Medical Radiology

Diagnostic Imaging

For further volumes:
http://www.springer.com/series/4354

Robert Hermans
Editor

Head and Neck Cancer Imaging

Foreword by
Maximilian F. Reiser

Springer

Prof. Robert Hermans
Department of Radiology
University Hospital Leuven
Herestraat 49
3000 Leuven
Belgium
e-mail: robert.hermans@uzleuven.be

ISSN 0942-5373
ISBN 978-3-642-17868-9 e-ISBN 978-3-642-17869-6
DOI 10.1007/978-3-642-17869-6
Springer Heidelberg Dordrecht London New York

Library of Congress Control Number: 2011941617

Cover design: eStudio Calamar, Berlin/Figueres

Printed on acid-free paper

Springer is part of Springer Science+Business Media (www.springer.com)

To my wife, Isabelle
And our children, Simon, Lies, Thomas and Tim

Bob Hermans

Foreword

Cancer treatment in the very complex head and neck region is largely dependant on the nature of the lesion, its local extension and the stage of the tumor. The rapid technological development of imaging, in recent years, provides us with an increasingly detailed and reliable visualization of these pathological features. For the treatment strategy as well as the management of the patient, the role of the radiologist within the multidisciplinary team becomes more and more important.

With this second edition of Head and Neck Cancer Imaging, we hope to provide the radiologist with detailed clinical background on the head and neck region in order to fully understand the clinical significance of imaging findings. At the same time we hope to inform all other members of interdisciplinary cancer treatment teams on the specific possibilities, advantages and limitations which modern imaging technology provides for the detection, evaluation, treatment, monitoring and follow-up of head and neck malignancies.

This book offers a comprehensive, up-to-date review of state-of-the-art head and neck cancer imaging, including numerous illustrative graphics and images.

The editor, R. Hermans, of the radiological department of the Leuven University, is an internationally recognized expert in head and neck radiology and was already in charge of the very successful first edition of this book. The authors of the individual chapters were invited to contribute because of their outstanding experience and expertise and their major contributions to the radiological literature on the topic.

I would like to thank the editor and all authors for their great efforts which resulted in this excellent volume.

München — Maximilian F. Reiser

Preface

The head and neck is a region of considerable anatomical and functional complexity, making the accurate staging of a head and neck neoplasm a challenging task. Many neoplasms in this region originate from the mucosa, and are detectable by the clinician. However, the submucosal tumor extension, as well as the possible regional and distant disease spread cannot be completely assessed based on the clinical examination alone.

Modern imaging modalities visualize the head and neck structures to an unprecedented level of detail. If carefully performed and interpreted, these techniques allow a comprehensive evaluation of the extent of head and neck neoplasms.

The radiologist is an important member of the multidisciplinary team managing head and neck cancer patients. Recent and ongoing research is enforcing the impact of imaging in oncologic patient care. These new developments are not only focusing on technical advances, such as PET-CT or diffusion-weighted MRI. Also, the impact of existing imaging techniques in treatment choice, in monitoring tumor response and following-up patients after treatment has now been established.

This purpose of this book is to provide a comprehensive review of state-of-the-art head and neck cancer imaging. Several distinguished head and neck radiologists have contributed to this book, fully covering the field of advanced imaging in the head and neck cancer patient.

Compared to the previous edition of this book, several chapters have been rewritten, incorporating recent insights and knowledge. In other chapters, the increasing role of metabolic and functional imaging is included in more detail where appropriate.

Clinical-diagnostic techniques, as well as therapeutic strategies, also have changed significantly over the past years; in this regard I would like to thank my colleague-clinicians from Leuven who contributed to this book. Care has been taken to situate the role of imaging within these developments.

The ultimate goal of all medical actions is to provide our patients with the best possible therapy for their health problems. Hopefully this book contributes to achieving this purpose.

Leuven — Robert Hermans

Contents

Contributors

Kunwar S. S. Bhatia Department of Diagnostic Radiology and Organ Imaging, Faculty of Medicine, Prince of Wales Hospital, The Chinese University of Hong Kong, New Territories, Hong Kong SAR, China

Vincent F. H. Chong Yong Loo Lin School of Medicine, National University of Singapore, 21 Lower Kent Ridge Road, Singapore, 119077, Singapore

Christian Czerny Division of Neuroradiology–Musculoskeletal-Radiology, Department of Radiology, University Hospital Vienna, Waehringer Guertel 18-20, 1090, Vienna, Austria, e-mail: christian.czerny@meduniwien.ac.at

Pierre R. Delaere Department of Otorhinolaryngology, Head and Neck Surgery, University Hospitals Leuven, Herestraat 49, 3000, Leuven, Belgium, e-mail: Pierre.delaere@uz.kuleuven.ac.be

Frédérique Dubrulle Plateau commun d'imagerie, Hôpital Huriez CHRU Lille, 59000, Lille, France, e-mail: F-DUBRULLE@CHRU-LILLE.FR

Davide Farina Department of Radiology, University of Brescia, Piazzale Spedali Civili 1, 25123, Brescia, Italy, e-mail: nappaje@yahoo.it

Rick L. M. Haas Department of Radiology University Medical Center Utrecht, Heidelberglaan 100, 3584 CX, Utrecht, The Netherlands

Robert Hermans Department of Radiology, University Hospitals Leuven, Herestraat 49, 3000, Leuven, Belgium, e-mail: robert.hermans@uzleuven.be

Vincent Chong Fook Hin Department of Diagnostic Radiology, Singapore of Diaginostic Radiology, Outram Road, 169608, Singapore, Singapore, e-mail: vincent_chong@nuhs.edu.sg

Ann D. King Department of Diagnostic Radiology and Organ Imaging, Faculty of Medicine, Prince of Wales Hospital, The Chinese University of Hong Kong, New Territories, Hong Kong SAR, China, e-mail: king2015@ cuhk.edu.hk

Marc Keberle Radiology, Brüderkrankenhaus St. Josef, Husener-Str. 46, 33098, Paderborn, Germany, e-mail: m.keberle@bk-paderborn.de

Frederik De Keyzer Department of Radiology, University Hospitals Leuven, Herestraat 49, 3000, Leuven, Belgium

Sandra Nuyts Department of Radiation Oncology, University Hospital Gasthuisberg, Herestraat 49, 3000, Leuven, Belgium, e-mail: Sandra.Nuyts@uz.kuleuven.ac.be

Frank A. Pameijer Department of Radiology, University Medical Center Utrecht, Heidelberglaan 100, 3584 CX, Utrecht, The Netherlands, e-mail: f.a.pameijer@umcutrecht.nl

Polly S. Richards Imaging KGV Wing, St Bartholomew's Hospital, West Smithfield, London, EC1A 7BE, UK, e-mail: Polly.Richards@bartsandthelondon. nhs.uk

Ilona M. Schmalfuss Department of Radiology, Division of Neuroradiology, North Florida/South Georgia Veterans Administration and University of Florida College of Medicine, 1601 SW Archer Road, Gainesville, FL, 32608, USA; Department of Radiology, Malcolm Randall VA Medical Center and University of Florida College of Medicine, 1601 SW Archer Road, Gainesville, FL, 32608, USA, e-mail: Ilonaschmalfuss@yahoo.com

Vincent Vandecaveye Department of Radiology, University Hospitals Leuven, Herestraat 49, 3000, Leuven, Belgium

Vincent Vander Poorten Department of Otorhinolaryngology, Head and Neck Surgery, University Hospitals Leuven, Catholic University Leuven, Leuven, Belgium, e-mail: Vincent.Vanderpoorten@uz.kuleuven.ac.be

Introduction: Epidemiology, Risk Factors, Pathology, and Natural History of Head and Neck Neoplasms

Vincent Vander Poorten

Contents

Abstract

This introductory chapter sets the scene for the book by defining the complex domain in which the head and neck radiologist is expected to make his diagnosis. The epidemiology of epithelial and non-epithelial head and neck tumors is discussed representing up-to-date frequency measures. The known risk factors are subsequently reported. After that the clinical and pathological specifics of the most frequent tumors are presented, along with the expected natural history, so that the head and neck radiologist is aware of the different stages of the disease and the radiological "snapshots" that can result from imaging at different points in the evolution of the disease. Both macroscopic and microscopic aspects are illustrated by to-the-point clinical and light-microscopical pictures.

Head and neck cancer can be divided into two major groups. The largest group, the epithelial malignancies of the mucosal membranes of the upper aerodigestive tract, is called head and neck squamous cell carcinoma (HNSCC) and accounts for 90% of all head and neck neoplasms (Greenlee et al. 2001). The second important but smaller group are the "glandular neoplasms", arising in the thyroid and in the salivary glands.

Skin cancer is considered a separate entity and so is non-melanoma skin cancer of the head and neck. Non-melanoma head and neck skin cancer includes mainly squamous cell carcinoma and basal cell carcinoma, the latter being 3–4 times more frequent than the former (IARC 2008a). Infrequent head and neck

V. Vander Poorten (✉)
Department of Otorhinolaryngology,
Head and Neck Surgery,
University Hospitals Leuven,
Catholic University Leuven, Leuven, Belgium
e-mail: Vincent.Vanderpoorten@uz.kuleuven.ac.be

R. Hermans (ed.), *Head and Neck Cancer Imaging*, Medical Radiology. Diagnostic Imaging,
DOI: 10.1007/174_2011_370, © Springer-Verlag Berlin Heidelberg 2012

neoplasia include localized lymphoma, soft tissue and bone sarcoma, and neuroectodermal tissue tumors (paraganglioma, olfactory neuroblastoma, neuroendocrine carcinoma, malignant melanoma). For information about these types we refer the reader to the specific head and neck oncology literature.

In this introductory chapter the first paragraph deals with epidemiology and risk factors of head and neck neoplasms. An overview of the pathology and natural history of the most frequent benign and malignant head and neck neoplasms is outlined in the second paragraph.

1 Epidemiology: Frequency Measures and Risk Factors

1.1 Frequency Measure: Incidence

Head and Neck Cancer, excluding skin cancer and Hodgkin and Non Hodgkin lymphoma localized in the head and neck, is the sixth most frequent cancer worldwide. The currently estimated world incidence of epithelial malignancies of the mucous membranes is over 600,000 new cases per year, and these are 160,000 laryngeal, 389,000 oral, and 65,000 pharyngeal cancer cases, resulting in 300,000 deaths yearly (IARC 2008b). Thus, in 2008 6.8% percent of the incidence of cancer could be attributed to these neoplasms (Ferlay et al. 2010). Likewise, in the European Union 5% of the cancer burden was caused by oral, pharyngeal, and laryngeal cancer, and 1% by thyroid cancer (IARC CancerBase N°4 1999). Comparing the two largest groups, HNSCC and thyroid cancer, a definite gender difference in incidence is apparent. As an example, the most recent world incidence of laryngeal SCC shows a male–female ratio of 6/1, whereas for incidence of thyroid cancer, the odds are opposite with a ratio of 1/3 (Ferlay et al. 2010). The incidence of thyroid cancer has been steadily increasing in the last 40 years with a factor of 2.3, mainly due to a rise in papillary thyroid cancer, while the incidence of other types remained unchanged. This rise is mainly due to better detection methods and awareness, but also to a true rise in incidence as reflected by an increased incidence of large tumors and tumors displaying extrathyroidal extension (Morris and Myssiorek 2010; Sipos and Mazzaferri 2010). The incidence of salivary gland cancer is at the subpercentual level when looking at cancer in general, but is responsible for between 1 and 7% of head and neck cancer incidence (Kane et al. 1991; Spiro and Spiro 2001).

There is an important geographical variation in head and neck cancer incidence. A specifically high incidence is observed in much of Southern Asia, Australia, Brazil, Southern Africa, and parts of Central and Southern Europe. Nasopharyngeal cancer typically arises in southern China (Mehanna et al. 2010). The incidence of hypopharyngeal cancer is typically very high in Northern France (10/100,000 males/year) as compared to e.g. the United States of America (2/100,000 males/year). The incidence of laryngeal cancer in Northern Spain (20/100,000/year) is about 200 times as high as compared to certain regions in China (0.1/100,000/year) (IARC 1997; Hoffman et al. 1998). Besides probable differences in genetic susceptibility, a different prevalence of strong risk factors (e.g. Calvados drinking, smoking habits) undoubtedly explains these differences. In the same way, observed differences in incidence among races (higher incidence in African versus Caucasian Americans) (Day et al. 1993), and among men and women, can be largely attributed to differences in risk factor exposure (De Rienzo et al. 1991).

1.2 Risk Factors for the Development of Head and Neck Malignancies

1.2.1 Risk Factors for Development of HNSCC

The most important risk factor is chronic use of tobacco (smoking and smokeless such as betel quid chewing) and alcohol (Fig. 1). The reason that these factors are so important is twofold: a strong association with the disease on the one hand, and a very high prevalence among the population on the other. They are two independent risk factors that have been shown clearly to act in a multiplicative way when combined. Figure 2 shows that a 5.8 times increased risk for development of oral and pharyngeal cancer is observed in non-smokers who use 30 or more drinks/week, a 7.4 times increased risk in smokers not using alcohol with a history of 40 or more pack-years (smoking 20 cigarettes/day during 40 years), whereas the person combining the two has a 38 times increased risk (Blot et al. 1988; Hashibe et al. 2007).

Fig. 1 Smoking is the most prevalent and most powerful risk factor for the development of HNSCC. A doubled incidence of Warthin's tumor of the parotid gland has also been observed

Conversely, after cessation of the use of tobacco, the risk of oral mucosal dysplasia and cancer falls to the level in the population that never smoked after 15–20 years (Marron et al. 2010; Morse et al. 1996).

A recent pooled analysis based on over 11,000 cases and 16,000 controls shows that approximately 72% of HNSCC cancers are attributable to these two exposures, ranging from 64% for oral cavity cancer, over 72% for pharyngeal cancer, to 89% for laryngeal cancer. The strong interaction Blot et al. already described in 1988 between the two exposures was again confirmed (Hashibe et al. 2007).

The carcinogens in tobacco are nitrosamines, polycyclic aromatic hydrocarbons, and aldehydes. Nitrosamines are alkylating agents that induce mutational events. Alcohol acts as a solvent and thus enhances permeability of the mucosa for the toxic substances in tobacco.

A direct effect of alcohol is ascribed to mucosal enzymatic formation (alcohol dehydrogenase) of the carcinogenic acetaldehyde. This was recently supported by the finding that individuals homozygous for the *2 allele of aldehyde dehydrogenase 2 (ALDH2), who do not support alcohol intake because of their inability to metabolize acetaldehyde, have a significantly reduced incidence of head and neck cancer. People who have an efficient *1*1 homozygous variant allele of ALDH2 do produce acetaldehyde and do develop HNSCC, whereas *1*2 heterozygous ALDH2 patients who have a sixfold increased level of acetaldehyde in their blood following alcohol consumption due to a sixfold reduced metabolism of acetaldehyde have the highest incidence of HNSCC (Boccia et al. 2009).The sites that are most at risk for alcohol induced carcinogenesis are the oro- and hypo-pharyngeal mucosal surfaces (Brugere et al. 1986), much more than the glottic larynx, where only very high alcohol intakes can be shown to independently increase HNSCC risk.

Indirectly, alcohol consumption brings along intake of non-alcoholic carcinogenic compounds in alcoholic drinks e.g. nitrosodimethylamine in beer and tannin in wine. Furthermore, high intake of alcoholic beverages entails nutritional deficiencies, which in turn also increases the risk of HNSCC development. With poor nutrition, the proven protective effect of high intake of fruits and vegetables is lost. Indeed, a diet rich in fresh fruit and vegetables is associated with a 50–70% reduction in the incidence of HNSCC (De Stefani et al. 1999). Especially dark yellow vegetables, citrus fruits (rich in vitamin C) and the carotene-rich vegetables (fresh tomatoes, carrots, pumpkins) are protective, mainly due to antioxidant micronutrients in these vegetables such as vitamin C, vitamin E, beta carotene, and flavonoids (La Vecchia et al. 1997). Less proven but also suggested protective is the use of olive oil (Franceschi et al. 1999) and high fibre intake (De Stefani et al. 1999). A recent study pooling available data indicates a significant protective effect of coffee drinking on the risk of developing oral and pharyngeal cancer (Galeone et al. 2010).

Given the factors enumerated above, it is understandable that socio-economic status is strongly associated with the development of HNSCC. A total of 75% of patients live in the lower social classes, in terms of level of education and income. One in three patients has no partner and one in six patients is unemployed at the time of diagnosis. This social situation is a risk factor for having the direct risk factors of tobacco, alcohol, and poor dietary habits. There is also a lower level of oral hygiene. Once cancer is established, people in lower socio-economic groups will seek medical help later because of less education

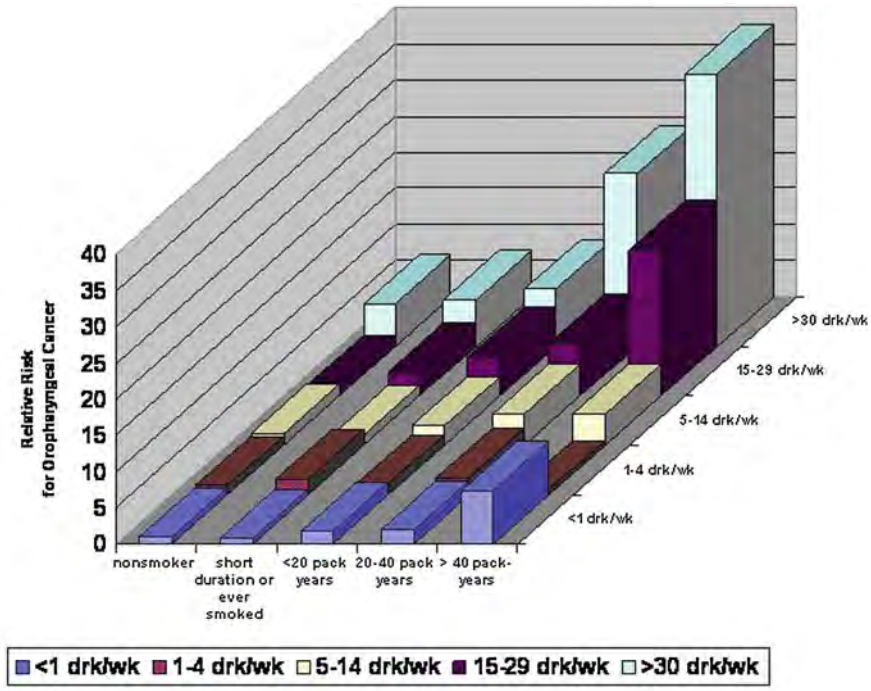

Fig. 2 Relative risk for oropharyngeal cancer for males according to amount of tobacco and alcohol use. (based on data from Blot WJ, et al. Cancer Research 1988; 48:3282–7, with permission)

and more difficult access to the health system, and thus will present with more advanced stages of disease. Another reason for advanced disease at presentation lies in the fact that often a significant part of caloric intake is provided for by alcohol and thus symptoms such as dysphagia for solid food will become problematic later. Stage at presentation is the strongest negative prognostic factor for outcome of treatment in HNSCC. Treatment of the advanced stages of HNSCC often has a serious impact on physical and psychological functioning. Great effort is needed to adapt to the resulting altered body image, to get integrated back into society, and also to achieve the change in lifestyle needed to prevent occurrence of second primary HNSCC. Unfortunately, following treatment, patients in lower social classes are often isolated to face this difficult challenge. Return to occupation thus becomes an illusion for the majority of these patients (Lefebvre et al. 2001). It is clear that a lower socio-economic environment is a strong negative prognostic factor for the oncologic results following treatment, and also for survival in general because of the impact of many of the comorbidities that result from the previous way of living (pulmonary insufficiency, atherosclerosis, liver disease, etc.) (Robertson et al. 2010).

Recently the role of genetic predisposition, previously suggested by small studies, has been confirmed. A family history of HNSCC in a first degree relative is associated with a 1.7 fold increased risk of developing the disease (Conway et al. 2009). This is attributed to polymorphisms in genes encoding enzymes for the metabolism of tobacco and alcohol, reduced metabolism implying an increased risk of the disease. A meta-analysis of 31 studies showed that a polymorphism in *GSTM1*, which encodes glutathione S transferase, involved in the metabolism of xenobiotics, was associated with a 1.23 increased risk of developing head and neck cancer (Hashibe et al. 2003). In the same way ALDH2 zygozity has been linked to differences in HNSCC development, as previously outlined (Boccia et al. 2009).

Viral infections also have been implicated in the carcinogenesis of HNSCC (Franceschi et al. 1996). Human Papilloma Virus (HPV) DNA is in the spotlight nowadays and held responsible for the recently observed increased incidence of oropharyngeal squamous cell carcinoma. This incidence showed no change between 1975 and 1999 but increased by 22% between 1999 and 2006 in the United States. The United Kingdom has seen a 51% increase in oral and oropharyngeal squamous cell carcinoma in men. This increased incidence seems accounted for by a rise in HPV-related oropharyngeal carcinoma, itself related to

altered sexual behavior (Heck et al. 2010). In a recent trial 64% of oropharyngeal cancers included were found to be HPV positive and these had a significantly better treatment outcome (Ang et al. 2010). Epstein–Barr Virus (EBV) is strongly associated with nasopharyngeal cancer. EBV antibody titres are much higher in cases than in controls, and biopsy specimens of undifferentiated nasopharyngeal carcinoma patients are 100% EBV positive and monoclonal as to this virus (Jeannel et al. 1999). EBV titres following treatment are used to monitor patients for disease recurrence. Patients infected with the human immunodeficiency virus (HIV) are at higher risk of developing HNSCC and Kaposi's sarcoma.

Among environmental factors, chronic sun exposure induces skin and lip cancer. Occupational factors have been implied in HNSCC development. Working in industries associated with higher exposure to aromatic amines and phenoxy herbicides confines an elevated risk for all sites. A specific strong association has been repeatedly described between specific industries and the development of sinonasal cancer. The rate of development of SCC of the sinonasal tract is increased 250 times in workers exposed to nickel (Pedersen et al. 1973).Working with wood in environments without an aspiration system for dust particles results in a 500–1,000 fold increase in the baseline incidence of sinonasal "intestinal type" adenocarcinoma and has led in several countries to the recognition of this cancer as an occupational disease and to stringent safety precautions to minimize dust exposure (Acheson et al. 1968).

1.2.2 Risk Factors for Development of Glandular Neoplasms

Radiation exposure is the only firmly established environmental risk factor for the development of thyroid carcinoma. The information comes from scrutinized follow-up of atomic bomb survivors in Japan and atomic disaster survivors in Chernobyl (UNSCEAR 2000). Typically, a low-dose exposure (e.g. about 3 Gy) results in the development of mainly papillary thyroid carcinoma, some 5–10 years later. The risk follows a linear dose–effect relationship and the incidence can be increased by more than 30 times (Drozdovitch et al. 2010).

Radiation exposure also results in an increased incidence of both benign (Warthin's tumour) and malignant (mucoepidermoid carcinoma) salivary gland tumors in follow-up studies in the same cohorts (Saku et al. 1997). For Warthin's tumor, also a doubled incidence has been observed in smokers versus non-smokers (Gallo and Bocciolini 1997). Epstein–Barr Virus has been implicated in the genesis of bilateral Warthin's tumors and undifferentiated carcinoma of the salivary gland (Gallo 2001).

2 Pathology and Natural History of Frequent Benign and Malignant Head and Neck Neoplasms

In tumor pathology, tumor typing is the first important subject. Within different tumor types, the second subject is detection of features with prognostic significance, such as grading, perineural, or vascular invasion, and radicality of resection margins. Regarding histological typing of head and neck neoplasms, it has already been mentioned that a far majority consists of HNSCC. A detailed discussion of all tumor types encountered in the head and neck is beyond the scope of this chapter and for this the reader is referred to the surgical and pathological literature. What follows is an overview of the clinical course and pathological specificities for the most frequent tumor types.

2.1 Epithelial Neoplasms of the Mucous Membranes

2.1.1 Tumor Typing and Clinical Behavior

2.1.1.1 Benign Lesions

Benign papillary lesions are less frequently a reason for seeking medical attention than malignant and premalignant lesions. Oral, pharyngeal, and laryngeal sites can display squamous papillomas, which are white lesions with a wart-like appearance with no signs of deeper invasion. Part of these lesions (e.g. juvenile laryngeal papillomatosis) have been ascribed to HPV, type 6 and 11. Sinonasal papillomas are also called Schneiderian papillomas and can be exophytic, endophytic (inverted), or oncocytic in presentation. Especially the inverted papilloma is considered premalignant (Fig. 3). Most symptomatic epithelial neoplasms of the mucous

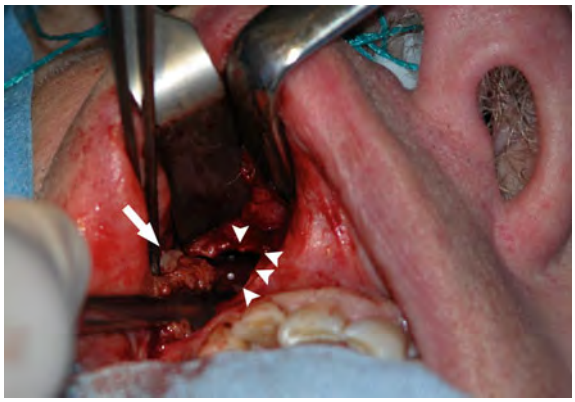

Fig. 3 Inverted papilloma (*arrow*) of the maxillary sinus being removed by Caldwell–Luc approach (antrostomy:*arrowheads*)

Fig. 4 Erythroplakia (*arrowheads*) with areas of nodular leukoplakia (*arrows*) of the tonsil, glossotonsillar sulcus, anterior tonsillar pillar, and hard and soft palate

membranes of the upper aerodigestive tract that bring patients to the doctor will turn out premalignant or malignant.

2.1.1.2 Premalignant Lesions

Premalignant lesions will often not be visualized on routine imaging studies. Macroscopically, we consider leukoplakia and related lesions: homogeneous leukoplakia versus non-homogeneous leukoplakia (nodular leukoplakia, erythroplakia, proliferative verrucous leukoplakia; Fig. 4). On the microscopical level epithelial hyperplasia, dysplasia, and carcinoma in situ can be discerned.

Leukoplakia is a descriptive clinical term used to describe "a white plaque or patch that cannot be characterized, clinically or histopathologically, as any other disease"(World Health Organization Collaborating Centre for Oral Precancerous Lesions 1978). Furthermore, in order to be designated as leukoplakia, the lesion should not be associated with any known physical (frictional keratosis, candidal leukoplakia) or chemical agent, except tobacco. It should also be impossible to scrape off the lesion.

Homogeneous leukoplakia is histologically either hyperortho- or hyperpara-keratosis and rarely shows dysplasia. Less frequent is non-homogeneous leukoplakia (nodular leukoplakia, erythroplakia, proliferative verrucous leukoplakia), mostly associated with dysplasia and thus much more at risk for becoming really malignant (Batsakis 2003). Dysplasia can be "mild", meaning that there is an increased number of mitotic figures and an abnormal cytologic appearance (loss of an orderly nuclear mosaic pattern, decreased nuclear/cytoplasmatic ratio, and an irregular random nuclear placement) only in the basal epithelial layer, whereas suprabasal mitosis and cytologic abnormality indicates "moderate" dysplasia. In "severe" dysplasia the atypical cells with mitotic activity can be observed everywhere from the basal to the superficial layers. The yearly malignant transformation rate of homogeneous leukoplakia is between 2 and 6% and is higher as the patient is older, female, and as the lesion persists for a longer time. The malignant transformation rate in non-homogeneous (speckled) leukoplakia and erythroplakia is more than 50% (Silverman et al. 1996).

2.1.1.3 Malignant Lesions

Less frequent specific clinical entities are verrucous carcinoma, papillary SCC, basaloid squamous cell carcinoma, and sarcomatous SCC, increasingly aggressive in that order. Verrucous carcinoma is an exophytic papillomatous low grade SCC, very well differentiated, without potential for regional or distant metastasis (Medina et al. 1984). Papillary SCC displays an exophytic growth with a poorly differentiated cell layer lining a central fibrovascular core. Its behavior is more aggressive than verrucous carcinoma, wherein metastasis is observed. Basaloid SCC and sarcomatoid SCC are highly aggressive SCC variants.

Most HNSCC are simply called "invasive squamous cell carcinoma" and can be graded into well, moderately, and poorly differentiated, paralleling the amount of keratin formation by cells. SCC cells by definition produce intercellular bridges. (Figs. 5, 6) Absence of these bridges is one of the features of undifferentiated SCC. This type of tumor occurs most frequently in the nasopharynx and is often diagnosed

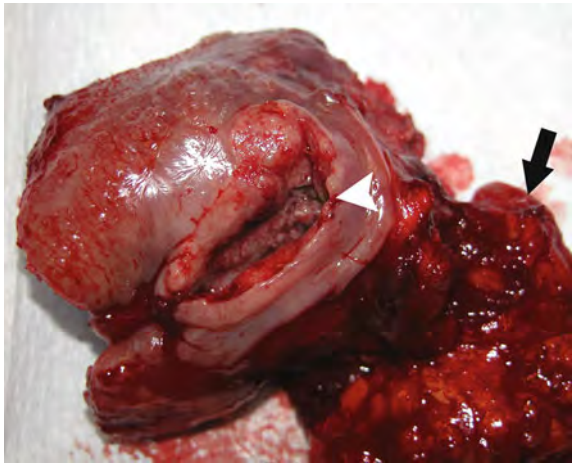

Fig. 5 Hemiglossectomy for ulcerative and deeply invasive well-differentiated squamous cell carcinoma of the lateral tongue (*arrowhead*). Specimen in continuity with radical neck dissection (*arrow*)

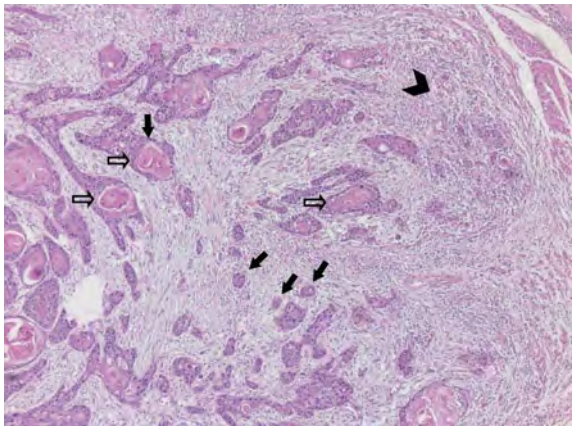

Fig. 6 Microscopical appearance of the same tumor. Note the diffuse infiltrative aspect of the tumor islets (*arrows*), the dense mononuclear inflammatory reaction (*arrowhead*), and the formation of keratin pearls (*hollow arrows*) Picture courtesy of Prof. Raf Sciot

because of massive neck lymph node metastasis already present at initial diagnosis, frequently bilaterally, and involving the posterior neck (region V).

2.1.2 Natural History Before and at Diagnosis

The presenting symptoms of HNSCC depend very much on the site of origin within the head and neck and the functions that thus are interfered with. Table 1 lists the typical alarming symptoms that

Table 1 Alarming symptoms and signs urging specialist referral

Symptoms
Throat pain
Hoarse voice
Swallowing impairment
Neck lump
Unilateral ear pain—hearing loss
Stridor
Epistaxis—haemoptoe
Unilateral nasal obstruction
Signs
Cranial nerve palsy (recurrent laryngeal, abducens, sympathetic chain, facial,…)
Red or white patch on oral mucosa
Ulceration of mucous membranes
Swelling
Unilateral serous otitis
Prooptosis
Neck lump
Skin infiltration
Hypoesthesia (mental nerve, infraorbital nerve,…)

demand urgent specialist referral. Many patients with oral and pharyngeal cancer will present at an advanced disease stage, because of the late occurrence of symptoms and the social situation with more difficult medical access. Patients with glottic cancer tend to present at earlier stages, given the rapid voice disturbance of even a small vocal cord lesion. Early glottic cancer is also not likely to result in regional metastasis and thus often has a good prognosis following radiotherapy or surgery, with 5-year survival rates of 70–100% (Lydiatt and Lydiatt 2001). Advancing stage, and origin of SCC in other anatomical subsites of the upper aerodigestive tract, are associated with lesser chances for successful treatment, and for the specifics the reader is referred to the specific head and neck oncological literature.

2.1.3 Natural History Following Diagnosis and Successful Treatment of Malignant HNSCC

The annual incidence of second primary cancer following successful treatment of an index HNSCC is 3–7%. A known feature in HNSCC is field

cancerization of the upper aerodigestive tract: several synchronous and also metachronous primary carcinomas and areas of moderate to severe dysplasia—carcinoma in situ are observed with areas of normal mucous membranes in between. This is caused by exposure of the entire upper aerodigestive tract to the same carcinogens—usually combined alcohol and tobacco. Patients are especially at risk of developing lung cancer, esophageal and gastric cancer, and a new localization of HNSCC. A change in lifestyle is essential to decrease the incidence of second primaries, but this is often complicated by the social context of the patient.

2.1.4 Microscopical Negative Prognostic Findings

Table 2 lists the important findings to routinely determine during microscopical analysis following resection of a primary HNSCC and its regional lymph nodes. These features carry a worse prognosis and thus contribute to the decision making on the need for further therapy, c.q. postoperative (chemo) radiotherapy. Many of these parameters (cTNM classification, perineural growth, tumour thickness, extracapsular spread in metastatic lymph nodes) can already be strongly suspected on a preoperative high quality imaging study.

Table 2 Histopathological negative prognostic factors in HNSCC

(p)TNM classification (Size of primary tumor, number/laterality of positive nodes, size of largest node)
Vascular invasion
Perineural growth
Resection margins (e.g. <5mm is considered "close margins" in oral cancer)
Thickness
Invasive front
Differentiation
Exophytic versus endophytic growth pattern
Field cancerization
Mitotic index
Presence of extracapsular spread in metastatic lymph nodes

2.2 Glandular Neoplasms

2.2.1 Thyroid Neoplasia

2.2.1.1 Benign Disease: Multinodular Enlargement

Benign multinodular goitre affects almost one in three persons worldwide (Delange 2000). Iodine deficiency is the most frequent contributory factor. In areas where iodine supply is sufficient, the prevalence of clinically detectable goitres is less than 4%, and results from elevated Thyroid Stimulating Hormone (TSH) levels or from elevated stimulation of the TSH receptor (such as in Graves' disease and nonatrophic Hashimoto's goitres). Most patients with multinodular goitre are asymptomatic. Medical concerns arise when compressive symptoms appear (Fig. 7), when autonomous hyperfunction appears, or when malignancy is feared. The latter is feared in rapidly enlarging goitres, enlarging lymph nodes, especially in patients with prior radiotherapy to the neck, or when fine needle aspiration cytology (FNAC) of dominant nodules indicates

Fig. 7 Large multinodular goitre with pharyngeal, esophageal, and tracheal compression

papillary carcinoma or a microfollicular lesion. A microfollicular lesion can be follicular carcinoma in about one in ten patients. Ultrasound is crucial in determining which nodule in a multinodular goitre merits evaluation by FNAC (Cooper et al. 2006; Frates et al. 2005) (see " Thyroid and Parathyroid Neoplasms").

Macroscopically, following thyroidectomy, we usually see a polynodular, soft, and globally enlarged thyroid gland (Fig. 8). There may be one or more larger nodules which deserve subsequent microscopical analysis. Up to 70% of hyperplastic nodules are clonal, neoplastic proliferations (Kopp et al. 1994). Microscopically, within the nodules, there is a varied pattern of large and small follicles, usually with

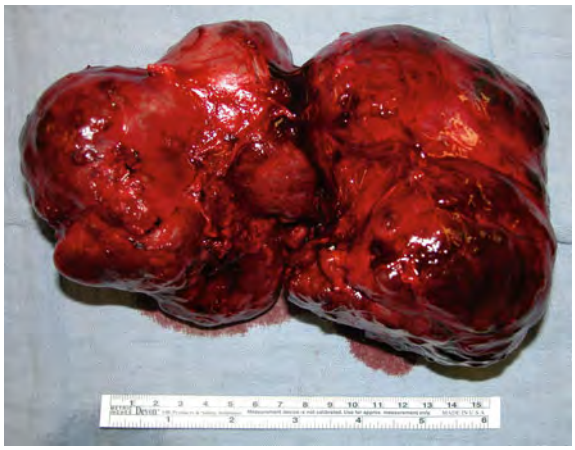

Fig. 8 The same goitre following resection

Fig. 9 Thyroidectomy specimen showing papillary carcinoma on cut surface in the left lobe and the isthmus. *Posterior view*. The specimen is inked to assess resection margins

abundant colloid. There is an often oedematous stroma with fibrosis, macrophages, hemosiderin, and calcifications.

2.2.1.2 Benign Disease: Uninodular Enlargement—the Solitary Thyroid Nodule

Any clinically visible or palpable nodule, and "any discrete macroscopic intrathyroidal lesion clearly distinguishable from the adjacent normal thyroid parenchyma" on ultrasonography or Technetium scanning should lead to actions to estimate the chance of malignancy (Hay and Klee 1993). As for multinodular goitre, the next step will be an ultrasound guided FNAC in any nodule showing worrisome features. A solitary thyroid nodule can be a degenerative lesion such as a cyst or a degenerative colloid nodule, or a benign or malignant neoplastic lesion. The global incidence of cancer in patients with a thyroid nodule is 10%, increasing for women or men older than 50 to 30 and 45% respectively (Tezelman and Clark 1995). The rest will be benign, where nine out of ten will be follicular adenomas, the remainder being mostly Hürthle cell adenomas. Macroscopically, adenomas are well demarcated from the adjacent parenchyma, and fleshy and pale, sometimes cystic or hemorrhagic on cut surface. The microscopic appearance of a solitary adenomatous nodule displays large and small follicles with a lot of colloid and a stromal component with hemosiderin, macrophages, fibrotic changes, and often calcifications. A Hürthle cell variant displays oncocytic cells, with an intensely eosinophylic cytoplasm due to a lot of abnormal mitochondria, and large vesicular nuclei.

2.2.1.3 Malignant Disease

An important issue in suspected malignant thyroid disease is the avoidance of iodine containing contrast medium in imaging studies for thyroid lesions. "Differentiated thyroid cancer" (see below) are tumors concentrating iodine due to preserved expression of the sodium–iodine symporter (NIS). They hence can be effectively and selectively treated with radioactive iodine. This treatment, however, will be delayed by about 3 months following an imaging study using iodine contrast medium, due to saturation of the iodine binding capacity of the targeted thyroid cancer cells.

Generally, a distinction is made between "differentiated thyroid cancer" with a relatively good (papillary, follicular, mixed papillary follicular carcinoma) to intermediate (Hürthle cell carcinoma) prognosis, and cancers with worse (medullary thyroid cancer) to fatal prognosis (anaplastic thyroid cancer). Of malignant tumors, the thyroid harbors both the tumors with the best (papillary) and the worst (anaplastic carcinoma) prognoses.

2.2.1.4 Papillary Thyroid Cancer

Papillary cancer is the most frequent thyroid cancer (85% belong to this group) (Sipos and Mazzaferri 2010). Overall women are affected three times more frequently than men. The clinical picture is usually a symptomless thyroid swelling, although enlarged lymph nodes may be the presenting feature (Fig. 9). Indeed, regional metastasis to the paratracheal (level VI–VII) and cervical (level II, III, and IV) lymph nodes is observed in one out of two patients at

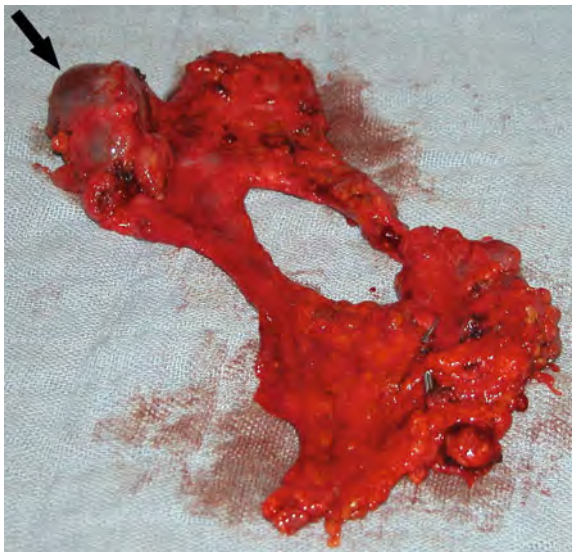

Fig. 10 Functional neck dissection specimen showing a typical *black* cystic metastatic neck node of papillary thyroid carcinoma (*arrow*)

presentation (Fig. 10). Distant metastasis usually occurs late in the disease course.

Following thyroidectomy, macroscopically typical features are multifocality and bilaterality, occuring in up to 87% of specimens (Russell et al. 1963). Lymph node metastasis is often cystic and dark bluish in appearance (Fig. 10).

Microscopically only 3% is true papillary carcinoma and 97% is "follicular variant of papillary carcinoma". Both forms have an equally good prognosis, with overall up to 95% of patients surviving 20 years following treatment (Hay and Klee 1993).

Essential for the diagnosis are the papillae with a central fibrovascular core and an epithelial lining showing the typical nuclear features with overlapping nuclei and nuclear grooves, making an FNAC diagnosis possible. Psammoma bodies, calcific concretions with concentric laminations, are observed in about 1 in 2 of these tumors, mostly already on FNAC. (Fig. 11).

Genetically, about 39% of papillary cancers display a *BRAF* proto-oncogene mutation. This aspect was extensively studied by many authors and found associated with extrathyroidal extension, multicentricity, advanced stage, nodal metastasis, advanced age at presentation and higher frequency of recurrent or persistent disease. Other authors, however, were not able to confirm this negative prognostic effect of a *BRAF* mutation.

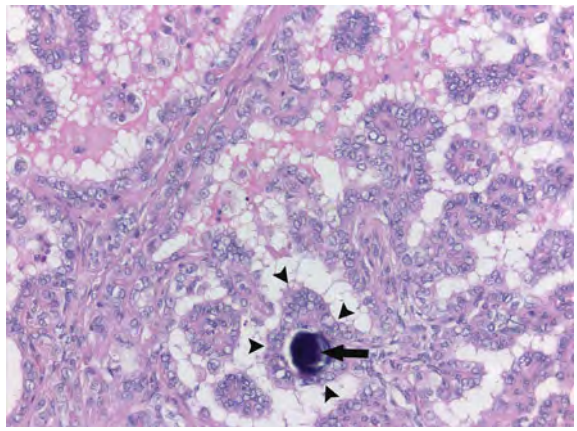

Fig. 11 Microscopical appearance of papillary thyroid cancer. Psammomabody (*arrow*) and papillary growth pattern (*arrowheads*). Picture courtesy of Prof. Raf Sciot

Rare subforms of papillary cancer with definite worse prognosis are the "tall cell" and "insular" variants (Sipos and Mazzaferri 2010).

2.2.1.5 Follicular Thyroid Cancer

About one in ten thyroid malignancies are follicular carcinomas. These are macroscopically solitary, encapsulated tumors. The features discriminating them from their benign follicular adenoma counterparts are microscopical vascular invasion and full thickness capsular invasion into the adjacent normal thyroid parenchyma. To be able to search the entire capsule for areas of invasion, all solitary nodules where FNAC suggests a "follicular lesion", should be excised with capsule and surrounding thyroid tissue. A minimal capsular invasion defines a subgroup of minimally invasive follicular carcinomas, behaving essentially as follicular adenomas. The tendency for vascular invasion in invasive follicular carcinoma explains that metastasis is primarily haematogenous to the lungs and the bones, rather than to the cervical lymph nodes, as observed in papillary cancer. Prognosis is somewhat less than for papillary carcinoma, with an overall 20-year survival of 81% (Shaha et al. 1995).

2.2.1.6 Hürthle Cell Carcinoma

Hürthle cell carcinomas are also solitary, encapsulated tumors that are distinguished from their benign counterparts by the presence of capsular and vascular invasion. They have an intermediate prognosis of about 65% 20-year survival (Shaha et al. 1995).

2.2.1.7 Medullary Carcinoma

Somewhat less than one in ten are medullary thyroid carcinomas (MTC). MTC is a malignant tumor of the calcitonin-secreting parafollicular C cells. These cells are embryologically maximally located in the upper two-thirds of the thyroid and this explains that tumors are usually found in that upper part of the gland. The tumors can occur in a usually unifocal sporadic form presenting in the age group of 40–60 years and constituting about 80% of MTC. An autosomal dominant hereditary form, due to a mutation in the Retinoblastoma (RET) proto-oncogen, can occur within the framework of Multiple Endocrine Neoplasia syndromes (MEN 2a: MTC, phaeochromocytoma, and parathyroid hyperplasia and MEN 2b: MTC, phaeochromocytoma and multiple mucosal neurinomas) or as familial medullary thyroid cancer (FMTC) without associated endocrinopathy. These hereditary forms usually occur earlier in life and are often multifocal in both thyroid lobes. In patients with MTC, lymph node metastasis, often bilateral, is frequently present at diagnosis and has a negative prognostic impact.

Microscopically, the diagnosis is suggested by the presence of amyloid and confirmed by immunostaining for calcitonin, chromogranin an carcino embryonic antigen (CEA). The 20-year survival following adequate treatment of MTC is about 65% (Moley 1995).

2.2.1.8 Anaplastic Carcinoma

About 5% of thyroid cancers are anaplastic carcinomas. This is a highly lethal variant which is rapidly progressive and almost universally fatal. Patients are usually 60–75 years old and present with a rapidly enlarging mass in the neck. Frequently, at presentation there are already signs of invasion of the surrounding structures: hoarseness due to recurrent laryngeal nerve paralysis, respiratory obstruction following tracheal compression or invasion, dysphagia due to esophageal invasion. Surgical treatment is almost never satisfactory and can only exceptionally be considered in the rare patient where disease is still intrathyroidal. Most patients are treated with radiotherapy with or without chemotherapy and survival is measured in months (Fig. 12).

The clinical diagnosis can sometimes be confirmed by FNAC, but often an incisional biopsy is performed to rule out thyroid lymphoma. Macroscopically, the surgeon performing an incisional biopsy sees a gray, hard, necrotic, and hemorrhagic tumor. Microscopically, there is a high mitotic index, marked cellular pleomorphism, necrosis, and tumor extension in blood vessels.

Fig. 12 Anaplastic thyroid carcinoma, growing through the dehiscent incision of the previous biopsy, during the radiotherapy. Note the tattoo on the skin of the patient demarcating the radiation field (*arrows*)

2.2.2 Salivary Gland Neoplasia

A distinction is made between the paired major salivary glands (parotid, submandibular, and sublingual) and the minor salivary glands. The latter are the 500–1,000 seromucous glands that are found throughout the entire upper aerodigestive tract, located in the oral cavity including lips, floor of mouth, cheek mucosa, tongue, soft and posterior hard palate, but also the nasal cavity, paranasal sinuses, nasopharynx, middle ear, Eustachian tube, oropharynx, hypopharynx, and even trachea (Ellis and Auclair 1996a). The majority of tumors (64–80%) arise in the parotids, 15–32% of which are malignant. Seven to 11% arise in the submandibular glands, 41–45% being malignant. Less than 1% of salivary gland tumors occur in the sublingual gland, most of these (70–90%), however, are malignant. Minor salivary gland tumors form 9–23% of the entire group, one in two being malignant (Ellis and Auclair 1996b). This observation results in the didactic rule "the smaller

the salivary gland, the less frequent a tumour arises in it, but the more frequently malignancy is involved".

2.2.2.1 Tumor Typing and Clinical Behavior

The extensive list of salivary gland tumor types is listed in Table 3, which is based on the 2005 World Health Organization Classification (Barnes et al. 2005). The key features of the most frequent benign and malignant types are briefly presented.

2.2.2.2 Benign Tumors

Pleomorphic Adenoma

Pleomorphic adenoma is definitely the most frequent salivary gland tumor and accounts for up to 70% of parotid tumors, 50% of submandibular salivary gland tumors, 35% of the minor salivary gland tumors, and 6% of sublingual tumors (Ellis and Auclair 1996b). Patients typically present with a long-standing, painless swelling (Fig. 13). Macroscopically, the tumor is well delineated from the normal salivary tissue, and this explains the old bad surgical practice to "shell the tumour out". The tumor is gray to white and lobulated on cut surface (Fig. 14). Microscopy shows a "mixture" of epithelial and mesenchymal (stromal) components in a varying combination and this explains the name "pleomorphic" adenoma or "mixed" tumor (Fig. 15). The tumor is notorious for recurring, often in a multinodular way, following inadequate surgery. A 2–23% rate of becoming malignant, the so-called carcinoma ex pleomorphic adenoma, has been reported (Gnepp 1993). The rate of malignant degeneration increases with time of presence of the lesion (Eneroth and Zetterberg 1974).

Warthin's Tumor

Warthin's tumor is the second most frequent benign salivary gland tumor. It occurs exclusively in the parotid gland and the adjacent level II lymph nodes. Between 6 and 10% of parotid tumors are Warthin's tumors (Ellis and Auclair 1996b). There is a male to female preponderance of 5 to 1. Warthin's tumors can occur bilaterally in about 10% of patients (Heller and Attie 1988). Microscopically, there is typically a two-layered eosinophylic epithelium and a lymphoid stroma, hence the name adenolymphoma.

Table 3 The WHO 2005 histologic classification of benign and malignant salivary gland tumors (Barnes et al. 2005)

Adenomas
1. Pleomorphic adenoma
2. Myoepithelioma (myoepithelial adenoma)
3. Basal cell adenoma
4. Warthin's tumor (adenolymphoma)
5. Oncocytoma (oncocytic adenoma)
6. Canalicular adenoma
7. Lymphadenoma
7.1. Sebaceous
7.2. Non-sebaceous
8. Ductal papilloma
8.1. Inverted ductal papilloma
8.2. Intraductal papilloma
8.3. Sialadenoma papilliferum
9. Cystadenoma
Carcinomas
1. Acinic cell carcinoma
2. Mucoepidermoid carcinoma
3. Adenoid cystic carcinoma
4. Polymorphous low grade adenocarcinoma
5. Epithelial myoepithelial carcinoma
6. Clear cell carcinoma, not otherwise specified (NOS)
7. Basal cell adenocarcinoma
8. Sebaceous carcinoma
9. Sebaceous lymphadenocarcinoma
10. Cystadenocarcinoma
11. Low grade cribriform cystadenocarcinoma
12. Mucinous adenocarcinoma
13. Oncocytic carcinoma
14. Salivary duct carcinoma
15. Adenocarcinoma NOS
16. Myoepithelial carcinoma
17. Carcinoma in pleomorphic adenoma
18. Carcinosarcoma
19. Metastasizing pleomorphic adenoma
21. Small cell carcinoma
22. Large cell carcinoma
23. Lymphoepithelial carcinoma
24. Sialoblastoma

Fig. 13 Typical picture of a long-standing symptomless swelling in the *left* parotid region, following excision the diagnosis of pleomorphic adenoma was confirmed

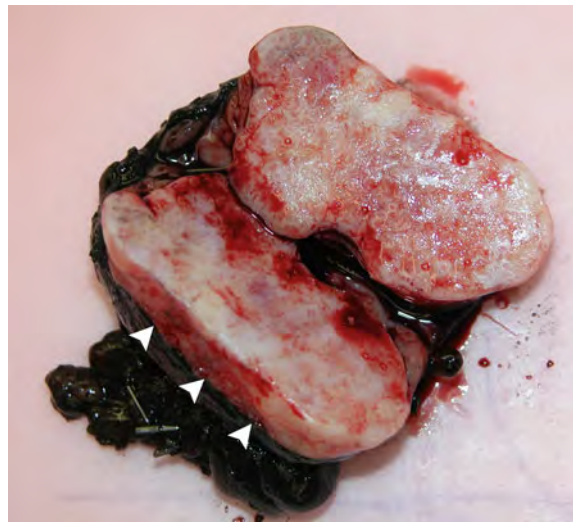

Fig. 14 Pleomorphic adenoma of the submandibular gland with a mainly mesenchymal-chondroid differentiation. *Grey* to *white* and lobulated on cut surface. Specimen inked for assessment of resection margins. Note the tumor looks easy to "shell out" (*arrowheads* demarcating the normal submandibular gland parenchyma that spontaneously retracts upon bisection of the gland)

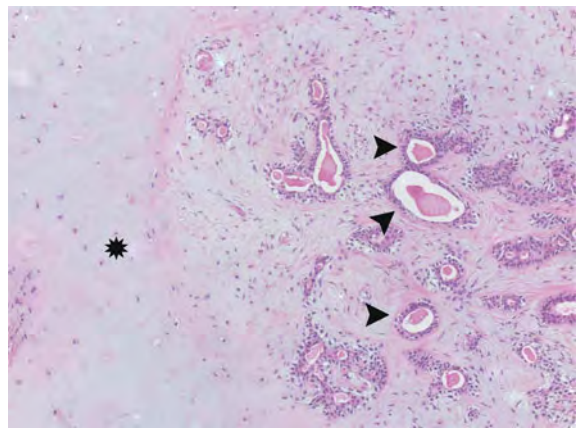

Fig. 15 Microscopical appearance of the same pleomorphic adenoma. Note the chondromyxoid matrix (*asterisk*), in which ductal structures (*arrows*) can be noted. Picture courtesy of Prof. Raf Sciot

2.2.2.3 Malignant Tumors

Mucoepidermoid Carcinoma

About one in six (Vander Poorten et al. 2003) to one in three (Spiro 1986) salivary gland cancers are mucoepidermoid carcinomas. Macroscopically, the cut surface is solid but can contain cysts. Microscopically, the tumor consists of a variable combination of glandular cells lining cystic spaces and epidermoid basaloid type cells forming solid areas (Fig. 16). A histological grading system is based on the relative proportion of mucinous versus epidermoid cells. Tumors containing 90% solid area made up of epidermoid cells are designated high grade (Seifert and Sobin 1992) and are associated with a 72% disease-specific death rate versus only 6–8% disease specific death rate in low grade, more mucus containing, low grade tumors (Healey et al. 1970).

Adenoid Cystic Carcinoma

Adenoid cystic carcinoma accounts for about one out of six parotid carcinomas (Vander Poorten et al. 2003). It occurs more frequently in other sites with about 45% of submandibular and minor salivary gland carcinomas being of this type (Vander Poorten et al. 1999a; Vander Poorten et al. 2000).

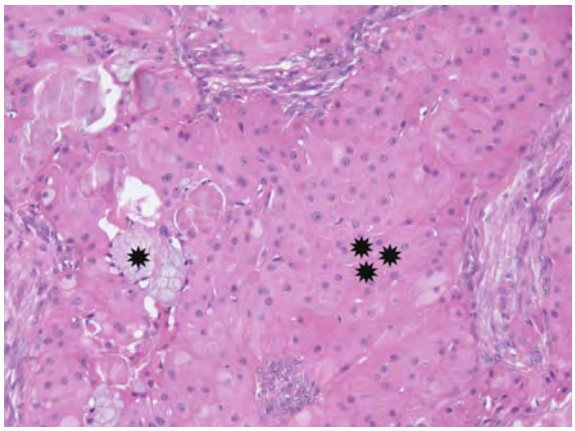

Fig. 16 Intermediate grade mucoepidermoid carcinoma of the parotid gland. Epithelial solid tumor (*3 asterisks*) with some islands of mucinous cells (*asterisk*). Picture courtesy of Prof. Raf Sciot

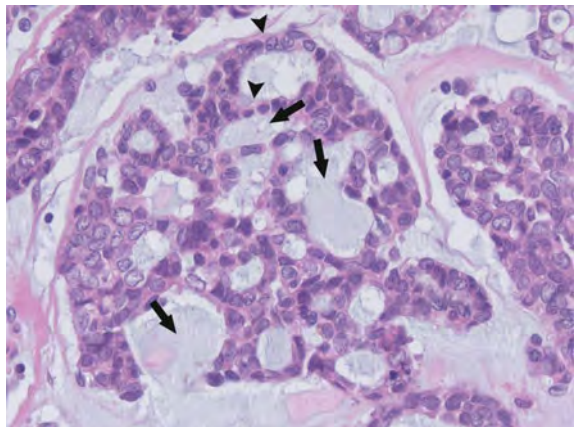

Fig. 18 Adenoid cystic carcinoma of the tongue base. Strands of tumor cells (arrowheads) grow in a cribriform pattern on a mucinous background (*arrows*) thus shaped as pseudolumina. Picture courtesy of Prof.Raf Sciot

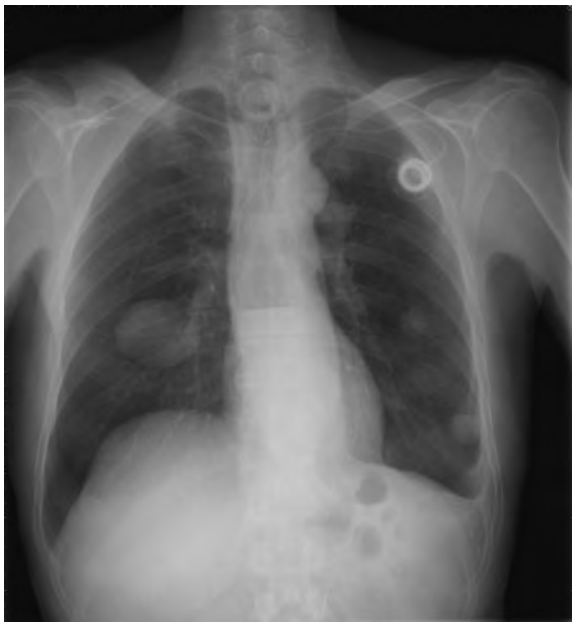

Fig. 17 Diffuse lung metastasis in a patient diagnosed with subglottic adenoid cystic carcinoma 10 years earlier

Macroscopically, it is an often infiltrating rather hard tumor with an irregular extension pattern. The tumor tends to extend via major cranial nerves and in this respect MR imaging is often essential to determine the real anatomical extent. It also has a well-known capacity for distant metastasis in about 40% of patients, (Spiro and Huvos 1992) mostly to the lungs (Fig. 17), and in these patients a protracted clinical course can result in disease-related deaths even after more than 10 years following the initial diagnosis (Spiro and Huvos 1992; Vander Poorten et al. 1999b). Microscopically, the tumor is often composed of cylindrical cystic spaces separated by solid septae of tumor cells, and this is called the "cribriform pattern" (Fig. 18).

Acinic Cell Carcinoma

About one in five parotid carcinomas is diagnosed as acinic cell carcinoma (Vander Poorten et al. 2003). The majority of these tumors have a clinically low grade course, and following adequate resection, low stage tumors are not considered to need additional radiotherapy (Armstrong et al. 1990). Macroscopically acinic cell carcinomas are solitary, well circumscribed, multilobular masses. Microscopically, typical acinar cells with cytoplasmic Periodic Acid Schiff's reagent positive glycogen granules are the main components. A more aggressive (papillocystic (Spiro et al. 1978), microcystic (Colmenero et al. 1991) subgroup is increasingly being distinguished, making up about 15% of acinic cell carcinomas (Hoffman et al. 1999) and requiring a more aggressive treatment.

Adenocarcinoma Not Otherwise Specified (NOS)

Quite frequently a salivary gland adenocarcinoma lacks specific features allowing the pathologist to make a more specific diagnosis. About one in four salivary gland carcinomas cannot be accommodated in the other specific subtypes (Vander Poorten et al. 2003).

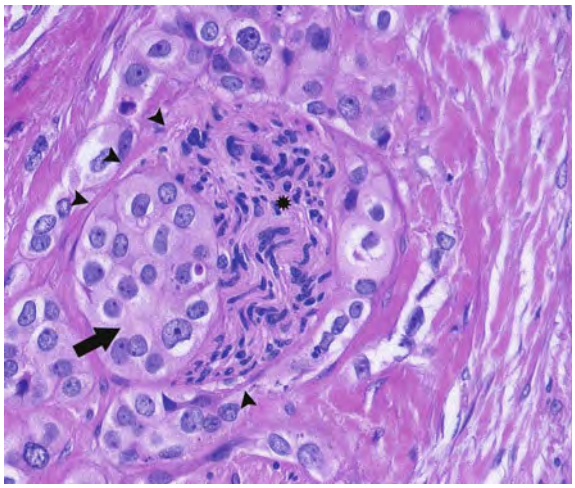

Fig. 19 Perineural growth in a high grade adenocarcinoma NOS of the parotid gland. *Arrowhead* demarcate perineurium, extended by tumor cells (*arrow*), compressing the nerve bundles (*asterisk*) Picture courtesy of Prof. Raf Sciot

Microscopically, they range from well-differentiated and low grade to high grade, invasive lesions, displaying perineural growth (Fig. 19).

Acknowledgment The author expresses his sincere gratitude to Raf Sciot, MD PhD, for providing the illustrative microscopic images corresponding to the clinical examples displayed in this chapter.

References

Acheson ED, Cowdell RH, Hadfield E et al (1968) Nasal cancer in woodworkers in the furniture industry. Br Med J 2:587–596

Ang KK, Harris J, Wheeler R et al (2010) Human papillomavirus and survival of patients with oropharyngeal cancer. N Engl J Med 363:24–35

Armstrong JG, Harrison LB, Spiro RH et al (1990) Malignant tumors of major salivary gland origin: a matched-pair analysis of the role of combined surgery and postoperative radiotherapy. Arch Otolaryngol Head Neck Surg 116:290–293

Barnes L, Eveson JW, Reichart P et al (2005) Pathology and genetics of head and neck tumours. World health classification of tumours. ed IARC, 210. IARC press, Lyon

Batsakis JG (2003) Clinical Pathology of Oral Cancer. In: Shah JP, Johnson NW, Batsakis JG (eds) Oral Cancer, 1st edn. edn. Martin Dunitz, Taylor and Francis Group, London, pp 77–129

Blot WJ, McLaughlin JK, Winn DM et al (1988) Smoking and drinking in relation to oral and pharyngeal cancer. Cancer Res 48:3282–3287

Boccia S, Hashibe M, Galli P et al (2009) Aldehyde dehydrogenase 2 and head and neck cancer: a meta-analysis implementing a Mendelian randomization approach. Cancer Epidemiol Biomarkers Prev 18:248–254

Brugere J, Guenel P, Leclerc A et al (1986) Differential effects of tobacco and alcohol in cancer of the larynx, pharynx, and mouth. Cancer 57:391–395

Colmenero C, Patron M, Sierra I (1991) Acinic cell carcinoma of the salivary glands: a review of 20 new cases. J Craniomaxillofac Surg 19:260–266

Conway DI, Hashibe M, Boffetta P et al (2009) Enhancing epidemiologic research on head and neck cancer: INHANCE—the international head and neck oncology consortium. Oral Oncol 45:743–746

Cooper DS, Doherty GM, Haugen BR et al (2006) Management guidelines for patients with thyroid nodules and differentiated thyroid cancer. Thyroid 16:109–142

Day GL, Blot WJ, Austin DF et al (1993) Racial differences in risk of oral and pharyngeal cancer: alcohol, tobacco, and other determinants. J Natl Cancer Inst 85:465–473

De Rienzo DP, Greenberg SD, Fraire AE (1991) Carcinoma of the larynx: changing incidence in women. Arch Otolaryngol Head Neck Surg 117:681–684

De Stefani E, Ronco A, Mendilaharsu M et al (1999) Diet and risk of cancer of the upper aerodigestive tract-II nutrients. Oral Oncol 35:22–26

Delange F (2000) Iodine deficiency. In: Braverman LE, Utiger RD (eds) Werner and Ingbar's the thyroid, 8th edn. edn. Lippincott, Williams and Wilkins, Philadelphia, pp 295–296

Drozdovitch V, Khrouch V, Maceika E et al (2010) Reconstruction of radiation doses in a case-control study of thyroid cancer following the chernobyl accident. Health Phys 99:1–16

Ellis GL, Auclair PL (1996a) The normal salivary glands. In: Ellis GL, Auclair PL (eds) Tumors of the salivary glands. Armed Forces Institute of Pathology, Washington DC, pp 1–23

Ellis GL, Auclair PL (1996b) Salivary gland tumors: general considerations: site specific tumor differences. In: Ellis GL, Auclair PL (eds) Tumors of the salivary glands. Armed Forces Institute of Pathology, Washington DC, p 32

Eneroth CM, Zetterberg A (1974) Malignancy in pleomorphic adenoma: a clinical and microspectrophotometric study. Acta Otolaryngol 77:426–432

Ferlay J, Shin HR, Bray F et al (2010) Estimates of worldwide burden of cancer in 2008: GLOBOCAN 2008. Int J Cancer 127:2893–2917

Franceschi S, Munoz N, Bosch XF et al (1996) Human papillomavirus and cancers of the upper aerodigestive tract: a review of epidemiological and experimental evidence. Cancer Epidemiol Biomarkers Prev 5:567–575

Franceschi S, Favero A, Conti E et al (1999) Food groups, oils and butter, and cancer of the oral cavity and pharynx. Br J Cancer 80:614–620

Frates MC, Benson CB, Charboneau JW et al (2005) Management of thyroid nodules detected at us: society of radiologists in utrasound consensus conference statement. Radiology 237:794–800

Galeone C, Tavani A, Pelucchi C et al (2010) Coffee and tea intake and risk of head and neck cancer: pooled analysis in the

international head and neck cancer epidemiology consortium. Cancer Epidemiol Biomarkers Prev 19:1723–1736
Gallo O (2001) Aetiology and molecular changes in salivary gland tumours. In: Mc Gurk M, Renehan AG (eds) Controversies in the management of salivary gland tumours, 1st edn. edn. Oxford University Press, Oxford, pp 13–23
Gallo O, Bocciolini C (1997) Warthin's tumour associated with autoimmune diseases and tobacco use. Acta Otolaryngol 117:623–627
Gnepp DR (1993) Malignant mixed tumors of the salivary glands: a review. Pathol Annu 28:279–328
Greenlee RT, Hill-Harmon MB, Murray T et al (2001) Cancer statistics. CA Cancer J Clin 51:15–36
Hashibe M, Brennan P, Strange RC et al (2003) Meta- and pooled analyses of GSTM1, GSTT1, GSTP1, and CYP1A1 genotypes and risk of head and neck cancer. Cancer Epidemiol Biomarkers Prev 12:1509–1517
Hashibe M, Brennan P, Benhamou S et al (2007) Alcohol drinking in never users of tobacco, cigarette smoking in never drinkers, and the risk of head and neck cancer: pooled analysis in the international head and neck cancer epidemiology consortium. J Natl Cancer Inst 99:777–789
Hay ID, Klee GG (1993) Thyroid cancer diagnosis and management. Clin Lab Med 13:725–734
Healey WV, Perzin KH, Smith L (1970) Mucoepidermoid carcinoma of salivary gland origin. Classification, clinical-pathologic correlation, and results of treatment. cancer 26(2):368–388
Heck JE, Berthiller J, Vaccarella S et al (2010) Sexual behaviours and the risk of head and neck cancers: a pooled analysis in the international head and neck cancer epidemiology (INHANCE) consortium. Int J Epidemiol 39:166–181
Heller KS, Attie JN (1988) Treatment of Warthin's tumor by enucleation. Am J Surg 156:294–296
Hoffman HT, Karnell LH, Funk GF et al (1998) The national cancer data base report on cancer of the head and neck. Arch Otolaryngol Head Neck Surg 124:951–962
Hoffman HT, Karnell LH, Robinson RA et al (1999) National cancer data base report on cancer of the head and neck: acinic cell carcinoma. Head Neck 21:297–309
IARC (1997) Cancer incidence in five continents, vol VII. IARC Sci Publ (143): i–xxxiv, pp 1–1240
IARC CancerBase N°4. EUCAN (1999) Cancer incidence, mortality and prevalence in the European Union 1997, version 4.0. IARC Press, Lyon
IARC (2008a). Non-melanoma skin cancer. World cancer report. Cancer site by site. Boyle P, Levin B (eds) international agency for research on cancer, Lyon, pp 398–403
IARC (2008b). Head and neck cancers**.** World cancer report. Cancer site by site. Boyle P, Levin B (eds) international agency for research on cancer, Lyon, pp 331–337
Jeannel D, Bouvier G, Hubert A (1999) Nasopharyngeal cancer. In: Newton R, Beral V, Weiss RA (eds) Infections and human cancer. Cold Spring Harbor Press, Plainview, New York, pp 125–156
Kane WJ, McCaffrey TV, Olsen KD et al (1991) Primary parotid malignancies: a clinical and pathologic review. Arch Otolaryngol Head Neck Surg 117:307–315
Kopp P, Kimura ET, Aeschimann S et al (1994) Polyclonal and monoclonal thyroidnodules coexist within human multinodular goiters. J Clin Endocrinol Metab 79:134–139
La Vecchia C, Tavani A, Franceschi S et al (1997) Epidemiology and prevention of oral cancer. Oral Oncol 33:302–312
Lefebvre J, Lartigau E, Kara A et al (2001) Oral cavity, pharynx and larynx cancer. environment-related prognostic factors. In: Gospodarowicz MK, Henson DE, Hutter RVP, O'Sullivan BO, Sobin LH, Ch Wittekind (eds) UICC prognostic factors in cancer. Wiley-Liss, New York, pp 151–165
Lydiatt WM, Lydiatt DD (2001) The larynx: early stage disease. In: Shah JP (ed) Cancer of the head and neck. BC Decker, Hamilton, London, pp 169–184
Marron M, Boffetta P, Zhang ZF et al (2010) Cessation of alcohol drinking, tobacco smoking and the reversal of head and neck cancer risk. Int J Epidemiol 39:182–196
Medina JE, Dichtel W, Luna MA (1984) Verrucous-squamous carcinomas of the oral cavity: a clinicopathologic study of 104 cases. Arch Otolaryngol 110:437–440
Mehanna H, Paleri V, West CM et al (2010) Head and neck cancer—part 1: epidemiology, presentation, and prevention. BMJ 341:664–666
Moley JF (1995) Medullary thyroid cancer. Surg Clin North Am 75:405–420
Morris LG, Myssiorek D (2010) Improved detection does not fully explain the rising incidence of well-differentiated thyroid cancer: a population-based analysis. Am J Surg 200:454–461
Morse DE, Katz RV, Pendrys DG et al (1996) Smoking and drinking in relation to oral epithelial dysplasia. Cancer Epidemiol Biomarkers Prev 5:769–777
Pedersen E, Hogetveit AC, Andersen A (1973) Cancer of respiratory organs among workers at a nickel refinery in Norway. Int J Cancer 12:32–41
Robertson G, Greenlaw N, Bray CA et al (2010) Explaining the effects of socio-economic deprivation on survival in a national prospective cohort study of 1909 patients with head and neck cancers. Cancer Epidemiol 34:682–688
Russell WO, Ibanez ML, Clark RL (1963) Thyroid carcinoma: classification, intraglandular dissemination, and clinicopathologic study based upon whole organ sections of 80 glands. Cancer 16:1425–1460
Saku T, Hayashi Y, Takahara O et al (1997) Salivary gland tumors among atomic bomb survivors, 1950–1987. Cancer 79:1465–1475
Seifert G, Sobin LH (1992) The world health organization's histological classification of salivary gland tumors. [A commentary on the 2nd edn.]. Cancer 70:379–385
Shaha AR, Loree TR, Shah JP (1995) Prognostic factors and risk group analysis in follicular carcinoma of the thyroid. Surgery 118:1131–1136
Silverman S Jr, Gorsky M, Kaugars GE (1996) Leukoplakia, dysplasia, and malignant transformation. Oral Surg Oral Med Oral Pathol Oral Radiol Endod 82:117
Sipos JA, Mazzaferri EL (2010) Thyroid cancer epidemiology and prognostic variables. Clin Oncol (R Coll Radiol) 22:395–404
Spiro RH (1986) Salivary neoplasms: overview of a 35-year experience with 2, 807 patients. Head Neck 8:177–184
Spiro RH, Huvos AG (1992) Stage means more than grade in adenoid cystic carcinoma. Am J Surg 164:623–628

Spiro JD, Spiro RH (2001) Salivary Tumors. In: Shah JP, Patel SG (eds) Cancer of the Head and Neck. Decker BC, Hamilton, pp 240–250

Spiro RH, Huvos AG, Strong EW (1978) Acinic cell carcinoma of salivary origin: a clinicopathologic study of 67 cases. Cancer 41:924–935

Tezelman S, Clark OH (1995) Current management of thyroid cancer. Adv Surg 28:191–221

UNSCEAR (2000) The united nations scientific committee on the effects of atomic radiation. Health Phys 79: 314

Vander Poorten VLM, Balm AJM, Hilgers FJM et al (1999a) Prognostic factors for long term results of the treatment of patients with malignant submandibular gland tumors. Cancer 85:2255–2264

Vander Poorten VLM, Balm AJM, Hilgers FJM et al (1999b) The development of a prognostic score for patients with parotid carcinoma. Cancer 85:2057–2067

Vander Poorten VLM, Balm AJM, Hilgers FJM et al (2000) Stage as major long term outcome predictor in minor salivary gland carcinoma. Cancer 89:1195–1204

Vander Poorten VL, Hart AA, van der Laan BF et al (2003) Prognostic index for patients with parotid carcinoma: external validation using the nationwide 1985–1994 dutch head and neck oncology cooperative group database. Cancer 97:1453–1463

World Health Organization Collaborating Centre for Oral Precancerous Lesions (1978) Definitions of leukoplakia and related lesions: an aid to studies on oral precancer. Oral Surg Oral Med Oral Pathol 46:518–539

Clinical and Endoscopic Examination of the Head and Neck

Pierre R. Delaere

Contents

Abstract

Head and neck neoplasms present with variable signs and symptoms, depending on their site of origin and extension pattern. Thorough clinical examination, aided by modern endoscopic devices, is a cornerstone of the pre- and post-therapeutic evaluation of the patient suffering head and neck cancer. This chapter reviews the possibilities, but also the limitations of the clinical examination for each of the major subsites in the head and neck region.

1 Introduction

Head and neck neoplasms present with variable signs and symptoms, depending on their site of origin and extension pattern. Thorough clinical examination, aided by modern endoscopic devices, is a cornerstone of the pre- and post-therapeutic evaluation of the patient suffering head and neck cancer. This chapter reviews the possibilities, but also the limitations of the clinical examination for each of the major subsites in the head and neck region.

2 Neck

Clinical examination still remains an important method of assessing regional lymph nodes. The presence of a clinically palpable, unilateral, firm, enlarged lymph node in the adult should be considered metastatic until proven otherwise. External examination of the neck represents an important

P. R. Delaere (✉)
Department of Otorhinolaryngology,
Head and Neck Surgery,
University Hospitals Leuven,
Herestraat 49, 3000 Leuven, Belgium
e-mail: Pierre.delaere@uz.kuleuven.ac.be

R. Hermans (ed.), *Head and Neck Cancer Imaging*, Medical Radiology. Diagnostic Imaging,
DOI: 10.1007/174_2011_371, © Springer-Verlag Berlin Heidelberg 2012

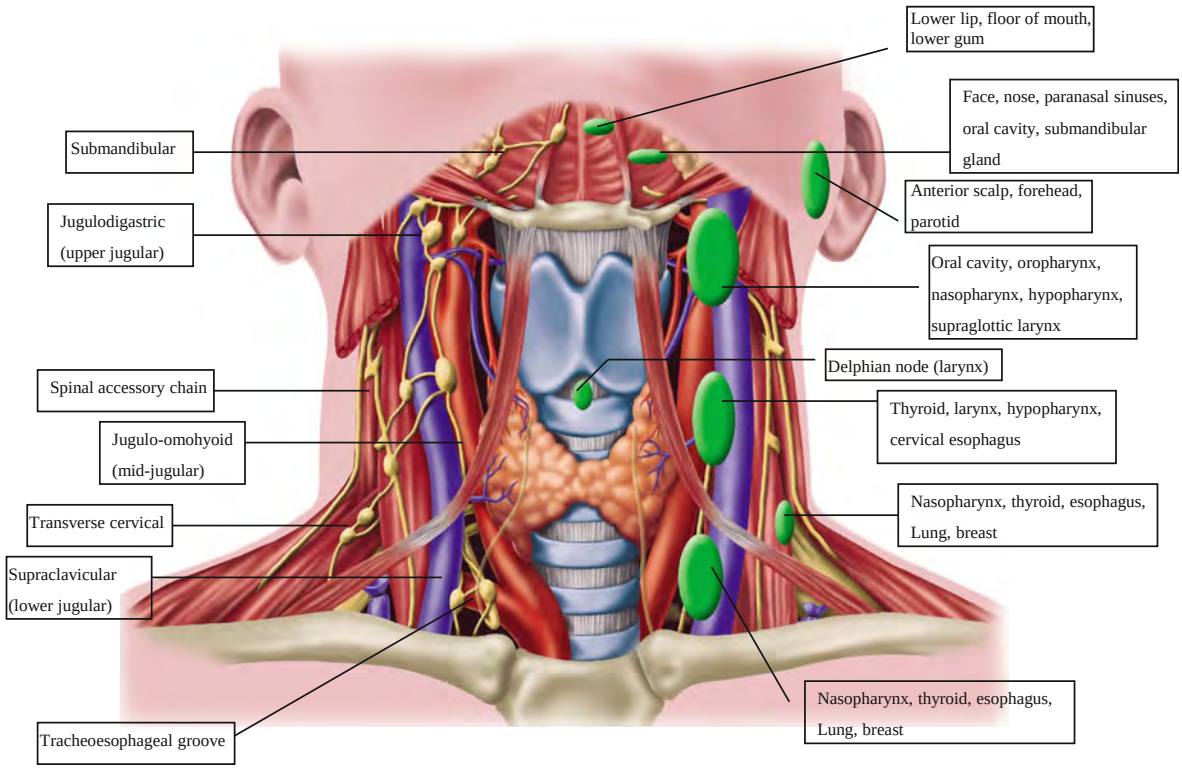

Fig. 1 The regional lymph nodes of the head and neck region; the major regional lymphatic chains are annotated on the *left*. These regional lymph node groups drain a specific primary site as first echelon lymph nodes (indicated on *right*)

starting point in the examination of the patient. It is important to remember that some cervical masses may escape the very best surgical palpation. It is essential that an orderly and systematic examination of the lymphatic fields on both sides of the neck is performed (Stell and Maran 1972).

Regional lymphatic drainage from the mucosa of the upper aerodigestive tract, salivary glands, and the thyroid gland occurs to specific regional lymph node groups (Shah 1990). They should be appropriately addressed in treatment planning for a given primary site. The major lymph node groups of the head and neck are shown in Fig. 1. Cervical lymph nodes in the lateral aspect of the neck primary drain the mucosa of the upper aerodigestive tract. These include the submental and submandibular group of lymph nodes located in the submental and submandibular triangles of the neck. Deep jugular lymph nodes include the jugulodigastric, jugulo-omohyoid, and supraclavicular group of lymph nodes adjacent to the internal jugular vein. Lymph nodes in the posterior triangle of the neck include the accessory chain of lymph nodes located along the spinal accessory nerve and the transverse cervical chain of lymph nodes in the floor of the posterior triangle of the neck. The retropharyngeal lymph nodes are at risk of metastatic dissemination from tumors of the pharynx. The central compartment of the neck includes the Delphian lymph node overlying the thyroid cartilage in the midline draining the larynx, and the perithyroid lymph nodes adjacent to the thyroid gland. Lymph nodes in the tracheoesophageal groove provide primary drainage to the thyroid gland as well as the hypopharynx, subglottic larynx, and cervical esophagus. Lymph nodes in the anterior superior mediastinum provide drainage to the thyroid gland and the cervical esophagus.

The localization of a palpable metastatic lymph node often indicates the potential source of a primary tumor. In Fig. 1 the regional lymph node groups draining a specific primary site as first echelon lymph nodes are depicted.

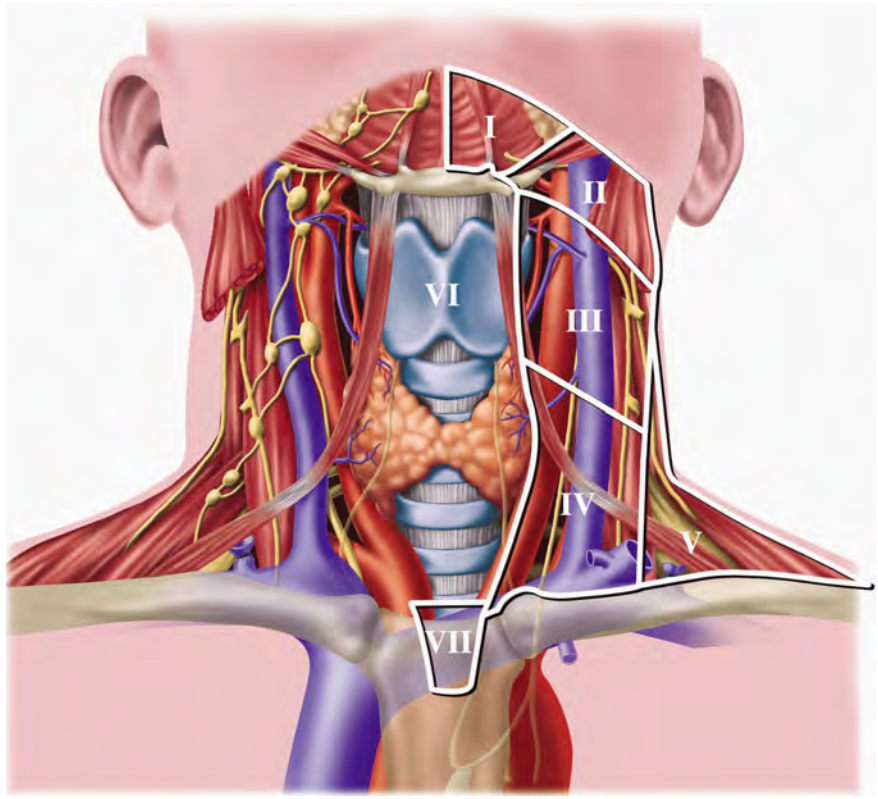

Fig. 2 Level system of cervical lymph nodes: seven levels are distinguished (labeled I–VII)

In order to establish a consistent and easily reproducible method for description of regional cervical lymph nodes, providing a common language between the clinician, the pathologist, and radiologist, the Head and Neck Service at Memorial Sloan–Kettering Cancer Center has described a leveling system of cervical lymph nodes (Fig. 2). This system divides the lymph nodes in the lateral aspect of the neck into five nodal groups or levels. In addition, lymph nodes in the central compartment of the neck are assigned Levels VI and VII.

- *Level I*: *Submental group and submandibular group*. Lymph nodes in the triangular area bounded by the posterior belly of the digastric muscle, the inferior border of the body of the mandible, and the hyoid bone.
- *Level II*: *Upper jugular group*. Lymph nodes around the upper portion of the internal jugular vein and the upper part of the spinal accessory nerve, extending from the base of the skull up to the bifurcation of the carotid artery or the hyoid bone. Surgical landmarks: base of skull superiorly, posterior belly of digastric muscle anteriorly, posterior border of the sternocleidomastoid muscle posteriorly, and hyoid bone inferiorly.
- *Level III*: *Mid-jugular group*. Lymph nodes around the middle third of the internal jugular vein.
- Surgical landmarks: hyoid bone superiorly, lateral limit of the sternohyoid muscle anteriorly, the posterior border of sternocleidomastoid muscle posteriorly, and the caudal border of the cricoid cartilage inferiorly.
- *Level IV*: *Lower jugular group*. Lymph nodes around the lower third of the internal jugular. Surgical landmarks: cricoid superiorly, lateral limit of the sternohyoid muscle anteriorly, posterior border of the sternocleidomastoid muscle posteriorly, and clavicle inferiorly.
- *Level V*: *Posterior triangle group*. Lymph nodes around the lower portion of the spinal accessory nerve and along the transverse cervical vessels. It is bounded by the triangle formed by the clavicle, posterior border of the sternomastoid muscle, and the anterior border of the trapezius muscle.
- *Level VI*: *Central compartment group*. Lymph nodes in the prelaryngeal, pretracheal, (Delphian),

Table 1 N staging of lymph node metastasis from squamous cell carcinoma of the head and neck except nasopharynx (UICC, International Union Against Cancer 2009)

Nx	Regional lymph nodes cannot be assessed
N0	No regional lymph node metastasis
N1	Metastasis in a single ipsilateral lymph node, <3 cm in greatest dimension
N2a	Metastasis in single ipsilateral lymph node >3 cm but <6 cm in greatest dimension
N2b	Metastasis in multiple ipsilateral lymph nodes, none >6 cm in greatest dimension
N3	Metastasis in a lymph node >6 cm in greatest dimension

paratracheal, and tracheoesophageal groove. The boundaries are: hyoid bone to suprasternal notch and between the medial borders of the carotid sheaths.

- *Level VII*: *Superior mediastinal group*. Lymph nodes in the anterior superior mediastinum and tracheoesophageal grooves, extending from the suprasternal notch to the innominate artery.

Some nodes in the neck are more difficult to palpate than others. Thus the retropharyngeal and highest parajugular nodes are almost impossible to detect by palpation until they are very large.

Structures in the neck which may be mistaken for enlarged lymph nodes are the transverse process of the atlas, the carotid bifurcation and the submandibular salivary gland.

Physical examination of the neck for lymph node metastasis has a variable reliability (Watkinson et al. 1990). A meta-analysis comparing computed tomography (CT) with physical examination (PE) yielded the following results: sensitivity, 83 (CT) versus 74% (PE); specificity, 83 (CT) versus 81% (PE): and accuracy, 83 (CT) versus 77% (PE). Overall, PE identified 75% of pathologic cervical adenopathy; this detection rate increased to 91% with addition of CT (Merritt et al. 1997).

The American Joint Committee on Cancer and the International Union against Cancer has agreed upon a uniform staging system for cervical lymph nodes. The exact description of each N stage of lymph node metastasis from squamous carcinomas of the head and neck is described in Table 1. Squamous carcinomas of the nasopharynx and well-differentiated thyroid carcinomas have a different biology and cervical metastases from these tumors are assigned different staging systems.

An enlarged metastatic cervical lymph node may be the only physical finding present in some patients whose primary tumors are either microscopic or occult at the time of presentation. A systematic search for a primary tumor should be undertaken in these patients prior to embarking upon therapy for the metastatic nodes. If a thorough head and neck examination, including fiberoptic nasolaryngoscopy, CT or MRI-study, and PDG-PET scan, fails to show a primary tumor, then the diagnosis of metastatic carcinoma to a cervical lymph node from an unknown primary is established.

3 Nose and Paranasal Sinuses

The nasal cavity is the beginning of the upper airway and is divided in the midline by the nasal septum. Laterally, the nasal cavity contains the nasal conchae, the inferior concha being part of the nasal cavity, and the superior and middle conchae being composite parts of the ethmoid complex. The nasal cavity is surrounded by air containing bony spaces called paranasal sinuses, the largest of which, the maxillary antrum, is present on each side. The ethmoid air cells occupy the superior aspect of the nasal cavity, and separate it from the anterior skull base at the level of the cribriform plate. Superoanteriorly, the frontal sinus contained within the frontal bone forms a biloculated pneumatic space. The sphenoid sinus at the superoposterior part of the nasal cavity is located at the roof of the nasopharynx. The adult ethmoid sinus is narrowest anteriorly in a section known as the ostiomeatal complex and this is the site of drainage of the maxillary and frontal sinuses (Fig. 3).

Since all of the paranasal sinuses are contained within bony spaces, primary tumors of epithelial origin seldom produce symptoms until they are of significant dimensions, causing obstruction, or until they have broken through the bony confines of the involved sinus cavity. Tumors of the nasal cavity often produce symptoms of nasal obstruction, epistaxis, or obstructive pansinusitis early during the

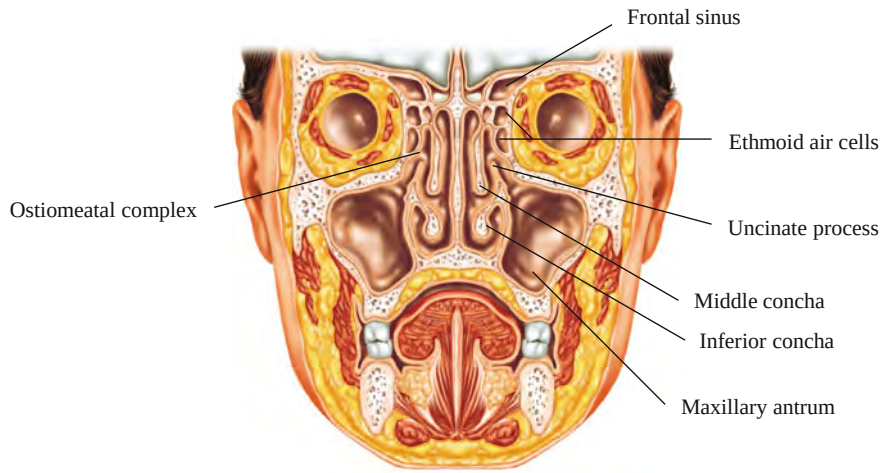

Fig. 3 Coronal section through maxillofacial region, showing proximity of orbit and anterior cranial fossa to nasal cavity and paranasal sinuses. Disease of the sinuses and nasal cavity may spread directly into adjacent structures with catastrophic results

course of the disease. Unilateral epistaxis, obstruction, or sinusitis should raise the index of suspicion regarding the possibility of a neoplastic process. Tumors of the maxillary antrum may present with symptoms of obstructive maxillary sinusitis. Swelling of the upper gum or loose teeth may be the first manifestation of a malignant tumor of the maxillary antrum. Locally advanced tumors may present with anesthesia of the skin of the cheek and upper lip, diplopia, proptosis, nasal obstruction, epistaxis, a mass in the hard palate or upper gum, or a soft tissue mass in the upper gingivobuccal sulcus. Advanced tumors may present with trismus and visible or palpable fullness of the check. Trismus usually is a sign of pterygoid musculature invasion. Epistaxis may be the first manifestation of tumors of the ethmoid or frontal sinus. This may be accompanied by frontal headaches or diplopia. Occasionally anosmia may be present in patients with esthesioneuroblastoma. Anesthesia in the distribution of the fifth cranial nerve or paralysis of the third, fourth, or sixth cranial nerve may be the first manifestation of a primary tumor of the sphenoid sinus. Although sinonasal malignancy is rare, persistent nasal symptoms should always be investigated, particularly if unilateral. Tumors of the nasal cavity and paranasal sinuses are the most challenging to stage. Endoscopic evaluation of the nasal cavity is crucial in accurate clinical assessment of an intranasal lesion. Fiber optic flexible endoscopy provides adequate visualization of the lower half of the nasal cavity. Therefore, lesions presenting in the region of the inferior turbinate, middle meatus, and the lower half of the nasal septum can be easily visualized by office endoscopy.

Rigid endoscopic evaluation with telescopes generally requires adequate topical anesthesia as well as shrinkage of the mucosal surfaces of the interior of the nasal cavity with the use of topical cocaine. A set of 0, 30, 70, and 90° telescopes should be available for appropriate evaluation of the interior of the nasal cavity (Fig. 4). Diagnostic nasal endoscopy allows the characterization of intranasal anatomy and identification of pathology not otherwise visible by traditional diagnostic techniques, such as the use of a headlight, speculum, and mirror (Bolder and Kennedy 1992; Levine 1990).

4 Nasopharynx

The nasopharynx is the portion of the pharynx bounded superiorly by the skull base and the sphenoid and laterally by the paired tori of the eustachian tubes, with the Rosenmüller's fossa. Anteriorly the posterior choanae form the limit of the space, and inferiorly an artificial line drawn at the level of the hard palate delimits the nasopharynx from the oropharynx.

Presenting symptoms of nasopharyngeal cancer may include a neck mass, epistaxis, nasal obstruction, otalgia, decreased hearing, or cranial neuropathies. Approximately 85 percent of patients have cervical adenopathy and 50 percent have bilateral neck involvement (Lindberg 1972). Serous otitis media may occur due to Eustachian tube obstruction. Cranial

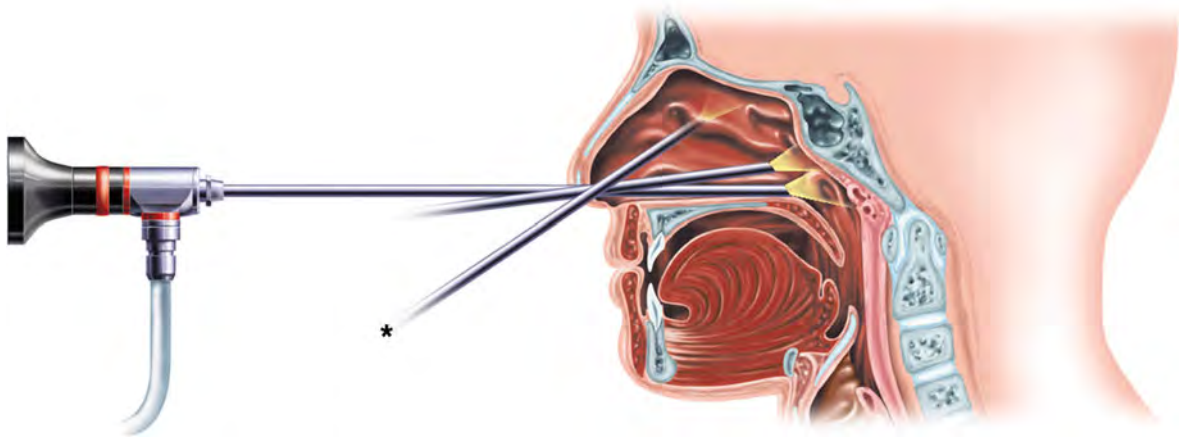

Fig. 4 The rigid endoscope allows for detailed examination of the nasal cavity. The scope can be rotated laterally under the *middle* turbinate into the posterior aspect of the *middle* meatus (*asterisk*). An excellent view of the *middle* turbinate, uncinate process, and surrounding mucosa can be obtained

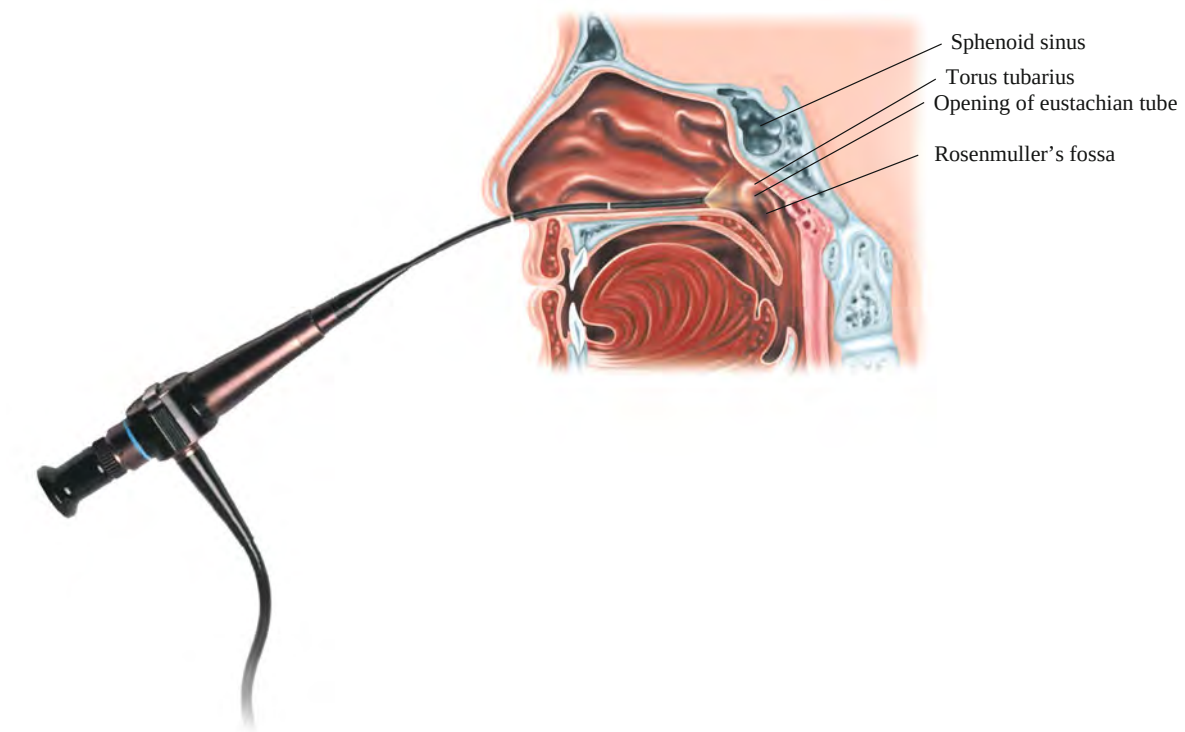

Fig. 5 Examination of nasopharynx with flexible scope

nerve VI is most frequently affected but multiple cranial nerves may be involved.

Nasopharyngeal carcinoma has a tendency for early lymphatic spread. The lateral retropharyngeal lymph node (of Rouvier) is the first lymphatic filter but is not palpable. The common first palpable node is the jugulodigastric and/or apical node under the sternomastoid which are second echelon nodes. Bilateral and contralateral lymph node metastases are not uncommon.

Nasendoscopy (Fig. 5) using the flexible scope gives a good view of the nasal floor, the walls of the nasopharynx and the fossa of Rosenmüller. Nasopharyngeal tumors in any quadrant including the fossa of Rosenmüller can be seen and accurately biopsied. For the nasopharynx, also rigid 0 and 30° sinus endoscopes can be similarly used in the clinical setting. Under anesthesia, should this be necessary, these are the scopes of choice for visual assessment and biopsy.

Evidence of lower cranial nerve deficits may be apparent from palatal or glossal paralysis and atrophy. A full evaluation of the remaining cranial nerves should include visual assessment and examination of the tympanic membranes.

5 Oral Cavity

The oral cavity extends from the vermilion borders of the lips to the junction of the hard and soft palates superiorly and to the line of the circumvallate papillae inferiorly. Within this area are the lips, buccal mucosa, alveolar ridges with teeth and gingiva, retromolar trigone, floor of mouth, anterior two-thirds of the tongue, and hard palate (Fig. 6).

All mucosal surfaces of the mouth require thorough and systematic examination. The oral cavity is lined by a mucous membrane which is a non-keratinizing stratified squamous epithelium and is therefore pink. It contains taste buds and many minor salivary glands. All mucosal surfaces should be examined using tongue blades under optimal lighting conditions.

The clinical features of the primary tumors arising in the mucosal surface of the oral cavity are variable. The tumor may be ulcerative, exophytic, or endophytic, or it may be a superficial proliferative lesion. Most patients with a mouth cancer present with a painful ulcer. Squamous carcinomas with excessive keratin production and verrucous carcinomas present as white heaped-up keratotic lesions with varying degrees of keratin debris on the surface. Bleeding from the surface of the lesion is a characteristic for malignancy and should immediately raise the suspicion for a neoplastic process. Endophytic lesions have a very small surface component but have a substantial amount of soft tissue involvement beneath the surface.

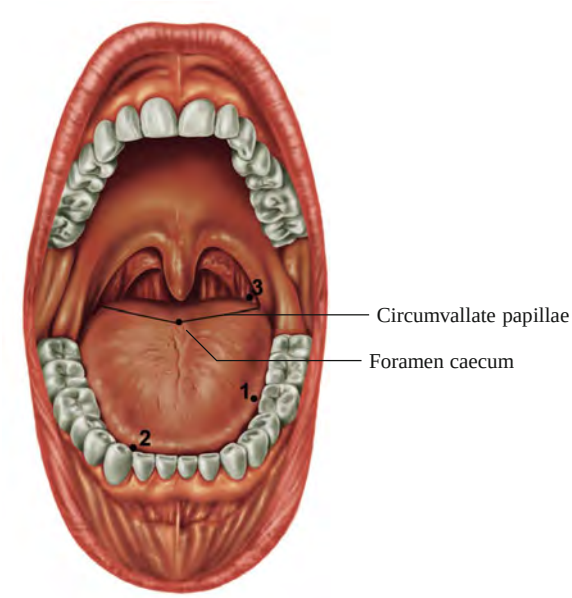

Fig. 6 Oral cavity and oropharynx. The posterior limits of the oral cavity are the anterior tonsillar pillars, the junction of the anterior two-thirds and posterior one-third of the tongue (i.e. the circumvallate papillae) and the junction of the hard and soft palate. The soft palate and the tonsil are therefore part of the oropharynx. Carcinoma of the anterior two-thirds of the tongue is the most frequent site for a mouth cancer and the lateral border (*1*) is the most common location. Carcinoma of the floor of the mouth most commonly occurs anteriorly either in the midline or more usually to one side of the midline (*2*). Carcinoma of the oropharynx most commonly occurs in the slit between tonsil and base of tongue, at the level of the anterior tonsillar pillar (*3*)

Oral salivary tumors may present as a nodule, a non-ulcerative swelling or more usually as an ulcerative lesion. Metastatic tumors may also present as submucosal masses. Mucosal melanoma shows characteristic pigmentation.

Macroscopic lesions should be evaluated for mobility, tenderness and be palpated with the gloved finger to detect submucosal spread. This is particularly important in tongue lesions extending posteriorly into the posterior third and tongue base. The distance from the tumor to the mandible and the mobility of the lesion in relation to the mandible are critical elements in determining the management of perimandibular cancers. The indications for examination under anesthesia include an inadequate assessment of the extent of the disease by history and physical examination and imaging, or the presence of symptoms referable to the trachea, larynx, hypopharynx, and

esophagus that need endoscopic assessment. It is not cost-effective screening to perform panendoscopy on all patients with oral cavity cancer (Benninger et al. 1993; Hordijk et al. 1989).

Palpation of the neck is of course essential in the assessment of a patient with mouth cancer. Neck nodal disease is the single most important factor determining the method of treatment, and also prognosis is determined by the presence of metastatic nodes. Full examination of the neck must be carried out to detect any lymph node metastases and each level must be carefully palpated, particularly the upper and middle deep cervical nodes deep to the sternomastoid, from behind the patient, using the tips of the fingers. Carcinoma of the oral tongue has the greatest propensity for metastasis to the neck among all oral cancers. The primary echelon of drainage is level II but other levels may be also involved.

6 Oropharynx

The oropharynx is that part of the pharynx which extends from the level of the hard palate above to the hyoid bone below. The anterior wall of the oropharynx is formed by the base or posterior third of the tongue bounded anteriorly by the v-shaped line of circumvallate papillae (Fig. 6). When present, the initial symptoms of oropharyngeal cancer are often vague and non-specific, leading to a delay in diagnosis. Consequently, the overwhelming majority of patients present with locally advanced tumors.

Presenting symptoms may include sore throat, foreign-body sensation in the throat, altered voice or referred pain to the ear that is mediated through the glossopharyngeal and vagus nerves. Over two-thirds of patients present with a neck lump. As the tumor grows and infiltrates locally, it may cause progressive impairment of tongue movement which affects speech and swallowing.

Most tumors of the oropharynx can be easily seen with good lighting, but those originating in the lower part of the oropharynx and tongue base are best viewed with a laryngeal mirror. The patient should be asked to protrude the tongue, to rule out injury to the hypoglossal nerve. Trismus is a sign of invasion of the masticator space. Sensory and motor function should be assessed, particularly mobility of the tongue as well as fixation. Fiberoptic nasopharyngeal endoscopy has greatly enhanced the ease of examination of these tumors, particularly in assessing the lower extent of the tumor and also the superior extent if the nasopharynx is involved. The extent of involvement is often underestimated on inspection, and bimanual palpation of the tumor must be undertaken in all patients. Careful palpation should be carried out to estimate the extent of infiltration, but this examination may be limited by patient tolerance; thorough palpation under general anesthetic is advisable. Advanced tumors that cause trismus may also be better assessed under a general anesthetic. A detailed examination and biopsy under general anesthetic may be the only accurate method of assessing the extent of tumors such as those of the tongue base that may be in a submucosal location.

Examination of the neck must be carried out systematically and each level must be carefully palpated to detect lymph node enlargement or deep invasion of the tumor.

Nodal metastases from squamous cell carcinomas are typically hard and when small are generally mobile. As they enlarge, those in the deep cervical chain initially become attached to the structures in the carotid sheath and the overlying sternomastoid muscle with limitation in vertical mobility, but later become attached to deeper structures in the prevertebral region with absolute fixation.

Lymphomas on the other hand have a rubbery consistency and are generally larger and multiple with matting together of adjacent nodes. Cystic degeneration in a metastatic jugulodigastric node from a squamous carcinoma of the oropharynx may have a similar presentation to a brachial cyst but the latter is a far less likely diagnosed in the older patient.

7 Larynx

The larynx communicates with the oropharynx above and the trachea below. Posteriorly it is partly surrounded by the hypopharynx. It may be functionally divided into three important areas. The supraglottis contains epiglottis, aryepiglottic folds, arytenoids, false cords, and includes the laryngeal ventricle. The glottis includes the vocal cords and anterior commissure and posterior commissure. The subglottis is

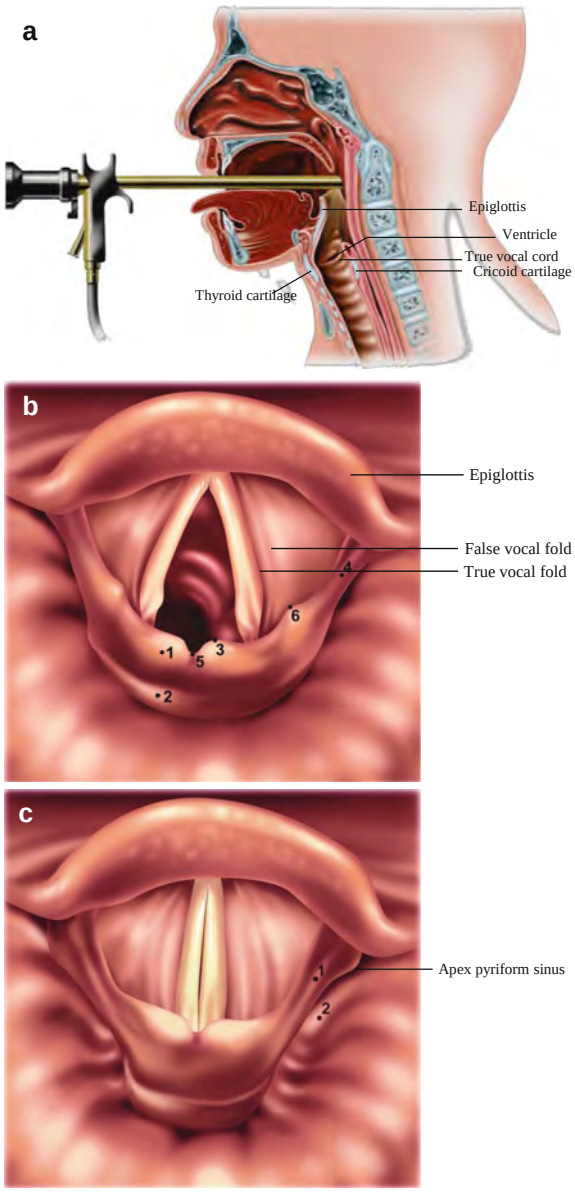

Fig. 7 Indirect laryngoscopy with Hopkins rod telescope. **a** Sagittal view. **b** View during quiet breathing. The arytenoid cartilages (*1*) articulate with facets on the superior surface of the posterior arch of the cricoid cartilage (*2*). A small mass of cartilage, the corniculate cartilage (*3*), usually articulates with the apex of the arytenoid and is located within the inferomedial part of the aryepiglottic fold (*4*). In the midline the mucosa forms a shallow notch between the two corniculate cartilages, known as the posterior commissure (*5*). On the lateral aspect of the corniculate cartilages, within the aryepiglottic folds, are the cuneiform cartilages (*6*). During laryngoscopy the corniculate and cuneiform cartilages appear as small paired swellings in the aryepiglottic folds lying on either side of the posterior commissure. **c** View during phonation. The aryepiglottic folds (*1*) define the anteromedial border of the pyriform fossae (*2*)

limited by the undersurface of the true cords to the inferior margin of the cricoid cartilage (Fig. 7a).

Patients with primary tumors of the larynx usually present with complaints of hoarseness of voice, discomfort in the throat, dysphagia, odynophagia, sensation of something stuck in the throat, occasional respiratory obstruction, hemoptysis, or with referred pain in the ipsilateral ear. Hoarseness is an early symptom of glottic cancer but may be seen later in advanced supraglottic or subglottic tumors indicating spread to the vocal cord, arytenoid, or cricoarytenoid joint. Submucosal spread within the paraglottic space can occur from these sites to produce hoarseness without mucosal irregularity. Dyspnoea and stridor occur with bulky supraglottic tumors or in the presence of vocal cord fixation. In most instances the diagnosis is made by a thorough clinical examination which includes mirror examination of the larynx for adequate assessment of the surface extent of the primary tumor and mobility of the vocal cords.

Examination must be carried out carefully to identify the possible spread of tumor beyond the larynx either directly or by metastasis to the regional lymph nodes. A neck mass almost always indicates lymphatic metastasis but may result from direct extension of the tumor into the soft tissues of the neck. The most frequent site of secondary deposits is the ipsilateral deep cervical chain, usually in the upper/middle region (level II, III). Glottic tumors rarely metastasize, while deposits in the lymph nodes are more frequent from supraglottic lesions. Examination must include an assessment of the number, mobility, and level of the lymph nodes. Some anterior swelling of the larynx, by widening or by penetration of tumor through the cricothyroid membrane, may be felt.

The use of the 70 or 90° Hopkins rod telescope (Fig. 7a) allows a high resolution view of the larynx. It allows assessment of vocal cord function, high quality photography, and is the ideal instrument for videostroboscopy of the larynx. The clinical appearance of a normal larynx seen through a rigid telescope is shown in Fig. 7b. This view of the normal larynx provides adequate visualization of all the anatomic sites of the supraglottic and glottic larynx as well as the hypopharynx. The dynamic function of the larynx should also be observed and recorded by asking the patient to phonate. During phonation, the vocal cords adduct while the pyriform sinuses are opening up, revealing their apices (Fig. 7c). Stroboscopy is useful

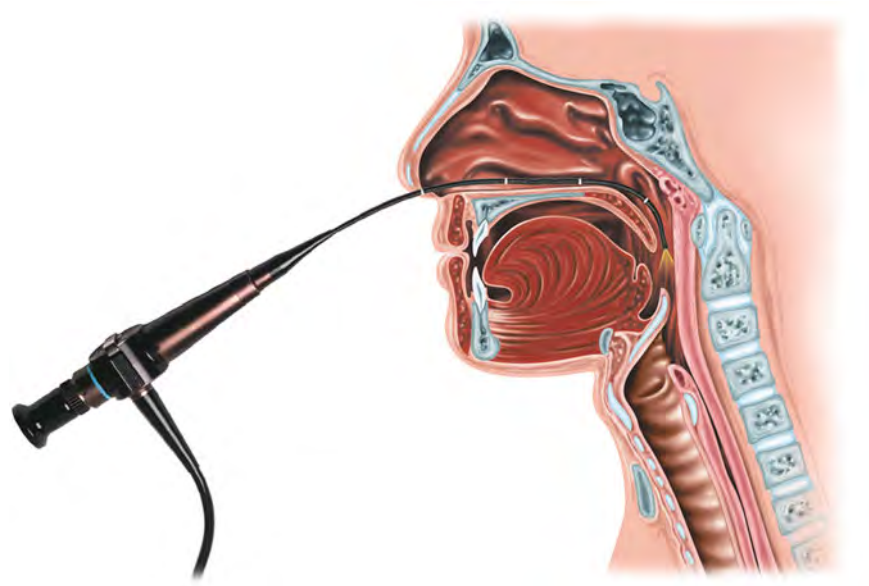

Fig. 8 Flexible laryngoscopy. Fiberoptic laryngeal nasendoscopy provides a clear image of the larynx, laryngopharynx, and base of tongue

for the differentiation of functional from anatomical defects (Sercarz et al. 1992) and has been employed in the early detection of glottic cancer. In the latter setting, preservation of the mucosal wave suggests that a lesion is not invasive (Zhao 1992).

Technological advance is producing increasingly smaller diameter fiberoptic endoscopes for examination of the human body. The flexible nasendoscope can be used to examine the postnasal space, pharynx, and larynx, down to the level of the vocal cords. Flexible nasolaryngoscopy (Fig. 8) is generally carried out in a normal anatomical position and during normal respiration, unlike the rather distorted position achieved by indirect laryngoscopy or the use of the Hopkins rods. Additionally, flexible endoscopy can be used to directly observe the pharyngeal phase of swallowing, giving complementary information to that obtained by videofluoroscopy. Test swallows of milk or colored food can be examined (Logemann 1983).

Direct laryngoscopy under general anesthesia is the only reliable way to assess mucosal lesions of the larynx and pharynx (Phelps 1992; Parker 1992), and more often enables adequate biopsies to be sampled than with flexible techniques (Ritchie et al. 1993). If a tumor is detected, its limits in all directions should be determined both by sight and palpation.

The introduction of the operating microscope has facilitated detailed examination of the larynx (Kleinsasser 1965) (Fig. 9). Use of various telescopes (0, 30, 70, and 120°) provides an excellent and detailed view of the lesion.

Clinical examination is limited by the fact that certain areas of the larynx are inaccessible to both visualization and palpation; nevertheless involvement of these structures has an important bearing on staging as well as on management. Information from radiological imaging and operative endoscopy must be utilized in conjunction with physical findings to obtain an accurate pretreatment TNM staging record. Particularly supraglottic tumors are frequently understaged because the pre-epiglottic and paraglottic spaces cannot be assessed clinically.

8 Hypopharynx and Cervical Esophagus

The hypopharynx links the oropharynx superiorly to the larynx and esophagus below. Its boundaries are roughly the hyoid and valleculae above and the cricoid below. Common sites for squamous cell cancers are the pyriform sinuses, the posterior pharyngeal wall and the postcricoid space.

Patients with primary tumors of the hypopharynx usually present with the complaints of discomfort in the throat, dysphagia, odynophagia, sensation of something stuck in the throat, referred pain in the ipsilateral ear, hemoptysis, hoarseness of voice, or

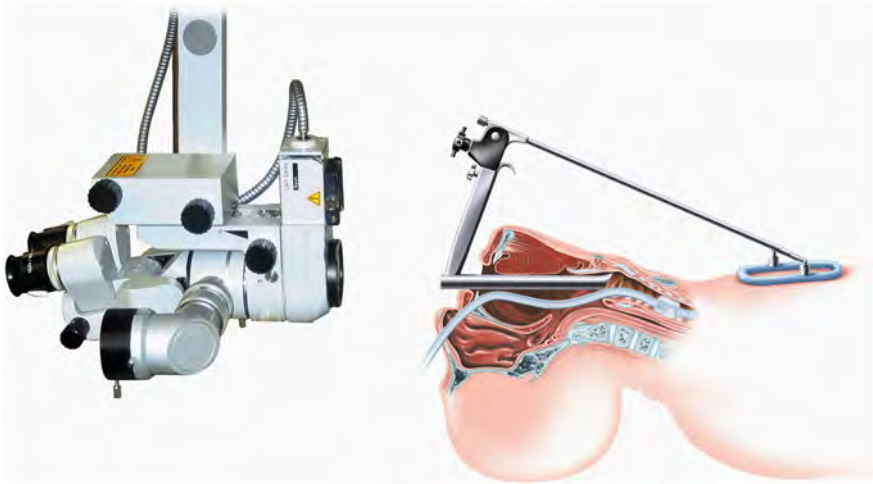

Fig. 9 The arrangement for stable microlaryngoscopy. After placement of the laryngoscope the laryngostat is attached and the tension tightened until the view is just adequate. The microscope is then brought into position and focused

shortness of breath. In most instances, diagnosis is made by a thorough clinical examination including mirror examination of the hypopharynx and larynx, as well as either rigid telescopic or fiberoptic nasolaryngopharyngoscopic examination for adequate clinical assessment of the primary tumor.

While clinical examination permits the diagnosis of a primary tumor of the hypopharynx, direct laryngoscopy and esophagoscopy under general anesthesia are essential for accurate assessment of the tumor extent and to obtain a biopsy for histologic diagnosis.

The important features to be assessed during endoscopic examination under anesthesia include the site of origin of the primary tumor, and its local extension to the other sites within the hypopharynx and adjacent regions.

In patients with a malignant tumor of the upper respiratory or upper digestive tract, it is advisable to perform flexible esophagogastroduodenoscopy; the detection rate of a synchronous primary tumor is about 3–13% (Levine and Nielson 1992).

9 Salivary Glands

The parotid glands are located in close proximity to the cartilage of the external auditory canal. Anteriorly the gland abuts both the lateral and posterior border of the ramus of the mandible and the overlying masseter muscle, while inferiorly it rests medially on the posterior belly of the digastric muscle, as well as the sternocleidomastoid muscle laterally. Medially the parotid is adjacent to the parapharyngeal space, while superiorly it reaches the arch of the zygoma. The facial nerve courses through the parotid gland. The parotid gland is arbitrarily divided into a 'superficial' and 'deep' lobe by the plane of the facial nerve. Numerous lymph nodes are localized within, and adjacent to, the capsule of the parotid gland, serving as the first echelon drainage for the temporal scalp, portions of the cheek, the pinna, and the external auditory canal. For this reason, the parotid gland may harbor metastatic cutaneous malignancy from these sites.

The submandibular glands are located in the anterior triangle of the neck, and are bounded superiorly and laterally by the body of the mandible. The mylohyoid muscle is located anterior to the gland, while the hyoglossus muscle lies medial to the gland. The submandibular (Wharton's) duct exists the gland medial to the mylohyoid muscle, then courses anteriorly and superiorly into the anterior floor of mouth (Fig. 10).

Located beneath the mucosa of the floor of the mouth, the small sublingual glands drain directly into the oral cavity through numerous small ducts.

The majority of neoplastic lesions of salivary glands appear as a lump without other symptoms.

Swellings in the retromandibular sulcus, the immediate preauricular region, and over the masseter are, in most cases, of parotid gland origin. Although about 10% of parotid gland tumors arise medial to the plane of the facial nerve in the deep 'lobe' of the

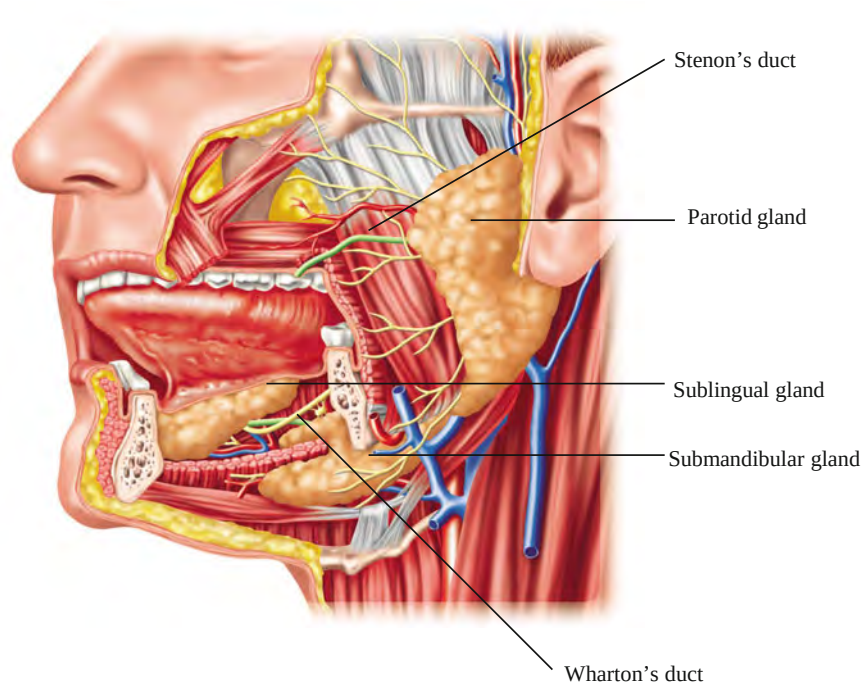

Fig. 10 Anatomic relations of the parotid, submandibular, and sublingual salivary gland

gland, more than three-fourths of these deep lobe tumors will present as a typical parotid mass.

In the parotid gland pleomorphic adenomas present as round, firm, reasonable well-demarcated tumors, with a tendency to nodularity as they grow. Their site of election is between the ascending ramus of the mandible anteriorly, and the mastoid process and sternomastoid posteriorly, usually in the tail of the gland. Occasionally they arise in the immediate preauricular region, where they tend to be small. Warthin's tumors lie almost invariably in the lower pole of the gland, are ovoid in shape, and vary in consistency between soft and firm, depending on whether or not they have been exposed to previous inflammation; these tumors can occur bilaterally.

Weakness or paralysis of the facial nerve in a previously untreated patient almost always indicates that a tumor is malignant (Spiro et al. 1975; Borthune et al. 1986). Careful assessment should be made of the facial nerve and the nerves traversing the nearby carotid space (cranial nerve IX and XII) if a deep lobe or parapharyngeal space tumor is suspected.

It is often difficult to distinguish between a tumor arising within the submandibular gland or an enlarged node close to the gland or on its outer surface. Bimanual palpation is essential to differentiate between the two, since a node lying on the outer surface of the salivary gland is unlikely to be palpated by a finger in the mouth, whereas a tumor of the gland itself is more readily compressible bimanually. Pleomorphic adenomas of the submandibular gland are usually large, quite hard, and nodular, but may be confused with a slowly growing malignancy such as an adenoid cystic carcinoma. Submandibular gland neoplasms also need evaluation of the lingual and hypoglossal nerves.

The assessment of intraoral minor salivary gland neoplasms depends on the location of the tumor. Palatal lesions are the most common, usually giving the appearance of being fixed, whether they are benign or malignant, because of the tight adherence of the mucous membrane to bone. Tumors of the hard or soft palate are often fusiform, firm to hard in consistency and nodular. Again the distinction between mixed tumor and adenoid cystic carcinoma may be difficult to make.

A salivary gland tumor arising from the deep lobe of the parotid gland, or from a minor salivary gland in the parapharyngeal space, may cause secondary displacement of the palatotonsillar region.

Swelling detectable both in the pharynx and parotid region indicates a very bulky tumor originating from within the deep lobe of the parotid gland. This parotid swelling can be visible externally, but the technique of bimanual palpation will elicit the characteristic sign of ballottement between the examining fingers, typical of masses occupying such a wide area. The absence of both a visible swelling in the parotid gland and ballottement suggests an origin exclusively in the parapharyngeal space.

10 Thyroid Gland

The thyroid gland lies within the pretracheal fascia in the front of the neck, and consists of two symmetrical lobes united in the midline by an isthmus that overlies the second to fourth tracheal rings (Fig. 1). There is often a pyramidal lobe, which may extend as high as the top of the thyroid cartilage.

The incidence of palpable thyroid nodules is estimated at only 4–7% of the general adult population. They occur more frequently in women and they are increasing with age (Mazzaferri et al. 1988). Slightly less than 5% of thyroid nodules are found to be malignant (Gharib and Goellner 1993). Most patients with differentiated carcinoma present with a palpable nodule in the thyroid gland of varying size, consistency, and local extent. The primary tumor may present as a solitary, well-defined, intrathyroidal discrete palpable nodule or it may manifest with diffuse involvement of the thyroid gland with or without extrathyroid extension and fixation to the structures in the central compartment of the neck, or it may present as multiple palpable nodules. The most common location of palpable metastatic lymph nodes from thyroid cancer is at levels III, IV, or V in the lateral neck. Procedures commonly used for the initial evaluation of thyroid nodules are: ultrasound, radionuclide imaging, and fine-needle aspiration biopsy (FNAB).

Anaplastic carcinoma of the thyroid gland usually manifests in the older population with a very short history of a rapidly enlarging thyroid mass. Physical examination reveals a diffusely enlarged firm to hard ill-defined thyroid mass with significant extrathyroid extension to adjacent soft tissues. The mass appears fixed and inseparable from the laryngotracheal–esophageal complex.

11 Role of Imaging Studies

The clinical evaluation allows to appreciate the mucosal layer of the head and neck region quite well. However, the deep extent of potentially infiltrating lesions can only be judged indirectly. Some regions, such as the base of the skull, pterygopalatine and infratemporal fossa, orbits and brain are beyond clinical evaluation, but critical management decisions have to be made based on the involvement of these structures; imaging findings are of the utmost importance in such cases. Perineural and/or perivascular spread, eventually leading to tumor progression or recurrences at distance from the primary tumor can often only be detected by imaging.

Metastatic adenopathies can be identified, sometimes still in a subclinical stage or at places not accessible for clinical examination, such as the retropharyngeal or paratracheal lymph nodes. Also, information on extranodal tumor spread and the relation to critical structures such as the carotid arteries, is necessary for determining the optimal patient management, and can be deduced from imaging studies.

Imaging is needed in submucosal lesions, covered by an intact mucosa. The origin and extent of such lesions is often difficult to determine based on the clinical evaluation alone. Imaging may provide important clues to the diagnosis, as representative biopsies may be difficult to obtain in deep-seated lesions.

All these findings can profoundly influence the staging and management of the patient with head and neck cancer. Finally, imaging may be used to monitor tumor response and to try to detect recurrent or persistent disease before it becomes clinically evident, possibly with a better chance for successful salvage.

The single most important factor in the optimal use of all this information is the mutual cooperation between the radiologist and the physicians in charge of patient care.

References

Benninger MS, Enrique RR, Nichols RD (1993) Symptom-directed selective endoscopy and cost containment for evaluation of head and neck cancer. Head Neck 15:532–536

Bolder WE, Kennedy DW (1992) Nasal endoscopy in the outpatient clinic. Otolaryngol Clin North Am 25:791–802

Borthune A, Kaalhus O, Vermund H (1986) Salivary gland malignant neoplasms: treatment and prognosis. Int J Radiat Oncol Biol Phys 12:747–754

Gharib H, Goellner JR (1993) Fine needle aspiration biopsy of the thyroid: an appraisal. Ann Int Med 118:282–289

Hordijk GJ, Bruggink T, Ravasz LA (1989) Panendoscopy: a valuable procedure? Otolaryngol Head Neck Surg 101:426–428

Kleinsasser O (1965) Weitere technische entwicklung und erste ergebnisse der 'endolaryngealen microchirurgie'. Zeitschrift für Laryngologie, Rhinologie und Otologie 44:711–727

Levine HL (1990) The office diagnosis of nasal and sinus disorders using rigid nasal endoscopy. Otolaryngol Head Neck Surg 102:370–373

Levine B, Nielson EW (1992) The justifications and controversies of panendoscopy-a review. Ear Nose Throat J 71:335–343

Lindberg RD (1972) Distribution of cervical lymph node metatstases from squamous cell carcinoma of the upper respiratory and digestive tracts. Cancer 29:1446–1450

Logemann JA (1983) Evaluation and treatment of swallowing disorders. College Hill Press, San Diego

Mazzaferri EL, de los Santos ET, Rofagha-Keyhani S (1988) Solitary thyroid nodule: diagnosis and management. Med Clin North Am 72:1177–1211

Merritt RM, Williams MF, James TH et al (1997) Detection of cervical metastasis. A meta-analysis comparing computed tomography with physical examination. Arch Otolaryngol Head Neck Surg 123:149–152

Parker R (1992) Laryngoscopy, microlaryngoscopy and laser surgery. In: McGregor IA, Howard DJ (eds) Rob and smith's operative surgery: head and neck, part 2, 4th edn. Oxford, Butterworth, pp 451–463

Phelps PD (1992) Carcinoma of the larynx-the role of imaging in staging and pre-treatment assessments. Clin Radiol 46:77–83

Ritchie AJ, McGuigan J, Stenvenson HM et al (1993) Diagnostic rigid and flexible oesophagoscopy in carcinoma of the oesophagus: a comparison. Thorax 48:115–118

Sercarz JA, Berke GS, Ming Y et al (1992) Videostroboscopy of human vocal fold paralysis. Ann Otol Rhinol Laryngol 101:567–577

Shah JP (1990) Patterns of nodal metastases from squamous carcinomas of the upper aerodigestive tract. Am J Surg 160:405–409

Spiro RH, Huvos AW, Strong EW (1975) Cancer of the parotid gland: a clinicopathologic study of 288 primary cases. Am J Surg 130:452–459

Stell PM, Maran AGD (eds) (1972) Pre-operative considerations. In: Head and neck surgery. William Heinnemann Medical, London, p 6

UICC, International Union Against Cancer (2009) TNM classification of malignant tumors, 7th edn. Wiley, New York, p 37

Watkinson JC, Johnston D, James D et al (1990) The reliability of palpation in the assessment of tumours. Clin Otolaryngol 5:405–410

Zhao R (1992) Diagnostic value of stroboscopy in early glottic carcinoma. Chung Rua Ehr Pi Yan Hou Ko Tsa Chih 27:175–176

Imaging Techniques

Robert Hermans, Frederik De Keyzer, Vincent Vandecaveye, and Laurens Carp

Contents

Abstract

Various imaging techniques are used to investigate the presence and extent of head and neck neoplasms, including ultrasound, computed tomography, magnetic resonance imaging and nuclear imaging techniques. To obtain the most optimal results, close attention should be paid to a correct technical execution of the imaging study. This chapter provides information on the relative advantages and disadvantages of each of the available imaging techniques, as well as on patient preparation, contrast agent or tracer injection, data acquisition, and image reconstruction, reformatting and display. The possible value of some newer imaging techniques, such as diffusion-weighted MRI and dynamic contrast-enhanced MRI is also reviewed.

1 Introduction

Various imaging techniques are used in the evaluation of patients with head and neck cancer, before, during and after treatment. Each of these imaging techniques has its own advantages and disadvantages.

Many head and neck neoplasms arise from the mucosal lining; when a patient is referred for imaging, the histological diagnosis often was already established by endoscopic biopsy. Therefore, imaging should primarily supply information on the submucosal extension depth of the primary tumor, including its relation to surrounding structures, as well as on the presence of regional and/or distant metastasis, or a second primary tumor.

R. Hermans (✉) · F. De Keyzer · V. Vandecaveye
Department of Radiology, University Hospitals Leuven, Herestraat 49, 3000 Leuven, Belgium
e-mail: robert.hermans@uzleuven.be

L. Carp
Service of Nuclear Medicine, University Hospital Antwerp, Wilrijkstraat 10, 2650 Edegem, Belgium

R. Hermans (ed.), *Head and Neck Cancer Imaging*, Medical Radiology. Diagnostic Imaging,
DOI: 10.1007/174_2011_372, © Springer-Verlag Berlin Heidelberg 2012

The purpose of this chapter is to describe the various techniques available for imaging the head and neck cancer patient, and to provide general rules for their use. Specialized imaging applications are described in the following chapters where appropriate.

2 Plain Radiography

In the past, a variety of conventional methods were applied to stage head and neck cancer, including soft tissue views of the neck, plain films of the facial skeleton, xeroradiography, plain film tomography, laryngography and barium swallow. The value of these studies to stage head and neck cancer is very limited; these techniques are now replaced by cross-sectioning imaging modalities.

Barium swallow remains an indispensable method in the early phase after pharyngeal surgery, to rule out or confirm the presence of fistulae. This technique is also essential in the evaluation of functional disorders (such as bolus retention, delayed passage and aspiration) after surgery or radiotherapy.

3 Ultrasonography

Ultrasonography is a widely used technique for the evaluation of the thyroid gland (see "Thyroid and Parathyroid Neoplasms"), neck lymph nodes (see "Neck Nodal Disease") and salivary glands, as it offers visualization of these structures with high spatial resolution, at a low cost and without using ionizing radiation.

Ultrasonography in combination with fine needle aspiration cytology (FNAC) is the most accurate method for neck nodal staging in most head and neck cancers (Van Den Brekel et al. 1991). However, execution of this procedure is time consuming, and the obtained results are operator-dependent (Takes et al. 1996). Also, in a multicenter study where both computed tomography and ultrasound of the neck were applied for staging of head and neck cancer, the addition of ultrasound-guided FNAC did not provide significant additional value (Takes et al. 1998).

4 Computed Tomography and Magnetic Resonance Imaging

Nowadays, in most patients computed tomography (CT) or magnetic resonance imaging (MRI) is performed for pretherapeutic staging of a head and neck malignancy. Both techniques can supply the information needed by the clinician for adequate treatment planning.

A common question is which of these techniques should be used in a particular patient. The most widely used technique is CT, as it has a number of important advantages over MRI:

- wide availability
- relative low cost
- easy to execute this in a reproducible way
- short examination time, resulting in less image quality degradation caused by motion, such as swallowing and respiration
- superior bone detail
- high quality multiplanar imaging on multidetector CT systems
- easy extend of the study into the upper thoracic cavity or intracranial cavity, if needed
- easier interpretation, especially regarding nodal involvement (Curtin et al. 1998).

However, CT also has a number of disadvantages compared to MRI:

- relative low soft tissue contrast resolution
- administration of iodinated contrast agent is necessary
- severe image quality degradation by dental fillings or other metallic foreign objects (Fig. 1)
- radiation exposure.

The advantages of MRI over CT in the evaluation of head and neck cancer are its superior soft tissue contrast resolution, and the absence of radiation exposure. Overall, the image quality is not or less hampered by the presence of dental fillings than in CT, but also MRI studies may be severely jeopardized by metallic implants (Fig. 2). The disadvantages of MRI are mainly related to the long acquisition time, making the technique sensible to motion artifacts which cause a non-diagnostic study (Fig. 3). It is also technically more challenging with MRI to properly

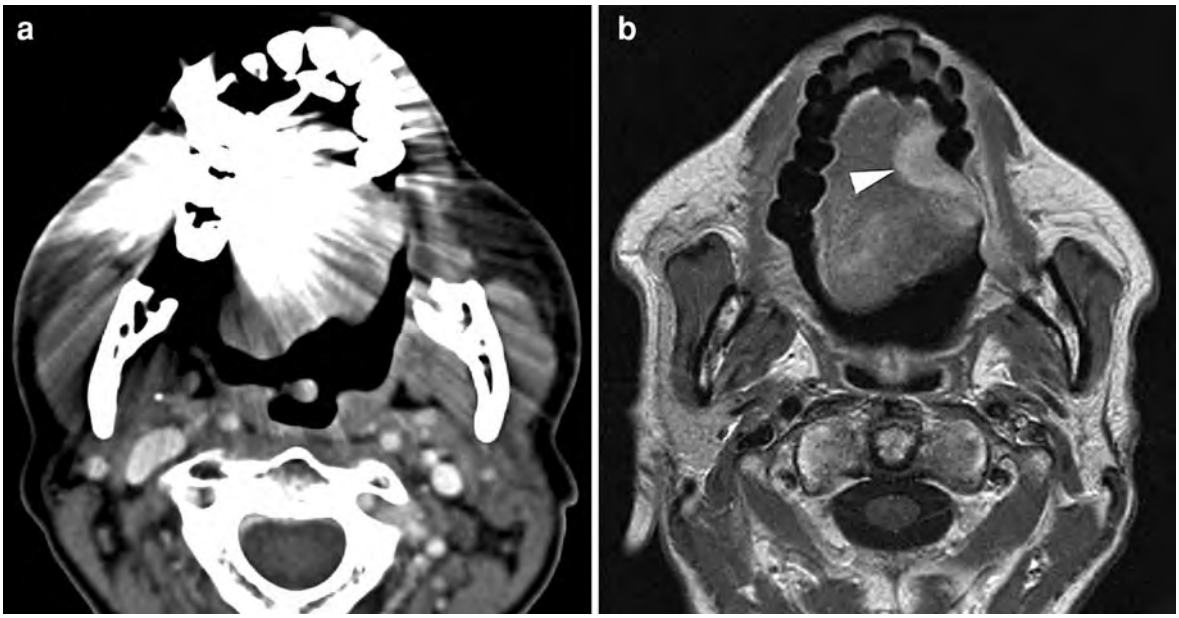

Fig. 1 Patient suffering left-sided oral tongue cancer. **a** Axial contrast-enhanced CT-image. As the image quality is severely hampered by artifacts arising from dental fillings, the primary tumor is not visible. A complementary MR-study was advised. **b** Gadolinium-enhanced T1-weighted image, not affected by presence of dental fillings, clearly shows the primary tumor (*arrowhead*)

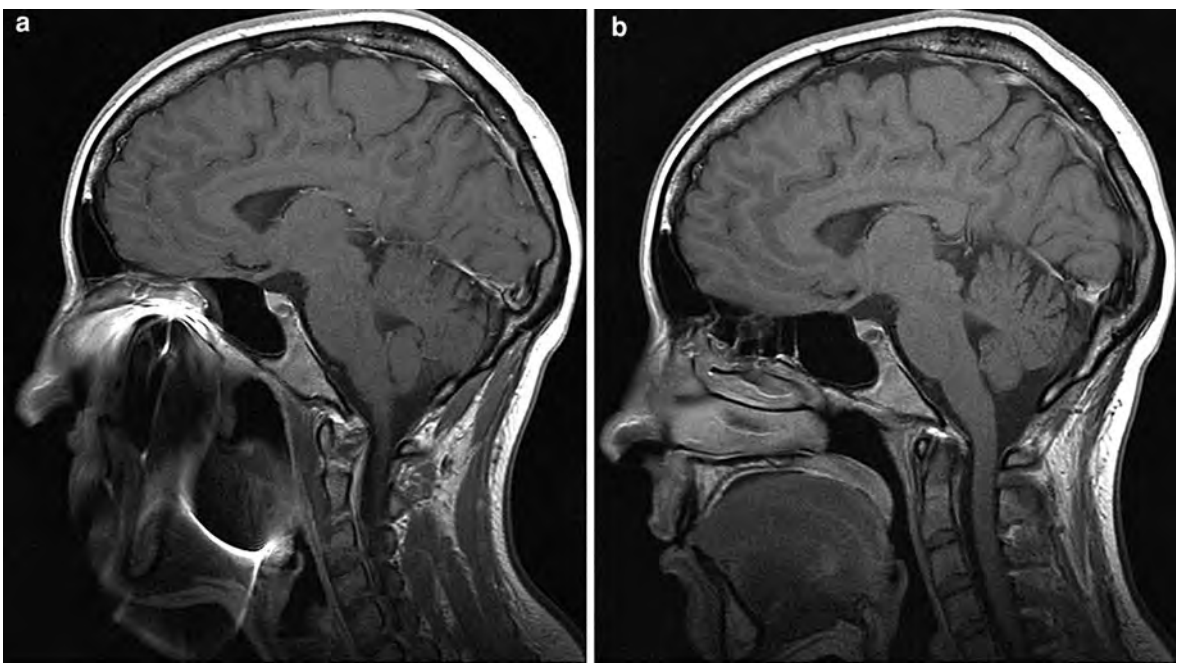

Fig. 2 Patient referred for MR-study of the maxillofacial region and skull base because of unilateral facial pain. **a** Initial MR-study was non-conclusive, as artifacts caused by fixed orthodontic material severely degrade image quality. **b** After removal of the orthodontic material by the dentist, optimal image quality was achieved

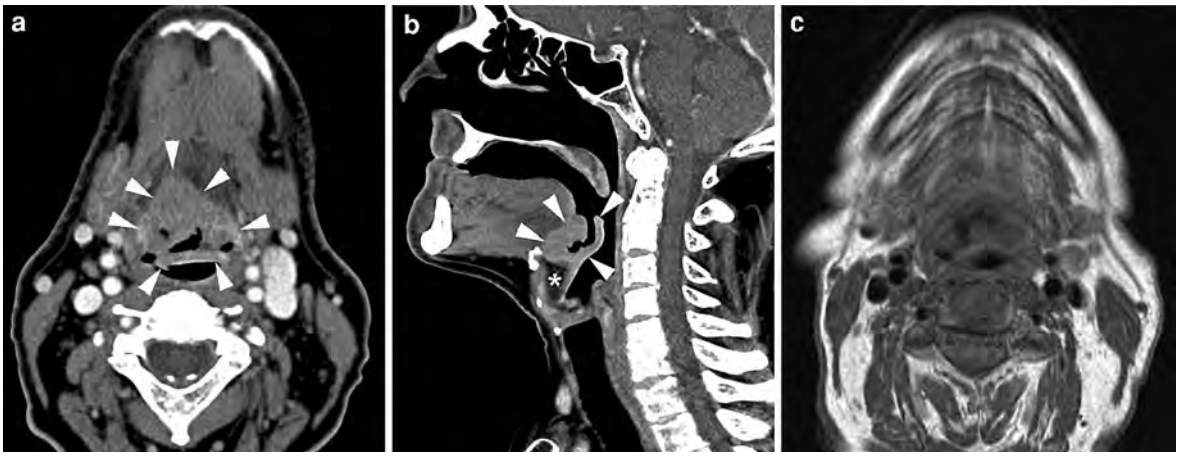

Fig. 3 Patient suffering tongue base cancer. **a**, **b** Axial and sagittal reformatted contrast-enhanced MDCT-images clearly show tumor extent into tongue base and involvement of free epiglottic rim (*arrowheads*), as well as the relationship of the tumor to the pre-epiglottic space (*asterisk*). **c** For study purposes, a MR-study was performed in this patient one day later. Because of motion artifacts, the tumor is not confidently discernable. This MR-study was considered non-diagnostic

stage both primary tumor and neck nodal disease in a single study. The lower availability of MRI, resulting in a longer waiting list, and its higher cost should also be taken into consideration.

In many institutions, CT is the preferred imaging method for evaluation of laryngeal and hypopharyngeal cancer, as well as of oral cavity and oropharyngeal cancer. These cancer sites constitute about 80–85% of all head and neck malignancies (excluding skin cancer and lymphoma) in Europe and the USA. In most cases, a dedicated CT study will provide all answers needed by the clinician; in such a setting, MRI is used as complementary tool to solve remaining questions.

Because of its higher contrast resolution, MRI is the preferred imaging method in rarer head and neck malignancies, such as nasopharyngeal cancer and sinonasal cancer. There is no consensus regarding the use of CT or MRI as primary imaging tool in salivary gland cancer, although there is a tendency among head and neck radiologists to choose for MRI.

4.1 Computed Tomography

CT can be regarded as the 'workhorse' of head and neck cancer imaging. It is not possible to define the ideal imaging protocol, as available equipment varies. The minimal requirements for an optimal diagnostic study will be outlined.

4.1.1 Patient Positioning

The images are obtained with the patient supine and during quiet respiration. The neck should be in slight extension. The head is aligned in the cephalocaudal axis in order to make it possible to compare symmetric structures. Malposition may result in an appearance that simulates disease. Every effort should be made to make the patient feel comfortable; this will help the patient dropping the shoulders to a position as low as possible (Wirth et al. 2006).

This patient-friendly position is applicable for all indications if multidetector spiral CT (MDCT) is used, as this modality allows retrospective high quality reformatting in every spatial plane. In case an incremental or single-spiral CT technique has to be used, additional direct coronal imaging is needed in the evaluation of sinonasal and skull base neoplasms. This can be realized by hyperextension of the neck, either in supine or prone position, and tilting the gantry to a position perpendicular to the hard palate.

4.1.2 Contrast-Agent Injection

While evaluating a patient suffering head and neck cancer, a proper injection method of iodinated contrast agent is crucial to obtain state-of-the art CT-images. Optimal tissue enhancement, allowing correct discrimination of tumoral from normal tissue, and a high neck vessel density must be realized at the same time. Several contrast-agent injection protocols have been described, some of them being fairly

complicated. For all practical purposes, a single bolus technique with an injection rate of 1–2 cc/s is appropriate on modern CT machines (Keberle et al. 2002). A total amount of 100 ml is sufficient in MDCT; a somewhat higher volume (up to 150 ml) may be required when an incremental or single-slice spiral CT technique is used.

It is essential to wait long enough before starting the acquisition, as the contrast agents need some time to diffuse in the normal and pathologic soft tissues. If re-angulation of the gantry at the oral level is performed (see below), the contrast injection needs not to be paused while changing the gantry angle. If one uses an MDCT-machine, allowing a rapid entire neck examination without gantry angulation, the scan should be started only after injection of the entire contrast volume. A subsequent saline injection at the same injection rate is recommended. The contrast-agent injection protocol for evaluation of the head and neck, as currently used in Leuven is: 1.5 cc/s contrast agent up to 100 ml, followed by 30 ml saline at the same rate; image acquisition starts 80 s after initiation of the injection.

4.1.3 Data Acquisition and Image Reconstruction

4.1.3.1 General Comments

On a lateral scout view, the area of interest is indicated. For a routine head and neck imaging study, images are acquired from the top of the sphenoid sinus to the lower border of the sternoclavicular joints. It makes sense to scan from cranial to caudal: this allows the contrast medium concentration in the subclavian vein, at the side of injection, to drop to a similar or only slightly higher level compared to other neck vessels, reducing artifacts at the level of the thoracic inlet.

When performing a routine study of the face, sinonasal region or skull base, images are acquired from the top of the frontal sinus to the submental region.

The field of view (FOV) must be as small as possible, to optimize spatial resolution. The recommended FOV for neck studies varies between 16 and 20 cm, depending on the size of the patient. The selected FOV also depends on the type of pathology: in a study performed for squamous cell cancer, the posterior part of the perivertebral space not necessarily needs to be included in the FOV as it is unlikely to encounter pathology in that region; however, for example in skin cancer and lymphoma, this part of the neck should also be visualized, as (sub) occipital adenopathies may be present.

The optimal display slice thickness for evaluation of neck structures is 3 mm; adjacent slices should be obtained. Somewhat thinner slices (2 mm) are apt for the evaluation of the facial bones, sinonasal cavities and orbits. In laryngeal and hypopharyngeal neoplasms, it is useful to reconstruct an additional series of images coned down to the laryngohypopharyngeal region, with a FOV of about 10 cm and a slice thickness of 2 mm. Also the evaluation of the temporal bone requires a coned down FOV (about 9 cm), and a thin slice thickness of 0.5–1 mm.

Image reconstruction is always done in a soft tissue algorithm. Additional images, reconstructed in a high-resolution (bone detail) algorithm, are always generated in sinonasal cavity, skull base and temporal bone studies.

In patients suffering neoplastic disease, the lower slices including the upper part of the lungs should also be reviewed in lung window, as unknown metastatic disease or second primary tumors may then become visible.

4.1.3.2 Incremental CT and Single-Slice Spiral CT

Even in this era of MDCT, studies of acceptable quality can be obtained using an incremental or single-slice spiral CT technique. The disadvantage of these techniques is the compromise that has to be made between slice thickness and acquisition time. As these techniques do not allow obtaining very high quality reformattings from the native images, the gantry angle should be changed at the mouth level. From the skull base down to the oral cavity, the image plane should be parallel to the hard palate, while from the oral cavity down to the thoracic inlet, the image plane should be parallel to the vocal cords. The vocal cord plane sometimes can be recognized on the lateral scout views; if this cannot be seen, the gantry should be tilted parallel to the intervertebral disk space at the level of C4–C5 or C5–C6. Adherence to this protocol generates images reproducibly showing head and neck anatomy; furthermore, dental filling artifacts are avoided at the level of the oral cavity.

The CT examination is performed as contiguous 3 mm thick scans, or as a spiral study reconstructed as contiguous 3 mm sections. The spiral technique uses 3 mm thick scans with a 3-5 mm/s table speed, and a

pitch of 1:1–1:1.6; these parameters may vary slightly according to the CT machine.

4.1.3.3 Multidetector Spiral CT

State-of-the-art CT of the head and neck requires the use of MDCT. The rapid acquisition results in a volumetric data set, reconstructed to a stack of thin and overlapping native images; this reduces partial volume averaging and motion artifacts. Furthermore, full advantage of the injected contrast agent is accomplished by optimal timing between injection and image acquisition. Disadvantage of this technique is the overall higher radiation exposure.

The native images cannot routinely be used for display: the large amount of native images is difficult to handle, and the signal/noise level of these images is relatively low. Therefore, a new set of images needs to be reformatted from these native images for display. These images are routinely reformatted in the axial plane, mimicking the image display as it is obtained in incremental or single-slice spiral CT: for neck studies, adjacent 3 mm thick images are reformatted parallel to the hard palate from the skull base to the oral cavity, and parallel to the vocal cords from the oral cavity to the thoracic inlet (Fig. 4). Reformatting in other planes and/or with a thinner slice thickness is done according to the organ of interest (see above) and/or the findings on the axial images (Fig. 5).

The data acquisition with MDCT is usually done with zero gantry tilt. However, in some patients, this causes problems at the level of the oral cavity when dental fillings are present. Also, in patients with short necks or a high position of the shoulders, the image quality may be suboptimal at the level of the larynx due to artifacts arising from the shoulder girdle. To avoid these problems, some head and neck radiologists continue to use gantry tilting in MDCT, as described for the incremental and single-slice spiral CT technique, although this makes it impossible to obtain reformatted images in the coronal or sagittal plane at the level of the oral cavity. An alternative is to perform a complete head and neck study without gantry tilt, and acquire additional images the level of the oral cavity and oropharynx, if dental filling artefacts are present, with a tilted gantry (Fig. 6). Yet another solution is to obtain additional images with the mouth widely opened; this may bring the pathology out of the dental filling artifacts (Fig. 7) (Henrot et al. 2003).

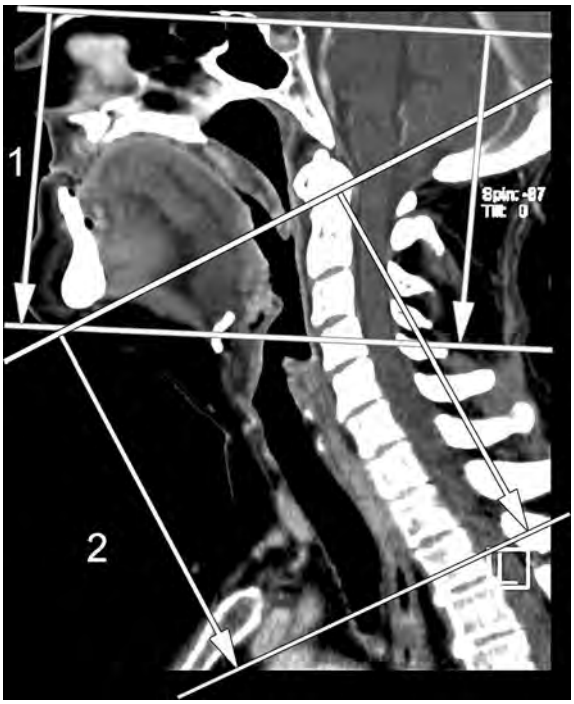

Fig. 4 Routine head and neck CT-study. Midline sagitally reformatted image from native axial MDCT-images. The data acquisition extended from just above the sphenoid sinus to the thoracic inlet. From the native images, two sets of axial images are routinely reformatted for display: the first set (1), parallel to the hard palate, from the skull base to the lower margin of the mandible; the second set (2), parallel to the vocal cords (or C4–C5/C5–C6 intervertebral space), from the oral cavity to the thoracic cavity. The two image sets should be overlapping

More technical details on the MDCT-parameters used currently in the University Hospitals of Leuven are summarized in Table 1 and 2.

4.1.4 Dynamic Maneuvers

The data acquisition is routinely performed while the patient continues breathing. Dynamic maneuvers during scanning can improve the visualization of particular anatomic structures. During prolonged phonation of [i], arytenoid mobility can be judged and a better visualization of the laryngeal ventricle can be achieved; the slight distention of the pyriform sinuses may also allow better delineation of the aryepiglottic folds (Lell et al. 2004). A modified Valsalva maneuver (blowing air against closed lips, puffing out the cheeks) produces substantial dilatation of the hypopharynx, allowing better visualization of the pyriform sinuses, including the postcricoid region (Robert et al. 1993) (Fig. 8).

Fig. 5 **a** Axial MDCT-image (3 mm thick) shows lymph node on right side, appearing centrally hypodense (*arrowhead*): central necrosis or partial volume averaging of fatty nodal hilum? **b** Additionally, a thinner (1.5 mm) reformatting was made through this lymph node in the coronal plane. On this section, the hypodense nodal region shows fat density and communicates with the outer nodal border: fatty metaplasia in nodal hilum. Normal lymph node

This modified Valsalva maneuver may also be of use in the evaluation of oral cavity tumors, as the inner cheek walls and gingivobuccal sulci become better visible.

The success rate of these dynamic maneuvers is variable, especially when an incremental CT technique is used, and is strongly depending on the cooperation of the patient. These problems are largely overcome by MDCT, as the patient has to perform the maneuver only once during one rapid acquisition.

Dynamic maneuvers are mainly helpful in showing superficial tumor spread, while the purpose of imaging is describing deep tumor extent. Also, abnormal mobility of the vocal cord is more accurately seen during clinical examination than on dynamic imaging studies. Therefore, the added value of acquiring images during a dynamic maneuver in staging head and neck neoplasms is, on average, limited.

4.1.5 Three-Dimensional Image Reformatting

Three-dimensional (3D) display of the data set is most often done to evaluate the bony structures of the maxillofacial skeleton in congenital abnormalities or traumatic lesions. Meaningful 3D display of the often subtle osteolytic changes seen in head and neck malignancies is rarely possible. However, in some cases of extensive bone destruction, 3D displays are helpful for the surgeon in planning bone resection (Fig. 9).

Virtual endoscopy of the larynx and hypopharynx has been studied; otolaryngologists rank such 3D images as more beneficial than radiologists, usually in bulky masses that precluded definitive direct endoscopic evaluation (Silverman et al. 1995). This technique does not show the adjacent soft tissues, and its clinical role is not exactly defined (Magnano et al. 2005).

4.2 Magnetic Resonance Imaging

MRI of the head and neck can be performed on low-field or high-field machines. At comparable measuring time, the high-field (≥1.5T) machines provide a better signal-to-noise ratio and a higher spatial resolution. Currently, the experience on 3T systems regarding the investigation of head and neck tumors is steadily increasing.

4.2.1 Patient Positioning

Similar to CT, the image acquisition is performed with the patient in supine position, and during quiet respiration. The head and neck should be aligned and symmetrically positioned. Every effort should be

Fig. 6 Axial MDCT-image at level of oral cavity and oropharynx, obtained with a zero degree gantry tilt (**a**), is severely degraded by artifacts arising from dental fillings. By obtaining additional images with angulation of the gantry around the dental fillings (**b**), optimal image quality could be achieved at this level (**c**, **d**). (Courtesy of Ilona Schmalfuss, MD, Gainesville, Fl, USA)

made to make the patient feel as comfortable as possible. The patient should be instructed not to move during the examination, and to try not to cough during the image acquisition. The patient should not be prohibited to swallow as this is hardly feasible in clinical practice as the imaging sequences take several minutes each.

4.2.2 Coils

The choice of the receiver coil is dictated by the localization of the disease process. If the tumor is localized in the oral cavity or infrahyoid part of the neck, the neck coil should be used. When the patient suffers neoplastic disease at the level of the skull base, sinonasal cavities, face, parotid glands or nasopharynx, the head coil should be selected. A disadvantage of using a single receive coil however is the inability to cover the entire neck for evaluation of nodal stations.

This may be of particular importance in nasopharyngeal, tongue or oropharyngeal cancer which are frequently associated with adenopathies throughout the neck. Modern machines, at field strengths of 1.5 and 3 T, allow to image the entire head and neck, either by a combination of a standard head coil and 2-channel dedicated surface coil or an integrated head-neck coil of 12 or more coil elements.

A possible drawback of combining head and neck coils is that both coils have a distinctive coil design, inducing heterogenous recipient field characteristics at the crossover between the two coils, which translates into local signal loss, distortion and heterogeneous incomplete fat saturation. This drawback can be partially

Fig. 7 Patient suffering cancer of the lateral tongue edge. **a**, **b** Sagittal and axial reformatted CT-image, obtained after a standard MDCT acquition with closed mouth (**a**). This study did not show the extent of the primary tumor because of dental filling artifacts (**b**). Tilting the gantry would not have solved the problem in this patient, as the dental fillings are close to the tumor. **c**, **d** Because of a contra-indication for MRI, an additional CT-study was performed with the mouth of the patient widely opened (**c**). This brings the region of the tongue tumor (**d**, *arrowheads*) out of the dental filling artifacts

overcome by meticulous shimming, coil and patient position and the use of sequences with short echo-trains. As such, an integrated head-neck coil that provides a homogeneous pattern of full receiver coil coverage with a high signal-to-noise ratio and minimized artifacts is preferred for imaging of the entire head and neck.

4.2.3 Standard Sequences

After obtaining scout images, a standard examination of the head and neck should start with a T2-weighted turbo spin-echo (TSE) sequence. Compared to a conventional T2-weighted spin-echo (SE) sequence, a TSE sequence takes less time to perform, reducing motion artifacts and improving image quality. However, the high signal intensity of fat on a T2-weighted TSE sequence can be a disadvantage, as this may reduce the contrast between a tumor and the surrounding tissues. The contrast can be improved by performing the sequence with either a chemical shift-moderated fat suppression technique (chemical shift-selective fat suppression or water-selective excitation) or by applying an additional inversion recovery preparation pulse with a short inversion time (SPIR, SPAIR, STIR).

The high signal intensity of fat and bone marrow on a plain T1-weighted SE or TSE sequence is often very helpful to determine tumor extent, as it contrasts clearly with the low signal intensity of most tumors. Repetition of this sequence after injection of gadolinium-DTPA, and comparison with the pre-injection sequence, allows to determine the areas of contrast-enhancement and to differentiate these areas from fat.

A fat-saturated T1-weighted SE sequence after injection of gadolinium-DTPA may be helpful, as the contrast between enhancing tissue and fat is increased, but at the cost of some more susceptibility artifacts and a longer acquisition time.

Table 1 MDCT data acquisition and native image reconstruction parameters

		16-row	64-row	128- row
Neck[a] Face[b] Sinonasal cavities[b]	Collimation	16 × 0.75 mm	64 × 0.6 mm	128 × 0.6 mm
	Feed/rotation	10.2	17.3 mm	30.7 mm
	Rotation time	1 s	1 s	1 s
	kV	120	120	120
	mAs_{eff}	250[c]	250[c]	230[c]
	$slice_{eff}$	1 mm	1 mm	1 mm
	slice interval	0.7 mm	0.7 mm	0.5 mm
Temporal bone[b] Skull base[b]	Collimation	2 × 0.6 mm	12 × 0.3 mm	16 × 0.3 mm
	Feed/rotation	1.2 mm	1.8 mm	4 mm
	Rotation time	1 s	1 s	1 s
	kV	140	140	140
	mAs_{eff}	220	260	240
	$slice_{eff}$	0.6 mm	0.6 mm	0.4 mm
	slice interval	0.2 mm	0.2 mm	0.2 mm

mAs_{eff} = effective mAs
$slice_{eff}$ = effective slice thickness
[a] soft tissue algorithm
[b] both soft tissue and bone detail algorithm in tumoral pathology
[c] effectively used mAs may be lower (determined by automatic exposure control system)

Table 2 MDCT-image reformatting for display

	Slice thickness	Slice interval	Image plane
Neck	3 mm	3 mm	Axial + coronal + sagittal
Face, sinonasal cavities, skull base (soft tissue detail)	2 mm	2 mm	Axial + coronal + sagittal
Temporal bone, skull base (bone detail)	0.8 mm	1	Axial + coronal (sagittal if needed)

Depending on the investigated region, a slice thickness of 3–4 mm is optimal, with an interslice gap of 0–50%. The FOV is similar to what is described above for CT. The imaging matrix should be at least 256 × 256, but in recent years more often a base matrix of 384 or 512 is advocated, especially for lesions in and around the skull base and sinonasal cavities.

The plane of section is chosen according to the localization of the disease process. For most neck lesions, it is appropriate to start with a T2- and T1-weighted sequence in the axial plane, and to continue with a gadolinium-enhanced axial, coronal and sagittal T1-weighted sequence. In general, the axial plane should be, similar as for CT, parallel with the hard palate when dealing with suprahyoid pathology, and parallel with the vocal cords when dealing with infrahyoid pathology. In naso-ethmoidal neoplasms, it may be more useful to start the study with a coronal T2- and T1-weighted sequence, in order to better evaluate potential spread to the anterior cranial fossa.

The use of very fast imaging such as single-shot techniques is usually not recommended. Single-shot techniques have in general a lower signal-to-noise ratio and are very sensitive to magnetic field inhomogeneities (susceptibility effects). Also, single-shot sequences often yield a somewhat blurred image, impairing visualization of thin structures or making accurate delineations. In case of uncooperative patients or when fast scan time is absolutely required, patient positioning and shimming should be performed with the utmost precision. If patient movement is within limits, a segmented approach, probing the entire k-space into several separate acquisitions and thereby reducing the echo-train length, is preferable to minimize the above-mentioned drawbacks.

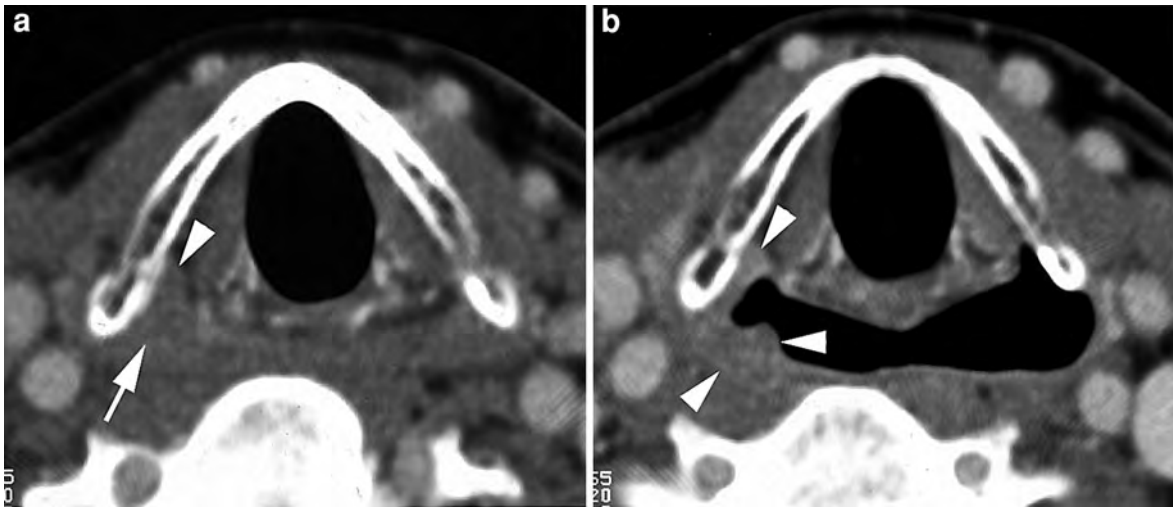

Fig. 8 Contrast-enhanced single-slice spiral CT-images in a patient suffering cancer of the pyriform sinus. **a** Axial image during quiet breathing shows subtle soft tissue thickening in the apex of the right pyriform sinus (*arrow*); some evidence of subtle infiltration or displacement of the paraglottic space fat is present (*arrowhead*). **b** Axial image obtained during modified Valsalva maneuver. The right pyriform sinus expands somewhat less than the opposite one; the mucosal irregularity produced by the cancer is now better visible (*arrowheads*)

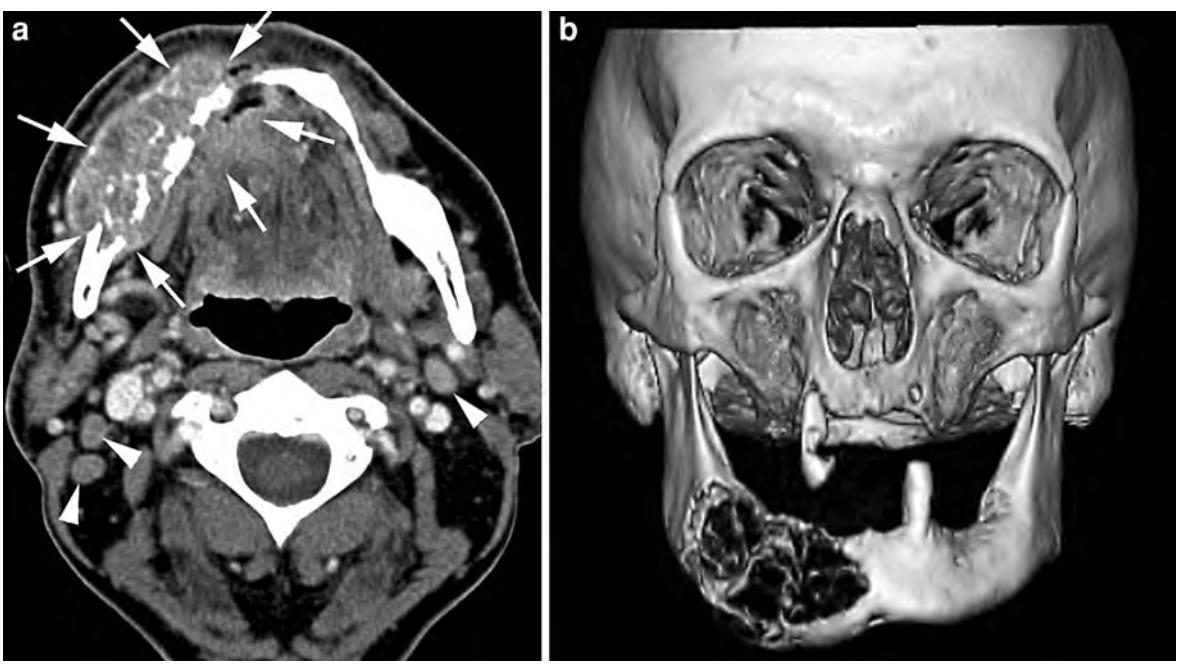

Fig. 9 **a** Axial contrast-enhanced MDCT-image. Large floor of the mouth cancer, massively invading the right side of the mandible (*arrows*). Several small but inhomogenously enhancing adenopathies are visible on both sides of the neck (*arrowheads*). **b** Extent of mandibular bone destruction can easily be appreciated on 3D reformatting

The use of parallel imaging grants the benefit of a reduced scan time with the same image quality, or a comparable scan time but with a better image quality. In practice this means that patient movement artifacts can be reduced and signal-to-noise ratio increased, making parallel imaging an ideal addition to head and neck MR imaging. However, as successful application of the parallel imaging reconstruction algorithm is very dependent on both magnetic field and receiver coil homogeneity, a combined use of several head and neck coils (see above) limits the use of parallel imaging. When using the newer systems with a large number of homogeneous receiver coils, application of parallel imaging is encouraged for comprehensive evaluation of the head and neck area.

Example parameters for head and neck MRI are listed in Table 3.

4.2.4 Contrast Agents

In MR-studies for head and neck neoplasms, obtaining sequences before and after injection of gadolinium-DTPA (at a dose of 0.1–0.2 mmol/kg body weight) is mandatory. Most neoplasms will show increased signal intensity after contrast-agent injection. This will usually increase the contrast between the tumor and the surrounding lesions. However, tumors infiltrating bone marrow may become less well visible after contrast injection, as their signal intensity may become similar to that of the surrounding bone marrow; this problem can be solved by obtaining a fat-suppressed sequence

Table 3 Example parameters for full head and neck examination at **a** 1.5T with combination of head and neck coils and at **b** 3T with integrated head and neck coil

Parameter	Pre-contrast T2-weighted imaging	Pre-contrast diffusion-weighed imaging	Dynamic contrast-enhanced imaging	Pre- and Post-contrast T1-weighted imaging
(*A*) *1.5T*				
Sequence type	T2-weighted Turbo spin-echo (TSE)	Spin-echo echoplanar imaging (SE-EPI)	3D spoiled gradient echo	T1-weighted Turbo spin-echo (TSE)
Field of view (mm)	203 × 250	203 × 250	225 × 300	203 × 250
Matrix	291 × 512	104 × 128	134 × 256	333 × 512
Pixel size (mm)	0.70 × 0.49	1.95 × 1.95	1.68 × 1.17	0.61 × 0.5
Number of slices	48	48	48	30
Slice thickness (mm)	4	4	4.4	4
Interslice gap (mm)	0.4	0.4	0	0
TR/TE (ms)	3,080/106	7,400/84	4.3/1.6	532/8.3
Phase encoding direction	Anteroposterior	Anteroposterior	Anteroposterior	Anteroposterior
Averages	2	3	1	2
Phase partial Fourier	0.875	0.75	0.75	1
Bandwidth (Hz/pixel)	136	1,502	350	195
Turbo factor/echo-train length ()	19	104	–	7
Parallel imaging factor	–	–	–	–
B-values (s/mm^2)	–	0, 50, 100, 500, 750, 1,000	–	–
Saturation	–	Fatsat	–	- (If needed)
Scan time (min:sec)	5:42	6:03	3:29 for 25 measurements	5:11

(continued)

Table 3 continued

Parameter	Pre-contrast T2-weighted imaging	Pre-contrast diffusion-weighed imaging	Dynamic contrast-enhanced imaging	Pre- and Post-contrast T1-weighted imaging
(*B*) *3T*				
Sequence type	T2-weighted Turbo spin-echo (TSE)	Spin-echo echoplanar imaging (SE-EPI)	3D spoiled gradient echo	T1-weighted Turbo spin-echo (TSE)
Field of view (cm)	240 × 220	228 × 190	294 × 395	240 × 220
Matrix	377 × 440	116 × 100	248 × 360	303 × 400
Pixel size (mm)	0.64 × 0.50	1.96 × 1.90	1.19 × 1.10	0.79 × 0.55
Number of slices	54	2 stacks of 28	162	55
Slice thickness (mm)	3.5	4	1.3	3.5
Interslice gap (mm)	0.4	0.4	0	0.35
TR/TE (ms)	4,476/90	5,045/64	3.4/1.65	666/16
Phase encoding direction	Anteroposterior	Anteroposterior	Anteroposterior	Anteroposterior
Averages	2	2	1	2
Phase partial Fourier	1	0.689	0.625	1
Bandwidth (Hz/pixel)	194	2,896	1,206	196
Turbo factor/ echo-train length ()	24	61	–	7
Parallel imaging factor	2	2	2	3
B-values (s/mm^2)	–	0, 50, 100, 500, 750, 1,000	–	–
Saturation	–	Short tau inversion recovery (STIR)	Spectral selection attenuated inversion recovery (SPAIR)	- (If needed)
Scan time (min:sec)	3:48	2 × 2:47	3:15 for 20 measurements	3:39

(see above). Tumor necrosis becomes better visible after injection of gadolinium; this is of particular importance in staging the neck nodes (see "Neck Nodal Disease").

Ultra-small superparamagnetic iron oxide (USPIO) particles are captured by macrophages in normally functioning lymph nodes. As a result, signal intensity reduction is observed in tissues accumulating these particles because of the susceptibility effects of iron oxide. Metastatic lymph nodes show a hyperintensity on sequences weighted to these effects. Some promising results have been obtained in the head and neck, but technical problems regarding motion, susceptibility artifacts and spatial resolution still need to be solved (Sigal et al. 2002).

4.2.5 Additional MRI Techniques

Although defining the extent of the primary tumor is often possible based on anatomical criteria, identification of small nodal metastasis remains challenging. Also the distinction of post-therapeutic tissue changes from residual tumor may be difficult. In recent years, progress has been made in the application

of functional MRI in head and neck imaging (Vandecaveye et al. 2010).

While the clinical application of MR-spectroscopy (MRS) remains challenging, dynamic contrast-enhanced MRI (DCE-MRI) and diffusion-weighted MRI (DWI) can now be used as complementary imaging tools in the locoregional imaging evaluation of head and neck cancer.

4.2.5.1 Dynamic Contrast-Enhanced Magnetic Resonance Imaging

The tumoral vascular network is substantially different from a morphological and functional point of view compared to normal blood vessels, resulting in a heterogeneous blood flow, with increased capillary permeability (Carmeliet and Jain 2000).

DCE-MRI uses serial imaging with high temporal resolution over a lesion or anatomical area prior to, during and after the bolus injection of a gadolinium-based contrast agent to depict the perfusion properties of tumoral lesions. For head and neck imaging, a T1-weighted gradient-echo sequence is usually preferred over T2*-based dynamic susceptibility contrast MRI (DSC-MRI). Compared with DSC-MRI, DCE-MRI requires less contrast agent and is far less prone to susceptibility artifacts. Most importantly, the signal intensity changes caused by the contrast agent are much slower than in DSC-MRI, and therefore a lower time resolution is allowed (around 4–8 s/volume), providing the opportunity to obtain larger anatomical coverage and higher spatial resolution images, while retaining perfusion information (Fig. 10). Also, the positive contrast enhancement used in the T1-weighted DCE-MRI allows more easy lesion identification compared to the negative contrast-enhancement of the T2*-weighted DSC-MRI.

In both normal and tumoral tissue, the injected contrast will leak from the vessels into the interstitial space with a variable rate and will start to wash out when the interstitial concentration exceeds the intravascular concentration. The main parameters influencing this rate of interstitial contrast leakage are contrast inflow into the tissue, vessel wall permeability and the total vessel surface area (Padhani 2003).

The signal intensity curve, obtained from the consecutive sequences over time, holds information about tumor perfusion, tracer uptake and blood volume. After the contrast injection, the enhancement pattern will typically consist of three phases: the upslope or rapid arterial enhancement, the point of maximum enhancement and delayed washout. The dynamic signal enhancement on T1-weighted DCE-MRI can be assessed by semi-quantitative evaluation of the signal intensity curve or by quantification of the change of contrast-agent concentration using pharmacokinetic modeling techniques. Semi-quantitative parameters evaluate discrete points of the signal intensity curve while ignoring the information in the rest of the curve; these include the maximal contrast-enhancement, time to maximal contrast-enhancement (time to peak) and the speed of arterial contrast-enhancement (initial slope) (Fig. 10). Their main advantage is their robustness, facilitating their use in clinical routine, although it should be kept in mind that semi-quantitative parameters do not reflect contrast medium concentration in tissues and may show variability because of scanner settings and differences in interpatient cardiovascular physiology (Padhani 2003). Therefore, in order to decrease intra- and interpatient variability during treatment follow-up, normalization of contrast-uptake may be done by analyzing contrast-enhancement in a feeding artery and normalizing the tissue measurements to this arterial input function (AIF) (Port et al. 2001).

For quantitative analysis, the entire contrast-time-curve is fitted by a curve model based on biological assumptions, such as blood volume, blood flow or permeability. Quantitative parameters that are investigated include the volume transfer constant of the contrast agent (K^{trans}) and the rate constant (k_{ep}), which are calculated based on a two compartment model correlating the tissue tracer concentration to the difference between arterial plasma and interstitial fluid concentrations (Tofts and Kermode 1991). These parameters have the advantage that they show closer correlation to underlying biologic processes of the vasculature, such as the permeability surface area and flow. However, quantified models are more complex to analyze, less robust and more susceptible to artifacting, making them more difficult to use in clinical routine.

An intermediate solution to quantify perfusion is the use of the initial area under the signal intensity curve (IAUC) or contrast medium concentration curve (IAUGC) (Padhani 2003).

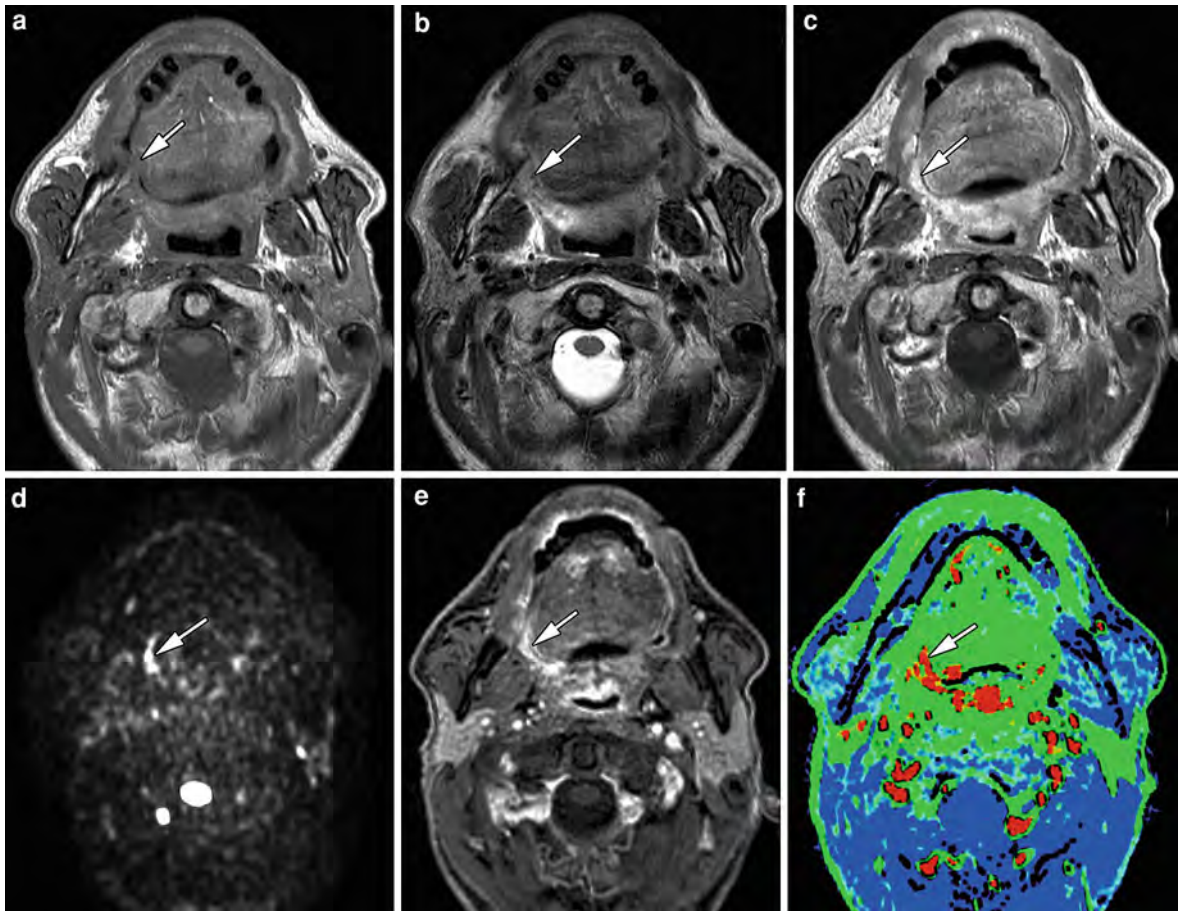

Fig. 10 Patient with persistent pain in the right oropharyngeal area, 4 months after end of chemoradiotherapy for a base of tongue cancer. T1-weighted (**a**), T2-weighted (**b**) and contrast-enhanced T1-weighted spin-echo sequence (**c**) show some soft tissue thickening in the right glossotonsillar sulcus and anterior tonsillar pillar (*arrow*). B1000 diffusion-weighted weighted image (**d**) shows hyperintensity in this area, while the native dynamic contrast-enhanced image (**e**) and corresponding perfusion map (*initial slope*, **f**) indicate hypervascularity (*arrows*). These findings are suspect for persistent or recurrent tumor. Histopathology after surgical resection confirmed presence of squamous cell carcinoma

4.2.5.2 Diffusion-Weighted Magnetic Resonance Imaging

DWI allows for tissue characterization based on changes in the random movement of tissue water molecules (Le Bihan et al. 1988). In solid malignant tumors, the high cellular density, intact cellular membranes and diminished extravascular extracellular space (EES), restricts the random movement of water (Fig. 10). Contrary, in necrosis and inflammation, the low cellular density and increased EES facilitates the random water movement.

Spin-echo EPI-based DWI (SE-EPI-DWI) is most frequently used for imaging of head and neck cancer. The major advantage of an EPI readout sequence is the inherent rapidity as it is a single-shot sequence without the need for refocusing radiofrequency pulses. This allows to scan relatively large volumes with multiple b-values in a short time period, making the technique suitable for the simultaneous evaluation of the primary tumor site and all nodal stations in the head and neck (Vandecaveye et al. 2010). As a drawback, SE-EPI-DWI is highly sensitive to susceptibility artifacts, possibly reducing diagnostic quality. Single-shot turbo spin-echo (SS-TSE)-DWI may be considered as an alternative sequence for EPI-DWI, as this sequence lacks these kinds of artifacts (De Foer et al. 2008). However, because of the inherent need of 180° spin-echo pulses, SS-TSE-DWI

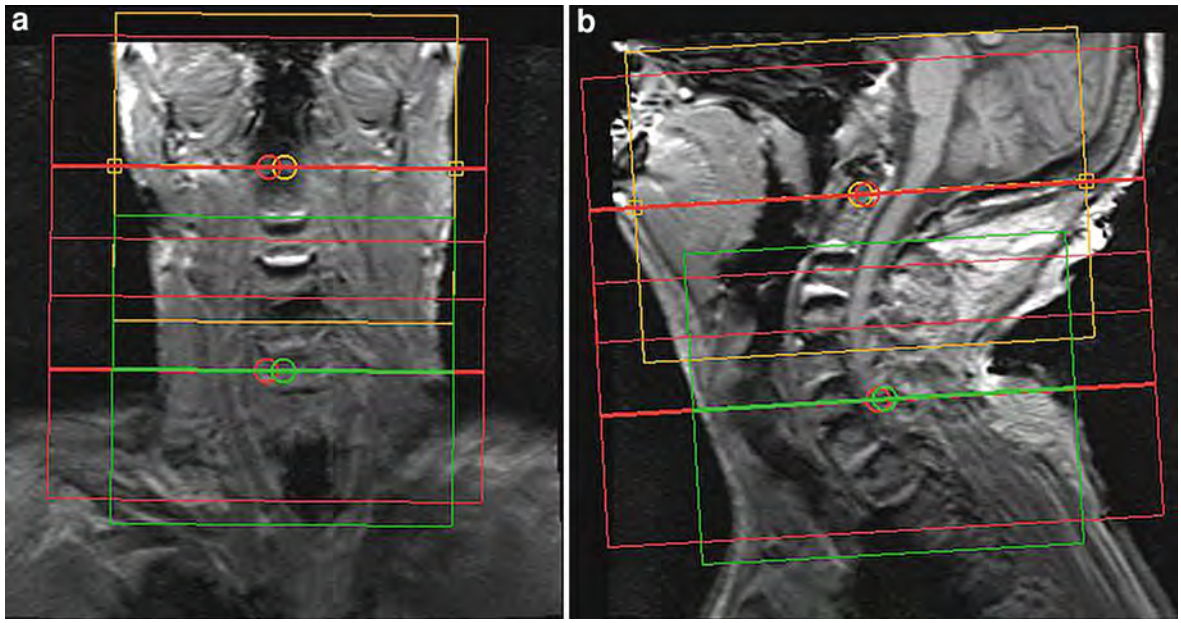

Fig. 11 Localizer image in the coronal (**a**) and sagittal plane (**b**), obtained on a 3T system. The imaging volumes (*red boxes*) are divided into two sub-volumes, respectively extending from the skull base to the level of the hyoid and from the hyoid to the thoracic inlet. Shim boxes (*green box and orange box*) have been adapted in the phase encoding direction, excluding the air around the head and neck

is limited by a high specific absorption rate (SAR), and is time consuming; therefore it cannot be used for screening of the entire neck or for examinations that require the inclusion of multiple b-values. Additionally, the higher echo time (TE) of SS-TSE-DWI compared to SE-EPI-DWI leads to an unfavorable SNR making the detection of tumoral lesions more difficult. Therefore, SS-TSE-DWI is only useful for evaluation of a limited anatomical area, where susceptibility artifacts make the application of SE-EPI-DWI nearly impossible.

Because of the sensitivity of DWI to artifacts, a number of technical optimizations are pivotal to preserve diagnostic imaging quality. First, it is important that the shortest possible TE is selected, maximizing the signal-to-noise ratio, and minimizing susceptibility and fat-shift artifacts. This requires the scanner to be equipped by a strong gradient system and the use of a high bandwidth. Second, one should rather not use unrealistically high DW imaging matrices, as this increases the echo-train length, introducing T2* and susceptibility artifacts. In most clinical settings, an imaging matrix of 128 is sufficient, although in low-susceptibility areas it can be increased up to 192. The third and most important issue concerns positioning of the shim block, which should be placed manually instead of using the automatic shim leading to a strong decrease of distortion artifacts (Fig. 11). Currently, no uniform guidelines exist to optimize shimming, but usually, the shim should be tailored around the total head and neck, excluding large areas of air surrounding the neck at 3T MR-systems. At 1.5T MR-systems, or when using a combination of a standard head coil and 2-channel dedicated surface coil, the shim box should only cover the spine and deep muscles of the neck, while excluding as much as possible any moving or air-containing structures.

Finally, when DWI needs to cover the entire head and neck, the imaging volume can be subdivided into two separate but spatially linked scan volumes; one extending from the skull base down to the level of the hyoid, and the second one extending further down to the aortic arch. This allows closer positioning of each imaging stack to the isocenter of the magnet, minimizing geometric distortion and failed fat suppression at the slices further away from the isocenter.

DWI can be evaluated in a qualitative and quantitative way. Qualitative analysis using DWI at a single high b-value (usually b = 1000 s/mm^2) offers

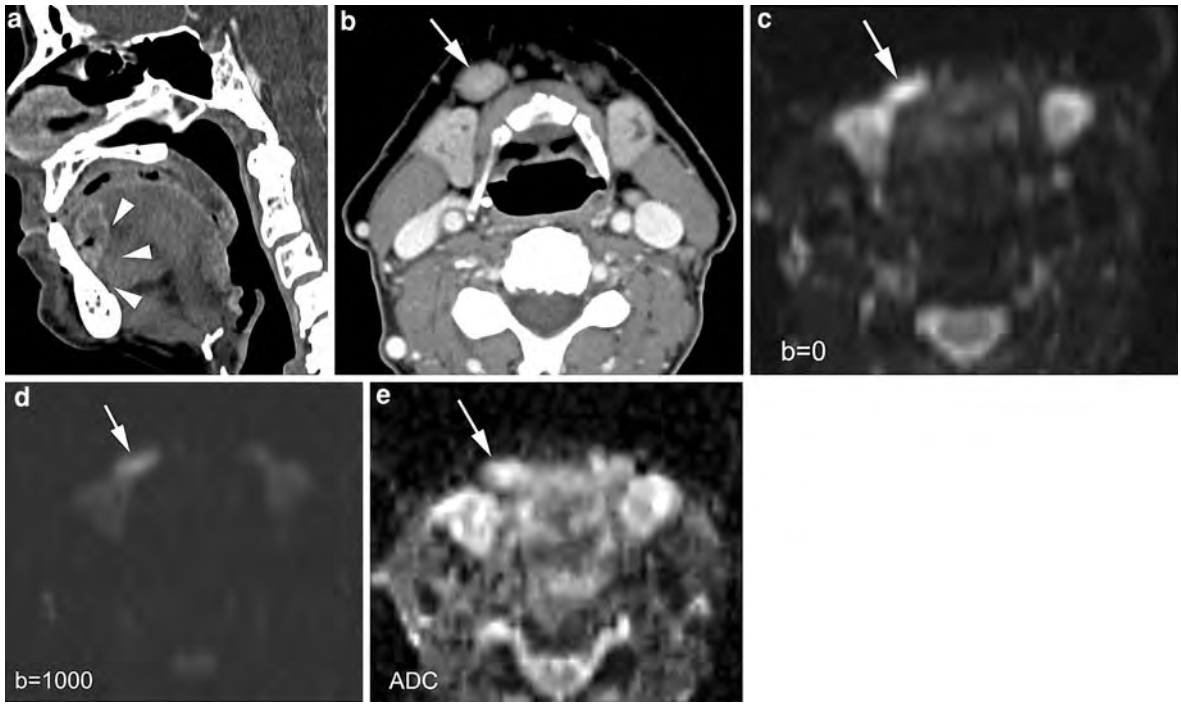

Fig. 12 Patient suffering floor of the mouth cancer. **a** Sagittal contrast-enhanced MDCT-image shows primary tumor at the junction of the floor of the mouth and oral tongue (*arrowheads*). **b** Axial MDCT-image. Slightly enlarged lymph node (minimal axial diameter 12 mm) in the submandibular region (*arrow*): suspect for metastatic adenopathy. **c**–**e** Axial diffusion-weighted MR-images. Compared to the b = 0 image (**c**), the signal clearly reduced in the adenopathy (*arrow*) on the b = 1000 image (**d**), indicating easy diffusion of water protons. The ADC-map (**e**) shows a relative high signal (ADC >0.00130 mm^2/s). These findings are consistent with a benign adenopathy. After neck dissection, histologically no tumor was found in this lymph node

high sensitivity for detection of tumoral disease but has relatively low specificity (Takahara et al. 2004). Such images can be used for the rapid depistation of potentially tumoral localizations. However, DWI-based tissue characterization, especially of lymph nodes, often requires additional calculation of the apparent diffusion coefficient (ADC) (Fig. 12).

In head and neck DWI, 3 up to 6 b-values ranging from 0 to 1000 s/mm^2 are preferentially used. The large number of b-values improves the accuracy of the ADC-calculation, by minimizing the influence of movement and noise propagation. Also, in highly vascular tumors, the addition of non-zero low b-values can be used to eliminate vascular contributions that may falsely increase ADC values by an additional but variable influence of microperfusion (Thoeny et al. 2005). A DWI-sequence with six b-values and 4 mm slice thickness typically takes around 5 min on a 1.5 Tesla system, and around 3 min on a 3 Tesla system.

5 Nuclear Imaging

5.1 Physical Aspects

Positron emission tomography (PET) allows evaluation of the biodistribution of small amounts of positron-emitting radiopharmaceuticals and is considered the most sensitive and specific technique for in vivo imaging of metabolic pathways and receptor−ligand interactions in the tissues of men (Jones 1996). PET uses radioisotopes of natural elements, such as oxygen-15, carbon-11, nitrogen-13 and fluorine-18, which can be used for labeling of most biomolecules, without altering their biochemical properties.

Positron-emitting isotopes decay by emission of a positron, which is the positively charged antiparticle of the electron. Positrons are formed during the decay of nuclides that have a large number of protons in their nuclei compared with the number of neutrons,

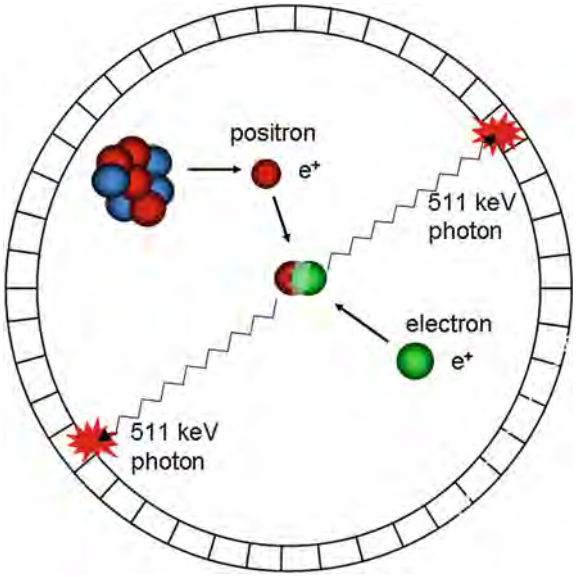

Fig. 13 After the decay of a positron-emitting radioisotope, the positron annihilates with an electron, resulting in the creation of two annihilation photons, each having an energy of 511 keV. In a PET camera, a large number of detectors are installed in a ring-shaped pattern around the patient, enabling the simultaneous detection of the opposed photons within a narrow time-window, the so-called "coincidence detection"

which makes them unstable. After its emission, the positron travels a short distance until it annihilates with an electron. In this process, the positron and electron masses are converted into 2 photons that travel apart in nearly opposite directions (180°) with an energy of 511 keV each (Fig. 13). PET tomographs are designed to detect these photon pairs and to reconstruct tomographic images of the regional tracer distribution. Detector pairs are installed in a ring-shaped pattern for the detection of the opposed photons within a narrow time-window, enabling the so-called "coincidence detection". Because of this "electronic" collimation, PET does not require collimators as they are necessary in single photon measurements with gamma cameras. This results in a significantly higher sensitivity of PET compared to SPECT. The sensitivity of PET can be further improved by adding extra detector rings, increasing the axial coverage (Townsend 2008). Compared with SPECT, PET has a relatively high spatial resolution of 4–6 mm. Recent PET cameras are equipped with detectors of smaller size, enabling the detection of smaller lesions which is particularly important in patients with head and neck cancer. However, the physics of PET impose certain well-known limitations on the spatial, temporal and contrast resolution that can be attained in a particular situation. Both the range the positron travels until annihilation and the residual momentum of the positron–electron pair degrade the spatial resolution and will limit the resolution of future whole body PET cameras to approximately 2 mm.

5.2 Radiopharmaceuticals

5.2.1 ^{18}Fluorodeoxyglucose

The tracer most commonly used worldwide is Fluorine-18-labeled 2-fluoro-2-deoxy-D-glucose, [^{18}F]FDG. This is a D-glucose molecule in which a hydroxyl group in the 2-position is replaced by a positron-emitting ^{18}F. Several decades ago, Warburg et al. described the higher rate of glucose metabolism in cancer cells compared to non-malignant tissue (Warburg 1956). After malignant transformation, there is an increased expression of epithelial glucose transporter proteins and an up-regulation of hexokinase activity. After intravenous injection, FDG distributes throughout the body in proportion to glucose metabolism of tissues. Glucose transporters facilitate FDG uptake in tumor cells and hexokinase subsequently phosphorylates FDG to FDG-6-phosphate. FDG-6-phosphate is not metabolized in the glycolytic pathway because it lacks a hydroxyl group in position-2. As most tumor cells do not contain significant amounts of glucose-6-phosphatase, FDG-6-phosphate will accumulate in the cell, resulting in the so-called "metabolic trapping" (Fig. 14) (Pauwels et al. 1998).

It has been demonstrated that increased FDG uptake by malignant cells, although a function of the proliferative activity, is mainly related to the number of viable tumor cells (Higashi et al. 1993). However, some benign tumors can also consume considerable amounts of glucose, as can be seen in Warthin tumors of the parotid gland. In addition, inflammatory tissue may exhibit an increased FDG uptake due to glycolytic activity in neutrophils, eosinophils, macrophages and proliferating fibroblasts, to a degree sometimes more marked than in malignant cells, resulting in a false positive FDG-signal (Kubota et al. 1992). This can be a problem in the field of therapy monitoring, where posttreatment inflammation may raise the overall FDG uptake, causing an

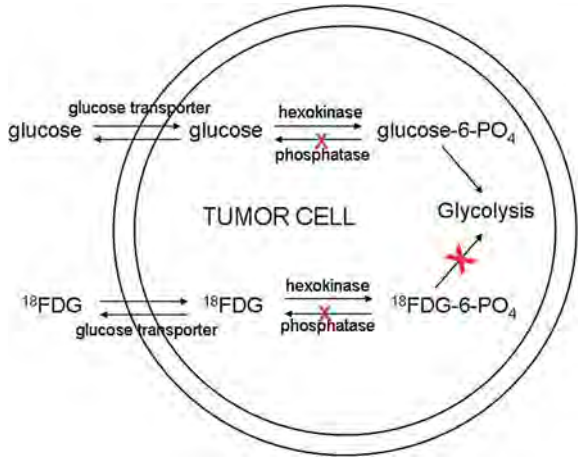

Fig. 14 Uptake kinetics of glucose and FDG in a tumor cell. Glucose transporters facilitate FDG uptake in tumor cells and hexokinase subsequently phosphorylates FDG. The phosphorylated product FDG-6-phosphate is not metabolized in the glycolytic pathway and the activity of glucose-6-phosphatase in tumor tissue is low, resulting in the metabolic trapping of FDG-6-phosphate in the tumor cell

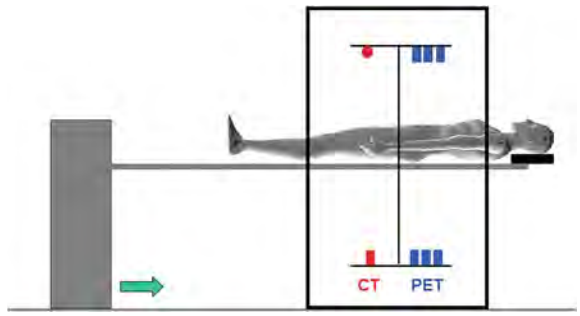

Fig. 15 A schematic design of a modern PET/CT camera, combining a PET camera and a diagnostic CT-scanner within one gantry. A standard whole body FDG-PET/CT protocol is started 60 min after the intravenous injection of FDG and includes a low-dose spiral CT acquisition without contrast, followed by a PET acquisition of the same region and followed by a complementary contrast-enhanced CT-study

underestimation of treatment effectivity and a decrease in the specificity of FDG-PET (Schöder et al. 2009). For this reason FDG-PET after radiotherapy should not be performed before 8–12 weeks after the end of treatment of head and neck tumors. Alternatively, some more tumor-specific tracers have been proposed, which should be less sensitive to inflammatory conditions.

5.2.2 ^{18}Fluorothymidine

^{18}F-labeled fluorothymidine, ^{18}FLT, is utilized in oncology as a marker of cellular proliferation. Thymidine is a native nucleoside, which is used by cells for DNA replication. FLT enters the cell, undergoes phosphorylation by thymidine kinase 1 and is being accumulated in the cytosol instead of being trapped into DNA. Thymidine kinase 1 activity is high in proliferating cells and low in quiescent cells.

5.2.3 ^{18}FET and ^{11}C-MET

Labeled amino acid analogs like ^{18}F-fluoro-ethyl-tyrosine (^{18}FET) and ^{11}C-methionine (^{11}C-MET) have been developed for tumor detection. Increased amino acid metabolism results in an accumulation of amino acids in tumor cells. Compared to FDG, the uptake of amino acids in inflammatory cells is lower.

5.3 Technical Aspects of FDG-PET and Integrated FDG-PET/CT in Head and Neck Cancer

FDG-PET relies on the detection of metabolic alterations in cancer cells, independent of structural features as provided by morphologic imaging techniques like contrast-enhanced CT and MRI. Especially in the post-treatment setting, morphologic imaging modalities have distinct limitations in accurate identification of viable tumor within residual masses, in the identification of small tumor deposits (e.g. in normal-size lymph nodes), and in the characterization of secondary enlarged inflammatory lymph nodes (McCabe and Rubinstein 2005). Postradiation changes and anatomic distortions limit the diagnostic accuracy of these anatomic-based imaging studies in the head and neck region. Since biochemical and cellular changes precede size reduction, there is an increasing interest in reponse imaging in-vivo using molecular imaging with FDG-PET. Moreover, FDG-PET has an advantage over conventional imaging because of its whole body coverage and its sensitivity to distant lesions that may be missed by conventional imaging.

A major limitation of FDG-PET in the neck is the inadequate anatomic information inherent in metabolic imaging. The interpretation of FDG-PET images of the head and neck is particularly difficult because of the presence of multiple sites showing a variable degree of physiological FDG accumulation, such as the salivary glands, lymphoid tissues, muscles and

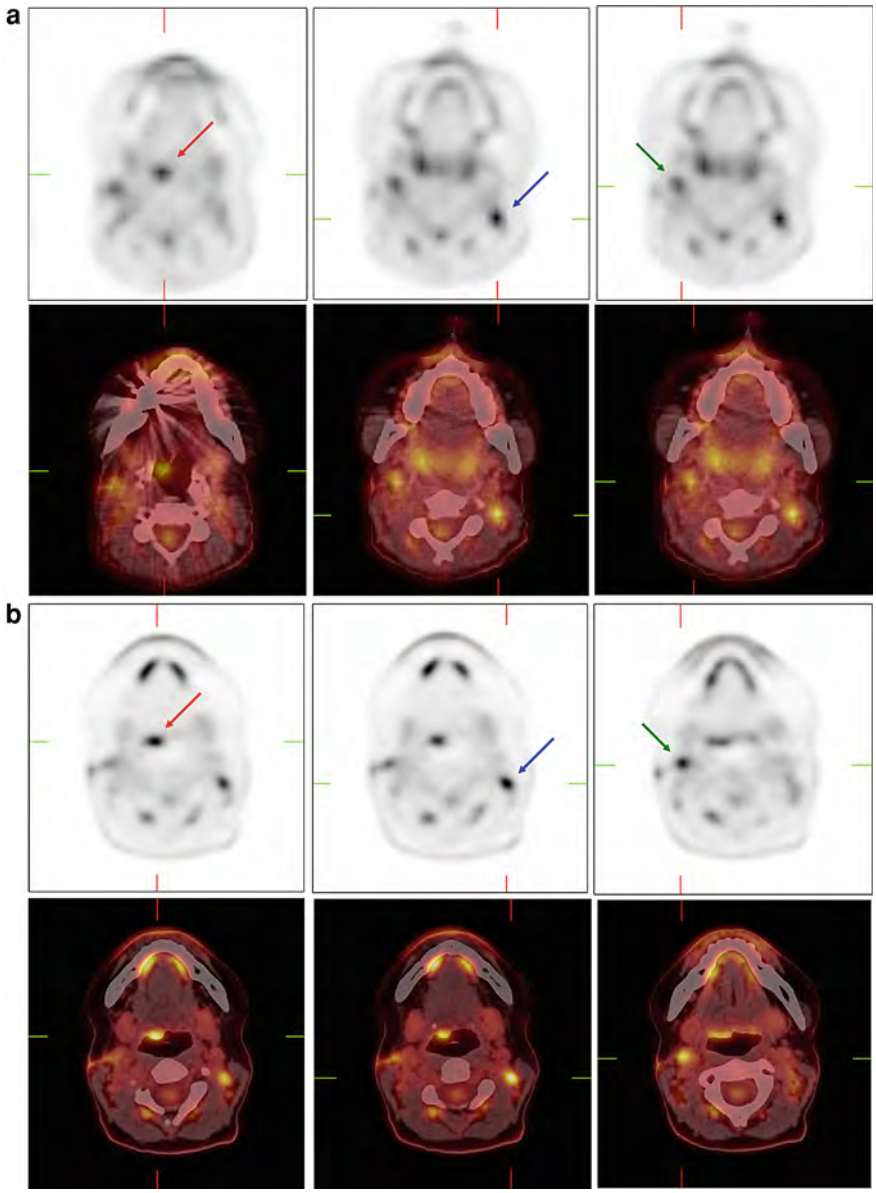

Fig. 16 FDG-PET and fused FDG-PET/CT slices illustrating the improvement in image quality between standard whole body images and dedicated high-resolution head and neck images in a patient with a lymph node positive for squamous cell carcinoma on the right side of the neck, and an unknown primary tumor. **a** Whole body images demonstrate avid FDG uptake at the base of the tongue (*red arrow*) and at both sides of the neck (*blue and green arrows*). Interpretation of these FDG spots is difficult because of CT-related artifacts, insufficient image resolution of both PET and CT, and the presence of FDG uptake in brown fat and muscle. **b** Dedicated head and neck images clearly show the primary tumor at the base of the tongue (*red arrow*) and a positive lymph node at both sides of the neck (*blue and green arrows*). These dedicated fused head and neck images allow easy differentiation between tumor and physiological FDG uptake in brown fat or muscle

brown adipose tissue ("USA-Fat"). The introduction of combined PET/CT scanners has overcome this problem by providing coregistered metabolic and anatomic information (Fig. 15). Combined PET/CT has proven to be more accurate than stand-alone FDG-PET by improving the differentiation between physiologic and pathologic FDG uptake and by providing a more accurate tumor localization, hence reducing the number of equivocal findings (Goshen et al. 2006). In addition, FDG-PET image quality can be improved by instructing patients not to speak during the FDG uptake phase and by pharmacological interventions with diazepam, reducing muscular uptake, or with propranolol, reducing FDG uptake in brown adipose tissue.

Until today, independent of the tumor type, clinically combined PET/CT imaging is usually performed as a whole body imaging tool, which has intrinsic limitations in terms of resolution (affecting sensitivity) and false positive findings (affecting specificity). Moreover, the CT-part of this examination is most often performed as a low-dose non-diagnostic non-contrast CT, which is

sufficient for attenuation correction and anatomic correlation of the PET images, but does not offer the image quality of a diagnostic CT-scan. Hence, this whole body approach using general reconstruction algorithms is less suitable for imaging of a complex and dense anatomic region like the neck. Recent data advocate the use of high-resolution head and neck PET/CT protocols for the detection of small lymph node metastases in the neck (Vogel et al. 2005; Rodrigues et al. 2009). In such a setting, whole body imaging is being performed for the detection of metastatic disease, while dedicated high-resolution head and neck PET/CT imaging is added for the detection of the primary tumor and/or lymph node metastases in the neck. Ideally, dedicated head and neck PET/CT imaging is being perfomed with the arms down (along the side of the patient) and should include a diagnostic CT-scan with the use of intravenous contrast. The PET acquisition and reconstruction parameters should be optimized for the head and neck region and smaller pixels should be used, reducing the partial volume effect which causes an underestimation of FDG activity in all lesions smaller than twice the spatial resolution. These improvements enable to optimize integrated FDG-PET/CT imaging for the detection of small primary tumors and small nodal metastases in the head and neck region (Fig. 16).

Because of further technical improvements and the introduction of newer, more specific radiopharmaceuticals, the role of PET/CT imaging in the management of head and neck tumors is likely to become even more important in the future.

References

Carmeliet P, Jain RK (2000) Angiogenesis in cancer and other diseases. Nature 407:249–257

Curtin HD, Ishwaran H, Mancuso AA et al (1998) Comparison of CT and MR imaging in staging of neck metastases. Radiology 207:123–130

De Foer B, Vercruysse JP, Bernaerts A et al (2008) Detection of postoperative residual cholesteatoma with non-echo-planar diffusion-weighted magnetic resonance imaging. Otol Neurotol 29:513–517

Goshen E, Davidson T, Yahalom R et al (2006) PET/CT in the evaluation of patients with squamous cell cancer of the head and neck. Int J Oral Maxillofac Surg 35:332–336

Henrot P, Blum A, Toussaint B, Troufleau P, Stines J, Roland J (2003) Dynamic maneuvers in local staging of head and neck malignancies with current imaging techniques: principles and clinical applications. Radiographics 23: 1201–1213

Higashi K, Clavo AC, Wahl RL (1993) In vitro assessment of 2-fluoro-2-deoxy-D-glucose, L-methionine and thymidine as agents to monitor the early response of a human adenocarcinoma cell line to radiotherapy. J Nucl Med 34:773–779

Jones T (1996) The imaging science of positron emission tomography. Eur J Nucl Med 23:807–813

Keberle M, Tschammler A, Hahn D (2002) Single-bolus technique for spiral CT of laryngopharyngeal squamous cell carcinoma: comparison of different contrast material volumes, flow rates, and start delays. Radiology 224:171–176

Kubota R, Yamada S, Kubota K et al (1992) Intratumoural distribution of fluorine-18-fluorodeoxyglucose in vivo: high accumulation in macrophages and granulation tissues studied by microautoradiography. J Nucl Med 33:1972–1980

Le Bihan D, Breton E, Lallemand D, Aubin ML, Vignaud J, Laval-Jeantet M (1988) Separation of diffusion and perfusion in intravoxel incoherent motion MR imaging. Radiology 168:497–505

Lell MM, Greess H, Hothorn T, Janka R, Bautz WA, Baum U (2004) Multiplanar functional imaging of the larynx and hypopharynx with multislice spiral CT. Eur Radiol 14:2198–2205

Magnano M, Bongioannini G, Cirillo S et al (2005) Virtual endoscopy of laryngeal carcinoma: is it useful? Otolaryngol Head Neck Surg 13:776–782

McCabe KJ, Rubinstein D (2005) Advances in head and neck imaging. Otolaryngol Clin North Am 38:307−319 vii

Padhani AR (2003) MRI for assessing antivascular cancer treatments. Br J Radiol 76:S60–S80

Pauwels E, McCready VR, Stoot JH et al (1998) The mechanism of accumulation of tumour-localising radiopharmaceuticals. Eur J Nucl Med 25:277–305

Port RE, Knopp MV, Brix G (2001) Dynamic contrast-enhanced MRI using Gd-DTPA: interindividual variability of the arterial input function and consequences for the assessment of kinetics in tumors. Magn Reson Med 45:1030–1038

Robert YH, Chevalier D, Rocourt NL et al (1993) Dynamic maneuver acquired with spiral CT in laryngeal disease. Radiology 189:298–299

Rodrigues RS, Bozza FA, Christian PE et al (2009) Comparison of whole-body PET/CT, dedicated high-resolution head and neck PET/CT, and contrast-enhanced CT in preoperative staging of clinically M0 squamous cell carcinoma of the head and neck. J Nucl Med 50:1205–1213

Schöder H, Fury M, Lee N, Kraus D (2009) PET monitoring of therapy response in head and neck squamous cell carcinoma. J Nucl Med 50 Suppl 1:74S−88S

Sigal R, Vogl T, Casselman J et al (2002) Lymph node metastases from head and neck squamous cell carcinoma: MR imaging with ultrasmall superparamagnetic iron oxide particles (Sinerem MR)—results of a phase-III multicenter clinical trial. Eur Radiol 12:1104–1113

Silverman PM, Zeiberg AS, Sessions RB, Troost TR, Zeman RK (1995) Three-dimensional imaging of the hypopharynx and larynx by means of helical (spiral) computed tomography. Comparison of radiological and otolaryngological evaluation. Ann Otol Rhinol Laryngol 104:425–431

Takahara T, Imai Y, Yamashita T, Yasuda S, Nasu S, Van Cauteren M (2004) Diffusion weighted whole body imaging with background body signal suppression (DWIBS):

technical improvement using free breathing, STIR and high resolution 3D display. Radiat Med 22:275–282

Takes RP, Knegt P, Manni JJ et al (1996) Regional metastasis in head and neck squamous cell carcinoma: revised value of US with US-guided FNAB. Radiology 198:819–823

Takes RP, Righi P, Meeuwis CA et al (1998) The value of ultrasound with ultrasound-guided fine-needle aspiration biopsy compared to computed tomography in the detection of regional metastases in the clinically negative neck. Int J Radiat Oncol Biol Phys 40:1027–1032

Thoeny HC, De Keyzer F, Vandecaveye V et al (2005) Effect of vascular targeting agent in rat tumor model: dynamic contrast-enhanced versus diffusion-weighted MR imaging. Radiology 237:492–499

Tofts PS, Kermode AG (1991) Measurement of the blood-brain barrier permeability and leakage space using dynamic MR imaging. 1. Fundamental concepts. Magn Reson Med 17: 357–367

Townsend D (2008) Dual-modality imaging: combining anatomy, function. J Nucl Med 49:938–955

van den Brekel MW, Castelijns JA, Stel HV et al (1991) Occult metastatic neck disease: detection with US and US-guided fine-needle aspiration cytology. Radiology 180:457–461

Vandecaveye V, De Keyzer F, Dirix P et al (2010) Applications of diffusion-weighted magnetic resonance imaging in head and neck squamous cell carcinoma. Neuroradiology 52:773–784

Vogel WV, Wensing BM, van Dalen JA et al (2005) Optimised PET reconstruction of the head and neck area: improved diagnostic accuracy. Eur J Nucl Med Mol Imaging. 32:1276–1282

Warburg O (1956) On the origin of cancer cells. Science 123:309–314

Wirth S, Meindl T, Treitl M, Pfeifer KJ, Reiser M (2006) Comparison of different patient positioning strategies to minimize shoulder girdle artifacts in head and neck CT. Eur Radiol 16:1757–1762

Laryngeal Neoplasms

Robert Hermans

Contents

R. Hermans (✉)
Department of Radiology, University Hospitals, Herestraat 49, 3000 Leuven, Belgium
e-mail: Robert.Hermans@uz.kuleuven.ac.be

Abstract

Most laryngeal neoplasms are squamous cell cancers, and the larynx is a relative frequent site of head and neck malignancy. Although most laryngeal cancers are detected clinically, and their superficial extent can be well evaluated by endoscopic examination, imaging is required to evaluate the frequent submucosal spread of these tumors. Accurate staging of laryngeal cancer requires imaging, and the radiological findings affect tumor staging and treatment choice. This chapter reviews the normal anatomy of the larynx, and focuses on the imaging findings in laryngeal squamous cell cancer, both before and after treatment. The prognostic value of imaging-derived parameters is explained. The radiological findings in less common laryngeal tumor types are also reviewed.

1 Introduction

The larynx is one of the most frequent head and neck cancer sites. Nearly all laryngeal malignancies are squamous cell carcinomas. Cigarette smoking and excessive alcohol consumption are well-known risk factors. An important factor in the treatment planning of laryngeal neoplasms is the accuracy of pretherapeutic staging. As most laryngeal tumors are mucosal lesions, they often can be seen directly or indirectly, but the limitations of clinical and endoscopic tumor evaluation are well recognized. The clinical and radiological evaluation of laryngeal tumors are complementary; the combination of the obtained information will lead to the most accurate determination of tumor extent. Imaging

R. Hermans (ed.), *Head and Neck Cancer Imaging*, Medical Radiology. Diagnostic Imaging,
DOI: 10.1007/174_2011_373, © Springer-Verlag Berlin Heidelberg 2012

may be used to monitor tumor response and to detect recurrent or persistent disease as early as possible.

2 Normal Laryngeal Anatomy

Essentially, the larynx consists of a supporting skeleton, a mucosal surface, and in between a soft tissue layer containing fat, some ligaments and muscular structures (Figs. 1, 2, 3, 4).

2.1 Laryngeal Skeleton

The laryngeal skeleton is made up of cartilage and fibrous bands. The foundation of the larynx is the cricoid cartilage. The cricoid cartilage is the only complete cartilaginous ring in the airway. Its horizontal ring-shaped part is known as the arch (arcus), while the higher posterior part is called the lamina. Two paired facets are found at the upper margin of the lamina, allowing articution with the arytenoid cartilages.

The largest supporting cartilage is the thyroid cartilage, essentially consisting out of two wings or laminae. The teardrop-shaped epiglottis extends downward and attaches to the inner side of the thyroid cartilage. Only a small part of the epiglottis extends above the hyoid bone, the suprahyoid or free margin of the epiglottis.

The vocal ligament stretches from the vocal process of the arytenoid to the inner side of the thyroid cartilage; it forms the medial support of the true vocal cord. The ventricular ligament stretches from the upper arytenoid to the thyroid cartilage, forming the medial margin of the false cord. The epiglottis is held in place by the hyo-epiglottic ligament, running through the fatty preepiglottic space.

2.2 Mucosal Layer and Deeper Laryngeal Spaces

All these structures are covered by mucosa; the inner larynx is dominated by two prominent parallel bands, the true and false cords, separated by a slit-like opening towards the laryngeal ventricle. The true cord largely consists of a muscle, running parallel and lateral to the vocal ligament, between the arytenoid and thyroid cartilage, hence known as the thyro-arytenoid muscle. The false cord largely consists of fat. In between the cords, the ventricle rises into the laryngeal tissue space between the mucosa and supporting skeleton. The relationship of pathological

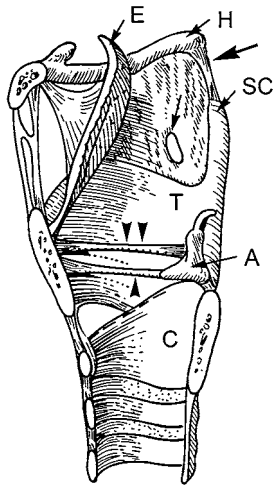

Fig. 1 Lateral diagram of the larynx showing the cartilaginous skeleton (mucosa, intrinsic laryngeal muscles, and paraglottic fat removed). The vocal ligament (*single arrowhead*) stretches from the vocal process of the arytenoid *A* to the anterior thyroid cartilage. The ventricular ligament (*double arrowhead*) runs from the upper arytenoid to the anterior thyroid cartilage. *T* thyroid lamina; *SC* superior cornu (of thyroid). The superior cornua are attached to the hyoid by the thyrohyoid ligament (unlabeled *thick arrow*), which forms the posterior margin of the thyrohyoid membrane. *C* cricoid cartilage; *E* epiglottis; *H* hyoid bone. Note: The small structure at the upper tip of the arytenoid is the corniculate cartilage. It has no clinical significance, but is occasionally seen on CT. The small hole (unlabeled *thin arrow*) in the thyrohyoid membrane transmits the internal branch of the superior laryngeal nerve that provides sensation to the laryngeal mucosa

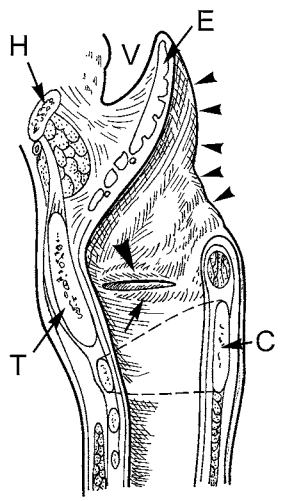

Fig. 2 Lateral diagram of the larynx sectioned sagittally in the midline. The slitlike ventricle separates true vocal cord (unlabeled *arrow*) and false vocal cord (large *arrowhead*). *Small arrowheads*, aryepiglottic fold; *T* thyroid cartilage; *C* cricoid cartilage (lamina); *dashed line*, projection of the arch of the cricoid cartilage; *E*: epiglottis; *H* hyoid bone; *V* vallecula

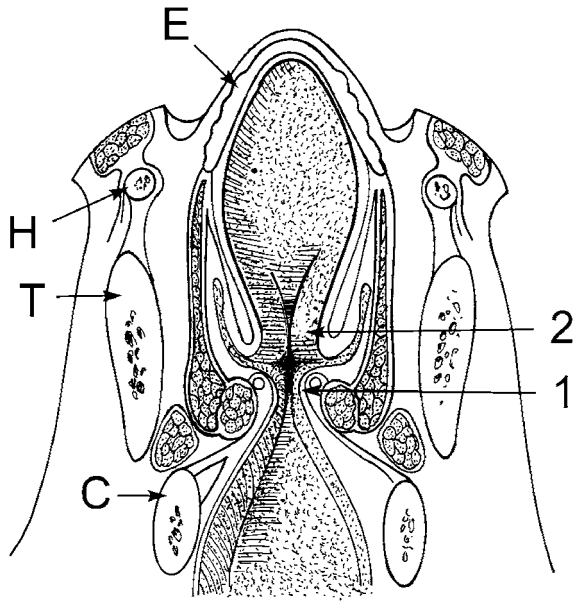

Fig. 3 Coronal diagram of the larynx showing the laryngeal subsites. *1* True vocal cord (TVC) consist mainly of the bellies of the thyroarytenoid muscle. *2* False vocal cord (FVC) consists mainly of fatty tissue. TVC and FVC are separated by the slitlike laryngeal ventricle (sinus of Morgagni), extending superolaterally as the sacculus laryngis or appendix. *E* epiglottis; *H* hyoid bone; *T* thyroid cartilage; *C* cricoid cartilage

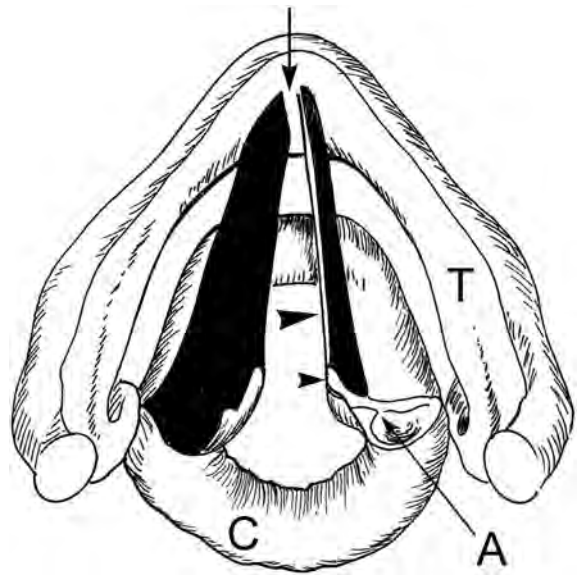

Fig. 4 *Inner view* of the larynx, seen from above, after removal of most soft tissues. *A* arytenoid cartilage; *C* cricoid lamina; *T*, thyroid cartilage. The bulk of the TVC is made up of the thyroarytenoid muscle (in *dark*) running from the inner aspect of the thyroid lamina to the arytenoid cartilage, paralleling the vocal ligament (*large arrowhead*). The thyroarytenoid muscle can be separated in two bellies. Only the medial portion (vocalis muscle) is seen on the right. The vocal ligament extends from the vocal process (*small arrowhead*) to the anterior commissure (unlabeled *arrow*)

conditions among these three parallel structures is significant in the evaluation of laryngeal cancer.

Above the false cords, from the arytenoid cartilages, the mucosa reflects upwards towards the epiglottis, forming the aryepiglottic folds.

The part of the larynx at the level of the true vocal cords is called the glottis. The region beneath the undersurface of the true vocal cords until the undersurface of the cricoid cartilage is the subglottis. Above the level of the true vocal cords is the supraglottis. Within these different levels, further subsites are distinguished, important for staging purposes (Table 1).

The bare area between the anterior attachment of the true vocal cords, where no or only minimal soft tissue is present against the cartilage, is known as the anterior commissure. The area between the arytenoids is known as the posterior commissure.

The fat-containing space between the mucosa and the supporting skeleton is variable in size. The part of this deep space, anterior to the epiglottis, is known as the preepiglottic space. This preepiglottic space is continuous with the more lateral submucosal spaces, extending into the aryepiglottic folds and false vocal cords. These lateral spaces are known as the paraglottic spaces. At the level of the glottis, the paraglottic spaces are reduced to a very thin strip of fat just lateral to the thyro-arytenoidal muscles.

Table 1 Subsites within the larynx (UICC 2009)

Supraglottis
Suprahyoid epiglottis (including tip, lingual, and laryngeal surfaces)
infrahyoid epiglottis
Aryepiglottic fold, laryngeal aspect
Arytenoid
Ventricular bands (false vocal cords)
Glottis
True vocal cords
Anterior commissure
Posterior commissure
Subglottis

The paraglottic fat tissue is continuous with a thin infraglottic fat plane, bordered by the conus elasticus. The preepiglottic and paraglottic spaces together are sometimes called the paralaryngeal space (Sato et al. 1993).

2.3 Normal Radiological Anatomy

The normal radiological anatomy of the larynx is shown in Fig. 5.

The appearance of the laryngeal cartilages can vary considerably, depending on the degree of ossification and the amount of fatty marrow in the ossified medullar space. In children, the CT density of the laryngeal cartilages is similar to soft tissue. The (endochondral) ossification of hyaline cartilage starts early in the third decade of life. A high degree of variation exists between individuals (Yeager et al. 1982). The thyroid cartilage shows the greatest variability in ossification; its ossification may also occur in an asymmetrical fashion. The cricoid and arytenoids show less pronounced variability in ossification. The epiglottis and vocal process of the arytenoids are composed of yellow fibrocartilage; this type of cartilage usually does not ossify.

3 Squamous Cell Carcinoma

Squamous cell carcinoma, originating from the mucosal lining, is the most common malignant tumor in the larynx. Mucosal abnormalities can be far better evaluated by the clinician than with even sophisticated imaging methods such as CT or MRI. However, these tumors have the tendency to spread submucosally, and this extension into the deeply lying tissue planes may be difficult to evaluate by clinical examination alone.

The clinical criteria used for giving a tumor a particular T-classification are site-dependent; in the larynx involvement of different laryngeal subsites and reduced vocal cord mobility are important criteria. The local staging criteria for glottic, supraglottic, and subglottic cancer, as well as the stage grouping, are summarized in Tables 2, 3, 4 and 5. About 65–70% of laryngeal cancers originate at the glottic level, and about 30% at the supraglottic level; laryngeal cancer originating from the subglottic region is rare.

The regional (neck) staging criteria for laryngeal cancer are similar to those for oro- and hypopharyngeal cancer and sinonasal cancer.

The validity of any classification is dependent on the diagnostic methods employed. It is recognized that clinical classification of laryngeal cancer is insufficient when compared with pathologic classification (Pillsbury and Kirchner 1979). As some criteria (such as vocal cord fixation or impaired mobility) are prone to subjective interpretation, difficulties occur to clinically determine the extension of a laryngeal tumor, or to reproduce this assessment (Takes et al. 2010). A marked improvement in accuracy is obtained when the results of CT or MRI are added to the clinical findings (Sulfaro et al. 1989; Katsantonis et al. 1986; Zbären et al. 1996). Imaging is mainly of benefit in detecting deep soft tissue extension, such as in the preepiglottic space, the laryngeal cartilages, and base of tongue. Findings from imaging studies frequently result in an upclassification of the disease.

For categorization of a given laryngeal tumor, the UICC and AJCC are not very precise regarding their recommendations for the use of imaging methods such as CT and MRI. The AJCC, for example, states that a variety of imaging procedures are valuable in evaluating the extent of disease, particularly for advanced tumors; these techniques include laryngeal tomograms, CT and MRI studies, but when to use either or all of these imaging methods is not indicated. Without further specification as to the type of imaging, the UICC recommends that imaging should be included in the diagnostic workup.

Although the benefit of CT in the classification of laryngeal cancer is already known for a long time, not all patients with clinically advanced cancer are being examined with this tool; the reasons for this are not clear (Barbera et al. 2001).

In the United States, in the period 1990–1992 about 37% of patients with laryngeal cancer had a CT study (Shah et al. 1997). Large regional variation exists in the use of CT for staging purposes of laryngeal cancer. This variation cannot always be attributed to the availability of these imaging modalities. In Ontario, about 20% of patients with glottic and 42% of patients with supraglottic cancer underwent CT during the period 1982–1995 (Barbera et al. 2001); in the same period, the overall rate of CT use varied between 10.4 and 50.5% among the regional cancer centers in this province.

One may argue that patients with clinically localized disease would benefit more from such a CT study, as upclassification of the cancer may result in a

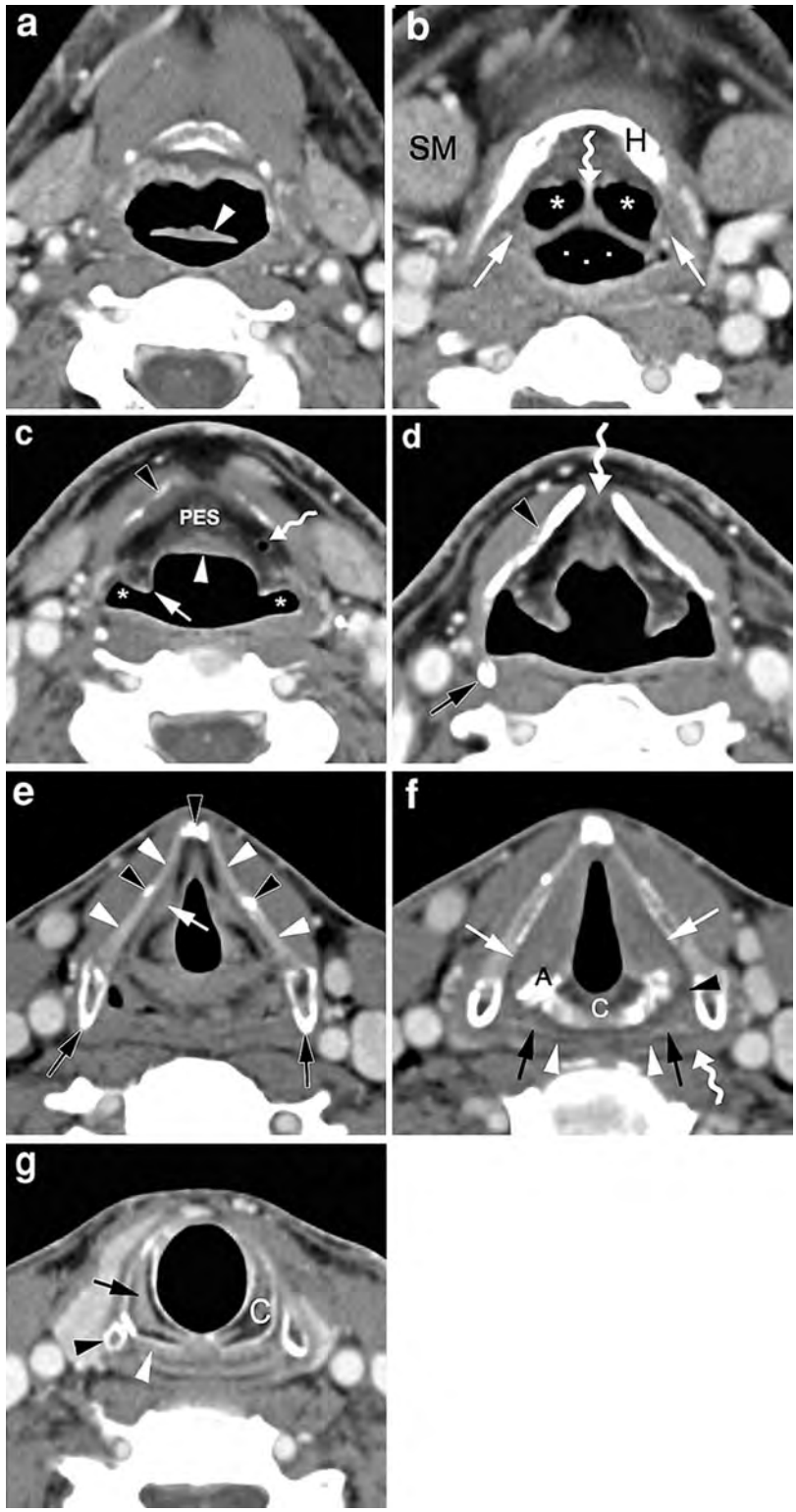

Fig. 5 Axial CT images through normal appearing larynges (different patients), from cranial to caudal, illustrating normal radiological anatomy. **a** Level of the free epiglottic margin (*arrowhead*), at the superior edge of the hyoid bone. **b** Level of the hyoid bone (*H*). The glosso-epiglottic ligament separates both valleculae (*asterisks*). The epiglottis separates the oropharyngeal valleculae from the laryngeal vestibule (*dots*). The pharyngo-epiglottic folds (*arrows*) correspond to the anterocranial margin of the piriform sinuses. Submandibular salivary gland (*SM*). **c** Level of superior margin of thyroid cartilage (*black arrowhead*). Epiglottis (*white arrowhead*), aryepiglottic fold (*arrow*), piriform sinuses (*asterisks*). The fatty space in front of the epiglottis is the preepiglottic space (*PES*). The more lateral fatty spaces are called the paraglottic spaces; in the left paraglottic space, the air-containing tip of the laryngeal ventricle is seen (*curved arrow*). **d** Level of thyroid cartilage (*black arrowhead*). Thyroid notch (*curved arrow*). Superior thyroid cornu (*arrow*). **e** Level of false vocal cords. Within the fatty paraglottic space, some tissue with higher density can be seen, corresponding to intrinsic laryngeal muscles and the collapsed laryngeal ventricles (*white arrow*). The thyroid cartilage shows areas of calcification (*black arrowheads*), ossification (*black arrows*) and non-calcified cartilage (*white arrowheads*). **f** Level of true vocal cords. Arytenoid cartilage (*A*, partially ossified); lamina of cricoid cartilage (*C*). The fatty paraglottic spaces are reduced to a thin fatty line (*white arrows*) between the thyroid cartilage and vocal muscles. Posteriorly, the paraglottic spaces are continuous with the anterior submucosal fat plane in the retrocricoidal part of the hypopharynx (*black arrowhead*). Hypopharyngeal mucosa (*black arrows*), posterior submucosal fat plane in retrocricoidal hypopharynx (*white arrowheads*), pharyngeal constrictor muscle (*curved arrow*). **g** Level of subglottis. Arch of cricoid cartilage (*C*). The denser areas correspond to islands of non-ossified cartilage within the otherwise ossified cricoid. Inferior thyroid cornu (*black arrowhead*). Posterior crico-arytenoid muscle (*white arrowhead*)

Table 2 T-staging of glottic cancer (UICC 2009)

T1	Tumor limited to vocal cord(s) with normal mobility (may involve anterior or posterior commissure)
	T1a: limited to one vocal cord
	T2b: involving both vocal cords
T2	Extension into supra- and/or subglottis, and/or with impaired vocal cord mobility
T3	Vocal cord fixation and/or invasion of paraglottic space, and/or inner cortex of the thyroid cartilage
T4	Extralaryngeal tumor spread
	T4a: Tumor invading through the outer cortex of the thyroid cartilage, or tissues beyond the larynx (e.g. trachea, soft tissues of the neck, deep/extrinsic muscles of the tongue[a], strap muscles, thyroid gland, esophagus)
	T4b: Tumor invading prevertebral space, mediastinum, or encasing carotid artery

[a] Genioglossus, hypoglossus, palatoglossus, and styloglossus muscle

Table 3 T-staging of supraglottic cancer (UICC 2009)

T1	Tumor limited to one subsite of supraglottis with normal vocal cord mobility
T2	Tumor invades mucosa of more than one adjacent subsite of supraglottis, glottis or region outside of supraglottis, without fixation of the larynx
T3	Vocal cord fixation or invasion of postcricoid area, preepiglottic and/or paraglottic space, and/or inner cortex of thyroid cartilage
T4	Extralaryngeal tumor spread
	T4a: Tumor invading through thyroid cartilage, or tissues beyond the larynx (e.g. trachea, soft tissues of the neck, deep/extrinsic muscles of the tongue[a], strap muscles, thyroid gland, esophagus)
	T4b: Tumor invading prevertebral space, mediastinum, or encasing carotid artery

[a] Genioglossus, hypoglossus, palatoglossus, and styloglossus muscle

Table 4 T-staging of subglottic cancer (UICC 2009)

T1	Tumor limited to subglottis
T2	Tumor extends to vocal cord(s) with normal or impaired mobility
T3	Vocal cord fixation
T4	Extralaryngeal tumor spread
	T4a: Tumor invades cricoid or thyroid cartilage, and/or invades tissues beyond the larynx (e.g. trachea, soft tissues of the neck, deep/extrinsic muscles of the tongue[a], strap muscles, thyroid gland, esophagus)
	T4b: Tumor invading prevertebral space, mediastinum, or encasing carotid artery

[a] Genioglossus, hypoglossus, palatoglossus, and styloglossus muscle

Table 5 Stage grouping of laryngeal cancer (UICC 2009)

Stage 0	Tis	N0	M0
Stage I	T1	N0	M0
Stage II	T2	N0	M0
Stage III	T1, T2	N1	M0
	T3	N0, N1	M0
Stage IVa	T4a	N0, N1, N2	M0
	T1, T2, T3	N2	M0
Stage IVb	T4b	Any N	M0
	Any T	N3	M0
Stage IVc	Any T	Any N	M0

Fig. 6 Contrast-enhanced axial CT-images in a patient with a clinically T3 glottic cancer on the *left side*. **a** Level of true vocal cords. The left true vocal cord appears thickened and slightly enhancing. The tumor reaches the anterior commissure (*black arrowhead*). The left paraglottic space is infiltrated [compare to normal opposite side (*arrows*)]. Marked sclerosis of the left arytenoid (*white arrowhead*). There appears to be some sclerosis of the left thyroid lamina. **b** Level of subglottis. Enhancing soft tissue thickening on left side (*arrowheads*). Note slight sclerosis cricoid arch on the left (*curved arrow*). Slight enhancement is seen anteromedially to the subglottis, corresponding to subtle extralaryngeal tumor spread or peritumoral inflammation (*arrow*). **c** Level of false vocal cords. Soft tissue infiltration of the paraglottic space along the thyroid cartilage (*arrows*). Area of non-ossified thyroid cartilage (*arrowhead*); as the surrounding ossified thyroid cartilage shows no abnormalities, most likely normal variant. The patient was treated by extended hemilaryngectomy. Pathologic examination confirmed glottic squamous cell carcinoma extending in the subglottic and supraglottic regions without evidence of extralaryngeal tumor extension. The arytenoid showed focal neoplastic invasion; in the other cartilages only inflammatory changes were noted

change in patient management. In The Netherlands, a national guideline states that all patients with a supraglottic carcinoma, and all patients with a glottic carcinoma (except T1-lesions limited to one vocal cord, not involving the anterior commissure) should undergo a high-quality CT or MRI study (Nationale Werkgroep Hoofd-Halstumoren 2000).

3.1 General Imaging Findings

Criteria used for tumor involvement are abnormal contrast enhancement, soft tissue thickening, presence of a bulky mass, infiltration of fatty tissue (even without distortion of surrounding soft tissues), or a combination of these. Any tissue thickening between the airway and the cricoid arch is considered to represent subglottic tumor.

Several studies have compared the CT/MRI findings with the results of whole organ sectioning after total or partial laryngectomy, showing that both techniques are accurate methods to visualize laryngeal pathology (Zbären et al. 1996). These studies correlating whole organ sectioning and imaging have also revealed some pitfalls. Small foci of mucosal tumor may be difficult to detect or may be invisible, and associated inflammatory and edematous changes may cause overestimation of the tumor extent. Distortion of adjacent normal structures may mimic tumoral involvement.

Gross cartilage invasion can be detected with CT. Due to the large variability in the ossification pattern of the laryngeal cartilages, CT often fails to detect early cartilage invasion. Nonossified hyaline cartilage shows more or less the same density values as tumor on CT images. Demonstration of tumor on the extralaryngeal side of the cartilage is a reliable, but late sign of cartilage invasion. Asymmetrical sclerosis, defined as thickening of the cortical margin and/or increased medullary density, comparing one arytenoid to the other, or one side of the cricoid or thyroid cartilage to the other side, is a sensitive but nonspecific finding on CT (Fig. 6) (Becker et al. 1995). Erosion or lysis has been found to be a specific criterion for neoplastic invasion in all cartilages (Fig. 7). Other signs, such as cartilaginous blow-out or bowing, a serpiginous contour or obliteration of the medullary space are not very reliable for cartilage invasion. The combination of several diagnostic CT-criteria for neoplastic invasion of the laryngeal cartilages seems to constitute a reasonable compromise: when extralaryngeal tumor and erosion or lysis in the thyroid, cricoid and arytenoid cartilages was combined with sclerosis in the cricoid and arytenoid

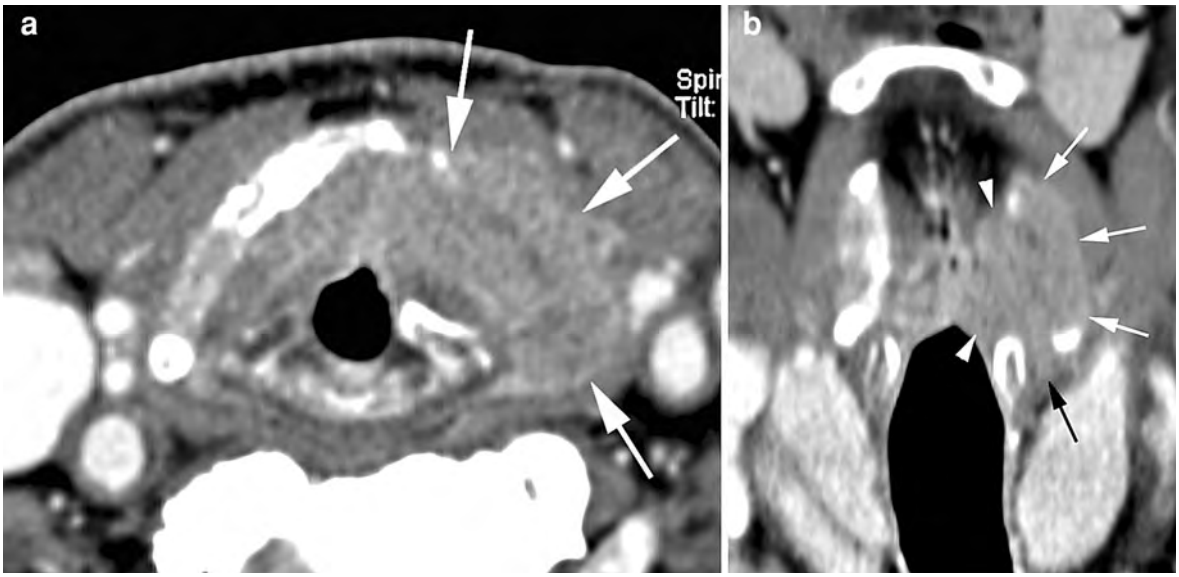

Fig. 7 Contrast-enhanced CT-images in a patient with a large left-sided glottic squamous cell carcinoma. **a** Axial image. The tumor mass massively invades and destructs the left wing of the thyroid cartilage, growing into the extralaryngeal soft tissues (*arrows*). **b** Coronal reformatting. Involvement of the glottic and supraglottic laryngeal level (*arrowheads*) is seen, as well as massive destruction of left thyroid cartilage wing and extralaryngeal tumor spread (*white arrows*). Extralaryngeal extension also occurs through the lateral cricothyroid membrane (*black arrow*)

(but not the thyroid) cartilages, an overall sensitivity of 82%, an overall specificity of 79%, and an overall negative predictive value of 91% was obtained (Becker et al. 1995).

The controversy on which modality should be preferred to image the larynx dealt for a great part with the accuracy to detect cartilage invasion. MRI was recommended to be the best method to determine the status of the cartilages in the presence of a laryngeal tumor (Becker et al. 1997b). MRI is a more sensitive technique than CT to detect cartilage abnormalities. Areas of cartilage abnormality will result in an increase in signal intensity T2-weighted images and contrast-enhanced T1-weighted MRI images. However, due to its high sensitivity for intracartilaginous alterations MRI causes in a considerable number of cases a false positive result, as distinction between true cartilage invasion and reactive inflammation, edema, fibrosis, or ectopic red bone marrow is not possible (Becker et al. 1995). Peritumoral inflammatory changes without tumoral invasion are common coincidental findings in laryngeal cartilages, especially in the thyroid cartilage. The positive diagnosis of neoplastic invasion of the thyroid cartilage should be made with caution on MRI; it has been suggested that one should rather talk about 'abnormal signal intensity in the cartilage' instead of 'invasion of cartilage' (Castelijns et al. 1996a). A more recent study suggests that reactive inflammatory changes and true neoplastic involvement of the laryngeal cartilages can be better distinguished by comparing the T2-weighted and postcontrast T1-weighted cartilage signal intensity with that of the adjacent tumor tissue. If the cartilage signal intensity on these sequences is higher than that of the tumor, this more likely indicates inflammation; the reported specificity of this sign is 82% (Fig. 8) (Becker et al. 2008).

3.2 Neoplastic Extension Patterns of Laryngeal Cancer

3.2.1 Glottic Cancer

3.2.1.1 Local Tumor Spread

The most common site of involvement is the anterior portion of the vocal cord, usually at the free margin or upper surface. Involvement of the anterior commissure

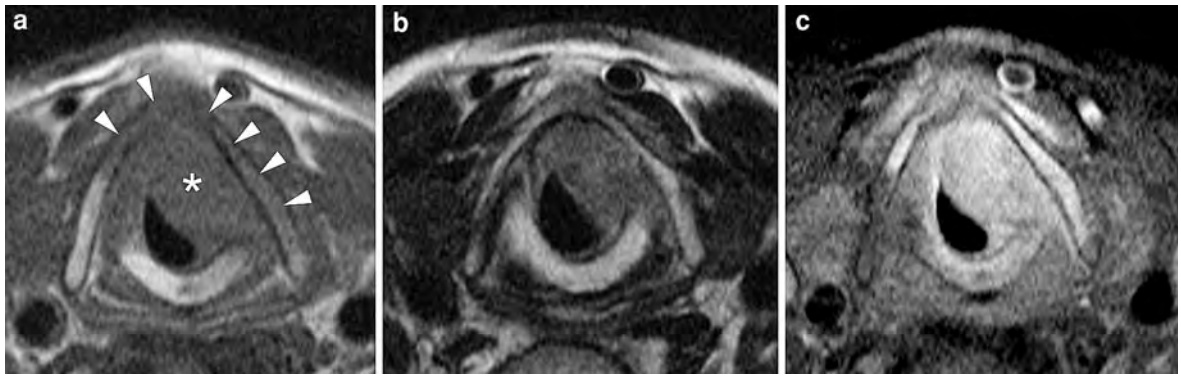

Fig. 8 Axial MR-images in a patient suffering from transglottic cancer. A large soft tissue mass is seen, centered on the left glottis/subglottis, extending over the midline. On the T1-weighted spin echo image (**a**), signal loss is seen in the adjacent part of the thyroid cartilage (*arrowheads*). On the T2-weighted image, the tumor shows a lower signal intensity than the thyroid cartilage. On the gadolinium-enhanced T1-weighted image, both the tumor and the cartilage show similar enhancement. This cartilage signal behavior suggests cartilagineous inflammation, rather than tumoral invasion. Total laryngectomy was performed; no neoplastic cartilage involvement was present

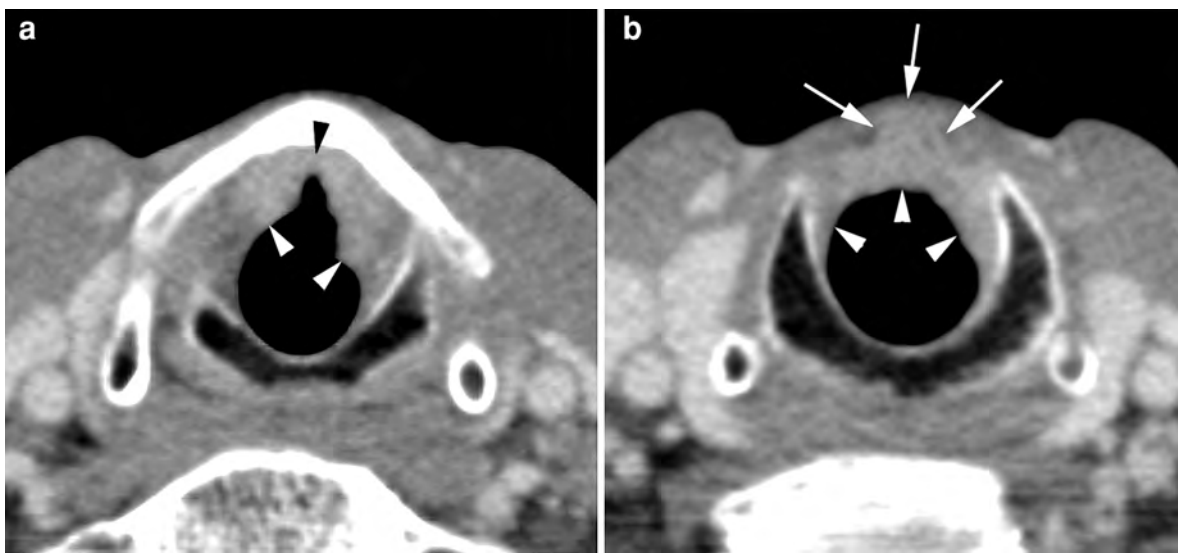

Fig. 9 Axial contrast-enhanced CT-images in a patient with squamous cell carcinoma of the anterior glottic region. **a** Thickening and slightly increased enhancement of lower surface of true vocal cords (*white arrowheads*) and anterior commissure (*black arrowhead*) is seen. **b** Soft tissue thickening at the subglottic level (*arrowhead*); extralaryngeal extension (*arrows*) occurred, through the cricothyroid membrane

is commonly present and such lesions may extend over the midline in the contralateral vocal cord. As the amount of normal soft tissue visible at the level of the anterior commissure is somewhat variable (Kallmes and Phillips 1997), radiological detection of subtle tumor spread into this structure by imaging can be challenging; however, usually the anterior commissure can be well evaluated during endoscopic examination.

Lesions limited to the anterior commissure are rarely seen (<2%). Lesions involving the anterior commissure may directly invade the thyroid cartilage; involvement of the anterior subglottic region, lower preepiglottic space, as well as extralaryngeal spread through the cricothyroid ligament may occur (Fig. 9).

When the tumor arises from the posterior side of the vocal cord, posterior extension over the medial facet

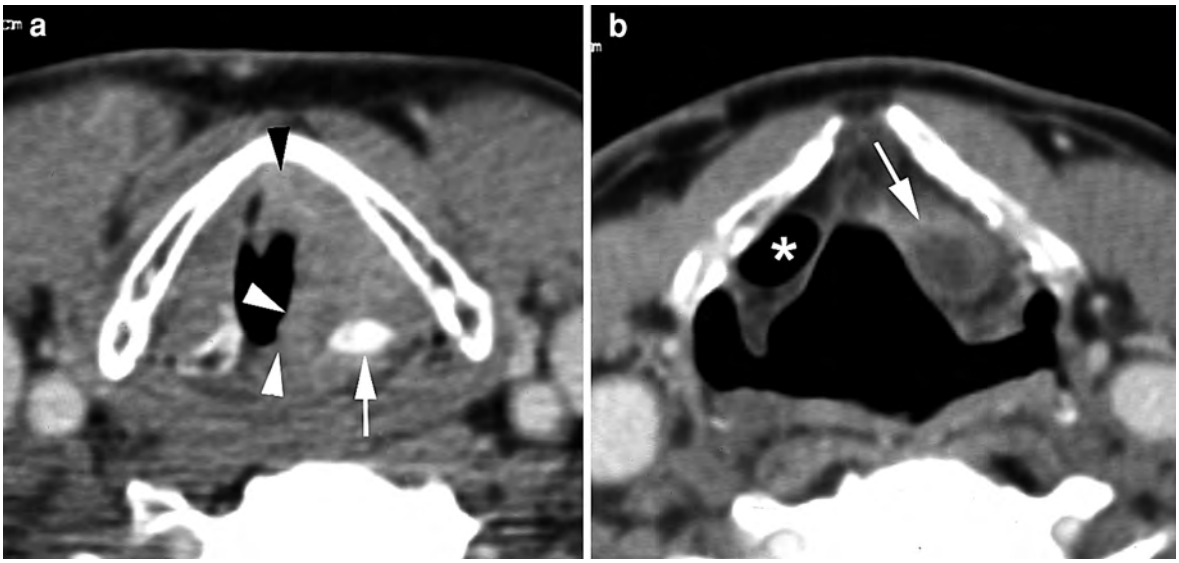

Fig. 10 Axial contrast-enhanced CT-images in a patient with a clinically T3 glottic cancer on the left side. **a** Level of true vocal cords. The left true vocal cord is markedly thickened. The lesion extends into the anterior commissure (*black arrowhead*), and grows over the medial facet of the arytenoid into the posterior commissure (*white arrowheads*). The left paraglottic space is infiltrated. The left arytenoid cartilage appears sclerotic (*arrow*). B. Level of the aryepiglottic folds. Secondary fluid-filled laryngocoele (*arrow*). Air-filled ventricle in the right paraglottic space (*asterisk*). The patient was treated by total laryngectomy. Pathologic examination confirmed squamous cell carcinoma, invading the anterior commissure and spreading to the right true vocal cord. The left arytenoid cartilage was invaded by the neoplasm

of the arytenoid cartilage, eventually involving the posterior commissure may occur (Fig. 10). The redundant mucosa at the level of the posterior commissure should not be misinterpreted as evidence for tumor spread. From the region of the posterior commissure, invasion of the cricoarytenoid joint may occur.

Obstruction of the opening of the ventricular orifice may be the cause of a fluid-filled laryngocele (also called a saccular cyst) (Fig. 10). Most laryngoceles are not caused by an obstructive mass, but an underlying neoplasm has to be excluded, both clinically and radiologically.

Extension into the subglottis may occur along the mucosal surface, or submucosally after penetration of the conus elasticus. As the upper airway wall gradually slopes from the free edge of the true vocal cords towards the inner side of the cricoid ring, the precise border between the undersurface of the true vocal cord and subglottic level is difficult to define on axial cross-sectional imaging. When soft tissue thickening is seen adjacent to a glottic neoplasm along the inner side of the cricoid, the lesion is extending into the subglottis. Coronal images, either direct MR-images or coronally reformatted CT-images, may be helpful to evaluate more subtle subglottic tumor extension. A more precise manner to measure the inferior extent of glottic/subglottic cancer is by referring to the lateral free margin of the true vocal cord.

Lateral spread of the cancer causes infiltration of the vocal ligament and muscle. In a more advanced stage, the paraglottic space is infiltrated and the perichondrium of the thyroid cartilage is reached (Fig. 6). The tumor is diverted by the thyroid cartilage to grow further in the paraglottic space, extending cranially into the supraglottic region of the larynx, or caudally into the subglottic region. A glottic cancer growing inferiorly may be diverted by the conus elasticus, laterally and extralaryngeally, to grow through the opening between the thyroid and cricoid cartilage (Fig. 7).

Erosion and eventually break-through of the thyroid cartilage with extralaryngeal tumor spread are not commonly seen, being usually late phenomenons in advanced lesions (Figs. 7, 11). Neoplastic cartilage involvement usually occurs in ossified parts of the laryngeal framework, most frequently at the inferior margin of the thyroid cartilage, upper margin of the cricoid cartilage or at the level of the anterior commissure (Kurita et al. 1985). These sites correspond to

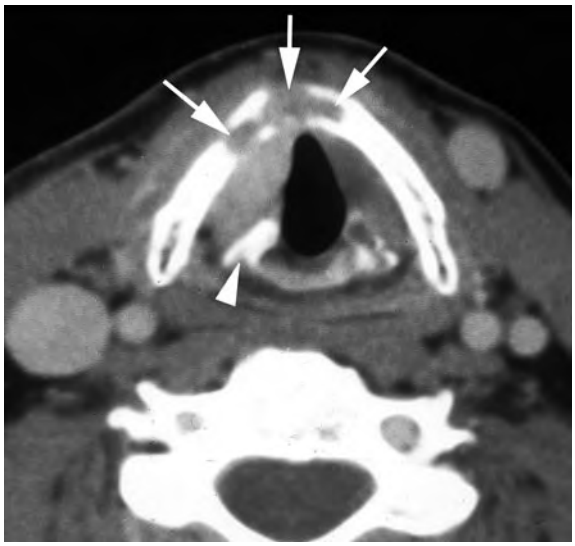

Fig. 11 Axial contrast-enhanced CT-image in a patient with a clinically T3 glottic cancer on the right side. Thickening and increased enhancement of the right true vocal cord. Sclerosis of the right arytenoid cartilage (*arrowhead*) and lysis of the anterior part of the thyroid cartilage, containing enhancing tissue (*arrows*). The patient was treated by definitive radiotherapy; long-term local tumor control was achieved

the attachment site of ligaments and membranes to the cartilages.

With extralaryngeal growth, tumor extension into non-fatty soft tissue structures surrounding the larynx may be present. Neoplastic invasion of the thyroid gland mostly occurs in glottic cancer showing subglottic extension or invading the thyroid cartilage (Dadas et al. 2001). Invasion of the subcutaneous layers and eventually skin may be seen in anteriorly spreading cancer. Posterior spread to the retrocricoid hypopharynx and eventually esophagus may occur (Fig. 12).

Rarely, a cancer originating at the level of the anterior commissure grows predominantly into the thyroid cartilage, without causing clear tumoral abnormalities at endoscopic examination. In such cases, imaging studies show an irregularly shaped, lytic expansion of the anterior part of the thyroid cartilage (Fig. 13). In the absence of mucosal changes, it may be difficult to prove the presence of cancer by routine biopsy. A deep, surgical biopsy may be required. In selected cases, an image-guided fine-needle aspiration or tru-cut biopsy can be an alternative method to obtain representative cytological or histological material (Preda et al. 2010).

A prelaryngeal abscess is another rare presentation of a glottic squamous cell carcinoma invading the anterior part of the thyroid. Presumably the neoplasm, or a combination of the neoplasm and an associated locally aggressive infection, erodes through the thyroid cartilage and offers bacteria a pathway to the prelaryngeal soft tissues (Fig. 14) (Op de beeck et al. 2001). The main differential diagnosis in such cases is infected thyroglossal duct cyst. Infection coexisting with malignancy complicates the clinical picture and may lead to a delayed diagnosis of malignancy. Therefore, careful follow-up after the initial treatment should be initiated if the etiology of the prelaryngeal infection remains obscure, especially in patients with an increased risk of developing head and neck cancer (alcohol and/or tobacco abusers). Repeated imaging studies may be helpful in coming to a correct diagnosis.

Cancer involving the glottic and supraglottic regions is also called transglottic cancer. However, the definition of transglottic cancer varies from author to author. Usually, tumors crossing the laryngeal ventricle involving both the false and true vocal cords are called transglottic cancer; most agree that the use of this term also implies that the subglottic region is involved, and that the true vocal cord is fixed (Mancuso et al. 1989).

Verrucous carcinoma is a variant of squamous cell carcinoma occurring in 1–2% of patients with glottic cancer. The histologic diagnosis of this type of cancer is difficult, and must be correlated with the gross appearance of the tumor. Clinically, it appears as an accretion or papillary mass with a warty surface or filiform projections, and it may extend over a large area. It is often 'under diagnosed' as a benign hyperplasia. Repeated and deep biopsy may be necessary to confirm the diagnosis. On CT and MR studies, verrucous carcinoma is difficult to differentiate from other types of squamous cell carcinoma, although an exophytic soft tissue mass originating from the true vocal cords, displaying an irregular surface and no or minimal submucosal extension, may suggest the diagnosis (Becker et al. 1998).

3.2.1.2 Lymphatic Spread

Usually, glottic cancer only metastasizes to the neck lymph nodes when growing beyond the glottic region. Level III is the most commonly affected level. Neck adenopathies are very uncommonly encountered in small (T1) lesions, but the risk increases to about 8 and 30% in respectively T2 and T3-lesions. Imaging studies may detect these adenopathies at an earlier stage than clinical examination alone (see also "Neck Nodal Disease").

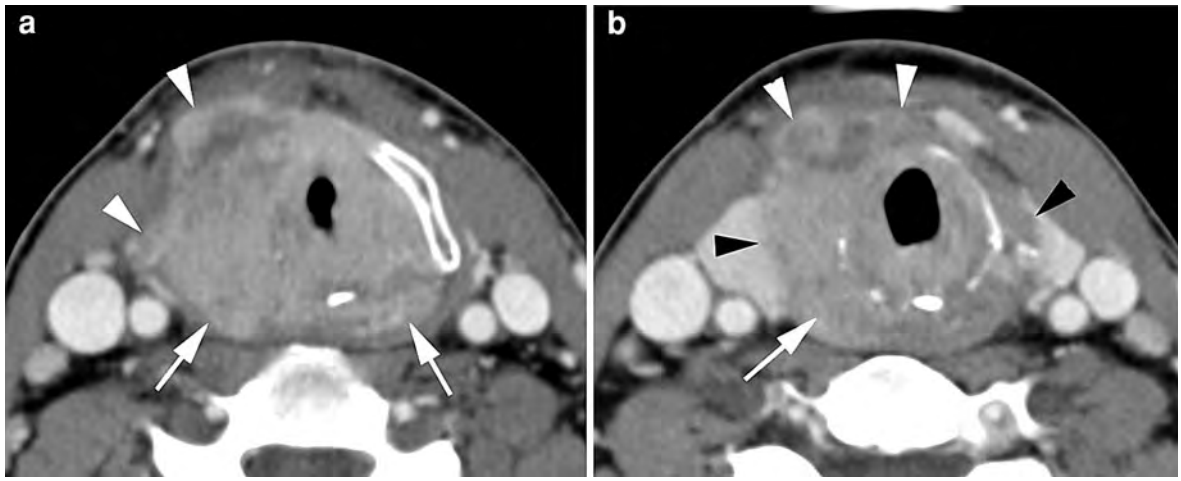

Fig. 12 Axial contrast-enhanced CT-images in a patient with extensive glottic squamous cell carcinoma. **a** Level of true vocal cords. Circumferential neoplastic involvement of the glottis, with massive destruction of the thyroid cartilage and extralaryngeal spread into the soft tissue anterolateral to the larynx (*white arrowheads*). Posterior tumor spread into the hypopharynx is at this level visible on both sides (*arrows*). **b** Circumferential involvement of the subglottis, including massive lysis of cricoid cartilage. Extralaryngeal spread into the prelaryngeal soft tissues (*white arrowheads*), as well as in both lobes of thyroid gland (*black arrowheads*). Involvement of retrocricoidal part of hypopharynx on the *right* side (*arrow*)

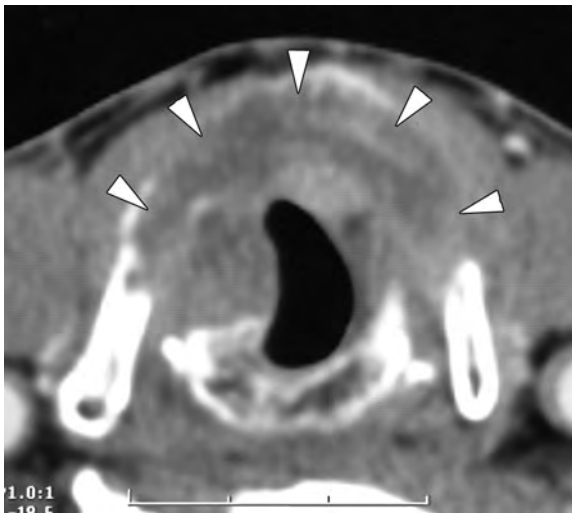

Fig. 13 Patient presenting with history of chronic laryngitis since two years. Endoscopic examination shows edema of the anterior commissure, and scarring of the vocal cords. The axial CT-image shows thickening and distortion of the laryngeal soft tissues, as well as osteolysis and expansion of a large part of the thyroid cartilage (*arrowheads*). These findings are very suspect for a malignant lesion. Deep biopsy revealed squamous cell cancer

3.2.2 Supraglottic Cancer

Essentially, the radiological signs are similar to those in glottic cancer, but supraglottic cancers often show a larger tumor volume at first presentation.

Clinically visible tumor extension and radiological tumor volume are not always correlated, because of submucosal spread in the preepiglottic space and/or paraglottic space. Laryngeal cartilage invasion is rarely seen in supraglottic cancer.

3.2.2.1 Suprahyoid Epiglottis

Lesions of the suprahyoid epiglottis may grow exophytically. Others invade the epiglottic tip and spread to adjacent structures, such as the valleculae, tongue base, and preepiglottic space; soft tissue ulceration and amputation of the epiglottic tip may be present (Fig. 15).

3.2.2.2 Infrahyoid Epiglottis

As the infrahyoid epiglottis contains tiny perforations, such lesions easily infiltrate the preepiglottic space; from this space, they may spread upwards towards the valleculae and tongue base, or downwards to the epiglottic petiolus. Invasion of the anterior commissure or subglottic spread are rare, but may be seen in advanced cases.

Extension into the aryepiglottic folds and false vocal cords may be seen; extension to the true vocal cords mostly occurs in advanced cases (Fig. 16).

3.2.2.3 Aryepiglottic Fold and Arytenoid

Aryepiglottic fold tumors may present as exophytic lesions, or infiltrative masses invading the paraglottic

Fig. 14 Axial contrast-enhanced CT-images. **a** Supraglottic level. Large fluid collection (*stars*) with rim enhancement is seen in the prelaryngeal soft tissues, displacing the strap muscles (*arrows*) anteriorly. **b** Glottic level. The large fluid collection extends downwards to this level. Thickening and enhancement of the left true vocal cord (*arrow*). **c** Same level as *b* bone window. Fragmentation of the anterior part of the thyroid cartilage (*arrows*). Sclerosis of left arytenoid cartilage (*arrowhead*)

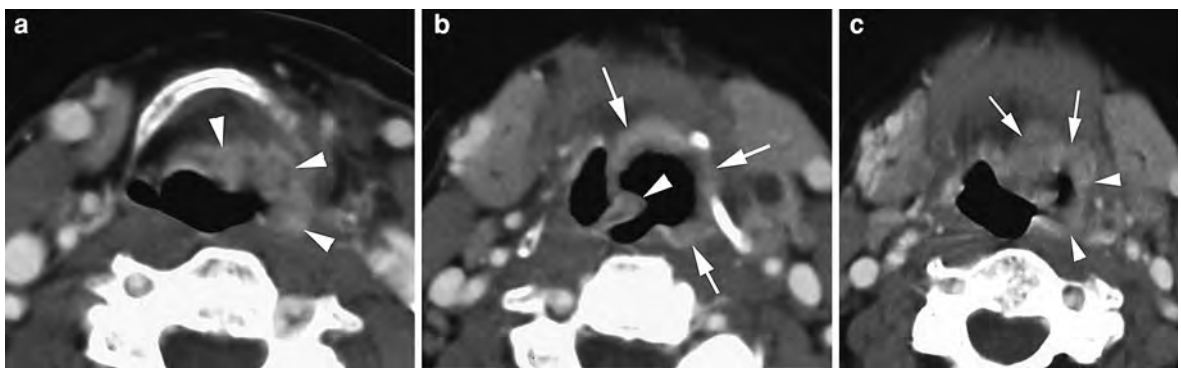

Fig. 15 Contrast-enhanced axial CT-images in a patient with a supraglottic squamous cell carcinoma. **a** Level of hyoid bone. Thickening and increased enhancement of the epiglottis, as well as infiltration of the preepiglottic and paraglottic space, with extension into the left aryepiglottic fold, is seen. Involvement of the upper part of the left piriform sinus can not be excluded. **b** Level of free epiglottic margin. The epiglottic tip (*arrowhead*) is amputated on the left side. The margins of the left vallecula are occupied by tumoral tissue, and there is extension into the posterolateral wall of the oropharynx. **c** At a slightly higher level, invasion of the tongue base (*arrows*), as well as posterolateral oropharyngeal wall (*arrowheads*), is seen. Pathological neck lymph nodes are ipsilaterally present

space. Along the paraglottic space, they may spread towards the false and eventually true vocal cords. Invasion of the cricoarytenoid joint may be seen. Extension towards the piriform sinus commonly occurs, and it may be difficult to distinguish between a primary piriform sinus cancer and supraglottic cancer.

3.2.2.4 False Vocal Cords

Submucosal tumor spread is commonly present in these lesions, with involvement of the paraglottic space at the level of the infrahyoid epiglottis/aryepiglottic fold and/or at the level of the true vocal cord (Fig. 17). Subglottic tumor spread is seen in advanced cases.

3.2.2.5 Lymphatic Spread

As the supraglottic region has a rich network of lymphatic channels, lymphadenopathy is frequently present in supraglottic cancer. At presentation, about 50–60% of patients with supraglottic cancer have clinically manifest lymphadenopathy. The incidence of neck metastasis is about 30% in T1 and T2-lesions, and about 70% in T3 and T4-lesions. Neck level II is most commonly affected, to a lesser extent level III.

3.2.3 Subglottic Cancer

Subglottic cancer is a rare malignant lesion. Apart from squamous cell carcinoma, also adenoid cystic carcinoma is frequently located at this level. By the

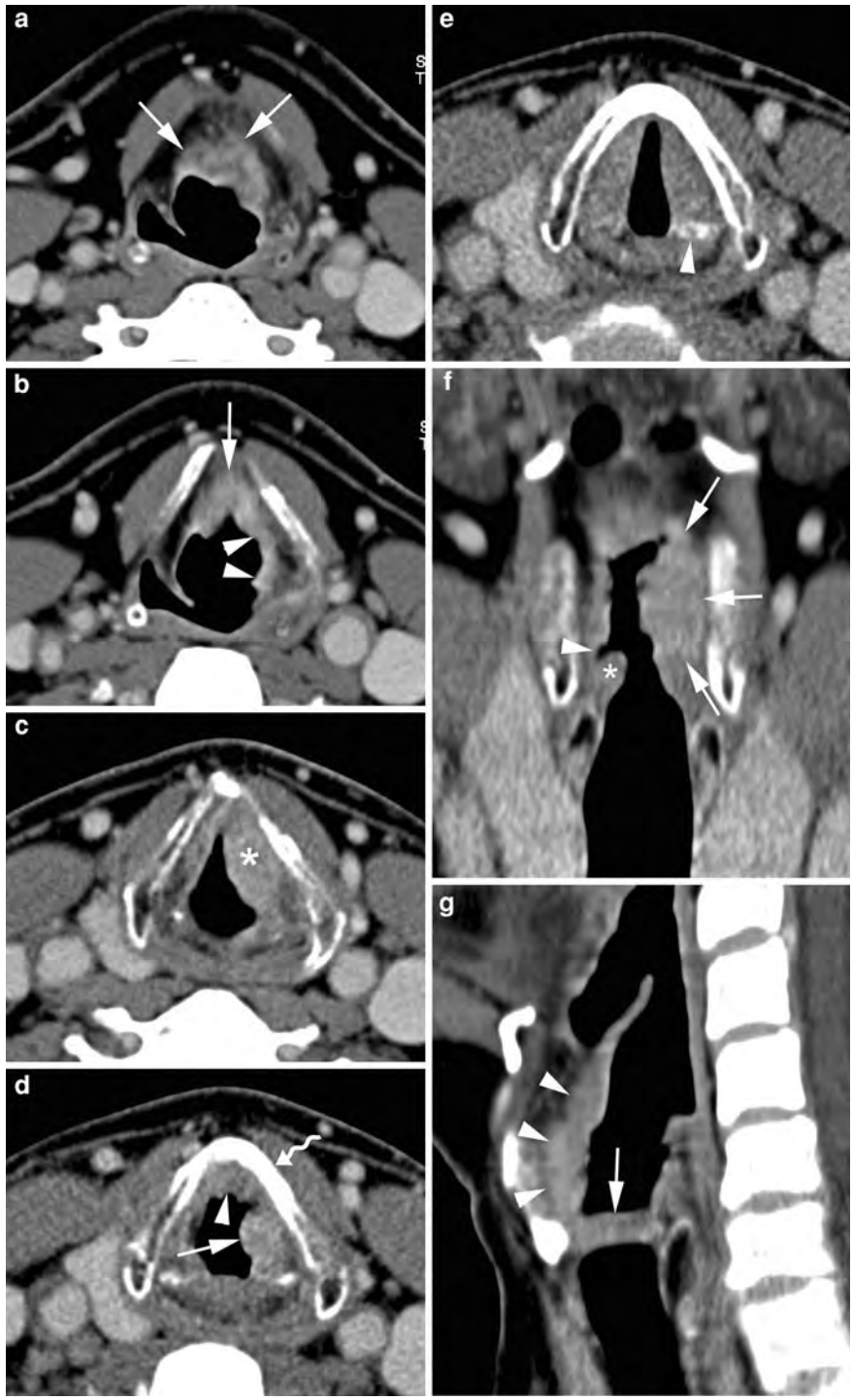

Fig. 16 Contrast-enhanced CT-images in a patient with supraglottic squamous cell carcinoma. **a** Axial image. Thickening and increased enhancement of the infrahyoid epiglottis, with infiltration of the preepiglottic space (*arrows*). **b** Axial image, more inferiorly, shows downwards tumor extension along the epiglottis and preepiglottic space (*arrow*), as well as posterolateral growth into the aryepiglottic fold. **c** Axial image, more inferiorly, shows tumoral infiltration of the left false vocal cord. **d** Axial image, level of ventrical entrance. Tumoral soft tissue thickening just above the level of the anterior commissure (*arrowhead*), as well as just above the level of the true vocal cord (*arrow*). Sclerosis of left thyroid cartilage wing (*curved arrow*). **e** Axial image, level of true vocal cords. Apart from sclerosis of left arytenoid cartilage (*arrowhead*), no abnormalities are seen. **f** Coronal image. The tumor mass (*arrows*) extends throughout the left paraglottic space, abutting and slightly displacing downwards the upper margin of the true vocal cord. Normal right true vocal cord (*asterisk*), right laryngeal ventricle (*arrowhead*). **g** Sagittal image.Tumoral thickening of the infrahyoid epiglottis (*arrowheads*), extending down to the level just above the anterior commissure. True vocal cord (*arrow*)

time of diagnosis, subglottic cancer has usually invaded the true vocal cords, and it may be difficult to distinguish between a cancer originating in the glottis or subglottis. Subglottic cancer is commonly bilateral or even circumferential at presentation. Cricoid cartilage invasion occurs early; extralaryngeal extension, anteriorly through the cricothyroid membrane or inferiorly into the trachea, is also commonly present.

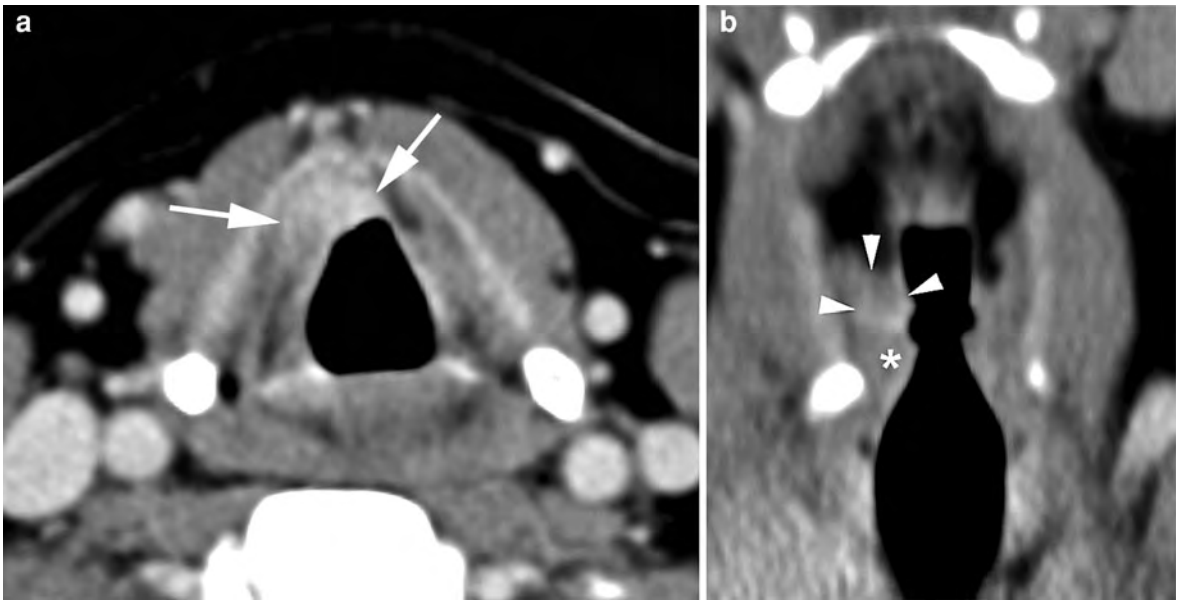

Fig. 17 Patient presenting with hoarseness. Squamous cell carcinoma of the left false vocal cord. **a** Axial contrast-enhanced CT-image shows small infiltrating lesion (*arrows*) in the right paraglottic space, at the level of the false vocal cords; the lesion extends into the anterior midline (lower part of preepiglottic space, level of epiglottic petiole). **b** Coronal reformatting. Enhancing soft tissue lesion in the right false vocal cord (*arrowheads*), just above the normal true vocal cord (*asterisk*)

Lymphatic dissemination is seen in about 10% of cases; among the lymph nodes which may become involved are the Delphian node and paratracheal lymph nodes.

Imaging shows a subglottic soft tissue mass (normally no soft tissue is seen between the subglottic air column and the cricoid cartilage), more or less with circumferential extension along the cricoid cartilage. The findings may include cricoid cartilage alterations (sclerosis, lysis), intratracheal soft tissue thickening, and infiltration of the glottic and prelaryngeal soft tissues (Fig. 18).

4 Prognostic Factors for Local Outcome of Laryngeal Cancer

4.1 Treatment Options

4.1.1 Glottic Cancer

Carcinoma in situ can often be controlled by stripping the cord or laser treatment; radiotherapy is used after rapid or multiple recurrences of such superficial cancer (Million 1992).

In T1 and T2 tumors radiation treatment is usually preferred, as the voice quality is better than after partial laryngectomy, and fewer complications are encountered. Patients with well-defined lesions suitable for transoral laser excision with a good functional outcome can be treated with either laser or radiotherapy (Mendenhall et al. 2004).

Favorable T3 and T4 tumors, confined to one side of the larynx without significant airway compromise, may be cured either with radiotherapy or total laryngectomy with possible postoperative irradiation. Failures after radiotherapy may be cured by salvage laryngectomy. Such a strategy yielded similar locoregional control rates and survival for T3 tumors either treated with radiotherapy alone with surgery in reserve, or with primary surgery (with or without adjuvant irradiation), but with a significantly higher likelihood of voice preservation in the first group (Mendenhall et al. 1992, 1997). This concept of 'radical radiotherapy with surgery for salvage' is a subject of discussion, as according to some authors this treatment policy means that a number of patients will die in order that others could save their larynx; furthermore, the costs are thought to be higher than if

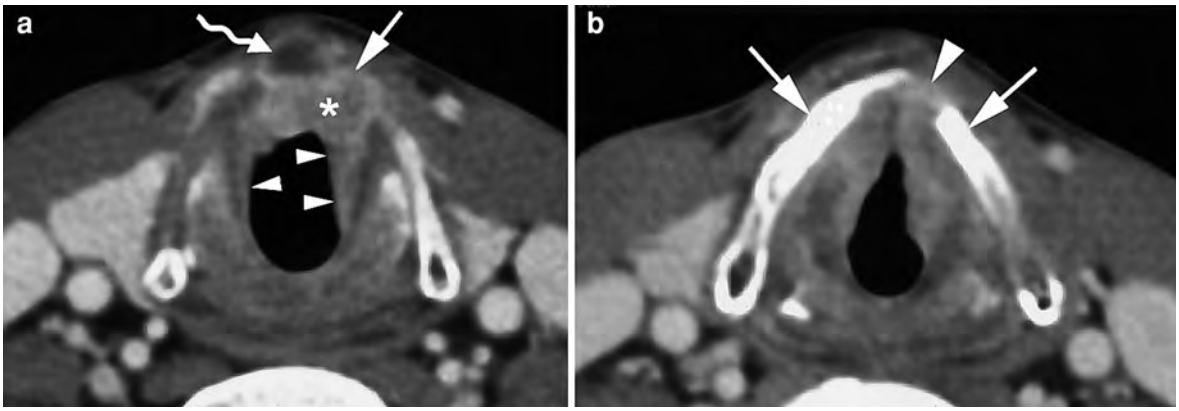

Fig. 18 Patient suffering from subglottic squamous cell carcinoma. Axial contrast- enhanced CT-images. **a** Anterior subglottic soft tissue thickening (*asterisk*), with bilateral posterior spread along the subglottic wall (*arrowheads*). Extralaryngeal spread through the cricothyroid membrane (*arrow*). Centrally hypodense nodule (*curved arrow*), presumably corresponding to necrotic prelaryngeal ('Delphian') lymph node. **b** Section 9 mm cranial to *A*. The soft tissue mass extends into the anterior commissure and both true vocal cords. Some sclerosis (*arrows*) of the thyroid cartilage is visible; the adjacent area of absent cartilage ossification (*arrowhead*) may correspond to lysis of previously ossified cartilage

surgery is used as first treatment, due to the intensive follow-up and retreatment needed in a substantial fraction of patients (DeSanto 1984).

Patients with advanced disease are in the unfavorable group for radiotherapy advised to undergo total laryngectomy (Million 1992). Some patients who refuse total laryngectomy or are medically unsuited for this procedure may be cured by radiotherapy; Van Den Bogaert et al. (1983) reported in advanced glottic cancer (T3 and T4-lesions) a 5-year local control rate of 23%.

Parsons et al. (1998) reported an overall 5-year local control of 52% in 43 T4 laryngeal tumors (26 supraglottic, 11 glottic, and 6 subglottic cancers), treated by irradiation with curative intent. 'Nonbulky' tumors tended to have a better prognosis than 'bulky' ones (67 vs. 38% local control rate); 'bulkiness' was assessed clinically and by CT. Twenty (46%) of the patients in this study were thought to be suitable for radical radiotherapy based on relative low tumor volume; it is unlikely that irradiation would produce a 50% rate of local control in all (unselected) T4 laryngeal cancers.

As in supraglottic carcinoma, there are indications that imaging is helpful in the selection of patients into the 'favorable' glottic carcinoma group, with a reasonable chance of voice sparing cure by radiotherapy (see below).

Nowadays, patients with advanced laryngeal cancer (stages III and IV) are offered concurrent chemoradiotherapy, with further surgery reserved for salvage, as treatment option. Platinum-based concomittant chemoradiotherapy improves the likelihood of organ preservation, with locoregional control rates of about 75% (Forastiere et al. 2003). The drawbacks of this approach are the acute and late toxic side effects, which are more frequent than after radiotherapy alone. Treatment complications, such as treatment-induced severe dysphagia, chronic lung aspiration, laryngeal radionecrosis, and others, may occur, reducing the benefit of larynx preservation in a number of patients (Lambert et al. 2010). Although the survival after concurrent radiotherapy is somewhat improved, the probability of developing distant metastases later on is estimated to be around 15–20%, less good than initially expected.

In selected patients with advanced glottic cancer, extended partial laryngectomy may still be feasible. Extended hemilaryngectomy with tracheal autotransplantation allows to remove half of the larynx, including the full height of the cricoid; the resection can be extended to include the apex of the piriform sinus. This allows to perform a partial laryngectomy in patients with arytenoid cartilage fixation and subglottic tumor extension reaching the upper border of the cricoid cartilage (Delaere et al. 2000, 2007, Delaere and Hermans 2003 (see below).

Verrucous carcinoma is not consistently responsive to irradiation; although debated, an anaplastic transformation may follow such a treatment (Ferlito et al. 1998). Therefore, in patients with this type of tumor surgery is usually recommended as the treatment of choice.

4.1.2 Supraglottic Cancer

Patients with a T1, T2, or a 'favorable' T3 lesion can be treated with either irradiation or supraglottic laryngectomy (Robbins et al. 1987; Lee et al. 1990; Million 1992). The selection is at the preference of the patient and the physician in charge. A 'favorable' T3 tumor is classified as T3 due to preepiglottic space involvement (visible on CT) or limited extension to the medial wall of the piriform sinus or postcricoid area, and not due to vocal cord fixation which precludes supraglottic laryngectomy (Million 1992). Supraglottic laryngectomy probably produces a higher initial local control rate but, based on anatomic and coexisting medical considerations, is suitable for a smaller subset of patients and has a higher risk of complications compared with radiotherapy (Hinerman et al. 2002). Patients with pulmonary or cardiac disease are not good candidates for this procedure, as essentially all patients aspirate to some degree after the operation. The proportion of patients suitable for conservative surgery in an unselected population with supraglottic cancer is estimated to be about 15–20%.

Fifty percent or more of patients who undergo a supraglottic laryngectomy will have a combined treatment with radiotherapy (Weems et al. 1987; Lee et al. 1990). Radiotherapy increases the morbidity of supraglottic laryngectomy (Steiniger et al. 1997). If such a combined treatment can be anticipated (clinically positive neck nodes), or the likelihood of conversion of partial to total laryngectomy during surgery is high, radical radiotherapy is preferred over surgery (Weems et al. 1987).

T3 cancers with a fixed vocal cord have lower local control rates after radiotherapy than those with normal mobility (Mendenhall et al. 1996).

Bulky, endophytic T3 lesions and most T4 lesions are considered unfavorable for radiotherapy; often they will show vocal cord fixation and/or airway compromise. Partial (if feasible) or total laryngectomy, with or without postoperative radiotherapy, is an option in these patients, as the local control rates are better for the surgically treated patients than for those treated by radiotherapy alone (Weems et al. 1987). Patients who are medically unfit for total laryngectomy or refuse this procedure are treated with radiotherapy; in T3 and T4 tumors anatomically unsuitable for conservation surgery, local control can be achieved by radiotherapy in 40–63% of patients (Mendenhall et al. 1996).

There is a need for better selection of patients with a T3 lesion, medically suitable for partial laryngectomy, into the favorable group for radiotherapy; in this way a more informed treatment choice can be made. Imaging findings can be helpful to select patients in which radiotherapy has a good chance of success (see below).

Some selected T4 lesions may also be not as unfavorable for radiotherapy as is suggested by their staging: minimal cartilage invasion or minimal neck soft tissue extension may not influence the local outcome when treated by RT (Million 1992; Parsons et al. 1998).

As for glottic cancers, chemotherapy is useful as concurrent therapy in patients with advanced tumors (see above). CT-determined parameters, such as tumor volume, are helpful to select patients likely to benefit from such combined treatment (Mendenhall et al. 2003).

4.2 Impact of Imaging on Treatment Choice and Prognostic Accuracy

Very few studies are available on the impact of imaging on treatment choice and the accuracy of predicting treatment outcome in laryngeal cancer. Such an impact depends on the treatment policy of laryngeal cancer in a given center (Barbera et al. 2001). Charlin et al. (1989) studied the impact of CT on management, working in an institution where at that time all cancers with a small to moderate tumor volume and no sign of deep infiltration were treated by radiotherapy alone, larger cancers and those with signs of deep infiltration by conservation surgery when local extension allowing it, and total laryngectomy with postoperative radiotherapy was performed for tumors with vocal cord fixation, cartilage destruction and other signs of deep major infiltration. Charlin et al. (1989) observed a change in therapeutic attitude with CT in 10 out of 66 consecutive patients (15.1%). In all ten patients radiotherapy was thought

to be the best treatment after endoscopic evaluation; this was changed to conservative surgery in seven and total laryngectomy with postoperative irradiation in three patients.

In other centers, nearly all laryngeal cancers are treated by radical radiotherapy, surgery being used as a salvage procedure. In such institutions the impact of laryngeal imaging on initial treatment selection can be anticipated to be of less importance. However, the radiological findings may influence the definition of radiation portals, which require an exact knowledge of the local extension of the tumor, the status of the neck lymph nodes, and the location of metastatic neck adenopathies.

In a retrospective multicenter study, the incorporation of CT information did not improve the ability of the T-classification for predicting local failure or cause-specific survival (Barbera et al. 2001). However, as noted by these authors, the ability of CT to improve the predictive value of the T-classification is constrained by the definitions of the T-classifications, which do not take into account other prognostic information provided by CT.

Archer et al. (1984) have proposed a classification system of laryngeal cancer based on CT findings. This classification used the localization of the tumor mass relative to the arytenoid cartilage, as visible on CT studies. The rationale was that tumors with their plane of maximal size at or below the mid-body of the arytenoid cartilage have a much higher likelihood of cartilage invasion. In more than half of their cases such cartilage invasion was only detectable by microscopic study of the resection specimen. This alternative classification system has not been adopted.

4.3 Use of Imaging Parameters as Prognostic Factors for Local Outcome Independently from the TN-Classification

4.3.1 Predicting Local Outcome After Radiotherapy

4.3.1.1 Tumor Volume and Deep Tissue Infiltration

Success in controlling a tumor by radiotherapy depends on killing all clonogenic cells. The probability of cure depends, among other factors, on the initial number of clonogenic cells. There are indications that the clonogen number increases linearly with tumor volume (Johnson et al. 1995).

Large primary tumor volume is already for a long time known to be a reason of poor local outcome of laryngeal cancer after definitive radiation treatment (Fletcher et al. 1975). Clinical estimation of tumor volume in various advanced head and neck cancers treated in a multicenter EORTC trial, correlated with survival and locoregional control after radiation treatment (Van Den Bogaert et al. 1995), but the volume classes defined in this study (<10 ml, 10–30 ml, 30–100 ml, >100 ml) are too rough to be applicable to less advanced head and neck cancers. Overgaard et al. (1986) reported laryngeal tumor diameter (<2 cm, 2–3.9 cm, >4 cm) to be of significant importance to both probability of local control and survival in glottic and supraglottic tumors. However, tumor diameters are a rough and potentially inaccurate estimation of tumor volume due to invisible deep tumor extension (Marks et al. 1979; Van Den Bogaert et al. 1983).

Three-dimensional tumor visualization as offered by modern cross-sectional imaging techniques allows more accurate estimation of the tumor volume. To determine the volume of a particular structure, its borders are traced on consecutive images, either manually or with some (semi-)automated method. The segmented surface on each image is then calculated. This procedure can be done on the screen of a workstation, using a mouse-controlled cursor, or indirectly using a digitizer. The obtained surfaces are then multiplied by the slice interval. The summation of all these obtained volumes represents the total volume of the structure of interest. This technique is called the summation-of-areas technique (Breiman et al. 1982).

Gilbert et al. (1987) were the first to report the prognostic value of CT-determined laryngeal tumor volume for outcome after definitive radiation therapy. Their study consisted of 37 patients with T2–T4 laryngeal cancer (both from glottic and supraglottic origin). The mean tumor volume for patients failing radiotherapy in their study was 21.8 ml, and for patients primarily controlled this was 8.86 ml; tumor volume significantly predicted disease-free interval and outcome with radiotherapy.

Glottic and supraglottic tumors should be considered separately in such studies, as the anatomic situation, and correlated extension pattern is very

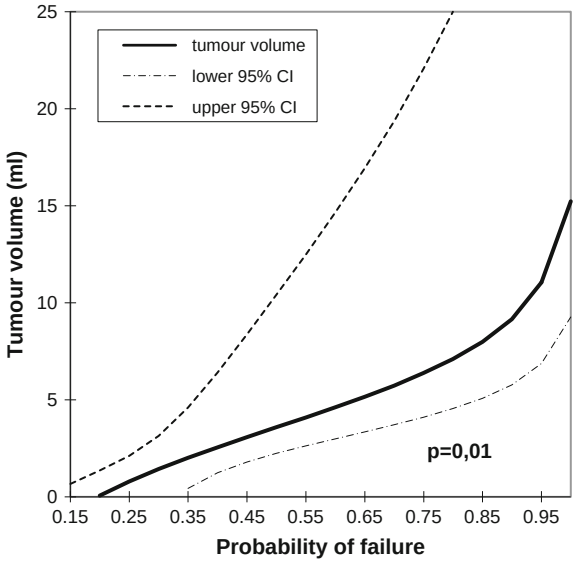

Fig. 19 Glottic cancer: probability of local failure after definitive radiation therapy versus CT-determined primary tumor volume. Local failure rate is significantly higher with larger primary tumor volume. The 95% confidence intervals for tumor volume are indicated (from Hermans et al. (1999a), with permission)

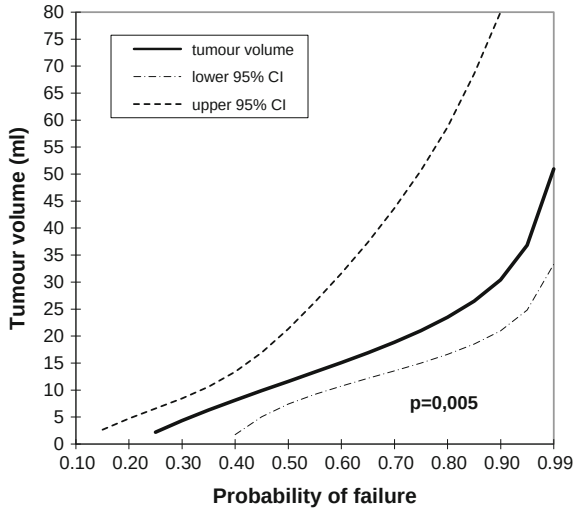

Fig. 20 Supraglottic cancer: probability of local failure after definitive radiation therapy versus CT-determined primary tumor volume. As for glottic cancer, local failure rate is significantly higher with larger primary tumor volume. The 95% confidence intervals for tumor volume are indicated (from Hermans et al. (1999b), with permission)

different for glottic versus supraglottic tumors. Freeman et al. (1990) and Mancuso et al. (1999) were able to identify those patients with T1–T4 supraglottic carcinomas who had a higher likelihood of local control based on pretreatment CT volumetric analysis (tumors <6 ml had a probability of 89% of local control, while tumors >6 ml had only a control rate of 40%). In another study, a significant difference in local outcome after radiotherapy was found in supraglottic cancer, with local control rates for tumors with volumes greater than or less than 8 ml being 20 and 70%, respectively (Kraas et al. 2001).

Lee et al. (1993) and Pameijer et al. (1997) could stratify in a similar way patients with T3 glottic carcinoma into groups with different likelihoods of local control (tumors of ≤3.5 ml had a local control probability of 85%, while tumors of >3.5 ml had only a local control rate of 22%). On the other hand, Mukherji et al. (1995), in a study on 28 patients with T2 glottic carcinoma, were not able to distinguish groups with significantly different local control rates using CT-determined tumor volume. However, in another study in patients with a T2 laryngeal cancer, a tumor volume of >4 ml predicted a significantly worse local outcome rate (Lo et al. 1998).

The results of the studies by Hermans et al. (1999a, b) corroborate well these previous findings. Both for glottic and supraglottic cancers, tumor volume was found to be a significant prognostic indicator of local control. In glottic cancer, failure probability analysis showed a clear relation between larger tumor volume and increasing risk for local failure (Fig. 19); a tumor volume of 3.5 ml correlated with a risk for local failure of approximately 50%. From the graph published by Pameijer et al. (1997), an approximately 40% chance of local failure in T3 glottic cancer with a similar tumor volume can be inferred. Also for supraglottic cancer, Hermans et al. (1999b) found a significant relation between tumor volume and risk for local failure (Fig. 20). Compared to glottic cancer, larger supraglottic tumor volumes were found for similar local control rates; similar results can be inferred from other publications (Mancuso et al. 1999). The reason for this different critical tumor volume between glottic and supraglottic cancer is not clear; it might be related to a different local environment in the glottic and supraglottic regions, but also (and maybe predominantly) to the more exophytic growth pattern exhibited by supraglottic tumors.

However, tumor volume was not found to be an independent predictor of local outcome when a multivariate analysis was performed. In glottic carcinoma,

involvement of the paraglottic space at the level of the true vocal cord and involvement of the preepiglottic space were found to be independent predictors of local outcome (Hermans et al. 1999a). Deep involvement of the paraglottic space at the glottic level, as seen on imaging studies is also called the 'adjacent sign'. This sign was found to be the only independent predictor of local outcome and survival in a series of 130 patients suffering from T1 to T2 glottic cancer (Murakami et al. 2005). In a study where MRI was used as imaging method, intermediate signal in the thyroid cartilage on a T2-weighted sequence, and hypopharyngeal extension were found as independent predictors of local control (Ljumanovic et al. 2007). However, these authors did not include involvement of the paraglottic space in their analysis; as mentioned below, cartilage signal alterations can be regarded as an indirect parameter reflecting tumor spread in the deep tissues.

In supraglottic carcinoma, involvement of the preepiglottic space and subglottic extension were the strongest independent predictors of local control (Hermans et al. 1999b). Also, in a study using MRI as imaging tool, preepiglottic space involvement, as well as abnormal signal intensities in the thyroid cartilage adjacent to the anterior commissure and/or cricoid cartilage were the independent predictors of local control (Ljumanovic et al. 2004). Again, these cartilage abnormalities can be regarded as reflecting extensive invasion of the deep laryngeal tissues (see below).

Tumor volume and degree of involvement of the laryngeal deep tissues are correlated to some extent. However, these descriptive CT-parameters may also reflect a more aggressive tumoral behavior, which could explain their stronger association with local recurrence. Fletcher and Hamberger (1974) stated that the preepiglottic space is poorly vascularized; they suggested that the anoxic compartment of tumors invading this space must be significant, and thus relatively radioresistant.

Although currently few data are available, imaging-determined tumor volume does seem to predict the local outcome in patients suffering advanced head and neck cancer, including laryngeal cancer, when treated by chemoradiotherapy (Hoebers et al. 2008).

4.3.1.2 Cartilage Involvement

Laryngeal cartilage invasion is often considered to predict a low probability of radiation therapy alone to control the primary tumor site and to indicate an increased risk of late complications, such as severe edema or necrosis (Lloyd et al. 1981; Castelijns et al. 1990).

Before the era of computer assisted cross-sectional imaging only gross cartilage destruction, usually occurring in large volume laryngeal tumors, could be detected clinically or by conventional radiography. More limited laryngeal cartilage invasion can be detected with modern cross-sectional imaging methods (Becker et al. 1995). Earlier studies described an association between CT-depicted cartilage involvement in laryngeal carcinoma and poor outcome after radiation therapy (Silverman 1985; Isaacs et al. 1988). However, according to others, involvement of laryngeal cartilage is not necessarily associated with a reduced success rate of radiation therapy (Million 1989). More recent studies correlating laryngeal cartilage abnormalities, detected on CT, with local outcome after RT seem to corroborate this last point of view.

The cartilage most often showing abnormalities is the arytenoid cartilage; usually this cartilage appears sclerotic. An abnormal appearance of this cartilage was not found to be associated with poorer local control, and may be unimportant in terms of prognosis (Tart et al. 1994; Hermans et al. 1999a). The majority of sclerotic arytenoid cartilages do not contain tumor within ossified bone marrow, which can help to explain why radiation therapy is efficient in a large percentage of patients with isolated arytenoid sclerosis on CT (Becker et al. 1997).

Pameijer et al. (1997) found a lower probability of local control in patients with T3 glottic carcinoma, when both arytenoid and cricoid showed sclerosis. These authors assume that if both the arytenoid and cricoid cartilage are sclerotic, the probability of microscopic cartilage invasion will increase. Hermans et al. (1999b) also found that cricoid cartilage abnormalities in glottic carcinoma yielded a statistically significant lower control rate. Ten out of the 13 patients with sclerosis of the cricoid in this study had also sclerosis of the arytenoid cartilage, corresponding with the 'double sclerosis'-situation described by Pameijer et al. (1997). However, the multivariate analysis performed in the study by Hermans et al. (1999a) showed that an abnormal appearing cricoid cartilage is not an independent predictor of poor local control in glottic carcinoma: it lost significance when paraglottic and preepiglottic space involvement were

entered in the statistical model. Even relatively subtle cartilage abnormalities, as detected in this study population (sclerosis of the cartilage being the most frequent alteration seen), seem to be correlated with deep tumor extension. More destructive cartilage changes are associated with very bulky tumors, which are not selected for radiation therapy.

There are only few data available on the correlation between thyroid cartilage abnormalities as seen on CT and local outcome of glottic cancer after definitive radiation therapy. Some studies explicitly excluded patients showing evidence of thyroid cartilage involvement (Mukherji et al. 1995; Pameijer et al. 1997). In the study by Hermans et al. (1999a), where tumor visible on both sides of the cartilage and lysis of ossified cartilage were used as signs of thyroid cartilage invasion, only a limited number of patients with glottic carcinoma had an abnormal appearance of this cartilage. No evidence was found that thyroidal cartilage involvement on itself as seen on CT is associated with a poorer local outcome after definitive radiation therapy, but as said, the number of patients in this study with signs of neoplastic involvement of this cartilage was small.

No conclusions can be drawn concerning cricoid or thyroid cartilage abnormalities on CT in supraglottic carcinoma, due to the limited number of patients selected for radiation therapy with abnormalities of these cartilages.

On MRI, cartilage involvement in patients with small-sized tumors (under 5 ml) is not correlated with tumor recurrence; abnormal MR signal pattern in cartilage combined with large tumor volume (above 5 ml) worsens the prognosis significantly (Castelijns et al. 1996b). Consequently, abnormal MR signal pattern in laryngeal cartilage should not automatically imply laryngectomy, especially in lesions with smaller volumes. It is incorrect to postulate that radiotherapy cannot cure a substantial number of lesions with cartilage involvement on MRI. Castelijns et al. agree with Million (1989) that minimal cartilage involvement in patients with low staged tumors does not imply a bad prognosis (Castelijns et al. 1995, 1996a). Similar to CT, the presence of cartilage abnormalities on MRI studies may be just reflecting a large tumor volume and deep tumor spread, and as such being only indirectly correlated with local outcome after radiotherapy (Ljumanovic et al. 2004, 2007).

Recent experience shows that organ preservation after chemoradiotherapy is possible in advanced laryngeal cancer invading the cartilage, or even spreading through the cartilage, as visible on imaging studies (Knab et al. 2008; Worden et al. 2009). However, the use of organ preservation as end point in such studies may be questioned; in patients with pretreatment gross cartilage destruction, a poor functional outcome may be expected because of breakdown of a significant part of the larynx during tumor regression (Wolf 2010). As discussed above, quantification of tumor bulk may be a more reliable way to predict success of therapy.

4.3.1.3 Imaging of the Tumoral Micro-Environment

Multiple factors determine the resistance of tumors against radiation treatment and chemotherapy. Tumors may show an intrinsic, genetically determined inherent resistance. However, extrinsic physiological (environmental) factors are also important. Most critical is the presence of less or inadequate and heterogeneous vascular networks leading to chronic 'diffusion-limited' tumor hypoxia.

There is strong evidence that for some human tumors treatment may fail due to the presence of hypoxia (Overgaard and Horsman 1996). The presence of tumor hypoxia needs to be identified and quantified, not only as predictor of outcome, but also to select patients for concomitant radiosensitising therapy to overcome the hypoxia effect. Treatments such as hyperbaric oxygen or carbogen (95–98% O_2 with 2–5% CO_2) breathing during RT have been extensively investigated and initiated in clinics (Kaanders et al. 2002). The adequate appreciation of tumor hypoxia may also lead to the efficient use of hypoxia-directed treatments such as bioreductive drugs or gene therapy.

Direct quantification of tumor oxygenation can thus be expected to be of important prognostic and therapeutic value. However, till date, one has to rely on invasive methods, e.g. biopsy-based immunohistochemistry techniques, or the use of Eppendorf oxygen-sensitive electrodes to screen tumors for hypoxia. However, oxygen-sensitive needle electrodes can only to a certain extent be used, as some primary tumors (such as laryngeal cancers) are deeply seated and difficult to reach.

There is a clear need for non-invasive methods to investigate the tumoral micro-environment. Nuclear

imaging methods (such as PET-imaging) may provide important information about tumor physiology. There is increasingly more evidence that CT and MR-studies, classically used to demonstrate the anatomic position and extent of tumors, are able to provide additional, biological information (Rijpkema et al. 2001, 2002; Hermans et al. 2003; Bisdas et al. 2009).

For example, breathing a hyperoxic hypercapnic gas mixture may have an effect on both blood flow and oxygenation. To study these effects in the clinic a combination of blood oxygen level dependent (BOLD)-MRI and dynamic contrast-enhanced MRI techniques seems suitable. The effects of breathing a hyperoxic hypercapnic gas mixture (98% O_2 + 2% CO_2) were assessed by functional MRI techniques in patients with head and neck tumors (Rijpkema et al. 2002). The main conclusion of this study was that breathing this gas mixture improved tumor blood oxygenation. No changes in tumor vascularity were found as assessed by the gadolinium uptake rate (Rijpkema et al. 2001). Functional MRI proved to be a promising tool to investigate both tumor oxygenation and vascularity and might be developed into a predictive tool for treatments using hyperoxygenation for other types of tumors as well.

4.3.2 Predicting Local Outcome After Surgery

One study addressed the correlation between volume of supraglottic cancer, as assessed on imaging studies, and outcome after surgical therapy. This study examined a small population with few local recurrences; patients with a tumor volume over 16 ml were found to have a significantly worse local outcome than those with smaller volumes (Mukherji et al. 2000). The threshold tumor volume in this surgical series is greater than the threshold tumor volumes reported for supraglottic cancer treated by radiotherapy (see above). This can be expected as during laryngectomy the tumor is resected en bloc. The endolaryngeal soft tissues of the larynx are contained within a cartilaginous framework; the primary tumor should therefore be completely contained within the resected specimen in a successfully performed laryngectomy. Large tumors are more likely invading the laryngeal framework and grow extralaryngeally (Mukherji et al. 2000).

It is often suggested that cartilage involvement precludes voice-sparing partial laryngectomy (Tart et al. 1994; Becker et al. 1995; Castelijns et al. 1996a). However, one study indicated that cartilage alterations, as seen on preoperative CT, are not correlated with the local outcome of patients treated by a speech-preserving surgical technique: no increased local failure rate was observed in the patients with cartilage alterations (1 of 11) over those without cartilage abnormalities (1 of 5) (Thoeny et al. 2005). The used surgical technique in this study (extended hemilaryngectomy with tracheal autotransplantation) allows resection of the hemilarynx, including half of the cricoid cartilage. Therefore, areas of possible neoplastic cartilage involvement are very likely to be included in the resection specimen. The inability of other speech-preserving surgical techniques to adequately resect areas of laryngeal framework invasion may falsely lead to the belief that cartilage involvement, in itself, is a contraindication for partial laryngectomy (Thoeny et al. 2005).

4.3.3 Towards Risk Profiles Incorporating Imaging Findings

As staging procedure, CT and MRI have an important function in corroborating clinical findings and ruling out more extensive disease. Accurate staging is critical in decision making in oncology (Barbera et al. 2001). However, to what extent CT or MRI influence treatment decisions in laryngeal cancer is currently not very clear, and likely varies from institute to institute. This influence depends on the conducted treatment policy, more precisely on the relative role of radiotherapy and surgery as primary treatment modality in more advanced laryngeal cancer.

The parameters defined in the T-classification are mainly based on clinical examination; the addition of modern imaging methods in staging laryngeal cancer may influence the prognostic information about the T-classification itself, by causing stage migration (Piccirillo and Lacy 2000; Champion and Piccirillo 2004). Furthermore, imaging-derived parameters such as tumor volume and depth of invasion in the deep tissues are stronger related to local outcome than the T-categories.

Pure morphologic criteria cannot explain entirely the biologic behavior of a tumor and its response to treatment. Ongoing research focuses on the evaluation with radiological methods of tumor microvascularisation, perfusion, and oxygenation, factors known to be of important prognostic value.

New classification systems should be conceived, incorporating not only morphologic tumor extent as within the present TNM system, but also including other variables with independent prognostic significance (Takes et al. 2010).

5 Posttreatment Imaging in Laryngeal Cancer

5.1 Expected Findings After Treatment

After treatment of a head and neck cancer, a number of tissue changes become visible on CT and MR images of the neck. These expected alterations should be known, so that they are not misinterpreted as evidence of persistent or recurrent tumor.

Imaging may be used to monitor tumor response and to try to detect recurrent or persistent disease before it becomes clinically evident, possibly with a better chance for successful salvage.

Treatment complications, such as soft tissue or cartilage/bone necrosis, are less frequent than tumor recurrences, but these conditions may be clinically sometimes difficult to distinguish. Although definitive distinction between necrosis and recurrent tumor may also be radiologically difficult, imaging findings may be helpful in guiding the choice of treatment and assessing the response to specific treatment (Hermans 2004).

5.1.1 Expected Tissue Changes After Radiotherapy

Within the first two weeks after radiotherapy, there is an acute inflammatory reaction within the deep tissues. Increased permeability, due to detachment of the lining endothelial cells within small blood and lymphatic vessels, results in interstitial edema. After this initial period of a few weeks, there is progressive thickening of the connective tissue. Endothelial proliferation is also seen, eventually resulting in complete obstruction of the vessels. The reduction in venous and lymphatic drainage results in further accumulation of interstitial fluid. Then the fibrosis becomes progressively more advanced but the interstitial edema may be reduced by formation of collateral capillary and lymphatic channels.

The changes visible on posttreatment CT and MR images depend on the radiation dose and rate, the irradiated tissue volume, and the time elapsed since the end of radiation therapy (Mukherji et al. 1994a; Nömayr et al. 2001). Changes that may be seen include (Fig. 21):

- Thickening of the skin and platysma muscle
- Reticulation of the subcutaneous fat and the deep tissue fat layers
- Edema in the retropharyngeal space
- Increased enhancement of the major salivary glands, followed by size reduction of these glands: postirradiation sialadenitis
- Atrophy of lymphatic tissue, in both the lymph nodes and Waldeyer's ring
- Thickening and increased enhancement of the pharyngeal walls
- Thickening of the laryngeal structures, with increased density of the fat in the preepiglottic and paraglottic spaces.

These tissue changes are most pronounced during the first few months after the end of radiation therapy, and diminish or even resolve with time. It is important to note that the expected tissue changes after radiation therapy appear symmetrical, unless the neck was irradiated using asymmetric radiation portals.

The laryngeal cartilages do not show changes after irradiation. Reduction in the degree of cartilage sclerosis in the neighborhood of the tumor has been described, and this appears to correlate with local control (Pameijer et al. 1999).

5.1.2 Expected Findings After Laryngeal Surgery

The limits of surgical therapy are determined by the balance between obtaining cure by radical resection of the tumor, and leaving the patient in a functionally and esthetically acceptable situation. More extensive resections are possible by the introduction of various reconstructive materials, such as pedicled or free soft tissue flaps, grafts, and protheses.

5.1.2.1 Laser Resection

The expected findings after transoral laser excision of a laryngeal cancer depend on the amount of tissue resected. The laryngeal soft tissues may appear normal, showing a focal tissue defect (Fig. 22). After a more extensive resection, the laryngeal soft tissue may be replaced by scar, appearing as homogeneous but relatively dense tissue with a straighter inner border (Maroldi et al. 2001); in such cases, differentiation with recurrent tumor may be difficult and

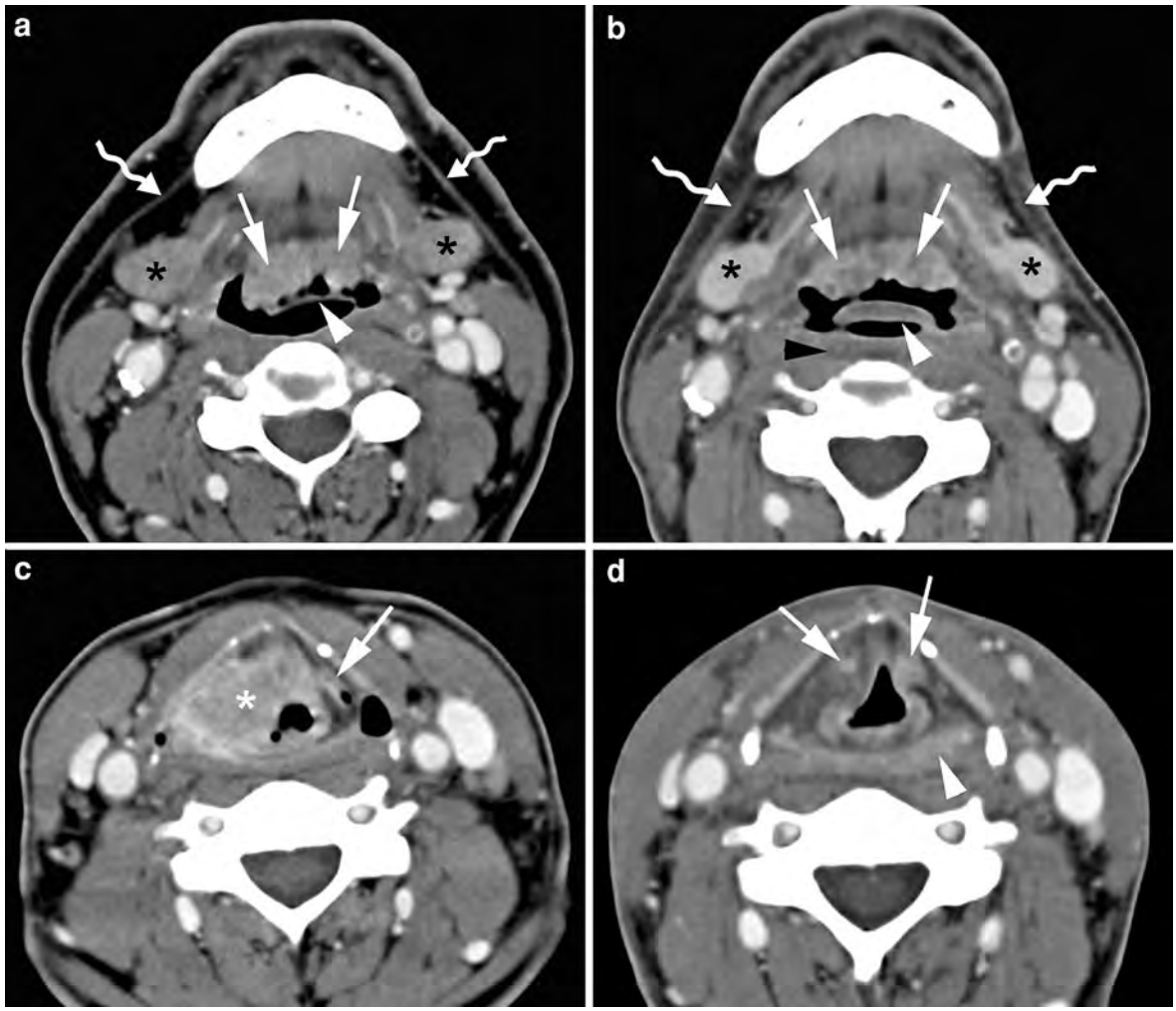

Fig. 21 Patient with supraglottic squamous cell carcinoma, staged T3N0, treated by definitive radiotherapy. Axial contrast-enhanced CT images are shown, obtained just before and 3 months after completion of radiation treatment. **a**, **b** Level of lingual tonsil. After radiotherapy (**b**), apart from diffuse increased attenuation of the neck fatty tissue, thickening of the free edge of the epiglottis (*white arrowhead*), platysma muscles (*curved arrows*), and oropharyngeal walls is seen. Slight amount of retropharyngeal edema is present (*black arrowhead*). Note also increased enhancement of the submandibular salivary glands (*asterisks*), corresponding to radiation sialadenitis, and volume reduction of lingual tonsil (*arrows*). **c**, **d**. Level of supraglottis. Before radiotherapy (*c*), a large supraglottic tumor mass (*asterisk*) is seen, infiltrating the preepiglottic and right paraglottic space; normal left ventricle, containing air bubble, in left paraglottic space (*arrow*). After radiotherapy (*d*), the tumor mass disappeared; increased attenuation of the paraglottic fat spaces, somewhat more pronounced in former tumor bed; no mass lesion can be recognized. Laryngeal ventricle is now visible on both sides (*arrows*). Thickening and increased enhancement of the hypopharyngeal walls (*arrowhead*)

correlation with endoscopic findings is necessary. In case of doubt, biopsy is warranted.

5.1.2.2 Partial Laryngectomy

The aim of partial laryngectomy is to combine radical tumor resection with preservation of laryngeal function. This requires continuity and patency of the airway, separation of the airway and digestive tract, and sparing or reconstruction of the glottic phonation function.

Traditional partial laryngectomies include horizontal supraglottic laryngectomy and vertical hemilaryngectomy, but more complex surgical techniques are also being employed (Maroldi et al. 1997, 2001;

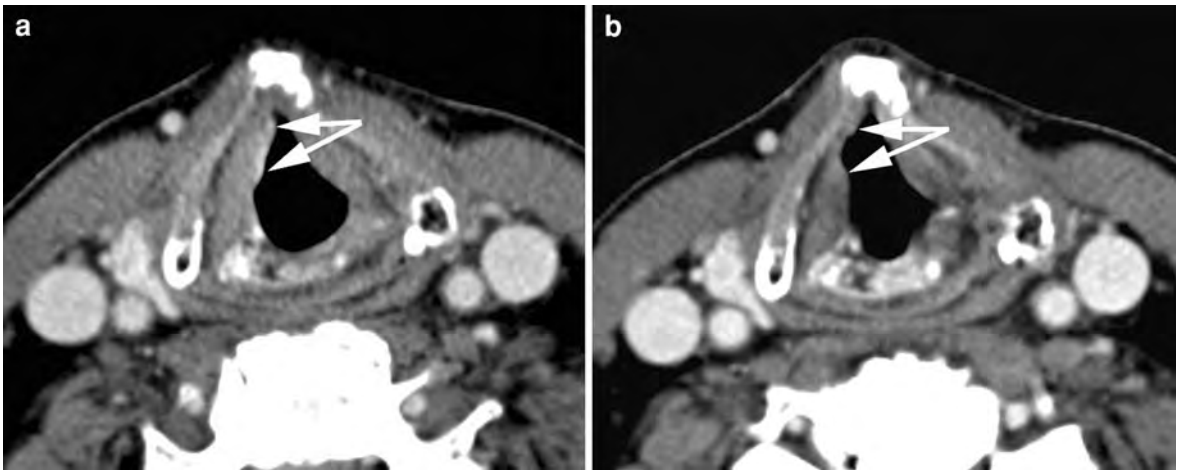

Fig. 22 **a** Recurrent glottic squamous cell cancer, presenting as soft tissue thickening (*arrows*), two years after radiotherapy for a right-sided glottic cancer (T2N0). **b** Situation 7 months after partial cordectomy by transoral laser resection: a soft tissue defect is seen in the anterior half of the right true vocal cord (*arrows*); no evidence for recurrent cancer

Delaere et al. 2007). The postoperative radiological findings depend on the technique employed. Changes in the laryngeal framework offer landmarks for interpreting postoperative findings. However, a somewhat different appearance for the same technique may be encountered among different patients, depending on technical adaptations needed for adequate tumor resection. The postoperative soft tissue changes are less predictable, depending on individual differences in healing, and variations in amount of edema and scarring (Maroldi et al. 2001). The differentiation between redundant or hypertrophic mucosa, as well as scar tissue, from recurrent cancer, may be difficult.

Horizontal supraglottic laryngectomy can be performed in supraglottic cancer staying above the level of the ventricles; this procedure is not performed when the tumor infiltrates both arytenoids (one arytenoid can be resected), the posterior commissure, the postcricoid area, the apex of the sinus piriformis, the glottis, or the thyroid cartilage. Minimal tongue base invasion is not a contraindication. Almost all of the larynx above the level of the ventricles is removed. The residual thyroid cartilage is pulled upwards and sutured to the hyoid bone.

Limited glottic cancer can be treated by vertical hemilaryngectomy. The most limited variant of this procedure is a cordectomy, where the entire vocal cord is removed from the anterior commissure to the vocal process of the arytenoid. In a frontolateral laryngectomy, the true and false vocal cords are removed, as well as the greatest part of the ipsilateral thyroid cartilage, including the angle to encompass the anterior commissure; the vocal process of the arytenoid can also be included. In a frontal laryngectomy, the anterior portion of both vocal cords is removed, together with the anterior commissure; a modified frontal laryngectomy is Tucker's' near-total' technique, using the epiglottis as reconstructive tissue (Fig. 23).

If more extensive involvement of the arytenoid is present (possibly with involvement of the cricoarytenoid joint) and/or subglottic extension is present, these procedures are not performed. Extended hemilaryngectomy may then be an alternative. During this procedure, half of the larynx, including half of the cricoid cartilage, is removed. The large defect in the larynx is reconstructed with a tracheal patch, revascularized by a freely transplanted radial forearm soft tissue flap. Full height cricoid defects can be closed using this patch in a position comparable to unilateral laryngeal paralysis. This is a functional reconstruction, allowing the patient to breathe and speak through his larynx, and swallow without aspiration (Delaere et al. 2007) (Fig. 24).

Some advanced glottic and supraglottic cancers can be treated by supracricoid partial laryngectomy (SPL), entailing en bloc resection of all tissues between the

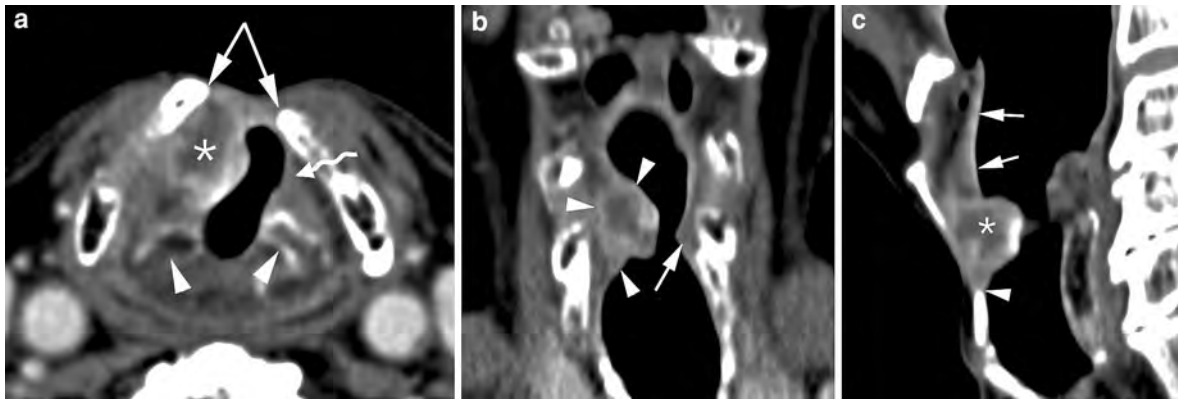

Fig. 23 Contrast-enhanced CT-images in a patient who was treated by a frontal laryngectomy (according to Tucker) for a carcinoma in the anterior commissure. Three years later, he presents with increasing dysphonia. Clinically, swelling of the right false vocal cord is noted with an intact mucosa. **a** Axial section at the level of the arytenoid cartilages (*arrowheads*). Defect in the anterior part of the thyroid cartilage (*arrows*); the anterior part of the left true vocal cord (*curved arrow*) has been resected. On the right side, a centrally necrotic soft tissue mass is seen (*asterisk*), indicating tumor recurrence. **b** Coronal reformatting. Level of true vocal cord is indicated on *left* side by *arrow*. The recurrent tumor on the *right* (*arrowheads*) grows from the false vocal cord region into the true vocal cord; early subglottic extension may be present (*lower arrowhead*). **c** Sagittal reformatting. The upper part of the epiglottis (*arrows*) has a more anterior course as normally expected, as this structure was used to close the thyroid cartilage defect. The recurrent tumor (*asterisk*) abuts the upper margin of the arch of the cricoid cartilage, appearing sclerotic (*arrowhead*). No neoplastic cartilage invasion was present histologically

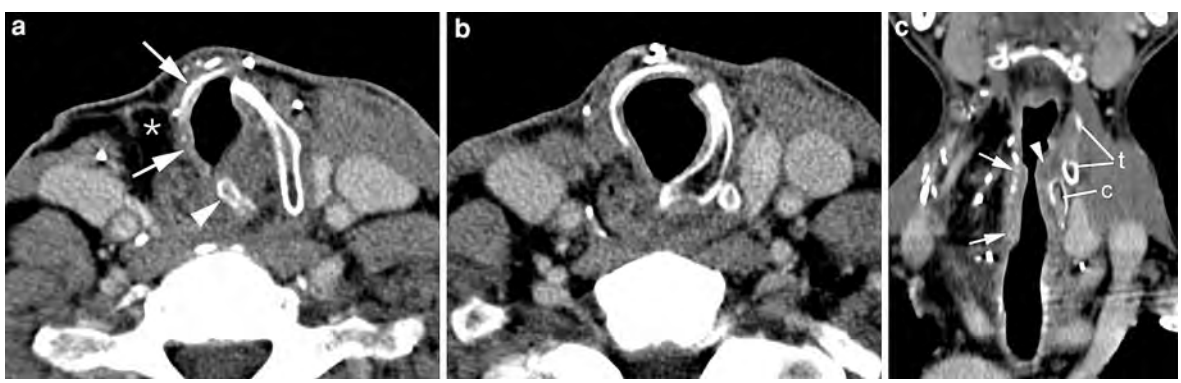

Fig. 24 Contrast-enhanced CT images in a patient treated by extended hemilaryngectomy for a right-sided true vocal cord carcinoma. **a** Axial section at the level of the left true vocal cord. Left arytenoid (*arrowhead*). The right hemilarynx was resected, and the defect closed by a tracheal patch (*arrows*). The fatty structure along the tracheal patch (*asterisk*) corresponds to the radial forearm fascial flap. **b** Axial section at the level of the subglottis. The subglottic airway is reconstructed by the tracheal transplant. **c** Coronal reformatting shows restoration of the laryngeal airway by the tracheal transplant (*arrows*). Left true vocal cord (*arrowhead*); cricoid cartilage (*c*); thyroid cartilage (*t*)

upper margin of the cricoid cartilage and the inferior margin of the hyoid bone, including the true and false vocal cords. Only the arytenoid on the less involved site is left in place. For glottic cancers without involvement of the supraglottis, the upper two-thirds of the epiglottis can be preserved; this variant is known as SPL with cricohyoidoepiglottopexy (CHEP) (Gavilan 2000).

5.1.2.3 Total Laryngectomy

Complete removal of the larynx may be required as primary treatment of extensive laryngeal cancer or for salvage of tumor recurrence after radiation treatment or failed partial laryngectomy.

When the larynx is removed, the airway and upper digestive tract become completely separated. The

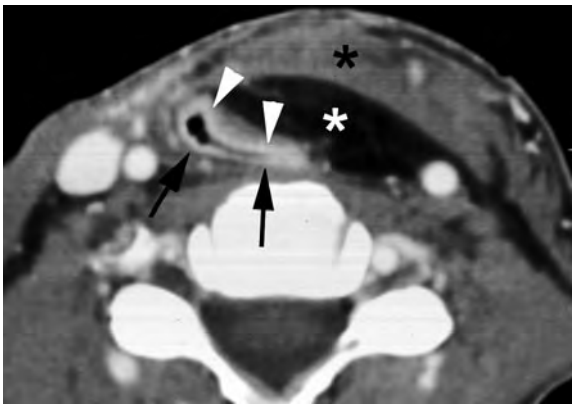

Fig. 25 Axial contrast-enhanced CT image. Situation after total laryngectomy. The neopharynx is reconstructed by residual pharyngeal tissue (*arrows*) and a musculocutaneous soft tissue flap (pectoral major flap), containing skin (*arrowheads*), subcutaneous fat (*black asterisk*) and muscle (*white asterisk*)

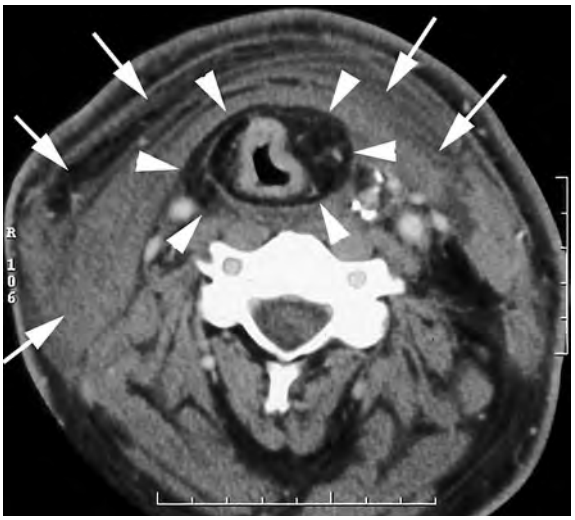

Fig. 26 Axial contrast-enhanced CT-image, in a patient treated by total laryngectomy. The neopharynx is reconstructed by a free radial forearm flap (*arrowheads*); inner enhancing rim is skin); the soft tissues are anteriorly covered by a pedicled pectoralis major flap (*arrows*)

airway will then end at a tracheostomy in the base of the neck. If, following the laryngectomy, not sufficient hypopharyngeal tissue is left for creating a neopharyngeal lumen of acceptable diameter, a soft tissue flap is used to create a wider lumen. A pedicled pectoralis major musculocutaneous flap is commonly used for this purpose (Fig. 25). The pectoralis major flap has an excellent blood supply. The skin of the flap borders the lumen, while the bulk of the flap fills the soft tissue neck defect, creating a more acceptable aesthetic appearance. On imaging studies, the pectoralis major flap appears initially as a bulky soft tissue structure, showing the characteristics of muscle; gradually, denervation atrophy appears, causing volume loss and fatty replacement of the muscle. At the time of imaging, the muscle denervation may be incomplete; fiber-like structures with muscle density within the flap should not be confused with tumor recurrence. Sometimes a radial forearm flap is used to create a neopharynx (Fig. 26), or an intestinal structure is transplanted to function as neopharynx.

Between the proximal trachea and esophagus, a small one-way valve (such as a Provox voice prothesis) is placed, allowing escape of air from the proximal trachea to the esophagus if the tracheostome is closed by the patient. In this way the patient has a lot of air available for producing pharyngeal speech, allowing more rapid speech rehabilitation. Such a valve is visible on imaging studies as a small tube, situated in the wall between the proximal trachea and upper esophagus (Fig. 27).

Commonly during laryngectomy, tissue of the thyroid gland is removed. Unilateral thyroidectomy may be performed, to facilitate surgical access to the larynx and to remove at the same time a site of potential direct spread of the cancer. Another option is to remove the isthmus of the thyroid gland, leaving the two thyroid lobes. This remnant thyroid tissue is usually easy to recognize because it shows a high density, related to the high iodine concentration in the gland and its strong vascularisation. However, as the normal shape of the thyroid gland is lost, these remnants usually show a rounded or oval appearance. Thyroid tissue may appear inhomogeneous due to the presence of nodular hyperplasia, adenomas, or cysts. It is important that these thyroid remnants are not confused with recurrent cancer; unlike recurrent cancer, these have well-defined borders (Fig. 28).

5.2 Persistent or Recurrent Cancer

5.2.1 Imaging Strategies and Findings

Posttreatment imaging is useful to confirm the presence of clinically suspected tumor recurrence.

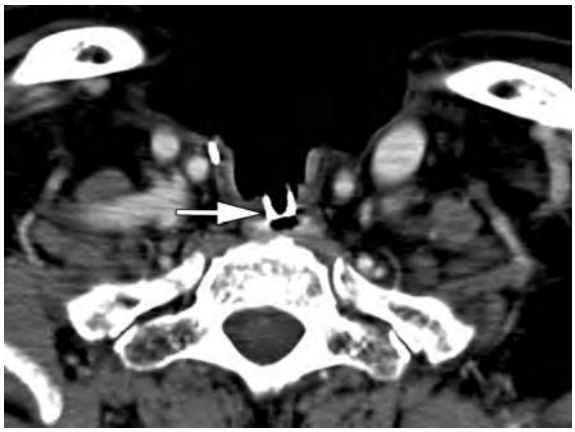

Fig. 27 Axial CT-image at the level of the tracheostomy, in a patient who underwent total laryngectomy. Normal appearance of a voice prothesis (*arrow*), placed through the tracheo-esophageal septum

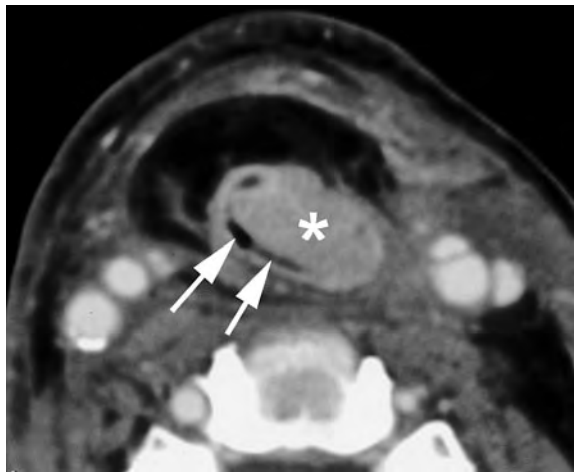

Fig. 29 Axial contrast-enhanced CT-image, after total laryngectomy for squamous cell carcinoma. Enhancing soft tissue mass (*asterisk*) at the anterolateral side of the neopharyngeal lumen (*arrows*): recurrent cancer

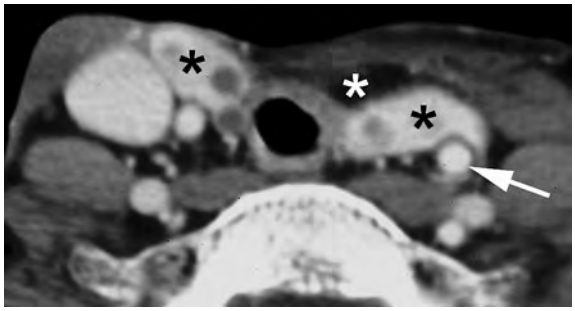

Fig. 28 Axial contrast-enhanced CT image. The neopharynx is seen lying between both thyroid lobes (*black asterisks*). The thyroid isthmus was resected during the laryngectomy. The inhomogeneous appearance of the thyroid lobes is caused by nodular hyperplasia. Absence of left internal jugular vein along the common carotid artery (*arrow*), resected during radical neck dissection. Soft tissue flap (*white asterisk*)

On CT or MRI, tumor recurrence appears after radiation therapy as a soft tissue mass at the primary site and/or as an enlarged (and/or centrally liquefied) neck adenopathy. After surgical treatment, the most reliable imaging finding in recurrent tumor is an enhancing soft tissue mass (Figs. 23, 29); after partial laryngectomy, destruction of residual laryngeal cartilage may be seen.

Early tumor recurrence may be difficult to distinguish from tissue changes induced by therapy. Therefore, it is recommended to obtain a follow-up CT or MR study after surgical, radiation or combined treatment for a laryngeal neoplasm with high-risk profile (Hermans et al. 2000; Schwartz et al. 2003). Probably the best time to obtain such a baseline study is about 3–6 months after the end of treatment. Such a baseline study allows treatment-caused changes in the head and neck tissues to be documented. By comparing subsequent studies with the baseline study, it becomes possible to detect with more confidence tumor recurrences or treatment complications, and this at an earlier stage than is possible with clinical follow-up alone (Fig. 30). In patients with laryngeal cancer, CT is an adequate imaging modality for pre- and posttreatment imaging, but similar results can be obtained using MRI (Ljumanovic et al. 2008).

There is evidence that the baseline study after radiotherapy carries important predictive information regarding the eventual local outcome: several studies show that CT may be useful in the early differentiation of treatment responders from non-responders in irradiated laryngeal and hypopharyngeal cancer (Hermans et al. 2000; Mukherji et al. 1994b).

Based on the appearance of the larynx/hypopharynx on an early post-radiotherapy CT study, a prediction of long-term local outcome can be made according to the following scores: 1 = expected post-radiotherapy changes, i.e. complete resolution of the tumor at the primary site and symmetrically appearing laryngeal and hypopharyngeal tissues, as described

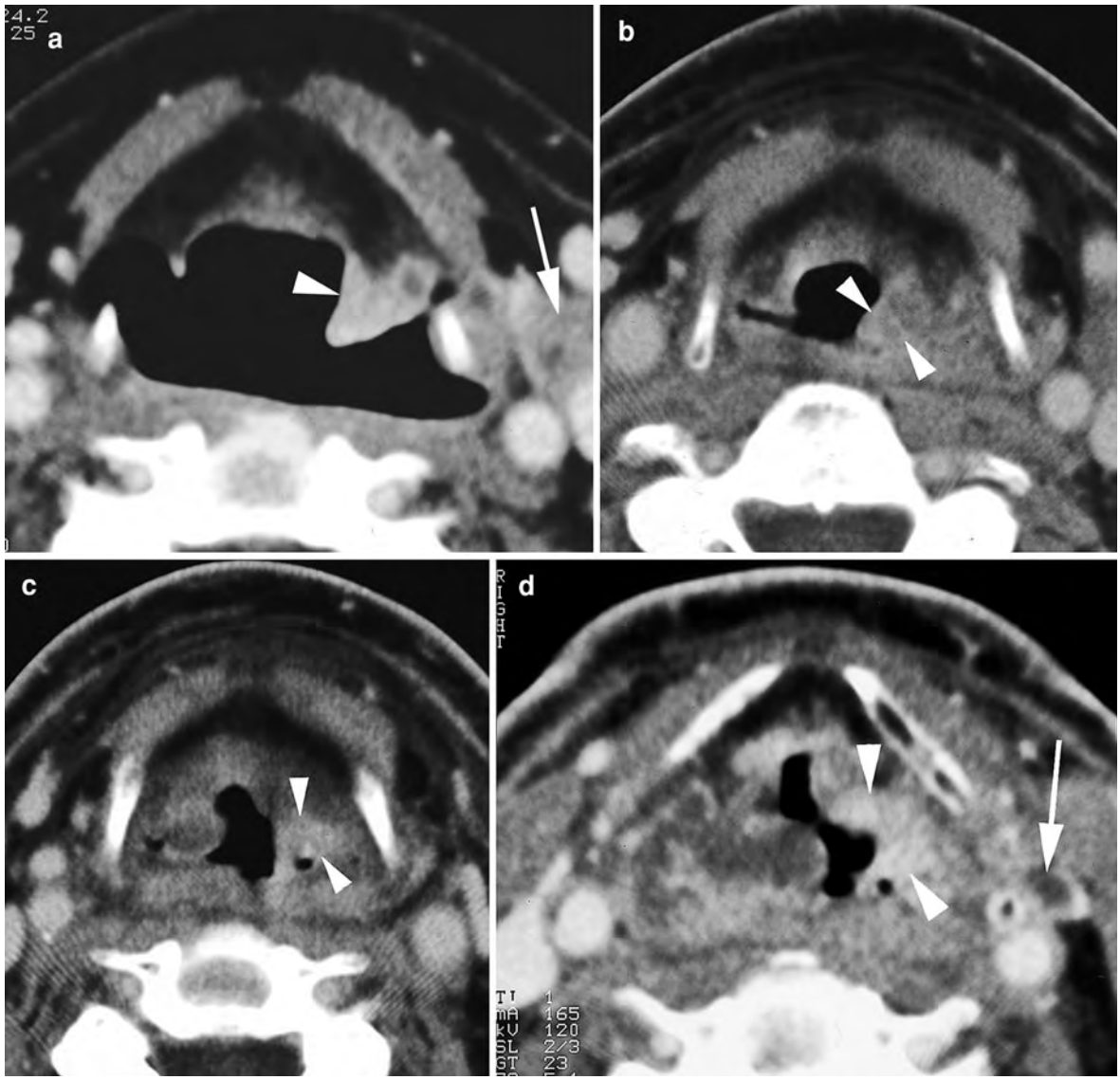

Fig. 30 **a** Pretreatment CT-image of patient with T2 supraglottic squamous cell carcinoma, shows infiltrating lesion within the left aryepiglottic fold (*arrowhead*). A pathologic lymph node is seen along the left internal jugular vein (*arrow*). **b** Three months after radiation treatment. Clinical examination showed pronounced laryngeal edema, but no evidence of tumor. On CT, thickening of the supraglottic soft tissues is seen, more pronounced in the left aryepiglottic fold (*arrowheads*); the density within the left aryepiglottic fold is also somewhat higher than in the surrounding tissues. This is a non-specific finding (score 2), warranting further imaging follow-up. **c** Nine months after radiation treatment. Clinically favourable evolution. However, CT shows more pronounced enhancement in the left aryepiglottic fold compared to the previous study (*arrowheads*). This was reported as suspicious for tumor recurrence. Direct laryngoscopy was performed but showed no mucosal abnormalities; biopsies were negative. **d** One year after radiation treatment. Apart from increasing generalized laryngeal edema, the enhancing mass in the aryepiglottic fold is now extending more anteriorly into the left paraglottic space (*arrowheads*). Also note appearance of small necrotic lymph node in the left neck (*arrow*). Direct laryngoscopy, performed after the CT study, showed caking of necrotic tissue over the left aryepiglottic fold, suspect for tumor recurrence. Biopsy revealed squamous cell carcinoma. The patient died with progressive locoregional disease seven months later

above; 2 = focal mass with a maximal diameter of <1 cm and/or asymmetric obliteration of laryngeal tissue planes; 3 = focal mass with a maximal diameter of >1 cm, or <50% estimated tumor volume reduction (Pameijer et al. 1999; Hermans et al. 2000).

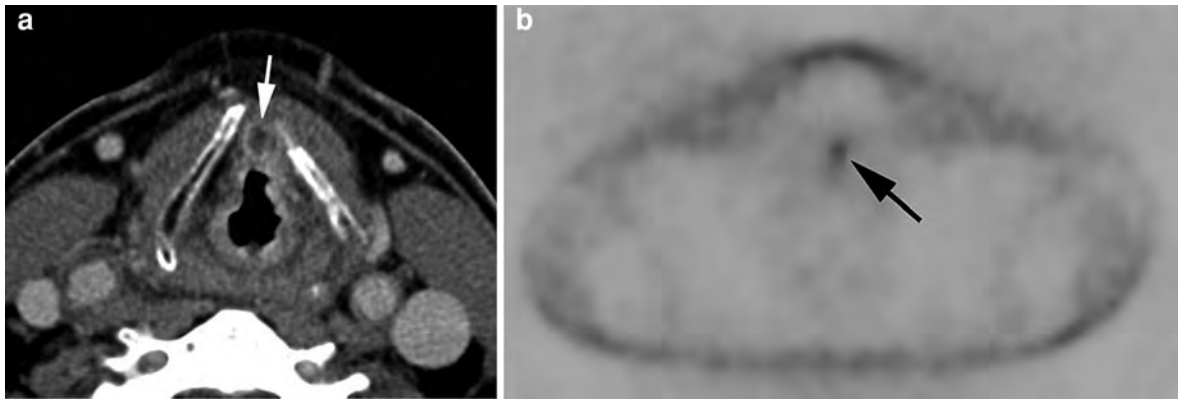

Fig. 31 Same patient as in Fig. 16. Six months after radiotherapy, clinical suspicion of tumor recurrence. **a** Axial contrast-enhanced CT-image shows centrally hypodense nodular lesion in the preepiglottic space (*arrow*) suggesting necrotic tumor. Biopsies were negative. **b** FDG-PET image shows faint tracer accumulation at the level of the supraglottis. Total laryngectomy was performed; histological analysis of the resection specimen confirmed presence of squamous cell carcinoma

The post-radiotherapy CT-score 1 was shown to be a very strong predictor of long-term local control; patients with such findings on post-radiotherapy CT will probably not benefit from further follow-up imaging studies. Conversely, patients with a first follow-up examination classified as CT-score 3 do very poorly; almost all these patients will develop a local failure (Pameijer et al. 1999). Further exploration in such post-radiotherapy CT-score 3 patients is warranted. FDG or thallium PET or SPECT-imaging may prove to be a useful intermediate step in cases where biopsy is considered too risky, or if a biopsy result is returned as negative (Fig. 31). Indeed, the predictive value of a negative biopsy for local control is reported to be only 70% (Keane et al. 1993); this is likely due to sampling error, as tumor recurrences initially develop submucosally and can therefore not be accurately targeted. In cases of contradiction between the clinical findings, CT findings, results of radionucleide studies and/or biopsy, close clinical follow-up and repeat imaging studies are needed.

The local outcome of patients initially classified as post-radiotherapy CT-score 2 is indeterminate. Unless clinical examination is already suspect for local failure, further follow-up CT studies are needed in these patients; a time interval of 3 to 4 months is recommended, to be continued up to 2 years after completion of radiation treatment.

Some authors recommend FDG-PET as the initial baseline study, in patients treated with advanced disease with low clinical suspicion of recurrence, and in patients with nonspecific symptoms that could indicate recurrence but without a clinically obvious mass; cross-sectional imaging should then be performed for an equivocal or positive PET-study, or as the initial study in patients with a suspicious palpable mass or biopsy proved recurrent tumor (Mukherji and Wolf 2003).

False positive findings are frequent if CT, MRI (using conventional sequences), as well as PET is used earlier than 3–4 months after the end of radiotherapy. This is caused by radiotherapy-induced tissue changes. These tissue changes, such as edema, inflammation, fibrosis, and necrosis are expected to show low cellularity on histological examination, in contrast with recurrent or persistent tumour. Diffusion-weighted MRI takes advantage of this completely different microstructure, which will be reflected by a different signal intensity and ADC-value. Based on ADC-values, diffusion-weighted MRI allows differentiation of tumoral tissue from post-radiotherapy alterations and tissue necrosis with high accuracy, and this both in early and late tumour recurrences. In the head and neck, sensitivities in the range of 84–93% and specificities in the range of 90–96% were reported (Vandecaveye et al. 2007; Abdel Razek et al. 2007, 2008). Also in the larynx, diffusion-weighted MRI allows to differentiate tumor recurrence from inflammation and necrosis (Vandecaveye et al. 2007). However, further validation and standardisation of this imaging technique is needed.

5.2.2 Potential Value of Imaging Surveillance

Use of this imaging-based information could lead to more prompt salvage surgery and potentially improve the survival of these patients (Hermans et al. 2000). However, few data regarding the value of posttreatment surveillance in patients with head and neck cancer are available. Some authors argue that routine follow-up is indispensable, as patients with asymptomatic locoregional recurrences, discovered during surveillance, have a significant better postrecurrence survival than those patients where recurrent disease was found by symptoms (De Visscher and Manni 1994). Other authors point out that the apparently longer survival of patients with recurrent tumor diagnosed by testing, may be due to lead time bias (i.e. early diagnosis falsely appears to prolong survival) (Schwartz et al. 2003). This statement probably is true for patients treated by combined-modality therapy for advanced head and neck cancer, who are known to do extremely poorly after relapse and rarely have an effective treatment option available (Cooney and Poulsen 1999). However, in single modality treated patients, where a reasonable chance of salvage exists after locoregional recurrence (e.g. 35–60% surgical salvage rate for irradiated laryngeal cancer), imaging surveillance may be worthwhile to add to the clinical follow-up in order to further improve the salvage rate. More studies are required to elucidate this question.

5.3 Treatment Complications

5.3.1 Complications After Surgery

Most surgical complications occur early after treatment, and are dealt with on a clinical basis. Imaging may be required in the detection and follow-up of a fistula after partial or total laryngectomy. Many of these fistulas will close spontaneously, but some may need reintervention.

After conservative surgery, swallowing coordination may be impaired. The postoperative swallowing function can be analyzed by videofluoroscopy or videofluorography, providing information allowing the planning of rehabilitation (Maroldi et al. 2001). In some cases, surgical intervention may be required; in case of severe aspiration, total laryngectomy may be necessary.

Imaging may also be of use in the confirmation of flap failure due to necrosis (Fig. 32).

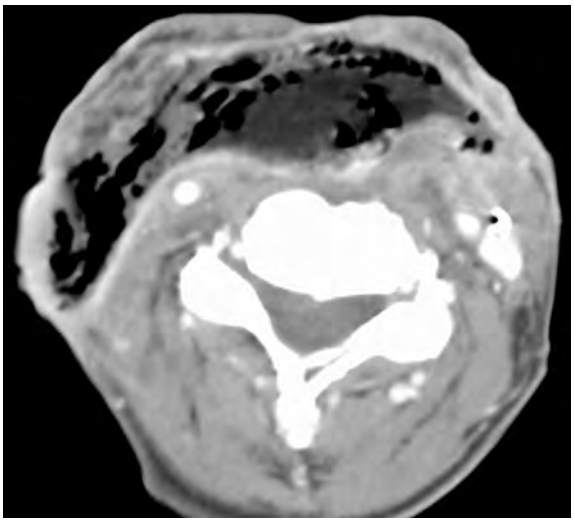

Fig. 32 Axial contrast-enhanced CT image. A few weeks before this CT study, total laryngectomy was performed, with neopharyngeal reconstruction by a pectoralis major flap. The patient suffers now from persistent fistulisation. Throughout the pectoralis major flap, large, confluent gas bubbles are visible, indicating flap necrosis. Flap necrosis was surgically confirmed

A voice prosthesis may cause an inflammatory reaction in the surrounding tissues, and infections may also occur. Clinically, the differentiation with tumor recurrence is not always obvious, and also on imaging, such inflammation causes a soft tissue thickening which may be difficult to differentiate from tumor recurrence. More severe cases of infection complicating a voice prosthesis have been reported, including cervical osteomyelitis and mediastinitis. The presentation may be insidious, with symptoms such as dysphagia, swollen neck and reduced cervical mobility (Malik et al. 2007).

Another complication that may be seen after total laryngectomy is dislocation of the voice prosthesis causing dysphagia (Fig. 33).

5.3.2 Complications After Radiotherapy

5.3.2.1 Laryngeal Necrosis

Acute effects of radiotherapy (skin and mucosal reactions) occur during or immediately after treatment, and usually settle spontaneously.

Persisting severe edema and radionecrosis of the larynx are uncommon treatment complications with an incidence of about 1%. The occurrence of laryngeal necrosis peaks during the 12 months following treatment, which is more or less contemporaneous

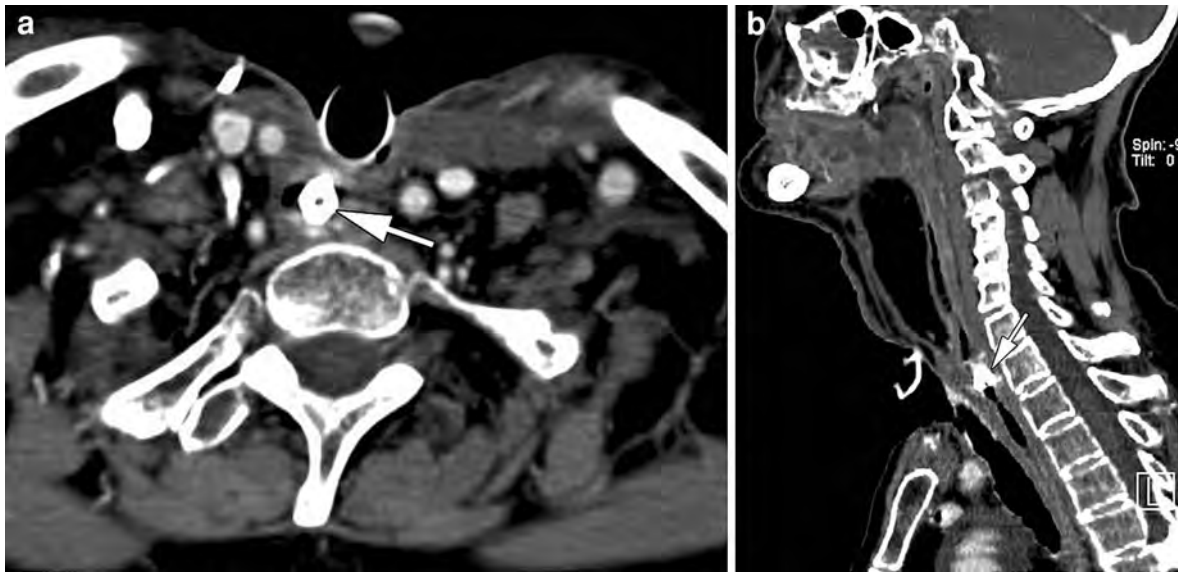

Fig. 33 Axial (**a**) and coronal (**b**) CT-image in a patient presenting with dysphagia after total laryngectomy; no evidence for tumor recurrence was seen, but the voice prosthesis (*arrow*) was seen to be dislodged into the neopharynx, explaining the patient's complaints. At endoscopy, the prothesis was found completely embedded within the neopharyngeal mucosa

with the peak incidence of tumor recurrence. However, cases of laryngeal necrosis more than 10 years after radiation treatment do occur (O'Brien 1996). These late effects after radiation treatment are largely due to impaired vascular and lymphatic flow, caused by endothelial damage and fibrosis (Alexander 1963). Cartilage itself is resistant to the effect of irradiation (see above). Cartilage changes usually occur when the perichondrium is broached by trauma or tumor, exposing the underlying irradiated cartilage to microorganisms in the airway (Keene et al. 1982); this may lead to infectious perichondritis, possibly resulting in necrosis and laryngeal collapse.

Patients with laryngeal necrosis often have neck and/or ear pain, some degree of dysphagia, and anterior neck swelling. Hoarseness and dyspnea are caused by increasing edema with impairment of vocal cord mobility, resulting in cord fixation. Inflammatory changes in the overlying skin or cutaneous fistulae may be present. Palpation of the laryngeal region usually is painful. On imaging studies, a variable degree of laryngeal soft-tissue swelling is seen (Hermans et al. 1998). These soft tissue changes surrounding the necrotic cartilage can be very pronounced and may be the only visible abnormality, making the differentiation with recurrent tumor very difficult. Furthermore, laryngeal necrosis and tumor recurrence may occur simultaneously. In laryngeal necrosis, some fluid may be seen surrounding the cartilages (Fig. 34). Cartilaginous abnormalities are often visible, but in some patients they may only become apparent on follow-up CT studies.

Necrosis of the thyroid cartilage may cause fragmentation and collapse of this cartilage with or without gas bubbles visible adjacent to or in it. Patients with arytenoid cartilage necrosis may show anterior dislocation of this cartilage; this could be due to cricoarytenoidal joint effusion, secondary to inflammation or infection. Progressive lysis of the arytenoid is possible, showing a crumbly aspect evolving to complete disappearance (De Vuysere et al. 1999). Also, sloughing of the arytenoid cartilage into the airway has been described (Hermans et al. 1998). The adjacent part of the cricoid cartilage may appear sclerotic. Cricoidal sclerosis or destruction may be also seen in association with lysis of the thyroid cartilage (Fig. 35).

On MR studies, laryngeal necrosis may appear as focal swelling of the laryngeal soft tissues, loss of the normal high signal in the medullary space of ossified laryngeal cartilage on T1-weighted images, and enhancement of the affected cartilage after injection of gadolinium (Bousson et al. 1995).

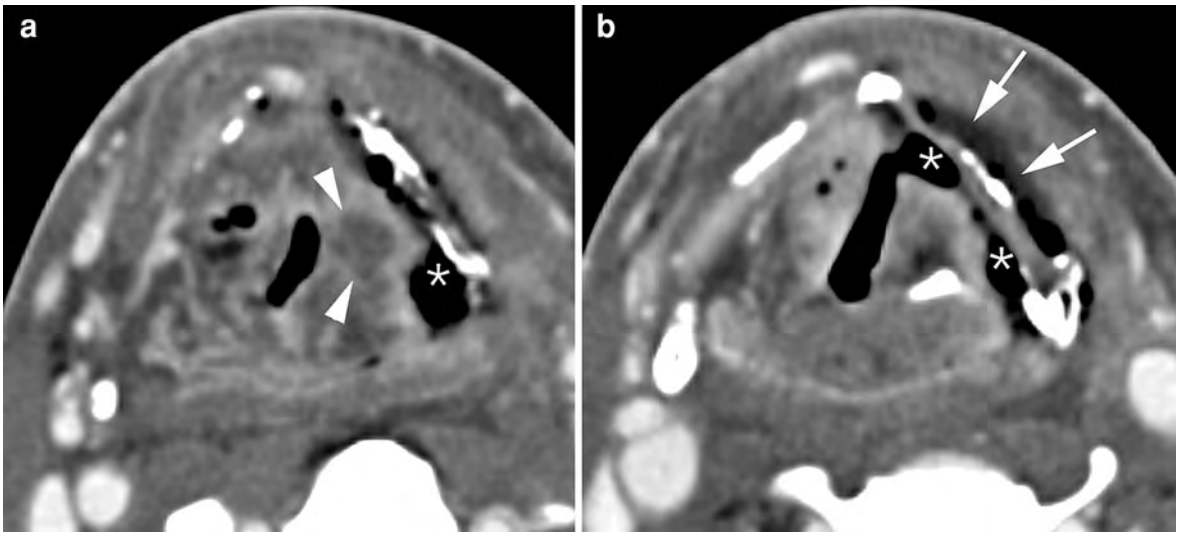

Fig. 34 Axial contrast-enhanced CT-images. Patient treated five months earlier by irradiation for T3 supraglottic cancer, suffering from progressive dysphagia. Laryngoscopy showed a fixed left vocal cord, suspect for tumor recurrence. **a** On a background of expected changes after radiation therapy, a centrally hypodense nodular area of soft tissue thickening is seen in the left aryepiglottic fold (*arrowheads*). Furthermore, a large soft tissue defect (*asterisk*), connecting the left piriform sinus with the denuded thyroid cartilage lamina, is seen. The thyroid lamina appears slightly irregular, and is abutted by air. **b** At a lower level, soft tissue defects are seen to connect to the left piriform sinus, as well as to the laryngeal ventricle (*asterisks*). Fluid layer at the outer side of the thyroid cartilage (*arrows*). A FDG-PET study was strongly positive at the level of the supraglottis. Because of a rapidly deteriorating clinical situation, total laryngectomy was performed. Histologic examination revealed extensive tissue necrosis, but no laryngeal tumor recurrence

In some cases, the imaging findings allow better differentiation between tumor recurrence and chondronecrosis than clinical examination alone. Studies on post-radiotherapy surveillance of laryngeal and hypopharyngeal cancer (Mukherji et al. 1994b; Pameijer et al. 1999) showed that progressive cartilage alterations on post-radiotherapy CT studies predicted poor local outcome, either due to tumor recurrence or chondroradionecrosis. In these studies gas bubbles in the vicinity of cartilage and cartilage collapse were not observed in cases of tumor recurrence. Such findings can be regarded as suggestive of radionecrosis; nevertheless, a co-existent tumor recurrence may be difficult to exclude, depending on the associated tissue alterations (Fig. 34).

It has been suggested that FDG-PET may allow differentiation between tumor recurrence and tissue necrosis as complication of therapy (Anzai et al. 1996; McGuirt et al. 1998). However, false positive results may occur as tissue necrosis may be associated with an important inflammatory reaction, increased metabolism and thus increased uptake of the tracer, suggesting tumor recurrence.

As already mentioned above, diffusion-weighted MRI may be a useful complementary method to differentiate between tissue necrosis and persistent or recurrent cancer (Vandecaveye et al. 2007).

5.3.2.2 Other Complications After Radiotherapy

Fibrosis after radiotherapy may lead to contraction and hardening of the cervical tissues. Fibrosis-induced laryngeal dysfunction may lead to aspiration due to immobilization of the epiglottis and/or delayed closure of the laryngeal vestibulum and glottis; secondary aspiration may be caused by ineffective clearance of the pharynx. Dysphagia may be caused by pharyngeal or upper esophageal stenosis, occuring in 3–4% of patients irradiated for head and neck cancer; rarely, this may evolve to complete obstruction of the upper digestive tract (Laurell et al. 2003; Maple et al. 2006).

Fibrosis of the masticatory muscles may occur, particularly if they were involved by the cancer. The MRI-signal characteristics of fibrosis are variable; often, follow-up studies are needed to rule

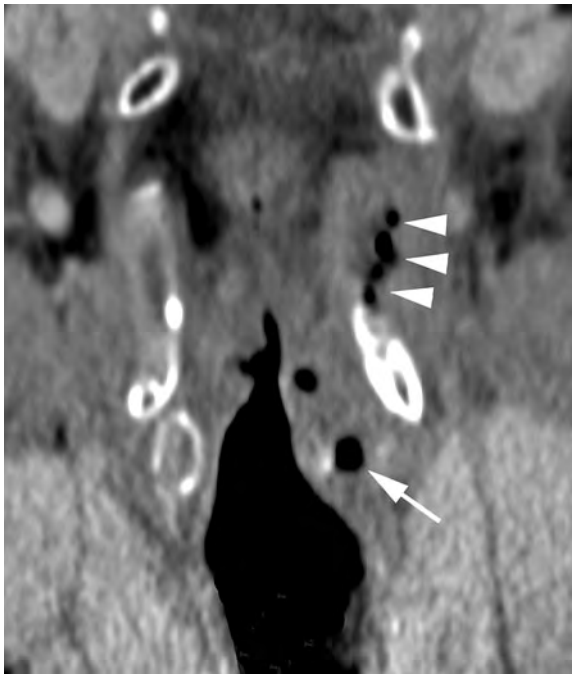

Fig. 35 Coronal reformatting of contrast-enhanced laryngeal CT-study. The patient was treated two years earlier with radiotherapy for a T2 glottic carcinoma, and now present with increasing breathing and swallowing difficulties. Laryngeal soft tissue thickening is seen, more pronounced on the left side. Lysis of the left part of the cricoid arcus, with presence of an intracartilaginous gas bubble (*arrow*); also the upper part of the left thyroid cartilage wing appears lytic and contains several gas bubbles (*arrowheads*). The image is suggestive for extensive laryngeal necrosis. Total laryngectomy was performed; histopathologic study confirmed extensive radionecrosis, without evidence of tumor recurrence

out tumor recurrence with a sufficient degree of confidence.

Other long-term complications of radiotherapy include arteriopathy, delayed central nervous system reaction, radiation myelopathy, cranial nerve palsy and secondary tumors (Becker et al. 1997b).

6 Non-Squamous Cell Laryngeal Neoplasms

The vast majority of laryngeal mass lesions are squamous cell carcinomas, and most of them clinically show mucosal alterations. Non-squamous cell carcinomas typically grow beneath an intact mucosal layer. Clinical and endoscopical diagnosis of a submucosal laryngeal mass lesion is more difficult, and the initial biopsy results of such lesions may be returned as inconclusive or negative.

CT and MR studies demonstrate the presence and extension of such submucosal mass lesion. However, the radiological differentiation between a benign and malignant submucosal mass may be difficult. Signs suggesting malignancy include cartilage destruction, the presence of adenopathies, and a multifocal appearance and/or widely infiltrating behavior.

A variety of epithelial non-squamous neoplasms, and non-epithelial neoplasms can be encountered within the larynx (De Foer et al. 1996). The following discussion is limited to malignant lesions.

6.1 Minor Salivary Gland Neoplasms

Minor salivary glands are found throughout the mucosa of the oral and upper respiratory tract. In the larynx, these glands are located in the supra- and subglottic region; the glottis is devoid of minor salivary glands. The incidence of malignant tumors is considerably higher in minor salivary glands than in the large salivary glands; adenoid cystic carcinoma is the most frequent neoplasm of the minor salivary glands, but also adenocarcinoma and muco-epidermoid carcinoma arise from these glands.

Adenoid cystic carcinoma is a misleading name as macroscopic cystic structures are unusual in this tumor. It is sometimes called cylindroma, an old name which is better abandoned as it includes several nonrelated types of neoplasms.

About 25–35% of minor salivary gland tumors are adenoid cystic carcinomas. This tumor is mainly seen in the fourth, fifth and sixth decade of life.

The radiographic characteristics of adenoid cystic carcinoma are nonspecific. In the larynx, these tumors usually present as a submucosal soft tissue mass in the subglottis (Fig. 36). As they grow submucosally, they are often locally more extensive than clinically suspected.

6.2 Mesenchymal Malignancies

6.2.1 Chondrosarcoma

Chondrosarcomas are the most frequent laryngeal sarcomas. Cartilaginous tumors of the larynx account for less than 1% of all laryngeal tumors. Both chondroma and chondrosarcoma are encountered in the

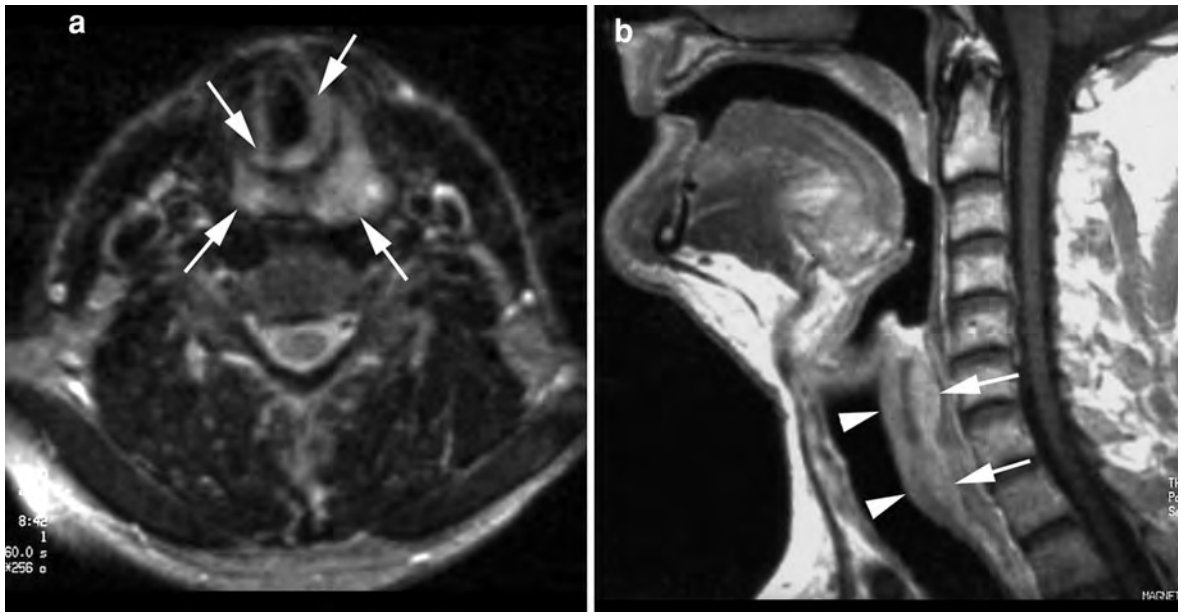

Fig. 36 Patient presenting with hoarseness; endoscopically, a submucosal mass lesion is suspected. The axial T2-weighted MR image (**a**) shows a hyperintense mass lesion (*arrows*) in the subglottis and distal hypopharynx. On the sagittal gadolinium-enhanced T1-weighted image (**b**), the mass is seen to infiltrate the larynx (*upper arrowhead*), proximal trachea (*lower arrowhead*), distal hypopharynx (*upper arrow*) and proximal oesophagus (*lower arrow*)

larynx, with 70% arising from the cricoid cartilage, and the thyroid cartilage being the next most common site of origin.

These cartilaginous tumors may be asymptomatic, or present with hoarseness, dyspnea or dysphagia. At presentation, the lesion is usually less than 2 to 3 cm in diameter. On pathological examination, a lobular growth pattern with low cellularity is seen; nuclear atypia and mitoses are not encountered (Devaney et al. 1995).

True chondromas of the larynx are probably very rare. It is difficult to firmly establish the diagnosis of benign laryngeal chondroma on a small amount of tissue obtained by biopsy. Low-grade chondrosarcoma may also show a lobular growth pattern. Compared to chondroma, low-grade chondrosarcoma may display only minimally increased cellularity and nuclear atypia, a pattern overlapping with benign chondromas; there is also no appreciable degree of mitotic activity in such lesions (Devaney et al. 1995).

On CT studies, cartilaginous tumors of the larynx appear as hypodense, well circumscribed masses centered within the laryngeal cartilage, with coarse or stippled calcification within the lesion (Wang et al. 1999) (Fig. 37). The imaging findings do not allow to

Fig. 37 Coincidently discovered mass lesion in cricoid cartilage, on occasion of a MR study of the cervical spine. Clinical examination showed submucosal swelling underneath the left true vocal cord. Axial CT-image (bone window) confirms an expansile lesion in the left posterolateral part of the cricoid arch; the lesion contains punctiform calcifications. The patient was treated by extended hemilaryngectomy; histological examination showed low-grade chondrosarcoma

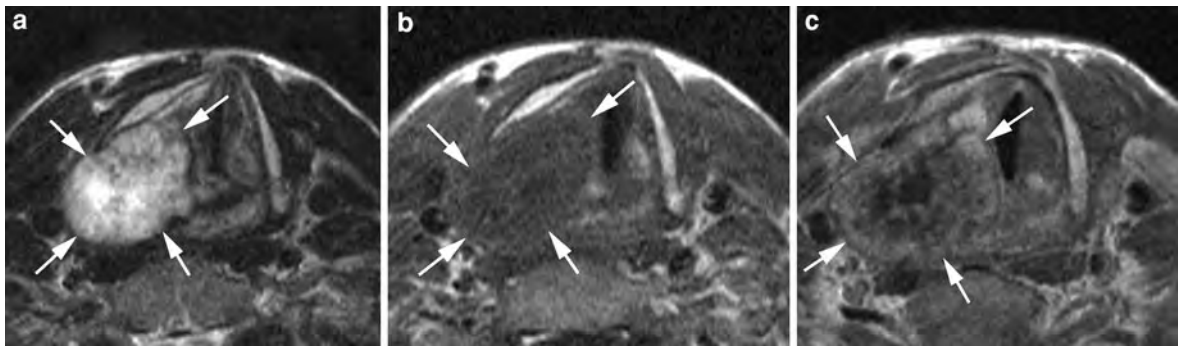

Fig. 38 MR appearance of a large low-grade chondrosarcoma originating from the cricoid cartilage. **a** Axial T2-weighted spin echo image shows a lobulated mass (*arrows*) with high signal intensity. **b** Axial T1-weighted spin echo image. **c** Gadolinium-enhanced axial T1-weighted spin echo image shows irregular enhancement of the mass lesion

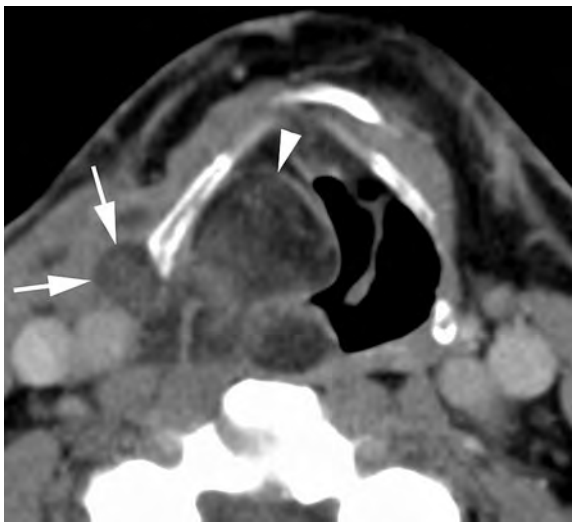

Fig. 39 Axial contrast-enhanced CT-image. Soft tissue mass centered in the right paraglottic space (*arrowhead*), extending into the hypopharynx as well as extrapharyngeally (*arrows*). The tumor appears inhomogeneously, consisting of tissue with negative and positive density values. Liposarcoma

distinguish between a benign and malignant chondroid tumor, although in high-grade chondrosarcomas nodal metastasis in the head and neck may rarely be seen. MRI is less specific for diagnosing such a lesion as it does not depict the intratumoral calcifications as well as CT; on MRI, the tumor matrix has shows a relative high signal intensity on T2-weighted images; the tumor enhancement after injection of gadolinium is variable (Fig. 38).

Cystic-appearing chondrosarcomas have been reported, and may mimic a fluid-filled laryngocoele when originating from the thyroid cartilage (De Foer et al. 1996).

Surgery is the only curative modality in laryngeal cartilaginous tumors. Low-grade chondrosarcomas may locally recur if incompletely resected, but have only limited risk of metastasic disease. Therefore, in all laryngeal cartilaginous tumors a conservative approach is followed whenever possible, directed towards voice-sparing partial laryngectomy. However, total laryngectomy may be the appropriate treatment in lesions involving larger portions of the cricoid cartilage, interfering with surgical reconstruction of a functional larynx, or when the diagnosis of high grade chondrosarcoma is established (Devaney et al. 1995; Wang et al. 1999).

6.2.2 Other Mesenchymal Malignancies

Other types of laryngeal sarcomas are extremely rare. These include osteosarcoma, malignant fibrous histiocytoma, fibrosarcoma, liposarcoma (Fig. 39), angiosarcoma, synovial sarcoma, rhabdomyosarcoma, leiomyosarcoma and Kaposi's sarcoma. These tumors usually appear radiologically as a huge and infiltrating supraglottic mass lesion.

6.3 Hematopoietic Malignancies

6.3.1 Lymphoma

Non-Hodgkin lymphoma is a heterogeneous group of neoplasms originating from lymphocytes or their derivatives. Non-Hodgkin lymphoma has varying

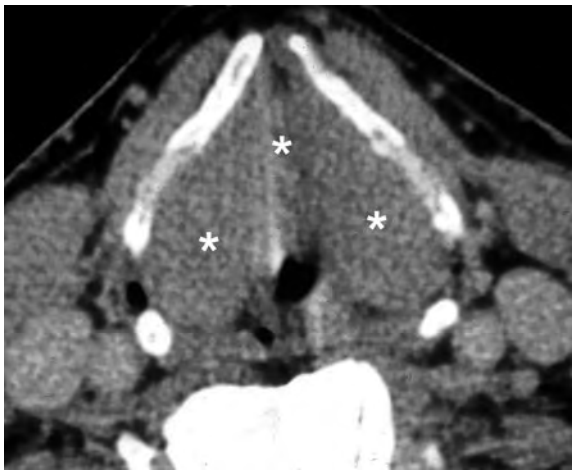

Fig. 40 Axial contrast-enhanced CT image shows diffuse soft tissue infiltration of the deep fatty laryngeal spaces (paraglottic and preepiglottic space), corresponding to non-Hodgkin lymphoma

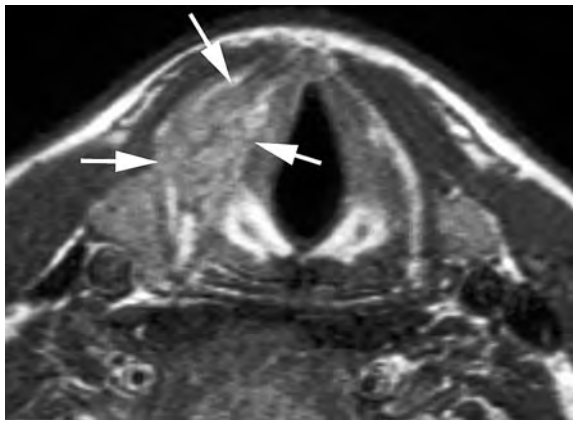

Fig. 41 Patient known with localized bladder cancer, treated by endoscopic resection. Because of pain during swallowing, an imaging study of the neck was performed. Gadolinium-enhanced axial T1-weighted spin echo image shows enhancing and expansile mass lesion (*arrows*) in the right thyroid cartilage wing. Resection was performed; pathologic examination revealed urothelial cancer, histologically similar to the previously removed bladder tumor: metastasis. The patient died a few months later due to widespread and rapidly progressive metastatic disease

clinical presentations and different courses and prognoses (see "Neck Lymphoma")

Non-Hodgkin lymphoma is a disease of the middle-aged and elderly, with only few cases occurring before the age of 40. It represents about 5% of head and neck malignancies. About 11% of non-Hodgkin lymphomas present with lesions in this region, and about 50% of patients with head and neck disease have systemic disease.

Non-Hodgkin lymphoma can involve virtually any site in the extracranial head and neck. Nodal involvement is common, but in several studies extranodal spread is reported to occur more frequently than nodal enlargement. In the head and neck, two distinct extranodal sites are recognized: extranodal lymphatic spread or involvement of Waldeyer's ring, and extranodal extralymphatic spread. Extranodal extralymphatic non-Hodgkin lymphoma occurs most commonly in the sinonasal cavities and orbits, but it may infiltrate any tissue of the head and neck, such as the deep spaces, skeletal structures, larynx and thyroid gland. Laryngeal non-Hodgkin lymphoma often shows on imaging studies a large submucosal mass lesion in the supraglottic region; extension to the glottis, subglottis, laryngeal cartilage and strap muscles is less frequent (King et al. 2004) (Fig. 40).

Whenever an infiltrating mass is present in the extracranial head and neck region, lymphoma is a possible cause (Hermans et al. 1994).

6.3.2 Plasma Cell Neoplasms

Plasma cell neoplasms are relatively unusual malignancies of the head and neck region. Multiple myeloma, solitary plasmacytoma of bone, and extramedullary plasmacytoma are plasma cell neoplasms. Multiple myeloma is a fatal disease with a mean survival of 2–3 years. Progression to multiple myeloma is the most important prognostic factor for solitary plasmocytoma of bone and extramedullary plasmocytoma; extramedullary plasmocytoma has a better prognosis than solitary plasmacytoma of bone.

The incidence of laryngeal plasmacytoma with respect to all malignant tumors of the larynx is small (Maniglia and Xue 1983). Approximately 6–18% of extramedullary plasmocytomas in the head and neck region occur in the larynx. The most common laryngeal sites are the epiglottis, followed by the vocal cords, false cords, ventricles, and subglottis. Laryngeal plasmacytomas are generally submucosal lesions, but can also be polypoid and may involve multiple contiguous sites of the larynx (Nofsinger et al. 1997).

The imaging findings of extramedullary plasmocytoma in the larynx are non-specific. The major role of imaging is to confirm the presence of a tumor mass and show the extent of the lesion.

6.3.3 Metastasis

The larynx is an rare site for metastasis. In most cases, the metastasis involves the supra- or subglottic submucosa, or the ossified laryngeal framework. The most common primary tumors are malignant melanoma, renal cell carcinoma, gastro-intestinal cancer, breast cancer and pulmonary cancer (Batsakis et al. 1985; Nicolai et al. 1996). Laryngeal metastasis may be asymptomatic, or cause symptoms similar to primary laryngeal tumors (Fig. 41).

References

Abdel Razek AA, Kandeel AY, Soliman N, El-shenshawy HM, Kamel Y, Nada N, Denewar A (2007) Role of diffusion-weighted echo-planar MR imaging in differentiation of residual or recurrent head and neck tumors and posttreatment changes. Am J Neuroradiol 28:1146–1152

Abdel Razek AA, Megahed AS, Denewer A, Motamed A, Tawfik A, Nada N (2008) Role of diffusion-weighted magnetic resonance imaging in differentiation between the viable and necrotic parts of head and neck tumors. Acta Radiol 49:364–370

Alexander FW (1963) Micropathology of radiation reaction in the larynx. Ann Otol Rhinol Laryngol 72:831–841

Anzai Y, Carroll WR, Quint DJ et al (1996) Recurrence of head and neck cancer after surgery or irradiation: prospective comparison of 2-deoxy-2-(F-18)fluoro-D-glucose PET and MR imaging diagnoses. Radiology 200:135–141

Archer CR, Yeager VL, Herbold DR (1984) Improved diagnostic accuracy in laryngeal cancer using a new classification based on computed tomography. Cancer 53:44–57

Barbera L, Groome PA, Mackillop WJ, Schuze K, O'Sullivan B, Irish JC, Warde PR, Schneider KM, Mackenzie RG, Hodson DI, Hammond JA, Gulavita SPP, Eapen LJ, Dixon PF, Bissett RJ (2001) The role of computed tomography in the T classification of laryngeal carcinoma. Cancer 91:394–407

Batsakis JG, Luna MA, Byers RM (1985) Metastases to the larynx. Head Neck Surg 7:458–460

Becker M, Zbären P, Laeng H, Stoupis C, Porcellini B, Vock P (1995) Neoplastic invasion of the laryngeal cartilage: comparison of MR imaging and CT with histopathologic correlation. Radiology 194:661–669

Becker M, Zbären P, Delavelle J et al (1997a) Neoplastic invasion of the laryngeal cartilage: reassessment of criteria for diagnosis at CT. Radiology 203:521

Becker M, Schroth G, Zbären P et al (1997b) Long-term changes induced by high-dose irradiation of the head and neck region: imaging findings. RadioGraphics 17:5–26

Becker M, Moulin G, Kurt AM, Zbaren P, Dulgerov P, Marchal F, Zanaret P, Lehmann W, Rufenacht DA, Terrier F (1998) Atypical squamous cell carcinoma of the larynx and hypopharynx: radiologic features and pathologic correlation. Eur Radiol 8:1541–1551

Becker M, Zbären P, Casselman JW, Kohler R, Dulguerov P, Becker CD (2008) Neoplastic invasion of laryngeal cartilage: reassessment of criteria for diagnosis at MR imaging. Radiology 249:551–559

Bisdas S, Nguyen SA, Anand SK, Glavina G, Day T, Rumboldt Z (2009) Outcome prediction after surgery and chemoradiation of squamous cell carcinoma in the oral cavity, oropharynx, and hypopharynx: use of baseline perfusion CT microcirculatory parameters vs. tumor volume. Int J Radiat Oncol Biol Phys 73:1313–1318

Bousson V, Marsot-Dupuch K, Lashiver X et al (1995) Nécrose post-radique du cartilage cricoïde: un cas inhabituel. J Radiol 76:517–520

Breiman RS, Beck JW, Korobkin M, Glenny R, Akwari OE, Heaston DK, Moore AV, Ram PC (1982) Volume determinations using computed tomography. Am J Roentgenology 138:329–333

Castelijns JA, Golding RP, van Schaik C, Valk J, Snow GB (1990) MR findings of laryngeal cartilage invasion by laryngeal cancer: value in predicting outcome of radiation therapy. Radiology 174:669–673

Castelijns JA, van den Brekel MWM, Smit EMT, Tobi H, van Wagtendonk FW, Golding RP, Venema HW, van Schaik C, Snow GB (1995) Predictive value of MR imaging-dependent and non-MR imaging dependent parameters for recurrence of laryngeal cancer after radiation therapy. Radiology 196:735–739

Castelijns JA, Becker M, Hermans R (1996a) The impact of cartilage invasion on treatment and prognosis of laryngeal cancer. Eur Radiol 6:156–169

Castelijns JA, van den Brekel MWM, Tobi H, Smit EMT, Golding RP, van Schaik C, Snow GB (1996b) Laryngeal carcinoma after radiation therapy: correlation of abnormal MR imaging signal pattern in laryngeal cartilage with the risk of recurrence. Radiology 198:151–155

Champion GA, Piccirillo JF (2004) The impact of computed tomography on pretherapeutic staging in patients with laryngeal cancer: demonstration of the Will Rogers' phenomenon. Head Neck 26:972–976

Charlin B, Brazeau-Lamontagne L, Guerrier B, Leduc C (1989) Assessment of laryngeal cancer: CT scan versus endoscopy. J Otolaryngol 18:283–288

Cooney TR, Poulsen MG (1999) Is routine follow-up useful after combined-modality therapy for advanced head and neck cancer? Arch Otolaryngol Head Neck Surg 125:379–382

Dadas B, Uslu B, Cakir B, Ozdogan HC, Calis AB, Turgut S (2001) Intraoperative management of the thyroid gland in laryngeal cancer surgery. J Otolaryngol 30:179–183

De Foer B, Hermans R, Van der Goten A, Delaere PR, Baert AL (1996) Imaging features in 35 cases of submucosal laryngeal mass lesions. Eur Radiol 6:913–919

de Visscher AVM, Manni JJ (1994) Routine long-term follow-up in patients treated with curative intent for squamous cell carcinoma of the larynx, pharynx and oral cavity. Arch Otolaryngol Head Neck Surg 120:934–939

Delaere PR, Hermans R (2003) Tracheal autotransplantation as a new and reliable technique for the functional treatment of advanced laryngeal cancer. Laryngoscope 113:1244–1251

Delaere P, Vander Poorten V, Vanclooster C, Goeleven A, Hermans R (2000) Results of larynx preservation surgery for advanced laryngeal cancer through tracheal autotransplantation. Arch Otolaryngol Head Neck Surg 126:1207–1215

Delaere P, Goeleven A, Vander Poorten V, Hermans R, Hierner R, Vrancks J (2007) Organ preservation surgey for advanced unilateral glottic and subglottic cancer. Laryngoscope 117:1764–1769

DeSanto LW (1984) T3 glottic cancer: options and consequences of the options. Laryngoscope 94:1311–1315

Devaney KO, Ferlito A, Silver CE (1995) Cartilaginous tumors of the larynx. Ann Otol Rhinol Laryngol 104:251–255

Ferlito A, Rinaldo A, Mannara GM (1998) Is primary radiotherapy an appropriate option for the treatment of verrucous carcinoma of the head and neck? J Laryngol Otol 112:132–139

Fletcher GH, Hamberger AD (1974) Causes of failure in irradiation of squamous-cell carcinoma of the supraglottic larynx. Radiology 111:697–700

Fletcher GH, Lindberg RD, Hamberger A, Horiot JC (1975) Reasons for irradiation failure in squamous cell carcinoma of the larynx. Laryngoscope 85:987–1003

Forastiere AA, Goepfert H, Maor M, Pajak TF, Weber R, Morrison W, Glisson B, Trotti A, Ridge JA, Chao C, Peters G, Lee DJ, Leaf A, Ensley J, Cooper J (2003) Concurrent chemotherapy and radiotherapy for organ preservation in advanced laryngeal cancer. N Engl J Med 349:2091–2098

Freeman DE, Mancuso AA, Parsons JT, Mendenhall WM, Million RR (1990) Irradiation alone for supraglottic larynx carcinoma: Can CT findings predict treatment results? Int J Radiation Oncology Biol Phys 19:485–490

Gavilan J (2000) Cancer of the glottis. In: Ferlito A (ed) Diseases of the larynx. Arnold, London, p 615

Gilbert RW, Birt D, Shulman H, Freeman J, Jenkin D, MacKenzie R, Smith C (1987) Correlation of tumor volume with local control in laryngeal carcinoma treated by radiotherapy. Ann Otol Rhinol Laryngol 97:514–518

Hermans R (2004) Post-treatment imaging of head and neck cancer. Cancer Imaging 4:1–10. doi:10.1102/1470-7330.2004.0007

Hermans R, Horvath M, De Schrijver T, Lemahieu SF, Baert AL (1994) Extranodal non-Hodgkin lymphoma of the head and neck. J Belge Radiol 77:72–77

Hermans R, Pameijer FA, Mancuso AA et al (1998) Computed tomography findings in chondroradionecrosis of the larynx. Am J Neuroradiol 19:711–718

Hermans R, Van den Bogaert W, Rijnders A, Doornaert P, Baert AL (1999a) Predicting the local outcome of glottic cancer treated by definitive radiation therapy: value of computed tomography determined tumor parameters. Radiother Oncol 50:39–46

Hermans R, Van den Bogaert W, Rijnders A, Baert AL (1999b) Value of computed tomography determined tumor parameters as outcome predictor of supraglottic cancer treated by definitive radiation therapy. Int J Radiat Oncol Biol Phys 44:755–765

Hermans R, Pameijer FA, Mancuso AA et al (2000) Laryngeal or hypopharyngeal squamous cell carcinoma: can follow-up CT after definitive radiotherapy be used to detect local failure earlier than clinical examination alone? Radiology 214:683–687

Hermans R, Meijerink M, Van den Bogaert W, Rijnders A, Weltens C, Lambin P (2003) Tumor perfusion rate determined noninvasively by dynamic computed tomography predicts outcome in head-and-neck cancer after radiotherapy. Int J Radiat Oncol Biol Phys 57:1351–1356

Hinerman RW, Mendenhall WM, Amdur RJ, Stringer SP, Villaret DB, Robbins KT (2002) Carcinoma of the supraglottic larynx: treatment results with radiotherapy alone or with planned neck dissection. Head Neck 24:456–467

Hoebers FJ, Pameijer FA, De Bois J, Heemsbergen W, Balm AJ, Schornagel JH, Rasch CR (2008) Prognostic value of primary tumor volume after concurrent chemoradiation with daily low-dose cisplatinum for advanced-stage head and neck carcinoma. Head Neck 30:1216–1223

Isaacs JH, Mancuso AA, Mendenhall WM, Parsons JT (1988) Deep spread patterns in CT staging of T2–4 squamous cell laryngeal carcinoma. Otolaryngol Head Neck Surg 99: 455–464

Johnson CR, Thames HD, Huang DT, Schmidt-Ullrich RK (1995) The tumor volume and clonogen number relationship: tumor control predictions based upon tumor volume estimates derived from computed tomography. Int J Radiat Oncol Biol Phys 33:281–287

Kaanders JH, Bussink J, van der Kogel AJ (2002) ARCON: a novel biology-based approach in radiotherapy. Lancet Oncol 3:728–737

Kallmes DF, Phillips CD (1997) The normal anterior commissure of the glottis. Am J Roentgenol 168: 1317–1379

Katsantonis GP, Archer CR, Rosenblum BN, Yeager VL, Friedman WH (1986) The degree to which accuracy of preoperative staging of laryngeal carcinoma has been enhanced by computed tomography. Otolaryngol Head Neck Surg 95:52–62

Keane TJ, Cummings BJ, O' Sullivan B et al (1993) A randomized trial of radiation therapy compared to split course radiation therapy combined with Mitomycin C and 5 Fluorouracil as initial treatment for advanced laryngeal and hypopharyngeal squamous carcinoma. Int J Radiat Oncol Biol Phys 25:613–618

Keene M, Harwood AR, Bryce DP et al (1982) Histopathological study of radionecrosis in laryngeal carcinoma. Laryngoscope 92:173–180

King AD, Yuen EH, Lei KI, Ahuja AT, Van Hasselt A (2004) Non-Hodgkin lymphoma of the larynx: CT and MR imaging findings. Am J Neuroradiol 25:12–15

Knab BR, Salama JK, Solanki A, Stenson KM, Cohen EE, Witt ME, Haraf DJ, Vokes EE (2008) Functional organ preservation with definitive chemoradiotherapy for T4 laryngeal sqaumous cell carcinoma. Ann Oncol 19:1650–1654

Kraas JR, Underhill TE, D'Agostino RB Jr, Williams DW III, Cox JA, Greven KM (2001) Quantitative analysis from CT is prognostic for local control of supraglottic carcinoma. Head Neck 23:1031–1036

Kurita S, Hirano M, Matsuoka H, Tateishi M, Sato K (1985) A histopathological study of carcinoma of the larynx. Auris Nasus Larynx 12 (Suppl 2): S172–S177

Lambert L, Fortin B, Soulières D, Guertin L, Coulombe G, Charpentier D, Tabet JC, Bélair M, Khaouam N, Nguyen-Tan PF (2010) Organ preservation with concurrent chemoradiation for advanced laryngeal cancer: are we succeeding? J Radiat Oncol Biol Phys 76:398–402

Laurell G, Kraepelien T, Mavroidis P, Lind BK, Fernberg JA, Beckman M, Lind MG (2003) Structure of the proximal esophagus in head and neck carcinoma after radiotherapy. Cancer 97:1693–1700

Lee NK, Goepfert H, Wendt CD (1990) Supraglottic laryngectomy for intermediate-stage cancer: U.T. M.D. Anderson cancer center experience with combined therapy. Laryngoscope 100:831–836

Lee WR, Mancuso AA, Saleh EM, Mendenhall WM, Parsons JT, Million RR (1993) Can pretreatment computed tomography findings predict local control in T3 squamous cell carcinoma of the glottic larynx treated with radiotherapy alone? Int J Radiat Oncol Biol Phys 25:683–687

Ljumanovic R, Langendijk JA, Schenk B, van Wattingen M, Knol DL, Leemans CR, Castelijns JA (2004) Supraglottic carcinoma treated with curative radiation therapy: identification of prognostic groups with MR imaging. Radiology 232:440–448

Ljumanovic R, Langendijk JA, van Wattingen M, Schenk B, Knol DL, Leemans CR, Castelijns JA (2007) MR imaging predictors of local control of glottic squamous cell carcinoma treated with radiation alone. Radiology 244:205–212

Ljumanovic R, Langendijk JA, Hoekstra OS, Knol DL, Leemans CR, Castelijns JA (2008) Pre- and post-radiotherapy MRI results as a predictive model for response in laryngeal carcinoma. Eur Radiol 18:2231–2240

Lloyd GAS, Michaels L, Phelps PD (1981) The demonstration of cartilaginous involvement in laryngeal carcinoma by computerized tomography. Clin Otolaryngol 6:171–177

Lo SM, Venkatesan V, Matthews TW, Rogers J (1998) Tumor volume: implications in T2/T3 glottic/supraglottic squamous cell carcinoma. J Otolaryngol 27:247–251

Malik T, Bruce I, Cherry J (2007) Surgical complications of tracheo-oesophageal puncture and speech valves. Curr Opin Otolaryngol Head Neck Surg 15:117–122

Mancuso AA, Harnsberger HR, Dillon WP (1989) Workbook for MRI and CT of the head and neck, 2nd edn. William & Wilkins, Baltimore, p 183

Mancuso AA, Mukherji SK, Schmalfuss I, Mendenhall W, Parsons J, Pameijer F, Hermans R, Kubilis P (1999) Preradiotherapy computed tomography as a predictor of local control in supraglottic carcinoma. J Clin Oncol 17:631–637

Maniglia A, Xue JW (1983) Plasmacytoma of the larynx. Laryngoscope 93:903–906

Maple JT, Petersen BT, Baron TH, Kasperbauer JL, Wong Kee Song LM, Larson MV (2006) Endoscopic management of radiation-induced complete upper esophageal obstruction with an antegrade-retrograde rendezvous technique. Gastrointest Endosc 64:822–828

Marks JE, Freeman RB, Lee F, Ogura JH (1979) Carcinoma of the supraglottic larynx. Am J Roentgenol 132:255–260

Maroldi R, Battaglia G, Nicolai P, Maculotti P, Cappiello J, Cabassa P, Farina D, Chiesa A (1997) CT appearance of the larynx after conservative and radical surgery for carcinomas. Eur Radiol 7:418–431

Maroldi R, Farina D, Battaglia G, Palvarini L, Maculotti P (2001) Imaging after laryngeal surgery. In: Hermans R (ed) Imaging of the larynx. Springer, Berlin, pp 124–125

McGuirt WF, Greven KM, Keyes JW Jr et al (1998) Laryngeal radionecrosis versus recurrent cancer: a clinical approach. Ann Otol Rhinol Laryngol 107:293–296

Mendenhall WM, Parsons JT, Stringer SP, Cassisi NJ, Million RR (1992) Stage T3 squamous cell carcinoma of the glottic larynx: a comparison of laryngectomy and irradiation. Int J Radiation Oncology Biol Phys 23: 725–732

Mendenhall WM, Parsons JT, Mancuso AA, Stringer SP, Cassisi NJ (1996) Radiotherapy for squamous cell carcinoma of the supraglottic larynx: an alternative to surgery. Head Neck 18:24–35

Mendenhall WM, Parsons JT, Mancuso AA, Pameijer FJ, Stringer SP, Cassisi NJ (1997) Definitive radiotherapy for T3 squamous cell carcinoma of the glottic larynx. J Clin Oncol 15:2394–2402

Mendenhall WM, Morris CG, Amdur RJ, Hinerman RW, Mancuso AA (2003) Parameters that predict local control after definitive radiotherapy for squamous cell carcinoma of the head and neck. Head Neck 25:535–542

Mendenhall WM, Werning JW, Hinerman RW, Amdur RJ, Villaret DB (2004) Management of T1–T2 glottic carcinomas. Cancer 100:1786–1792

Million RR (1989) The myth regarding bone or cartilage involvement by cancer and the likelihood of cure by radiotherapy. Head Neck 11:30–40

Million RR (1992) The larynx.so to speak: everything I wanted to know about laryngeal cancer I learned in the last 32 years. Int J Radiat Oncol Biol Phys 23:691–704

Mukherji SK, Wolf GT (2003) Evaluation of head and neck squamous cell carcinoma after treatment (editorial). Am J Neuroradiol 24:1743–1746

Mukherji SK, Mancuso AA, Kotzur IM et al (1994a) Radiologic appearance of the irradiated larynx. Part I. Expected changes. Radiology 193:141–148

Mukherji SK, Mancuso AA, Kotzur IM et al (1994b) Radiologic appearance of the irradiated larynx. Part II. Primary site response. Radiology 193:149–154

Mukherji SK, Mancuso AA, Mendenhall W, Kotzur IL, Kubilis P (1995) Can pretreatment CT predict local control of T2 glottic carcinomas treated with radiation therapy alone? Am J Neuroradiol 16:655–662

Mukherji SK, O'Brien SM, Gerstle RJ, Weissler M, Shockley W, Stone JA, Castillo M (2000) The ability of tumor volume to predict local control in surgically treated squamous cell carcinoma of the supraglottic larynx. Head Neck 22:282–287

Murakami R, Nishimura R, Baba Y, Furusawa M, Ogata N, Yumoto E, Yamashita Y (2005) Prognostic factors of glottic carcinomas treated with radiation therapy: value of the adjacent sign on radiological examinations in the sixth edition of the UICC TNM staging system. Int J Radiat Oncol Biol Phys 61:471–475

Nationale werkgroep hoofd-halstumoren (2000) Richtlijn Larynxcarcinoom. Kwaliteitsinstituut voor de Gezondheidszorg, Utrecht

Nicolai P, Puxeddu R, Cappiello J, Peretti G, Battocchio S, Facchetti F, Antonelli AR (1996) Metastatic neoplasms to the larynx: report of three cases. Laryngoscope 106:851–855

Nofsinger YC, Mirza N, Rowan PT, Lanza D, Weinstein G (1997) Head and neck manifestations of plasma cell neoplasms. Laryngoscope 107:741–746

Nömayr A, Lell M, Sweeney S et al (2001) MRI appearance of radiation-induced changes of normal cervical tissues. Eur Radiol 11:1807–1817

O'Brien P (1996) Tumor recurrence or treatment sequelae following radiotherapy for larynx cancer. J Surg Oncol 63:130–135

Op de beeck K, Hermans R, Delaere PR, Van den Bogaert W, Marchal G (2001) Laryngeal squamous cell carcinoma presenting as a prelaryngeal neck abscess: report of two cases. Eur Radiol 11:2479–2483

Overgaard J, Horsman MR (1996) Modification of hypoxia-induced radioresistance in tumors by the use of oxygen and sensitizers. Semin Radiat Oncol 6:10–21

Overgaard J, Hansen HS, Jørgensen K, Hjelm-Hansen M (1986) Primary radiotherapy of larynx and pharynx carcinoma—an analysis of some factors influencing local control and survival. Int J Radiat Oncol Biol Phys 12:515–521

Pameijer FA, Mancuso AA, Mendenhall WM, Parsons JT, Kubilis MS (1997) Can pretreatment computed tomography predict local control in T3 squamous cell carcinoma of the glottic larynx treated with definitive radiotherapy? Int J Radiat Oncol Biol Phys 37:1011–1021

Pameijer FA, Hermans R, Mancuso AA et al (1999) Pre- and post-radiotherapy computed tomography in laryngeal cancer: imaging-based prediction of local failure. Int J Radiat Oncol Biol Phys 45:359–366

Parsons JT, Mendenhall WM, Stringer SP, Cassisi NJ (1998) T4 laryngeal carcinoma: radiotherapy alone with surgery reserved for salvage. Int J Radiat Oncol Biol Phys 40:549–552

Piccirillo JF, Lacy PD (2000) Classification and staging of laryngeal cancer. In: Ferlito A (ed) Diseases of the larynx. Arnold, London, pp 563–564, 574

Pillsbury HR, Kirchner JA (1979) Clinical vs histopathologic staging in laryngeal cancer. Arch Otolaryngol 105:157–159

Preda L, De Fiori E, Rampinelli C, Ansarin M, Petralia G, Maffini F, Alterio D, Bonello L, Chiesa F, Bellomi M (2010) US-guided transcutaneous tru-cut biopsy of laryngo-hypopharyngeal lesions. Eur Radiol 20:1450–1455

Rijpkema M, Kaanders JH, Joosten FB, van der Kogel AJ, Heerschap A (2001) Method for quantitative mapping of dynamic MRI contrast agent uptake in human tumors. J Magn Reson Imaging 14:457–463

Rijpkema M, Kaanders JH, Joosten FB, van der Kogel AJ, Heerschap A (2002) Effects of breathing a hyperoxic hypercapnic gas mixture on blood oxygenation and vascularity of head-and-neck tumors as measured by magnetic resonance imaging. Int J Radiat Oncol Biol Phys 53:1185–1191

Robbins KT, Davidson W, Peters LJ, Goepfert H (1987) Conservation surgery for T2 and T3 carcinomas of the supraglottic larynx. Arch Otolaryngol Head Neck Surg 114:421–426

Sato K, Kurita S, Hirano M (1993) Location of the preepiglottic space and its relationship to the paraglottic space. Ann Otol Rhinol Laryngol 102:930–934

Schwartz DL, Barker J, Chansky K et al (2003) Postradiotherapy surveillance practice for head and neck squamous cell carcinoma—too much for too little? Head Neck 25: 990–999

Shah JP, Karnell LH, Hoffman HT, Ariyan S, Brown GS, Fee WE, Glass AG, Goepfert H, Ossoff RH, Fremgen A (1997) Patterns of care for cancer of the larynx in the United States. Arch Otolaryngol Head Neck Surg 123: 475–483

Silverman PM (1985) Medullary space involvement in laryngeal carcinoma. Arch Otolaryngol 111:541–542

Steiniger JR, Parnes SM, Gardner GM (1997) Morbidity of combined therapy for the treatment of supraglottic carcinoma: supraglottic laryngectomy and radiotherapy. Ann Otol Rhinol Laryngol 106:151–158

Sulfaro S, Barzan L, Querin F, Lutman M, Caruso G, Comoretto R, Volpe R, Carbone A (1989) T staging of the laryngohypopharyngeal carcinoma. Arch Otolaryngol Head Neck Surg 115:613–620

Takes RP, Rinaldo A, Silver CE, Piccirillo JF, Haigentz M, Suares C, Vander Poorten V, Hermans R, Rodrigo JP, Devaney KO, Ferlito A (2010) Future of the TNM classification and staging system in head and neck cancer. Head Neck 2010 (Epub ahead of print)

Tart RP, Mukherji SK, Lee WR, Mancuso AA (1994) Value of laryngeal cartilage sclerosis as a predictor of outcome in patients with stage T3 glottic cancer treated with radiation therapy. Radiology 192:567–570

Thoeny HC, Delaere PR, Hermans R (2005) Correlation of local outcome after partial laryngectomy with cartilage abnormalities on CT. Am J Neuroradiol 26:674–678

UICC, International Union Against Cancer (2009) TNM classification of malignant tumors, 7th edn. Wiley-Liss, New York, pp 40–41

Van den Bogaert W, Ostyn F, Van der Schueren E (1983) The primary treatment of advanced vocal cord cancer: laryngectomy or radiotherapy? Int J Radiat Oncol Biol Phys 9:329–334

Van den Bogaert W, van der Schueren E, Horiot JC, De Vilhena M, Schraub S, Svoboda V, Arcangeli G, de Pauw M, van Glabbeke M (1995) The EORTC randomized trial on three fractions per day and misonidazole in advanced head and neck cancer: prognostic factors. Radiother Oncol 35:100–106

Vandecaveye V, De Keyzer F, Nuyts S, Deraedt K, Dirix P, Hamaekers P, Vander Poorten V, Delaere P, Hermans R (2007) Detection of head and neck squamous cell carcinoma with diffusion weighted MRI after (chemo) radiotherapy: correlation between radiologic and histopathologic findings. Int J Radiat Oncol Biol Phys 67:960–971

Vuysere De, Hermans R, Delaere P et al (1999) CT findings in laryngeal chondroradionecrosis. J Belge Radiol 82: 16–18

Wang SJ, Borges A, Lufkin RB et al (1999) Chondroid tumors of the larynx: computed tomography findings. Am J Otolaryngol 20:379–382

Weems DH, Mendenhall WM, Parsons JT, Cassisi NJ, Million RR (1987) Squamous cell carcinoma of the supraglottic larynx treated with surgery and/or radiation therapy. Int J Radiat Oncol Biol Phys 13:1483–1487

Wolf GT (2010) Routine computed tomography scanning for tumor staging in advanced laryngeal cancer: implications for treatment selection. J Clin Oncol 28:2315–2317

Worden FP, Moyer J, Lee JS et al (2009) Chemoselection as a strategy for organ preservation in patients with T4 laryngeal squamous cell carcinoma with cartilage invasion. Laryngoscope 119:1510–1517

Yeager VL, Lawson C, Archer CR (1982) Ossification of the laryngeal cartilages as it relates to computed tomography. Invest Radiol 17:11–19

Zbären P, Becker M, Laeng H (1996) Pretherapeutic staging of laryngeal cancer: clinical findings, computed tomography and magnetic resonance imaging versus histopathology. Cancer 77:1263–1273

Hypopharynx and Proximal Esophagus

Ilona M. Schmalfuss

Contents

Abstract

Cancers of the hypopharynx and proximal esophagus typically present at an advanced stage. They are often underestimated on clinical examination as they tend to grow in a submucosal fashion. On imaging, evaluation of the normally present fat planes within the post-cricoid musculature and around the hypopharynx as well as proximal esophagus is essential for mapping of the tumor boundaries. Cartilage invasion, tumor volume and involvement of the pyriform sinus apex are important variables in stratification of patients into favorable and unfavorable treatment groups. Patients with favorable tumors typically receive radiation therapy while patients with unfavorable tumors usually undergo surgical resection and subsequent reconstructive surgery. Both treatments cause some alteration of the tissue planes with additional marked distortion of the normal anatomy seen with surgical resection. The growth patterns of tumors arising from the different subsites within the hypopharynx and proximal esophagus, pretreatment considerations for staging and treatment planning purposes, as well as posttreatment complications and surveillance issues will be discussed in this chapter.

1 Introduction

Cancers of the hypopharynx and proximal esophagus represent one of the most difficult diseases for the head and neck surgeons to manage as they pose a significant diagnostic challenge. The trend of these cancers

I. M. Schmalfuss (✉)
Department of Radiology, Division of Neuroradiology, North Florida/South Georgia Veterans Administration and University of Florida College of Medicine, 1601 SW Archer Road, Gainesville, FL 32608, USA
e-mail: Ilonaschmalfuss@yahoo.com

R. Hermans (ed.), *Head and Neck Cancer Imaging*, Medical Radiology. Diagnostic Imaging,
DOI: 10.1007/174_2011_374, © Springer-Verlag Berlin Heidelberg 2012

to grow in submucosal fashion combined with the complex functions of the hypopharynx, esophagus and adjacent larynx requires detailed mapping of the tumor boundaries to yield the most optimal treatment selection, determine the extent of possible surgical resection and subsequent reconstructive surgery. Consequently, cross-sectional imaging plays a critical role in the evaluation of hypopharyngeal and esophageal cancers.

Computer tomography (CT) is a well-established and in most institutions the preferred method for evaluation of the hypopharynx and the cervical esophagus. The short acquisition time is the main advantage of CT over Magnetic Resonance (MR) imaging (Wenig et al. 1995). Up to 16% of MR studies focusing on the hypopharynx and cervical esophagus have been reported to be non-diagnostic secondary to claustrophobia or motion artifacts (Becker 1998). MR imaging is however superior in the evaluation of the esophageal verge and cervical esophagus because of better soft tissue delineation and lack of obscuration of these structures by beam-hardening artifacts caused by the shoulders as may be seen with CT. Multi-planar capabilities of MR play a markedly less important role in our days as the wide utilization of multi-slice helical CT scanners and interactive picture archive computer systems allow reformation of the volumetric CT data sets in any desirable plane. In recent years, positron emission tomography–computed tomography (PET–CT) with fluorine-18 fluorodeoxyglucose (18F-FDG) has become an important adjunctive tool in staging and follow-up of patients with head and neck cancer, in particular in advanced tumor stages as this is typically the case with hypopharyngeal cancers.

2 Anatomy

2.1 Descriptive Anatomy

The hypopharynx is the portion of the pharynx that extends from the oropharynx to the esophageal verge. It continues inferiorly as the cervical esophagus to the level of the thoracic inlet. The anterior boundary of the hypopharynx and the cervical esophagus is formed by the larynx and the trachea, respectively. The retropharyngeal space forms the posterior boundary. There is no clear anatomical barrier between the hypopharynx and the oropharynx as well as the hypopharynx and the cervical esophagus. The hypopharynx is divided into three distinct regions: pyriform sinus, postcricoid region and posterior hypopharyngeal wall:

The *pyriform sinus* (one on each side) is formed by the anterior, medial and lateral walls and resembles an inverted pyramid. The base of the pyramid at the level of the pharyngoepiglottic folds constitutes the entrance of the pyriform sinus. The pyriform sinus apex located at the inferior margin of the cricoid cartilage, represents the tip of the inverted pyramid. The aryepiglottic folds separate the pyriform sinus posteriorly from the larynx anteromedially. More inferiorly, the pyriform sinus abuts the posterior margin of the paraglottic space. This close anatomical proximity explains the frequently seen involvement of the larynx in patients diagnosed with pyriform sinus cancer. The thyrohyoid membrane separates the pyriform sinus from the lateral neck compartment. The superior laryngeal neurovascular bundle courses through the thyrohyoid membrane. The sensory axons of the superior laryngeal nerve continue superiorly to join the Arnold nerve within the jugular foramen, giving rise to referred otalgia that can be the presenting symptom of pyriform sinus cancer. In addition, the superior laryngeal neurovascular bundle causes a "weak" point within the thyrohyoid membrane facilitating tumor spread out of the visceral compartment into the extrapharyngeal soft tissues.

The *postcricoid region* represents the anterior wall of the hypopharynx. It extends from the posterior surface of the arytenoid cartilage to the esophageal verge.

The *posterior hypopharyngeal wall* forms the posterior boundary of the hypopharynx stretching from the aryepiglottic folds superiorly to the esophageal verge inferiorly. There is no defined boundary of the hypopharyngeal wall towards the oropharynx superiorly and towards the esophagus inferiorly. The retropharyngeal space separates the vertebral and paravertebral structures from the posterior hypopharyngeal wall and allows the pharynx to move freely during swallowing.

The wall of the hypopharynx constitutes four layers: the outer fascial layer originating from the buccopharyngeal facia, the muscular layer, the fibrous layer arising from the pharyngeal aponeurosis and the mucosal lining of stratified squamous epithelium over loose stroma that can be identified on cross-sectional images as a thin fat plane (see under *Imaging*

Anatomy). The muscular layer is formed by the posterior cricoarytenoid muscle anteriorly and the middle or inferior constrictor muscles posteriorly. The inferior constrictor muscle continues inferiorly to blend with the cricopharyngeus muscle forming the upper esophageal sphincter at the esophageal verge. Slightly more inferiorly, the esophageal verge assumes a round to oval shape as it transitions to the cervical esophagus. At the cervical esophagus level, the muscular layer consists of inner circular and outer longitudinal muscle fibers that are protected on the inside by nonkeratinizing squamous epithelium over loose areolar tissue. Externally, the muscular layer is covered by a fascial sheath. The cervical esophagus is located posterior to the trachea where it often causes impression upon the posterior fibrous wall of the trachea. A thin layer of fatty tissue separates the fibrous wall of the trachea from the esophagus and may be referred to as the "common wall". Laterally, the cervical esophagus abuts the tracheoesophageal (TE) groove. It houses the recurrent laryngeal nerve and the TE groove lymph nodes as part of the nodal group VI. Occasionally, the parathyroid and/or the thyroid gland extend into the TE groove.

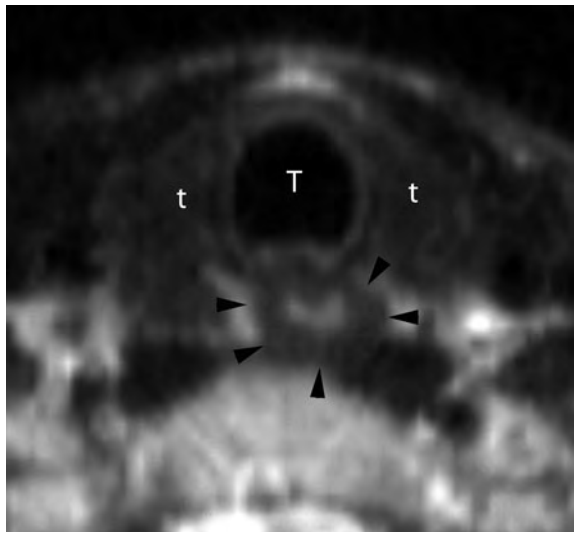

Fig. 1 Axial T2-weighted image through the cervical esophagus demonstrating the normal homogeneous low attenuation of the muscular wall of the esophagus (*arrowheads*) in comparison to the hypertintense mucosa centrally and the paraesophageal fat planes laterally. T = trachea, t = thyroid

2.2 Imaging Anatomy

On cross-sectional images, all three portions of the hypopharynx are seen posterior to the arytenoid and cricoid cartilages while only the pyriform sinuses and the posterior pharyngeal wall constitute the hypopharynx above the arytenoid cartilage level. The hypopharyngeal cross-sectional anatomy posterior to the cricoid cartilage is therefore very complex: the postcricoid region lies directly posterior to the cricoid cartilage, the inferior portion of the pyriform sinuses laterally on each side and the posterior hypopharyngeal wall posteriorly. The fact that the hypopharynx is typically collapsed during cross-sectional imaging, bringing the mucosa of the postcricoid region and of the posterior hypopharyngeal wall in direct contact to form a single mucosal layer complicates the already difficult hypopharyngeal anatomy at that level. Therefore, knowledge of the normal appearance and of normative data is essential for detection of abnormalities (Schmalfuss et al. 2000).

The anteroposterior (AP) dimensions of the postcricoid portion of the hypopharynx show little variations from the upper to lower margin of the cricoid cartilage. However, an AP diameter over 10 mm should be considered abnormal (Schmalfuss et al. 2000). The postcricoid area is usually slightly thinner than the posterior pharyngeal wall with 2.5 and 3.5 mm in average, respectively (Schmalfuss et al. 2000). In contrast to the AP measurements, the transverse dimension of the postcricoid portion of the hypopharynx tapers from the upper to the lower margin of the cricoid cartilage. Therefore, lack of normal tapering should raise the suspicion for an underlying abnormality and initiate a search for additional abnormal findings such as obscuration of the intramural or surrounding fat planes (see below). The esophageal diameter depends upon the amount of intraluminal air and is therefore not a useful indicator for underlying pathology. The thickness of the esophageal wall, however, is relatively constant with less than 5 mm and consequently a key marker for detection of an underlying lesion (Schmalfuss et al. 2000). In addition, the internal attenuation of the esophageal wall is helpful as it should be homogeneously iso-attenuated to the surrounding musculature on CT and T2-weighted images (Fig. 1) and shows no enhancement following contrast administration (Schmalfuss et al. 2000; Quint et al. 1985).

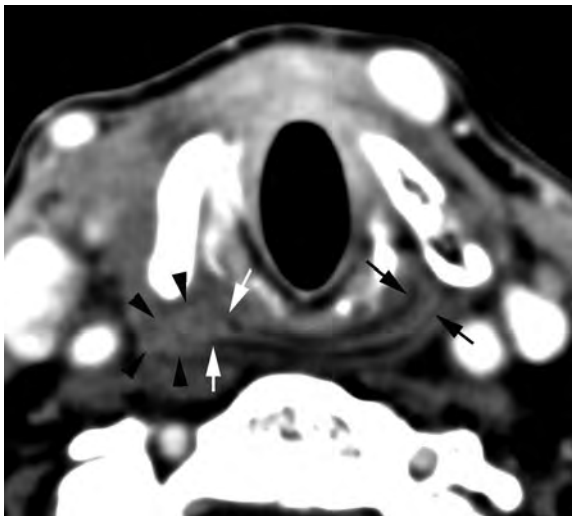

Fig. 2 Axial contrast-enhanced CT image through the postcricoid region shows normal submucosal fat planes on the *left* (*black arrows*) and abrupt cutoff of the submucosal fat planes on the *right* (*white arrows*) caused by a small pyriform sinus tumor on the *right* (*arrowheads*)

Fig. 3 Axial contrast-enhanced CT image through the mid cricoid level demonstrates asymmetric appearance of the submucosal fat planes. As in this patient, the submucosal fat planes are usually more prominent on the *left* (*black arrows*) than on the *right* (*white arrows*) which might be related to the preferred left-sided location of the cervical esophagus (not demonstrated)

The assessment of intramural and surrounding fat planes is critical in the workup of patients with suspected hypopharyngeal or upper esophageal abnormality as obliteration of these fat planes might be the only sign of an underlying cancer (Fig. 2). Overall, the fat planes are more frequently seen with CT than with MR. The gradient-echo T2-weighted images are superior to the T1- or T2-weighted images in the visibility of the intramural fat planes while there are no preferences between the various MR sequences for demonstration of the surrounding fat planes (Schmalfuss et al. 2000).

In the postcricoid portion of the hypopharynx, the visibility of the *intramural fat planes* decreases from the upper to the lower cricoid cartilage level with 85–30%, respectively. The intramural fat planes are usually symmetric in appearance at the upper cricoid cartilage level but show marked asymmetry at the mid and lower cricoid cartilage levels in approximately one-third of the patients (Fig. 3). Typically, the left intramural fat plane is more obvious which might be due to the commonly seen left-sided location of the esophagus (Schmalfuss et al. 2000).

The *surrounding fat planes* lateral to the postcricoid portion of the hypopharynx and cervical esophagus are most constantly seen. The left surrounding fat plane is markedly more commonly visible than the right while the posterior fat plane is least frequently appreciated (Fig. 4a). In addition, the visibility of the surrounding fat planes varies by location with the best visibility around the esophageal verge (Fig. 4b). The fat planes of the TE groove contain a subset of group VI lymph nodes. These lymph nodes should be considered normal if homogeneous in attention and less than 1 cm in largest diameter (Schmalfuss et al. 2000; Glazer et al. 1985). In adults, these are rarely larger than 5 mm in short axis. Hence, the classically used cutoff value of 1 cm may not be applicable to the elderly. Small but round appearing TE lymph nodes, especially when heterogeneously enhancing, should be considered suspicious in the presence of a hypopharyngeal or esophageal cancer.

The common wall of the trachea and esophagus is formed by the fibrous wall of the posterior trachea, anterior esophageal wall and adipose tissue in-between (Figs. 5 and 6). The common wall is more frequently seen with MR than with CT. Contrast enhanced T1-weighted images are superior to other MR sequences (Fig. 6). In addition, its different components can be most distinctly separated at the esophageal verge with a gradual decline more inferiorly. Evaluation of the common wall of the trachea and the esophagus is an essential step in the surgical treatment planning process of patients with cancer

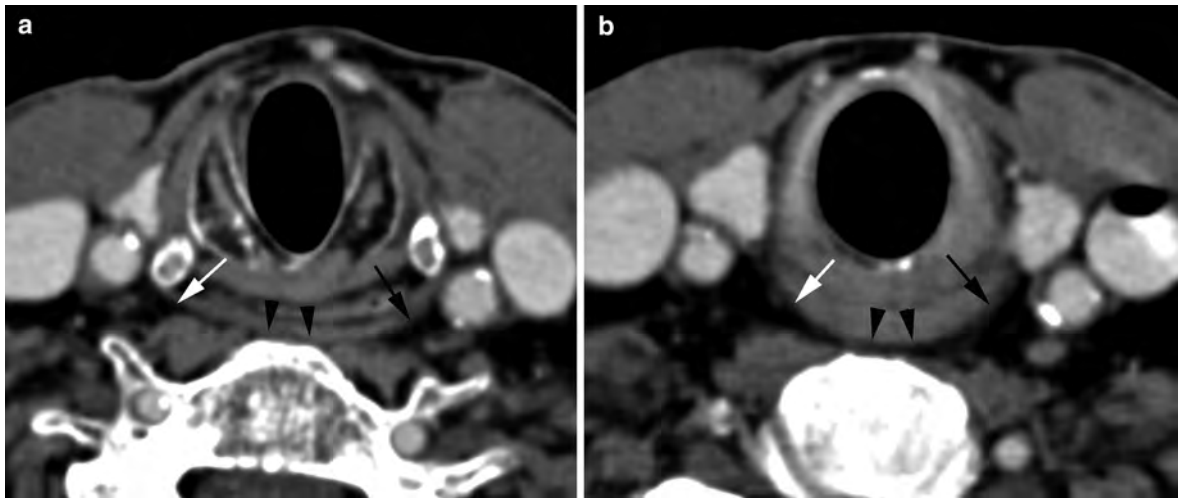

Fig. 4 Axial contrast-enhanced CT images through the mid (**a**) and lower cricoid cartilage (**b**) show the typically seen variable size of the different surrounding fat planes. The left surrounding fat plane is usually the largest (*black arrows*) and the posterior fat plane is the least appreciable (*arrowheads*). At the esophageal verge (**b**), the surrounding fat planes are usually more easily visible than at adjacent levels. *White arrow* = right-sided surrounding fat plane

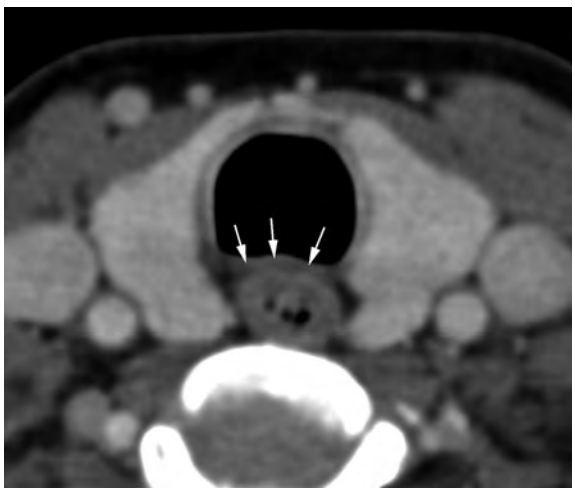

Fig. 5 Axial contrast-enhanced CT image demonstrates the normal appearance of the common wall of the trachea and esophagus with a thin layer of fat (*arrows*) visualized between the trachea anteriorly and the esophagus posteriorly

arising from the esophagus, trachea or adjacent anatomical structures such as the thyroid gland.

3 Pathology

The hypopharynx and cervical esophagus are in the vast majority involved by squamous cell malignancies followed by infiltration by surrounding tumors such as thyroid gland and bronchogenic carcinomas. Other types of tumors are very rare.

3.1 Non-Squamous Cell Malignancies

Non-squamous cell malignancies of the hypopharynx and cervical esophagus are extremely rare and include various sarcomas, lymphomas and malignant minor salivary gland tumors (Becker 1998; Matsuki et al. 1999; De Campora et al. 1987; Tom et al. 1981; Miyazaki et al. 2004; Mouret 1999; Artico et al. 2004; Kitamoto 2003). These tend to grow submucosally and hence are more difficult to see and to biopsy (Becker et al. 2008).

Lipo- and synovial sarcomas are the most commonly reported types of sarcomas involving the hypopharynx and cervical esophagus (Mouret 1999; Artico et al. 2004). Hypopharyngeal liposarcoma most commonly involves older males. Patients typically present with local symptoms and rarely with nodal or distant metastasis. The prognosis does not seem to be affected by the tumor size but rather the grade of the tumor. Low grade liposarcomas are less locally aggressive and rarely metastasize but still show a high local recurrence rate. In contrast, high grade tumors demonstrate a much more aggressive growth pattern and metastasize frequently. The imaging findings vary dependent upon the grade and

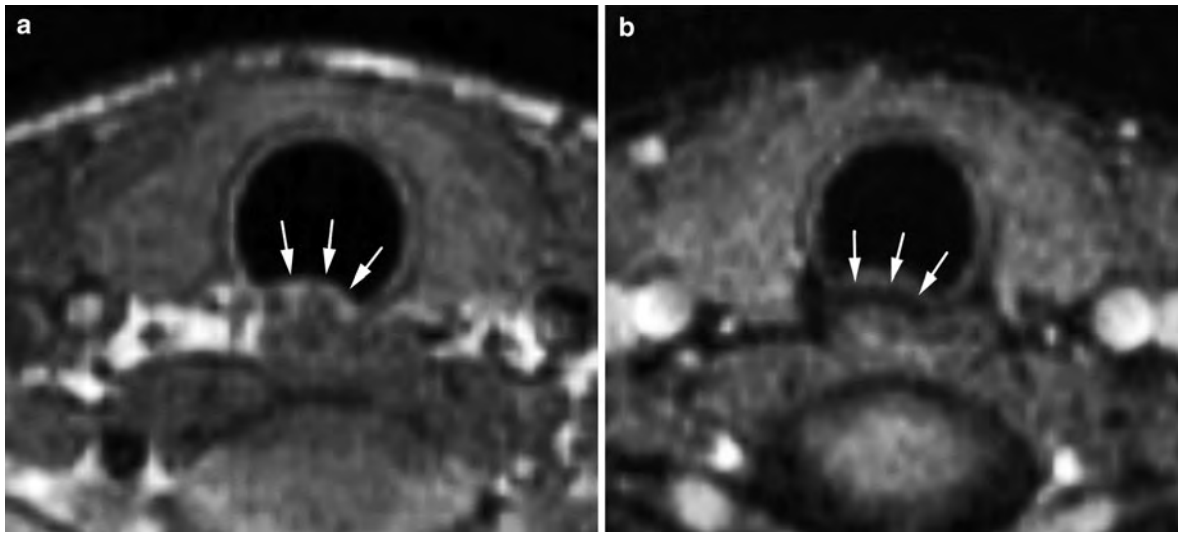

Fig. 6 Axial non-enhanced T1 (**a**) and gradient echo T2-weighted (**b**) images illustrate the dependency of visibility of the thin layer of fat within the common wall of the trachea and esophagus (*arrows*) with this fat plane more completely visible on the gradient exho T2 image (*arrows* in **b**)

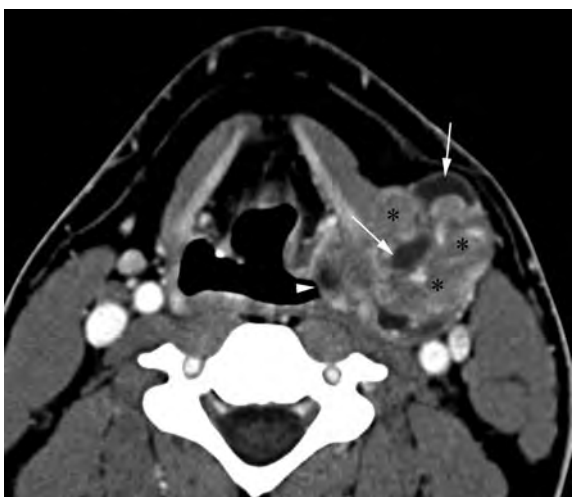

Fig. 7 Axial contrast-enhanced CT image through the upper thyroid cartilage level shows a large mass arising from the lateral wall of the pyriform sinus on the *left* (*arrowhead*) with gross extension into the lateral compartment of the neck. This mass has heterogeneous density with solid (*asterisks*) and cystic (*arrows*) portions that is characteristic for synovial sarcoma but not typically seen with squamous cell carcinoma

differentiation of the tumor, with well-differentiated low grade tumors almost resembling benign lipomas, while high grade undifferentiated tumors may be indistinguishable to squamous cell malignancies.

Synovial hypopharyngeal sarcoma is most likely the second most common sarcoma type involving the hypopharynx. Only 3% of the synovial sarcomas involve the head and neck region with the hypopharynx being most commonly involved (Rangheard et al. 2001). Typically, they affect young adults and adolescents. Although synovial sarcomas are often seen adjacent to joints they do not originate from synovial tissue but rather from pluripotential mesenchymal cells located near articular surfaces, tendons, tendon sheaths, juxta-articular membranes and facial aponeuroses. They are characterized by a reciprocal translocation between chromosomes X and 18 and are divided into a monophasic and biphasic form (Artico et al. 2004; Rangheard et al. 2001). The monophasic form is more common and is constituted of one cell type (epithelial or spindle cells), whereas the biphasic form is very rare and is composed of epithelial and spindle cells. As liposarcomas, they usually present with local symptoms and rarely with nodal or distant metastatic disease. On cross-sectional imaging studies, synovial sarcomas classically display a well-defined, multilocular mass with heterogeneous enhancement (Fig. 7) (Quint et al. 1985). No significant imaging differences have been reported between the mono- and biphasic form. The tumor size primarily influences patient's prognosis. Presence of calcifications is also a favorable prognostic factor (Hirsch et al. 1997; Bukachevsky et al. 1992; Mamelle et al. 1986). Wide excision with postoperative radiation

therapy is currently considered the optimal treatment of the different sarcoma types.

Lymphoma involving the hypopharynx and cervical esophagus is extremely rare (Miyazaki et al. 2004; Kitamoto et al. 2003). Mucosa-associated lymphoid tissue (MALT) lymphoma—a non-Hodgkin's lymphoma—is the most commonly reported subtype of lymphoma in those regions. None of the published case reports refers to cross-sectional imaging findings; however, the reported cases describe a smooth-surfaced, submucosal mass rather than a mucosal lesion as suggested by its name (Miyazaki et al. 2004; Kitamoto et al. 2003). MALT lymphoma of other regions have been described to show increased signal intensity on the T2, decreased attenuation on the T1 weighted images and strong, rapid enhancement following intravenous contrast administration (Takahara et al. 2005; Espinosa et al. 2005). Therefore, MALT lymphoma should be considered in the differential diagnosis if such MR imaging findings are seen in a patient with a submucosal lesion of the hypopharynx and/or cervical esophagus.

Salivary gland malignancies are also rare in the hypophaynx and cervical esophagus. Mucoepidermoid and adenoid cystic carcinomas are the most commonly reported subtypes (Matsuki et al. 1999; De Campora et al. 1987). Adenoid cystic tumors typically arise in salivary gland tissue and minor salivary glands; however, some authors also suggested their origin in common mucosal glands. When arising in common mucosal glands, as this would be the case in the hypopharynx and cervical esophagus, adenoid cystic carcinomas have been shown particularly malignant, with high incidence of local recurrence and distant metastatic disease. The cross-sectional imaging findings of adenoid cystic carcinoma arising from the salivary gland tissue or minor salivary glands have been reported; however, it is uncertain whether the more aggressive subtype of adenoid cystic carcinoma arising from the common mucosal glands follows the same imaging characteristics. Mucoepidermoid carcinoma is composed of signet-ring and squamous cells. None of the published cases mentions the cross-sectional imaging findings of mucoepidermoid carcinoma of the hypopharynx and/or cervical esophagus, however, as these tumors range between low and high grade malignancies their imaging features would be expected to range from a well-defined lesion to an aggressive, locally advanced malignancy. Their prognosis is also variable and certainly depends upon the grade of the tumor, however, there seems to be also a difference in location with a reported overall 5-year survival rate of 77% for the mucoepidermoid carcinoma of the hypopharynx and 0% 2-year survival rate from the esophagus (Matsuki et al. 1999; Damiani et al. 1981).

3.2 Squamous Cell Malignancies

3.2.1 Risk Factors

Chronic tobacco and alcohol abuse represent the main risk factors. Therefore, older males are most commonly involved by this type of tumor with slowly increasing incidence in females as tobacco use in females is still on the rise. Postcricoid area cancers though represent an exception; they occur most commonly in females and are associated with Plummer–Vinson syndrome, which is rarely seen in the United States or continental Europe but more often encountered in the United Kingdom (Zbären and Egger 1997). Postcricoid region hypopharyngeal tumors are hypothesized to be caused by food stasis resulting from hypopharyngeal or esophageal webs as seen with Plummer–Vinson syndrome. In addition, these patients also present with iron deficiency anemia.

The incidence of human papilloma virus (HPV) in hypopharyngeal and cervical esophageal cancer is markedly lower than for oropharyngeal cancer with a reported odd ratio of 15 versus 179, respectively (Ribeiro et al. 2011).

3.2.2 Clinical Presentation

Most commonly, patients with hypopharyngeal and/or cervical esophageal cancer present with a neck mass, secondary to metastatic nodal involvement and/or dysphagia, odynophagia, globus sensation and/or otalgia. Weight loss and a characteristic change in voice to "hot potato" voice can also be seen. Typically, these cancers present at an advanced stage; they also have a high tendency to metastasize to the draining nodal chains early on. Therefore, it is not surprising that up to 75% of patients have nodal metastatic disease at presentation. In addition, elective dissections in patients with clinically N0 neck have shown a high incidence of occult nodal metastasis with a frequency of 30%. Up to 40% of

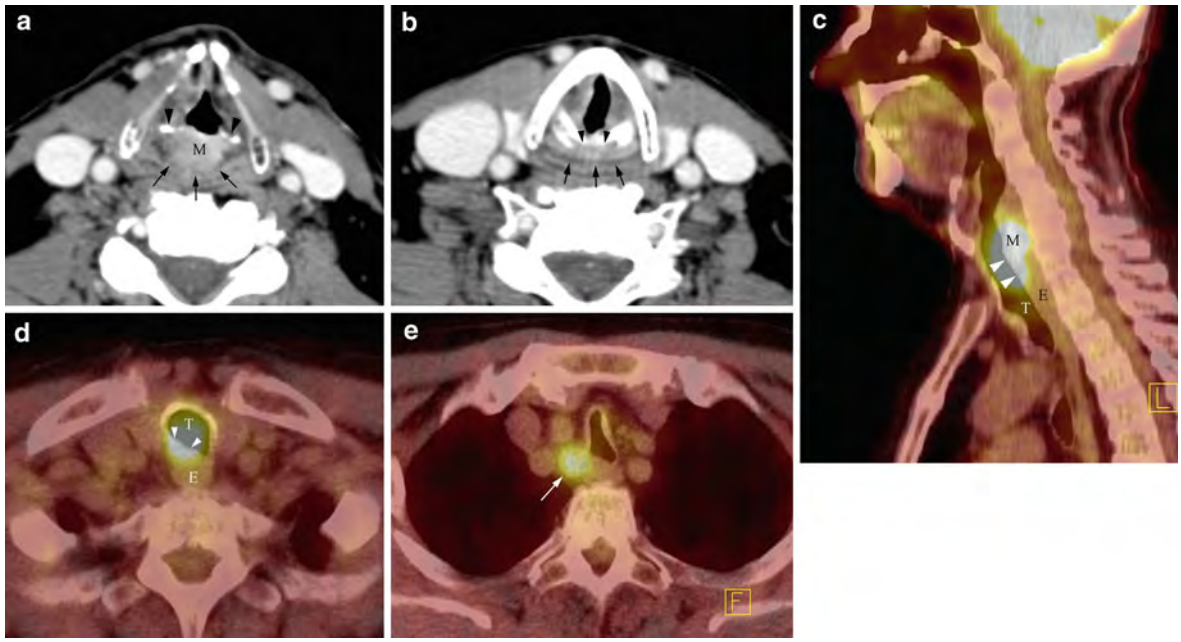

Fig. 8 Axial contrast-enhanced CT image at the hypopharynx level (**a**) reveals a small mass (*M* in **a**) between the arytenoids cartilages (*arrowheads* in **a**) that partially infiltrates the anterior submucosal fat plane (*arrows* in **a**). Slightly more inferiorly, the axial contrast-enhanced CT image (**b**) shows restoration of the submucosal fat plane (*arrows* in **b**) suggesting that the tumor is localized to the interarytenoid region (*M* in **a**). Closer evaluation, however, discovers a large erosion (*arrowheads* in **b**) of the cricoid cartilage posteriorly. Since this is symmetric in distribution, it can be mistaken for asymmetric ossification of the cricoid cartilage. The fused PET–CT image in sagittal plane (**c**) reveals even further inferior extent of the mass (*M* in **c**) with involvement of the common wall (*arrowheads* in **c** and **d**) between the trachea (*T* in **c** and **d**) and esophagus (*E* in **c** and **d**) down to the thoracic inlet level as confirmed on the axial fused PET–CT image (**d**). Axial fused PET–CT image (**e**) through the upper lungs detects an abnormal group VI lymph node (*arrow* in **e**) on the right, the expected lymphatic drainage pathway for postcricoid cancers

patients also have distant metastasis at the time of presentation (Million 1994; Kraus et al. 1997; Spector et al. 2001).

3.2.3 Growth Pattern

Hypopharyngeal malignancies like to spread in submucosal fashion that is often undetectable on clinical and/or endoscopic examination (Million 1994; Saleh et al. 1993). Nevertheless, the different subtypes of hypopharyngeal malignancies show distinct grows patterns, as described below.

Postcricoid region cancers like to invade the posterior aspect of the larynx causing vocal cord paralysis and hoarseness. The cricoarytenoid joint itself is usually not involved (Fig. 8). In addition, these tumors have a high propensity to grow posterior–lateral to involve the pyriform sinuses (100%) and inferiorly to involve the trachea (71%) and/or cervical esophagus (71%) (Fig. 8) (Aspestrand et al. 1990). Tracheal or esophageal invasion is not detectable by endoscopic evaluation in half of the patients.

The growth pattern of pyriform sinus cancers depends on their site of origin or involvement. Tumors arising from or infiltrating the lateral wall of the pyriform sinus like to invade the posterior aspect of the thyroid cartilage, extend into the soft tissues of the lateral compartment of the neck and the paraglottic space of the true vocal cord (Fig. 9) (Zbären and Egger 1997). Direct infiltration of the intrinsic laryngeal muscles is rarely seen. In contrast, tumors arising from or infiltrating the medial wall of the pyriform sinuses show early laryngeal invasion and vocal cord fixation in 60% of the patients (Figs. 10 and 11) (Becker 1998; Zbären and Egger 1997; Nowak et al. 1999). They also have a high propensity for contralateral tumor extension with 87%, higher frequency of submucosal tumor spread than the other tumor subtypes with 56% and perineural tumor

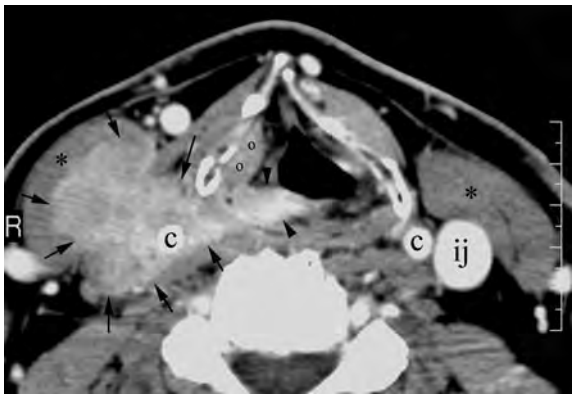

Fig. 9 Axial contrast-enhanced CT image through the mid thyroid cartilage level shows a large squamous cell carcinoma arising from the pyriform sinus on the *right* (*arrowheads*) with huge extension into the lateral compartment of the neck (*arrows*) causing marked flattening and lateral displacement of the sternocleidomastoid muscle (*asterisks* on *right*) when compared to its normal appearance on the *left* (*asterisks* on *left*). In addition, this mass results in complete occlusion of the internal jugular vein on the *right* when compared to the *left side* (*ij* on *left*). The common carotid artery (*c*) is also surrounded by the mass on the *right* (*c* on *right*) when compared to its normal appearance on the *left* (*c* on *left*). Please note also the submucosal involvement of the false vocal cord on the *right* (*o*)

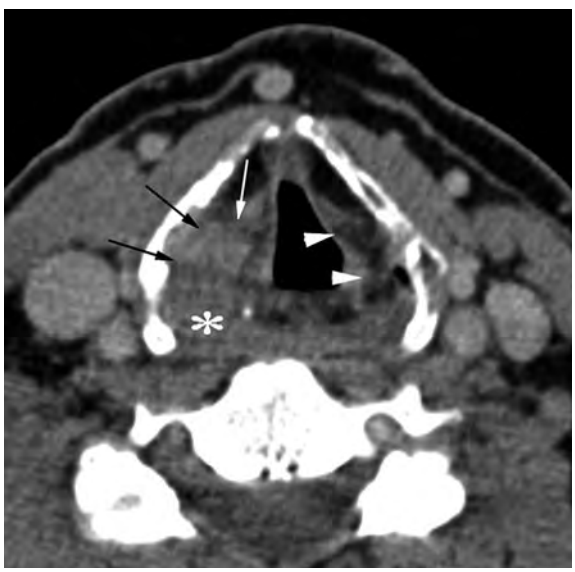

Fig. 10 Axial contrast-enhanced CT image through the false vocal cord level shows submucosal extension of the right pyriform sinus tumor (*asterisks*) into the right false vocal cord (*arrows*) that is seen as obliteration of the paraglottic fat plane when compared to the normal appearance on the *left* (*arrowheads*). This portion of the tumor was not appreciable on endoscopic examination

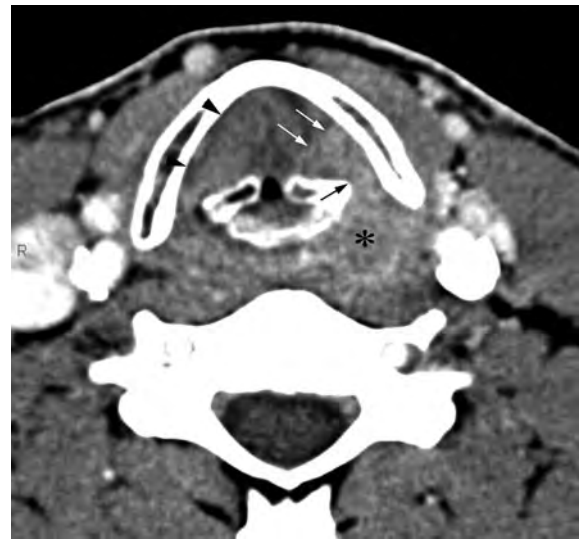

Fig. 11 Axial contrast-enhanced CT image through the true vocal cord level demonstrates a large pyriform sinus cancer on the *left* (*asterisks*) that is extending in submucosal fashion into the left true vocal cord (*white arrows*). The extension into the true vocal cord is slightly higher in density than the normal vocal cord tissues; also slight widening of the distance between the arytenoid and thyroid cartilage (*black arrow*), the disorganization of the intrinsic vocal cord musculature and the obliteration of the paraglottic fat plane provide additional clues to the glottic extent of the primary tumor. Note that the normal paraglottic fat plane (*arrowheads* on *right*) at the true vocal cord level are significantly more difficult to delineate than at the false vocal cord level (compare with Fig. 9)

invasion in almost 45% of patients (Figs. 10 and 11) (Zbären and Egger 1997).

Posterior hypopharyngeal wall cancers like to grow in craniocaudal direction with potential extension from the nasopharynx all the way to the esophagus (Nowak et al. 1999). As the craniocaudal extension of these tumors may solely be superficial, the full extent of the tumor may not be detectable on cross-sectional examination; therefore correlation with clinical findings is critical for staging and treatment planning purposes. Rarely, these tumors cause infiltration of the prevertebral fascia or musculature at the time of presentation. Even when there is obliteration of the prevertebral fat planes on CT and/or MR studies, the diagnosis of prevertebral fascia or muscle invasion cannot be made as the accuracy of CT in predicting prevertebral musculature involvement has been reported to be low with 55% (Righi et al. 1996). Therefore, surgical exploration has to be done for definitive diagnosis. In contrast,

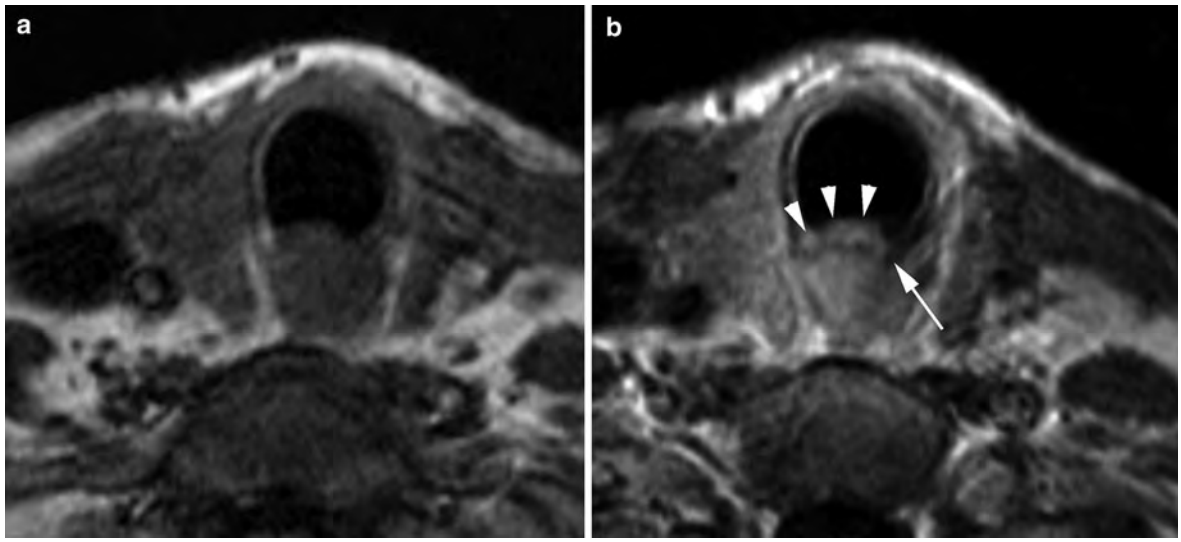

Fig. 12 Axial non-enhanced T1- (**a**) and contrast-enhanced T1- (**b**) weighted images through the upper esophagus show lack of patent esophageal lumen caused by an esophageal cancer that is difficult to appreciate on the non-enhanced T1-weighted image (**a**). The contrast-enhanced T1-weighted image clearly shows gross involvement of the common wall of the trachea and esophagus (*arrowheads*) that enhances in comparison to the non-enhancing normal tracheal wall (*arrows*); this provides a critical clue to the correct diagnosis

preservation of the prevertebral fat planes is helpful as the negative predicative value for prevertebral musculature involvement is high with 82% (Righi et al. 1996). When the tumor breaks through the pharyngeal constrictor muscle, it can spread freely and unsuspected by clinical examination along the facial planes to reach the skull base superiorly and the upper mediastinum inferiorly.

Cervical esophageal tumors like to infiltrate adjacent anatomical structures, such as the trachea, TE groove housing the recurrent laryngeal nerve, and adjacent vasculature (Figs. 12 and 13). In addition, they incline to spread in a submucosal fashion to involve the hypopharynx (Fig. 13).

The exact assessment of the craniocaudal extension of hypopharyngeal tumors into the cervical esophagus and vice versa is crucial for planning of surgical resection (limited vs. extensive resection) (Fig. 13). Since hypopharyngeal tumors can spread in a superficial or submucosal pattern, a combination of clinical examination and cross-sectional study should be used in the treatment planning process.

3.2.4 Nodal Chain Involvement

The different hypopharyngeal tumor subtypes and the cervical esophagus have slightly different lymphatic drainage pathways: the postcricoid area tumors primarily drain into groups III, IV and VI lymph nodes (Fig. 8); the pyriform sinus tumors tend to metastasize into groups II, III and V lymph nodes; and the posterior hypopharyngeal wall cancers like to involve the retropharyngeal lymph nodes and secondarily the internal jugular chain lymph nodes. Retropharyngeal lymph nodes are only rarely involved with the other hypopharyngeal cancer subtypes and are seen in 15% of patients, however, only when there is concomitant involvement of the lateral nodal chain groups (Million 1994). Cervical esophageal cancer drains into group VI and mediastinal lymph nodes. The group VI lymph nodes are involved in 71% of patients at presentation (Weber et al. 1993).

3.2.5 Detection of Distant Metastasis

The incidence of distant metastasis has been reported to be up to 40% at the time of presentation with delayed metastatic disease seen in 18% (Million 1994; Kraus et al. 1997; Spector et al. 2001). The risk of distant metastases is dependent upon tumor stage with T4 tumors and advanced regional nodal disease carrying the highest risk. Lungs, followed by liver and bones are the most commonly affected. FDG PET imaging has shown to have 1.5 times higher rate of

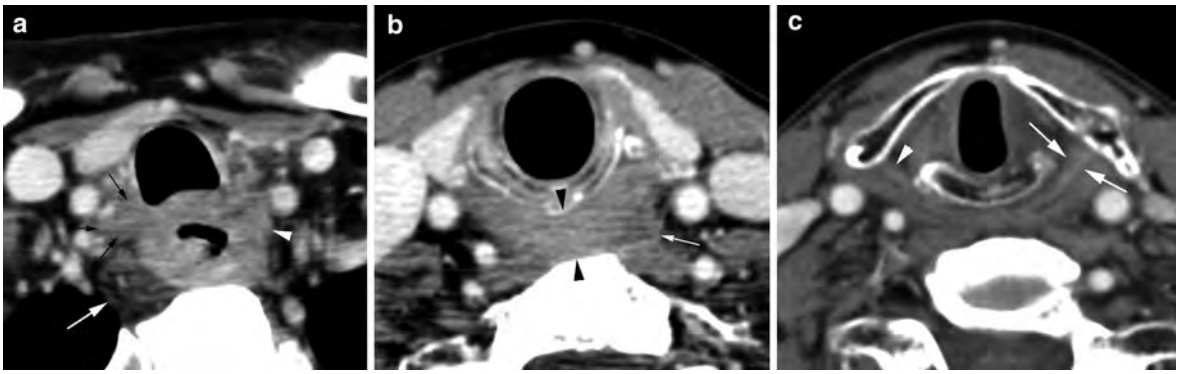

Fig. 13 Axial contrast-enhanced CT images through the cervical esophagus (**a**), esophageal verge (**b**) and postcricoid level (**c**) show marked wall thickening of the upper esophagus caused by a large esophageal cancer with clear signs of tumor growth beyond the serosal layer, delineated as indistinct appearance of the outer esophageal margin (*arrowhead* in **a**), "dirty" appearance of the paraesophageal fat on *right* (*white arrow*) and gross extension into the TE groove on the *right* (*black arrows* in **a**). Superiorly, the tumor is involving the esophageal verge which is slightly larger in anterior posterior diameter (between *arrowheads* in **b**) than typically seen. In addition, there is partial obscuration of the left-sided surrounding fat plane (*arrow* in **b**) consistent with extra-esophageal tumor growth, providing additional clue for involvement of the esophageal verge. The tumor continues superiorly to involve the postcricoid region on the *left* (*arrows* in **c**) when compared to the normal appearance on the *right* (*arrowhead* in **c**)

detection of metastatic foci than CT alone at a price of slightly lower specificity (Ng et al. 2008). Therefore, the utilization of both imaging tools in combination (PET–CT) yields the best results and has been reported to change the treatment in 13% of patients.

3.2.6 TNM Classification

The staging system of the primary hypopharynx and cervical esophageal cancers and associated nodal metastatic disease is outlined in Tables 1 and 2, respectively (American joint committee on cancer 2010). The recommended staging of cervical esophageal lesions is identical to that of the intrathoracic esophagus.

3.3 Secondary Involvement by Other Tumors

Infiltration of the hypopharynx and cervical esophagus by surrounding tumors is rare. It may occur with advanced head and neck tumors as well as thyroid, tracheal and bronchogenic carcinomas (Roychowdhury et al. 2000). MR is more sensitive than CT for detection of hypopharyngeal and/or esophageal invasion by an adjacent malignancy due to its higher soft tissue definition. Focal areas of increased T2 signal intensity raise the suspicion for invasion (Fig. 14). Focal enhancement following contrast administration might also be a sign of infiltration; however, it is not as specific as the T2 changes (Fig. 14). Circumferential mass at the level of the cervical esophagus has been reported to be the most sensitive and specific sign of invasion (accuracy, 100%). In contrast, intact adjacent fat planes, absence of wall thickening and normal T2 wall signal intensity indicate no invasion with a very high degree of confidence (Roychowdhury et al. 2000).

4 Cross-Sectional Imaging

Cross-sectional imaging with CT and MR is critical in the evaluation of patients with hypopharyngeal and/or cervical esophagus malignancies (Wenig et al. 1995; Becker 1998; Aspestrand et al. 1990; Nowak et al. 1999; Prehn et al. 1998; Thabet et al. 1996). Overall, it has been shown that the clinical tumor stage increases in up to 90% of patients with cross-sectional imaging. Changes in T-stage account for two-thirds of the tumor up-staging due to detection of lateral soft tissue involvement in 88%, and bone or cartilage invasion in 23% of patients. In one-third of the patients the N-stage was responsible for the tumor up-staging. Comparison of the accuracy of tumor staging with pathological findings revealed that the clinical examination is less

Table 1 Staging of primary tumors of the hypopharynx

Primary tumor	
Tis	Carcinoma in situ
T1	Tumor limited to one subsite of hypopharynx and/or ≤2 cm in greatest dimension
T2	Tumor invades more than one subsite of hypopharynx or an adjacent site, or measures >2 cm but ≤4 cm in greatest diameter without fixation of hemilarynx or extension into the esophagus
T3	Tumor >4 cm in greatest dimension or with fixation of the hemilarynx or extension into esophagus
T4	
T4a	Moderate advanced local disease: Tumor invades thyroid/cricoid cartilage, hyoid bone, thyroid gland or central compartment soft tissues (=prelaryngeal strap muscles and subcutaneous fat)
T4b	Very advanced local disease: Tumor invades prevertebral fascia, encases carotid artery or involves mediastinal structures
Regional lymph nodes	
NX	Regional lymph nodes cannot be assessed
N0	No regional lymph node metastasis
N1	Metastasis in a single lymph node, ≤3 cm in greatest dimension
N2	
N2a	Metastasis in a single ipsilateral lymph node >3 cm but ≤6 cm in greatest dimension
N2b	Metastasis in multiple ipsilateral lymph nodes, none >6 cm in greatest dimension
N2c	Metastasis in bilateral or contralateral lymph nodes, none >6 cm in greatest dimension
N3	Metastasis in a lymph node >6 cm in greatest dimension
	Note: Metastases at the level VII are considered regional lymph node metastasis.

Source Adapted from American joint committee on cancer (2010)

Table 2 Staging of primary tumors of the cervical esophagus

Primary tumor	
Tis	High-grade dysplasia
T1	Tumor invades the lamina propria, muscularis mucosae or submucosa
T1a	Tumor invades lamina propria or muscularis mucosae
T1b	Tumor invades submucosa
T2	Tumor invades muscularis propria
T3	Tumor invades adventitia
T4	Tumor invades adjacent structures
T4a	Resectable tumor invading pleura, pericardium or diaphragm
T4b	Unresectable tumor invading other adjacent structures, such as aorta, vertebral body, trachea
Regional lymph nodes	
NX	Regional lymph nodes cannot be assessed
N0	No regional lymph node metastasis
N1	Metastasis in 1–2 regional lymph nodes
N2	Metastasis in 3–6 regional lymph nodes
N3	Metastasis in ≥7 regional lymph nodes

Source Adapted from reference American joint committee on cancer (2010)

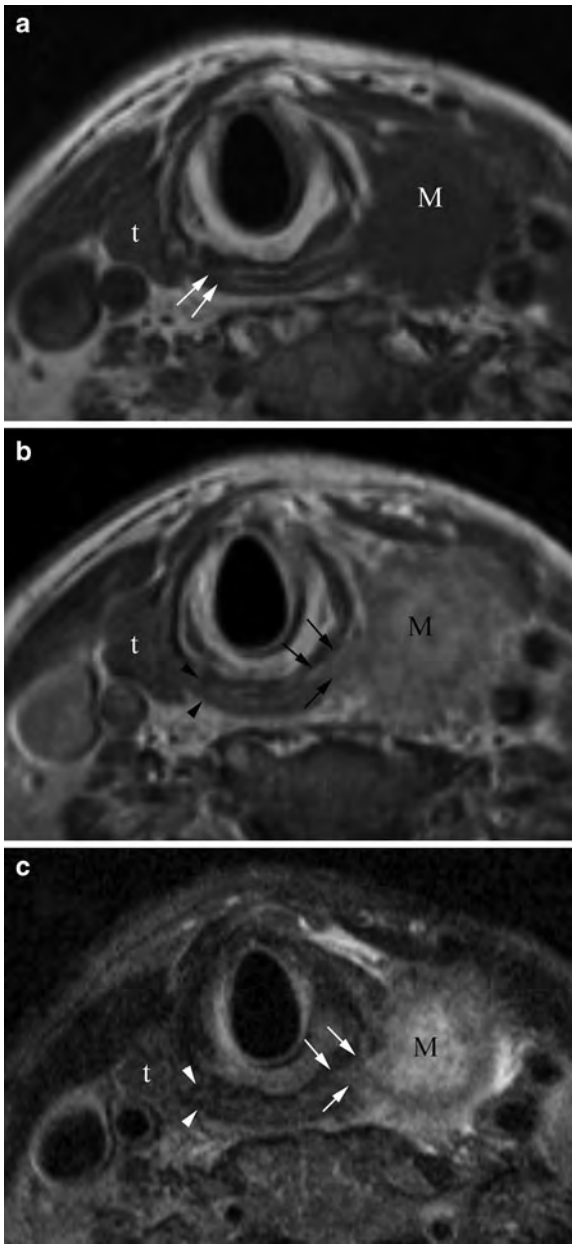

Fig. 14 Axial non-contrasted T1- (**a**), contrast-enhanced T1- (**b**) and T2- (**c**) weighted images show a large mass arising from the left thyroid lobe (*M*). This mass is invading the left hypopharynx which is not well seen on the non-contrasted T1-weighted image (**a**) as there is no significant infiltration of the submucosal fat planes on the *left* when compared to their normal appearance on the *right* (*arrows* in **a**). The enhanced T1- (**b**) and the T2- (**c**) weighted images clearly show the invasion by the thyroid cancer as the muscular layers are obscured by an enhancing or hyperintense lesion, respectively, when compared to the normal appearance of the hypopharyngeal musculature on the *right* (*arrowheads* in **b** and **c**). *t* = normal right lobe of the thyroid gland

accurate with 58% than CT and MR imaging with 80 and 85% accuracy, respectively. These facts emphasize the essential role of cross-sectional imaging in staging of hypopharyngeal and esophageal cancers. Interestingly, none of the other cancers of the head and neck region shows such a significant impact of cross-sectional imaging upon staging.

CT and MR imaging is, however, only helpful when performed with an appropriate protocol covering the potential sites of tumor spread, utilizing the appropriate imaging study, sequence and window display. Although each radiologist has personal preferences and there are vendor-related variations in hardware and software, the subsequent generic imaging guidelines should be followed:

1. Image the patient in supine position with the neck slightly extended to elongate the airway. Use dedicated neck coil for MR imaging to improve the spatial resolution and signal to noise ratio.
2. Perform images in axial plane from the body of the mandible to the thoracic inlet. Obtain MRI images parallel to the true vocal cords and review the volumetrically acquired CT images in the same plane. Increase the upper extent to the skull base if posterior pharyngeal wall cancer is suspected to capture the entire possible extent of the tumor and to include all retropharyngeal lymph nodes.
3. Utilize a slice thickness of $\leq$3 mm for CT and contiguous 3 mm images for MR imaging for adequate display of the pertinent anatomical structures. Utilize the multi-planar reformations capabilities of the volumetric CT acquisition to review images in different planes.
4. Use a field-of-view of $\leq$16 cm through the neck. Additional reconstructions of the CT images through the hypopharynx with a field-of-view of 10 cm are recommended to increase spatial resolution. Magnification of the images performed with the larger field-of-view is not sufficient as the special resolution will stay the same.
5. Use image matrix of at least 256 $\times$ 256 for MR and 512 $\times$ 512 for CT for optimal spatial resolution.
6. Inject intravenous contrast for better tumor border delineation and detection of nodal metastatic foci. Scan in the capillary phase as tumor might not significantly enhance when scanned too early, e.g. during the arterial phase.

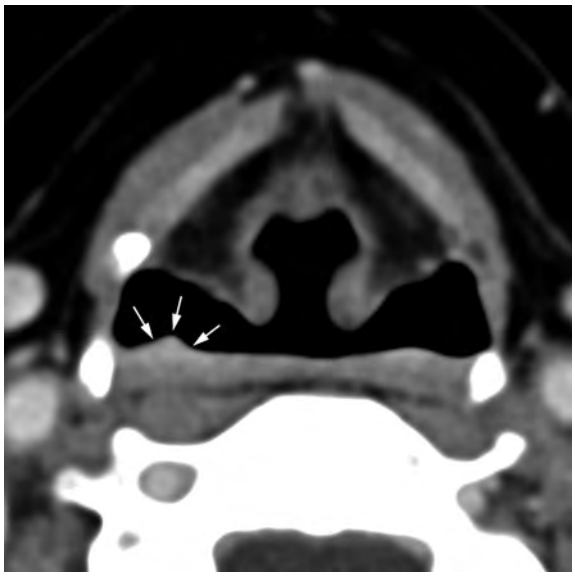

Fig. 15 Axial contrast-enhanced CT image performed during valsalva maneuver reveals a tiny mass along the posterior pharyngeal wall (*arrows*) on the right side that would have been difficult to detect with collapsed pyriform sinus as typically seen during quiet breathing

7. *MRI*: A minimum of noncontrasted and contrast T1-weighted images and fast spin-echo T2-weighted images should be performed to emphasize soft tissue detail. Other sequences may be included to better evaluate certain structures such as the intramural fat planes (see Sect. 2.2).
8. *CT*: Reconstruction of the images through the laryngeal cartilages in bone algorithm is helpful for detection of cartilage destruction and/or sclerosis.
9. Utilize the multi-planar capabilities of both imaging modalities to facilitate the assessment of craniocaudal tumor extension.
10. Consider scanning of patient during modified vasalva maneuver when small tumor is suspected to open the piriform sinuses (Fig. 15) (see also "Imaging Techniques").

5 Radiologist's Role

5.1 Pretreatment

The radiologist's pretreatment role is multifold: detection of the subsite of origin of the primary tumor, delineation of the extent of the primary tumor, assessment of the nodal status and detection of a second primary cancer. When the full extent of the primary tumor is assessed and reported, the following pertinent issues have to be emphasized as they may influence the T staging of the tumor.

5.1.1 Submucosal Spread

As mentioned before, hypopharyngeal and/or esophageal cancers like to grow in a submucosal fashion and, therefore, remain undetectable in a significant number of patients on clinical and endoscopic examination (Figs. 10 and 11) (Saleh et al. 1993). Occasionally, the entire tumor is submucosal in location and difficult or impossible to biopsy endoscopically. In such cases, the radiologist may offer percutaneous biopsy under CT guidance.

5.1.2 Cartilage Involvement

Cartilage involvement may be studied with CT and MR. Both modalities struggle with the problem of lack of ossification of the different cartilages in the younger patient and heterogeneous as well as variable ossification with advanced age (Yeager et al. 1982). This is particularly true for the thyroid cartilage. Since the different cartilages tend to ossify in a symmetric fashion, asymmetric attenuation might be a helpful hint for presence of cartilage invasion and needs to be included in the pretreatment assessment of CT and/or MR studies (Fatterpekar et al. 2004).

The role of CT and MR in detection of cartilage involvement has been studied extensively in the past decades and has shown that non-removal of an involved cartilage carries a risk of 50–60% of leaving tumor behind. The overall consensus is that MR is the most sensitive imaging modality in detection of cartilage involvement; however, it suffers from low specificity as inflammation, edema and sclerosis can show similar MR findings as tumor invasion (Wenig et al. 1995; Becker 1998; Becker et al. 1995; Castelijns et al. 1988; Zbären et al. 1996). For CT, the reported sensitivity is lower but the overall specificity is higher than for MR (Becker et al. 1997). Therefore, a combination of both studies might be the most effective strategy in the evaluation process of cartilage invasion by cancer (Yousem and Tufano 2002). In addition, the specificity of both imaging modalities depends upon the cartilage type. The thyroid cartilage has the lowest specificity due to its variable ossification and the arytenoid cartilage has the highest.

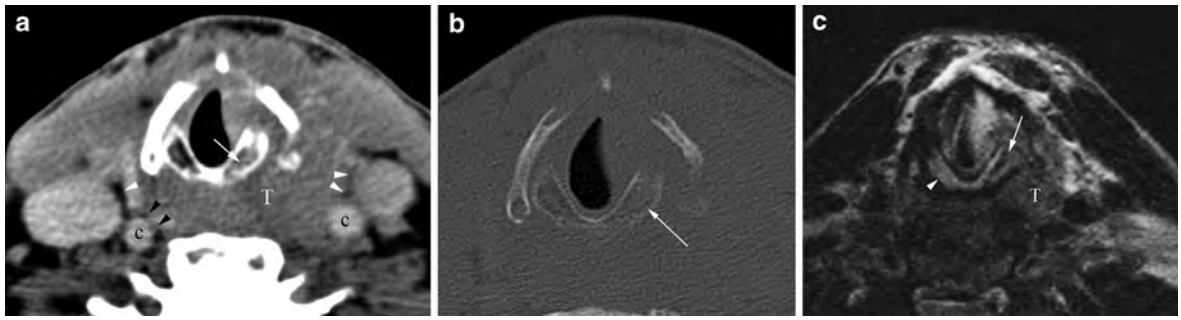

Fig. 16 Axial contrast-enhanced CT images displayed in soft tissue (**a**) and bone (**b**) windows show a large pyriform sinus mass on the left (*T*) that is causing subtle sclerosis of the left cricoid cartilage (*white arrow* in **a** and **b**). The T2 weighted (**c**) image at the same level confirms the sclerosis as the normally seen high signal intensity of the cricoid cartilage (*arrowhead* in **c**) is replaced by dark signal intensity on the *left* (*arrow* in **c**). In addition, this mass partially obliterates the left lateral surrounding fat plane (*white arrowheads* on *left* in **a**) when compared to its normal appearance on the right (*white arrowhead* on *right* in **a**). There is also obliteration of the normally seen fat plane around the common carotid artery (*c*) on the *left* when compared to its normal appearance on the *right* (*black arrowheads* in **a**)

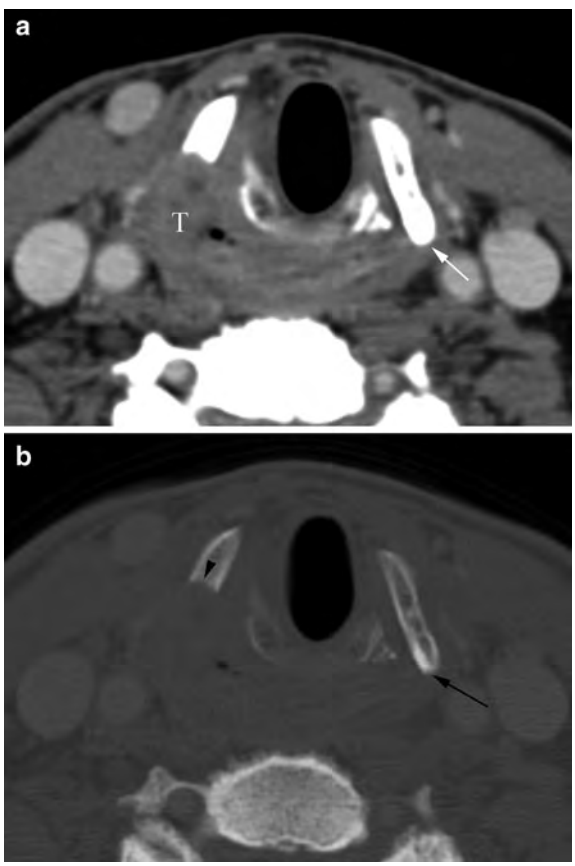

Fig. 17 Axial contrast-enhanced CT images displayed in soft tissue (**a**) and bone (**b**) windows show severe foreshortening of the posterior thyroid cartilage caused by extensive pyriform sinus cancer (*T*) involvement on the *right*, when compared to its normal length on the *left* (*arrow*)

Therefore, the diagnosis of thyroid cartilage involvement by tumor should only be made with caution with both imaging modalities.

Cartilage involvement can manifest as cartilage sclerosis (Fig. 16), cortical erosions or lysis (Fig. 17) and bone marrow replacement (Fig. 18). Cartilage sclerosis is discernible as increased density on CT and decreased attenuation on all MR sequences with lack of enhancement following contrast administration (Fig. 16). It has been shown to be the most sensitive criterion for cartilage invasion; however, it often corresponds to "benign" reactive inflammation secondary to the adjacent tumor or occasionally to a normal anatomical variation as reported for the arytenoid cartilage (Schmalfuss et al. 2000; Becker et al. 1997; Munoz et al. 1993). Therefore, it is not surprising that the positive predictive value of cartilage sclerosis for tumor invasion has been reported to be only about 50%. Cartilage erosion or lysis manifests as serpiginous or gapping cartilage contour while bone marrow replacement shows increased density on CT and decreased signal intensity on T1-weighted images in relation to the uninvolved fatty replaced bone marrow seen in older patients, with marked enhancement following contrast administration (Figs. 17 and 18). None of the criteria alone showed sufficient sensitivity and specificity for cartilage invasion and therefore, the highest degree of accuracy could only be reached when combining sclerosis, erosions or lysis and extralaryngeal tumor extension together. Since not all of these criteria are present in

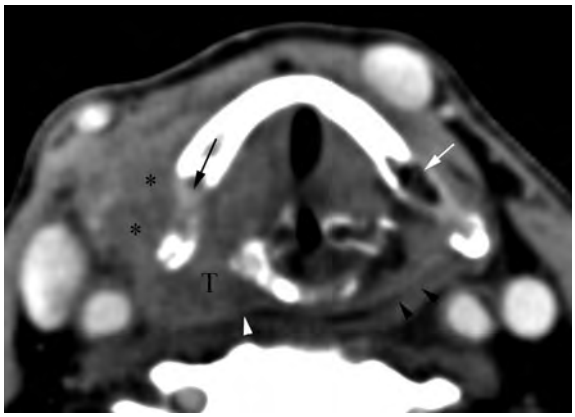

Fig. 18 Axial contrast-enhanced CT image through the arytenoid cartilage level demonstreates replacement of the normally seen fatty bone marrow (*white arrow*) by soft tissue density (*black arrow*) caused by bone marrow replacement of this portion of the thyroid cartilage by a pyriform sinus cancer on the right (*T*). Note the abrupt cutoff of the submucosal fat planes caused by the tumor on the *right* (*white arrowhead*) when compared to their normal appearance on the *left* (*black arrowheads*). The tumor also wraps around the posterior border of the thyroid cartilage to involve the strap muscles (*asterisks*)

each patient simultaneously, a significant false negative rate would be expected. Nevertheless, cross-sectional imaging is valuable as an excellent negative predictor for cartilage invasion with reported high negative predictive values of 92–100% (Becker 1998; Castelijns et al. 1988; Becker et al. 1995; Zbären et al. 1996).

5.1.3 Tumor Volume

In the past decade, focus was placed on stratifying patients in high- or low-risk groups to help in the selection of the most optimal treatment plan based on outcome measures. Besides cartilage invasion, tumor volume and amount of disease at the pyriform sinus apex have been identified to be critical prognostic factors in patients with T1 and T2 stage pyriform sinus cancer (Pameijer et al. 1998). A tumor volume of 6.5 ml demarcated the threshold between favorable and non-favorable to reach control at the primary site with radiation therapy alone. Similar threshold criteria were also detected in regard to pyriform sinus apex involvement. A tumor diameter of <10 mm at the level of the base of the arytenoid cartilage and upper 3 mm of the cricoid cartilage (="minimal apical disease") has been shown to have a favorable prognosis to reach control at the primary site with radiation therapy alone, in contrast to tumor diameter of ≥10 mm (="bulky apical disease") (Pameijer et al. 1998). The results of tumor volume and apical disease combined, classified the patients into different risk groups with the following criteria and local control rates if treated with radiation therapy alone:

- *Low-risk group*. Tumor volume <6.5 ml and no or minimal pyriform apex disease resulted in a control rate of 94% (Fig. 19).
- *Moderate risk group*. Tumor volume of <6.5 ml and bulky apical disease or tumor volume ≥6.5 ml and no or minimal pyriform apex disease demonstrated local control rates of 50% (Fig. 20).
- *High-risk group*. Tumor volume of ≥6.5 ml and bulky apical disease yielded a survival rate of 0% (Fig. 21).

Therefore, tumor volume and extent of disease at the pyriform apex level should be included in the radiological report for all T1 and T2 stage pyriform sinus cancers. Thresholds for tumor volume and/or extent of pyriform apex disease for other types of hypopharyngeal and/or other T stages are still unknown.

More recently, CT perfusion imaging has shown promising results in predicting outcome in patients with head and neck cancers with a 14 times higher risk of recurrent tumor detected in patients with low permeability surface area product (<18 mL/min/100 g) (Bisdas et al. 2009). Similar but less profound risk of recurrence (sixfold) was seen with low maximal blood flow values.

5.2 During Treatment

At present, the radiologist is only rarely involved during the treatment phase of patients with hypopharyngeal or cervical esophageal cancer, unless the patient develops complications related to the therapy, such as fistula and abscess formation or vascular rupture requiring percutaneous intervention.

5.3 Posttreatment

As it is true for the pretreatment evaluation of patients with hypopharyngeal or cervical esophageal cancer, cross-sectional imaging plays a crucial role in the detection of recurrent cancer. It has been reported that

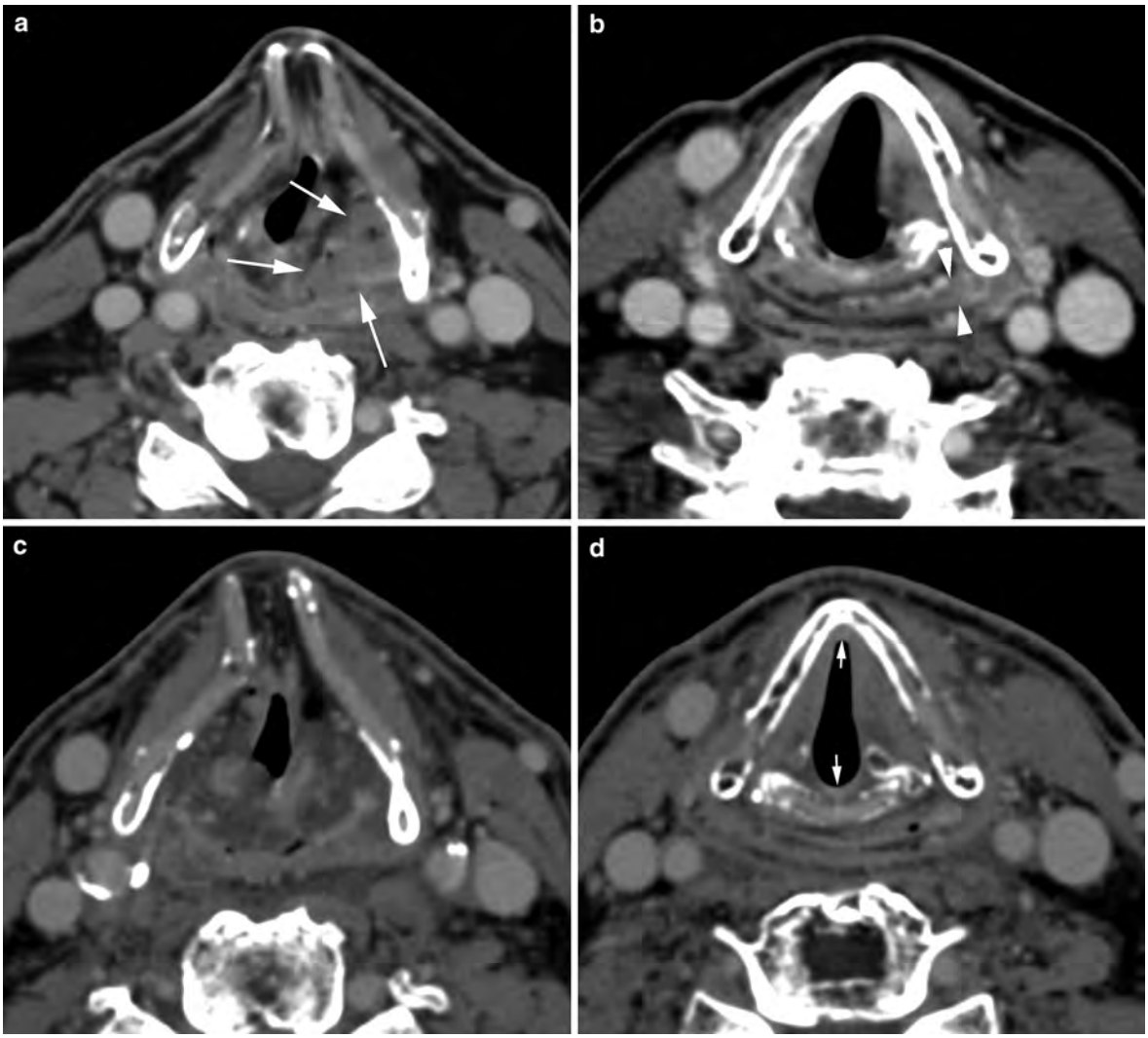

Fig. 19 Axial contrast-enhanced CT images through the false (**a**) and true (**b**) vocal cord level reveals a pyriform sinus cancer (*arrows* in **a**) of <6.5 ml with minimal involvement at the pyriform sinus apex (*arrowheads* in **b**) that carries a favorable prognosis to be controlled at the primary site with radiation therapy alone as demonstrated on the matched posttreatment images (**c**, **d**). Note the diffuse swelling of the false vocal cords (**c**) as well as anterior and posterior commissure (*arrows* in **d**) that represent the expected findings following radiation therapy

up to 40% of recurrent tumors are detected with cross-sectional imaging prior to their discovery on clinical examination (Hermans et al. 2000). This is on one side due to the similarity of post-radiotherapy changes to recurrent tumor on clinical examination and on the other side due to potential submucosal location of recurrent tumors. Therefore, the referring physicians rely on imaging surveillance even more in patients with hypopharyngeal or cervical esophageal cancer than in patients with other head and neck tumor types. Since the treatment options of patients with tumors of the hypopharynx and cervical esophagus vary from radiation therapy alone to total laryngectomy in combination with various reconstructive techniques and/or radiation therapy, the cross-sectional imaging findings significantly vary from patient to patient (Kraus et al. 1994). Superimposed posttreatment complications, such as abscess or fistula formation, may further complicate this issue. Therefore, to allow easier and faster detection of recurrent or persistent tumor, a CT and/or MR imaging study 3 to 4 months after completion of the treatment is recommended in all patients.

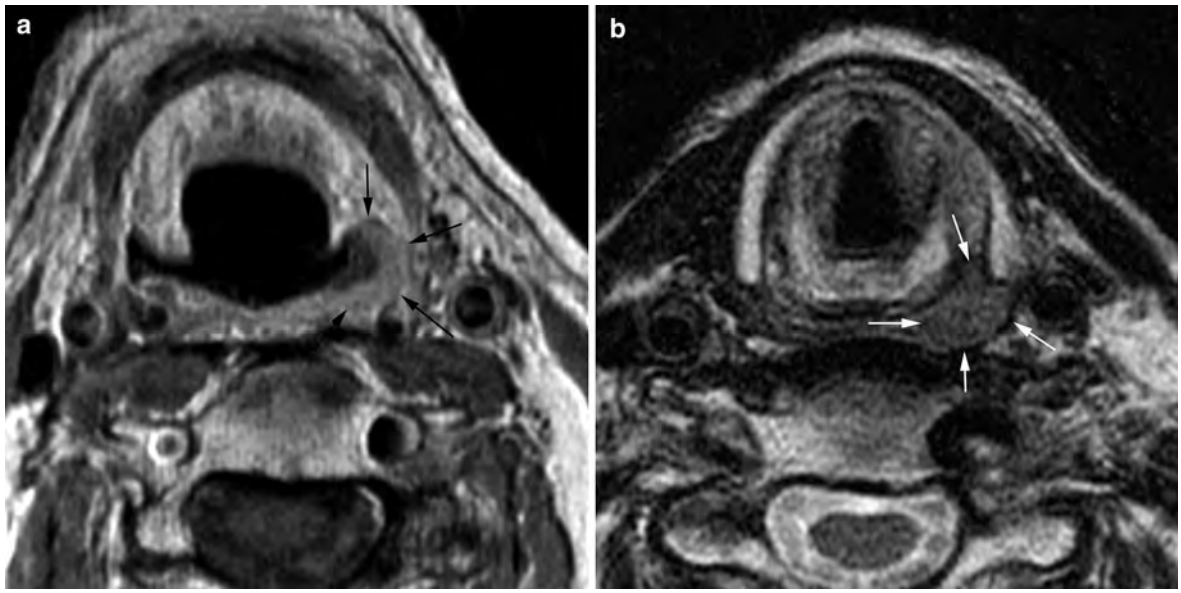

Fig. 20 Axial contrast-enhanced T- (**a**) and T2- (**b**) weighted image at the entrance site of the pyriform sinus (**a**) and pyriform sinus apex (**b**) levels shows a small pyriform sinus cancer (*arrows* in **a**). The small volume is favorable for reaching control at the primary site with radiation therapy alone. However, since there is bulky apical involvement (*arrows* in **b**) the chance for the patient to be cured with radiation therapy alone decreases to about 50%

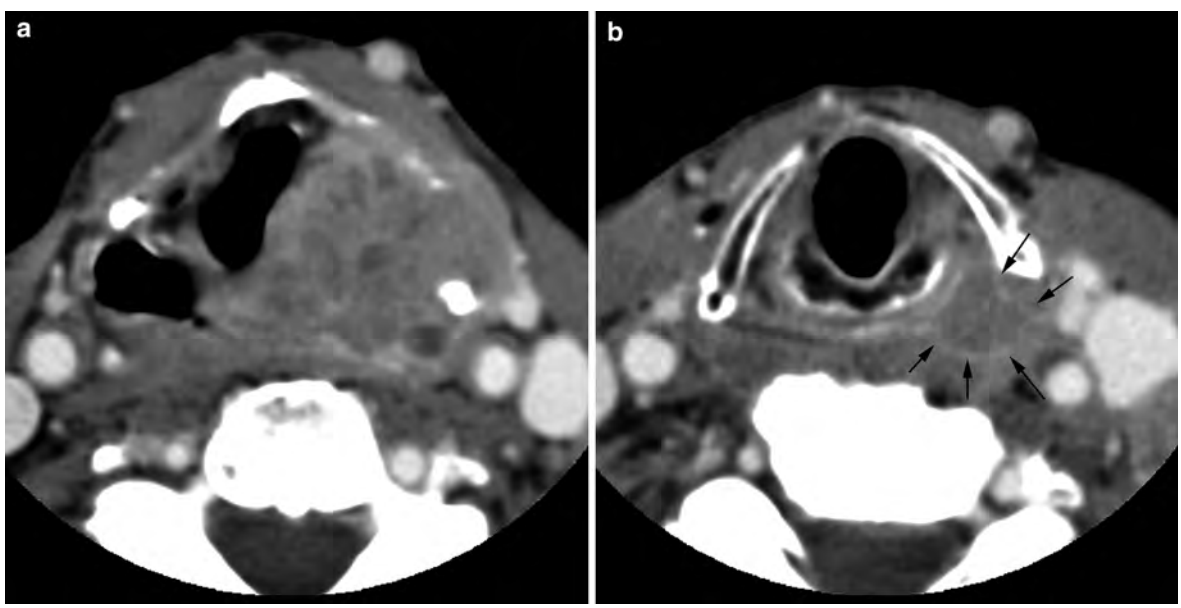

Fig. 21 Axial contrast-enhanced CT images through the upper thyroid (**a**) and mid cricoid (**b**) cartilage levels show a huge pyriform sinus cancer on the left with bulky disease at the pyriform sinus apex (*arrows* in **b**). Because of the size and the bulky apical disease this patient has extremely poor chance to be cured with radiation therapy alone, and therefore surgical resection should be the preferred treatment choice

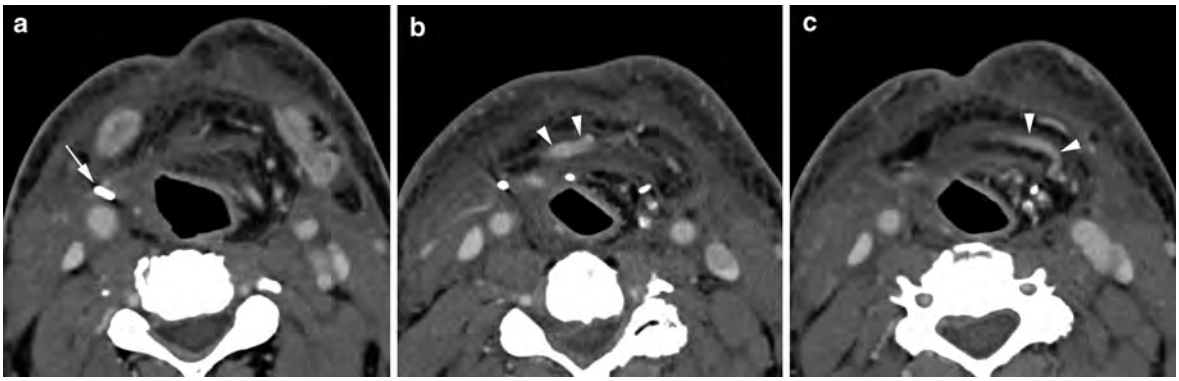

Fig. 22 Sequential axial contrast-enhanced CT images through the mid-neck in a patient after total laryngectomy and total pharyngectomy, demonstrates a radial forearm flap forming a neopharynx. The surgical clip at the external carotid artery vascular anastomosis (*arrow* in **a**) of the large vessel (*arrowheads* in **b** and **c**) that comes with the free flap suggests the nature of the reconstructive surgery

FDG PET–CT is another imaging tool to be considered; it is in particular useful in patients' status post reconstructive surgery and in patients with initially advanced tumor stage.

5.3.1 Post Surgery

Knowledge of the type of surgery and familiarity of expected postsurgical changes of the different types of reconstructive techniques is critical in the assessment of radiological post-treatment studies. A jejunal free flap with microvascular anastomosis is the most commonly used reconstructive method for patients who require total pharyngectomy and show only limited invasion of the cervical esophagus. Since the jejunum is already a tube only two anastomotic sutures are required during surgery. This decreases the risk of post-operative stricture and fistula formation (Reece et al. 1995). In addition, it tolerates post-surgical radiation therapy better than gastric or colonic interposition (Uppaluri and Sunwoo 2005). However, if the jejunal conduit is chosen too long, a kink in the "neopharynx" may develop causing dysphagia and stasis symptoms. Gastric pull-up is the reconstruction method of choice in patients with longer esophageal involvement. It has a low frequency of fistula formation, but the patients often complain of dumping and reflux symptoms. On cross-sectional studies, the jejunal interposition has a thin and regular wall while the gastric interposition shows polypoid folds of redundant mucosa. Both conduits should be surrounded by a "clean" fat plane. Colonic interposition is currently the least favorable method of hypopharyngeal reconstruction as it is associated with the highest rate of morbidity and mortality with 70 and 20%, respectively (Surkin et al. 1984). Therefore, it is only rarely performed at present.

Pectoralis major myocutaneous and radial forearm flaps may be used for subtotal hypopharyngeal defects in which a posterior stripe of mucosa remains intact (Uppaluri and Sunwoo 2005). The lack of pliability and the bulky nature of the pectoralis flap make circumferential tubing difficult, especially in obese or muscular patients (Schuller 1980). In contrast, the radial forearm flap offers thin, flexible tissue that is easy to form. It also has the tendency to remodel over time allowing better swallowing function than with other reconstructive surgeries including jejunal interposition (Anthony et al. 1994). The radial forearm flap is a well-vascularized free flap with a large-caliber donor vessel and long vascular pedicle that is connected as end-to-end or end-to-side anastomoses to the external carotid artery or its branches, as also done with the jejunal conduit (Fig. 22) (Uppaluri and Sunwoo 2005). The vascular anastomosis might be seen on contrast-enhanced CT images. In contrast, the pectoralis major myocutaneous flap does not require a vascular anastomosis as the myocutanous flap does not represent a free flap but is formed by rotation of the pectoralis major muscle superiorly with subsequent transposition over the clavicle through a widely undermined subcutaneous tunnel. Typically, the pectoralis major muscle can therefore be followed to the upper chest on cross-sectional imaging (Fig. 23). If the type of reconstructive

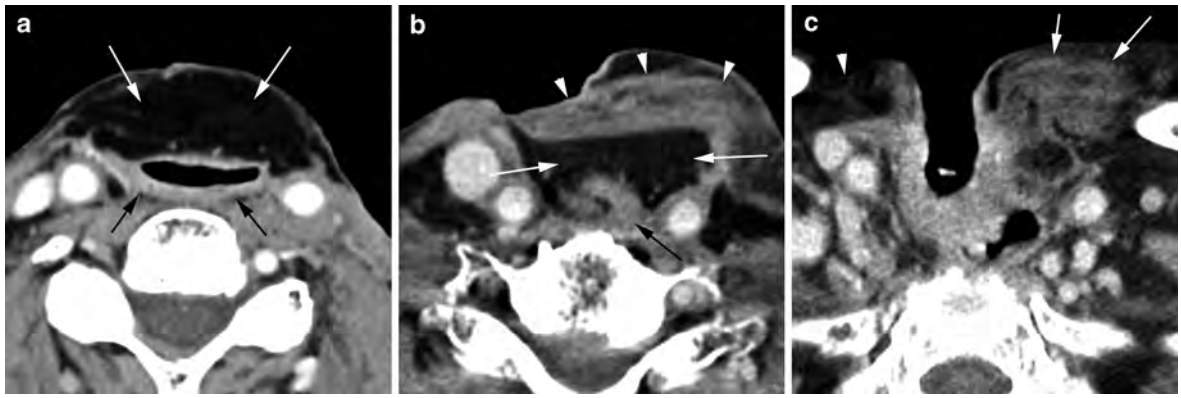

Fig. 23 Sequential axial contrast-enhanced CT images extending from the mid-neck to thoracic inlet demonstrate the expected changes following total laryngectomy and partial pharyngectomy with pectoralis major muscle reconstruction of the neopharynx. At the mid-neck level, only fatty tissue (*white arrows* in **a**) is seen anterior to the smoothly walled appearing neopharynx (*black arrows* in **a**). More inferiorly, the muscular component (*white arrowheads* in **b**) of the flap is appreciated anteriorly while the fatty tissue component (*white arrows* in **b**) is seen posteriorly, immediately anterior to the neopharynx (*black arrow* in **b**). At the thoracic inlet level, a muscular connection is seen anteromedial to the clavicle (*white arrows* in **c**) where normally only fatty tissue is observed (*arrowhead* in **c**)

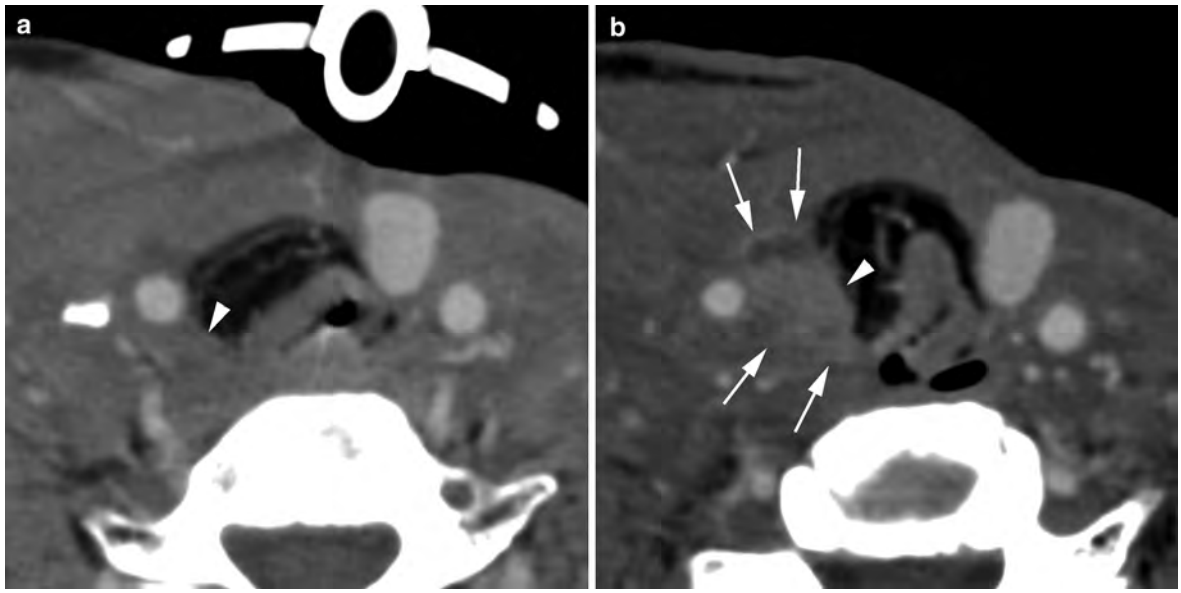

Fig. 24 Axial contrast-enhanced CT images of a patient status post total laryngectomy and partial pharyngectomy with pectoralis major flap reformation; imaging was performed immediately post surgery (**a**) and 3 months later (**b**); a large recurrent tumor along the lateral margin of the surgical bed (*arrows* in **b**) is seen 3 months after surgery. Note the changes in the contour of the fatty component of the pectoralis major flap with convex appearance (*arrowhead* in **b**) on the follow-up study and concave appearance on the immediate post surgical examination (*arrowhead* in **a**). Sometimes this contour change may be the only hint for recurrent disease

surgery is not known, this muscular connection might provide a helpful hint.

After surgery, recurrent tumors typically occur at the margins of the resection or within the deep tissues of the neck (Fig. 24). On cross-sectional images, the appearance of the mucosa is not very helpful in evaluating recurrent tumor because single or multiple irregular-appearing folds are typically seen with

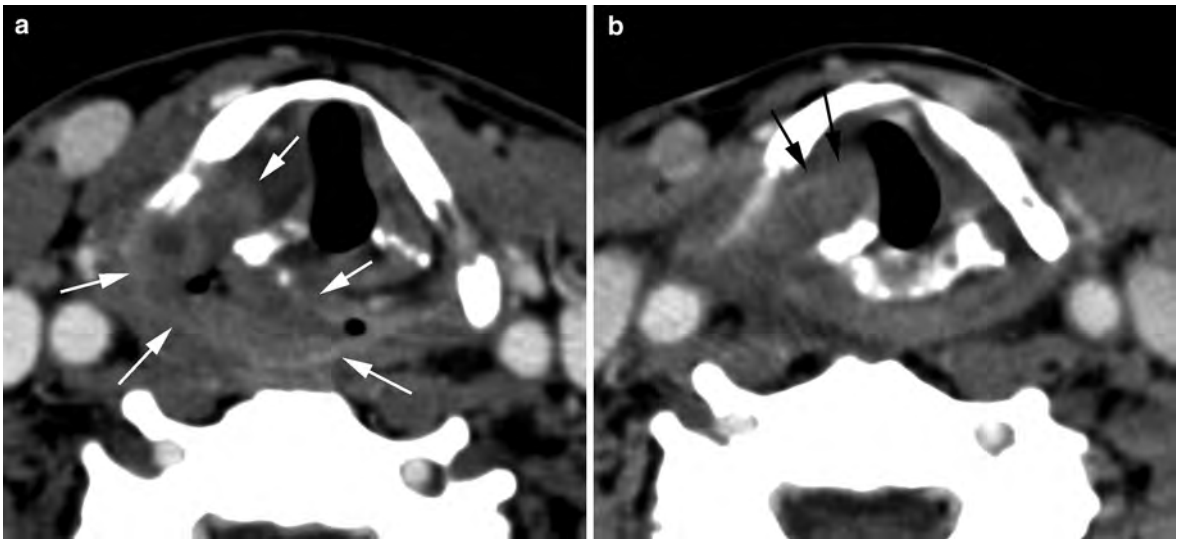

Fig. 25 Axial contrast-enhanced CT images pre (**a**) and post (**b**) radiation therapy for a large pyriform sinus cancer on the *right* (*arrows* in **a**) show marked decrease of the tumor at the pyriform sinus level with persistent mass in the right true vocal cord (*arrows* in **b**) that is over 1 cm in largest diameter. Such an appearance is strongly suspicious for persistent disease and the patient should undergo biopsy and/or PET–CT examination

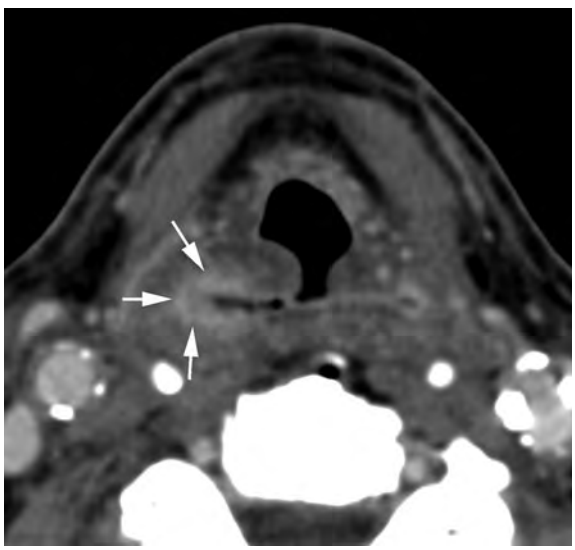

Fig. 26 Axial contrast-enhanced CT image performed 3 months following completion of radiation therapy shows asymmetric thickening of the mucosa in the upper pyriform sinus on the right (*arrows*) when compared to the left that is <1 cm in thickness. Since the pyriform sinus tumor did not completely resolve, a 3- to 4-months follow-up CT study is warranted to exclude persistent tumor; this appearance can also be caused by asymmetric radiation therapy-induced mucositis or non-viable tumor. Biopsy is only recommended if there is also clinical suspicion for persistent tumor

gastric pull-up and less commonly with jejunal interposition. The evaluation of cross-sectional imaging studies should therefore focus on regular thickness and attenuation of the muscular wall and on smooth outer border of the neopharyngeal wall (Becker 1998). Close evaluation of the fat planes surrounding the neopharynx is in particular essential as recurrent tumor might become only visible by subtle obliteration of fat planes. If however, the surgical reconstruction resulted in distortion or partial obliteration of fat planes or if baseline postsurgical imaging studies are not available for comparison, early detectibility of recurrent tumors becomes challenging. In such cases, an FDG PET–CT examination may be very helpful (see also "Positron Emission Tomography in Head and Neck Cancer").

5.3.2 Post Radiation Therapy

The post radiation therapy changes can be divided into general, localized to the primary site and related to the laryngeal cartilages. The general post radiation therapy changes within the neck have been described in detail by Mukherji et al. (1994a) (Fig. 19c and d).

In contrast, the work of Hermans et al. (2000) focuses on changes at the primary tumor-specific site as seen on the 3- to 4-months follow-up CT

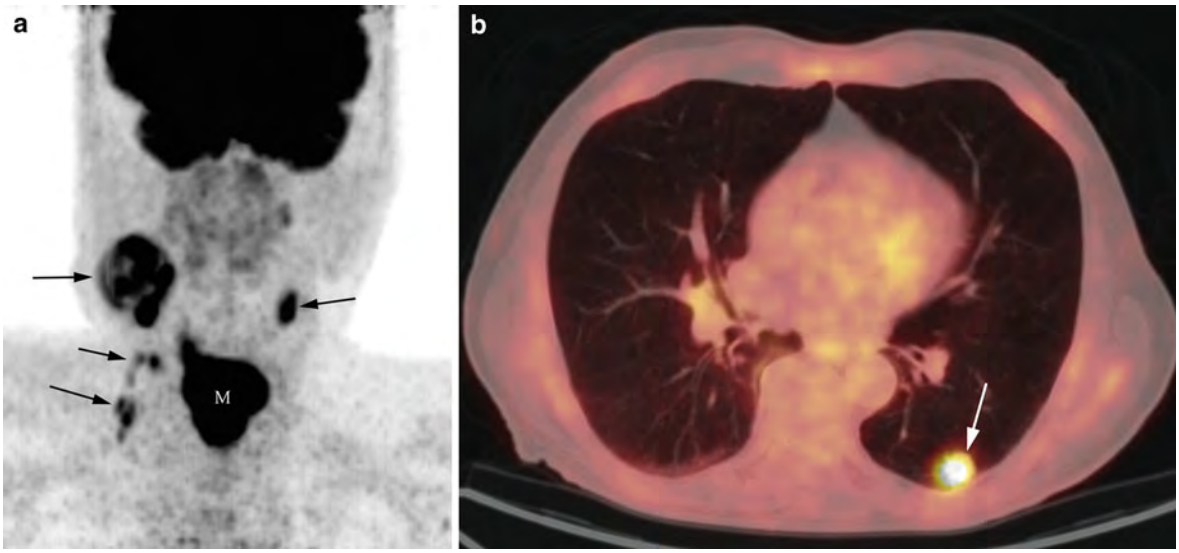

Fig. 27 Coronal PET image (**a**) of the neck demonstrates a large hypopharyngeal mass (*M* in **a**) with bilateral metastatic lymph nodes (*arrows* in **a**). The axial fused PET–CT image (**b**) reveals a second mass (*arrow* in **b**) in the posterior left lung that was biopsy proven to be lung cancer—a common combination in patients with hypopharyngeal cancer

examinations. Based on the response of the tumor and the clinical outcome three groups of patients were stratified:

1. Patients with complete resolution of the tumor and symmetric-appearing soft tissue planes on the CT examination at 3 to 4 months following completion of radiation therapy showed an excellent clinical outcome as none of the patients presented with local recurrence over at least a 2-year follow-up period (Fig. 19c and d). Therefore, this patient group requires clinical follow-up and cross-sectional imaging only if suspicion for recurrent tumor is raised on the clinical examination.
2. Patients with tumor volume reduction of <50% or a persistent mass of ≥1 cm in diameter have a high likelihood of local failure (Fig. 25). Therefore, in these patients further investigation with FDG PET–CT examination or biopsy is warranted (Hermans et al. 2000; Mukherji et al. 1994b).
3. Patients with a residual mass of <1 cm in diameter and/or asymmetry of the soft tissue planes have an intermediate prognosis and, therefore, cross-sectional follow-up at 3- to 4-months' intervals should be performed if there is no clinical suspicion for recurrent tumor (Fig. 26). Two consecutive stable studies after the baseline study are consistent with control at the primary site. An FDG PET–CT examination might be also beneficial in these patients, however, it might be false negative if the lesion is too small.

Hermans et al. (2000) also described post radiation alterations of the cartilages and its significance for recurrent disease in the same study. Based on their results, cartilage alteration associated with a persistent mass of ≥1 cm in diameter should be considered as local failure and appropriate salvage surgery needs to be considered. Cartilage alteration associated with minimal soft tissue asymmetry requires close follow-up as it can be related to recurrent tumor or chondroradionecrosis.

Distinction of recurrent tumor from chondroradionecrosis may pose a diagnostic challenge as the clinical symptoms of both entities are similar, endoscopy with biopsy yields a correct diagnosis only in 43% of patients and CT and/or conventional MRI techniques are hampered by expected post chemo- and/or radiotherapy tissue alterations (Zbären et al. 2008). Although the imaging findings of chondroradionecrosis (anterior dislodgement of the arytenoids cartilage, cartilage fragmentation and collapse, gas bubbles around the involved cartilage) are well established, these represent rather late changes of the disease process (Hermans et al. 1998). The issue is even more complicated as early on just soft tissue

fullness might be present mimicking recurrent tumor, and as chondroradionecrosis might co-exist with recurrent tumor. In such cases, the utilization of FDG PET–CT imaging is only helpful if no abnormal FDG uptake is found. In such a scenario no recurrent tumor was found by Terhaard et al. (2001) with a high negative predictive value of 89%. In contrast, a positive FDG PET–CT examination is inconclusive as inflammatory changes associated with chondroradionecrosis may show similar FDG uptake as recurrent tumor. In such cases, diffusion weighted imaging might be beneficial as the signal intensity of inflammatory tissue is reduced on high *b*-value images in contrast to increased signal intensity seen with recurrent tumor (Vandecaveye et al. 2006; Zbären et al. 2008).

5.4 Detection of Second Primary Tumors

The radiologist is required to search for a second primary in patients with hypopharyngeal or cervical esophagus cancer as these patients have a higher incidence of a second primary (15%) than the remainder of head and neck malignancies (Million 1994). Interestingly, in only 25% of patients a second primary is found at the time of the diagnosis of the hypopharyngeal or cervical esophageal cancer (synchronous lesions) while the majority is discovered on follow-up studies (metachronous lesion) with a reported rate of occurrence of 4% per year (Chu et al. 2010). Therefore, search for a second primary has to be conducted on every study performed in patients with history of hypopharyngeal or cervical esophageal cancer. Lung and esophageal cancers are the most commonly detected second primary tumors outside of the head and neck area (Fig. 27).

References

American Joint Committee on Cancer (2010) AJCC cancer staging manual, 7th edn. Springer, New York

Anthony JP, Singer MF, Mathes SJ (1994) Pharyngoesophageal reconstruction using the tubed free radial forearm flap. Clin Plast Surg 21:137–147

Artico R, Bison E, Brotto M (2004) Monophasic synovial sarcoma of hypopharynx: care report and review of the literature. Acta Otorhinolaryngol Ital 24:33–36

Aspestrand F, Kolbenstvendt A, Boysen M (1990) Carcinoma of the hypopharynx: CT staging. J Comput Assist Tomogr 14:72–76

Becker M (1998) Larynx and hypopharynx. Radiol Clin North Am 36:891–920

Becker M, Zbären P, Laeng H, Stoupis C, Porcellini B, Vock P (1995) Neoplastic invasion of the laryngeal cartilage: comparison of MR imaging and CT with histopathologic correlation. Radiology 194:661–669

Becker M, Zbären P, Delavelle J, Kurst AM, Egger C, Rufenacht DA, Terrier F (1997) Neoplastic invasion of the laryngeal cartilage: reassessment of criteria for diagnosis at CT. Radiology 203:521–532

Becker M, Burkhardt K, Dulguerov P, Allal A (2008) Imaging of the larynx and hypopharynx. Eur J Radiol 66: 460–479

Bisdas S, Nguyen SA, Anand SK, Glavina G, Day T, Rumboldt Z (2009) Outcome prediction after surgery and chemoradiation of squamous cell carcinoma in the oral cavity, oropharynx, and hypopharynx: Use of baseline perfusion CT microcirculatory parameters vs. tumor volume. Int J Radiat Oncol Biol Phys 73:1313–1318

Bukachevsky RP, Pincus RL, Shechtman FG, Sarti E, Chodsh P (1992) Synovial sarcoma of the head and neck. Head Neck 14:44–48

Castelijns JA, Gerritsen GJ, Kaiser MC, Valk J, van Zanten TE, Golding RG, Meyer CJ, van Hattum LH, Sprenger M, Bezemer PD (1988) Invasion of laryngeal cartilage by cancer: comparison of CT and MR imaging. Radiology 167:199–206

Chu PY, Chang SY, Huang JL, Tai SK (2010) Different patterns of second primary malignancy in patients with squamous cell carcinoma of larynx and hypopharynx. Am J Otolaryngol 31:168–174

Damiani JM, Damiani KK, Hauck K, Hyams VJ (1981) Mucoepidermoid-adenosquamous carcinoma of the larynx and hypopharynx: a report of 21 cases and a review of the literature. Otolaryngol Head Neck Surg 89:235–243

De Campora E, Croce A, Biocciolo G, Radici M (1987) Adenoid-cystic carcinoma (cylindroma) of the pyriform sinus in pediatric age. Int J Pediatr Otorhinolaryngol 14:235–242

Espinosa LA, Daniel BL, Jeffrey SS, Nowels KW, Ikeda DM (2005) MRI features of mucosa-associated lymphoid tissue lymphoma in the breast. AJR Am J Roentgenol 185: 199–202

Fatterpekar GM, Mukherji SK, Rajgopalan P, Lin Y, Castillo M (2004) Normal age-related signal changes in the laryngeal cartilages. Neuroradiology 46:678–681

Glazer GM, Gross BH, Quint LE, Francis IR, Bookstein FL, Orringer MB (1985) Normal mediastinal lymph nodes: number and size according to American thoracic society mapping. AJR Am J Roentgenol 144:261–265

Hermans R, Pameijer FA, Mancuso AA, Parsons JT, Mendenhall WM (1998) CT findings in chondroradionecrosis of larynx. AJNR Am J Neuroradiol 19:711–718

Hermans R, Pameijer FA, Mancuso AA, Parson JT, Mendenhall WM (2000) Laryngeal and hypopharyngeal squamous cell carcinoma: can follow-up CT after definitive radiation therapy be used to detect local failure earlier than clinical examination alone? Radiology 214:683–687

Hirsch RJ, Yousem DM, Loevner LA, Montone KT, Chalian AA, Hayden RE, Weinstein GS (1997) Synovial sarcomas of the head and neck: MR findings. AJR Am J Roentgenol 169:1185–1188

Kitamoto Y, Hasegawa M, Ishikawa H, Saito J, Yamakawa M, Kojima M, Nakano T (2003) Mucosa-associated lymphoid tissue lymphoma of the esophagus: a case report. J Clin Gastroenterol 36:414–416

Kraus DH, Pfister DG, Harrison LB, Shah JP, Spiro RH, Armstrong JG, Fass DE, Zelefsky M, Schantz SP, Weiss MH (1994) Larynx preservation with combined chemotherapy and radiation therapy in advanced hypopharyngeal cancer. Otolaryngol Head Neck Surg 111:31–37

Kraus DH, Zelefsky MJ, Brock HA, Huo J, Harrison LB, Shah JP (1997) Combined surgery and radiation therapy for squamous cell carcinoma of the hypopharynx. Otolaryngol Head Neck Surg 116:637–641

Mamelle G, Richard J, Luboinski B, Schwaab F, Eschwege F, Micheau C (1986) Synovial sarcoma of the head and neck: an account of four cases and review of the literature. Eur J Surg Oncol 12:347–349

Matsuki A, Nishimaki T, Suzuki T, Kanda T, Hatakeyama K (1999) Esophageal mucoepidermoid carcinoma containing signet-ring cellos: three case reports and a literature review. J Surg Oncol 71:54–57

Million RR (1994) Pharyngeal walls, pyriform sinus, postcricoid pharynx. In: Million RR (ed) Management of head and neck cancer. JB Lippincott, Philadelphia, pp 502–532

Miyazaki T, Kato H, Masuda N, Nakajima M, Manda R, Fukuchi M, Tsukada K, Kojima M, Nakajima T, Kuwano H (2004) Mucosa-associated lymphoid tissue lymphoma of the esophagus: case report and review of the literature. Hepatogastroenterology 51:750–753

Mouret P (1999) Liposarcoma of the hypopharynx. A case report and review of the literature. Rev Laryngol Otol Rhinol 120:39–42

Mukherji SK, Mancuso AA, Kotzur IM, Mendenhall WM, Kubilis PS, Tart RP, Lee WR, Freeman D (1994a) Radiologic appearance of the irradiated larynx. Part I. Expected changes. Radiology 183:141–148

Mukherji SK, Mancuso AA, Kotzur IM, Mendenhall WM, Kubilis PS, Tart RP, Freeman D, Lee WR (1994b) Radiologic appearance of the irradiated larynx. Part II. Primary site response. Radiology 183:149–154

Munoz A, Ramos A, Ferrando J et al (1993) Laryngeal carcinoma: sclerotic appearance of the cricoid and arytenoids cartilage—CT-pathological correlation. Radiology 189:433–437

Ng SH, Chan SC, Liao CT, Chang JT, Ko SF, Wang HM, Chin SC, Lin CY, Huang SF, Yen TC (2008) Distant metastases and synchronous second primary tumors in patients with newly diagnosed oropharyngeal and hypopharyngeal carcinomas: evaluation of (18)F-FDG PET and extended-field multi-detector row CT. Neuroradiology 50:969–979

Nowak B, Di Martino E, Janicke S, Cremerius U, Adam G, Zimny M, Reinartz P, Bull U (1999) Diagnostic evaluation of malignant head and neck cancer by F-18-FDG PET compared to CT/MRI. Nuklearmedizin 38:312–318

Pameijer FA, Mancuso AA, Mendenhall WM, Parson JT, Mukherji SK, Hermans R, Kubilis PS (1998) Evaluation of pretreatment computed tomography as a predictor of local control in T1/T2 pyriform sinus carcinoma treated with definitive radiotherapy. Head Neck 20:159–168

Prehn RB, Pasic TR, Harari PM, Brown WD, Ford CN (1998) Influence of computed tomography on pretherapeutic tumor staging in head and neck cancer patients. Otolaryngol Head Neck Surg 119:628–633

Quint L, Glazer G, Orringer M (1985) Esophageal imaging by MR and CT: study of normal anatomy and neoplasms. Radiology 156:727–731

Rangheard AS, Vanel D, Viala J, Schwaab G, Casiraghi O, Sigal R (2001) Synovial sarcomas of the head and neck: CT and MR imaging findings of eight patients. AJNR Am J Neuroradiol 22:851–857

Reece GP, Schusterman MA, Miller MJ, Kroll SS, Robb GL, Baldwin BJ, Luethcke DR (1995) Morbidity and functional outcome of free jejunal transfer reconstruction for circumferential defects of the pharynx and cervical esophagus. Plast Reconstr Surg 96:1307–1316

Ribeiro KB, Levi JE, Pawlita M, Koifman S, Matos E, Eluf-Neto J, Wunsch-Filho V, Curado MP, Shangina O, Zaridze D, Szeszenia-Dabrowska N, Lissowska J, Daudt A, Menezes A, Bencko V, Mates D, Fernadez L, Fabianova E, Gheit T, Tommasino M, Boffetta P, Brennan P, Waterboer T (2011) Low human papillomavirus prevalence in head and neck cancer: results from two large case-control studies in high-incidence regions. Int J Epidemiol 40(2):489–502

Righi PD, Kelley DJ, Ernst R, Deutsch MD, Gaskill-Shipley M, Wilson KM, Gluckman JL (1996) Evaluation of the prevertebral muscle invasion by squamous cell carcinoma. Can computed tomography replace open neck exploration? Arch Otolaryngol Head Neck Surg 122: 660–663

Roychowdhury S, Loevner LA, Yousem DM, Chalian A, Montone KT (2000) MR imaging for predicting neoplastic invasion of the cervical esophagus. AJNR Am J Neuroradiol 21:1681–1687

Saleh E, Mancuso AA, Stringer S (1993) Relative roles of computed tomography and endoscopy for determining the interior extent of pyriform sinus carcinoma: correlative histopathologic study. Head Neck 15:44–52

Schmalfuss IM, Mancuso AA, Tart R (2000) Postcricoid region and cervical esophagus: normal appearance at CT and MR imaging. Radiology 214:237–246

Schuller DE (1980) Limitations of the pectoralis major myocutatenous flap in head and neck cancer reconstruction. Arch Otolaryngol 106:709–714

Spector JG, Sessions DG, Haughey BH, Chao KS, Simpson J, El Mofty S, Perez CA (2001) Delayed regional metastases, distant metastases, and second primary malignancies in squamous cell carcinomas of the larynx and hypopharynx. Laryngoscope 111(6):1079–1087

Surkin MI, Lawson W, Biller HF (1984) Analysis of the methods of pharyngoesophageal reconstruction. Head Neck 6:953–970

Takahara Y, Kawashima H, Han YS, Sugimura N, Nakatani T, Tanaka K, Hino M (2005) Primary mucosa-associated lymphoid tissue (MALT) lymphoma of the urinary bladder. Hinyokika Kiyo 51:45–48

Terhaard CH, Bongers V, van Rijk PP, Hordijk GJ (2001) F-18-fluoro-deoxy-glucose-positron-emision tomography

scanning in detection of local recurrence after radiotherapy for laryngeal/pharyngeal cancer. Head Neck 23: 933–941

Thabet HM, Sessions DG, Gado MH, Gnepp DA, Harvey JE, Talaat M (1996) Comparison of clinical evaluation and computed tomographic diagnostic accuracy for tumors of the larynx and hypopharynx. Laryngoscope 106:589–594

Tom LW, Wurzel JM, Wetmore RF, Lowry LD (1981) Mucoepidermoid carcinoma of the hypopharynx. Otolaryngol Head Neck Surg 89:753–757

Uppaluri R, Sunwoo JB (2005) Neoplasms of the hypopharynx and cervical esophagus. In: Cummings CW (ed) Otolaryngology—Head and Neck Surgery. Elsevier Mosby, Philadelphia, pp 1859–1931

Vandecaveye V, De Keyzer F, Vander Poorten V et al (2006) Evaluation of the larynx for tumour recurrence by diffusion-weighted MRI after radiotherapy: initial experience in four cases. Br J Radiol 79:681–687

Weber RS, Marvel J, Smith P, Hankins P, Wolf O, Goepfert H (1993) Paratracheal lymph node dissection for carcinoma of the larynx, hypopharynx, and cervical esophagus. Otolaryngol Head Neck Surg 108:11–17

Wenig BL, Ziffra KL, Mafee MF, Schild JA (1995) MR imaging of squamous cell carcinoma of the larynx and hypopharynx. Otolaryngol Clin North Am 28:6009–6019

Yeager VL, Lawson C, Archer CR (1982) Ossification of laryngeal cartilages as it relates to computed tomography. Invest Radiol 17:11–19

Yousem DW, Tufano RP (2002) Laryngeal imaging. Magn Reson Imaging Clin N Am 10:451–465

Zbären P, Egger C (1997) Growth pattern of piriform sinus carcinomas. Laryngoscope 107:511–518

Zbären P, Begger M, Laeng H (1996) Pretherapeutic staging of laryngeal cancer: clinical findings, computed tomography and magnetic resonance imaging versus histopathology. Cancer 77:1263–1273

Zbären P, Weidner S, Thoeny HC (2008) Laryngeal and hypopharyngeal carcinomas after (chemo)radiotherapy: a diagnostic dilemma. Curr Opin Otolaryngol Head Neck Surg 16:147–153

Neoplasms of the Oral Cavity

Marc Keberle

Contents

Abstract

This chapter deals with benign and malignant neoplasms of the oral cavity. It starts with an overview of the relevant anatomy of the floor of the mouth, the tongue, the lips and gingivobuccal regions, the hard palate,and the region of the retromolar trigone. Moreover, the preferred imaging modalities are briefly discussed. The section "Pathology" contains all relevant benign lesions like congenital lesions (such as vascular malformation, dermoid cyst, and lingual thyroid), inflammatory conditions (such as phlegmon, abscess, and ranula), and benign neoplasms (such as pleomorphic adenoma, lipoma, rhabdomyoma, hemangioma, schwannoma, and others). More thoroughly, malignant neoplasms (such as squamous cell cancer, adenoid cystic cancer, mucoepidermoid carcinoma) and their predominant anatomic sites are presented with state-of-the-art illustrations. The chapter ends with a section on recurrent cancer.

1 Anatomy

Predominantly, oral cavity lesions are clinically apparent. Except for important information on the differential diagnosis, cross-sectional imaging provides the clinician with the crucial pretherapeutic information on deep tumor infiltration. In this regard, the clinician exactly needs to know which anatomic structures (Figs. 1, 2, 3, 4, 5 and 6) are involved (Ferner and Staubesand 1982).

The oral cavity is the most anterior part of the aerodigestive tract. Its borders are the lips ventrally,

M. Keberle (✉)
Radiology, Brüderkrankenhaus St. Josef,
Husener-Str. 46, 33098 Paderborn, Germany
e-mail: m.keberle@bk-paderborn.de

R. Hermans (ed.), *Head and Neck Cancer Imaging*, Medical Radiology. Diagnostic Imaging,
DOI: 10.1007/174_2011_375, © Springer-Verlag Berlin Heidelberg 2012

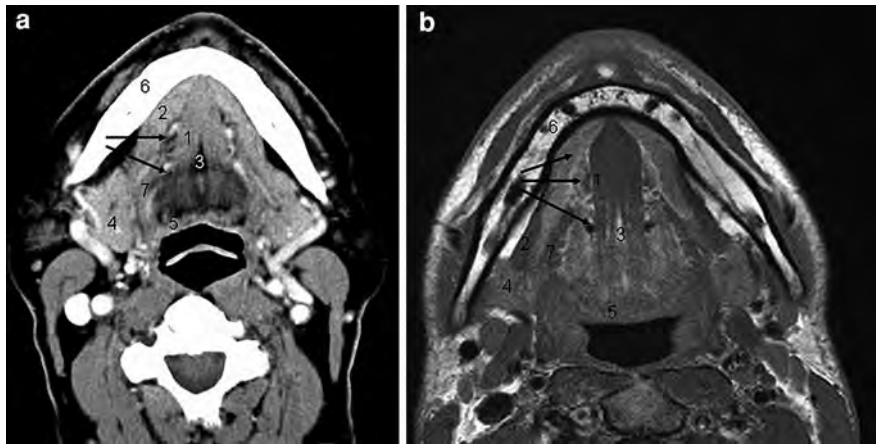

Fig. 1 Axial CT (**a**) and MRI (**b**) of the floor of the mouth. *1* geniohyoid muscle, *2* mylohyoid muscle, *3* fatty lingual septum, *4* submandibular gland, *5* base of the tongue, *6* mandible, *7* hyoglossus muscle, *arrows*: sublingual (fat) space with lingual artery and vein

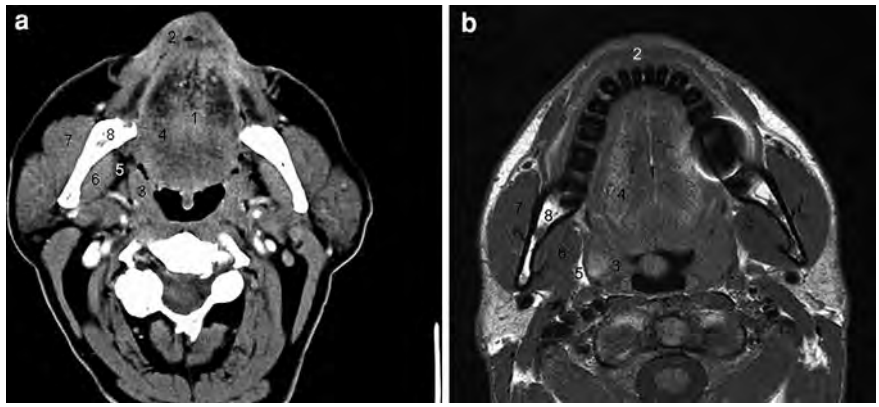

Fig. 2 Axial CT (**a**) and MRI (**b**) at the level of the tongue. *1* tongue with fatty lingual septum, *2* (lower) lip, *3* palatopharyngeal muscles and palatopharyngeal arch, *4* intrinsic lingual muscles fibers, *5* parapharyngeal fat space, *6* medial pterygoid muscle, *7* masseter muscle, *8* mandible

Fig. 3 Axial CT (**a**) and MRI (**b**) at the level of the maxilla. *1* maxilla, *2* mandible, *3* lateral pterygoid muscle, *4* soft palate, *5* tongue, *6* parapharyngeal fat space, *7* masseter muscle, *8* buccinator muscle, *9* area of the retromolar trigone (with bony pterygoid process on CT), *arrows*: (Stensen's) parotid duct

the mylohyoid muscle caudally, the gingivobuccal regions laterally, the circumvallate papillae and the anterior tonsillar pillar dorsally, and the hard palate cranially. The center of the oral cavity is filled out by the tongue.

1.1 The Floor of the Mouth

The floor of the mouth is considered the space between the mylohyoid muscle and the caudal mucosa of the oral cavity. The mylohyoid muscle has

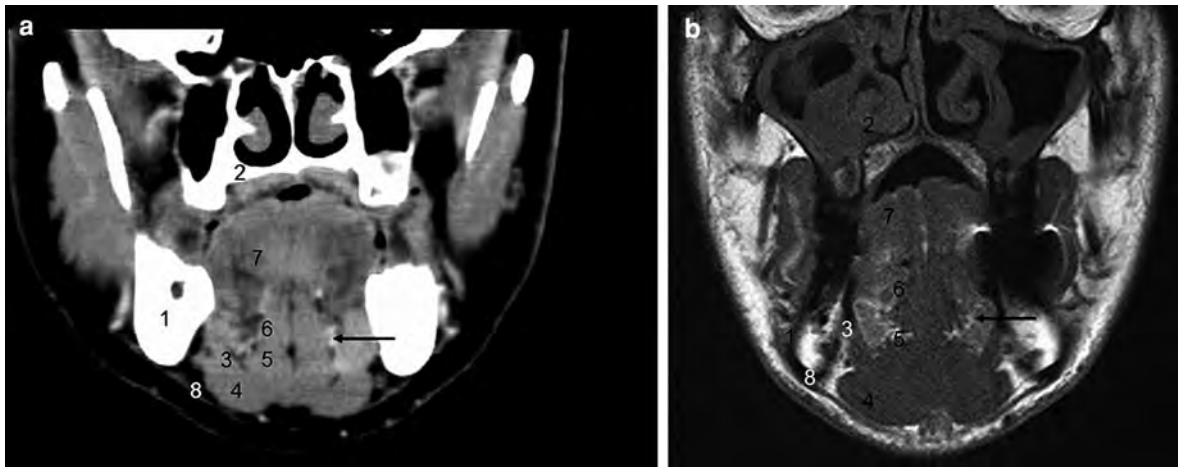

Fig. 4 Coronal CT (**a**) and MRI (**b**) at more anterior aspects of the oral cavity. *1* mandible, *2* (maxillary) hard palate with a tiny nerval canal, *3* mylohyoid muscle, *4* anterior belly of digastric muscle, *5* geniohyoid muscle, *6* genioglossus muscle, *7* intrinsic lingual muscles, *8* submandibular fat space, *arrows*: sublingual fat space with lingual artery and vein

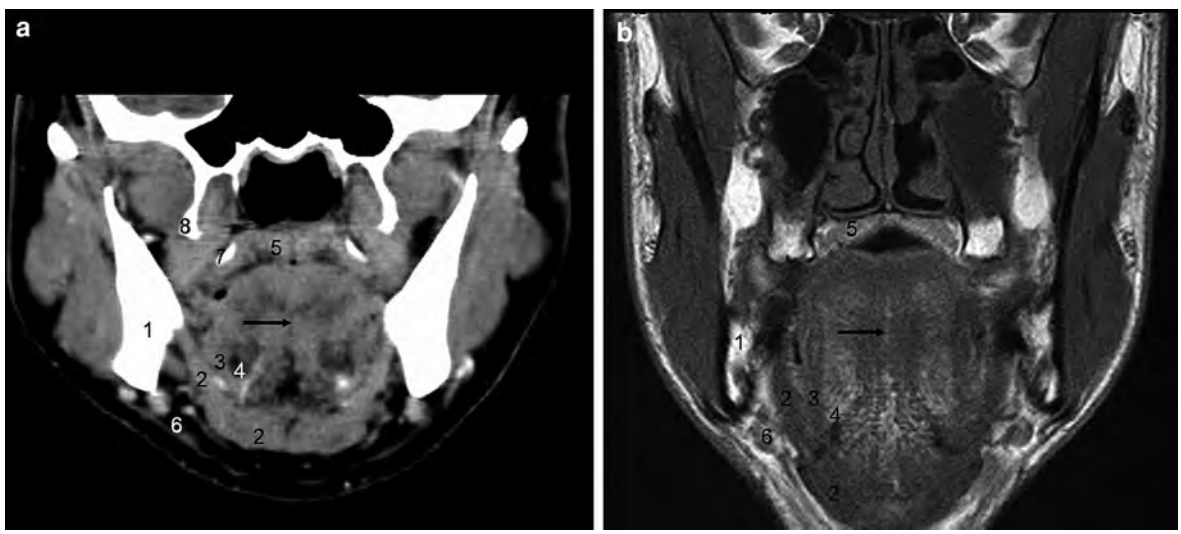

Fig. 5 Coronal CT (**a**) and MRI (**b**) at more posterior aspects of the oral cavity. *1* mandible, *2* mylohyoid muscle, *3* hyoglossus muscle, *4* sublingual fat space (with lingual artery and vein), *5* soft (on CT) and hard (on MRI) palate, *6* submandibular fat space, *7* medial pterygoid process, *8* lateral pterygoid process, *arrow*: fatty lingual septum

the form of a hammock which is attached to the mandible ventrally and laterally on both sides but with a free dorsal margin. Coronal planes nicely demonstrate the anatomy of the mylohyoid as well as the geniohyoid muscles (Figs. 4 and 5). The geniohyoid muscles are paired sagittally orientated slender muscles on the superior surface of the mylohyoid muscle. In the median, they arise from the inner surface of the mandible and pass dorsally to insert onto the anterior surface of the hyoid bone. Above these muscular landmarks is the primarily fat-filled bilateral sublingual space. It comprises the following important paired structures: the sublingual gland, the hyoglossus muscle, the lingual artery, vein, and nerve, Wharton's (submandibular) duct, and dorsally the tip of the submandibular gland as it surrounds the dorsal margin of the mylohyoid muscle. Anatomically noteworthy is that in the sagittal plane the hyoglossus

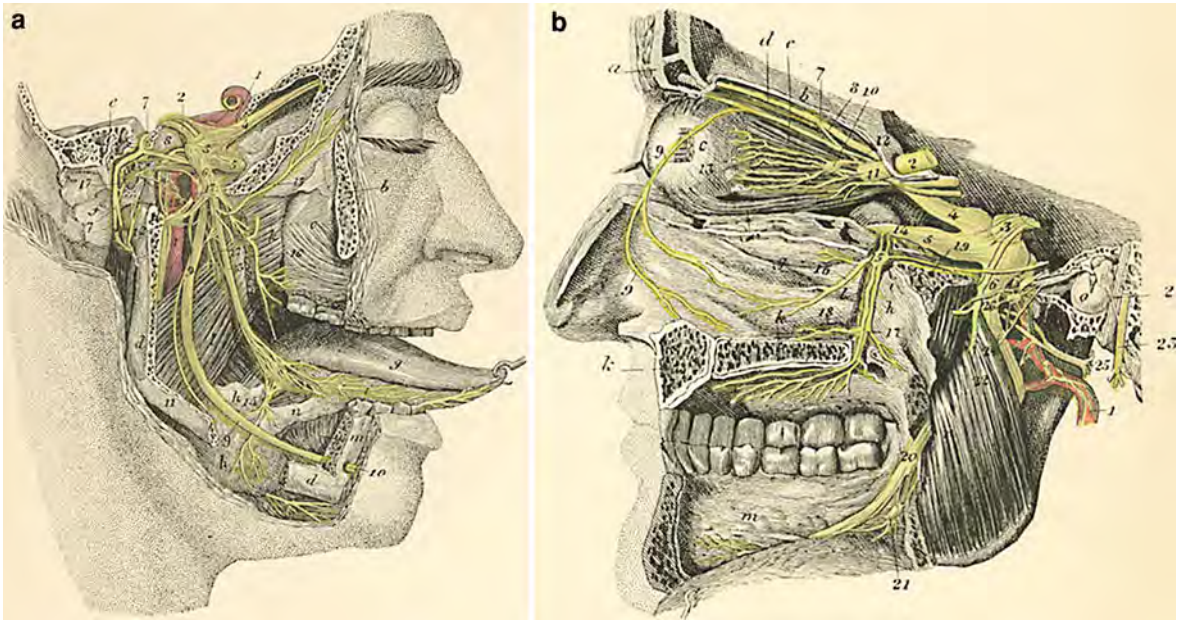

Fig. 6 Anatomic views of the trigeminal nerve (from Bergman and Afifi 2002, with permission) (**a**) *a* Greater wing of the sphenoid bone, *b* Zygomatic bone, *c* Maxilla, *d* Mandible, *e* Petrous part of temporal bone, *f* Mastoid process, *g* Tongue, *h* Submandibular gland, *i* Sublingual gland, *k* Medial pterygoid muscle, *l* Lateral pterygoid muscle, *m* Genioglossus muscle, *n* Hyoglossus muscle. *1* internal carotid artery, *2* trigeminal nerve, *3* trigeminal ganglion, *4* trigeminal nerve (V/1, ophthalmic division), *5* trigeminal nerve (V/2, maxillary division), *6* trigeminal nerve (V/3, mandibular division), *7* facial nerve, *8* great superficial petrosal nerve, *9* inferior alveolar nerve, *10* mental nerve, *11* mylohyoid nerve, *12* anterior auricular nerve (with middle meningeal artery), *13* lingual nerve, *14* submandibular ganglion, *15* deep temporal nerve, *16* buccinator nerve, *17* chorda tympani, *18* internal carotid plexus (sympathetic nerves) (**b**) *a* Frontal bone (frontal sinus), *b* Roof of the orbit (frontal bone), *c* Ocular bulb, *d* M. levator palpbrae superioris, *e* M. ocular superior rectus, *f* M. ocular inferior rectus, *g* Wall of the nasal cavity, *h* Pterygoid process, *i* Sphenopalatine foramen, *k* Hard palate, *l* Pterygopalatine canal, *m* Mandible, *n* Medial pterygoid muscle, *o* Tympanic membrane (with an auditory bone). *1* maxillary artery, *2* optic nerve, *3* trigeminal nerve with trigeminal ganglion, *4* trigeminal nerve (V/1, ophthalmic division), *5* trigeminal nerve (V/2, maxillary division), *6* trigeminal nerve (V/3, mandibular division), *7* frontal nerve, *8* nasal nerve, *9* ethmoidal nerve, *10* ciliary ganglion, *11* ciliary ganglion, short ciliary nerves, *12* ciliary ganglion, long ciliary nerves, *13* ciliary ganglion and ciliary nerves, *14* pterygopalatine nerves, *15* pterygopalatine ganglion, *16* posterior superior nasal nerves, *17* pterygopalatine nerve, *18* posterior inferior nasal nerves, *19* greater superficial petrosal nerve, *20* lingual nerve, *21* submandibular ganglion, *22* pterygoid nerve, *23* facial nerve in the facial canal, *24* chorda tympani, *25* anterior auricular nerve, *26* otic ganglion

muscle separates Wharton's duct and the hypoglossal and lingual nerves, which course laterally, from the lingual artery and vein, which lie medially (compare Figs. 1 and 5).

1.2 The Tongue

While the posterior third of the tongue—located dorsally of the circumvallate papillae—forms part of the oropharynx, the two anterior thirds of the tongue belong to the oral cavity. The tongue contains a complex mixture of various intrinsic and extrinsic muscles. Intrinsic muscles are made up by longitudinal, transverse, vertical, and oblique fibers which are not connected with any structure outside the tongue (Figs. 2, 4, and 5). The extrinsic muscles have their origin external to the tongue (Figs. 1 and 4): the genioglossus (chin), hyoglossus (hyoid bone), and styloglossus (styloid process) muscles. Both intrinsic and extrinsic muscles of the tongue receive their innervation from the (XII) hypoglossus nerve. Sensory fibers are carried by the lingual nerve, a branch of the (V3) mandibular nerve (Fig. 6). The tongue is sagitally divided in two halves by a fatty midline septum (Figs. 1, 2, 3, 4, and 5).

Table 1 List of oral cavity pathologies

Benign lesions
Congenital
Vascular malformations
Venous
Arterial
Lymphatic
Capillary
(Epi-)Dermoid cysts
Lingual thyroid
Thyroglossal duct cyst
Digastric muscle aplasia
Inflammatory
Cervical phlegmone (e.g. odontogenic)
Abscess (± sialolithiasis)
Sialadenitis (± sialolithiasis)
Ranula
Simple
Plunging (or diving)
Ludwig's angina
Neoplastic
Pleomorphic adenoma
Lipoma
Rhabdomyoma
Hemangioma
Lymphangioma
Schwannoma
Leiomyoma
Neurofibromatosis
Fibroma
Aggressive fibromatosis
Others
Osseous lesions (see "Malignant Lesions of the Masticator Space")
Pseudotumor
Hemiatrophy of the tongue (or of other muscles)
Malignant lesions
Squamous cell carcinoma (major sites in descending frequency)
Lips
Floor of the mouth
Retromolar trigone
Tongue
Adenoid cystic carcinoma
Mucoepidermoid carcinoma
Lymphoma
Non-Hodgkin's Lymphoma
Burkitt-Lymphoma
Sarcoma (Rhabdomyo-, Lipo-, Fibro-, Angio-, Leiomyo-)
Adenocarcinoma
Malignant schwannoma
Metastases
Melanoma
Osseous malignancies (see "Malignant Lesions of the Masticator Space")

1.3 The Lips and Gingivobuccal Regions

Externally, the lips are covered by keratinizing stratified squamous epithelium, and internally, by nonkeratinizing stratified squamous mucosa. The vestibule of the mouth separates lips and cheeks from the alveolar processes of the mandible and maxilla. The gingiva is the mucosa on both the lingual and the buccal aspects of the alveolar processes. The junction of the gingival with the buccal mucosa is called gingivobuccal region. At the level of the second maxillar molar tooth Stensens' (parotid) duct opens within the buccal mucosa (Fig. 3). Moreover, minor salivary glands are relatively frequent in the gingivobuccal regions. Dorsally, the vestibules open into the dorsal part of the oral cavity.

1.4 The Hard Palate and the Region of the Retromolar Trigone

While the soft palate is part of the oropharynx, the mucosal layer beneath the hard palate belongs to the oral cavity. There are several openings for palatine nerves piercing the hard palate (compare Figs. 4 and 6). The strategic region posterior to the last maxillary molar tooth is called the retromolar trigone (Fig. 3). The retromolar trigone has a connection to the buccinator space laterally, to the anterior tonsillar pillar (part of the oropharynx), the mandible, and to the pterygomandibular space dorsally (and via this way to the anterior parts of the parapharyngeal space and the skull base cranially), and to the palate medially.

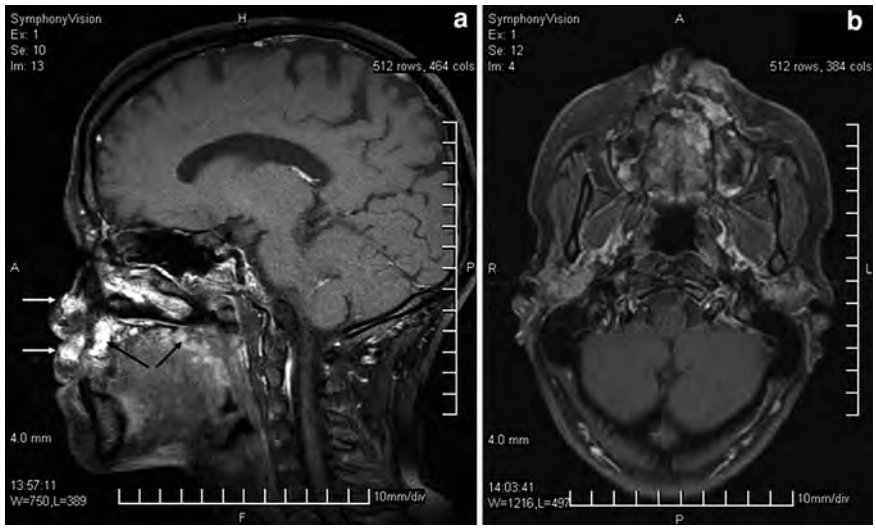

Fig. 7 MRI of a venous vascular malformation in a 25-year-old man. Fat-saturated sagittal (**a**) and axial (**b**) post-contrast T1-weighted images reveal a heterogenous rather strongly contrast-enhancing mass at the upper lip, hard and soft palate, maxilla, and the nose

1.5 Lymphatic Drainage

The lips predominantly drain to the submental and/or submandibular (level 1) lymph nodes. The major lymphatic drainage of the floor of the mouth is to the submental, submandibular, and/or internal jugular nodes (levels 1 and 2). The oral tongue drains mainly to the submandibular and internal jugular nodes (levels 1 and 2), often with bilateral involvement in case of a carcinoma of the tongue.

2 Preferred Imaging Modalities

In children, to avoid radiation exposure, ultrasound, and MRI are the methods of first choice. In contrast to more cranial parts of the oral cavity and of the oropharynx, the floor of the mouth, the base of the tongue, and the neck can be evaluated with ultrasound (compare Figs. 11 and 19). High frequency transducers should be used. For the evaluation of the most ventral part of the floor of the mouth the transducer has to be tilted accordingly. Contrast-enhanced MRI offers several diagnostic advantages over ultrasound; it allows covering of the entire oral cavity and has a higher diagnostic accuracy, especially regarding the exact evaluation of the extension and differential diagnosis of a lesion.

In adults, CT and MRI are the most frequently used imaging modalities. The administration of intravenous contrast agent is a rule. Only in rare circumstances, such as the detection of calculi, an initial (or sole) native CT may be necessary (or sufficient). The most frequent diagnostic problem of CT are dental filling artifacts, whereas the interpretation of MRI is most frequently limited by motion artifacts because of swallowing. As a result of these diagnostic drawbacks, one can recommend to use CT for lesions which are primarily located in the floor of the mouth and the base of the tongue because the latter structures can be scanned without disturbing artifacts from dental fillings. On the other hand, MRI can generally be recommended for lesions predominantly involving the tongue and the palate (Sigal et al. 1996). However, to specifically answer the question of bone involvement (hard palate, mandible) CT is generally regarded to be slightly superior over MRI so that sometimes both methods add up to the final diagnosis.

3 Pathology

3.1 Benign Lesions

3.1.1 Congenital Lesions

3.1.1.1 Vascular malformations

Although vascular malformations are predominantly present at birth, they can manifest with symptoms later on (Table 1). Generally, vascular malformations tend to involve muscle and bone (Figs. 7 and 8). They usually grow slowly, however, rapid growth can be linked with endocrine changes during life. In contrast

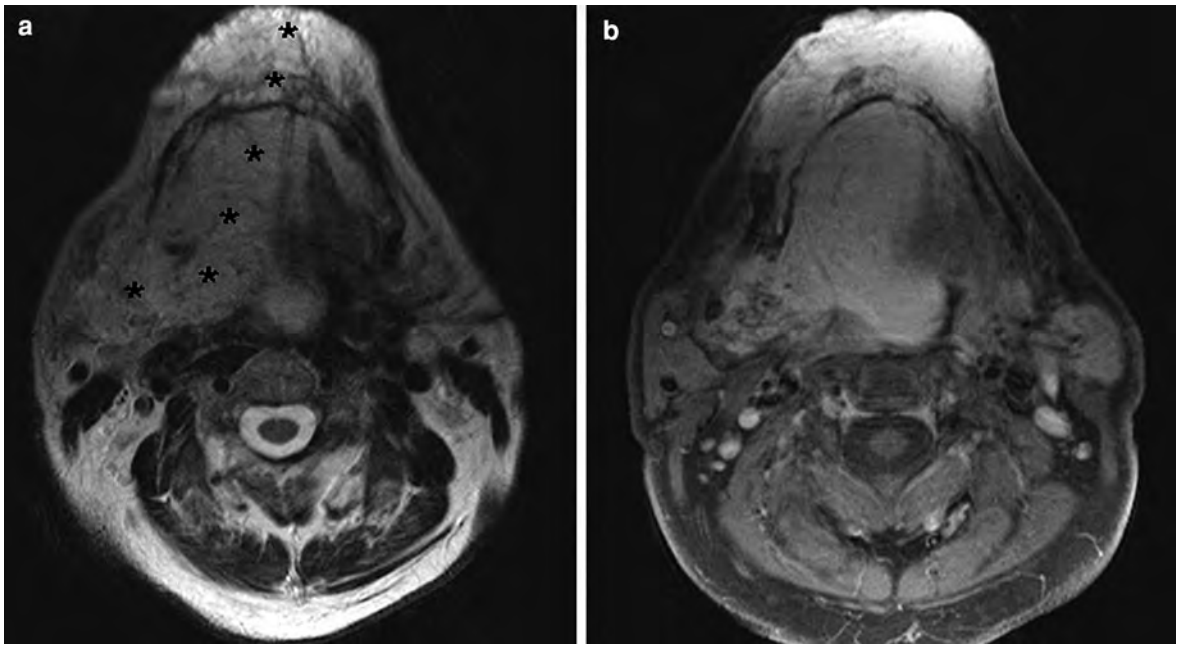

Fig. 8 MRI of a venous malformation with hardly any flow-voids in a 65-year-old male. The lesion shows diffuse extension through the mandible and the mylohyoid muscle into the lower lip and the submandibular region. Moreover, there is midline crossing and extension to the base of the tongue. On T2, the lesion is quite hyperintense (**a**) and on the post–contrast image there is a rather homogeneous strong contrast enhancement (**b**)

to hemangiomas, vascular malformations do not involute during childhood (Mulliken 1988, Figs. 7 and 8). Main therapeutic options are steroid injection, embolization, laser therapy, and/or surgical resection (if possible). Based on the predominant type of anomalous vessel involved, capillary (e.g. nevus flammeus in Sturge–Weber-Syndrome), venous, or arterial malformations are distinguished (Baker et al. 1993). In rare circumstances, they may appear as "lymphatic" malformations which can also be secondary after infection, tumor, or trauma, such as surgery (Kennedy 1989; Smoker 2003).

In the oral cavity, venous malformations are the most frequent vascular malformations (Figs. 7 and 8). In contrast to arterial malformations, these are slow-flow malformations. On CT, they are usually isodense to muscle (however phleboliths are characteristic) and demonstrate variable contrast enhancement. On MR they are isointense to muscle on T1-weighted images but quite hyperintense on T2; contrast enhancement is usually heterogenous, often with rather strongly enhancing components (Fig. 7). Arterial malformations are high-flow lesions with tortuous and enlarged vessels and usually show flow-voids (Baker et al. 1993). Some vascular malformations comprise both slow- and high-flow components. In lymphatic malformations, on the other hand, only septae and/or cyst walls enhance.

3.1.1.2 (Epi-)Dermoid cysts

When epithelial remnants become enclaved during early midline closure of the first and second branchial arches, (epi-)dermoid cysts can be the result (King et al. 1994). These lesions occur in or close to the midline (Figs. 9 and 10), both cranial and caudal to the mylohyoid muscle. Coronal or sagittal slices are useful to show their relation to the latter muscle because the surgical approaches differ (Vogl et al. 1993).

Fatty contents (either as fat drops or as a fat-fluid level) are pathognomonic for dermoid cysts (Fig. 10). However, without fatty contents a differentiation is not possible (Koeller et al. 1999). In case of an epidermoid cyst (Fig. 9), an entirely fluid-filled lesion is visible (CT: <20HU; MR: hypointense signal on T1 and hyperintense on T2). A slight rim enhancement around these cysts can sometimes be noted.

In contrast to epidermoid cysts, dermoid cysts have malignant potential (King et al. 1994).

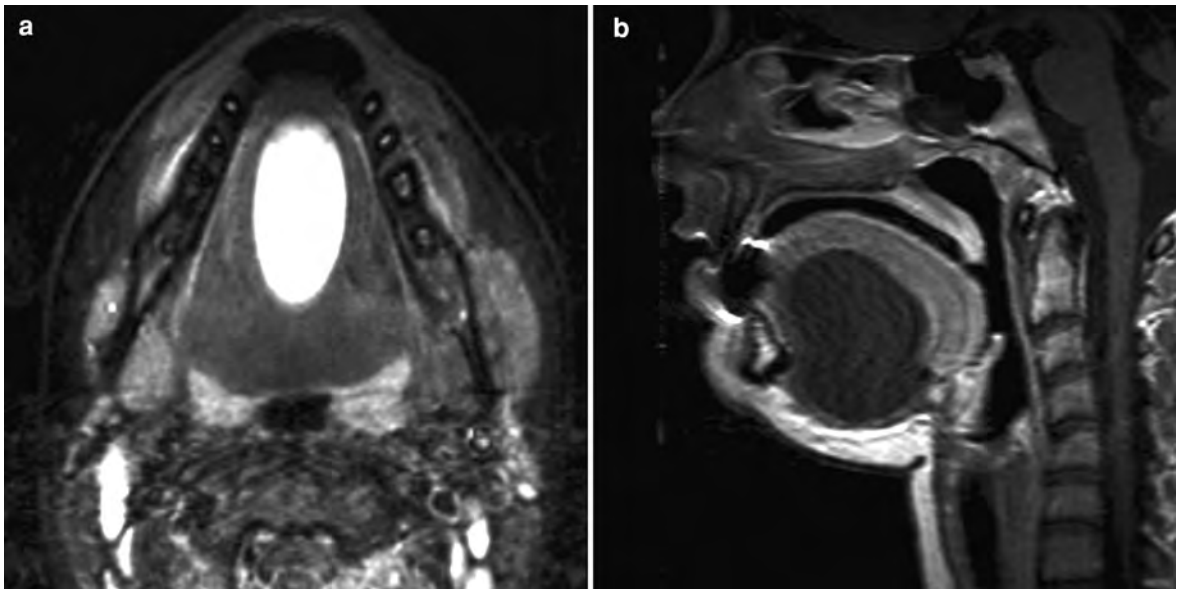

Fig. 9 MRI of an epidermoid of the floor of the mouth and the tongue in a 21-year-old female. The lesion is strictly located in the midline. On T2, it presents well delineated with a very bright homogeneous signal (**a**). On post-contrast T1, there is no enhancement—the sagittal image nicely shows the relation of the epidermoid to the more caudal mylohyoid muscle (**b**). (With courtesy of Nicole Freling, MD, Amsterdam, the Netherlands)

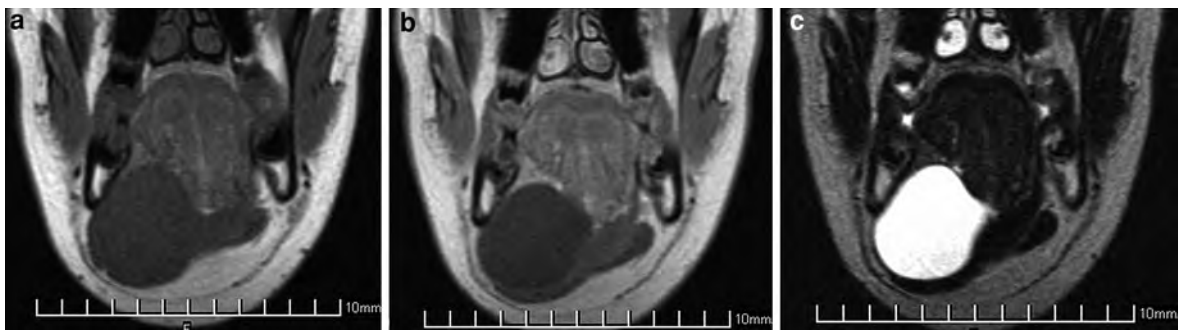

Fig. 10 MRI of a dermoid of the floor of the mouth in a 15-year-old male. Median and *right* paramedian lesion which is difficult to distinguish from the more caudal mylohyoid muscle on native T1 (**a**). After contrast administration, the dermoid does not enhance (**b**). On T2, there is slight heterogeneity within the cyst suggesting a dermoid rather than an epidermoid (**c**)

3.1.1.3 Lingual thyroid

If the thyroid gland does not descend from the foramen cecum, the midline dorsum of the tongue is the most common location for an ectopic thyroid gland (Fig. 11), whereas thyroglossal duct cysts predominantly occur at the level of the hyoid bone or below (Douglas and Baker 1994). Mostly, women are affected. Lingual thyroids are usually small and discovered incidentally. In larger symptomatic cases surgery is the first therapeutical option. However, in more than 50% of the patients no other functioning thyroid tissue is present, so that complete resection may be problematic.

Comparable to a thyroid gland in its normal location, a lingual thyroid is hyperdense on precontrast CT. On precontrast MRI, it may be only slightly hyperintense on both T1- and T2-weighted images. Thyroid tissue, generally, shows strong contrast enhancement (Johnson and Coleman 1989).

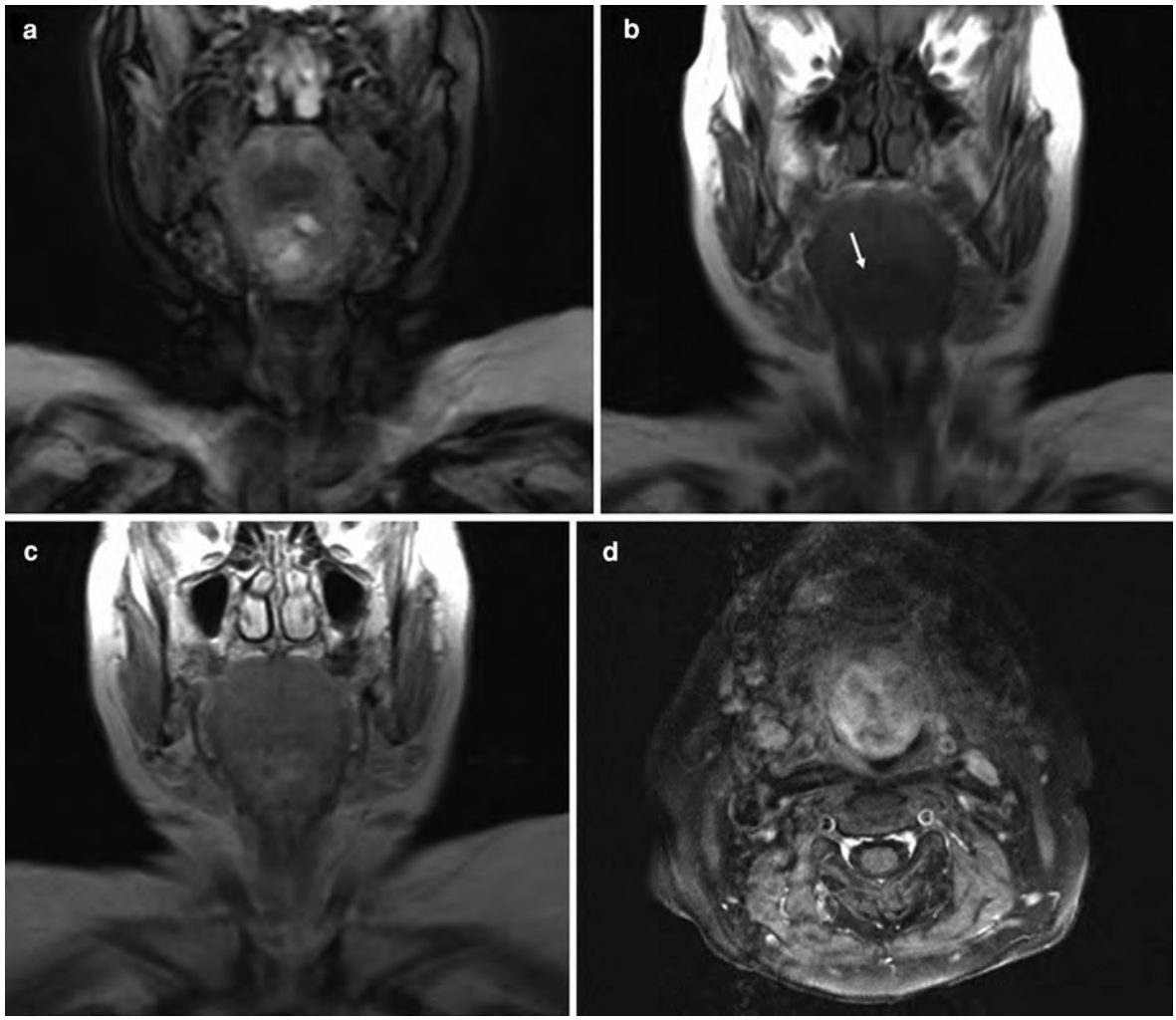

Fig. 11 MRI of a 65-year-old female with a large lingual thyroid affecting the tongue as well as the floor of the mouth. The T2-weighted image (**a**) reveals an inhomogeneous mass with some very hyperintense cysts. On the native T1-weighted image, the mass is slightly hypointense compared to the tongue (**b**). After contrast agent has been given, the respective coronal (**c**) and fat-saturated axial (**d**) images show irregular rather strong enhancement of the lesion. Histology after laser resection revealed a lingual thyroid with regressive cystic changes (goiter). The lesion has been present since childhood but enlarged after orthotopic strumectomy

3.1.2 Inflammatory Conditions

3.1.2.1 Cervical phlegmone and abscess (and sialolithiasis)

Dental infection or ductal obstruction of the salivary glands are the main causes of oral inflammations, both mainly involving the sublingual and/or submandibular spaces (Smoker 2003; Yousem et al. 2000). Phlegmones are diffuse inflammatory processes which in contrast to abscesses do not contain central necrotic components and/or air. Native CT and MRI show edematous changes, contrast enhancement is diffuse. If Wharton's duct is obstructed (e.g. in case of sialolithiasis) the respective submandibular gland as well as the duct can be enlarged (Fig. 12). Either native CT or a bone-window setting of a post-contrast CT best unveils hyperdense calculi which may be missed in a soft-tissue-window setting after contrast enhancement or with other modalities. A clinical important issue is the exclusion of osteomyelitis (Fig. 13). In mild cases, CT is known to be

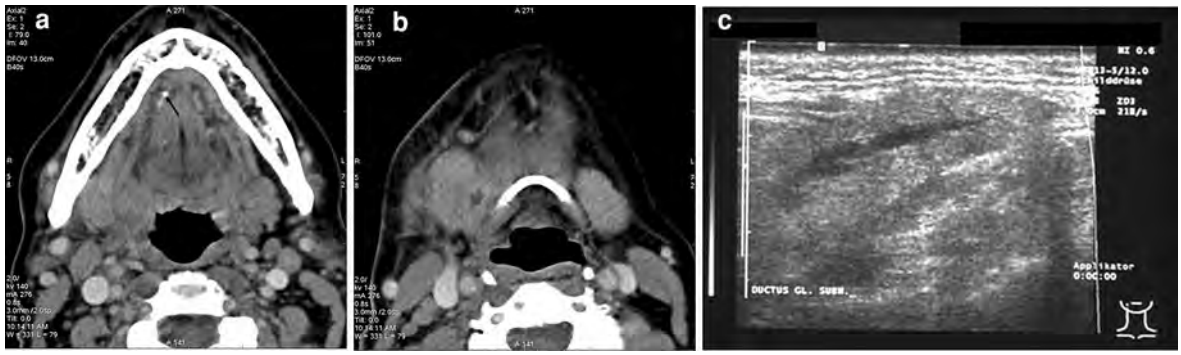

Fig. 12 CT of a submandibular abscess due to an obstruction of Wharton's (submandibular) duct by a stone (female, 57 years). In the anterior *right* floor of the mouth, a small stone can be seen at the level of the aperture of the duct (**a**). The *right* submandibular duct is swollen and contains an abscess *right* at its tip behind the mylohyoid muscle (**b**); the surrounding fat contains inflammatory edematous streaks. An ultrasound image of the enlarged submandibular gland showing the dilated duct (**c**)

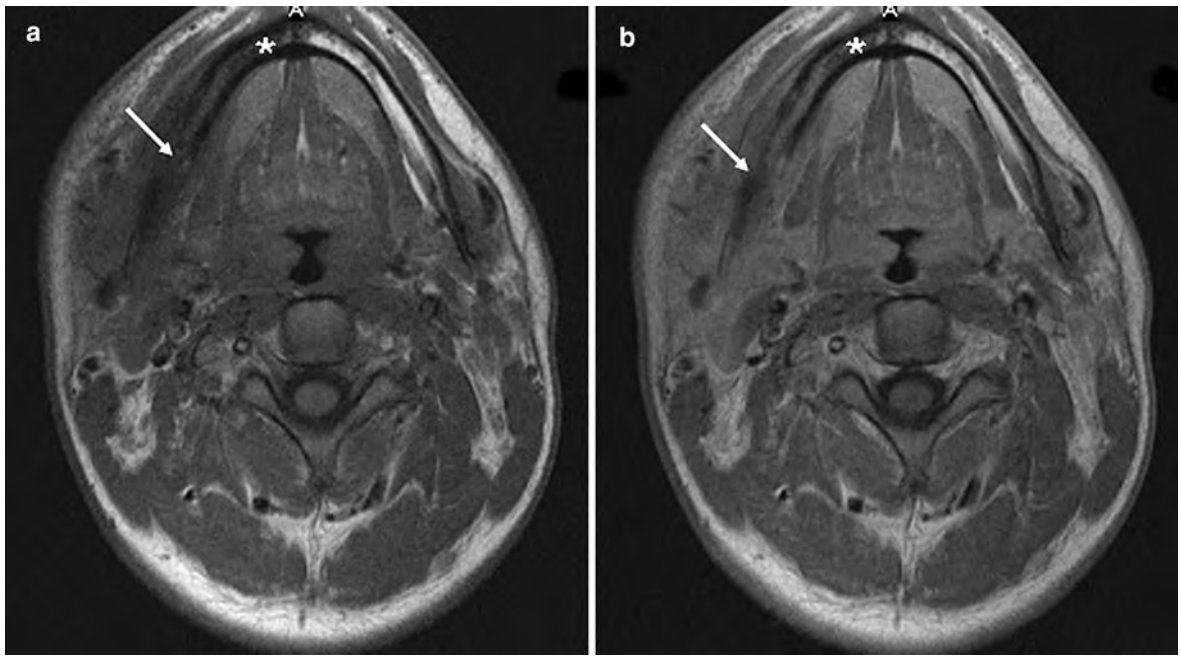

Fig. 13 Axial MRI of a 23-year-old man with multifocal osteomyelitis (Sapho-Syndrome). The pre-contrast (**a**) as well as the post-contrast (**b**) images show a diffuse (contrast enhancing) lesion within and on both sides of the mandible. The cortex is partly eroded (*arrow* on both images) and the bone marrow yields hypointense signal alterations due to inflammatory edema (*star* on both images)

superior in the evaluation of the mandibular cortex, whereas MRI appears better regarding medullar bone involvement.

3.1.2.2 Ranulas

In case of obstruction of the duct of the sublingual gland patients can present with a ranula, a true epithelium-lined "mucus retention cyst". They are located above the mylohyoid muscle, fill out the sublingual space and, thus, mostly have an oval configuration (Fig. 14). But they can also grow to an enormous size and then have a more roundish shape. In contrast to a "simple ranula", a ranula can present ruptured and extend dorsally (or caudally through

Fig. 14 CT of a 57-year-old male who noted a swelling at the *right* floor of the mouth. The typical simple ranula is hypodense (18HU), well delineated, and without contrast enhancement

gaps in the mylohoid muscle) into the submandibular space and then is called a diving or plunging ranula (Coit et al. 1987). The bulk of the latter typically lies—more posteriorly—medial to the submandibular gland with a typical anterior extension to the sublingual space (suggesting its sublingual origin).

On CT, ranulas present as hypodense, non-enhancing, thin-walled, solitary, paramedian lesions (Coit et al. 1987). Accordingly, on MR, ranulas have homogeneous high signal on T2 and low signal on T1. However, plunging ranulas, as these are pseudocysts, are to a various extent surrounded with granulation tissue so that a slight circular enhancement may be present on post-contrast images.

3.1.3 Benign Tumors

3.1.3.1 Pleomorphic adenoma

In adults, pleomorphic adenomas are the most common benign neoplasms of the oral cavity. On histology, pleomorphic adenomas contain epithelial as well as fibromyxoid tissue, and with increasing size, there are often cystic changes, central necrosis and/or calcfications (Som and Brandwein 2003). As pleomorphic adenomas can originate from the sublingual glands as well as from minor salivary glands, these tumors can be found throughout the oral cavity. Complete resection is recommended because pleomorphic adenomas tend to recur.

The varying mixture of epithelial and fibromyxoid tissues as well as possible degenerative changes of this tumor result in their "pleomorphic" heterogenous imaging appearance with a varying signal on T2 and varying contrast enhancement (especially concerning larger tumors—Okahara et al. 2003; Keberle et al. 2005). In contrast to malignant tumors, pleomorphic adenomas show a rather slow growth pattern and are well-circumscribed tumors (Fig. 15).

3.1.3.2 Lipoma

Other benign neoplasms are much rarer. Of all mesenchymal tumors, lipoma is the most common in the oral cavity (Smoker 2003). To some extent, lipomas can contain other tissues and present as fibro-, angio-, myxo-, or chondrolipomas. Lipomas occur virtually all over the oral cavity with the cheek as the most common location. Imaging features are pathognomonic with homogeneous low-density values of around 100HU on CT, no contrast enhancement, and high-signal intensity on T1-weighted MR-images. Lipomas are clearly defined tumors, sometimes separated by thin septae and do not infiltrate neighboring anatomic structures.

3.1.3.3 Rhabdomyoma

In contrast to rhabdomyosarcomas, rhabdomyomas are benign tumors. They originate from striated muscle and, within the oral cavity, they have a predilection for the floor of the mouth and the tongue (Smoker 2003). In adults, rhabdomyomas mostly affect middle-aged men. The second age group is early childhood (usually during the first two years of life). Like lipomas, they do not infiltrate and, thus, complete resection is rarely a problem.

On both native CT and T1-weighted MRI rhabdomyomas have the density/intensity of muscle; slight enhancement is seen on post-contrast images. They are usually only slightly hyperintense on T2-weighted MR-images.

3.1.3.4 Hemangiomas

Hemangiomas occur only in early childhood (Mulliken and Glowacki 1982), and in this age-group they are the most common benign tumors. They are true neoplasms mostly containing endothelial and

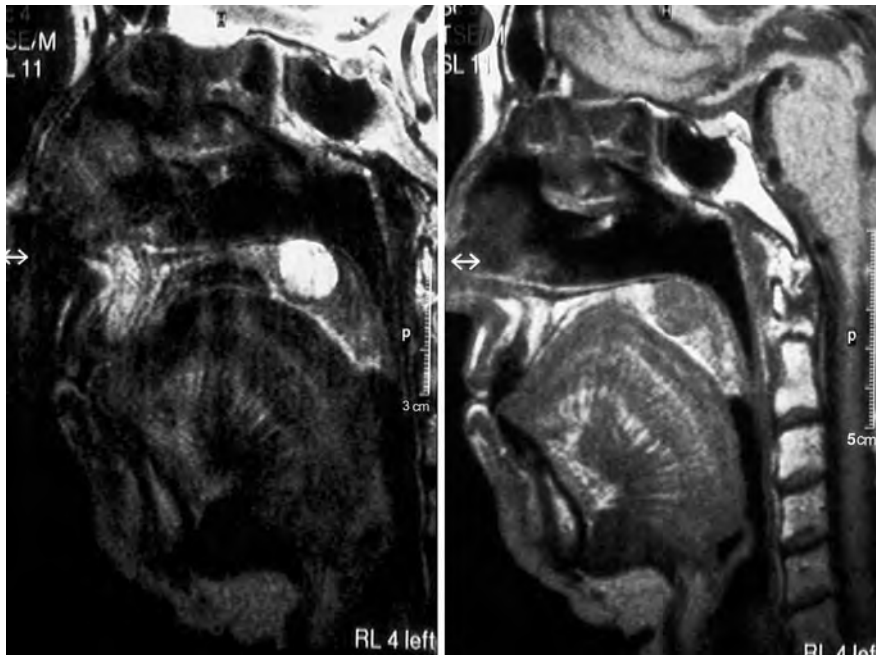

Fig. 15 Sagittal MR-images of a 34-year-old male showing a pleomorphic adenoma between hard and soft palate. On the T2-weighted image, the lesion is homogeneously hyperintense, round and well delineated (**a**). The post–contrast T1-weighted image shows only slight enhancement (**b**). (With courtesy of Nicole Freling, MD, Amsterdam, the Netherlands)

Table 2 Squamous cell carcinoma of the oral cavity: T-Staging (UICC 2009)

T1	Tumor ≤2 cm in greatest diameter
T2	Tumor >2 cm but <4 cm in greatest diameter
T3	Tumor ≥4 cm in greatest diameter
T4a	*Oral cavity*: cortical bone, deep/extrinsic muscles of the tongue, maxillary sinus, skin of face *Lips*: cortical bone, inferior alveolar nerve, floor of the mouth, skin (chin or nose)
T4b	Masticator space, pterygoid process, skull base, internal carotid artery

Note superficial erosion alone of bone or tooth socket by gingival primary is not sufficient to classify a tumor as T4

fibrous tissues. They grow rapidly, and usually involute by adolescence. Only if hemangiomas are gravely symptomatic or are cosmetically problematic therapy, for example with laser, is performed rather than a "wait-and-see policy". In this regard, color Doppler or MRI may be useful tools in order to show high-flow lesions which are more amenable to laser therapy than low-flow lesions.

It is a diagnostic challenge and not always possible to differentiate hemangiomas from vascular malformations. In opposition to the latter, hemangiomas are usually well-defined subcutaneous tumors, which do not infiltrate bone or muscle. Vascular malformations are isointense on T1-weighted, rather hyperintense on T2-weighted MR-images (Baker et al. 1993), and on contrast-enhanced images, they usually show bright enhancement with a varying homogeneity; high-flow arteriovenous shunts can be seen as well.

3.1.3.5 Schwannomas

Schwannomas are rare benign tumors originating from nerve sheaths. Within the oral cavity they are most frequently found in the tongue of the adult population (Al-Ghamdi et al. 1992). Surgical excision is the treatment of choice.

They are usually isointense (isodense) on T1-weighted MR-images (on CT). On T2, solid components of schwannomas are rather hyperintense. Moreover, cystic tumor components may be present. After the administration of contrast agent a "target-like" appearance is a characteristic sign (Beaman et al. 2004).

3.1.3.6 Miscellaneous benign tumors and tumor-like lesions

Other benign tumors within the oral cavity are even rarer. For completion they are listed in Table 1. Some of them, such as an exostosis, are straightforward diagnoses, others require tissue sampling for identification.

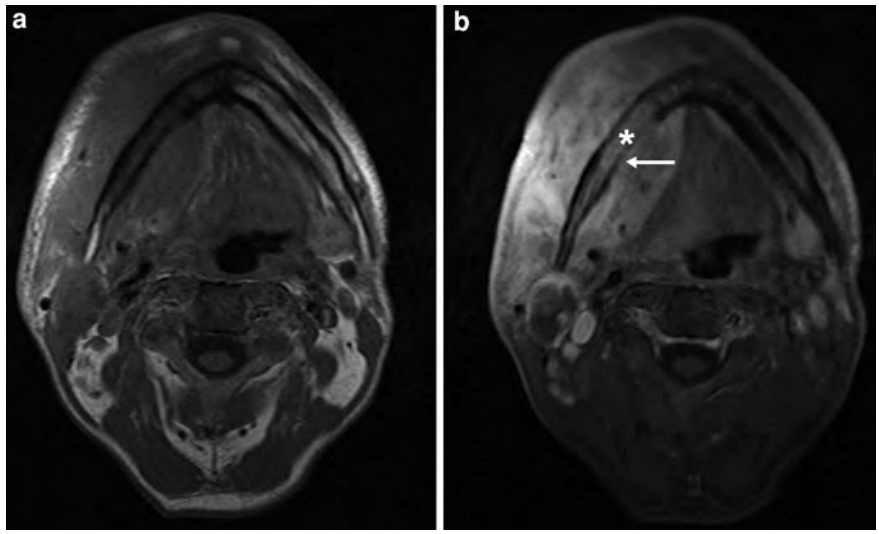

Fig. 16 Pre-contrast (**a**) and post-contrast (**b**) T1-weighted axial MRI showing carcinomatous infiltration of the mandible. Erosion of the bony cortex (*arrow*). The post-contrast image differentiates between hypointense edema and hyperintense tumor infiltration (*star* on **b**) of the bone marrow. (With courtesy of Bodo Kress, MD, Heidelberg, Germany)

3.2 Squamous Cell Cancer

3.2.1 General Considerations

In adulthood, most lesions in the oral cavity sent for imaging are malignant. The most frequent question to answer is whether there is deep infiltration in already clinically detected and biopsied oral cancer. Squamous cell cancer (SCC) predominantly affects men between 50 and 70 years of age (Ferlay et al. 1999; Cawson 1998). Most important risk factors are a long history of tobacco and/or alcohol abuse. Oral SCC originates from the mucosa and, therefore, allows for an easy clinical access regarding detection and biopsy. This holds especially true for the lower lip which is the most comman site for SCC of the oral cavity. Furthermore, local extension of a tumor of the lip can usually be sufficiently determined clinically so that cross-sectional imaging is only needed in very large tumors (e.g. to exclude mandibular infiltration). Besides for the lips, any intraoral mucosal surface can be affected, however three specific intraoral sites are predominantly affected. In descending frequency, the floor of the mouth, the retromolar trigone, and the ventrolateral tongue are involved (Mashberg and Myers 1976).

Small superficial T1-tumors are often not visible on both CT- and MR-images (Keberle et al. 1999). With increasing size, SCC infiltrates deeper submucosal structures. As a result, CT and MRI show a tumor mass and allow for an accurate evaluation of deep tumor infiltration (Kösling et al. 2000; Leslie et al. 1999). This results in the possibility of staging SCC of the oral cavity according to the TNM-system (UICC 2009, Table 2). In spite of the invasive character of SCC, bony structures and arteries resemble anatomic barriers and are infiltrated rather late in the course of the disease.

Regarding bony structures, cortical tumor infiltration can best be detected as erosion and/or lysis of the adjacent cortex on CT-images with a bone-window setting (Van den Brekel et al. 1998; Mukherji et al. 2001). A soft-tissue mass within the bony marrow is a direct sign and can be seen on both CT- and MR-images. Especially, pre-contrast in combination with fat-saturated post-contrast T1-weighted MR-images are very helpful to detect bone marrow invasion (Fig. 16).

Furthermore, an important aspect regarding malignancies of the oral cavity is the invasion of nerves and vessels of neurovascular bundles, such as in the sublingual space (Mukherji et al. 1996; Smoker 2003). While vascular invasion yields a greater risk of remote as well as lymph node metastases, nerve involvement can lead to tumor extension along nerve routes (perineural extension) far beyond the expected tumor margins (compare Figs. 6 and 17). Perineural extension may be asymptomatic and is often not easy to detect with all imaging modalities. Therefore, perineural extension results in a greater likelihood of positive resection margins and/or remote tumor remnants. As a consequence, it is crucial to look for direct or indirect signs for perineural tumor extension.

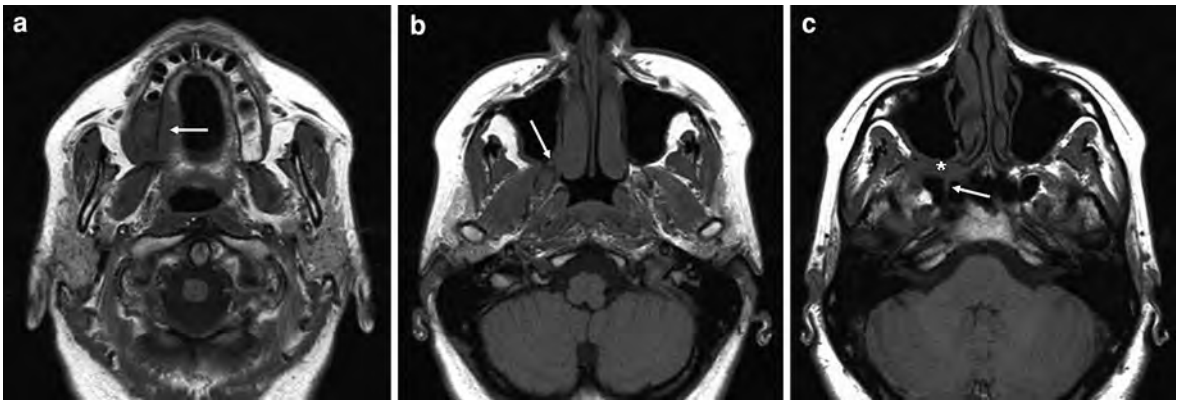

Fig. 17 Axial pre-contrast T1-weighted MRI of an adenoid cystic carcinoma at the *right* maxillary alveolar ridge (**a**); the signal loss inside the bone represents medullar tumor infiltration. The patient complained of *right*-sided facial headache and an anesthesia of the palate, as a result of extensive perineural tumor spread. Accordingly, (**b**) shows soft-tissue thickening in the region of the greater palatine canal containing the greater palatine nerve (*arrow*) and (**c**) shows tumor extension into the *right* pterygopalatine fossa (*star*) extending laterally in the infratemporal fossa, anterolaterally along the wall of the maxillary sinus, and posteriorly in the pterygoid (Vidian) canal (*arrow*). (With courtesy of Robert Hermans, MD, PhD, Leuven, Belgium)

Direct signs are thickened (Fig. 17) and contrast-enhanced nerves. Indirect signs are invasion of sublingual space and widening of bony foramina or canals.

In general, SCC has a similar density to muscle on pre-contrast images (on both, CT- and MR-images—Yasumoto et al. 1995; Keberle et al. 2002). Nonetheless, native T1-weighted MR-images are of great value to delineate the tumor because the characteristic architecture of the tongue musculature is usually altered by the lesion. Furthermore, native T1-weighted images as well as post-contrast CT-images yield the best contrast versus normal fat (e.g. the fatty tissue of the sublingual space). On T2-images, SCC is slightly hyperintense. On post-contrast images there is moderate enhancement, so that fat-saturated MR-images have to be obtained. With increasing size, SCC (and respective metastases) often present with a central necrosis.

Cervical lymph node metastases occur in approximately 50% of the patients with SCC of the oral cavity (Magrin and Kowalski 2000; Smoker 2003). In tumors crossing the median (midline) there is often bilateral lymph node involvement. This holds especially true for tumors of the tongue. Lymph node involvement is generally accepted to be the single most important prognostic parameter (Magrin and Kowalski 2000). In addition to CT and MRI, ultrasound is known to be a very valuable tool regarding the detection and differentiation of cervical lymph nodes (see also "Neck Nodal Disease").

In general, therapeutic options comprise of surgery, radiation therapy, and chemotherapy. The latter is increasingly used as inductive chemotherapy in order to reduce the size of the tumor prior to surgery. Furthermore, surgery and radiation therapy are often combined. Clear extension beyond the midline in tongue cancer often precludes surgical resection as this would imply total glossectomy; primary radiation therapy, in combination with chemotherapy, is usually performed in such circumstances. While smaller tumors can be removed with laser or classic surgery, larger tumors often require extensive surgery with tissue reconstruction. An additional invasion of the mandibular cortex requires marginal (cortical) mandibulectomy. Invasion of the mandibular marrow instead requires complete mandibular resection of the infiltrated segment (segmental mandibulectomy) with local reconstruction.

As a result there is a large variety of therapeutic options so that for any individual an exact evaluation of the tumor extension is essential.

3.2.2 Lip Cancer

As already mentioned, the lips are the most frequent location regarding SCC of the oral cavity (Fig. 18).

However, only very large tumors require local evaluation of deep tumor extension by CT or MRI. In this regard, pretherapeutically important anatomic structures are the mandibular cortex, the mandibular marrow, and the inferior alveolar and/or mental nerves (regarding the imaging criteria of perineural and mandibular infiltration see Sect. 3.2.1).

3.2.3 Floor of the Mouth Cancer

Most tumors of the floor of the mouth originate in its anterior aspects. Here small superficial tumors are readily diagnosed by clinical means. In order to evaluate a tumor's deep infiltration and for TN-staging, cross-sectional imaging is needed (Figs. 19 and 20). Considering the latter facts, in ultrasound, the transducer has to be tilted so that the anterior part of the floor of the mouth can be evaluated accordingly (Mende et al. 1996; Keberle et al. 2000). SCC of the floor of the mouth preferentially infiltrates the surrounding soft tissues first before the mandible and/or the mylohyoid muscle are invaded (Lenz and Hermans 1996). Medially, the tumor can cross the midline, invade the contralateral neurovascular bundle and if there is also cranial extension of the tumor the tongue can be involved. As previously mentioned, large tumor involvement of the contralateral tongue and/or neurovascular bundle often precludes radical surgical resection (Mukherji et al. 1997). Dorsally and caudally, SCC of the floor of the mouth can spread to deeper cervical tissues. Usually, it comes to a dorsal spread first along the mylohyoid muscle and the inner surface of the mandible which are natural borders. Dorsally, Wharton's duct or the submandibular gland itself can be infiltrated. Both can result in inflammatory changes of the gland due to duct obstruction (Yousem et al. 2000). Enlargement of the submandibular gland and dilatation of the duct are important indirect tumor signs. On the other hand, oropharyngeal tumors at the base of the tongue tend to infiltrate the floor of the mouth ventrally (resulting in a T4a-oropharyngeal tumor if extrinsic muscles of the tongue are involved, Fig. 21). The same tumor stage applies for oral cavity tumors in case of invasion of extrinsic muscles of the tongue and/or lateral (as well as anterior) infiltration of the mandible (Table 2). Interestingly, caudal infiltration of the mylohyoid muscle is not regarded a T4-stage according to UICC-guidelines (Table 2). The coronal plane facilitates the evaluation of the mylohyoid as well as extrinsic tongue muscles (Lell et al. 1999).

Fig. 18 CT in a 55-year-old pipe-smoking male with a squamous cell carcinoma of the lower lip. The contrast-enhancing mass is on both sides of the midline, the adjacent soft tissues are edematously swollen. In level II there are bilateral lymph node metastases with central necrosis

The mandible is best evaluated in the axial plane. CT is regarded to be superior for the demonstration of cortical infiltration whereas MRI is more sensitive for evaluation of bone marrow infiltration (Fig. 16). Infiltration of the mandibular cortex leads only to marginal (cortical) mandibulectomy, while infiltration of the bone marrow requires complete segmental resection.

Tumors of the anterior part of the floor of the mouth in particular result in submental (level I; best seen on coronal slices; Lell et al. 1999) and/or submandibular (also level I) lymph node metastases (Fig. 20a).

3.2.4 Retromolar Trigone Cancer

SCC of the retromolar trigone are localized in the superoposterior part of the oral cavity and often involve oropharyngeal subregions (Fig. 22). These tumors are rarer than tumors of the lips or of the floor of the mouth, however, they are more difficult to detect by clinical means. Dorsally, the cranial part of the tonsillar pillar, the lateral aspect of the soft palate, as well as the pharyngeal tonsil can be affected. Deeply, along the pterygomandibular space, the

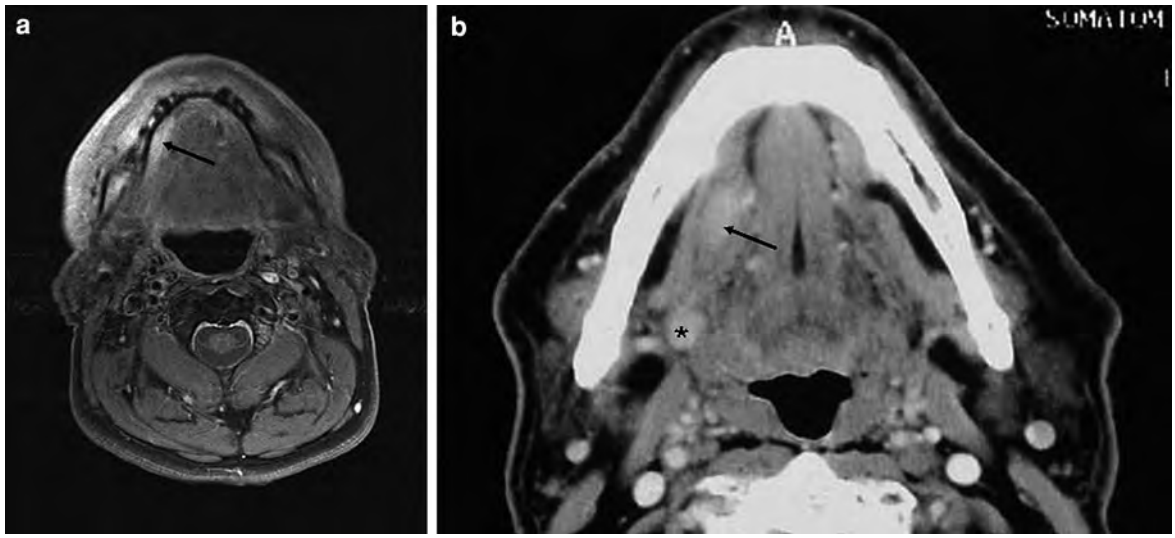

Fig. 19 MRI of a 54-year-old man with a small T1-tumor (SCC) in the anterior part of the floor of the mouth (**a**). A fat-saturated axial T1-weighted MR-image shows the small hyperintense mass adjacent to the attachment of the mylohyoid muscle at the inner mandibular surface. The cortex is intact. **b** A different patient (63 years, male) presented with a squamous cell carcinoma of the *right* floor of the mouth. At CT, the small T1-tumor almost completely fills out the sublingual (fat) space and lies directly between the medially located ipsilateral neurovascular bundle (and hyoglossus muscle) and the laterally located mylohyoid muscle. A lymph node metastasis can be seen on the same slice (*star*)

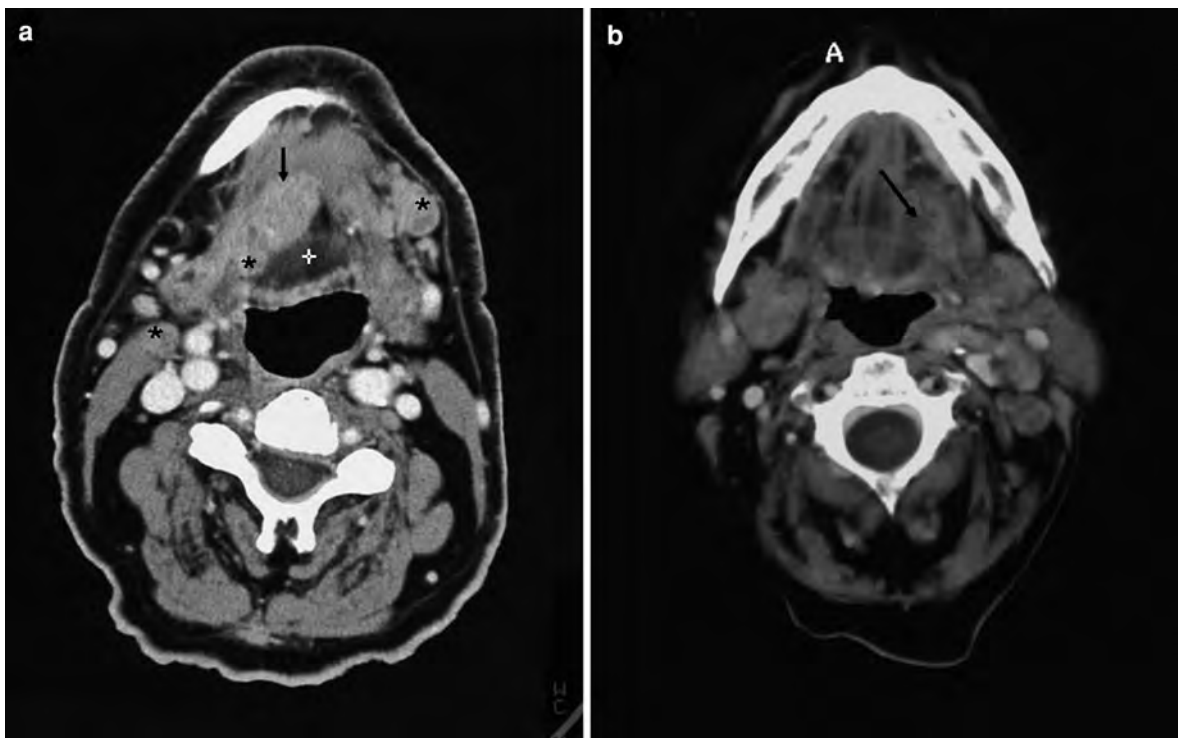

Fig. 20 CT of 62-year-old man with a squamous cell carcinoma lying more deeply in the floor of the mouth (**a**). The tumor is located between the mylohyoid muscle and the partially presented transverse (intrinsic) muscles of the tongue (*cross*). Note the bilateral lymph node metastases. Different patient (**b**) with a SCC with central necrosis on the *left* side of the floor of the mouth. At CT, the tumor (*arrow*) is located between the geniohyoid and the hyoglossus muscles. Note the ipsilateral lymph node metastasis with central necrosis

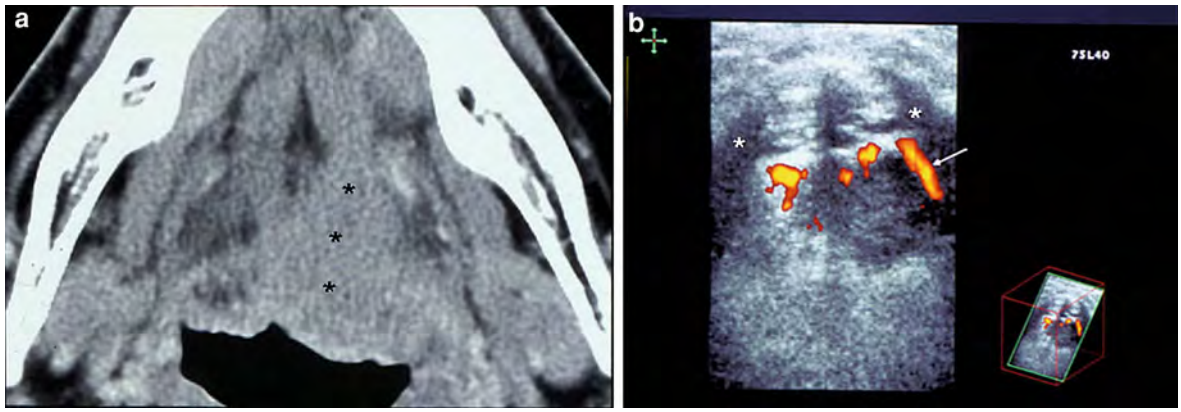

Fig. 21 CT of a 56-year-old man with an oropharyngeal (T4) squamous cell carcinoma of the base of the tongue and deep tumor infiltration into the geniohyoid and genioglossus muscles of the floor of the mouth (*stars*) and midline crossing (**a**). The corresponding ultrasound nicely shows the relation to the lingual artery (*arrow* and *stars* indicate the mylohyoid muscle on both sides, **b**)

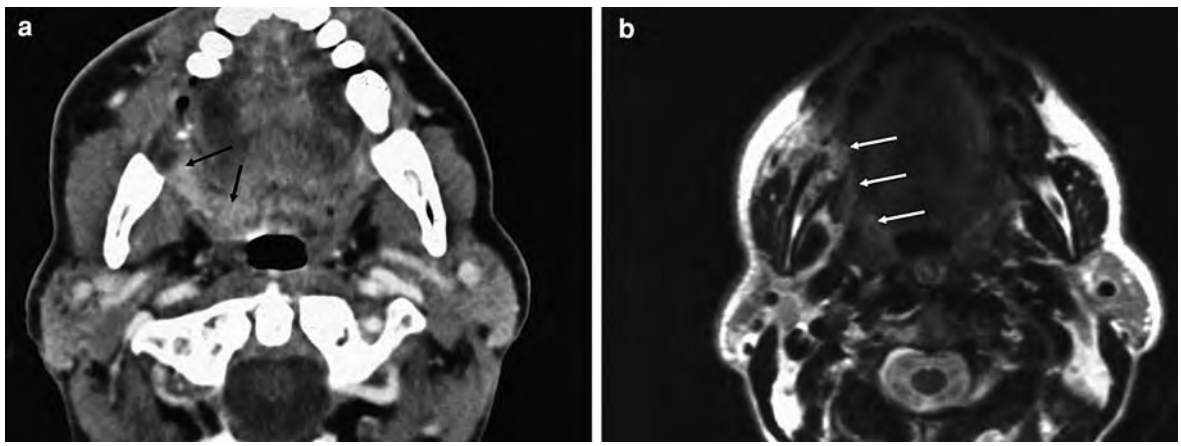

Fig. 22 Axial CT (**a**) and axial T2-weighted MRI (**b**) of a male patient with squamous cell carcinoma of the *right* retromolar trigone (*arrows*) extending medially to the soft palate. The contrast-enhancing (**a**) mass is hyperintense on the T2-weighted MR-image (**b**, With courtesy of Sabrina Kösling, MD, Halle, Germany)

mandible, superior pharyngeal constrictor muscle, the pterygoid processes, the medial pterygoid muscle (eventually causing trismus), and the masticator and the parapharyngeal spaces (and this way even the skull base) can be infiltrated. Especially, in case of tumor extension into the pterygopalatine fossa, one always has to watch for perineural tumor spread (Mukherji et al. 1997). Ventrally and cranially, the gingival and/or buccal mucosa as well as the maxillary alveolar ridge (the latter being a T4a-stage) are possibly infiltrated (Table 2). Medially, the tumor may extend toward the hard palate; laterally, the buccinator space can be infiltrated.

3.2.5 Tongue Cancer

The ventrolateral surface of the tongue is involved more often than the rest of the tongue (Fig. 23). These tumors invade easily the intrinsic muscles of the tongue. The floor of the mouth with the ipsilateral neurovascular bundle (Fig. 24), the base of the tongue, the gingival mucosa and eventually the oropharyngeal tonsils, the soft palate, and the mandible may become invaded. Again, it is crucial to evaluate tumor extension in relation to the midline and to the contralateral neurovascular bundle and sublingual space.

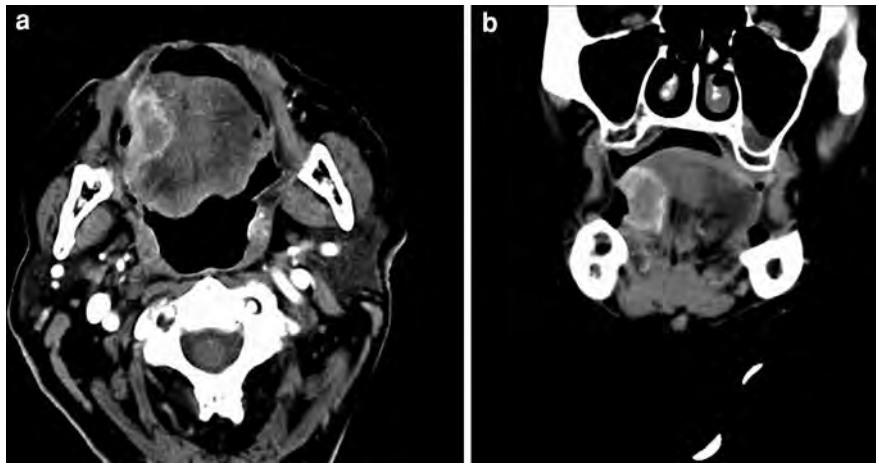

Fig. 23 CT with axial (**a**) as well as coronal reformation (**b**) in a 49-year-old male with a T2 squamous cell carcinoma of the ventrolateral tongue. The tumor does not cross the midline and, thus can more easily be removed than the masses shown in Figs. 21 and 24 (e.g. by hemiglossectomy)

3.2.6 Hard Palate, Gingival and Buccal Cancer

Tumor location at the mucosal layer beneath the hard palate eventually implies close evaluation of the adjacent bone (Fig. 25). This can best be achieved on coronal MR- or CT-images (bone window). Furthermore, the incisive canal and the greater and lesser palatine canals have to be inspected closely for potential perineural tumor spread along the respective palatine nerves (nerve V/2) toward the pterygopalatine fossa. While CT can demonstrate asymmetric pathologic widenings (sometimes cortical erosions) of the respective bony canals, MRI superiorly displays perineural spread as thickening (Fig. 17) and/or contrast enhancement of the nerve.

SCC of the gingival or buccal mucosa may eventally invade the mandibular or maxillary cortex (Figs. 16 and 26), which is usually best seen on axial slices.

3.3 Other Malignant Tumors

3.3.1 Adenoid Cystic Carcinoma

Malignant tumors other than SCC are quite rare. Adenoid cystic carcinoma (ACC) originates from the minor salivary glands which can be found everywhere in the oral cavity (Figs. 17, 25b, and 27, Cawson 1998). They usually occur in the fifth to seventh decade of life, men and women are affected about equally. The long-term prognosis is worse in comparison to SCC (Friedman et al. 1986). This is mainly caused by the propensity of adenoid cystic carcinoma for perineural tumor spread and deep local invasion (Sigal et al. 1992; Parker and Harnsberger 1991). On the other hand, lymphatic metastases are much rarer than in SCC, but hematogenous spread, mainly to the lungs and liver, does occur. Perineural invasion mainly affects the maxillary (V2) and/or the mandibular (V3) nerves. To avoid underestimation of tumor spread, in this regard, the latter nerves, the pterygopalatine fossa (V2), the foramen rotundum (V2), the pterygoid canal (canal containing mixed para- and orthosympathic nerve entering the pterygopalatine canal), the foramen ovale (V3), and the cavernous sinus have to be inspected thoroughly. It is important to note that in some cases of ACC tumor-free areas ("skip areas") along the nerves have been reported. On CT-images, perineural spread might be identified by enlargement of skull base foramina, whereas enlarged nerves are usually not directly visualized. On MR-images, perineural tumor spread can directly be visualized as an enlarged nerve with a varying extent of contrast enhancement. The primary tumor itself cannot be distinguished from SCC by cross-sectional imaging (Becker et al. 1998); perineural spread can also occur in SCC. Thus, differentiation of ACC and SCC requires histopathologic analysis.

3.3.2 Mucoepidermoid Carcinoma

As adenoid cystic carcinoma, mucoepidermoid carcinoma also arises from minor salivary glands. An important aspect to mucoepidermoid carcinoma is the wide range of histological subclassifications (Som and Brandwein 2003; Smoker 2003). Low-grade

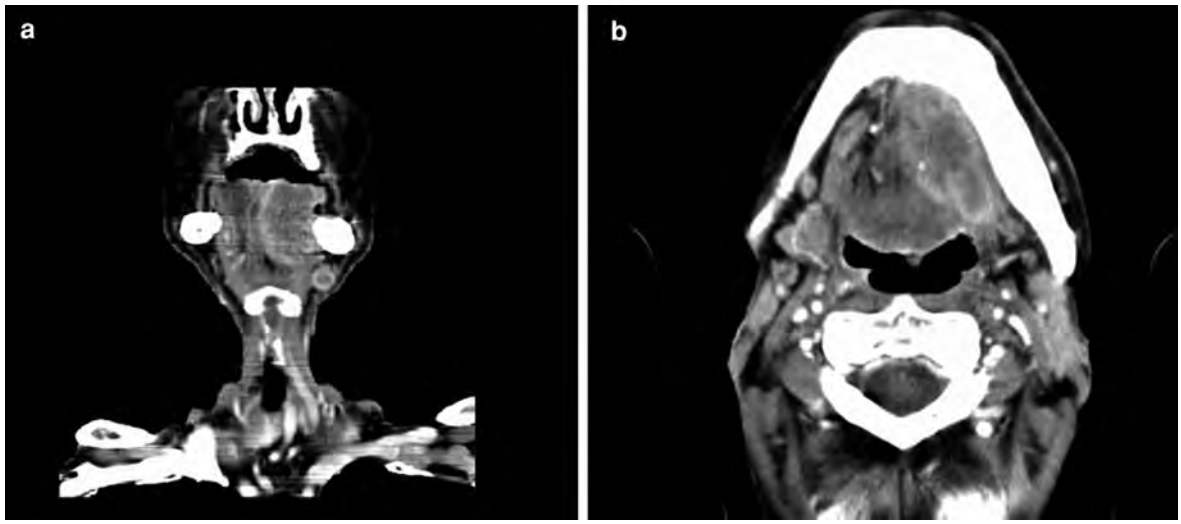

Fig. 24 CT with coronal (**a**) and axial (**b**) reconstructions of a 60-year-old male with a huge squamous cell carcinoma of the tongue. The tumor extends into the floor of the mouth and reaches the mandible as well as the midline but without crossing it. The tumor shows a strong rim enhancement and appears to surround the ipsilateral neurovascular bundle. Beneath the mylohyoid muscle is a small submandibular lymph node metastasis (level I)

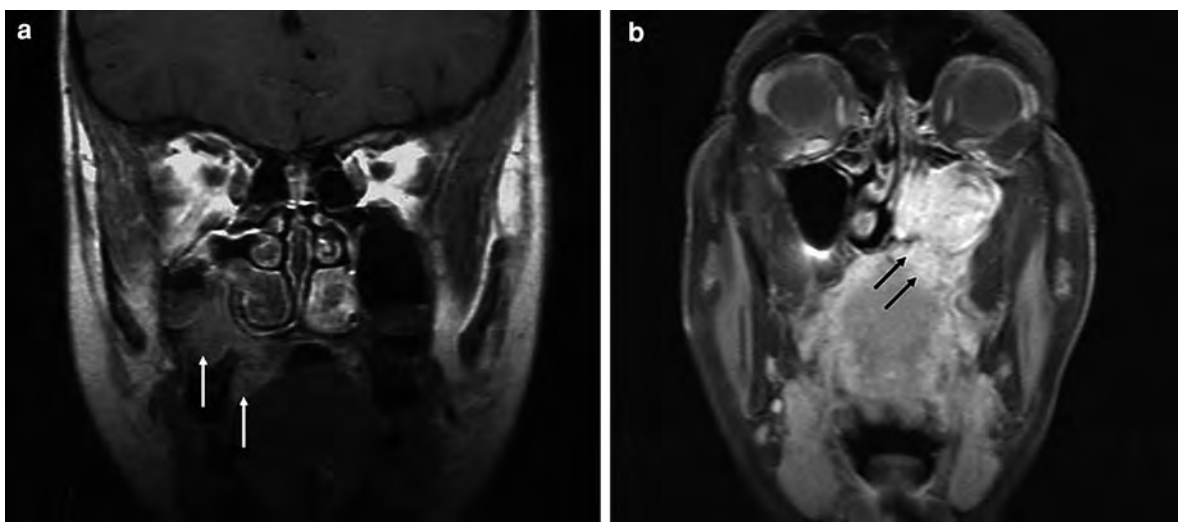

Fig. 25 Coronal MRI (post-contrast T1-weighted) in a 72-year-old male showing a mildly enhancing squamous cell carcinoma of the hard palate with infiltration of bone and extension into the *right* maxillary sinus (**a**). **b** shows an adenoid cystic carcinoma in a 84-year-old female (fat-saturated T1-weighted post-contrast MRI) of the hard palate with severe extension into the maxillary sinus. Although, adenoid cystic carcinoma is often associated with perineural infiltration, this patient did not present with the latter form of tumor spread

mucoepidermoid carcinoma have a very good prognosis. On imaging studies they appear as well-delineated solid tumors. Cystic tumor components and even calcifications can be present. On the other hand, high-grade mucoepidermoid carcinoma have a very poor prognosis. The latter tumors are ill-defined and have similar imaging characteristics as SCC or ACC.

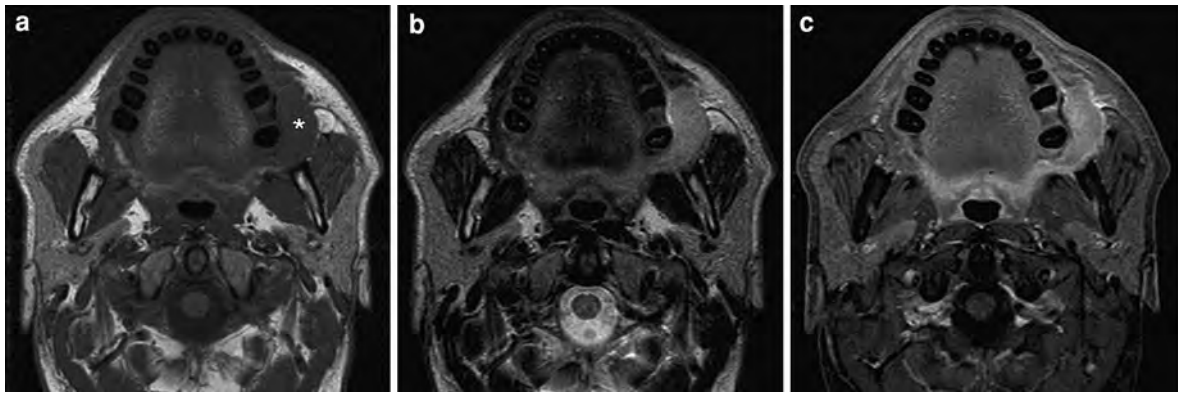

Fig. 26 Axial MRI in a 60-year-old female with a swollen cheek and histologically proven squamous cell carcinoma of the gingival mucosa at the level of the *left*-sided 7th and 8th maxillary molar teeth. Isointense mass on native T1 (**a**), hyperintense mass on T2 (**b**), and homogeneously enhancing hyperintense mass on fat-saturated post-contrast T1 (**c**). The adjacent maxillary cortex is not invaded. The tumor grows behind the 8th molar into the region of the retromolar trigone. (With courtesy of Nicole Freling, MD, Amsterdam, the Netherlands)

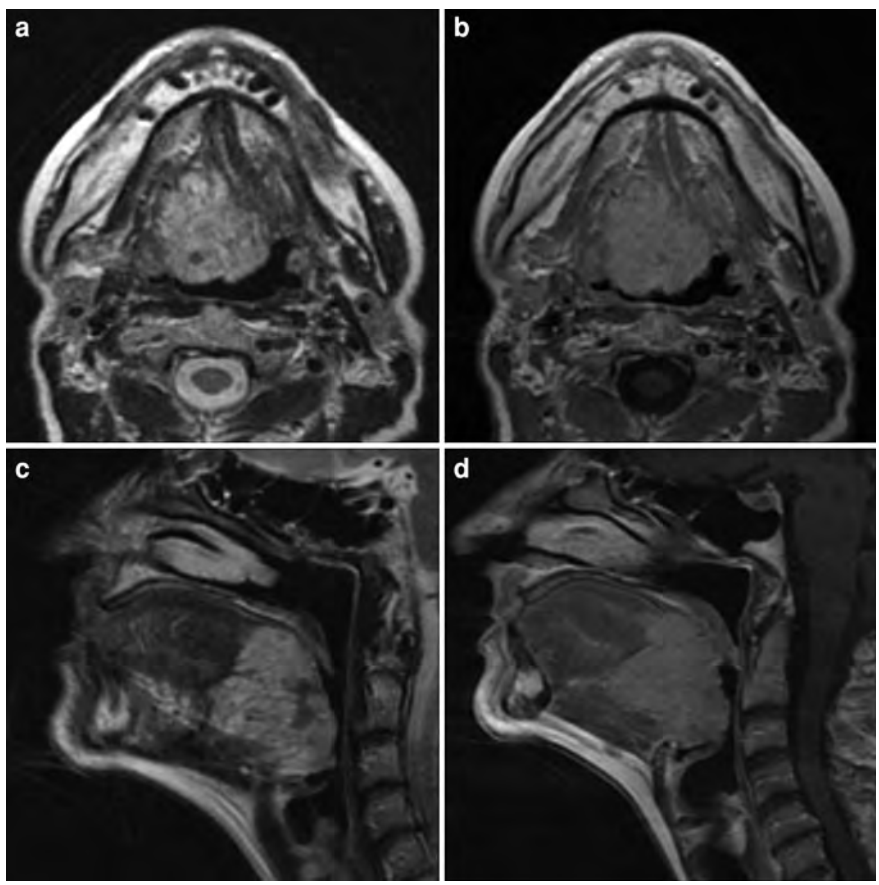

Fig. 27 MRI of a 56-year-old female with a short history of dysphagia. Axial T2–(**a**) and post-contrast T1-weighted (**b**) images of an irregular slightly heterogenous hyperintense adenoid cystic carcinoma of the tongue which infiltrates the floor of the mouth and clearly crosses the midline. Thus, there were no surgical options. Sagittal T2–(**c**) and post-contrast T1-weighted (**d**) images better show the entire longitudinal and sagittal extension of the tumor. Posteriorly, the tumor infiltrates the base of the tongue. (With courtesy of Nicole Freling, MD, Amsterdam, the Netherlands)

Fig. 28 CT of a 50-year-old female with multi-focal non-Hodgkin's lymphoma also involving her *left* masseter muscle, cheek, and lip (*arrows*)

3.3.3 Miscellaneous

Other malignancies in the oral cavity are extremely rare. However, lymphoma, especially non-Hodgkin's lymphoma (NHL), merits some attention (see also "Neck Lymphoma"). Extranodal involvement of the oropharynx by NHL or Burkitt-lymphoma can reach a considerable size and, this way extend ventrally to affect the oral cavity (Fig. 28). NHL tends to present with homogeneous masses, usually, originating from lymphatic tissues of the base of the tongue or the pharyngeal tonsils (see also Table 1). Necrotic tumor components are rare as opposed to carcinomas. This also applies to cervical lymph nodes and more remote tumor sites which are mostly present in NHL (Lee et al. 1987).

Other extremely rare malignancies include sarcoma (rhabdomyo-, lipo-, fibro-, angio-, and leiomyosarcoma). Among these, rhabdomyosarcoma merit further attention since these tumors are the most frequent malignancies during the first two decades of life (Peters et al. 1989). Several histopathologic subtypes occur in rhabdomyosarcomas, which have a predilection for the head and neck region. In the oral cavity, the floor of the mouth and the tongue are more frequently involved than the rest of the oral cavity. On precontrast images, they have the density of muscle. Mostly, there is heterogenous contrast enhancement. On MR, rhabdomyosarcomas may be slightly hyperintense on T2-weighted images. Both, well- and ill-defined masses have been reported.

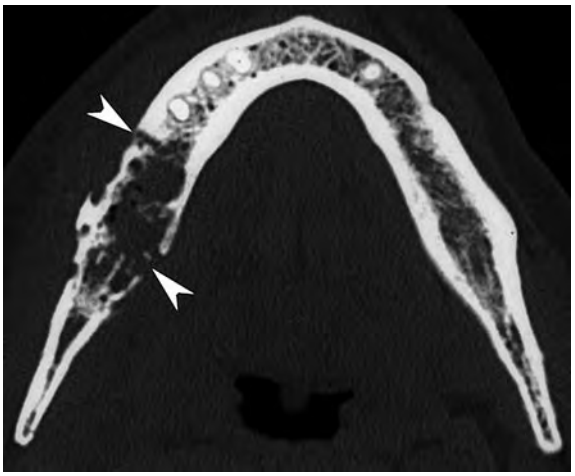

Fig. 29 Axial CT-image (bone window) of a patient treated by external irradiation 10 years earlier for a *right*-sided parotid malignancy, now presenting with oral pain and mucosal dehiscence. Extensive resorption of *right*-sided mandibular spongiosa and destruction of both lingual and buccal cortex, complicated by a pathologic fracture (*arrowheads*). Intra-osseous air bubbles are seen. Histopathologic examination showed necrotic bone with signs of osteomyelitis (With courtesy of Robert Hermans, MD, PhD, Leuven, Belgium)

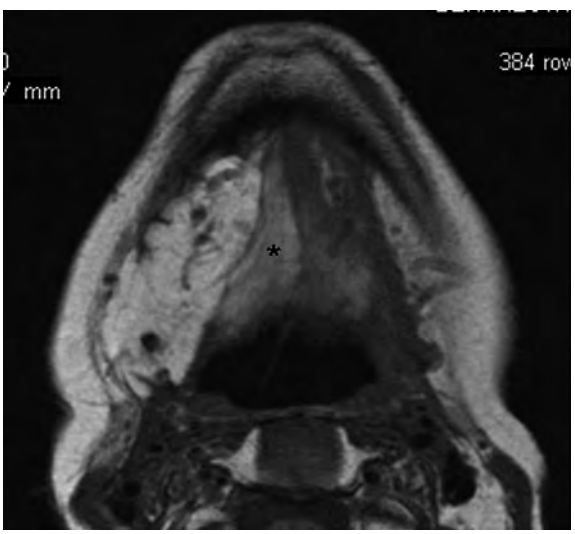

Fig. 30 Axial MRI of 63-year-old male patient after resection of a squamous cell carcinoma with flap reconstruction on the *right* side (**a**). On the one hand, note the flow-voids of the arterial supply and the the fatty transformation of the myocutaneous flap itself. And on the other hand, note the fatty transformation of the muscles (*star*) between the flap and the midline due to muscle denervation. The borders of the flap and of the anatomic structures are smooth, there is no evidence for recurrent tumor

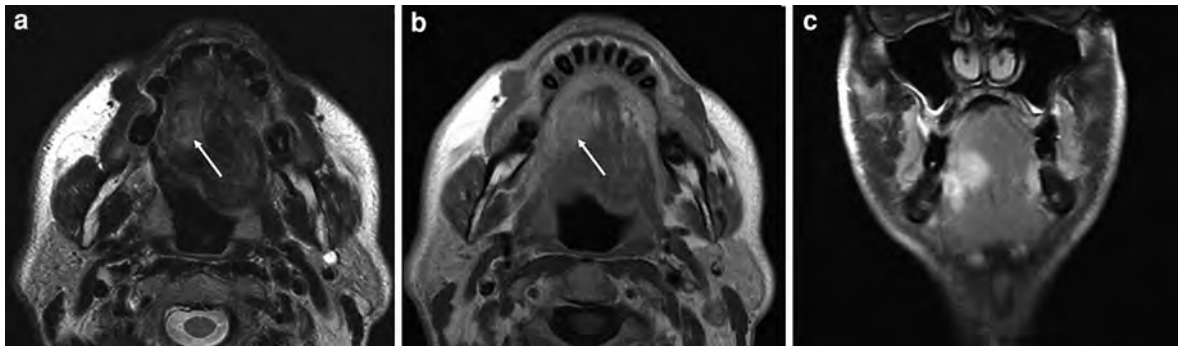

Fig. 31 MRI of a 56-year-old man with a local recurrence after resection of a squamous cell carcinoma of the tongue and respective asymmetric changes of the anatomy. The T2-weighted image shows a small hyperintense lesion (*arrow*) deeply between floor of the mouth and tongue (**a**). The respective post-contrast axial (**b**) and coronal (**c**) T1-weighted images demonstrate contrast enhancement of the lesion

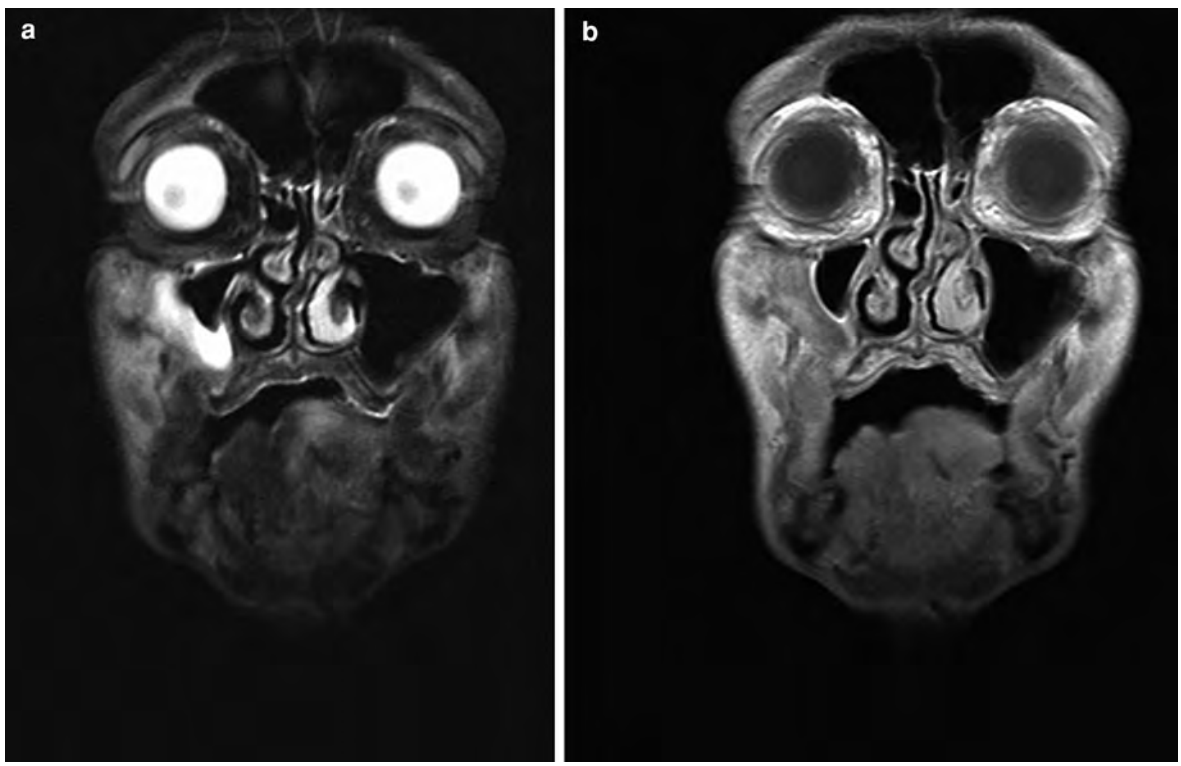

Fig. 32 Coronal MRI of a 50-year-old male with a local recurrence at the *left* tongue. Both, the T2-weighted (**a**) as well as the T1-weighted post-contrast (**b**) images show a hyperintense lesion

3.4 Recurrent Cancer

In the oral cavity, there are typical post-therapeutic imaging findings which should not be misinterpreted with recurrent tumor. After radiation therapy these alterations are generally unspecific and consist in mucosal thickening, edematous changes, and later fibrotic changes (for a more general description of tissue changes after radiotherapy, see "Laryngeal Neoplasms").

A specific complication in the oral cavity after radiation therapy may be osteoradionecrosis (Fig. 29) which usually presents with local lysis, sclerosis,

and eventually bone destruction (Hermans 2003; Weber et al. 2003). On the other hand, recurrent tumor may infiltrate the mandible or maxilla. Although sometimes difficult, CT is the imaging modality of choice to differentiate osteoradionecrosis and recurrent tumor with bony infiltration. An adjacent soft-tissue mass suggests the presence of bony tumor infiltration, whereas a typical moth-eaten appearance and sequestrations favor the diagnosis of osteoradionecrosis.

Specific post-operative changes in the oral cavity can be seen after hemiglossectomy (Lell et al. 2000). Often the tip of the tongue is inverted toward the resected side. Sometimes soft-tissue reconstructions (e.g. myocutaneous flaps) are performed to reduce functional impairment after surgery (Fig. 30, Hudgins et al. 1994). Because of denervation, transformation of muscle into fat and eventually atrophy of the transplanted flap occur.

In contrast to primary carcinoma, which start out superficially, recurrent tumor mainly grows deeply so that for clinicians it is difficult to find recurrent tumor in an early stage (Fig. 31). However, because of the aforementioned expected post-therapeutic tissue changes and the possible presence of other post-therapeutic lesions (e.g. inflammatory changes, granulation tissue, etc.), it is challenging to find a recurrent cancer on imaging studies. In general, the signs for recurrent tumor are similar to the pre-therapeutic situation (see also "Laryngeal Neoplasms").

There is a predisposition for local recurrences in the tongue (Fig. 32). The reason for this are the rather close resection margins in patients with tumors that are close to or just across the midline in order to avoid severe post-operative swallowing disorders (Keberle et al. 2003).

Rather than evaluating anatomic features associated with tumor growth, FDG PET/CT assesses abnormal metabolic activity of tumor and, in this way, avoids some of the difficulties inherent in examining the post-treatment head and neck (Lapela et al. 1995; Lin and Alavi 2005). However, except for a high-negative predictive value (91%), a very variable positive predictive value has been reported in different studies (5–91%), which can partly be explained by disturbing dental artifacts and/or false positive uptake of post-therapeutic inflammatory tissue. (Goodwin 1998; Seitz et al. 2009—see also "Positron Emission Tomography in Head and Neck Cancer").

References

Al-Ghamdi S, Black MJ, Lafond G (1992) Extracranial head and neck schwannomas. J Otolaryngol 107:186–188

Baker LL, Dillion WP, Hieshima GB et al (1993) Hemangiomas and vascular malformations of the head and neck: MR characterization. Am J Neuroradiol 14:307–314

Beaman FD, Kransdorf MJ, Menke DM (2004) Schwannoma: radiologic–pathologic correlation. Radiographics 24: 1477–1481

Becker M, Moulin G, Kurt A et al (1998) Non-squamous cell neoplasms of the larynx: radiologic–pathologic correlation. Radiographics 18:1189–1209

Bergman RA, Afifi AK (2002) Nerves of the eyes, nose, and mouth: Atlas of human anatomy. Copyright protected material used with permission of the authors and the University of Iowa's Virtual Hospital, www.vh.org

Cawson RA (1998) Lucas's pathology of tumors of the oral tissues, 5th edn. Churchill Livingstone Harcourt Brace & Co Ltd, Edinburgh

Coit WE, Harnsberger HR, Osborn AG et al (1987) Ranulas and their mimics. Radiology 263:211–216

Douglas PS, Baker AW (1994) Lingual thyroid. Br J Oral Maxillofac Surg 32:123–124

Ferlay J, Bray F, Sankila R et al (1999) EUCAN: Cancer incidence, mortality and prevalence in the European Union 1995, version 2.0. IARC CancerBase No. 4., Lyon, IARCPress

Ferner H, Staubesand J (1982) Sobotta—Atlas of human anatomy. Urban & Schwarzenberg, Munich

Friedman M, Levin B, Grybauskas V et al (1986) Malignant tumors of the major salivary glands. Otolaryngol Clin North Am 19:625–636

Goodwin WJ (1998) PET and recurrent squamous cell carcinoma of the head and neck: a surgeon's view. Am J Neuroradiol 19:1189–1196

Hermans R (2003) Imaging of mandibular osteoradionecrosis. Neuroimaging Clin North Am 13:597–604

Hudgins PA, Burson JG, Gussack GS et al (1994) CT and MR appearance of recurrent malignant head and neck neoplasms after resection and flap reconstruction. Am J Neuroradiol 15:1694–1698

Johnson JC, Coleman LL (1989) Magnetic resonance imaging of a lingual thyroid gland. Pediatr Radiol 19:461–462

Keberle M, Kenn W, Tschammler A et al (1999) Current value of double-contrast pharyngography and of computed tomography for the detection and for staging of hypopharyngeal, oropharyngeal and supraglottic tumors. Eur Radiol 9:1843–1850

Keberle M, Jenett M, Kessler C et al (2000) New possibilities in the diagnosis and documentation using 3D power Doppler ultrasound with carcinoma of the floor of the mouth as illustration. Ultraschall Med 21:26–31

Keberle M, Tschammler A, Hahn D (2002) Single-bolus technique for spiral CT of laryngopharyngeal squamous cell carcinoma: comparison of different contrast material volumes, flow rates, and start delays. Radiology 22: 171–176

Keberle M, Hoppe F, Dotzel S et al (2003) Prognostic value of pretreatment CT regarding local control in oropharyngeal cancer after primary surgical resection. Fortschr Röntgenstr 175:61–66

Keberle M, Ströbel P, Relic A (2005) Simultaneous pleomorphic adenomas of the parotid and the submandibular gland. Fortschr Röntgenstr 177:436–438

Kennedy TL (1989) Cystic hygroma–lymphangioma: a rare and still unclear entity. Laryngoscope 99:1–10

King RC, Smith BR, Burk JL (1994) Dermoid cysts in the floor of the mouth. Review of the literature and case reports. Oral Surg Oral Med Oral Pathol 78:567–576

Koeller KK, Alamo L, Adair CF et al (1999) Congenital cystic masses of the head and neck: radiologic–pathologic correlation. Radiographics 19:121–146

Kösling S, Schmidtke M, Vothel F et al (2000) The value of spiral CT in the staging of carcinomas of the oral cavity and of the oro- and hypopharynx. Radiologe 40: 632–639

Lapela M, Grenman R, Kurki T et al (1995) Head and neck cancer: detection of recurrence with PET and 2-(F-18)Fluoro-2-deoxy-D-glucose. Radiology 197:205–211

Lee YY, van Tassel P, Nauert C et al (1987) Lymphomas of the head and neck: CT findings at initial presentation. Am J Neuroradiol 8:665–671

Lell M, Baum U, Koester M et al (1999) The morphological and functional diagnosis of the head–neck area with multiplanar spiral CT. Radiologe 39:932–938

Lell M, Baum U, Greess H et al (2000) Head and neck tumors: imaging recurrent tumor and post-therapeutic changes with CT and MRI. Eur J Radiol 33:239–247

Lenz M, Hermans R (1996) Imaging of the oropharynx and the oral cavity. Part II: pathology. Eur Radiol 6:536–549

Leslie A, Fyfe E, Guest P et al (1999) Staging of squamous cell carcinoma of the oral cavity and oropharynx: a comparison of MRI and CT in T- and N-staging. J Comput Assist Tomogr 23:43–49

Lin EC, Alavi A (2005) Head and neck Cancer. In: Lin EC, Alavi A (eds) PET and PET/CT. Thieme, New York, pp 95–99

Magrin J, Kowalski L (2000) Bilateral radical neck dissection: results in 193 cases. J Surg Oncol 75:232–240

Mashberg A, Myers H (1976) Anatomical site and size of 222 early asymptomatic oral squamous cell carcinomas. Cancer 37:2149–2157

Mende U, Zöller J, Dietz A et al (1996) The sonography in the primary staging of head and neck tumors. Radiologe 36:207–216

Mukherji SK, Weeks SM, Castillo M et al (1996) Squamous cell carcinomas that arise in the oral cavity and tongue base: can CT help predict perineural or vascular invasion? Radiology 198:157–162

Mukherji SK, Pillsbury HR, Castillo M (1997) Imaging squamous cell carcinomas of the upper aerodigestive tract: what clinicians need to know? Radiology 205:629–646

Mukherji SK, Isaacs DL, Creager A et al (2001) CT detection of mandibular invasion by squamous cell carcinoma of the oral cavity. Am J Roentgenol 177:237–243

Mulliken JB (1988) Vascular malformations of the head and neck. In: Mulliken JB, Young AE (eds) Vascular birthmarks, hemangiomas and malformations. WB Saunders, Philadelphia, pp 301–342

Mulliken JB, Glowacki J (1982) Hemangiomas and vascular malformations in infants and children: a classification based on endothelial characteristics. Plast Reconstr Surg 69:412–420

Okahara M, Kiyosue H, Hori Y et al (2003) Parotid tumors: MR imaging with pathological correlation. Eur Radiol 13(Suppl. 4): L25–L33

Parker GD, Harnsberger HR (1991) Clinical-radiologic issues in perineural tumor spread of malignant diseases of the extracranial head and neck. Radiographics 11:383–399

Peters E, Cohen M, Altini M et al (1989) Rhabdomyosarcoma of the oral and paraoral region. Cancer 63:963–966

Seitz O, Chambron-Pinho N, Middendorp M et al (2009) 18F-Fluorodeoxyglucose-PET/CT to evaluate tumor, nodal disease, and gross tumor volume of oropharyngeal and oral cavity cancer: comparison with MR imaging and validation with surgical specimen. Neuroradiology 51:677–686

Sigal R, Monnet O, de Baere T et al (1992) Adenoid cystic carcinoma of the head and neck. Radiology 184:95–101

Sigal R, Zagdanski A, Schwaab G et al (1996) CT and MR imaging of squamous cell carcinoma of the tongue and floor of the mouth. Radiographics 16:787–810

Smoker WRK (2003) The oral cavity. In: Som PM, Curtin HD (eds) Head and neck imaging, 4th edn. Mosby, St. Louis, pp 1377–1464

Som PM, Brandwein MS (2003) Salivary glands: anatomy and pathology. In: Som PM, Curtin HD (eds) Head and neck imaging, 4th edn. Mosby, St. Louis, pp 2005–2133

UICC Union international contre le cancer (2009) TNM classification of malignant tumours, 7th edn. Wiley-Liss, New York, pp 26–27

Van den Brekel MWM, Runne RW, Smeele LE et al (1998) Assessment of tumour invasion into the mandible: the value of different imaging techniques. Eur Radiol 8: 1552–1557

Vogl TJ, Steger W, Ihrer S et al (1993) Cystic masses in the floor of the mouth: value of MR imaging in planning surgery. Am J Roentgenol 161:183–186

Weber AL, Kaneda T, Scrivani SJ et al (2003) Jaw: cysts, tumors, and nontumorous lesions. In: Som PM, Curtin HD (eds) Head and neck imaging, 4th edn. Mosby, St. Louis, pp 930–994

Yasumoto M, Shibuya H, Takeda M et al (1995) Squamous cell carcinoma of the oral cavity: MR findings and value of T1-versus T2-weighted fast spin-echo images. Am J Roentgenol 164:981–987

Yousem DM, Kraut MA, Chalian AA (2000) Major salivary gland imaging. Radiology 216:19–29

Neoplasms of the Oropharynx

Robert Hermans

Contents

Abstract

Squamous cell carcinoma is the most common neoplasm originating in the oropharynx. Cigarette smoking and excessive alcohol consumption are well-known risk factors. Infection by high-risk human papillomavirus (HPV) is also a well-recognized risk factor for development of oropharyngeal cancer, and these patients have a better prognosis than those with tobacco or alcohol-induced cancers. As in other head and neck sites, the clinical examination and imaging studies are complementary in the evaluation of the tumor extent. Accurate staging is important in the pretreatment planning of oropharyngeal malignancies. After a review of the normal anatomy, this chapter describes the imaging findings in oropharyngeal cancer, focusing on tumor extent patterns in the different oropharyngeal subsites.

1 Introduction

Head and neck cancer commonly originates from the oropharynx. As in most head and neck sites, squamous cell cancer is the most frequently encountered malignant disease. Cigarette smoking and excessive alcohol consumption are well-known risk factors. Infection by high-risk human papillomavirus (HPV) is also a well-recognized risk factor for development of oropharyngeal cancer, and these patients have a better prognosis than those with tobacco or alcohol-induced cancers (Psyrri et al. 2009).

R. Hermans (✉)
Department of Radiology,
University Hospitals, Herestraat 49,
3000 Leuven, Belgium
e-mail: Robert.Hermans@uz.kuleuven.ac.be

R. Hermans (ed.), *Head and Neck Cancer Imaging*, Medical Radiology. Diagnostic Imaging,
DOI: 10.1007/174_2011_376,

The accuracy of pretherapeutic staging is important in the treatment planning of oropharyngeal neoplasms; clinical examination and imaging studies are complementary in precisely evaluating tumor extent. As an adjunct to clinical surveillance, imaging can be used to monitor tumor response and to detect recurrent or persistent disease as early as possible.

2 Normal Anatomy

The pharynx is divided into three sections: the nasopharynx lies behind the nasal cavity, the oropharynx behind the oral cavity, and the hypopharynx (merging with the proximal oesophagus at the lower level of the cricoid bone) behind the larynx.

The pharyngeal constrictor muscles compose the posterior and lateral wall of the pharynx. They all insert on a midline localised fibrous raphe. This posterolateral wall of the pharynx is a continuous structure, without markings allowing separation in a naso-, oro-, or hypopharyngeal level.

The soft palate separates the nasopharynx from the oropharynx. On imaging studies, often one uses a line extending the level of the hard palate as demarcation line on the lateral and posterior wall; an alternative is to use a horizontal line through the C1–C2 articulation (Chong et al. 1999). Direct sagittal MR-images, or sagitally reformatted CT-images are well suited for defining the border between the naso- and oropharynx.

The oropharynx is separated from the hypopharynx by the pharyngo-epiglottic folds. The border between the oropharynx and oral cavity is more complex, being ring-like and composed of several structures. The upper part of this ring is formed by the junction between the hard and soft palate; therefore, the hard palate is a structure belonging to the oral cavity, while the soft palate is an oropharyngeal structure (actually only its lower surface—the upper surface belongs to the nasopharynx). A mucosal fold, known as the anterior tonsillar pillars, forms the lateral parts of the ring. These mucosal folds mark the anterior border of the tonsillar fossa. The lower part of the ring is formed by a row of small structures on the back of the tongue, the circumvallate papillae. These papillae are on a V-shaped line, with the tip of the V pointing posteriorly. By definition, the posterior third of the tongue (called tongue base) is part of the oropharynx, and not of the oral cavity (Hermans and Lenz 1996).

Table 1 Subsites within the oropharynx (UICC, International Union Against Cancer 2009)

Anterior wall
Base of tongue (posterior to circumvallate papillae or posterior third)
Vallecula
Lateral wall
Tonsil
Tonsillar fossa and tonsillar (faucial) pillars
Glossotonsillar sulci
Posterior wall
Superior wall
Inferior surface of soft palate
Uvula

The soft palate is a complex structure, composed of muscles, some fat, and lymphoid tissue. Two muscles, arising from the skull base, take part in the formation of the soft palate. The more medial one is the levator veli palatini, the more lateral one the tensor veli palatini. These muscles have an important role during deglutition and phonation. They also form a functional unit with the Eustachian tube; their action opens the Eustachian tube fissure during swallowing and yawning. Dysfunction of the Eustachian tube causes serous otitis, a common finding in nasopharyngeal cancer.

The anterior and posterior tonsillar pillars define the triangular tonsillar fossa. Both pillars are mucosal folds produced by the underlying muscular structures. The anterior muscle is the palatoglossal muscle, connecting the soft palate with the tongue base. The posterior muscle is the palatopharyngeal muscle, which takes part in the formation of the muscular pharyngeal wall. Oropharyngeal cancers commonly arise on the anterior tonsillar pillar, using this muscle and the overlying mucosa as a pathway to spread into the soft palate and tongue base. The tonsillar fossa harbors the palatine tonsil, consisting of encapsulated lymphoid tissue. The palatine tonsil is one of the major tonsils in the lymphoid ring of Waldeyer; the other major tonsils are the lingual tonsil in the tongue base, and the pharyngeal tonsil in the roof of the nasopharynx.

The pit between the tongue base and the free edge of the epiglottis is divided by a median mucosal fold running from the base of the tongue to the epiglottis; this fold is the glosso-epiglottic fold, and separates

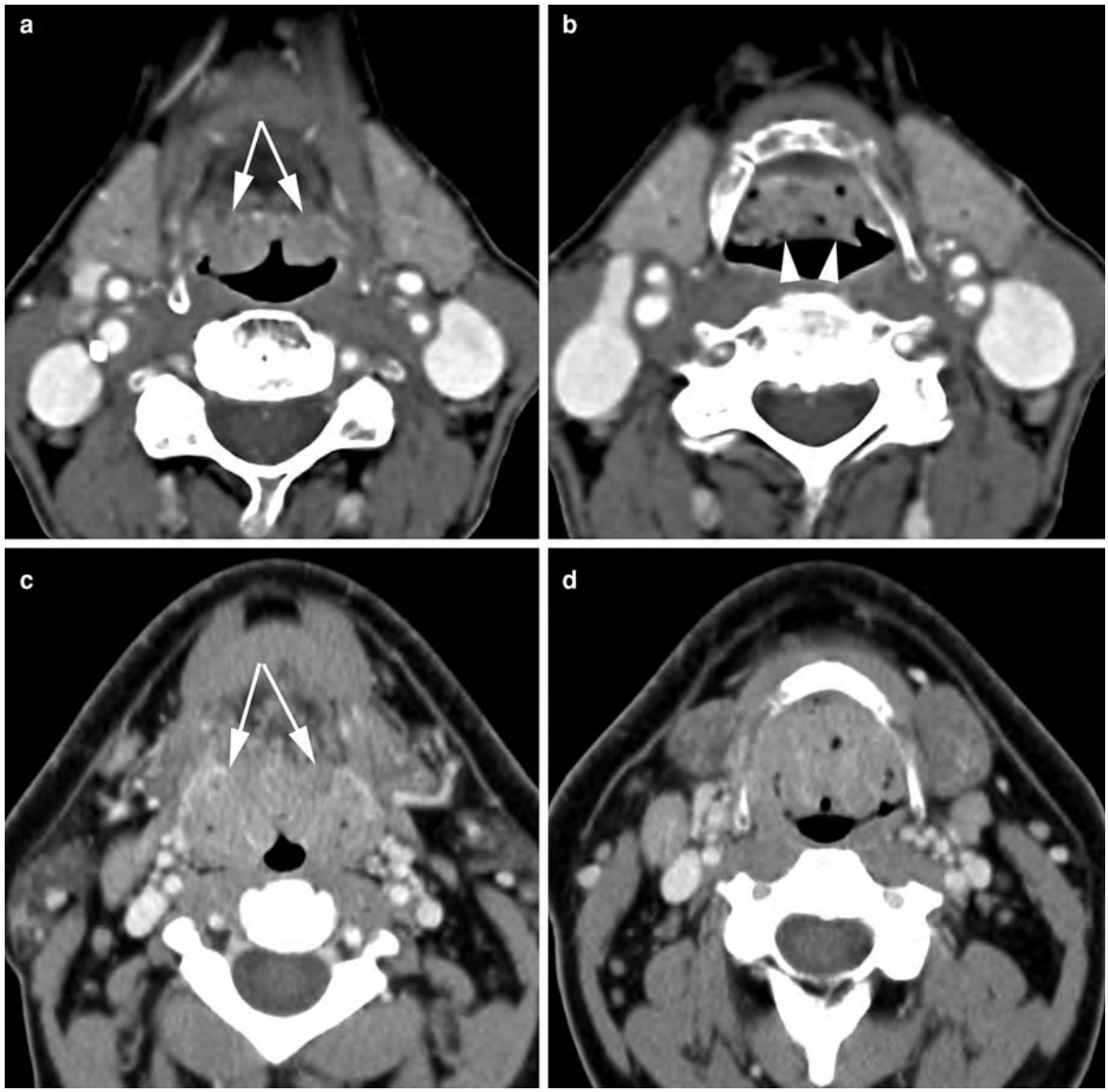

Fig. 1 Contrast-enhanced CT images in a 63-year-old patient. The study was performed because of a parotid tumor. The lingual tonsil appear prominent. The symmetric appearance, lack of invasion in the tongue base tissues (*arrows*, **a**), and the presence of air-filled crypts, as visible at the vallecular level (**b**), indicate benign enlargement of the tonsillar lymphoid tissue. Epiglottic rim, *arrowheads* (**b**). No biopsies were obtained. **c–d** Contrast-enhanced CT images in a 40-year-old patient, complaining of globus sensation. Large volume of the lingual tonsil, narrowing the oropharyngeal airway, both at the level of the tongue base (**a**) and valleculae (**b**). The tissue appears symmetrical, does not invade the tongue base (*arrows*) and contains air-filled crypts, suggesting benign enlargement of the tonsillar lymphoid tissue. Because of the large size of this tonsil, and the associated symptoms, biopsies were obtained on three occasions over a period of 6 months: histological examination always showed follicular hyperplasia, without evidence of tumor

both valleculae. The valleculae are part of the oropharynx. Anatomically, the lingual side of the free epiglottic margin is the posterior border of the valleculae. For staging purposes, it is important to know that the entire epiglottis is considered as part of the larynx. Spread of oropharyngeal cancer to the

Table 2 T-staging of oropharyngeal carcinoma (UICC, International Union Against Cancer 2009)

Tis	Carcinoma in situ
T1	Tumor ≤2 cm in greatest dimension
T2	Tumor >2 cm but ≤4 cm in greatest dimension
T3	Tumor measures >4 cm in greatest dimension or extension to lingual surface of epiglottis
T4a	Tumor invades any of the following : larynx[a], deep/extrinsic muscle of the tongue (genioglossus, hyoglossus, palatoglossus, and styloglossus), medial pterygoid, hard palate, and mandible
T4b	Tumor invades any of the following: lateral pterygoid muscle, pterygoid plates, lateral nasopharynx, skull base, or encases the carotid artery

[a] Mucosal extension to lingual surface of epiglottis from primary tumors of the tongue base and vallecula does not constitute laryngeal invasion

larynx will upstage such a tumor to the T4a category; however, mucosal spread to the lingual surface of the epiglottis is considered as T3 disease (UICC, International Union Against Cancer 2009).

Underneath the vallecular floor a laryngeal fat plane is present, known as the pre-epiglottic fat plane; this fatty tissue is sometimes used by oropharyngeal tumors to dive into the larynx, an extension that is occult to the examining clinician.

The different subsites of the oropharynx, important for staging purposes, are summarized in Table 1.

The largest part of the tongue base is composed of muscles, both intrinsic and extrinsic. On axial imaging, these intrinsic muscular fibers may produce a relative high density in the tongue base on CT-images, which should not be confused with an infiltration mass lesion; the regular and symmetric appearance of these normal muscles allows avoidance of this pitfall.

The lingual artery is the main arterial supply to the tongue. It is a branch of the external carotid artery, arising just distal from the superior thyroid artery and proximal to the facial artery. Three segments can be distinguished (Portugalli et al. 2003):

- a proximal segment, running anterosuperior from the external carotid artery, entering the tongue base just above the hyoid bone, medial to the hyoglossal muscle. The hypoglossal nerve crosses the origin of the lingual nerve, but runs lateral to the hyoglossal muscle.
- a middle segment, running along the medial side of the hypoglossal muscle.
- a branching distal segment, dividing into the deep lingual artery and sublingual artery.

The lingual nerve, a branch of the third portion of the trigeminal nerve, enters the tongue at a higher level than the lingual artery; this nerve enters the tongue from the parapharyngeal space, lateral to the stylohyoid and hyoglossal muscle. The lingual nerve contains sensitive and sensory (via the chorda tympani, branch of the facial nerve) fibers for the anterior two-thirds of the tongue. The sensory and sensitive innervation of the tongue base is via the glossopharyngeal nerve.

The lymphoid tissue within the ring of Waldeyer can appear prominent in younger subjects, prolapsing into the pharyngeal lumen. The amount of the lymphoid tissue decreases with age. Patients older than 40 years are not expected to have a significant amount of residual lymphatic tissue, but small tags of tissue may persist. The volume of the tonsils may increase because of an upper respiratory tract infection, but also because of an extranodal lymphoma localisation. A persistent or asymmetric appearing lingual tonsil can cause problems, as differentiation with a malignant tumor is not always possible. Clues, which may help to differentiate, are air-filled crypts and the presence of small calcifications within the lymphatic tissue. Lymphatic tissue does not invade the deeper structures (Fig. 1; see also Fig. 9). However, one should always stay prudent, and in case of doubt, obtaining biopsies is warranted.

The parapharyngeal space runs from the skull base to the submandibular salivary glands. It essentially consists of fat and is bordered medially by the pharyngeal walls and laterally by the infratemporal space (containing the masticatory muscles). Contrary to the superficial tissues of the oropharynx, which may appear somewhat asymmetric, this deeper lying parapharyngeal space should always appear symmetric; any asymmetry should be treated with extreme caution (Farina et al. 1999). The parapharyngeal space has a small anterior extension between the oropharyngeal wall and the medial pterygoid muscle; this narrow space is known as the pterygomandibular space, reaching the mandible; it contains the lingual nerve. This small pterygomandibular space is actually a crossroads of several structures belonging to different spaces. The anterior tonsillar pillar, connecting the soft palate to the tongue base, and using the pterygomandibular space as access to the

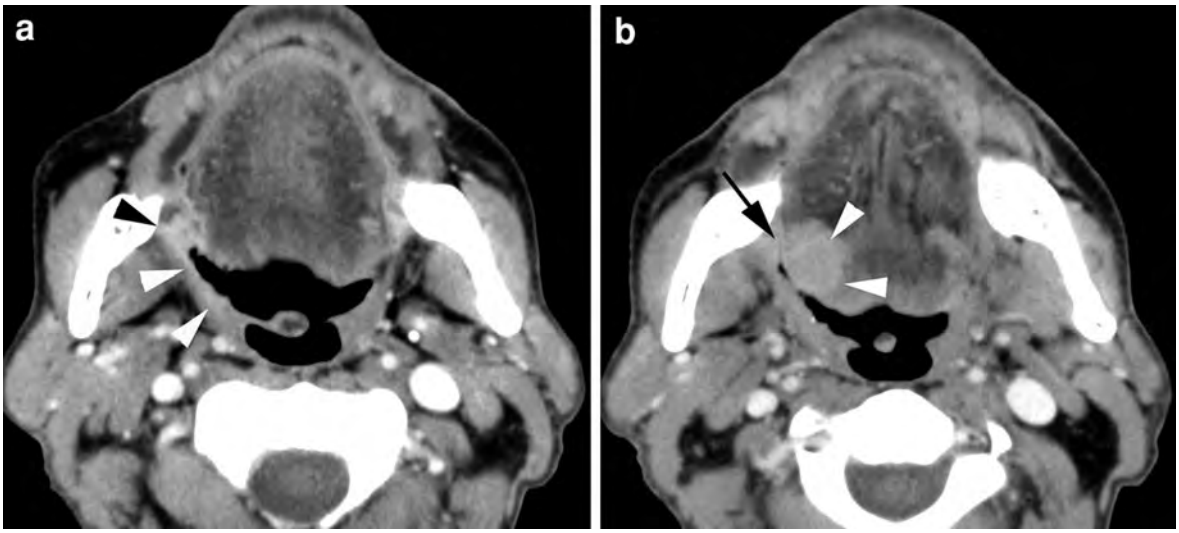

Fig. 2 Axial contrast-enhanced CT images in a patient with *right-sided* tonsillar cancer. **a** Soft tissue thickening and increased enhancement is seen in the *right* anterior tonsillar pillar (*white arrowhead*), extending into pterygomandibular raphe (*black arrowhead*). **b** The enhancing soft tissue mass extends along the glossotonsillar sulcus (*arrow*) into the tongue base (*arrowheads*)

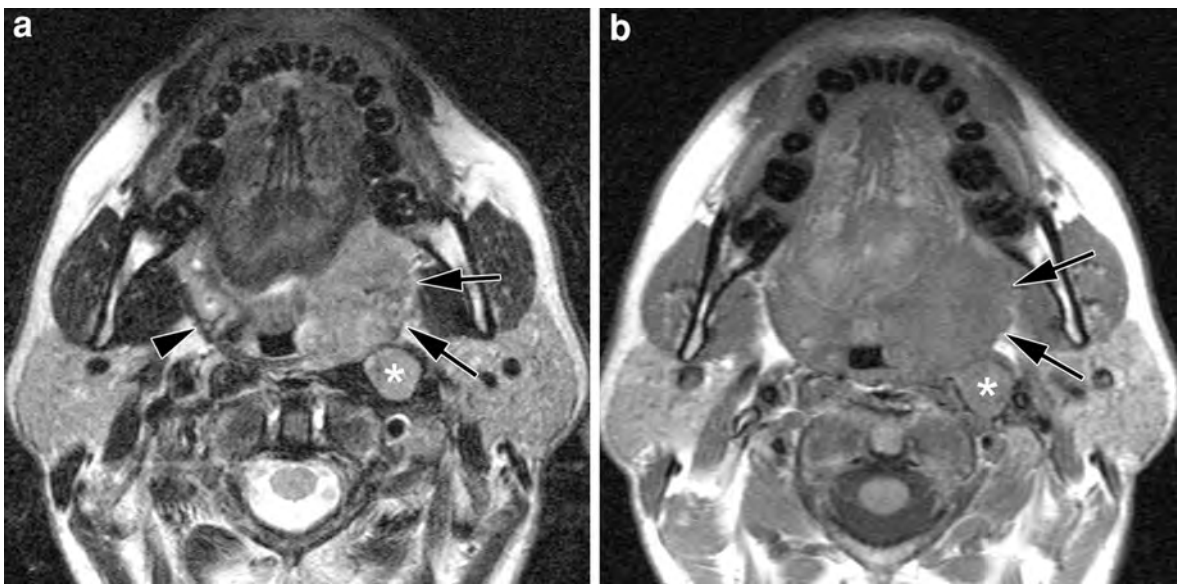

Fig. 3 Axial T2-weighted (**a**) and plain T1-weighted spin echo image (**b**) in a patient with a *left-sided* tonsillar cancer. The soft tissue mass involves the palatine tonsil, grows through the pharyngeal constrictor muscle into the parapharyngeal space (*arrows*, compare to opposite side). The mass lesion reaches the retromolar trigone, and slightly compresses the tongue base. Retropharyngeal adenopathy (*asterisk*). Normal pharyngeal constrictor muscle on *right side* (*arrowheads*)

parapharyngeal space, is very close, as well as the retromolar trigonum of the mandible, a small triangular bony space, localised just behind the third lower molar. The mucosal surface at the level of the retromolar trigone also covers the fibrous pterygomandibular raphe. On the posterior side of this raphe, part of the pharyngeal constrictor muscle originates, while on the anterior side, the buccinator muscle takes its origin, eventually forming the muscular substrate of the cheek.

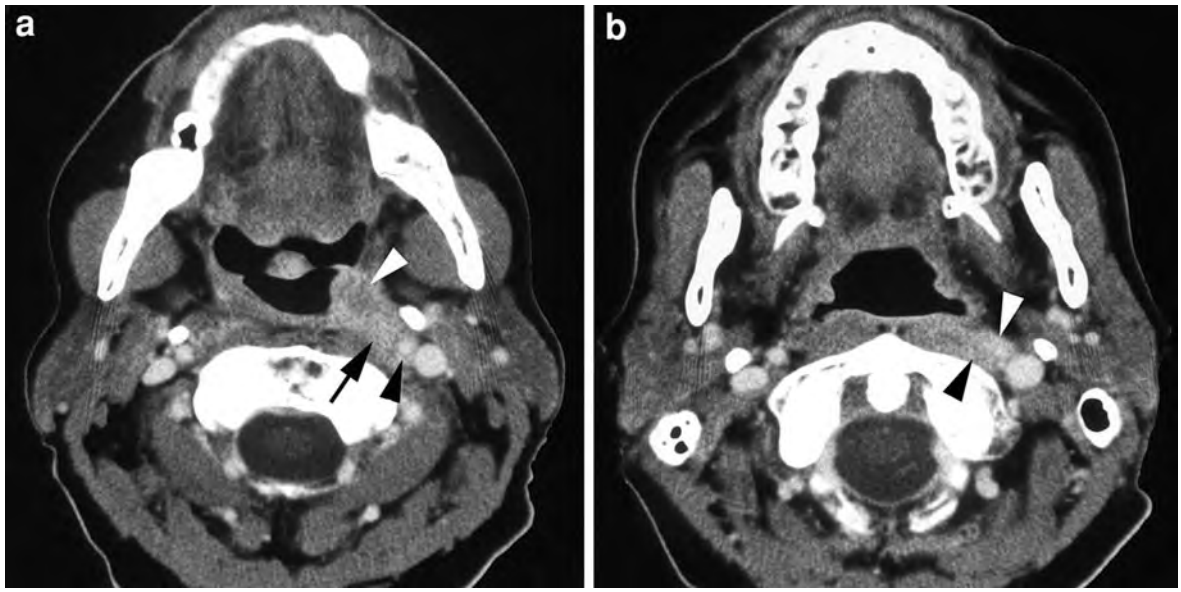

Fig. 4 Patient presenting with *left-sided* otalgia. Clinical examinations show *left-sided* tonsillar tumor. Axial contrast-enhanced CT-images. **a** Level of oropharynx: enhancing mass lesion in *left* oropharyngeal tonsil (*white arrowhead*), extending into the retrostyloid compartment of the parapharyngeal space (*arrow*), encasing the internal carotid artery (*black arrowhead*). **b** Level of nasopharynx. Submucosal perivascular tumor extension (*arrow*) along the internal carotid artery (*arrowhead*)

Fig. 5 Contrast-enhanced CT image in a patient with a *right sided* tonsillar cancer. The mass extends into the infratemporal space, parapharyngeal, and carotid space (*arrows*). Encasement of the external carotid artery (*white arrowhead*), and partial encasement of the internal carotid artery (*black arrowhead*). Laterally, the mass is bordered by the posterior belly and the digastric muscle and parotid gland (*curved arrow*)

The parapharyngeal space and its neoplastic pathology is discussed in detail in "Parapharyngeal Space Neoplasms".

3 Squamous Cell Carcinoma

Squamous cell carcinoma is the most frequent malignant tumor of the oropharynx (90%). Most patients complain of sore throat, otalgia, or dysphagia; more advanced, invasive tumors may cause severe pain and trismus.

The T-staging is based on tumor size, and involvement of adjacent structures (Table 2). The most common site of origin of oropharyngeal cancer is the anterior tonsillar pillar.

3.1 Tonsillar Cancer

Nearly all tonsillar cancers originate from the anterior tonsillar pillar. These cancers commonly spread anteroinferiorly to the tongue base, and superomedially to the soft palate, both along the palatoglossal muscle.

Fig. 6 Contrast-enhanced CT images in a patient with tongue base cancer. **a** Axial image. An ulcerated, contrast-enhancing soft tissue mass is seen in the base of the tongue (*arrowheads*). Irregular tumor margins are present. The lesion crosses the midline, and approaches the left lingual artery (*curved arrow*). Large, necrotic adenopathy on left side. **b** Sagittal reformatted image (paramedian section on left side). The anterior spread in the floor of the mouth can be well appreciated (*white arrowhead*); again, close relationship with the proximal part of the lingual artery is seen (distal branches indicated by *arrows*). The lesion extends into the vallecula (*black arrowhead*); the preepiglottic space (*asterisk*) is not involved

Anterolateral spread, along the pharyngeal constrictor muscle to the pterygomandibular raphe and retromolar trigone, is also commonly seen (Fig. 2). Advanced lesions may invade the mandible, spread along the pharyngeal wall to the hypo- and/or nasopharynx, or invade the parapharyngeal space through the pharyngeal wall (Figs. 3, 4). Spread to the infratemporal space, with involvement of the muscles of mastication and neurovascular structures in this space may be seen in advanced cases (Fig. 5).

Lesions originating from the posterior tonsillar pillar are rare; these may spread inferiorly along the palatopharyngeal muscle.

3.2 Tongue Base Cancer

Cancer in the tongue base tends to grow silently and deeply, and is often larger than suspected at clinical examination. Tumors may spread, along the palatoglossal muscle, cornering the glossotonsillar sulcus, to involve the anterior tonsillar pillar.

Anterior spread into the floor of the mouth and/or tongue body may occur, along the mylo- and/or hyoglossal muscle, and/or along the lingual neurovascular bundle (Fig. 6). Tongue base cancer may also grow in a retrograde fashion along the lingual vessels towards the external carotid artery (Dubin et al. 2002). Vascular and perineural tumor spread is associated with reduced local and regional tumor control and reduced patient survival. A tumor mass with an overall diameter of more than 2 cm on imaging predicts vascular and perineural tumor spread (Mukherji et al. 1996). Infiltration of the normal fatty tissue planes in the base of the tongue, of the fat in the sublingual space, as well as irregular tumor margins are also associated with an increased risk of vascular and perineural tumor spread. Such findings are related to overall tumor bulk.

Spread to the valleculae and piriform sinuses, and into the pre-epiglottic space may be seen. Retrograde tumor growth sometimes occurs along the styloid musculature (Fig. 7).

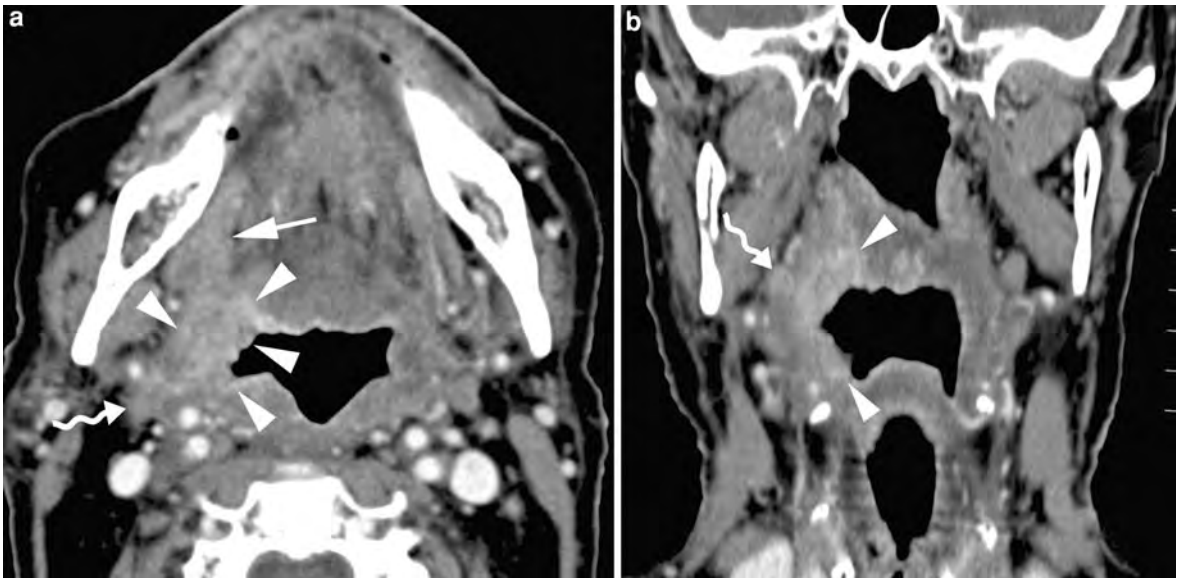

Fig. 7 Patient treated by irradiation for right-sided tonsillar cancer 5 years earlier; clinically an area suspicious for recurrent cancer is seen on the right tonsil. **a** Axial contrast-enhanced CT image. Area of soft tissue thickening and increased enhancement in right tonsillar area, extending into tongue base (*arrowheads*): recurrent cancer. Some anterior extension along the hyoglossus muscle is suspected (*arrow*). The lesion abuts the styloglossal muscle, which has a slightly irregular contour (*curved arrow*). The fat planes surrounding the external and internal carotid artery are obliterated, but do not show increased enhancement: probably post-radiotherapy. **b** Coronal reformatted image. The cancer is extending into the soft palate (*upper arrowhead*) and down to the pharyngo-epiglottic fold (*lower arrowhead*). Obliteration of fat planes along the styloglossal muscle, showing increased enhancement: perimuscular tumor extension

Extension of a tongue base cancer across the midline usually precludes surgical cure, as one lingual neurovascular pedicle needs to be conserved for sufficient functional recovery to allow safe swallowing (Fig. 8).

Differentiation of tongue base cancer from normal lymphoid tissue on the surface of the tongue base may be difficult on imaging studies; a reliable criterion to diagnose cancer is infiltration of the deeper soft tissue structures (see above) (Fig. 9).

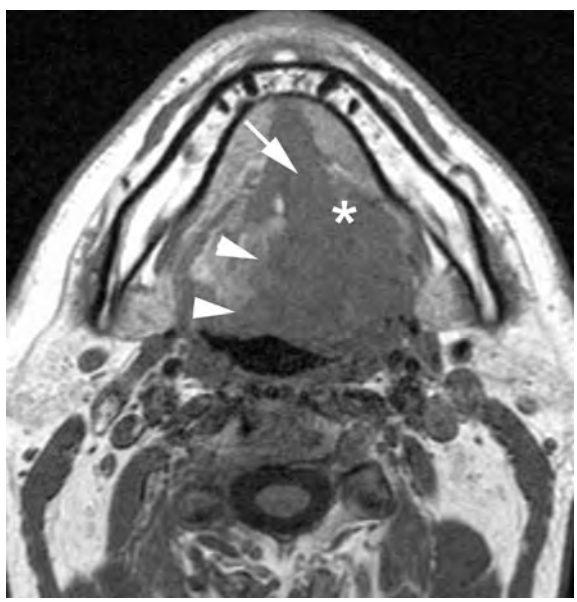

Fig. 8 Patient with a left-sided tongue base cancer. Axial plain T1-weighted spin echo image show soft tissue mass growing over the midline (*arrowheads*), involving the left sublingual space (*asterisk*) and genioglossus/geniohyoid muscle (*arrow*)

3.3 Soft Palate Cancer

Soft palate cancer may spread laterally and inferiorly along the tonsillar pillars. Superior spread to the nasopharynx occurs in advanced disease (Fig. 10). Carcinoma of the soft palate may occasionally spread perineurally along palatine branches of the maxillary nerve (Ginsberg and DeMonte 1998).

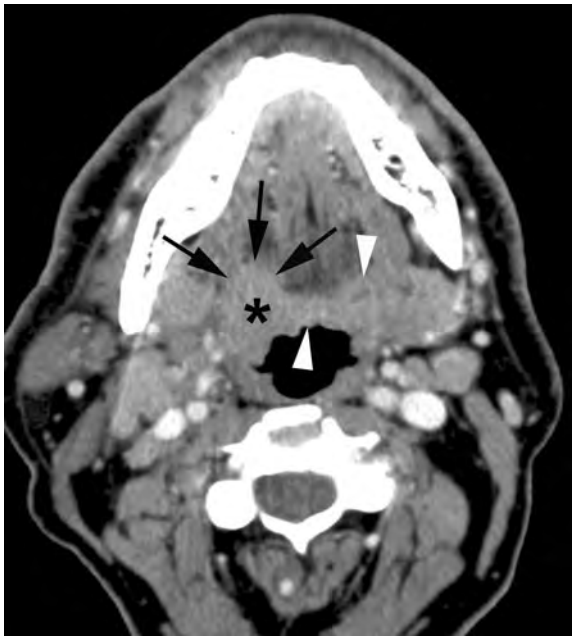

Fig. 9 Axial contrast-enhanced CT-image in a patient with a right-sided tongue base cancer (*asterisk*). The lesion shows the same density as the lingual tonsil (*arrowheads*), but can be identified because it infiltrates the deeper tissues of the tongue base (*arrows*, compare to opposite side)

3.4 Posterior Oropharyngeal Wall Cancer

Isolated cancer in the posterior oropharyngeal wall is rare (Fig. 11); more commonly, this wall is invaded by cancers originating from the lateral oropharyngeal wall. Along the posterior wall, mucosal or submucosal spread to the hypopharynx and/or nasopharynx is possible.

Fixation to or direct invasion of the prevertebral fascia precludes the possibility of surgical resection of pharyngeal cancer, and is associated with a poor prognosis. The absence of prevertebral space involvement is reliably predicted on CT and MR-images by demonstrating the preservation of the retropharyngeal fat plane. The negative predictive value of this sign varies between 82 and 97.5% (Righi et al. 1996; Hsu et al. 2005). However, cross-sectional imaging is poor in predicting involvement of the prevertebral space. Obliteration of the retropharyngeal fat plane, asymmetric enlargement of the prevertebral muscles (on CT studies), and thickening and signal abnormalities (on MR studies) are all unreliable signs to diagnose extension into this space (Righi et al. 1996; Loevner et al. 1998; Hsu et al. 2005) (Fig. 11). Open neck exploration with direct evaluation of the prevertebral muscles is superior to CT and MRI and should be considered in these patients. However, the decision to surgical resection is influenced in these patients by a number of factors in addition to involvement of the prevertebral space, including carotid artery encasement, perineural spread, retropharyngeal adenopathy, and overall patient performance status. Also, the majority of lesions on the posterior pharyngeal wall are treated by radiotherapy or combined chemotherapy and radiotherapy, as the reported cure rates are similar to those of surgery alone or combined surgery and radiotherapy (Million et al. 1994). Nevertheless, as surgical reconstruction methods improve, resection with postoperative radiotherapy can be considered in selected cases (Julieron et al. 2001).

3.5 Lymphatic Spread

Lymphatic spread usually occurs in a predictable way, from superior to inferior, the upper parajugular lymph nodes (level II) being the first echelon at risk. Retropharyngeal adenopathy is relatively common and usually associated with lymphadenopathy in other neck levels; isolated retropharyngeal adenopathy without involvement of other lymph nodes also occurs, particularly in posterior oropharyngeal wall cancer (Bussels et al. 2006).

Bilateral adenopathies are commonly seen in soft palate cancer, as well as in base of the tongue cancer.

The imaging criteria for diagnosing metastatic neck adenopathy are described in "Neck Nodal Disease".

4 Treatment

Oropharyngeal cancer is treated with curative intent by radiotherapy, surgery, or a combination of both modalities. Depending on the anatomical localisation, small lesions (T1 or T2) are treated by either radiotherapy or surgery; cancer of the soft palate or uvula is treated by irradiation, as surgery of these structures interferes with palatal function. If possible, surgery can be considered as an option in larger lesions (T3 or T4), followed by radiotherapy.

Nowadays, patients with advanced oropharyngeal cancer (stages III and IV) (Table 3) are offered concurrent chemoradiotherapy, with surgery reserved

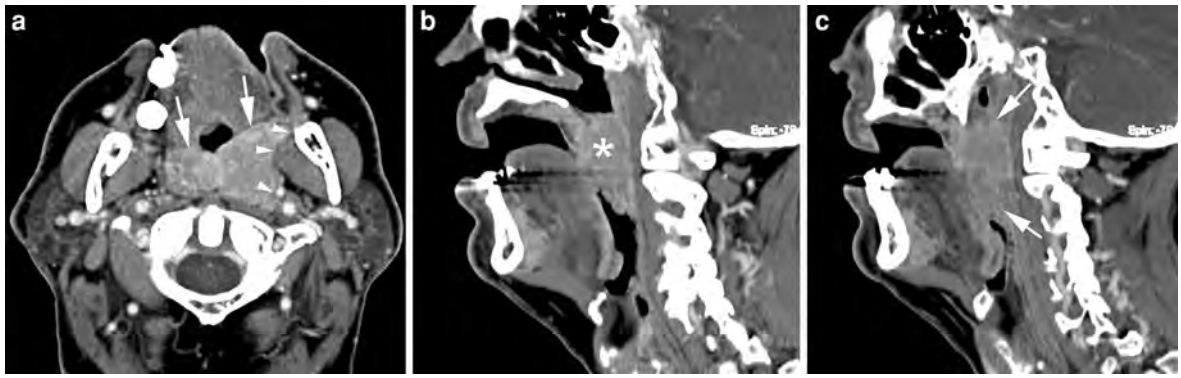

Fig. 10 Contrast-enhanced CT-images in a patient with soft palate cancer. **a** Axial image. Pronounced thickening and increased enhancement of the soft palate (*arrows*); the mass extends into the region of the retromolar trigone, and pushes the left lateral pharyngeal wall towards the parapharyngeal space (*arrowheads*). **b** and **c** Sagittal reformatted images (**c** more lateral than **a**), showing the soft palate tumor (*asterisk*); superior extension into the lower part of the nasopharynx (*upper arrow*) and into the lateral oropharyngeal wall (*lower arrow*) is seen

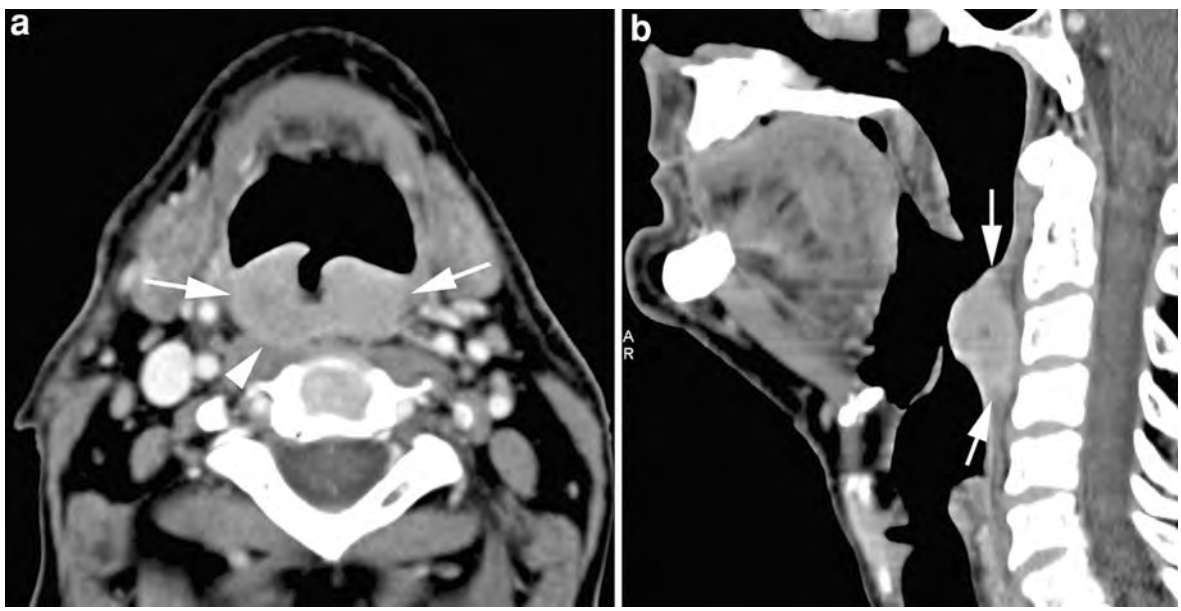

Fig. 11 Contrast-enhanced CT-images in a patient with cancer of the posterior oropharyngeal wall. **a** Axial image. Contrast-enhancing soft tissue mass (*arrows*), showing ulceration. On the *right side*, the lesion obliterates the retropharyngeal fat plane and abuts the prevertebral muscle (*arrowhead*); invasion of this muscle cannot be excluded. **b** Coronal reformatted image, showing the craniocaudal extent of the lesion (*arrows*). The mass remains limited to the oropharyngeal level. The patient was treated by radiotherapy

for salvage, as treatment option (Cohan et al. 2009). Platinum-based concomittant chemoradiotherapy results in locoregional control rates of about 75% (Nuyts et al. 2009). However, acute and late toxic side effects are more frequent than after radiotherapy alone (Dirix and Nuyts 2010). Treatment complications, such as treatment-induced severe dysphagia, chronic lung aspiration, radionecrosis, and others, may also

Table 3 Stage grouping of oropharyngeal carcinoma (UICC, International Union Against Cancer 2009)

Stage 0	Tis	N0	M0
Stage I	T1	N0	M0
Stage II	T2	N0	M0
Stage III	T1, T2	N1	M0
	T3	N0, N1	M0
Stage IVa	T4a	N0, N1, N2	M0
	T1, T2, T3	N2	M0
Stage IVb	T4b	any N	M0
	any T	N3	M0
Stage IVc	any T	any N	M0

occur. Although the survival after concurrent chemoradiotherapy is somewhat improved, the probability of developing distant metastases later on is estimated to be around 15–20%, less good than initially expected.

Several studies indicated, in glottic, supraglottic, hypopharyngeal, and nasopharyngeal squamous cell carcinoma, the value of CT-determined primary tumor volume as the prognostic parameter for local outcome after radiation treatment; increasing volume of the primary tumor indicates an increased likelihood of local failure (Mukherji et al. 2004). Such imaging-derived information is helpful for better stratifying patients in a low- or high-risk group for local failure than the clinical examination alone. This opens perspectives for treatment modulation in patients with head and neck squamous cell carcinoma. It also allows the identification of a patient group potentially benefiting from frequent posttherapy imaging surveillance, in order to identify tumor persistence or recurrence at an early stage.

However, studies on oropharyngeal cancer in general (Nathu et al. 2000), and tonsillar cancer in particular (Hermans et al. 2001), revealed an only marginal impact of CT-determined primary tumor volume on local outcome, while T-category was very significantly correlated with local outcome. Despite the pronounced variability within each T-category, tumor volume could not be used to separate patients within the same T-category in groups with different local outcomes (Hermans et al. 2001). Why the relation between tumor volume and local outcome is less pronounced in oropharyngeal cancer compared to other head and neck sites, is not clear. Clinically, a relation between the growth pattern of a cancer and its response to radiotherapy has been noted, with exophytically growing cancers generally being more radiosensitive than infiltrating cancers. This may

Fig. 12 A patient with a *right-sided* T3 oropharyngeal tonsillar cancer, treated by definitive radiotherapy. Anatomically corresponding axial contrast-enhanced CT- images are shown, obtained just before and 6 months after completion of radiation treatment. Before treatment (**a**), part of the oropharyngeal cancer is seen (*white arrows*). After radiotherapy (**b**), the oropharyngeal tissues appear symmetrical. Volume reduction and increased enhancement of the parotid salivary glands (*asterisks*) correspond to radiation sialadenitis. Slight retropharyngeal edema (*black arrows*)

Fig. 13 **a** Axial contrast-enhanced CT image, obtained 4 months after completion of radiotherapy for a T2N1 oropharyngeal cancer. Expected changes after radiotherapy are seen, no evidence for local disease. **b**. Because of left sided odynophagia and otalgia, a new CT study was obtained 2 months later. Slight soft tissue thickening and increased enhancement is seen in the left anterior tonsillar pillar (*arrow*) extending into glossotonsillar sulcus (*arrowhead*) (compare with A). Clinically, this abnormality corresponded to a small granulomatous lesion. Biopsy revealed squamous cell cancer

be related to a larger anoxic compartment in deeply growing cancers, as suggested by Fletcher and Hamberger (1974) in a study on supraglottic cancer.

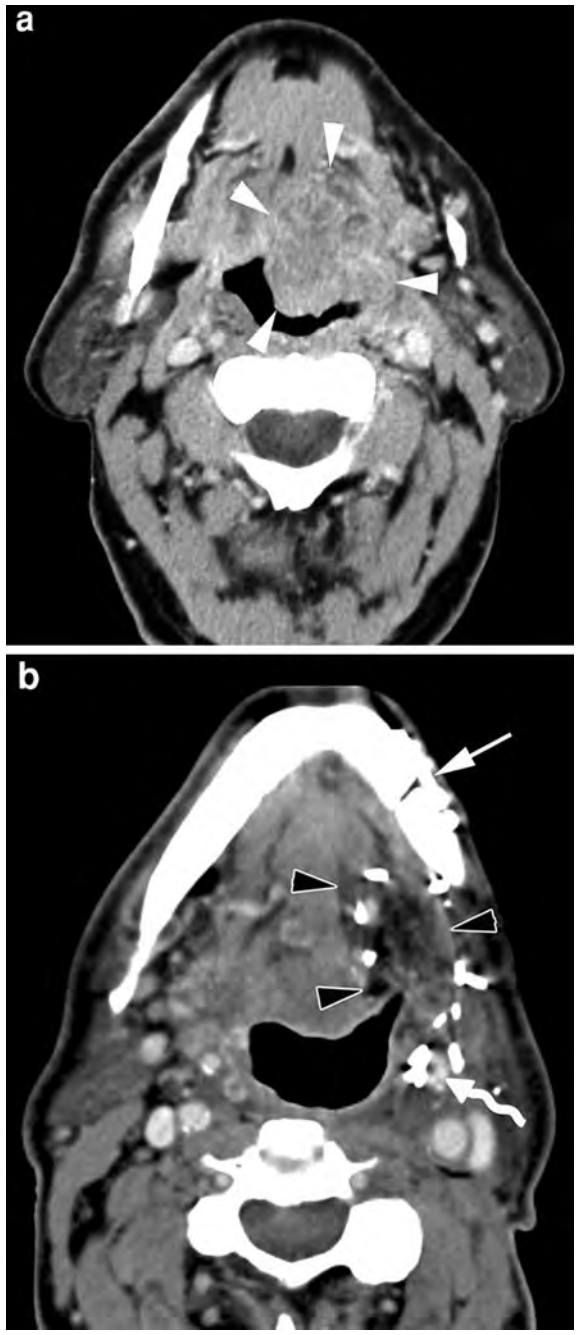

Fig. 14 Contrast-enhanced CT-images in a patient with a T3 squamous cell cancer of the tongue base. **a** Large tumor mass, slightly extending over the midline and growing into the lateral pharyngeal wall (*arrowheads*). **b** CT-study obtained 1 year after surgical resection and postoperative radiotherapy. The tumor was approached after splitting the mandible (osteotomy site and osteosynthetic plate, *white arrow*). The soft tissue defect was closed by a radial forearm flap (*black arrowheads*), whose vascular pedicle was anastomosed to the external carotid artery (*curved arrow*). The high density opacities correspond to surgical clips

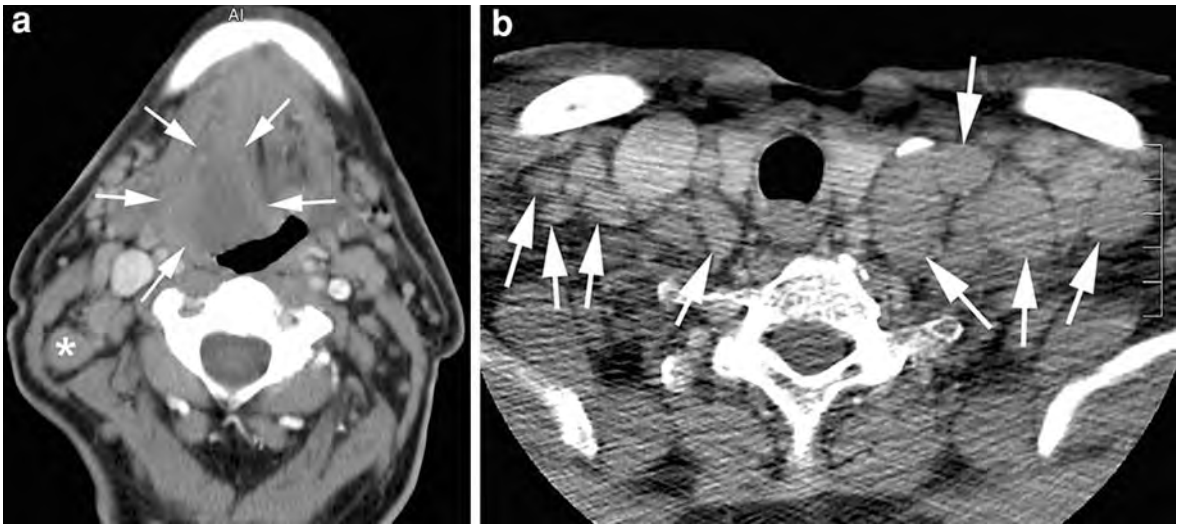

Fig. 15 Axial contrast-enhanced CT-images. **a** Infiltrating soft tissue mass (*arrows*) in the right tongue base. Ipsilaterally, a slightly enlarged lymph node is seen in level II (*asterisk*). Several of such lymph nodes were seen throughout both sides of the neck. **b** Bilaterally in the neck base, homogeneous adenopathies are present, larger on the left side. The distribution of the adenopathies is atypical for tongue base cancer, making the imaging findings suspect for non-Hodgkin lymphoma; this was confirmed histologically

Fig. 16 Axial T2-weighted spin echo image. Well-demarcated hyperintense soft tissue mass (*arrowhead*) posterolaterally in the tongue base. Biopsy revealed mucoepidermoid carcinoma

In this context, the variable degree of deep tissue infiltration by oropharyngeal cancer may dilute the volume effect.

5 Posttreatment Imaging

The expected neck tissue changes after radiotherapy are described in "Laryngeal Neoplasms". Within the oropharyngeal region, mainly thickening of the muscular pharyngeal walls, reduced volume of the tonsillar lymphoid tissue, some degree of retropharyngeal edema, and increased attenuation of the fatty tissue planes is expected. After successful irradiation, the tumor bed is expected to show similar characteristics as the surrounding normal tissues (Fig. 12).

Although currently no hard data are available on the value of surveillance imaging for oropharyngeal cancer after radiotherapy, obtaining a baseline follow-up CT or MR study 3–6 months after the end of therapy can be considered. In a number of cases, local failure can be detected at an earlier stage than by clinical examination alone. Persisting or recurring tissue asymmetry and/or increased tissue enhancement after therapy, are suspect for persisting or recurring tumor (Fig. 13). Such findings need further exploration; when no clinical correlate is apparent, one may opt to perform an additional nuclear imaging study or to obtain a follow-up CT/MR-study about 4 months later. In case of persisting or progressive tissue changes, tissue sampling is required. Initial

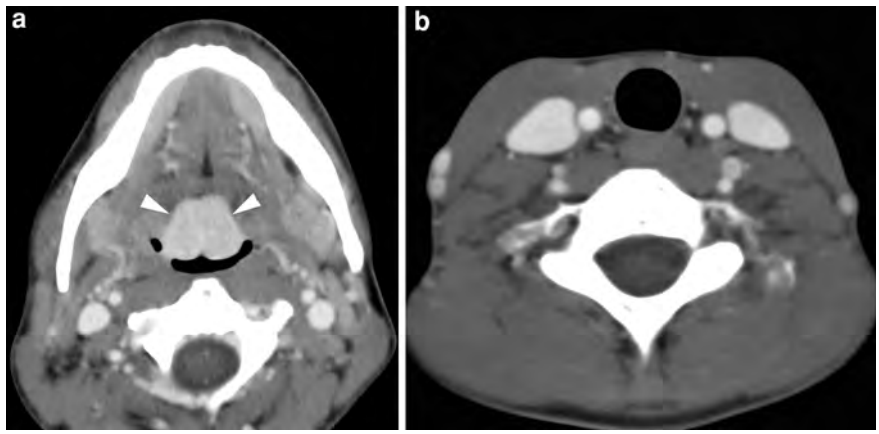

Fig. 17 Axial contrast-enhanced CT images in a patient with progressive dysphagia. **a** Strongly enhancing soft tissue mass (*arrowheads*) in tongue base midline, compatible with ectopic thyroid tissue. **b** Absence of thyroid gland at its normal position

Fig. 18 Axial contrast-enhanced CT image in a patient with a progressive neck swelling. Mass lesion (*arrowhead*) centered in and destructing the hyoid bone, with extension to surrounding structures, causing narrowing of the oropharyngeal airway. The lesion was resected; pathological study revealed papillary thyroid carcinoma, presumably arising from ectopic thyroid tissue. There was no evidence for a primary cancer in the thyroid gland

experience suggests that diffusion-weighted MRI might be helpful to identify persisting or recurrent cancer at an early stage after treatment (Vandecaveye et al. 2007).

When an oropharyngeal cancer is treated primarily by surgery, often extensive removal of soft tissues, possibly also including mandibular bone, is needed to obtain oncologically safe resection margins. To reconstruct the created tissue defects, and to obtain a better functional and/or cosmetic result, tissue transfer from a body donor site to the oropharyngeal region may be required. These flaps are vascularized by local vessels, anastomosed to the flap by microvascular techniques. Different kinds of free flaps are in use, for example cutaneous flaps to reconstruct defects in the oropharyngeal cavity, or osseous flaps (e.g. fibula) to reconstruct mandibular defects (Fig. 14). A CT or MR study, obtained about 4 months after the end of such a complex procedure, may be helpful as a baseline study allowing earlier diagnosis of subsequent tumor recurrence.

6 Other Neoplastic Disease

6.1 Non-Hodgkin Lymphoma

Because of the abundant lymphoid tissue in the oropharynx (lingual and palatine tonsils), non-Hodgkin lymphoma occurs in this region as extranodal lymphatic disease. The diagnosis of lymphoma can often be suggested based on the imaging findings, as these tumors frequently appear large and homogeneous on imaging studies. Also, adenopathies may be present at sites unusual for an untreated carcinoma (Fig. 15), or the oropharyngeal lesion may be associated with another extranodal neck lymphoma localisation (Hermans et al. 1994). Such findings, occurring in patients without risk factors for head and neck carcinoma, are suggestive of lymphoma.

Neck lymphoma is described in more detail in "Neck Lymphoma".

Fig. 19 Axial T2-weighted spin echo image (**a**) in a 32-year-old patient shows a sharply demarcated, hyperintense mass in the tongue base on the left side. The sagittal gadolinium-enhanced T1-weighted spin echo image (**b**) shows homogeneous lesion enhancement, with some areas of liquefaction. Biopsy revealed schwannoma

6.2 Salivary Gland Tumors

These oropharyngeal neoplasms originate from minor salivary glands. In the soft palate, these are often benign pleiomorphic adenomas, but in other oropharyngeal sites malignant tumors, such as mucoepidermoid and adenoid cystic carcinoma, predominate (Watkinson et al. 2000) (Fig. 16).

6.3 Other

The thyroid gland is formed during embryologic life as an epithelial proliferation from the ventral pharyngeal wall; this proliferation is known as the medial thyroid anlage and the place where it arises corresponds later to the foramen caecum, at the border between the oral tongue and the tongue base. This medial thyroid analage migrates downwards along the neck midline to its final position. Ectopic thyroid tissue can be found anywhere along this tract, but most commonly in the tongue. Patients with a lingual thyroid gland have no thyroid tissue in the neck in 70–80% of the cases (Fig. 17). Ectopic thyroid is subject to the same diseases as the anatomically correct positioned thyroid, such as nodular hyperplasia and rarely neoplastic degeneration (Fig. 18). Development of a mass lesion is often the reason why this ectopic thyroid tissue becomes symptomatic.

Other benign tumoral lesions, such as hemangioma or schwannoma, may be encountered in the oropharynx. As these masses occur submucosally, imaging is required to estimate their extent. A specific soft tissue diagnosis is usually not possible based on imaging findings, and tissue sampling is required for diagnosis (Fig. 19).

References

Bussels B, Hermans R, Reijnders A, Dirix P, Nuyts S, Van den Bogaert W (2006) Retropharyngeal nodes in squamous cell carcinoma of the oropharynx: implications for target volume delineated. Int J Radiat Oncol Biol Phys 65: 733–738

Chong VFH, Mukherji SK, Ng SHH et al (1999) Nasopharyngeal carcinoma: review of how imaging affects staging. JCAT 23:984–993

Cohan DM, Popat S, Kaplan SE, Rigual N, Loree T, Hickx WL Jr (2009) Oropharyngeal cancer: current understanding and management. Curr Opin Otolaryngol Head Neck Surg 17:88–94

Dirix P, Nuyts S (2010) Evidence-based organ-sparing radiotherapy in head and neck cancer. Lancet Oncol 11:85–91

Dubin MG, Ebert CS, Mukherji SK, Pollock HW, Amjadi D, Shockley WW (2002) Computed tomography's ability to

predict sacrifice of hypoglossal nerve at resection. Laryngoscope 112:2181–2185
Farina D, Hermans R, Lemmerling M et al (1999) Imaging of the parapharyngeal space. J Belge Radiol 82: 234–239
Fletcher GH, Hamberger AD (1974) Causes of failure in irradiation of squamous-cell carcinoma of the supraglottic larynx. Radiology 111:697–700
Ginsberg LE, DeMonte F (1998) Imaging of perineural tumor spread from palatal carcinoma. Am J Neuroradiol 19: 1417–1422
Hermans R, Lenz M (1996) Imaging of the oropharynx and oral cavity. Part I: Normal anatomy. Eur Radiol 6:362–368
Hermans R, Horvath M, De Schrijver T et al (1994) Extranodal non-Hodgkin lymphoma of the head and neck. J Belge Radiol 77:72–77
Hermans R, Op de beeck K, Van den Bogaert W et al (2001) The relation of CT-determined tumor parameters and local and regional outcome of tonsillar cancer after definitive radiation treatment. Int J Radiat Oncol Biol Phys 50:37–45
Hsu WC, Loevner LA, Karpati R et al (2005) Accuracy of magnetic resonance imaging in predicting absence of fixation of head and neck cancer to the prevertebral space. Head Neck 27:95–100
Julieron M, Kolb F, Schwaab G et al (2001) Surgical management of posterior pharyngeal wall carcinomas: functional and oncologic results. Head Neck 23:80–86
Loevner LA, Ott IL, Yousem DM et al (1998) Neoplastic fixation to the prevertebral compartment by squamous cell carcinoma of the head and neck. Am J Roentgenol 170: 1389–1394
Million RR, Cassisi NJ, Mancuso AA (1994) Hypopharynx: pharyngeal walls, pyriform sinus, postcricoid pharynx. In: Million RR, Cassisi NJ (eds) Management of head and neck cancer: a multidisciplinary approach. J.B. Lippincott Co, Philadelphia, p 516
Mukherji SK, Weeks SM, Castillo M et al (1996) Squamous cell carcinomas that arise in the oral cavity and tongue base: can CT help predict perineural or vasculair invasion? Radiology 198:157–162
Mukherji SK, Schmalfuss IM, Castelijns J, Mancuso AA (2004) Clinical applications of tumor volume measurements for predicting outcome in patients with squamous cell carcinoma of the upper aerodigestive tract. Am J Neuroradiol 25:1425–1432
Nathu RM, Mancuso AA, Zhu TC, Mendenhall WM (2000) The impact of primary tumor volume on local control for oropharyngeal squamous cell carcinoma treated with radiotherapy. Head Neck 22:1–5
Nuyts S, Dirix P, Clement PMJ, Vander Poorten V, Delaere P, Schoenaers J, Hermans R, Van den Bogaert W (2009) Impact of adding concomittant chemotherapy to hyperfractionated radiotherapy for advanced head-and-neck squamous cell carcinoma. Int J Radiat Oncol Biol Phys 73:1088–1095
Portugalli V, Borghesi A, Mossi F, Farina D, Maroldi R (2003) VIBE sequence in the diagnostic work-up of malignant neoplasms of the oropharynx. Scientific poster ECR 2003. http://epos.myecr.org/
Psyrri A, Gouveris P, Vermorken JB (2009) Human papillomavirus-related head and neck tumors: clinical and research implication. Curr Opin Oncol 21:201–205
Righi PD, Kelley DJ, Ernst R et al (1996) Evaluation of prevertebral muscle invasion by squamous cell carcinoma. Can computed tomography replace open neck exploration? Arch Otolaryngol Head Neck Surg 122:660–663
UICC, International Union Against Cancer (2009) TNM classification of malignant tumors, 7th edn. Wiley-Liss, New York, pp 30–33
Vandecaveye V, De Keyzer F, Nuyts S, Deraedt K, Dirix P, Hamaekers P, Vander Poorten V, Delaere P, Hermans R (2007) Detection of head and neck squamous cell carcinoma with diffusion weighted MRI after (chemo)radiotherapy: correlation between radiologic and histopathologic findings. Int J Radiat Oncol Biol Phys 67:960–971
Watkinson JC, Gaze MN, Wilson JA (2000) Stell & Maran's head & neck surgery, 4th edn. Butterworth Heinemann, Oxford, pp 322, 338

Neoplasms of the Nasopharynx

Cheng K. Ong and Vincent F. H. Chong

Contents

Abstract

Nasopharyngeal carcinoma (NPC) is the most common malignant tumour of the nasopharynx, although a wide variety of other nasopharyngeal tumours are also seen. NPC is believed to be the outcome of a unique interaction between underlying genetic susceptibility and surrounding environmental influences. While NPC is usually diagnosed through endoscopic examination and biopsy, imaging plays a central role in accurate tumour mapping and treatment planning, which are critical for optimal therapeutic outcome. Post-treatment imaging is equally important, for early detection of tumour recurrence or treatment complications, which would lead to timely interventions, thereby improving survival and reducing morbidity. This chapter provides a detailed description of the imaging anatomy and pathologic anatomy of the nasopharynx, incorporating the latest TNM classification of NPC. Follow-up issues, particularly on tumour recurrence and treatment complications are discussed. An overview on other neoplasms of the nasopharynx is also presented.

1 Introduction

A wide variety of malignant neoplasms may originate from the nasopharynx, of which the nasopharyngeal carcinoma (NPC) is by far the most common. NPC is a squamous cell carcinoma (SCC) with three histopathologic subtypes: keratinising SCC (WHO type 1), non-keratinising carcinoma (WHO type 2) and undifferentiated carcinoma (WHO type 3).

C. K. Ong (✉)
Department of Diagnostic Radiology,
National University Hospital, 5 Lower Kent Ridge Road,
Singapore 119074, Singapore
e-mail: cheng_kang_ong@nuhs.edu.sg

V. F. H. Chong
Yong Loo Lin School of Medicine,
National University of Singapore,
21 Lower Kent Ridge Road, Singapore 119077, Singapore

R. Hermans (ed.), *Head and Neck Cancer Imaging*, Medical Radiology. Diagnostic Imaging,
DOI: 10.1007/174_2011_377, © Springer-Verlag Berlin Heidelberg 2012

NPC is a unique malignancy, representing the outcome of interactions between underlying genetic susceptibility and surrounding environmental factors. It shows a remarkably distinct geographic and racial distribution. The incidence is highest in the Southern Chinese population of Guangdong province and Hong Kong (up to 50/100,000 population), so much so that it is known as the "Canton tumour" (Hepeng 2008). Intermediate incidence is reported in Southeast Asia, Alaskan Eskimos and the Mediterranean basin (15–25/100,000 population) (Chan et al. 2002; Parkin et al. 2002). Epidemiological studies have linked childhood consumption of locally preserved food to the development of NPC in these high-risk populations (Yu and Yuan 2002).

NPC is more common in males, with a male to female ratio of 2–3:1. It has a bimodal age distribution, peaking at 50–60 years of age with a smaller peak during late childhood (Jeyakumar et al. 2006).

The link between Epstein–Barr virus (EBV) and NPC was first discovered by Old et al. (1966). It is currently hypothesised that EBV plays a critical role in transforming nasopharyngeal epithelial cells into invasive tumours (Lo et al. 2004). Most patients with NPC show consistently high titres of EBV-specific IgA antibodies and these antibodies are useful screening markers for early detection of NPC.

NPC is distinct from the other head and neck squamous cell carcinomas. It shows aggressive local infiltration with a high propensity for cervical nodal metastasis despite apparently early primary lesions. Systemic spread is also common in locally advanced disease. Radiation therapy remains the primary treatment modality for early disease, while concurrent chemoradiation therapy is now the standard of care for locally advanced tumours in order to improve local control and limit distant metastasis (NCCN 2008; Chan and Felip 2008). Surgery plays a minor role, reserved for resection of residual or recurrent disease in the nasopharynx or cervical nodes.

2 Imaging Anatomy of the Nasopharynx

The nasopharynx is an inverted J-shaped muscular-aponeurotic sling suspended from the central skull base (Teresi et al. 1987). The roof of the nasopharynx abuts the basisphenoid and slopes posteroinferiorly along the clivus to the upper cervical vertebrae. Anteriorly, it merges with the nasal cavity. Inferiorly, the soft palate separates the nasopharynx from the oropharynx. On axial imaging, the C1/C2 junction is generally accepted as the level of demarcation between nasopharynx and oropharynx (Dubrulle et al. 2007).

The pharyngobasilar fascia, a tough aponeurosis that extends from the superior constrictor muscle to the skull base, provides the principal framework for maintaining the configuration of the nasopharynx. The foramen lacerum is within the confines of the pharyngobasilar fascia and is thus part of the nasopharyngeal roof. This foramen presents a route for nasopharyngeal tumours to access the cavernous sinus and intracranial cavity.

The eustachian tube and levator veli palatini muscle enter the nasopharynx through the sinus of Morgagni, a posterolateral defect in the pharyngobasilar fascia. The eustachian tube opens anteriorly (on axial images) and inferiorly (on coronal images) to the torus tubarius (distal cartilaginous end of the eustachian tube). The lateral pharyngeal recess (fossa of Rosenmueller) is seen posterior (on axial images) and superior (on coronal images) to the torus tubarius, partly due to the inverted J-configuration of the torus tubarius. The lateral pharyngeal recess is the most common site of origin of NPC (Fig. 1). However, these recesses may show an asymmetric expansion in normal individuals, and such asymmetry should not be mistaken as evidence for tumour (Fig. 1).

The parapharyngeal space is lateral to the nasopharynx and separates it from the masticator space. Displacement or obliteration of the parapharyngeal fat is an important sign of tumour infiltration. The carotid space is located posterior to the parapharyngeal space and forms the posterolateral border of the nasopharynx. Between the nasopharyngeal mucosal space and the prevertebral muscles is the retropharyngeal space, within which are the medial and lateral retropharyngeal nodes. The lateral retropharyngeal nodes (nodes of Rouviere) constitute the first echelon nodes in the lymphatic drainage of the nasopharynx. The medial retropharyngeal nodes are rarely visible on imaging.

3 Imaging of Pathologic Anatomy of the Nasopharynx

NPC is commonly isodense to muscle on non-enhanced CT. It is usually hypo- to iso-intense and mildly hyperintense to muscle on T1-weighted and

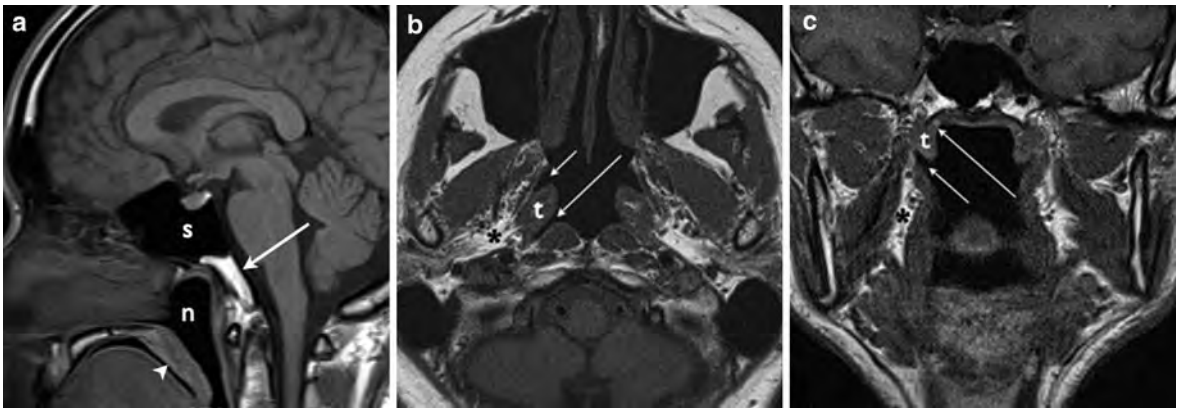

Fig. 1 Imaging anatomy of the nasopharynx. **a** Sagittal T1-weighted MR image shows the nasopharynx (n), sphenoid sinus (s), clivus (*arrow*) and soft palate (*arrowhead*). **b** Axial T1-weighted MR image shows the right eustachian tube opening (*short arrow*), torus tubarius (t) and lateral pharyngeal recess (*long arrow*). The hyperintense fat in the parapharyngeal space lies laterally (*asterisk*). Note asymmetry of the lateral pharyngeal recesses, a not infrequent finding. **c** Coronal T1-weighted MR image shows the right lateral pharyngeal recess (*long arrow*), torus tubarius (t) and eustachian tube opening (*short arrow*). The parapharngeal space is again seen laterally (*asterisk*)

T2-weighted MR images, respectively. Mild to moderate tumour enhancement is often seen following intravenous contrast on both CT and MRI.

3.1 Tumour Spread

Most NPC originate from the lateral pharyngeal recess and spread submucosally with early infiltration of the deep cervical spaces. Tumour involvement of the adjacent eustachian tube orifice or levator veli palatini (which opens the orifice during swallowing) commonly results in serous otitis media (Fig. 2). Beyond the nasopharynx, NPC spreads along well-defined routes and the following patterns of spread may be seen in various combinations (Sham et al. 1991a; Chong and Fan 1998a).

3.1.1 Anterior Spread

NPC often extends anteriorly into the nasal cavity. The latest seventh edition (2009) of the international union against cancer (UICC) TNM Classification of Malignant Tumours, which was published in collaboration with the American joint committee on cancer (AJCC), has reclassified NPC invading the nasal cavity as T1 lesions instead of the previously designated T2a (Tables 1 and 2).

From the nasal fossa, tumours may spread through the sphenopalatine foramen into the pterygopalatine fossa. The earliest imaging sign of pterygopalatine fossa involvement is obliteration of the normal fat content (Fig. 3). The pterygopalatine fossa is a major crossroad within the deep face, from where tumours may infiltrate:

- The maxillary nerve and spread perineurally through the foramen rotundum into the intracranial cavity.
- Along the vidian canal posteriorly through the foramen lacerum into the petrous carotid canal.
- Laterally through the pterygomaxillary fissure into the masticator space (Fig. 3).
- Superiorly through the inferior orbital fissure into the orbital apex, with subsequent intracranial extension via the superior orbital fissure (Fig. 4).

Advanced tumours may also erode the walls of the maxillary sinus.

3.1.2 Lateral Spread

This is the most common direction of tumour spread, often through the sinus of Morgagni (essentially a gap in the barrier that is the pharyngobasilar fascia) posterolaterally into the parapharyngeal space. Further laterally, the tumour may invade the masticator space (Fig. 5). Invasion of the muscles of mastication (notably the medial and lateral pterygoid muscles) often cause trismus (Chong 1997). Within the masticator space, the mandibular nerve is vulnerable to tumour infiltration, resulting in denervation atrophy of the muscles of mastication.

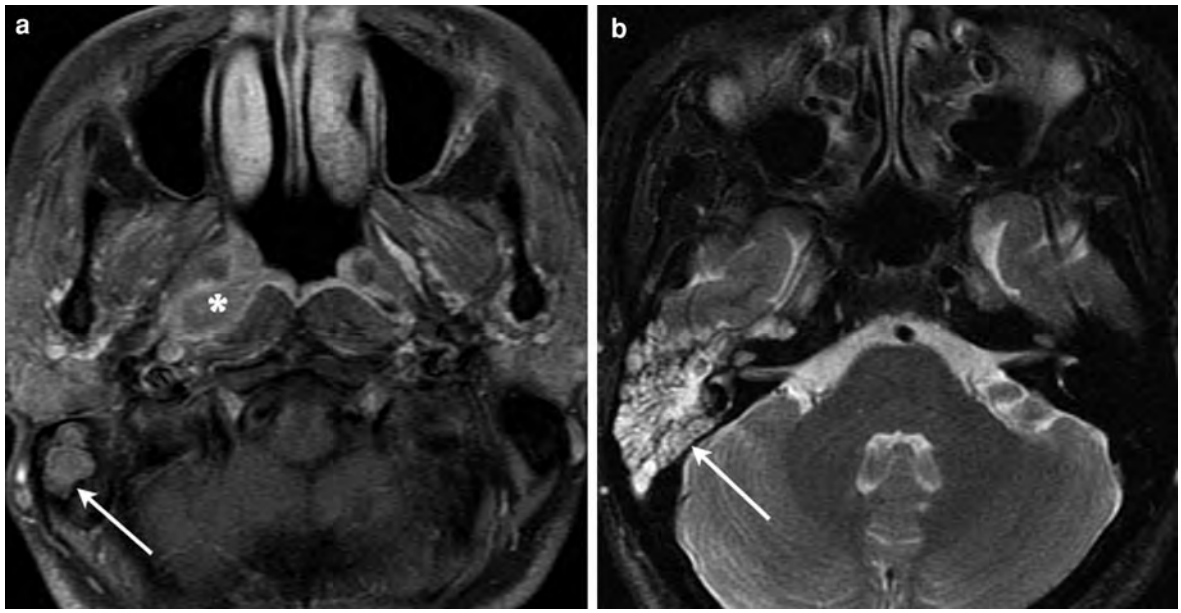

Fig. 2 32-year-old man with right-sided conductive hearing loss. **a** Axial contrast-enhanced fat-saturated T1-weighted MR image shows a nasopharyngeal carcinoma arising from the right lateral pharyngeal recess (*asterisk*). Fluid within the air-cells in the right mastoid tip is evident (*arrow*). **b** Axial fat-saturated T2-weighted image more superiorly shows prominent right serous otomastoiditis (*arrow*), secondary to eustachian tube dysfunction

Table 1 Nasopharyngeal carcinoma: seventh edition TNM classification (2009)

T—primary tumour	
T1	Tumour confined to nasopharynx, or extends to oropharynx and/or nasal cavity
T2	Tumour with parapharyngeal extension
T3	Tumour invades bony structures of skull base and/or paranasal sinuses
T4	Tumour with intracranial extension and/or involvement of cranial nerves, hypopharynx, orbit, or with extension to the infratemporal fossa/masticator space
N—regional lymph nodes	
Nx	Regional lymph nodes cannot be assessed
N0	No regional lymph node metastasis
N1	Unilateral metastasis, in cervical lymph node(s), and/or unilateral or bilateral metastasis in retropharyngeal lymph nodes, 6 cm or less in greatest dimension, above the supraclavicular fossa
N2	Bilateral metastasis in cervical lymph node(s), 6 cm or less in greatest dimension, above the supraclavicular fossa
N3	Metastasis in cervical lymph node(s) >6 cm in dimension or in the supraclavicular fossa
-N3a	->6 cm in dimension
-N3b	-extension in the supraclavicular fossa

Note**:** Midline nodes are considered ipsilateral nodes

Animal models show that in the first 4 weeks of muscle denervation, there is a relative decrease in intracellular water with a relative increase in extracellular water, although the total amount of tissue water remains unchanged (Chong 2004). With time, muscular atrophy associated with fatty

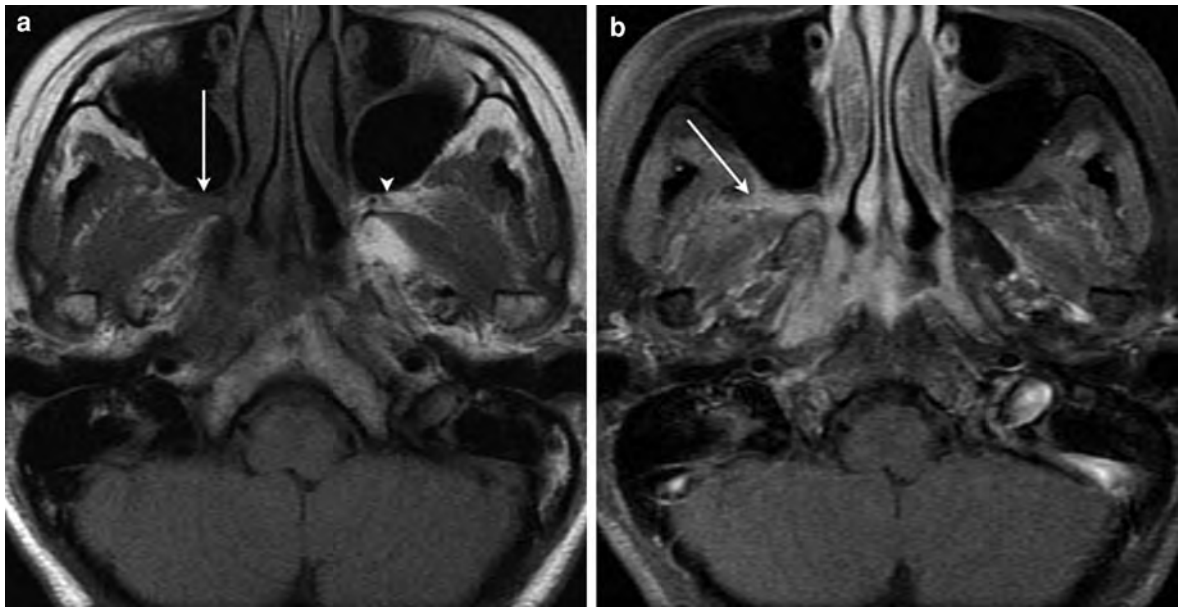

Fig. 3 **a** Axial T1-weighted MR image shows a nasopharyngeal carcinoma spreading through the right sphenopalatine foramen into the right pterygopalatine fossa (*arrow*). Note the normal hyperintense fat in the contralateral pterygopalatine fossa (*arrowhead*). **b** Axial contrast-enhanced fat-saturated T1-weighted MR image shows the tumour invading the right masticator space through the pterygomaxillary fissure (*arrow*)

Fig. 4 A series of three axial contrast-enhanced CT images from inferior to superior. Image **a** shows a nasopharyngeal carcinoma extending through an enlarged left sphenopalatine foramen (*arrow*) into the pterygopalatine fossa (*asterisk*). Image **b** shows the tumour spreading superiorly through the inferior orbital fissure into the left orbital apex (*arrow*). Image **c** shows the carcinoma infiltrating intracranially via the superior orbital fissure and involving the left cavernous sinus (*arrows*)

infiltration takes place. In the acute to subacute phases, T2-weighted MR images show hyperintense signals in the muscles simulating oedema. This is because the T2 of extracellular water is longer than the T2 of intracellular water. Increased enhancement is also seen in these muscles, due to the underlying increase in perfusion and accumulation of contrast medium in the extracellular space. In the chronic phase, there is muscle atrophy with hyperintense signals on T1 and fast spin-echo T2-weighted MR images due to fatty replacement. This should be distinguished from direct tumour infiltration of the muscles, which often result in an increase (rather than decrease) in the muscle bulk. The MR signal changes

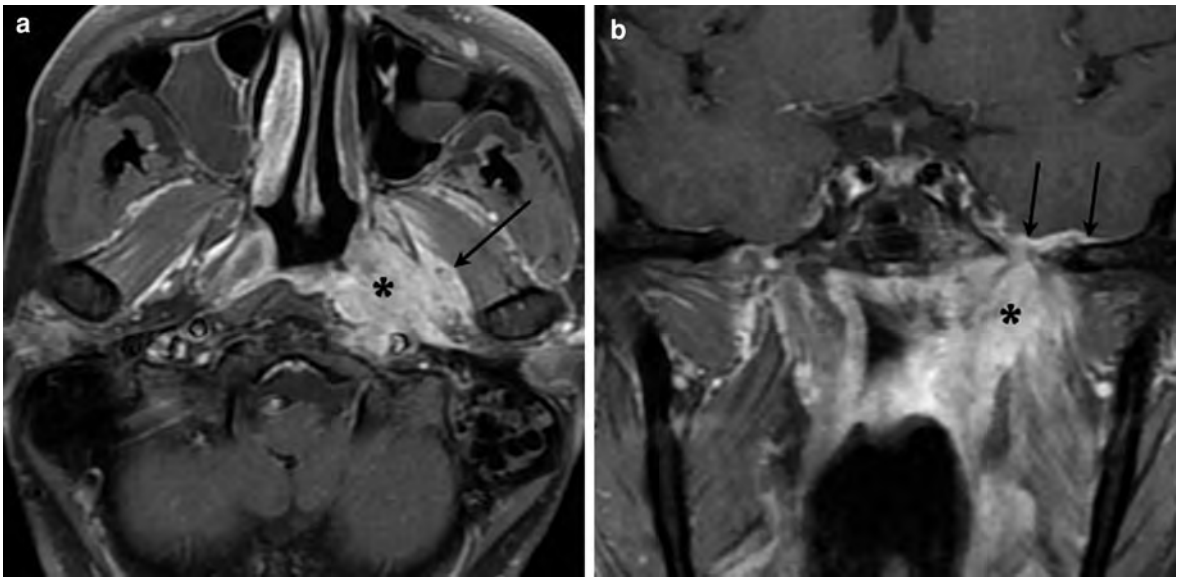

Fig. 5 Nasopharyngeal carcinoma with perineural spread. **a** Axial contrast-enhanced fat-saturated T1-weighted MR image shows a left-sided nasopharyngeal carcinoma (*asterisk*) that spreads laterally across the parapharyngeal space to invade the left masticator space (*arrow*). **b** Coronal contrast-enhanced fat-saturated T1-weighted MR image shows the tumour (*asterisk*) spreading perineurally along the left mandibular nerve through the foramen ovale into the intracranial cavity, with resultant dural thickening and enhancement on the floor of the left middle cranial fossa (*arrows*)

in denervation atrophy are also more generalised and higher in intensity than malignant infiltration of the muscles.

3.1.3 Posterior Spread

Posteriorly, NPC may infiltrate the retropharyngeal and prevertebral spaces. In neglected patients with advanced diseases, the vertebrae are destroyed with tumour growing into the spinal canal. Posterolateral extension of tumour often involves the nasopharyngeal carotid space and compromises the glossopharyngeal, vagus, spinal accessory and hypoglossal nerves (Fig. 6). Subsequent superior perineural or perivascular spread may then invade the jugular foramen and gain access into the posterior cranial fossa (Chong and Fan 1996).

Involvement of the hypoglossal nerve results in hypotonia and atrophy of the tongue musculature. The imaging features are similar to those observed in the muscles of mastication following tumour infiltration of the mandibular nerve, although they may be subtle in the early stage of disease. The affected side of the tongue may also be seen to drop posteriorly in the axial images of a supine patient (Chong and Fan 1998b) (Fig. 6). It is important to note that this posterior displacement of the denervated tongue may simulate an apparent increase in its longitudinal dimension mimicking a mass, and should be recognised for what it actually is (Harnsberger and Dillon 1985).

3.1.4 Superior Spread

The foramen lacerum is within the confines of the pharyngobasilar fascia and for a long time, it was believed to provide an unimpeded route of tumour extension into the intracranial cavity. Many NPC also spread superiorly through direct skull base erosion (Sham et al. 1991b) (Fig. 7). Skull base invasion is seen in approximately 12% of the patients on CT, and up to 31% on MRI (Chong et al. 1996; Roh et al. 2004).

Once the tumour invades the masticator space, the mandibular nerve also serves as a natural conduit of least resistance for perineural tumour spread through the foramen ovale into the intracranial cavity (Ong and Chong 2010). Dural thickening and enhancement along the floor of the middle cranial fossa may represent the earliest signs of intracranial extension (Fig. 5). However, it should also be noted that dural thickening per se does not indicate definite

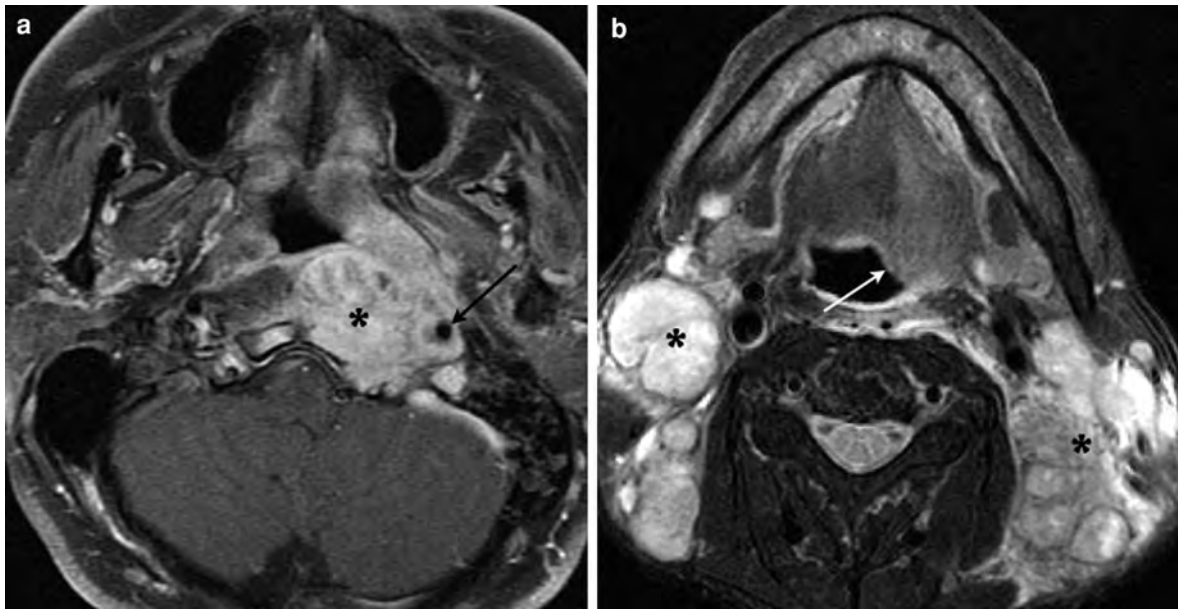

Fig. 6 Hypoglossal denervation. **a** Axial contrast-enhanced fat-saturated T1-weighted MR image shows a locally advanced nasopharyngeal carcinoma (*asterisk*) extending to the left carotid space, encasing the internal carotid artery (*arrow*). **b** Axial fat-saturated T2-weighted MR image of the same patient shows atrophy and increased signal intensity in the left half of the tongue, due to tumour involvement of the left hypoglossal nerve. This denervated side of the tongue is also seen to drop posteriorly in this supine patient as a result of hypotonia (*arrow*). Multiple enlarged cervical lymph nodes are evident bilaterally (*asterisks*)

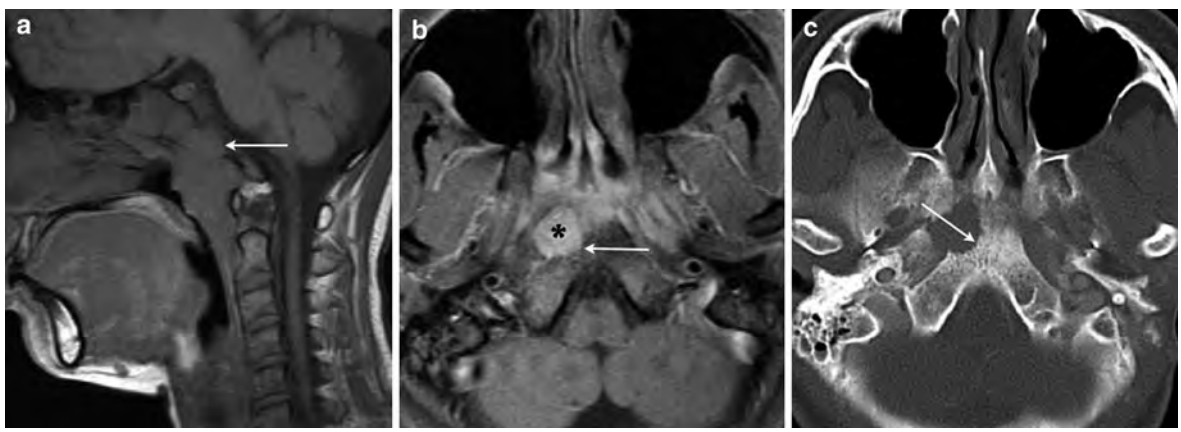

Fig. 7 **a** Sagittal T1-weighted MR image shows a nasopharyngeal carcinoma with predominantly superior spread and direct invasion of the skull base (*arrow*). **b** Axial contrast-enhanced fat-saturated T1-weighted MR image shows the enhancing tumour (*asterisk*) infiltrating the clivus (*arrow*). **c** The corresponding axial bone-algorithm CT image shows tumour erosion on the right side of the clivus (*arrow*)

malignant infiltration, as it may be secondary to reactive inflammation.

3.1.5 Inferior Spread

Many NPC show preferential spread inferiorly along the submucosal plane or through the retropharyngeal space, thus escaping clinical or endoscopic detection. Inferior tumour extension into the oropharynx is readily appreciated on coronal or sagittal MR images. On axial sections, the oropharynx is deemed involved when the tumour is seen below the C1/C2 junction (Fig. 8).

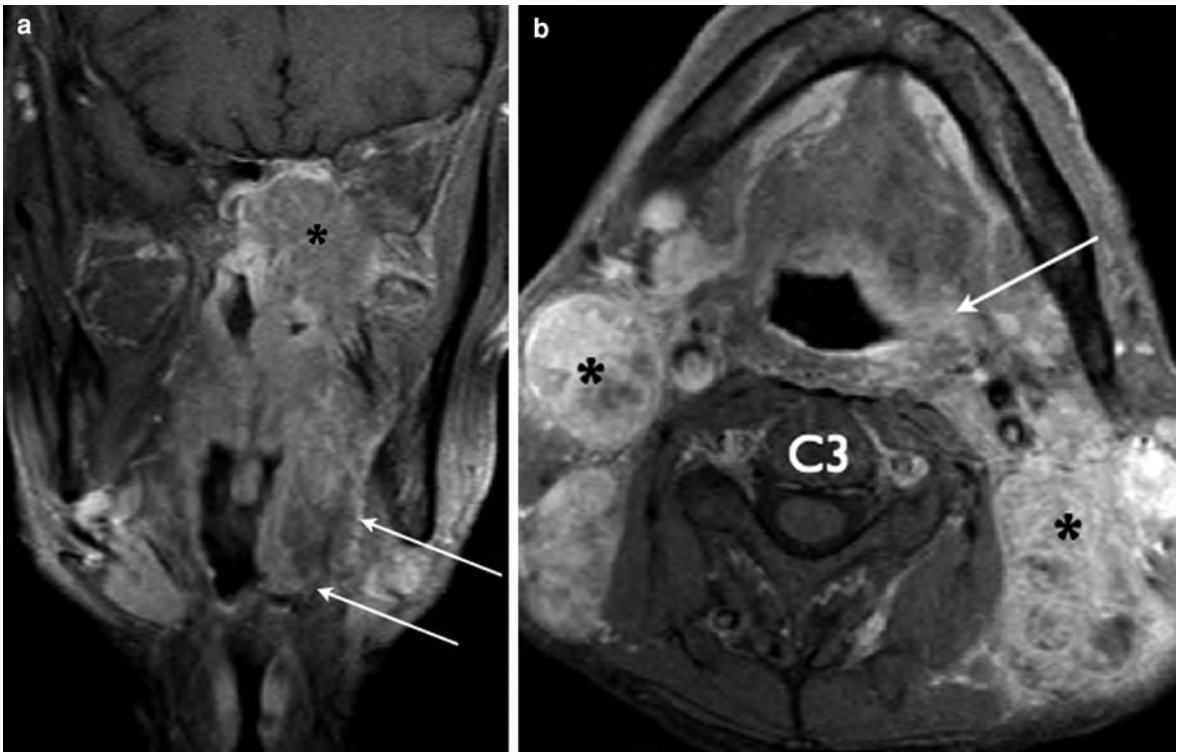

Fig. 8 **a** Coronal contrast-enhanced fat-saturated T1-weighted MR image shows a large left-sided nasopharyngeal carcinoma with skull base erosion and intracranial extension (*asterisk*), as well as inferior spread into the oropharynx (*arrows*). **b** Axial contrast-enhanced fat-saturated T1-weighted MR image at the level of C3 shows tumour along the left side of the oropharynx (*arrow*). Extensive bilateral cervical lymphadenopathy is evident (*asterisks*)

As per the seventh edition of TNM Classification, NPC extending into the oropharynx is now considered as T1 tumours, as compared to the previously designated T2a lesions (Table 1).

3.2 Nodal Metastasis

Cervical nodal metastasis is very common in NPC, and is often the initial presenting complaint. Enlarged cervical nodes are evident in up to 75% of patients at presentation, with 80% of them having bilateral lymphadenopathy (Chong and Ong 2008).

Although retropharyngeal nodes are generally considered as the first echelon nodes of NPC, they are only seen in 65% of patients with nodal involvement (Chong et al. 1995) (Fig. 9). In the remaining 35% of patients, the metastases bypass the retropharyngeal nodes and spread directly to the internal jugular nodes. On MRI, the short axes of the normal lateral retropharyngeal nodes are usually less than 4.5 mm. Any lateral retropharyngeal node with a short axis of 5 mm or more should be regarded as malignant (Lam et al. 1997; King et al. 2000). As medial retropharyngeal nodes are usually not visible, any medial retropharyngeal nodes detected on MRI should be considered as highly suspicious of metastatic involvement (Wang et al. 2009). Retropharyngeal lymphadenopathy is now, for the first time, included in the latest edition of TNM Classification (Table 1).

Cervical nodal metastases in NPC, as a rule, show an orderly inferior spread and the affected nodes in the upper neck are generally larger than those more inferiorly. This reflects the route of spread of the tumour cells along the lymphatic system and has prognostic implications. The cervical nodes may be viewed as successive defensive barriers, with the supraclavicular nodes being the last line of defence.

The supraclavicular fossa is formed by three points: (1) the superior margin of the sternal end of the clavicle; (2) the superior margin of the lateral end of the clavicle; (3) the point where the neck meets the

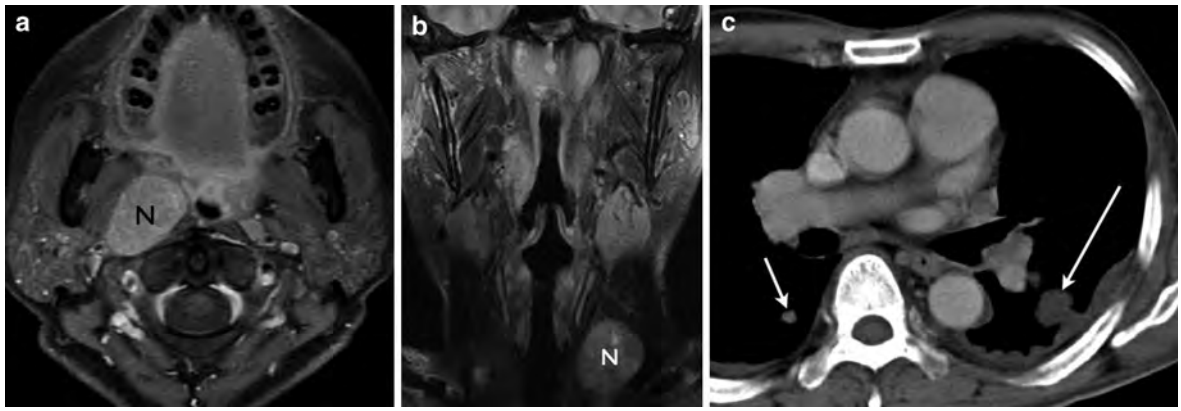

Fig. 9 Lymphadenopathy in nasopharyngeal carcinoma. **a** Axial contrast-enhanced fat-saturated T1-weighted MR image shows an enlarged right lateral retropharyngeal node (N), the first echelon node for nasopharyngeal carcinoma. **b** Coronal fat-saturated T2-weighted MR image shows an enlarged malignant left supraclavicular node (N). **c** Axial contrast-enhanced CT image of the thorax of the same patient reveals a metastasis in the left lung with pleural involvement (*long arrow*). A right pulmonary metastasis is also seen (*short arrow*)

shoulder. Nodes in the supraclavicular fossa include caudal portions of levels IV and V. Failure of supraclavicular nodes to contain the malignant cells results in spilling into the thoracic duct and eventually the systemic circulation. Supraclavicular lymphadenopathy (N3b disease) is therefore associated with a high risk of systemic metastasis.

3.3 Systemic Metastasis

NPC has a high incidence of distant metastasis (up to 41%) when compared with the other head and neck tumours (5–24%). Common sites of metastasis include bone (20%), lung (13%) and liver (9%) (Sham et al. 1990).

The risk of metastasis increases with more advanced primary tumours. Tumours infiltrating the parapharyngeal space often invade the parapharyngeal venous plexus (which drains via the retropharyngeal and facial veins into the internal jugular vein) and result in dissemination of disease through the systemic circulation (Xiao et al. 2002).

In addition, Kumar et al. showed that there was a direct correlation between the prevalence of metastasis and the N-classification of NPC. The positive yield of their metastatic work-up was 0, 1.8, 4.8 and 14.3% for N0, N1, N2 and N3 diseases, respectively (Kumar et al. 2004).

3.4 Tumour Volume

Primary tumour volume is a significant independent prognostic factor in malignant tumours, including NPC (Wei and Sham 2005). Larger tumours are associated with increased tumour clonogens and other adverse radiobiologic factors such as tumour hypoxia, and thus relative radioresistance (Johnson et al. 1995; Lartigau et al. 1993; Bentzen et al. 1991).

There is approximately a 1% increase in the risk of local control failure with every 1 cm^3 increase in the primary tumour volume (Sze et al. 2004). Early studies have also revealed a positive correlation between NPC tumour volume and the TNM classification system (Chong et al. 2006). Such observations have prompted suggestions to incorporate tumour volume into the TNM staging system. In the current system, a small tumour involving a critical area is often assigned a higher T-classification than a larger tumour confined within a defined anatomic site (Chen et al. 2004).

However, technical difficulty in standardising accurate tumour volume measurement has prevented it from being used routinely in daily practice. Measurement of tumour volume is tedious and involves operator-dependent tracing of the tumour outline. Several semi-automated systems of tumour volume measurement are now available for NPC, reducing inter- and intra-operator variability (Rasch et al. 1997; Chong et al. 2004).

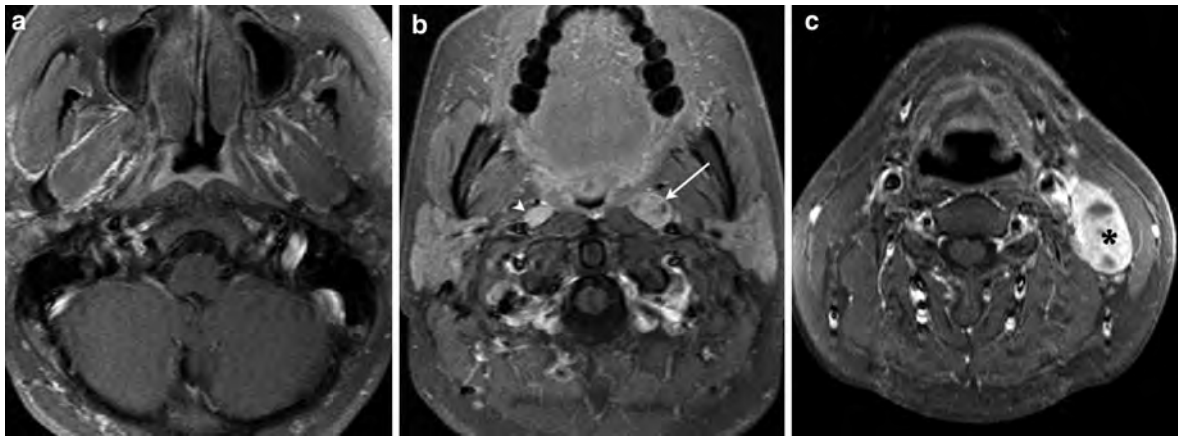

Fig. 10 Occult nasopharyngeal carcinoma in a 61-year-old male who presented with left cervical lymphadenopathy. **a** Axial contrast-enhanced fat-saturated T1-weighted MR image through the nasopharynx shows no evidence of any tumour, particularly in the lateral pharyngeal recesses. **b** Axial contrast-enhanced fat-saturated T1-weighted MR image at the level of the oropharynx shows an enlarged left lateral retropharyngeal node with evidence of necrosis (*arrow*). A smaller right lateral retropharyngeal lymph node is also seen (*arrowhead*). **c** Axial contrast-enhanced fat-saturated T1-weighted MR image at the level of the hypopharynx shows a markedly enlarged and necrotic left cervical node (*asterisk*), the presenting complaint of the patient

4 Clinical Imaging

Multi-planar magnetic resonance imaging (MRI), using a dedicated head and neck coil, is the modality of choice for evaluation of NPC. Axial and coronal contrast-enhanced T1-weighted images with fat saturation allow precise mapping of the tumour (particularly submucosal infiltration, skull base marrow replacement, perineural and intracranial spreads), and thus accurate staging of the disease (Chong et al. 1999; Lau et al. 2004). High resolution bone-algorithm computed tomography (CT) remains valuable in depicting early skull base cortical bone erosions.

Imaging of the nasopharynx is required in three groups of patients:

- those who present with cervical lymphadenopathy with no endoscopic evidence of any nasopharyngeal lesion;
- those who present with a nasopharyngeal mass for radiologic evaluation and staging;
- those who have undergone treatment for tumour surveillance and assessment of possible treatment complications.

4.1 Occult Malignancy

NPC may spread submucosally with relatively normal endoscopic findings. These patients commonly present with enlarged cervical lymph nodes (Fig. 10). Imaging is mandatory in such patients, especially in the high-risk population. MRI is superior to CT in detecting and delineating submucosal tumours.

As noted above, the lateral pharyngeal recesses may appear asymmetric in normal individuals, and this should not be confused as sign of underlying malignancy (Fig. 1). Residual nasopharyngeal lymphoid tissue may also occasionally mimic neoplasms. T2-weighted MR images show optimal contrast between the hyperintense lymphoid tissue and the underlying lower signal intensity muscles. Lymphoid tissues enhance following intravenous contrast, but is located superficially and never penetrates the underlying muscles.

4.2 Staging of Malignancy

Most patients undergo imaging evaluations following endoscopic confirmation of a nasopharyngeal mass. With the advent of 3D conformal radiation therapy

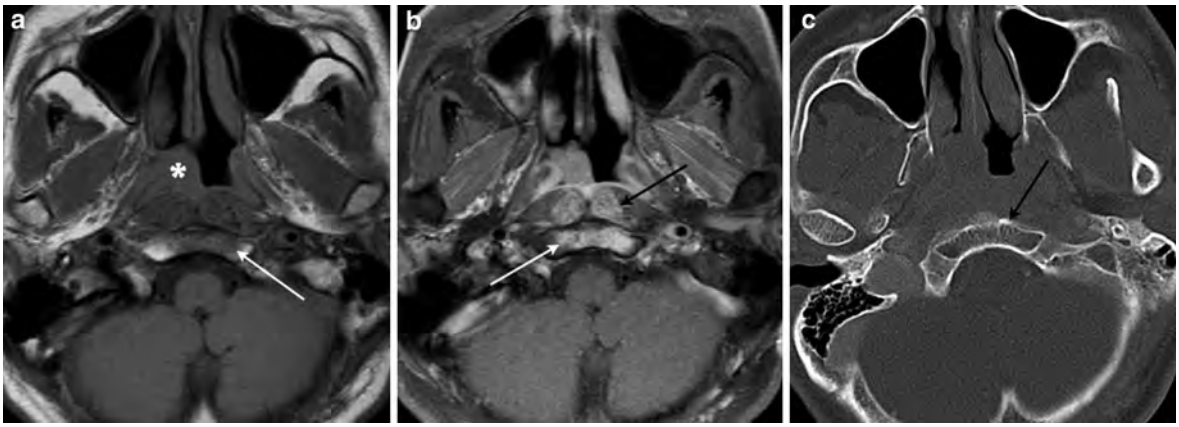

Fig. 11 **a** Axial T1-weighted MR image shows a right nasopharyngeal carcinoma (*asterisk*), with marrow signal change in the clivus (*arrow*). **b** Axial contrast-enhanced fat-saturated T1-weighted MR image shows enhancement in the marrow of the clivus (*white arrow*), as well as the prevertebral muscles (*black arrow*). **c** Axial bone-algorithm CT image, however, shows no definite evidence of bone erosion (*arrow*)

and intensity modulated radiation therapy (IMRT), MRI is the preferred imaging modality for more accurate tumour mapping.

One prominent issue related to the use of MRI in NPC staging is the significance of skull base marrow signal changes (Fig. 11). These marrow changes may represent tumour infiltration, reactive inflammation or both. As histopathologic verification of skull base lesions cannot be easily performed, the specificity of this observation remains unknown. If these changes are considered tumour invasion, MRI will upstage a certain number of patients. Nevertheless, in clinical practice, skull base with marrow changes detected on MRI is included within the radiation treatment field.

The detection of systemic metastasis alters prognosis and treatment planning. Imaging surveillance (which may include chest X-ray or CT of the thorax, ultrasound or CT of the abdomen and whole body bone scan) is indicated in patients with advanced disease who are more susceptible to metastasis. On the other hand, since the incidence of metastasis is relatively low in patients with early NPC (stage I and II), the validity of metastatic work-up in every patient diagnosed with NPC remains debatable.

There is evidence that flurodeoxyglucose positron emission tomography (FDG-PET) or PET CT has a higher sensitivity and specificity in detecting visceral and skeletal metastases when compared with CT thorax and abdomen and whole body radioisotope bone scan, respectively (Liu et al. 2007a, b; Chua et al. 2009; Ng et al. 2009). Nevertheless, the role of PET and PET CT in the routine staging of NPC is yet to be fully established.

4.3 Follow-up

Patients are often followed up clinically at 1 to 2-monthly intervals in the first year, 2 to 3-monthly intervals in the second year, 3 to 4-monthly intervals in the third year and 6-monthly intervals thereafter. The primary aims of post-treatment imaging include early detection of recurrent disease and treatment complications, which allow early treatment, thereby decreasing morbidity and improving survival rates.

4.3.1 Tumour Recurrence

The distinction between residual and recurrent tumour is important as it affects the treatment strategies and management plans. Residual disease is defined as incomplete tumour resolution following 3 months of therapy. On the other hand, designation of tumour recurrence necessitates documentation of a disease free period.

Residual disease after radiation therapy may be due to firstly, the relative radio-insensitivity of the tumour; secondly, a "geographic miss" on the irradiation field; thirdly, insufficient radiation dose and fourthly, too long the duration taken to deliver the dose. Residual or recurrent tumour is usually detected

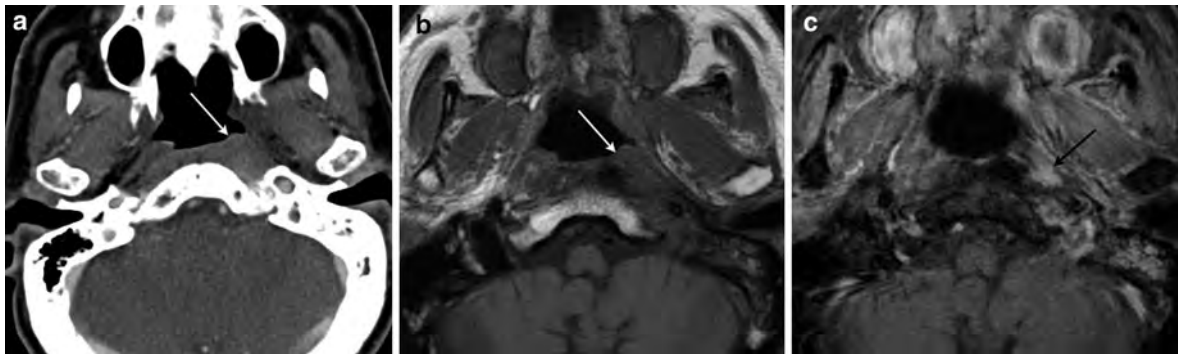

Fig. 12 Post-treatment fibrosis mimicking residual or recurrent tumour. **a** Axial contrast-enhanced CT image 12 months following treatment for a left-sided nasopharyngeal carcinoma shows residual bulky soft tissue in the region of the left lateral pharyngeal recess (*arrow*). **b** Axial T1-weighted MR image 4 -years later shows persistent prominent soft tissue in the region of the left lateral pharyngeal recess (*arrow*). **c** Axial contrast-enhanced fat-saturated T1-weighted MR image shows some enhancement deep in the left lateral pharyngeal recess (*arrow*). Biopsy was performed due to concern of a recurrent tumour. The histology showed squamous mucosa with parakeratosis and lymphoplasmacytic infiltrate, but no evidence of dysplasia or malignancy

by endoscopy. Imaging may confirm deep recurrences suspected on the basis of clinical symptomology but are not apparent on endoscopy, and delineate the tumour extent.

Post-radiation granulation tissue and fibrosis may mimic recurrent tumour, especially on CT since their attenuation values are similar. Even on MRI, early fibrous tissue is often indistinguishable from neoplasm as it appears hyperintense on T2-weighted images and show contrast enhancement, due to its hypercellularity and hypervascularity, respectively. On the other hand, mature scar, which is hypocellular and hypovascular is characterised by low T2 signal intensity and does not show contrast enhancement.

Differentiating tumour recurrence from fibrosis on imaging can be challenging (Fig. 12). Regular follow-up is therefore essential. Imaging studies at 6 and 12 months after radiation therapy are important. These scans can be used as baseline studies for comparison with future imaging over the next few years. A stable appearance provides reassurance that the abnormality seen is most likely due to underlying post-radiation changes. PET CT is useful in detecting post-treatment NPC recurrence, by co-registering tracer uptake with anatomic information. A systematic review of 21 studies showed that FDG-PET was significantly more sensitive (95%) in detecting residual or recurrent NPC when compared with MRI (78%) and CT (76%) (Liu et al. 2007a, b).

4.3.2 Treatment Complications

The complications of radiation therapy for NPC may be categorised into neurological and non-neurological sequelae. The advent of intensity modulated radiation therapy (IMRT) has resulted in a significant decrease in the severity and frequency of these complications.

4.3.3 Neurological Complications

4.3.3.1 Temporal Lobe Necrosis

NPC shows a high propensity of skull base invasion and intracranial extension through perineural spread, which necessitates adequate radiation coverage of the skull base and middle cranial fossa. The effective radiation dose for tumour control often exceeds the tolerance limit of neural tissues, resulting in significant risk of radiation-induced brain injury.

The reported incidence of temporal lobe necrosis is relatively low, ranging from 0 to 6% (Lee et al. 2005, 2009; Yeh et al. 2005; Kam et al. 2004). However, temporal lobe necrosis is probably under diagnosis as approximately 16% of these patients remain asymptomatic while up to 39% of them present with vague and non-specific symptoms (Lee et al. 1992). The latent period ranges from 1.5 to 13 years, with a median of 5 years.

The medial and inferior aspects of the temporal lobes are particularly at risk, since they are included in the radiation field. Cerebral oedema is the earliest radiologic features, followed by necrosis. Necrotic

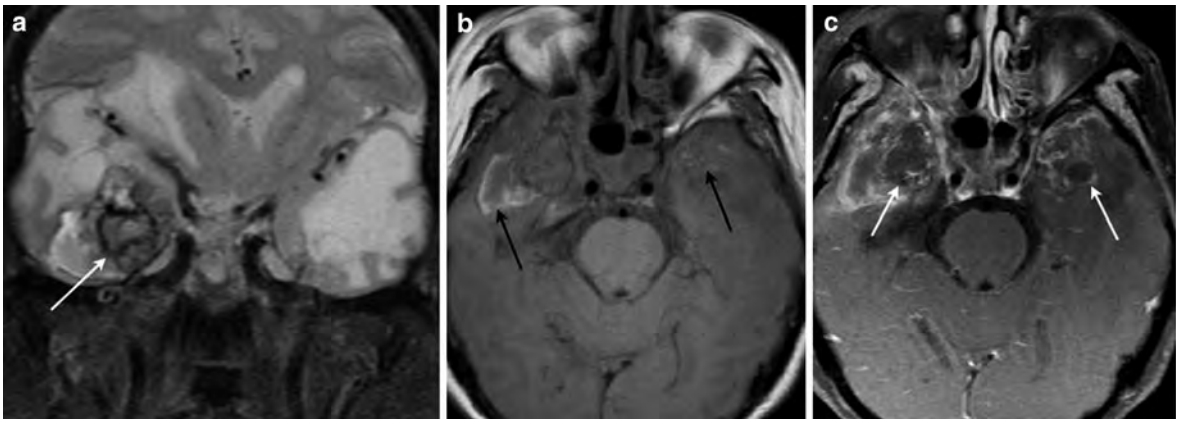

Fig. 13 Radiation-induced temporal lobe necrosis. **a** Coronal fat-saturated T2-weighted MR image shows bilateral cystic temporal lobe necrosis with florid cerebral oedema. The low signal intensities in the right temporal lobe are due to associated haemorrhage (*arrow*). **b** Axial T1-weighted MR image shows hyperintense methaemoglobin (*arrows*) in both temporal lobes, more so on the right side, in keeping with subacute haematomas. **c** Axial contrast-enhanced fat-saturated T1-weighted MR image shows bilateral heterogeneous intra-axial enhancement characteristic of temporal lobe necrosis (*arrows*)

foci in the white matter are characteristically associated with florid oedema, while grey matter lesions may show minimal or no oedema (Chong et al. 2000). Mild injuries may heal completely but extensive damage usually results in temporal lobe atrophy or macrocystic encephalomalacia (Fig. 13).

The differential diagnosis of temporal lobe necrosis includes intracranial tumour recurrence and cerebral metastasis. Intracranial tumour recurrence is almost always an extra-axial lesion, while temporal lobe necrosis is an intra-axial process. In addition, NPC with intracranial extension, unlike temporal lobe necrosis, is often not associated with significant cerebral oedema. Cerebral metastasis is exceedingly rare in NPC, and is usually low on the list of differential diagnosis in clinical practice. PET CT is able to differentiate these entities. Temporal lobe necrosis typically shows no tracer uptake while recurrent or metastatic tumour commonly demonstrates increased metabolic activity.

4.3.3.2 Brainstem and Spinal Cord Encephalomyelopathy

Data collected prior to the early 1980s showed that radiation-induced brainstem and cervical cord encephalomyelopathy occurred in up to 3% of patients (Mesic et al. 1981). However, with the advent of more sophisticated radiation therapy technology, the incidence of brainstem and spinal cord injury is extremely rare (Lee et al. 2005, 2009; Kam et al. 2004).

This major complication has a median latent period of 3 years, (range 0.4–9 years) (Lee et al. 1992). The anteriorly located corticospinal tracts along the brainstem and cervical cord are at the highest risk of radiation-induced injury. These patients therefore usually present with progressive spastic paraparesis or quadraparesis, with eventual severe motor disability. On MRI, brainstem and cervical cord encephalomyelopathy shows decreased signal intensity on T1-weighted images and increased signal intensity on T2-weighted images.

4.3.3.3 Cranial Neuropathy

Cranial nerves are relatively radioresistant. The reported incidence of radiation-induced cranial neuropathy ranges from 0.3 to 6% (Flores et al. 1986; Lee et al. 1992). This entity is diagnosed by exclusion, as the involved cranial nerves usually appear radiologically unremarkable. In particular, perineural invasion by recurrent tumour must be excluded. The hypoglossal nerve is the most commonly affected cranial nerve, followed by the optic and abducens nerves. Note that multiple cranial nerve palsies may also be encountered in brainstem encephalopathy.

4.3.4 Non-neurological Complications

4.3.4.1 Xerostomia

The parotid glands, which account for up to 80% of saliva production from the major salivary glands, are

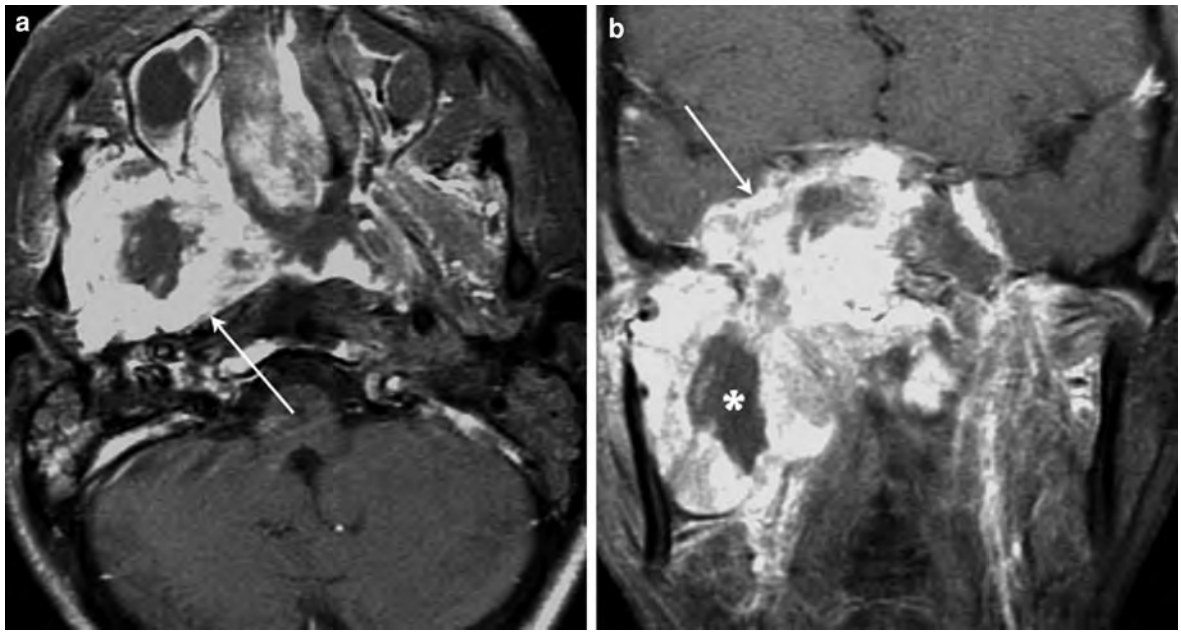

Fig. 14 Radiation associated tumour. **a** Axial contrast-enhanced fat-saturated T1-weighted MR image shows a large necrotic tumour in the right masticator space (*arrow*), in a patient who completed radiotherapy for right-sided nasopharyngeal carcinoma 9 years ago. **b** Coronal contrast-enhanced fat-saturated T1-weighted MR image shows a necrotic tumour in the right masticator space (*asterisk*) with superior extension into the intracranial cavity (*arrow*). The histology revealed malignant fibrohistiocytoma, thought to be radiation associated

Table 2 Nasopharyngeal carcinoma: stage grouping

Stage 0	Tis	N0	M0
Stage I	T1	N0	M0
Stage II	T1 T2	N1 N0, N1	M0 M0
Stage III	T1, T2 T3	N2 N0, N1, N2	M0 M0
Stage IVA	T4	N0, N1, N2	M0
Stage IVB	Any T	N3	M0
Stage IVC	Any T	Any N	M1

often exposed to radiation during treatment of NPC. As a result, nearly all patients have some degree of xerostomia. Associated dysphagia, dental caries and oral infection such as candidiasis are common complaints. Radiologically, these glands show atrophy and not infrequently, intense post-contrast enhancement.

4.3.4.2 Radiation-Induced Fibrosis

Radiation-induced fibrosis is predominantly a clinical diagnosis. It may manifest as rigidity of soft tissue in the neck, trismus and dysphagia (O'Sullivan and Levin 2003). Trismus is due to fibrosis of temporomandibular joints and the adjacent muscles of mastication. When severe, it often results in dysphagia, which may be further compounded by pharyngeal mucositis and lower cranial nerve palsies (Murphy and Gilbert 2009).

4.3.4.3 Radiation Associated Tumours

The tumour induction potential of ionising radiation is well recognised. However, ascribing a second tumour as the direct consequence of irradiation is often difficult. Three diagnostic criteria are required: firstly, a difference in the histopathology of the second tumour from the primary neoplasm; secondly, the second tumour should arise from within the irradiation field; and thirdly, an arbitrary latent period of at least 5 years (Kong and Lu 2009).

The exact incidence of radiation associated tumour following NPC treatment is unknown, but has been estimated as between 0.4 and 1.2% (Steeves and Bataini 1981; Kong et al. 2006). Various tumours have been reported, which include sarcomas, malignant

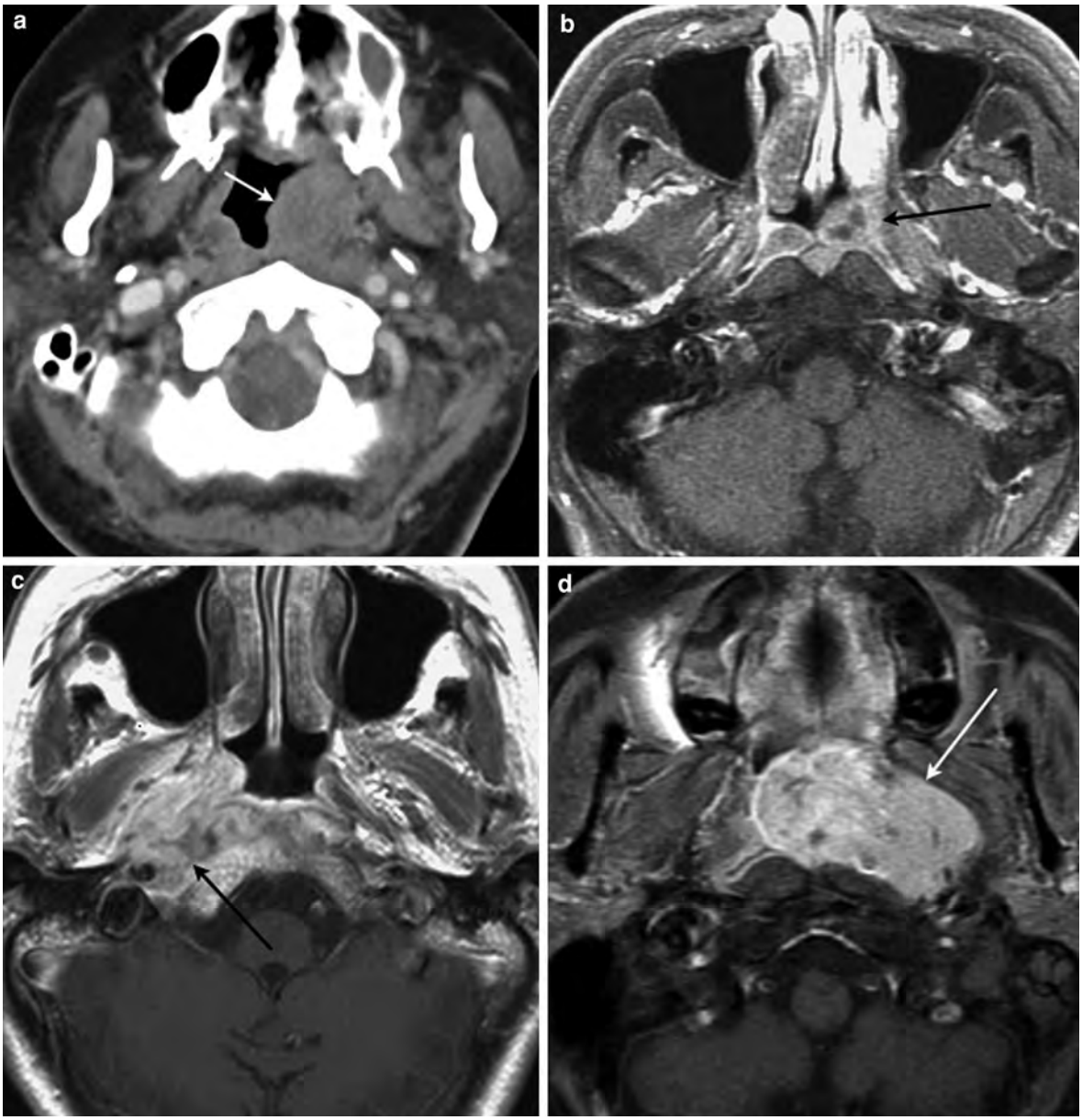

Fig. 15 **a** Nasopharyngeal non-Hodgkin's lymphoma. Axial contrast-enhanced CT image shows a left nasopharyngeal tumour (*arrow*) with no significant invasion of the adjacent deep cervical spaces. **b** Nasopharyngeal mucosa-associated lymphoid tissue (MALT) lymphoma. Axial contrast-enhanced T1-weighted MR image shows a left nasopharyngeal tumour (*arrow*). The tumour is largely confined to the pharyngeal mucosal space. **c** Nasopharyngeal extramedullary plasmacytoma. Axial contrast-enhanced T1-weighted image shows an enhancing tumour arising from the right lateral pharyngeal recess (*arrow*). Histology revealed monoclonal neoplastic plasma cells in keeping with plasmacytoma. **d** Nasopharyngeal haemangiopericytoma. Axial contrast-enhanced T1-weighted MR image shows an intensely enhancing left nasopharyngeal tumour (*arrow*) with intralesional flow voids due to prominent tumour vessels

fibrohistiocytoma (Fig. 14), gliomas, schwannomas, meningiomas, thyroid tumours and squamous cell carcinomas.

5 Other Neoplasms of the Nasopharynx

Several other tumours, albeit much less common, may arise from the nasopharynx. At times, it may be impossible to differentiate these tumours from NPC on imaging alone and histologic confirmation is necessary. The principal differential diagnoses of NPC include nasopharyngeal non-Hodgkin's lymphoma (NHL) and minor salivary gland carcinoma.

Nasopharyngeal NHL is usually encountered in conjunction with systemic disease. It may affect all age group but is more commonly seen in middle and old age. Nasopharyngeal NHL, in contrast to NPC, often shows minimal or no infiltration of the adjacent deep neck spaces (King et al. 2003). Skull base erosion is rare. The lymph nodes in NHL appear usually not necrotic (see also "Neck and Nodal Disease" and "Neck Lymphoma").

Minor salivary gland neoplasms of the nasopharynx are seen in middle age patients, with no sex predilection. Nodal metastasis is rare in these tumours, which are otherwise often indistinguishable from NPC on imaging (Jones et al. 1998).

Nasopharyngeal plasmacytoma, haemangiopericytoma, melanoma and rhabdomyosarcoma have also been reported (King et al. 2003; Palacious et al. 2005; Mortele et al. 2001; Nikolidakis et al. 2000) (Fig. 15).

References

Bentzen SM, Johansen LV, Overgaard J et al (1991) Clinical radiobiology of squamous cell carcinoma of the oropharynx. Int J Radiat Oncol Biol Phys 206:1197–1206

Chan AT, Teo PM, Johnson PJ (2002) Nasopharyngeal carcinoma. Ann Oncol 13:1007–1015

Chan AT, Felip E, Guidelines Working Group ESMO (2008) Nasopharyngeal cancer: ESMO clinical recommendations for diagnosis, treatment and follow-up. Ann Oncol 19(Suppl 2):ii81–82

Chen MK, Chen TH, Liu JP et al (2004) Better prediction of prognosis for patients with nasopharyngeal carcinoma using primary tumour volume. Cancer 100:2160–2166

Chong VFH (1997) Masticator space in nasopharyngeal carcinoma. Ann Otol Rhino Laryngol 106:979–982

Chong VF (2004) Imaging the cranial nerves in cancer. Cancer Imaging 4:S1–S5

Chong VFH, Fan YF (1996) Jugular foramen involvement in nasopharyngeal carcinoma. J Laryngol Otol 110:897–900

Chong VFH, Fan YF (1998a) Nasopharyngeal carcinoma. Semin Ultrasound CT MR 19:449–462

Chong VF, Fan YF (1998b) Hypoglossal nerve palsy in nasopharyngeal carcinoma. Eur Radiol 8:939–945

Chong VF, Ong CK (2008) Nasopharyngeal carcinoma. Eur J Radiol 66:437–447

Chong VF, Fan YF, Khoo JBK (1995) Retropharyngeal lymphadenopathy in nasopharyngeal carcinoma. Eur J Radiol 21:100–105

Chong VFH, Fan YF, Khoo JBK (1996) Nasopharyngeal carcinoma with intracranial spread: CT and MRI characteristics. J Comput Assist Tomogr 20:563–639

Chong VF, Mukherji SK, Ng SH et al (1999) Nasopharyngeal carcinoma: review of how imaging affects staging. J Comput Assist Tomogr 23:984–993

Chong VFH, Fan YF, Mukherji SK (2000) Radiation-induced temporal lobe changes: CT and MR imaging characteristics. AJR Am J Roentgenol 175:431–436

Chong VFH, Zhou JY, Khoo JBK et al (2004) Tumour volume measurement in nasopharyngeal carcinoma. Radiology 231:914–921

Chong VFH, Zhou JY, Khoo JBK et al (2006) Correlation between MR imaging derived nasopharyngeal carcinoma tumour-volume and TNM system. Int J Radiat Oncol Biol Phys 64:72–76

Chua ML, Ong SC, Wee JT et al (2009) Comparison of 4 modalities for distant metastasis staging in endemic nasopharyngeal carcinoma. Head Neck 31:346–354

Dubrulle F, Souillard R, Hermans R (2007) Extension patterns of nasopharyngeal carcinoma. Eur Radiol 17:2622–2630

Flores AD, Dickson RI, Riding K et al (1986) Cancer of the nasopharynx in British Columbia. Am J Clin Oncol 9:281–291

Harnsberger HR, Dillon WP (1985) Major motor atrophic patterns in the face and neck: CT evaluation. Radiology 155:665–670

Hepeng J (2008) Zeng Yi profile. a controversial bid to thwart the 'cantonese cancer'. Science 321:1154–1155

Jeyakumar A, Brickman TM, Jeyakumar A et al (2006) Review of nasopharyngeal carcinoma. Ear Nose Throat J 85:168–170, 172–173, 184

Johnson CR, Thames HD, Huang DT et al (1995) The tumour volume and clonogens number relationship: tumour control predictions based upon tumour volume estimates derived from computed tomography. Int J Radiat Oncol Biol Phys 332:281–337

Jones AS, Beasley NJ, Houghton DJ et al (1998) Tumors of the minor salivary glands. Clin Otolaryngol Allied Sci 23:27–33

Kam MK, Teo PM, Chau RM et al (2004) Treatment of nasopharyngeal carcinoma with intensity-modulated radiotherapy: the Hong Kong experience. Int J Radiat Oncol Biol Phys 60(5):1440–1450

King AD, Ahuja AT, Leung SF et al (2000) Neck node metastases from nasopharyngeal carcinoma: MR imaging of patterns of disease. Head Neck 22:275–281

King AD, Lei KI, Richards PS et al (2003) Non-Hodgkin's lymphoma of the nasopharynx: CT and MR imaging. Clin Radiol 58:621–625

Kong L, Lu JJ (2009) Second primary tumor. In: Schwab M (ed) Encyclopedia of cancer. Springer, Berlin

Kong L, Lu JJ, Hu C et al (2006) The risk of second primary tumors in patients with nasopharyngeal carcinoma after definitive radiotherapy. Cancer 107(6):1287–1293

Kumar MB, Lu JJ, Loh KS et al (2004) Tailoring distant distant metastatic imaging for patients with clinically localized undifferentiated nasopharyngeal carcinoma. Int J Radiat Oncol Biol Phys 58:688–693

Lam WW, Chan YL, Leung SF et al (1997) Retropharyngeal lymphadenopathy in nasopharyngeal carcinoma. Head Neck 19:176–181

Lartigau E, Le Radant AM, Lambin P et al (1993) Oxygenation of head and neck tumors. Cancer 717:2319–2325

Lau KY, Kan WK, Sze WM et al (2004) Magnetic resonance for T-staging of nasopharyngeal carcinoma, the most informative pair of sequences. Jpn J Clin Oncol 34:171–175

Lee AW, Law SC, Ng SH et al (1992) Retrospective analysis of nasopharyngeal carcinoma treated during 1976–1985: late complications following megavoltage irradiation. Br J Radiol 65(778):918–928

Lee AW, Lau WH, Tung SY et al (2005) Preliminary results of a randomized study on therapeutic gain by concurrent chemotherapy for regionally advanced nasopharyngeal carcinoma: NPC-9901 Trial by the Hong Kong nasopharyngeal cancer study group. J Clin Oncol 23(28):6966–6975

Lee AW, Ng WT, Hung WM et al (2009) Major late toxicities after conformal radiotherapy for nasopharyngeal carcinoma patients and treatment related risk factors. Int J Radiat Oncol Biol Phys 73(4):1121–1128

Liu FY, Lin CY, Chang JT et al (2007a) 18F-FDG PET can replace conventional work-up in primary M staging of nonkeratinizing nasopharyngeal carcinoma. J Nucl Med 48:1614–1619

Liu T, Xu W, Yan WL et al (2007b) FDG-PET, CT, MRI for diagnosis of local residual or recurrent nasopharyngeal carcinoma, which one is the best? a systematic review. Radiother Oncol 85:327–335

Lo AK, Huang DP, Lo KW et al (2004) Phenotypic alterations induced by the Hong Kong-prevalent Epstein-Barr virus-encoded LMP1 variant (2117-LMP1) in nasopharyngeal epithelial cells. Int J Cancer 109:919–925

Mesic JB, Fletcher GH, Goepfert H (1981) Megavoltage irradiation of epithelial tumors of the nasopharynx. Int J Radiat Oncol Biol Phys 7:447–452

Mortele B, Lemmerling M, Seynaeve P et al (2001) Hemangiopericytoma of the parotid gland: CT and MR features. Eur Radiol 11:1073–1075

Murphy BA, Gilbert J (2009) Dysphagia in head and neck cancer patients treated with radiation: assessment, sequelae, and rehabilitation. Semin Radiat Oncol 19(1):35–42

NCCN (2008) Clinical practice guidelines in oncology: head and neck cancers.v.2.2008. National Comprehensive Cancer Network, Washington

Ng SH, Chan SC, Yen TC et al (2009) Staging of untreated nasopharyngeal carcinoma with PET/CT: comparison with conventional imaging work-up. Eur J Nucl Med Mol Imaging 36:12–22

Nikolidakis A, Skoulakis C, Papadakis C et al (2000) Solitary extramedullary plasmacytoma of the nasopharynx. J Otolaryngol 29:254–257

O'Sullivan B, Levin W (2003) Late radiation-related fibrosis: pathogenesis, manifestations, and current management. Semin Radiat Oncol 13(3):274–289

Old LJ, Boyse EA, Oettgen HF et al (1966) Precipitating antibody in human serum to an antigen present in cultured Burkitt's lymphoma cells. Proc Natl Acad Sci U S A 56:1699–1704

Ong CK, Chong VF (2010) Imaging of perineural spread in head and neck tumours. Cancer Imaging 10:S92–98

Palacious E, Restrepo S, Mastrogiovanni L et al (2005) Sinonasal hemangiopericytomas: clinicopathologic and imaging findings. Ear Nose Throat J 84:99–102

Parkin DM, Whelan SL et al (eds) (2002) Cancer incidence in five continents, vol VIII. IARC scientific publications, Lyon

Rasch C, Keus R, Pameijer FA et al (1997) The potential impact of CT-MRI matching on tumor volume delineation in advanced head and neck cancer. Int J Radiat Oncol Biol Phys 394:841–848

Roh JL, Sung MW, Kim KH et al (2004) Nasopharyngeal carcinoma with skull base invasion: a necessity of staging subdivision. Am J Otolaryngol 25:26–32

Sham JST, Cheung YK, Chan FL et al (1990) Nasopharyngeal carcinoma: pattern of skeletal metastases. Br J Radiol 63:202–205

Sham JST, Cheung YK, Choy D et al (1991a) Nasopharyngeal carcinoma: CT evaluation of patterns of tumour spread. AJNR 12:265–270

Sham JST, Cheung YK, Choy D et al (1991b) Cranial nerve involvement and base of skull erosion in nasopharyngeal carcinoma. Cancer 68:422–426

Steeves RA, Bataini JP (1981) Neoplasms induced by megavoltage radiation in the head and neck region. Cancer 47:1770–1774

Sze WM, Lee AW, Yau TK et al (2004) Primary tumour volume of nasopharyngeal carcinoma: prognostic significance for local control. Int J Radiat Oncol Biol Phys 59:21–27

Teresi LM, Lufkin RB, Vinuela F et al (1987) MR imaging of the nasopharynx and floor of the middle cranial fossa—part I: Normal anatomy. Radiology 164:811–816

Wang XS, Hu CS, Ying HM et al (2009) Patterns of retropharyngeal noe metastasis in nasopharyngeal carcinoma. Int J Radiat Oncol Biol Phys 73:194–201

Wei WI, Sham JST (2005) Nasopharyngeal carcinoma. Lancet 365:2041–2054

Xiao GL, Gao L, Xu GZ (2002) Prognostic influence of parapharyngeal space involvement in nasopharyngeal carcinoma. Int J Radiat Oncol Biol Phys 52:957–963

Yeh SA, Tang Y, Lui CC et al (2005) Treatment outcomes and late complications of 849 patients with nasopharyngeal carcinoma treated with radiotherapy alone. Int J Radiat Oncol Biol Phys 62(3):672–679

Yu MC, Yuan JM (2002) Epidemiology of nasopharyngeal carcinoma. Semin Cancer Biol 12:421–429

Parapharyngeal Space Neoplasms

Robert Hermans

Contents

Abstract

While primary neoplasms of the parapharyngeal space (PPS) are rare, secondary displacement or infiltration of this space, by pathology originating in neighboring spaces, is more commonly seen. An important role of imaging in the evaluation of PPS pathology, is to identify the space of origin. In combination with the imaging characteristics of the mass, this allows to reduce the differential diagnosis to a limited number of possibilities. This chapter reviews the key anatomical features of the PPS, and explains the imaging approach to mass lesions at this level.

1 Introduction

The parapharyngeal space (PPS) is a deep space of the neck shaped as a tilted up pyramid with its base attaching to the skull base and the apex reaching the level of the hyoid bone, and almost exclusively containing fat.

Primary neoplasms arising in this space are rare, accounting for only 0.5% of all head and neck tumors (Olsen 1994; Miller et al. 1996; Pang et al. 2002). About 70–80% of the tumors originating from the PPS itself are benign (Luna-Ortiz et al. 2005).

The PPS is more commonly displaced or infiltrated by lesions arising in adjacent structures and spaces, including the pharynx, as well as the parotid, masticator and retropharyngeal spaces.

Small tumors of the PPS are often incidental findings. Larger tumors cause aspecific symptoms, including sore throat, ear fullness, dysphagia and, less

R. Hermans (✉)
Department of Radiology, University Hospitals,
Herestraat 49, 3000 Leuven, Belgium
e-mail: Robert.Hermans@uz.kuleuven.ac.be

R. Hermans (ed.), *Head and Neck Cancer Imaging*, Medical Radiology. Diagnostic Imaging,
DOI: 10.1007/174_2011_378, © Springer-Verlag Berlin Heidelberg 2012

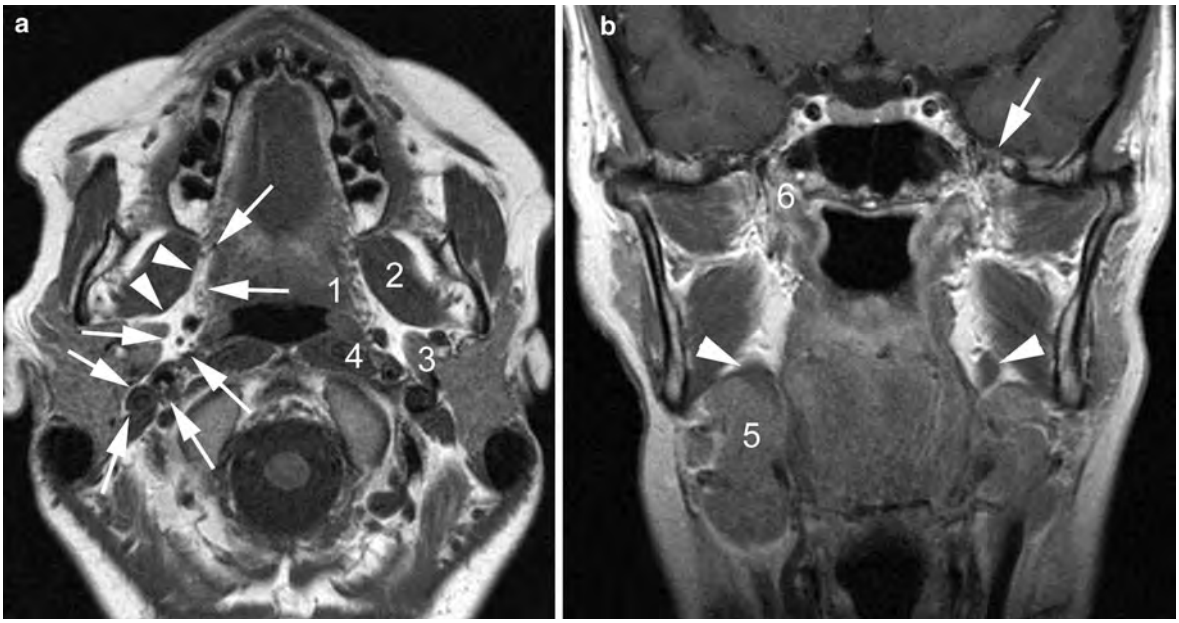

Fig. 1 **a** Axial T1-weighted spin echo image at the level of the soft palate. The boundaries of the parapharyngeal space (PPS) (including prestyloid and retrostyloid compartment) are indicated by *arrows* and *arrowheads* on the *right*. On the *left*, the adjacent spaces are labeled: pharyngeal mucosal space (1), masticator space (2), parotid space (3), retropharyngeal/prevertebral space (4). **b** Coronal T1-weighted spin echo images through prestyloid compartment of the PPS. Inferiorly, this space is closed by the submandibular gland (5), while superiorly, it reaches the skull base (6). The foramen ovale (*arrow*), through which exits the mandibular nerve, communicates with the masticator space. The styloglossal muscles run through the PPS (*arrowheads*)

frequently, jaw pain combined with cranial nerves palsy. The last two symptoms are suggestive of a malignant lesion. Because of their deep location, the clinical assessment of tumors in this region is limited, commonly causing a delay between the onset of symptoms and diagnosis. Large lesions cause a bulging of the lateral oro- and/or naso-pharyngeal wall. When a PPS lesion grows laterally, facial swelling may result at the level of the parotid or submandibular region. Rarely, the mandible will be displaced by a slowly growing tumor (Farina et al. 1999).

An important role of imaging in the evaluation of PPS pathology, is to identify the space of origin. Lesions arising from the adjacent spaces displace the PPS in a particular way; in combination with the imaging characteristics of the mass, this information allows to reduce the differential diagnosis to a limited number of possibilities. Imaging studies should also identify hypervascular neoplasms, in order to avoid biopsy and its possible complications.

2 Anatomy

2.1 Fascial Layers and Compartments

The PPS is *medially* in close contact with the pharynx, bordered by the middle layer of the deep cervical fascia (also known as buccopharyngeal fascia) (Figs. 1 and 2). Superiorly, the pharyngeal constrictor muscle does not reach the skull base, and at that level, the lumen of the nasopharynx is held open by the thick pharyngobasilar fascia. This fascia lies within the middle layer of the deep cervical fascia. The pharyngobasilar fascia is interrupted at the level of the sinus of Morgagni, an opening through which the cartilagineous part of the Eustachian tube and the levator veli palatini muscle enter the nasopharynx. This area should be carefully inspected on imaging studies of the nasopharynx, as it is a common route of spread for nasopharyngeal carcinomas to the PPS and skull base (Fig. 3).

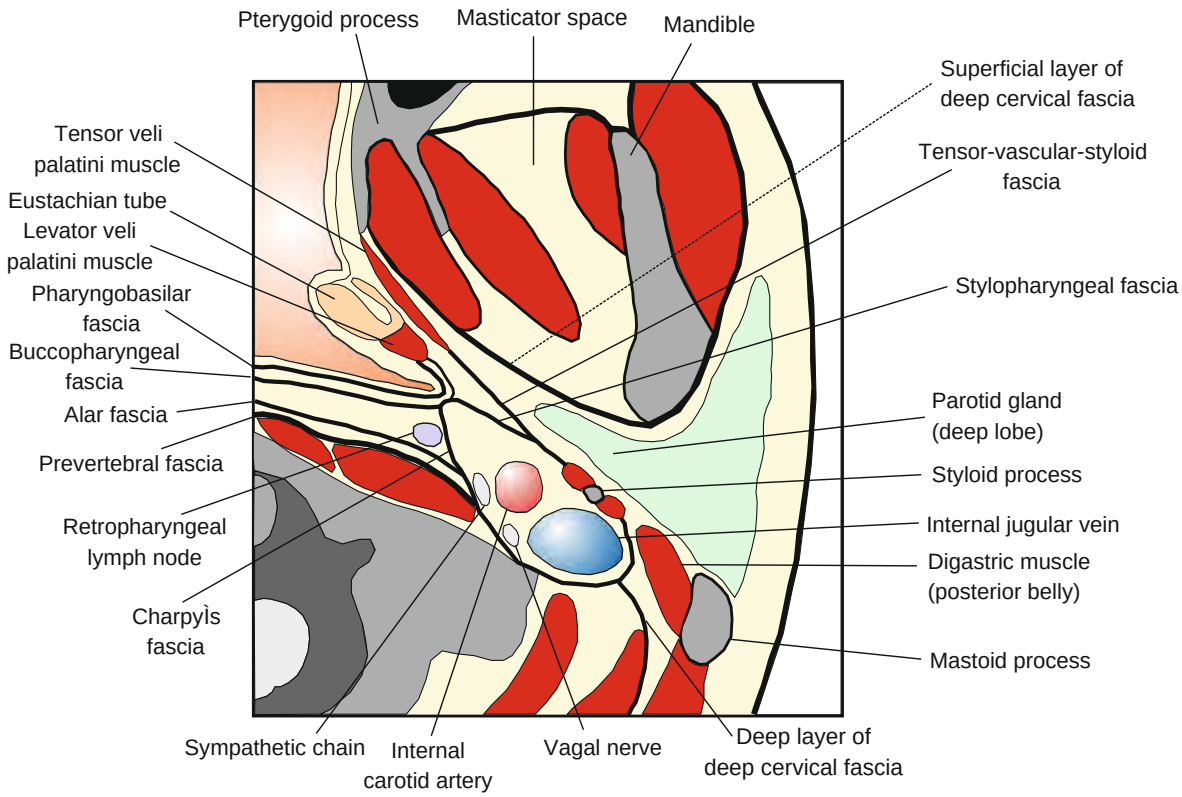

Fig. 2 Topographical anatomy of the PPS in the axial plane, including the different fascial layers at this level

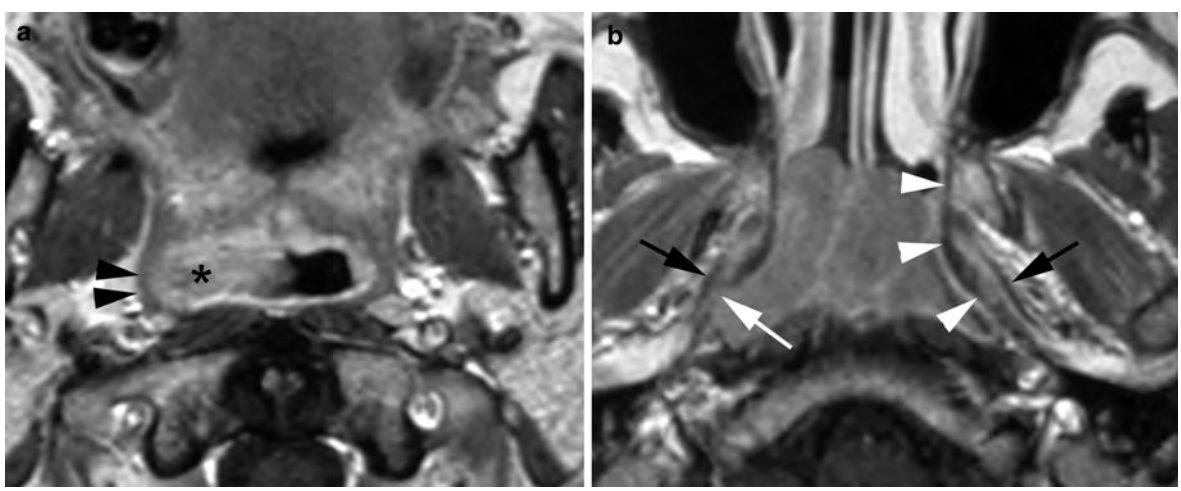

Fig. 3 Axial gadolinium-enhanced T1-weighted spin echo images, showing the relationship between the superior constrictor muscle, the pharyngobasilar fascia and a nasopharyngeal cancer. **a** Axial section at level of soft palate. The superior constrictor muscle (*arrowheads*) is surrounding the nasopharynx; the tumor (*asterisk*) is confined to the nasopharyngeal lumen. **b** At a higher level, the nasopharyngeal lumen is bordered by the pharyngobasilar fascia (*arrowheads*). Bilaterally, the tensor veli palatini muscle (*black arrow*) is visible on the outer side of this fascial layer. On the right, the tumor extends into the PPS through the pharyngobasilar fascia (*white arrow*); this site likely corresponds to the sinus of Morgagni

The superficial layer of the deep cervical fascia is *lateral* to the PPS, separating this space from the masticator space. This fascia curves around the medial surface of the pterygoid muscles and extends from the mandible to the skull base, where it attaches just medial to foramen ovale. As a consequence, the mandibular nerve (V3), as it courses through this foramen, directly enters the masticator space.

In its *posterolateral* portion, the PPS is in contact with the deep lobe of the parotid gland. The existence of a fascial layer at this level is controversial.

The *anterior* border of the PPS is the pterygomandibular raphe. *Inferiorly*, the PPS gradually becomes narrower and ends at the level of the hyoid bone and the superior margin of the submandibular salivary gland.

The *posterior* border of the PPS is the most complex and controversial; different descriptions are found in the literature. Some authors consider the PPS completely separated from the more posterior carotid space: the anterior surface of the carotid sheath (made up of the three layers of deep cervical fascia) draws the borderline between the two spaces (Som and Curtin 1995). Others consider the carotid space to be a part of the PPS (Mukherji and Castillo 1998).

Three more fascial structures are described, acting as anatomical landmarks subdividing the PPS. The most important one is the *tensor-vascular-styloid fascia* (TVS), a layer that extends from the inferior border of tensor veli palatini muscle, posterolaterally and inferiorly to the styloid process and muscles (Fig. 2). Anteriorly, it reaches the pterygomandibular raphe and therefore it closes the gap between the skull base, the tensor veli palatini muscle and the styloid process (Som and Curtin 1995). The other two are the *stylopharyngeal fascia,* and *Charpy's fascia*, also known as '*cloison sagitalle*' (Fig. 2).

The TVS fascia allows to further subdivide the PPS into two compartments: the *prestyloid* compartment, lying between the pterygoid muscles and the TVS fascia, and the *retrostyloid* compartment, just medial to the TVS fascia itself and including the carotid space (Maroldi et al. 1994; Nasser and Attia 1990).

The PPS mainly contains fat tissue and loose connective tissue. In the prestyloid compartment ectopic minor salivary glands and vascular structures (pharyngeal ascending and internal maxillary artery, pharyngeal venous plexus) are found. The retrostyloid PPS contains the internal carotid artery (ICA), the internal jugular vein (IJV), the cranial nerves IX-X-XI-XII and the sympathetic plexus. Lymph nodes of the deep cervical chain, known as the jugulodigastric lymph nodes, are only found below the level of the posterior belly of the digastric muscle (Gregoire et al. 2003).

2.2 Radiological Anatomy

Because of its higher contrast resolution, MRI is preferred over CT when dealing with pathology at the level of the PPS.

In the axial plane the prestyloid compartment of the PPS is recognized as a triangular fat-filled space (Fig. 1) with maximum width at the level of the soft palate. The pharyngobasilar fascia is sometimes visible on MRI as a hypointense line (Fig. 3).

The sinus of Morgagni itself is not visible on MR, but the Eustachian tube, particularly at the torus tubarius, where it opens in the nasopharyngeal lumen, can be used as an anatomical landmark.

The TVS, stylopharyngeal and Charpy's fascia cannot be routinely identified on MR. Their course can be mentally outlined on axial scans by using the tensor veli palatini muscle and styloid process as anatomical landmarks.

The lateral fascial border of the PPS is not identified, but its cranial attachment lies just medial to foramen ovale (Fig. 1). MR is able to depict the course of the mandibular nerve—from Meckel's cave, through the foramen ovale—and also the proximal segment of the main terminal branch, the inferior alveolar nerve, as it runs to the entrance of the mandibular canal.

The ICA and IJV, just medial to the styloid process, generally show a flow void on a T1- and T2-weighted MR sequence.

3 Imaging Findings in Parapharyngeal Space Lesions

3.1 Primary Lesions of the Parapharyngeal Space

As indicated, primary lesions of the PPS are rare and most are benign. These lesions can be classified based on histology (mainly salivary gland tumors, neurogenic

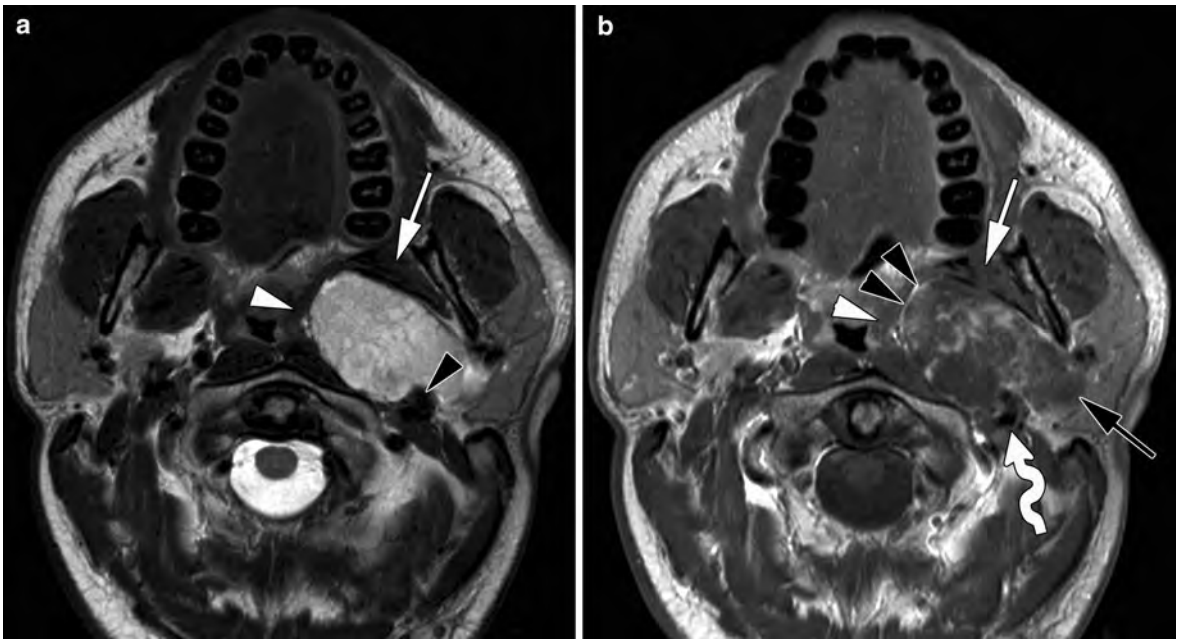

Fig. 4 Axial T2-weighted (**a**) and gadolinium-enhanced T1-weighted spin echo image (**b**) in a patient with a coincidentally discovered PPS tumor. The lesion cannot be separated from the deep lobe of the parotid gland (*black arrow*), and largely fills the prestyloid compartment; a thin layer of fat is still visible at the anteromedial margin of the tumor (*black arrowheads*, **b**). The pharyngeal wall (*white arrowheads*) and medial pterygoid muscle (*white arrow*) are displaced. The large vessels (*curved arrow*) are displaced posteriorly. The styloid process and styloid musculature produces an indentation in the posterior tumor margin (*black arrowhead*, **a**) Pleomorphic adenoma of the deep parotid lobe

tumors and paragangliomas), or according to the compartment of origin (prestyloid or retrostyloid).

3.1.1 Prestyloid Lesions

The overwhelming majority of neoplasms in the prestyloid compartment are salivary gland tumors. Most other lesions in this compartment are related to anomalies of the branchial apparatus.

Pleomorphic adenoma is the most frequent salivary tumor. Histologically, both epithelial and mesenchymal elements are found, hence the name 'mixed tumor'. These tumors may arise from ectopic minor salivary glands, localised in the prestyloid compartment along the embryological growth path of the parotid gland. However, much more frequently they originate from the deep lobe of the parotid gland, extending exophytically into the PPS.

The most reliable sign of a primary PPS tumor is the presence of a fat layer separating the tumor from the deep lobe of the gland. A deep parotid lobe tumor appears as a more or less dumbbell-shaped mass, connected to the parotid gland, potentially widening the stylomandibular tunnel, and displacing anteromedially the PPS fat (Fig. 4).

Fig. 5 Axial plain T1-weighted spin echo image in a patient with a right-sided peritonsillar swelling, rapidly increasing over a few hours' time. A soft tissue mass (*asterisk*) is seen in the prestyloid compartment of the PPS; the periphery of the mass, mainly on the tonsillar side, shows spontaneous hyperintensity, compatible with recent hemorrhage (*arrows*). Pathologic examination showed pleomorphic adenoma

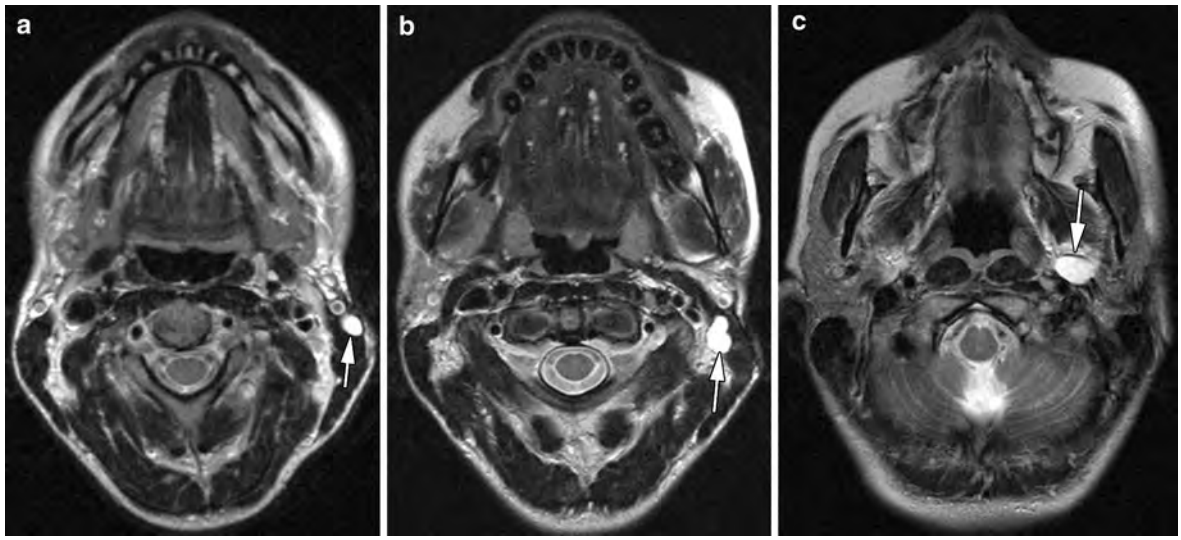

Fig. 6 Axial T2-weighted spin echo images (**a**–**c**) in a patient presenting with an infra-auricular swelling, 9 years after surgery for pleomorphic adenoma. Several bright nodular lesions (*arrows*) are seen, superficial and deep to the sternocleidomastoid muscle, as well as in the prestyloid compartment of the PPS (*arrow*, **c**). Reoperation confirmed recurrent pleomorphic adenoma

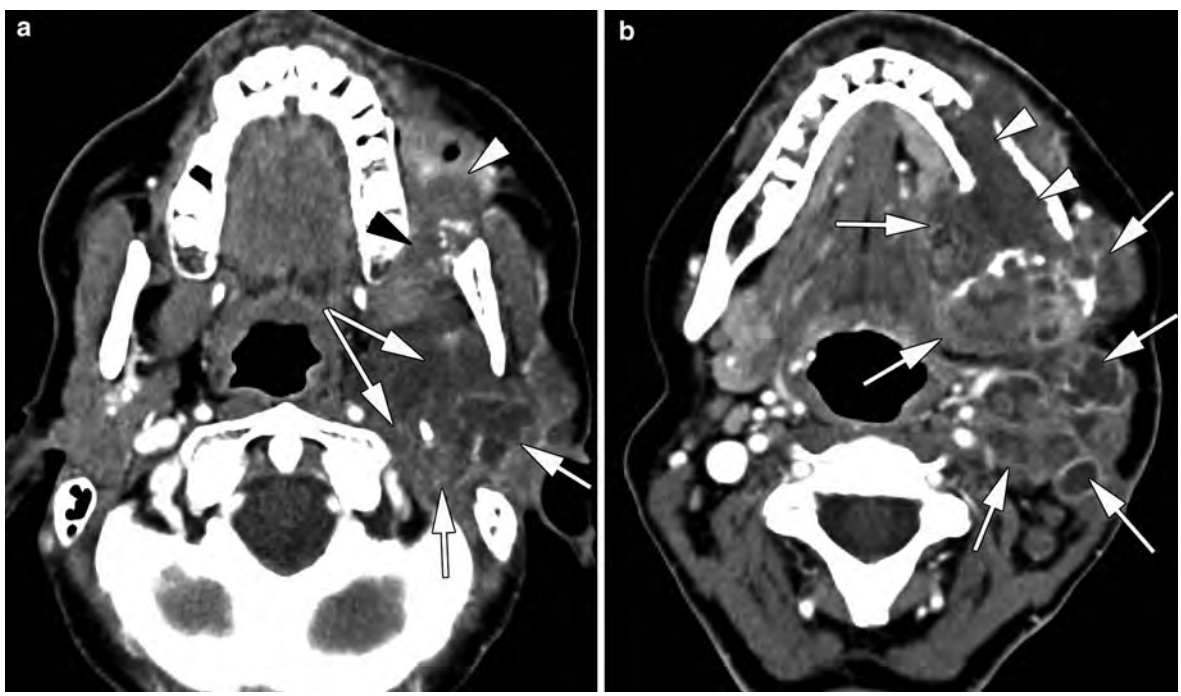

Fig. 7 Patient in her fifth decade, with a history of pleomorphic adenoma of the deep lobe of the left parotid gland. After initial resection, a recurrence was resected about 1 year ago. The patient now presents with peri-auricular pain and trismus, and a palpable mass in the pre-auricular and submandibular region. CT shows a large mass lesion in the parotid space, pre- and retro-styloid compartment of the PPS (*arrows*, **a**), extending into the masticator and buccinator space (*arrowheads*, **a**), and into the floor of the mouth, and peri-jugular and submandibular region (*arrows*, **b**). Massive osteolysis of the left mandibular body is seen (*arrowhead*, **b**). Some adenopathies are seen in level II on the *left side*. The lower sections of this CT study also revealed lung metastases. Although repeat biopsies always showed pleomorphic adenoma, the clinical behavior and radiological appearance are compatible with malignant degeneration of this tumor. Palliative chemotherapy was initiated. The patient died of progressive disease 1 year later

Fig. 8 Patient in his fourth decade, presenting with a painful swelling in the left parotid region. Axial T2-weighted image shows tumoral lesion in the prestyloid compartment of the PPS, extending into the deep lobe of the parotid gland. The lesion appears not as bright as pleomorphic adenomas *usually* do (compare with Fig. 4). Also, there is some doubt about the relationship between the mass lesion and medial pterygoid muscle (*arrowhead*): subtle invasion cannot be excluded. Because of adherence to the surrounding structures, the surgical resection of the lesion was difficult. Histological examination revealed adenocarcinoma

Pleomorphic adenomas usually show the following MR appearance: hyperintense signal intensity on T2-weighted sequences, related to their myxoid component, and often pronounced enhancement with focal areas of hypointensity on T1-weighted sequences. Various signal intensities may be seen in a pleomorphic adenoma, because of hemorrhage, calcifications and necrosis (Fig. 5).

Although pleomorphic adenoma is a benign tumor, it may recur locally if only a tumorectomy is performed, as the lesion has a thin and incomplete capsule. Most frequently, these relapses are multifocal and appear very hyperintense on T2-weighted sequences (Fig. 6).

Malignant transformation of the epithelial component of a pleomorphic adenoma, called 'carcinoma ex pleomorphic adenoma' or 'malignant mixed tumor', is the principal reason to remove all pleomorphic adenomas surgically. It manifests itself clinically by a sudden increase in tumor size, sometimes accompanied by pain and facial palsy. The radiological appearance may be relatively unremarkable compared to the 'benign' mixed tumor, or it may show infiltration into and destruction of surrounding structures (Fig. 7).

Salivary malignancies are not frequent, with mucoepidermoid and adenoid cystic carcinoma being the most common histologic types. CT and MR characteristics do not allow a reliable differentiation of a malignant from a benign lesion, although an overall low T2-signal intensity in a salivary gland tumor must raise the suspicion of a malignant tumor. The presence of infiltration into adjacent structures suggests malignancy (Fig. 8).

Much rarer neoplasms in the prestyloid compartment are lipomas (Kakani et al. 1992; Smith et al. 2006) and muscular neoplasms, such as rhabdomyomas and rhabdomyosarcomas. Rhabdomyosarcoma is, apart from lymphoma, the most common malignant head and neck neoplasms in children; the PPS is one of the sites of predilection of this tumor (Fig. 9).

Anomalies of the second branchial apparatus represent a spectrum of manifestions, ranging from a fistula to an isolated cyst (Piccin et al. 2008). One end of the spectrum is a fistula between the anterior side of the sternocleidomastoid muscle and the pharyngeal wall at the level of the palatine tonsil. The other end of the spectrum is a cyst, potentially localised anywhere along this tract. The most typical localisation of such a cyst is just below the mandibular angle, posterior to the submandibular salivary gland, lateral to the vessels and anterior to the sternocleidomastoid muscle. As the trajectory of such a branchial apparatus anomaly runs through the PPS, such cysts may also occur within the PPS (Fig. 10). Thickened, irregular walls may be seen in branchiogenic cysts that are or have been infected. In the absence of a history of inflammation, an atypical cystic lesion should also raise the possibility of a cystic retropharyngeal adenopathy, as can be seen with papillary thyroid carcinoma (Fig. 11) (Lombardi et al. 2004; Heimgartner et al. 2009).

3.1.1.1 Retrostyloid Lesions

A *retrostyloid* tumor can easily be identified when an anteromedial displacement of the ICA is present.

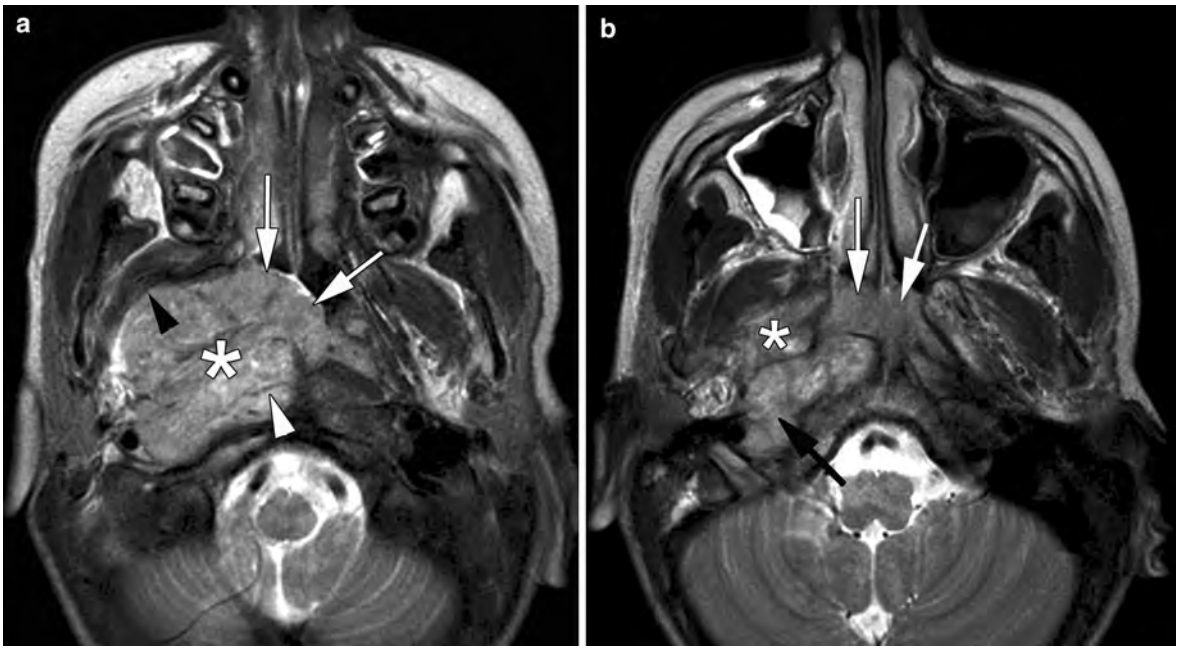

Fig. 9 Axial T2-weighted spin echo images in a 11-year-old child, presenting with facial pain, mainly during mastication, decreased hearing on the right side and weight loss. Large mass lesion (*asterisk*) centered on the right PPS, extending in the nasopharyngeal lumen (*white arrows*). The mass is displacing the muscles of mastication (*black arrowhead*). Invasion of the prevertebral space (*white arrowhead*) and apex of the right petrous bone (*black arrow*) is seen. Biopsy revealed embryonal rhabdomyosarcoma

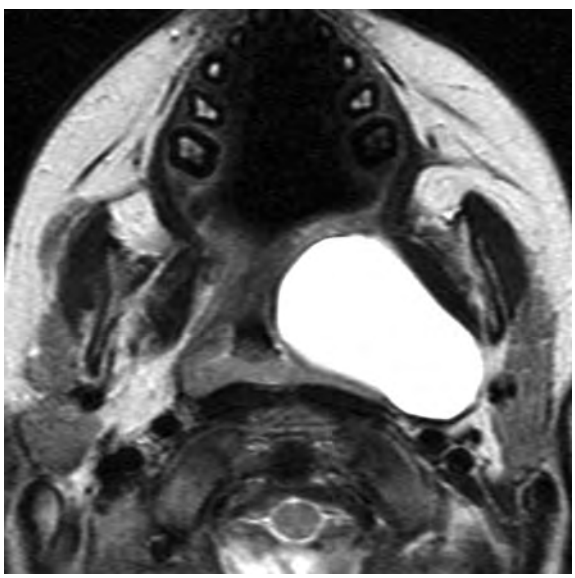

Fig. 10 Young child presenting with peritonsillar swelling. Axial T2-weighted spin echo image shows a cystic mass in the prestyloid compartment of the PPS, displacing the pharyngeal wall. The cyst was resected and confirmed to be a branchiogenic cyst

These lesions also displace the prestyloid PPS fat anteriorly. The most common primary lesions in this compartment are neurogenic tumors (17–25% of all PPS neoplasms) and paragangliomas (10–15%).

Schwannomas more frequently arise from the vagal nerve. Malignant degeneration has seldom been reported (Al Otieshan et al. 1998). The typical MR appearance of a schwannoma is that of an ovoid mass with a slightly hyperintense signal on T2-weighted images; the lesion can be heterogeneous because of areas of hemorrhage or cystic degeneration. After the administration of a contrast agent, marked enhancement may lead to a misdiagnosis of a hypervascular tumor. Actually, a schwannoma is a relatively hypovascular lesion and the enhancement is due to extravascular leakage through abnormally permeable vessels with poor venous drainage (Fig. 12).

Rarely, flow voids may become visible in an extracranial schwannoma, corresponding to dilated abnormal vessels (Kato et al. 2010); this may cause confusion with a paraganglioma, being a hypervascular tumor, where such flow voids correspond to feeding arteries or

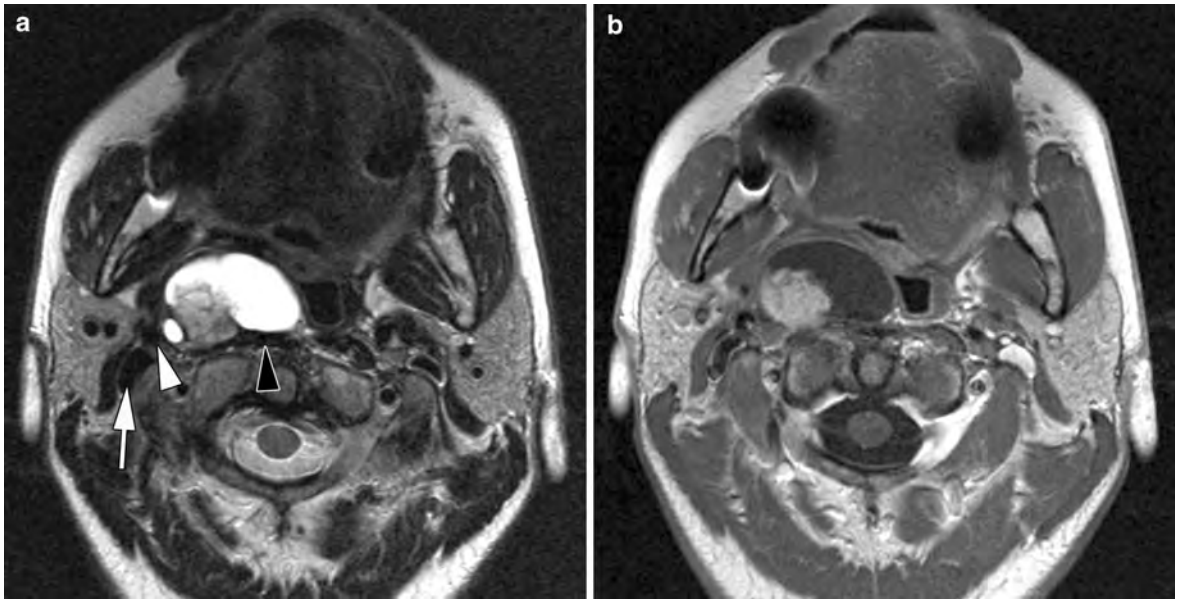

Fig. 11 Asymptomatic, 42-year-old female patient, with coincidentally discovered peritonsillar swelling on right side. Axial T2-weighted (**a**) and gadolinium-enhanced T1-weighted (**b**) spin echo images show largely cystic lesion, filling the prestyloid compartment of the PPS. The mass is centered between the prevertebral muscle (*black arrowhead*) and internal carotid artery (*white arrowhead*), a typical localisation for a retropharyngeal adenopathy. The internal carotid artery and the internal jugular vein (*white arrow*) are displaced posterolaterally. The cystic mass contains a solid component, showing enhancement. A lesion showing such appearance, especially in a young female patient, should raise the possibility of metastastic papillary thyroid cancer, a diagnosis that eventually was confirmed

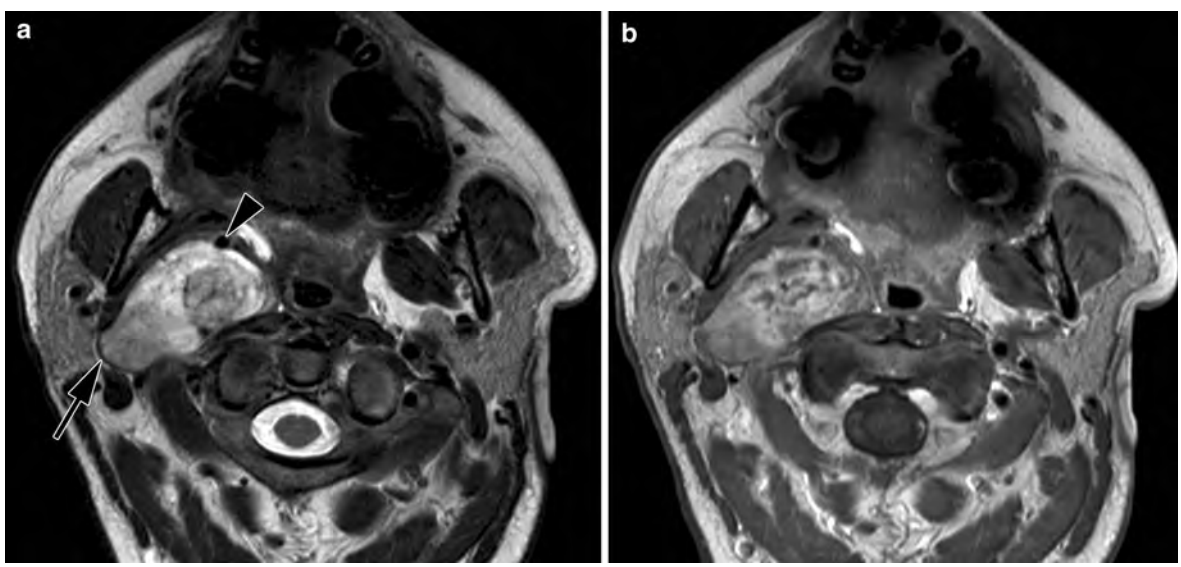

Fig. 12 T2-weighted (**a**) and gadolinium-enhanced T1-weighted (**b**) spin echo images, showing a heterogeneous mass lesion in the retrostyloid compartment of the PPS, displacing the internal carotid artery (*arrowhead*) anteromedially, and the internal jugular vein (*arrow*) posterolaterally. These findings are compatible with a schwannoma, most likely originating from the vagal nerve. As this lesion is causing few complaints, for the moment the patient is followed-up conservatively

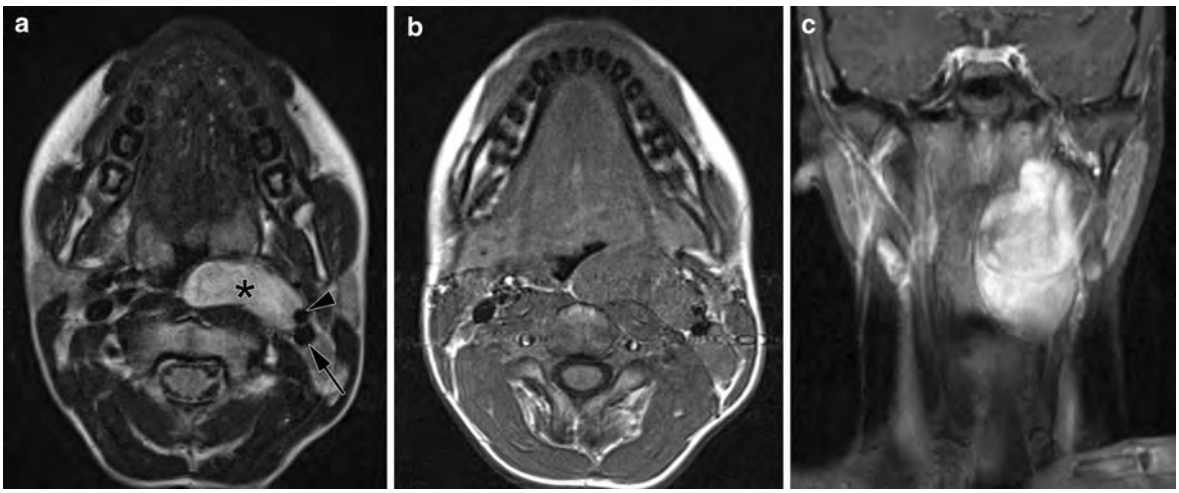

Fig. 13 A teenage patient, with a coincidently discovered parapharyngeal mass lesion; no clinical symptoms. Axial T2-weighted spin echo image (**a**) shows hyperintense mass, displacing the internal carotid artery (*arrowhead*) and internal jugular vein (*arrow*) laterally. Compared to the axial plain T1-weighted image (**b**) the coronal gadolinium-enhanced T1-weighted image (**c**) shows considerable enhancement of this lesion. The main differential diagnosis was retropharyngeal adenopathy, or neurogenic tumor originating from the sympathetic chain. Surgical exploration showed a sympathetic chain tumor; pathological examination revealed ganglioneuroma

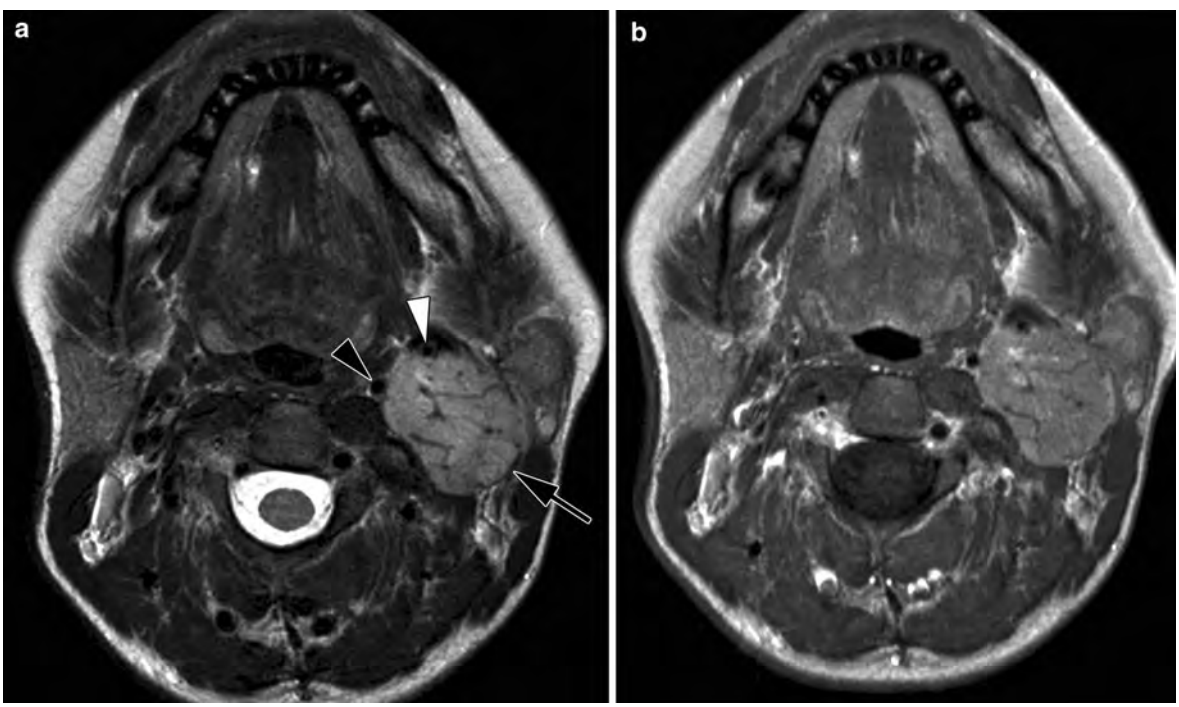

Fig. 14 Axial T2-weighted (**a**) and gadolinium-enhanced T1-weighted spino echo image (**b**) in a patient presenting with a submandibular swelling. A mass lesion is seen in the retrostyloid compartment of the PPS, separating the internal carotid artery (*black arrowhead*) and internal jugular vein (compressed, *arrow*). The lesion also displaces the external carotid artery (*white arrowhead*) somewhat anteriorly, but is not centered on the carotid bifurcation. Within the tumor, several vessel-like signal voids are seen, indicating hypervascularity. These findings are compatible with a glomus vagale tumor; this diagnosis was confirmed after resection and pathological examination

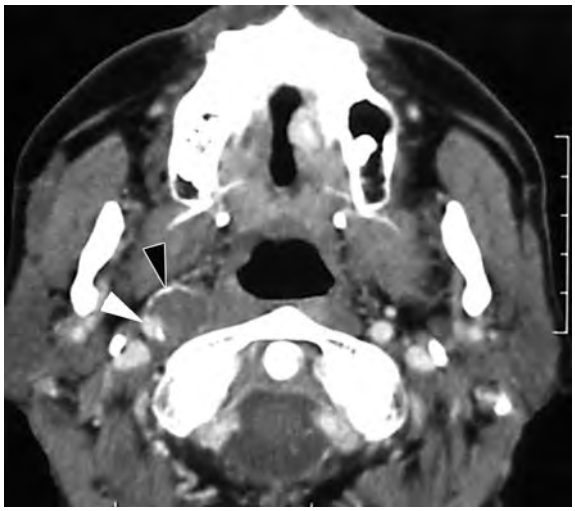

Fig. 15 Axial contrast-enhanced CT-image shows nodular lesion in the retrostyloid compartment of the PPS. At first sight one may think about retropharyngeal adenopathy. However, the narrowed lumen of the internal carotid artery (*white arrowhead*) is within the peripheral part of the mass, which also shows some peripheral calcifications (*black arrowhead*): these findings are compatible with an internal carotid artery aneurysm

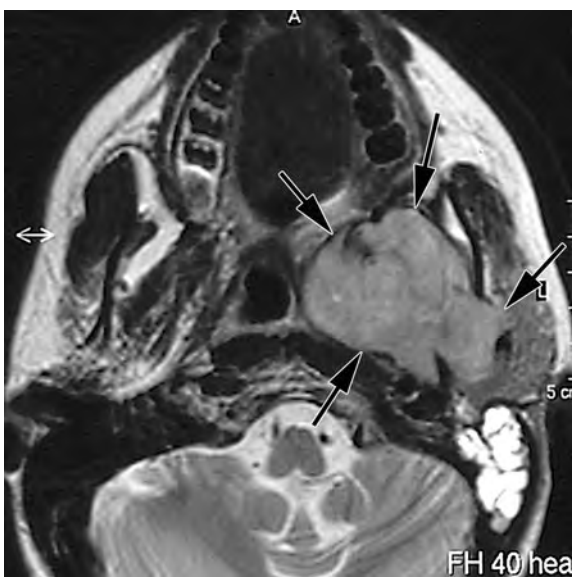

Fig. 16 Axial T2-weighted (**a**) and plain T1-weighted spin echo image (**b**) in a 22-year-old patient presenting with hearing loss on left side and increasing difficulties with mastication. A soft tissue mass (*black arrows*) is seen on deep side of mandible, extending into the PPS; a thin layer of fat can be recognized on the posteromedial side of the mass (*white arrow*). The lesion involves the deep lobe of the parotid gland. Contrary to the patient shown in Fig. 4, the pterygoid musculature cannot be recognized anymore, suggesting that the point of origin is within the masticator space. Fluid is present in the mastoid, secondary to dysfunction of the eustachian tube. Biopsy revealed rhabdomyosarcoma

Fig. 17 Axial gadolinium-enhanced T1-weighted spin echo image in a patient suffering nasopharyngeal carcinoma. The tumor extends posterolaterally (*small arrow*) in the retrostyloid compartment of the PPS, and remains sharply demarcated from the prestyloid compartment by the tensor veli palatini muscle (*arrowhead*) and tensor-vascular-styloid fascia (*large arrow*), although the fat plane is somewhat pushed laterally

Fig. 18 Axial contrast-enhanced CT image at level of nasopharynx. Retropharyngeal adenopathy in a patient suffering squamous cell cancer of the neck (unknown primary). A retropharyngeal adenopathy is typically situated between the prevertebral muscle (*arrowhead*) and the internal carotid artery (*arrow*); large adenopathies, such as in this case, displace the prestyloid fat anterolaterally

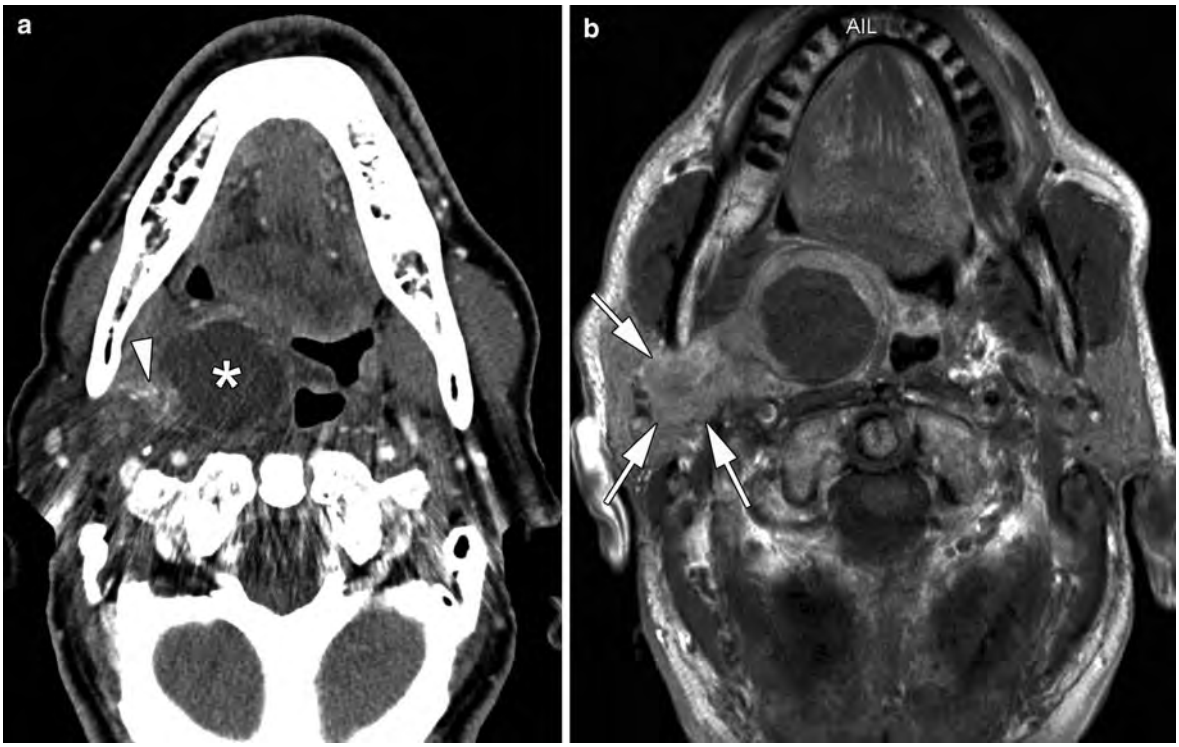

Fig. 19 Elderly patient presenting with right-sided throat pain. Clinical examination shows a swollen tonsil, no fever. Axial contrast-enhanced CT image (**a**) shows a large fluid-filled mass lesion (*asterisk*) in the prestyloid compartment of the PPS; this may be confused with a peritonsillar abscess. However, a solid component (*arrowhead*) with some small calcifications is seen at its lateral side, suggesting a tumor originating from the deep parotid lobe. The gadolinium-enhanced T1-weighted image (**b**) better shows the solid tumor component in the parotid gland (*arrows*). Transoral aspiration of the cystic component revealed hemorrhagic fluid. The patient was lost to follow-up; most likely, this lesion corresponds to a pleiomorphic adenoma containing hemorhagic component in the PPS

draining veins. If necessary, the differentiation can be made by obtaining a dynamic contrast-enhanced study: a schwannoma will nearly always show a slow, steady increase in enhancement, while paragangliomas show a rapidly increasing enhancement.

Schwannomas originating from the cervical sympathetic chain are an exception to the rule that a retrostyloid tumor displaces the ICA anteromedially: as this chain is lying medial to the ICA (see Fig. 2), the vessels will be displaced laterally. Such a sympathetic chain schwannoma may therefore be confused with a retropharyngeal adenopathy (Fig. 13) (Yuen et al. 2006; Saito et al. 2007; Kahraman et al. 2009).

Paragangliomas (also called glomus tumors) arise from chemoreceptor cells, basically present at three different anatomical sites: at the level of the nodose ganglion of vagal nerve, just below the skull base (vagal paraganglioma), at the carotid bifurcation (carotid paraganglioma) and at the level of the jugular foramen (jugular paraganglioma). A marked enhancement and, at MR, a 'salt and pepper' pattern are quite typical: this is due to the presence of tortuous large caliber vessels (detected as flow voids) within the mass (Fig. 14). Nevertheless, this pattern can be difficult to see or even absent, particularly in small lesions with predominantly small caliber feeding vessels. (Som and Curtin 1995). Carotid body tumors typically splay the internal and external carotid artery and may extend superiorly in the PPS. A vagal paraganglioma is centered in the retrostyloid compartment of the PPS; it only rarely reaches the carotid bifurcation. A jugular paraganglioma is centered in the jugular foramen, often eroding the surrounding bone and extending into the middle ear (Swartz et al. 1998). CT and MR allow an accurate diagnosis of glomus tumors in most cases.

Several vascular anomalies may be encountered in the retrostyloid compartment. Sometimes the ICA shows a tortuous course, running behind the posterior

pharyngeal wall: correct assessment avoids a disasterous biopsy of a misinterpreted submucosal pharyngeal lesion. An occlusion of ICA, or an IJV thrombosis, is sometimes encountered; MR shows a complex pattern of signal intensities of the intraluminal clot reflecting the different phases of hemoglobin degradation. MR is an accurate technique to diagnose dissection of the ICA. Aneurysms of the extracranial part of the ICA occur; rarely these aneurysms cause cranial nerve palsy. The diagnosis of such an aneurysm is usually straightforward (Fig. 15).

3.2 Secondary Lesions of the Parapharyngeal Space

To identify the site of origin of a lesion arising from a space neighboring the PPS, its relationships with the PPS fat and the large vessels must be carefully assessed. *Masticator space* neoplasms displace this fat plane posteromedially (Fig. 16) while a tumor originating from the pharynx will usually infiltrate the retrostyloid compartment (Fig. 17), displacing the fat tissue laterally. A *retropharyngeal* lesion (most often a retropharyngeal adenopathy) displaces the fat of the PPS anterolaterally (Fig. 18).

Large and aggressively behaving neoplasms, such as sometimes seen in sarcoma, nasopharyngeal cancer or lymphoma, may show a transspatial growth pattern; in such circumstances, a precise diagnosis on imaging studies is not possible.

Secondary involvement of the PPS may also be observed in benign multicompartmental lesions, such as hemangioma and lymphangioma.

Parapharyngeal abscess is a rare event in the era of broad spectrum antibiotics, generally secondary to head and neck infections of odontogenic, pharyngeal, tonsillar, otomastoideal or salivary origin. Sometimes, a PPS tumor may mimick on imaging a parapharyngeal abscess at first sight; this issue can be solved by correlation with the clinical findings (Fig. 19).

4 Conclusion

Imaging has an important role in the characterisation of mass lesions originating from the PPS or its neighboring spaces. A good knowledge of the local anatomy is a prerequisite, and in combination with the imaging characteristics of the mass, a precise diagnosis, or at least a limited list of differential diagnoses, can be put forward in most cases.

References

Al Otieschan AA, Saleem M, Manohar MB, Larson S, Atallah A (1998) Malignant schwannoma of the parapharyngeal space. J Laryngol Otol 112:883–887

Farina D, Hermans R, Lemmerling M, Op de beeck K (1999) Imaging of the parapharyngeal space. J Belge Radiol 82:234–240

Grégoire V, Levendag P, Ang KK et al (2003) CT-based delineation of lymph node levels and related CTVs in the node-negative neck: DAHANCA, EORTC, GORTEC, NCIC, RTOG consensus guidelines. Radiother Oncol 69:227–236

Heimgartner S, Zbaeren P (2009) Thyroid carcinoma presenting as a metastasis to the parapharyngeal space. Otolaryngol Head Neck Surg 140:435–436

Kahraman A, Yildirim I, Kilic MA, Okur E, Demirpolat G (2009) Horner's syndrome from giant schwannoma of the cervical sympathetic chain: case report. B-ENT 5: 111–114

Kakani RS, Bahadur S, Kumar S, Tandon DA (1992) Parapharyngeal lipoma. J Laryngol Otol 106:279–281

Kato H, Kanematsu M, Mizuta K et al (2010) "Flow-void" sign at MR imaging: a rare finding of extracranial head and neck schwannoma. J Magn Reson Imaging 31:703–705

Lombardi D, Nicolai P, Antonelli AR, Maroldi R, Farina D, Shaha AR (2004) Parapharyngeal lymph node metastasis: an unusual presentation of papillary thyroid carcinoma. Head Neck 26:190–196

Luna-Ortiz K, Navarrete-Alemán JE, Granados-García M, Herrera-Gómez A (2005) Primary parapharyngeal space tumors in a Mexican cancer center. Otolaryngol Head Neck Surg 132:587–591

Maroldi R, Battaglia G, Maculotti P, Bondioni MP, Gheza G, Chiesa A (1994) Diagnostica per immagini delle lesioni dello spazio parafaringeo. In: Mosciaro O (ed) I Tumori parafaringei. Studio Forma, Verona, pp 69–103

Miller FR, Wanamaker J, Lavertu P, Wood BG (1996) Magnetic resonance imaging and the management of parapharyngeal space tumors. Head Neck 18:67–77

Mukherji SK, Castillo M (1998) A simplified approach to the spaces of the suprahyoid neck. Radiol Clin N Am 36:761–780

Nasser JG, Attia EL (1990) A conceptual approach to learning and organizing the surgical anatomy of the skull base. J Otolaryngol 19:114–121

Olsen KD (1994) Tumors and surgery of the parapharyngeal space. Laryngoscope 104:1–28

Pang KP, Goh CH, Tan HM (2002) Parapharyngeal space tumours: an 18 year review. J Laryngol Otol 116: 170–175

Piccin O, Cavicchi O, Caliceti U (2008) Branchial cyst of the parapharyngeal space: report of a case and surgical

approach considerations. Oral Maxillofac Surg 12: 215–217

Saito DM, Glastonbury CM, El-Sayed IH, Eisele DW (2007) Parapharyngeal space schwannomas: preoperative imaging determination of the nerve of origin. Arch Otolaryngol Head Neck Surg 133:662–667

Smith JC, Snyderman CH, Kassam AB, Fukui MB (2006) Giant parapharyngeal space lipoma: case report and surgical approach. Skull Base 12:215–220

Som PM, Curtin HD (1995) Lesions of the parapharyngeal space. Role of MR imaging. Otolaryngol Clin N Am 28:515–542

Swartz JD, Harnsberger HR, Mukherji SK (1998) The temporal bone: contemporary diagnostic dilemmas. Radiol Clin N Am 36:819–854

Yuen HW, Goh CH, Tan TY (2006) Enlarged cervical sympathetic ganglion: an unusual parapharyngeal space tumour. Singap Med J 47:321–323

Malignant Lesions of the Masticator Space

Christian Czerny and Riste Saat

Contents

Abstract

The masticator space is a deep facial space containing the mandibular ramus and the muscles of mastication. The third branch of the trigeminal nerve is also part of the masticator space. Malignancies arising of the masticator space are mostly of mesenchymal origin, such as osteosarcomas, rhabdomysarcomas or angiosarcomas, but also Non-Hodgkin lymphomas are encountered. Beside these primary malignancies, secondary malignancies may involve the masticator space. Malignancies from the surrounding tissues can invade the masticator space, and occasionally a metastasis may occur in this space. The malignant masticator space lesions and their imaging characteristics are described in this chapter, as well as the differential diagnosis with benign entities.

1 Introduction

The masticator space is a deep facial space surrounded by the superficial layer of the deep cervical fascia. The content of the masticator space consists of muscles of the mastication which are the temporalis muscle, the masseter muscle, the lateral and medial pterygoid muscles (Chong and Fan 1996; Aspestrand and Boysen 1992).

These muscles attach to the ascending part of the mandibula, the mandibular ramus. Furthermore, it contains the third branch of the trigeminal nerve (V3), the mandibular nerve. The third branch of the trigeminal nerve leaves the skull base through the oval foramen, passes between the lateral and medial

C. Czerny (✉) · R. Saat
Division of Neuroradiology–Musculoskeletal-Radiology, Department of Radiology, University Hospital Vienna, Waehringer Guertel 18-20, 1090 Vienna, Austria
e-mail: christian.czerny@meduniwien.ac.at

R. Saat
Department of Radiology, HUCH, Meilahti Hospital, PL 340, Haartmaninkatu 4, 00029 Helsinki, Finland

R. Hermans (ed.), *Head and Neck Cancer Imaging*, Medical Radiology. Diagnostic Imaging,
DOI: 10.1007/174_2011_379, © Springer-Verlag Berlin Heidelberg 2012

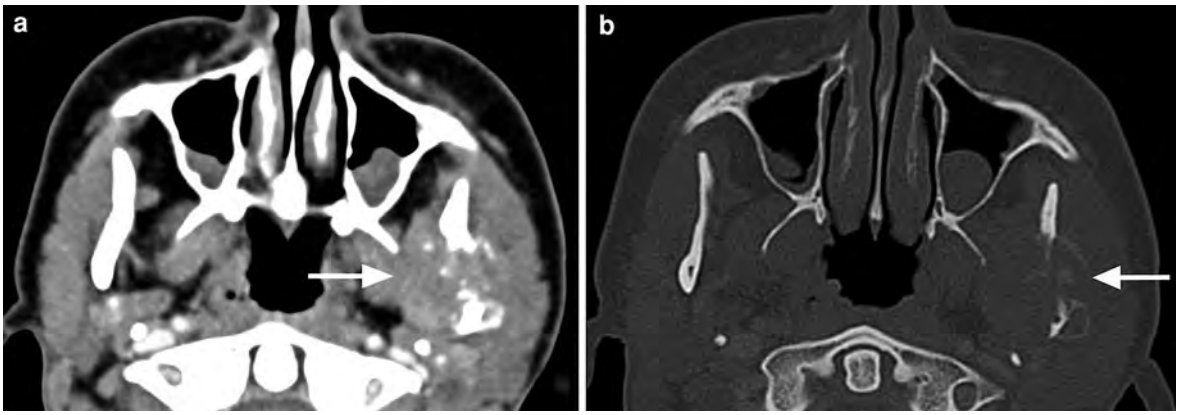

Fig. 1 Malignant intrinsic lesion of the left masticator space in a 55-year-old female with trismus and pain of the left V3 territory with biopsy-proven osteosarcoma. **a** Contrast-enhanced axial CT image shows a soft tissue mass causing osteolysis of the left mandibular ramus with soft tissue infiltration (*arrow*). **b** Axial CT image in bone-window-level-setting shows an irregular unsharply demarcated osteolytic region with periostal reaction of the left mandibular ramus (*arrow*)

pterygoid muscles, and then enters the mandible through the mandibular foramen. The V3 nerve provides the motor innervation of the masticator muscles, and carries sensory information from the mandibular teeth, gums, and lower lip and chin region.

Primary malignancies arising from/within the masticator space are mostly of mesenchymal origin (Galli et al. 2010; Mendenhall et al. 2010; Palacios and Valvassori 2000). Secondary malignancies involving the masticator space arise from the surrounding structures—such as the oral cavity, pharynx or the parotid gland—or correspond to metastasis from other regions of the body (Nishikawa et al. 2010; Loehn et al. 2009; Glaser et al. 1997).

The spectrum of primary malignant lesions includes osseous lesions such as mandibular osteosarcoma, which is the most common primary malignancy in this space (Fig. 1). Other osseous tumors are e.g. chondrosarcomas or plasmocytoma. Malignant tumors arising within the muscles and fascias are rhabdomyosarcomas or fibrosarcomas, and those arising from the nerve may be neurosarcomas (Gosau et al. 2008; Toranzo-Fernandez et al. 2000; Chemello et al. 1988). Other primary malignancies seen in this space are hemangiosarcomas and Non-Hodgkin's lymphoma (Daniels et al. 1996).

The clinical symptoms of malignant lesions of the masticator space are swelling, numbness, pain and trismus. The nerval symptoms of pain and numbness are also caused by involvement of V3, which may serve as a route for perineural tumor spread into the skull base (Hyare et al. 2010). Trismus is a reactive mouth opening impairment and caused by infiltration of the masticator muscles by a malignant tumor or an inflammatory process like an abscess.

2 Imaging Techniques

The different imaging techniques of multidetector-CT (MDCT), and magnetic resonance imaging (MRI), as well as PET-CT and their ability to depict tumoral lesions are described earlier in this book (see "Imaging Techniques").

MDCT of the masticator space is performed in the axial plane beginning cranially from the suprasellar region down to the base of the neck. Symmetrical imaging of the head and neck region is important as some pathologies may be very subtle and the comparison of one side with the other allows to detect and delineate the lesion.

The investigation is performed with intravenous administration of iodinated contrast material. The images are obtained in a soft-tissue- and bone-window-level setting. Coronal and sagittal images may be reconstructed from the axial sections. The section thickness of the different imaging planes should be 3 mm or less, without interval.

MRI is performed with a dedicated head and neck coil. The predominant plane is the axial plane, but also coronal and sagittal planes are obtained. The standard sequences are STIR or T2-weighted fat-suppressed

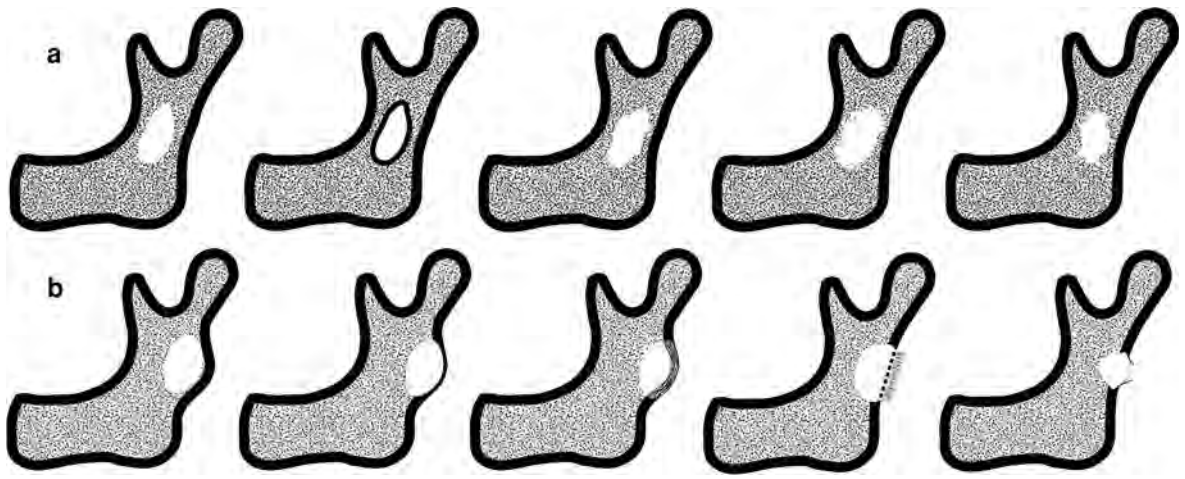

Fig. 2 **a** Forms of osteolysis (A1) geographic no margin (A2) geographic sclerotic margin (A3) geographic unsharp margin (A4) motheaten (A5) permeative **b** Forms of cortical reactions (B1) bulging of corticalis (B2) thinning of corticalis (B3) thinning and lamellating (B4) sunburst (B5) Codman triangle

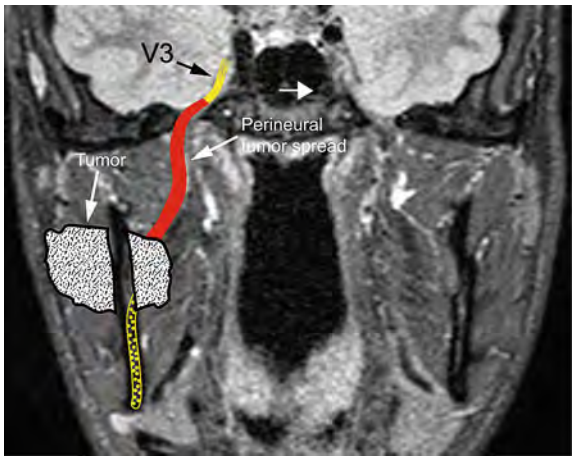

Fig. 3 Graph illustrating perineural tumor spread along the V3 through the oval foramen by a tumor growing around the mandibular nerve

sequences followed by T1-weighted sequences before and after the intravenous application of contrast material. In addition, also T1-weighted contrast enhanced sequences with fatsuppression may be performed. The injection of contrast material is mandatory as it enables to better delineate the tumor extent, including possible perineural spread. The section thickness should not be thicker than 3–4 mm and the matrix should be high, if possible 512 × 512 depending on the scanner technology.

PET is nowadays performed in combination with MDCT (PET-CT, see "Imaging Techniques").

3 General Imaging Findings

The most important goal of imaging is to correctly depict the anatomic extent of the lesion and to determine whether the lesion originates primarily from the structures of the masticator space or invades the masticator space from outside (Chong and Fan 1996). The depiction of the epicentre of the mass as well as the displacement of structures—such as the fatty tissues—may be helpful to exactly localize and characterize the type of lesion.

Malignant tumors arising from the mandible may show a characteristic pattern of bone destruction and periosteal reaction, as has been described for the peripheral skeleton and can also be applied at the mandible.

The radiological appearances of bone destruction has been summarized in a classification system by Lodwick. This system is very useful to describe the aggressiveness of a bone tumor. Lodwick described three types (grading) of destruction (Lodwick et al. 1980):

1. Geographic destruction.
2. Moth-eaten like destruction.
3. Permeative destruction.

These types of destruction correspond to the biological activity and aggressiveness of the lesion. Geographic destruction mostly occurs in benign lesion, while moth-eaten like destruction and

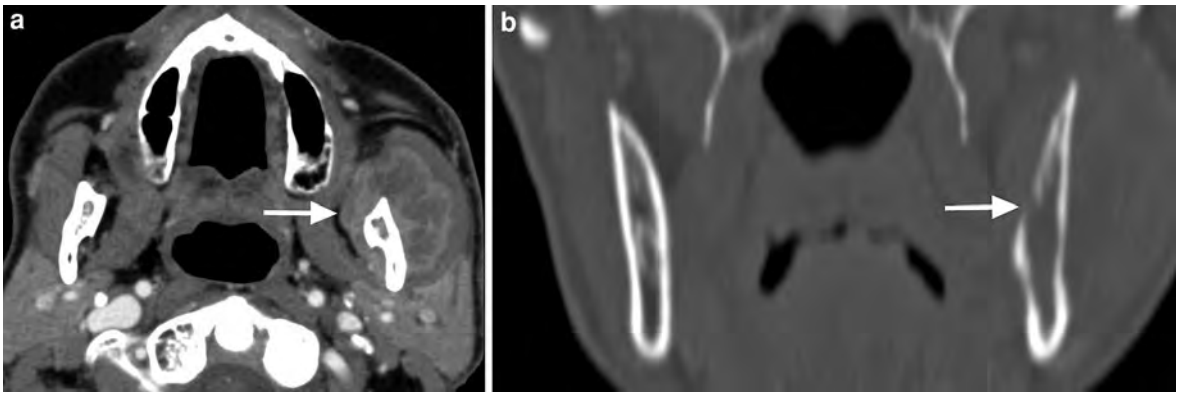

Fig. 4 Malignant intrinsic lesion of the left masticator space in a 67-year-old female with trismus and dysaesthesia of the left V3 territory with biopsy-proven osteosarcoma. **a** Axial contrast-enhanced CT image shows a soft tissue mass in the masticator space surrounding the left mandibular ramus (*arrow*). **b** Coronal CT image in bone-window-level-setting shows an irregular unsharp osteolysis of the cortical and spongiotic structures of the left mandibular ramus (*arrow*); final diagnosis was osteosarcoma of the mandible

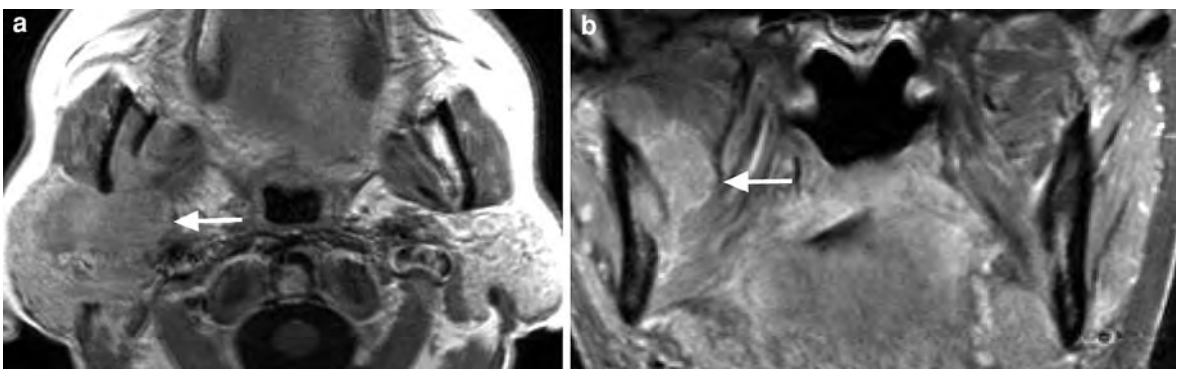

Fig. 5 Malignant intrinsic lesion of the right masticator space in a 72-year-old male with numbness and pain of the right V3 territory with biopsy-proven multiple myeloma. **a** Axial T1-weighted MR image after i.v. contrastmaterial shows a mass (*arrow*) infiltrating the right mandible and the adjacent parotid gland. **b** Coronal fat-suppressed T1-weighted MR image after i.v. contrastmaterial shows the mass (*arrow*) infiltrating the right mandible and the adjacent masticator muscles. Biopsy revealed plasmocytoma of the right mandible

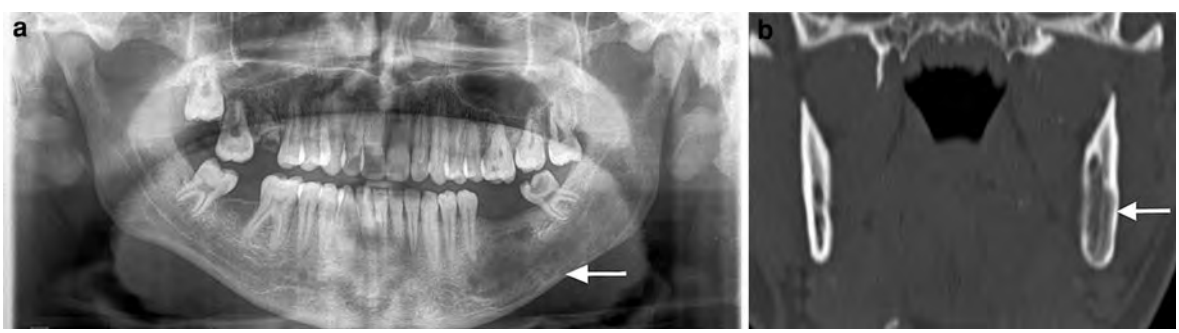

Fig. 6 Malignant intrinsic lesion of the left masticator space in a 32-year-old female with dysaesthesia of the left V3 territory with biopsy-proven Ewing sarcoma. **a** Panoramic radiograph reveals unsharp permeative osteolysis (*arrow*) of the left mandibular ramus. **b** Coronal CT image in bone-window-level-setting shows unsharp-diffuse osteolysis of the left mandibular ramus (*arrow*)

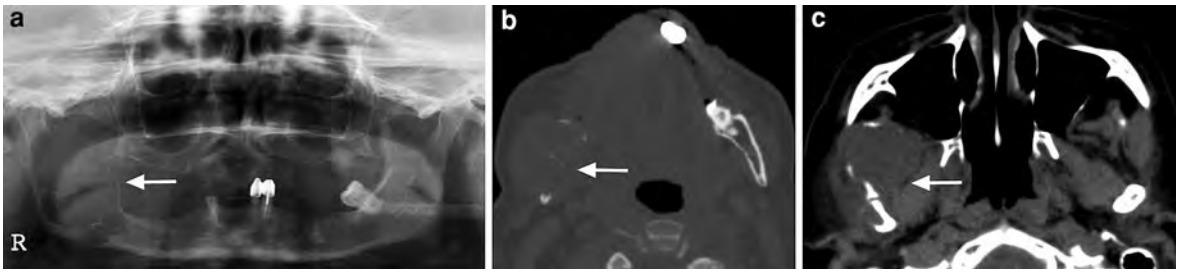

Fig. 7 Malignant intrinsic lesion of the right mandible in a 57-year-old male with progressive swelling of the right cheek and dysaesthesia of the right inferior alveolar nerve with biopsy-proven fibromyxosarcoma. **a** Panoramic radiograph reveals lobulated slightly unsharply marginated osteolysis of the right mandibular ramus (*arrow*). **b** Axial CT image in bone-window-level-setting shows an irregular unsharp osteolysis of the right mandibular ramus (*arrow*). **c** Axial CT image in soft window shows osteolytic and a soft tissue mass infiltrating around the mandibular ramus

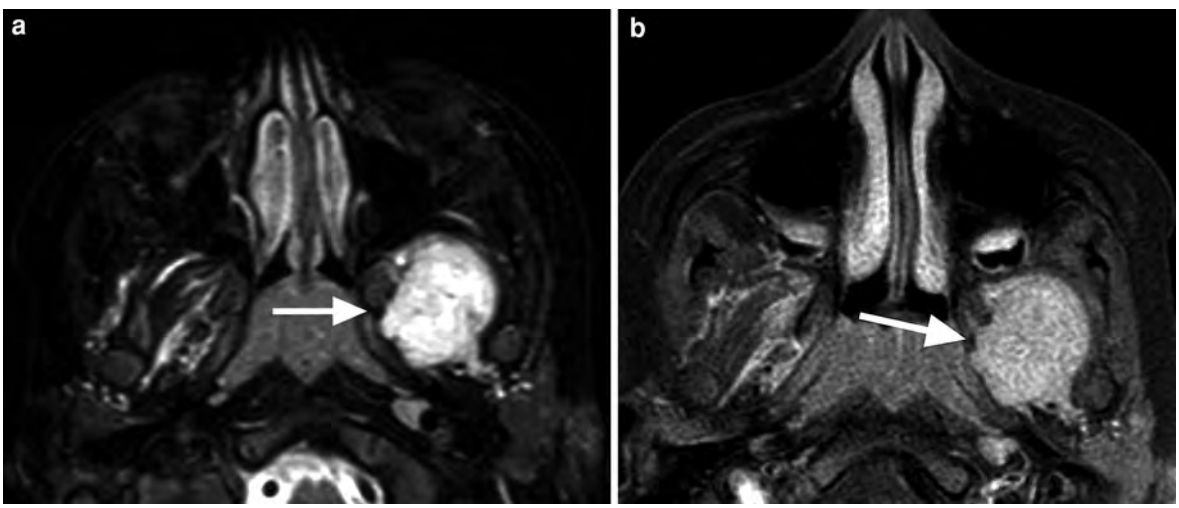

Fig. 8 Malignant intrinsic lesion of the left masticator space in a 5-year-old boy presenting with trismus. **a** Axial T2w fat-suppressed MR image shows a hyperintense mass (*arrow*) in the left masticator space within the lateral pterygoid muscle. **b** Axial T1w fat suppressed MR image after contrastmaterial application shows an enhancing mass (*arrow*) with the epicentre in the left lateral pterygoid muscle. Biopsy revealed an embryonic pleomorphic rhabdomyosarcoma

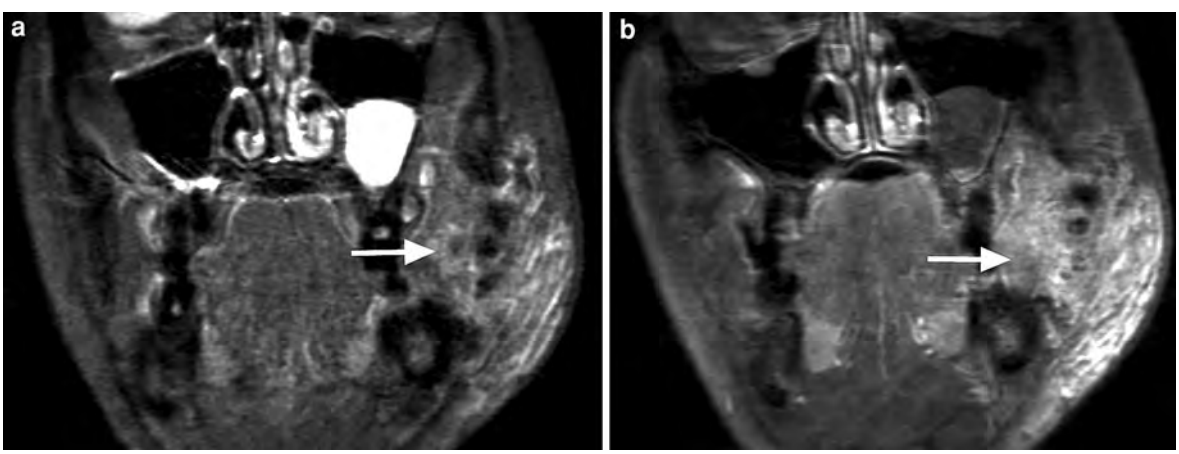

Fig. 9 Malignant intrinsic lesion of the left masticator space in a 64-year-old male with trismus. **a** T2-weighted MR image with fatsuppression shows an ill-defined hyperintense mass (*arrow*) containing hypointense structures, with its epicentre around the left mandibular ramus and infiltration of the adjacent masticator muscles. **b** Coronal contrast-enhanced MR image T1-weighted shows an ill-defined mass with a "salt-and-pepper-sign" (*arrow*). This was histologically diagnosed as an angiosarcoma

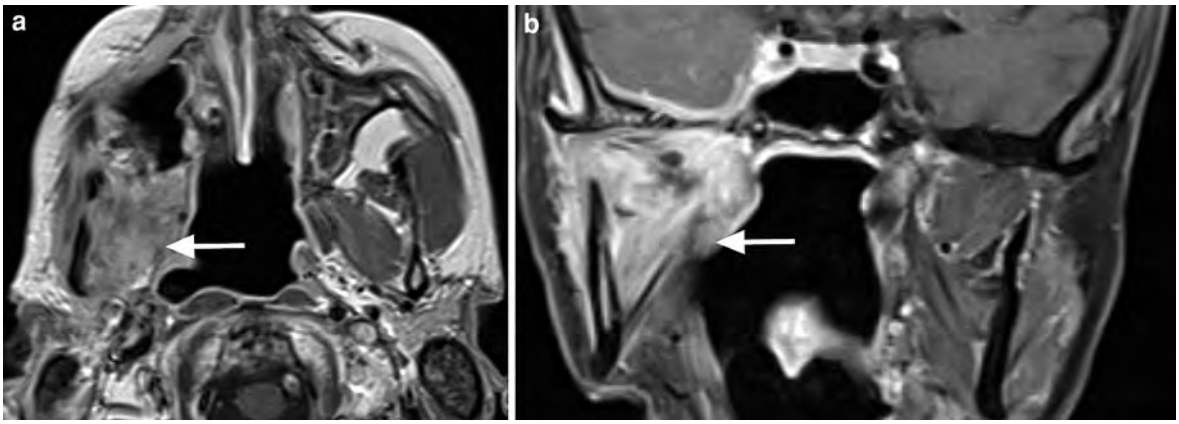

Fig. 10 Malignant extrinsic lesion of the right masticator space in a 49-year-old female with numbness and pain of the right V3 territory with recurrent perineural tumor spread by an adenoid cystic carcinoma of the parotid gland. **a** Axial contrast-enhanced T1-weighted MR image shows a mass (*arrow*) primarily originating from the right parotid gland infiltrating the right mandible and the masticator muscles. **b** The coronal image also shows an enhancement in the right mandible and the masticator muscles and also perineural tumor extension along the V3 with meningeal enhancement (*arrow*). Histology revealed recurrent adenoid cystic carcinoma

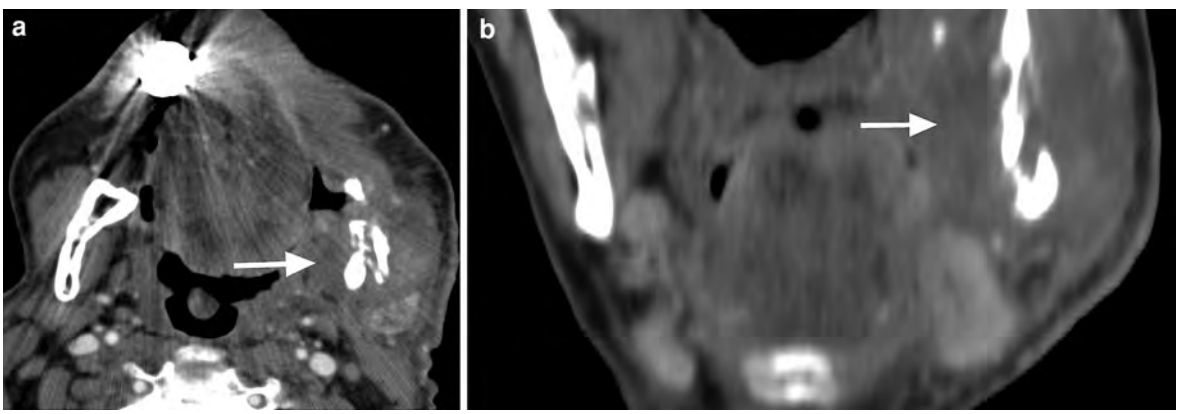

Fig. 11 Malignant extrinsic lesion of the left masticator space in a 48-year-old male with pain in the left V3 territory by invasion of the mandible by a surgically proven squamous cell carcinoma of the left tonsil. **a, b** Axial and coronal CT image after i.v. contrast-material application shows osteolysis of the mandibular ramus, surrounded by an enhancing soft tissue (*arrow*)

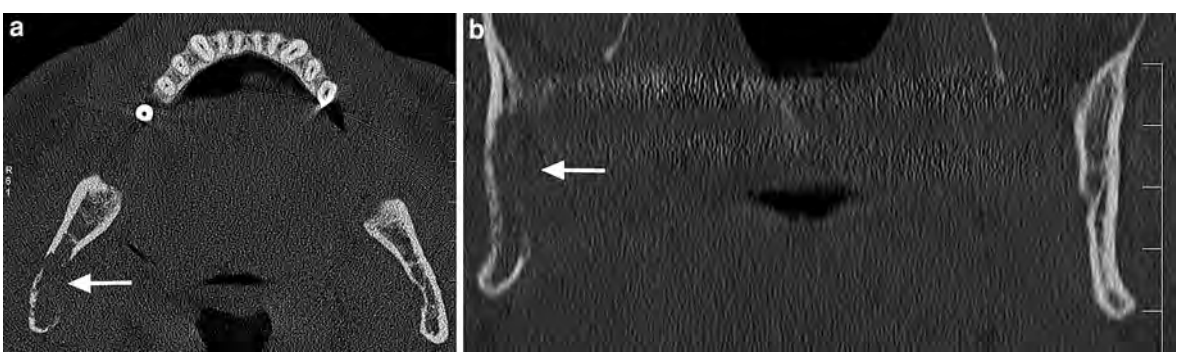

Fig. 12 Malignant secondary lesion of the right mandible in a 55-year-old female with dysaesthesia of the right V3 territory. **a**, **b** Axial and coronal CT image in bone-window-level-setting shows an irregular unsharply marginated osteolysic area (*arrow*) in the right mandibular ramus. Further investigation revealed metastasis from thyroid carcinoma

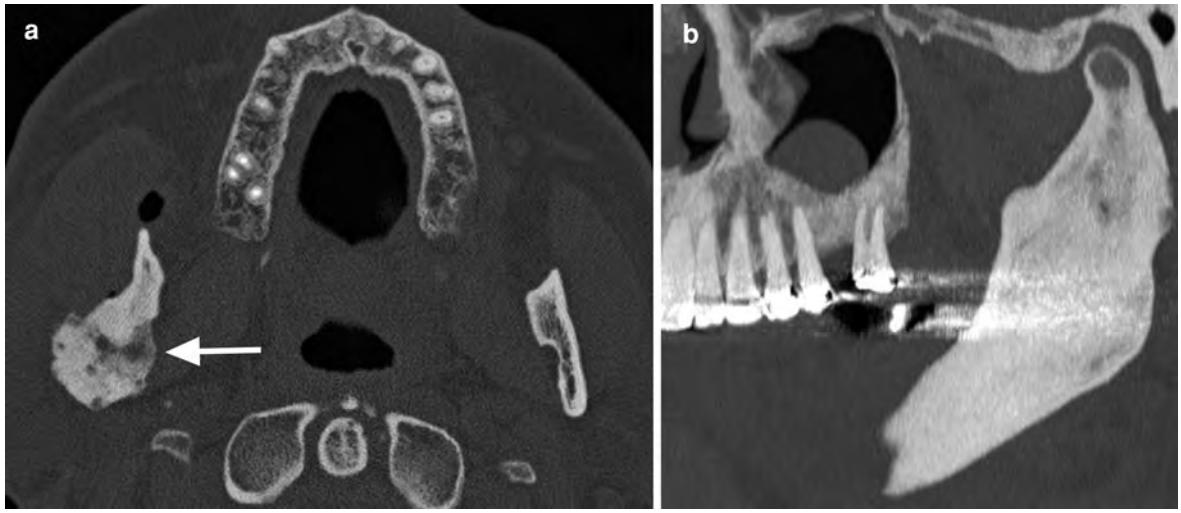

Fig. 13 Malignant secondary lesion of the right mandible in an 83-year-old male with dysaesthesia of the right V3 territory caused by a osteoblastic metastasis of a prostatic carcinoma. **a, b** Axial and sagittal CT image in bone-window-level-setting shows sclerotic osteoblastic lesion of the right mandibular ramus (*arrow*)

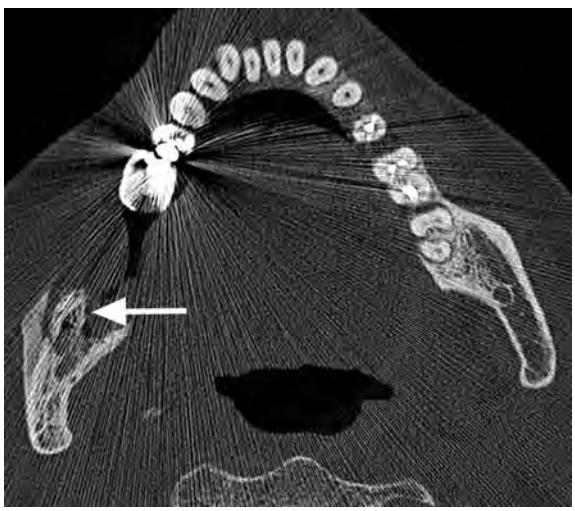

Fig. 14 Intrinsic lesion of the right mandible in a 69-year-old female with dysaesthesia of the right V3 territory caused by bisphosphonates related osteonecrosis. Axial CT image in bone-window-level setting shows lamellating periosteal reaction and sclerosis and fragmentation of the right ascending ramus of the mandible (*arrow*)

permeative destruction are usually seen in very aggressive tumors (Fig. 2). Sometimes moth-eaten like destructions or a mixture of moth-eaten like destruction and permeative destruction may be seen in inflammatory processes; the differential diagnosis may then be difficult based on imaging alone, and the correct diagnosis can often only be obtained by biopsy.

Furthermore, Lodwick described several types of periosteal reactions indicating the grade of aggressiveness. Bulging and thinning of the cortex without periosteal reaction reflects more benign types, while thinning or disruption of the cortex, with a periosteal reaction such as a so-called sunburst or Codmans' triangle indicates malignancy.

In addition to the destruction of the bone, primarily osseous tumors often display a soft tissue component. In some tumors, this soft tissue component may show a calcified matrix. In some tumors such as the chondrosarcoma, characteristic popcorn-like calcifications may be seen.

Malignant tumors arising from the soft tissues of the masticator space may invade the mandible and cause bony destruction, which mostly appears irregular and has unsharp margins. Metastasis within the bone may be either osteolytic, or osteoblastic as is seen for example in prostate cancer (Glaser et al. 1997).

When the V3 is involved by the tumor, signs of muscle atrophy may be seen. Initially, denervation atrophy may result in an increased contrast enhancement of the muscles; later, the muscles will show volume decrease and fatty atrophy, which is easily

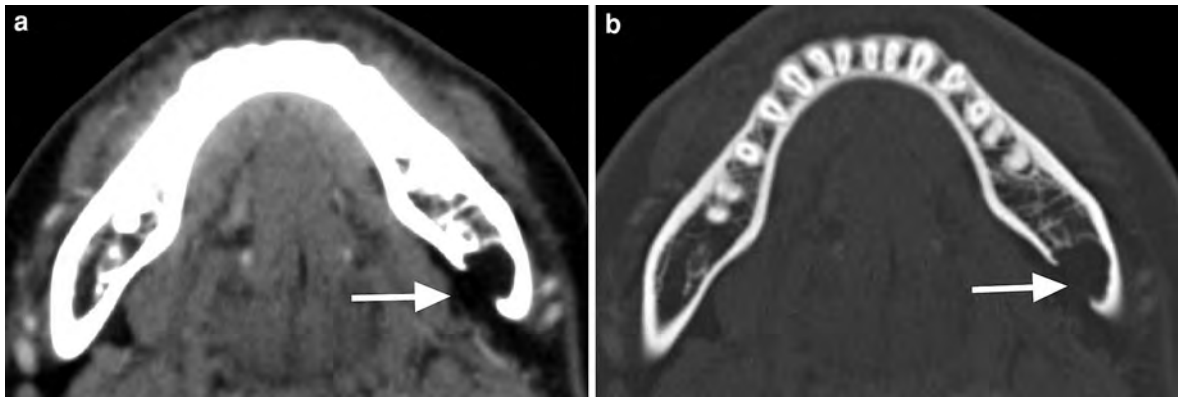

Fig. 15 Intrinsic variant on the lingual side of the left mandible in a 25-year-old male without any clinical symptoms. **a** Axial contrast-enhanced CT image shows a bony defect containing fatty tissue in the left mandibular angle (*arrow*). **b** Axial CT image in bone-window-level-setting shows a regular margin of the bony defect (*arrow*). This appearance is characteristic of a Staphne cyst

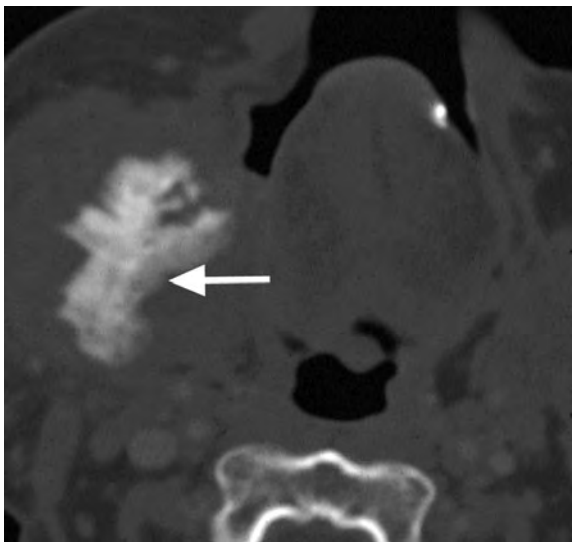

Fig. 16 Intrinsic lesion of the right mandible in a 75-year-old male with numbness in the territory of the right inferior alveolar nerve territory caused by biopsy-proven chronic osteomyelitis. Axial CT image in bone-window-level-setting shows sunburst-like periostal reaction (*arrows*) of the right mandibular ramus

seen on MRI. Also, increased contrast enhancement and potential thickening of the V3 nerve is a sign of perineural tumor invasion (Fig. 3) (Maroldi et al. 2008).

These general radiologic findings should be taken into consideration together with the clinical information to establish for most accurate diagnosis.

4 Imaging Findings of Primary Malignancies

The most common primary malignant bone tumor in the masticator space is the osteosarcoma (Figs. 1 and 4) (Kim et al. 2010; dos Santos and Cavalcanti 2002; Zorzan et al. 2001). MDCT in bone-window-level setting excellently depicts the periosteal and cortical changes which are destructive and sometimes accompanied with a so-called "sunburst" periosteal reaction. This is characteristic for a highly malignant bone tumor. MRI depicts the osseous invasion better than CT (Chidzonga and Mahomva 2007). Especially, T1-weighted contrast enhanced sequences with fatsuppression delineate the tumor extent. PET-CT is a valuable tool to show distant metastasis.

Very rarely primary bone malignancies such as multiple myeloma or plasmocytoma may also be seen in the mandibule (Fig. 5). In these cases, if no periosteal or cortical reactions are present, MRI depicts the intraosseous-spongiotic extension of the tumor replacing the normal bone marrow. Other tumors, such as the Ewing sarcoma may arise in the mandible and are sometimes depicted as a subtle osteolytic region on panoramic radiographs of the mandible (Fig. 6). The tumor extension is much better seen on MDCT or MR images.

Fibrosarcoma or rhabdomyosarcoma may cause an unsharp, lobulated mandibular destruction, as seen on panoramic radiographs or on an MDCT in a

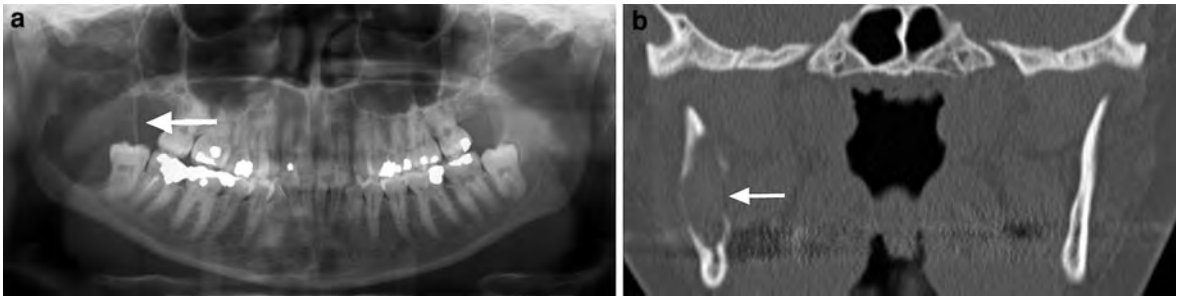

Fig. 17 Benign intrinsic lesion of the right mandible in a 26-year-old male with subtle numbness of the right inferior alveolar nerve. **a** Panoramic radiograph reveals lobulated smooth osteolysic area (*arrow*) in the right mandibular ramus. **b** Coronal CT image in bone-window-level-setting shows a smooth-sharply demarcated osteolytic area in the right mandibular ramus (*arrow*). Further investigation revealed a keratocyst

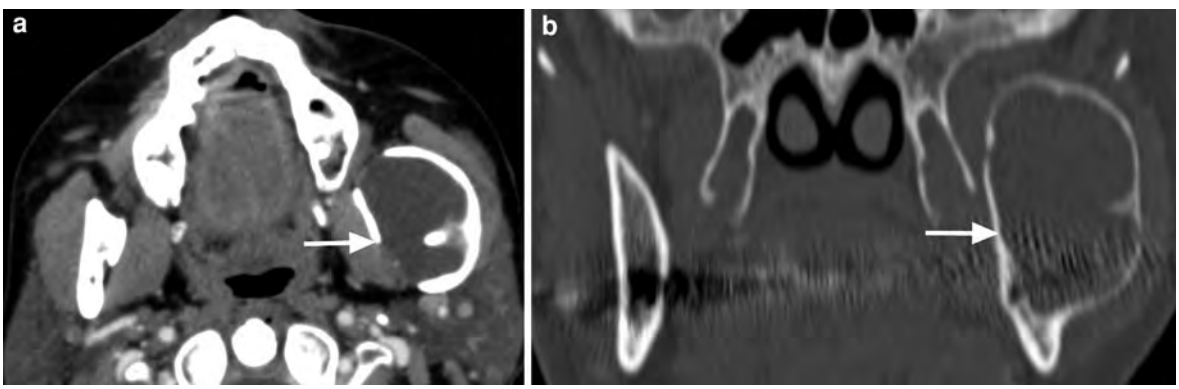

Fig. 18 Benign intrinsic lesion of the left mandible in a 42-year-old male with numbness in the territory of the left inferior alveolar nerve. **a** Axial contrast-enhanced CT image shows an expansile, largely non-enhancing soft tissue mass (*arrow*) within the left mandibular ramus. **b** Coronal CT image in bone-window-level-setting shows smoothly marginated osteolysis with scalloping of the left mandibular ramus (*arrow*). This was caused by an ameloblastoma

bone–window-level setting (Fig. 7) (Gosau et al. 2008; Chemello et al. 1988). Contrast-enhanced MDCT or MRI will show a mass originating from the soft tissues of the masticator space with bony destruction.

The presence of a mass within the masticator muscles in a child is highly suggestive for a rhabdomyosarcoma (Fig. 8). These tumors may be hyperintense on STIR or T2-weighted fatsuppressed images with a strong contrast enhancement on T1-weighted images. The mass appears sometimes lobulated with subtle irregular-unsharp margins infiltrating the surrounding tissues.

Because of its excellent soft tissue contrast resolution, MRI may show signs indicating that the tumor originates from vascular structures (Daniels et al. 1996). The "salt-and-pepper-sign" is a characteristic of vascular tumors and is seen e.g. in angiosarcomas (Fig. 9). Apart from this pattern, MRI may also show diffuse infiltration of such a tumor into the surrounding tissues.

5 Imaging Findings of Secondary Malignancies

The masticator space can be invaded by malignancies surrounding or lying close to the masticator space. These secondary neoplasms can be of parotid gland origin. When invading the masticator space, these tumors may reach the V3 and grow perineurally, especially adenoid cystic carcinomas are notorious for their tendency to grow along nerves (Figs. 3 and 10) (Maroldi et al. 2008; Laine et al. 1990).

Squamous cell carcinomas originating from the retromolar trigone and from the oropharyngal tonsil can also infiltrate the masticator space, sometimes appearing like a tumor primarily arising from the masticator space (Fig. 11).

The masticator space can also be affected by metastasis. Such metastasis may occur in the soft tissues or in the mandible. Bony metastasis can be osteolytic (e.g. from lung or breast cancer) or osteoblastic (e.g. from prostate cancer) (Glaser et al. 1997; Nishikawa et al. 2010). Osteolytic metastasis produce an irregular-unsharp lysis of the bone, while osteoblastic metastasis appear mostly very sclerotic on conventional radiographs or on MDCT in a bone-window-level setting (Figs. 12 and 13).

6 Posttreatment Imaging

Also after treatment, imaging plays an important role in the management of the patient.

The treatment options for malignancies in the masticator space depend on the histology and extent of the lesion; this may be either surgery, chemotherapy or chemoradiotherapy, or a combination of these (Nishikawa et al. 2010). Posttreatment imaging may delineate complications e.g. after surgery or show tumor response or non-response after therapy. Also tumor recurrence may be depicted by imaging before becoming clinically apparent.

Treatment of bone metastasis, or of osteoporosis by bisphosphonates may cause osteonecrosis of the mandible (Fig. 14) (Bisdas et al. 2008; Studer et al. 2004). In these patients, osteolytic and osteosclerotic changes of the bone can be seen sometimes with fragmentation and sequestration, well delineated on MDCT in a bone-window-level setting or on a so-called Dental-CT. Similar imaging findings may be seen in patients with mandibular osteoradionecrosis, but in a different clinical context.

7 Benign Conditions Mimicking Malignancy

Some benign conditions may radiologically mimic malignant pathologies.

A Stafne cyst is a focal cortical depression in the lingual cortex of the posterior mandible. On panoramic radiography, it appears as a cystic lesion. The bony "defect" either contains fat or salivary gland tissue (Fig. 15) (Dorman and Pierse 2002). It has a typical radiologic appearance and location and should not be misinterpretated as a potentially suspect lesion.

Osteomyelitis is an important differential diagnosis and sometimes has an appearance similar to malignancies primarily arising from the mandible. In some cases osteomyelitis—especially when chronic—may mimic a malignant tumor as it may show periosteal and cortical reactions resembling a sunburst-appearance of an osteosarcoma (Fig. 16) (Schuknecht and Valavanis 2003). The clinical history of the patient combined with laboratory data and imaging findings lead to the correct diagnosis.

Dentogenic cysts, keratocysts or odontogenic tumors, such as ameloblastoma, may extend in the ascending ramus of the mandible (Kaneda et al. 2003). In most of these cases smooth osteolysis with cortical thinning and scalloping can be seen radiologically (Figs. 17 and 18). The combination of clinical information and radiological findings often allows to establish the dentogenic origin of these lesions.

Intra-osseous vascular malformations may cause mandibular osteolysis; the identification of large feeding vessels allows to make the diagnosis. A biopsy should not be performed in such cases to avoid significant bleeding.

8 Summary

Primary and secondary malignancies of the masticator space are rare entities. Many different kinds of malignant neoplasms can be seen in this space.

By determining the point of origin of the neoplasm, and combining imaging findings with clinical data, in most cases the differential diagnosis can be limited to a number of entities.

References

Aspestrand F, Boysen M (1992) CT and MR imaging of primary tumors of the masticator space. Acta Radiol 33(6):518–522

Bisdas S, Chambron Pinho N, Smolarz A, Sader R, Vogl TJ, Mack MG (2008) Bisphosphonate-induced osteonecrosis of the jaws: CT and MRI spectrum of findings in 32 patients. Clin Radiol 63(1):71–77

Chemello PD, Nelson CL, Tomich CE, Sadove AM (1988) Embryonal rhabdomyosarcoma arising in the masseter

muscle as a second malignant neoplasm. J Oral Maxillofac Surg 46(10):899–905
Chidzonga MM, Mahomva L (2007) Sarcomas of the oral and maxillofacial region: a review of 88 cases in Zimbabwe. Br J Oral Maxillofac Surg 45(4):317–318
Chong VF, Fan YF (1996) Pictorial review: radiology of the masticator space. Clin Radiol 51(7):457–465
Daniels RL, Haller JR, Harnsberger HR (1996) Hemangiopericytoma of the masticator space. Ann Otol Rhinol Laryngol 105(2):162–165
Dorman M, Pierse D (2002) Ectopic salivary gland tissue in the anterior mandible: a case report. Br Dent J 193(10):571–572
dos Santos DT, Cavalcanti MG (2002) Osteosarcoma of the temporomandibular joint: report of 2 cases. Oral Surg Oral Med Oral Pathol Oral Radiol Endod 94(5):641–647
Galli F, Flor N, Villa C, Franceschelli G, Pompili G, Felisati G, Biglioli F, Cornalba GP (2010) The masticator space value of computed tomography and magnetic resonance imaging in localisation and characterisation of lesions. Acta Otorhinolaryngol Ital 30(2):94–99
Glaser C, Lang S, Pruckmayer M, Millesi W, Rasse M, Marosi C, Leitha T (1997) Clinical manifestations and diagnostic approach to metastatic cancer of the mandible. Int J Oral Maxillofac Surg 26(5):365–368
Gosau M, Draenert FG, Winter WA, Mueller-Hoecker J, Driemel O (2008) Fibrosarcoma of the childhood mandible. Head Face Med 16(4):21
Hyare H, Wisco JJ, Alusi G, Cohen M, Nabili V, Abemayor E, Kirsch CF (2010) The anatomy of the nasopharyngeal carcinoma spread through the pharyngobasilar fascia to the trigeminal mandibular nerve on 1.5T MRI. Surg Radiol Anat 32(10):937–944
Kaneda T, Minami M, Kurabayashi T (2003) Benign odontogenic tumors of the mandible and maxilla. Neuroimaging Clin N Am 13(3):495–507
Kim GT, Lee JK, Choi BJ, Kim J, Han SH, Kwon YD (2010) Malignant transformation of monostotic fibrous dysplasia in the mandible. J Craniofac Surg 21(2):601–603
Laine FJ, Braun IF, Jensen ME, Nadel L, Som PM (1990) Perineural tumor extension through the foramen ovale: evaluation with MR imaging. Radiology 174(1):65–71
Lodwick GS, Wilson AJ, Farrel C, Virtama P, Dittrich F (1980) Determination of growth rates of focal lesions of bone from radiographs. Radiology 134(3):577–583
Loehn B, Walvekar RR, Harton A, Nuss D (2009) Mandibular metastasis from a skull base chordoma: report of a case with review of literature. Skull Base 19(5):363–368
Maroldi R, Farina D, Borghesi A, Marconi A, Gatti E (2008) Perineural tumor spread. Neuroimaging Clin N Am 18(2): 413–429
Mendenhall WM, Fernandes R, Werning JW, Vaysberg M, Malyapa RS, Mendenhall NP (2010) Head and neck osteosarcoma. Am J Otolaryngol [Epub ahead of print: 18 Nov]
Nishikawa H, Nakashiro K, Sumida T, Sugita A, Hamakawa H (2010) Mandibular osteoblastic metastasis of poorly differentiated carcinoma of the thyroid gland. Int J Oral Maxillofac Surg 39(3):301–304
Palacios E, Valvassori G (2000) Masticator space tumor, malignant schwannoma. Ear Nose Throat J 79(8):550
Schuknecht B, Valavanis A (2003) Osteomyelitis of the mandible. Neuroimaging Clin N Am 13(3):605–618
Studer G, Grätz KW, Glanzmann C (2004) Osteoradionecrosis of the mandible in patients treated with different fractionations. Strahlenther Onkol 180:233–240
Toranzo-Fernandez JM, Noyola-Frias MA, Sanchez-Hermosillo E, Gonzalez-Mendoza E (2000) Rhabdomyosarcoma in children: report of two cases. J Clin Pediatr Dent 25(1):87–90
Zorzan G, Tullio A, Bertolini F, Sesenna E (2001) Osteosarcoma of the mandibular condyle: case report. J Oral Maxillofac Surg 59(5):574–577

Neoplasms of the Sinonasal Cavities

Davide Farina and Roberto Maroldi

Contents

Abstract

The paranasal sinuses are a complex framework of air cavities, variable in number and size, located in an overall small anatomical area. The high variety of tissues present in this region accounts for the extremely wide range of benign and malignant tumors, only a minority of which display a typical imaging appearance. However, imaging plays a pivotal role in treatment planning either allowing to select tumors amenable to purely endoscopic resection and, in advanced malignant tumors, detecting tumor invasion in crucial anatomic areas (such as the orbit, anterior skull base and masticator space). Detailed knowledge of the anatomy is the key to exploit all the information provided by imaging, not only at staging, but also during follow-up. A pattern of expected anatomic changes is predictable based on the treatment strategy, and serves as a guide to detect recurrent tumors.

1 Introduction

An extremely wide range of benign and malignant tumors may arise in the nose and paranasal sinuses, actually reflecting the high variety of tissues present in such a restricted anatomical area. Incidence is overall rare: among benign histotypes, for example, inverted papilloma (IP) is reported to occur in 0.6–1.5/100.000 inhabitants per year, whereas osteoma is found in 3% of CT scans of the paranasal sinuses. Malignancies account for less than 3–6% of all head and neck neoplasms; in Europe their reported incidence in males is 0.8–1/100.000 inhabitants per year and in females it is

D. Farina (✉) · R. Maroldi
Department of Radiology,
University of Brescia,
Piazzale Spedali Civili 1,
25123 Brescia, Italy
e-mail: nappaje@yahoo.it

R. Hermans (ed.), *Head and Neck Cancer Imaging*, Medical Radiology. Diagnostic Imaging,
DOI: 10.1007/174_2011_381, © Springer-Verlag Berlin Heidelberg 2012

0.4/100.000 inhabitants. Different from benign tumors, malignancies show some variation in geographical distribution: the overall incidence is higher in parts of Africa and Japan than in the United States (Gras Cabrerizo et al. 2007).

Certain malignant tumors are correlated with occupational risk factors: prolonged exposure to woodwork dust is associated with the development of adenocarcinoma, exposure to chrome or nickel is associated with squamous cell carcinoma (SCC). Conversely, no correlation was seen with tobacco and alcohol abuse (Thompson 2006).

As for the site of origin, maxillary sinus is the most commonly involved followed by the ethmoid cavity; conversely, frontal or sphenoid sinus tumors are rarely the site of origin (Samant and Kruger 2007).

Tumors arising in the paranasal sinuses have abundant place to grow without causing many symptoms; in addition, signs and symptoms are both non specific and late, thus sinonasal tumors are generally diagnosed in advanced stages. Unilateral nasal obstruction is by far the most common complaint, which may be associated with nasal discharge. Sometimes, symptoms may predict the tumor site: headache, neurological deficits and pain suggest skull base and/or cavernous sinus involvement; trismus and loosening of teeth are more common in maxillary sinus tumors; proptosis or epiphora may herald orbital involvement. On inspection, facial deformity may be observed as the result of anterior maxillary sinus wall destruction or of extensive spread of SCC arising from the skin covering the nasal vestibule. Epistaxis is more commonly seen in highly vascularized lesions such as lobular capillary hemangioma and juvenile angiofibroma.

2 Normal Radiological Anatomy

The paranasal sinuses are a complex framework of air cavities, variable in number and size that, from the functional point of view, may be subdivided into two distinct compartments. The anterior compartment includes anterior ethmoid cells, frontal and maxillary sinus and drains its secretions in the middle meatus; the posterior compartment is composed of posterior ethmoid cells and sphenoid sinus and drains in the superior meatus. The anatomic separation between the two compartments is outlined by the basal lamella of the middle turbinate, i.e. the attachment of the turbinate to the lateral nasal wall or medial orbital wall. From the oncologic perspective, however, the relevant anatomy is not represented by air cavities and drainage pathways, but rather by the relationships of the paranasal sinuses with the adjacent structures and spaces.

The orbits are separated from the ethmoid by the lamina papyracea—the name itself implying the frailty of this bony wall—and by the fused periosteal layer of the seven orbital bones (i.e. the periorbita). The orbital floor is a thicker lamina separating the orbit from the maxillary sinus, below. On the anterior part of the lamina papyracea and, caudally, along the anterior part of the medial maxillary sinus wall, is the nasolacrimal duct, best seen on axial scans as it courses from the medial aspect of the orbit down to the inferior meatus.

Cranially, a complex bone layer, namely, the fovea ethmoidalis, demarcates the sinonasal cavity from the anterior cranial fossa. On both sides of the midline the horizontal part of the roof is composed of the lamina cribrosa, which is extremely thin and, as the name suggests, perforated by multiple olfactory fila. The lateral part of the fovea ethmoidalis is composed of the vertical lamina of the ethmoid and the thick frontal bone to which it attaches. Posterior to the lamina cribrosa, the nasal vault is a flat bone surface, named ethmoid and sphenoid planum (Fig. 1).

Posterior to maxillary sinuses is the pterygopalatine fossa (PPF), a slit-like space mainly containing fat tissue, crossed by the sphenopalatine artery and by the greater and lesser palatine nerves. These nerves run through the whole vertical extension of the fossa to reach—in its upper part—the inferior surface of the sphenopalatine ganglion. From the posterior surface of the ganglion exits the vidian nerve, which courses horizontally through the pterygoid root to reach the middle cranial fossa, at the level of the anterior foramen lacerum. A few millimeters above, the maxillary nerve crosses the uppermost part of the PPF horizontally, coming from the foramen rotundum (located on the lateral sphenoid sinus wall) and coursing through the inferior orbital fissure, to end in its terminal branch—the infraorbital nerve—which runs into the infraorbital canal along the orbital floor. There is direct connection between the maxillary nerve and the sphenopalatine ganglion through a small amount of fibers named sphenopalatine nerves (Fig. 1).

Just above the inferior orbital fissure—and freely communicating with it—is the superior orbital fissure, located between the ala minor and ala major of the

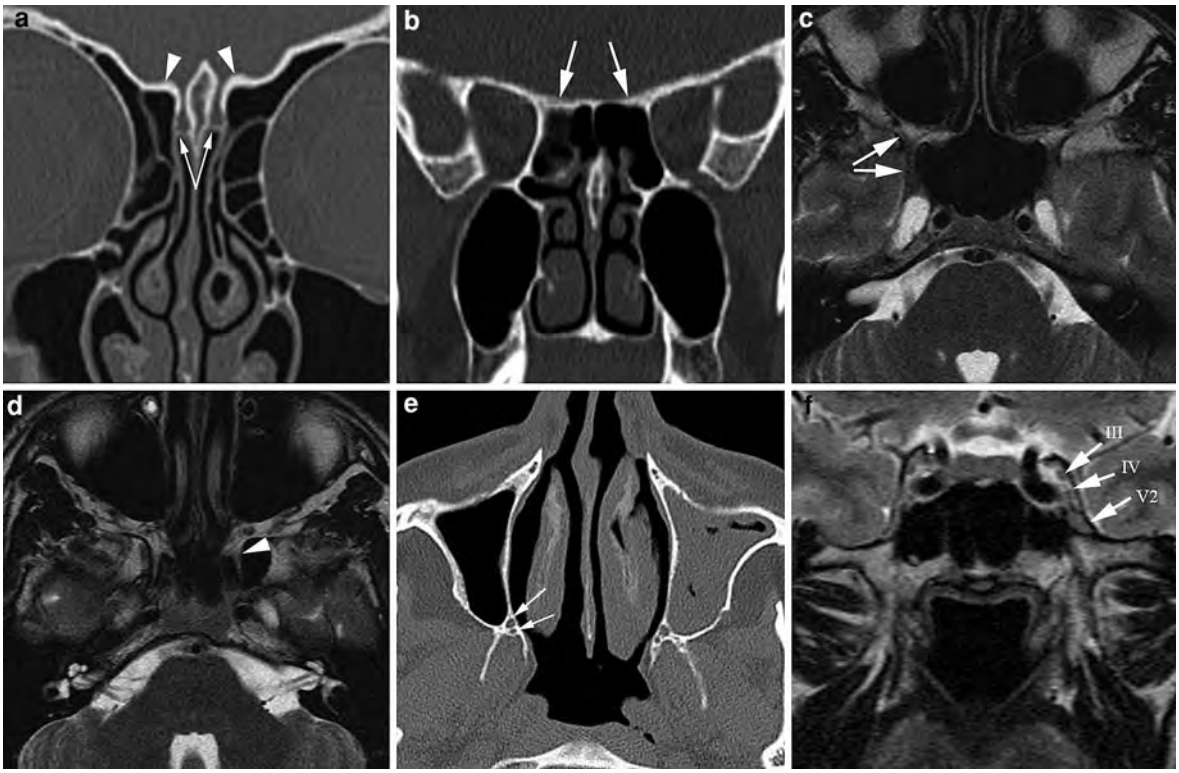

Fig. 1 Normal anatomy. **a**, **b** The fovea ethmoidalis is made up by the thin cribriform plate (*small arrows*) and the frontal bone (*arrowheads*); posteriorly, the ethmoid planum demarcates the sinonasal cavity from the anterior cranial fossa (*large arrows*). **c–e** The maxillary nerve draws a curvilinear course from the foramen rotundum (*large arrows*), through the PPF, to reach the orbital floor. Few millimeters below, the vidian canal (*arrowhead*) can be seen, larger in its anterior opening. The palatine nerves canals (*small arrows*) can be seen entering the most caudal part of the PPF, at the junction between medial and posterior maxillary sinus wall. **f** Lateral to the sphenoid sinuses, within the cavernous sinus the oculomotor (*III*), trochlear (*IV*), and maxillary nerve (*V2*) can be seen on a high resolution TSE T2 sequence

sphenoid: this fissure is crossed by the oculomotor (III), the trochlear (IV), the abducens (VI) and the ophthalmic nerve (V1), as they run from the cavernous sinus to the orbit (Fig. 1).

Finally, the pterygomaxillary fissure provides direct communication between the PPF and, laterally, the infratemporal fossa, whereas the sphenopalatine foramen connects the upper part of the PPF with the nasal fossa, medially.

3 Indications for Imaging Studies

Endoscopy of the nasal cavities should be the first diagnostic step in the work-up of patients complaining of the abovementioned symptoms, in order to confirm the presence of a neoplastic lesion and, in some cases, to obtain clues about its nature. Cross-sectional imaging is subsequently performed to assess deep tumor extent basically to four areas which may significantly modify the surgical approach (in some cases precluding it): orbit, anterior skull base, pterygopalatine and infratemporal fossa, cavernous sinus. Nodal metastases are overall rather infrequent, although they may represent a major issue in skin tumors of the nasal vestibule and in malignant tumors involving the lower part of the nasal cavity and maxillary sinuses, potentially involving the oral cavity; cross-sectional imaging plays a pivotal role in the detection of retropharyngeal nodes, not detectable by ultrasound.

As a general rule, MRI is commonly considered the technique of choice for the evaluation of paranasal sinus tumors because of its unsurpassed contrast

resolution; through adequate manipulation of acquisition parameters lesions may be differentiated from surrounding structures such as cortical or spongiotic bone, nerves, vessels. On the other hand, CT is preferred in the assessment of osteoma and fibrous dysplasia because the excellent spatial resolution of modern scanners (0.5–0.75 mm) allows to assess the relationships between the lesion and sinus drainage pathways or skull base neurovascular foramina.

4 Imaging Appearance and Extension Patterns of Sinonasal Neoplasms

4.1 Appearance of the Tumor Mass on CT and MRI

Most lesions appear as solid, moderately enhancing masses on both CT and MRI; diffuse involvement of sinus cavities and bone remodeling with sinus expansion are more typically observed in inflammatory conditions, as opposed to unilateral involvement and focal bone destruction, more frequently seen in malignant tumors. Yet, substantial overlap exists, making the discrimination between aggressive inflammatory lesions (such as Wegener's granulomatosis or invasive fungal infections), benign and malignant tumors sometimes extremely difficult. In the majority of cases, CT density and MRI signal intensity do not allow consistent tissue characterization. Calcifications, for instance, may be seen in variable amounts in a wide range of histotypes—both benign and malignant—including epithelial tumors (such as inverted papilloma, adenocarcinoma, SCC) and non-epithelial tumors (such as schwannoma and esthesioneuroblastoma). On MRI, T2 signal is similarly unreliable: the vast majority of tumors will display intermediate signal; though much rarer, hyperintensity is also aspecific, being shared by neurogenic, vascular and minor salivary gland tumors. Only a small number of histotypes display pathognomonic MRI or multislice CT (MSCT) features, such as inverted papilloma, juvenile angiofibroma, fibrous dysplasia and osteoma (see below). Melanoma may appear typically hyperintense on plain spin echo (SE) T1 sequences due to the paramagnetic properties of melanin; yet this substance is not produced by all melanoma subtypes.

Recently, the role of diffusion-weighted sequences in the characterization of lesions has been investigated in several head and neck regions, but not in the nose and paranasal sinuses (Vandecaveye et al. 2010). This lack of data might be due to the technical difficulties imposed by the numerous air–soft tissue interfaces in this region. At our institution, in an unpublished series, we found statistically significant difference between the ADC value of 34 sinonasal SCCs (0.88×10^{-3} mm^2/s) and 9 inverted papillomas (1.29×10^{-3} mm^2/s). Nonetheless, the practical utility of this observation in the clinical routine is questionable, as a large majority of tumors is accessible—and thus characterized—at endoscopic biopsy.

Besides characterization, imaging plays a pivotal role in discriminating tumor from the associated secretions, retained within sinus cavities obstructed by the mass: on contrast enhanced MSCT, most tumors appear solid and hyperdense, whereas inflammatory secretions show fluid-like density values. However, the discrimination is far more evident on MRI: generally, this is obtained on T2 sequences, as the signal of retained secretions is markedly higher than that of tumor. When progressive dehydration of entrapped mucus occurs, T2 signal drops and T1 signal rises, thus the discrimination may be clearer on T1 sequences (Som et al. 1989).

4.2 Extension Towards Neighboring Structures

The key points for presurgical assessment of sinonasal neoplasms are—on one hand—the thin interfaces that separate the air cavities from the orbit and the anterior cranial fossa, and—on the other hand—the deep spaces of the suprahyoid neck that provide indirect connection with the central skull base and from there, with the middle cranial fossa.

4.2.1 Orbit

The interface between the orbit and the ethmoid cells, maxillary and frontal sinus is made of three juxtaposed layers: stratified squamous epithelium investing the sinus cavities, bone (extremely thin in the medial wall and slightly thicker at the orbital floor and roof) and connective tissue, i.e. the periorbit. In normal conditions, the only element of the interface shown by MSCT is the hyperdense bone, whereas the interface

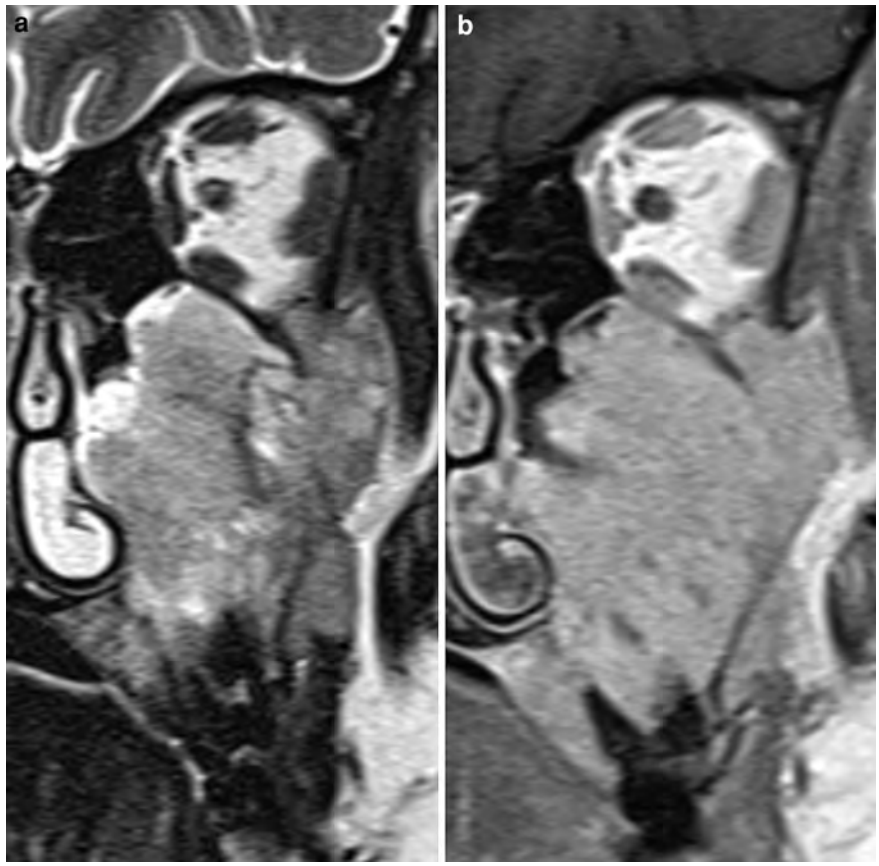

Fig. 2 **a**, **b** Adenoid cystic carcinoma of the left maxillary sinus. A hypointense layer composed of the juxtaposition of bone and periorbit sharply demarcates the tumor from the orbital fat and inferior rectus muscle. Such findings indicate absence of orbital invasion

is nearly invisible on MRI because the thin mucosal lining is barely perceptible and the hypointensity of bone and periosteum is indistinguishable from that of air within the sinus. Whenever air is replaced by tumor, thickened mucosa or retained secretions, the added signals of bone and periosteum can be detected on MRI, particularly on turbo spin echo (TSE) T2. As the neoplasm grows, the mineral component of bone is remodeled and eroded: when this occurs, no demarcation between lesion and orbital content can be shown by MSCT, whereas the periorbita is still seen on MRI (Kim et al. 2006). This sign, which has negative predictive value as high as 100% (Maroldi et al. 1997), is essential since evidence in the literature shows that orbital exenteration can be avoided on condition that the periorbit is not grossly invaded (Fig. 2). On the other hand, partial effacement of the periorbita or the detection of an irregular and nodular interface between tumor and orbital fat are predictors of invasion on MRI, yielding positive predictive value and accuracy of 86 and 95.4%, respectively (Fig. 3).

4.2.2 Anterior Cranial Fossa

Four elements compose the interface between sinonasal cavities and anterior cranial fossa, namely mucosa investing the ethmoid roof, bone, dura and cerebrospinal fluid (CSF). As for the orbit, the main landmark for MSCT is represented by bone, whereas MRI may provide more sophisticated information: whenever a lesion abuts the ethmoid roof, bone is sandwiched between the lesion and CSF and seen especially on TSE T2 as a hypointense line (Ishida et al. 2002). If the bone framework is interrupted, contrast enhanced SE T1 is the key sequence: as the tumor contacts the dura, this layer appears thickened and enhancing due to peritumoral inflammation, dural hypertrophy and increased vascularization (Fig. 4). According to Eisen (1996), dural infiltration is suggested by thickening superior to 5 mm, nodular interface between the lesion and intracranial content, encroachment of the dura and pial enhancement, with sensitivity and specificity of 88 and 100%, respectively (Fig. 5).

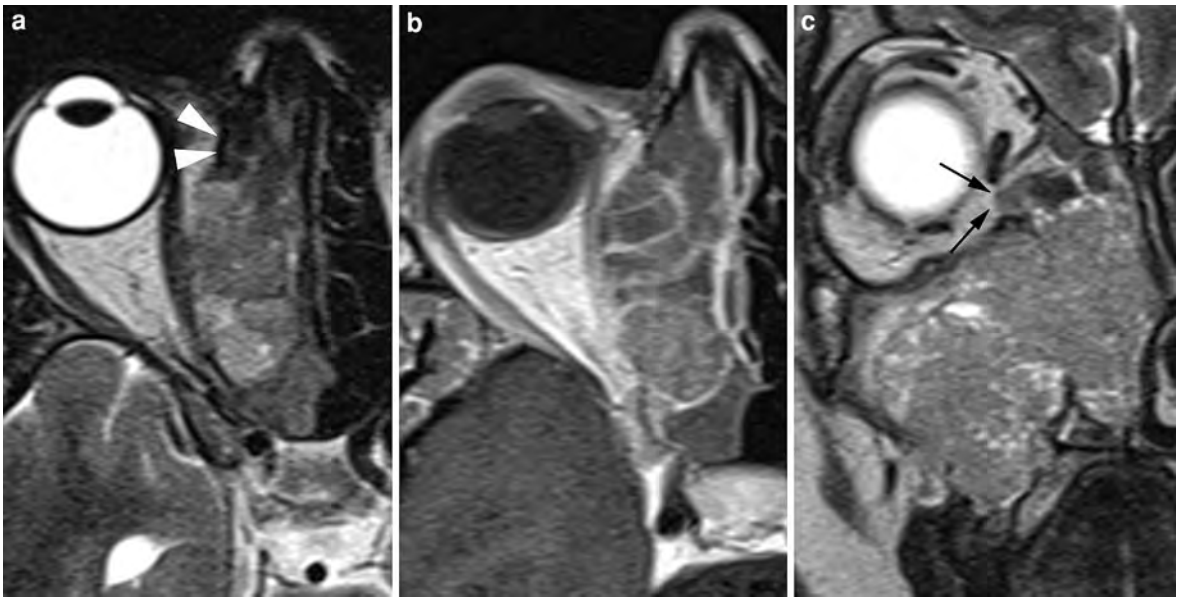

Fig. 3 37 year female, affected by sinonasal undifferentiated carcinoma. The lesion contacts and displaces the right lamina papyracea. On axial TSE T2 (**a**) and contrast enhanced SE T1 (**b**), a hypointense demarcation between tumor and orbital fat can be seen only in the anterior third (*arrowheads*). On coronal TSE T2 (**c**) a small nodule of solid tissue protrudes within the orbit (*arrows*). Overall, findings indicate orbital invasion

4.2.3 Invasion of Deep Spaces and Perineural Spread

Tumor arising from or invading the maxillary sinus may have access—through the invasion of its posterolateral wall—to the PPF. This may occur through bone destruction (easily detected by both MSCT and MRI) or, less frequently through permeative invasion. This last pattern, specifically seen in adenoid cystic carcinoma and in lymphoma, manifests as tumor growth on both surfaces of a cortical bone that shows subtle moth-eaten erosions without gross destruction. Similarly, in spongiotic bones the pattern may manifest as extensive invasion of medullary spaces in the absence of gross cortical erosions (Fig. 6). Such findings are much more easily detected with MRI, in particular plain SE T1 sequence is by far superior to MSCT in the detection of medullary bone changes. Once the tumor gains access to the PPF, a complex network of nerve fibers (maxillary and vidian nerve, palatine and sphenopalatine nerves) offers a framework which may convey tumor cells very far from the primary site. This phenomenon, referred to as perineural spread, is defined as the accumulation of tumor cells around the nerve circumference or within any of the three layers of the nerve sheath (epineurium, perineurium and endoneurium). Segmental nerve damage is often associated: this manifests as nerve enhancement due to increased permeability of the endoneurial capillaries and disruption of the perineurium (Carter et al. 1983; Kobayashi et al. 1993; Sartoretti-Schafer et al. 1994). As enlarged nerve segments course through the skull base, bone remodeling, widening and, eventually, erosion of fissures, foramina and canals, may be seen. Retrograde (centripetal) spread along the peripheral branches of the trigeminal nerve may result in Meckel's cave or, even further, cisternal segment invasion. Cavernous sinus invasion is heralded by enlargement, increased convexity and enhancement, although the latter, particularly on MSCT can be difficult to discriminate from physiologic venous enhancement (Maroldi et al. 2008) (Fig. 7). When perineural spread occurs along a motor branch, paralysis and atrophy of the corresponding muscles may be observed as indirect signs.

Overall, MRI is superior to MSCT in detecting perineural spread even if MSCT is better in demonstrating subtle bone changes: in two recent papers (Hanna et al. 2007; Gandhi et al. 2011) MRI had a sensitivity of 100%. Nonetheless, MRI has limitations that should not be neglected: false positives may

Fig. 4 **a**, **b** 53 year male affected by sinonasal SCC. The tumor is in contact with the ethmoid fovea, however both coronal (**a**) and sagittal (**b**) TSET2 demonstrate a thin hypointense barrier separating the tumor from the anterior cranial fossa. **c**, **d** 48 year, male. Sinonasal SCC. The lesion abuts the ethmoid roof, TSE T2 in coronal plane (**c**) shows focal interruption of the hypointense layer (*arrows*), although a thin layer of hyperintense CSF separates the lesion from the olfactory tract. After contrast application (**d**), SET1 shows reactive thickening and enhancement of the dura (*arrows*). Thickness of the dura (inferior to 5 mm) and sharp interface in the area of contact indicate intracranial but extradural tumor extension

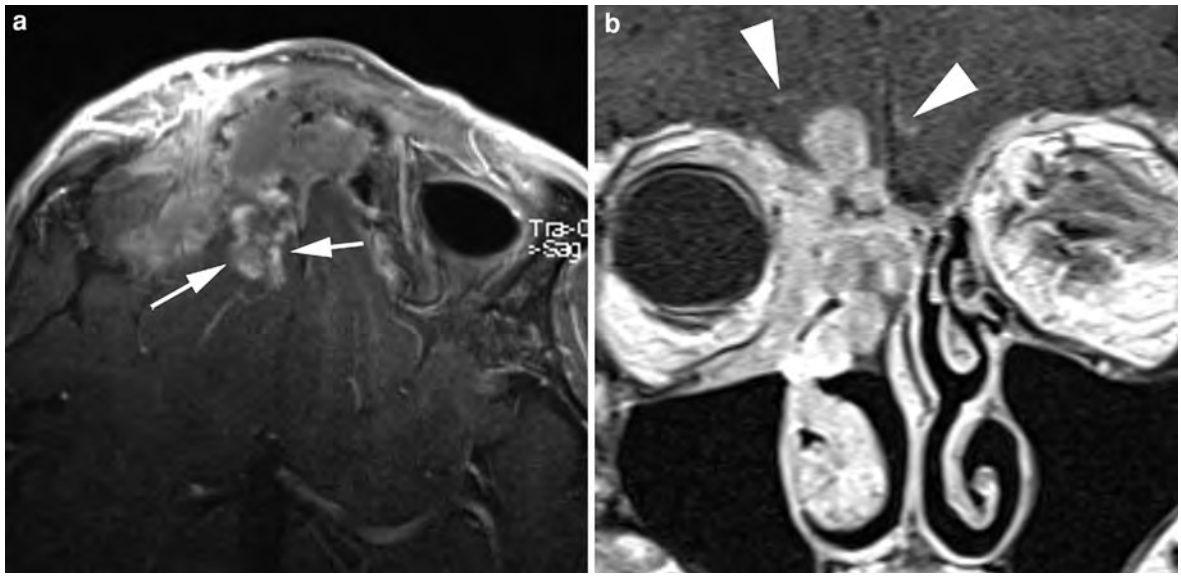

Fig. 5 50 year, male affected by nasoethmoid sarcoma, possibly secondary to the radiation treatment the patient received for retinoblastoma during infancy. Post contrast axial SE T1, acquired applying surface coils (**a**) and coronal SE T1 (**b**) demonstrate a mass lesion invading the orbit and the anterior cranial fossa. The intracranial part of the lesion displays nodular morphology (*arrows*); focal leptomeningeal enhancement is seen in both frontal lobes (*arrowheads*). Findings suggest dural invasion

decrease its specificity down to 85%. This is mainly related to nerve enhancement possibly seen in several non-neoplastic lesions such as inflammation, ischemia, infarct, trauma, demyelination and axonal degeneration. Furthermore, when the accuracy of MRI is weighted on per patient (rather than per nerve) basis, incomplete mapping may occur in 20–37% of cases. This can be due to microscopic spread—below the resolution of the technique—which also accounts for the presence of *skip lesions*: occasionally, perineural spread skips the foraminal segment of a nerve, resurfacing more centrally. Such a phenomenon is observed in hard or soft palate tumors which "resurface" into the PPF while leaving the caliber of palatine canals normal, or in PPF lesions reaching the Gasserian ganglion with normal appearing foramen rotundum. As a consequence, thorough care should be paid both during image acquisition (to the selection of the appropriate CT and MRI field-of-view and coverage) and during image analysis (to the systematic analysis of the whole course of the possibly involved nerves).

Finally, from the PPF tumor may spread laterally across the pterygomaxillary fissure to reach the infratemporal fossa: invasion of this space is clearly demonstrated on both MSCT and MRI scans as the replacement of the fat pad, normally filling this fossa, by solid enhancing tissue.

5 Tumor Types

5.1 Epithelial Tumors

5.1.1 Inverted Papilloma

IP is an epithelial tumor originating from the schneiderian membrane of the mucosa that lines the nasal cavity and paranasal sinuses. Although essentially benign, foci of SCC may be found in 7–15% of the resected specimens; furthermore, IP shows high propensity to recur (4–22% of cases) (Lombardi et al. 2011). However, according to the surgical literature (Lund 2000) "the term recurrence merely indicates residual disease in the majority of cases and is directly related to the surgical approach and the 'care' with which the IP is removed". Surgery is the mainstay of treatment. Before the endoscopic era, medial maxillectomy by lateral rhinotomy or midfacial degloving was considered the gold standard; nowadays, the vast majority of IP are resected through a purely transnasal endoscopic approach, while combined or external

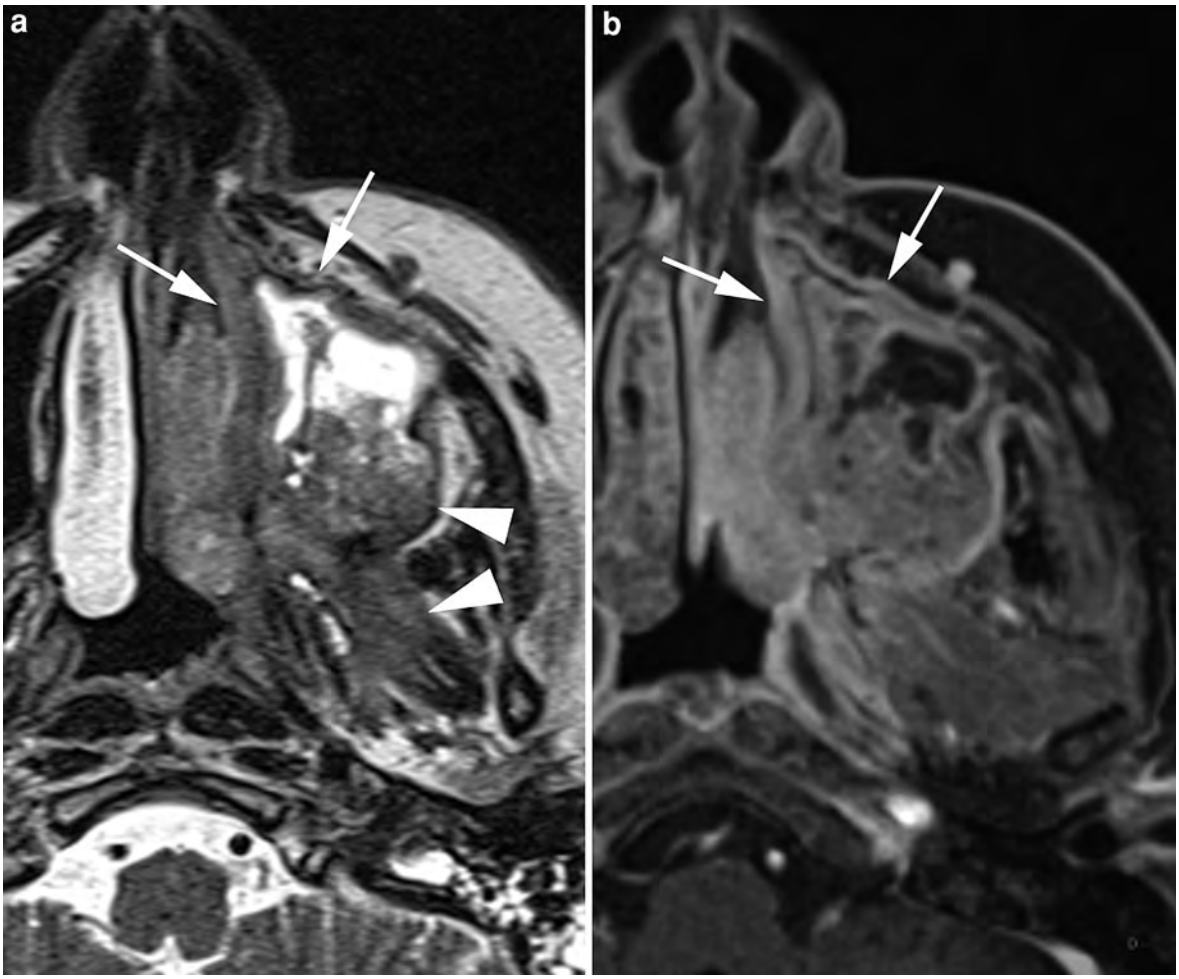

Fig. 6 Adenoid cystic carcinoma of the left maxillary sinus, axial TSE T2 (**a**) and post contrast VIBE (**b**). Hypointense and enhancing tumor tissue is shown on both sides of the anterior and medial maxillary sinus wall (*white arrows*), although the hypointense bone is apparently not destructed: findings indicate permeative invasion. The posterolateral sinus wall is invaded, the tumor infiltrates the masticator space and infratemporal fossa (*arrowheads*)

approaches are only occasionally used. Cross-sectional imaging is essential in the selection of proper treatment: for example, massive involvement of the frontal sinus or of a supraorbital cell (i.e. an etmoid cell pneumatizing the orbital roof, posterior to frontal sinus) contraindicates purely endoscopic resection. This clearly emphasizes the need to obtain an accurate discrimination between tumor and retained secretions.

MSCT appearance of IP is nonspecific: most often this polypoid lesion originates from the lateral nasal wall or from the nasal septum and shows lobulated margins (when an air interface allows to appreciate the peripheral borders) and possibly containing coarse. Focal bone remodeling and sclerosis are also frequently seen.

On MRI a characteristic columnar pattern may be seen, either on TSET2 or on SET1 sequences: this reflects the histologic architecture of the lesion, i.e. juxtaposition of several layers of proliferating epithelium invaginating in the underlying stroma. The hyperplastic epithelium appears hypointense on T2 because it is highly cellular, and enhances mildly on postcontrast T1; the underlying edematous stroma appears hyperintense on T2, and shows more pronounced enhancement on postcontrast T1 because of its rich vascularisation. Such a pattern has a very high positive predictive value (95.8%) (Ojiri et al. 2000;

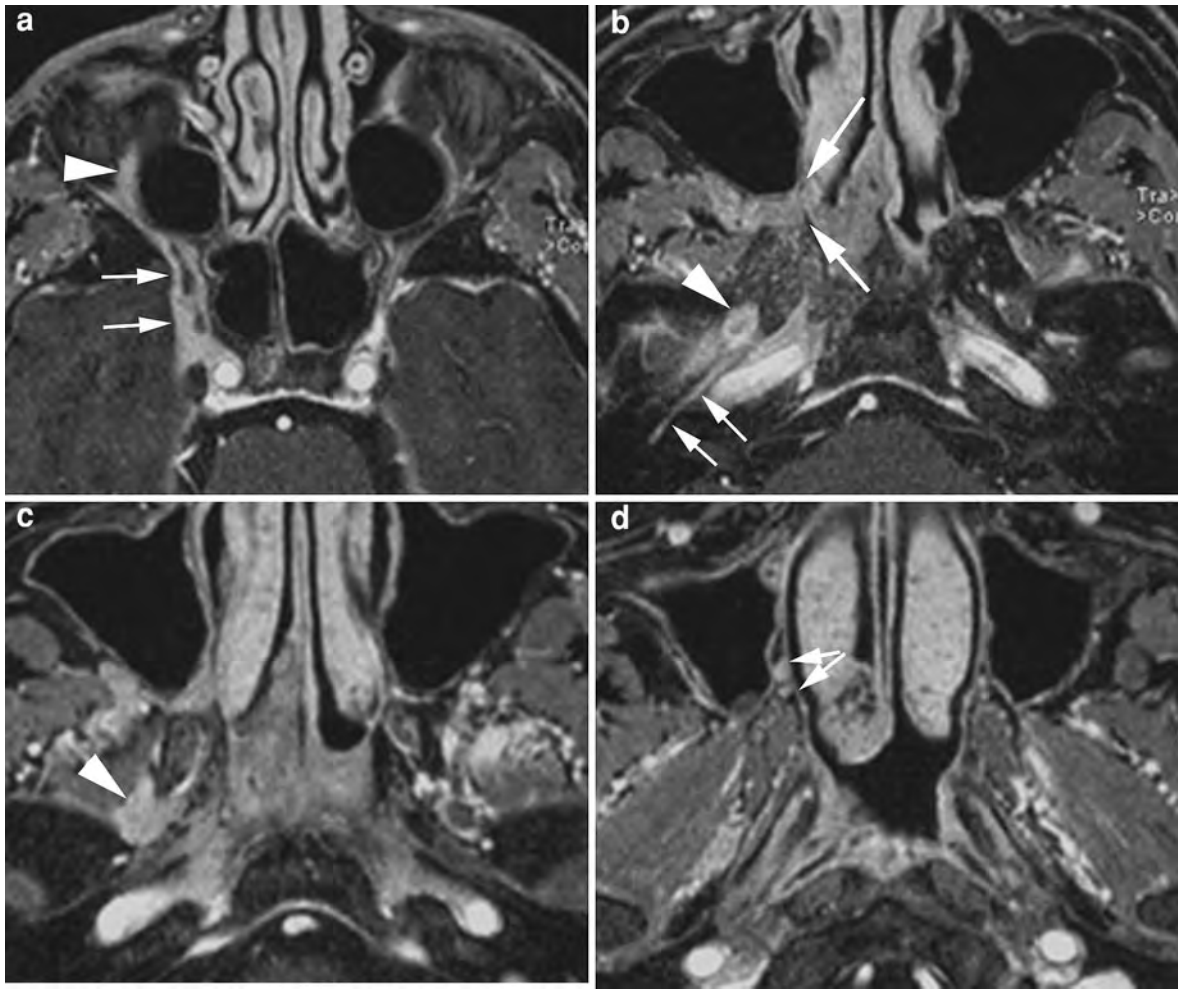

Fig. 7 58 year male. Perineural tumor spread in adenoid cystic carcinoma. Post contrast VIBE sequence shows the nasopharyngeal tumor growing through the sphenopalatine foramen (*arrows* in **b**) to reach the PPF. From this site tumor spreads antegradely and retrogradely along palatine nerves (*arrows* in **d**), infraorbital nerve (*arrowhead* in **a**) and maxillary nerve (*arrows* in **a**), mandibular nerve (*arrowheads* in **b** and **c**) and along the greater superficial petrosal nerve (*arrows* in **b**)

Maroldi et al. 2004b); similar MRI appearance was incidentally found in ameloblastoma (particularly the plexiform subtype), although associated with a much more aggressive pattern of growth (see also Sect. 5.2.3.3).

The site of origin of the IP is not infrequently identified on cross-sectional imaging as a sclerotic bone spur, equally detected with MSCT and MRI (Fig. 8). Such information is essential, as accurate subperiosteal dissection of the mucosa close to the insertion of the tumor and drilling of the underlying bone may achieve better tumor control (Lombardi et al. 2011), thus considerably decreasing recurrence rate.

5.1.2 Squamous Cell Carcinoma

SCC is generally regarded as the most frequent malignant histotype, accounting for about 60% of all malignancies (Thompson 2006). The literature data indicate the maxillary sinus and the nasal cavity as the most common sites of origin (25–58 and 25–35% of cases, respectively); SCC rarely arises from the ethmoid, frontal or sphenoid sinus. Peak incidence is in the sixth and seventh decades, with a male predominance (2:1). Occupational factors (including nickel, chromium, thorotrast and radium exposure) are associated with an increased risk. Surgery is the mainstay of treatment, combined with radiotherapy

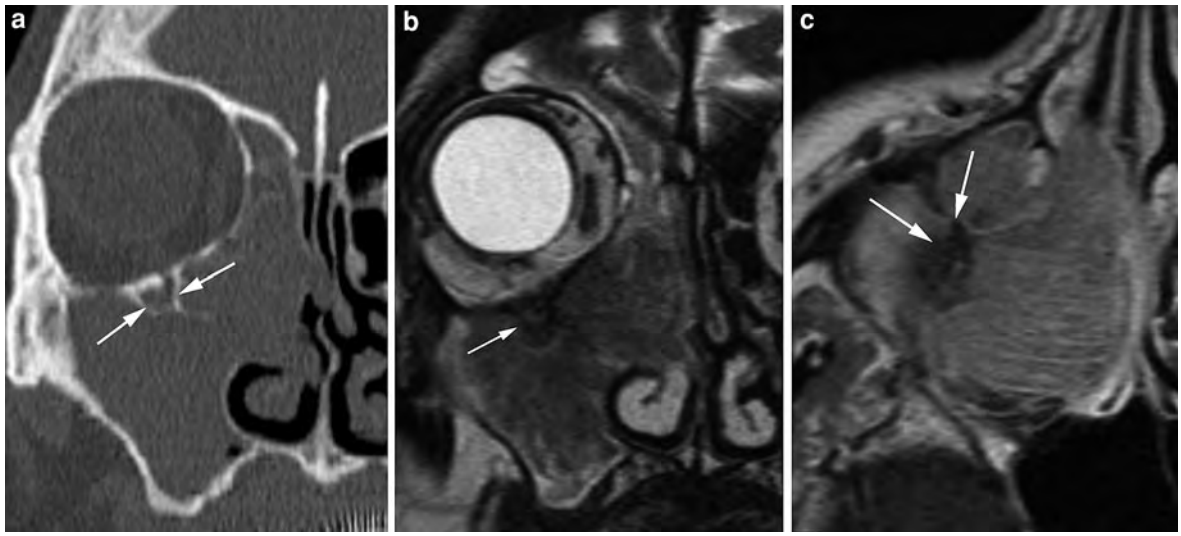

Fig. 8 82 year male complaining of nasal obstruction. MSCT (**a**) shows unilateral opacification of right sinus cavities, suggesting the presence of a lesion obstructing the middle meatus. On MRI, a maxillary sinus lesion is demonstrated protruding through an enlarged ostium into the nasal fossa. Both TSE T2 (**b**) and contrast enhanced SE T1(**c**) show a rather peculiar striated pattern consistent with inverted papilloma (confirmed at biopsy). *Arrows* point to the spur representing the attachment site of the lesion

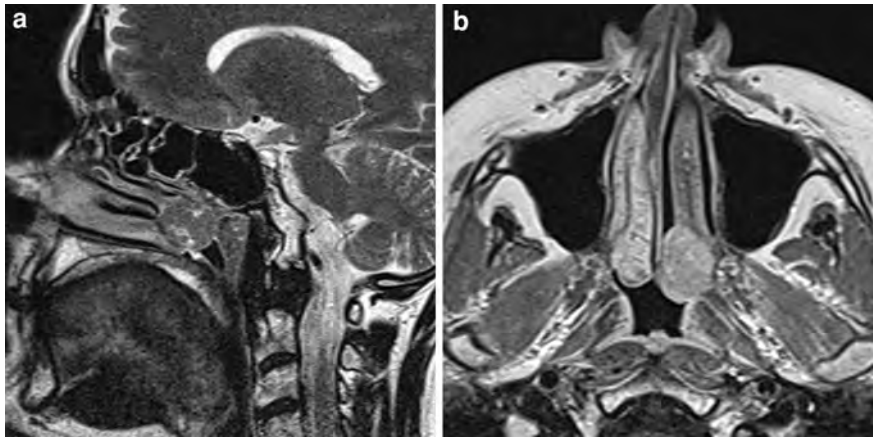

Fig. 9 70 year, male affected by SCC. TSE T2 (**a**) and contrast enhanced SE T1 (**b**). Rarely sinonasal tumors are diagnosed in an early stage, as in this small mass, arising from the posterior tip of the middle turbinate

according to location and stage; chemotherapy may also be used, as a neoadjuvant or postoperatively.

SCC does not show specific MSCT or MRI characteristics (Fig. 9). The main goal of imaging is to determine the submucosal extent of sinonasal neoplasms, as both surgical and radiotherapeutic management require an accurate mapping of tumor extent (Maroldi et al. 1997; Hermans et al. 1999). The prognosis is overall poor (5-year survival rate is reported to be 50%, recurrence rate is 56%), worsened by involvement of critical anatomical areas (Suarez et al. 2004), even more so when multiple subsites are simultaneously invaded.

5.1.3 Sinonasal Undifferentiated Carcinoma and Neuroendocrine Carcinoma

SNUC is a malignant tumor with slight male predominance and peak of incidence in the fifth and sixth decades. Short-time history of symptoms (mainly consisting of nasal obstruction with epistaxys), large

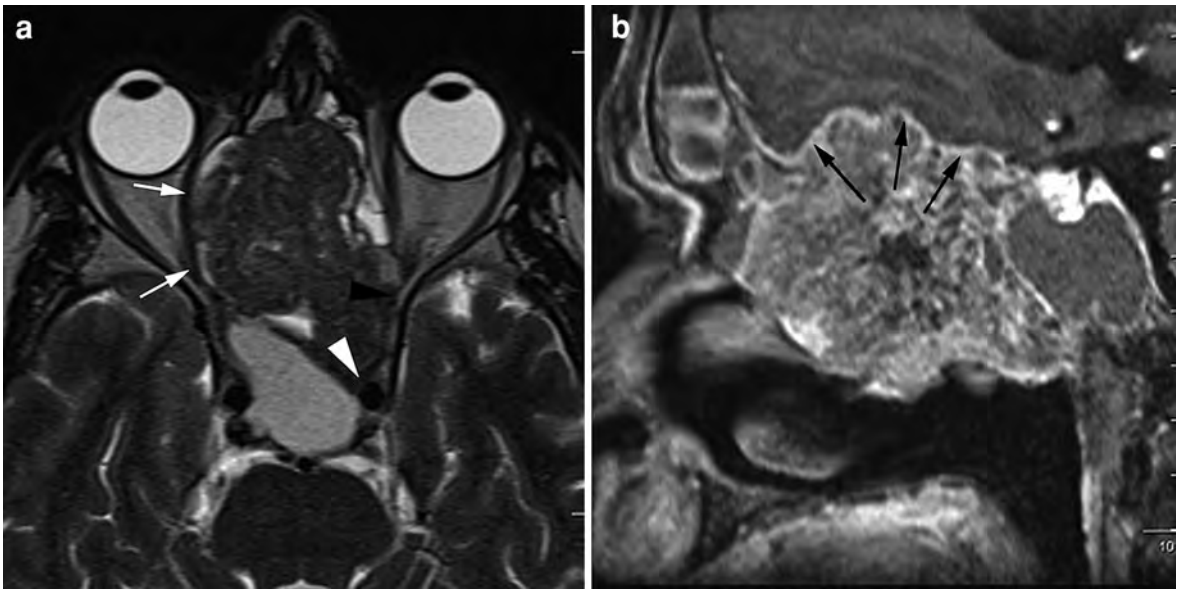

Fig. 10 46 year, male affected by SNUC. On TSE T2 (**a**), the large ethmoid mass cannot be demarcated by the medial wall of the right orbit (*white arrows*), invades the left sphenoid sinus contacting the orbital apex (*black arrowhead*) and the carotid canal (*white arrowhead*). On the sagittal reformations of VIBE (**b**), although the ethmoid roof is invaded, the displaced and enhancing dura (*black arrows*) is not substantially thickened and therefore probably not invaded

size at presentation and rather high incidence of nodal metastases (15–20% of cases) denote the aggressive nature of this neoplasm. Although generally classified within neuroectodermal tumors, the exact origin is still debated: the lack of neuroectodermal differentiation in a substantial number of cases has also suggested a possible origin from the Schneiderian epithelium (Rischin and Coleman 2008). On cross-sectional imaging, SNUC lacks distinctive features (Fig. 10): usually, it appears as a solid mass arising from the ethmoid or from the upper part of nasal cavities, simultaneously involving multiple sites and with high propensity to invade the orbit and the skull base; calcifications are usually absent (Raghavan and Phillips 2007). Multimodal treatment is generally applied although no clear consensus has been reached about the sequence; prognosis is overall poor with 5-year survival in the range between 43 and 63%.

The classification of sinonasal neuroendocrine carcinoma (SNEC) (Fig. 11) is also a matter of debate: it is not clear whether it should be considered as a distinct entity (the less differentiated counterpart of olfactory neuroblastoma) or classified as SNUC. However, treatment principles are similar to SNUC (Rischin and Coleman 2008).

5.1.4 Adenocarcinoma

Adenocarcinoma is a malignant neoplasm more frequently observed in the ethmoid, with predilection for men in the fifth to seventh decade. It is composed of epithelial cells, arranged in a glandular or gland-like pattern. Under the term adenocarcinoma all glandular malignancies that cannot be assigned to another more definable class (such as adenoid cystic carcinoma, acinic cell carcinoma or mucoepidermoid carcinoma) are collected. Although in many cases it arises from salivary glands, a variant with histologic features resembling colonic adenocarcinoma exists, referred to as intestinal-type adenocarcinoma (ITAC). Interestingly, this subtype may manifest in two distinct clinical variants (Sklar and Pizarro 2003).

Occupational ITAC is strongly related to softwood dust and leather dust inhalation; in woodworkers the risk is estimated to be increased by 900 times, the time interval for tumor development is about 40 years. When related to occupational hazard, ITAC more commonly arises in the ethmoid or nasal vault, shows marked male predilection and bears better prognosis (possibly because symptoms manifest earlier, before the tumor invades critical areas). Sporadic ITAC (i.e. unrelated to occupational exposure) arises

Fig. 11 70 year, male affected by neuroendocrine carcinoma. TSE T2 (**a**) and SE T1 (**b**). The mass is probably arising from the upper third of the nasal fossa—note lateral displacement of the middle turbinate (*arrows*)—and does not invade the anterior cranial fossa

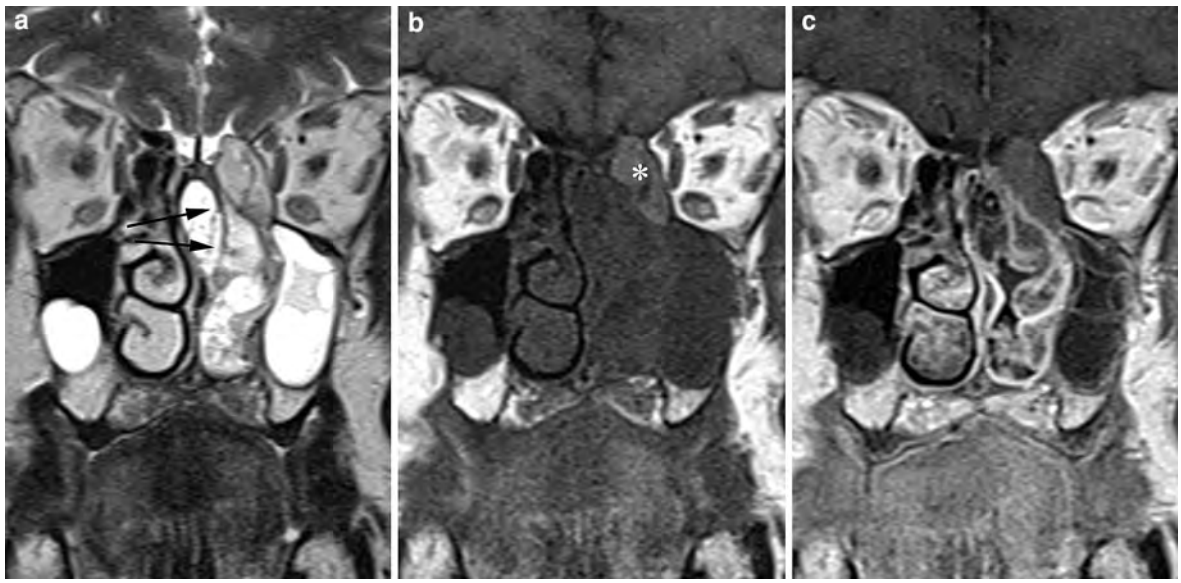

Fig. 12 59 year male, affected by intestinal-type adenocarcinoma. The left nasal fossa is occupied by a heterogenous mass with hyperintense TSE T2 signal (**a**) and irregular enhancement (**c**). The mass displaces the left middle turbinate laterally (*arrows*), thus obstructing the middle meatus. The left maxillary sinus is occupied by inflammatory secretions; (**b**) expansion of an anterior ethmoid cell filled with spontaneously T1 hyperintense material corresponds to mucocele (*asterisk*)

in the maxillary sinus, is more frequent in women and shows shorter survival times.

Imaging appearance of adenocarcinoma is overall nonspecific. ITAC may show a mixed solid–fluid pattern due to mucus produced by tumoral cells (Fig. 12). This may hamper the discrimination between the lesion and retained secretions (or mucocele) due to sinus blockage; meticulous attention should therefore be paid to the presence of any solid component within a mucocele, combining the

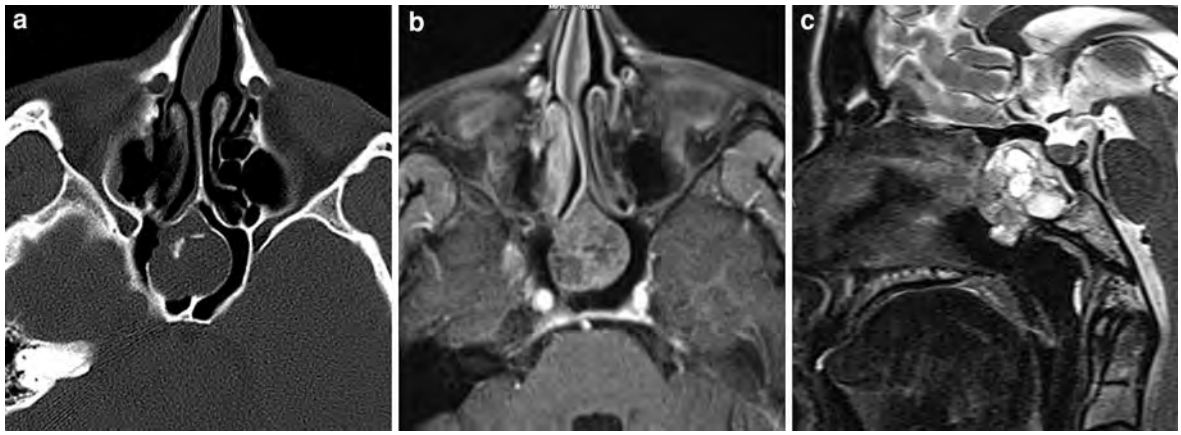

Fig. 13 26 year male complaining with headache; incidental finding on screening sinus MSCT (**a**). Sphenoid sinus tumors are overall quite rare: the TSE T2 hyperintense (**c**) and enhancing (**b**) mass vegetating into the left sinus turned out to be adenoid cystic carcinoma. Chordoma and chondrosarcoma had been considered in the differential diagnosis although the normal aspect of the clivus and midline location made these hypotheses less likely. Note some coarse calcifications within the mass (**a**)

information provided by pre- and postcontrast sequences and by diffusion-weighted sequences (when not degraded by artifacts).

5.1.5 Adenoid Cystic Carcinoma

There are 450–750 minor salivary glands scattered in the whole head and neck area, including sinonasal cavities. Adenoid cystic carcinoma (ACC) (Fig. 13) is a variant of adenocarcinoma arising from minor salivary glands; 10–25% of all head and neck ACC arise in the sinonasal tract. Age distribution is wide, although this tumor is rarely seen below the third and above the eighth decade.

ACC is characterized by an extremely slow but relentless growth rate: as a consequence, recurrences are frequent and regular follow-up should be prolonged far longer than the conventional 5-year period. Nodal metastases are uncommon (5%), whereas distant metastases (mostly to the lung, liver and brain) are seen in over 50% of patients during their clinical history (Maroldi et al. 2004c). Treatment consists of surgical resection plus postoperative adjuvant radiation therapy; ACC is considered radiosensitive more than radiocurable and, consequently, radiation therapy is believed to be delaying rather than preventing recurrences (Wiseman et al. 2002).

Imaging findings reflect the peculiar tendency of this tumor to grow submucosally and subperiosteally, thus permeating bone and soft tissues (Fig. 6). Invasion of muscles, vessels and fat tissue may be detected on imaging studies as effacement and encasement with no or very limited mass effect. Similarly, replacement of spongiotic bone may occur with minimal changes of the cortical bone; furthermore, tumor growth on both surfaces of a cortical bone (such as the posterolateral maxillary sinus wall) may be seen with only focal bone destruction.

Predictably, all these findings are much better demonstrated on MRI, because of its high contrast resolution: plain SE T1 and 3d GE T1 with fat suppression are key sequences. The first one, in particular, maximizes the signal gap between tumor and fat tissue, thus allowing to detect even subtle signs of infiltration of bone marrow and improving the assessment of the invasion of deep spaces. However, it should be emphasized that rather frequently a significant discrepancy occurs between MRI staging and actual tumor spread demonstrated during intraoperative mapping. Both the radiologist and the otolaryngologist should be aware of this inconsistency, which is basically the effect of microscopic diffusion below the threshold of MRI detection.

The combination of high contrast and spatial resolution (submillimetric voxel size), such as offered by 3d GE T1 is essential to map tumor spread along nerves (Fig. 7). Clearly, the FOV has to be adjusted in order to track the entire course of the trigeminal nerve (most common path of perineural spread for sinonasal ACC), as well as the greater superficial petrosal

Table 1 UICC 2009 staging of nasal cavity and ethmoid sinus tumors (Sobin et al. 2010)

T1	Tumor restricted to one subsite of nasal cavity or ethmoid sinus, with or without bony invasion
T2	Tumor involves two subsites in a single site or extends to involve an adjacent site within the nasoethmoidal complex, with or without bone invasion
T3	Tumor extends to invade the floor or medial wall or floor of the orbit, maxillary sinus, palate, or cribriform plate
T4a	Tumor invades any of the following: anterior orbital contents, skin of nose or cheek, minimal extension to anterior cranial fossa, pterygoid plates, sphenoid or frontal sinuses
T4b	Tumor invades any of the following: orbital apex, dura, brain, middle cranial fossa, cranial nerves other than maxillary nerve, nasopharynx, or clivus

Table 2 UICC 2009 staging of maxillary sinus tumors (Sobin et al. 2010)

T1	Tumor limited to the mucosa, with no erosion or destruction of bone
T2	Tumor causing bone erosion or destruction, including extension into the hard palate and/or middle nasal meatus, except extension to the posterior wall of maxillary sinus wall and pterygoid plates
T3	Tumor invades any of the following: bone of posterior wall of maxillary sinus, subcutaneous tissues, floor or medial wall of orbit, pterygoid fossa, ethmoid sinuses
T4a	Tumor invades any of the following: anterior orbital contents, skin of cheek, pterygoid plates, infratemporal fossa, cribriform plate, sphenoid or frontal sinuses
T4b	Tumor invades any of the following: orbital apex, dura, brain, middle cranial fossa, cranial nerves other than maxillary division of trigeminal nerve (V2), nasopharynx or clivus

nerve, coursing along the edge of the petrous bone and connecting the vidian nerve to the facial nerve. Adequate coverage will significantly decrease understaging (and undertreatment) due to the presence of skip lesions and the above described resurfacing phenomenon.

5.1.6 Staging of Sinonasal Carcinomas

The staging of sinonasal neoplasms is based on endoscopic and imaging findings. Two different staging systems have been formulated for ethmoid tumors and maxillary sinus tumors, reported in Tables 1 and 2, respectively.

5.2 Non-Epithelial Tumors

5.2.1 Neuro-Ectodermal Tumors

5.2.1.1 Olfactory Neuroblastoma

Olfactory neuroblastoma (ONB), also referred to as esthesioneuroblastoma, is a rare malignant tumor (2% of all sinonasal tumors) arising from the olfactory epithelium normally found in the cribriform plate, the ethmoid roof, the upper part of the nasal septum and the superior turbinates (Thompson 2009). A bimodal incidence (second and sixth decades) with slight male predominance is reported. Rarely, ONB may manifest with hypertension and hyponatriemia, due to vasopressin secretion.

ONB is clinically staged according to the Kadish classification as limited to the nasal cavity (stage A), involving nose and paranasal sinuses (stage B) and extending beyond the nasal cavity and paranasal sinuses (stage C). This simple classification correlates well with both the natural history and prognosis (McFadden et al. 2009).

As most tumors are diagnosed in an advanced stage, on cross-sectional imaging ONB is often seen as a dumbbell-shaped mass growing across the cribriform plate. On MSCT, the mass exhibits spontaneous hyperdensity (reflecting high cellularity) and calcifications of variable size. The MRI pattern is composed of intermediate T2 signal and T1 hypointensity; cystic areas may be found, capping the intracranial part of the tumor. Both iodine and paramagnetic contrast enhancement is strong (Fig. 14), sometimes making the differential diagnosis with vascular tumors difficult. Treatment consists of surgical resection (open craniofacial resection, cranio-endoscopic or purely endoscopic resection) supplemented with postoperative radiation treatment; a combination of chemo- and radiotherapy is used in unresectable tumors.

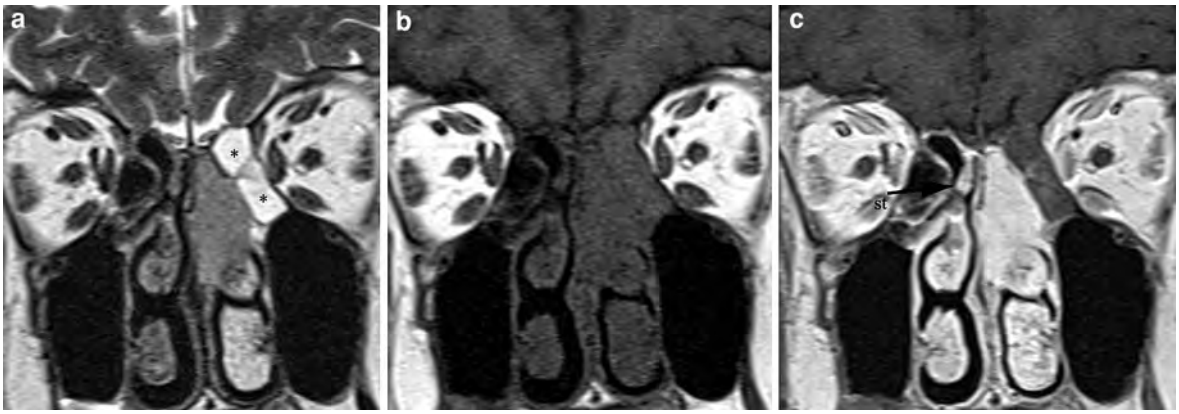

Fig. 14 **a–c** Olfactory neuroblastoma. A strongly enhancing mass with intermediate TSE T2 signal intensity originates from the left ethmoid roof and encases the superior turbinate (*st*). The mass is limited to the nasal cavity; the paranasal sinuses and the anterior cranial fossa are not invaded (Kadish stage A). Retained secretions are seen into the posterior ethmoid cells (*asterisks*)

5.2.1.2 Ewing Sarcoma and Peripheral Neuroectodermal Tumor

Ewing sarcoma and peripheral neuroectodermal tumor (PNET) are small round cell tumors mainly occurring in young subjects in their first–second decade, with 1.5:1 male:female ratio. Sinonasal involvement is rare, actually less than 1% of Ewing sarcomas have head and neck localization. The discrimination between Ewing sarcoma, PNET and other small cell tumor such as lymphoma, melanoma, embryonal rhabdomyosarcoma and ONB is often difficult and based on immunohistochemical and ultrastructural features (Toda et al. 1999). Although imaging features are aspecific, the peculiar age range of Ewing sarcoma may guide the diagnosis, particularly in children presenting with fractures insufficiently explained by the trauma suffered (Howarth et al. 2004).

5.2.1.3 Melanoma

Sinonasal melanoma arises from melanocytes that migrated during embryonal life from the neural crest to the mucosa investing the nasal cavity and sinuses. The nasal septum and lateral nasal wall are the most common sites of origin, by far outnumbering the paranasal sinuses, among which maxillary sinus is the most frequent. Peak of incidence is observed between the fifth and seventh decade, with slight male prevalence.

On imaging studies, melanoma appears as a solid soft tissue mass with local invasion and relatively high tendency to nodal spread. Three peculiar aspects may help to characterize this histotype. A T1 spontaneous hyperintensity, atypical for nearly all other benign and malignant sinonasal tumors, is much more frequently exhibited by the melanotic variant; this is explained by the paramagnetic properties of melanin as well as by intralesional hemorrhage (Kim et al. 2000). Secondly, flow voids may be demonstrated on MRI sequences at the periphery and into the lesion, representing its rich vascular network; such finding explains the frequent epistaxes occurring in patients affected by melanoma (Kim et al. 2000) (Fig. 15). Finally, perineural extension is shown by the desmoplastic variant (Raghavan and Phillips 2007) and demonstrated on cross-sectional imaging by the signs previously discussed in Sect. 4.2.3.

Surgery (open or endoscopic approach) is the mainstay of treatment, adjuvant radiotherapy may be indicated to increase local tumor control or as a palliation in unresectable lesions. However, the overall prognosis is quite poor: local recurrence may be as high as 37%, distant metastasis will occur in approximately 50% of cases (Roth et al. 2010).

5.2.2 Vascular and Soft Tissue Tumors

5.2.2.1 Vascular Tumors

Juvenile Angiofibroma

Juvenile angiofibroma (JAF) is a highly vascular mass characterized by three distinctive features: it occurs nearly exclusively in male adolescents; it originates in

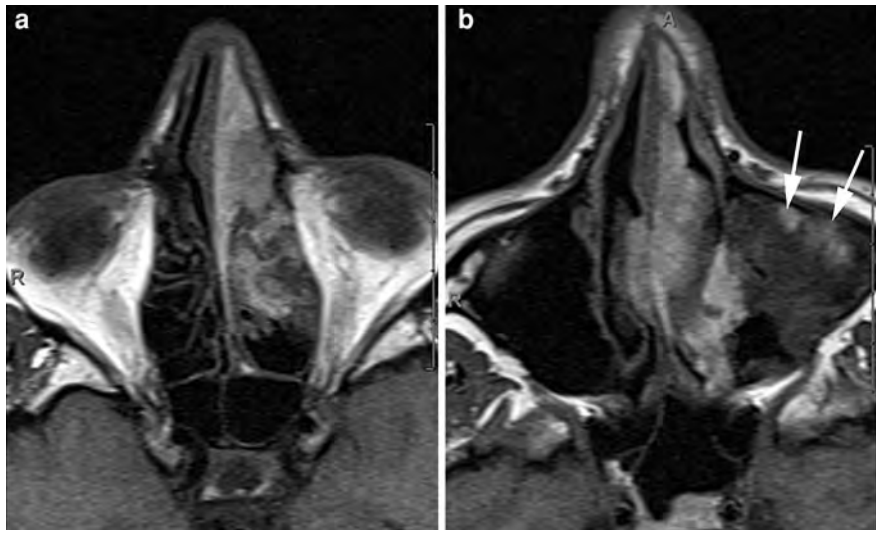

Fig. 15 **a**, **b** 51 year, female. Melanoma of the nasal cavity. The lesion is spontaneously hyperintense due to the paramagnetic properties of melanin, thus its extension can be clearly depicted on plain SE T1. Also the focal hyperintensities within the left maxillary sinus (*arrows*) turned out to be melanoma

the posterior nasal fossa, close to the sphenopalatine foramen; it is composed of irregular vessels set in a fibrous stroma (Das and Kirsch 2005; Nicolai et al. 2010). The typical clinical symptoms are nasal obstruction and epistaxis.

Not only pathogenesis is unknown: actually, the exact nature of JAF is debated, as increasing evidence suggests that its immunohistochemical and electron microscopic profile is consistent with a vascular malformation rather than a tumor. Despite its benign nature, JAF exhibits a locally aggressive pattern of growth typically manifesting at the pterygoid root: destruction of the sphenoid sinus walls (particularly the floor and lateral wall) is commonly seen along with replacement of spongiotic bone, quite often also extending to the greater sphenoid wing. Furthermore, JAF shows propensity to grow in an enlarged vidian canal and foramen rotundum. Although the lesion may reach the cavernous sinus, dural invasion is rare. Surgery is the treatment of choice; in recent years microendoscopic surgery was introduced, producing satisfactory results in small- and medium-sized lesions (Nicolai et al. 2010).

On cross-sectional imaging (Fig. 16), JAF appears as a solid, brightly enhancing lesion vegetating in the posterior nasal cavity and nasopharynx and invading the pterygopalatine and infratemporal fossa; flow voids are detected on MRI images. Such a typical appearance (combined with the typical clinical pattern) in nearly all cases allows to avoid biopsy which would be extremely dangerous to perform. A combination of TSE T2 and SE T1 (before and after contrast administration) is essential, not only for characterization of JAF, but also for the assessment of spongiotic bone invasion; when JAF approaches the cavernous sinus, submillimetric 3d GE T1 sequences allow to define the relationships between the lesion and vascular or nervous structures. The role of MSCT is restricted by the issue of radiation exposure and by the lack of contrast resolution in grading medullary bone involvement; however in selected cases, a volumetric data set acquired with MSCT is the basis for intraoperative navigation systems, which allow safer control of critical structures such as the internal carotid artery and the optic nerve. Angiography is invariably included in the work-up; embolization, performed 24–72 h prior to surgery, allows to minimize intraoperative blood loss (Nicolai et al. 2010).

Prognosis is overall favorable although residual lesions may occur, generally regarded as persistent rather than recurrent lesions. Persistences may be intentionally left (when close relationships with crucial structures would imply an inacceptably high surgical risk) or may be the result of incomplete surgical drilling of involved bone structures after removal of JAF. As in both cases persistent lesions are deeply seated in the submucosa, imaging is an essential complement to endoscopic assessment (Kania et al. 2005).

Lobular Capillary Hemangioma

Lobular capillary hemangioma (LCH), also referred to as pyogenic granuloma, is a benign vascular tumor

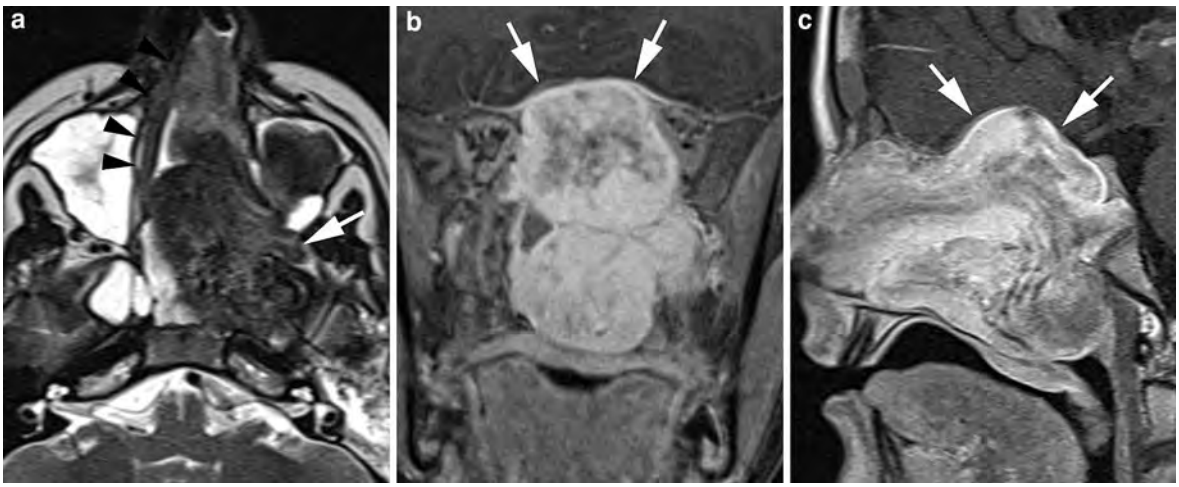

Fig. 16 14 year male, affected by juvenile angiofibroma. A large, intensely enhancing mass (**b**, **c**) occupies the left nasal fossa laterally displacing the nasal septum (*arrowheads* in **a**), nasopharynx and sphenoid sinuses. TSE T2 (**a**) shows several vascular flow voids into the lesion. Through an enlarged sphenopalatine foramen (*arrows*) the mass protrudes into the PPF. The lesion encroaches the ethmoid planum and sphenoid sinus roof, displacing the dura, appearing thickened and enhancing (*arrows* in **b**, **c**)

composed of capillaries arranged in lobules into an edematous and fibroblastic stroma. In the sinonasal tract, LCH more frequently arises from the anterior nasal septum, although skin and oral mucosa are the preferred head and neck sites of origin. Pathogenesis is unclear, several hypotheses have been proposed, including trauma, hormonal imbalances, viral oncogenes, underlying microscopic arteriovenous malformations and production of angiogenetic factors.

On MSCT, LCH appears as a soft tissue density mass (Simo et al. 1998; Karagama et al. 2002) that may cause bone remodeling and destruction (Lance et al. 1992); the MRI pattern consists of T2 hyperintensity and spontaneous T1 hypointensity. Bright enhancement is obtained after contrast agent administration (Maroldi et al. 2004a) (Fig. 17). Similar findings are shared by several other highly vascularized sinonasal lesions, both benign and malignant, such as haemangioma, haemangiopericytoma, JAF, paraganglioma and highly vascularized metastases (i.e. from kidney, thyroid, lung and breast cancer). Unfortunately, JAF is the only differential diagnosis that can be readily ruled out, based on the typical site of origin, pattern of growth, age and sex of the patient.

Endoscopic resection is feasible, also for large-sized lesions, without significant blood loss; consequently, preoperative embolization is generally not necessary. No recurrence was observed in a series of 40 patients treated endoscopically and followed up, on average, for 5 years (Puxeddu et al. 2006).

Angiomatous Polyp

The angiomatous polyp is a sinochoanal polyp whose vascular pedicle is strangled by the pressure exerted by the bony walls of the foramen through which it exits the sinus cavity of origin to reach the nasal cavity (De Vuysere et al. 2001). Such compression may trigger a cascade of dilatation and stasis of feeder vessels, necrosis (which in some cases prevails) and neovascularization. The site and pattern of growth of the lesion as well as its mixed appearance (fluid-like intensity/density of the sinusal component, intense enhancement of its vascular compromised portion) are sufficient clues for the diagnosis on imaging studies (Fig. 18).

Hemangiopericytoma

Hemangiopericytoma (HPC) is a vascular tumor that can either be benign or malignant and may be found in any part of the body; 15–20% of cases arise from the head and neck, 5% in the sinonasal region. HPC originates from pericytes, mesenchymal cells covering the outer surface of capillaries, implied in flow regulation and vasoconstriction (Kuo et al. 2005; Stomeo et al. 2004). Interestingly, four cases of

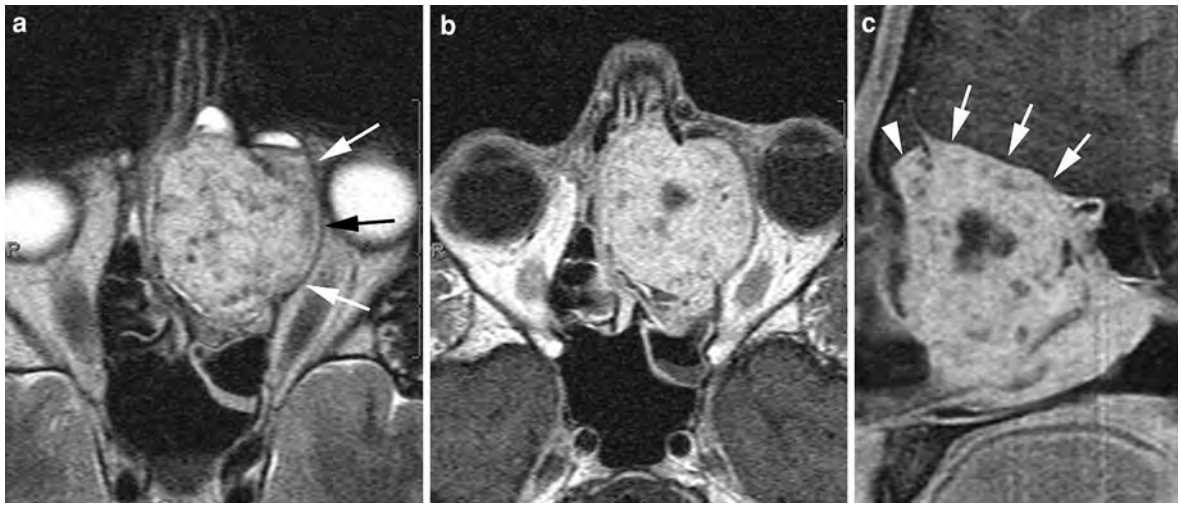

Fig. 17 23 year male. A large mass with hyper TSE T2 signal (**a**) and bright contrast enhancement (**b**, **c**) fills the ethmoid cells and protrudes into the frontal sinus (*arrowhead*). The sharp interface between the lesion and both the orbital and intracranial content (*arrows*) indicates low aggressiveness. Pathologic examination of the surgical specimen revealed lobular capillary hemangioma

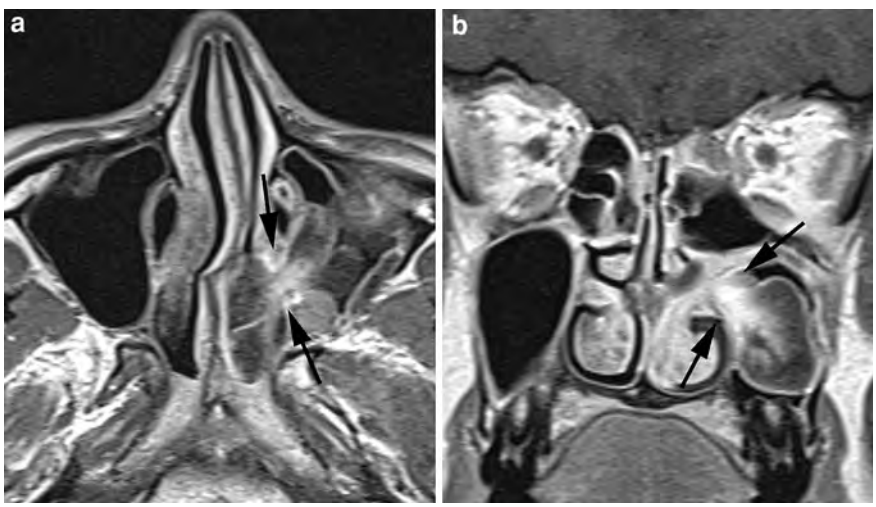

Fig. 18 **a**, **b** 26 year female. Post contrast SE T1 shows an antrochoanal polyp. The vascular compromised part of the lesion, strangled as it courses through an accessory ostium (*arrows*), is referred to as angiomatous polyp

oncogenic osteomalacia (a rare condition manifesting with muscle weakness, bone pain and frailty) have been described in patients affected by HPC (Beech et al. 2007).

On both MSCT and MRI, HPC appears as an indistinct soft tissue mass with moderate to bright contrast enhancement; bone changes (remodeling, destruction) are generally also found. Lesions arising in the sinonasal tract do not show aggressive behavior, distant metastases are rare.

Wide surgical excision is the treatment of choice; recurrences, mostly due to incomplete resection, range in the literature between 7 and 40% and may occur up to 15 years after initial treatment; such natural history warrants prolonged clinical and imaging follow-up.

5.2.2.2 Soft Tissue Tumors

Peripheral Nerve Sheath Tumor

Peripheral nerve sheath tumors are overall rare entities, generally benign in nature. Schwannoma more commonly affects the ethmoid followed by the nasal septum and maxillary sinus, usually as a solitary lesion. Neurofibroma is classically described as

localized, diffuse and plexiform. Rarely malignant transformation (spindle cell sarcoma) may occur. Triton tumor is a neoplasm composed of peripheral nerve fibers and well-differentiated striated muscle fibers, described as either benign or malignant (Castro et al. 2005; Nicolai et al. 2000).

Nasal Glioma

Nasal glioma is a congenital fronto-nasal mass composed of dysplastic neuroglial tissue and fibrovascular tissue. This mass is thought of as a cephalocele that lost connection to the skull base. It is usually found at birth or during infancy as a subcutaneous lesion located on the nasal dorsum, typically at the glabella, on the midline (although this is not the rule) (Hedlund 2006; Aguilar Mandret et al. 2004). MRI should be considered the imaging technique of choice, not only for its low invasiveness, but also because it better depicts the absence of connections with the brain; the lesion displays hypointense T1 signal (as compared to gray matter) and T2 hyperintensity (due to gliosis); no contrast enhancement is expected.

Meningioma

Meningioma may be found in the sinonasal cavities in four different forms: as the direct extension of a lesion arising in anterior cranial fossa; as a metastasis of an intracranial meningioma; as an extracranial neoplasm arising from arachnoid cells located in the sheath surrounding cranial nerves in their course through skull base foramina; as an extracranial lesion with no connection with the anterior cranial fossa (Thompson and Gyure 2000; Rushing et al. 2009). The nasal cavity is the most common site of sinonasal meningiomas.

Imaging appearance is equivalent to that of intracranial meningiomas: MSCT density is generally homogeneous, MRI signal is iso- to hyperintense on T2 sequences and iso- to hypointense on T1, compared with gray matter; contrast enhancement is bright. Bone erosion, sclerosis and hyperostosis may be found.

Rhabdomyosarcoma

Rhabdomyosarcoma is the most common sinonasal malignant tumor in children, characterized by aggressive local behavior and early metastases. Three subtypes (embryonal, alveolar and pleomorphic) are described, however the differentiation may be difficult at histology. As the nasal symptoms produced by this tumor are similar to allergic or infectious diseases, at the time of diagnosis rhabdomyosarcoma is often a large mass invading adjacent structures. On MRI, TSE T2 signal is hyperintense to muscle. Contrast enhancement is heterogeneous; necrosis, calcifications and hemorrhage are rare (Hagiwara et al. 2001).

5.2.3 Osseous and Cartilaginous Tumors

5.2.3.1 Osteosarcoma

Head and neck osteosarcoma more commonly affects the jaw and mandible, it rarely arises in the sinonasal tract. Specific risk factors have been described, including preexisting bone abnormalities—among which Paget's disease, giant cell tumor, osteogenesis imperfecta, osteoblastoma and others—and previous radiation therapy for other malignancies (Galera-Ruiz et al. 2001). Sinonasal osteosarcomas are mostly high grade lesions, however distant metastases (to other bones, lymphnodes and lungs) are less frequent than for high grade tumors arising from long bones.

On MSCT, osteosarcoma appears as a soft tissue mass containing coarsely calcified new bone which exhibits an aggressive pattern of growth, resulting in mixed sclerotic and lytic lesions. On MRI, the calcified osteoid matrix is less obviously demonstrated, however medullary bone invasion and soft tissue infiltration are more accurately depicted (Vlychou et al. 2007).

Treatment consists of wide surgical resection, followed by chemotherapy in high grade lesions; radiation therapy is indicated as completion treatment when clear surgical margins are not achieved. Local recurrence is the most common pattern of failure, emphasizing the role of MRI and MSCT during follow-up.

5.2.3.2 Chondrosarcoma

Chondrosarcoma generally affects long bones, ribs and pelvis; a sinonasal localization is overall uncommon, in 60% of cases occurring in the alveolar process of the maxilla, although several cases of nasal septal chondrosarcoma are reported. Sinonasal chondrosarcomas tend to be high grade lesions, different from laryngeal lesions which more commonly are low grade (Yamamoto et al. 2002).

MSCT appearance consists of a soft tissue matrix with scattered calcifications (which may represent a

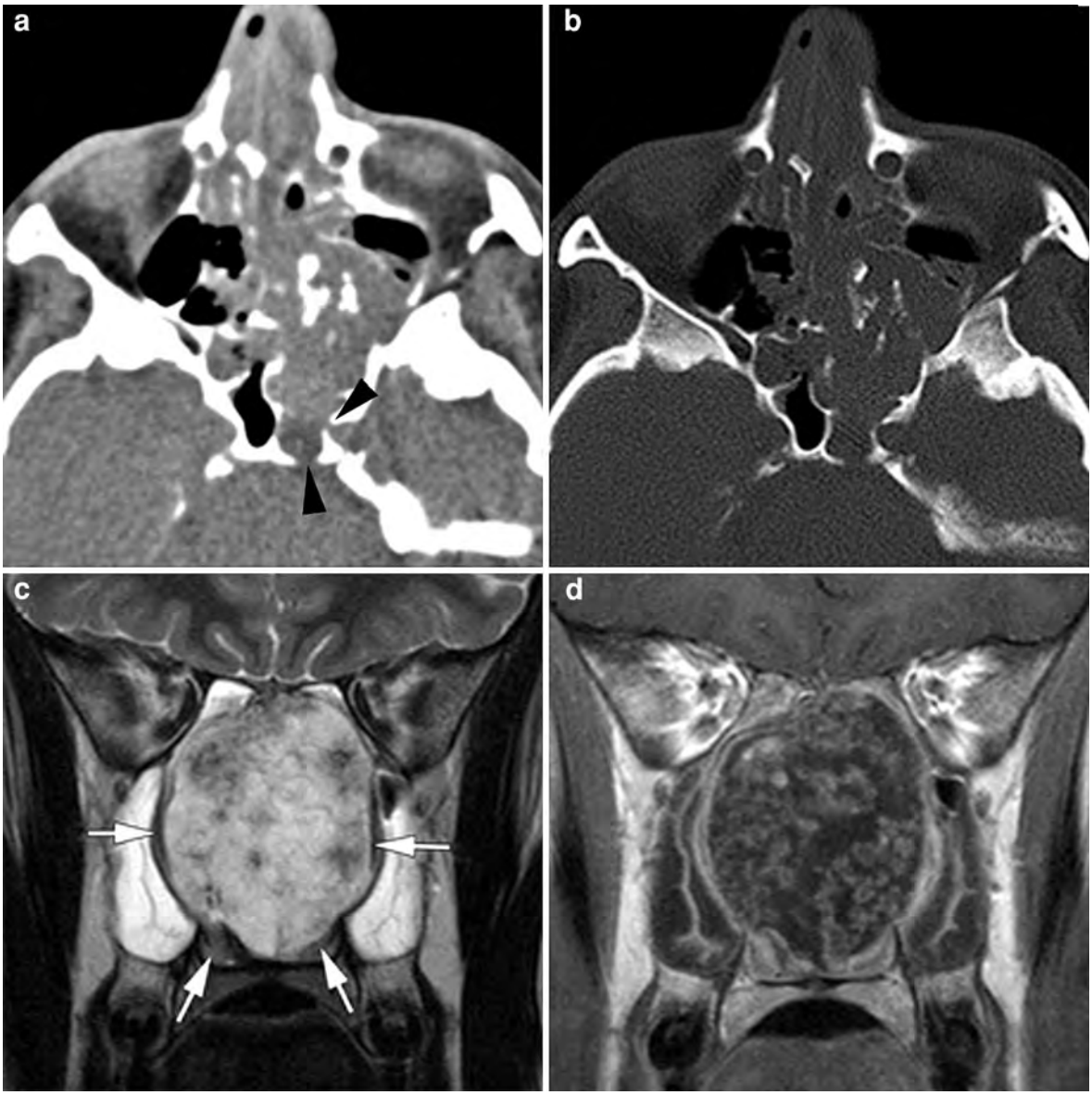

Fig. 19 Sinonasal chondrosarcoma. **a**, **b** In a 65 year female, MSCT shows a large soft tissue mass with coarse calcifications located in the left posterior ethmoid and sphenoid sinus. Focal demineralization of the posterior wall of the sphenoid sinus and the carotid canal is seen (*arrowheads*); however, the low density of the material in the posterior part of the sinus might indicate chronically retained inflammatory secretions. **c**, **d** 15 year, male. Both nasal fossae are completely occupied by a mass displaying hyper T2 signal and a typical 'rings and arcs' pattern on post-contrast SE T1. The nasal septum is not recognizable, the inferior and middle turbinates (*arrows*) are pushed against the lateral nasal wall (**c**, **d** courtesy of Robert Hermans, MD, Ph.D, Leuven, Belgium)

helpful hint for the differential diagnosis) and bone destruction. On MRI, chondrosarcoma exhibits bright T2 signal and T1 hypointensity with variable, heterogeneous contrast enhancement (Momeni et al. 2007). Typically, scalloped margins and intralesional septa display enhancement, whereas cartilage and mucoid matrix do not, resulting in a peculiar rings and arcs pattern. Although calcifications are less evident than on MSCT, the T2 hyperintensity (uncommon for neoplasms) and pattern of enhancement may suggest chondrosarcoma on MRI (Fig. 19).

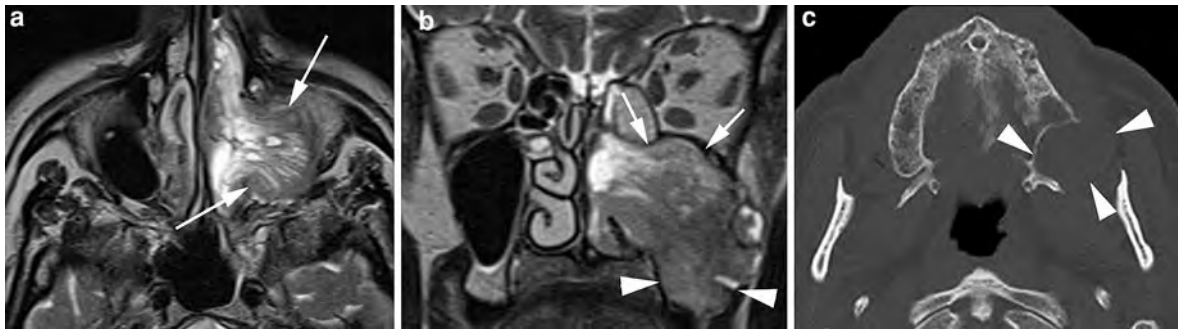

Fig. 20 **a–c** 73 year male. The left maxillary sinus is occupied by a mass protruding in the nasal fossa. Although the upper part of the mass (*arrows*) shows a columnar pattern resembling inverted papilloma, the destruction of the posterolateral sinus wall (**b**) indicates a more aggressive pattern of growth. Involvement of the alveolar process of maxillary bone (*arrowheads*) suggests odontogenic origin. Pathology proved the lesion to be ameloblastoma

As the differentiation between chondrosarcoma and its benign counterpart—i.e. chondroma—can be challenging even at pathology, wide surgical resection is the treatment of choice. Five-year survival for sinonasal lesions is 40–60%, recurrences occur in 60% of patients within 5 years from treatment.

5.2.3.3 Ameloblastoma

Ameloblastoma is a benign but locally aggressive neoplasm which is believed to originate from remnants of the odontogenic epithelium, from the lining of odontogenic cysts or from the basal membrane of the overlying oral mucosa. The mandible largely outnumbers the maxilla as the site of origin (80 vs. 15–20% of cases), rarely extraosseous peripheral ameloblastoma arising from the sinonasal cavities has been described. Maxillary ameloblastomas tend to occur at older age (fifth and sixth vs. second and third decade) and to show more aggressive behavior than those originating from the jaw.

On cross-sectional imaging, ameloblastoma of the maxilla may appear as a uni- or multilocular cystic and solid lesion arising from the alveolar ridge. Bone remodeling and destruction are often seen, along with maxillary sinus and nasal cavity invasion. A peripheral (generally incomplete) bony shell may surround the lesion (Schafer et al. 1998); the presence of multiple septa within the lesion may result in a honeycomb appearance; in 10% of cases a dental element may be embedded into the lesion (Minami et al. 1996). MRI appearance of plexiform ameloblastoma may be similar to the columnar pattern of inverted papilloma: this is due to the presence of thin septa and papillary projections of solid tissue within the lesion, both enhancing after contrast administration (Fig. 20).

Surgery is the treatment of choice; local recurrence is very frequent, mainly due to osseous invasion. In some recurrent tumors, radiation therapy has also been proposed. Distant metastasis may rarely occur even in the absence of cytological signs of malignancy of the primary lesion.

5.2.4 Hematologic Tumors

5.2.4.1 Lymphoma

Two distinct manifestations of *extranodal extralymphathic non-Hodgkin lymphoma* may be observed in the sinonasal region.

Diffuse large B-cell lymphoma more commonly affects the maxillary sinus although nasal cavity, ethmoid and frontal sinus are also often involved; peak of incidence is at the sixth decade. B-cell lymphoma appears as a soft tissue mass causing bone destruction. Such pattern is quite nonspecific, however the simultaneous involvement of lymph nodes (generally without necrosis) and of Waldeyer ring may suggest the diagnosis (Chain and Kingdom 2007; Lee et al. 2003) (Fig. 21).

NK/T-cell lymphoma mainly involves the nasal cavity, palate and upper airway, presenting as a midline bone destructive lesion; for this reason, it was described in the past as lethal midline granuloma, a misnomer currently completely abandoned. Imaging shows destruction of the nasal septum, inferior turbinates and sometimes hard palate. The soft tissue component of the tumor may appear as a layer

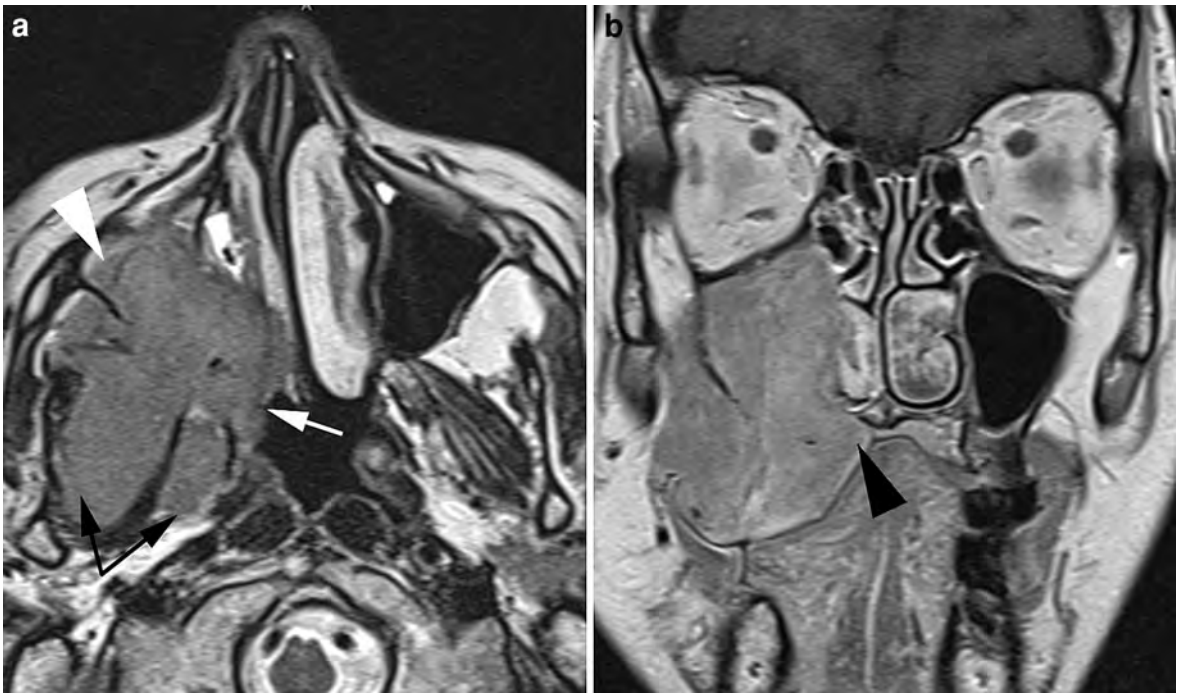

Fig. 21 70 year, female affected by B-cell lymphoma. The mass lesion arising from the right maxillary sinus encroaches the posterolateral wall to invade the infratemporal fossa (*arrowhead*), PPF (*white arrow*) and masticator space (*black arrows*). Downwards extension to the alveolar process and hard palate (*black arrowhead*) is also seen. Signal intensity is homogenous on both TSE T2 (**a**) and SE T1 (**b**)

investing bone structures while leaving their shape unaltered, or as a mass with necrotic areas; contrast enhancement is variable. These findings are not pathognomonic, the list of differential diagnoses includes infections (bacterial and fungal), aggressive inflammatory diseases (such as Wegener's granulomatosis, sarcoidosis, polyarteritis nodosa and systemic lupus) and toxic lesions (mainly cocaine abuse). Beyond precisely assessing disease spread, imaging may therefore be helpful in selecting the target lesion for sinonasal biopsy (Borges et al. 2000) (Fig. 22).

5.2.4.2 Granulocytic Sarcoma

Also known as chloroma, granulocytic sarcoma is a rare tumor composed of precursors of the granulocyte series, including myeloblasts, promyelocytes and myelocytes. This tumor may develop during the course of, or as a presenting sign of a variety of myeloproliferative disorders among which is acute myelogenous leukemia; seldom, granulocytic sarcoma may even precede leukemia by weeks or months (Guermazi et al. 2002). Although more commonly described in the orbit (actually it was first described as a green ocular tumor hence the name *chloroma*), this lesion may also be found in the sinonasal region and nasopharynx. Imaging shows a homogeneously enhancing soft tissue mass, on MRI displaying iso- to hypeintense T2 signal.

5.2.4.3 Plasmacytoma

Plasmacytoma is a soft tissue mass composed of monoclonal plasma cells most commonly affecting the sinonasal cavities, followed by the nasopharynx and oropharynx, and manifesting in 90% of cases as a solitary mass (Megat Shiraz et al. 2008). About 15–20% of plasmacytomas convert into multiple myeloma, although such transformation is thought to occur in intramedullary lesions, whereas extramedullary lesions (such as sinonasal plasmacytoma) are generally solitary lesions. Imaging findings (soft tissue mass, bone destruction) are completely nonspecific.

5.2.5 Fibro-Osseous Disease

Fibrous dysplasia is a non-neoplastic slowly progressive bone disorder characterized by expansion of

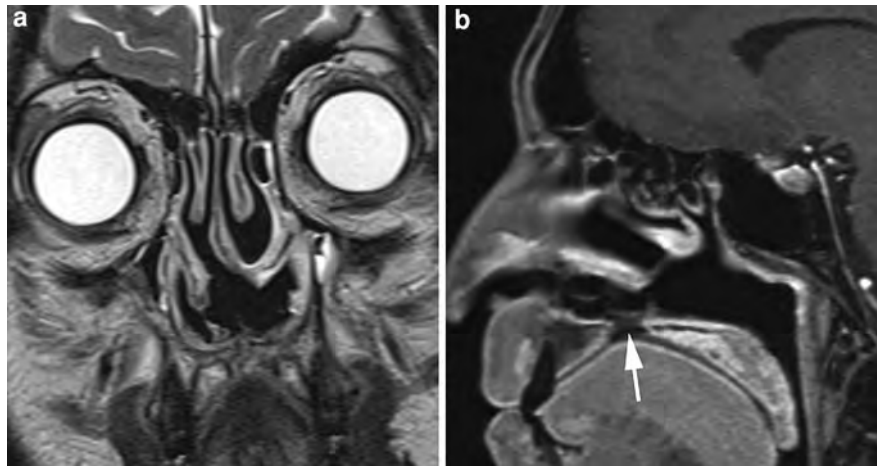

Fig. 22 37 year male. NK/T-cell lymphoma. TSE T2 (**a**) shows destruction of the nasal septum and bulbous part of the inferior turbinates; a focal erosion of the palate (*arrow*) is demonstrated on postcontrast VIBE (**b**)

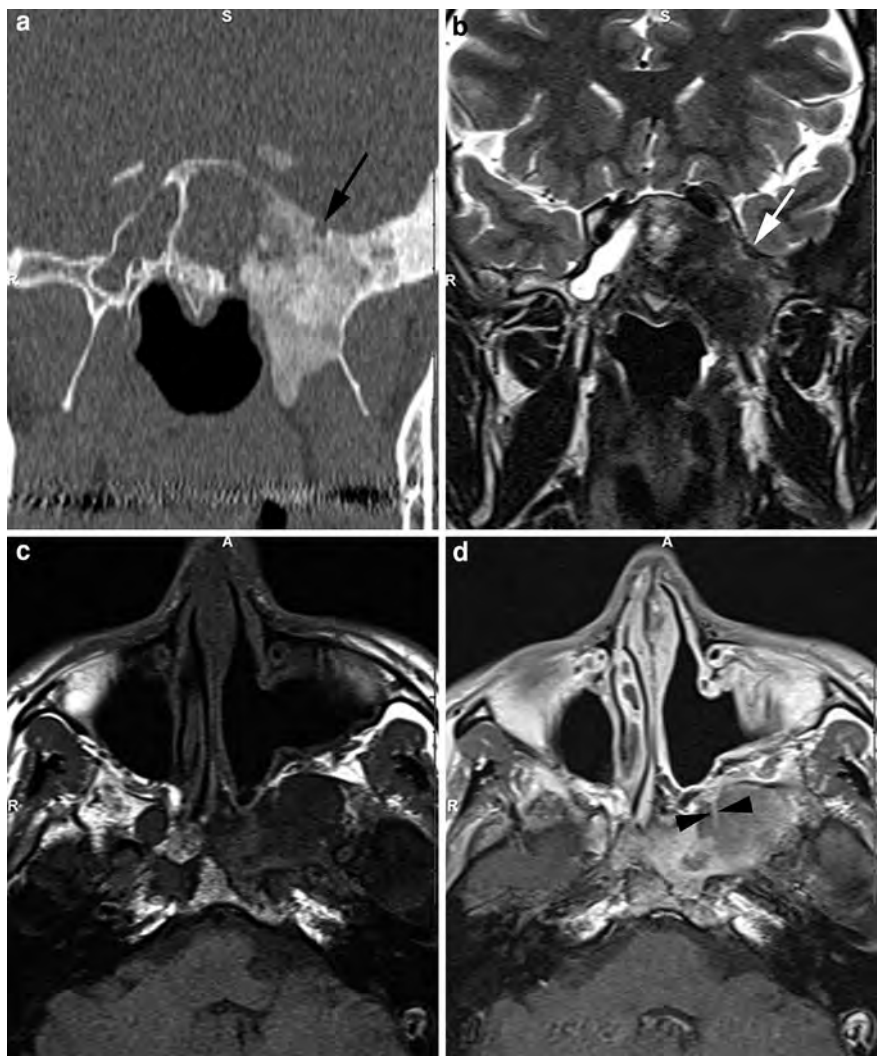

Fig. 23 Fibrous dysplasia. CT image (**a**) shows the left greater sphenoid wing, pterygoid root and medial pterygoid plate to be grossly enlarged. Spongiotic bone is replaced by immature woven bone with a typical ground glass appearance on MSCT. MRI pattern on TSE T2 (**b**) and SE T1 before (**c**) and after (**d**) contrast agent are less characteristic, although bone expansion is clearly shown also with this technique. Note narrowing of the foramen rotundum (*arrow*) and vidian canal (*arrowheads*)

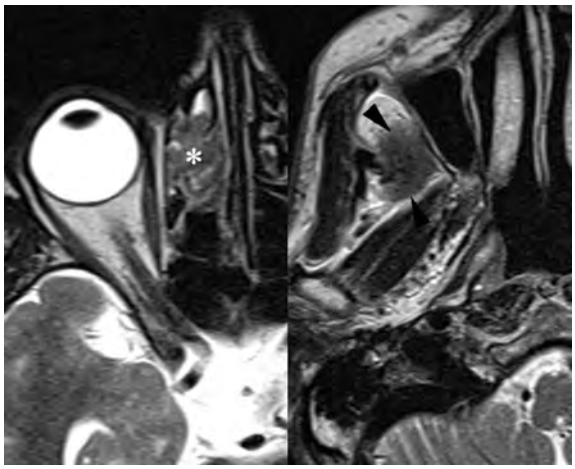

Fig. 24 59 year male, affected by lung carcinoma, complaining of trismus. Two metastases are shown on TSE T2, located in the ethmoid (*asterisk*) and masticator space (*arrowheads*)

the involved segments, secondary to replacement of medullary bone with fibrous tissue and immature woven bone. This condition may have three different presentations, namely the monostotic form (accounting for 70% of cases), the polyostotic form (~30%) and, rarely (<3%) McCune–Albright syndrome, in which endocrine dysfunction, precocious puberty and cutaneous hyperpigmentation add to the clinical scenario. Age of onset is variable, earlier for the polyostotic form, whereas the monostotic is more commonly diagnosed around the third and fourth decade, quite often as incidental finding; these two forms show no gender distribution whereas McCune–Albright syndrome shows female predilection (Lustig et al. 2001).

The sinonasal tract is more commonly involved by the polyostotic form; the ethmoid is the most common site (71% of cases) followed by the sphenoid (43%), frontal (33%) and maxillary bone (29%). Symptoms are mainly related to progressive enlargement of involved bone causing pressure and displacement of soft tissue and cranial nerves; orbital bone involvement may produce proptosis, visual disturbances and diplopia; sphenoid lesions may cause trigeminal neuropathy.

Ossifying fibroma is a benign fibroosseous tumor with locally aggressive pattern of growth that originates from mesenchymal blast cells, more often localized in the jaw and mandible. Age of onset matches that of fibrous dysplasia, female incidence prevails.

Fibrous dysplasia and ossifying fibroma share overlapping histologic features, making the differential diagnosis challenging, particularly when biopsy does not achieve an adequate sample. Some imaging findings may be helpful for the characterization of the lesion (Fig. 23). Fibrous dysplasia is displayed on MSCT as a poorly circumscribed bone expansion with ground glass density, covered by a thin and generally unaffected cortex; according to the prevalence of fibrous tissue or osseous component, density may range between radiolucency and sclerosis. On the other hand, ossifying fibroma is often a well-defined lesion with moderate to high density, bordered by a peripheral calcified shell. On MRI, the osseous or calcified matrix of such lesions is less distinctly demonstrated, however this technique allows more accurate assessment of soft tissue invasion or cranial nerve involvement. Signal intensity and contrast enhancement are highly variable and therefore of limited help for characterization, although T2 signal is reported to be hyperintense for ossifying fibroma as opposed to hypointensity exhibited by fibrous dysplasia.

Aneurysmal bone cysts may develop both in ossifying fibroma and fibrous dysplasia: on imaging studies, they are characterized by cystic appearance with peripheral calcified border; fluid–fluid levels are more readily shown on MRI but may be detected also with adequate MSCT window setting (Kendi et al. 2003).

Treatment of fibrous dysplasia is dictated by its benign nature and by the clinical scenario: surgery is indicated when imaging findings are insufficient to characterize a lesion incidentally found or to relieve symptoms due to compression of nerves or soft tissues; radiation therapy is contraindicated because of the risk of malignant degeneration. Medical treatment with bisphosphonates, aimed at decreasing osteoclastic activity, still needs validation on large series of patients (Berlucchi et al. 2005).

5.2.6 Metastasis

Rarely, the nose and paranasal sinus are the site of a distant metastasis, mostly of renal cell, breast or lung carcinoma. Signs and symptoms are similar to those caused by benign and malignant lesions. Imaging appearance is nonspecific, although intense enhancement is expected in hypervascular metastases, such as those produced by renal cell carcinoma and

Fig. 25 **a–d** Sinonasal SCC, follow-up obtained 6 months after radical maxillectomy including resection of the left hemipalate. The surgical defect was repaired rotating a temporalis muscle flap. Although partially effaced by edema and intense contrast enhancement (due to subacute denervation), the striated appearance of muscular fibers is still recognizable

melanoma. Maxillary sinus (33%) is the most commonly involved site followed by sphenoid sinus (22%), ethmoid (14%) and frontal sinus (9%); simultaneous involvement of more than one cavity occurs in as many as 22% of cases (Prescher and Brors 2001) (Fig. 24).

6 Imaging After Therapy

Detailed information about the natural history of the primary tumor along with a precise report of the surgical procedure adopted is the key to the correct assessment of the normal postoperative MRI findings.

Actually, the anatomy of the nose and paranasal sinuses may be significantly altered, not only after open surgery but also as a consequence of endoscopic resections.

The Draf-III procedure, for example, entails resection of the nasal septum (upper part) and of frontal intersinus septum, and drilling of the floor of frontal sinuses; as a result a large communication between the nasal fossae and frontal sinuses is created.

Extended maxillectomies, including posterolateral sinus wall resection, almost invariably produce large scars within the adjacent infratemporal and pterygopalatine fossae. These are seen as sharp plaques of T2 hypointense tissue, with variable degrees of enhancement, quite often bright in the early follow-up studies. Diffusion weighted imaging may be of help in the discrimination between post surgical scar and residual/recurrent tumor: in a review of 131 patients (personal unpublished data) followed up for SCC of the head and neck, the 40 recurrences appeared bright on b-1,000 images, as opposed to mature scars, which were as dark as the background normal tissues.

More demolitive procedures may require *reconstructive surgery*, to address either functional or cosmetic issues. Duraplasty, for example, aims at recreating a separation between endocranium and

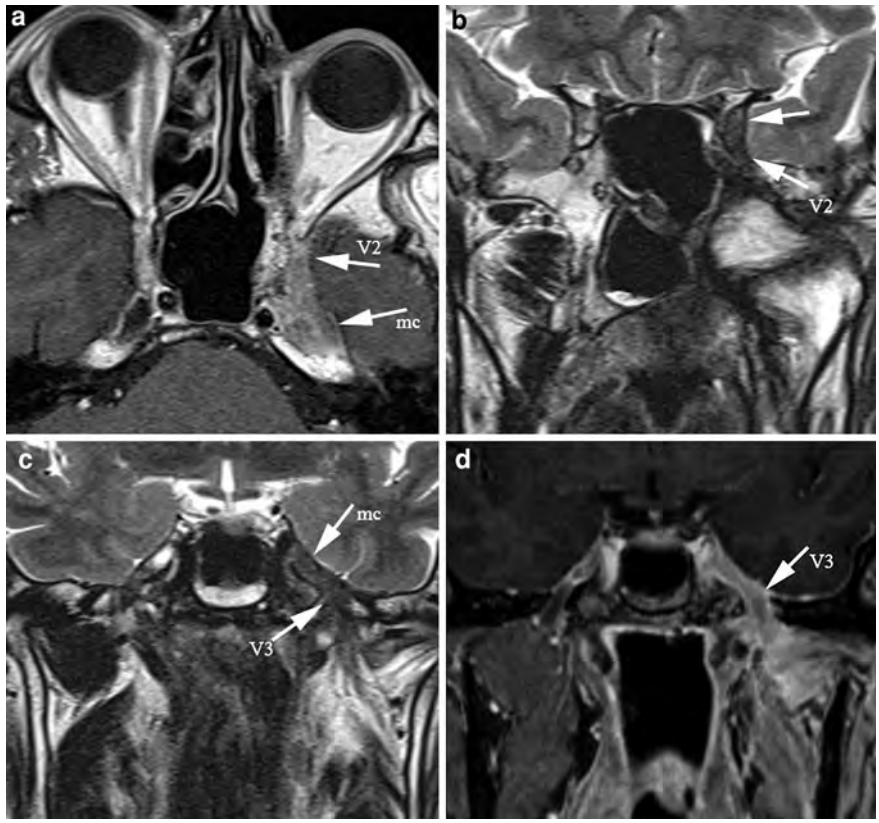

Fig. 26 **a–d** Sinonasal SCC (same patient as Fig 25, 1 year later): recurrent tumor with perineural spread. Solid tissue with hypointense TSE T2 signal and contrast enhancement is seen in the superior orbital fissure (*arrow*) and along the course of the maxillary nerve (*V2*). The tumor reaches the Meckel's cave (*mc*) and from there grows antegradely along the mandibular nerve (*V3*)

sinonasal cavity after anterior skull base and dural resection, performed with either open or transnasal endoscopic approach (Nicolai et al. 2011). In endoscopic surgery, this is achieved by harvesting three fascial layers (ilio-tibial tract has been recently advocated), the first intradural, the second intracranial extradural, the third extracranial. In open surgery, skull base defects are generally repaired with galeal pericranial flaps or microvascular free flaps (Boyle et al. 1998).

Duraplasty generally shows intermediate to hypointense T2 signal and variable degrees of enhancement. However, morphology is far more relevant than signal pattern, as the thickness of the duraplasty is expected to be regular all along its anteroposterior extension; additionally such a duraplasty is not infrequently seen to shrink over time. As a consequence, it is mandatory to add sagittal acquisitions to the normal MRI protocol, ideally both on TSE T2 and after contrast administration (Farina et al. 2010).

Muscular flaps, commonly harvested by rotating the temporalis muscle, are used to fill the gaps created by radical maxillectomy and/or orbital resection. Signal pattern of such flaps may sometimes be confusing, particularly when subacute denervation results in bright contrast enhancement. As a general rule, the identification of the tendon (hypointense on all sequences) and of the normal striated pattern of muscles helps to discriminate flaps from recurrent lesions (Fig. 25).

Thickening of sinonasal mucosa is common after treatment, particularly if radiotherapy is associated to surgery, and generally does not represent a challenge for the radiologist. It manifests as swelling and ballooning of the mucosa with hyperintense T2 signal; after contrast application, the epithelial lining enhances whereas the underlying edematous submucosa does not. Sometimes, the chronic inflammation may lead to the formation of synaechiae which may block the drainage of secretions with sinus cavities, finally resulting in mucocele formation. Although the detection of an expanded sinus cavity may raise concerns, the differentiation of mucocele from recurrent tumor is possible in nearly all cases based on signal pattern (dessiccated secretions often display hyperintense T1 signal without enhancement, which

is very uncommon in tumors) and bone changes (mucocele produces bone remodeling rather than destruction).

Awareness of the pattern of expected changes on MRI scans is crucial: any inconstency in such patterns should be considered suspect for tumor recurrence until otherwise proven. Recurrences are actually detected as nodules of variable size, located at the interface between native and reconstructed tissues (flaps, duraplasty). Rarely, recurrences manifest as linear/en-plaque lesions: this mainly occurs when the relapsing tumor grows along nerves or vessels (Fig. 26).

Signal pattern is rarely pathognomonic, however as a rule of thumb this is expected to replicate that of the primary. The added value of diffusion-weighted imaging is far from being validated in the literature. The overall rarity and histologic variety of sinonasal tumor makes the collection of large series difficult; furthermore, anatomic distortion and lack of spatial resolution limit the reliability of this technique. However, when the quality of images is sufficient, the combination of hyperintensity on b-1,000 images and diffusion restriction on the ADC map ($<1 \times 10^{-3}$ mm^2/s) may be adopted as a pragmatic rule for the detection of recurrent lesions.

Nodal recurrences, overall seen in up to 13% of patients, are more common in tumors arising for the maxillary sinus. Although ultrasound is regarded as the technique of choice for neck surveillance, retropharyngeal nodes should always be carefully scrutinized on follow-up MRI scans.

References

Aguilar Mandret F, Oliva Izquierdo MT, Valles Fontanet J (2004) Glioma nasal: a proposito de un caso. Acta Otorrinolaringol Esp 55:346–350

Beech TJ, Rokade A, Gittoes N et al (2007) A haemangiopericytoma of the ethmoid sinus causing oncogenic osteomalacia: a case report and review of the literature. Int J Oral Maxillofac Surg 36(10):956–958

Berlucchi M, Salsi D, Farina D et al (2005) Endoscopic surgery for fibrous dysplasia of the sinonasal tract in pediatric patients. Int J Pediatr Otorhinolaryngol 69:43–48

Borges A, Fink J, Villablanca P et al (2000) Midline destructive lesions of the sinonasal tract: simplified terminology based on histopathologic criteria. Am J Neuroradiol 21(2):331–336

Boyle JO, Shah KC, Shah JP (1998) Craniofacial resection for malignant neoplasms of the skull base: an overview. J Surg Oncol 69(4):275–284

Carter RL, Foster CS, Dinsdale EA et al (1983) Perineural spread by squamous carcinomas of the head and neck: a morphological study using antiaxonal and antimyelin monoclonal antibodies. J Clin Pathol 36(3):269–275

Castro DE, Raghuram K, Phillips CD (2005) Benign triton tumor of the trigeminal nerve. Am J Neuroradiol 26: 967–969

Chain JR, Kingdom TT (2007) Non-Hodgkin's lymphoma of the frontal sinus presenting as osteomyelitis. Am J Otolaryngol 28:42–45

Das S, Kirsch CFE (2005) Imaging of lumps and bumps in the nose: a review of sinonasal tumours. Cancer Imaging 5:167–177

De Vuysere S, Hermans R, Marchal G (2001) Sinochoanal polyp and its variant, the angiomatous polyp: MRI findings. Eur Radiol 11:55–58

Eisen MD, Yousem DM, Montone KT et al (1996) Use of preoperative MR to predict dural, perineural, and venous sinus invasion of skull base tumors. Am J Neuroradiol 17(10):1937–1945

Farina D, Borghesi A, Botturi E et al (2010) Treatment monitoring of paranasal sinus tumors by magnetic resonance imaging. Cancer Imaging 10:183–193

Galera-Ruiz H, Sanchez-Calzado JA, Rios-Martin JJ et al (2001) Sinonasal radiation-associated osteosarcoma after combined therapy for rhabdomyosarcoma of the nose. Auris Nasus Larynx 28(3):261–264

Gandhi MR, Panizza B, Kennedy D (2011) Detecting and defining the anatomic extent of large nerve perineural spread of malignancy: Comparing "targeted" MRI with the histologic findings following surgery. Head Neck 33(4):469–475

Gras Cabrerizo JR, Sarandeses García A, Montserrat I, Gili JR et al (2007) Revision of carcinomas in paranasal sinuses. Acta Otorrinolaringol Esp 58(6):266–275

Guermazi A, Feger C, Rousselot P et al (2002) Granulocytic sarcoma (chloroma): imaging findings in adults and children. A J Roentgenol 178:319–325

Hagiwara A, Inoue Y, Nakayama T et al (2001) The botryoid sign: a characteristic feature of rhabdomyosarcomas in the head and neck. Neuroradiology 43:331–335

Hanna E, Vural E, Prokopakis E et al (2007) The sensitivity and specificity of high-resolution imaging in evaluating perineural spread of adenoid cystic carcinoma to the skull base. Arch Otolaryngol Head Neck Surg 133:541–545

Hedlund G (2006) Congenital frontonasal masses: developmental anatomy, malformations, and MR imaging. Pediatr Radiol 36(7):647–662

Hermans R, De Vuysere S, Marchal G (1999) Squamous cell carcinoma of the sinonasal cavities. Semin Ultrasound CT MR 20(3):150–161

Howarth KL, Khodaei I, Karkanevatos A et al (2004) A sinonasal primary Ewing's sarcoma. Int J Pediatr Otorhinolaryngol 68:221–224

Ishida H, Mohri M, Amatsu M (2002) Invasion of the skull base by carcinomas: histopathologically evidenced findings with CT and MRI. Eur Arch Otolaryngol 259(10):535–539

Kania RE, Sauvaget E, Guichard JP et al (2005) Early postoperative CT scanning for juvenile nasopharyngeal angiofibroma: detection of residual disease. Am J Neuroradiol 26:82–88

Karagama YG, Howarth K, Steel PRM et al (2002) Lobular capillary haemangioma of the nasal vestibule: a rare entity. Int J Pediatr Otorhinolaryngol 66:71–75

Kendi ATK, Kara S, Altinok D et al (2003) Sinonasal ossifying fibroma with fluid–fluid levels on MR images. Am J Neuroradiol 24:1639–1641

Kim SS, Han MH, Kim JE et al (2000) Malignant melanoma of the sinonasal cavity: explanation of magnetic resonance signal intensities with histopathologic characteristics. Am J Otolaryngol 21(6):366–378

Kim HJ, Lee TH, Lee HS et al (2006) Periorbita: computed tomography and magnetic resonance imaging findings. Am J Rhinol 20(4):371–374

Kobayashi S, Yoshizawa H, Hachiya Y et al (1993) Vasogenic edema induced by compression injury to the spinal nerve root. Distribution of intravenously injected protein tracers and gadolinium-enhanced magnetic resonance imaging. Spine 18(11):1410–1424

Kuo FY, Lin HC, Eng HL et al (2005) Sinonasal hemangiopericytoma-like tumor with true pericytic myoid differentiation: a clinicopathologic and immunohistochemical study of five cases. Head Neck 27(2):124–129

Lance E, Schatz C, Nach R et al (1992) Pyogenic granuloma gravidarum of the nasal fossa: CT features. J Comput Assist Tomogr 16(4):663–664

Lee HJ, Im JG, Goo JM et al (2003) Peripheral T-cell lymphoma: spectrum of imaging findings with clinical and pathologic features. Radiographics 23(1):7–26

Lombardi D, Tomenzoli D, Buttà L et al (2011) Limitations and complications of endoscopic surgery for treatment for sinonasal inverted papilloma: a reassessment after 212 cases. Head Neck 33(8):1154–1161. doi:10.1002/hed.21589

Lund VJ (2000) Optimum management of inverted papilloma. J Laryngol Otol 114:194–197

Lustig LR, Holliday MJ, McCarthy EF et al (2001) Fibrous dysplasia involving the skull base and temporal bone. Arch Otolaryngol Head Neck Surg 127(10):1239–1247

Maroldi R, Farina D, Battaglia G et al (1997) MR of malignant nasosinusal neoplasms. Frequently asked questions. Eur J Radiol 24(3):181–190

Maroldi R, Berlucchi M, Farina D et al (2004a) Benign neoplasms and tumor-like lesions. In: Maroldi R, Nicolai P (eds) Imaging in treatment planning for sinonasal diseases. Springer, Berlin

Maroldi R, Farina D, Palvarini L et al (2004b) Magnetic resonance imaging findings of inverted papilloma: differential diagnosis with malignant sinonasal tumors. Am J Rhinol 18(5):305–310

Maroldi R, Lombardi D, Farina D et al (2004c) Malignant neoplasms. In: Maroldi R, Nicolai P (eds) Imaging in treatment planning for sinonasal diseases. Springer, Berlin

Maroldi R, Farina D, Borghesi A et al (2008) Perineural tumor spread. Neuroimaging Clin N Am 18(2):413–429

McFadden Bragg T, Scianna J, Kassam A et al (2009) Clinicopathological review: esthesioneuroblastoma. Neurosurgery 64:764–770

Megat Shiraz MAR, Jong YH, Primuharsa Putra SHA (2008) Extramedullary plasmacytoma in the maxillary sinus. Singapore Med J 49(11):310–311

Minami M, Kaneda T, Ozawa K et al (1996) Cystic lesions of the maxillomandibular region: MR distinction of odontogenic keratocysts and ameloblastomas from other cysts. Am J Roentgenol 166:943–949

Momeni AK, Roberts CC, Chew FS (2007) Imaging of chronic and exotic sinonasal disease: review. Am J Roentgenol 189:35–45

Nicolai P, Tomenzoli D, Berlucchi M et al (2000) Malignant triton tumor of the ethmoid sinus and nasal cavity. Ann Otol Rhinol Laryngol 109(9):880–886

Nicolai P, Bolzoni Villaret A, Farina D et al (2010) Endoscopic surgery for juvenile angiofibroma: a critical review of indications after 46 cases. Am J Rhinol Allergy 24:67–72

Nicolai P, Castelnuovo P, Bolzoni Villaret A (2011) Endoscopic Resection of Sinonasal Malignancies. Curr Oncol Rep 13(2):138–144. doi:10.1007/s11912-011-0151-6

Ojiri H, Ujita M, Tada S et al (2000) Potentially distinctive features of sinonasal inverted papilloma on MR imaging. A J Roentgenol 175(2):465–468

Prescher A, Brors D (2001) Metastases to the paranasal sinuses: case report and review of the literature. Laryngorhinootologie 80:583–594

Puxeddu R, Berlucchi M, Ledda GP et al (2006) Lobular capillary hemangioma of the nasal cavity: a retrospective study on 40 patients. Am J Rhinol 20(4):480–484

Raghavan P, Phillips CD (2007) Magnetic resonance imaging of sinonasal malignancies. Top Magn Reson Imaging 18(4): 259–267

Rischin D, Coleman A (2008) Sinonasal malignancies of neuroendocrine origin. Hematol Oncol Clin N Am 22:1297–1316

Roth TN, Gengler C, Huber GF et al (2010) Outcome of sinonasal melanoma: clinical experience and review of the literature. Head Neck 32(10):1385–1392

Rushing EJ, Bouffard JP, McCall S et al (2009) Primary extracranial meningiomas: an analysis of 146 cases. Head Neck Pathol 3(2):116–130

Samant S, Kruger E (2007) Cancer of the paranasal sinuses. Curr Oncol Rep 9:147–151

Sartoretti-Schefer S, Wichmann W, Valavanis A (1994) Idiopathic, herpetic, and HIV-associated facial nerve palsies: abnormal MR enhancement patterns. Am J Neuroradiol 15(3):479–485

Schafer DR, Thompson LDR, Smith BC et al (1998) Primary ameloblastoma of the sinonasal tract: a clinicopathologic study of 24 cases. Cancer 82(4):667–674

Simo R, De Carpentier J, Rejali D et al (1998) Paediatric pyogenic granuloma presenting as a unilateral nasal polyp. Rhinology 36:136–138

Sklar EML, Pizarro JA (2003) Sinonasal intestinal-type adenocarcinoma involvement of the paranasal sinuses. Am J Neuroradiol 24:1152–1155

Sobin L, Gospodarowicz M, Wittekind C (2010) TNM classification of malignant tumours. Blackwell, Hoboken

Som Dillon PM, Fullerton GD et al (1989) Chronically obstructed sinonasal secretions: observations on T1 and T2 shortening. Radiology 172(2):515–520

Stomeo F, Fois V, Cossu A et al (2004) Sinonasal haemangiopericytoma: a case report. Eur Arch Otorhinolaryngol 261(10):555–557

Suarez C, Llorente JL, Fernandez De Leon R et al (2004) Prognostic factors in sinonasal tumors involving the anterior skull base. Head Neck 26(2):136–144

Thompson LDR (2006) Sinonasal carcinomas. Curr Diag Pathol 12:40–53

Thompson LDR (2009) Olfactory neuroblastoma. Head Neck Pathol 3:252–259

Thompson LDR, Gyure KA (2000) Extracranial sinonasal tract meningiomas: a clinicopathologic study of 30 cases with a review of the literature. Am J Surg Pathol 24(5):640–650

Toda T, Atari E, Sadi AM et al (1999) Primitive neuroectodermal tumor in sinonasal region. Auris Nasus Larynx 26:83–90

Vandecaveye V, De Keyzer F, Dirix P et al (2010) Applications of diffusion-weighted magnetic resonance imaging in head and neck squamous cell carcinoma. Neuroradiology 52: 773–784

Vlychou M, Ostlere SJ, Kerr R et al (2007) Low-grade osteosarcoma of the ethmoid sinus. Skeletal Radiol 36(5): 459–462

Wiseman SM, Popat SR, Rigual NR et al (2002) Adenoid cystic carcinoma of the paranasal sinuses or nasal cavity a 40-year review of 35 cases. Ear Nose Throat J 81(8):510–514

Yamamoto S, Motoori K, Takano H et al (2002) Chondrosarcoma of the nasal septum. Skeletal Radiol 31:543–546

Parotid Gland and Other Salivary Gland Tumors

Frédérique Dubrulle and Raphaëlle Souillard-Scemama

Contents

F. Dubrulle (✉) · R. Souillard-Scemama
Plateau commun d'imagerie,
Hôpital Huriez CHRU Lille,
59000, Lille, France
e-mail: F-DUBRULLE@CHRU-LILLE.FR

Abstract

Parotid gland masses are most frequently benign tumors. In order to determine the most appropriate therapy, MR imaging is the best imaging tool to evaluate tumor topography, locoregional extension, relationship with the facial nerve and even its nature, benign or malignant. MR diffusion-weighted images and dynamic contrast-enhanced sequences are helpful to differentiate benign from malignant tumors, and in case of atypical tumors. This chapter reviews the imaging characteristics of parotid gland and other salivary glands tumors.

1 Introduction

The parotid gland is the largest salivary gland. It is located in the parotid space. The parotid gland can be affected by a variety of pathologic processes, especially neoplastic. Parotid tumors represent less than 3% of all head and neck tumors and are most frequently benign. These tumors require surgery in most cases and imaging is essential in the workup of these lesions.

2 Anatomy

The parotid space is a paired lateral suprahyoid neck space surrounded by the superficial layer of the deep cervical fascia. This space extends from the external auditory canal and the mastoid tip superiorly to the angle of the mandible below. It contains the parotid gland, intra- and extra-parotid lymph nodes. The

R. Hermans (ed.), *Head and Neck Cancer Imaging*, Medical Radiology. Diagnostic Imaging,
DOI: 10.1007/174_2011_383, © Springer-Verlag Berlin Heidelberg 2012

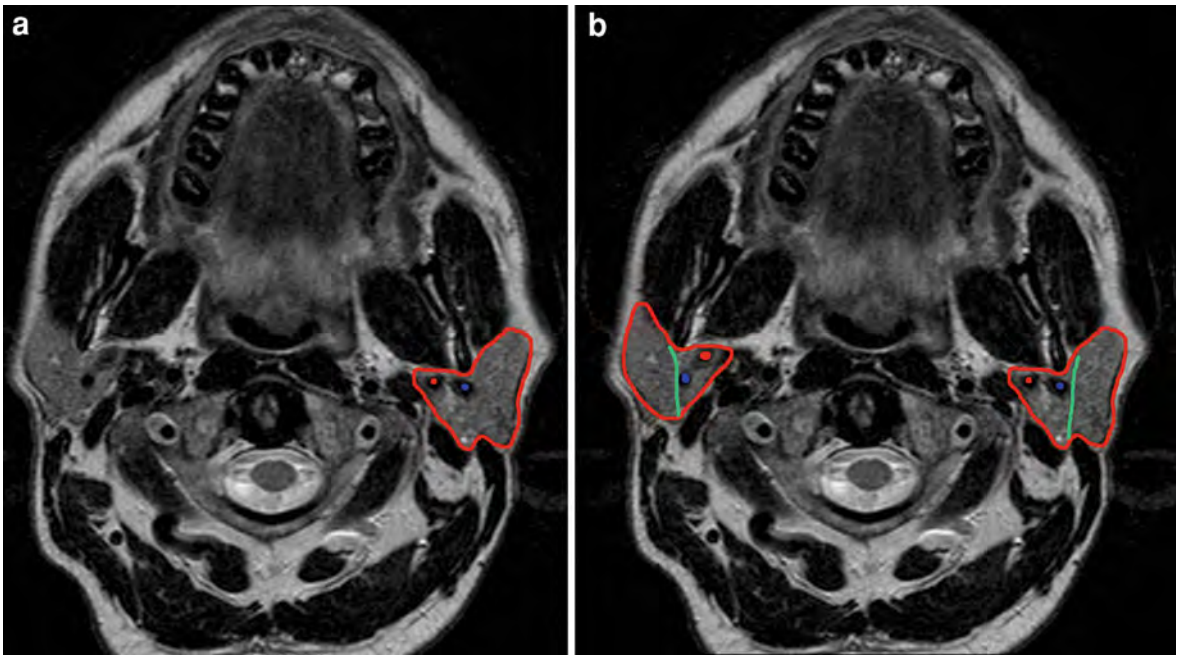

Fig. 1 Anatomy of the parotid space The parotid space (surrounded in *red*) is made of the parotid gland, the retromandibular vein (*blue circle*), the external carotid artery (*red circle*) and intra- and extra-parotid lymph nodes. It also contains the facial nerve, which is not directly seen on imaging; it is used as a reference plane (*green line*) to separate the parotid gland into an external superficial lobe and an internal deep lobe

gland contains about 20 intraglandular lymph nodes which are considered normal if their transverse diameter is less than 8 mm. The gland also contains extracranial branches of the facial nerve, and vessels: the external carotid artery and the retromandibular vein just behind the mandibular ramus (Fig. 1).

The facial nerve exits the skull base via the stylomastoid foramen and continues within the parotid gland from its posterior and superior part to its anterior and inferior part, lateral to the retromandibular vein. It then divides into superior temporo-facial branches and inferior cervical branches. By convention, the facial nerve is used as a reference plane within the gland to separate the external superficial lobe and the internal deep lobe, but actually there is no true anatomic division. The facial nerve is not seen with imaging and its course can only be estimated (Fig. 1; Harnsberger 2004).

The parotid space is directly lateral to the anterior part of the parapharyngeal space (prestyloid space), without real anatomic division between these two spaces. The deep portion of the parotid gland bulges in the prestyloid compartment in which deep lobe tumors can extend (Fig. 2). The prestyloid compartment also contains fat tissue, accessory salivary glands and a prestyloid branch of the mandibular nerve (V3).

Anterior to the parotid space is the masticator space or infratemporal fossa, which contains the pterygoid muscles.

Posterior to the prestyloid parapharyngeal space is the carotid space or retrostyloid space (Fig. 2).

There is an anatomic division between these different spaces (the masticator space, the carotid space and the anterior parapharyngeal space). Benign tumors will respect these anatomic limits whereas they will be infiltrated by malignant tumors.

The parotid gland also contains salivary ducts. The main parotid duct, or Stensen's duct, emerges from the anterior part of the parotid gland, runs over the masseter muscle and in the superficial cervical fascia and then abruptly courses medially to pierce the buccinator muscle, forming a nearly 90° angle with this muscle, terminating in the buccal mucosa at the level of the second upper molar (Fig. 3).

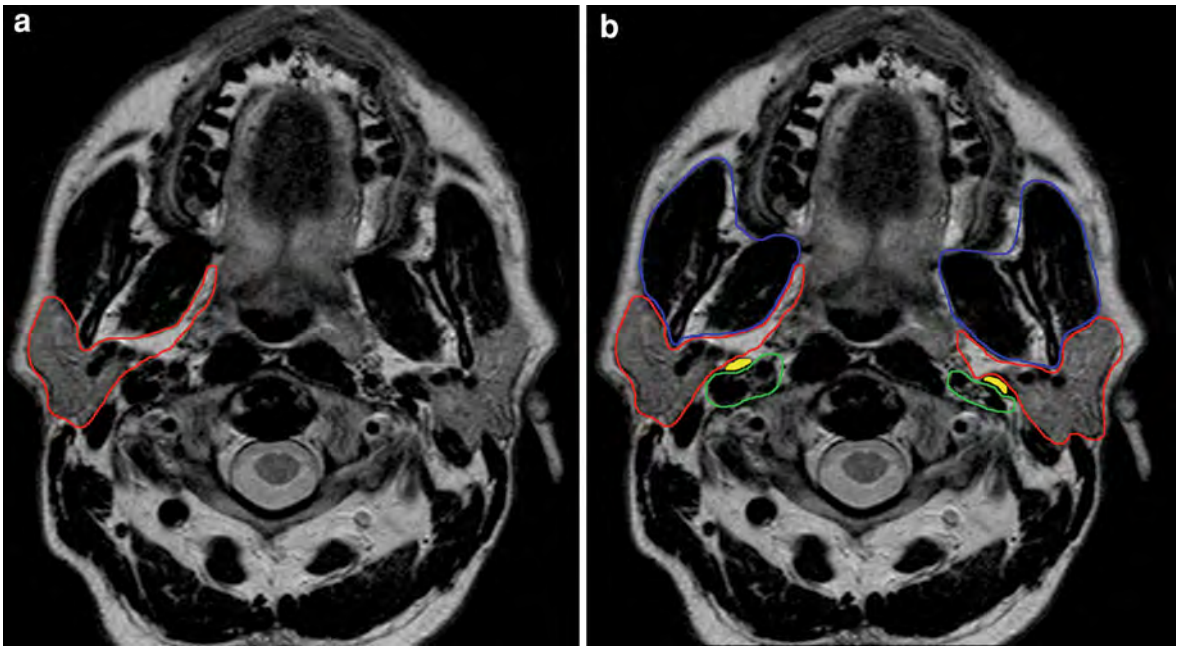

Fig. 2 Lateral and internal to the parotid space is the anterior part of the parapharyngeal space (or prestyloid compartment—both surrounded in *red*); there is no real anatomic division between these two spaces. The most internal part of the deep parotid lobe bulges in the prestyloid compartment. Posterior (retrostyloid) part of the parapharyngeal space, also called the carotid space (surrounded in *green*), separated from the anterior parapharyngeal space by the styloid process (indicated in *yellow*) as well as muscles and a fascial layer originating from it (see also "Parapharyngeal Space Neoplasms"). Masticator space (surrounded in *blue*)

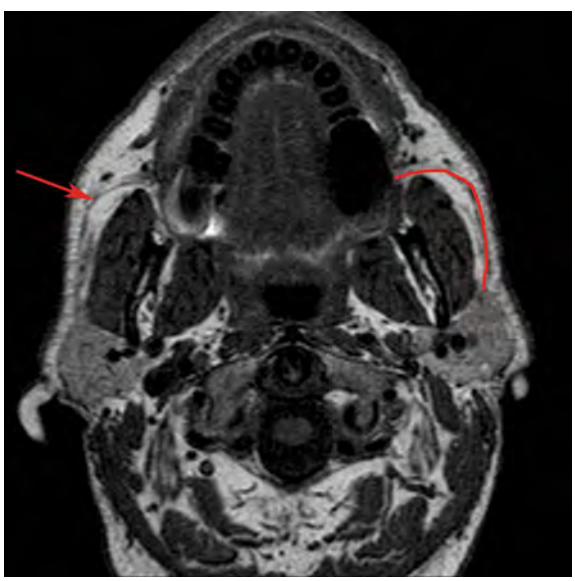

Fig. 3 The main parotid salivary duct canal or Stensen's duct (in *red*) emerges from the anterior part of the parotid gland, runs over the masseter muscle and in the superficial cervical fascia, then forms a 90° angle (*arrow*), pierces the buccinator muscle to terminate in the oral cavity at level of the second upper molar

3 Imaging Issues

When a patient presents with a palpable mass of the parotid space, the radiologist has to answer several key questions, which are essential to the head and neck surgeon in order to determine the best therapy (Harnsberger 2004; Shah 2002; Vogl et al. 1999):

- *Is the mass intra or extraparotid*?
  Small, intraparotid masses are easy to identify. For large and deep lobe masses, the knowledge of the different cervical spaces is essential. The pattern of displacement of the prestyloid parapharyngeal space has to be analyzed.
- *Is the parotid space mass single or multiple? Unilateral or bilateral*?
  Multiple lesions are suggestive for specific tumors: for example, bilateral tumors are suggestive of Warthin tumor; multiple cystic formations suggest Sjögren syndrome or benign lymphoepithelial lesions possibly related to HIV.
- *Does the tumor show benign or malignant characteristics*?

The surgical approach will depend on these characteristics. If malignancy is suspected, is there evidence of perineural spread along the facial nerve or branches of the trigeminal nerve? In that case, the therapeutic attitude will be different.

- *Is the tumor limited to the superficial lobe of the parotid*?
  A superficial parotidectomy is sufficient for a benign, well-circumscribed, superficial lobe lesion. On the other hand, a superficial lesion extending in the deep lobe requires a total parotidectomy (O'Brien 2003).
- *What is the relationship of the mass to the facial nerve*?
  The facial nerve is not seen on imaging but its intraparotid course can be estimated (plane between the stylomastoid foramen and the lateral border of the retromandibular vein).
- *Is it possible to determine the histologic type of a benign tumor*?
  A pleomorphic adenoma of the parotid gland will require surgery, whereas Warthin tumor in elderly patients may be followed up clinically and by imaging.

In order to answer all these key questions, MR imaging is the primary modality of choice for parotid gland tumors (Joe and Westesson 1994; Shah 2004).

The classical sequences used are: axial and coronal turbo spin-echo T2-weighted and spin-echo T1-weighted sequences with a slice thickness of 2–3 mm and a spin-echo T1-weighted sequence after contrast administration. A sequence with fat saturation after contrast administration is useful to better visualize potential perineural extension along the facial nerve or intracranial extension. This sequence is also useful to analyze correctly the tumoral enhancement.

A sequence to analyze the cervical lymph nodes is necessary if a malignant tumor is suspected. MR sialography can be useful if a pseudo-tumoral pathology such as Sjögren syndrome is suspected.

Diffusion-weighted sequence with calculation of an apparent diffusion coefficient (ADC) map may be interesting to better characterize non-specific tumors (Ikeda et al. 2004) or to improve the distinction between benign and malignant tumor, high cellularity in malignant tumors coming along with a decreased ADC value (Eida et al. 2007). To improve the reproductibility, calculation of the ADC tumor/ADC normal parotid gland ratio is recommended (Tassart et al. 2010).

Dynamic contrast-enhanced MR imaging (DCE-MRI) is a technique recently introduced for the evaluation of salivary glands tumors: a T1-weighted sequence is repeated every 30 s for 5 min during and after bolus injection of gadolinium. Two parameters are analyzed: the time to peak enhancement (T_{peak}) and the washout ratio (WR), which are determined from time–signal intensity curves (TICs) (Yabuuchi et al. 2003). Four types of curves can be described (Table 1). This dynamic technique is helpful to differentiate benign from malignant tumors (Yabuuchi et al. 2003), and for further tissue characterization in benign tumors (Yabuuchi et al. 2003; Ikeda et al. 2004; Alibek et al. 2007; Hisatomi et al. 2007; Tassart et al. 2010).

Table 1 Different types of dynamic contrast enhancement of parotid tumors

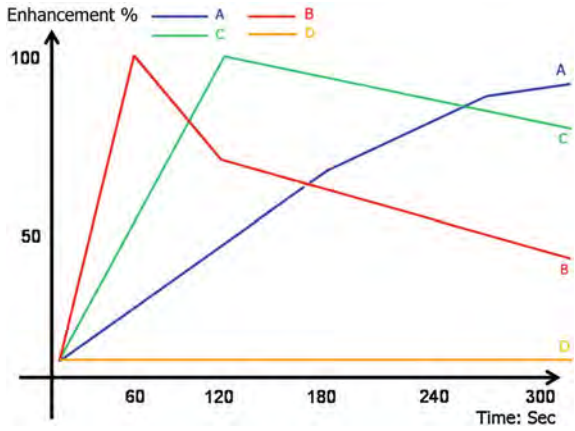

Evolution of the tumoral enhancement on dynamic contrast-enhanced T1-weighted sequence repeated every 30 s during 5 min; evaluation of TICs. Four TIC patterns can be observed
Type A progressive contrast enhancement of the tumor with a delayed time to peak enhancement ($T_{peak} > 120$ s) and a poor WR (<10% at 5 min): 75% of pleomorphic adenomas and other types of benign adenomas
Type B early enhancement ($T_{peak} < 120$ s) and high washout pattern (WR > 30% at 5 min) suggestive of Warthin tumor
Type C early enhancement ($T_{peak} \leq 120$ s) and low washout pattern, (WR < 30% at 5 min) suggestive of malignant tumors
Type D flat curve without enhancement suggestive of cystic lesion

Courtesy Marc Tassart, MD, Paris, France

4 Benign Parotid Tumors

Benign tumors of the parotid gland represent about 85% of all parotid tumors (Okahara et al. 2003).

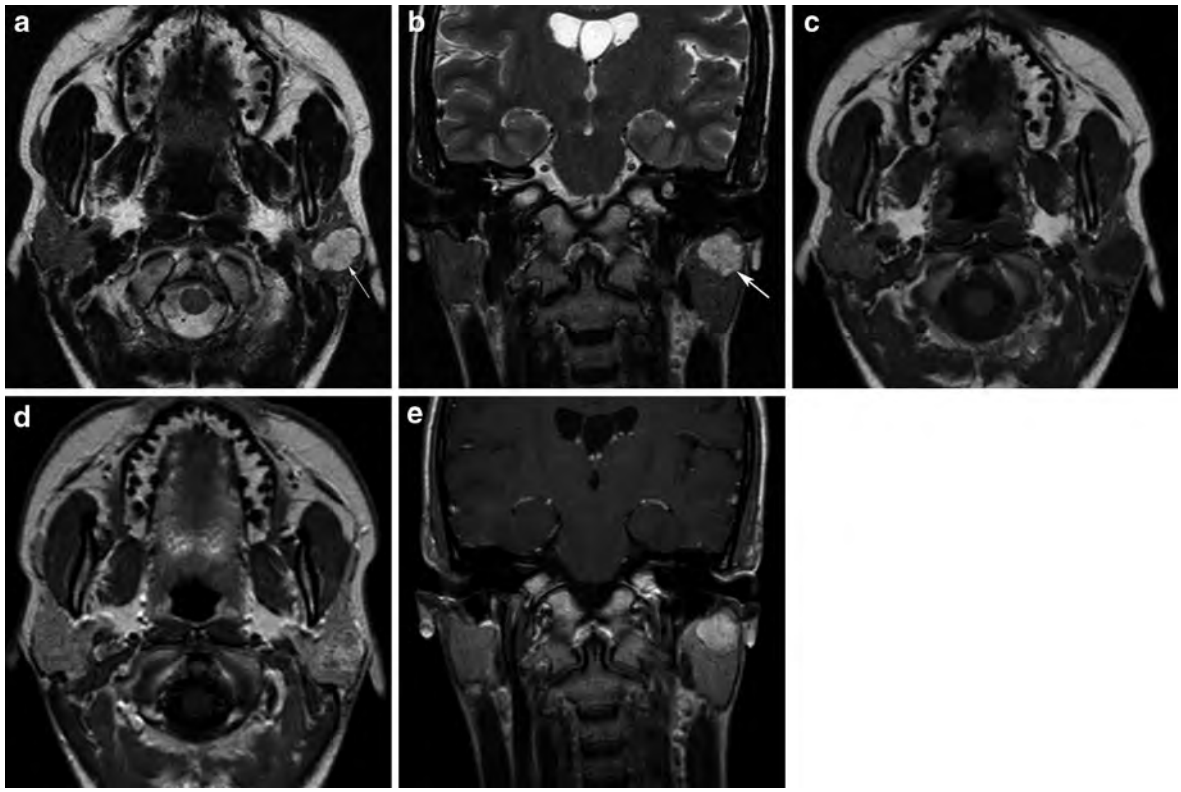

Fig. 4 Typical pleomorphic adenoma, or benign mixed tumor, of the superficial lobe of the left parotid gland: a lobulated, well-circumscribed lesion with high T2-weighted (*arrow*, **a**, **b**) and low T1-weighted signal intensity (**c**). It shows clear enhancement on contrast-enhanced T1-weighted images (**d**), appearing more homogeneous on delayed contrast-enhanced images (**e**)

4.1 Benign Mixed Tumor or Pleomorphic Adenoma

4.1.1 General Description

This is the most common parotid gland tumor and it represents 70–80% of all tumors of the parotid gland. The lesion is usually solitary. Of all pleomorphic adenomas, 90% occur in the superficial lobe. If the lesion originates from the deep lobe, it can become large, extending in the anterior parapharyngeal space without causing symptoms.

There is a female predominance (sex ratio: 2/1). Facial nerve paralysis is uncommon.

4.1.2 Histological Findings

Pleomorphic adenoma is encased in a capsule that may be incomplete. It contains epithelial, myoepithelial and stromal (mucoid, myxoid, chondroid) cellular components. Calcifications are rare. Sites of cystic changes and hemorrhage may be present, especially if the tumor is large.

The lesion may show multicentric outgrowth through its capsule. The risk of recurrence is very high when only an enucleation of the tumor is performed. Therefore, in some centers, total parotidectomy is routinely performed for pleomorphic adenoma, in order to limit the risk of recurrence as much as possible.

4.1.3 Imaging Findings

- Typically, pleomorphic adenoma is a solitary, well-circumscribed mass. It may be lobulated. This tumor has low T1-weighted and high T2-weighted signal intensities. It may demonstrate a low T2-weighted signal intensity capsule. It shows homogeneous enhancement on T1 contrast-enhanced images, well illustrated on delayed contrast-enhanced T1-weighted images with fat saturation (Figs. 4, 5; Ikeda et al. 1996).

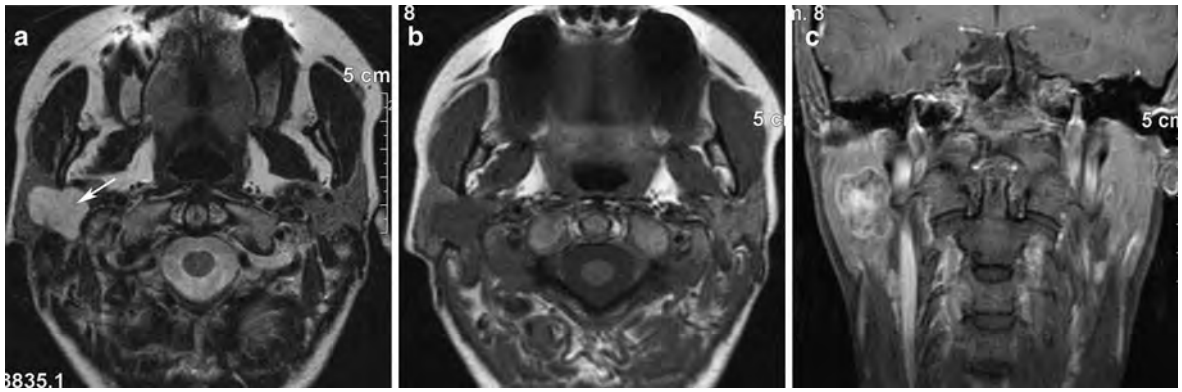

Fig. 5 Large pleomorphic adenoma of the right parotid gland extending to the deep lobe of the parotid gland (*arrow*). The tumor appears well-circumscribed and lobulated with high T2-weighted (**a**), low T1-weighted signal intensity (**b**) and heterogeneous enhancement on contrast-enhanced images (**c**)

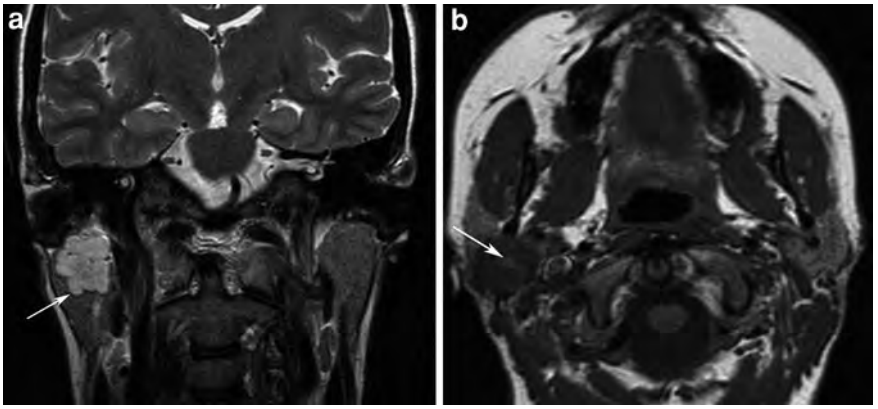

Fig. 6 Pleomorphic adenoma of the right parotid gland: a well-delineated, lobulated tumor showing a typically high T2-weighted signal intensity and a low-signal intensity "capsule" (*arrow*, **a**). On the plain T1-weighted images (**b**), the tumor has a low-signal intensity with small regions of high T1-weighted signal intensity, corresponding to hemorrhagic areas (*arrow*)

Imaging findings may be less typical in case of larger tumors, but the lesion remains lobulated and well-circumscribed. Areas of hemorrhage appear as regions of high-signal intensity on both T1- and T2-weighted images (Fig. 6). Myxoid degeneration appears as heterogeneous and intermediate T2-weighted signal intensity (Fig. 7). In these large tumors, signal intensity can be heterogeneous on early contrast-enhanced images but it can appear more homogeneous on delayed contrast-enhanced, fat-suppressed T1-weighted images (Fig. 4).

An extension to the deep lobe of the parotid gland must be looked for and reported.

Large tumors of the deep lobe are usually mixed tumors (Figs. 8, 9).

Pleomorphic adenoma presents no restricted diffusion with high ADC value and ADC tumor/normal parotid gland ratio >1.2 (nearly two most frequently). These characteristics can be useful to differentiate pleomorphic adenomas from all other types of parotid gland tumors (Yerli et al. 2007).

- Dynamic contrast-enhanced MRI typically shows a progressive contrast enhancement of the tumor with a delayed time to peak enhancement ($T_{peak} > 120$ s) and a poor WR (<10% at 5 min), corresponding to an A curve on the TICs patterns (Yabuuchi et al. 2003; Hisatomi et al. 2007).
- Non-typical forms of pleomorphic adenoma are rare. These lesions have a low T2-weighted signal intensity which corresponds to fibrous tissue (Fig. 10). The correct diagnosis may be difficult but a solitary, well-circumscribed, encapsulated lesion is suggestive of benign tumor (Harnsberger 2004). Diffusion-weighted sequence and dynamic contrast-enhanced MRI can be helpful in this case showing respectively a typical high ADC value, and a characteristic intensity time curve type A.

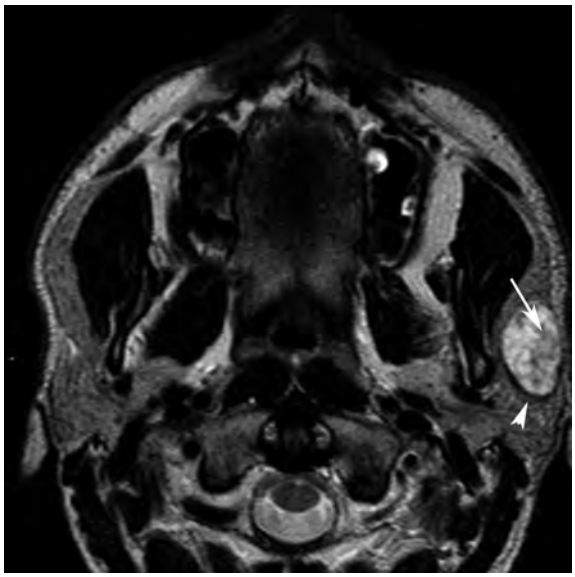

Fig. 7 Pleomorphic adenoma of the left parotid gland with a high T2-weighted signal intensity and small heterogeneous areas of lower signal intensity, related to myxoid degeneration (*arrow*). The capsule is well identified (*arrowhead*)

Fig. 8 Pleomorphic adenoma extending to the left anterior parapharyngeal space with typical high signal on T2-weighted images

- Calcified lesions are uncommon; these calcifications occur after a long evolution.
- Recurrent pleomorphic adenoma tends to be multifocal and more aggressive (Fig. 11). To improve the detection of nodular recurrences, a T2-weighted sequence with fat suppression (fat sat), or STIR sequence, is very useful (Tassart et al. 2010).
- Malignant degeneration within a pleomorphic adenoma is rare but exists in 3–5% (Tassart et al. 2010). The most common type of malignancy associated with pleomorphic adenoma is a carcinoma ex pleomorphic adenoma, or sometimes an adenocarcinoma. Malignant characteristics are then present on imaging studies. The hypercellularity due to the malignant degeneration results in low-signal intensity on T2-weighted sequence, and low ADC values (Kato et al. 2008) with an ADC tumor/ADC normal parotid gland ratio lower than 1.

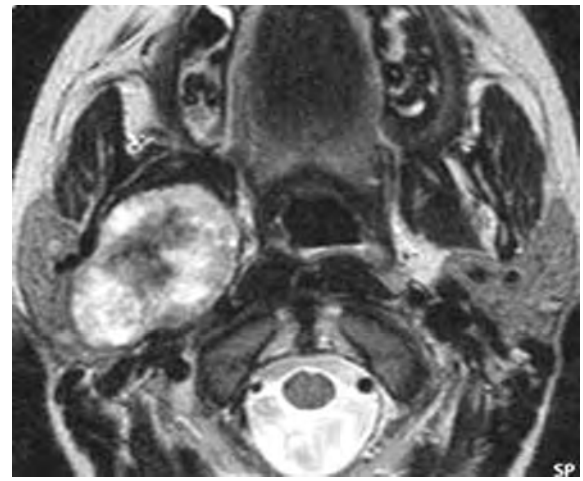

Fig. 9 Large pleomorphic adenoma of the deep lobe of the right parotid gland with non-homogeneous, high-signal intensity on this T2-weighted image. Larger tumors typically show slightly heterogeneous signal intensity

4.1.4 Differential Diagnosis

- *Warthin tumor or papillary cystadenoma lymphomatosum*
  Especially in case of non-typical imaging findings of pleomorphic adenoma (see Sect. 6).
- *Malignant tumor*
  Features suggesting malignancy are heterogeneous enhancement, an infiltrating mass with irregular margins, perineural tumor spread or infiltration of adjacent fat tissue.
- *Non-Hodgkin lymphoma of the parotid*
  The clinical presentation may be suggestive (see "Neck Lymphoma").
- *Parotid nodal metastasis* (often from skin carcinoma or melanoma, sometimes systemic metastasis).

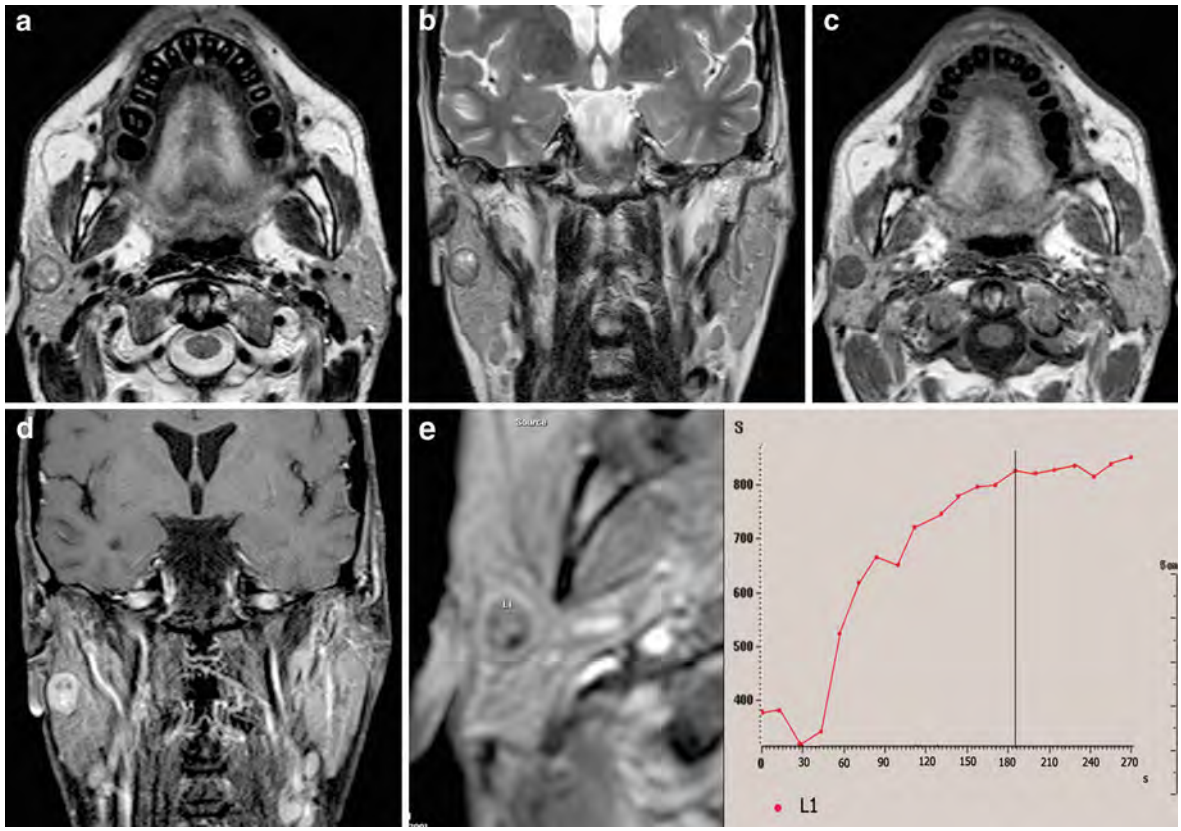

Fig. 10 Atypical pleomorphic adenoma of the right parotid gland, with low heterogenous T2-weighted signal intensity (**a**, **b**), and low T1-weighted signal intensity (**c**). This tumor shows however benign characteristics: a well-delineated, sharply outlined mass with homogeneous enhancement on post-contrast images (**d**) and a typical A curve on the dynamic contrast-enhanced sequence with a progressive contrast enhancement ($T_{peak} > 120$ s)

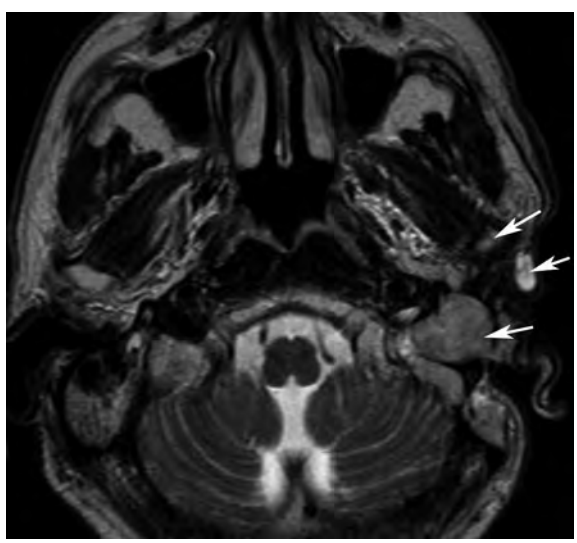

Fig. 11 Multifocal recurrent pleomorphic adenoma after partial parotidectomy (*arrows*)

4.2 Warthin Tumor or Papillary Cystadenoma Lymphomatosum

4.2.1 General Description

This is the second most frequent benign tumor arising in the parotid gland and it represents 10–25% of all parotid tumors.

It is more common in males than in females (sex ratio: 3/1). The mean age for presentation is 60 years. About 90% of patients with this tumor are cigarette smokers. This diagnosis should not be suggested before age of 40 years (Harnsberger 2004).

It arises almost exclusively in the lower portion of the superficial lobe of the parotid gland. There is a bilateral involvement in 15–20% of patients, which presents simultaneously or metachronously, the contralateral location may be discovered on imaging only.

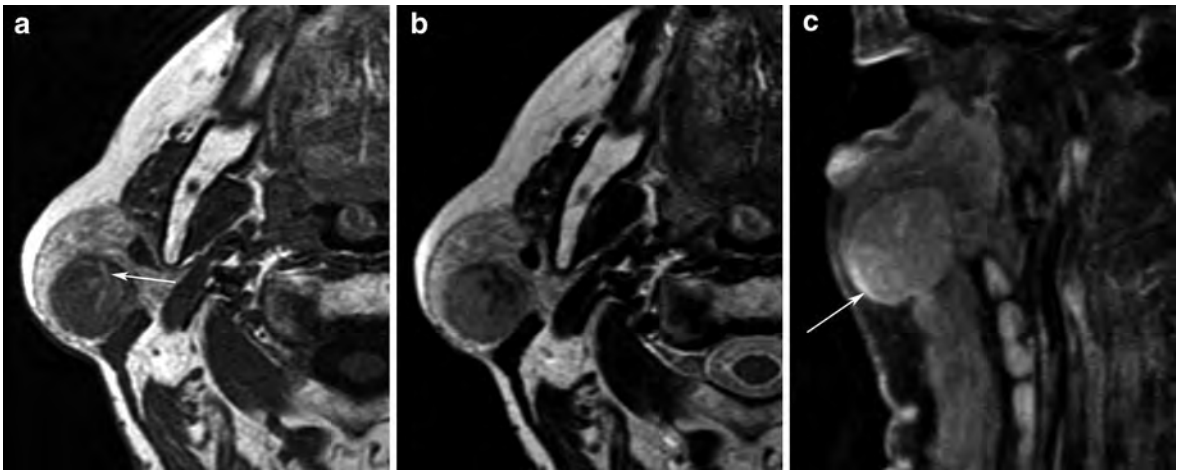

Fig. 12 Typical Warthin tumor in the superficial lobe of the right parotid gland showing a low T1-weighted signal intensity with small high-signal intensity areas (*arrow*, **a**), a low T2-weighted signal intensity (**b**), and a mild enhancement more pronounced in the periphery of the mass (*arrow*, **c**)

These are slow-growing tumors and malignant transformation is uncommon, occurring in less than 1% of Warthin tumors.

The recommended treatment is superficial parotidectomy, sparing the intraparotid facial nerve. Considering the slow-growing nature of this tumor and its very low risk of degeneration, a clinical and radiological follow-up can be proposed especially in elderly people in whom the diagnosis of Warthin tumor is suspected on imaging.

4.2.2 Histological Findings

The papillary cystadenoma lymphomatosum is encapsulated. It arises within the lymphoid tissue of the parotid gland and is composed of lymphoid stroma and epithelium. The epithelial component is characterized by cystic spaces; it can show hemorrhagic areas. For these reasons, Warthin tumors tend to be nonhomogeneous on imaging.

4.2.3 Imaging Findings

Warthin tumor has typically a heterogeneous appearance on imaging, due to cystic and hemorrhagic changes, with overall benign characteristics: a well-circumscribed lesion measuring 2–4 cm in diameter.

The tumor presents low T1-weighted signal intensity, with small areas of high-signal intensities due to accumulation of proteinous fluid, cholesterol crystals or hemorrhagic changes. Such areas are seen in about 60% of the cases and are typical of the diagnosis of Warthin tumor (Figs. 12, 13; Ikeda et al. 2004).

The tumor has intermediate and high T2-weighted signal intensities. The high-signal intensities areas correspond to cystic foci.

Warthin tumor shows a mild enhancement on post-contrast-enhanced T1-weighted images. Cystic spaces show no enhancement. A typical aspect of the tumor is a ring enhancement (Fig. 12). Fat-suppressed, contrast-enhanced T1-weighted images illustrate better the heterogeneous enhancement of the tumor. DCE-MRI shows typical cases a curve with early enhancement ($T_{peak} < 120$ s) and high washout pattern (WR > 30% at 5 min), corresponding to a B curve on TICs patterns (Yabuuchi et al. 2003; Hisatomi et al. 2007) (Fig. 13). This high washout, as well as the presence of cystic portions explain that these tumors show mild enhancement on post-contrast T1-weighted sequences.

Multiple lesions in one parotid gland or bilaterally have to be looked for. Bilateral lesions in the lower parts of the parotid glands are virtually pathognomonic (Fig. 14).

Warthin tumor may extend to the deep lobe of the parotid gland. On the other hand, a primary location in the deep lobe is very rare.

On diffusion-weighted images, the tissular compartment of Warthin tumors typically presents a very low ADC value (Ikeda et al. 2004; Yerli et al. 2007).

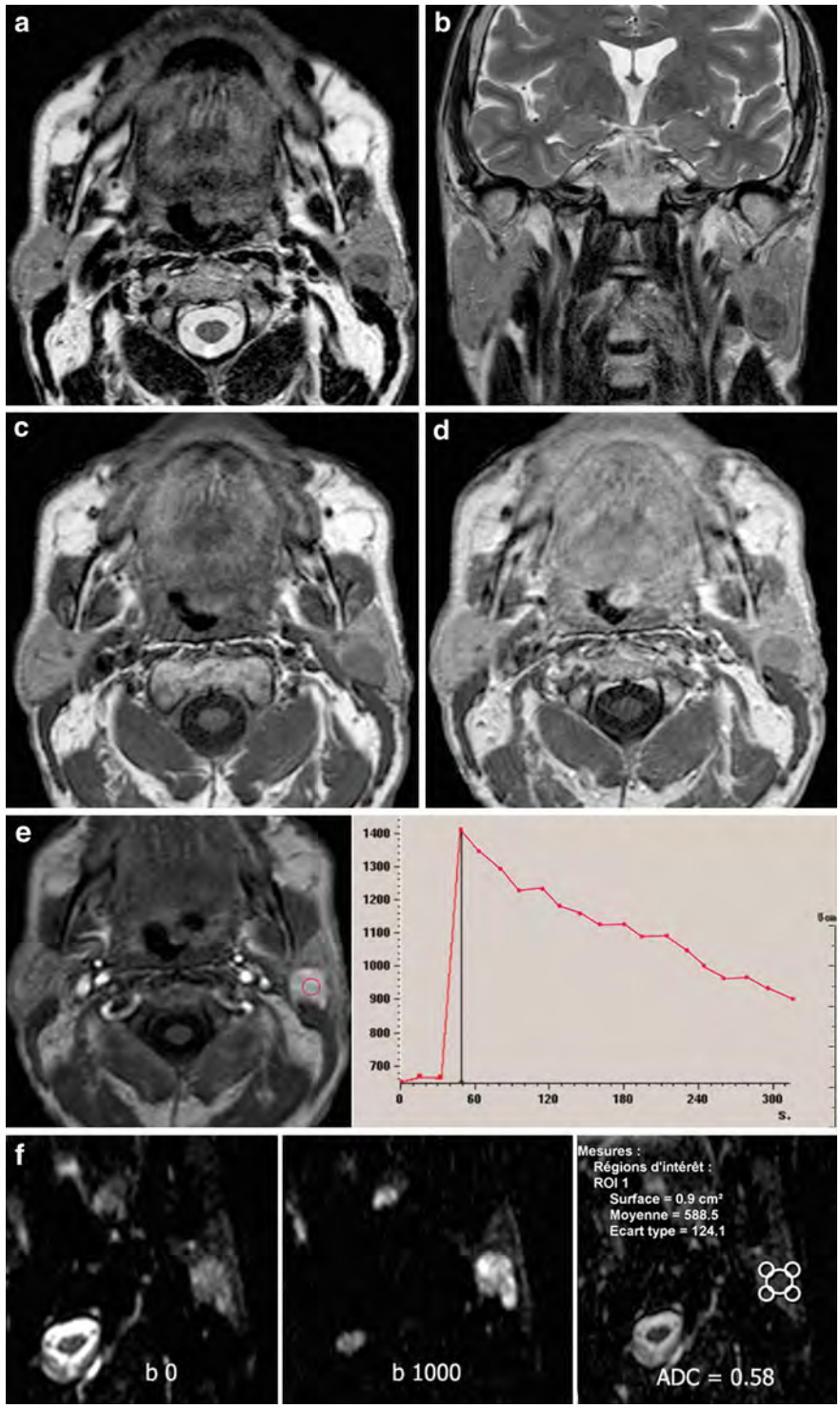

Fig. 13 Well-defined tumor of the left inferior parotid gland with low-signal intensity on both T2-weighted images (**a**, **b**) and T1-weighted images (**c**). Post-contrast T1-weighted images demonstrate mild contrast enhancement (**d**). DCE-MRI shows a typical B curve with an early enhancement ($T_{peak} < 120$ s) and a high washout pattern (**e**); diffusion-weighted sequence confirms an important diffusion restriction, with a high-signal intensity at b factor of 1,000 s/mm^2 and a very low ADC value of 0.58 (**f**). These features are typical of a Warthin Tumor

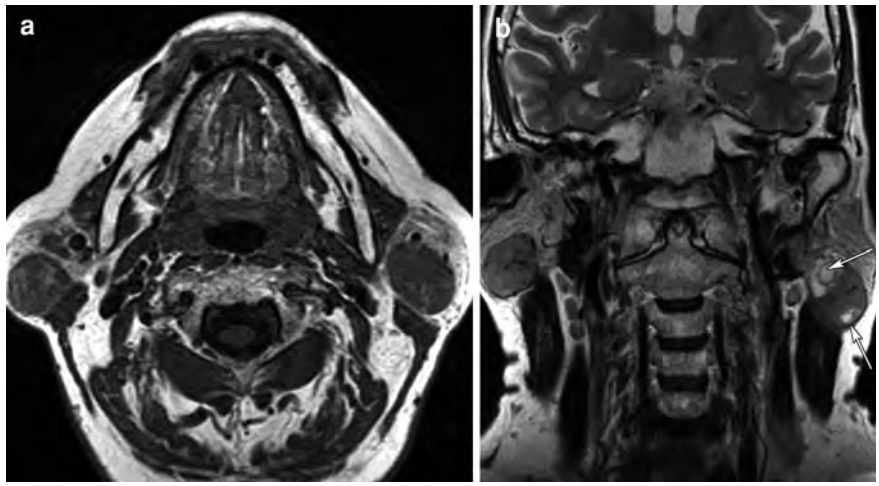

Fig. 14 Typical bilateral Warthin Tumor with low T1-weighted (**a**) and T2-weighted (**b**) signal intensity. Note the small spontaneous hyperintense areas (due to hemorrhagic changes and cholesterol crystals) on the T1-weighted sequence (**a**). Cystic areas show high T2-weighted signal intensity within the left lesion (**b**)

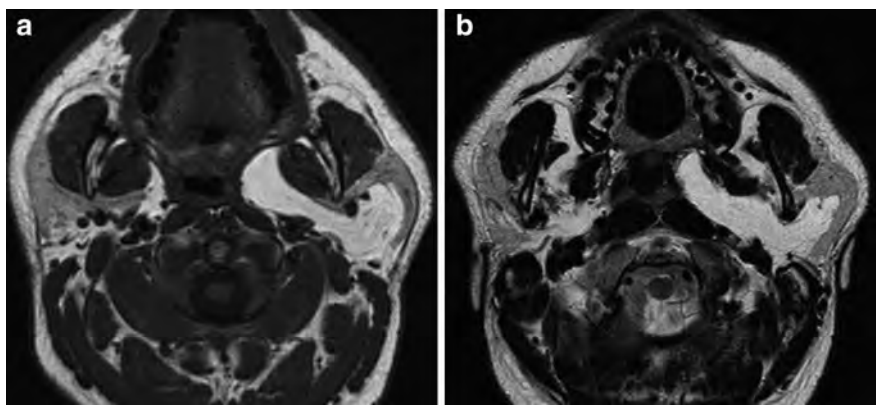

Fig. 15 Lipoma of the left parotid gland extending to the deep lobe and the anterior parapharyngeal space, showing a spontaneous high T1-weighted (**a**) and a high T2-weighted signal intensity (**b**)

4.2.4 Differential Diagnosis

- Atypical pleomorphic adenoma.
- Benign lymphoepithelial lesions in HIV-positive patients.
- Malignant tumor with few malignant characteristics on imaging.

4.3 Other Benign Tumors

4.3.1 Lipoma

It represents 1% of all parotid gland tumors. CT and MR findings are characteristic: well-circumscribed lesion with negative H.U.-values on CT, showing high T1-weighted and high T2-weighted signal intensities, without enhancement on contrast-enhanced T1-weighted images. The high T1-weighted signal intensity disappears on fat-suppressed sequences (Fig. 15).

4.3.2 Neurogenic Tumor

A schwannoma of the intraparotid portion of the facial nerve may occur but remains rare in this extratemporal localization. Facial nerve palsy is exceptional.

Imaging findings are nonspecific but show characteristics of a benign tumor, centered on the facial nerve plane, with low T1-weighted, high T2-weighted signal intensities and homogeneous strong enhancement. Some authors describe a higher signal intensity surrounding the periphery of the tumor on T2-weighted images as a suggestive sign for schwannoma

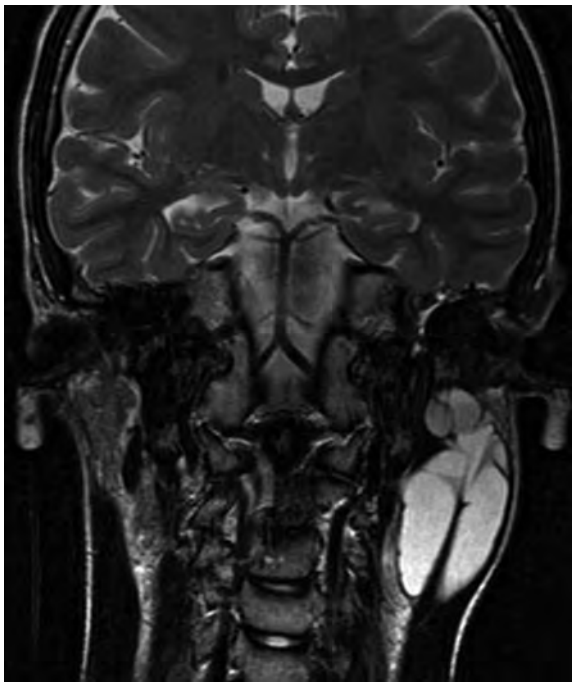

Fig. 16 Cystic lymphangioma of the inferior pole of the left parotid gland. Typical aspect of a lobulated, septated, cystic mass showing a high T2-weigthed signal intensity

(Shimizu et al. 2005). When large in size, cystic changes may occur, making the diagnosis on imaging more difficult. Extension through the stylomastoid foramen and along the third portion of the facial nerve has to be looked for very carefully, this aspect being very suggestive for the diagnosis of schwannoma (Shimizu et al. 2005). The differential diagnosis is perineural extension of a malignant tumor (in particular in adenoid cystic carcinoma), but in such a case the tumor is ill-defined, with low-signal intensity on T2-weighted sequence (Tassart et al. 2010).

4.4 Congenital Tumors

4.4.1 Lymphangioma

Lymphangioma is rare in adults, more common in children. It presents as lobulated, multiloculated, cystic mass with septations. Some of the cystic areas can show spontaneous high-signal intensity due to hemorrhagic changes. Sometimes fluid–fluid levels are seen. Cystic foci do not enhance. Cystic lymphangioma often occurs in the lower portion of the parotid gland (Fig. 16).

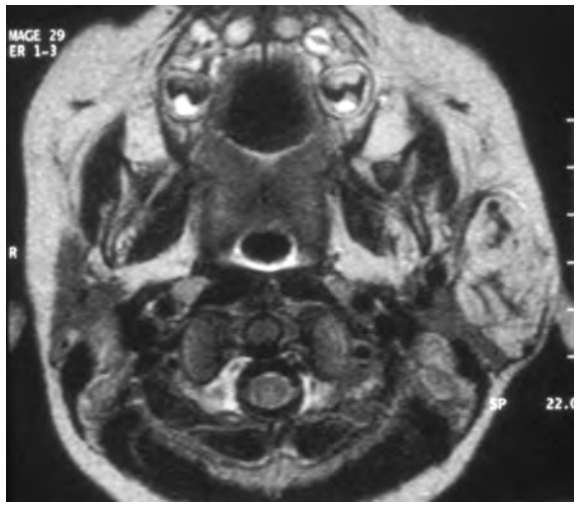

Fig. 17 Infantile capillary hemangioma: a large solid mass of the left parotid space showing intense enhancement and containing multiple enlarged vascular signal voids (*arrow*)

Mixed vascular malformations exist, such as the cavernous lymphangioma, composed of (enhancing) solid areas and dilated lymphatic spaces.

4.4.2 Infantile Hemangioma

This is the most frequent tumor of the parotid space in infants and young children. This tumor shows a 3-phase evolution: rapid growth until the age of about 10 months, then stabilization and finally regression with sometimes an incomplete involution with residual calcifications.

Imaging findings are a large solid mass which shows intermediate T1-weighted, high T2-weighted signal intensities, and intense and fast enhancement with multiple enlarged vascular signal voids (Fig. 17).

4.5 Cystic Tumors

4.5.1 Solitary Cystic Lesion

A solitary cystic lesion of the parotid gland is rare (Som et al. 1995). The cystic nature of the lesion has to be confirmed on imaging using specific sequences (in particular diffusion-weighted sequence). Actually, most of parotid gland tumors show high T2-weighted signal intensity, so this finding does not systematically correspond to a cystic lesion. A cystic formation shows low T1-weighted signal intensity without any enhancement

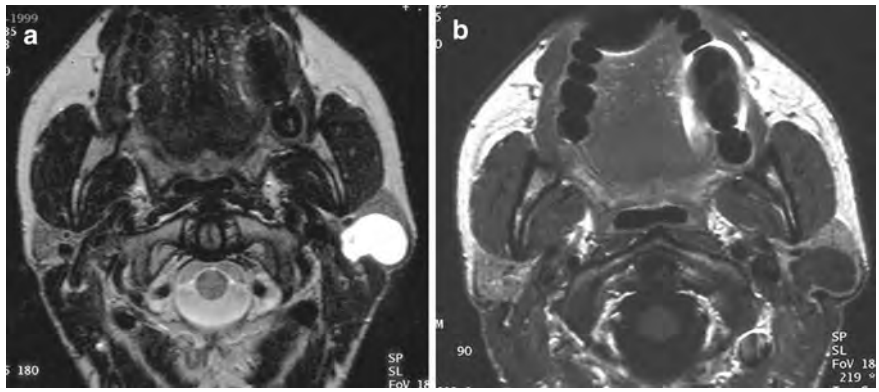

Fig. 18 Solitary simple cystic lesion of the left parotid gland with a high T2-weighted (**a**) and a low T1-weighted signal intensity without any contrast enhancement (**b**)

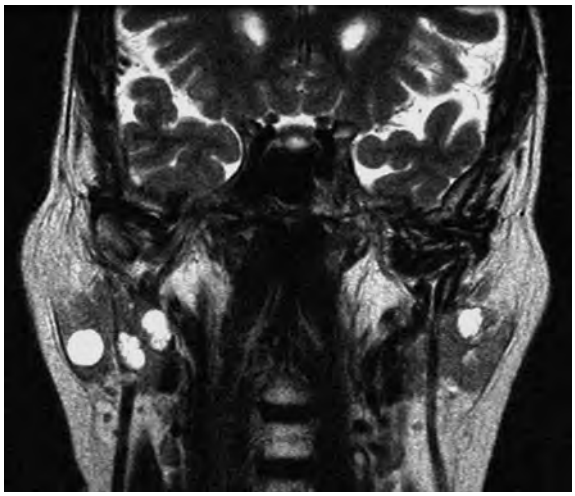

Fig. 19 Multpile bilateral cystic lesions in a HIV-positive patient, corresponding to benign lymphoepithelial lesions

on contrast-enhanced T1-weighted sequence. It has a high T2-weighted signal intensity including T2-weighted sequence with long echo time (Fig. 18). Cystic lesion appears hypointense on diffusion-weighted sequence at b factor of 800 or 1,000 s/mm^2.

A cystic lesion of the parotid gland is suggestive of first branchial cleft abnormality and a fistulous connection in or around the external auditory canal must be looked for (Van der Goten et al. 1997). If the cyst appears to be unilocular and non-communicating, the differential diagnosis is between a non-communicating branchial cleft cyst and a simple cyst of the parotid gland.

4.5.2 Dermoid Cysts

Dermoid cysts may occur in the parotid space. Their heterogeneous structure (fat, bone, skin adnexa) is highly suggestive of this diagnosis.

4.5.3 Epidermoid Cysts

Rarely epidermoid cysts occur in the parotid gland. Signal intensity is typical on MRI: low T1-weighted signal intensity, high T2-weighted signal intensity and no enhancement on contrast-enhanced T1-weighted images. Diffusion-weighted sequence is very helpful because epidermoid cysts show high-signal intensity at b factor of 800 or 1,000 s/mm^2, with a very low ADC value (around 0.5 $\times$ 10^{-3} mm^2/s).

These are slow-growing tumors and a simple follow-up imaging study can be proposed.

4.5.4 Multiple Intraparotid Cystic Lesions

Multiple intraparotid cystic lesions must evoke the possibility of benign lymphoepithelial lesions, as may be seen in HIV-positive patients (Holliday et al. 1998).

The etiology remains unknown, probably from inflammatory origin.

Imaging findings are multiple, bilateral cystic and solid masses, enlarging both parotid glands, associated with tonsillar hyperplasia and bilateral cervical adenopathy.

These lesions are well-circumscribed, sometimes heterogeneous, with low T1-weighted and high T2-weighted signal intensities (Fig. 19).

The clinical profile should help in the diagnosis.

5 Malignant Parotid Tumors

Malignant tumors represent 15% of all parotid tumors. Clinical symptoms suggestive for malignancy are: facial nerve paralysis, pain, skin infiltration, a rapidly enlarging lesion and cervical adenopathy. Prognosis depends on histologic grade.

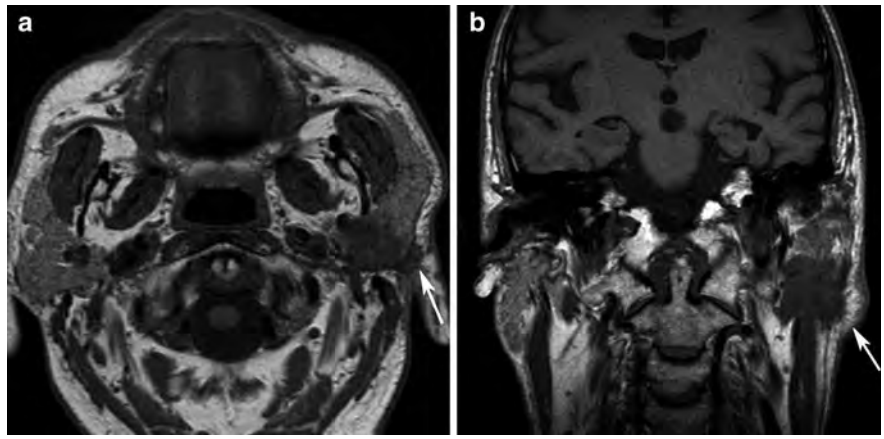

Fig. 20 Malignant tumor of the left parotid gland, with ill-defined margins, infiltrating the adjacent subcutaneous fat tissue (*arrow*), well appreciated on pre-contrast T1-weighted images (**a**, **b**)—Adenocarcinoma

5.1 Histologic Classification

- *Adenocarcinoma, squamous cell carcinoma and undifferentiated carcinoma*
  These malignant tumors have a predilection for men and most cases occur over the age of 60 years. They are most frequently rapidly growing tumors, presenting with facial nerve paralysis and early infiltration of the infratemporal fossa. The prognosis of these cancers is very bad.
- *Adenoid cystic carcinoma*
  This malignant tumor occurs more commonly in the submandibular gland and the minor salivary glands. Adenoid cystic carcinoma is a slow-growing, widely infiltrative tumor with a tendency for perineural spread along the facial nerve and trigeminal nerve (auriculotemporal nerve and mandibular nerve). A significant number of patients develop late intracranial recurrence due to perineural infiltration. Distant metastases develop in 40–50%.
- *Mucoepidermoid carcinoma*
  It has a female predominance and is most frequently seen in the 40- to 60-year age group. Prognosis depends on the histologic grade. Low-grade mucoepidermoid carcinoma may have a clinical and radiological presentation of a benign tumor. High-grade tumors have a high risk of local recurrence and distant metastases.
- *Non-Hodgkin lymphoma*
  It develops from intraparotid lymph nodes and is frequently associated to a systemic lymphoma with cervical lymphadenopathy and other lymphoma localizations. Patients suffering Sjögren syndrome have an increased risk of developing parotid lymphoma.
- *Intraparotid metastases*
  The vast majority of parotid metastases of known primary tumors originate from the skin in the head and neck region.
- *Liposarcoma and rhabdomyosarcoma*
  These are rare parotid neoplasms.

5.2 Imaging Findings

5.2.1 Parotid Cancer

The aim of imaging is to identify the malignant features of a tumor in order to initiate the best therapy as soon as possible. Subtle signs of malignancy (Figs. 20, 21, 22, 23; Freling et al. 1992) that have to be scrutinized include the following:

- Ill-defined margins, indicating an invasive mass, including infiltration of the adjacent fat tissue, which can be an early and only sign suggesting malignancy, best depicted on precontrast T1-weighted images;
- cervical lymphadenopathy;
- extension to the adjacent deep facial spaces (Fig. 24) such as the masticator and parapharyngeal space;
- perineural spread along the facial nerve or trigeminal nerve, better depicted on contrast-enhanced images with fat saturation, is typically seen in adenoid cystic carcinoma (Fig. 25; Harnsberger 2004; Som and Curtin 1996);
- low T2-weighted signal intensity may indicate malignancy (Som and Biller 1989), but may also be seen in some benign tumors;

Fig. 21 Malignant tumor of the right parotid gland, with poorly defined margins and infiltrating the subcutaneous adjacent fat tissue (*arrow*) showing a low T1-weighted (**a**), a low T2-weighted signal intensity (*arrow*, **b**) and mild enhancement on the contrast-enhanced T1-weighted image (*arrow*, **c**)—Mucoepidermoid carcinoma

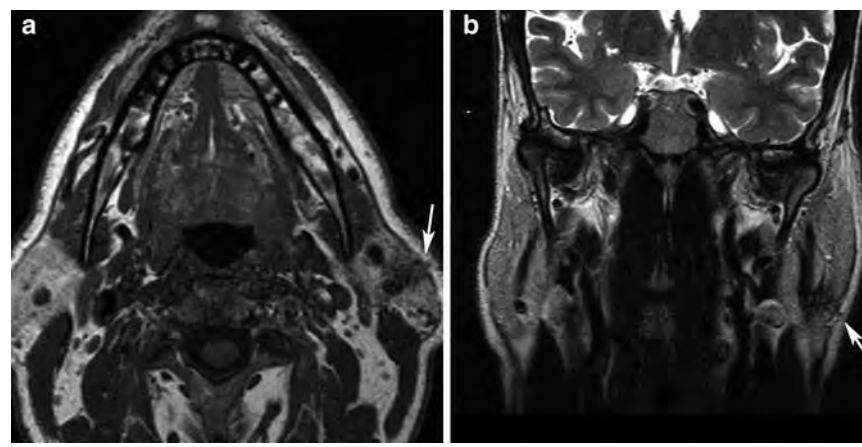

Fig. 22 Small malignant tumor of the inferior pole of the left parotid gland (**a**). The ill-defined margins, low T2-weighted signal intensity (**b**) and infiltration of the adjacent fat tissue suggestive of malignancy (*arrow*)—Mucoepidermoid carcinoma

- the hypercellularity of malignant tumors results in low ADC values (Kato et al. 2008) with an ADC tumor/ADC normal parotid gland ratio lower than 1; in such a case, the only differential diagnosis is a Warthin tumor;
- DCE-MRI depicts an early peak of enhancement (but slower than in a Warthin tumor) and a low washout pattern, inferior to 30% at 5 min (curve type C).

Therefore, combination of diffusion-weighted imaging and DCE-MRI is useful to differentiate a malignant tumor from a Warthin tumor (Yabuuchi et al. 2003; Hisatomi et al. 2007).

If a malignant tumor is suspected on imaging, a fine needle aspiration may be performed. This allows differential diagnosis with a benign tumor in 85–90% of the cases (Zbaren et al. 2001).

The typical treatment of these malignant tumors is wide surgical resection, lymph node dissection and radiation therapy.

5.2.2 Non-Hodgkin Lymphoma

Non-Hodgkin lymphoma often has more specific imaging features: multiple homogeneous nodal lesions with intermediate T1-weighted and T2-weighted signal intensities and moderate enhancement, rarely necrotic. Usually, there is also cervical lymphadenopathy showing the same signal intensity on all MR sequences (Fig. 26). The submandibular gland as well as the lacrimal glands may also be involved. In lymphoma, the ADC value is particularly low with a ratio often inferior to 0.5 (Tassart et al. 2010).

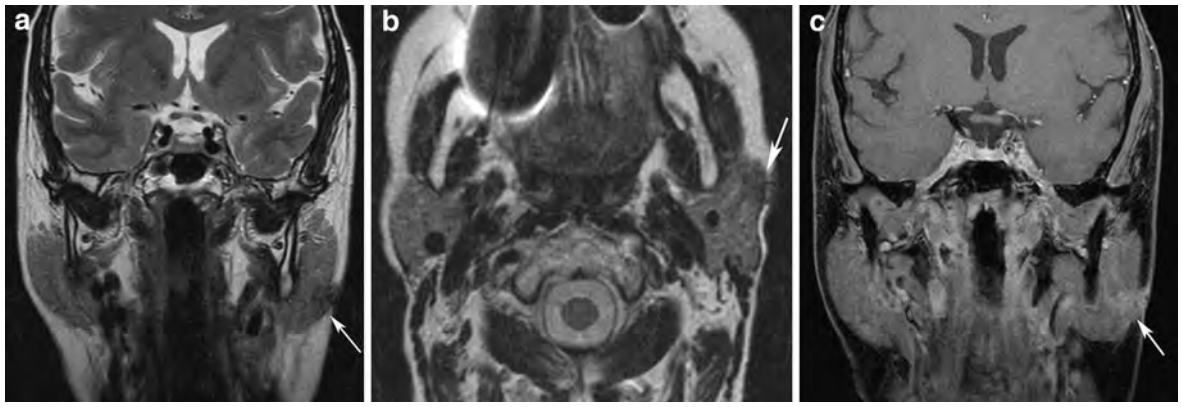

Fig. 23 Malignant tumor in the superficial lobe of the left parotid gland, with low T2-weigthed signal intensity (*arrow*, **a**). The infiltration of the adjacent fat tissue is well identified on pre-contrast T1-weighted image (*arrow*, **b**), as well as on the contrast-enhanced T1-weighted images with fat saturation (*arrow*, **c**)—Adenocarcinoma

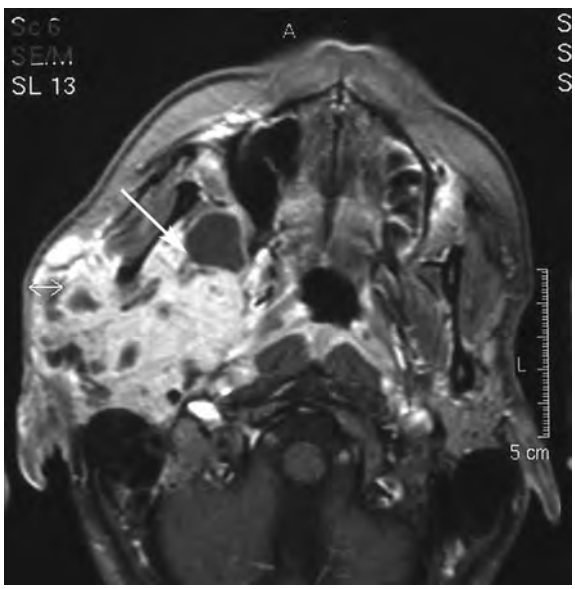

Fig. 24 Adenoid cystic carcinoma of the right parotid gland extending to the parapharyngeal space and the infratemporal fossa (*arrow*)

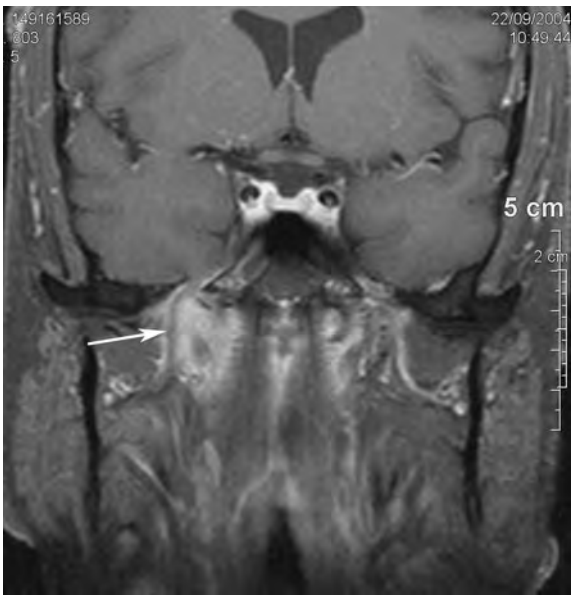

Fig. 25 Adenoid cystic carcinoma of the deep lobe of the right parotid gland, showing perineural spread along the mandibular branch of the trigeminal nerve (*arrow*) toward the foramen ovale

Parotid lymphomas are uncommon but a history of autoimmune disease, especially Sjögren syndrome, previous lymphoma, HIV with a painful, rapidly enlarging parotid gland, is suggestive of this diagnosis (Loggins and Urquhart 2004).

Fine needle aspiration may confirm the diagnosis. However, the histologic diagnosis has to be confirmed by a larger tissue sample. The treatment consists of chemotherapy, possibly associated with radiotherapy.

6 Difficult Cases

- Real difficult cases in imaging parotid gland tumors are rare and represent less than 10% of the cases. However, it can be impossible to differentiate an atypical parotid benign tumor, such as atypical pleomorphic adenoma, from a malignant tumor showing few typical malignant characteristics.

Fig. 26 Multiple homogeneous nodular lesions of the left parotid gland (**a**, **b**, *arrow*), associated with bilateral lymphadenopathy (**c**, *arrows*) showing the same intermediate signal as the parotid lesions on all sequences, corresponding to lymphoma

Table 2 ADC values in parotid gland tumor

ADC Value in parotid gland tumor		
Very low < 0.8 x 10-3 mm2/sec	**Low < 1.2** x 10-3 mm2/sec	**High > 1.2** x 10-3 mm2/sec
Lymphoma	Malignant tumor	Pleomorphic adenoma
Epidermoid cyst	Warthin tumor	Other adenoma tumor
	Lipoma	Cystic tumor

Benign tumors show in majority a high ADC value except Warthin tumor, lipoma and epidermoid cyst. All malignant tumors present a low ADC value

Diffusion-weighted sequences are helpful in such situations (Table 2). The lesion's signal intensity at b factor of 1,000 s/mm^2 and the ADC value have to be evaluated. Pleomorphic adenoma appears hypointense on diffusion-weighted sequence at b factor of 1,000 s/mm^2, with an ADC value >1.2 (Fig. 27). On the other hand, malignant tumors, including lymphoma, show a much lower ADC value <1.2. If the ADC value is >1.2, suggestive of a pleomorphic adenoma, surgery of the lesion can be proposed. If the ADC value is <1.2, fine needle aspiration can be done in order to first exclude malignancy. However, there is no consensus whether to perform fine needle aspiration or not. As said, this procedure allows differentiation of benign tumors from malignant tumors in 85–90% of all cases (Zbaren et al. 2001; Lim et al. 2003). On the contrary, a specific histologic diagnosis for benign tumors is possible only in 40% of cases (Hamilton et al. 2003), except for cystadenolymphoma for which a diagnosis is possible in 74% of cases (Parwani and Ali 2003).

- It can also be very hard to differentiate an atypical pleomorphic adenoma showing low T2-weighted signal intensity from a Warthin tumor. In such situation, MR diffusion-weighted imaging is very helpful: a pleomorphic adenoma appears hypointense on diffusion-weighted sequence at b factor of 1,000 s/mm^2, with ADC value >1.2, whereas a Warthin tumor presents a high-signal intensity at b factor of 1,000 s/mm^2 with a low ADC value, lower than the one observed in case of malignant tumor (Ikeda et al. 2004; Habermann et al. 2009).
- Diffusion-weighted imaging also allows making the difference between a simple intraparotid cyst and an epidermoid cyst. An epidermoid cyst shows a high signal on diffusion-weighted images at b factor of 1,000 s/mm^2 with a very low ADC value (around 0.5), in favor of this diagnosis.
- Combination of diffusion-weighted sequence and dynamic contrast-enhanced MRI is very helpful in these difficult cases.

7 Pseudo-Tumors of the Parotid Gland

7.1 Sjögren Syndrome

This is a chronic systemic auto-immune disease that affects salivary and lacrimal glands.

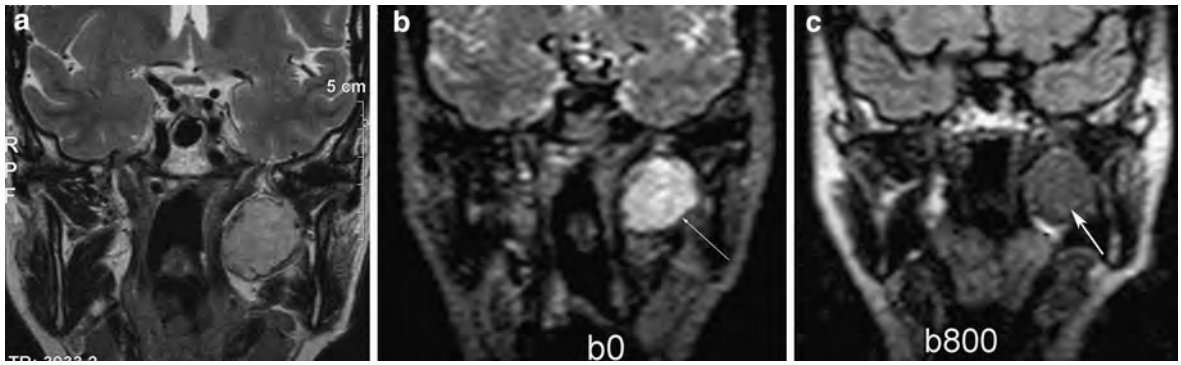

Fig. 27 Pleomorphic adenoma of the deep lobe of the right parotid gland, appearing hyperintense on T2-weighted images (**a**), hyperintense on a diffusion-weighted image with b factor of 0 s/mm^2 (arrow, **b**) and hypointense with b factor of 800 s/mm^2 (*arrow*, **c**); the ADC value is >1.2

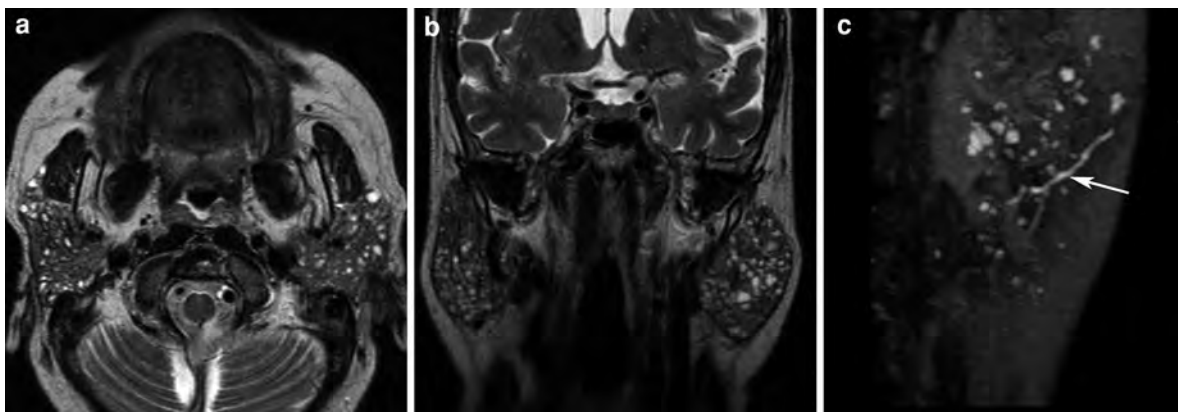

Fig. 28 Miliary pattern appearance of multiple cystic lesions throughout both enlarged parotid glands, showing high T2-weighted signal intensity, in a patient affected by Sjögren syndrome (**a**, **b**). These cystic lesions and the normal salivary ducts (*arrow*) are well seen on MR sialography (**c**)

The best diagnostic clue on imaging is bilateral enlargement of both parotid glands, usually asymmetric, with multiple small cystic and solid lesions; sometimes calcifications are present.

On MR imaging, a miliary pattern of small cysts throughout both parotids is diagnostic of Sjögren's syndrome. The small collections show low T1-weighted, high T2-weighted signal intensities; the small cysts do not enhance, while the surrounding parenchyma shows mild enhancement. MR sialography suggests the diagnosis of Sjögren syndrome by showing multiple cystic lesions while the salivary ducts appear normal (Fig. 28; Ohbayashi et al. 1998; Izumi et al. 1996).

The differential diagnosis includes benign lymphoepithelial cystic lesions in HIV-positive patients; cystic areas are usually larger in this pathology.

A solid tumoral mass, developing in the parotid gland in a patient with Sjögren syndrome, is suspect for lymphoma.

7.2 Sarcoidosis

Sarcoidosis is a systemic disease. The parotid glands are affected in 10–30% of patients. It can present with solid and cystic lesions involving both parotid glands, often associated with cervical adenopathy.

Differential diagnosis must be made with non-Hodgkin lymphoma, in which the imaging pattern commonly consists of bilateral, solid, nodal-appearing intraparotid masses. The clinical presentation is usually suggestive of the diagnosis.

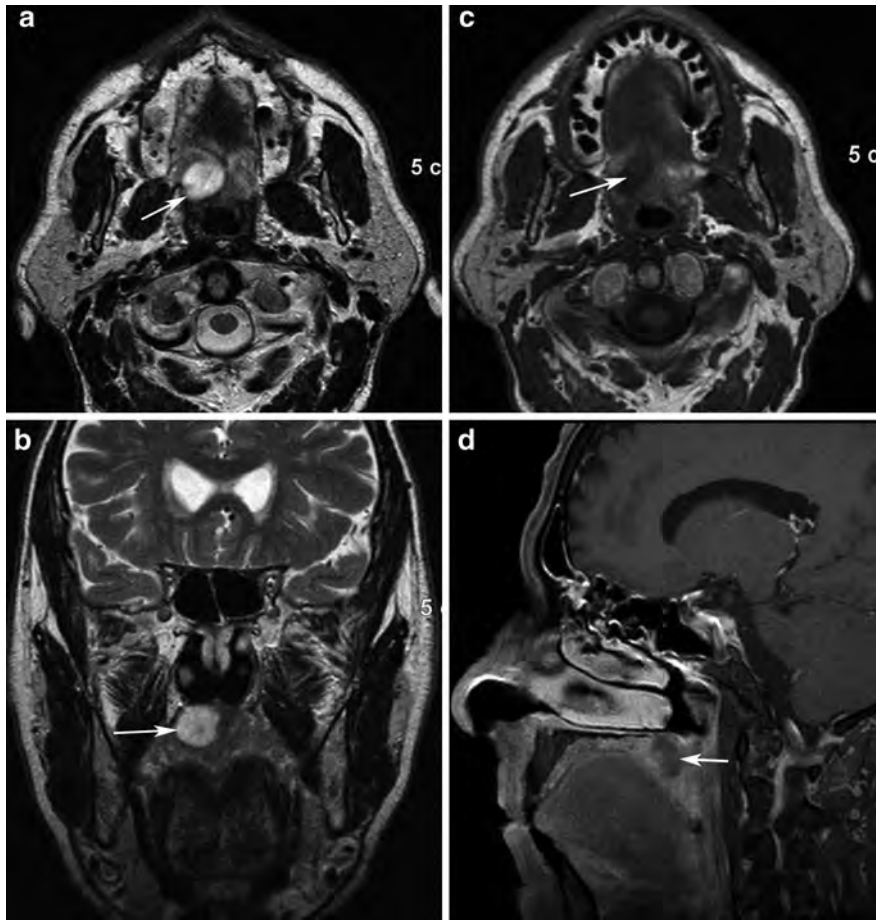

Fig. 29 Mucoepidermoid tumor of a minor salivary gland at the junction of hard palate and soft palate: an ovoid, well-demarcated lesion showing high, heterogeneous T2-weighted (**a**, **b**), and low T1-weighted signal intensity (**c**), with mild contrast enhancement (**d**)

7.3 Intraparotid Lymph Nodes

Presence of multiple intraparotid lymph nodes can be caused by lymphoid hyperplasia, lymphoma, sarcoidosis or metastasis from a cervicofacial tumor, in particular from a skin cancer in 60% (especially melanoma—Tassart et al. 2010). Intraparotid metastasis from extrafacial tumors are rare.

8 Tumors of the Other Salivary Glands

The paired submandibular and sublingual glands are referred to as major salivary glands, such as the parotid glands. The minor salivary glands are submucosal clusters of salivary tissue present in the oral cavity, particularly at the junction of hard palate and soft palate, pharynx, upper respiratory tract, as well as in the anterior parapharyngeal space. While parotid tumors are frequently benign, other salivary glands tumors are often malignant.

Fig. 30 Chronic sialadenitis: multiple calcified lithiasis (*arrows*) within the left submandibular gland and Wharton's duct

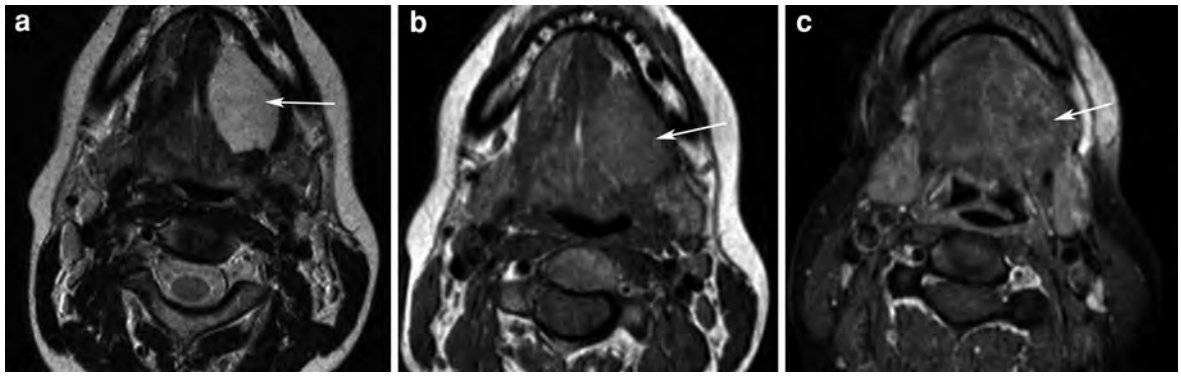

Fig. 31 Adenoid cystic carcinoma of the left sublingual gland: huge mass appearing hyperintense on T2-weighted image (*arrow*, **a**), hypointense on T1-weighted image (*arrow*, **b**), showing a moderate and heterogeneous enhancement on contrast-enhanced T1-weighted image (*arrow*, **c**)

8.1 Minor Salivary Glands Tumors

- Adenoid cystic carcinoma and mucoepidermoid carcinoma are the most frequent malignancies. A tumor of the palate is suspicious of a minor salivary gland tumor. Perineural spread toward the maxillar branch of the trigeminal nerve (V2) is suggestive of adenoid cystic carcinoma. Cervical lymphadenopathy may be present. Treatment consists of wide surgical resection, often associated with radiotherapy. Mucoepidermoid carcinoma often mimics a benign tumor (a well-defined, non-infiltrative tumor) and has a better prognosis than adenoid cystic carcinoma (Fig. 29).
- Pleomorphic adenoma of minor salivary gland origin in the anterior parapharyngeal space is rare (see "Parapharyngeal Space Neoplasms"). These are usually slow-growing, large tumors without much clinical symptoms, presenting with the MR characteristics of a pleomorphic adenoma: a well-defined, lobulated mass with low T1-weighted, high T2-weighted signal intensities and important enhancement. These lesions often appear heterogeneous (Fig. 8). The differential diagnosis is a pleomorphic adenoma arising in the deep lobe of the parotid gland (Fig. 9).

8.2 Submandibular Gland Tumors

- The role of imaging is to determine whether a submandibular lesion is either a salivary gland tumor or an adenopathy. In case of a salivary localization, the lesion appears to be malignant in 55% of patients (Kaneda et al. 1996).
- Adenoid cystic carcinoma and mucoepidermoid carcinoma are the most frequent submandibular gland tumors. On MR imaging, these tumors are usually poorly defined, with low T1-weighted, intermediate T2-weighted signal intensities and heterogeneous enhancement. The surrounding structures, such as the adjacent cervical deep spaces, muscles, mandible and cervical lymph nodes, have to be analyzed in order to rule out tumoral involvement. Treatment consists of a wide resection with neck dissection, and frequently adjuvant radiotherapy. Imaging follow-up must last a very long time because of the possibility of late recurrence.
- Benign mixed tumor is the most frequent benign tumor arising in the submandibular gland. MR imaging characteristics are similar to those of intraparotid pleomorphic adenoma. Typical appearance on CT is a hypodense, lobulated mass with heterogeneous enhancement related to cystic and hemorrhagic changes.

  Fine needle aspiration of submandibular gland tumors has poor sensitivity and specificity. Surgical resection of the submandibular gland may be proposed if the lesion is small, homogeneous, well-defined, showing MR characteristics of a benign mixed tumor. Wide surgical resection associated with neck dissection has to be performed if the lesion is larger, heterogeneous, ill-defined and suggestive of a malignant tumor.
- Chronic sialadenitis due to obstruction of the ductal system can clinically simulate a tumoral lesion of the submandibular space. Imaging is very useful to look for the obstructive calculus in Wharton's duct

Fig. 32 Small mucoepidermoid tumor of the left sublingual gland showing a high T2-weighted signal intensiy (*arrow*, **a**) and an important enhancement on contrast-enhanced T1-weighted images (*arrow*, **b**), associated with two small adjacent submandibular adenopathies (*arrow*, **c**)

Fig. 33 Cystic formation in the anterior part of the right sublingual space, compressing the genioglossal muscles and extending over the midline. Confirmed simple ranula (Courtesy Robert Hermans, MD, PhD, Leuven, Belgium)

and the inflammatory modifications of the submandibular gland. On imaging, the involved gland is usually enlarged, diffusely densely enhancing, associated with dilatation of the main salivary duct, often containing a calculus at its distal part. Lithiasis is well depicted on CT (Fig. 30).

8.3 Sublingual Gland Tumors

- About 80% of the sublingual gland tumors are malignant. Again, the two main etiologies are adenoid cystic carcinoma and mucoepidermoid carcinoma (Sumi et al. 1999).
  On MR imaging, these tumors are more or less well-circumscribed and present low T1-weighted signal intensity, intermediate T2-weighted signal intensity and a heterogeneous enhancement (Fig. 31). Extension outside the sublingual space has to be looked for, such as extension to the mandible or to the cervical lymph nodes. These lesions are usually well-circumscribed in case of mucoepidermoid tumor (Fig. 32).
  Treatment consists of a wide resection with neck dissection, most often associated with radiation therapy. Because of the risk of recurrence, a long-term follow-up is recommended.
- A ranula is a mucous retention cyst that originates from the sublingual gland. It most commonly results from trauma or inflammation. A ranula occurs in two forms. The first one, the simple ranula, is a retention cyst that remains located in the sublingual space (Fig. 33). The second type is the plunging ranula, which is a mucocele extending through the mylohyoid muscle, to the submandibular space.
  On MR imaging, the simple ranula is a cystic formation with low T1-weighted, high T2-weighted signal intensity and a thin enhancement ring on

contrast-enhanced images. The plunging ranula appears as a multi-lobulated cystic formation; it sometimes shows spontaneous high T1-weighted signal intensity because of its protein concentration, high T2-weighted signal intensity with much more important enhancement of the cyst wall.

On CT, a ranula has usually a low attenuation because of its high water content; the cyst wall may enhance after contrast administration.

The differential diagnosis includes epidermoid cysts and cystic hygromas of the sublingual space.

9 Conclusion

Most of parotid gland lesions are benign tumors. The best imaging approach to analyze parotid gland tumors is MR imaging. In many cases, the MRI findings are indicative of benign or malignant nature. In case of benign tumors, an etiologic diagnosis can sometimes be suggested on MRI. MR diffusion-weighted and dynamic contrast-enhanced sequences appear to be helpful in improving the diagnostic yield in case of atypical or difficult cases.

References

Alibek S, Zenk J, Bozzato A, Lell M, Grunewald M, Anders K, Rabe C, Iro H, Bautz W, Greess H (2007) The value of dynamic MRI studies in parotid tumors. Acad Radiol 14:701–710

Eida S, Sumi M, Sakihama N, Takahashi H, Nakamura T (2007) Apparent diffusion coefficient mapping of salivary gland tumors: prediction of the benignancy and malignancy. AJNR Am J Neuroradiol 28:116–121

Freling NJM, Molenaar WM, Vermey A, Mooyaart EL, Panders AK, Annyas AA, Thijn CJP (1992) Malignant parotids tumors: clinical use of MR imaging and histologic correlation. Radiology 185:691–696

Habermann CR, Arndt C, Graessner J, Diestel L, Petersen KU, Reitmeier F, Ussmueller JO, Adam G, Jaehne M (2009) Diffusion-weighted echo-planar MR imaging of primary parotid gland tumors: is a prediction of different histologic subtypes possible? AJNR Am J Neuroradiol 30(3):591–596

Hamilton BE, Salzman KL, Wiggins RH, Harnsberger HR (2003) Earring lesions of the parotid tail. AJNR Am J Neuroradiol 24(9):1757–1764

Harnsberger HR (2004) Diagnostic imaging head and neck, 1st edn. Amirsys, Salt Lake City, part III—Sect 7:2–36 and Sect 4:26–48

Hisatomi M, Asaumi J, Yanagi Y, Unetsubo T, Maki Y, Murakami J, Matsuzaki H, Honda Y, Konouchi H (2007) Diagnostic value of dynamic contrast-enhanced MRI in the salivary gland tumors. Oral Oncol 43:940–947

Holliday RA, Cohen WA, Schinella RA, Rothstein SG, Persky MS, Jacobs JM, Som PM (1998) Benign lymphoepithelial parotid cyst and hyperplastic cervical adenopathy in AIDS-risk patients: a new CT appearence. Radiology 168:439–441

Ikeda K, Katoh T, Ha-Kawa SK, Iwai H, Yamashita T, Tanaka Y (1996) The usefulness of MR in establishing the diagnosis of parotid pleiomorphic adenoma. AJNR Am J Neuroradiol 17:55–59

Ikeda M, Motoori K, Hanazawa T, Nagai Y, Yamamoto S, Ueda T, Funatsu H, Ito H (2004) Warthin tumor of the parotid gland: diagnostic value of MR imaging with histopathologic correlation. AJNR Am J Neuroradiol 25(7): 1256–1262

Izumi M, Eguchi K, Ohki M, Uetani M, Hayashi K, Kita M, Nagataki S, Nakamura T (1996) MR imaging of parotid gland in Sjogren's symdrome: a proposal for new criteria. AJR Am J Roentgenol 166:1483–1487

Joe VQ, Westesson PL (1994) Tumors of the parotid gland: MR imaging characteristics of various histologic types. AJR Am J Roentgenol 163:433–438

Kaneda T, Minami M, Ozawa K, Akimoto Y, Kawana T, Okada H, Yamamoto H, Suzuki H, Sasaki Y (1996) MR of submandibular gland: normal and pathologic states. AJNR Am J Neuroradiol 17:1575–1581

Kato H, Kanematsu M, Mizuta K, Ito Y, Hirose Y (2008) Carcinoma ex pleomorphic adenoma of the parotid gland: radiologic–pathologic correlation with MR imaging including diffusion-weighted imaging. AJNR Am J Neuroradiol 29:865–867

Lim LH, Chao SS, Goh CH, Ng CY, Goh YH, Khin LW (2003) Parotid gland surgery: a review of 118 cases in an Asian population. Head Neck 25(7):543–548

Loggins JP, Urquhart A (2004) Preoperative distinction of parotid lymphomas. J Am Coll Surg 199(1):58–61

O'Brien CJ (2003) Current management of benign parotid tumors: the role of limited superficial parotidectomy. Head Neck 25(11):946–952

Ohbayashi N, Yamada I, Yoshino N, Sasaki T (1998) Sjogren syndrome: comparison of assessments with MR sialography and conventional sialography. Radiology 209:683–688

Okahara M, Kiyosue H, Hori Y, Matsumoto A, Mori H, Yokoyama S (2003) Parotid tumors MR imaging with pathological correlation. Eur Radiol 13(Suppl 4):L25–L33

Parwani AV, Ali SZ (2003) Diagnostic accuracy and pitfalls in fine-needle aspiration interpretation of Whartin tumor. Cancer 99(3):166–171

Shah GV (2002) MR imaging of salivary glands. Magn Reson Imaging Clin N Am 10(4):631–662

Shah GV (2004) MR imaging of salivary glands. Neuroimaging Clin N Am 14(4):777–808

Shimizu K, Iwai H, Ikeda K, Sakaida N, Sawada S (2005) Intraparotid facial nerve schwannoma a report of five cases and an analysis of MR imaging results. AJNR Am J Neuroradiol 26(6):1328–1330

Som PM, Biller HF (1989) High-grade malignancies of the parotid glands: identification with MR imaging. Radiology 173:823–826

Som PM, Curtin HD (1996) Salivary glands in head and neck imaging, 3rd edn. Mosby, St. Louis, pp 823–914

Som PM, Brandwein MS, Silvers A (1995) Nodal inclusion cysts of the parotid gland and parapharyngeal space: a discussion of lymphoepithelial, AIDS-related parotid, branchial cyst, cystic Whartin's tumors and cysts in Sjogren's symdrome. Laryngoscope 105(10):1122–1128

Sumi M, Izumi M, Yonetsu K, Nakamura T (1999) Sublingual gland: MR features of normal and diseased states. AJR Am J Roentgenol 172(3):717–722

Tassart M, El Amri A, Bourdet C, Lefevre M, Perie S, Facon D, Marsault C (2010) Salivary gland pathology. In: Dubrulle F, Martin-Duverneuil MoulinG (eds) Imagerie en ORL. Elsevier Masson, Paris

Van der Goten A, Hermans R, Van Hover P, Crevits I, Baert AL (1997) First branchial complex anomalies: report of 3 cases. Eur Radiol 7:102–105

Vogl TJ, Balzer J, Mack M, Steger W (1999) Salivary glands in differential diagnosis in head and neck imaging. Thieme Stuttgart, New York, pp 237–253

Yabuuchi H, Fukuya T, Tajima T, Hachitanda Y, Tomita K, Koga M (2003) Salivary gland tumors: diagnostic value of gadolinium-enhanced dynamic MR imaging with histopathologic correlation. Radiology. 226:345–354

Yerli H, Agildere AM, Aydin E, Geyik E, Haberal N, Kaskati T, Oguz D, Ozluoglu LN (2007) Value of apparent diffusion coefficient calculation in the differential diagnosis of parotid gland tumors. Acta Radiol 48:980–987

Zbaren P, Schar C, Hotz MA, Loosli H (2001) Value of fine needle aspiration cytology of parotid gland masses. Laryngoscope 111:1989–1992

Malignant Lesions of the Central and Posterior Skull Base

Ilona M. Schmalfuss

Contents

Abstract

Imaging interpretation of skull base lesions can be challenging because of their infrequent occurrence, the complex nature of the skull base and the ability of normal anatomical variations to mimic pathology. Since the majority of skull base lesions are accidentally detected and inaccessible for biopsy, the clinicians heavily rely upon the accurate image interpretation by the radiologist. The main goals of the image analysis are to distinguish normal anatomical variations form true pathology, recognize medically treatable conditions and to differentiate benign "do-not-touch" lesions from malignant processes that might require aggressive treatment. The imaging features and preferential location of the different malignant skull base lesions and their benign counterparts will be discussed in this chapter. After the diagnosis of a malignancy is established, the radiologist's main role is the delineation of the extent of the suspected malignant skull base lesion for treatment planning.

1 Introduction

Evaluation of skull base lesions is challenging. On the one hand, the skull base is not directly accessible for clinical evaluation, and an underlying lesion is suspected based on neurological deficits. On the other hand, cross-sectional radiological studies are excellent in demonstrating a skull base lesion and its extent, but their evaluation is intimidating to the majority of radiologists. There are three main reasons for the intimidation of radiologists: The anatomical

I. M. Schmalfuss (✉)
Department of Radiology,
Malcolm Randall VA Medical Center
and University of Florida College of Medicine,
1601 SW Archer Road, Gainesville, FL 32608, USA
e-mail: Ilonaschmalfuss@yahoo.com

R. Hermans (ed.), *Head and Neck Cancer Imaging*, Medical Radiology. Diagnostic Imaging,
DOI: 10.1007/174_2011_386, © Springer-Verlag Berlin Heidelberg 2012

complexity of the skull base, the ability of normal anatomical structures to mimic pathology and the rarity of skull base lesions preventing dedicated training throughout residency and even during fellowship. In addition, inappropriate choice of an imaging study, imaging parameters and/or sequences may amplify the insecurity of the radiologist.

Recognition of anatomical mimics and of medically treatable conditions is essential as the majority of skull base lesions are inaccessible for biopsy. The biopsy route may extend through normal pertinent anatomical structures, such as inner ear in case of a petrous apex lesion, or may need to be performed through the intracranium. Differentiation of malignant from benign lesions is also critical as a different surgical intervention may apply, the lesion might be vascular in nature preventing a biopsy, or occasionally treatment might be conducted without a tissue diagnosis, e.g. radiation therapy in case of paragangliomas. In addition, determination of the exact origin and extent of a lesion is crucial for radiation therapy and even more for surgical planning purposes. All these points will be addressed in this chapter.

2 Anatomy

The anatomy of the skull base is very complex; not only do the bony structures play an important role but also the cranial nerves and vasculature coursing through it. Knowledge of the location of the different neural and vascular foramina and channels, as well as of the different neuronal connections, can therefore explain the wide range of clinical symptoms and facilitate the detection of extracranial tumor spread.

The skull base is formed by the ethmoid, sphenoid, occipital, frontal and temporal bones. It is divided into three regions: anterior, central and posterior skull base. Only the central and the posterior skull base will be discussed in this chapter as the anterior skull base is included in "Neoplasms of the Sinonasal Cavities". The distinction of the central to posterior skull base is ambiguous as the roof of the petrous apex represents part of the central skull base, while the posterior margin borders the posterior skull base. Since the majority of the malignant petrous apex lesions are surgically approached from the posterior fossa, the petrous apex will be included in the posterior skull base in the subsequent discussion.

2.1 Central Skull Base

The sphenoid bone forms the middle portion of the central skull base. It is subdivided into the central sphenoid body housing the sella and the sphenoid sinuses, the greater sphenoid wings forming the boundary to the anterior skull base, the lesser sphenoid wings and the pterygoid processes that are protruding below the skull base and serve as attachments for the medial and lateral pterygoid muscles. Parts of the temporal bones compose the lateral portions of the central skull base and are formed by the mastoid, tympanic, petrous and squamous bones. The greater sphenoid wing is connected via the sphenosquamous suture and the petrosphenoidal fissure with the squamous and petrous portions of the temporal bone, respectively. The anterior portion of the squamous bone creates the lateral border of the central skull base while the petrous bone together with the clivus form the anterior boundary of the posterior skull base. The petrous bone and the clivus are separated by the petro-occipital fissure.

The central skull base represents the floor of the middle cranial fossa which is primarily filled with the temporal lobes laterally and the cavernous sinuses medially. The cavernous sinuses are located between the dura and the periostium of the body of the sphenoid bone and between the superior orbital fissure anteriorly and the petrous apex posteriorly. Each cavernous sinus contains a complex venous plexus surrounding the internal carotid artery and the cranial nerve VI. The cranial nerve VI enters the cavernous sinus through a small bony channel within the medial petrous apex called Dorello's canal. The cranial nerves III–V are actually located within the dural leaflet that form the lateral boundary of the cavernous sinus rather than within the cavernous sinus itself. These cranial nerves and the internal carotid artery exit the intracranium through different foramina located within the central skull base.

The superior orbital fissure and the optic canal are the most anterior openings of the central skull base. The optic nerve, optic nerve sheath and the ophthalmic artery course through the optic canal. The cranial nerves III, IV and VI as well as the lacrimal, frontal and nasociliary branches of the first division of the trigeminal nerve (V1) exit the cavernous sinus into the orbital apex through the superior orbital fissure. The foramen rotundum is located just inferior to the

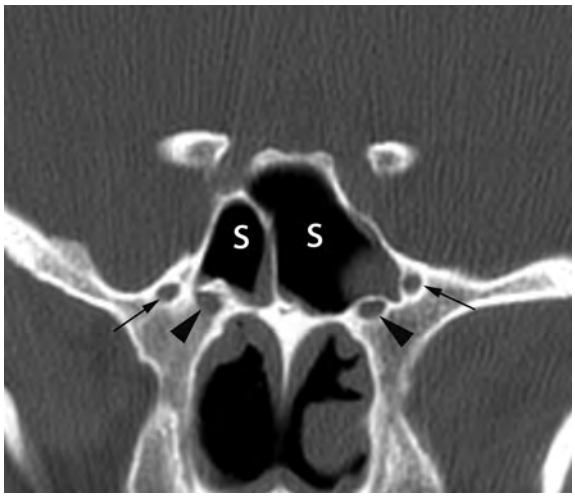

Fig. 1 Coronal CT image displayed in bone window demonstrating the relationship between the foramen rotundum (*arrows*) and vidian canal (*arrowheads*) to each other and the sphenoid sinus (*s*) within the central skull base

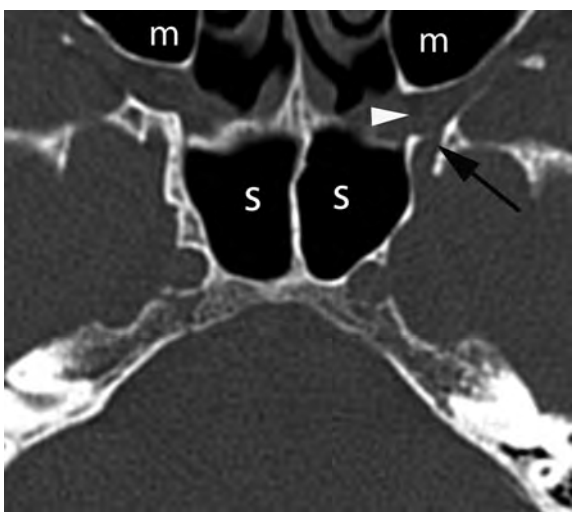

Fig. 2 Axial CT image displayed in bone window illustrates the communication of the foramen rotundum (*arrow*) with the pterygopalatine fossa (*arrowhead*) located immediately posterior to the maxillary sinus (*m*). *s*, Sphenoid sinus

superior orbital fissure and houses the second division of the trigeminal nerve (V2) (Fig. 1). The foramen rotundum communicates anteriorly with the pterygopalatine fossa where a few ganglionic branches leave V2 to travel to the pterygopalatine ganglion (Fig. 2; Moore et al. 1999). V2 gives off the zygomatic and the posterior superior alveolar nerves and then continues anteriorly as the infraorbital nerve within the

Fig. 3 Axial CT image of the central skull base displayed in bone window shows the larger foramen ovale (*black arrows*) on each side and the smaller foramen spinosum (*black arrowheads*) posterior lateral to it. Both assume an oval shape. The *white arrowheads* demarcate the vidian canal that extends from the pterygopalatine fossa (*white arrows*) to the foramen lacerum within the petrous apex (not demonstrated at this level). *s* Sphenoid sinus

infraorbital canal. The third division of the trigeminal nerve (V3) courses through the central skull base within the foramen ovale situated posterior and lateral to the foramen rotundum (Fig. 3). V3 travels inferiorly to enter the masticator space. Just superomedial to the foramen ovale is a groove within the central skull base, located immediately posterior to the cavernous sinus, containing the Meckel's cave. The Meckel's cave houses the trigeminal ganglion anteroinferiorly, where the three divisions of the trigeminal nerve are merging together, and the trigeminal cistern (Kaufman and Bellon 1973; Williams et al. 2003). The trigeminal ganglion gives rise to multiple individual rootlets that course superiorly through the trigeminal cistern. The individual rootlets give the trigeminal cistern a speckled appearance on coronal high resolution images before they merge together to form the main trunk of the trigeminal nerve just posterior to the trigeminal cistern.

The foramen spinosum and the lacerum portion of the carotid canal are the most posterior foramina of the central skull base. The foramen spinosum is located just posterolateral to the foramen ovale and contains the middle meningeal artery, a distal branch of the external carotid artery, and the meningeal branch of the facial nerve (Fig. 3). The middle meningeal artery branches off into multiple small vessels

Fig. 4 Axial CT image displayed in bone window illustrates the close relationship between the clivus (*c*) centrally and the internal carotid artery canal within the petrous apex laterally (*arrows*). The Eustachian tube courses parallel to the internal carotid artery canal through the petrous bone (*black arrowheads*). The *white arrowheads* demarcate the Eustachian tube openings within the middle ear cavities

intracranially that form grooves within the superior surface of the central skull base and along the inner table of the frontal and anterior parietal skull. The lacerum portion of the carotid canal is located more medially within the body of the sphenoid bone, at the junction of the petrous apex and clivus (Tauber et al. 1999). It represents the exit site of the internal carotid artery from the carotid canal within the petrous portion of the temporal bone (Fig. 4). The internal carotid artery continues superiorly as the carotid siphon to lie within a sigmoid-shaped groove along the sphenoid bone within the cavernous sinus. The internal carotid artery exits the cavernous sinus medial to the anterior clinoid process. The vidian canal courses inferior to the carotid siphon within the sphenoid bone forming a direct communication between lacerum portion of the carotid canal and the pterygopalatine fossa (Fig. 3; Chong and Fan 1998). It contains the vidian nerve that is composed of preganglionic parasympathetic fibers of the greater superficial petrosal nerve, the postganglionic sympathetic fibers of the deep petrosal nerve and sensory fibers from the cranial nerve VII.

2.2 Posterior Skull Base

The posterior skull base is shaped like a cup. The clivus and the petrous apex create the anterior boundary while the occipital bone forms the posterior and inferior borders of the posterior skull base. The lateral boundary of the posterior skull base is established by the occipital bone posteriorly and the mastoid and petrous portions of the temporal bone superoanteriorly and inferoanteriorly, respectively. The occipitomastoid suture connects the occipital bone with the mastoid portion of the temporal bone. The different anatomical structures of the posterior fossa create numerous grooves, crests and foramina within the posterior skull base.

The cerebellar hemispheres cause two indentations along the posterior surface of the posterior skull base with a midline internal occipital crest in between. The occipital crest provides the attachment for the falx cerebelli and extends from the foramen magnum to the internal occipital protuberance. One vertical and two horizontal grooves extend superiorly and laterally from the internal occipital protuberance housing the superior sagittal sinus and the transverse sinuses, respectively. The horizontal grooves are extending anteroinferiorly to continue as the sigmoid sulci that contain the sigmoid sinus on each side. The sigmoid sinus subsequently enters the jugular foramen and continues through the skull base into the neck as the internal jugular vein.

The jugular foramen and the foramen magnum are the largest openings of the posterior skull base. The jugular foramen lies at the posterior end of the petrooccipital fissure and is bordered by the petrous bone of the temporal bone anteriorly and the occipital bone posteriorly. It is partially subdivided by the jugular spine into two compartments: the pars venosa and the pars nervosa (Fig. 5; Inserra et al. 2004; Sen et al. 2001). Only occasionally the bony jugular spine continues as a fibrous or osseous septum posteriorly to completely separate these two compartments. The pars venosa lies posterolateral and contains the internal jugular bulb laterally and the cranial nerves X and XI medially (Fig. 5). The pars nervosa is located anteromedially and contains the cranial nerve IX medially and often the inferior petrosal sinus laterally (Fig. 5). The internal carotid artery enters the skull base anterior to the jugular foramen (Fig. 5). Therefore, all three of these cranial nerves lie between the internal jugular vein and the internal carotid artery below the skull base, with the cranial nerve IX being the most anterolateral and the cranial nerve XI the most posteromedial in position.

The cranial nerve XI is very unique as it extends through the posterior skull base twice. Once to exit

Fig. 5 Axial CT image of the right jugular fossa displayed in bone window shows the jugular spine (*arrow*) dividing the jugular foramen into the pars venosa (*pv*) laterally and pars nervosa (*pn*) medially. The internal carotid artery (*c*) lies anterior to the pars venosa (*pv*)

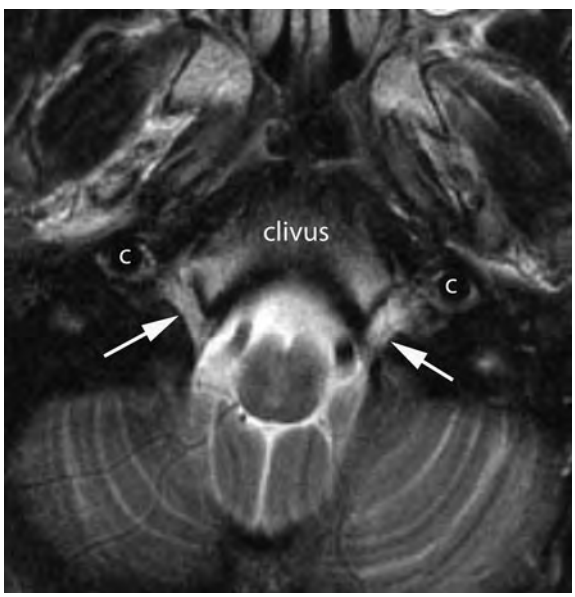

Fig. 6 Axial T2-weighted image through the lower clivus demonstrates the oblique course of the hypoglossal canal (*arrows*) along the lateral edge of the clivus on each side. The exit of the hypoglossal canal (*arrows*) is in close proximity to the internal carotid artery (*c*)

the skull base through the jugular foramen as mentioned above and once to enter the posterior cranial fossa through the foramen magnum as parts of its fibers originate from the cervical spinal cord. The remaining cranial nerve XI fibers originate from the medulla oblongata and merge with the cervical spinal cord fibers at the foramen of magnum. The cranial nerves XI lie posterior to the vertebral arteries that ascend from cervical to intracranial through the foramen mangum. The vertebral arteries give rise to the posterior cerebellar arteries that course posteroinferiorly to supply the inferior cerebellar hemispheres. In turn, the paired posterior spinal arteries arise either from the intracranial portion of the vertebral arteries or occasionally from the posterior cerebellar arteries and continue inferiorly through the foramen magnum to supply the spinal cord.

The posterior skull base has few additional, smaller openings. The porus acusticus is the medial opening of the internal auditory canal along the posterior surface of the petrous bone. It contains the cranial nerves VII and VIII as well as branches of the anterior inferior cerebellar artery that supply the inner ear. Inferior and posterior to it are the openings of the cochlear and vestibular aqueducts, respectively. The vestibular aqueduct courses almost parallel to the posterior margin of the petrous bone between the vestibule and the intracranium and contains the endolymphatic duct. In contrast, the cochlear aqueduct runs almost parallel to the internal auditory canal between the basal turn of the cochlea and the intracranium within the inferior aspect of the petrous bone and transmits the perilymphatic duct (Mukherji et al. 1998). Even more inferiorly within the petrous bone is the hypoglossal foramen located just inferomedial to the jugular foramen (Fig. 6). It contains the cranial nerve XII, the hypoglossal venous plexus and a meningeal branch of the ascending pharyngeal artery. Below the skull base, the cranial nerve XII continues inferiorly between the internal carotid artery and the internal jugular vein.

3 Clinical Presentation

Only few skull base lesions present with specific, disease-related symptoms that significantly help to narrow the differential diagnosis. The Gradenigo's triad represents one of them and is characterized by

Table 1 Clinical symptoms of cranial nerve palsies

Cranial nerve	Symptoms
Cranial nerve III (oculomotor nerve)	Diplopia due to inability to move the ipsilateral eye superiorly, inferiorly and medially Ptosis Fixed and dilated pupil
Cranial nerve IV (trochlear nerve)	Dilopia due to inability to move the ipsilateral eye inferiormedial
Cranial nerve V (trigeminal nerve)	Loss of sensation or dysaesthesia in the ipsilateral face Ipsilateral loss of jaw clenching and side to side movement
Cranial nerve VI (abducens nerve)	Diplopia due to inability to move the ipsilateral eye laterally
Cranial nerve VII (facial nerve)	Loss of taste in the anterior 2/3 of the tongue Ipsilateral facial drop
Cranial nerve VIII (vestibulocochlear nerve)	Ipsilateral sensorineural hearing loss Dizziness
Cranial nerve IX (glossopharyngeal nerve)	Loss of oropharyngeal sensation Loss of taste and sensation to the posterior 1/3 of tongue
Cranial nerve X (vagus nerve)	Nasal speech due to ipsilateral palatal weakness Hoarseness due to ipsilateral vocal cord paralysis
Cranial nerve XI (spinal accessory nerve)	Weakness and wasting of the ipsilateral sternocleidomastoid and trapezius muscles
Cranial nerve XII (hypoglossal nerve)	Wasting and fasciculation of the tongue Tongue tip deviation to paralyzed side on protrusion

ipsilateral cranial nerve VI paralysis, severe facial pain in V1 distribution and inflammatory disease of the middle ear and/or mastoid air cells (Gradenigo 1904). As the triad indicates, this symptom complex has been associated with extensive acute inflammatory disease of the ear. However, less than 50% of the patients present with all three of these symptoms. In particular, cranial nerve VI palsy has been described as the least reliable clinical sign of the triad making distinction to other skull base entities more difficult (Price and Fayad 2002). Hence, the majority of patients with skull base pathology present with non-specific neurological symptoms related to the mass effect caused by the lesion. These symptoms can be related to cranial nerve dysfunction, vascular compromise or direct compression of the brain or orbital structures. The clinical symptoms of cranial nerve palsies are summarized in Table 1.

4 Normal Anatomical Variations

Normal anatomical variations are asymptomatic and typically discovered incidentally in patients that seek medical attention for an unrelated reason (Schmalfuss and Camp 2008). Asymmetric aeration of the petrous apex is the most common entity that is mistaken for a petrous apex mass, in particular on MR imaging (Fig. 7). CT certainly is easier to interpret in this regard, however, close attention to the imaging characteristics can facilitate the correct diagnosis on MR images as well. In particular, lack of mass effect and increased T1 signal intensity of the fatty bone marrow within the unaerated petrous apex is characteristic (Fig. 7a). Asymmetric accumulation of fluid within the petrous apex air cells will show intermediate T1 and high T2 signal intensity and may be mistaken for a chondrosaroma; however, the lack of mass effect and of contrast enhancement as well as often accompanied fluid within the middle ear cavity and/or mastoid air cells should question such a diagnosis (Schmalfuss 2009).

A high riding jugular bulb or a jugular bulb diverticulum might be mistaken for a mass within the jugular foramen. Close evaluation of all images in the different planes and on the various sequences typically reveals inconsistency of the flow pattern, with the classic flow void seen in at least one plane or on one sequence in such cases.

Mottled fatty replacement of the bone marrow may mimic a diffuse infiltrative process of the skull base that might be impossible to distinguish from lymphoma, leukemia, multiple myeloma or diffuse metastatic disease. Correlation to clinical symptoms, age, gender and history of an underlying malignancy

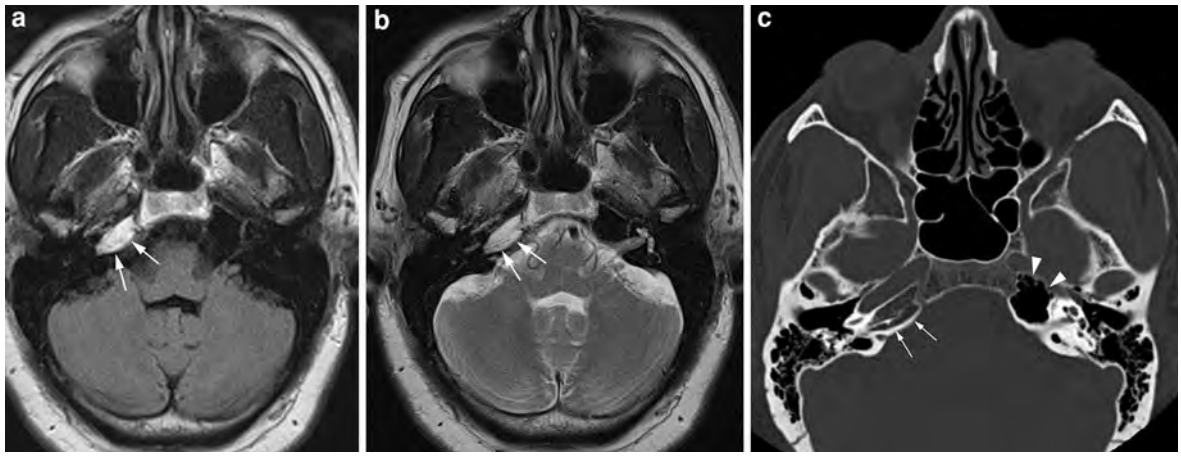

Fig. 7 Axial non-contrast enhanced T1- (**a**) and T2-weighted (**b**) images demonstrate increased signal intensity within the right petrous apex (*arrows* in **a** and **b**) that is often mistaken for a small cholesterol granuloma. The axial CT image displayed in bone window however, reveals the true nature of this "lesion" as it shows preserved diploic trabeculations within the non-aerated petrous apex (*arrows* in **c**) when compared to the aerated petrous apex on the left (*arrowheads* in **c**). The non-aerated petrous apex is increased in T1 signal intensity (*arrows* in **a** and **b**) in this patient due to fatty bone marrow but may also assume lower intensity when red bone marrow is present in this location, e.g. in young patients

might help to develop a risk profile that does or does not warrant further evaluation with bone scan, bone marrow biopsy or cross-sectional follow up.

5 Pathology

The skull base is composed of different tissue components and houses a variety of structures that can serve as the origin of skull base masses. Therefore, the spectrum of possible skull base abnormalities is very broad. Skull base lesions overall are rare, with metastatic disease and lymphoma, accounting for most of the lesions. Primary malignancies of the skull base are even more scarce but can be mistaken for benign lesions, and vice versa, creating a diagnostic dilemma. In addition, some of the benign entities show an aggressive growth pattern that might require more aggressive treatment. Therefore, the discussion of pathology of the skull base will also include benign entities that can be mistaken for, or that need to be treated more like a malignant lesion.

Skull base lesions can be divided into two broad categories: diffuse or localized abnormalities. Diffuse involvement of the skull base may manifest as diffuse replacement of the bone marrow or as multi-focal lesions. Localized lesions in turn can be subdivided into region specific and region-non-specific entities. This approach in evaluation of skull base abnormalities is an important starting point. The exact location of the lesion together with its imaging characteristics, patient's demographics and clinical presentation might then further narrow the differential diagnostic considerations.

5.1 Malignant Lesions Causing Diffuse or Multi-focal Skull Base Involvement

Multiple myeloma, lymphoma, leukemia and metastatic disease are the main malignant entities able to cause diffuse replacement of the bone marrow or multifocal involvement of the skull base (Figs. 8, 9). Often, the skull and the visualized portions of the cervical spine are also affected (Fig. 8a). Although any primary cancer can metastatize to the skull base, prostate, lung and breast cancer outnumber the other malignancies (Laigle-Dondey et al. 2005; Layer et al. 1999).

5.2 Mimics of Malignant Lesions Causing Diffuse or Multi-focal Skull Base Involvement

Diffuse replacement of the fatty bone marrow by red bone marrow due to chronic anemia may mimic

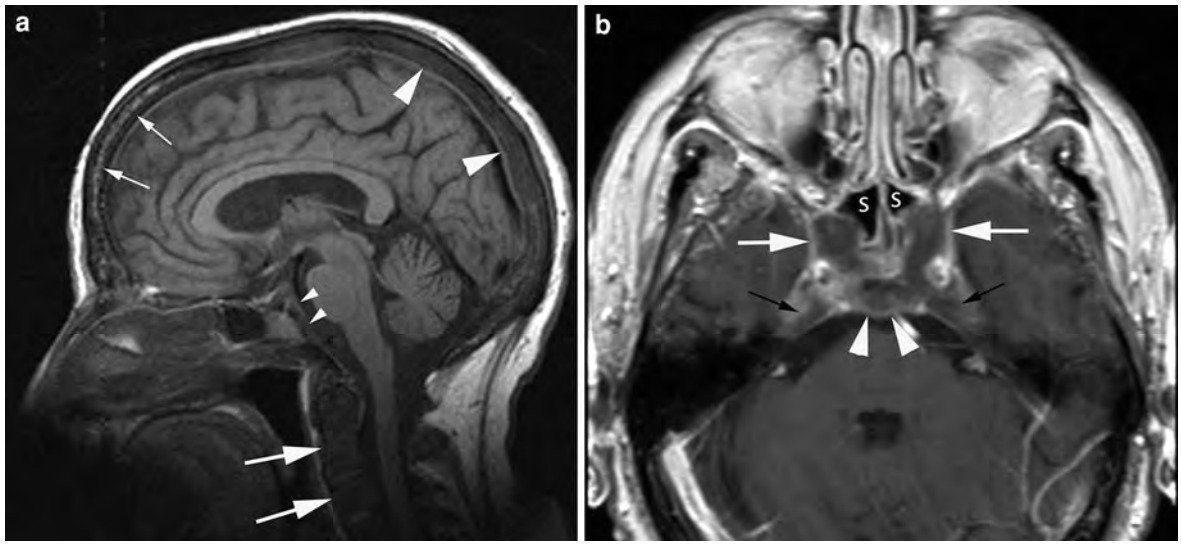

Fig. 8 Sagittal, non-contrast enhanced T1-weighted image (**a**) demonstrates completely replaced fatty bone marrow by diffuse metastatic disease in the majority of the skull (*large arrowheads* in **a**) and cervical spine (*large arrows* in **a**) while the bone marrow of the frontal skull is more mottled in appearance (*small arrows* in **a**) that is consistent with less extensive involvement. In addition, there is lack of fatty bone marrow within the clivus (*small arrowheads* in **a**) due to involvement by metastatic disease. The extent of the skull base metastasis is markedly better seen on the axial, contrast enhanced T1-weighted image (**b**) showing posterior bulging of the clivus (*arrowheads* in **b**), extension into the petrous apex bilaterally (*black arrows* in **b**), into the cavernous sinuses (*white arrows* in **b**) and into the sphenoid sinuses (*s* in **b**)

diffuse infiltration of the skull base by an underlying malignant entity. MR imaging findings are often not helpful as both entities result in decreased intensity of the bone marrow on T1- and fast spin-echo T2 weighted images and show enhancement following intravenous contrast administration (Laigle-Dondey et al. 2005; Yildrim et al. 2005; Loevner et al. 2002). CT may or may not provide additional clues as not all patients with multiple myeloma, lymphoma, leukemia or metastatic disease show bony destruction within the diploic space or early erosions of the inner and/or outer table. Therefore, clinical history and laboratory results might provide the most helpful information in some patients. Bone marrow expansion can also occur and mimic diffuse malignant involvement of the skull base and skull. It is usually seen with severe anemia such as hemolytic anemia or thalassemia (Yildrim et al. 2005; Tunaci et al. 1999). MR might deliver ambiguous results but CT usually solves the dilemma as the bone thickening caused by the bone marrow expansion is disproportionate to the preserved diploic trabecula and the intactness of the inner and outer tables of the skull (Fig. 10). Sites of extrapoetic bone marrow, such as within the paranasal sinuses, might occasionally also be seen, supporting the benign nature of the bone marrow expansion (Tunaci et al. 1999; Joseph et al. 2004).

Gorham, or vanishing bone disease, is an extremely rare bone disorder that can occur at any age and affects both genders equally. This disease is characterized by osteolysis of unknown etiology associated with angiomatous proliferation within the bone or adjacent soft tissues (Gorham et al. 1954). It can manifest as single or multiple lytic lesions involving any bone, but the calvarium and the mandible are most commonly affected (Fig. 11). Since it is such a rare entity, metastatic disease or multiple myeloma is by far the most common cause of multiple lytic bony lesions.

5.3 Non-region Specific, Localized Malignant Skull Base Lesions

All malignancies that can cause diffuse or multi-focal involvement of the skull base (metastatic disease, lymphoma, leukemia and plasmocytoma) as well as different sarcomas can present as localized lesions anywhere in the skull base. These might be difficult to distinguish from each other without further clinical

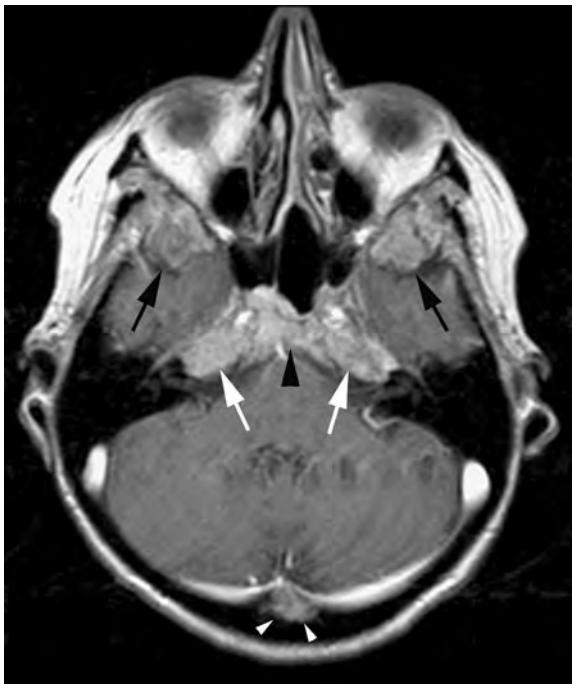

Fig. 9 Axial, contrast enhanced T1-weighted image through the upper orbit level shows replacement of the fatty bone marrow with associated bony expansion in the greater sphenoid wings bilaterally (*black arrows*), clivus (*black arrowhead*), petrous apices (*white arrows*) and in the occipital skull (*white arrowheads*) related to multiple myeloma

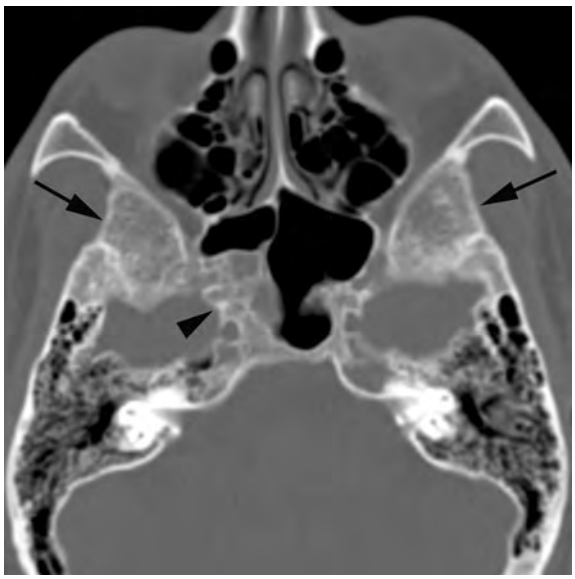

Fig. 10 Axial CT displayed in bone window demonstrates marked expansion of the greater sphenoid wings (*arrows*) that is also more cystic in appearance within the body of the sphenoid bone on the right (*arrowhead*). Thalassemia is the underlying cause of bony expansion in this patient

information. In general, metastatic disease is more aggressive in appearance and causes frank bone destruction even in early stages, while localized lymphoma and leukemia (often referred to as chloroma) show more permeative growth pattern with preservation of the diploic trabecula and of the cortical bony margins even with large tumors (Figs. 12, 13). In addition, it has been reported that highly cellular tumors with small extracellular compartment, such as lymphoma, leukemia and Ewing' sarcoma, often demonstrate pronounced restricted diffusion on the diffusion weighted images (DWI), with increased signal intensity on the DWI and reduced signal intensity on the apparent diffusion coefficient (ADC) maps (Guo et al. 2002; Mascalchi et al. 2005). In contrast, metastatic disease shows markedly less frequently restricted diffusion. Therefore, DWI might be a useful tool in narrowing the differential diagnostic possibilities in patients with inconclusive conventional MR and clinical findings.

Ewing's sarcoma is a rare and highly malignant neoplasm of the bone arising from the primitive neuroectoderm (Rueda-Franco and Lopez-Correla 1995; Kozlowski et al. 1991). It most commonly involves the long bones, pelvis, ribs and only very rarely the skull base and vault. It typically occurs in children between 5 and 13 years of age. Neurological deficits are the leading clinical symptoms caused by the mass effect from the tumor. Aggressive chemotherapy is the primary and usually successful treatment choice for Ewing's sarcoma, while surgery is reserved for cranial nerve decompression and radiation therapy for tumors unresponsive to chemotherapy (Carlotti et al. 1999). On imaging, Ewing's sarcoma presents as an osteolytic lesion causing erosions of the inner and/or outer table in association with an extracranial soft tissue mass of variable size and a significant epidural component causing local mass effect upon the adjacent brain parenchyma. The epidural component of the tumor rarely invades the dura or the brain parenchyma. On CT, the tumor itself is usually iso- to hyperdense and shows heterogeneous enhancement following intravenous contrast administration. MR is superior in delineation of the epidural component to adjacent dura and brain parenchyma. In addition, the restricted diffusion seen on the DWI part of the study might provide useful hints to the nature of the mass (Guo et al. 2002; Mascalchi et al. 2005).

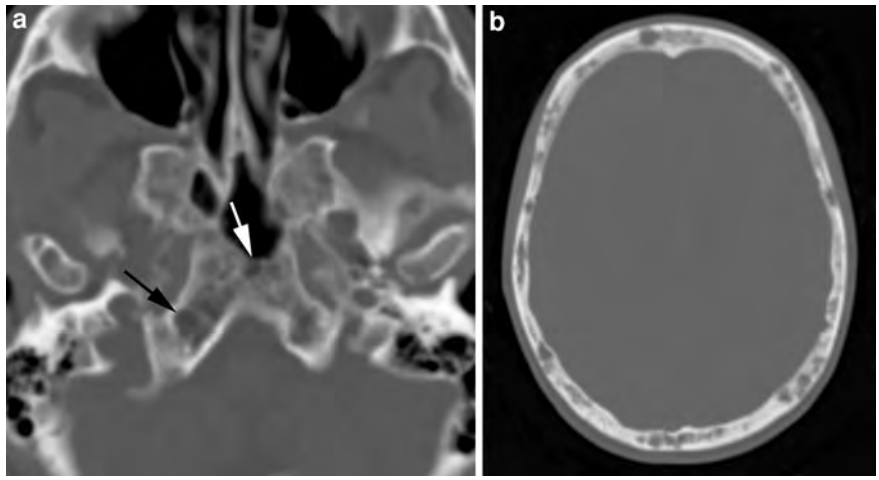

Fig. 11 Axial CT images displayed in bone window through the central skull base (**a**) and skull (**b**) show multiple small pounched out skull base (*arrows* in **a**) and numerous skull lesions caused by Gorham's disease

Fig. 12 Axial CT image displayed in bone window shows destruction of the sphenoid body (*arrowheads*) and clivus (*arrow*) caused by an aggressive skull base metastasis

Osteosarcoma is the second most common primary bone tumor after multiple myeloma of the skeleton. It typically arises from the metaphysis of the long bones, especially of the femur and proximal tibia. It only very rarely involves the skull and skull base. Secondary osteosarcomas are also rare and usually occur in the setting of previous radiation therapy or arise from benign lesions with malignant potential such as Paget's disease, multiple osteochondromatosis and chronic osteomyelitis (Salvati et al. 1993; Shinoda et al. 1993). The imaging characteristics depend on the type of the osteosarcoma. While parosteal osteosarcoma is limited to the outer table, the other types of osteosarcomas show inner and outer table involvement with associated involvement of the subdural space and brain parenchyma in approximately 40% of cases (Garland 1945). The degree of intracranial involvement is inversely related to patient's prognosis (Whitehead et al. 1998). Small fluid–fluid levels may be seen in cases of telangiectatic osteosarcoma. Radical surgical excision is the treatment of choice which is usually not feasible in the skull base. Therefore, patients with skull base osteosarcomas carry a worse prognosis than patients with osteosarcomas of other parts of the skeleton.

5.4 Mimics of Non-region Specific, Localized Malignant Skull Base Lesions

Fibrous dysplasia of the skull base is relatively common and is a developmental anomaly of the bone forming mesenchyma in which the transformation of woven to lamellar bone is disturbed. This causes an arbitrary arrangement of the bony trabeculae that are embedded in an overgrowth of a well-vascularized fibrous stroma. It represents a benign lesion, with extremely low potential for malignant transformation that usually occurs secondary to radiation therapy (Utz et al. 1989). Fibrous dysplasia is often mistaken for a skull base tumor as it can assume any appearance on MR imaging (Fig. 14; Chong and Fan 1998; Utz et al. 1989). It may show low intensity on all

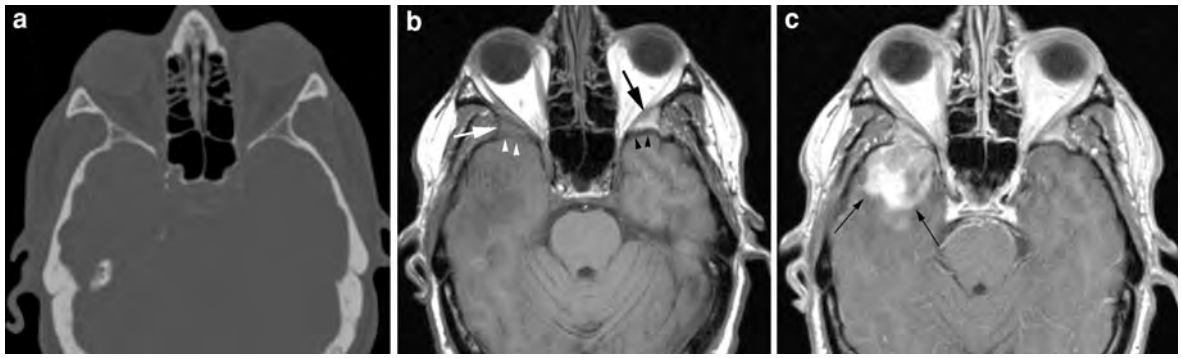

Fig. 13 Axial CT image displayed in bone window (**a**) demonstrates normal appearance of the greater sphenoid wings bilaterally. On the non-contrast enhanced T1-weighted image (**b**) diffuse infiltration of the bone marrow within the right greater sphenoid wing (*white arrow* in **b**) is noted when compared to its normal appearance on the left (*black arrow* in **b**) that is obscured on the post-contrast enhanced T1 weighted image (**c**). Also notice that the posterior cortex of the greater sphenoid wing on the left is markedly thicker in appearance (*black arrowheads* in **b**) than on the right (*white arrowheads* in **b**). The contrast-enhanced T1 weighted image (**c**) also shows the gross extension of the greater sphenoid wing mass into the middle cranial fossa and the brain invasion (*arrows* in **c**). The discrepancy of the imaging findings between CT and MR in regard to bone involvement is characteristic of lymphoma—the diagnosis in this patient

sequences reflecting the high degree of mineralization but can also demonstrate any other combination of signal intensities on the various sequences, without or with mild to extensive enhancement, reflecting the different degrees of fibrous and cystic components. In contrast, plain radiographs and CT show characteristic imaging features with bone marrow expansion, "ground-glass" appearance and preservation of the adjacent cortex (Fig. 14d). Occasionally, fibrous dysplasia presents as a lytic lesion. It is usually unilateral and monostotic in nature. It can occur anywhere in the skull but prefers the anterior and central skull base. It spares the membranous labyrinth, facial nerve canal and the internal auditory canal. Clinically, it is silent in the majority of cases and is usually incidentally found on imaging. The symptomatic patients seek medical attention because of cosmetically undesirable skull and/or facial deformities, or neurological symptoms caused by narrowing of the skull base neural foramina and subsequent cranial nerve compression that may benefit from decompressive surgery.

Langerhans cell histiocytosis is a group of idiopathic neoplasms characterized by proliferation of mature eosinophilic and specialized bone marrow-derived Langerhans cells. Three major types have been described based on clinical course: acute, fulminant, disseminated form (Letterer–Siwe disease), intermediate form (Hand–Schüller–Christian disease) and indolent/chronic form (eosinophilic granuloma) (Satter and High 2008). Eosinophilic granuloma represents the localized form of Langerhans cell histocytosis and is the variety most commonly seen by radiologists. It typically occurs in children between 5 and 15 years of age (Howarth et al. 1999). The lesions are usually asymptomatic but may manifest with bone pain, palpable soft tissue mass or symptoms related to mass effect such as proptosis or cranial nerve neuropathies (Miller et al. 1978). Usually eosinophilic granuloma presents as unifocal bony lesions, typically involving the frontal and temporal bones (DiNardo and Wetmore 1989). On imaging, eosinophilic granuloma presents as a radiolucent, round to oval punch-out bony defect without sclerosis of its margins, with an enhancing soft tissue mass within the bony defect. Hand–Schüller–Christian disease is a chronic, systemic and multi-focal variant of Langerhans cell histiocytosis with peak onset between 2 and 10 years of age. These patients typically present with diabetes insipidus, exophthalmos, chronic otorrhea and hearing loss related to multi-focal and/or bilateral skull and skull base involvement. Other organs (lymph nodes in 50%, liver in 20%, spleen in 30%) and skin may also be involved (Howarth et al. 1999). Letterer–Siwe disease is a diffuse, systemic and most severe form of Langerhans cell histocytosis. It presents in children less than 2 years of age with skin eruption, anemia and hepatosplenomegaly. It is universally fatal within

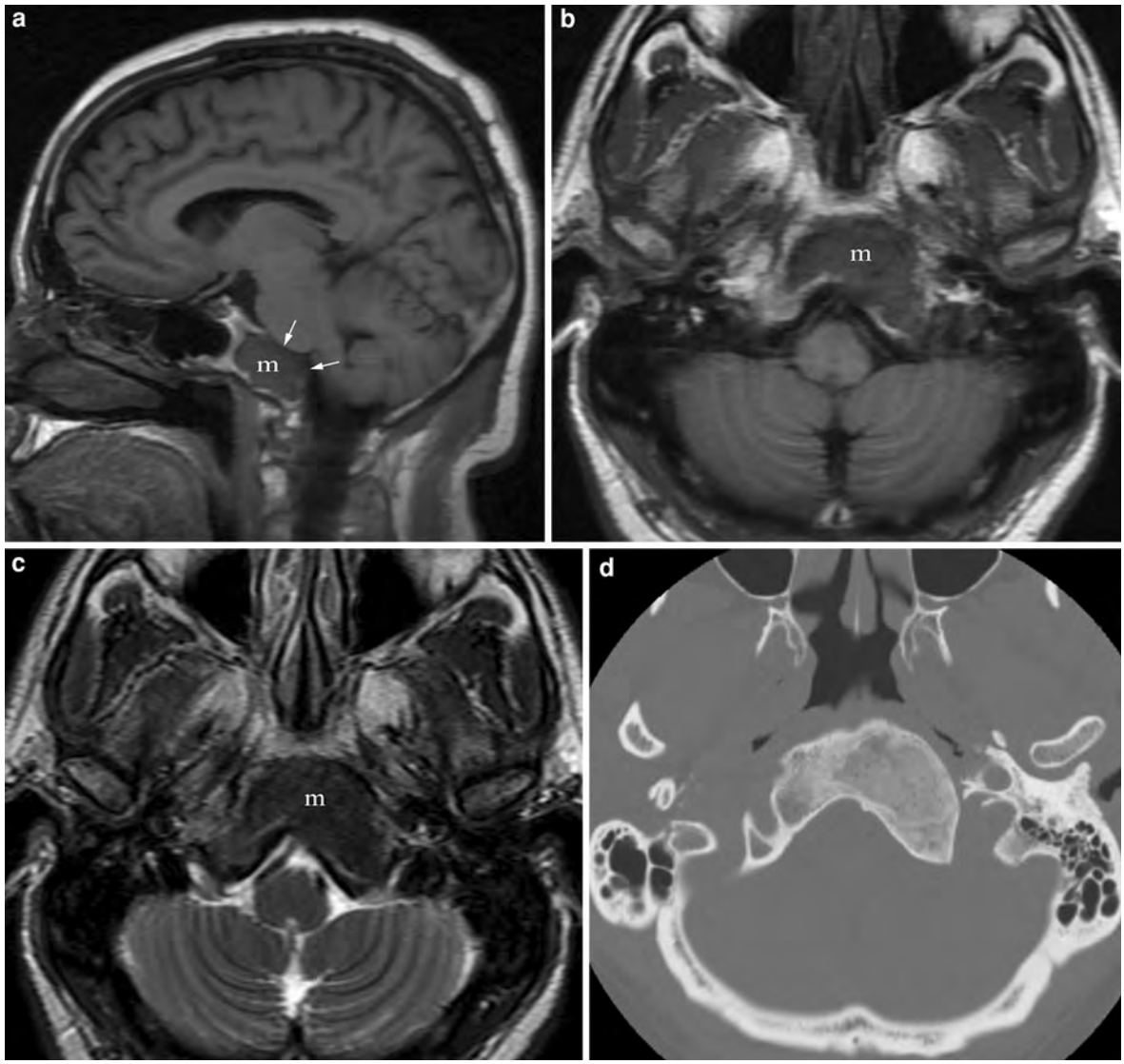

Fig. 14 Sagittal T1-weighted image through the head (**a**) demonstrates markedly abnormal bone marrow signal within the clivus (*m* in **a**) with disruption of the posterior cortex and extension into the posterior fossa (*arrows* in **a**) that is concerning for metastatic disease. The axial T1- (**b**) and T2-weighted (**c**) images through the mid clivus reveal that the lesion (*m* in **b** and **c**) is rather markedly expansile than destructive in nature and of very low signal intensity on the T2-weighted images (*m* in **b**) suggesting a benign fibrous tumor. The benign nature of the lesion was confirmed with CT (**d**) that better illustrates the expansile growth pattern and underlying ground-glass opacification characteristic for fibrous dysplasia

few years. While solitary bone lesions are treated locally with curettage or excision, systemic chemotherapy and/or bone marrow transplantation is indicated in the systemic forms of the disease (Howarth et al. 1999).

Dermoid tumors are uncommon lesions and represent inclusion cysts rather than true neoplasms. They derive from misplaced ectodermal elements during the process of neural tube closure. The tumors are usually well-defined and multi-lobulated in appearance. They have an outer connective tissue capsule lined with stratified squamous epithelium and contain hair follicles, different glands, desquamated epithelial keratin and most importantly some lipid material. This composition influences the heterogeneous appearance of these tumors on imaging.

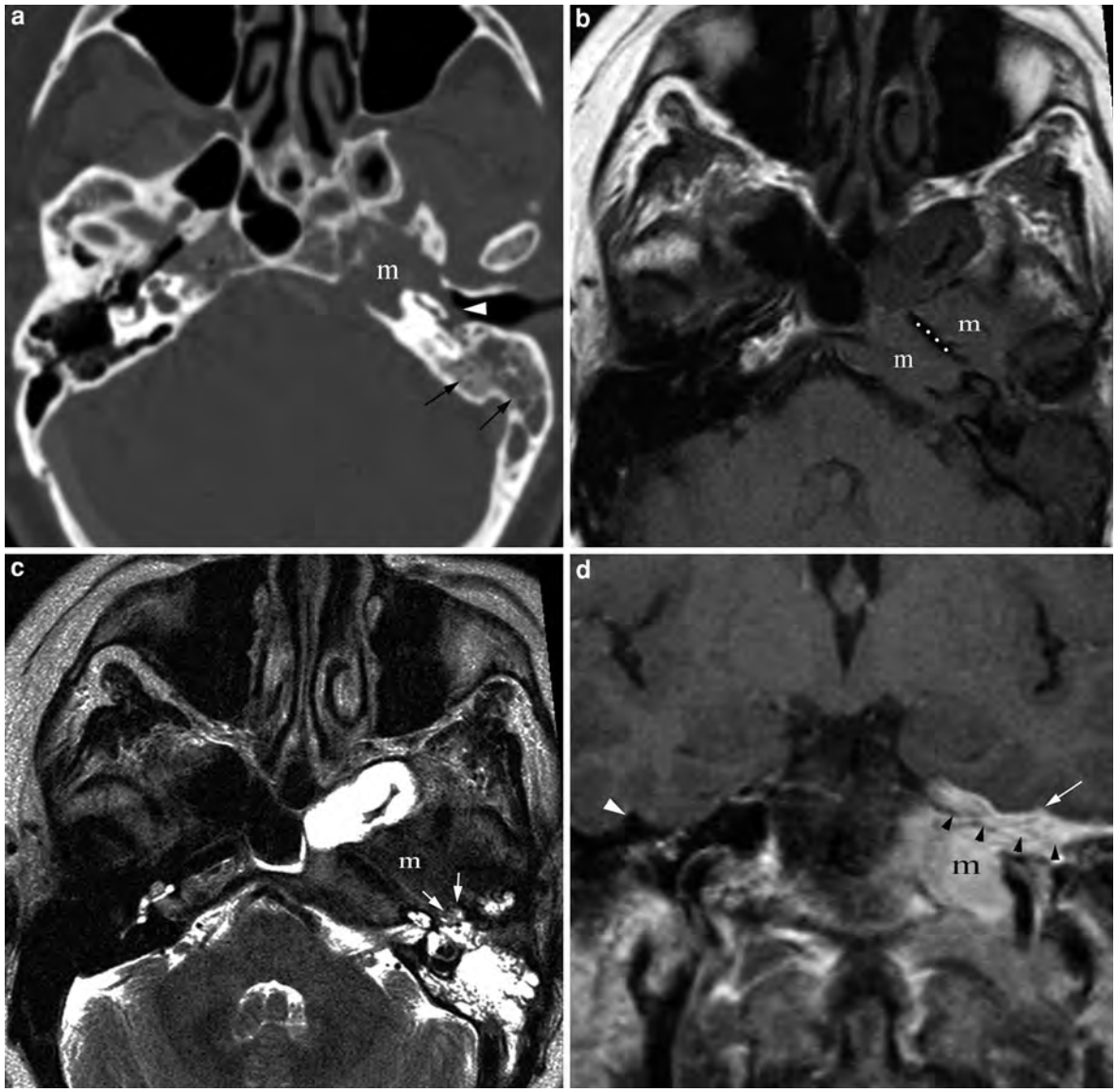

Fig. 15 Axial CT image (**a**) at the level of the sphenoid sinus incidentially discovered a destructive lesion *(m* in **a**) in the left petrous apex causing obstructive changes in the mastoid air cells (*arrows* in **a**) and complete opacification of the middle ear cavity (*arrowhead* in **a**) that could be related to direct involvement or obstructive changes. The axial T1-weighted image (**b**) reveals that the lesion (*m* in **b**) is completely surrounding the internal carotid artery (*dotted line* in **b**) within the petrous canal while the T2-weighted image (**c**) is better able to demarcate the boundary (*arrows* in **c**) between lesion (*m* in **c**) and obstructive changes within the middle ear cavity. The Gadolinium enhanced, coronal T1-weighted image (**d**) shows the superior extension of the lesion (*m* in **d**) with thick plate-like involvement of the dura *(black arrowheads* in **d**) and early invagination into the sulci of the inferior temporal lobe (*arrow* in **d**) when compared to their normal appearance on the right (*white arrowhead* in **d**). Biopsy revealed inflammatory pseudotumor rather than the initially suspected metastatic lesion

Nevertheless, these tumors typically contain various amounts of lipid material visible on imaging as very low density on CT images and high signal intensity on T1-weighted images, facilitating the correct diagnosis (Smirniotopoulos and Chiechi 1995; Gormley et al. 1994). Contrast enhancement is uncommon. Dermoid tumors involving the central nerves system typically present as a midline intracranial mass. Skull, skull

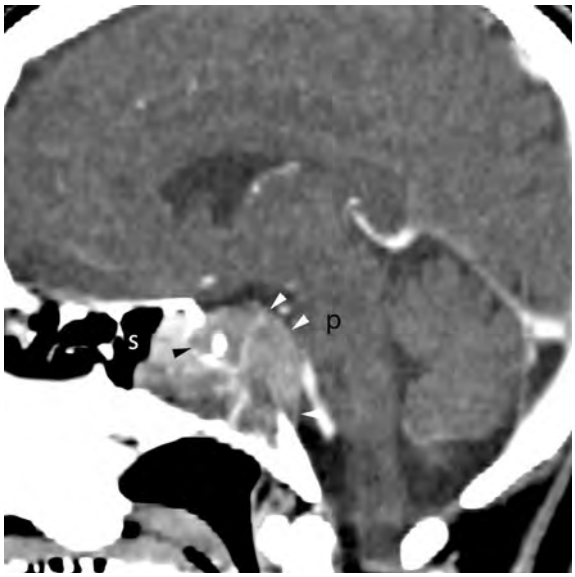

Fig. 16 Contrast enhanced, sagittal multi-planar CT reformation displayed in soft tissue window illustrates a large central skull base mass with gross invasion of the sphenoid sinus (*s*). In addition, the clivus (*c*) is almost completely involved by this mass that also bulges posteriorly into the prepontine cistern (*white arrowheads*) where it flattens the pons (*p*). The sella (*black arrowhead*) is also involved without significant suprasellar component. This represented an invasive pituitary gland adenoma. Notice the discrepancy between the suprasellar and the intraclival component that is more characteristic of aggressive pituitary gland tumor variants

base and orbit represent the most common extracranial locations of dermoid tumors in the head and neck region (Cummings et al. 2004). Complete surgical excision is the standard treatment. Resectability, however, depends upon the location of the tumor, e.g. encroachment upon vasculature and nerves.

Inflammatory pseudotumors of the skull base are rare. They represent idiopathic, non-neoplastic lesions that typically show locally aggressive behavior and marked enhancement mimicking malignant skull base neoplasm (Fig. 15; Garg et al. 2010). No specific imaging features have been reported and therefore, the diagnosis can only be made by biopsy and/or resection. Proliferation of the fibroblasts with intermixed inflammatory cells is seen on pathological evaluation. Surgical resection and/or corticosteroid administration are usually the treatment option of first choice, with radiation therapy reserved for recurrent disease (Williamson et al. 2003).

5.5 Malignant Central Skull Base Lesions

Invasive and malignant pituitary gland tumors are rare and represent a continuum of disease, as pituitary carcinomas usually occur in the setting of pre-existing invasive pituitary gland tumors (Ragel and Couldwell 2004). Both show locally aggressive growth pattern with tendency for early skull base invasion, in contrast to the slowly growing benign pituitary gland tumors that like to decompress into the suprasellar cistern (Fig. 16). Distinct immunohistochemical markers (interleukin 6 and heat shock protein 27) that have been found to be elevated in invasive types but not in the benign variants of pituitary gland tumors are thought to be responsible for this biological aggressiveness of the invasive tumor variants (Gandour-Edwards et al. 1995). Often these tumors are large at presentation or fast growing on serial follow-up. Otherwise, they show similar imaging characteristics to their benign variants. Their large size and local aggressive growth pattern sometimes make them difficult to distinguish from other malignant central skull base lesions (Figs. 16, 17). The majority of invasive variants of pituitary gland tumors are endocrinologically active with 42% secreting adrenocorticotrophic hormone (ACTH) and 33% prolactin. The presence of metastatic disease distinguishes the invasive pituitary gland tumor from the carcinoma form (Ragel and Couldwell 2004). Metastatic disease primarily occurs in the central nervous system (cerebrum, cerebellum, spinal cord, leptomeninges and subarachnoid space) and search for it needs to be conducted in suspected invasive pituitary gland tumor as metastatic lesions might be already present on the initial imaging study. Systemic metastases most commonly involve lymph nodes, bone, liver and ovaries. Overall, pituitary carcinomas have a very poor prognosis with a reported 1-year survival rate of 34%. For the patient it is critical that the radiologist recognizes the invasive nature of a pituitary gland tumor, as an aggressive treatment plan is critical prior to development of metastatic disease.

Neuroblastoma is an embryonal malignancy arising from neuroblasts of the sympathetic nervous system (Brodeur and Castleberry 2001). They can occur as primary or secondary neuroblastomas of the skull base. The primary neuroblastomas arise from the olfactory bulb and are discussed in

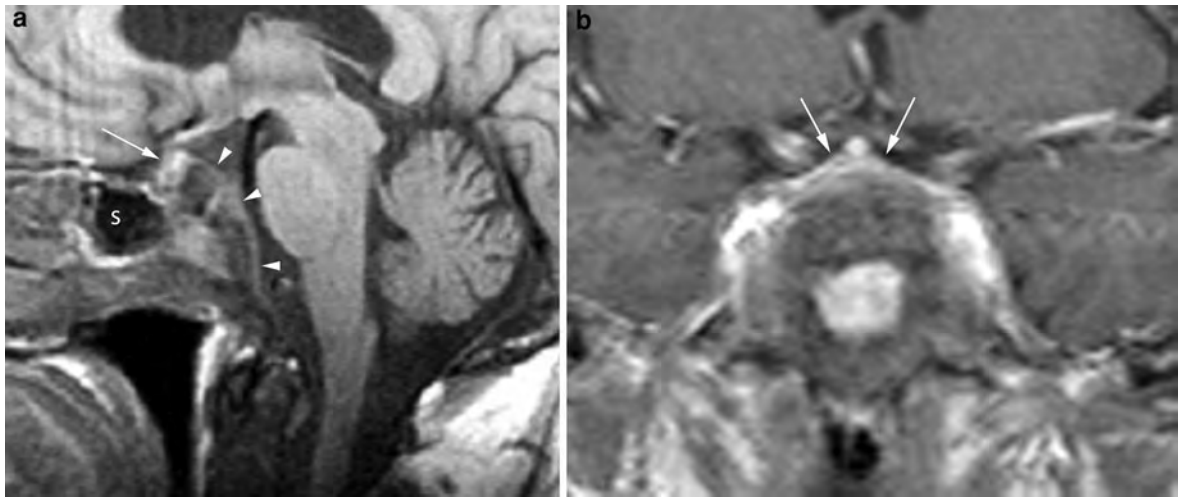

Fig. 17 Sagittal (**a**) and coronal (**b**) contrast enhanced T1-weighted images demonstrate a large central skull base mass completely involving the clivus. The extent of the mass is similar to Fig. 16 although the sphenoid sinus (*s* in **a**) is not involved and the posterior bulging into the prepontine cistern (*arrowheads* in **a**) is not as extensive. More important, however, is that the pituitary gland can be seen as it is displaced anterior and superior on the sagittal view (*arrow* in **a**) and is markedly flattened on the coronal view (*arrows* in **b**) obviating an invasive pituitary tumor as the etiology of this skull base mass. This represented a metastatic lesion

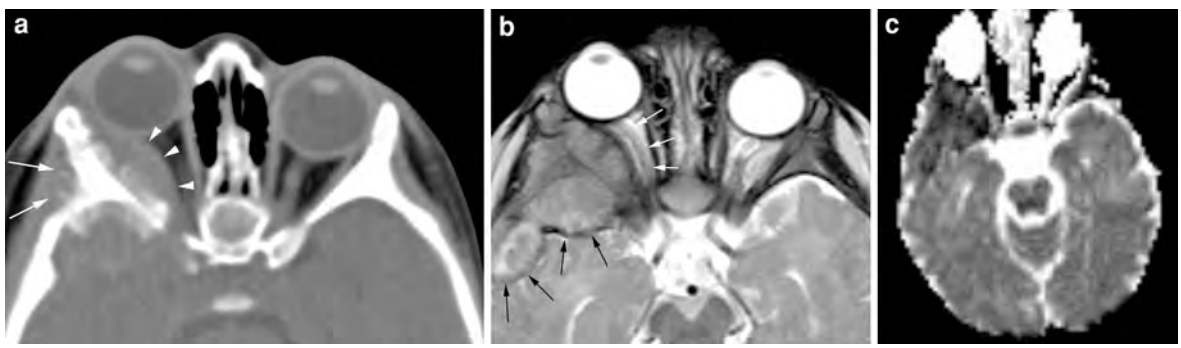

Fig. 18 Axial CT image displayed in soft tissue window (**a**) shows a large mass centered in the greater sphenoid wing on the right side (*arrows* in **a**) with extensive periosteal reaction and an orbital component (*arrowheads* in **a**). The intracranial component (*black arrows* in **b**) is markedly better seen on the axial T2-weighted image (**b**) that also displays the displacement of the optic nerve sheath complex medially (*white arrows* in **b**). The ADC map (**c**) shows lower attenuation than the adjacent brain parenchyma consistent with restricted diffusion that is characteristic of small blue cell tumors such as neuroblastoma metastasis

"Neoplasms of the Sinonasal Cavities". Secondary neuroblastomas represent metastatic disease to the skull base with a tendency for orbital wall involvement including the portions formed by the greater sphenoid wings (Fig. 18). Little has been reported in regard to imaging findings of metastatic neuroblastoma to the skull base, however, since neuroblastoma is a small cell tumor with high cellularity and little extracellular space it is not surprising that it shows restricted diffusion on DWI (Fig. 18c). Patients with orbital involvement may present with proptosis, periorbital ecchymosis, diplopia or vision loss. Otherwise, the symptoms are related to the primary lesions, "blueberry muffin" resembling skin disease or a paraneoplastic systemic syndrome with myoclonic jerking and random eye movements (=opsoclonus) (Brodeur and Castleberry 2001). The treatment and prognosis of neuroblastoma depends upon tumor stage, age of the patient, histological and molecular features.

In the central skull base region, schwannomas may arise from cranial nerve III–VI. Benign trigeminal nerve (cranial nerve V) schwannomas are the most

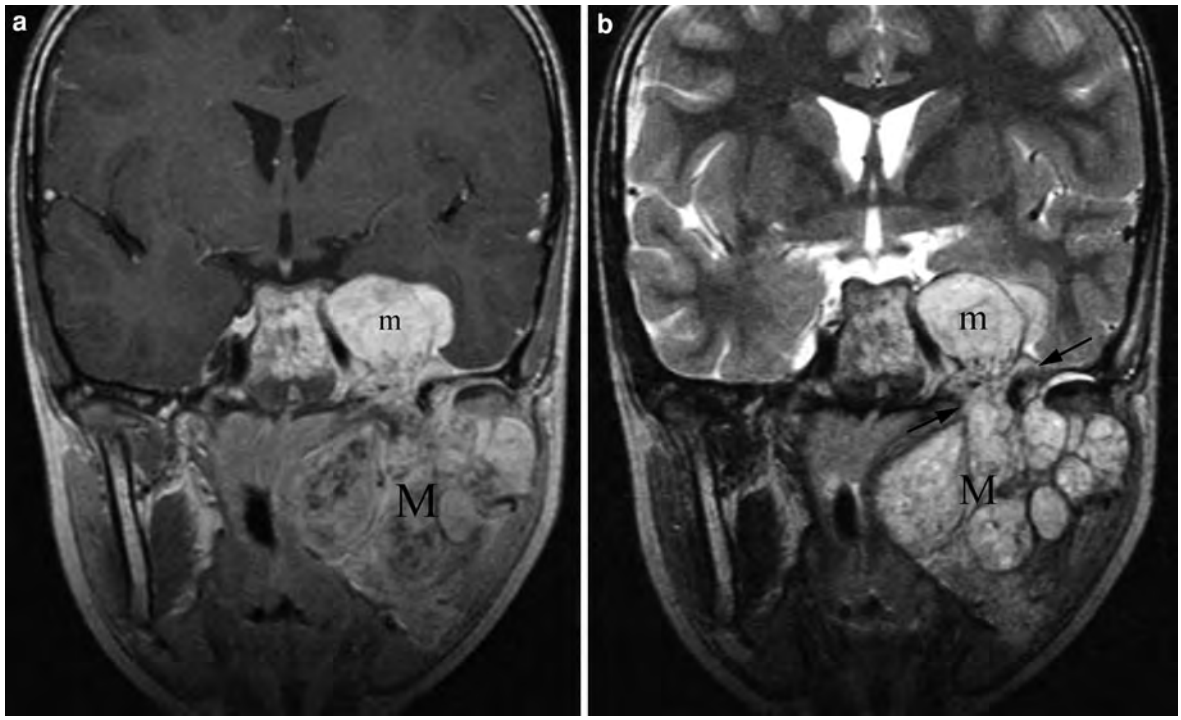

Fig. 19 Gadolinium enhanced, coronal T1- (**a**) and T2-weighted (**b**) images through the central skull base show a large, markedly enhancing left cavernous sinus mass on the left (*m* in **a** and **b**) that extends through the foramen ovale (*arrows* in **b**) along the mandibular division of the trigeminal nerve to completely occupy the infratemoral fossa (*M* in **a** and **b**). The very large size of the neuronal tumor in a patient without neurofibromatosis has to raise the concern for a malignant variant, requiring more aggressive treatment, as was the case in this patient

common cranial nerve tumors with a reported incidence of up to 0.4% of all intracranial tumors. Malignant schwannomas are even more rare. All but trigeminal nerve malignant schwannomas have been linked to neurofibromatosis type 1 (Stone et al. 2001). Malignant schwannomas of the trigeminal nerve are rather sporadic in occurrence with no known risk factors. The clinical presentation of the benign and malignant variants of central skull base schwannomas is similar, related to dysfunction of the cranial nerve primarily involved and mass effect-related dysfunction of the remaining cranial nerves within the cavernous sinuses. There are no characteristic imaging features distinguishing between benign and malignant types of schwannomas either. The more aggressive nature of the schwannoma may be suggested when rapid tumor growth or extensive nerve involvement is seen (Fig. 19). In addition, presence of early erosions of the skull base foramina that are disproportionate to the size of the schwannoma might provide important clues (Stone et al. 2001). Due to the rarity of malignant schwannomas little is known in regard to most optimal treatments. Complete surgical resection is certainly the main goal but usually not feasible. In addition, it has been reported that malignant schwannomas have 50% local recurrence rate despite negative surgical margins and adjuvant radiotherapy (Jabre et al. 2000). Therefore, the overall prognosis is poor with a reported 5-year survival between 38 and 65% (Stone et al. 2001).

Primary extra-dural meningioma of the skull base is rare with its malignant variant being extraordinarily uncommon (Van Tassel et al. 1991). Both entities will be discussed in this section together as their imaging findings overlap and the benign form may mimic malignant central skull base lesions. Primary extra-dural meningiomas are thought to arise from ectopic meningocystes or arachnoid cap cells that are trapped in a fracture line or suture during trauma or molding of the head at birth, respectively (Turner and Laird 1966; Azar-Kian et al. 1974). Most commonly extra-dural meningiomas are therefore intra-osseous in

Fig. 20 Axial CT images displayed in bone (**a**) and soft tissue (**b**) windows show slight sclerosis of the greater sphenoid wing on the right (*white arrow* in **a**) when compared to the left (*black arrow* in **a**) with marked periosteal region (*arrowheads* in **a**) and a large orbital component (*m* in **b**) causing mild proptosis. These CT findings and mass location are typical of an extra-dural, intra-osseous meningioma. Axial contrast-enhanced CT image of the same patient performed 6 months later (**c**) shows moderate enlargement of the orbital component (*m* in **b**) with more pronounced protosis and a new large intracranial component (*arrows* in **c**) that extended superiorly to involve the lower half of the frontal lobe (not demonstrated). The rapid growth pattern of this mass is consistent with a malignant meningioma that was confirmed surgically and on pathological evaluation

nature and often involve the greater sphenoid wing which is in part related to the high number of sutures in this location (Fig. 20). In contrast to the intradural variant, there is no gender preference and the extra-dural type shows a bimodal peak with manifestation at older age as well as in the second decade of life (Lang et al. 2000). More than half of these lesions are hyperostotic on plain films and CT studies potentially mimicking prostatic cancer metastasis or fibrous dysplasia (Fig. 20a). Only approximately 35% present as osteolytic and 6% mixed lesions (Crawford et al. 1995; Tokgoz et al. 2005). Spiculated appearing periosteal reaction might be present (Fig. 20a). Often a soft tissue component of variable size is seen which might be difficult to distinguish from adjacent musculature and/or dura on CT images (Fig. 20b, c). MR is superior in this regard due to its increased soft tissue detail. As on CT, extra-dural meningiomas may show variable internal signal characteristics and different degrees of contrast enhancement primarily reflecting the degree of hyperostosis. Interestingly, it has been shown that the extra-dural type of meningiomas has a higher incidence of malignant degeneration than the intradural variant with a reported risk of 11 and 2%, respectively (Tokgoz et al. 2005). It has been described that meningiomas presenting with osteolysis and an extracranial soft tissue component are more likely aggressive, and therefore, more often malignant in nature (Fig. 20). In addition, it has been shown that malignant meningiomas have the tendency to show restricted diffusion on DWI (Fillippi et al. 2001). Complete surgical resection is the treatment of first choice.

5.6 Mimics of Malignant Central Skull Base Lesions

Cephalocele is a rare entity, in which brain tissue and/or meninges are protruding through a bony defect from intracranial to extracranial. In the central skull base region, intra-sphenoidal and trans-sphenoidal cephaloceles have been encountered (Jabre et al. 2000). Trans-sphenoidal cephaloceles are usually congenital in nature. They are typically midline in position and therefore may present on imaging as a midline bony gap associated with a cystic nasopharyngeal mass. This type of cephalocele is usually complex in nature containing optic nerves, hypothalamus or other adjacent midline structures. These patients might present with pituitary gland dysfunction due to protrusion of the pituitary gland into the meningoencephalocele or more commonly because of associated maldevelopment of the sella and pituitary gland. The intra-sphenoidal cephaloceles are typically lateral in location and most commonly post-traumatic in nature. These usually contain variable amounts of temporal lobe tissue and may present with seizures or rhinorrhea, bearing increased risk of meningitis. Therefore, they are often treated with surgery. On CT,

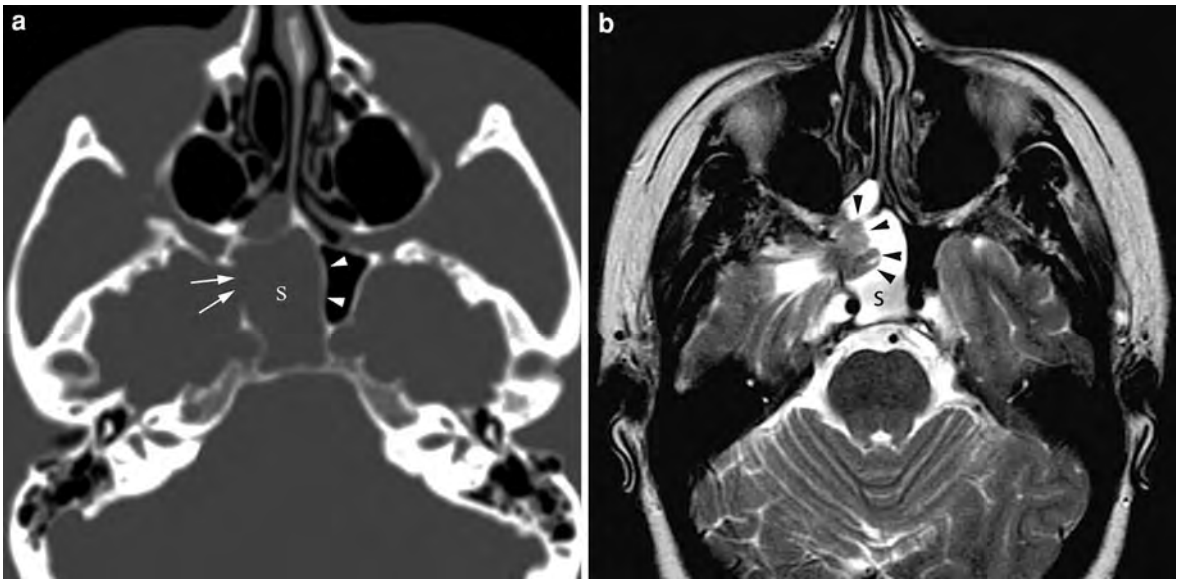

Fig. 21 Axial CT image displayed in bone window (**a**) demonstrates complete opacification of the sphenoid sinus on the right (*s*) with an approximately 1-cm bony gap in the lateral wall of the sphenoid sinus (*arrows* in **a**) and mild bowing of the sphenoid septum to the left (*arrowheads* in **a**). Although these imaging findings might be mistaken for a sphenoidal mucocele and less likely for an aggressive sphenoid sinus tumor, the direction of bowing of the edges of the bony gap suggests that this is an intracranial process secondary involving the sphenoid sinus. This is confirmed on the axial T2-weighed image (**b**) that clearly shows protrusion of brain tissue (*arrowheads* in **b**) into the sphenoid sinus (*s* in **b**) through the bony defect. These imaging findings are therefore consistent with a lateral intrasphenoidal encephalocele

a bony gap in the sphenoid body and partial or complete opacification of one or both sphenoid sinuses is seen (Bolger and Reger 2003). They may be mistaken for mucoceles or aggressive skull base masses when associated with mass effect within the sphenoid sinus (Fig. 21a). On MR the diagnosis is easier as the extracranial brain tissue and/or meninges are directly demonstrated in particular on T2-weighted images (Fig. 21). On CT, however, the location of the bony gap, the pattern of bone remodeling rather than destruction and potentially associated mild bowing of the involved bone towards the sphenoid sinus provide important diagnostic clues that warrant further evaluation with MRI.

5.7 Malignant Lesions at the Junction of Central to Posterior Skull Base

Chordomas represent rare, locally invasive and slowly growing tumors. Histologically, they resemble benign tumors, however, the majority of authors consider them as low grade malignancies due to their aggressive local growth pattern and their low risk for metastatic disease (Erden et al. 2003). They originate from embryonic remnants of primitive notochord at the spheno-occipital synchondrosis. The skull base is the second most common location. The majority of chondromas occur at the distal end of the notochord in the sacral region. Different histological subtypes have been reported such as chondroid and myxoid variants. Chordomas may present at any age but show a predilection for the fourth decade and males. The onset of symptoms is insidious, reflecting the slow growth pattern of these tumors. However, at some point these patients become symptomatic and most commonly present with headaches and diplopia secondary to cranial nerve VI palsy. This is not unexpected as the cranial nerve VI courses through the medial portion of the petrous apex within Dorello's canal, in close proximity to the spheno-occipital fissure. The vast majority of chordomas are midline in position with relative symmetric bilateral tumor growth. Only less than 15% of chordomas have been reported to originate from the petrous apex simulating a chondrosarcoma. On CT, chordomas classically present as large, relatively well-circumscribed, lytic bone lesions arising from the clivus (Fig. 22a). Often intra-tumoral

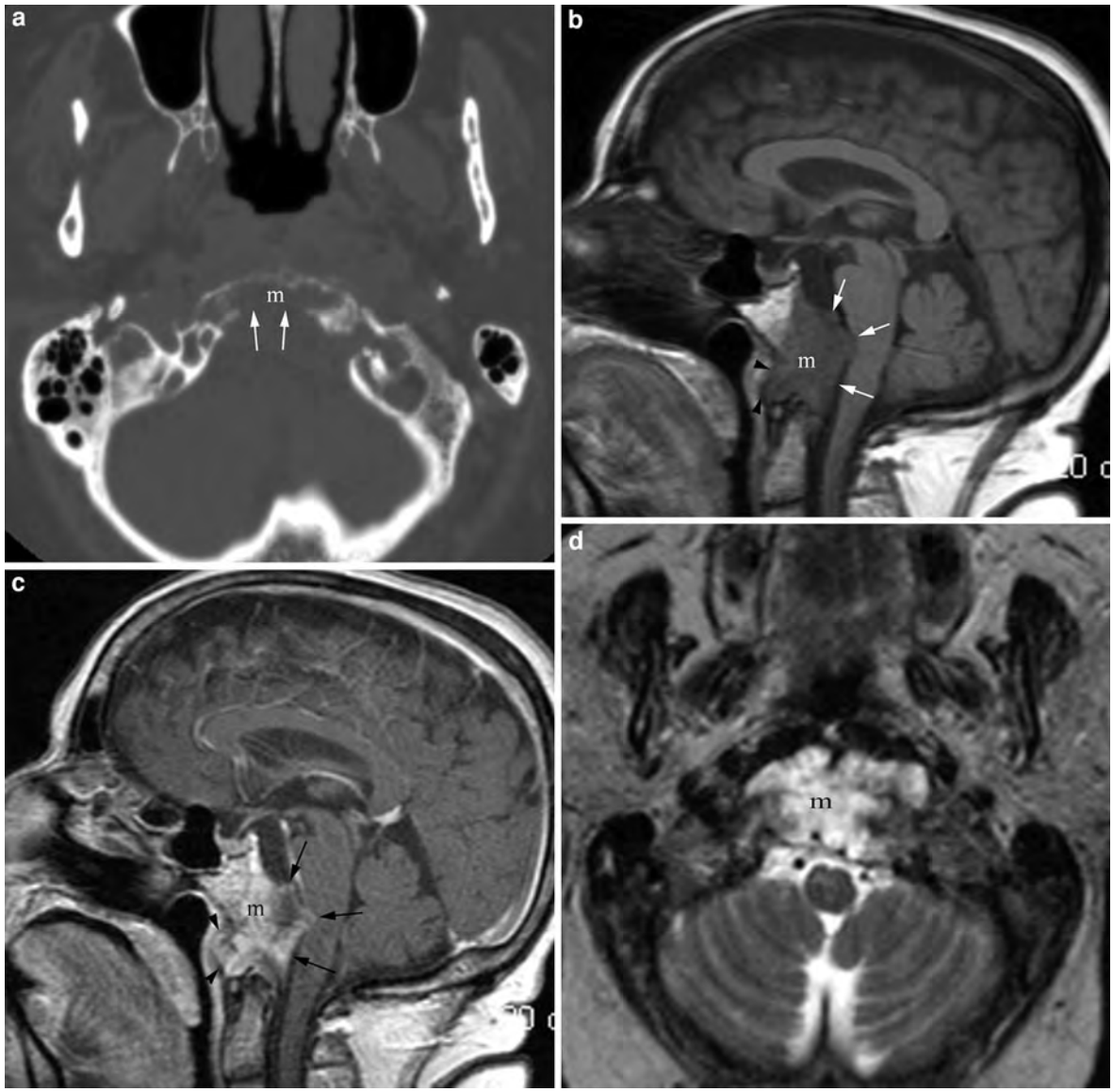

Fig. 22 Axial CT image displayed in bone window (**a**) demonstrates a moderate lytic clival mass (*m* in **a**) with complete posterior cortical disruption (*arrows* in **a**). The non-contrast enhanced (**b**) and contrast enhanced (**c**) T1-weighted images demonstrate the full extent of the markedly, heterogeneously enhancing lesion (*m* in **b** and **c**) with a small nasopharyngeal (*arrowheads* in **b** and **c**) and a large posterior fossa component (*arrows* in **b** and **c**). The clival origin of the lesion together with the marked hyper intensity on the axial T2-weighted (*m* in **d**) images is most consistent with chordoma which was confirmed with surgical biopsy

calcifications are seen, representing small bony sequestra left behind from bone destruction or true calcifications in case of the chondroid variant. The associated soft tissue mass is usually slightly hyperdense in appearance demonstrating moderate to marked enhancement following intravenous contrast administration. Although it is easy to detect a chordoma with CT, MR has been proven to be considerably superior in the delineation of the tumor extent, and is therefore the most pertinent study for treatment planning purposes. On MR imaging, chordomas show a low to intermediate T1 and high T2 signal intensity with small focal areas of decreased T2 intensity caused by tumoral calcifications or small

foci of intra-tumoral hemorrhage (Fig. 22a–c). Moderate to marked heterogeneous contrast enhancement is typically seen (Fig. 22b, c). Total surgical resection is the most optimal treatment but is usually not feasible. Therefore, post surgical radiation therapy is usually utilized to improve patient's prognosis, which is primarily affected by the amount of tumor tissue left behind within the surgical bed (Erden et al. 2003). Overall, the prognosis is poor with a reported 5-year survival rate of approximately 50% (Forsyth et al. 1993).

5.8 Malignant Posterior Skull Base Lesions

Chondrosarcomas are rare malignant cartilaginous tumors of variable aggressiveness (Evans et al. 1977). Their aggressiveness depends upon the tumor subtype and grade. The dedifferentiated and mesenchymal variants are more aggressive than the classic variant. The classic variant is the most common and represents a low grade chondrosarcoma. This type of chondrosarcoma shows the least aggressive growth pattern, minimal risk of metastatic disease and is often difficult to distinguish from chordomas histologically and clinically (Bourgouin et al. 1992). As with chordomas, headaches and diplopia related to cranial nerve VI palsy are the most common symptoms at presentation. However, chondrosarcomas usually occur in younger patients with a peak incidence in the second and third decades, and even more importantly they are off midline (petroclival) in location (Hassounah et al. 1985). Their paramedian location also predisposes these patients for lower cranial nerve deficits, in particular hearing loss. CT images typically demonstrate a destructive mass centered in the petrous apex with ring and arcs in it reflecting the chondroid nature of this tumor (Fig. 23a). Variable amount of soft tissue component is seen, typically isodense to the adjacent brain parenchyma, with some (but variable) enhancement following intravenous contrast administration. Chondrosarcomas have low to intermediate signal intensity on T1-, and high signal intensity on T2-weighted sequences, with variable enhancement pattern (Fig. 23b–d). As with chordomas, total surgical resection is the most desirable treatment in combination with radiation therapy if positive resection margins are present. Despite the histological and clinical similarities, the classic type of chondrosarcoma has been reported to have a better prognosis than chordomas with a 5-year survival rate of approximately 90%. This, however, is not true for the other chondrosarcoma variants (Forsyth et al. 1993; Evans et al. 1977).

Endolymphatic sac tumors are also very rare. They may occur sporadically or in association with von Hippel-Lindau disease (Luff et al. 2002). The patients typically present with hearing loss, tinnitus, vertigo and/or facial nerve dysfunction (Choyke et al. 1995). Bilateral involvement has been reported in von Hippel-Lindau disease patients. The majority of these tumors are low grade adenocarcinomas or papillary cystadenomas that are indistinguishable from each other based on imaging (Mukherji and Castillo 1996). On CT, local destruction is seen in the retrolabyrinthine petrous bone, at the aperture of the vestibular aqueduct, with characteristic intra-tumoral bone spiculi that might be associated with an enlarged vestibular aqueduct (Ragel and Couldwell 2004). The T1-weighted images demonstrate characteristic hyperintense foci within the tumor substance with extensive enhancement following intravenous contrast administration. Endovascular embolization prior to surgical resection may be required.

Paragangliomas are rare tumors of neural crest origin (Rao et al. 1999). In the posterior skull base, they are most commonly seen in the jugular fossa and are called glomus jugulare tumors. They arise from the paraganglion cells of the Jacobson or Arnold nerve which are branches of the cranial nerve IX and X, respectively (Rao et al. 1999). The majority of the paragangliomas are benign in nature. Up to 13% of glomus jugulare tumors have been reported to be malignant. Both types will be discussed in this section together as they both demonstrate with locally aggressive growth pattern making them indistinguishable from each other (Figs. 24, 25). Demographic data are not helpful either as both forms most commonly occur in middle-aged females that typically present with tinnitus (Brewis et al. 2000). It has been suggested that the incidence of pain is higher and the occurrence of hearing loss lower with the malignant variants. The main differentiating feature, however, is the existence of metastatic lesions in the malignant form (Fig. 25b). Metastatic disease most commonly spreads to the bone, lung and cervical

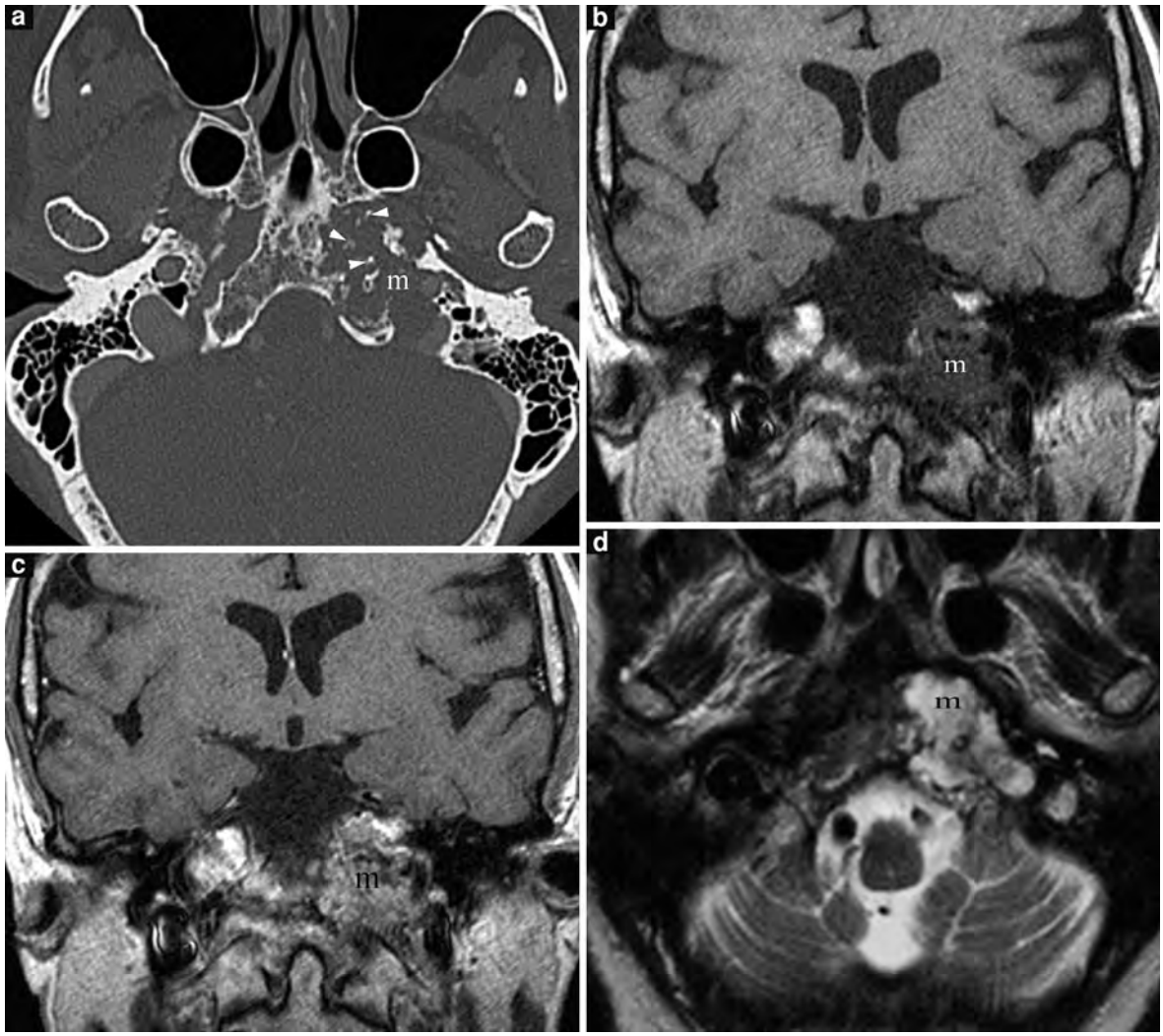

Fig. 23 Axial CT image displayed in bone window (**a**) shows a large, destructive mass (*m* in **a**) in the left petrous apex and left clivus with characteristic ring and arcs (*arrowheads* in **a**) appearance of chondrosarcomas. The MRI study confirms this suspicion by demonstrating a markedly enhancing mass in the petrous apex (*m* in **b** and **c**) on the T1-weighted images without (**b**) and with Gadolinium enhancement (**c**) with characteristic hyperintense signal intensity seen on the T2-weighted image (*m* in **d**)

lymph nodes and might present even years after the initial diagnosis and treatment (Fig. 25b). While nuclear medicine examination with Indium 111 labeled somatostatin analogs is an excellent way to evaluate for metastatic disease, CT and/or MR are primarily utilized to evaluate the primary tumor within the jugular fossa. On CT, glomus jugular tumor causes destruction of the walls of the jugular foramen and adjacent petrous bone giving the so-called "mouth eaten" appearance (Figs. 24, 25). On MR, a hypervascular mass with flow voids and extensive enhancement is seen in the jugular fossa region. On both studies, the tendency of the glomus jugulare to grow into the middle ear cavity and posterior fossa is seen, although the intracranial involvement is better demonstrated with MR (Fig. 24). In approximately 10% of patients, multifocal and/or bilateral involvement is seen. The benign forms of glomus jugulare can be treated with surgical resection following intra-arterial embolization, radiation therapy or both as the tumor is known to be radiosensitive and total surgical resection is often

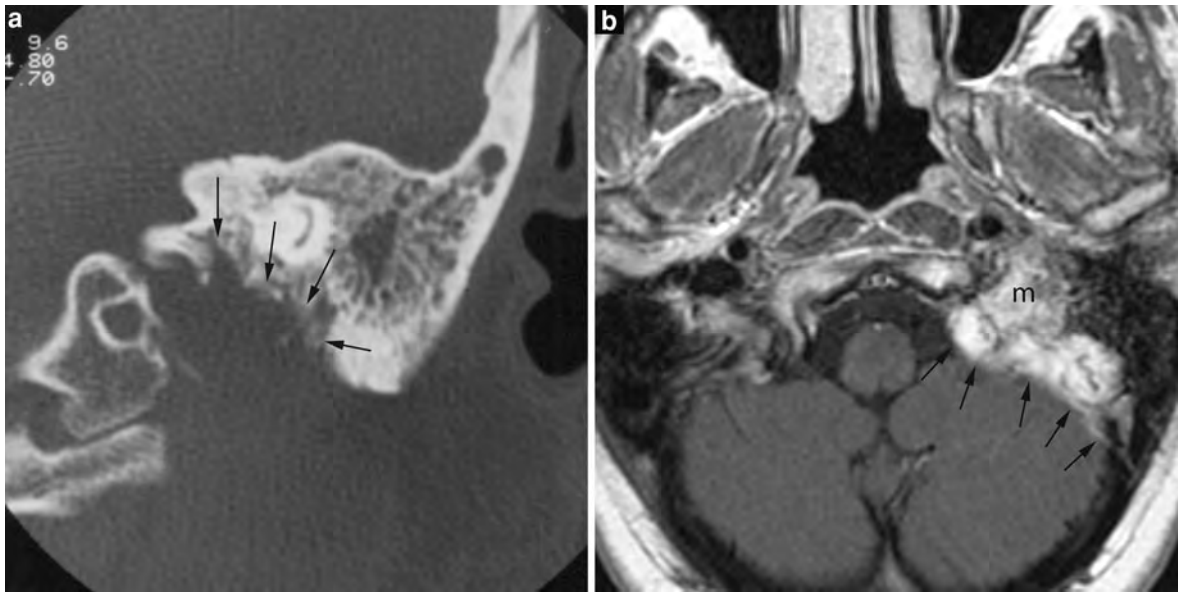

Fig. 24 Coronal CT image displayed in bone window (**a**) shows the marked erosions along the lateral and superior jugular foramen (*arrows* in **a**) caused by a large heterogeneously enhancing mass (*m* in **b**) as seen on this contrast enhanced axial T1-weighted image (**b**). The mass also extends into the posterior fossa (*arrows* in **b**) where it results in mild impression upon the left cerebellar hemisphere. The location and imaging findings are classic for a jugular foramen paraganglioma

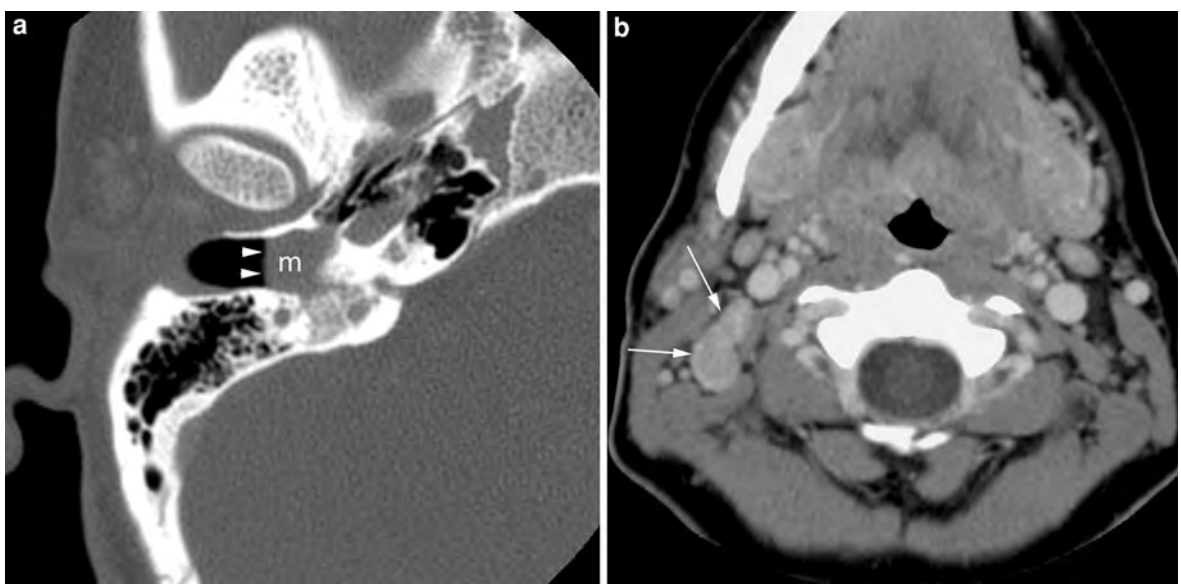

Fig. 25 Axial contrast-enhanced CT images through the middle ear displayed in bone window (**a**) and through the upper neck displayed in soft tissue window (**b**) from a 35-year-old female with tinnitus and hearing loss and with classic imaging findings of paraganglioma originating within the jugular foramen on other images. **a** Image illustrating the tendency of the jugular paragangliomas to grow into the middle ear cavity (*m* in **a**). The typpanic membrane is markedly displaced laterally (*arrowheads* in **a**). The image through the neck demonstrates abnormal group 2A lymph nodes on the right (*arrows* in **b**) allowing the diagnosis of malignant paraganglioma. This patient underwent right modified lymph node dissection confirming the nodal metastatic disease that was not suspected on clinical examination

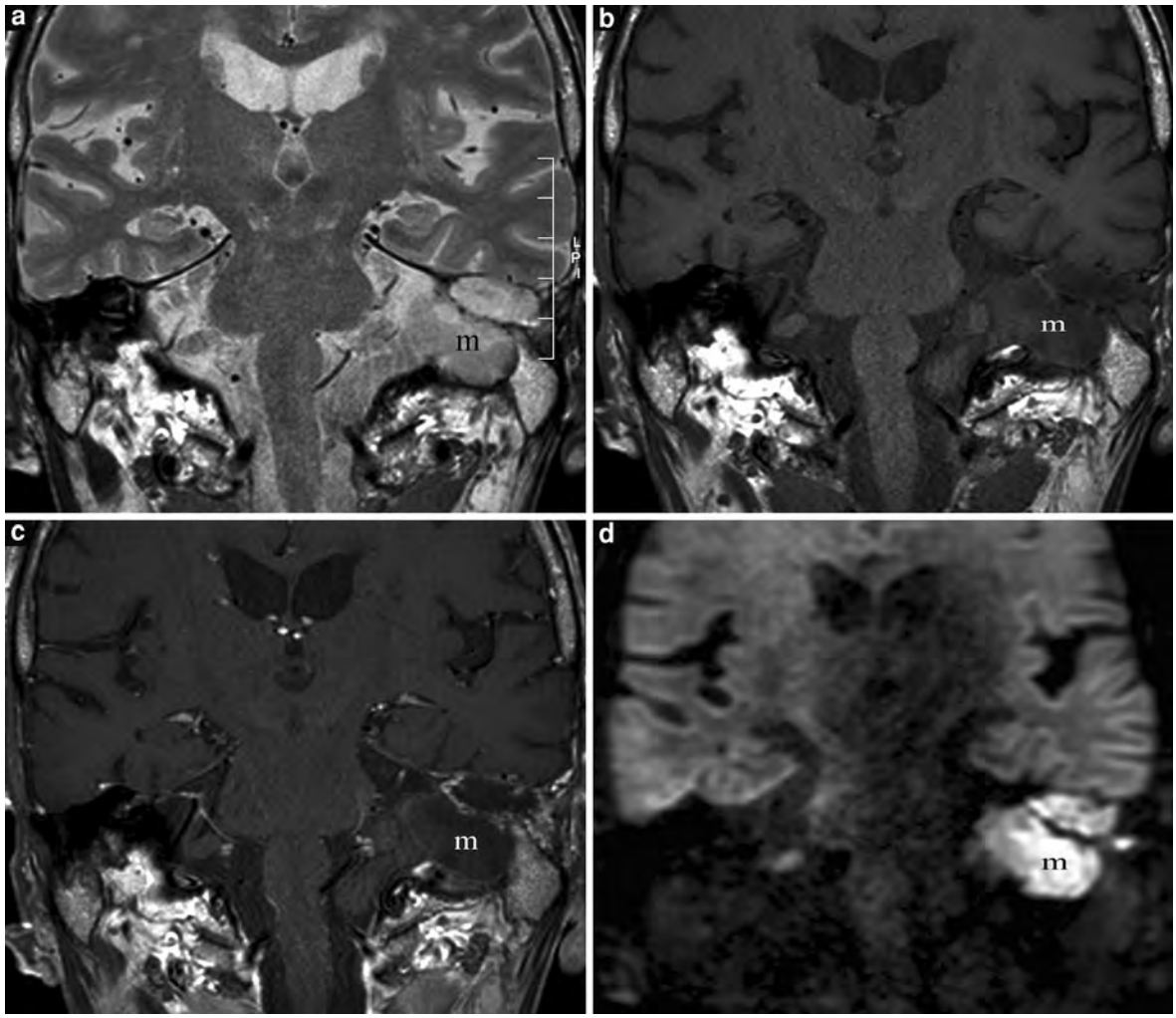

Fig. 26 Coronal T2-weighted image (**a**) demonstrates a large, hyperintense mass (*m* in **a**) in the right petrous apex region on the left side that might be mistaken for a chondrosarcoma because of its location and T2 signal intensity. The T1-weighted images pre- (**b**) and post-contrast administration (**c**), however, show lack of enhancement within the mass (*m* in **b** and **c**) which is very atypical for chondrosarcoma. In addition, the diffusion weighted image in coronal plane (**d**) shows restricted diffusion within the lesion (*m* in **d**). Cholesteatoma was confirmed on surgical specimen (Images courtesy of Robert Hermans, MD, PhD, Leuven, Belgium)

difficult. Since radiation therapy is known to leave a residual mass of variable activity behind, treatment of the malignant forms with radiation therapy alone is currently not recommended but rather surgical resection with post-operative radiation therapy. Utilization of Iodine 131 labeled MIBG for treatment of the metastatic lesions has been reported with mixed preliminary results (Bomanji et al. 2001). Paragangliomas are increasingly recognized to have a genetic predisposition, with mutations of the enzyme succinyl dehydrogenase (SDH) resulting in paraganglioma formation. Several types of mutation of this enzyme are known: SDHB mutation possibly leading to extra-adrenal pheochromocytomas, malignant paragangliomas and extra-paraganglial neoplasia; SDHD mutatation is associated with an increased incidence of multiple benign head and neck paragangliomas. Therefore, discovery of a paraganglioma should promp a genetic test in search of a possible SDH mutation (Barber et al. 2011).

Malignant schwannomas of the cranial nerve VII–XII demonstrate the same rarity, behavior and

imaging findings as the malignant schwannomas of the cranial nerve III–VI (see Sect. 5.5 for details).

5.9 Mimics of Malignant Posterior Skull Base Lesions

Congenital cholesteatoma is a rare disease arising from aberrant ectoderm that is trapped during embryogenesis within the temporal bone (Robert et al. 1995). Histologically, the lesion is lined with stratified squamous epithelium and filled with debris. It typically presents in children and young adults. It can occur anywhere within the temporal bone; when located in the petrous apex it might simulate a malignant lesion of the skull base. Petrous apex congenital cholesteatomas present with facial nerve palsy, sensorineural hearing loss and/or vertigo. On CT, a hypodense, non-enhancing expansile mass is seen with variable degree of bony destruction. Congenital cholesteatoma is usually low to intermediate in signal intensity on T1- and high signal intensity on T2-weighted images (Fig. 26a–c). Presence of restricted diffusion on DWI has also been reported which is not surprising as cholesteatomas histologically resemble epidermoid tumors (Fig. 26d; Aikele et al. 2003). The use of non- echo-planar DWI sequence is recommended in this area as it allows for thinner section thickness and higher imaging matrix with less associated susceptibility artifacts (De Foer et al. 2006). Surgical excision is the treatment of choice and recurrent disease is common with subtotal resection. In such patients, non-echo-planar DWI has shown to be a promising tool for evaluation of residual or recurrent disease as an alternative to exploratory second-look surgery (Dhepnorrarat et al. 2009; De Foer et al. 2010).

Cholesterol granuloma represents an accumulation of granulation tissue intermixed with blood products and cholesterol crystals within the middle ear or petrous apex (Farrior et al. 1981). Patients with cholesterol granuloma classically have a long-standing history of chronic otitis media. Lesions in the petrous apex are often quiet large at the time of diagnosis and may therefore present with hearing loss, tinnitus and/or cranial neuropathies (Goldofsky et al. 1991). On CT, cholesterol granulomas present as expansile, well-defined masses (Fig. 27a; Greenberg et al. 1988). When large, the site of origin might be difficult to determine making distinction to other types of petrous apex lesions, in particular petrous apex aneurysm, difficult. As cholesterol granulomas are often large at the time of initial scanning, CT images often show bony gaps that may be mistaken for bone destruction or erosions suggesting an aggressive or malignant lesion. On MRI, cholesterol granulomas are classically of increased signal intensity on the T1- and T2-weighted images, with no or minimal peripheral enhancement following contrast administration (Fig. 27b). Cholesterol cysts are essentially identical to cholesterol granulomas but occur in the absence of chronic middle ear disease. Mucoceles of the petrous apex share the same imaging characteristics as cholesterol granulomas on CT, but usually demonstrate decreased signal intensity on T1-weighted images. Mucoceles of the petrous apex are very rare and are felt to be related to post-inflammatory obstruction. All of these lesions are usually treated with surgical drainage.

Internal carotid artery aneurysms can occur within the cavernous sinuses, causing remodeling of the adjacent sphenoid bone, or within the petrous bone. The cavernous sinus aneurysms are more common and usually do not demonstrate a diagnostic dilemma. Petrous segment internal carotid aneurysms, in contrast, are rare. They can be congenital, post-traumatic or post-infectious in etiology (Liu et al. 2004). Aneurysms in this location are usually asymptomatic and are incidentally found on CT or MR studies performed for other indications. In symptomatic patients, symptoms are primarily non-specific in nature (headaches) or related to local mass effect (cranial neuropathies, Horner's syndrome or tinnitus). Embolic events have not been associated with petrous segment aneurysm even with larger mural thrombus formation (Liu et al. 2004). On CT, they usually present as an expansile mass with marked enhancement following intravenous contrast administration. The degree and homogeneity of enhancement depends upon the amount of mural thrombus and the size of patent lumen (Fig. 28). If no intravenous contrast is given, they may mimic a cholesterol granuloma, cholesterol cyst or a petrous apex mucocele. Close search for the internal carotid canal within the petrous bone and evaluation of the vector of the associated bone remodeling usually results in correct diagnosis. Contrast-enhanced CT and/or CT angiography might be then performed to confirm the

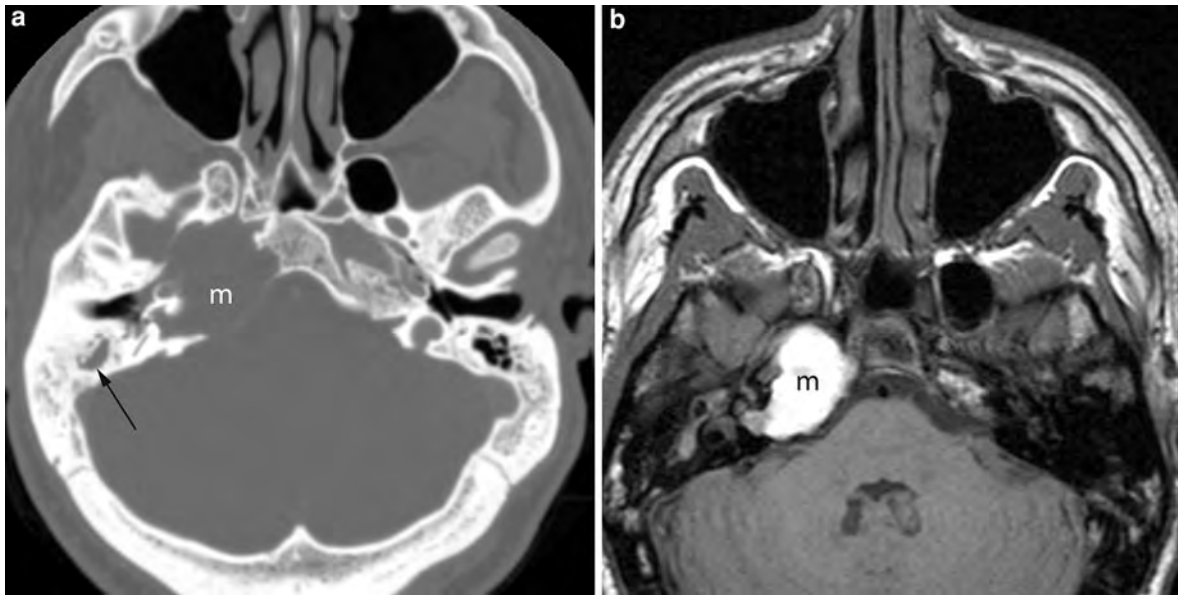

Fig. 27 Axial CT displayed in bone window (**a**) shows a large lytic lesion (*m* in **a**) centered within the petrous apex without signs of cartilageous matrix to suggest a chondrosarcoma. The non-contrast enhanced T1-weighted image in axial plane (**b**) shows spontaneous very high signal intensity of the mass (*m* in **b**) that is characteristic of cholesterol granulomas in contrast to the low to intermediate signal intensity seen in chondrosarcomas that occur in the same location. In addition, there is a small amount of fluid (*arrow* in **a**) present in the mastoid air cells on the right supporting the diagnosis of cholesterol granuloma

diagnosis and to classify the type of the aneurysms (Fig. 28). On MR, petrous apex aneurysms usually present with mixed signal intensity and enhancement pattern, related to the turbulent flow within the aneurysmal segment (Fig. 28). Even MR angiography is usually difficult to interpret as the turbulent flow causes signal drop-out due to reentry phenomenon or thrombus formation that underestimates the size or makes the aneurysm difficult to appreciate at all. This constellation of imaging findings may result in misdiagnosis of the aneurysm as a non-vascular benign and/or malignant skull base lesion. In the instance of present flow voids within the aneurysm, the aneurysm might be completely missed as the difference in signal intensity to adjacent petrous apex, in particular when the petrous apex is aerated, might be very small and therefore not appreciable to the radiologist's eye. The bottom line is that internal carotid artery aneurysms in this location might pose a diagnostic dilemma and the radiologist should consider it every time a petrous apex lesion is observed on CT or MRI to prevent a potential biopsy with usually fatal outcome. The treatment of petrous segment aneurysm remains challenging, in particular when the patient has no or minimal symptoms. Currently, a "wait and see" approach is applied to this latter patient group as these types of aneurysms do not suffer life-threatening bleeding episodes. Endovascular intervention (balloon or coil occlusion of the internal carotid artery and/or stent placement) or surgical trapping with revascularization bypass is currently reserved for symptomatic patients (Liu et al. 2004).

Petrous apicitis is usually caused by otitis media that extended anteromedially into the aerated petrous apex cells without or with progression to osteomyelitis in the early and delayed stages, respectively. Usually, the patients present with fever reflecting the acute nature of the infection in combination with some or all of the symptoms of the Gradenigo's triad (see Sect. 3) (Gradenigo 1904). In the early stages, obliteration of the petrous apex air cells with fluid, in association with otomastoid disease is seen. In the later stages, additional bony destruction with trabecular breakdown and cortical erosions is present, reflecting the degree of underlying osteomyelitis (Fig. 29a). All these changes are readily visible on CT. Petrous apicitis is prone for intracranial complications such as epidural or brain abscess formation,

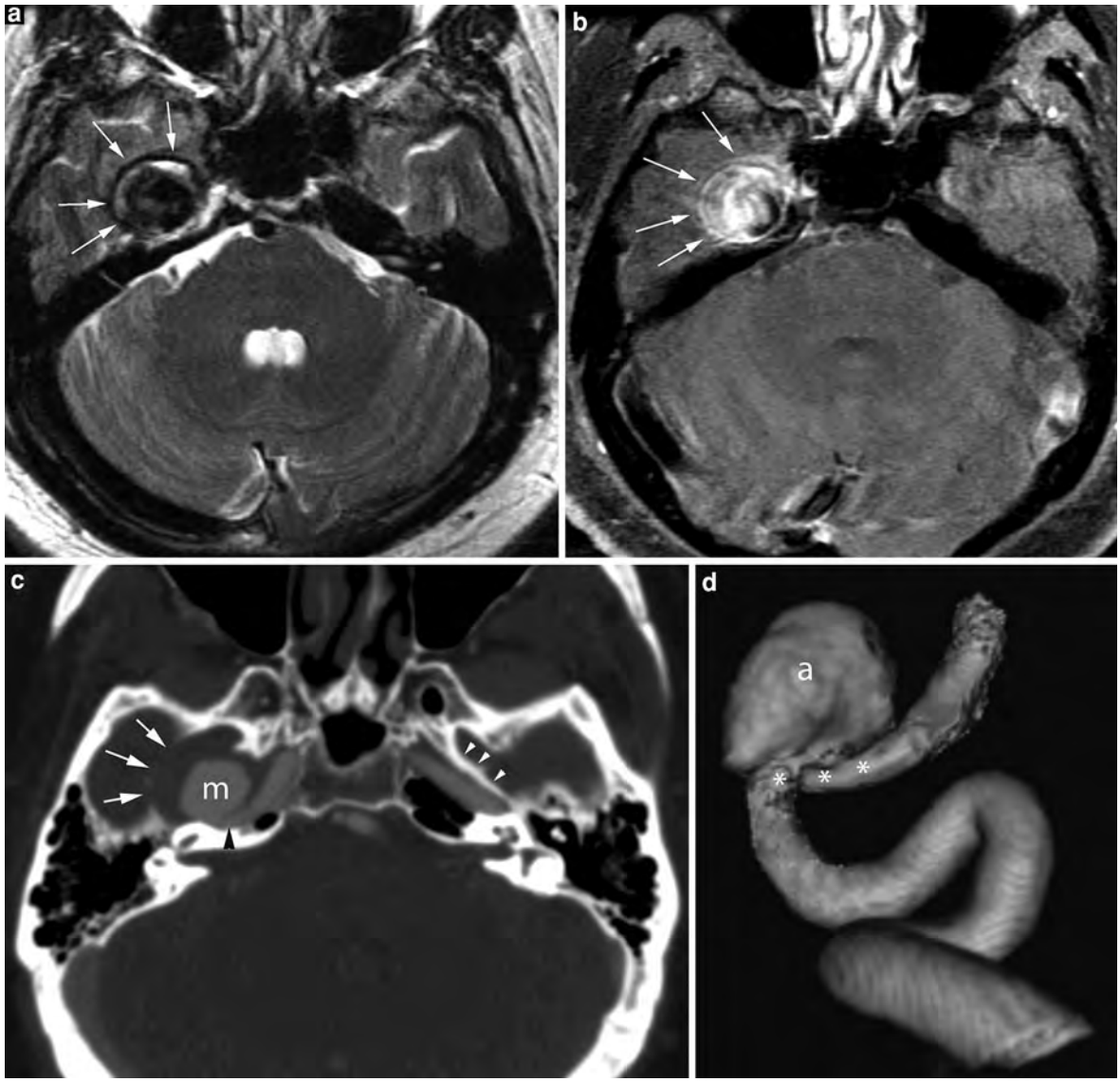

Fig. 28 These images are from a 76-year-old male patients who underwent MR examination for dementia. Axial T2-weighted image (**a**) shows a round and well-defined mass (*arrows* in **a**) of mixed signal intensity centered within the petrous apex. The mass (*arrows* in **b**) shows marked heterogeneous enhancement on the contrast-enhanced fat suppressed T1-weighted image (**b**). The imaging findings were therefore suspicious for an aneurysm of the petrous segment of the internal carotid artery and the patient underwent CT angiography for further evaluation. The contrast-enhanced source image displayed in an intermediate window (**c**) shows extensive lateral bowing of the lateral wall of the internal carotid canal on the right (*white arrows* in **c**) when compared to the left (*white arrowheads* in **c**) caused by a centrally markedly enhancing mass (*m* in **c**) that is contiguous with the internal carotid artery (*black arrowheads* in **c**). The gap between the enhancing central component (*m* in **c**) and the bony bowing (*white arrows* in **c**) reflects the degree of mural thrombus. The maximal intensity projection (MIP) image (**d**) nicely displays the patent portion of the saccular aneurysm (*a* in **d**) arising from the petrous segment of the internal carotid artery (*stars* in **d**)

subdural empyema, meningitis and sinus thrombosis or thromboplebitis (Fig. 29b). These possible complications are usually better delineated with MR imaging. Petrous apicitis, in particular when associated with osteomyelitis or intracranial complications, represents a surgical emergency requiring

Fig. 29 Axial CT image displayed in bone window (**a**) demonstrates marked dehiscence of the bony cortex (*arrows* in **a**) and fragmented appearance of the petrous apex on the left when compared to the right (*arrowheads* in **a**). The contrast-enhanced axial CT image displayed in soft tissue window shows an extra-dural fluid accumulation with marked ring enhancement (*arrows* in **b**). The constellation of the imaging findings together with fever and signs of otitis media on clinical examination are consistent with petrous apicitis complicated by an epidural abscess that was surgically proven

debridement of the petrous apex and drainage of possible abscesses or empyemas. However, recently, successful conservative treatment of uncomplicated petrous apicitis with new antibiotics has been reported (Burston et al. 2005).

6 Imaging Protocols

In view of the broad variety of lesions that can involve the skull base, it is not surprising that there is no single imaging protocol that fits all these entities. The imaging protocol will primarily depend upon availability, presenting symptoms, patient's history and extent of tumor. Overall, CT is usually the study of first choice as it is widely available and easily accessible. Based on symptoms, MR should be the initial diagnostic study for patients with cranial neuropathies, while CT is primarily reserved as a screening tool for more non-specific symptoms such as headaches and dizziness. Presence of risk factors for a certain disease process (e.g. chronic otomastoiditis or neurofibromatosis), or a history of underlying malignancy in combination with the clinical presentation, might raise the suspicion for a specific entity that it is better evaluated with one or the other imaging tool. The extent of the tumor is usually unpredictable based on clinical examination alone and therefore, review of the images while the patient is still on the scanner with immediate modification of the imaging protocol represents the most optimal work-up of patients with skull base lesions. Despite most optimal image quality a significant number of patients will end up with both—CT and MR—studies for narrowing of the differential diagnostic considerations and better delineation of the tumor margins (Figs. 13, 18, 21, 22).

Although no specific protocol is given here, the following issues need to be considered or followed to facilitate the most optimal quality of a cross-sectional study: CT and MRI should be obtained as a high resolution study with a small field of view (8–14 cm) that is coned down to the area of interest, such as the central skull base or temporal bone. The images should be performed with contiguous slices. It is recommended that CT images are acquired with a slice thickness of 1 mm or less in bone algorithm for optimal display of the bony details of the skull base. In the era of interactive capabilities of the picture archive computer system (PACS) such thin sections are also desirable in soft tissue algorithm to allow high quality multi-planar reformations that facilitate

better delineation of the lesion from adjacent anatomical structures. In contrast, such thin slices are not feasible nor desirable with MR, as the signal to noise would be too low and/or the imaging time too long. Therefore, MR images should be obtained with a slice thickness of 3 mm (Casselman 2005). When a large lesion is present, the slice thickness might need to be increased to 4 mm to be able to cover the entire tumor in a reasonable time frame.

High resolution fast spin-echo T2- and standard T1-weighted images, without and with intravenous contrast administration sequences, should be performed in axial and coronal planes (Casselman 2005). Some tumors also benefit from sagittal imaging, such as chordomas. The standard T1-weighted images without contrast agent are most sensitive for bony invasion, while the T2-weighted images are very helpful in delineation of the outer tumor margins (Figs. 13a, b, 23). Post-contrast agent T1-weighted images are most useful for evaluation of involvement of adjacent soft tissues (Fig. 23). Utilization of fat suppression techniques in the skull base is controversial as it is hampered by loss of most of the anatomical landmarks, and is predisposed for susceptibility artifacts. In addition, the suppression of fat makes the typically high signal difference between tumor and adjacent fatty bone marrow disappear on the plain images, and the detectibility of a lesion on the contrast-enhanced images will depend upon the degree of intra-lesional contrast accumulation. Therefore, it is advisable to obtain standard plain T1-weighted images without fat suppression in at least one imaging plane (preferentially the axial plane) that would supplement the fat suppressed images. Additional imaging sequences such as heavily T2-weighted high resolution volumetric acquisitions or MR angiography/venography might also be considered for further evaluation of the cisternal portions of the cranial nerves or of the intracranial vasculature, respectively. It is also recommended to perform larger field of view images (20–22 cm) through the entire head in non-enhanced T1 and fluid attenuation inversion recovery (FLAIR) weighing that could serve as an overview for optimal positioning of the subsequently acquired high resolution images; these would allow detectibility of additional lesions as well as possible complications related to the skull base mass such as infarction at the same time. Additional DWI through the entire head might not only further characterize the age of potential infarction, but also narrow the differential diagnosis in some instances.

7 Radiologist's Role

The radiologist's main role pretreatment is the delineation of the extent of the suspected malignant skull base lesion, including delineation of possible involvement of the neurovascular structures. Narrowing of the differential diagnostic considerations is certainly desirable but not as critical as the tumor extent. The radiologist might offer biopsy of a lesion when a soft tissue component is present below the skull base that is accessible for biopsy with CT guidance. Central skull base lesions can be often reached by placement of a guiding needle through the mandibular notch or through the buccal space along the anterior margin of the mandibular ramus. However, CT guided biopsy of the bony skull base itself is difficult due to the high frequency of traversing nerves and vessels.

During the treatment phase, the interventional radiologist might perform intra-arterial embolization of a vascular tumor prior to surgical resection or treat a petrous segment internal carotid aneurysm with balloon/coil occlusion.

Posttreatment imaging is critical as surgical resections are often subtotal in extent and radiation therapy may leave residual masses of unknown activity. To facilitate the radiologist's ability to detect recurrent tumor as soon as possible, it is advisable to obtain a baseline CT and/or MR study approximately 6 weeks following treatment, and to perform the subsequent follow-up examinations with the same imaging protocol and technique.

References

Aikele P, Kittner T, Offergeld C, Kaftan H, Huttenbrink KB, Laniado M (2003) Diffusion-weighted MR imaging of cholesteatoma in pediatric and adult patients who have undergone middle ear surgery. Am J Roentgenol 181: 261–265

Azar-Kian B, Sarwar M, Marc JA, Schlechter MM (1974) Intraosseous meningioma. Neuroradiology 6:246–253

Barber B, Ingram M, Khan S, Bano G, Hodson S, Vlahos I (2011) Clinicoradiological manifestations of paraganglioma syndromes associated with succinyl dehydrogenase enzyme mutation. Insights Imaging 2(4):431–438

Bolger WE, Reger C (2003) Temporal lobe encephalocele appearing as a lytic lesion of the skull base and pterygoid process. Ear Nose Throat J 82:268–272

Bomanji JB, Hyder SW, Gaze MN, Gacinovic S, Costa DC, Coulter C, Ell PJ (2001) Functional imaging as an aid to decision-making in metastatic paraganglioma. Br J Radiol 74:266–269

Bourgouin PM, Tampieri D, Robitaille Y, Robert F, Bergeron D, del Carpio R, Melancon D, Ethier R (1992) Low-grade myxoid chondrosarcoma of the base of the skull: CT, MRI, and histopathology. J Comput Assist Tomogr 16:268–273

Brewis C, Bottrill ID, Wharton SB, Moffat DA (2000) Metastases from glomus jugulare tumours. J Laryngol Otol 114:17–23

Brodeur GM, Castleberry RP (2001) Neuroblastoma. In: Pizzo PA, Poplack DG (eds) Principles and practice of pediatric oncology. Lippincott Williams & Wilkins, Philadelphia, p 796

Burston BJ, Pretorius PM, Ramsden JD (2005) Gradenigo's syndrome: successful conservative treatment in adult and paediatric patients. J Laryngol Otol 119:325–329

Carlotti CG Jr, Drake JM, Hladky JP, Teshima I, Becker LE, Ruthka JT (1999) Primary Ewing's sarcoma of the skull in children utility of molecular diagnostics, surgery and adjuvant therapies. Pediatr Neurosurg 31:307–315

Casselman JW (2005) The skull base: tumoral lesions. Eur Radiol 15:534–542

Chong VFH, Fan YF (1998) Radiology of the sphenoid bone. Clin Radiol 53:882–893

Choyke PL, Glenn GM, Walther MM, Patronas NJ, Linehan WM, Zbar B (1995) Von Hippel Lindau disease: genetic, clinical and imaging features. Radiology 146:629–642

Crawford TS, Kleinschmidt-DeMasters BK, Lillehei KO (1995) Primary intraosseous meningioma (Case report). J Neurosurg 83:912–915

Cummings TJ, George TM, Fuchs HE, McLendon RE (2004) The pathology of extracranial scalp and skull masses in young children. Clin Neuropathol 23:34–43

De Foer B, Vercruysse JP, Pilet B, Michiels J, Vertiest R, Pouillon M, Somers T, Casselman JW, Offeciers E (2006) Single-shot, turbo spin-echo, diffusion-weighted imaging versus spin-echo-planar, diffusion-weighted imaging in the detection of acquired middle ear cholestatoma. Am J Neuroradiol 27:480–482

De Foer B, Vercruysse JP, Bernaerts A et al (2010) Middle ear cholesteatoma: non-echo-planar diffusion-weighted MR imaging versus delayed gadolinium-enhanced T1-weighted MR imaging—value in detection. Radiology 255:866–872

Dhepnorrarat RC, Wood B, Rajan GP (2009) Postoperative non-echo-planar diffusion-weighted magnetic resonance imaging changes after cholesteatoma surgery: implications for cholesteatoma screening. Otol Neurotol 30:54–58

DiNardo LJ, Wetmore RF (1989) Head and neck manifestations of histocytosis-X in children. Laryngoscope 99:721–724

Erdem E, Angtuaco EC, Van Hemert R, Park JS, Al-Mefty O (2003) Comprehensive review of intracranial chordomas. Radiographics 23:995–1009

Evans HL, Ayala AG, Romsdahl MM (1977) Prognostic factors in chondrosarcoma of bone: a clinicopatholgogic analysis with emphasis on histologic grading. Cancer 40:818–831

Farrior B, Kampsen E, Farrior JB (1981) The positive pressure of cholesterol granuloma idiopathic blue eardrum: differential diagnosis. Laryngoscope 91:1286–1296

Filippi CG, Edgar MA, Ulug AM, Prowda JC, Heier LA, Zimmerman RD (2001) Appearance of meningiomas on diffusion-weighted images: correlating diffusion constants with histopathologic findings. Am J Neuroradiol 22:65–72

Forsyth PA, Cascino TL, Shaw EG, Scheithauer BW, O'Fallon JR, Dozier JC, Piepgras DG (1993) Intracranial chordomas: a clinocopathological and prognostic study of 51 cases. J Neurosurg 78:741–747

Gandour-Edwards R, Kapadia SB, Janecka IP, Martinez AJ, Barnes L (1995) Biologic markers of invasive pituitary adenomas involving the sphenoid sinus. Mod Pathol 8:160–164

Garg V, Temin N, Hildenbrand P, Silverman M, Catalano PJ (2010) Inflammatory pseudotumor of the skull base. Otolarngol Head Neck Surg 142:129–131

Garland LH (1945) Osteogenic sarcoma of the skull. Radiology 45:45–48

Goldofsky E, Hoffman RA, Holliday RA, Cohen NL (1991) Cholestrol cyst of the temoporal bone: diagnosis and treatment. Ann Otol Rinol Laryngol 100:181–186

Gorham LW, Wrighte AW, Schulz HH, Maxon FC (1954) Disappearing bones: a rare form of massive osteolysis, report of two cases, one with autopsy findings. Am J Medicine 17:674–681

Gormley WB, Tomecek FJ, Qureshi N, Malic GM (1994) Craniocerebral epidermoid and dermoid tumours: a review of 32 cases. Acta Neurochir (Wien) 128:115–121

Gradenigo G (1904) Sulla leptomeningite circonscritta e sulla paralisi dell' abducenta di origine otitica. Giornale dell'Accademia di medicina di Torino 10:59–84

Greenberg JJ, Oot RF, Wismer GL, Davis KR, Goodman ML, Weber AE, Montgomery WW (1988) Cholesterol granuloma of the petrous apex: MR and CT evaluation. Am J Neuroradiol 6:1205–1214

Guo AC, Cummings TJ, Dash RC, Provenzale JM (2002) Lyphomas and high-grade astrocytomas: comparison of water diffusibility and histological characteristics. Radiology 224:177–183

Hassounah M, Al-Mefty O, Akhtar M, Jenkins JR, Fox JL (1985) Primary cranial and intracranial chordosarcoma: a survey. Acta Neurosurgica 78:123–132

Howarth DM, Gilchrist GS, Mullan BP, Wiseman GA, Edmonson JH, Schomber PJ (1999) Langerhans cell histocytosis: diagnosis, natural history, management, and outcome. Cancer 85:2278–2290

Inserra MM, Pfeister M, Jackler RK (2004) Anatomy involved in the jugular foramen approach for jugulotympanic paragrangioma resection. Neurosurg Focus 17:41–44

Jabre A, Tabaddor R, Samaraweera R (2000) Transphenoidal meningoencephalocele in adults. Surg Neurol 54:183–187

Joseph M, Rajshekhar V, Chandy MJ (2004) Haematopoietic tissue presenting as a sphenoid sinus mass: case report. Neuroradiology 42:153–154

Kaufman B, Bellon EM (1973) The trigeminal nerve cistern. Radiology 108:597–602

Kozlowski K, Cambell J, Mc Alister W, Babyn P, Cama A, Masel J, Pelizza A, Taccone A (1991) Rare primary cranial

vault and base of skull tumours in children: report of 30 cases and short literature review. Radiol Med 81:213–224
Laigle-Donadey F, Taillibert S, Martin-Duverneuil N, Hildebrand J, Delattre JY (2005) Skull-base metastases. J Neurooncol 75:63–69
Lang FF, Macdonald OK, Fuller GN, DeMonte F (2000) Primary extradural meningiomas: a report of nice cases and review of literature from the era of computerized tomography scanning. J Neurosurg 93:940–950
Layer G, Steudal A, Schuller H, van Kaick G, Grunwald F, Riser M, Schild HH (1999) Magnetic resonance imaging to detect bone marrow metastases in the initial staging of small cell lung carcinoma and breast carcinoma. Cancer 85:1004–1009
Liu JK, Gottfried ON, Amini A, Couldwell WT (2004) Aneurysms of the petrous internal carotid artery: anatomy, origins, and treatment. Neursurg Focus 17:1–9
Loevner LA, Tobey JD, Yousem DM, Sonners AI, Hsu WC (2002) MR imaging characteristic of cranial bone marrow in adult patients with underlying systemic disorder compared with healthy control subjects. Am J Neuroradiol 23:248–254
Luff DA, Simmons M, Malik T, Ramsden RT, Reid H (2002) Endolymphatic sac tumours. J Laryngol Otol 116:398–401
Mascalchi M, Filippi M, Floris R, Fonda C, Gasparotti R, Villari N (2005) Diffusion-weighted MR of the brain: methodology and clinical application. Radiol Med (Torino) 109:155–197
Miller C, Lloyd TV, Johnson JC, Hunt WE (1978) Eosinophilic granuloma of the base of the skull: case report. J Neurosurg 49:464–466
Moore KL, Dalley AF (1999) Head and neck. In: Moore KL, Dalley AF (eds) Clinically oriented anatomy, 4th edn. Lippincott Williams & Wilkins, Philadelphia, pp 1093–1096
Mukherji SK, Castillo M (1996) Adenocarcinoma of the endolymphatic sac: imaging features and preoperative embolization. Neurordaiology 38:179–180
Mukherji SK, Baggett HC, Alley J, Carrasco VH (1998) Enlarged cochlear aqueduct. Am J Neuroradiol 19:330–332
Price T, Fayad G (2002) Abducens nerve palsy as the sole presenting symptom of petrous apicitis. J Laryngol Otol 116:726–729
Ragel BT, Couldwell WT (2004) Pituitary carcinoma: review of the literature. Neurosurg Focus 16:1–9
Rao AB, Koeller KK, Adair CF (1999) From the archives of the AFIP: Paragangliomas of the head and neck: radiologic–pathologic correlation. Radiographics 19:1605–1632
Robert Y, Carcasset S, Rocourt N, Hennequin C, Dubrulle F, Lamaitre L (1995) Congenital cholesteatoma of the temporal bone: MR findings and comparison with CT. Am J Neuroradiol 16:755–761
Rueda-Franco F, Lopez-Correla E (1995) Sarcomas in the central nervous system of children. Pediatric Neurosurg 22:49–56
Salvati M, Ciappetta P, Capone R, Santoro R, Raguso M, Raco A (1993) Osteosarcoma of the skull in a child: a case report and review of the literature. Childs Nerv Syst 9:437–439
Satter EK, High WA (2008) Langerhans cell histiocytosis: a review of the current recommendations of the Histiocyte Society. Pediatr Dermatol 25:291–295
Schmalfuss IM (2009) Petrous Apex. Neuroimaging Clin N Am 19:367–391
Schmalfuss IM, Camp M (2008) Skull Base: normal variants and Pseudolesions. Eur Radiol 18:1232–1243
Sen C, Hague K, Kacchara R, Jenkins A, Das S, Catalano P (2001) Jugular foramen: microscopic anatomic features and implications for neural preservation with reference to glomus tumors involving the temporal bone. Neurosurgery 48:838–847
Shinoda J, Kimura T, Funakoshi T, Iwata H, Tange K, Kasai C, Miyata Y (1993) Primary osteosarcoma of the skull. J Neurooncol 17:81–88
Smirniotopoulos JG, Chiechi MV (1995) Teratomas, dermoid, and epidermoids of the head and neck. Radiographics 15:1437–1455
Stone JA, Cooper H, Castillo M, Mukherji SK (2001) Malignant schwannoma of the trigeminal nerve. Am J Neuroradiol 22:505–507
Tauber M, van Loveren HR, Jallo G, Romano A, Keller JT (1999) The enigmatic foramen lacerum. Neurosurgery 44:386–391
Tokgoz N, Oner YA, Kaymaz M, Ucar M, Yilmaz G, Tali TE (2005) Primary intraosseous meningioma: CT and MRI appearance. Am J Neuroradiol 26:2053–2056
Tunaci M, Tunaci A, Engin G, Ozkorkmaz B, Dincol G, Acunas G, Acunas B (1999) Imaging features of thalassemia. Eur Radiol 9:1804–1809
Turner OA, Laird AT (1966) Meningioma with traumatic etiology. J Neurosurg 24:96–98
Utz JA, Krandorf MJ, Jelinek JS, Moser RP Jr, Berrey BH (1989) MR appearance of fibrous dysplasia. J Comput Assist Tomogr 13:845–851
Van Tassel P, Lee YY, Ayala A, Carrasco CH, Klima T (1991) Case report 680: intraosseous meningioma of the sphenoid bone. Skeletal Radiol 20:383–386
Whitehead RE, Melhem ER, Kasznica J, Eustace S (1998) Telangiectatic osteosarcoma of the skull base. Am J Neuroradiol 19:754–757
Williams LS, Schmalfuss IM, Sistrom CL, Inoue T, Tanaka R, Seoane ER, Mancuso AA (2003) MR imaging of the trigeminal ganglion, nerve and the perineural vascular plexus: normal appearance and variants with correlation to cadaver specimens. Am J Neuroradiol 24:1317–1323
Williamson RA, Paueksakon P, Coker NJ (2003) Inflammatory pseudotumor of the temporal bone. Otol Neurotol 24:818–822
Yildirim T, Agildere AM, Oguzkurt L, Barutcu O, Kizilkilic O, Kocak R, Alp Niron E (2005) MRI evaluation of cranial bone marrow signal intensity and thickness in chronic anemia. Eur J Radiol 53:125–130

Thyroid and Parathyroid Neoplasms

Polly S. Richards

Contents

Abstract

This chapter offers an overview of the epidemiology and aetiology, clinical and histological characteristics and classification, and staging of thyroid and parathyroid neoplasms before providing a more focused and illustrated description of the imaging findings. The indications and the role of ultrasound, ultrasound-guided fine needle aspiration, cross-sectional modalities and ^{18}F-FDG-PET in the diagnosis and follow-up of thyroid cancer are discussed, with reference to the particular imaging characteristics of different tumour types. The embryology of parathyroid gland development is addressed and the relative advantages of ultrasound, scintigraphy, cross-sectional modalities and percutaneous venous sampling in the management of hyperparathyroidism are described.

1 Thyroid Neoplasms

1.1 Introduction

The primary role of imaging in thyroid cancer is to distinguish between benign and malignant nodules, with the emphasis on ultrasound (US) and US-guided fine needle aspiration cytology (US-FNAC). Palpable thyroid nodules are present in 3–7% of the population but the incidence of benign nodular thyroid disease detected by high resolution US is probably over 60%, being highest in elderly women. Biologically significant thyroid cancers (those over 10 mm in size or associated with lymphadenopathy) are rare and the

P. S. Richards (✉)
Imaging KGV Wing, St Bartholomew's Hospital, West Smithfield, London, EC1A 7BE, UK
e-mail: Polly.Richards@bartsandthelondon.nhs.uk

R. Hermans (ed.), *Head and Neck Cancer Imaging*, Medical Radiology. Diagnostic Imaging,
DOI: 10.1007/174_2011_387, © Springer-Verlag Berlin Heidelberg 2012

prognosis is excellent. By comparison, microcarcinomas are common. The majority of these occult tumours are thought to be clinically insignificant, much in the same way that small prostate cancers appear to be in elderly men.

The investigation and management of thyroid nodules is controversial, but the ideal diagnostic pathway must be a balance between treating all biologically aggressive carcinomata and keeping the number of unnecessary diagnostic hemithyroidectomies and associated morbidity, anxiety and cost to a minimum. Pre-operative staging will depend on the histology of the tumour, but in the majority of cases it is not exhaustive. Imaging also has a role in the follow-up of patients treated for thyroid cancer.

1.2 Epidemiology and Aetiology

Thyroid cancer accounts for ~1% of all malignancies and causes around 0.5% of cancer deaths. The incidence is greater in women, peaking at 25–35 years. Thyroid cancer is rarest in childhood and adolescence but tends to present at a more advanced stage. However, due to a lower incidence of benign thyroid nodules in men and children, the risk of any single nodule being malignant in these groups is increased (Richards et al. 2010).

As most thyroid cancers are indolent in nature, their true incidence is likely to be higher than actually diagnosed; indeed, it is generally accepted that clinically occult papillary carcinomata under 1 cm in size are much more common. In a cadaveric series, microcarcinomas were reported in up to 38% of autopsy cases where death was due to an unrelated cause (Harach et al. 1984). Advances in US and US-FNAC techniques have resulted in greater detection of these occult cancers and may explain why thyroid malignancy has reportedly increased 2.4-fold over the last 30 years while 20-year survival has remained unchanged over the same period (Kent et al. 2007).

There is a geographical variation in the incidence of thyroid cancer, which is 15 times as common in Iceland and Hawaii than Northern Europe, thought to be due to dietary and environmental rather than genetic factors. Thyroid cancer is most common where the diet is iodine-rich but there is an increased proportion of follicular and anaplastic carcinomata in regions where dietary iodine is deplete (Richards et al. 2010).

Familial thyroid cancers occur and there is a genetic predisposition in the multiple endocrine neoplasia (MEN) syndromes, dyshormonogenesis and other inherited conditions such as Cowden disease and Gardner syndrome. An increased incidence of malignancy in nodules coexisting with Graves' disease has been suggested and Hashimoto's thyroiditis is associated with primary thyroid lymphoma.

There is a linear dose–response relationship between irradiation and the development of cancer. This is especially significant if received at a young age or if low-dose radiotherapy has been used (such as was once given for conditions ranging from adenoidal hypertrophy to thymic enlargement and tinea capitis) and is associated with a 40-fold increased risk. Higher-dose radiation treatment, including external beam radiotherapy and ^{131}I treatment for Graves' disease, is not associated with cancer induction (Richards et al. 2010).

Other aetiological factors include alcohol consumption and pregnancy. It has been postulated that this is due to transformation of indolent microcarcinomas by unknown endogenous or environmental factors. It is uncertain whether follicular adenomata have a tendency for malignant transformation, although it seems unlikely, as these are common lesions whereas follicular carcinoma is rare.

1.3 Classification and Staging

Primary thyroid cancer can arise from several different cell types and histological classification is an important determinant of prognosis. There are four main types of thyroid cancer: tumours arising from thyroid cells, ranging from papillary and follicular to anaplastic; medullary cancer arising from parafollicular C cells; primary thyroid lymphoma (PTL); and rare tumours arising from the stromal cells of the gland, such as sarcoma (Table 1, Hedinger et al. 1988). The International Union Against Cancer (UICC) TNM staging definitions for thyroid cancer are detailed in Table 2 (Sobin et al. 2009). Separate stage groupings are recommended for papillary, follicular, medullary and anaplastic carcinomata. All anaplastic carcinomata are considered stage IV disease.

Table 1 WHO histological classification of thyroid cancer (Hedinger et al. 1988)

Papillary carcinoma
Papillary/follicular carcinoma
Follicular carcinoma
Hürthle cell carcinoma
Medullary carcinoma
Anaplastic carcinoma
Small-cell carcinoma
Giant-cell carcinoma
Others
Lymphoma
Sarcoma
Carcinosarcoma
Secondary tumours
For clinical management thyroid cancer is generally divided into two categories: well differentiated or poorly differentiated

Table 2 UICC TNM classification of malignant tumours (Sobin et al. 2009)

Primary tumour (T)	
TX	Primary tumour cannot be assessed
T0	No evidence of primary tumour
T1	Tumour <2 cm in greatest dimension limited to the thyroid
T1a	Tumour ≤1 cm, limited to the thyroid
T1b	Tumour >1 cm but ≤2 cm in greatest dimension, limited to the thyroid
T2	Tumour >2 cm but not >4 cm in greatest dimension limited to the thyroid
T3	Tumour >4 cm in greatest dimension limited to the thyroid or any tumour with minimal extrathyroid extension (e.g. extension to sternothyroid muscle or perithyroid soft tissues)
T4a	Moderately advanced disease. Tumour of any size extending beyond the thyroid capsule to invade subcutaneous soft tissues, larynx, trachea, oesophagus or recurrent laryngeal nerve
T4b	Very advanced disease. Tumour invades prevertebral fascia or encases carotid artery or mediastinal vessels
All categories may be subdivided: (s) solitary tumour and (m) multifocal tumour (the largest determines the classification)	
All anaplastic carcinomata are considered T4 tumours	
T4a	Intrathyroidal anaplastic carcinoma
T4b	Anaplastic carcinoma with gross extrathyroid extension
Regional lymph nodes (N)	
Regional lymph nodes are the central compartment, lateral cervical, and upper mediastinal lymph nodes	
NX	Regional lymph nodes cannot be assessed
N0	No regional lymph node metastases
N1	Regional lymph node metastases
N1a	Metastases to Level VI (pretracheal, paratracheal and prelaryngeal/Delphian lymph nodes)
N1b	Metastases to unilateral, bilateral or contralateral cervical (Levels I, II, III, IV or V) or retropharyngeal or superior mediastinal lymph nodes (Level VII)
Distant metastases (M)	
MX	Distant metastases cannot be assessed
M0	No distant metastases
M1	Distant metastases

1.4 Imaging at Diagnosis

1.4.1 Indications for Imaging

The primary role of imaging in the diagnosis of thyroid cancer revolves around the assessment of nodules with US and FNAC. High frequency linear array transducers give such high spatial resolution that nodules as small as 1–2 mm can be easily detected. Nodules over 4 or 5 mm in size can be characterised with both grey-scale and Doppler and if necessary biopsied for FNAC. Lymph node staging in proven cases of malignancy is also largely by US, although cross-sectional and radionuclide techniques come into play to delineate the extent of local invasion, detect distant metastatic disease, and in the assessment of tumour recurrence. Scintigraphy is largely reserved for the detection of nodal and distant metastases and recurrence.

It is not appropriate to screen for thyroid cancer unless there are clinical factors known to increase the risk of cancer. Clinical assessment (including thyroid function) is all that is required to reassure the majority of patients with palpable nodules, without the need for further investigation. The clinical indications for US are summarised in Table 3.

1.4.2 Sonographic Characterisation of Thyroid Nodules

US can accurately locate, quantify and measure thyroid nodules but also allows for a degree of grey-scale characterisation. Much has been written about the ability of US to predict malignancy (Cappelli et al. 2007; Lin et al. 2005; Papini et al. 2002). The most specific grey-scale characteristic of thyroid cancer is microcalcification (86–96%). This is manifested by

Table 3 Clinical Indications for US

Age	Elderly (>70 years) and young (<14 years) at increased risk
Sex	Level of suspicion is higher in men
Onset	Rapid growth of a mass over a few weeks should initiate urgent FNAC. Masses developing over a few days usually result from haemorrhage into a benign nodule or cyst
Texture	Firm or hard on palpation
Solitary nodules	The risk of malignancy in any one nodule increases as the number of nodules in the gland decreases, although the overall risk of cancer per thyroid gland is constant, regardless of number of nodules present
Lymphadenopathy	
Signs of local	
Invasion	Fixation, dysphonia, dysphagia or dyspnoea
Family history	
Previous neck irradiation	

multiple small intranodular hyperechoic flecks with little or no posterior acoustic enhancement and is believed to correlate to psammoma bodies (Fig. 1a–c). As with all grey-scale features however, microcalcification has low sensitivity (26–59%) and therefore the overall diagnostic accuracy is reduced to around 85% (Cappelli et al. 2007).

As no single US feature has a high enough positive predictive value for cancer to reliably dictate which nodules should undergo FNAC, research has been directed towards the use of multiple US criteria in various combinations (Cappelli et al. 2007; Papini et al. 2002). In general, these studies point to the same few features that are significantly more common in malignant nodules: microcalcification (Fig. 1a–c), irregular margins (Fig. 2), hypoechogenicity compared to background thyroid tissue, tall shape (antero-posterior/transverse diameter ratio >1) and solidity (Cappelli et al. 2005, Fig. 3). The finding of two or more suspicious characteristics significantly increases the risk of cancer, as does the presence of extra-capsular extension (Fig. 4) and lymphadenopathy (Kim et al. 2002).

Although the majority of cystic nodules are benign and the majority of cancers are solid, a small proportion (~15%) of papillary thyroid cancer (PTC) can be macrocystic (Hatabu et al. 1991; Kessler et al. 2003, Fig. 5). For this reason it is important to sample the solid component of complex solid/cystic lesions as well as the fluid. Chaotic intranodular vascular pattern (Fig. 6a, b) and defects in or an absence of a hypoechoic halo may also have some predictive value (Fig. 7a, b, Papini et al. 2002).

The risk of any thyroid gland harbouring cancer is no longer thought to depend on the number of nodules present because, although the risk of cancer per nodule is lower in a multinodular goitre, it decreases in proportion to the number of nodules in the gland such that the overall rate of cancer per patient remains similar to that of a patient with a truly solitary nodule (Gharib et al. 2010). Nearly half of all clinically solitary nodules turn out to be multiple at US. As the risk of malignancy in a sonographically proven solitary nodule is highest, these should undergo FNAC (Leenhardt et al. 2002).

It is clearly established that nodule size is a poor indicator of cancer: around 30% of thyroid cancers are non-dominant within a multinodular goitre and the prevalence of cancer appears to be the same in palpable and non-palpable nodules at around 6% (Gharib et al. 2010). Strategies based on FNAC of palpable or dominant nodules are therefore inappropriate. Rather, cytological sampling of a multinodular goitre should be driven by sonographic appearances and often more than one nodule should be targeted.

1.4.3 US-Guided FNAC

US-FNAC of thyroid nodules and regional lymph nodes is simple to perform, has a low complication rate and causes minimal patient discomfort. There are no reported cases of seeding of malignant cells by FNAC of a thyroid cancer. Many differing techniques have been described for both acquiring and preparing FNA samples, but the technique adopted should take into account the reporting cytologist's preference (Baloch et al. 2008). US-FNAC is routinely performed without local anaesthetic at our institution, using either a 23- or 25- gauge venesection needle. Occasionally a spinal needle may be required for deeper lesions. No suction is applied and the material is drawn into the shaft of the needle by capillary action alone. This method produces a cellular sample with minimum haemodilution and a single pass is all that is required in most cases. In cases where suspicion of malignancy is high on US, a second pass is performed for calcitonin immunocytochemistry to aid

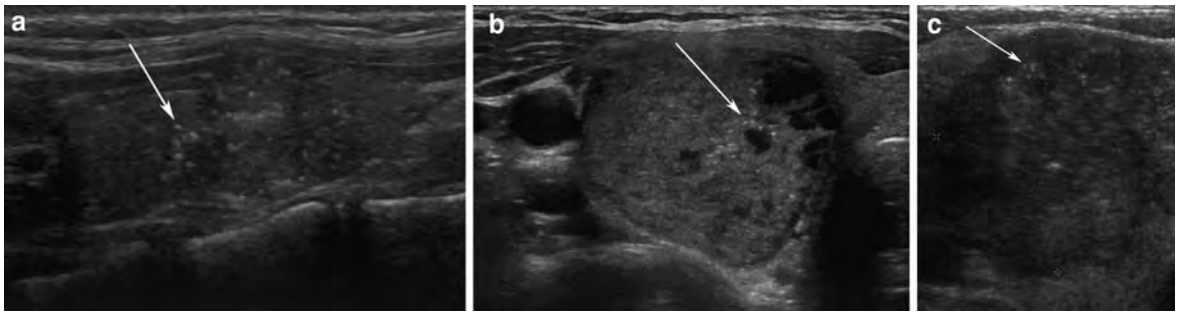

Fig. 1 **a–c** Punctate calcification on thyroid US (*arrow*) in three different cases of papillary thyroid carcinoma

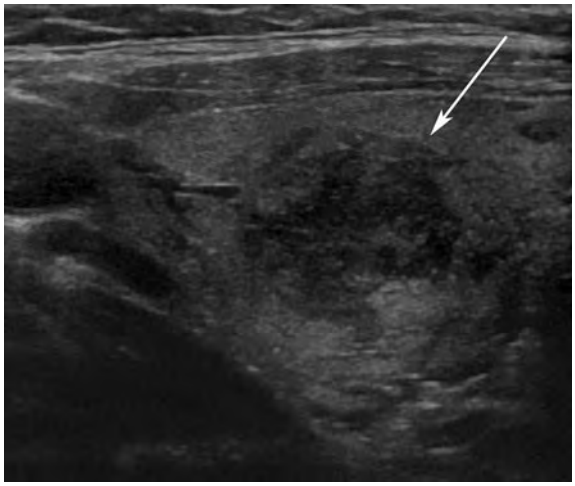

Fig. 2 Irregular, poorly defined nodular margins on thyroid US in a patient with macroscopically invasive follicular thyroid carcinoma

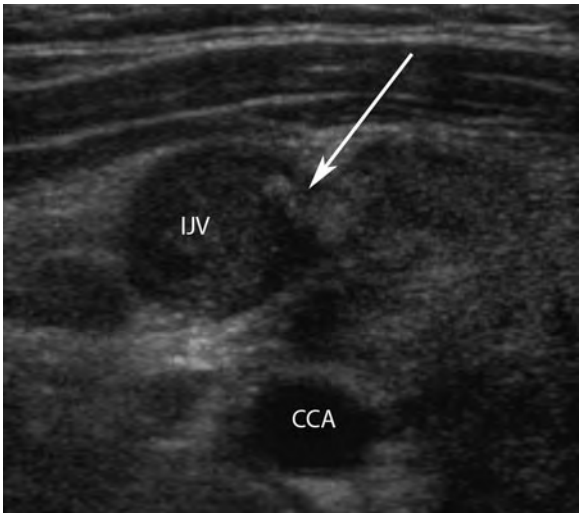

Fig. 4 Extracapsular extension into the carotid sheath by an anaplastic carcinoma of the right lobe of the thyroid with thrombosis of the internal jugular vein (*arrow*). CCA common carotid artery. IJV internal jugular vein

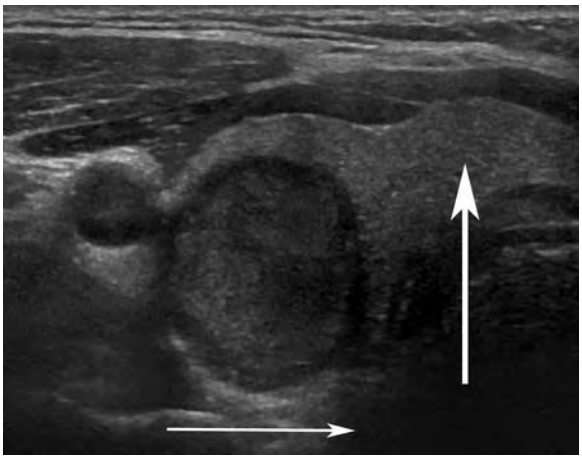

Fig. 3 Transverse thyroid US demonstrating papillary thyroid carcinoma with an antero-posterior dimension (*thick arrow*) greater than transverse (*thin arrow*)

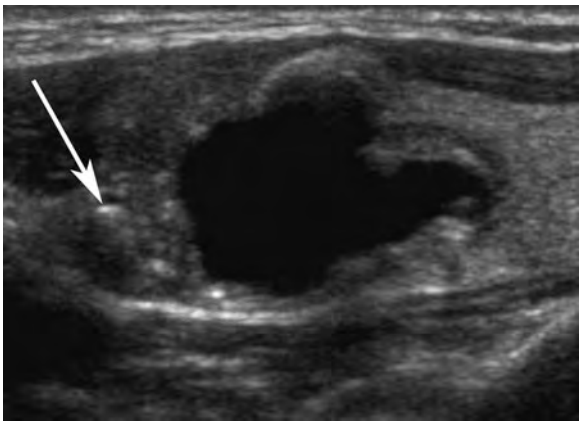

Fig. 5 Cystic papillary thyroid carcinoma on thyroid US with a mural thickening and irregularity demonstrating punctate calcification (*arrow*)

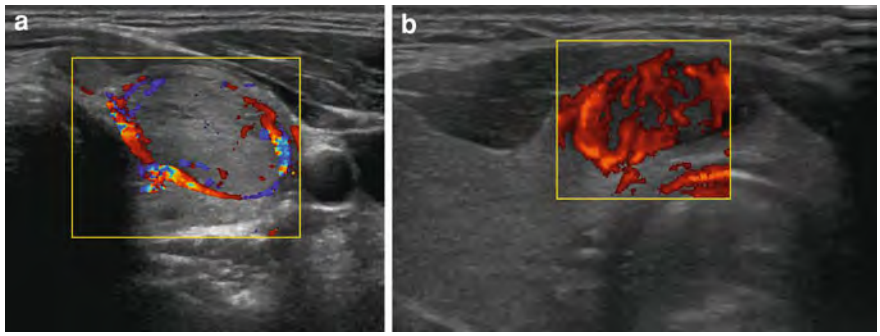

Fig. 6 Peripheral vascular distribution in a benign hyperplasic thyroid nodule on colour Doppler (**a**) and chaotic intranodular vascularity in a small follicular thyroid carcinoma on power Doppler (**b**)

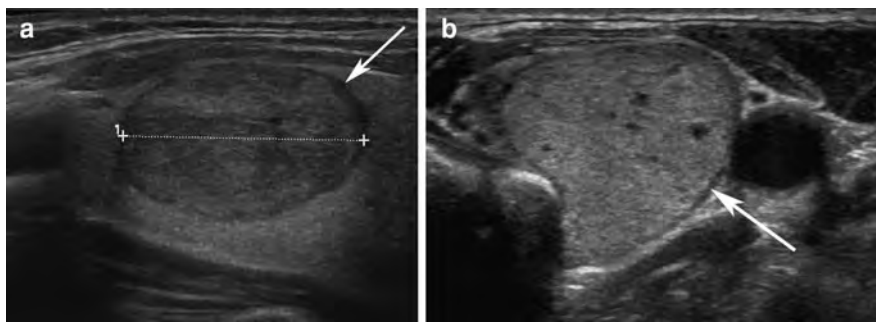

Fig. 7 **a**, **b** Thyroid US of two different follicular lesions demonstrating hypoechoic halos (*arrows*). Both lesions were follicular adenomata at histology

differentiation between papillary and medullary thyroid cancer. Core biopsy is useful to distinguish between poorly differentiated carcinoma and lymphoma, but is otherwise rarely required.

The reported sensitivity and specificity of thyroid FNAC ranges from 65 to 98% and 72 to 100%, respectively, with a positive predictive value of 50–96% (Cross et al. 2009). Thyroid FNAC samples are designated to six cytological categories (described in Table 4) along with an indication of the implied risk of malignancy (Cross et al. 2009; Ali and Cibas 2010). For a sample to be deemed adequate for diagnosis it must contain at least six groupings of well-preserved thyroid epithelial cells consisting of at least ten cells per group. Inadequate samples are classified as Class 1 and result from poor technique, haemodilution or the aspiration of cystic material. The reported rate of inadequate samples ranges from 2 to 21% with a mean of 17%. Repeat aspiration will result in a diagnostic sample in 50–60% and a delay of 2–3 months is recommended, unless there is clinical concern of malignancy (Gharib et al. 2010). The management of nodules that yield repeatedly inadequate samples should be decided on a case-by-case basis.

Class 3 samples contain follicular cells and include all follicular patterned lesions. If cells are abundant, with a paucity of colloid, this is suggestive of a follicular adenoma, but the possibility of a hyperplastic nodule, follicular variant papillary thyroid carcinoma or microinvasive follicular thyroid cancer (FTC) can only be excluded histologically, and diagnostic hemithyroidectomy is recommended (Gharib et al. 2010).

The decision to perform FNAC of a thyroid nodule should be a considered one because it commits the patient to a pathway with a significant chance of ending in hemithyroidectomy. This may be as high as 40% if surgery is performed whenever an FNAC sample is anything other than benign (Class 2). The ideal pathway is a balance between the chance of missing carcinomata of potential clinical aggressiveness and reducing the morbidity associated with unnecessary operations while keeping an eye on cost. Inconsistencies in opinion arise from the fact that not enough is yet known about how the diagnosis and treatment of microcarcinomas affect life expectancy and how the benefits of surgery compare to the risks.

The rising prevalence of microcarcinoma and the fact that nodal metastases, extracapsular extension

Table 4 ACE/AME/ETA thyroid nodule guidelines nomenclature (Cross et al. 2009; Ali and Cibas 2010)

AACE/AME/ETA thyroid nodule guidelines	Implied risk of malignancy (%)
Class I Non-diagnostic or unsatisfactory	0–10
Insufficient number of cells	
Other (obscuring blood, clotting artefact, etc.)	
Cyst fluid only	
Class II Benign	0–3
Includes hyperplastic nodule, colloid nodule, lymphocytic or granulomatous thyroiditis and benign cyst	
Class III Follicular lesion or atypia of undetermined significance	5–15
Class IV Follicular neoplasm or suspicious for a follicular neoplasm	15–30
Class V Suspicious for malignancy	60–75
Class VI Malignant	97–100

and aggressive histological features are sometimes seen with such small tumours has led to the suggestion that all sonographically visible nodules should undergo FNAC (Richards et al. 2010). Debate over the best strategy for the investigation and management of thyroid nodules has evolved over the last decade with the publication of several consensus statements and guidelines. More recently there has been a shift in attitude with more authorities advocating a less aggressive approach in view of the prevalence of benign nodules, the low incidence of biologically significant thyroid cancer and the fact that papillary carcinomata are so indolent (McDougall and Camargo 2007). Indeed in some institutions, including my own, a size threshold of 8–10 mm is applied to nodules with suspicious sonographic features below which US-FNAC is not performed, although patients are kept under regular sonographic review. The most recent guidelines from the American Association of Clinical Endocrinologists, Associazione Medici Endocrinologi and European Thyroid Association are recommended and provide a clear, comprehensive, evidence-based review which is beyond the scope of this chapter (Gharib et al. 2010).

1.4.4 Lymph Node Staging

US is the technique of choice for the assessment of cervical lymph nodes metastases in thyroid cancer. It has the highest spatial resolution of any imaging modality, allows assessment of internal nodal architecture and vascularity, and can be used to guide FNAC. Furthermore, both primary tumour and nodes can be evaluated at the same sitting. Metastatic nodes from differentiated thyroid cancer tend to be round and hypoechoic, with loss of the normal echogenic hilum and deranged vascularity. Nodal metastases in both papillary and medullary thyroid cancer (MTC) commonly demonstrate punctate calcification (Fig. 8a–c), and cystic components are a feature in 20% of metastatic nodes in PTC (Fig. 9). This may be so dominant as to be misinterpreted for a benign cervical cyst such as a branchial cleft cyst (King 2008).

1.4.5 Magnetic Resonance Imaging and Computed Tomography

Magnetic Resonance Imaging (MRI) and Computed Tomography (CT) characterisation of thyroid nodules and lymph nodes is poor. By comparison, these techniques are invaluable for the assessment of large tumour volume, retrotracheal and retrosternal extension, retropharyngeal and retrotracheal lymphadenopathy and the detection of local soft tissue and vascular invasion (Figs. 10 and 11). They also have a key role in the assessment of distant metastases to the lungs, liver and spine and in planning external radiotherapy (Miyakoshi et al. 2007; King 2008).

CT has greater spatial resolution than MRI over large volumes, is less prone to movement and pulsation artefact, and is the modality of choice for the assessment of mediastinal and pulmonary metastases. However, iodine-containing contrast temporarily blocks iodine uptake by follicular cells and will therefore delay subsequent radio-iodine scanning or therapy by at least 6 weeks. For this reason MRI is often the imaging modality of choice. CT remains the most useful adjunct to US for non-iodine avid tumours such as anaplastic carcinoma (AC) and medullary thyroid cancer, or when recurrent disease has become too poorly differentiated to take up iodine (Richards et al. 2010).

Thyroid nodules are common incidental findings on CT and MRI and have an uncertain risk of malignancy. A recent retrospective review of 122

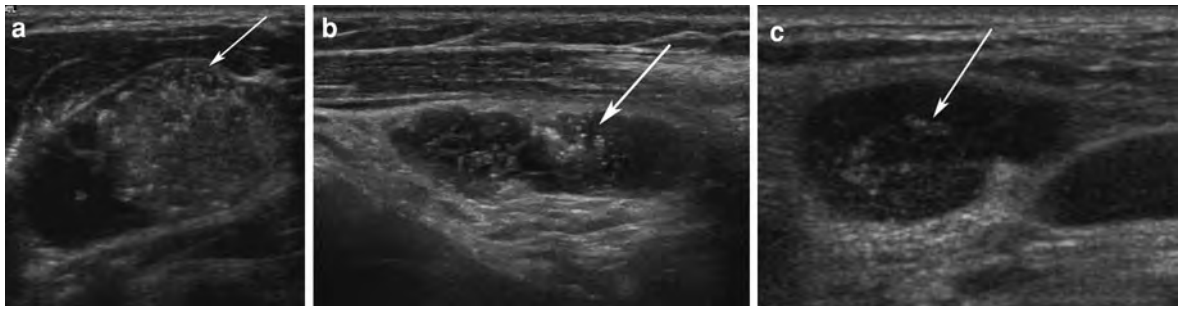

Fig. 8 **a–c** Three examples of metastatic cervical lymph nodes from papillary thyroid carcinoma demonstrating punctate calcification (*arrows*)

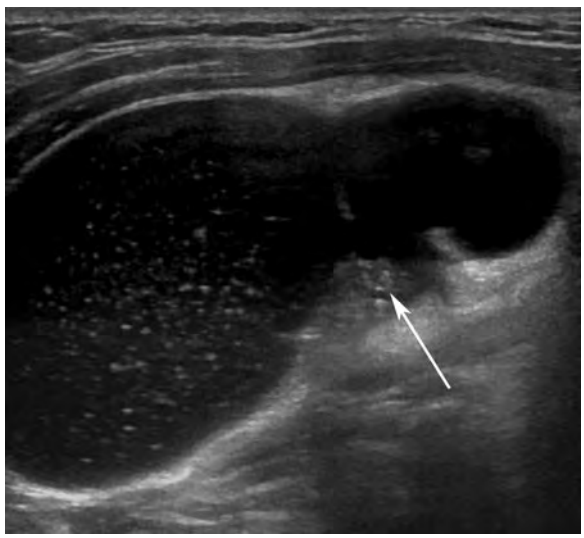

Fig. 9 Large metastatic cervical lymph node from papillary thyroid carcinoma which is largely cystic with a small mural nodule demonstrating punctate calcification (*arrow*)

Fig. 10 Axial contrast-enhanced CT of the thyroid demonstrating a large thyroid mass involving both lobes, with extracapsular extension and left internal jugular vein invasion (*arrow*). The trachea is displaced and the oesophagus is inseparable from the mass (*star*) which was an anaplastic carcinoma at histology

patients with incidental thyroid nodules detected on CT suggested the incidence of malignancy or potential malignancy was around 11% (Shetty et al. 2006), but there is no consensus on how to manage these patients. At our institution, size, age, thyroid function and other clinical risk factors are taken into consideration before committing patients to further work-up. Nodules under 1 cm are observed clinically.

1.4.6 Nuclear Medicine

The most widely used thyroid imaging agents are ^{123}I and ^{131}I, which are organified in thyroid follicles and therefore highly specific for thyroid tissue. Scintigraphy plays little role in the initial diagnosis of primary thyroid tumours, but radionuclides are useful in the detection of nodal and distant metastases and recurrence. Sensitivity depends on tumour volume and histology, and is reduced by increased total body iodine from diet, the use of intravenous iodinated contrast and some drugs such as amiodarone and carbimazole. ^{123}I produces the best whole body image quality in follow-up studies and is most sensitive for differentiated thyroid cancer metastases (Sarkar et al. 2002, Fig. 12). ^{131}I plays a major role in treatment.

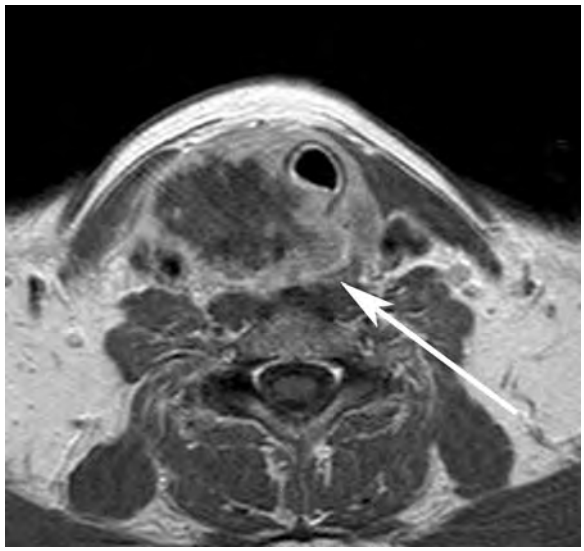

Fig. 11 T1-weighted axial MRI with gadolinium enhancement through the thyroid gland demonstrating an anaplastic carcinoma of the right thyroid with extracapsular extension and oesophageal invasion (*arrow*)

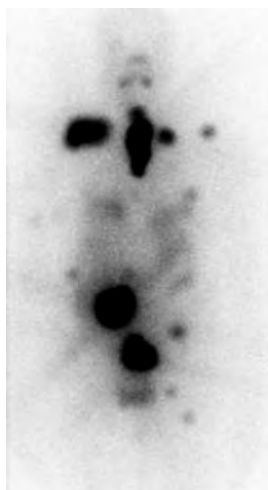

Fig. 12 ^{123}I whole body scintigraphy demonstrating widespread metastatic and nodal metastases from follicular thyroid carcinoma

A different spectrum of radioisotopes is required to assess medullary thyroid cancer. ^{111}In-labelled octreotide is the agent of choice (Fig. 13) and is excellent for demonstrating pulmonary metastases, but it is less sensitive for liver and lymph node metastases and false-positive uptake is seen in areas of inflammation and granulomatous disease.

Higher average 2-[F-18] fluoro-2-deoxy-D-glucose (^{18}F-FDG) uptake is seen in thyroid malignancies, but there is too great an overlap with benign adenomata

Fig. 13 ^{111}In-labelled octreotide scintigraphy abnormal uptake in a thyroid bed recurrence in a patient with medullary thyroid carcinoma (arrow).

for positron emission tomography (PET) to be useful in differentiating malignant from benign nodules (Robbins and Larson 2008). It has been shown to be useful in staging MTC and poorly differentiated thyroid cancers that are iodine non-avid (Fig. 14a–f). The reported sensitivity and specificity for localising MTC metastases when calcitonin levels are raised is 73–88% and 79–80%, respectively (Diehl et al. 2001; Zettinig et al. 2001; Finkelstein et al. 2008). Incidental focal thyroid uptake of both ^{18}F-FDG and ^{99m}Tc-sestamibi has a high risk of malignancy and these patients should be further assessed with US and FNAC (Eloy et al. 2009; Van den Bruel et al. 2002).

1.5 Clinical, Imaging and Histological Features, Treatment and Prognosis

1.5.1 Benign Thyroid Pathology

Typical imaging appearances of the various thyroid malignancies are described below but it is also important to mention benign nodular hyperplasia, as the vast majority of thyroid nodules will be hyperplastic. Histologically hyperplastic nodules reflect waves of focal hyperplasia and involution of thyroid tissue and are often filled with microcysts and colloid-laden follicles. Their sonographic appearance is very variable. Most often they are well-defined hypoechoic or isoechoic lesions with a spongiform texture manifested by multiple echogenic striations (Fig. 15). Frank cystic or haemorrhagic degeneration

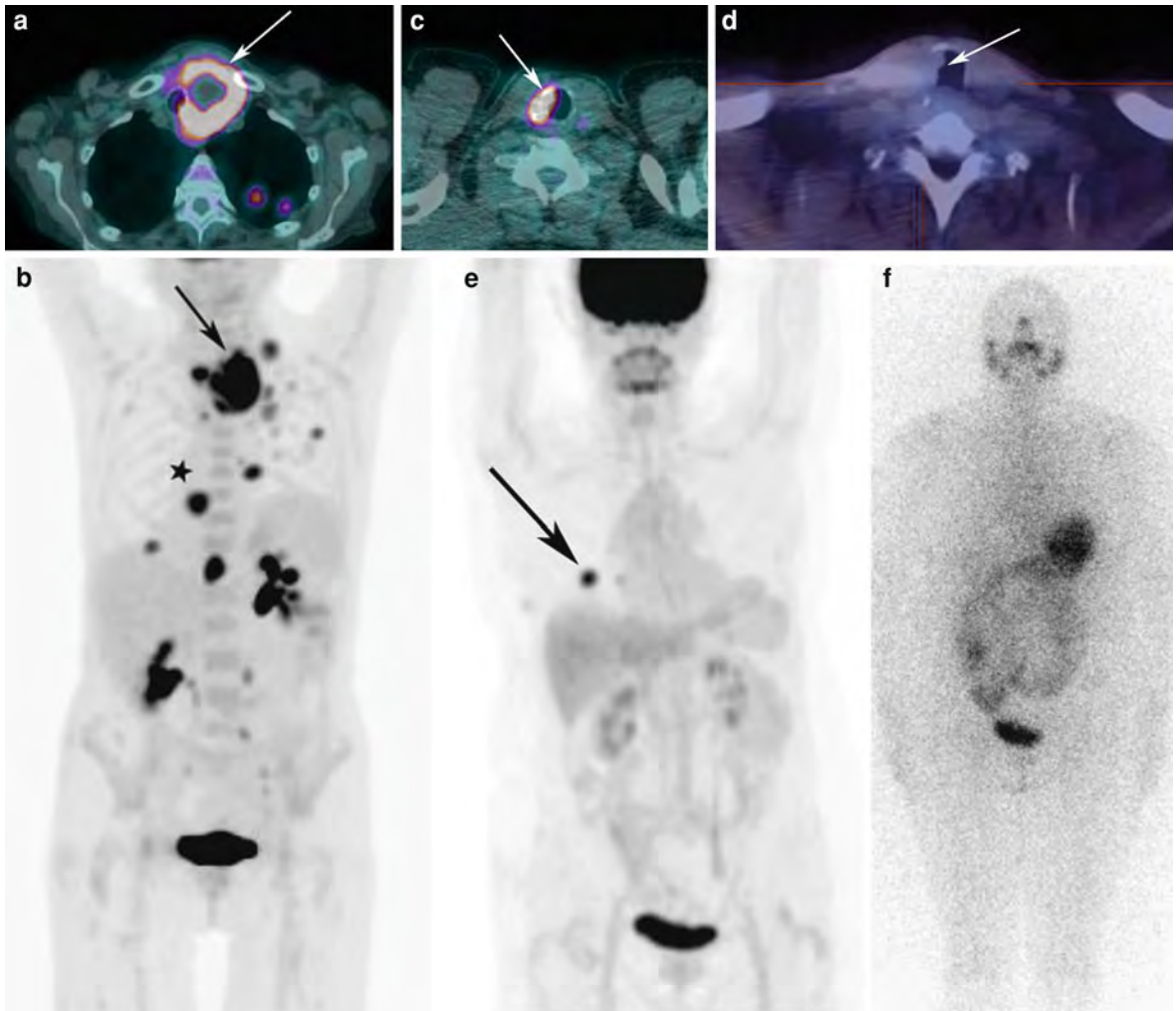

Fig. 14 ^{18}F-FDG-PET in anaplastic carcinoma demonstrating the primary thyroid lesion (*arrow*) and widespread metastases (**a**, **b**), in recurrent papillary thyroid carcinoma (*arrow*) (**c**) in a patient with iodine non-avid disease on ^{123}I scintigraphy (*arrow*) (**d**) and in a patient with pulmonary metastases (*arrow*) (**e**) from iodine non-avid follicular carcinoma on ^{123}I scintigraphy (**f**)

is common (Fig. 16a–c). The presence of colloid indicated by echogenic foci with comet-tail artefact is reassuring and has been reported to be 100% specific for benignity (Fig. 17a, b, Wong and Ahuja 2005).

Hashimoto's thyroiditis is associated with PTL and it is important to recognise, as it is often subclinical. Lymphocytic infiltration results in a large hypoechoic and often hypervascular gland in the acute phase. Hashimoto's thyroiditis is generally a diffuse process and multiple echogenic linear striations are characteristic (Fig. 18). Coexisting focal nodularity in Hashimoto's thyroiditis should be assessed carefully. If in doubt, the presence of lymphocytes on FNAC is reassuring (Cross et al. 2009).

Adenomata account for around 10% of thyroid nodules, are typically follicular in cell type and solitary. They are characteristically homogeneous with a hypoechoic halo and are usually isoechoic to background parenchyma (Fig. 7a, b). They can undergo central cystic change (Fig. 19) and may contain foci of coarse calcification. Follicular adenomata can only be differentiated from microinvasive FTC histologically and are therefore treated by a diagnostic hemithyroidectomy (Gharib et al. 2010).

1.5.2 Papillary Thyroid Carcinoma

PTC is the most common and least aggressive form of thyroid carcinoma. It accounts for around 85% of

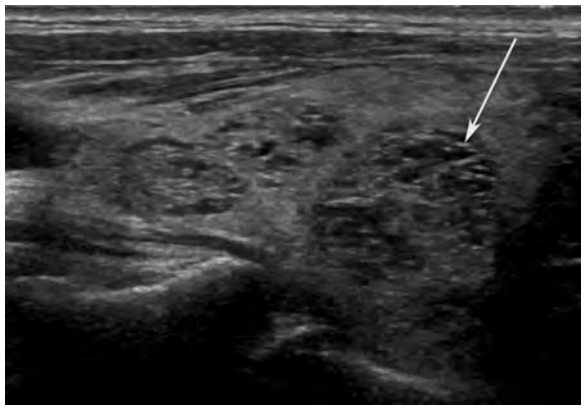

Fig. 15 Longitudinal thyroid US demonstrating multiple well-defined thyroid nodules with a spongiform texture with linear striations (*arrow*), typical of benign nodular hyperplasia

thyroid malignancy but causes only 0.3% of deaths from thyroid cancer, with a 20-year survival rate of over 90%. PTC has a bi-modal age distribution peaking at 25–30 years and then again at 50–60 years. It affects women three times more than men. Approximately 10–20% of PTC is multifocal. 5% of PTC is familial. It is more common in iodine-rich regions and is the main cancer induced by irradiation in childhood (Richards et al. 2010).

The characteristic feature of PTC is its indolent nature. It typically presents as a neck mass either from the primary tumour or a metastatic lymph node. 25% of cases in young adults and children present with lymph node enlargement. Despite this propensity to metastasise to nodes, regional nodal involvement has no bearing on overall prognosis in patients under the age of 45 years and small nodes may harbour cancerous cells for many years without further spread. Distant metastases occur in 5% of cases, mainly to the lungs and very rarely to bone, liver and brain (Richards et al. 2010).

PTC is typically solid and hypoechoic at US and may show ill-defined margins, tall shape and chaotic intranodular vascularity (Figs. 2, 3 and 6a, b). Although the majority of PTC tumours are solid, a small proportion (~15%) can be macrocystic (Fig. 5). Microcalcification is highly specific but only seen in about 40% (Fig. 1a–c). Metastatic lymph nodes also demonstrate microcalcification and are often cystic (43–70%) (Figs. 8a–c and 9). Occasionally, large, predominantly cystic nodal metastases are seen, often in conjunction with small primary tumours. Extensive punctate calcification may be detectable on CT, and cystic metastases from PTC are characteristically hyperintense on T1-weighted MRI due to a high thyroglobulin content or haemorrhage (King 2008, Fig. 20a, b).

Histologically, PTC can be encapsulated or locally infiltrating. Microscopic features include small papillae, 'ground-glass' or overlapping 'shingle-roofed' nuclei, small, spherical, calcified psammoma bodies and a desmoplastic reaction. Macroscopic calcification and necrosis may occur. Most PTC tumours have some follicular elements which may sometimes almost completely overshadow the papillary formations, but this does not affect prognosis. Several other variants of PTC have been described, including a follicular variant which can be diffuse sclerosing (occurs in children and young adults and has a good prognosis) or diffuse aggressive, an oxyphil cell variant which has biological behaviour closer to follicular carcinoma, and tall cell variant which predominates in older patients and has a more aggressive biological behaviour (Hedinger et al. 1988).

Treatment is by total thyroidectomy and central compartment neck dissection with removal of any sonographically abnormal cervical lymph nodes, followed by radio-iodine ablation. The prognosis in PTC is almost always excellent but is age-related and so, unlike other head and neck cancers, staging includes patient age as well as anatomical extent. In children and the young or early middle-aged, even with relatively advanced primary disease or lymph node metastases, a 100% cure rate can be achieved. In the older age group, the prime determinants of prognosis are tumour size and extent and the presence of distant metastases. Large tumours or extension outside the thyroid gland indicates a poor prognosis in older patients but has no impact on prognosis in younger patients. Similarly, pulmonary metastases are of concern in the elderly but not necessarily so in the young (Richards et al. 2010).

1.5.3 Follicular Thyroid Carcinoma

FTC accounts for 5–15% of thyroid malignancies and is three times more common in women, with a mean age of presentation of 50 years. The relative incidence of FTC is higher in iodine-deficient areas. FTC is associated with dyshormonogenesis, an uncommon cause of congenital hypothyroidism, and with Cowden's syndrome. Familial cases occur but are rare (Richards et al. 2010).

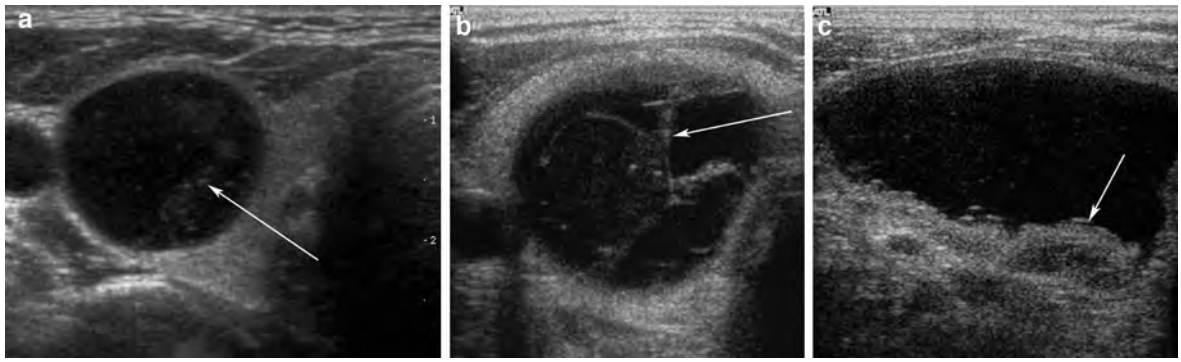

Fig. 16 Three different examples of haemorrhagic thyroid nodules demonstrating internal echogenic material (*arrow*) (**a**), septa (*arrow*) (**b**) and fluid/debris levels (*arrow*) (**c**)

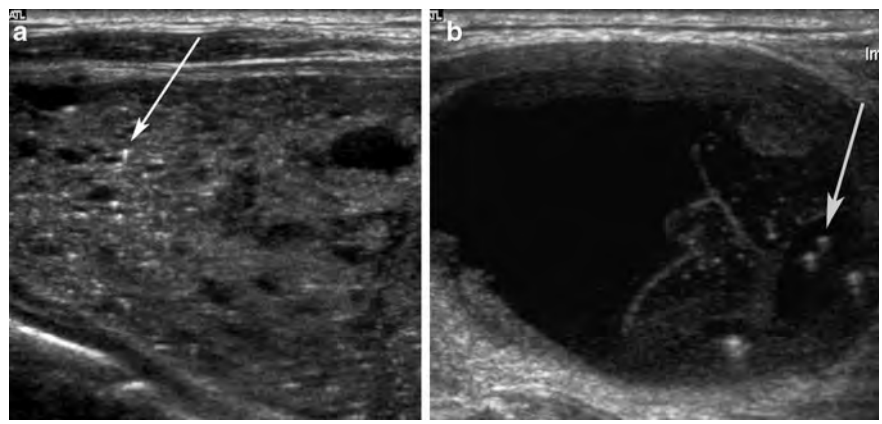

Fig. 17 Ring-down artefact from colloid (*arrows*) in a solid hyperplastic nodule (**a**) and a colloid cyst (**b**)

FTC is also an indolent tumour, but unlike PTC it tends to spread haematogenously to bone, liver or lungs rather than metastasise to regional lymph nodes. It is rarely multifocal. Patients usually complain of a symptomless neck mass, although large tumours may cause symptoms of local compression. 25% of patients with FTC will present with extrathyroidal invasion, 5–10% with cervical lymphadenopathy and 10–20% with distant metastases (Richards et al. 2010).

FTC most closely resembles normal thyroid tissue and when well differentiated can be impossible to distinguish from a follicular adenoma on US or FNAC, which typically yields hypercellular samples devoid of colloid (Fig. 21). The diagnosis of micro-invasive FTC requires histological confirmation of vascular invasion by tumour and is therefore often an unexpected finding following hemithyroidectomy for presumed benign disease. Microinvasive FTC is relatively slow-growing and rarely metastasises.

Macroscopically invasive FTC is more aggressive and can be diagnosed on cytology. This less well differentiated form typically contains follicular cells, but Askanazy, Hürthle or clear cells may also be found and tumours are subclassified according to the predominant cell type. Macroscopically invasive FTC appears heterogeneous on US, with an irregular margin and absent halo. Frankly invasive FTC is usually poorly differentiated and associated with the worst prognosis. On US it is hypoechoic and irregular and often demonstrates extracapsular spread and vascular invasion, which makes it indistinguishable from AC and PTL (King 2008, Fig. 22).

The treatment of pre-operatively confirmed FTC is the same as for PTC. While FTC has a good prognosis, it is less favourable than that of PTC. Prognosis depends on the degree of capsular and vascular invasion, the degree of tumour differentiation, tumour size and the presence of distant metastases. Once again, age is an important prognostic factor and is

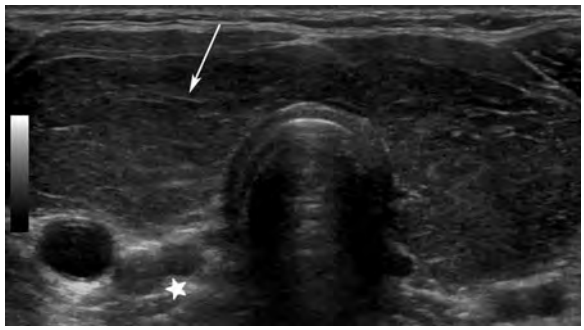

Fig. 18 Midline transverse US of the thyroid gland demonstrating a diffusely enlarged hypoechoic gland with linear striations (*arrow*) and a small reactive level VI lymph node (*star*) typical of Hashimoto's thyroiditis

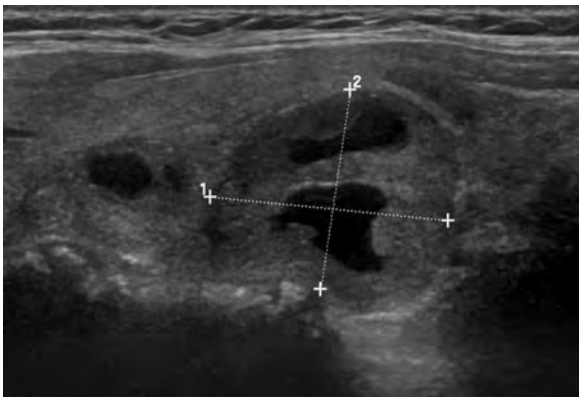

Fig. 19 Well-defined isoechoic lesion with two central cystic foci, which was found to be a follicular adenoma at histology

incorporated into the staging groups. Like PTC, the presence of lymph node metastases does not worsen prognosis in patients younger than 45 years but is significant in older patients (Richards et al. 2010).

1.5.4 Medullary Thyroid Cancer

MTC accounts for 3–9% of thyroid cancers and around 13% of thyroid cancer-related deaths. There is a slight female predominance. MTC is a neuroendocrine tumour which arises from parafollicular C-cells and may secrete a number of compounds, usually calcitonin. 75% of MTC is the sporadic form which occurs mainly in the fifth or sixth decade and is usually unilateral. The other 25% of MTC patients have a hereditary form, of which 65% occur in the context of MEN type II. The remainder of cases have a non-MEN familial form of the disease. All types of hereditary tumours are commonly multifocal (Richards et al. 2010).

MEN IIa is the most common form of hereditary MTC. Tumours occur in virtually every case with a peak age of incidence in the second or third decade. These patients are prone to other associated conditions such as phaeochromocytoma (<50%) and parathyroid hyperplasia (<50%). In MEN IIb the disease occurs in early childhood and is very aggressive. In these patients there is an association with phaeochromocytoma, mucosal neuromas, diffuse ganglioneuromas of the gastrointestinal tract, skeletal abnormalities and a 'Marfanoid habitus'. Non-MEN familial MTC usually arises in the fifth decade of life and is more indolent biologically (Richards et al. 2010).

Patients typically present with hard, painless nodular thyroid enlargement accompanied by cervical and mediastinal lymphadenopathy in 50%. 10–15% will also have distant metastases to lungs, liver and bone at presentation. In advanced tumours, symptoms from local compression and vascular invasion may be present. Excessive or ectopic hormone production may give rise to diarrhoea and flushing. Hereditary cases are usually diagnosed by screening with US and serum calcitonin.

MTC is usually similar in appearances to PTC on US, although punctate calcification is seen in the majority (80–90%), in this case due to amyloid formation (Fig. 23a, b). Microcalcification is also present in 50–60% of metastatic lymph nodes (Fig. 24) and may also be demonstrated on CT (Fig. 25, King 2008). Macroscopically, tumours are often well demarcated but only occasionally encapsulated and have a firm consistency. Calcification, necrosis, haemorrhage, cyst and bone formation are common. Microscopically MTC is a solid cellular tumour without follicles, and a variable amount of stromal amyloid due to calcitonin deposition is seen in upto 82% of cases. Inherited MTC is often smaller than sporadic because it is found by screening, and is accompanied by C-cell hyperplasia (Richards et al. 2010).

Surgery is the only treatment for MTC and patients require careful staging. Total thyroidectomy with routine central and bilateral modified neck dissection is recommended, unless there is evidence of distant metastases. External beam radiotherapy has been used for palliation, but radioactive iodine has no place in treatment.

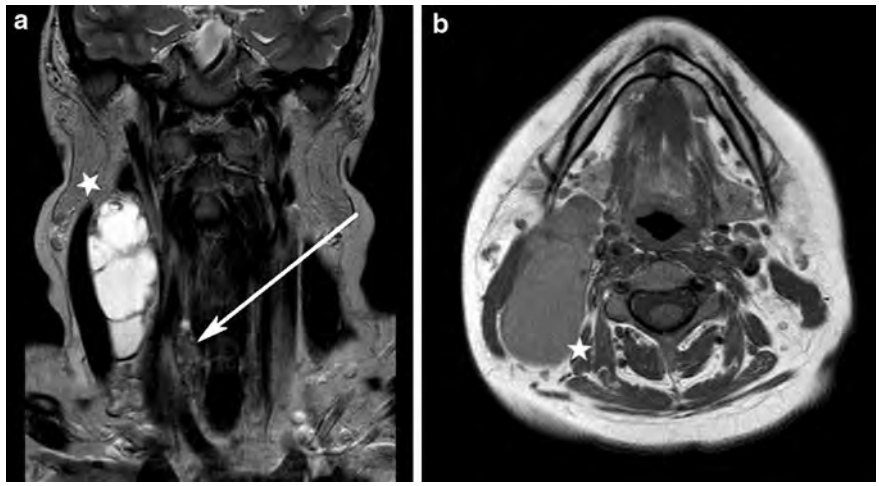

Fig. 20 **a**, **b** Coronal T2 and axial T1-weighted MRI of the neck demonstrating large right-sided metastatic cystic lymph nodes (*stars*) from a papillary thyroid carcinoma (*arrow*). The nodes are hyperintense on T1-weighted imaging, which is characteristic

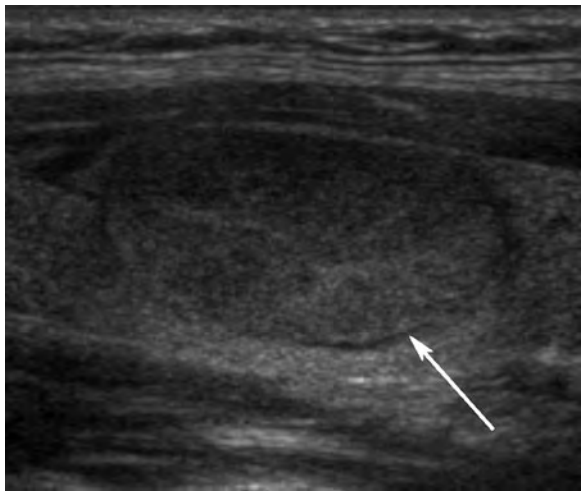

Fig. 21 Longitudinal thyroid US demonstrating a well-defined isoechoic lesion (*arrow*) which was a microinvasive follicular thyroid carcinoma at histology

Fig. 22 Transverse US of the right lobe of the thyroid demonstrating an irregular heterogenous hypoechoic mass which was a macroscopically invasive follicular thyroid carcinoma at histology

Despite the propensity to metastasise, MTC is relatively indolent, with a survival of 86% at 5 years and 65% at 10 years and, when confined to the thyroid gland, the prognosis is excellent. Prognostic factors include primary tumour size, the presence of lymph node and distant metastases, advanced age, association with MEN IIB and completeness of the surgical resection. Patients with the best prognosis are those who are diagnosed by provocative screening, prior to the appearance of palpable disease. All patients with MTC, including those with sporadic presentation, should be tested for RET proto-oncogene mutation and, if positive, family members should also be tested. Those with the gene should undergo prophylactic thyroidectomy at an early age (Richards et al. 2010).

1.5.5 Undifferentiated (Anaplastic) Thyroid Carcinoma

AC is rare, representing only 2% of all thyroid malignancies, but it is highly aggressive, with a median survival of only 6 months, and causes the majority of deaths from thyroid cancer. It is slightly

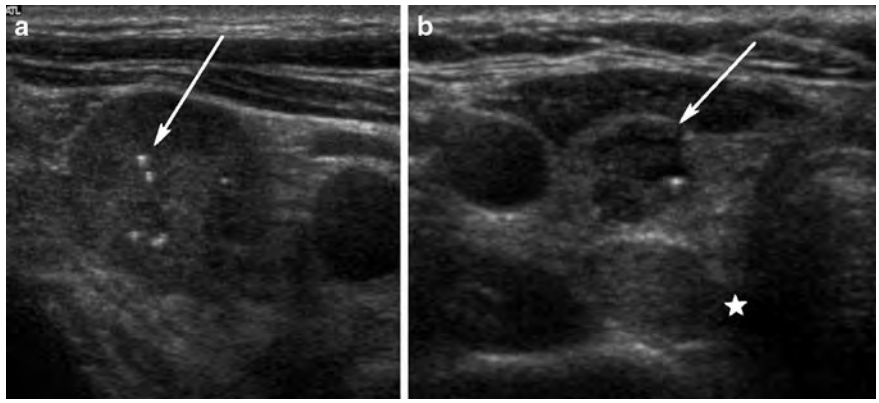

Fig. 23 Transverse US of the right lobe of the thyroid demonstrating a small irregular hypoechoic nodule (*arrow*) in the mid-pole, with echogenic foci representing punctate calcification (**a**). Histology confirmed medullary thyroid carcinoma. There is also parathyroid enlargement (*star*) in this patient with MEN IIa syndrome (**b**)

Fig. 24 Transverse US of the right deep cervical chain demonstrating an enlarged round metastatic lymph node from medullary thyroid carcinoma with punctate calcification (*arrow*)

Fig. 25 Axial contrast-enhanced CT of the neck demonstrating a metastatic right level II lymph node with a small calcified focus (*arrow*) from a medullary thyroid carcinoma

more common in females and usually presents after the fifth decade of life. Radiation is a recognised causative factor, reducing the age of presentation (Richards et al. 2010).

AC presents as a rapidly expanding, ill-defined hard neck mass often associated with symptoms and signs of local invasion and compression. Cervical lymphadenopathy is common and half of the patients have distant metastases at presentation. US appearances of AC are of a diffuse, ill-defined heterogeneous mass which usually involves the entire thyroid (Fig. 4). Necrosis and extracapsular spread are common, with invasion of adjacent tissues and vessels often requiring cross-sectional imaging to fully demonstrate (Figs. 10 and 11). ^{18}F-FDG-PET is useful for staging metastases (Fig. 14a, b).

The important differential diagnosis is of PTL, which sometimes requires histological assessment. AC is likely to arise as a result of transformation of a pre-existing PTC or FTC and areas of more differentiated thyroid carcinoma are often present at histology. Anaplastic transformation of differentiated carcinoma may also occur in metastases.

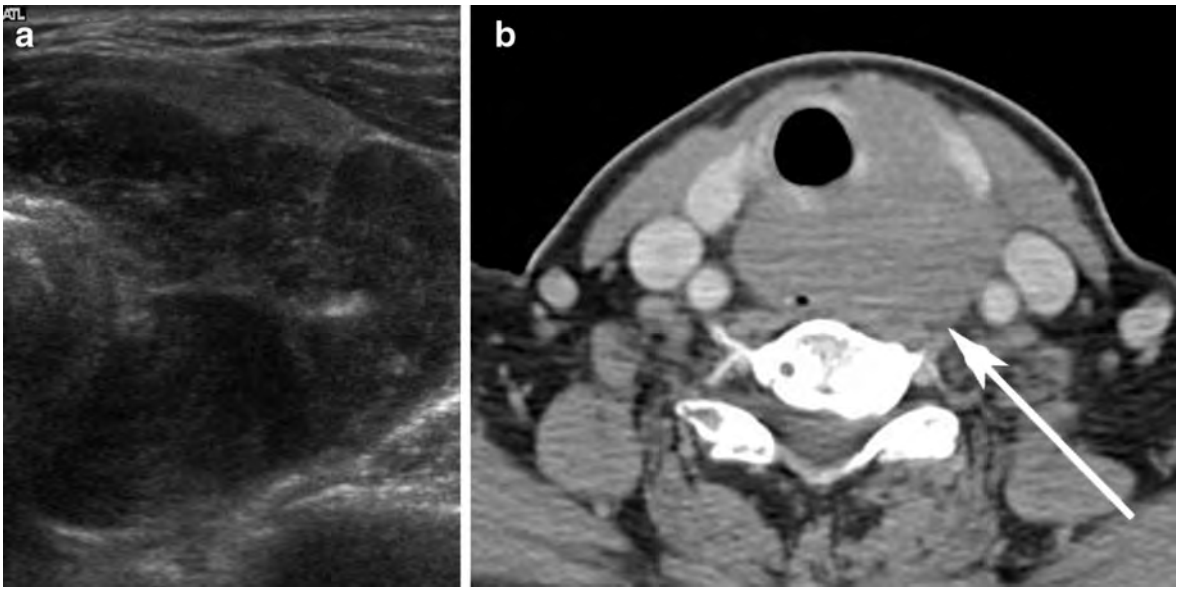

Fig. 26 Transverse thyroid US of a hypoechoic mass with posterior extracapsular spread extending into the retrotracheal region (**a**). Axial contrast-enhanced CT of the same patient demonstrating the left-sided thyroid mass with extracapsular spread (*arrow*) (**b**). Lymphoma was confirmed at histology

All patients with AC are considered to have stage IV disease (Sobin et al. 2009). Surgery with adjuvant chemoradiotherapy may be curative for smaller lesions, but treatment is usually palliative. External radiation with dexamethasone cover may slow tumour progression.

1.5.6 Primary Thyroid Lymphoma

PTL is another rare tumour representing 2% of all thyroid malignancies. It occurs most frequently in elderly women and is almost exclusively non-Hodgkin's lymphoma of a B-cell type. Eighty-five percent of cases occur on a background of Hashimoto's thyroiditis. It is postulated that chronic antigenic stimulation secondary to the autoimmune thyroiditis may lead to lymphoid proliferation which eventually undergoes transformation to a low-grade MALT lymphoma, with further transformation to large-cell lymphoma, which is the most common type seen clinically (Hedinger et al. 1988; Untch and Olson 2006).

Patients with large-cell thyroid lymphoma usually present with a rapidly growing thyroid nodule, frequently associated with lymphadenopathy, and symptoms of extracapsular spread. Sonographically there is usually a hypoechoic mass with poorly-defined margins and an absent halo, and evidence of Hashimoto's thyroiditis in the rest of the gland. The nodule is usually solitary but multifocal disease occurs. Diffuse or multifocal PTL is sonographically indistinguishable from AC on both US and cross-sectional imaging (Fig. 26a, b). Patients with the rarer and more indolent MALT lymphoma present with a slow-growing nodule. MALT lymphoma can coexist with large-cell lymphoma and, if too small a sample is obtained, the aggressive component could be missed, resulting in incorrect treatment (Richards et al. 2010).

Treatment is based on the lymphoma subtype and the extent of disease and follows protocols for NHL occurring in a nodal site. Primary MALT lymphoma is often treated with radiotherapy alone. Prognostic factors include age, performance status, elevated LDH, the number of extranodal sites involved and the Ann Arbor staging. The 5-year survival rate for patients was 50–86% (Richards et al. 2010).

1.5.7 Other Primary Tumours and Thyroid Metastases

Other primary tumours are rare and include sarcomas, squamous cell carcinoma and primary lymphomas arising from outside the thyroid. At autopsy, 17–24% of patients with known malignancy have thyroid

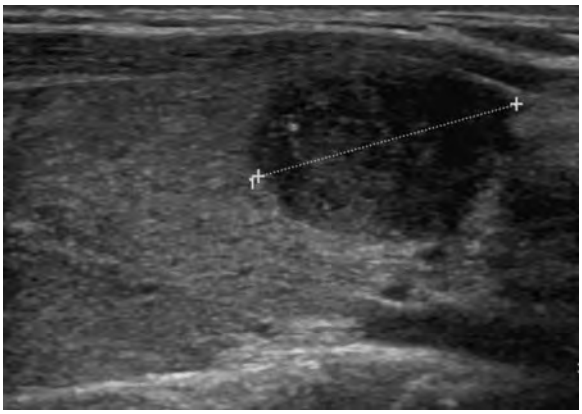

Fig. 27 Longitudinal thyroid US demonstrating a hypoechoic lesion in the inferior pole (callipers) which was metastasis from squamous cell carcinoma of the lung

metastases most commonly from renal, melanoma, breast and lung cancers, but these are usually only present when there is other metastatic disease (King 2008). Thyroid metastases are typically large, well-defined, multiple, markedly hypoechoic, found in the lower poles of the gland and associated with cervical lymphadenopathy (Fig. 27). The search for thyroid metastases has increased with the advent of ^{18}F-FDG-PET, which detects incidental thyroid pathology in 2–3% of cases; the reported risk of malignancy is 14–50%, usually primary thyroid cancers (Untch and Olson 2006).

1.6 Surveillance

Approximately 10–30% of patients develop recurrent disease, around 80% of which is confined to the neck, with 20% developing distant metastases, most commonly in the lungs. Post-treatment surveillance of thyroid cancer patients revolves around clinical examination, serological assessment of thyroglobulin or calcitonin, and regular chest X-rays. US and radioisotope studies are employed where recurrence is suspected, the latter also yielding information about therapy options. There are several pitfalls, however. Re-growth of normal thyroid tissue may be misinterpreted as recurrence. Stitch granulomata can have very similar appearances to PTC on US, being hypoechoic, with coarse echogenic foci which cast acoustic shadows. Finally, it is not uncommon for small metastatic cervical lymph nodes from PTC to persist for many years after ablation therapy (King 2008).

Both PTC and FTC may de-differentiate with time, losing the ability to accumulate iodine. At this stage there are no contraindications to iodinated contrast and ^{18}F-FDG-PET becomes a viable alternative to scintigraphy (Fig. 14c–f). ^{18}F-FDG-PET alone has been reported to be 70–95% sensitive, 25–80% specific and 64–90% accurate in these patients (Lind et al. 2003; Finkelstein et al. 2008).

2 Parathyroid Neoplasms

2.1 Introduction

Primary hyperparathyroidism (PHPT) usually results from a solitary benign parathyroid adenoma, although multiple parathyroid adenomata, parathyroid hyperplasia, rarely parathyroid carcinoma and very rarely ectopic parathormone secretion may be the cause. The need to differentiate between these pathologies, the variability in number and position of parathyroid glands and the morbidity associated with second-look surgery means that pre-operative radiological localisation has an important role. This is even more so with the recent interest in minimally invasive surgical techniques.

2.2 Anatomy and Embryology

Normal parathyroid glands are ellipsoid and around 5 mm in length. They have abundant fatty stroma, making them difficult to detect by most imaging modalities. Around 90% of people have two pairs of glands, although the total number of glands can range from 2 to 6. In parathyroid hyperplasia, activation of embryological rests leads to the development of more supernumerary glands.

Superior parathyroid glands develop with the thyroid from the fourth branchial pouch and migrate caudally during fetal development. Their final position is relatively constant, deep to the upper lobes of the thyroid in around 95%. Inferior parathyroid glands develop from the third branchial pouch and migrate inferiorly with the thymus to lie within a few centimetres of the inferior poles of the thyroid in most people. Their final position is determined by when

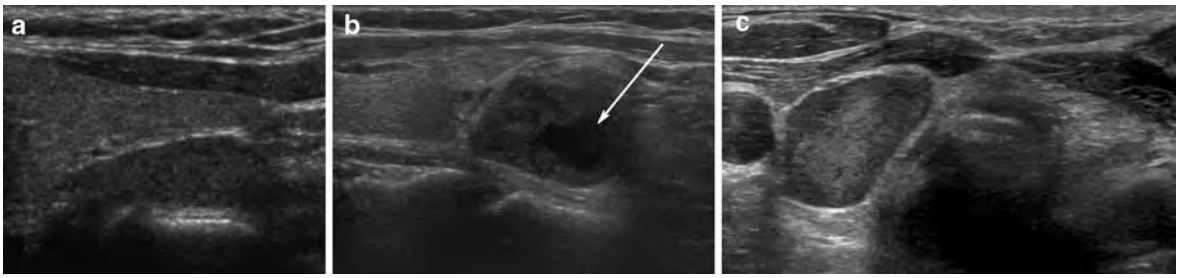

Fig. 28 Parathyroid enlargement on US. **a** longitudinal US demonstrating the elongated shape of enlarged parathyroid glands often seen, **b** longitudinal US demonstrating a parathyroid adenoma with central cystic characteristics and **c** transverse US demonstrating parathyroid enlargement in tertiary hyperparathyroidism

they disassociate from the thymus and is much more variable with ectopic inferior parathyroid glands occurring in up to 25%. They can lie anywhere between the carotid bifurcation and the mediastinum. Rarer ectopic locations include the retro-oesophageal, prevertebral and pretracheal spaces, within the thyroid or thymus, the aortopulmonary window or even in the pericardium (Johnson et al. 2007).

2.3 Epidemiology and Aetiology

PHPT is the most common endocrinological disorder. Symptomatic PHPT occurs in 1 in 500 women and 1 in 2000 men per year, usually presenting in their fifth to seventh decade, but asymptomatic PHPT detected on biochemical screening is probably even more prevalent. PHPT results from a single parathyroid adenoma in around 90%. The second most common cause is parathyroid hyperplasia, which occurs in around 6% and in which all the parathyroid glands are enlarged. Multiple, usually double, parathyroid adenomata occur in around 4%, with parathyroid carcinoma seen in around 1%, usually in a younger age group (Bilezikian et al. 2009).

The aetiology of parathyroid neoplasia is poorly understood, although previous external beam irradiation of the neck has been implicated. In most cases PHPT is sporadic, but there are both familial and genetic predispositions. Familial isolated hyperparathyroidism and familial hypocalciuric hypercalcaemia are rare diseases affecting multiple glands. Parathyroid hyperplasia is associated with MEN I and IIa. Parathyroid adenomata occur in MEN I but an association with parathyroid carcinoma is unproven. Adenomata and carcinomata are seen in the rare hyperparathyroidism-jaw tumour syndrome, 80% of which present with hypercalcaemia which is due to parathyroid carcinoma in 15% (Richards et al. 2010).

Secondary and tertiary hyperparathyroidism occurs in chronic renal failure when multi-gland hyperplasia or autonomous parathyroid adenomata develop in response to hypocalcaemia.

2.4 Clinical Features

Benign parathyroid enlargement per se is rarely symptomatic, as patients present with the signs or complications of hypercalcaemia such as polyuria, polydypsia and fatigue or renal stones, gastrointestinal ulcers, pancreatitis and bone disease.

The treatment of symptomatic PHPT is surgical and there are clearly-defined criteria for when to operate (AACE and AAES position statement 2005). The management of asymptomatic PHPT is more controversial but depends on calcium levels, bone mineral density, age and patient choice (Bilezikian et al. 2009). In experienced hands, surgery has a 90–95% cure rate in patients with a naive neck, preoperatively diagnosed with a single adenoma. Double parathyroid adenomata are usually bilateral and require both sides of the neck to be explored. Parathyroid hyperplasia also requires bilateral neck dissection and either subtotal parathyroidectomy, removing 3.5 glands, or total parathyroidectomy and autotransplantation of parathyroid tissue into the forearm to allow easy access, should the hyperparathyroidism recur (Johnson et al. 2007).

Parathyroid carcinoma is indolent but can be locally invasive and metastasise. Symptoms such as pain, dysphagia and dysphonia are concerning,

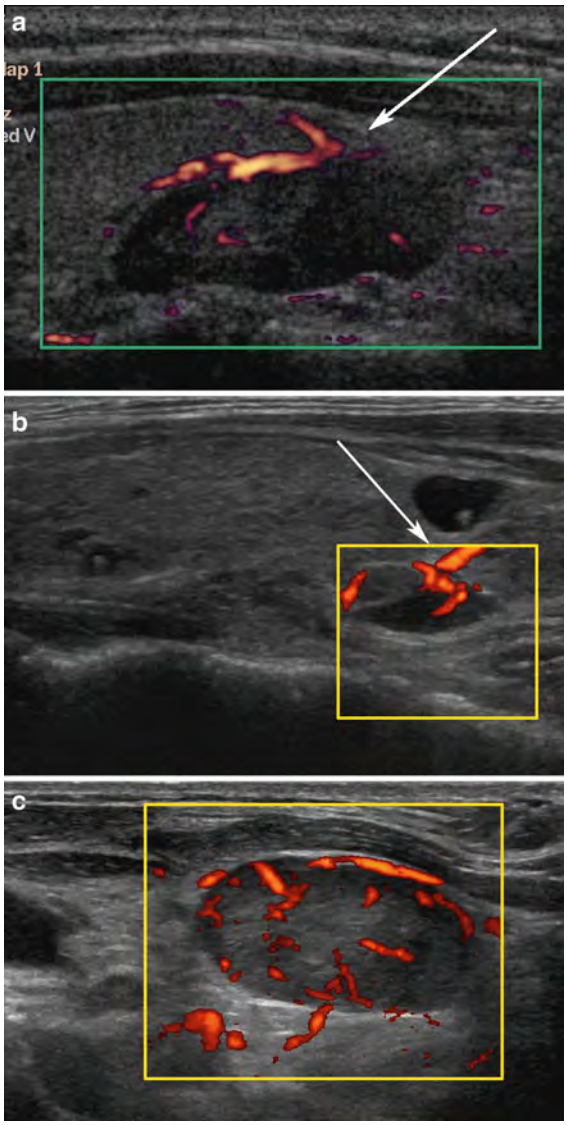

Fig. 29 Power Doppler studies of three different enlarged benign parathyroid glands. **a**, **b** vascular supply from a single pedicle which is not polar and appears to arise from the thyroid gland (*arrows*) and **c** a more chaotic pattern of vascularity

especially if associated with very high calcium or parathormone levels. Neither tumour size nor regional lymph node status is prognostically important, but distant metastases are associated with reduced survival. Primary and palliative treatment is surgical, with en-bloc resection including hemithyroidectomy and neck dissection when appropriate. Recurrence can be delayed and is reported in 30–70%. Five-year survival is around 50%, with patients usually dying from the complications of hypercalcaemia (Hedinger et al. 1988).

2.5 Classification and Staging

Parathyroid tumours arise from chief cells, transitional clear cells or can be of mixed cell type. The histological distinction between adenomata and carcinoma is difficult. Standard criteria for malignancy, such as mitoses and capsular invasion may be present in adenomata, as can macroscopic adhesions to surrounding structures. Conversely, carcinomata are often well differentiated. In general, clinical features and macroscopic behaviour are as important to the final pathological diagnosis as histology (AACE and AAES position statement 2005).

There are no staging criteria for parathyroid carcinoma, which is described as either localised, involving the parathyroid gland with or without local invasion, or metastatic. It most frequently metastasises to regional lymph nodes and lung, but may involve liver, bone, pleura, pericardium and pancreas.

2.6 Imaging

The role of imaging in PHPT is one of pre-operative localisation rather than diagnosis, as it is rarely able to differentiate between parathyroid hyperplasia, adenoma and carcinoma. Until recently the standard surgical technique was bilateral neck exploration with visualisation of all four parathyroid glands in order to exclude multi-gland hyperplasia or double adenomata. Pre-operative localisation was therefore reserved for patients undergoing redo operations. With the advent of focussed, minimally invasive techniques, pre-operative imaging is generally recommended in all patients whether or not they have had previous neck surgery (Bilezikian et al. 2009). The combination of scintigraphy and US is highly sensitive for single gland adenomata, but the pre-operative prediction of multi-glandular disease and double adenomata is less successful. Most centres therefore perform bilateral neck exploration whenever there are equivocal, negative or discordant results. Others advocate the use of US-FNA for parathormone (PTH) assay and percutaneous selective venous sampling to reduce the need for bilateral surgery.

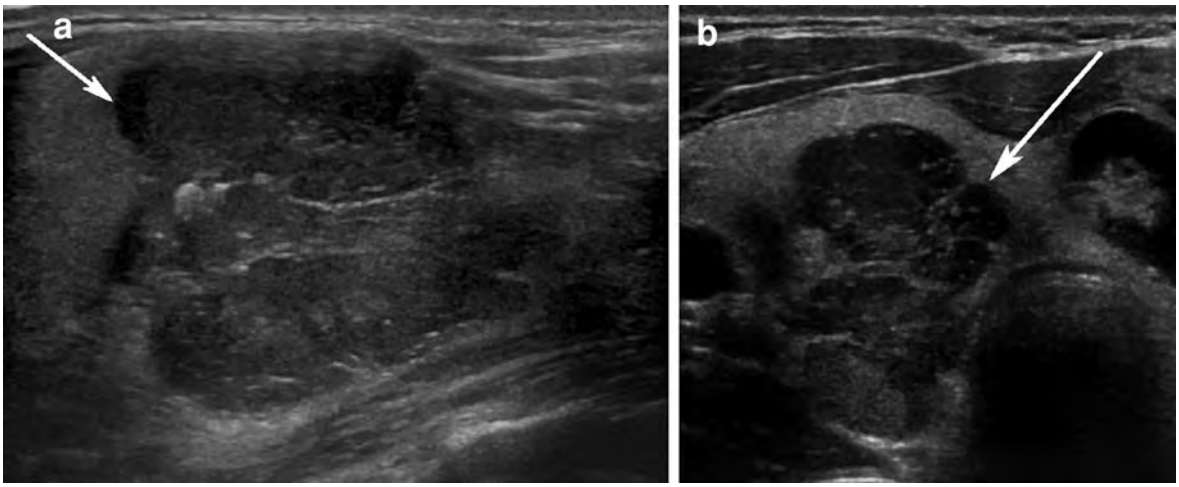

Fig. 30 Longitudinal (**a**) and transverse (**b**) US of the thyroid demonstrating an irregular heterogenous hypoechoic mass invading into the thyroid gland; this was parathyroid carcinoma at histology

Cross-sectional imaging has a less central role in imaging parathyroid glands but can be useful in suspected ectopia and post-operative patients.

2.6.1 US, Scintigraphy and ^{18}F-FDG-PET

US has advantages over scintigraphy in that it can accurately determine the anatomical relationship of an abnormal parathyroid gland to the thyroid, permits evaluation of coexisting thyroid and lymph node pathology and can be used to guide needles for FNA or percutaneous ethanol ablation when required. The reported sensitivity of US for a single parathyroid adenoma is similar to scintigraphy at around 80%, although this is operator-dependent (Haciyanli et al. 2003). As with scintigraphy, sensitivity falls to around 50% for multi-gland hyperplasia and even further for double adenomata to the region of 30% (Sugg et al. 2004).

Abnormal parathyroid glands are usually homogenously hypoechoic with an echogenic capsule and are oval in shape, with a craniocaudal axis, although they can be surprisingly elongated (Fig. 28a–c). Occasionally they can be isoechoic to thyroid and 4% undergo cystic or haemorrhagic degeneration. Typically they are hypervascular and reported to differ from lymph nodes by having a feeding vessel which enters the gland from one of the poles to supply it in a peripheral distribution, rather than the hilar architecture and more central distribution seen in nodes. When detected on power Doppler, the presence of such a polar feeding vessel has been reported to significantly increase the specificity of US for parathyroid enlargement (Rickes et al. 2003); however, in the author's experience, this has been an exceptionally rare finding (Fig. 29a–c).

Parathyroid adenomata are usually 0.8–3 cm in maximum diameter with a mean of 15 mm. Hyperplastic glands are typically 2–3 times smaller, but it is not uncommon for there to be a dominant gland in multigland hyperplasia, which can be misinterpreted as a solitary adenoma. Parathyroid carcinoma can be indistinguishable from adenomata but, when present, evidence of necrosis, haemorrhagic degeneration, deranged vascularity, calcification, local invasion and lymph node metastases are all concerning features (Fig. 30a, b). It is important to remember the association with MEN syndromes and assess the thyroid carefully for malignancy in every case of PHPT (Fig. 23a, b).

There are a number of pitfalls to be considered when performing US for parathyroid enlargement. Ectopic glands are often beyond the reach of US. Thyroid nodules may cause so much thyroid enlargement that parathyroid glands are displaced or obscured. Thyroid nodules can be pedunculated and mimic parathyroid enlargement, as can the reactive infrathyroid pretracheal lymph nodes seen with autoimmune thyroiditis. Intracapsular and even rarer intrathyroid parathyroid glands can be indistinguishable from thyroid nodules, although the presence of an independent extrathyroidal vascular supply is supportive evidence (Johnson et al. 2007).

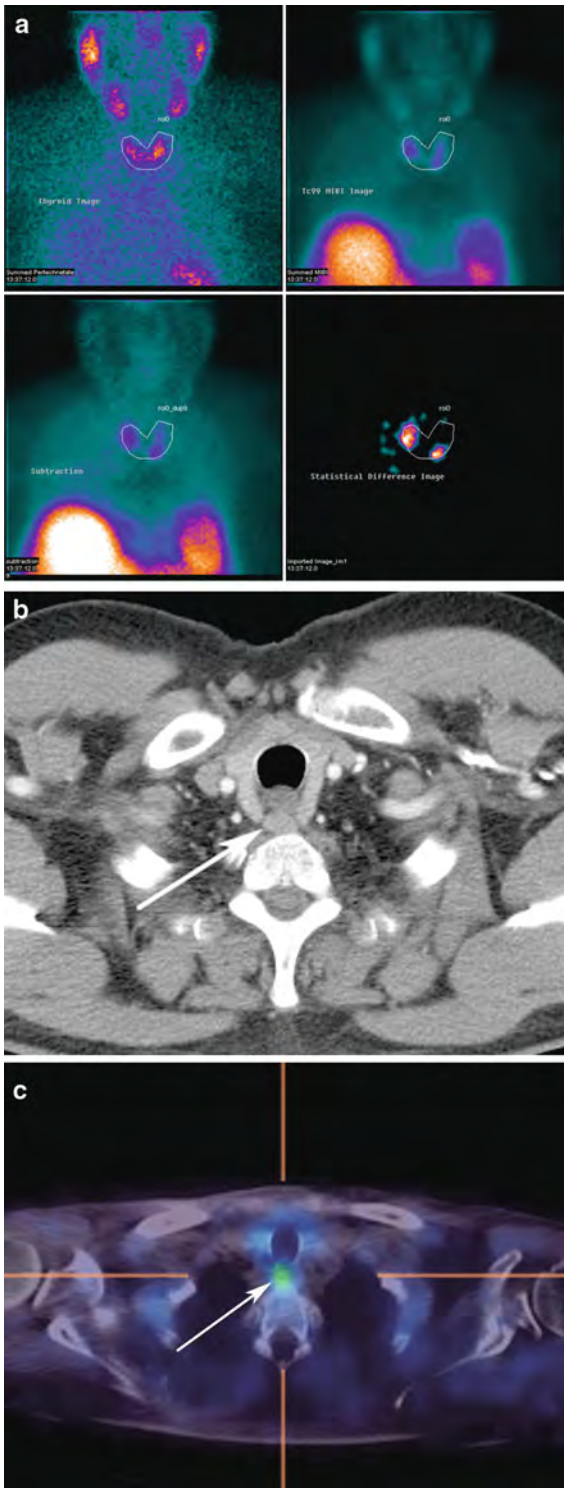

◀**Fig. 31** ^{99m}Technetium-labelled sestamibi scintigraphy: Thyroid retraction study demonstrating bilateral foci of increased uptake representing double parathyroid adenomata (**a**); axial contrast-enhanced CT of the lower neck (**b**) and axial SPECT with CT fusion (**c**) in a patient with a retro-oesophageal ectopic parathyroid adenoma (*arrows*)

US may be used under other circumstances. There is a role for US in pre-operative marking as well as intra-operatively. Occasionally US-FNA may be performed for PTH assay and is highly specific for the presence of parathyroid tissue. Although usually performed to treat tertiary hyperparathyroidism, percutaneous ethanol ablation has a role in patients with PHPT where there are medical co-morbidities or surgery is particularly high-risk. Under US guidance, ethanol is slowly injected into the abnormal parathyroid until blood flow into the gland can no longer be detected on power Doppler.

^{99m}Tc-sestamibi is the radioisotope of choice for imaging parathyroid glands. It is taken up by both thyroid and parathyroid tissue, but the latter is more avid and retained for longer by abnormal parathyroid glands than normal thyroid. These differences are exploited by the use of both initial and delayed 'wash-out' acquisitions. 3D single photon emission computed tomography (SPECT) is particularly useful in cases of ectopia (Fig. 31a–c). The concomitant use of ^{123}I or ^{99m}Tc-pertechnetate, which are preferentially taken up by the thyroid, permits subtraction imaging, but this has yet to be proven to be diagnostically advantageous.

The sensitivity of ^{99m}Tc-sestamibi scintigraphy varies between institutions but is similar to US at around 80%, the main advantage over US being the detection of ectopic glands, particularly in the mediastinum. As with US, sensitivity falls dramatically when a single adenoma is small (50% for glands weighing under 500 mg) or in the presence of multigland hyperplasia (44–73%) or double adenomata (30%) (Johnson et al. 2007). The reason why double adenomata are inherently difficult to detect is unclear and only partly explained by volume. Low mitochondrial activity has been suggested as a factor. False negative results may also occur when there is cystic or haemorrhagic degeneration within an abnormal parathyroid gland.

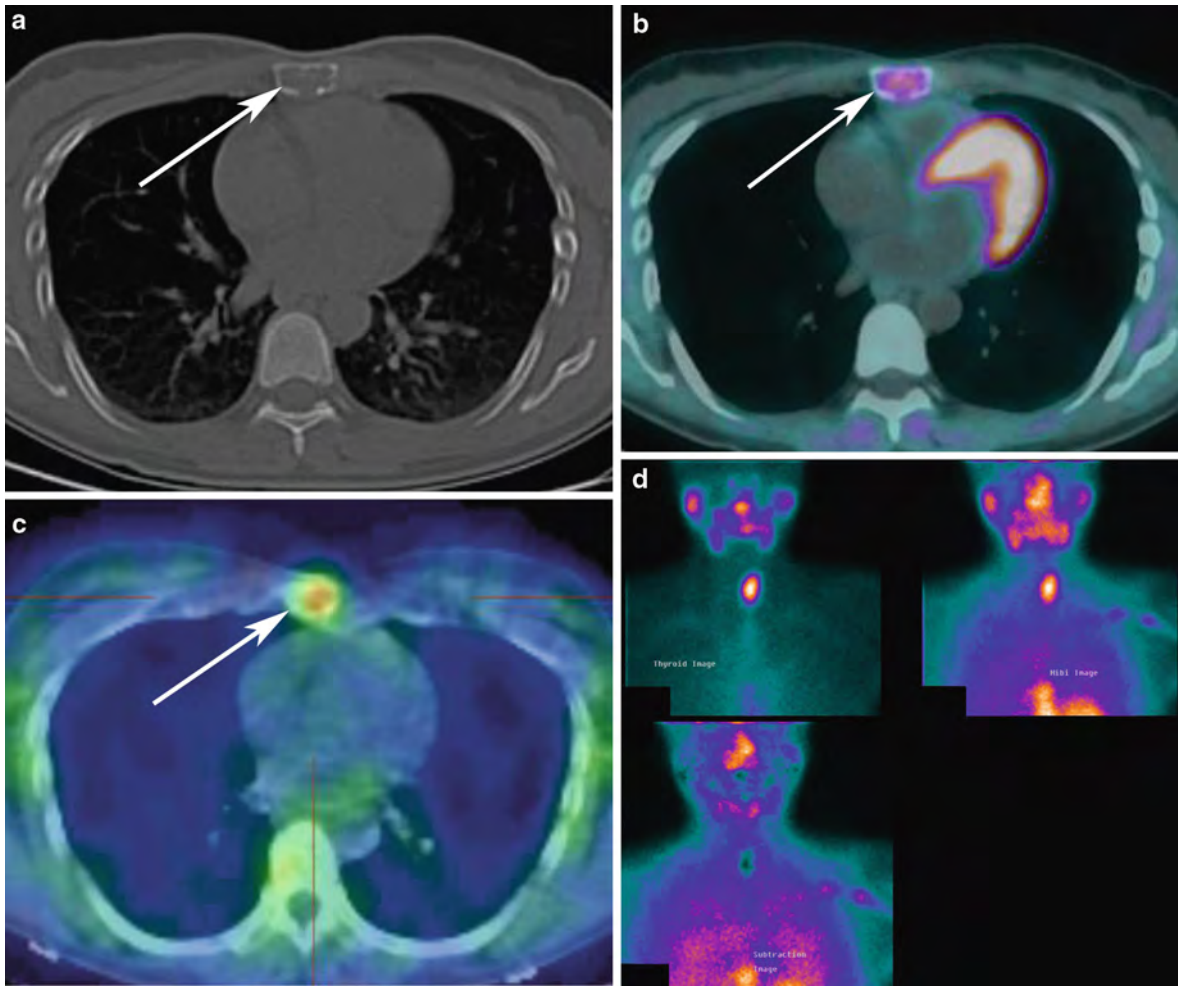

Fig. 32 Sternal metastasis from parathyroid carcinoma demonstrated on axial CT (**a**), ^{18}F-FDG-PET (**b**) and octreotide scintigraphy (**c**) (*arrows*) but not apparent on 99mTc-sestamibi (**d**)

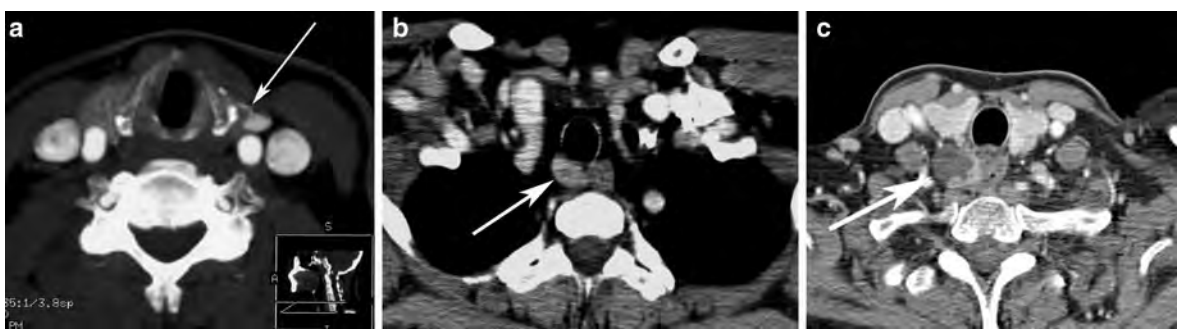

Fig. 33 Axial contrast-enhanced CT images demonstrating an enlarged parathyroid gland with a vascular pedicle (*arrow*) (**a**) and two examples of enlarged retrotracheal ectopic parathyroid glands (**b**, **c**) (*arrows*)

Interpretation of ^{99m}Tc-sestamibi scintigraphy is complicated by the presence of thyroid disease which can lead to false-positive results. Certain types of thyroid nodule and chronic thyroiditis may take up and retain sestamibi in a similar way to parathyroid tissue. Uptake has also been described

in follicular lymph node hyperplasia and chronic lymphadenitis.

Overall sensitivity can be slightly increased by using both US and scintigraphy when compared to either technique (Lumachi et al. 2000), but even when results are concordant, the detection of multigland disease and second adenomata is disappointing, having a reported positive predictive value of only 30% and a negative predictive value for single gland disease of only around 70% (Sugg et al. 2004; Rickes et al. 2003). For this reason, many institutions use intra-operative PTH assay during focussed minimally invasive surgery to reduce the risk of missing a double adenoma or multi-gland disease, even when pre-operative localisation is concordant.

If parathyroid carcinoma is suspected on US or when there are unusually high PTH levels, ^{18}F-FDG-PET and octreotide scintigraphy are both helpful in staging and may be more sensitive than ^{99m}Tc-sestamibi scintigraphy (Fig. 32a–d).

2.6.2 CT, MRI and Percutaneous Venous Sampling

CT or MRI, which may be co-registered with SPECT, provide cross-sectional anatomical detail which may help surgical planning, but studies are inconsistent as to the benefits in more routine cases. Most centres reserve these techniques for patients with non-concordant US and scintigraphy or where previous surgery has failed because the prevalence of supernumerary and ectopic glands is much higher in this group.

Contrast-enhanced MDCT is preferable to MRI because arterial-phase contrast enhancement can assist in differentiating vascular parathyroid tissue from lymph nodes and because there is less image degradation by pulsation artefact, which is particularly important when assessing the lower neck and mediastinum (Fig. 33a–c). The MRI signal characteristics of abnormal parathyroid glands are variable but typically follow those of lymph nodes, although occasionally there may be cystic or haemorrhagic features or evidence of fibrosis which allows them to be distinguished. Contrast-enhanced MRI is most advantageous when assessing patients with recurrent or persistent disease following parathyroidectomy, because of its ability to demonstrate parathyroid tissue within areas of post-operative fibrosis (Johnson et al. 2007).

Pre-operative percutaneous selective venous sampling is considered the gold-standard investigation for patients with recurrent disease following previous surgery and indeterminate results from other imaging modalities, with sensitivities as high as 90% being reported. False negative results are due to disruption of venous anatomy by previous surgery. The complication rate is low (Johnson et al. 2007).

References

Ali S, Cibas ES (2010) The Bethesda system for reporting thyroid cytopathology. Springer, New York

Baloch ZW, Cibas ES, Vlark DP, Layfield LJ, Ljung BM, Pitman MB, Abati A (2008) The national cancer institute: thyroid fine needle aspiration state of the science conference: a summation. Cytojournal 5:1–17

Bilezikian JP, Khan AA, Potts JT Jr (2009) Guidelines for the management of asymptomatic primary hyperparathyroidism: summary statement from the third international workshop. J Clin Endocrinol Metab 94:335–339

Cappelli C, Pirola I, Cumetti D, Micheletti L, Tironi AI (2005) The anteroposterior and transverse diameter ratio of non-palpable thyroid nodules a sonographic criteria for recommending fine-needle aspiration cytology? Clin Endocrinol 63:689–693

Cappelli C, Castellano M, Pirola I, Cumetti D, Agosti B, Gandossi E, Agabiti Rosei E (2007) The predictive value of ultrasound findings in the management of thyroid nodules. QJM 100:29–35

Cross P, Chandra A, Giles T, Johnson S, Kocjan G, Poller D, Stephenson T (2009) Guidance on reporting of thyroid cytology specimens. Royal College of Pathology, London

Diehl M, Risse JH, Brandt-Mainz K et al (2001) Fluorine-18 fluorodeoxyglucose positron emission tomography in medullary thyroid cancer: results of a multicentre study. Eur J Nucl Med 28:1671–1676

Eloy JA, Brett EM, Fatterpekar GM, Kostakoglu L, Som PM, Desai SC, Genden EM (2009) The significance and management of incidental [18F]fluorodeoxyglucose-positron-emission tomography uptake in the thyroid gland in patients with cancer. Am J Neuroradiol 30:1431–1434

Finkelstein SE, Grigsby PW, Siegel BA, Dehdashti F, Moley JF, Hall BL (2008) Combined [18F] Fluorodeoxyglucose positron emission tomography and computed tomography (FDG-PET/CT) for detection of recurrent, 131I-negative thyroid cancer. Ann Surg Oncol 15:286–292

Gharib H, Papini E, Paschke R, Duick DS, Valcavi R, Hegedüs L, Vitti P (2010) American Association of Clinical Endocrinologists, Associazione Medici Endocrinologi, and European thyroid association medical guidelines for clinical practice for the diagnosis and management of thyroid nodules. Endocrine Practice 16 (Suppl 1)

Haciyanli M, Lal G, Morita E, Duh QY, Kebebew E, Clark OH (2003) Accuracy of preoperative localization studies and intraoperative parathyroid hormone assay in patients with

primary hyperparathyroidism and double adenoma. J Am Coll Surg 197:739–746

Harach HR, Franssila KO, Wasenius VM (1984) Occult papillary carcinoma of the thyroid: a 'normal' finding in Finland: a systematic autopsy study. Cancer 56:531–538

Hatabu H, Kasagi K, Yamamoto K et al (1991) Cystic papillary carcinoma of the thyroid gland: a new sonographic sign. Clin Radiol 43:121–124

Hedinger C, Williams ED, Sobin LH (1988) Histological typing of thyroid tumors. In: international histological classification of tumors, World Health Organization, 2nd edn. Springer, Berlin

Johnson NA, Tublin ME, Ogilvie JB (2007) Parathyroid imaging: technique and role in the preoperative evaluation of primary hyperparathyroidism. AJR 188:1706–1715

Kent WDT, Hall SF, Isotalo PA et al (2007) Increased incidence of differentiated thyroid carcinoma and detection of subclinical disease. CMAJ 177:1357–1361

Kessler A, Rappaport Y, Blank A, Marmor S, Weiss J, Graif M (2003) Cystic appearance of cervical lymph nodes is characteristic of metastatic papillary thyroid carcinoma. J Clin Ultrasound 31:21–25

Kim EK, Park CS, Chung WY, Oh KK, Kim DI, Lee JT et al (2002) New sonographic criteria for recommending fine needle aspiration biopsy of nonpalpable solid thyroid nodules. AJR 178:687–691

King AD (2008) Imaging for staging and management of thyroid cancer. Cancer Imaging 8:57–69

Leenhardt L, Menegaux F, Franc B, Delbot T, Mansour G, Hoang C et al (2002) Selection of patients with solitary thyroid nodules for operation. Eur J Surg 168:236–241

Lin JD, Chao TC, Huang BY, Chen ST, Chang HY, Hsueh C (2005) Thyroid cancer in the thyroid nodules evaluated by ultrasonography and fine-needle aspiration cytology. Thyroid 15:708–717

Lind P, Kresnik E, Kumnig G et al (2003) ^{18}F-FDG-PET in the follow-up of thyroid cancer. Acta Med Austriaca 30: 17–21

Lumachi F, Zucchetta P, Marzola MC et al (2000) Advantages of combined technetium-99m-sestamibi scintigraphy and high-resolution ultrasonography in parathyroid localization: comparative study in 91 patients with primary hyperparathyroidism. Eur J Endocrinol 143:755–760

McDougall IR, Camargo CAS (2007) Treatment of micropapillary carcinoma of the thyroid: where do we draw the line? Thyroid 17:1093–1096

Miyakoshi A, Dalley RW, Anzai Y (2007) Magnetic resonance imaging of thyroid cancer. Top Magn Reson Imaging 18:293–302

Papini E, Guglielmi R, Bianchini A, Crescenzi A, Taccogna S, Nardi F et al (2002) Risk of malignancy in nonpalpable thyroid nodules: predictive value of ultrasound and color-Doppler features. J Clin Endocrinol Metab 87: 1941–1946

Richards PS, Avril N, Grossman AB, Reznek RH (2010) Thyroid cancer. In: Husband J, Reznek R (eds.) Imaging in oncology. Informa, London, Chap 10, pp 642–679

Rickes S, Sitzy J, Neye H, Ocran KW, Wermke W (2003) High-resolution ultrasound in combination with colour-Doppler sonography for preoperative localization of parathyroid adenomas in patients with primary hyperparathyroidism. Ultraschall Med 24:85–89

Robbins RJ, Larson SM (2008) The value of positron emission tomography (PET) in the management of patients with thyroid cancer. Best Pract Res Clin Endocrinol Metab 22:1047–1059

Sarkar SD, Kalapparambath TP, Palestro CJ (2002) Comparison of (123)I and (131)I for whole-body imaging in thyroid cancer. J Nucl Med 43:632–634

Shetty S, Maher MM, Hahn PF, Halpern EF, Aquino SL (2006) Significance of incidental lesions detected on CT: correlation among CT, sonography and pathology. AJR 187:1349–1356

Sobin L, Gospodarowicz M, Wittekind C (2009) TNM classification of malignant tumours (UICC), 7th edn. Wiley–Blackwell, New York, pp 58–62

Sugg SL, Krzywda EA, Demeure MJ, Wilson SD (2004) Detection of multiple gland primary hyperparathyroidism in the era of minimally invasive parathyroidectomy. Surgery 136:1303–1309

The American Association of Clinical Endocrinologists, the American Association of Endocrine Surgeons (2005) Position statement on the diagnosis and management of primary hyperparathyroidism. Endocr Pract 11:49–54

Untch BR, Olson JA (2006) Anaplastic thyroid carcinoma, thyroid lymphoma and metastases to thyroid. Surg Oncol Clin N Am 15:661–679

Van den Bruel A, Maes A, De Potter T et al (2002) Clinical relevance of thyroid fluorodeoxyglucose-whole body positron emission tomography incidentaloma. J Clin Endocrinol Metab 87:1517–1520

Wong KT, Ahuha AT (2005) Ultrasound of thyroid cancer. Cancer Imaging 5:167–176

Zettinig G, Leitha T, Niederle B et al (2001) FDG positron emission tomographic, radioiodine, and MIBI imaging in a patient with poorly differentiated insular thyroid carcinoma. Clin Nucl Med 26:599–601

Neck Nodal Disease

Kunwar S. S. Bhatia and Ann D. King

Contents

Abstract

Neck nodal metastases are common in head and neck cancer and influence prognosis profoundly. This chapter focuses on the commonest cancer type, squamous cell carcinoma, although other malignancies are also outlined. CT, MRI and US are the mainstay imaging modalities for routine nodal evaluation and are reliant on anatomic criteria, which are described in this chapter. 18F-FDG PET/CT provides functional information by virtue of tumour hypermetabolism although its role in staging is not established. Neck nodal distribution and nodal staging using the current levels-based and TNM systems respectively are described. Besides N stage, other nodal features demonstrable on imaging, including extracapsular spread and precise location, can influence therapy

K. S. S. Bhatia · A. D. King (✉)
Department of Diagnostic Radiology and Organ Imaging, Faculty of Medicine, Prince of Wales Hospital, The Chinese University of Hong Kong, New Territories, Hong Kong SAR, China
e-mail: king2015@cuhk.edu.hk

R. Hermans (ed.), *Head and Neck Cancer Imaging*, Medical Radiology. Diagnostic Imaging,
DOI: 10.1007/174_2011_382, © Springer-Verlag Berlin Heidelberg 2012

and prognosis. Anatomic imaging is particularly challenging in the post-treatment neck, especially for assessment of residual nodal cancer following chemoradiation. In this regard, 18F-FDG PET/CT may have some advantages; currently there is great interest in the development of other functional techniques such as diffusion-weighted MRI.

1 Introduction

Head and neck cancers commonly metastasize to cervical nodes. The frequency of nodal metastases from head and neck squamous cell carcinoma (HNSCC) is approximately 50% although this is variable, being dependent on factors such as the primary tumour site and stage. Nodal metastases cause morbidity and mortality by invading vital structures in the neck and by increasing the risk of more distant tumour spread. Nodal status is a very important prognostic indicator in HNSCC as metastatic cervical nodes reduce patient survival by 30–50% (Layland et al. 2005; Tankere et al. 2000) and multiple nodes, extranodal spread and lower cervical metastases are additional adverse prognostic factors. The treatment options of surgery and/or (chemo) radiotherapy are influenced by nodal status. Given the importance of nodal disease on patient outcomes, prompt detection of nodal metastases at initial presentation and after treatment is essential to prevent their rapid progression to more advanced and unsalvageable disease. Clinical palpation, although a valuable skill, is inaccurate for nodal detection and characterisation (Merritt et al. 1997; Johnson 1990) and therefore imaging has an essential role at every step of the patient pathway from initial diagnosis through to post therapeutic surveillance.

This chapter will review the normal nodal distribution and lymphatic drainage pathways in the head and neck region and the imaging features that are employed for distinguishing metastatic nodes from benign nodes using both anatomical and functional imaging criteria. Nodal staging and imaging strategies with respect to clinical and subclinical nodal disease, as well as prediction of therapeutic response and post therapeutic evaluation, are outlined. Emphasis throughout this chapter is on HNSCC although other head and neck carcinomas as well as lymphoma will be discussed briefly.

2 Nodal Group Classification and Pathways of Lymphatic Drainage

Early classifications of cervical nodal distribution were purely anatomical in that individual nodes or nodal groups were named according to the structures they were in close proximity to, such as submandibular nodes, jugulodigastric nodes, etc. While this classification remains useful today for describing specific nodes, over the years a levels-based system has emerged with the objectives of being simple, reproducible and relevant in the era of selective surgical and radiotherapy treatments as well as cross-sectional imaging. In this system, the majority of cervical nodes are assigned to one of six levels (I–VI) whose boundaries are readily identifiable on imaging. A further seventh level (VII) is sometimes used also which refers to nodes in the superior mediastinum (Som et al. 1999). Several neck nodal groups are located outside these levels and are still referred to anatomically such as the retropharyngeal, facial, parotid and periparotid, occipital and peri auricular nodal groups. A more detailed account of the levels-based system can be found in "Clinical and Endoscopic Examination of the Head and Neck" and by reference to the article by Som et al. (1999), but a brief summary is shown in Fig. 1 and illustrated by axial MRI images (Figs. 2a–f and 3a, b).

Lymphatic drainage in the head and neck tends to be site-specific and follow predictable pathways down the neck. The first draining node or nodal basin for a given site is termed the first echelon or sentinel node(s) and subsequent nodal basins are termed the second and third echelons, etc. The typical lymphatic drainage for different primary cancer sites in the head and neck is listed in Table 1. Awareness of this lymphatic drainage has relevance for nodal staging, treatment planning and to search for occult primary cancers. Midline structures such as the tongue, or sites with a particularly enriched lymphatic network, such as the pyriform sinus, frequently drain bilaterally. Furthermore, lymphatic drainage can vary between individuals and can be disrupted by previous infections, neck surgery and radiotherapy.

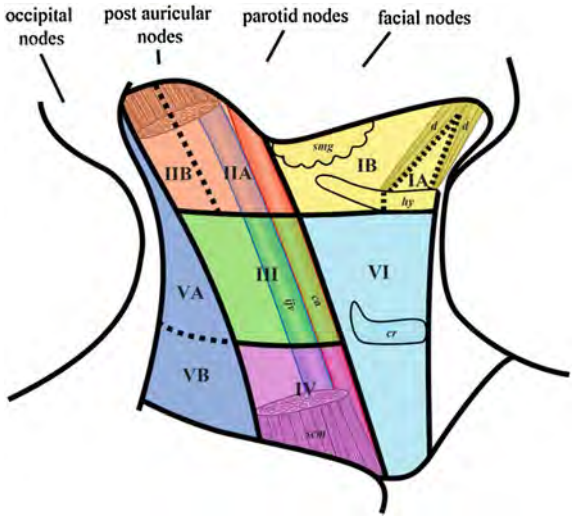

Fig. 1 Schematic illustration of the imaging-based level system of nodal distribution in the right side of the neck. *Solid lines* indicate boundaries of levels and *dotted lines* indicate level subdivisions. Facial, parotid, post auricular, occipital, retropharyngeal and superficial external jugular nodes (latter two groups are not shown) reside outside these levels and referred to by anatomical names. Level VII nodes are in the superior mediastinum (not shown). (*d* anterior belly of the digastric muscle, *ca* carotid artery (common and internal), *cr* cricoid cartilage, *hy* hyoid bone, *ijv* internal jugular vein, *smg* submandibular gland, *scm* sternocleidomastoid muscle)

3 Imaging Modalities

This section will provide a brief overview of the main modalities used for neck node evaluation, as well as of some of the newer functional imaging techniques which are presently in the domain of clinical research. Computed tomography (CT), magnetic resonance imaging (MRI), ultrasound (US) and (18)F-fluorodeoxyglucose positron emission tomography (FDG-PET) are the four main imaging modalities in routine clinical use for assessment of cervical nodal metastases. There is considerable variation in the reported accuracies of these modalities, which is unsurprising given the heterogeneity of study designs in terms of patient selection, imaging protocols, radiological diagnostic criteria and histopathological evaluation (Castelijns and van den Brekel 2002; van den Brekel et al. 1996). However, the choice of imaging technique is influenced also by other factors, which include the optimum modality for evaluating the primary site, available resources and radiological expertise. The limitations of conventional imaging for lymph node assessment have provided the impetus for research into new functional imaging techniques. These include techniques such as sentinel node lymphoscintigraphy and techniques that can be added to MRI such as diffusion-weighted imaging (DWI), proton magnetic resonance spectroscopy (MRS), dynamic contrast-enhanced MRI (DCE-MRI) and ultrasmall superparamagnetic iron oxide (USPIO) MRI, or added to CT such as dynamic contrast-enhanced CT. Some of these new techniques will be briefly mentioned at the end of this section.

3.1 CT and MRI

CT or MRI is the most widely used modality which reflects the fact that these modalities have acceptable and comparable accuracies for nodal malignancy, and because these can simultaneously assess the primary tumour and the neck nodes. A detailed account of the relative merits of CT and MRI is beyond the scope of this chapter although in general, MRI is excellent for soft tissue characterisation and does not involve ionising radiation, whereas CT is quicker to perform hence less susceptible to motion artifacts which make it especially suitable for dyspnoeic or claustrophobic patients. In practice whatever modality is used to stage the primary tumour is used also to stage the neck. Both modalities require intravenous contrast medium administration for optimum nodal characterisation.

3.2 US and US-Guided Fine-Needle Aspiration Cytology

US is the most practically useful imaging modality for cervical lymph nodes, although it is unsuitable in some deeply seated nodal groups such as those in the retropharyngeal space. US is quick, inexpensive, well tolerated, does not require intravenous contrast media and can display specific imaging features of discriminatory value more readily than CT or MRI, such as the nodal hilum and vascularity. A further major benefit of US is that it can be used to guide fine-needle aspiration for cytology (US-FNAC), which with sufficient experience can be performed successfully in nodes as small as 4 mm in diameter. The superiority of US-FNAC compared to US alone has

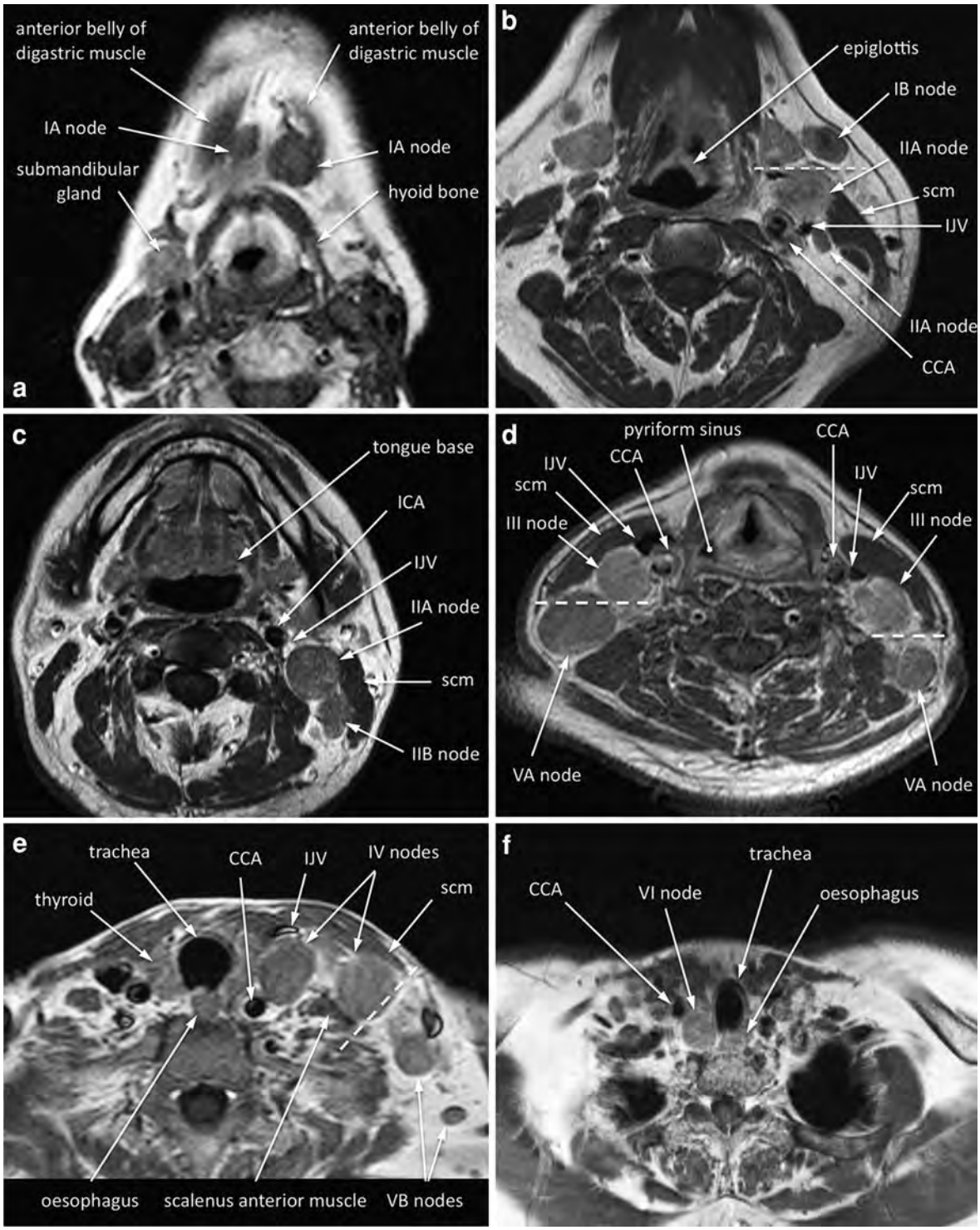
anterior belly of digastric muscle
anterior belly of digastric muscle
IA node
IA node
submandibular gland
hyoid bone
a
b
epiglottis
IB node
IIA node
scm
IJV
IIA node
CCA
c
tongue base
ICA
IJV
IIA node
scm
IIB node
d
pyriform sinus
CCA
IJV
CCA
IJV
scm
scm
III node
III node
VA node
VA node
e
trachea
CCA
IJV
IV nodes
scm
thyroid
oesophagus
scalenus anterior muscle
VB nodes
f
trachea
CCA
VI node
oesophagus

◀**Fig. 2** Distribution of cervical nodes using the imaging-based level system on axial T1 W post contrast MRI. (*CCA* common carotid artery, *ICA* internal carotid artery, *IJV* internal jugular vein, scm; sternocleidomastoid muscle) **a** Level IA (submental); nodes below the mylohyoid muscle, between the anterior bellies of the digastric muscles and hyoid bone. **b** Level IB (submandibular); nodes lateral to the anterior belly of digastric muscle and anterior to the posterior margin of the submandibular gland (the latter is denoted by a *dashed line*). Level II (upper internal jugular); nodes around the upper internal jugular vein. The lower limit is the inferior margin of the body of the hyoid bone. IIA nodes are anterior, medial or lateral, or posterior but inseparable from the vein. **c** Level IIA and Level IIB (upper internal jugular); nodes posterior to the upper internal jugular vein are IIA if inseparable from the vein and IIB if separable from the vein. **d** Level III (Mid jugular); nodes around the mid-internal jugular vein between the inferior margin of the body of the hyoid bone and inferior margin of the cricoid cartilage, lateral to the common carotid artery and anterior to the posterior margin of the sternocleidomastoid muscle. Level VA (upper posterior triangle); nodes posterior to posterior margin of the sternocleidomastoid muscle, anterior to the trapezius muscle and above the lower border of the cricoid cartilage (*dashed line* denotes the boundary between level III and VA). **e** Level IV (lower internal jugular); nodes around the lower internal jugular vein between the level of the cricoid cartilage and clavicle, lateral to the common carotid artery, and anterior to a line extending from the posterior margin of the sternocleidomastoid muscle to the posterolateral margin of the scalenus anterior muscle (denoted by a *dashed line*). Level VB (lower posterior triangle) nodes lie posterior to this line, anterior to the trapezius muscle and inferior to the cricoid cartilage. **f** Level VI (central compartment or visceral); nodes medial to the carotid arteries and extending between the hyoid bone and the manubrium. These include nodes along the thyroid gland, prelaryngeal and paratracheal nodes

been shown in several studies (Atula et al. 1997; Stuckensen et al. 2000; de Bondt et al. 2007). For example, one study documented 93% accuracy for US-FNAC compared to US alone (75%), CT (78%) and MRI (82%) (van den Brekel et al. 1993). Errors on US-FNAC are usually caused by sampling errors or cytological misinterpretation leading to false negative results. Because of its high accuracy, US-FNAC is well suited for investigating equivocal nodal findings in head and neck cancer patients, especially with the aim of distinguishing between patients with a N0 and a N+ neck, as this distinction has a major impact on clinical management. It is also performed in patients presenting with unexplained neck lymphadenopathy or suspected thyroid cancer where US is the initial imaging technique for assessing the primary site.

3.3 FDG-PET Imaging

Most head and neck cancers, including primary tumours as well as metastatic nodes, have increased glycolytic activity that can be detected using (18)F-fluorodeoxyglucose-PET (FDG-PET) imaging. Studies indicate that FDG-PET is superior to anatomic imaging techniques for the detection of nodal metastases in HNSCC (Schoder and Yeung 2004; Adams et al. 1998; Ng et al. 2006). However, FDG-PET is limited by its poorer spatial resolution and lack of anatomic detail. Combined PET/CT overcomes these limitations by permitting direct co-registration of functional and anatomic data, which translates into a higher accuracy for tissue characterisation than either PET or CT alone (Syed et al. 2005; Schwartz et al. 2005). In a recent study comparing imaging modalities for preoperative staging in HNSCC, FDG-PET/CT detected nodal metastases with 93% accuracy on a level-by-level basis, compared to 86% for patients evaluated by either CT or MRI (Roh et al. 2007). However, false negative and positive results occur using FDG-PET/CT thus, at present, there is no general consensus that using FDG-PET/CT for routine staging significantly improves clinical management (Ng et al. 2006; Hyde et al. 2003; Brouwer et al. 2004; Krabbe et al. 2008)

3.4 Diffusion-Weighted Imaging

DWI is the most developed of all the new functional MRI techniques. It evaluates free water motion (diffusion), which is quantified using apparent diffusion coefficients (ADCs) calculated from rate of signal loss on DWI images acquired with increasing diffusion encoding gradients (b-factors). DWI is non-invasive, relatively quick and can be performed with a large field of view to feasibly image most nodal groups in the neck. Nodal metastases show restricted diffusion and hence lower ADC values compared to normal nodes (Abdel Razek et al. 2006; de Bondt et al. 2009a; Holzapfel et al. 2009; Vandecaveye et al. 2009). However, to date there are few studies comparing DWI with conventional imaging, although one such study has shown that, for nodes between 4 and 9 mm, DWI achieved appreciably higher sensitivity than conventional turbo spin-echo MRI (76% vs. 7%) while specificity was only slightly lower (94% vs. 99.5%) (Vandecaveye et al. 2009).

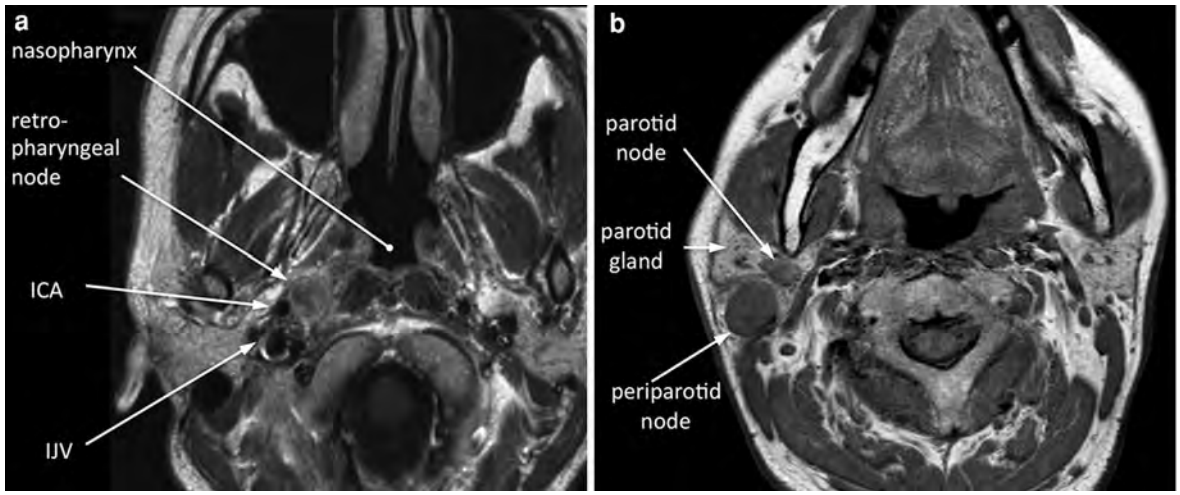

Fig. 3 Additional nodes not covered by the level-based system (Facial, post auricular and occipital nodes as well as level VII (superior mediastinal) nodes are not shown) (*ICA* internal carotid artery, *IJV* internal jugular vein). **a** Retropharyngeal nodes, medial to the internal carotid artery and posterolateral to the pharynx. **b** Parotid and periparotid nodes

Table 1 Primary head and neck cancers—main routes of nodal drainage

Site of primary cancer	Nodal groups
Nasopharynx	Retropharyngeal or level II (especially nodes posterior to the upper IJV), then in an orderly sequence down the neck. Submandibular and parotid nodes are uncommon at presentation. Bilateral nodes (including retropharyngeal nodes) in 60%
Oral cavity (oral tongue and floor of mouth and lip)	IA, IB, but lateral part of tongue and more posterior floor of mouth drain to IIA and IIB. Metastases from the lateral margin of the oral tongue may go directly to IV
Oropharynx (tongue base, palatine tonsil and soft palate)	IIA, IIB and sometimes IB. May spread directly to III and retropharyngeal nodes. Contralateral nodes in 20% of tumours in the base of the tongue and soft palate
Hypopharynx	III, IV and sometimes IIA, IIB. Posterior wall tumours also drain to retropharyngeal nodes. Increased risk of contralateral nodes if the tumour crosses the midline or involves the medial wall of the pyriform sinus
Larynx	Supraglottis and glottis: IIA, IIB, III. Subglottis: VI, IV, III. Incidence of nodal metastases from supraglottis is high due to high lymphatic density. (low lymphatic density in glottis hence low incidence from this subsite)
Sinonasal	Anterior nasal: IB. Posterior nasal/paranasal: retropharyngeal, II, III, IB
Salivary gland	Parotid: Intraparotid and periparotid nodes, II, III. Submandibular: IB. Sublingual: IA, IB. Minor salivary (mainly in the hard palate): II, III. Salivary cancers can skip to IV
Thyroid gland	Central compartment (VI: periglandular, paratracheal, paralaryngeal and prelaryngeal nodes) followed by the lateral compartment (initially III, IV then V) although spread may skip to lateral compartment first. Involvement of levels I and II are uncommon at first presentation
Skin	Depends on primary site but usually involves superficial nodal groups such as the (peri)parotid, post auricular, occipital nodes and superficial nodes along the external jugular vein

3.5 Magnetic Resonance Spectroscopy

Proton (1H) MRS measures tissue metabolites, which may then be used for tissue characterisation. Most research to date has focused on two metabolites, choline (Cho) and creatine (Cr), that can be detected in many tissues as spectral peaks at 3.22 and 3.03 ppm. Preliminary studies in HNSCC document

higher Cho/Cr ratios in both primary tumour and metastatic nodes compared to normal muscle (Mukherji et al. 1997; Bisdas et al. 2007; King et al. 2004a), and in metastatic nodes compared to reactive nodes (Bisdas et al. 2007). Furthermore, MRS has been shown to be of utility for differentiating cervical lymphadenopathies (King et al. 2005). Nevertheless, at present, MRS has important technical limitations that hamper a role in nodal staging. These include constraints on the minimum voxel size ($\sim 1\ cm^3$), contamination by surrounding tissues, and prolonged acquisition times which make MRS both susceptible to motion artifacts and unfeasible for assessing the entire neck.

3.6 Dynamic Contrast-Enhanced (DCE) MRI

DCE-MRI uses low molecular weight paramagnetic contrast agents such as gadolinium to assess the microvasculature and extravascular extracellular space of nodal cancers. In the head and neck region rapid serial imaging is performed using T1 W gradient recalled echo sequences as the intravenous contrast passes through the node, and the resultant data are analysed using time-intensity plots or pharmacokinetic models. Early work suggests that there may be a difference in the contrast enhancement of metastatic and normal nodes, with the former showing a delayed and lower peak enhancement, and slower washout phase (Fischbein et al. 2003).

3.7 Lymphoscintigraphy for Sentinel Node Localisation

Lymphoscintigraphy can be used for sentinel node localisation. It is already an established technique in malignant melanoma and breast cancer and currently is under investigation in HNSCC. Sentinel node imaging typically entails injecting Tc-99 m radiolabelled colloid into tissues around the primary tumour and mapping the subsequent lymphatic drainage including first echelon nodes using preoperative planar scintigraphy or single photon emission computed tomography (SPECT) as well as intraoperative hand held gamma detectors. The localised sentinel node is subsequently excised and examined for cancer, which is used to predict whether there is likely cancer in downstream nodes. In recent years, there has been significant interest in the role of sentinel node biopsy (SNB) for staging the clinical N0 neck in HNSCC. Accumulating evidence from pilot studies of SNB in oral/oropharyngeal HNSCC suggest this technique can achieve over 90% sensitivity and specificity for predicting overall neck nodal status. On the basis of these results, the risk of occult metastases after a negative SNB may be under 5%, hence SNB in these patients could eliminate the need for prophylactic neck dissections (Alvarez Amezaga et al. 2007; Alkureishi et al. 2010). The indications for SNB have still to be established. In this regard it may be unsuitable for floor of mouth tumours due their close proximity to the lymphatic basin which hinders sentinel nodal detection (Alkureishi et al. 2010). As a modification of the sentinel node technique, pilot studies have evaluated using US-guided FNAC instead of excision biopsy for radiolocalised sentinel nodes in N0 HNSCC (Nieuwenhuis et al. 2000, 2002; Hoft et al. 2002). However, the results thus far have been discouraging as this approach achieves poor sensitivities for predicting a positive nodal status and offers no practical diagnostic gains compared to conventional US-FNAC (Nieuwenhuis et al. 2000; van den Brekel et al. 1991).

4 Imaging Criteria for Malignant Nodes

The main imaging modalities used for initial nodal evaluation, namely CT, MRI and US, utilise anatomic criteria to differentiate malignant from benign nodes, although some centres supplement this with functional data from FDG-PET. Imaging features more suggestive of normal or reactive nodes include small size, oval shape, presence of central hilum, hilar vascularity, homogeneous cortex (Figs. 4, 5, 6) and minimal FDG uptake. By comparison, imaging features suggestive of metastatic nodes include nodal enlargement, rounded shape, absent hilum, peripheral or other non hilar vascularity, heterogeneous parenchyma which includes necrosis or cystic change, border irregularity suggestive of extracapsular tumour spread (ECS) (Figs. 4, 5, 6) and avid FDG uptake. Each criterion is discussed in more detail below.

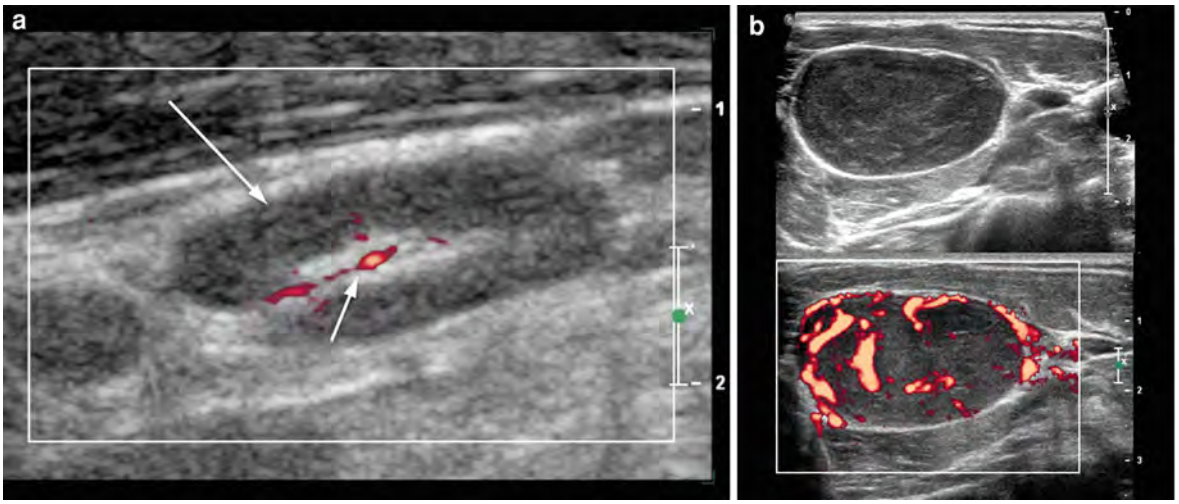

Fig. 4 **a** Grey scale US of a normal lymph node (*long arrow*) showing the peripheral cortex (*long arrow*) central echogenic hilum (*short arrow*) with hilar vascularity. **b** Grey scale US (*top*) with corresponding grey scale and power Doppler US (*below*) of a metastatic node from SCC. The node shows enlargement, long:short axis ratio <2, absent hilum, absent hilar vascularity and a peripheral disorganised vascular pattern

4.1 Size

Normal cervical lymph nodes range in size from a few millimeters to just over 2.5 cm in longitudinal diameter (Figs. 4, 5, 6). Nodal size declines with age and varies according to location. Nodes in the upper internal jugular chain, notably the jugulodigastric region, are usually the largest due to mild hyperplasia as a result of chronic exposure to repeated infections in the oral cavity and pharynx, while nodes towards the skull base and thoracic inlet tend to be smaller.

Nodal enlargement is an important feature of malignant infiltration although no threshold of nodal size is both highly sensitive and highly specific, which reflects the fact that moderately enlarged nodes in the neck are frequently reactive while small tumour deposits may not alter nodal dimensions. Over the years, numerous studies have investigated optimal size cut-offs for nodal metastases in HNSCC. One of the most influential is a CT-based study by van den Brekel et al. that documented short axis diameter thresholds of 11 mm for level II and 10 mm elsewhere as the most accurate overall, achieving 82% sensitivity and specificity. In addition, these thresholds could be lowered to 8–10 mm for groups of 3 or more nodes draining a primary tumour (van den Brekel et al. 1990). These criteria are still widely used today, albeit with minor modifications such as a lower threshold of 5 mm short axis diameter for retropharyngeal nodes (King et al. 2000).

Nevertheless, it should be highlighted that optimum size criteria are arbitrary and may be altered depending on whether a higher sensitivity or higher specificity is desired. One early study documented that lowering the short axis diameter cut-off from 15 to 5 mm increased the sensitivity of CT from 56 to 98% but lowered the specificity from 84 to 13% (Curtin et al. 1998). In addition, the patient population may influence optimum thresholds. Van den Brekel et al. performed another study of size criteria in HNSCC, this time using US, and found that thresholds achieving the highest global accuracy were 9 mm for level II and 8 mm for other levels (74% sensitivity and 78% specificity), whereas for a subgroup of patients without palpable nodes, optimal thresholds were lower, namely 7 mm for level II and 6 mm for other levels (80% sensitivity and 59% specificity) (van den Brekel et al. 1998a).

4.2 Shape

Normal or reactive nodes tend to be oval or reniform in shape and have a ratio of the longitudinal to transverse axis diameter (L/T) >2, while nodal metastases are more rounded resulting in a lower L/T

Fig. 5 **a** Axial CT post contrast showing normal jugulodigastric lymph nodes bilaterally (*long arrows*). The hilum, when seen, appears as a focal depression of the parenchyma (*short arrows*). A nodal vessel is seen emerging from the nodal hilum on the right (*arrowhead*). **b** Axial CT pre and post contrast (*left* and *right*) in a patient with HNSCC showing enlarged rounded right level IIA metastatic nodes. The more anterior node (*short arrow*) appears solid, whereas the posterior node (*long arrow*) is necrotic

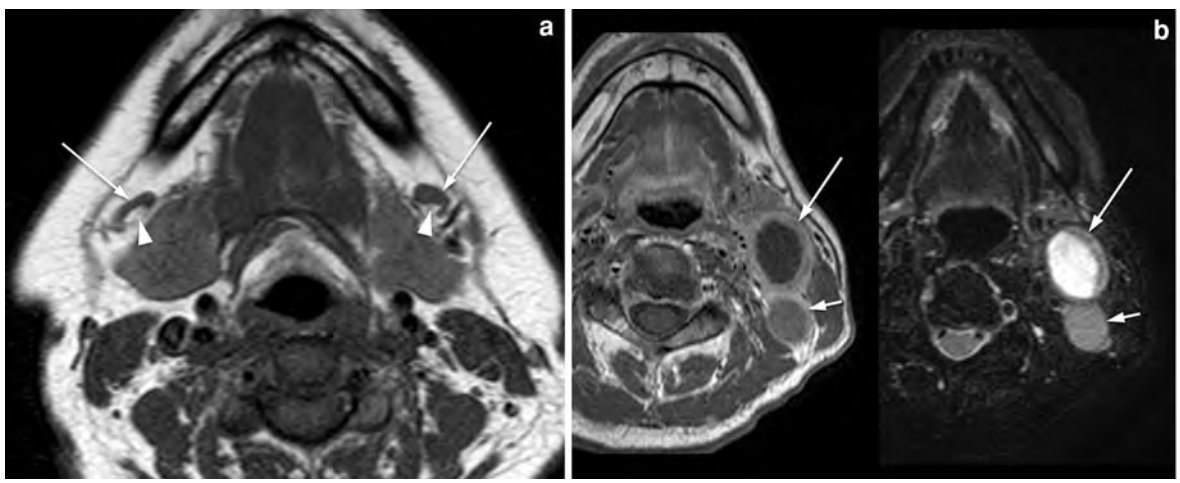

Fig. 6 **a** Axial T1 W MRI showing normal bilateral submandibular lymph nodes (*arrows*) with identifiable hila (*arrowheads*). **b** Axial T1 W post contrast MRI (*left*) and T2 W fat saturated MRI (*right*) showing metastatic left level IIA nodes (*arrows*) from nasopharyngeal carcinoma. The posterior node (*short arrow*) appears solid, whereas the anterior node (*long arrow*) is necrotic and has an ill-defined border suggestive of early extracapsular spread

ratio (Figs. 4, 5, 6). In clinical practice, a L/T ratio <2 is widely adopted as a criterion of malignancy. In one large study, nodal shape achieved 95% accuracy although it should be noted that the majority of these nodes were >1 cm (Steinkamp et al. 1995). Furthermore, normal nodes in the submandibular and parotid regions tend to be more rounded. The presence of eccentric cortical widening has been described in malignant nodes including in the neck (Vassallo et al. 1992), although this feature may also occasionally be found in normal or reactive nodes, especially those in the submandibular region.

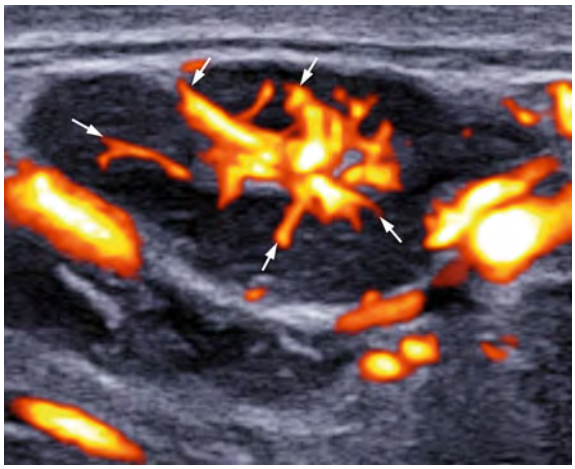

Fig. 7 Grey scale US with power Doppler showing a prominent reactive submandibular lymph node with florid hilar vascularity (*arrows*)

4.3 Hilum

Lymph nodes contain a hilum composed of arteries, veins, lymphatics and sometimes fat (Figs. 4, 5, 6). This is visualised optimally by US due to the presence of numerous reflective interfaces within the lymphatic sinuses. Using grey scale US, the hilum appears as an echogenic linear structure traversing into the centre of the node, and is detected in ~66% and >90% of normal nodes <5 and >5 mm, respectively (Ying et al. 2001). Conventional CT and MRI are generally less capable of depicting hila, although with careful attention a hilum is often identifiable, especially when there is fatty metaplasia. Loss of the nodal hilum can occur in malignant nodes due to direct invasion or compression by tumour. The reported sensitivity of this feature on conventional US varies widely between 44 and 95% (Vassallo et al. 1992; Ahuja et al. 2001a; Ahuja and Ying 2002; Ying et al. 1998). False negative results using this criterion are not surprising given that the majority of microscopic tumour deposits are located within the subcapsular sinuses, as afferent lymphatic channels enter the nodes peripherally (van den Brekel et al. 1996).

4.4 Vascular Pattern

The vascular architecture within lymph nodes can be assessed using power Doppler US, which in normal nodes typically extends into the hilum and branches outwards into the parenchyma (Figs. 4, 7). This hilar vascular pattern is more florid in reactive nodes. In contrast, metastatic nodes tend to display disorganised vascular patterns including peripheral cortical or subcortical vascularity, and focal areas of displaced or absent vascularity, with or without preservation of the hilar pattern (Ariji et al. 1998; Na et al. 1997a; Wu et al. 1998). Published studies using vascularity to differentiate metastatic from reactive nodes have reported sensitivities of 83–89% and specificities of 87–98% (Ariji et al. 1998; Wu et al. 1998). While vascular patterns are important, they are not always demonstrable in normal nodes, especially in those under 5 mm (Ying et al. 2001). Furthermore, abnormal vascular patterns are non-specific as they may occur in non-malignant lymphadenopathies (Ahuja et al. 2001b). Quantitative indices of vascular resistance including the resistive index (RI) and pulsatility index (PI) can be measured in intranodal vessels using spectral Doppler US. Several studies have shown that metastatic nodes have higher RI and PI than benign nodes (Na et al. 1997a; Wu et al. 1998; Ahuja et al. 2001b; Steinkamp et al. 1994; Dragoni et al. 1999). Measuring these indices is highly operator dependent and so currently there is no consensus on the optimal cut-offs for malignancy.

4.5 Parenchymal Heterogeneity and Necrosis

Normal parenchyma in the nodal cortex appears relatively uniform on conventional imaging whereas parenchymal heterogeneity is usually pathological (Figs. 4, 5, 6). Moreover, in the context of known HNSCC, nodal heterogeneity is specific for metastasis. These heterogeneous areas may be composed of variable amounts of solid tumour, deposits of keratin and necrotic tumour, which may or may not be cystic. Intranodal necrosis in HNSCC correlates with nodal size as it reflects tumour growth beyond its blood supply, and is identified in 56–63% of metastatic nodes >1.5 cm compared to 10–33% of nodes <1 cm (Friedman et al. 1993; Don et al. 1995). CT, MRI and US can all depict necrosis >3 mm in size; the accuracies of MRI and CT for detecting necrosis are similar (91–92%) and higher than that of US (84%) (King et al. 2004b). The lower accuracy of US may be explained partly by the fact that necrosis sometimes

can appear isoechoic to normal nodal parenchyma. Metastatic nodes can be almost entirely cystic and thus may cause initial diagnostic confusion with benign cystic lesions, namely branchial cleft cysts, especially if solitary and located along the mid to upper jugular chain. Nevertheless, the precise location, appearance and different clinical presentations of head and neck cancers and benign cysts can usually discriminate these conditions. Metastatic nodal calcification is rare at presentation in HNSCC (Eisenkraft and Som 1999; Gormly and Glastonbury 2004) and the presence of calcification should raise the suspicion of nodal metastases from thyroid cancer. Nodal calcification may also be found in benign pathologies, especially granulomatous diseases, as well as other untreated and treated malignancies such as adenocarcinoma and lymphoma (Eisenkraft and Som 1999).

4.6 Border Irregularity

In the absence of infection or previous treatment, loss of the normally smooth nodal border is highly suspicious for ECS (Figs. 6, 8, 9). The risk of ECS increases with nodal size, being present in approximately 50 and 75% of nodal metastases with a diameter of 2–3 cm and >3 cm, respectively (Snow et al. 1982; Collins 1987). In addition, ECS is reported to occur in 23% of metastatic nodes <1 cm, which accounts for 30% of all nodal ECS (Don et al. 1995; Collins 1987). ECS has major prognostic significance, which is discussed in a later section. The reported sensitivity and specificity of CT for ECS is 62–81% and 60–90% (Carvalho et al. 1991; Steinkamp et al. 1999; Xu et al. 1998; Souter et al. 2009) and of MRI is 74 and 72% (Steinkamp et al. 2002). Several early studies reported that MRI was inferior to CT for detecting ECS, although more recent studies indicate comparable accuracies (King et al. 2004c). Moreover, another MRI study documented that the presence of border irregularity on T2 W fat suppressed sequences achieved up to 87% sensitivity and 94% specificity for metastases, and encouragingly the accuracy remained high for nodes <10 mm in short axis diameter (up to 78% sensitivity and 97% specificity) (de Bondt et al. 2009b). Nevertheless, imaging detection of ECS is subjective and dependent on radiologists experience as it may be subtle or mistaken for perinodal inflammatory changes

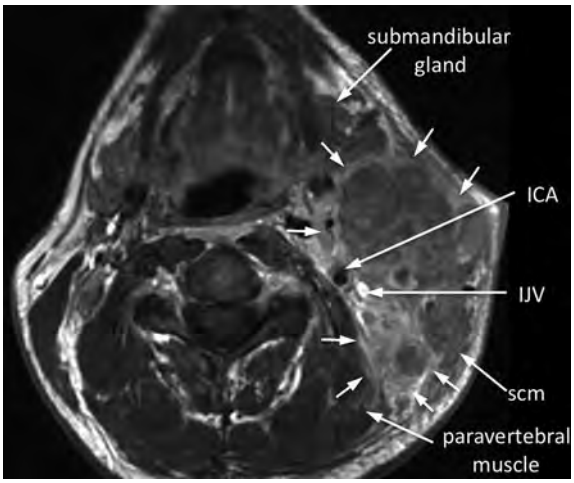

Fig. 8 Axial T1 W post contrast MRI in a patient with HNSCC showing metastatic left mid-upper internal jugular lymphadenopathy with gross extracapsular spread (*small arrows*). The enhancing nodal borders are ill defined and extend into the surrounding deep cervical fascia as well as invade the left sternocleidomastoid muscle and paravertebral muscles, both of which show abnormal enhancement. Tumour also contacts the left internal carotid artery and internal jugular vein. (ICA; internal carotid artery, IJV; internal jugular vein, scm; sternocleidomastoid muscle)

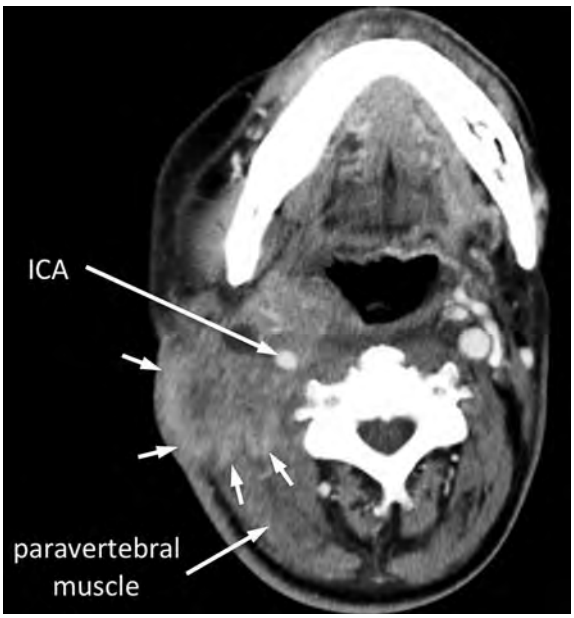

Fig. 9 Axial CT post contrast showing a heterogeneous right level II nodal mass with gross extracapsular spread. There is complete encasement of the right internal carotid artery (ICA), which is narrowed, as well as frank invasion of muscles and overlying skin (*short arrows*)

(Souter et al. 2009; Steinkamp et al. 2002; de Bondt et al. 2009b). It is noteworthy that metastatic nodes may appear paradoxically to have sharper, well-demarcated margins than benign nodes on grey scale US because of their reduced echogenicity, as this increases their conspicuity against the echogenic surrounding tissue (Shozushima et al. 1990).

4.7 FDG-PET Uptake

On FDG-PET, tissue FDG uptake can be assessed semi-quantitatively using standardised uptake values (SUVs). In normal nodes there is typically no or minimally increased SUV relative to background activity in the surrounding cervical tissue. By comparison, metastatic nodes typically show elevated SUVs, and the higher the SUV, the more likely a node is malignant. Despite these generalisations, at present there is no consensus in the literature regarding an appropriate SUV cut-off for malignancy, which partly reflects the overlap between uptake in benign and malignant nodes. False negative FDG-PET results are usually due to intrinsic low metabolic activity in small tumour deposits, and for this reason the utility of FDG-PET in patients with no palpable nodal disease is debated (Ng et al. 2006; Brouwer et al. 2004; Krabbe et al. 2008). Identification of metastatic nodes may be hampered also by low FDG uptake in markedly necrotic nodes, and when a node lies in close proximity to the primary tumour, as nodal uptake may be obscured by intense uptake at the primary site (King et al. 2008). False positive FDG-PET results can occur due to hypermetabolism in reactive nodes as well as other benign lymphadenopathies, recent biopsy and infection.

4.8 Functional MRI

On DWI, metastatic nodes show restricted diffusion and a low ADC (Fig. 10). Regions of necrosis, which are common in HSNCC, should be excluded from the ADC measurement as these reduce the discriminatory performance of DWI by increasing the ADC. In a recent study comparing SCC with benign nodes, DWI achieved 84% sensitivity and 94% specificity for metastases in nodes measuring >4 mm in short axis diameter (Vandecaveye et al. 2009). However, at present the optimum thresholds for discrimination of metastatic from benign nodes have still to be confirmed. On MRS, metastatic nodes have high Cho/Cr ratios (Fig. 11) but again optimum discriminatory thresholds have not been established.

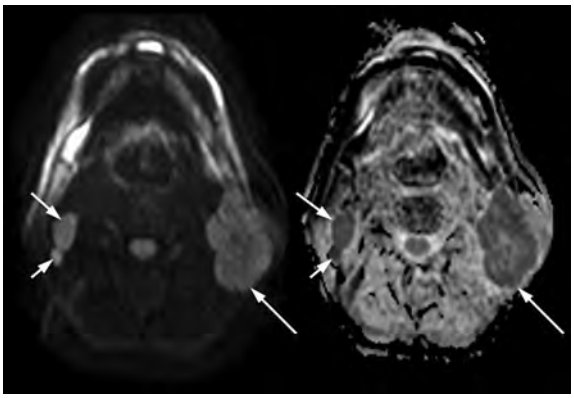

Fig. 10 Axial DWI-MRI diffusion image at b1000 (*left*) with corresponding ADC map (*right*) in a patient with HNSCC. Metastatic right level II nodes (*short arrows*) and a left level II nodal mass (*long arrow*) have a mean ADC of 0.94 and 1.04×10^{-3} mm^2/s respectively. These values are comparatively low, signifying restricted diffusion, which is compatible with malignant infiltration

5 Micrometastases

It should be noted that cancerous deposits may be microscopic, for instance comprising small clusters of cells, hence it is not feasible nor realistic to expect any of the current imaging modalities to detect these. Radiologically, the term micrometastases generally refers to tumour deposits <3 mm, which are not detected reliably by present day imaging techniques. These have been found in 25% of neck dissection specimens from patients with no clinicoradiological evidence of nodal disease (clinical N0) (van den Brekel et al. 1996). While micrometastases usually occur alongside larger deposits, in 10–25% of clinical N0 but pathologically positive neck dissection specimens, they are the sole manifestation of nodal malignancy (van den Brekel et al. 1992, 1996). Their exact clinical significance is unclear some of these could progress to clinically apparent disease if left untreated.

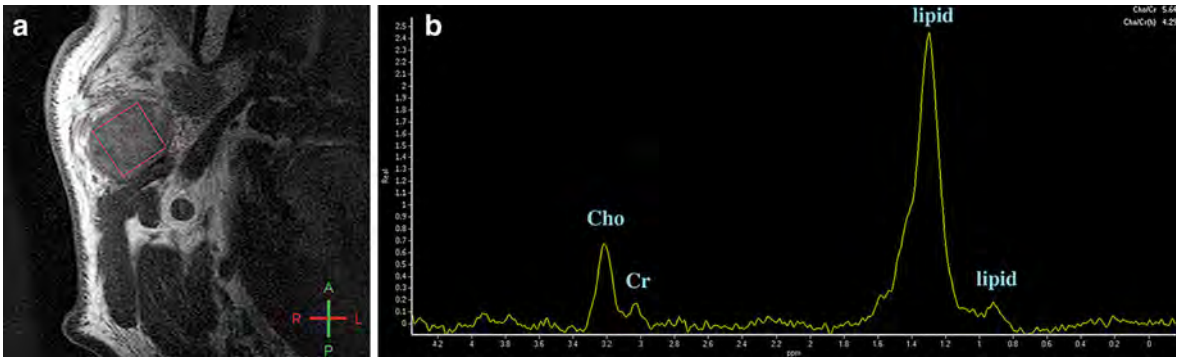

Fig. 11 Proton MRS of a metastatic periparotid node from HNSCC. a) Axial T1W post contrast MRI showing MRS voxel placement (red box). b) The corresponding MRS spectrum shows an elevated Cho peak and a high Cho/Cr ratio of 5.64, which is suggestive of malignancy. Lipid peaks are also demonstrated

6 Nodal Staging

Nodal staging of metastases from HNSCC is incorporated into the TNM system, which currently uses the 7th editions of the AJCC and UICC guidelines (Sobin et al. 2009; Edge et al. 2010). Staging evaluates nodal number (single or multiple), site (unilateral, contralateral or bilateral) and greatest dimension (using 3 and 6 cm thresholds). Of note, while diagnosis of a metastatic node entails measurement of the minimum axial diameter, staging entails measurement of the maximum diameter. In general, a single ipsilateral node ≤3 cm indicates N1 disease, any node >6 cm indicates N3; any other combination indicates N2 disease. N2 is further subdivided into N2a (single node >3 cm), N2b (multiple ipsilateral nodes) and N2c (bilateral or contralateral nodes). Nodal staging in HNSCC, nasopharyngeal carcinoma and thyroid cancer are summarised in Table 2. In HNSCC, the presence of metastatic nodes denotes a moderate or advanced overall stage III or IV.

Table 2 N staging of lymph node metastasis of head and neck cancers (AJCC/UICC 7th editions)

Primary site	N stage	Definition
Any	NX	Regional nodes cannot be assessed
	N0	No regional nodal metastasis
All excluding nasopharynx and thyroid	N1	Single ipsilateral ≤3 cm
	N2a N2b N2c	Single ipsilateral >3 cm and ≤ 6 cm Multiple ipsilateral ≤6 cm Bilateral or contralateral ≤6 cm
	N3	>6 cm in greatest dimension
Nasopharynx	N1	Unilateral cervical; unilateral or bilateral retropharyngeal; nodes above the supraclavicular fossa ≤6 cm
	N2	Bilateral cervical nodes above supraclavicular fossa ≤6 cm
	N3a N3b	>6 cm Supraclavicular fossa nodes
Thyroid	N1a	Level VI (pretracheal, paratracheal, prelaryngeal/Delphian lymph nodes)
	N1b	Unilateral, bilateral or contralateral cervical (levels I-V), retropharyngeal or superior mediastinal (level VII) nodes

7 Impact of Nodal Imaging on Patient Management

7.1 Detection of Metastatic Nodes

To understand the impact of imaging for identifying or excluding metastatic nodes, it is worth outlining the treatment strategies for the neck with (N+) and without (N0) clinicoradiological evidence of nodal metastases.

N+ neck: In patients with any evidence of metastatic neck nodal disease, definitive surgical treatment usually entails a radical or modified radical neck

dissection on the involved side(s). Both of these operations remove all lymph nodes within levels I–V operated(s), while these differ only in terms of whether extra-lymphatic structures (spinal accessory nerve, sternocleidomastoid muscle, internal jugular vein) are also removed (Robbins et al. 2002). In recent years several workers have advocated the use of a selective neck dissection (SND), which preserves at least one of the neck levels I–V to treat early node positive disease (localised, small volume nodes that lack ECS) (Andersen et al. 2002; Schmitz et al. 2009; Traynor et al. 1996) while minimising surgical morbidity. Radiotherapy fields usually encompass both sides of the neck although current radiotherapy regimes, which include intensity modulated radiotherapy (IMRT), deliver higher doses to positive nodes and lower doses to normal appearing nodal groups, especially those that lie close to important structures such as the parotid glands, oesphagus and spinal cord.

N0 neck: Depending on the primary site, up to 40% of necks in HNSCC with no palpable or radiological nodal metastases harbour occult nodal metastases (van den Brekel et al. 1996). Clinical management of these patients varies between a "watchful waiting" policy and elective treatment using radiotherapy or neck dissection. One surgical approach in the N0 neck is to perform a prophylactic unilateral SND on the same side as the primary tumour in order to diagnose and remove potential sites of occult metastases, and occasionally bilateral SNDs when the tumour is located in the midline. However, the optimal management of this subgroup is controversial in terms of how to balance the increased risk of unsalvageable recurrences that would occur under a "watchful waiting" policy in the minority of patients who have disease against the morbidity of prophylactic neck treatments in the majority of patients who do not have disease. To address this dilemma, many clinicians choose to surgically treat the neck electively if the risk of occult nodal metastases in the individual exceeds 20% (Weiss et al. 1994; Pfister et al. 2000; Pillsbury and Clark 1997). Patients with early T stage tumours in the glottis, parotid gland and paranasal sinuses have a low risk of nodal metastasis (<10%), hence the neck is usually managed by watchful waiting. Conversely, patients with tumours that have an advanced T-stage, are deeply invading (e.g. >4 mm in oral tongue cancers), have a high grade or are at high-risk sites (including the oropharynx, hypopharynx and supraglottis) usually undergo prophylactic neck treatment by surgery or radiotherapy (Shear et al. 1976; Martinez-Gimeno et al. 1995).

Based on the treatment stratifications described above, nodal imaging has the most impact on patient management in the following situations:

1. Distinguishing between patients with an N0 and an N+ neck. In this situation, finding even one single metastatic node in an otherwise normal neck could change management from a conservative "watchful waiting" policy to surgery/radiotherapy, or change the surgical approach from a limited to a more extensive neck dissection. Conversely, proving that a single indeterminate node is reactive rather than metastatic could have the opposite effect on management.
2. Identification of metastatic nodes outside the usual surgical and radiotherapy treatment fields including the contralateral neck, retropharyngeal, parotid, suboccipital, buccal, facial and level VI nodes; nodes adjacent to sites which may be preferentially spared during radiotherapy, such as the salivary glands. In these situations, the radiotherapy or surgical fields may need to be extended or the modality of treatment changed from one to the other.

To this end, US-FNAC is an invaluable ancillary investigation for any accessible lymph nodes with equivocal malignant features on imaging that will alter treatment (Dirix et al. 2006; Bussels et al. 2006).

7.2 Extracapsular Tumour Spread

Extracapsular tumour invasion of adjacent structures should be carefully documented as this may affect nodal resectability (Table 2) (Figs. 6, 8, 9). Tumour invasion of the internal or common carotid artery usually precludes neck dissection as the initial treatment due to the high risk of severe surgical morbidity combined with the risks of generally poor prognosis of these patients due to advanced disease (Freeman 2005). Unfortunately, imaging has a limited accuracy for detecting carotid invasion although, as a general rule, tumour directly contacting the vessel under 180° and over 270° of the vessel circumference indicates that vascular invasion is

probably absent and present, respectively (Steinkamp et al. 1999; Yousem et al. 1995; Yoo et al. 2000). In addition, some workers have documented that tumour fixation to the artery may be detected by palpation during US (Gritzmann et al. 1990; Mann et al. 1994).

Invasion of the prevertebral muscle or fascia tends to indicate unresectable disease to be within muscle. The presence of an intact fat plane between the tumour and the prevertebral fascia on imaging usually indicates that the fascia has not been breached, but the loss of this fat plane does not necessarily indicate that invasion is present.

Fortunately, tumoural invasion of the external carotid artery or its branches does not preclude surgery because these vessels can be sacrificed due to the rich collateral arterial supply in the head and neck region from the contralateral side. Similarly, the sternocleidomastoid muscle, internal jugular vein and skin can all be sacrificed if there is suspected involvement of these structures on imaging.

7.3 Identification of Patients at High Risk for Distant Metastases

Several nodal features at diagnosis are associated with a higher risk of developing distant metastases, including size >6 cm, >3 nodes involved, ECS and nodes in the lower neck/supraclavicular fossa (Alvi and Johnson 1997; de Bree et al. 2000; Leemans et al. 1993). These criteria may be used to decide whether further imaging, such as FDG-PET, is required to search for distant metastases centres recommend further imaging studies such as whole body PET-CT (Brouwer et al. 2006; Senft A et al. 2008).

8 Treatment Assessment

8.1 Prediction of Treatment Response to (Chemo)radiotherapy

There is currently great interest in identifying imaging markers with prognostic significance for (chemo)radiotherapy response which can be obtained either before treatment or early in a course of treatment, as these may facilitate better therapeutic stratification including dose escalations or cessation of (chemo)radiotherapy in favour of early conversion to surgery. Besides those markers already incorporated into the TNM staging (maximum nodal size, multiplicity and laterality), ECS is probably the most important as it indicates biologically aggressive disease as evidenced by increased risk of locoregional failure, distant metastases and reduced survival by as much as 50% (Myers et al. 2001; Larsen et al. 2009). At present most of the research regarding ECS is based on histology rather than imaging data. In the current edition of the TNM staging (Edge et al. 2010), ECS does not alter N stage *per se* although has been added as a descriptor (E+ or E– for clinical/radiologic evidence).

The prognostic significance of intranodal necrosis detected on imaging is unclear. A few studies using CT have documented that appreciable pre-treatment nodal necrosis is an independent risk factor for regional failure to (chemo)radiotherapy (Grabenbauer et al. 1998; Munck et al. 1991; Wang et al. 1996), which may be explained by the fact that tumour radiosensitivity is impaired by tissue hypoxia. Nevertheless, in clinical practice it is common for markedly necrotic nodes to demonstrate a complete response to (chemo)radiotherapy.

Several markers from functional imaging techniques obtained before treatment or early in the course of treatment show promise for prognostication. Early results suggest that local control is more likely to occur in nodes with higher vascularity as shown by a higher K trans on DCE-MRI (Kim et al. 2010). Nodes with a lower pre-treatment ADC and a higher early treatment rise in ADC on DWI (Fig. 12) (Kim et al. 2009; Vandecaveye et al. 2010) are also more likely to show tumour control. Using FDG-PET, primary tumours with a lower SUV are more likely to show an overall response in the neck (Schwartz et al. 2003; Wong et al. 2002). Furthermore, high pre-treatment FDG uptake in nodal metastasis in HNSCC may be a risk factor for distant recurrence (Kubicek et al. 2010).

8.2 Post Treatment Assessment

The majority of nodal metastases in HNSCC respond completely to (chemo)radiotherapy; in a minority of patients residual tumour persists, which may progress to surgically unsalvageable disease. Historically, regional control rates for early nodal disease treated

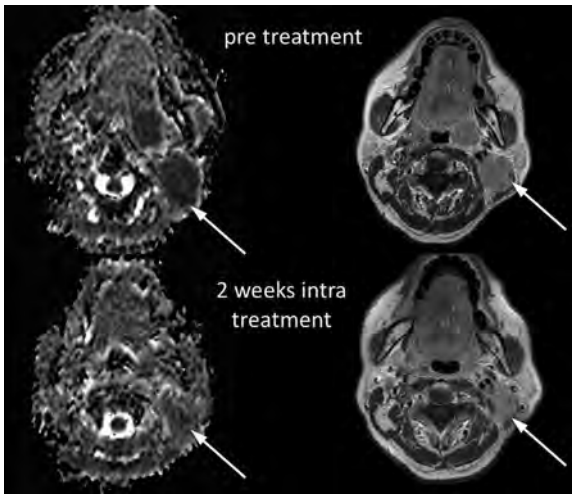

Fig. 12 Axial DWI-MRI ADC map (*left*) and T1 W post contrast MRI in a patient with a left tonsillar SCC and metastatic IIA node pretreatment (*upper row*) and 2 weeks intra treatment with concomitant chemoradiotherapy (*lower row*). The ADC of the node increased from 1.1×10^{-3} mm^2/s pretreatment to 1.5×10^{-3} mm^2/s at 2 weeks intra treatment. This indicates increased diffusion, which favours a treatment response. There has been no locoregional recurrence as of 3 years post treatment

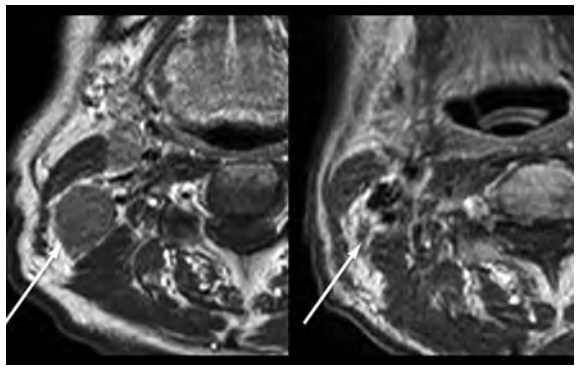

Fig. 13 Axial T1 W post contrast MRI showing right nodal metastases pretreatment (*left*) and 6 months post chemoradiotherapy (*right*). An enlarged right level II node (*arrow*) has reduced significantly in size following treatment although there is a small amount of residual soft tissue remaining. This was believed to represent a post treatment scar and there has been no regional recurrence as of 3 years post treatment

surgically or by radiotherapy were broadly equivalent, whereas for advanced nodal disease, control rates from radiotherapy alone were poor and suboptimal compared to radiotherapy followed by a planned neck dissection. For this reason, it was common practice to perform a neck dissection in this cohort, irrespective of whether or not there was evidence of a complete clinic-radiological response to radiotherapy. While this aggressive strategy reduced the risk of regional failures, this produced unnecessary surgical morbidity as up to two thirds of planned neck dissections were pathologically negative (Ojiri et al. 2002). Fortunately, with the development of more efficacious chemoradiotherapeutic regimens, there has been a shift towards a more conservative approach in terms of only performing neck dissection after (chemo)radiotherapy if there is clinical evidence of residual disease. This shift in practice places an even greater burden on imaging modalities to distinguish patients with post treatment regional failure who will require early salvage surgery, from patients with regional control, who can be placed under close imaging surveillance instead.

MRI and CT both have a high negative predictive value (94–97%) for residual nodal disease if the nodal metastases have essentially disappeared (Ojiri et al. 2002; Liauw et al. 2006; Yeung et al. 2008; Lin et al. 2007); under these circumstances patients may be spared surgery and undergo imaging surveillance instead. However, sterilised nodal metastases frequently regress incompletely, to leave behind a variable amount of scar tissue (Fig. 13). CT-based studies have documented residual nodes $\leq$1.5 cm with no focal abnormality (Liauw et al. 2006), or nodes with >90% reduction in size (Labadie et al. 2000) to be associated with tumour control. Larger residual masses or those containing a focal abnormality are non-specific as these may represent residual cancer or a benign mass of inflammatory tissue and fibrotic scarring. The documented positive predictive value of a post treatment mass is low, ranging between 36 and 59% (Ojiri et al. 2002; Liauw et al. 2006; Inohara et al. 2009). Ojiri et al. documented that 57% of hemi necks with nodes >15 mm were pathologically negative on neck dissection (Ojiri et al. 2002), and Yao et al. documented that post treatment nodes >50 mm could be disease-free (Yao et al. 2004). Difficulties in post treatment nodal assessment are partly due to the fact that anatomic abnormalities associated with malignancy can resolve very slowly after successful treatment, especially in nodes that were predominantly necrotic or had extracapsular invasion into adjacent muscles before treatment. The performance of US is similar to CT and MRI in that the disappearance of nodes usually indicates response (Furukawa and

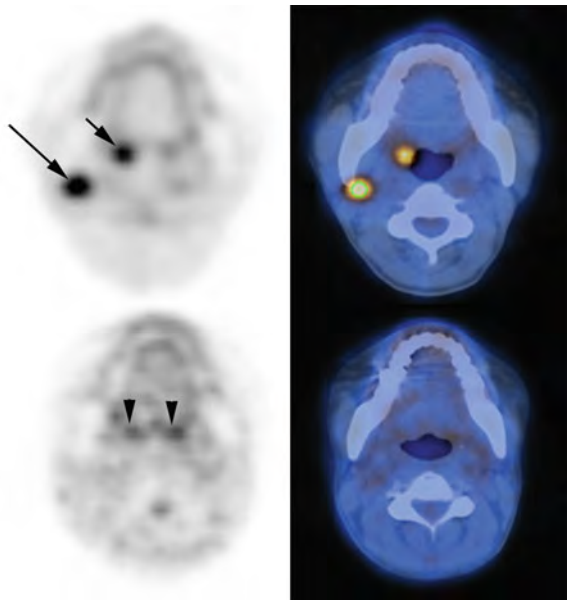

Fig. 14 Axial FDG-PET/CT at the oropharyngeal level in a patient with a right tonsillar SCC (*short arrow*) and a 1.8 cm metastatic right level II node (*long arrow*) before treatment (*top row*) and after completion of chemoradiation (*bottom row*). Pretreatment, both tumour sites show avid FDG uptake; tonsil SUVmax = 6.1, Level II node SUVmax = 4.3. Post treatment, neither site shows appreciable increased FDG uptake. The patient has had no recurrence as of 2 years post treatment. Mild physiological FDG uptake is present in lymphoid tissue in the tongue base (*arrowheads*)

Furukawa 2010; Yusa et al. 2000), whereas residual masses are non-specific. It has been shown that sonographic features associated with malignancy, namely abnormal vascularity, altered echogenicity, absent hilum and border irregularity can persist in the benign post treatment mass (Yusa et al. 2000). Furthermore, while US guided biopsy can be performed in these cases, this is prone to sampling errors due to the fact that residual cancer may be small and dispersed within larger areas of inflammation and scarring.

FDG-PET is now well established in the post treatment assessment of HNSCC (Fig. 14) and has become a part of routine imaging follow-up in some centres. The false positive and negative results from FDG-PET can be reduced by delaying the scan until at least several months after treatment. From the accumulating evidence which includes several review papers (Wong 2008; Isles et al. 2008; de Bree et al. 2009), the consensus appears to be that (1) FDG-PET/CT is more accurate than CT or MRI, (2) subjective assessment is often superior to SUV measurements, (3) FDG-PET/CT performed at least 10–12 weeks after treatment has a high negative predictive value (96%) although the positive predictive value is low (49%) (Isles et al. 2008).

Functional MRI and CT techniques can be easily incorporated into post treatment assessment and of these DWI appears to be the most promising. Successful treatment leads to cell death and a progressive rise in ADC so that benign post treatment residual masses have significantly higher ADCs than residual cancers, even as early as 3–6 weeks post treatment (de Bree et al. 2009; Vandecaveye et al. 2011). It is difficult to establish a universal ADC threshold for residual cancer due to differences in DWI protocols between institutions although several studies suggest a potential discriminatory cut-off $\sim 1.3 \times 10^{-3}$ mm^2/s (Vandecaveye et al. 2010; Abdel Razek et al. 2007; King et al. 2010) or a less than 20% rise in ADC values when compared to the pre-treatment DWI (Vandecaveye et al. 2011). One precaution when evaluating DWI is to exclude areas of frank necrosis from the ADC measurement as these may undergo early fibrotic organisation, which lowers the ADC and thus can simulate residual cancer. Using proton MRS, the persistence of a Cho peak after treatment may be a marker for residual cancer (King et al. 2010). Finally, preliminary studies suggest that residual cancers have greater vascularity than benign post treatment masses on DCE-MRI (Hoskin et al. 1999), although an optimum DCE parameter and threshold has not been established.

8.3 Post Treatment Surveillance

Even after employing anatomical imaging, functional imaging and imaging-guided biopsy, it may not be possible to distinguish between a nodal mass caused by residual cancer and one caused by benign post treatment inflammation and scarring. Currently, there is a shift towards less surgical intervention, even in those patients with residual nodal masses post chemo(radiation). Furthermore, some relapses occur at the tumour margin or from occult metastases, and these tumour recurrences may not manifest until much later in the post treatment period. Consequently, there is no substitute for close clinical and imaging surveillance.

The first post treatment baseline MRI or CT examination following chemo(radiotherapy) or surgery is usually performed between 4 and 8 weeks

after treatment (Liauw et al. 2006; Lell et al. 2000; Som et al. 1993), although in those patients with a low risk of residual disease this may be postponed to 4–6 months. Patients at a greater risk of locoregional relapse, including those with advanced disease treated by chemoradiotherapy, should undergo regular follow-up imaging. Most regional relapses/recurrences occur within the first 3 years of treatment, with the majority being diagnosed in the first 2 years. Imaging follow-up is therefore usually performed every 4–6 months for 2–3 years (Lell et al. 2000; Som et al. 1993), being more frequent in the earlier post treatment period. MRI or CT is the main technique for surveillance although some centres now include FDG-PET, either routinely as a post treatment baseline or more selectively for patients with a suspicious residual node on conventional imaging. US-FNAC also has a role in post treatment surveillance and has been specifically investigated for the early detection of occult nodal metastases in patients with an N0 neck (van den Brekel et al. 1999) who have undergone surgery at the primary site without an elective neck dissection. A watchful waiting strategy involving regular US follow-up, including every 8–10 weeks in the first year, has been shown to detect nodal recurrences early, thereby increasing the chances of performing salvage surgery (van den Brekel et al. 1999).

9 Brief Overview of Non-HNSCC Lymphadenopathies

9.1 Lymphoma

Cervical disease in Hodgkin's (HL) and non-Hodgkin's lymphomas (NHL) is described in "Neck Lymphoma". Neck HL nearly always presents as nodal involvement. In general about 50% of NHL in the head and neck shows neck node involvement (Chisin and Weber 1994; King et al. 2004d; Hanna et al. 1997), the incidence being greater in diffuse large cell lymphomas than Natural Killer/T cell lymphomas. The size criteria for the diagnosis of lymphomatous nodes are not well established in comparison to those for carcinoma. In general cut-offs between 1 and 1.5 cm are used although multiple smaller nodes are also considered suspicious (Cheson et al. 1999). Lymphomatous nodes show a spectrum of morphological imaging appearances. At one end of the spectrum, lymphomatous nodes have similar features to nodal metastases from HNSCC, including a round shape, loss of the hilum and in NHL necrosis, matting and extra capsular spread sometimes may be present (King et al. 2004d; Saito et al. 2001; Wang et al. 1999). At the other end of the spectrum, lymphomatous nodes have similar features to normal or reactive nodes, namely an oval shape, preserved hilum and hilar vascularity which may be florid. The hilum is frequently identified, even in markedly enlarged rounded nodes, although it may be compressed and eccentrically displaced (Fig. 15). Calcification prior to therapy is rare and described mainly in mediastinal rather than cervical nodes (Apter et al. 2002). DWI is especially promising for lymphoma detection as involved nodes have much lower ADC than SCC (Abdel Razek et al. 2006; Sumi et al. 2003; King et al. 2007) as well as normal nodes (Kwee et al. 2010). FDG-PET also shows promise in detecting disease in normal sized lymph nodes, which could influence radiotherapy planning. Both HL and NHL are FDG avid, and aggressive lymphomas tend to have higher SUV values than indolent lymphomas (Hicks et al. 2005). FDG-PET or FDG-PET/CT has been shown to be comparable or superior to morphological imaging techniques as well as gallium^{67} scintigraphy for detecting nodal lymphoma. In centres where

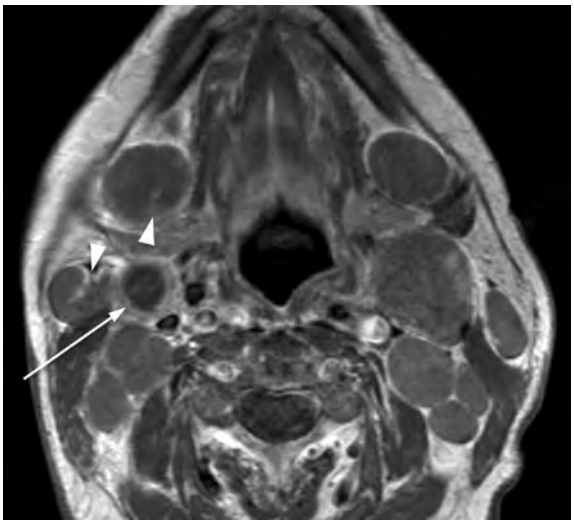

Fig. 15 Axial T1 W post contrast MRI showing a typical appearance of nodal lymphoma. There is gross lymphadenopathy with multiple enlarged rounded nodes, most of which appear solid although a right level II node demonstrates necrosis (*arrow*). Hila can be preserved even in grossly enlarged lymphomatous nodes (*arrowheads*)

PET/CT is available, it is increasingly becoming the main imaging investigation for staging and therapeutic monitoring (Collins 2006).

9.2 Other Head and Neck Carcinomas

(1) *Thyroid carcinoma*: Thyroid cancer commonly spreads to cervical lymph nodes (see "Thyroid and Parathyroid Neoplasms"). Papillary carcinoma is the most common thyroid cancer and it has the highest incidence of nodal metastases (30–90%), followed by medullary carcinoma (50%), anaplastic carcinoma (40%) and follicular carcinoma (10%). Medullary carcinoma has a greater propensity to spread bilaterally and to the mediastinum (Machens et al. 2002). See Table 1 for routes of nodal spread and Table 2 for nodal staging. Ultrasound is the method of choice for imaging nodal metastases from thyroid cancer in the neck. In addition to the general features of metastatic nodes described for HNSCC, nodal metastases from papillary carcinoma may show micro- and macrocalcifications, increased echogenicity compared to muscle, and cystic change (Fig. 16) (Ahuja et al. 1995; Rosario et al. 2005). Calcifications may also be detected by CT, and cystic change may be seen by both CT and MRI; in the latter modality the cystic area may have a characteristic high T1 W signal intensity (Som et al. 1994; King 2008). The presence of unexplained nodes with calcification on CT or high T1-W signal cystic regions on MRI should prompt the search for a primary thyroid papillary carcinoma. Metastatic nodes in the central compartment tend to be small and more difficult to detect or characterise than those in the lateral compartment. Nonetheless, special effort should be made to try to evaluate these, especially those in the lower paratracheal/paraoesphageal regions, as failure to resect these may be responsible for so-called thyroid bed tumour recurrences. Nodal metastases from papillary carcinoma are frequently smaller than 5 mm, for which FNAC may be technically difficult to perform. Fortunately, detection of these small nodes is less of a concern for surgical planning because they can be treated successfully by radioactive iodine post operatively (Wang et al. 1999; Lell et al. 2000). Iodine scintigraphy is used following surgery to identify residual nodal metastases in the neck and nodal metastases in the mediastinum, but it will miss iodine negative nodes (this tendency is greater in the less well differentiated cancers). These iodine negative nodes may sometimes be detectable using (Hyde et al. 2003) F-FDG-PET/CT.

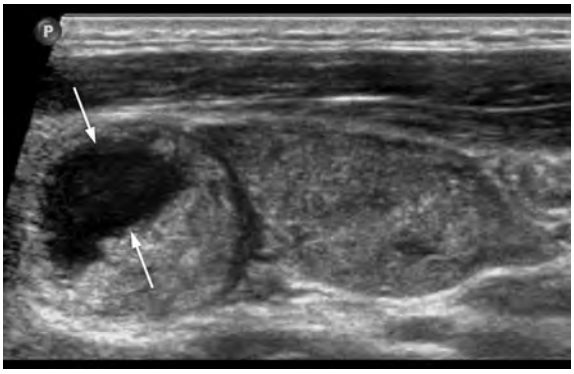

Fig. 16 Grey scale US showing nodal metastases from thyroid papillary carcinoma. The nodes are hyperechoic, with one showing an anechoic cystic component (*arrows*)

(2) *Salivary gland carcinoma*: The majority of nodal metastases from salivary malignancies arise from primaries in the submandibular gland (42%), followed by parotid gland (25%) and oral cavity (9%) (Terhaard et al. 2004; Lloyd et al. 2010). Similar halves overall survival, independent of T stage. The frequency of nodal metastases is related to the underlying histology, grade and T stage; in this respect many of the subtypes have a high risk whereas adenoid cystic carcinoma uncommonly involves lymph nodes (Ferlito et al. 2001). Routes of spread are shown in Table 1. Conventional imaging criteria for nodal metastases in salivary cancer are similar to those used for HNSCC. In general, salivary cancers are relatively radioresistant, hence documented nodal metastases are treated by neck dissection (Stennert et al. 2003). The incidence of occult nodal metastasis in salivary cancer ranges widely, between 12 and 48% (Stennert et al. 2003; Armstrong et al. 1992; Regis De Brito Santos et al. 2001; Rodriguez-Cuevas et al. 1995), and not surprisingly the optimal management of clinical N0 disease is debated (Stennert et al. 2003; Regis De Brito Santos et al. 2001; Frankenthaler et al. 1993; Medina 1998; Korkmaz et al. 2002). In practice, parotid and submandibular nodes are usually

Table 3 Summary of main points in the evaluation of cervical nodal metastases

Diagnosis	HNSCC: enlarged (size based on minimum axial diameter), round shape, absent hilum, peripheral vascularity, heterogeneous parenchyma (necrosis), ECS and avid FDG uptake. *(Lymphoma and some non-malignant lymphadenopathies can have a similar appearance)*
	Papillary thyroid carcinoma: in addition to the above, one may find calcification, cystic regions of high T1 W MR signal intensity and increased echogenicity
	Melanoma: high T1 W MR signal intensity may be seen
Staging	HNSCC: single ipsilateral node ≤3 cm indicates N1 disease, any node >6 cm indicates N3; any other combination indicates N2 disease (size based on maximum diameter)
	Thyroid and Nasopharyngeal carcinoma have separate staging systems
Impact on management	Distinguish between patients with an N0 and an N+ neck *(One single metastatic node in an otherwise normal neck may have a major impact on treatment and so indeterminate nodes may require further evaluation)*
	Look for metastatic nodes outside the usual treatment fields *(contralateral neck; retropharyngeal, parotid, post auricular, suboccipital, buccal, facial and level VI nodes; nodes adjacent to sites such as the salivary glands which may be preferentially spared during radiotherapy)*
	Extranodal tumour spread: indicator of poor prognosis *(unresectable disease may be present if there is nodal invasion of the common or internal carotid artery, pre- or paravertebral muscles. Internal jugular vein, sternocleidomastoid muscle, submandibular gland and skin involvement should be documented although these structures can be sacrificed)*
	Risk factor for distant metastases *(Multiple, bulky and low lying cervical adenopathies)*
Post treatment assessment	FDG-PET appears to be the most accurate modality provided it is performed at least 10–12 weeks after treatment. All imaging modalities have a high NPV but low PPV
	Surveillance: most nodal relapse/recurrence occurs within the first 3 years of treatment, with the majority of these cases being diagnosed in the first 2 years. Imaging follow-up is therefore usually performed every 4–6 months for 2–3 years, and is more frequent in the earlier post treatment period
New imaging techniques in the domain of clinical research	DWI appears to have a role for (chemo)radiotherapy monitoring in HNSCC: changes in ADC values early in the course of treatment (for predicting regional failure) and <6 weeks after the end of treatment (for identifying residual tumour) are promising

resected along with the primary tumour specimen, and these may undergo intraoperative frozen section histological analysis to determine whether to proceed to a comprehensive neck dissection.

(3) *Nasopharyngeal carcinoma*: Nasopharyngeal carcinoma commonly spreads to regional nodes and cervical lymphadenopathy may be the presenting feature (see also "Neoplasms of the Nasopharynx"). Nodal staging differs from that of HNSCC (Table 2) but the imaging criteria for nodal metastases are similar to those used for HNSCC. Lateral retropharyngeal nodes are common in this disease and are best identified by MRI (Fig. 3a). Routes of nodal spread are shown in Table 1. The presence of metastatic nodes in the lower neck or supraclavicular fossa increases the risk of distant metastases. With respect to post RT surveillance, it is common for benign nodes that have been spared from the radiation field (submental, paratracheal and suprasternal nodes) to become chronically enlarged due to altered lymphatic drainage.

(4) *Skin cancer*: Skin cancer of the head and neck involves the superficial nodal groups more commonly than in HNSCC (Table 1). The appearance of metastatic nodes from squamous cell carcinoma of the skin are similar to those of other HNSCC

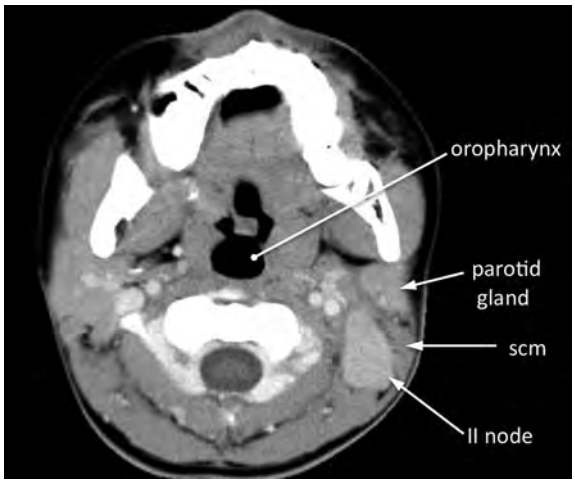

Fig. 17 Axial CT post contrast showing an enlarged homogeneous left level II lymph node. This was diagnosed as Castleman's disease

whereas nodal metastases from malignant melanoma tend to show less necrosis and extracapsular spread (van den Brekel et al. 1998b), and may have a high signal intensity on T1 W MR imaging due the paramagnetic effects of melanin. For malignant melanoma, the risk of developing nodal metastases is related to lesion thickness, with melanomas <1 mm thickness having a rate of nodal metastases of $<5\%$ while >4 mm thickness increases the risk to about 35% (McMasters and Swetter 2003).

9.3 Non-malignant Lymphadenopathy

Conventional imaging criteria using size, morphology or FDG uptake to identify metastatic lymphadenopathy are based on studies that predominantly compare metastatic nodes with normal and reactive lymph nodes. However, these same imaging criteria are much less accurate for differentiating metastatic nodes from other nodal pathologies. As a consequence, biopsy is almost invariably required for diagnosis. A detailed account of benign cervical lymphadenopathies is beyond the scope of this chapter although tuberculous lymphadenitis merits special attention as it is one of commonest causes of persistent cervical lymphadenopathy in the developing world as well as in parts of the developed world. Tuberculous nodes may be discrete, matted or form confluent masses (King et al. 1999) and may show calcification. Other imaging findings include nodal enlargement, necrosis, abscess formation, peri-adenitis and increased FDG uptake; all of these overlap with nodal metastases on imaging (Moon et al. 1997). Tuberculous nodes can also fistulate to the skin, which is highly suggestive of this diagnosis. Several non-infectious cervical lymphadenopathies may overlap with malignancy on imaging including Castleman's disease (Fig. 17), sarcoidosis, Rosai-Dorfman disease and Kikuchi-Fujimoto disease (Koyama et al. 2004; La Barge et al. 2008; Fulcher 1993; Na et al. 1997b).

10 Conclusion

Imaging of cervical nodal metastases has an important role in nodal detection, treatment planning and post treatment assessment. Imaging often requires a multimodality approach for the best results. A summary of the main points to be remembered when assessing nodal metastases are listed in Table 3.

References

Abdel Razek AA, Soliman NY, Elkhamary S, Alsharaway MK, Tawfik A (2006) Role of diffusion-weighted MR imaging in cervical lymphadenopathy. Eur Radiol 16:1468–1477

Abdel Razek AA, Kandeel AY, Soliman N et al (2007) Role of diffusion-weighted echo-planar MR imaging in differentiation of residual or recurrent head and neck tumors and posttreatment changes. Am J Neuroradiol 28:1146–1152

Adams S, Baum RP, Stuckensen T, Bitter K, Hor G (1998) Prospective comparison of 18F-FDG PET with conventional imaging modalities (CT, MRI, US) in lymph node staging of head and neck cancer. Eur J Nucl Med 25:1255–1260

Ahuja A, Ying M (2002) An overview of neck node sonography. Invest Radiol 37:333–342

Ahuja AT, Chow L, Chick W, King W, Metreweli C (1995) Metastatic cervical nodes in papillary carcinoma of the thyroid: ultrasound and histological correlation. Clin Radiol 50:229–231

Ahuja A, Ying M, King A, Yuen HY (2001a) Lymph node hilus: gray scale and power Doppler sonography of cervical nodes. J Ultrasound Med 20:987–992, quiz 94

Ahuja AT, Ying M, Ho SS, Metreweli C (2001b) Distribution of intranodal vessels in differentiating benign from metastatic neck nodes. Clin Radiol 56:197–201

Ahuja A, Ying M, Yuen YH, Metrewelli C (2001c) Power Doppler sonography to differentiate tuberculous cervical lymphadenopathy from nasopharyngeal carcinoma. AJNR 22:735–740

Alkureishi LW, Ross GL, Shoaib T et al (2010) Sentinel node biopsy in head and neck squamous cell cancer: 5-year follow-up of a European multicenter trial. Ann Surg Oncol 17:2459–2464

Alvarez Amezaga J, Barbier Herrero L, Pijoan del Barrio JI et al (2007) Diagnostic efficacy of sentinel node biopsy in oral squamous cell carcinoma. Cohort study and meta-analysis. Med Oral Patol Oral Cir Bucal 12E:235–243

Alvi A, Johnson JT (1997) Development of distant metastasis after treatment of advanced-stage head and neck cancer. Head Neck 19:500–505

Andersen PE, Warren F, Spiro J et al (2002) Results of selective neck dissection in management of the node-positive neck. Arch Otolaryngol Head Neck Surg 128:1180–1184

Apter S, Avigdor A, Gayer G, Portnoy O, Zissin R, Hertz M (2002) Calcification in lymphoma occurring before therapy: CT features and clinical correlation. Am J Roentgenol 178: 935–938

Ariji Y, Kimura Y, Hayashi N et al (1998) Power Doppler sonography of cervical lymph nodes in patients with head and neck cancer. Am J Neuroradiol 19:303–307

Armstrong JG, Harrison LB, Thaler HT et al (1992) The indications for elective treatment of the neck in cancer of the major salivary glands. Cancer 69:615–619

Atula TS, Varpula MJ, Kurki TJ, Klemi PJ, Grenman R (1997) Assessment of cervical lymph node status in head and neck cancer patients: palpation, computed tomography and low field magnetic resonance imaging compared with ultrasound-guided fine-needle aspiration cytology. Eur J Radiol 25:152–161

Bisdas S, Baghi M, Huebner F et al (2007) In vivo proton MR spectroscopy of primary tumours, nodal and recurrent disease of the extracranial head and neck. Eur Radiol 17:251–257

Brouwer J, de Bree R, Comans EF, Castelijns JA, Hoekstra OS, Leemans CR (2004) Positron emission tomography using [18F]fluorodeoxyglucose (FDG-PET) in the clinically negative neck: is it likely to be superior? Eur Arch Otorhinolaryngol 261:479–483

Brouwer J, Senft A, de Bree R et al (2006) Screening for distant metastases in patients with head and neck cancer: is there a role for (18)FDG-PET? Oral Oncol 42:275–280

Bussels B, Hermans R, Reijnders A, Dirix P, Nuyts S, Van den Bogaert W (2006) Retropharyngeal nodes in squamous cell carcinoma of oropharynx: incidence, localization, and implications for target volume. Int J Radiat Oncol Biol Phys 65:733–738

Carvalho P, Baldwin D, Carter R, Parsons C (1991) Accuracy of CT in detecting squamous carcinoma metastases in cervical lymph nodes. Clin Radiol 44:79–81

Castelijns JA, van den Brekel MW (2002) Imaging of lymphadenopathy in the neck. Eur Radiol 12:727–738

Cheson BD, Horning SJ, Coiffier B et al (1999) Report of an international workshop to standardize response criteria for non-Hodgkin's lymphomas. NCI Sponsored International Working Group. J Clin Oncol 17:1244

Chisin R, Weber AL (1994) Imaging of lymphoma manifestations in the extracranial head and neck region. Leuk Lymphoma 12:177–189

Collins SL (1987) Controversies in the management of cancer of the neck. In: Thawley SE, Panje WR (eds) Comprehensive management of head and neck tumours. Saunders, Philadelphia, pp 1386–1443

Collins CD (2006) PET in lymphoma. Cancer Imaging 6S: 63–70

Curtin HD, Ishwaran H, Mancuso AA, Dalley RW, Caudry DJ, McNeil BJ (1998) Comparison of CT and MR imaging in staging of neck metastases. Radiology 207:123–130

de Bondt RB, Nelemans PJ, Hofman PA et al (2007) Detection of lymph node metastases in head and neck cancer: a meta-analysis comparing US, USgFNAC, CT and MR imaging. Eur J Radiol 64:266–272

de Bondt RB, Hoeberigs MC, Nelemans PJ et al (2009a) Diagnostic accuracy and additional value of diffusion-weighted imaging for discrimination of malignant cervical lymph nodes in head and neck squamous cell carcinoma. Neuroradiology 51:183–192

de Bondt RB, Nelemans PJ, Bakers F et al (2009b) Morphological MRI criteria improve the detection of lymph node metastases in head and neck squamous cell carcinoma: multivariate logistic regression analysis of MRI features of cervical lymph nodes. Eur Radiol 19:626–633

de Bree R, Deurloo EE, Snow GB, Leemans CR (2000) Screening for distant metastases in patients with head and neck cancer. Laryngoscope 110:397–401

de Bree R, van der Putten L, Brouwer J, Castelijns JA, Hoekstra OS, Leemans CR (2009) Detection of locoregional recurrent head and neck cancer after (chemo)radiotherapy using modern imaging. Oral Oncol 45:386–393

Dirix P, Nuyts S, Bussels B, Hermans R, Van den Bogaert W (2006) Prognostic influence of retropharyngeal lymph node metastasis in squamous cell carcinoma of the oropharynx. Int J Radiat Oncol Biol Phys 65:739–744

Don DM, Anzai Y, Lufkin RB, Fu YS, Calcaterra TC (1995) Evaluation of cervical lymph node metastases in squamous cell carcinoma of the head and neck. Laryngoscope 105: 669–674

Dragoni F, Cartoni C, Pescarmona E et al (1999) The role of high resolution pulsed and color Doppler ultrasound in the differential diagnosis of benign and malignant lymphadenopathy: results of multivariate analysis. Cancer 85:2485–2490

Edge SB, Byrd DR, Compton CC, Fritz AG, Greene FL, Trotti A 3rd (2010) American joint committee on cancer, cancer staging manual, 7th edn. Springer, New York

Eisenkraft BL, Som PM (1999) The spectrum of benign and malignant etiologies of cervical node calcification. Am J Roentgenol 172:1433–1437

Ferlito A, Shaha AR, Rinaldo A, Mondin V (2001) Management of clinically negative cervical lymph nodes in patients with malignant neoplasms of the parotid gland. J Otorhinolaryngol Relat Spec 63:123–126

Fischbein NJ, Noworolski SM, Henry RG, Kaplan MJ, Dillon WP, Nelson SJ (2003) Assessment of metastatic cervical adenopathy using dynamic contrast-enhanced MR imaging. Am J Neuroradiol 24:301–311

Frankenthaler RA, Byers RM, Luna MA, Callender DL, Wolf P, Goepfert H (1993) Predicting occult lymph node metastasis in parotid cancer. Arch Otolaryngol Head Neck Surg 119: 517–520

Freeman SB (2005) Advanced cervical metastasis involving the carotid artery. Curr Opin Otolaryngol Head Neck Surg 13: 107–111

Friedman M, Roberts N, Kirshenbaum GL, Colombo J (1993) Nodal size of metastatic squamous cell carcinoma of the neck. Laryngoscope 103:854–856

Fulcher AS (1993) Cervical lymphadenopathy due to Kikuchi disease: US and CT appearance. J Comput Assist Tomogr 17:131–133

Furukawa MK, Furukawa M (2010) Diagnosis of lymph node metastases of head and neck cancer and evaluation of effects of chemoradiotherapy using ultrasonography. Int J Clin Oncol 15:23–32

Gormly K, Glastonbury CM (2004) Calcified nodal metastasis from squamous cell carcinoma of the head and neck. Australas Radiol 48:240–242

Grabenbauer GG, Steininger H, Meyer M et al (1998) Nodal CT density and total tumor volume as prognostic factors after radiation therapy of stage III/IV head and neck cancer. Radiother Oncol 47:175–183

Gritzmann N, Grasl MC, Helmer M, Steiner E (1990) Invasion of the carotid artery and jugular vein by lymph node metastases: detection with sonography. Am J Roentgenol 154:411–414

Hanna E, Wanamaker J, Adelstein D, Tubbs R, Lavertu P (1997) Extranodal lymphomas of the head and neck. A 20-year experience. Arch Otolaryngol Head Neck Surg 123: 1318–1323

Hicks RJ, Mac Manus MP, Seymour JF (2005) Initial staging of lymphoma with positron emission tomography and computed tomography. Semin Nucl Med 35:165–175

Hoft S, Muhle C, Brenner W, Sprenger E, Maune S (2002) Fine-needle aspiration cytology of the sentinel lymph node in head and neck cancer. J Nucl Med 43:1585–1590

Holzapfel K, Duetsch S, Fauser C, Eiber M, Rummeny EJ, Gaa J (2009) Value of diffusion-weighted MR imaging in the differentiation between benign and malignant cervical lymph nodes. Eur J Radiol 72:381–387

Hoskin PJ, Saunders MI, Goodchild K, Powell ME, Taylor NJ, Baddeley H (1999) Dynamic contrast enhanced magnetic resonance scanning as a predictor of response to accelerated radiotherapy for advanced head and neck cancer. Br J Radiol 72:1093–1098

Hyde NC, Prvulovich E, Newman L, Waddington WA, Visvikis D, Ell P (2003) A new approach to pre-treatment assessment of the N0 neck in oral squamous cell carcinoma: the role of sentinel node biopsy and positron emission tomography. Oral Oncol 39:350–360

Inohara H, Enomoto K, Tomiyama Y et al (2009) The role of CT and (18)F-FDG PET in managing the neck in node-positive head and neck cancer after chemoradiotherapy. Acta Otolaryngol 129:893–899

Isles MG, McConkey C, Mehanna HM (2008) A systematic review and meta-analysis of the role of positron emission tomography in the follow up of head and neck squamous cell carcinoma following radiotherapy or chemoradiotherapy. Clin Otolaryngol 33:210–222

Johnson JT (1990) A surgeon looks at cervical lymph nodes. Radiology 175:607–610

Kim S, Loevner L, Quon H et al (2009) Diffusion-weighted magnetic resonance imaging for predicting and detecting early response to chemoradiation therapy of squamous cell carcinomas of the head and neck. Clin Cancer Res 15: 986–994

Kim S, Loevner LA, Quon H et al (2010) Prediction of response to chemoradiation therapy in squamous cell carcinomas of the head and neck using dynamic contrast-enhanced MR imaging. Am J Neuroradiol 31:262–268

King AD (2008) Imaging for staging and management of thyroid cancer. Cancer Imaging 8:57–69

King AD, Ahuja AT, Metreweli C (1999) MRI of tuberculous cervical lymphadenopathy. J Comput Assist Tomogr 23: 244–247

King AD, Ahuja AT, Leung SF et al (2000) Neck node metastases from nasopharyngeal carcinoma: MR imaging of patterns of disease. Head Neck 22:275–281

King AD, Yeung DK, Ahuja AT, Leung SF, Tse GM, van Hasselt AC (2004a) In vivo proton MR spectroscopy of primary and nodal nasopharyngeal carcinoma. Am J Neuroradiol 25:484–490

King AD, Tse GM, Ahuja AT et al (2004b) Necrosis in metastatic neck nodes: diagnostic accuracy of CT, MR imaging, and US. Radiology 230:720–726

King AD, Tse GM, Yuen EH et al (2004c) Comparison of CT and MR imaging for the detection of extranodal neoplastic spread in metastatic neck nodes. Eur J Radiol 52:264–270

King AD, Lei KI, Ahuja AT (2004d) MRI of neck nodes in non-Hodgkin's lymphoma of the head and neck. Br J Radiol 77:111–115

King AD, Yeung DK, Ahuja AT et al (2005) Human cervical lymphadenopathy: evaluation with in vivo 1H-MRS at 1.5 T. Clin Radiol 60:592–598

King AD, Ahuja AT, Yeung DK et al (2007) Malignant cervical lymphadenopathy: diagnostic accuracy of diffusion-weighted MR imaging. Radiology 245:806–813

King AD, Ma BB, Yau YY et al (2008) The impact of 18F-FDG PET/CT on assessment of nasopharyngeal carcinoma at diagnosis. Br J Radiol 81:291–298

King AD, Yeung DK, Yu KH et al (2010) Pretreatment and early intratreatment prediction of clinicopathologic response of head and neck cancer to chemoradiotherapy using 1H-MRS. J Magn Reson Imaging 32:199–203

Korkmaz H, Yoo GH, Du W et al (2002) Predictors of nodal metastasis in salivary gland cancer. J Surg Oncol 80:186–189

Koyama T, Ueda H, Togashi K, Umeoka S, Kataoka M, Nagai S (2004) Radiologic manifestations of sarcoidosis in various organs. Radiographics 24:87–104

Krabbe CA, Dijkstra PU, Pruim J et al (2008) FDG PET in oral and oropharyngeal cancer. Value for confirmation of N0 neck and detection of occult metastases. Oral Oncol 44:31–36

Kubicek GJ, Champ C, Fogh S et al (2010) FDG-PET staging and importance of lymph node SUV in head and neck cancer. Head Neck Oncol 2:19

Kwee TC, Ludwig I, Uiterwaal CS et al (2010) ADC measurements in the evaluation of lymph nodes in patients with non-Hodgkin lymphoma: feasibility study. MAGMA 24:1–8

La Barge DV 3rd, Salzman KL, Harnsberger HR et al (2008) Sinus histiocytosis with massive lymphadenopathy (Rosai-Dorfman disease): imaging manifestations in the head and neck. Am J Roentgenol 191W:299–306

Labadie RF, Yarbrough WG, Weissler MC, Pillsbury HC, Mukherji SK (2000) Nodal volume reduction after concurrent chemo- and radiotherapy: correlation between initial CT and histopathologic findings. Am J Neuroradiol 21: 310–314

Larsen SR, Johansen J, Sorensen JA, Krogdahl A (2009) The prognostic significance of histological features in oral squamous cell carcinoma. J Oral Pathol Med 38:657–662

Layland MK, Sessions DG, Lenox J (2005) The influence of lymph node metastasis in the treatment of squamous cell carcinoma of the oral cavity, oropharynx, larynx, and hypopharynx: N0 versus N+. Laryngoscope 115:629–639

Leemans CR, Tiwari R, Nauta JJ, van der Waal I, Snow GB (1993) Regional lymph node involvement and its significance in the development of distant metastases in head and neck carcinoma. Cancer 71:452–456

Lell M, Baum U, Greess H et al (2000) Head and neck tumors: imaging recurrent tumor and post-therapeutic changes with CT and MRI. Eur J Radiol 33:239–247

Liauw SL, Mancuso AA, Amdur RJ et al (2006) Postradiotherapy neck dissection for lymph node-positive head and neck cancer: the use of computed tomography to manage the neck. J Clin Oncol 24:1421–1427

Lin D, Glastonbury CM, Rafaelian O, Eisele DW, Wang SJ (2007) Management of advanced nodal disease following chemoradiation for head and neck squamous cell carcinoma: role of magnetic resonance imaging. J Otolaryngol 36:350–356

Lloyd S, Yu JB, Ross DA, Wilson LD, Decker RH (2010) A prognostic index for predicting lymph node metastasis in minor salivary gland cancer. Int J Radiat Oncol Biol Phys 76:169–175

Machens A, Hinze R, Thomusch O, Dralle H (2002) Pattern of nodal metastasis for primary and reoperative thyroid cancer. World J Surg 26:22–28

Mann WJ, Beck A, Schreiber J, Maurer J, Amedee RG, Gluckmann JL (1994) Ultrasonography for evaluation of the carotid artery in head and neck cancer. Laryngoscope 104:885–888

Martinez-Gimeno C, Rodriguez EM, Vila CN, Varela CL (1995) Squamous cell carcinoma of the oral cavity: a clinicopathologic scoring system for evaluating risk of cervical lymph node metastasis. Laryngoscope 105:728–733

McMasters KM, Swetter SM (2003) Current management of melanoma: benefits of surgical staging and adjuvant therapy. J Surg Oncol 82:209–216

Medina JE (1998) Neck dissection in the treatment of cancer of major salivary glands. Otolaryngol Clin North Am 31:815–822

Merritt RM, Williams MF, James TH, Porubsky ES (1997) Detection of cervical metastasis: a meta-analysis comparing computed tomography with physical examination. Arch Otolaryngol Head Neck Surg 123:149–152

Moon WK, Han MH, Chang KH et al (1997) CT and MR imaging of head and neck tuberculosis. Radiographics 17:391–402

Mukherji SK, Schiro S, Castillo M, Kwock L, Muller KE, Blackstock W (1997) Proton MR spectroscopy of squamous cell carcinoma of the extracranial head and neck: in vitro and in vivo studies. Am J Neuroradiol 18:1057–1072

Munck JN, Cvitkovic E, Piekarski JD et al (1991) Computed tomographic density of metastatic lymph nodes as a treatment-related prognostic factor in advanced head and neck cancer. J Natl Cancer Inst 83:569–575

Myers JN, Greenberg JS, Mo V, Roberts D (2001) Extracapsular spread A significant predictor of treatment failure in patients with squamous cell carcinoma of the tongue. Cancer 92:3030–3036

Na DG, Lim HK, Byun HS, Kim HD, Ko YH, Baek JH (1997a) Differential diagnosis of cervical lymphadenopathy: usefulness of color Doppler sonography. Am J Roentgenol 168: 1311–1316

Na DG, Chung TS, Byun HS, Kim HD, Ko YH, Yoon JH (1997b) Kikuchi disease: CT and MR findings. Am J Neuroradiol 18:1729–1732

Ng SH, Yen TC, Chang JT et al (2006) Prospective study of [18F]fluorodeoxyglucose positron emission tomography and computed tomography and magnetic resonance imaging in oral cavity squamous cell carcinoma with palpably negative neck. J Clin Oncol 24:4371–4376

Nieuwenhuis EJ, Colnot DR, Pijpers HJ et al (2000) Lymphoscintigraphy and ultrasound-guided fine needle aspiration cytology of sentinel lymph nodes in head and neck cancer patients. Recent Results Cancer Res 157:206–217

Nieuwenhuis EJ, Castelijns JA, Pijpers R et al (2002) Wait-and-see policy for the N0 neck in early-stage oral and oropharyngeal squamous cell carcinoma using ultrasonography-guided cytology: is there a role for identification of the sentinel node? Head Neck 24:282–289

Ojiri H, Mendenhall WM, Stringer SP, Johnson PL, Mancuso AA (2002) Post-RT CT results as a predictive model for the necessity of planned post-RT neck dissection in patients with cervical metastatic disease from squamous cell carcinoma. Int J Radiat Oncol Biol Phys 52:420–428

Pfister DG, Ang K, Brockstein B et al (2000) NCCN practice guidelines for head and neck cancers. Oncology (Williston Park) 14:163–194

Pillsbury HC 3rd, Clark M (1997) A rationale for therapy of the N0 neck. Laryngoscope 107:1294–1315

Regis De Brito Santos I, Kowalski LP, Cavalcante De Araujo V, Flavia Logullo A, Magrin J (2001) Multivariate analysis of risk factors for neck metastases in surgically treated parotid carcinomas. Arch Otolaryngol Head Neck Surg 127:56–60

Robbins KT, Clayman G, Levine PA et al (2002) Neck dissection classification update: revisions proposed by the American Head and Neck Society and the American Academy of Otolaryngology-Head and Neck Surgery. Arch Otolaryngol Head Neck Surg 128:751–758

Rodriguez-Cuevas S, Labastida S, Baena L, Gallegos F (1995) Risk of nodal metastases from malignant salivary gland tumors related to tumor size and grade of malignancy. Eur Arch Otorhinolaryngol 252:139–142

Roh JL, Yeo NK, Kim JS et al (2007) Utility of 2-[18F] fluoro-2-deoxy-D-glucose positron emission tomography and positron emission tomography/computed tomography imaging in the preoperative staging of head and neck squamous cell carcinoma. Oral Oncol 43:887–893

Rosario PW, de Faria S, Bicalho L et al (2005) Ultrasonographic differentiation between metastatic and benign lymph nodes in patients with papillary thyroid carcinoma. J Ultrasound Med 24:1385–1389

Saito A, Takashima S, Takayama F, Kawakami S, Momose M, Matsushita T (2001) Spontaneous extensive necrosis in non-Hodgkin lymphoma: prevalence and clinical significance. J Comput Assist Tomogr 25:482–486

Schmitz S, Machiels JP, Weynand B, Gregoire V, Hamoir M (2009) Results of selective neck dissection in the primary management of head and neck squamous cell carcinoma. Eur Arch Otorhinolaryngol 266:437–443

Schoder H, Yeung HW (2004) Positron emission imaging of head and neck cancer, including thyroid carcinoma. Semin Nucl Med 34:180–197

Schwartz DL, Rajendran J, Yueh B et al (2003) Staging of head and neck squamous cell cancer with extended-field FDG-PET. Arch Otolaryngol Head Neck Surg 129:1173–1178

Schwartz DL, Ford E, Rajendran J et al (2005) FDG-PET/CT imaging for preradiotherapy staging of head-and-neck squamous cell carcinoma. Int J Radiat Oncol Biol Phys 61:129–136

Senft A, de Bree R, Hoekstra OS (2008) Screening for distant metastases in head and neck cancer patients by chest CT or whole body FDG-PET: a prospective multicenter trial. Radiother Oncol 87:221–229

Shear M, Hawkins DM, Farr HW (1976) The prediction of lymph node metastases from oral squamous carcinoma. Cancer 37:1901–1907

Shozushima M, Suzuki M, Nakasima T, Yanagisawa Y, Sakamaki K, Takeda Y (1990) Ultrasound diagnosis of lymph node metastasis in head and neck cancer. Dento-maxillofac Radiol 19:165–170

Snow GB, Annyas AA, van Slooten EA, Bartelink H, Hart AA (1982) Prognostic factors of neck node metastasis. Clin Otolaryngol Allied Sci 7:185–192

Sobin L, Gospodarowicz M, Wittekind C (2009) International union against cancer. TNM classification of malignant tumours, 7th edn. Wiley-Blackwell, New York

Som PM, Urken ML, Biller H, Lidov M (1993) Imaging the postoperative neck. Radiology 187:593–603

Som PM, Brandwein M, Lidov M, Lawson W, Biller HF (1994) The varied presentations of papillary thyroid carcinoma cervical nodal disease: CT and MR findings. Am J Neuroradiol 15:1123–1128

Som PM, Curtin HD, Mancuso AA (1999) An imaging-based classification for the cervical nodes designed as an adjunct to recent clinically based nodal classifications. Arch Otolaryngol Head Neck Surg 125:388–396

Souter MA, Allison RS, Clarkson JH, Cowan IA, Coates MH, Wells JE (2009) Sensitivity and specificity of computed tomography for detection of extranodal spread from metastatic head and neck squamous cell carcinoma. J Laryngol Otol 123:778–782

Steinkamp HJ, Maurer J, Cornehl M, Knobber D, Hettwer H, Felix R (1994) Recurrent cervical lymphadenopathy: differential diagnosis with color-duplex sonography. Eur Arch Otorhinolaryngol 251:404–409

Steinkamp HJ, Cornehl M, Hosten N, Pegios W, Vogl T, Felix R (1995) Cervical lymphadenopathy: ratio of long- to short-axis diameter as a predictor of malignancy. Br J Radiol 68:266–270

Steinkamp HJ, van der Hoeck E, Bock JC, Felix R (1999) The extracapsular spread of cervical lymph node metastases: the diagnostic value of computed tomography. Rofo 170:457–462

Steinkamp HJ, Beck A, Werk M, Felix R (2002) Extracapsular spread of cervical lymph node metastases: diagnostic value of magnetic resonance imaging. Rofo 174:50–55

Stennert E, Kisner D, Jungehuelsing M et al (2003) High incidence of lymph node metastasis in major salivary gland cancer. Arch Otolaryngol Head Neck Surg 129:720–723

Stuckensen T, Kovacs AF, Adams S, Baum RP (2000) Staging of the neck in patients with oral cavity squamous cell carcinomas: a prospective comparison of PET, ultrasound, CT and MRI. J Craniomaxillofac Surg 28:319–324

Sumi M, Sakihama N, Sumi T et al (2003) Discrimination of metastatic cervical lymph nodes with diffusion-weighted MR imaging in patients with head and neck cancer. Am J Neuroradiol 24:1627–1634

Syed R, Bomanji JB, Nagabhushan N et al (2005) Impact of combined (18)F-FDG PET/CT in head and neck tumours. Br J Cancer 92:1046–1050

Tankere F, Camproux A, Barry B, Guedon C, Depondt J, Gehanno P (2000) Prognostic value of lymph node involvement in oral cancers: a study of 137 cases. Laryngoscope 110:2061–2065

Terhaard CH, Lubsen H, Van der Tweel I, et al (2004) Salivary gland carcinoma: independent prognostic factors for locoregional control, distant metastases, and overall survival: results of the Dutch head and neck oncology cooperative group. Head Neck 26:681–692 (discussion 92–93)

Traynor SJ, Cohen JI, Gray J, Andersen PE, Everts EC (1996) Selective neck dissection and the management of the node-positive neck. Am J Surg 172:654–657

van den Brekel MW, Stel HV, Castelijns JA et al (1990) Cervical lymph node metastasis: assessment of radiologic criteria. Radiology 177:379–384

van den Brekel MW, Stel HV, Castelijns JA, Croll GJ, Snow GB (1991) Lymph node staging in patients with clinically negative neck examinations by ultrasound and ultrasound-guided aspiration cytology. Am J Surg 162: 362–366

van den Brekel MW, Stel HV, van der Valk P, van der Waal I, Meyer CJ, Snow GB (1992) Micrometastases from squamous cell carcinoma in neck dissection specimens. Eur Arch Otorhinolaryngol 249:349–353

van den Brekel MW, Castelijns JA, Stel HV, Golding RP, Meyer CJ, Snow GB (1993) Modern imaging techniques and ultrasound-guided aspiration cytology for the assessment of neck node metastases: a prospective comparative study. Eur Arch Otorhinolaryngol 250:11–17

van den Brekel MW, van der Waal I, Meijer CJ, Freeman JL, Castelijns JA, Snow GB (1996) The incidence of micrometastases in neck dissection specimens obtained from elective neck dissections. Laryngoscope 106:987–991

van den Brekel MW, Castelijns JA, Snow GB (1998a) The size of lymph nodes in the neck on sonograms as a radiologic criterion for metastasis: how reliable is it? Am J Neuroradiol 19:695–700

van den Brekel MW, Pameijer FA, Koops W, Hilgers FJ, Kroon BB, Balm AJ (1998b) Computed tomography for the detection of neck node metastases in melanoma patients. Eur J Surg Oncol 24:51–54

van den Brekel MW, Castelijns JA, Reitsma LC, Leemans CR, van der Waal I, Snow GB (1999) Outcome of observing the N0 neck using ultrasonographic-guided cytology for follow-up. Arch Otolaryngol Head Neck Surg 125: 153–156

Vandecaveye V, De Keyzer F, Vander Poorten V et al (2009) Head and neck squamous cell carcinoma: value of diffusion-weighted MR imaging for nodal staging. Radiology 251:134–146

Vandecaveye V, Dirix P, De Keyzer F et al (2010) Predictive value of diffusion-weighted magnetic resonance imaging during chemoradiotherapy for head and neck squamous cell carcinoma. Eur Radiol 20:1703–1714

Vandecaveye V, Dirix P, De Keyzer F et al (2011) Diffusion weighted magnetic resonance imaging early after (chemo) radiotherapy to monitor treatment response in head and neck squamous cell carcinoma. Int J Radiat Oncol Biol Phys [Epub ahead of print]

Vassallo P, Wernecke K, Roos N, Peters PE (1992) Differentiation of benign from malignant superficial lymphadenopathy: the role of high-resolution US. Radiology 183: 215–220

Wang HM, Ng SH, Wang CH, Liaw CC, Tsai MH, Lai GM (1996) Correlation between computed tomographic density of lymph node metastases and response to cisplatin-based chemotherapy in patients with head and neck squamous cell carcinoma in an area in which betel quid chewing is prevalent. Cancer 78:1972–1979

Wang P, Yu Q, Shi H (1999) CT findings of non-Hodgkin lymphoma in the head and neck. Zhonghua Kou Qiang Yi Xue Za Zhi 34:208–210

Weiss MH, Harrison LB, Isaacs RS (1994) Use of decision analysis in planning a management strategy for the stage N0 neck. Arch Otolaryngol Head Neck Surg 120:699–702

Wong RJ (2008) Current status of FDG-PET for head and neck cancer. J Surg Oncol 97:649–652

Wong RJ, Lin DT, Schoder H et al (2002) Diagnostic and prognostic value of [(18)F]fluorodeoxyglucose positron emission tomography for recurrent head and neck squamous cell carcinoma. J Clin Oncol 20:4199–4208

Wu CH, Chang YL, Hsu WC, Ko JY, Sheen TS, Hsieh FJ (1998) Usefulness of Doppler spectral analysis and power Doppler sonography in the differentiation of cervical lymphadenopathies. Am J Roentgenol 171:503–509

Xu W, Liu D, Lu Z (1998) CT scanning of the cervical lymph node metastases: compared with histologic sections. Lin Chuang Er Bi Yan Hou Ke Za Zhi 12:99–102

Yao M, Graham MM, Smith RB et al (2004) Value of FDG PET in assessment of treatment response and surveillance in head-and-neck cancer patients after intensity modulated radiation treatment: a preliminary report. Int J Radiat Oncol Biol Phys 60:1410–1418

Yeung AR, Liauw SL, Amdur RJ et al (2008) Lymph node-positive head and neck cancer treated with definitive radiotherapy: can treatment response determine the extent of neck dissection? Cancer 112:1076–1082

Ying M, Ahuja A, Metreweli C (1998) Diagnostic accuracy of sonographic criteria for evaluation of cervical lymphadenopathy. J Ultrasound Med 17:437–445

Ying M, Ahuja A, Brook F, Metreweli C (2001) Vascularity and grey-scale sonographic features of normal cervical lymph nodes: variations with nodal size. Clin Radiol 56:416–419

Yoo GH, Hocwald E, Korkmaz H et al (2000) Assessment of carotid artery invasion in patients with head and neck cancer. Laryngoscope 110:386–390

Yousem DM, Hatabu H, Hurst RW et al (1995) Carotid artery invasion by head and neck masses: prediction with MR imaging. Radiology 195:715–720

Yusa H, Yoshida H, Iwasa S et al (2000) Ultrasonographic assessment for response to radiochemotherapy of metastatic cervical lymph nodes in head and neck cancer: usefulness of grey-scale and color doppler sonography. Ultrasound Med Biol 26:1081–1087

Neck Lymphoma

Frank A. Pameijer and Rick L. M. Haas

Contents

Abstract

About 5% of malignant lymphomas in the head and neck are lymphomas. Frequently, lymphoma is not limited to the head and neck region, but also involves other parts of the body. The work-up of a patient with lymphoma requires a multidisciplinary approach. This chapter approaches lymphoma as a systemic disease describing the imaging work-up of patients with newly diagnosed head and neck lymphoma. This includes discussion of commonly applied imaging techniques such as, chest X-ray, computed tomography (CT), ultrasound, magnetic resonance imaging, and metabolic imaging (PET-CT). Both nodal disease, as well as non-nodal lymphoma manifestations (e.g. in Waldeyer's ring, larynx, orbit, lacrimal gland, parotid gland, sinonasal cavities, thyroid and bone) are discussed and illustrated with examples from daily practice. Frequently, imaging findings are non-specific. However, some imaging patterns can suggest the diagnosis of lymphoma.

F. A. Pameijer (✉)
Department of Radiology,
University Medical Center Utrecht,
Heidelberglaan 100, 3584 CX Utrecht,
The Netherlands
e-mail: f.a.pameijer@umcutrecht.nl

R. L. M. Haas
Department of Radiotherapy, The Netherlands Cancer Institute–Antoni van Leeuwenhoek Hospital,
Plesmanlaan 121, 1066 CX Amsterdam,
The Netherlands

R. Hermans (ed.), *Head and Neck Cancer Imaging*, Medical Radiology. Diagnostic Imaging,
DOI: 10.1007/174_2011_380, © Springer-Verlag Berlin Heidelberg 2012

1 Introduction

The most frequent group of neoplasms in the neck is the carcinomas, followed by the lymphomas. Only 5% of all neoplasms in the neck are malignant lymphomas. Lymphomas are neoplasms of the lymphoreticular system. They arise from lymphocytes and their derivates. Hodgkin's lymphoma (HL) and non-Hodgkin's lymphoma (NHL) are the most common malignancies of the hematopoietic system observed in the head and neck. Frequently, lymphoma is not limited to the head and neck region but also involves other parts of the body. This chapter approaches lymphoma as a systemic disease that can manifest itself in many forms in the head and neck. In many instances, the imaging findings are non-specific and tissue sampling remains the mainstay of making the diagnosis. However, some imaging patterns can strongly suggest the diagnosis of lymphoma.

1.1 Epidemiology

The malignant lymphomas, HL and NHL are the fifth most frequently occurring type of cancer in The United States comprising 5–6% of all malignancies. In the last years, an estimated 9260 new cases of HD and 81,850 new cases of NHL have been diagnosed in the United States (Jemal et al. 2007). The annual incidence rate of lymphomas in 1995–1999 was 19 cases per 100,000 persons. Rates of lymphomas historically have been about 40% higher in urban counties than in rural counties. The incidence rates of lymphomas in the United States tend to exceed those of most other countries. The rapid increase (1–5% annually) in lymphoma incidence in the 1970 and 1980s has been exceeded only by the increase in lung cancer in women and malignant melanomas in both sexes. The increase has been seen for males and females, for whites and blacks, and in all age groups (especially over 65 years of age), except for children. Malignant lymphomas in the head and neck usually presents as a neck lump, caused by lymphadenopathy (Cartwright et al. 1999; Vose et al. 2002).

1.2 Aetiology

The majority of lymphomas arise in lymph nodes, but primary extranodal disease now accounts for 20–30% of all cases. The most frequent primary extranodal sites are the stomach, small intestine, skin and brain. The incidence of extranodal disease has increased more rapidly than nodal disease.

Immunodeficiency, including both congenital and acquired conditions, especially in patients on immunosuppressive drugs after organ transplantation, is strongly associated with an increased lymphoma risk. Viruses like the Epstein-Barr virus appear to be important cofactors. A history of lymphatic malignancies in close relatives has been repeatedly shown to increase the risk of NHL by two- to three fold. Lymphomas may also cluster within families, not by an inherited genetic susceptibility, but because of shared environmental determinants (Cartwright et al. 1999; Vose et al. 2002).

1.3 Pathology and Classifications

In 1832, Thomas Hodgkin described a disease "lymphogranulomatosis maligna" that nowadays bears his name. From that moment on new lymphoma subtypes were recognized that closely resembled but were not exactly the disease discovered by Thomas Hodgkin, and were therefore epiphrased as NHL. Since the early 1960s in the previous century, several pathologists have attempted to produce classification systems in order to clarify the growing group of NHL's. Each new system was a revision of its predecessor adding new concepts and providing new names to the same entities. In 1982 a consensus system called the "Working Formulation" (WF) was produced combining several previous systems; the British National Lymphoma Investigation's Classification, the Rappaport Classification, the Lukes and Collins Classification, the Kiel Classification, the Dorfman Classification and the first World Health Organization (WHO) Classification. The WF lumped all diseases into three groups depending on their clinical behaviour; the low, intermediate and high-grade lymphomas abbreviated as LG-NHL, IG-NHL and HG-NHL.

The combination of several subtypes in just three groups was intended to help the clinician to distinguish lymphomas with more or less the same clinical course and comparable patient management. Soon, this lumping of different diseases in three groups without any biological basis was found to be artificial. In 1994, the WF was replaced by the Revised European-American Classification of Lymphoid Neoplasms, abbreviated as the REAL Classification (Harris et al. 1994). The basis of this system was a better understanding of the putative normal counterparts and their functions within specific sites of a normal lymph node,

Table 1 Nomenclature and prevalence of the four most important lymphoma entities

Official name from the WHO Classification (abbreviation)	Synonyms	Malignancy grade	Prevalence among the lymphomas (%)
Diffuse large B-cell lymphoma (DLBCL)	DLCL	Intermediate grade-NHL	30–40
Follicular lymphoma (FL)	Follicle center cell lymphoma (FCC), follicular centricity (cc) follicular centrocytic/centroblastic (cc/cb)	Low grade-NHL	15–25
Marginal zone lymphoma of MALT-type (MZL)	MALT lymphoma, maltoma	Low grade-NHL	~10
Mantle cell lymphoma (MCL)	(Relatively newly recognised entity)	Intermediate grade-NHL	~5

like the follicles, the germinal centers and the mantle- and marginal zones. The REAL Classification is based on a subdivision in three groups; B-cell neoplasms, T-cell/Natural Killer (NK)-cell neoplasms and Hodgkin's disease. The WHO Classification (2001) is a further refinement of the REAL system.

Clinicians still tend to communicate in terminology, which is a mixture derived from the WF, the REAL and the WHO systems. Table 1 simplifies the four most important lymphoma entities, their nomenclature and their prevalence among the lymphomas (Harris et al. 1994; WHO 2001). The indolent lymphomas are the former LG-NHL, the aggressive lymphomas used to be called IG-NHL or HG-NHL.

2 Hodgkin's Lymphoma

Originally, Thomas Hodgkin described in 1832 a disease "lymphogranulomatosis maligna" that afterward was called Hodgkin's disease. Since the WHO Classification of 2001, this entity is called HL. Historically, HL is further divided into four subtypes (see also Sect. 3; WHO classification 3.2.1–3.2.4):

1. nodular sclerosis (NS-HL; 40–60% of all HL)
2. lymphocyte predominant (LP-HL; ~2% of all HL)
3. mixed cellularity (MC-HL; 30–40% of all HL)
4. lymphocyte depleted (LD-HL; ~5% of all HL)

Most HL patients present in early stages predominantly with lymphadenopathy in the neck and upper mediastinum (see also Sect. 7). Extranodal spread in HL is very rare, splenic involvement being the most prevalent. Usually, only patients in advanced stage disease show organ involvement by HL. In those cases bone marrow infiltration, intrapulmonary spread (either as deposits or as a direct extension from hilar nodes into the lung parenchyma), liver and other organ involvement can be seen. From an imaging point of view, the following aspects should be emphasized:

- Neck nodes involved by HL usually have the same appearance as other lymphadenopathies. Sometimes, the imaging presentation is more characteristic and the diagnosis of lymphoma can be suggested by the radiologist (Table 3).
- NS-HL poses a problem in response assessment after therapy. Histologically, the malignant component of HL is embedded in a large amount of fibrous tissues (hence the name "sclerosis"). Frequently, residual masses are seen on ultrasound-, CT- or MRI investigations of the neck and mediastinum after successful treatment of NS-HL. These masses, though diagnosed as "partial response" on imaging do not necessarily contain viable lymphoma. In the past, for those cases the term CRu (Complete Response *unconfirmed*) was designated (Cheson et al. 1999). Both gallium-67-citrate scintigraphy and FDG-PET may help to decide on further treatment or not. Nowadays, a patient after the conclusion of treatment is either in Complete Response (CR) or in Partial Response (PR). In the recently published new "Cheson-criteria" based on combined findings from CT imaging and FDG-PET (Cheson 2008) the response category Cru does not exist longer. Residual masses (of PET-avid lymphomas) that become PET-negative after treatment are classified as CR.

3 Non-Hodgkin's Lymphomas (NHL) and Specific Entities

Worldwide, the incidence of NHL is about 5–10 times higher than the incidence of HL, largely dependent on regional differences. Of all cases of NHL, 80% is of

Table 2 Ann Arbor Staging system for Hodgkin's lymphoma

Stage	Description
I	Involvement of a single lymph node region
II	II = involvement of more than one lymphatic region on only one side of the diaphragm, IIE = localized involvement of one extralymphatic organ or site and its regional lymph nodes with or without other nodes on the same side of the diaphragm, IIS = involvement of more than one lymphatic region on only one side of the diaphragm plus involvement of the spleen, IIES = both
III	III = involvement of lymph node regions on both sides of the diaphragm, IIIE = involvement of lymph node regions on both sides of the diaphragm plus localized involvement of an extralymphatic organ or site, IIIS = involvement of lymph node regions on both sides of the diaphragm plus involvement of the spleen, IIIES = both
IV	Diffuse or disseminated involvement of one or more extralymphatic organs or tissues with or without associated lymph node enlargement. Organs considered distant include liver, bone, bone marrow, lung and/or pleura, and kidney.
Suffices	A Without symptoms
	B With symptoms
	Night sweats
	Unexplained fever >38° C
	Unexplained weight loss >10%, within last 6 months

B-cell origin and 20% is T-cell derived (Cartwright et al. 1999; Vose et al. 2002). The WHO Classification (Harris et al. 2000) of lymphoid neoplasms describes the following diseases:

1. B-cell neoplasms
   - 1.1. Precursor B-cell neoplasm
     - 1.1.1. Precursor B-lymphoblastic leukemia/lymphoma (precursor B-cell acute lymphoblastic leukemia)
   - 1.2. Mature (peripheral) B-cell neoplasms
     - 1.2.1. B-cell chronic lymphocytic leukemia/small lymphocytic lymphoma
     - 1.2.2. B-cell prolymphocytic leukemia
     - 1.2.3. Lymphoplasmacytic lymphoma
     - 1.2.4. Splenic marginal zone B-cell lymphoma (±villous lymphocytes)
     - 1.2.5. Hairy cell leukemia
     - 1.2.6. Plasma cell myeloma/plasmacytoma
     - 1.2.7. Extranodal marginal zone B-cell lymphoma of mucosa associated lymphoid tissues (MALT) type
     - 1.2.8. Nodal marginal zone B-cell lymphoma (±monocytoid B cells)
     - 1.2.9. Follicular lymphoma
     - 1.2.10. Mantle-cell lymphoma
     - 1.2.11. Diffuse large B-cell lymphoma
     - 1.2.12. Mediastinal large B-cell lymphoma
     - 1.2.13. Primary effusion lymphoma
     - 1.2.14. Burkitt's lymphoma/Burkitt cell leu-kemia
2. T-cell and natural killer (NK)-cell neoplasms
   - 2.1. Precursor T-cell neoplasm
     - 2.1.1. Precursor T-lymphoblastic lymphoma/leukemia (precursor T-cell acute lymphoblastic leukemia)
   - 2.2. Mature (peripheral) T-cell neoplasms
     - 2.2.1 T-cell prolymphocytic leukemia
     - 2.2.2 T-cell granular lymphocytic leukemia
     - 2.2.3 Aggressive NK-cell leukemia
     - 2.2.4 Adult T-cell lymphoma/leukemia (HTLV1+)
     - 2.2.5 Extranodal NK/T-cell lymphoma, nasal type
     - 2.2.6 Enteropathy-type T-cell lymphoma
     - 2.2.7 Hepatosplenic gamma–delta T-cell lymphoma
     - 2.2.8 Subcutaneous panniculitis-like T-cell lymphoma
     - 2.2.9 Mycosis fungoides/Sezary syndrome
     - 2.2.10 Anaplastic large-cell lymphoma, T/null cell, primary cutaneous type
     - 2.2.11 Peripheral T-cell lymphoma, not otherwise characterized

2.2.12 Angioimmunoblastic T-cell lymphoma
2.2.13 Anaplastic large-cell lymphoma, T/null cell, primary systemic type
3. Hodgkin's lymphoma (Hodgkin's disease)
3.1. Nodular lymphocyte-predominant Hodgkin's lymphoma
3.2. Classical Hodgkin's lymphoma
3.2.1. Nodular sclerosis Hodgkin's lymphoma (grades 1 and 2)
3.2.2. Lymphocyte-rich classical Hodgkin's lymphoma
3.2.3. Mixed cellularity Hodgkin's lymphoma
3.2.4. Lymphocyte depletion Hodgkin's lymphoma

Note The follicular (1.2.9) and diffuse large B-cell lymphomas (1.2.11) make up more than half of all lymphomas diagnosed (see also Table 1).

4 Work-up

The work-up of a patient with lymphoma requires a multidisciplinary approach involving close cooperation among the head and neck surgeon, the radiation oncologist, the pathologist, the medical oncologist or hematologist–oncologist and the radiologist.

4.1 Diagnosis

The diagnostic process to fully document new lymphoma patients, whether or not localized in the neck, comprises the following minimum requirements:

- Full history (including presence of fever, night-sweats and weight-loss; the so-called B-symptoms) and physical examination with emphasis on all peripheral lymph node regions (neck, axilla and groin), examination of Waldeyer's ring, liver, spleen and skin.
- Full blood count including a differential count of the leukocytes.
- Representative excision biopsy of an entire enlarged lymph node (in nodal disease).
- Bone marrow biopsy.
- Imaging of all lymphatic regions.

4.2 Initial Imaging

Standard radiological work-up of a newly diagnosed patient with head and neck lymphoma should include:

- Posteroanterior and lateral chest X-ray.
- Contrast-Enhanced Computed Tomography (CECT) of the neck, chest, abdomen and pelvis.
- Ultrasound of the neck may be useful as an adjunct study.
- Magnetic Resonance Imaging (MRI) may substitute CECT of the neck, especially if Waldeyer's ring is involved or extranodal head and neck disease is present.

This imaging strategy is usually sufficient to stage a lymphoma patient. CECT and MRI have completely replaced lymphangiography as a diagnostic tool in lymphoma patients. In recent years, positron emission tomography using 18-fluoro-deoxy-glucose PET has emerged as a powerful imaging tool for staging (Jerusalem et al. 2001; Moog et al. 1997) and response assessment of lymphomas (Cheson 2007). The use of PET is strongly recommended before treatment for patients with FDG-avid lymphomas (e.g., diffuse large B-cell lymphomas and Hodgkin's lymphoma) to better delineate and stage the disease (Fig. 1). As yet, PET imaging is not mandatory because of limitations imposed by cost and availability (Cheson 2007).

Recent improvements in MRI technology have resulted in the availability of sufficiently fast and diagnostic sequences to perform "whole-body magnetic resonance imaging" (WB-MRI). This MR-technique lacks the use of ionizing radiation which is an obvious advantage when compared to CT and PET-CT. Especially when combined with recently developed functional WB-MRI techniques such as diffusion-weighted imaging (DWI) (Takahara 2004; Kwee 2008), this technique seems promising. Preliminary data showed that initial staging of malignant lymphoma using WB-MRI (without DWI and with DWI) produced equal results to staging using CT (Fig. 2) in the majority of patients (Kwee 2009).

However, at present, CT remains the most commonly used imaging modality for staging malignant lymphoma because of its widespread availability and relatively low cost (Kwee 2008).

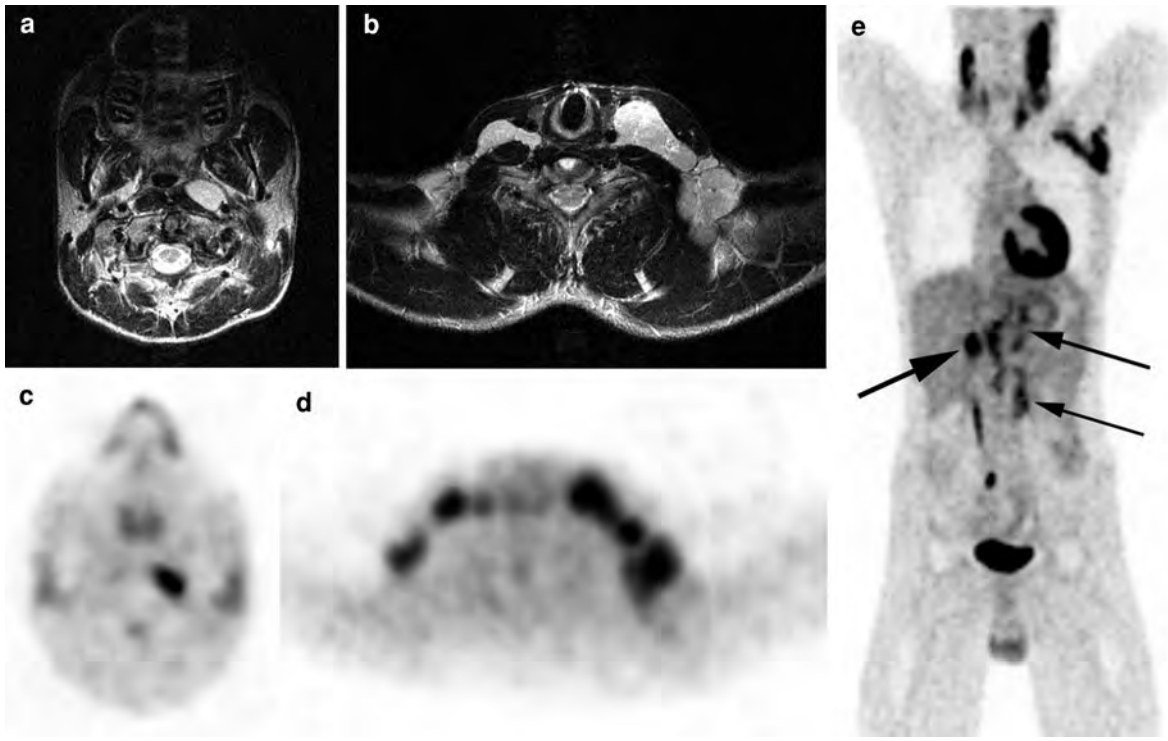

Fig. 1 Patient with Hodgkin's lymphoma (HL). Initial staging with MRI of the neck shows extensive lymphadenopathy. **a** Enlarged left retropharyngeal node. **b** Bilateral neck and left axillary adenopathy (presenting symptom). PET study confirms the MR-findings in the neck (**c** and **d**). **e** Periaortic lymph nodes (*slim arrows*) and lymphadenopathy in the liver hilus (*thick arrow*) also seen on abdominal CT (not shown), indicating Stage 3 disease HL. *Note* Normal activity in the heart, right ureter and bladder

4.3 Staging

Designed for Hodgkin's lymphoma the Ann-Arbor system is now used for staging all lymphomas (Table 2). The system was slightly modified after the Cotswold Convention (Lister et al. 1989; Smithers 1971).

5 Treatment

Management of lymphomas is very diverse and depends fully on the specific lymphoma subtype, the stage in which the patient is diagnosed, co-morbidity, the performance status and biological age of the patient. As a concept, lymphoma patients can be treated by chemotherapy, radiotherapy and immunotherapy, and usually in a combined modality approach.

Some frequently applied regimens are the following:

- *Chemotherapy, single agent*; Chlorambucil (oral), Cyclophosphamide (oral), Fludarabin (oral and iv.): in case of indolent lymphomas, predominantly follicular lymphoma.
- *Chemotherapy, multi-agent*; CVP (=COP), Chlorambucil + Vincristine (=Oncovin®) + prednisone in case of indolent lymphomas, CHOP (± Rituxan ®; CHOP = COP + Adriamycin), DHAP (Dexamethasone + high dose Ara-C + Cisplatin), VIM (VP-16 (=Etoposide) + Ifosphamide + Mesna) in case of aggressive lymphomas, predominantly DLCL, BEAM (BCNU + Etoposide + Ara-C + Melphalan) as a conditioning regimen before stem cell transplantations for aggressive lymphomas, ABVD (Adriamycin + Bleomycin + Vinblastin + Dacarbazine), MOPP (Mitoxin + Oncovin + Procarbazin + Prednisone), MOPP-ABV for Hodgkin's lymphoma.
- *IF-RT* (= *involved field radiotherapy*); all lymphomas; irradiation on the affected site only, no prophylactic irradiation to adjacent areas (Fig. 3).

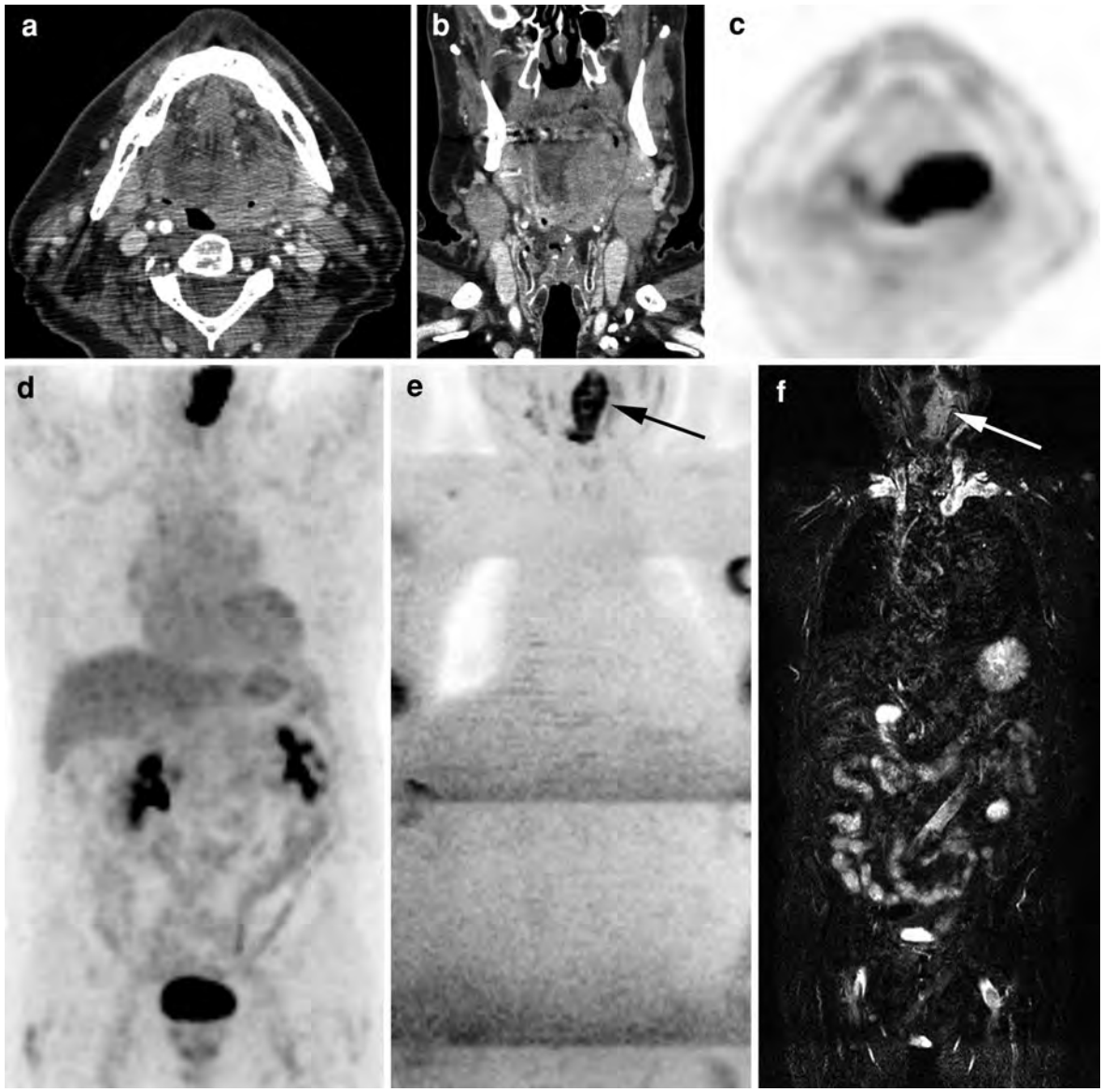

Fig. 2 Diffuse large B-Cell lymphoma (DLBCL) of the base of tongue (BOT). **a** Axial and coronal contrast-enhanced CT shows large enhancing lesion centered in the left BOT. **b** Axial and coronal PET study: area of increased metabolism correlates well with the abnormality on CT. **c**, **d** Staging of this patient with PET shows the large primary lesion in the left BOT. No pathological metabolic activity is detected outside the neck indicating Stage 1 disease. *Note* physiologic activity in the kidneys and bladder. **e**, **f** Good correlation with whole body MRI (WB-MRI) both on diffusion weighted imaging (**e**), as well as T2 short tau inversion recovery (**f**) that showed no areas of abnormal signal outside the primary lesion in the left BOT (*arrows*)

- *EF-RT* (=*extended field radiotherapy)*; all lymphomas; irradiation on the affected site plus prophylactic irradiation to adjacent areas.
- *[S]TNI = [sub]total nodal irradiation*; Hodgkin's lymphoma; this regimen of irradiation is now considered obsolete.

Table 3 Lymph node imaging features on US, CT and MRI for Hodgkin's and Non-Hodgkin's Lymphoma. For comparison, imaging features for squamous cell carcinoma nodes have been added (adapted from Harnsberger 2004)

Imaging features	Hodgkin's lymphoma	Non-Hodgkin's lymphoma	Squamous cell carcinoma
US	Well-defined enlarged round nodes with homogeneous appearance	Diffuse homogeneous decreased echogenicity characteristic	Round nodes with loss of hilar echogenicity
CT	Lobulated round nodal masses with variable enhancement. Central necrosis may be present. Calcification (pre-treatment) uncommon	Multiple bilateral ovoid masses in multiple nodal chains. Variable enhancement ranging from isodense to muscle to strong enhancement. Central necrosis may be present. Enhancement pattern may vary within same patient	Diffuse or rim-enhancement of nodes. Central necrosis is typical
MRI	T1WI: enlarged round iso- to hypointense nodes. T2WI: Nodes are hyperintense to muscle. T1 C+: variable: see CT	T1WI: enlarged nodes isointense to muscle. T2WI: Nodes are hyperintense to muscle. T1 C+: variable: see CT	T1WI: isointense to muscle; necrosis seen as hypointense focus. T2WI: hyperintense; necrosis shows focal marked hyperintensity. T1 C+: inhomogeneous

C+ contrast enhancement

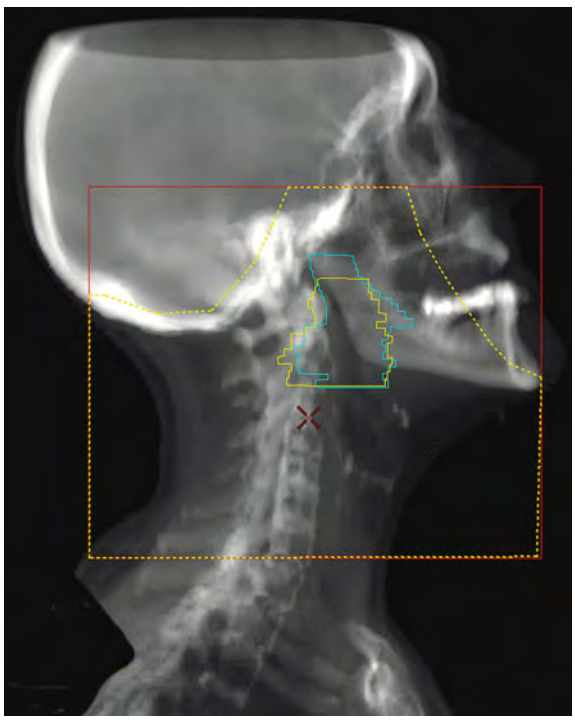

Fig. 3 Involved field radiotherapy (IF-RT). IF-RT planning of a patient with grossly enlarged tonsils due to NHL involvement (*left* tonsil delineated in *blue*, *right* tonsil in *yellow*). Total radiation volume for this treatment consist of Waldeyer's ring (both tonsils, base of tongue and nasopharyngeal adenoid) together with the occipital lymph nodes and the nodes in level I, II and III (*dashed yellow line*). The *red line* indicates the machine collimator

- *Combined modality regimens*; 3–4 × CHOP + IF-RT: aggressive lymphomas, predominantly DLCL in stage I or II, 3–4 × ABVD + IF-RT: Hodgkin's lymphoma, stage I or II.

6 Response Assessment

In principle, all imaging studies performed in the initial staging process will be repeated after completion of treatment. Imaging during treatment may also be indicated to decide on further management.

In hematology, response is assessed by the "Cheson-criteria" (Cheson 2008). This applies also to response evaluation in head and neck lymphoma. This is in contrast to response assessment in solid tumors, such as carcinomas and sarcomas, for which the RECIST criteria are used (Therasse 2000).

In recent years, PET has been an active area of investigation in response assessment in all kinds of tumors, including lymphoma. The advantage of PET, over conventional imaging techniques such as CT and MRI, is its ability to distinguish between viable tumor and residual mass lesions that contain only necrosis or fibrosis. The widespread use of PET in lymphoma patients warranted a reassessment of the previously established response criteria. In these "New response criteria for lymphomas" recommendations for the use of PET or PET-CT both for pretreatment imaging as

well as post-treatment response evaluation are included (Cheson 2008).

7 Nodal Disease

Per definition, this is lymphatic malignancy occurring *in pre-existing nodal chains* (in the head and neck). In hematology, lymph nodes are typically involved by contiguous spread. This is in contrast to solid tumors (i.e. squamous cell carcinoma of the head and neck) where specific lymph node groups are at a higher risk for metastatic involvement based on the preferential lymphatic drainage from the primary tumor site.

7.1 The Common Sites

For all imaging modalities depicting nodal disease, including US, CT and MRI, the cervical lymph nodes are described in terms of *levels* (Som et al. 2000; UICC 2009). In head and neck nodal disease, levels I–V are most frequently involved (Fig. 4).

In clinically suspected neck adenopathy, US may be helpful because it can be used to guide fine needle aspiration cytology (FNAC). An experienced cytopathologist can reliably diagnose lymphoid lesions from FNAC-smears, especially in the differential diagnosis from carcinomas. CT and MRI are better equipped for local tumor mapping and staging.

For practical purposes, nodal involvement with HL cannot be exclusively differentiated from nodes with NHL whatever imaging modality is used. In the head and neck, both entities typically present with multiple, uni- or bilateral non-necrotic enlarged lymph nodes involving usual and unusual nodal chains. However, certain imaging features are more characteristic for HL than for NHL.

General features in favor of *Hodgkin lymphoma* nodes

- HL presents in lymph nodes in about 98% of cases. When multiple nodes are present, the involved nodal groups are contiguous in about 90% of cases. This suggests a unifocal origin of the disease and subsequent dissemination through lymphatic pathways.
- Levels III and IV most frequently involved.
- Combination with mediastinal lymphadenopathy is frequent.

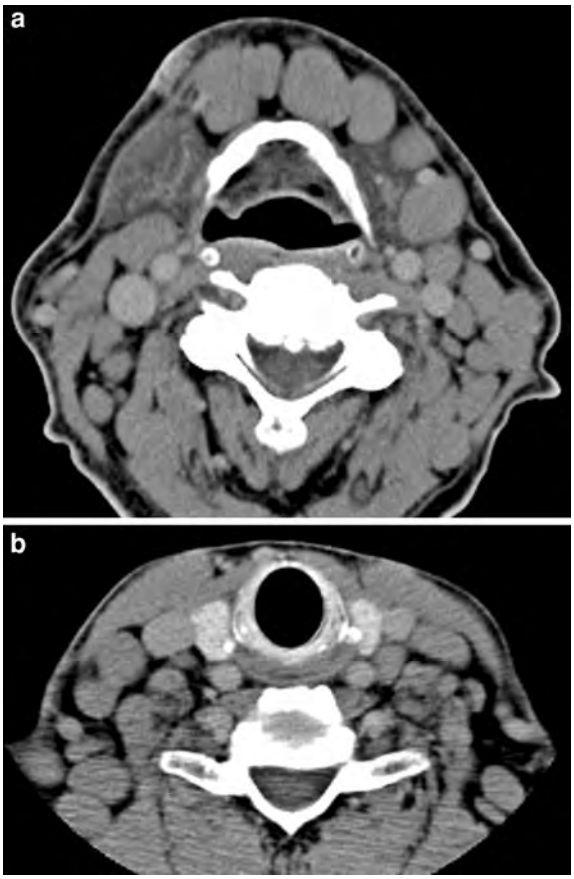

Fig. 4 **a**, **b** Nodal B-NHL. Axial contrast-enhanced CT shows bilateral enlarged level I–V cervical nodes without central necrosis

- Involvement of extranodal sites such as Waldeyer's ring is uncommon.

General features in favor of *Non-Hodgkin lymphoma* nodes

- NHL presents in a generalized fashion (including bone marrow infiltration) much more often than HL.
- Levels II–IV often involved.
- NHL often involves extranodal tissue, both Waldeyer's ring (extranodal *lymphatic*) as well as extranodal *extralymphatic* (orbit, salivary glands, sinonasal, etc.) tissue.

Specific lymph node imaging features for US, CT and MRI are shown in Table 3.

Note A minority of patients has enlarged lymph nodes *with* central necrosis on cross-sectional imaging. This imaging pattern is much more frequently seen in patients with head and neck squamous cell

cancer. Central necrosis in lymphoma patients usually indicates a higher malignancy grade.

7.2 The Uncommon Sites

Manifestations of nodal disease may also be seen in more uncommon sites including pre-tracheal nodes (level VI) and retropharyngeal nodes (Fig. 1). Other nodal sites, not included in the UICC nodal classification, include occipital, facial, buccal, peri-parotid and intraparotid lymph nodes. All these nodes may be sites of origin of lymphoma (Mancuso 1998). There are no differences in imaging appearance between these nodal groups and the level I–V nodes discussed above (Table 3).

8 Extranodal Disease

Per definition, this is lymphatic malignancy occurring *outside pre-existing nodal chains*. Extranodal lymphoma can be separated in extranodal *lymphatic* and extranodal *extralymphatic* disease (Hermans 2004). Extranodal areas predisposed to develop lymphoma are sites that are normally rich in lymphoid tissue such as Waldeyer's ring (extranodal lymphatic disease). Extranodal extralymphatic sites include the orbit, parotid gland, nasal cavity, paranasal sinuses, as well as the thyroid gland. Although anatomically in close proximity, lymphomas arising in these sites have distinct clinical characteristics. Factors that appear to influence the disease pattern include concurrent conditions, such as Sjögren's syndrome, and geographic factors particularly concerning sinonasal lymphomas (see also Sect. 8.4).

Patients with extranodal Hodgkin's lymphoma usually present with a painless mass or complain of systemic symptoms such as night sweats, fever and weight loss, whereas the clinical presentation of patients with extranodal NHL in the head and neck often mimic those of patients with squamous cell carcinoma (SCC) arising at the same site. Approximately 10% of patients with NHL present with extranodal primary lesions in the head and neck.

The treatment and prognosis of patients with head and neck lymphoma depends on the pathological subtype of disease and extent of involvement at time of presentation. The most common lymphoma is the diffuse large B-cell lymphoma (65%) in an early stage at presentation. In the parotid gland, however, the indolent histologies (marginal zone lymphoma and follicular lymphoma) prevail. Predominantly patients between 50 and 60 years of age are affected. The male to female ratio is 1.6:1, with the exception of lymphomas of the salivary glands, orbit and thyroid, which occur equally or more frequently in women.

The imaging findings of extranodal head and neck lymphomas are essentially the same as those found in SCC. In 80% of patients with primary extranodal NHL in the head and neck, additional nodal involvement is present. If a primary lesion is associated with large, homogeneously enhancing lymph nodes without central necrosis, the possibility of lymphoma may be suggested. However, this combination of imaging findings may also be encountered in SCC. Therefore, the diagnosis of lymphoma remains based on histologic tissue examination.

8.1 Waldeyer's Ring and the Upper Aerodigestive Tract

Waldeyer's ring comprises the lymphoid tissues located superiorly in the nasopharynx, laterally in both tonsillar fossae and inferiorly in the base of tongue. More than half of extranodal head and neck lymphomas occur in Waldeyer's ring, the tonsil being the most prevalent subsite (40–50% of cases). All subtypes of NHL can be found in Waldeyer's ring, but deposits of Hodgkin's lymphoma are rare (Aloulou et al. 2002; Hanna et al. 1997; Yuen and Jacobs 1999).

8.1.1 Nasopharynx

Patients with nasopharyngeal NHL may present with intermittent hearing loss secondary to unilateral or bilateral Eustachian tube obstruction or may have persistent epistaxis or nasal obstruction. Imaging of nasopharyngeal NHL shows two morphological types: a circumscribed, bulky, mucosa-based mass that has not invaded the deep structures around the pharynx (Fig. 5), and a mass with a much more infiltrative spread pattern. The latter type of primary nasopharyngeal lymphoma may invade the skull base and spread along nerves in a manner similar to that of SCC (King et al. 2003). Both diseases are commonly associated with cervical adenopathy.

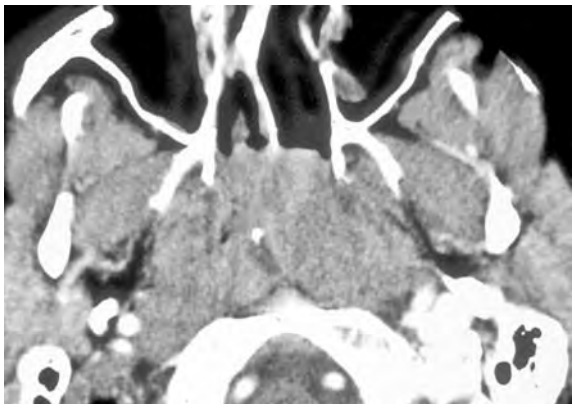

Fig. 5 Nasopharyngeal NHL. Axial contrast-enhanced CT shows a bulky mucosal mass filling the nasopharyngeal lumen and extending bilaterally into the choanae. *Note* the parapharyngeal fat is intact and there is no bony invasion of the clivus

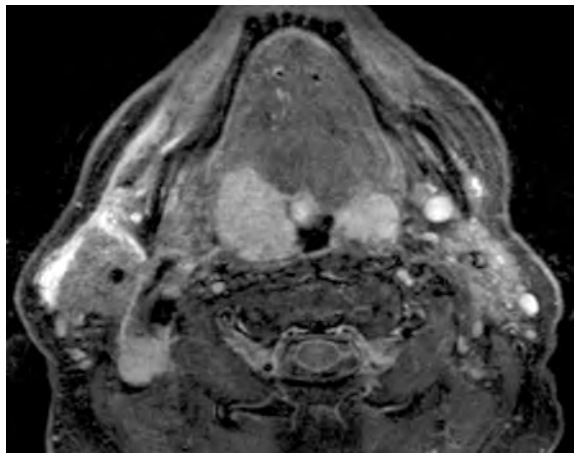

Fig. 6 Tonsillar NHL. Axial T2-weighted sequence (TIRM) demonstrates bilateral high signal intensity (SI) soft-tissue masses in the tonsil. *Note* that there is no invasion of the surrounding deep-tissue planes. There is an associated enlarged level II lymph node on the right with the same high SI appearance

In children and adolescents nasopharyngeal lymphoid tissue is prominent. These so-called "adenoids", or nasopharyngeal tonsils are located in the roof of the nasopharynx. Such tissue should not be mistaken as an abnormal mass. Normal lymphoid tissues show uniform enhancement after contrast medium injection and, on MRI, display a typical high signal intensity without invasion of adjacent structures.

8.1.2 Tonsillar Fossa

Patients with NHL of the tonsil usually have a unilateral sore throat or obstructive symptoms. Clinically, especially in younger patients, these lesions are difficult to differentiate from reactive hypertrophy. Frequently the diagnosis of NHL is delayed while patients are treated with prolonged courses of antibiotics or even with incision for a suspected tonsillar abscess.

Hermans et al. (1994) described two patterns of tonsillar involvement:

a) Involvement of only the tonsillar fossa. Imaging in these cases shows a unilateral or bilateral enlarged tonsil (Fig. 6), without infiltration of surrounding tissues.
b) Tonsillar involvement with extension to the pharyngeal wall. In this subgroup, two types of extension have been described. An infiltrating growth pattern, in which there is extension in the parapharyngeal fat plane and into the extrapharyngeal deep core tissues (masticator space, parotid space, etc.); this pattern mimics the growth pattern of carcinomas. The other subtype in this group consists of an exophytic pattern of growth in which the tumor stayed inside the pharyngeal walls but extended outside of the tonsillar margins expanding into the oral cavity (Fig. 7). Complete circumferential thickening of the pharyngeal wall without deep infiltration has been reported as quite specific for lymphoma (Hermans et al. 1994).

The signal intensity on T2-weighted, T1-weighted and T1-weighted contrast-enhanced MRI images is as a rule homogeneous and similar to that of normal tonsils. Large tumors can be mildly heterogeneous showing small foci of necrosis. Lymphadenopathy in the ipsilateral upper internal jugular chain can be seen and in those cases, the nodes will be of similar signal intensity to the primary tumor (Fig. 6). In 20% of tonsillar NHL gastrointestinal involvement can be diagnosed simultaneously (Hanna et al. 1997).

8.1.3 Base of Tongue

Patients with lymphoma in the base of tongue may have obstructive symptoms, sore throat and occasionally dysphagia or a change in voice. Clinically, these lesions are often submucosal, bulging and soft

Fig. 7 Tonsillar NHL. Contrast-enhanced multislice CT-images. **a** Axial contrast-enhanced CT shows a soft-tissue mass situated in the right tonsil (arrows). There is anterior extension (within the pharyngeal wall) along the glossotonsillar sulcus with slight displacement of the right tongue base. A grossly enlarged lymph node is present in level II (arrowhead). **b** Coronal reformatting shows the medial extension of the mass (arrows) with involvement of the soft palate. The level II lymph node contains a large area of central necrosis (arrowhead) (Courtesy R. Hermans, MD, PhD, Leuven, Belgium)

Fig. 8 Base of tongue base NHL. A female patient with dysphagia. Contrast-enhanced multislice CT-images. **a** Axial contrast-enhanced CT shows a large homogeneously enhancing mass centered in the left base of tongue. Note that there is no invasion of the surrounding deep-tissue planes. **b** Sagital reformatting demonstrating the exophytic nature of the mass

on palpation. As mentioned, the high concentration of lymphoid tissue in the base of tongue (tonsilla lingualis) predisposes this site to develop lymphoma. The typical imaging appearance on CT (Fig. 8) or MRI is a bulky, exophytic mass centered in the tongue base. Enhancement pattern and signal intensities are identical to tonsillar NHL.

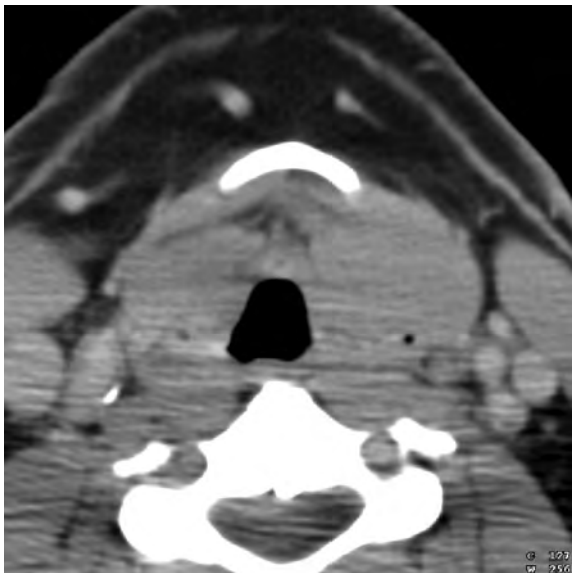

Fig. 9 Laryngeal NHL. Axial contrast-enhanced CT-image at the lower border of the hyoid bone shows bilateral large submucosal masses (Courtesy I. M. Schmalfuss, MD, Gainesville, Florida)

8.1.4 Larynx

Laryngeal involvement with NHL is very rare. Laryngeal lymphomas tend to have a large submucosal component most frequently centered in the supraglottis. The imaging characteristics are non-specific and comparable to SCC. Multiple lesions strongly suggest the diagnosis of NHL (Hermans et al. 1994). In addition, a laryngeal tumor with a large supraglottic submucosal component (Fig. 9) should alert the radiologist to the possibility of NHL (King et al. 2004).

8.2 Orbit

There are a variety of tumors and tumor-like lesions in the orbit, both benign and malignant. In an unselected series of 1,264 orbital lesions, 810 (64%) were benign and 454 (36%) were malignant. The percentage of malignant lesions was 20% in children, 27% in young adults and middle-aged patients and 58% in older patents (age range, 60–92 years). Lymphoma was the most common malignancy in older patients, representing 10% of cases (Shields et al. 2004). Lymphoid tumors of the orbit in children are extremely rare.

Besides malignant lymphoma, a spectrum of less malignant lymphoid orbital tumors exists ranging from the benign pseudolymphoma or pseudotumor to the reactive and atypical lymphoid hyperplasia. These two latter entities mimic orbital lymphoma, both from an imaging and from a histological point of view. The incidence of idiopathic inflammatory pseudotumor and lymphoid tumors seems to be equal (Yan et al. 2004). Any orbital tissue or combination of tissues may be involved in malignant lymphoma, as well as the less malignant lymphoid orbital tumors.

Anatomically, true lymphoid tissue is found in the subconjunctival and lacrimal glands, predisposing these sites for development of lymphoma. Orbital lymphomas can be subdivided into three groups; conjunctival, lacrimal and intra-orbital (true intraocular lymphomas are very rare). Orbital lymphomas are mostly indolent, low-grade lesions. Marginal zone lymphoma (MZL), synonym MALT lymphoma, followed by follicular lymphoma is the most prevalent diagnosis (Lee et al. 2005). If MZL is diagnosed, special attention should be focused to the other MZL-prevalent sites like the salivary glands, Waldeyer's ring and the stomach.

Treatment of orbital lymphomas is moderate dose irradiation (25–30 Gy) to the entire orbit with over 90% of local control (Agulnik et al. 2001; Pfeffer et al. 2004).

For imaging of the orbit, US, CT and MRI can be used.

8.2.1 Conjunctiva

Patients with lymphoma arising in the conjunctiva complain of local irritation, itching, ptosis or the sensation of a mass. Imaging shows unilateral or bilateral symmetrical swelling of the conjunctival tissues. These are smooth, sharply marginated ovoid lesion that shows moderate to strong enhancement (Fig. 10). In case of conjunctival involvement, differentiation has to be made from preseptal cellulitis, which is usually unilateral, and of sinonasal origin; preseptal pseudotumor is rare (Hermans et al. 1994).

8.2.2 Intra-orbital Lymphoma

Painless proptosis, diplopia and visual disturbance are the common presenting symptoms of patients with intraorbital lymphoma. On imaging, orbital lymphomas are homogeneous usually sharply marginated intra- or para-conal masses that occur most often in

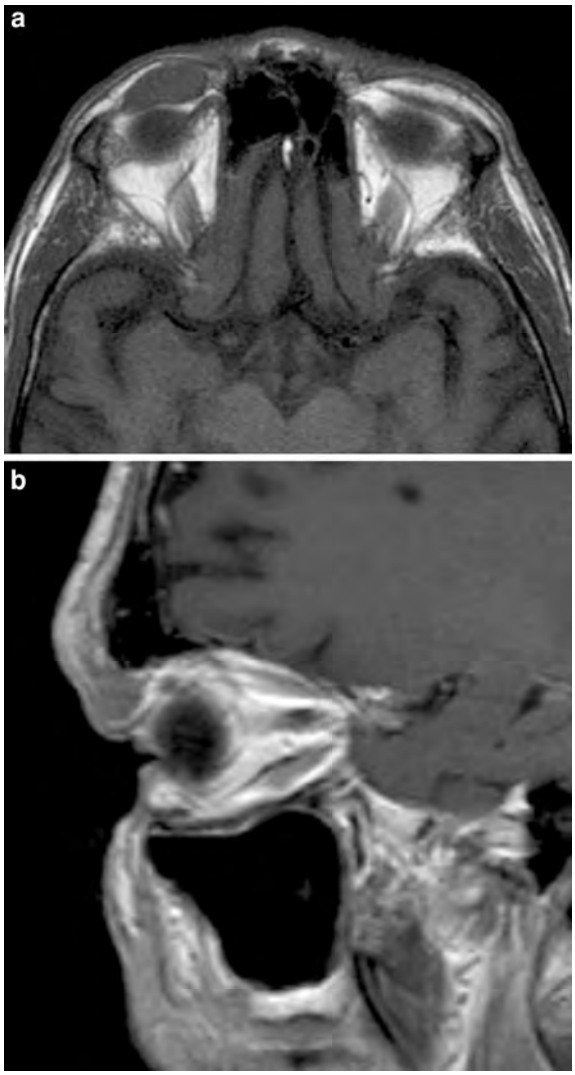

Fig. 10 Conjunctival NHL. T1-weighted MR-images. **a** Axial image at the cranial margin of the orbit shows an ovoid, sharply marginated, lesion located anterior to the right globe. **b** Post-contrast sagital image showing mild homogenous enhancement of the mass located in the upper eyelid

Fig. 11 Intra-orbital NHL. T1-weighted axial MR-images. **a** Non-enhanced image at the level of the optic nerve shows diffuse infiltration of the intraconal space of the left orbit. **b** Post-contrast fat-suppressed image showing moderate homogeneous enhancement of the intraconal mass Note that the lesion is 'molding' around the optic nerve

the anterior portion of the orbit, the retrobulbar area (Fig. 11), or in the superior orbital compartment. Mild to moderate enhancement is usually present. Based on the imaging findings alone, there is a differential diagnosis for these types of lesions including malignant lymphoma, pseudotumor, reactive hyperplasia, lacrimal gland tumors, optic nerve tumors and Graves' orbitopathy. This differential can be narrowed when the imaging features are interpreted in conjunction with the clinical signs and symptoms. A somewhat characteristic feature of orbital lymphoid tumors is the tendency to mold themselves around intraorbital structures without (bony) destruction (Fig. 11).

8.2.3 Lacrimal Gland

Lacrimal gland lymphoma may present with epiphora or as a painless mass noticed for cosmetic reasons. If lymphoma is restricted to the gland itself, the lesion is characteristically located in the supero-lateral orbital compartment. Cross-sectional imaging shows smooth, unilateral or bilateral (Fig. 12), enlargement of the lacrimal gland. If the gland is grossly enlarged, medial and forward displacement of the globe is the clue to the primary location.

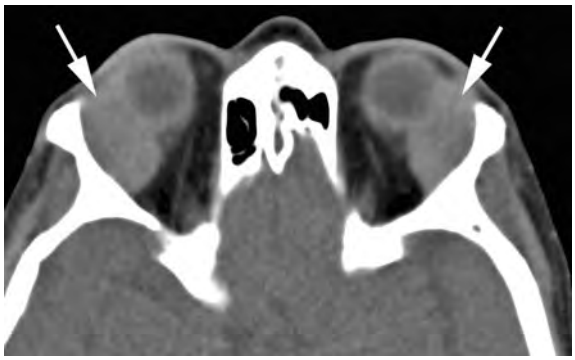

Fig. 12 Lacrimal gland NHL. Axial contrast-enhanced CT-image through the superior parts of the orbits shows symmetric enlargement of both lacrimal glands (arrows). There is mild medial and forward displacement of the globes (Courtesy R. Hermans, MD, PhD, Leuven, Belgium)

8.3 Salivary Glands

Primary lymphoma of the salivary glands is an uncommon tumor. The parotid gland is affected most often (80% of reported cases) followed by the submandibular gland (20%). There are only isolated reports of primary lymphoma in minor salivary glands; sites most commonly involved include the palate and gingiva.

8.3.1 Parotid Gland

Lymphoma of the parotid gland may arise within the parotid parenchyma (primary) or within the intraparotid lymph nodes (secondary).

Primary lymphoma of the parotid gland is rare, accounting for less than 5% of parotid tumors. These lymphomas are classified as MALT (mucosa-associated lymphoid tissue) lymphomas (see also Table 1). These low-grade lymphomas may involve any portion of the gastrointestinal tract where lymphoid tissue is part of the mucosal defence system. Lymphoid tissue is normally present in the parotid gland and absent in the submandibular and sublingual gland. When MALT lymphoma occurs in the salivary gland, as in other extranodal sites such as the stomach, it is usually an indolent neoplasm that tends to remain localized for long periods of time (Abbondanzo 2001; Palacios et al. 2004; Tonami et al. 2002, 2003; Yuen and Jacobs 1999). Patients with primary lymphoma of the parotid gland typically present with a painless parotid-region mass or with parotitis with progressive enlargement of the gland. After systemic work-up most patients are found to have early stage localized disease; i.e. Stage IIE (see also Table 2).

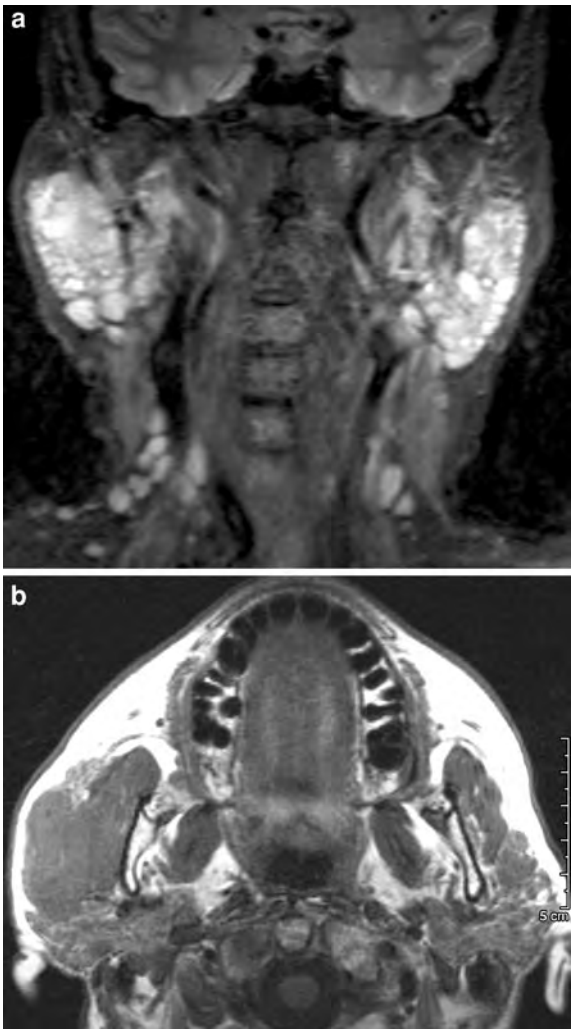

Fig. 13 Primary MALT lymphoma of the parotid gland. A female patient with Sjögren's syndrome with progressive parotid enlargement. T2-weighted (TIRM) MR-images. **a** Coronal image confirms bilateral parotid swelling. This is caused by innumerable small cysts indicative of chronic sialadenitis with cystic enlargement of terminal salivary ducts. Note multiple non-enlarged level IV nodes bilaterally. **b** Axial image shows an additional infiltrative mass located in the superficial lobe of the right parotid gland invading the masseter muscle. Biopsy of this mass revealed MALT lymphoma

Patients with Sjögren's syndrome have an increased risk of developing primary parotid lymphoma. Sjögren's syndrome, or sicca syndrome, is an autoimmune disease characterized by keratoconjunctivitis sicca, dryness of mucous membranes,

teleangiectasias of the face and bilateral parotid enlargement (Fig. 13). The syndrome is often associated with reumatoid arthritis and Raynaud's phenomenon. The risk of lymphoma in these patients has been estimated to be approximately 44 times the incidence expected in a generally healthy population (Yuen and Jacobs 1999). It may affect any area of the head and neck but may have its first manifestations in the parotid gland. Often these patients are scanned to survey for the possibility of lymphoma.

Lymphoma may also involve the salivary glands (usually parotid) secondary to systemic lymphoma. This secondary involvement is usually not classified as MALT lymphoma, but is more commonly a diffuse large cell lymphoma.

For imaging of suspected salivary gland tumors US, CT as well as MRI can be used. Because of their superficial position, the parotid, the submandibular and the sublingual glands can be imaged with high-resolution US transducers (Gritzmann et al. 2003). This is especially helpful in the diagnostic phase because US can be used to perform fine needle aspiration cytology.

Cross-sectional techniques are better equipped for local tumor mapping and staging purposes. On CT, primary lymphoma is characterized by, partial or total, replacement of the parotid gland by an infiltrating soft tissue mass (Fig. 13). Multiple solid, intraparotid masses are suggestive of secondary lymphoma (Fig. 14). These enlarged intraparotid lymph nodes are usually sharply marginated round to ovoid lesions with homogeneous attenuation. However, nodal necrosis can occur.

On MRI, primary and secondary lymphomas are characterized by homogeneous intermediate signal intensity (SI) on all imaging sequences. There is also a tendency to 'fade' into the SI of the parotid gland on T2-weighted and contrast-enhanced, fat-suppressed T1-weighted MR images.

In the setting of multiple intraparotid and/or periparotid lesions, the age of the patient is important in establishing a differential diagnosis. In younger patients, acute viral or bacterial infections should be considered. Acute otitis media can present with reactive lymphadenopathy of periparotid lymph nodes. Multiple intraparotid cystic lesions should alert the radiologist to the possibility of acquired immunodeficiency syndrome (AIDS). These cystic lesions or 'lymphoepithelial cysts' have been associated with HIV seropositivity. Presence of these abnormalities may be the first indication that the patient has AIDS. Most commonly, with HIV infection there is also a diffuse cervical adenopathy. In about one-third of the patients there is hyperplasia of Waldeyer's ring (Kirshenbaum et al. 1991).

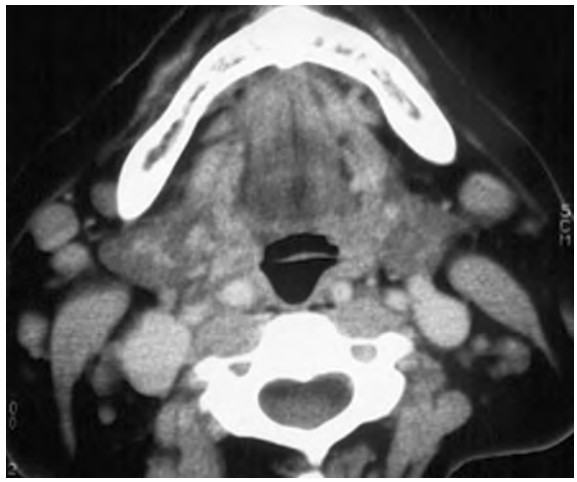

Fig. 14 Secondary parotid lymphoma. Axial contrast-enhanced CT-image shows multiple sharply marginated masses within and around both parotid glands representing enlarged intra- en peri-parotid lymph nodes (Courtesy R. Hermans, MD, PhD, Leuven, Belgium)

The differential diagnosis for elderly patients with multiple intraparotid masses should include lymphoma. Other lesions to be considered include Whartin's tumors and intraparotid metastases from SCC of the skin for unilateral involvement, and Whartin's tumors and melanoma for bilateral involvement.

8.4 Sinonasal Cavities

The incidence of nasal and paranasal lymphoma in the United States and Europe is low. However, lymphomas of the paranasal sinuses and nasal cavity are relatively prevalent in certain parts of Central and South America, East Asia, including Korea and seem to be associated with Epstein-Barr Virus infections (Chisin and Weber 1994; Koom et al. 2004).

Lymphomas arising in the sinonasal cavities are NHL and frequently are observed in patients who have disseminated lymphoma or AIDS. In the nasal cavity the extranodal Natural Killer (NK)/T-cell

lymphoma, nasal type (see also Sect. 4; entity 2.2.5,) is the most prevalent type which presents usually in Ann Arbor stage I (Table 2).

Sinonasal lymphoma most frequently occurs in the nasal cavity and maxillary sinus. Less often, lymphoma is found in the ethmoid sinuses, and only rarely it is found in the sphenoid and frontal sinuses. Patients with maxillary sinus lymphoma present with facial fullness, symptoms of sinusitis or odontogenic pain. Initial symptoms of nasal cavity lymphoma include nasal obstruction and/or epistaxis. Proptosis and epiphora, i.e. orbital and lacrimal gland extension indicate more widespread disease. Rarely, malignant lymphoma can present as a mass in the canine fossa. If isolated, this most likely represents lymphoma arising in the infraorbital lymph node group, i.e. nodal disease (Tart et al. 1993).

On CT and MRI imaging studies, lymphomas of the sinonasal cavities must be differentiated from the much more common entities of sinusitis, polyposis, as well as granulomatous processes such as Wegener's granulomatosis, and benign and malignant neoplasms (Yuen and Jacobs 1999).

The imaging appearance is non-specific. Lymphomas in the sinonasal cavities tend to be bulky soft tissue masses with moderate enhancement. The growth pattern may be expansile. However, in more advanced cases, aggressive bone erosion may be observed. Based on imaging alone, this more aggressive appearance of lymphoma cannot be differentiated from carcinoma (Fig. 15).

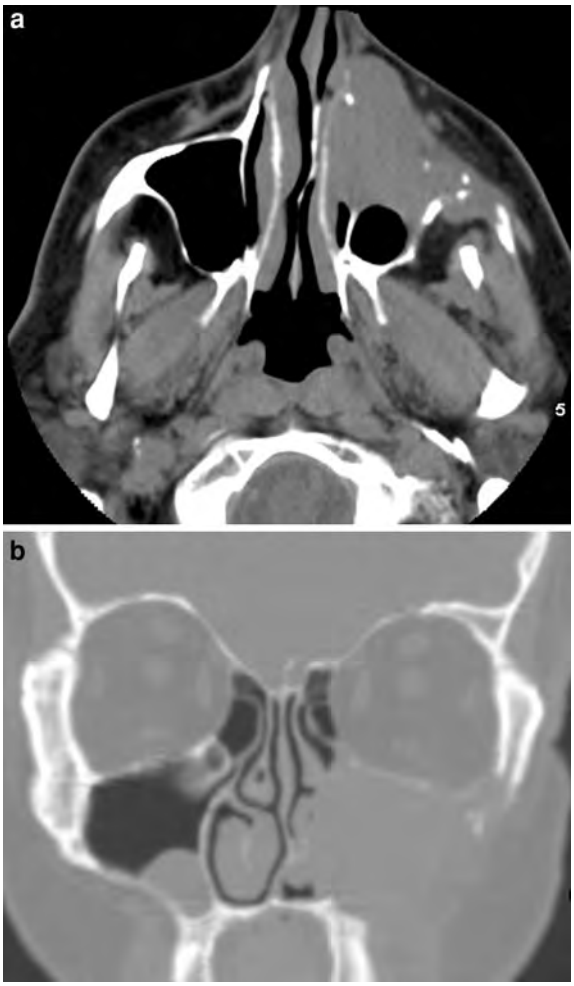

Fig. 15 Sinonasal NHL. Contrast-enhanced CT-images. **a** Axial image shows a soft-tissue mass with homogenous enhancement centered in the left maxillary sinus. Extensive bone destruction. The mass is extending into the nasal cavity and the soft tissues of the cheek. Subtle bony erosion of the postero-lateral sinus wall with beginning infiltration of the infratemporal fossa. **b** Coronal image (bone window setting) showing the extensive bony destruction. Note retention cyst in the right maxillary antrum

8.5 Thyroid

Lymphoma of the thyroid gland is an uncommon disease occurring primarily in older women. It may arise primarily from the thyroid or involve the gland as part of a systemic disease.

There is a strong association between thyroid lymphoma and Hashimoto's thyroiditis. Hashimoto's thyroiditis is an autoimmune disease characterized by circulating antithyroglobulin resulting in follicular atrophy, fibrosis, enlargement and firmness of the gland. Surveillance of these patients by yearly physical examination and US will facilitate discovery of lymphoma at an early stage. The diagnosis is established by (US-guided) biopsy (Fehr-Merhof 1999). The most common histologies are the diffuse large B-cell lymphomas (up to 70% of cases) and MALT lymphomas (in 6–27% of cases). Most patients have a short history of an enlarging thyroid or a neck mass causing tracheal compression or swallowing problems. Treatment for MALT lymphomas includes radiation therapy alone. In case of diffuse large B-cell lymphoma, patients will be treated by a combination of radiation with chemotherapy (Ansell et al. 1999; Michels et al. 2002; Widder and Pasieka 2004).

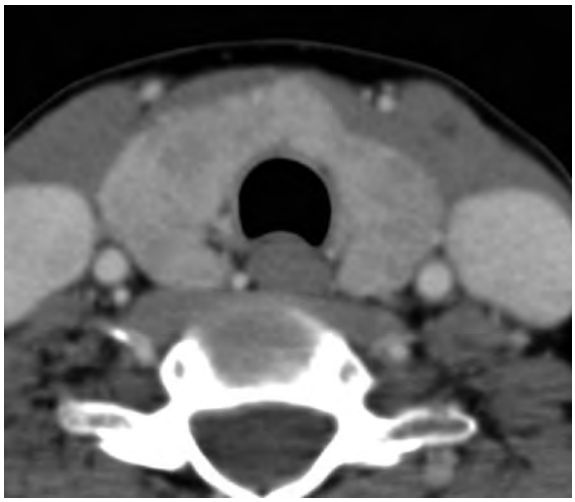

Fig. 16 Thyroid lymphoma. Axial contrast-enhanced CT-image shows diffuse enlargement of the thyroid gland by a relatively homogenous mass (Courtesy I.M. Schmalfuss, MD, Gainesville, Florida)

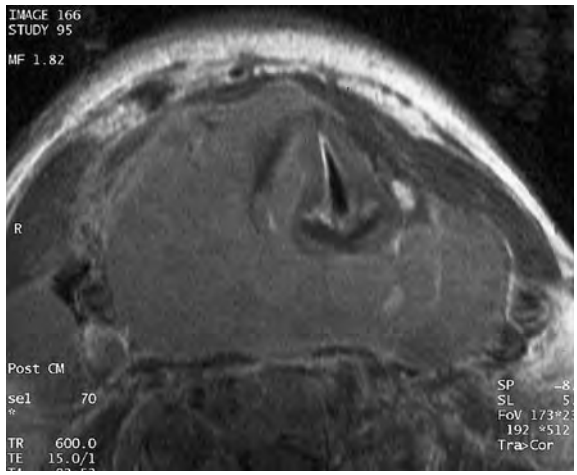

Fig. 17 Thyroid lymphoma. Axial contrast-enhanced MR-image shows diffuse enlargement of the thyroid gland with homogenous enhancement. Extensive retropharyngeal, as well as intralaryngeal extension. Note enlarged level III lymph node on the right with similar enhancement as the thyroid lymphoma (Courtesy R. Hermans, MD, PhD, Leuven, Belgium)

The imaging approach is based on prior clinical evaluation. Small lesions are ideally assessed with US, which is capable of discriminating between solid and cystic nodules. US-guided fine needle aspiration cytology/biopsy provides tissue for pathologic examination of thyroid nodules. On US, thyroid lymphoma may present as a focal mass or diffuse replacement of the thyroid gland. The mass is typically diffusely hypoechoic. CT and MRI are indicated for larger tumors, especially when extending outside the gland (Weber et al. 2000).

On CT, thyroid lymphoma may be seen as a focal mass, multiple thyroid nodules, or diffuse enlargement of the gland. On non-contrast CT the tumor demonstrates low attenuation. Following contrast administration, these tumors moderately enhance (Fig. 16). Associated cervical adenopathy may occur. Calcification and necrosis are unusual (Takashima et al. 1995). These two latter features are much more frequently seen in thyroid goiter.

The MRI-appearance of thyroid lymphoma is usually isointense on T1-weighted images with moderate homogeneous enhancement following contrast administration (Fig. 17). On T2-weighted sequences, the signal intensity is homogeneously bright (Takashima et al. 1995). Frequently occurring vascular invasion, associated lymphadenopathy and extension into the retropharyngeal area and mediastinum are depicted adequately both by CT and MRI (Fig. 17).

8.6 Bone

Bony disease in the setting of head and neck lymphoma is uncommon. Secondary infiltration and/or destruction (mimicking SCC) may occur (Fig. 15). However, there are some primary hematological bone disease entities in the head and neck.

8.6.1 Primary Lymphoma of Bone

The most common lymphoma affecting bone is the diffuse large B-cell lymphoma. Primary lymphoma of bone occurs most frequently in the mandible followed by the maxilla. In the mandible, most often there are ill-defined lytic destructive areas of variable size. These imaging features are non-specific and the differential diagnosis includes other primary neoplasm of bone, such as osteosarcoma and Ewing's sarcoma.

The jaw is a common site of presentation for the African type of Burkitt's lymphoma. This B-cell lymphoma occurs most frequently in children and young adults with 50% of cases arising in the maxilla or mandible (Fig. 18). This disease is found especially in Africa and other underdeveloped countries,

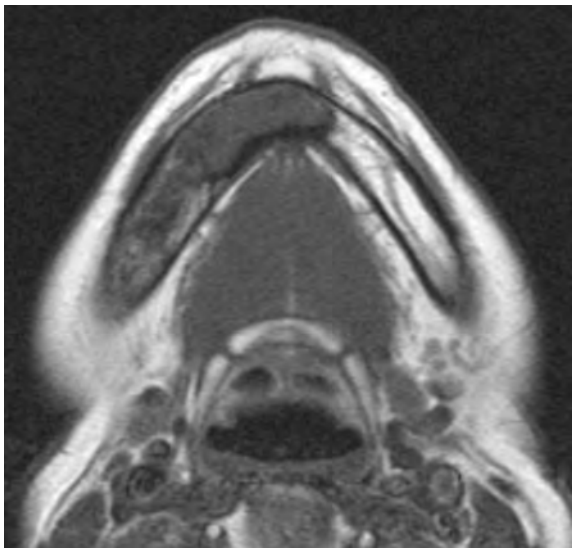

Fig. 18 Primary Burkitt's lymphoma of the mandible. Axial T1-weighted non-enhanced MR image shows replacement of the normal fatty marrow by a low signal intensity mass in the median and right part of the mandible, with expansion of the medullary cavity

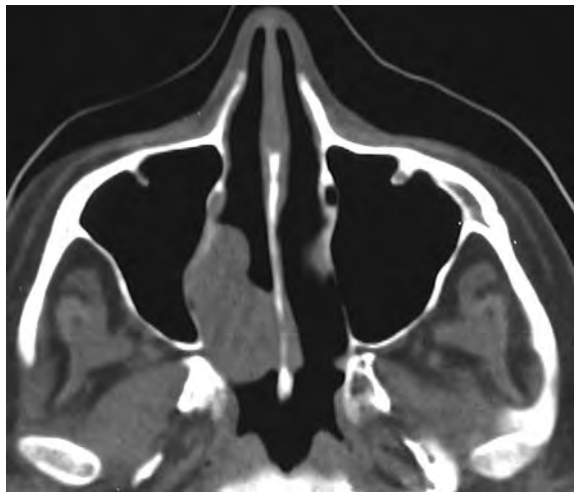

Fig. 19 Sinonasal plasmocytoma. Axial non-enhanced CT image (bone window setting) shows a smooth lobulated mass centered in the left nasal cavity. Note subtle remodelling of the medial wall of the left maxillary sinus

much less frequently in the United States and Europe. Association with Epstein–Barr Virus is postulated (Muwakkit et al. 2004; Rao et al. 2000; Weber et al. 2003).

8.6.2 Multiple Myeloma (Kahlers' Disease)

Multiple myeloma (MM) is characterized by a malignant proliferation of plasma cells with monoclonal immunoglobulin or immunoglobulin fragments in the patient's urine. This proliferation of neoplastic cells is associated with bone destruction and involves the bone marrow of the axial skeleton. Although single lesions occasionally occur (solitary plasmacytoma of bone), MM typically shows diffuse involvement of multiple bones. The typical radiographic appearance is that of 'punched-out' round to ovoid, regular radiolucencies in the skull and long bones with no circumferential bone sclerosis (Kesari and Bundock 2004). In the mandible, these lesions show a predilection for the angle, ramus and molar tooth regions. Solitary plasmacytomas of bone usually occur in the vertebra and skull.

8.6.3 Extramedullary Plasmocytoma

Extramedullary plasmocytoma (EMP) is a rare soft-tissue malignancy composed of plasma cells. Eighty percent of EMP's arise in the head and neck, most often occurring in the nasal cavity followed by the paranasal sinuses (Dimopoulos et al. 1999; Mendenhall et al. 2003). On CT, EMP's of the sinonasal cavities are smooth, homogeneous enhancing polypoid masses that remodel surrounding bone (Fig. 19). On MR imaging, they have intermediate signal intensity on all imaging sequences. EMP's markedly enhance because they are highly vascular. Spread to the regional lymph nodes is common in EMP; in solitary plasmocytomas of bone this is highly uncommon.

8.7 Skin

NHL in the head and neck may also be localized in the skin.

The cutaneous lymphomas can be distinguished in B- and T-cell types. Specific for the cutaneous T-cell lymphomas are the so-called mycosis fungoides and the Sezary syndromes, but they are more likely to be seen on the trunk and extremities than the head and neck (Foss 2004).

Crosti's syndrome should be mentioned. Originally called the reticulohistiocytoma of the dorsum by Crosti in 1951, this disease is nowadays considered a primary cutaneous B cell lymphoma of follicular center cell origin. This localized skin disease on the

back of the head and trunk has a very slowly progressive course, with many patients showing no systemic involvement even after prolonged follow-up (Berti et al. 1988).

When palpation is felt to be insufficient for local staging, CT or MRI can be used for mapping pretherapeutic disease extent and document response post-therapy.

9 Conclusion

Lymphoma should be approached as a systemic disease that can manifest itself in many forms in the head and neck. Frequently, the imaging findings are nonspecific and tissue sampling remains the mainstay of making the diagnosis. Sometimes, involvement of specific subsites or specific imaging patterns can strongly suggest the diagnosis of lymphoma. However, it should be kept in mind that lymphoma is a possible cause in any infiltrative soft tissue mass in the head and neck, irrespective of the location. In the work-up of a patient with a head and neck lesion, the radiologist may be the first one to suggest this diagnosis.

References

Abbondanzo SL (2001) Extranodal marginal-zone B-cell lymphoma of the salivary gland. Ann Diagn Pathol 5:246–254

Agulnik M, Tsang R, Baker MA et al (2001) Malignant lymphoma of mucosa-associated lymphoid tissue of the lacrimal gland: case report and review of literature. Am J Clin Oncol 24:67–70

Aloulou S, Farhat H, Bosq J et al (2002) Hodgkin's disease primarily involving the oropharynx: case report and review of the literature. Hematol J 3:164–167

Ansell SM, Grant CS, Habermann TM (1999) Primary thyroid lymphoma. Semin Oncol 26:316–323

Berti E, Alessi E, Caputo R et al (1988) Reticulohistiocytoma of the dorsum. J Am Acad Dermatol 19:259–272

Cartwright R, Brincker H, Carli PM et al (1999) The rise in incidence of lymphomas in Europe 1985–1992. Eur J Cancer 35:627–633

Cheson BD (2008) New response criteria for lymphomas in clinical trials. Ann Oncol 19:iv35–iv38

Cheson BD, Horning SJ, Coiffier B et al (1999) Report of an international workshop to standardize response criteria for non-Hodgkin's lymphomas. J Clin Oncol 17:1244–1253

Cheson BD, Pfistner B, Juweid ME et al (2007) Revised response criteria for malignant lymphoma. J Clin Oncol 25:579–586

Chisin R, Weber AL (1994) Imaging of lymphoma manifestations in the extracranial head and neck region. Leuk Lymphoma 12:177–189

Dimopoulos MA, Kiamouris C, Moulopoulos LA (1999) Solitary plasmacytoma of bone and extramedullary plasmacytoma. Hematol Oncol Clin North Am 13:1249–1257

Fehr-Merhof A, Flury R, Ruttimann S (1999) From Hashimoto thyroiditis to B-cell lymphoma of the thyroid gland. Schweiz Med Wochenschr 129:883–889

Foss F (2004) Mycosis fungoides and the Sezary syndrome. Curr Opin Oncol 16:421–428

Gritzmann N, Rettenbacher T, Hollerweger A et al (2003) Sonography of the salivary glands. Eur Radiol 13:964–975

Hanna E, Wanamaker J, Adelstein D et al (1997) Extranodal lymphomas of the head and neck. A 20-year experience. Arch Otolaryngol Head Neck Surg 123:1318–1323

Harnsberger RH (2004) Diagnostic imaging head and neck. 1st edn. Amirsys, Salt lake City, Utah

Harris NL, Jaffe ES, Stein H et al (1994) A revised European-American classification of lymphoid neoplasms: a proposal from the International Lymphoma Study Group. Blood 84:1361–1392

Harris NL, Jaffe ES, Diebold J et al (2000) World Health Organization classification of neoplastic diseases of the hematopoietic and lymphoid tissues: report of the Clinical Advisory Committee meeting-Airlie House, Virginia, November 1997. J Clin Oncol 17:3835–3849

Hermans R (2004) Extranodal lymphoma—neck. Cancer Imaging 4:1–5

Hermans R, Horvath M, De Schrijver T et al (1994) Extranodal non-Hodgkin lymphoma of the head and neck. J Belge Radiol 77:72–77

Jemal A, Siegel R, Ward E et al (2007) Cancer tatistics. CA Cancer J Clin 57:43–66

Jerusalem G, Beguin Y, Najjar F et al (2001) Positron emission tomography (PET) with 18F-fluorodeoxyglucose (18F-FDG) for the staging of low-grade non-Hodgkin's lymphoma (NHL). Ann Oncol 12:825–830

Kesari S, Bundock EA (2004) Punched-out skull. Arch Neurol 61:958–959

King AD, Lei KI, Richards PS et al (2003) Non-Hodgkin's lymphoma of the nasopharynx: CT and MR imaging. Clin Radiol 58:621–625

King AD, Yuen EH, Lei KI et al (2004) Non-Hodgkin lymphoma of the larynx: CT and MR imaging findings. Am J Neuroradiol 25:12–15

Kirshenbaum KJ, Nadimpalli SR, Friedman M et al (1991) Benign lymphoepithelial parotid tumors in AIDS patients: CT and MR findings in nine cases. Am J Neuroradiol 12:271–274

Koom WS, Chung EJ, Yang WI et al (2004) Angiocentric T-cell and NK/T-cell lymphomas: radiotherapeutic viewpoints. Int J Radiat Oncol Biol Phys 59:1127–1137

Kwee ThC, Takahara T, Ochiai R et al (2008) Diffusion-weighted whole-body imaging with background body signal suppression (DWIBS): features and potential applications in oncology. Eur Radiol 18:1937–1952

Kwee ThC, Quarles van Ufford HME, Beek FJ et al (2009) Whole-Body MRI, including Diffusion-Weighted Imaging, for the initial staging of malignant lymphoma. Invest Radiol 44:683–690

Lee JL, Kim MK, Lee KH et al (2005) Extranodal marginal zone B-cell lymphomas of mucosa-associated lymphoid tissue-type of the orbit and ocular adnexa. Ann Hematol 84:13–18

Lister TA, Crowther D, Sutcliffe SB et al (1989) Report of a committee convened to discuss the evaluation and staging of patients with Hodgkin's disease: Cotswolds meeting. J Clin Oncol 7:1630–1636

Mancuso AA (1998) Lymphoma: master of chicanery (editorial). Am J Neuroradiol 19:1808

Mendenhall WM, Mendenhall CM, Mendenhall NP (2003) Solitary plasmacytoma of bone and soft tissues. Am J Otolaryngol 24:395–399

Michels JJ, Delcambre C, Marnay J et al (2002) Primary thyroid lymphomas: clinicopathologic study of 30 cases and review of the literature. Ann Pathol 22:10–17

Moog F, Bangerter M, Diederichs CG et al (1997) Lymphoma: role of whole-body 2-deoxy-2-[F-18]fluoro-D-glucose (FDG) PET in nodal staging. Radiology 203:795–800

Muwakkit SA, Razzouk BI, Shabb NS et al (2004) Clinical presentation and treatment outcome of children with Burkitt lymphoma in Lebanon: a single institution's experience. J Pediatr Hematol Oncol 26:749–753

Palacios E, Larusso G, Rojas R et al (2004) Lymphoma of the parotid gland in Sjőgren's syndrome. Ear Nose Throat J 83:156

Pfeffer MR, Rabin T, Tsvang L et al (2004) Orbital lymphoma: is it necessary to treat the entire orbit? Int J Radiat Oncol Biol Phys 60:527–530

Rao CR, Gutierrez MI, Bhatia K et al (2000) Association of Burkitt's lymphoma with the Epstein-Barr virus in two developing countries. Leuk Lymphoma 39:329–337

Shields JA, Shields CL, Scartozzi R (2004) Survey of 1264 patients with orbital tumors and simulating lesions. Ophthalmology 111:997–1008

Smithers DW (1971) Summary of papers delivered at the Conference on Staging in Hodgkin's Disease (Ann Arbor). Cancer Res 31:869–870

Som P, Curtin H, Mancuso A (2000) Imaging-based classification for evaluation of neck metastatic adenopathy Am J Roentgenol 174:837–844

Takahara T, Imai Y, Yamashita T et al (2004) Diffusion weighted whole body imaging with background body signal suppression (DWIBS): technical improvement using free breathing, STIR and high resolution 3D display. Radiat Med 22:275–282

Takashima S, Nomura N, Noguchi Y et al (1995) Primary thyroid lymphoma: evaluation with US, CT and MRI. J Comput Assist Tomogr 19:282–288

Tart RP, Mukherji SK, Avino AJ et al (1993) Facial lymph nodes: normal and abnormal CT appearance. Radiology 188:695–700

Therasse P, Arbuck SG, Eisenhauer EA et al (2000) New guidelines to evaluate the response to treatment in solid tumors. European Organization for Research and Treatment of Cancer, National Cancer Institute of the United States, National Cancer Institute of Canada. J Natl Cancer Inst 92:205–216

Tonami H, Matoba M, Yokota H et al (2002) Mucosa-associated lymphoid tissue lymphoma in Sjőgren's syndrome: initial and follow-up imaging features. Am J Roentgenol 179:485–489

Tonami H, Matoba M, Kuginuki Y et al (2003) Clinical and imaging findings of lymphoma in patients with Sjőgren's syndrome. J Comput Assist Tomogr 27:517–524

UICC (2009) TNM classification of malignant tumours, 7th edn. Springer, Berlin Heidelberg

Vose JM, Chiu BC, Cheson BD et al (2002) Update on epidemiology and therapeutics for non-Hodgkin's lymphoma. Hematology 1:241–262

Weber AL, Randolph G, Aksoy FG (2000) The thyroid and parathyroid glands. CT and MR imaging and correlation with pathology and clinical findings. Radiol Clin North Am 38:1105–1129

Weber AL, Rahemtullah A, Ferry JA (2003) Hodgkin and non-Hodgkin lymphoma of the head and neck: clinical, pathologic, and imaging evaluation. Neuroimaging Clin N Am 13:371–392

Widder S, Pasieka JL (2004) Primary thyroid lymphomas. Curr Treat Options Oncol 5:307–313

World Health Organization Classification of Tumors (2001) Tumors of haematopoietic and lymphoid tissues. Jaffe ES, Harris HL, Stein H et al (eds). Oxford University Press, Oxford, pp 162–167

Yan J, Wu Z, Li Y (2004) The differentiation of idiopathic inflammatory pseudotumor from lymphoid tumors of orbit: analysis of 319 cases. Orbit 23:245–254

Yuen A, Jacobs C (1999) Lymphomas of the head and neck. Semin Oncol 26:338–345

Positron Emission Tomography in Head and Neck Cancer

Ilona M. Schmalfuss

Contents

Abstract

PET imaging complements CT and MRI in the staging process of head and neck malignancies. It has been shown to be helpful in detection of nodal metastasis, distant metastasis and unknown primary tumors leading to a change in TNM classification in up to 20% of patients. Tumor stage and CT tumor volumes have been well-established variables in the stratification process of patients into favorable and unfavorable treatment groups. PET imaging with its ability to capture biological activity and areas of hypoxia within tumors adds other important variables to consider, with high FDG activities and hypoxia representing unfavorable risk factors. Utilization of FDG activity- or hypoxia-tumor maps facilitates more individualized treatment planning, with the possibility to deliver higher radiation doses to unfavorable tumor areas. Posttreatment PET imaging can help to decide whether lymph node dissection is needed and facilitates the detection of persistent or recurrent tumors, in particular when significant alterations of the soft tissues planes are present. The strengths, weaknesses and limitations of PET imaging prior, during and after treatment will be discussed in this chapter.

1 Introduction

The prognosis of patients with head and neck cancer is closely related to tumor stage with advanced tumors carrying the most unfavorable prognosis. CT and/or MRI are well-established tools in staging of head and

I. M. Schmalfuss (✉)
Department of Radiology,
Malcolm Randall VA Medical Center,
University of Florida College of Medicine,
1601 SW Archer Road, Gainesville, FL 32608, USA
e-mail: ilonaschmalfuss@yahoo.com

R. Hermans (ed.), *Head and Neck Cancer Imaging*, Medical Radiology. Diagnostic Imaging,
DOI: 10.1007/174_2011_384,

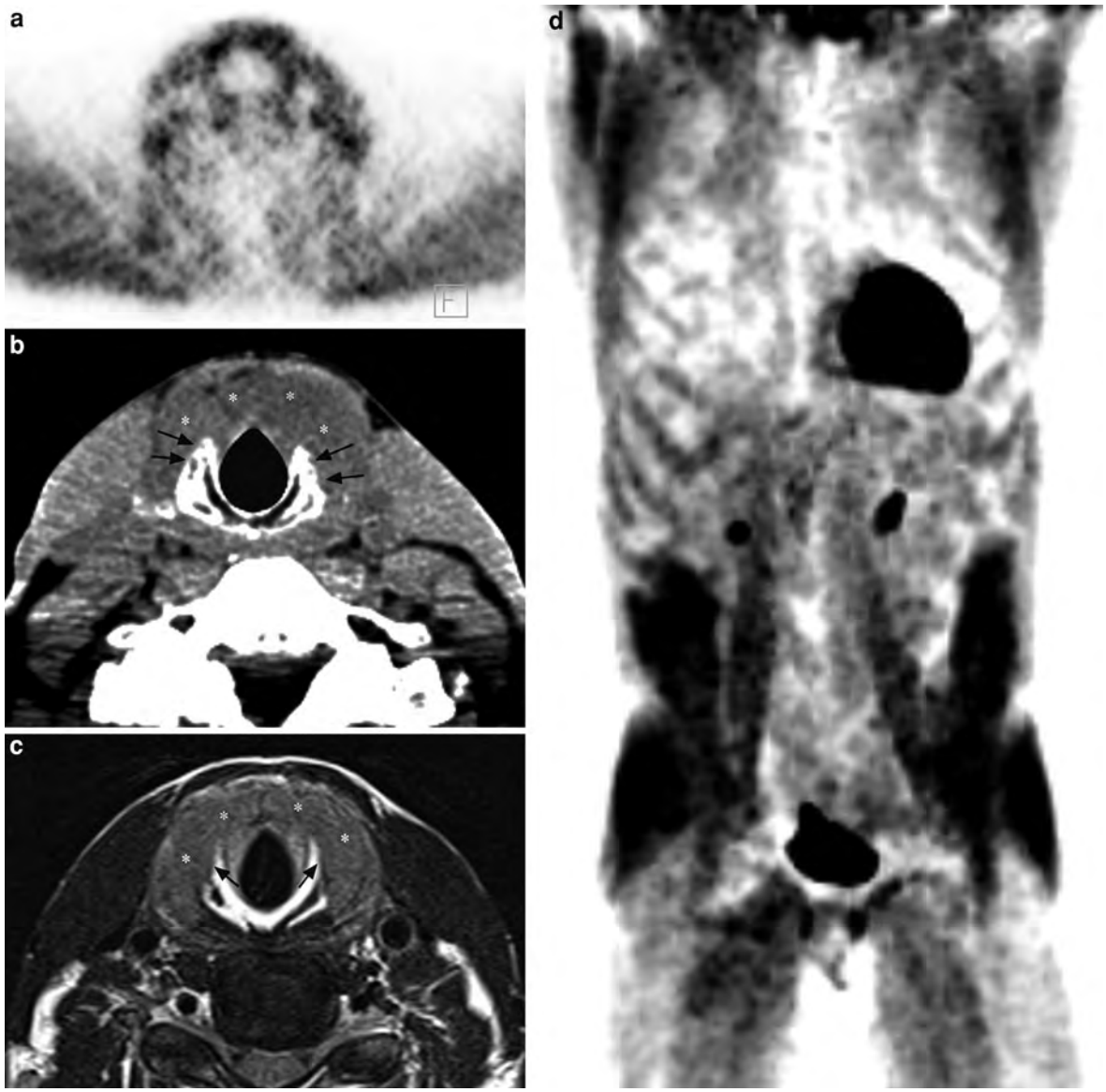

Fig. 1 Axial FDG-PET image (**a**) through the cricoid level demonstrates heterogeneous FDG uptake throughout the neck muscles without definitive focal uptake. Axial, non-contrast enhanced CT image at the same level (**b**) reveals gross infiltration of the strap muscles bilaterally (*) and signs of cricoid cartilage erosions bilaterally (*arrows* in **b**) which is also appreciated on the axial T2 weighted image (**c**) Biopsy confirmed undifferentiated squamous cell carcinoma. The false negative PET CT results are caused by diversion of FDG into muscles as better seen on the whole body image (**d**) that can be caused by elevated blood glucose, recent exercise or eating prior to scanning

neck malignancies, routinely used in clinical practice. These, however, have been shown to be deficient in detection of early nodal metastasis, distant metastasis and unknown primary tumors (Roh et al. 2007; Brouwer et al. 2006). Positron emission tomography's (PET) ability to measure the metabolic activity of tumors complements the anatomical information provided by CT and/or MRI studies. PET not only has been reported to yield higher detection rates of primary tumors and metastatic disease than CT and or MRI, but more importantly has led to a change in the TNM staging in 20% of patients, and treatment plan in about 14–57% of patients (Lonneux et al. 2010; Ha et al. 2006; Dietl et al. 2008). Consequently, PET is

gaining increasing clinical importance and utilization in the work-up of patients with head and neck cancer, in particular when used as integrated PET/CT scanner.

The technical aspects of PET and PET/CT are reviewed in "Imaging Techniques".

2 Clinical Applications

FDG-PET imaging is more complex and requires more careful patient preparation than CT and/or MRI, as FDG uptake is greatly influenced by different metabolic processes within the body. Blood glucose level >145 mg/dl (>8.0 mmol/l), fasting time <4 h and significant muscular activity within 24 h before FDG tracer administration divert FDG to muscles resulting in significantly reduced FDG uptake by the cancer (Fig. 1) and consequently carrying the risk of a false negative study (Vriens et al. 2010). This is in particular true for small tumors and metastatic deposits. For the injection of FDG tracer the site of intravenous line needs to be considered as well. Any extravasated radiotracer will be taken up by the lymphatic system yielding axillary lymph node FDG uptake in case of antecubital injection. Therefore, the opposite site for the injection should be selected in patients with suspected axillary lymph node involvement by tumor.

The degree of FDG tumor uptake is also impacted by the uptake time (Vriens et al. 2010). Too short or too long times between the tracer injection and the PET scan can lead to falsely negative results. When the time is too short (<60 min), there is insufficient clearance of the FDG tracer from the blood pool causing increased background activity that can mask tumor uptake. When the time is too long (>90 min), approximately half of the tracer activity will have decayed as the half-life of F^{18} is 110 min. This will lead to decreasing overall activity and increasingly "grainy" appearing images. Therefore, beginning of scanning 55–65 min after FDG injection is considered the most optimal imaging time resulting in completion of a whole body scan by 90–110 min after tracer injection.

To avoid muscular or brown fat uptake, the patient should be injected in a comfortably warm room and instructed to relax and avoid talking and moving during the entire uptake time. Unfortunately, the majority of patients with head and neck cancer suffer from smoking-induced emphysema and tend to be heavy breathers, facilitating muscular uptake in the laryngeal and respiratory musculature which might be asymmetric in nature. In addition, coughing or swallowing during the uptake phase often results in tracer accumulation in the cricopharyngeus muscle. These issues may prevent accurate staging of laryngeal and hypopharyngeal tumors or lead to misinterpretion of such uptake as a second or unknown primary tumor (Fig. 2). The situation becomes even more confusing when unilateral vocal cord paralysis is present and the uptake in the mobile vocal cord is mistaken for an underlying laryngeal tumor (Fig. 3). Therefore, pharmacological interventions might have to be applied in some patients as mentioned in "Imaging Techniques".

In the interpretation of FDG-PET scans maximum standardized uptake values (SUV_{max}) are utilized to distinguish between benign and malignant processes. In general, an SUV_{max} cut-off value of about three is applied, with values below three considered to be more likely benign and over three more likely malignant in nature. There is, however, a significant overlap between these two groups. Therefore, the SUV_{max} needs to be viewed just as an aid in the FDG-PET scan interpretation and should never be considered in isolation but rather in conjunction with other cross-sectional studies (CT and/or MRI) and the results of clinical examination.

2.1 Pretreatment

Squamous cell carcinoma is the most common tumor type involving the head and neck region and will be the main focus of this chapter. Accurate delineation of the malignant tumor is critical for tumor staging but is becoming even more important for treatment planning purposes as many new treatment developments focus upon preservation of the functionality of different head and neck structures. This approach in general results in as minimal as possible surgical intervention and as localized as possible high-dose radiation therapy delivery.

2.1.1 Primary Tumor Staging

FDG-PET has been reported to be slightly superior to the clinical examination and CT in staging of a

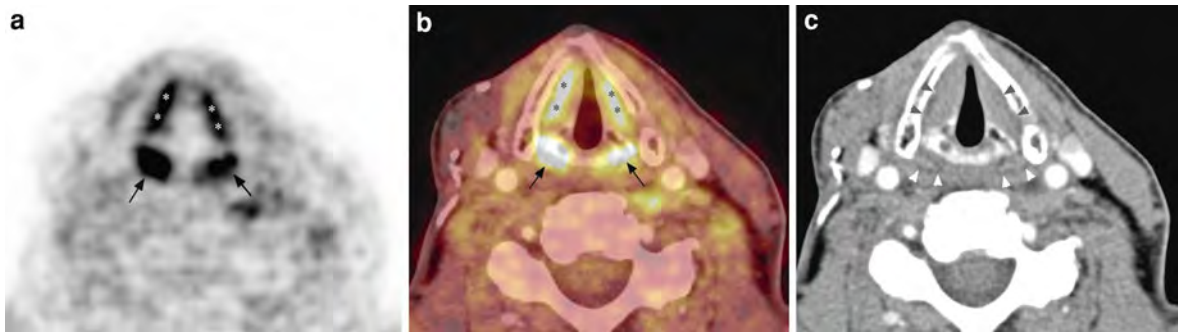

Fig. 2 Axial FDG-PET image (**a**) through the mid neck shows marked linear (* in **a**) and ovoid (*arrows* in **a**) FDG uptake bilaterally that localizes to the true vocal cords (* in **b**) and hypopharyngeal muscles (*arrows* in **b**) on the fused PET/CT image (**b**) Such uptake can be physiological in nature and related to speaking, swallowing and/or heavy breathing during the FDG uptake phase. Since it may mask an underlying tumor, correlation to clinical examination and careful evaluation of the paraglottic (*black arrowheads* in **c** and submucosal hypopharyngeal fat planes (*white arrowheads* in **c**) is required as seen on the axial contrast enhanced CT (**c**)

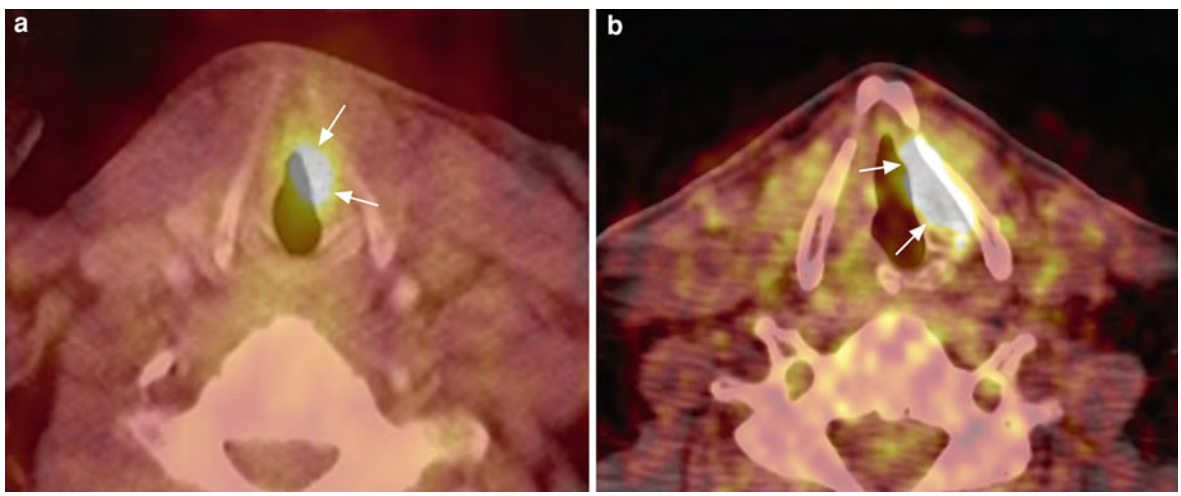

Fig. 3 Fused, axial PET/CT images (**a** and **b**) of two different patients reveal similar marked FDG uptake (*arrows* in **a** and **b**) within the left true vocal cord. The uptake in the first patient (**a**) was related to glottic squamous cell carcinoma while the uptake in the second patient (**b**) was physiological in nature. The asymmetry in FDG uptake in the second patient is caused by right vocal cord paralysis as noted on the clinical examination

primary tumor, with a similar sensitivity but higher specificity (Sigg et al. 2003). The sensitivity of FDG-PET is hampered by its lower resolution than CT and MRI as well as variable uptake in muscles, inflammation and lymphoid tissues.

The resolution of FDG-PET is around 5 mm, depending upon the used protocol, making detection of lesions <5 mm unreliable. In addition, partial volume averaging effects of lesions <1 cm in size might underestimate the FDG uptake and falsely classify it as benign. These issues are especially important for detection of small or superficial lesions as well as of perineural tumor spread (Daisne et al. 2004). Superficial lesions are easily detectable on clinical examination, however, perineural tumor spread is often clinically silent. Therefore, imaging might be the only tool to detect such type of tumor growth that typically carries poorer prognosis and significantly alters the treatment plan. MRI has been well established for detection of perineural tumor spread with reported sensitivity of 100% and specificity of 89%, but not all patients are able to undergo

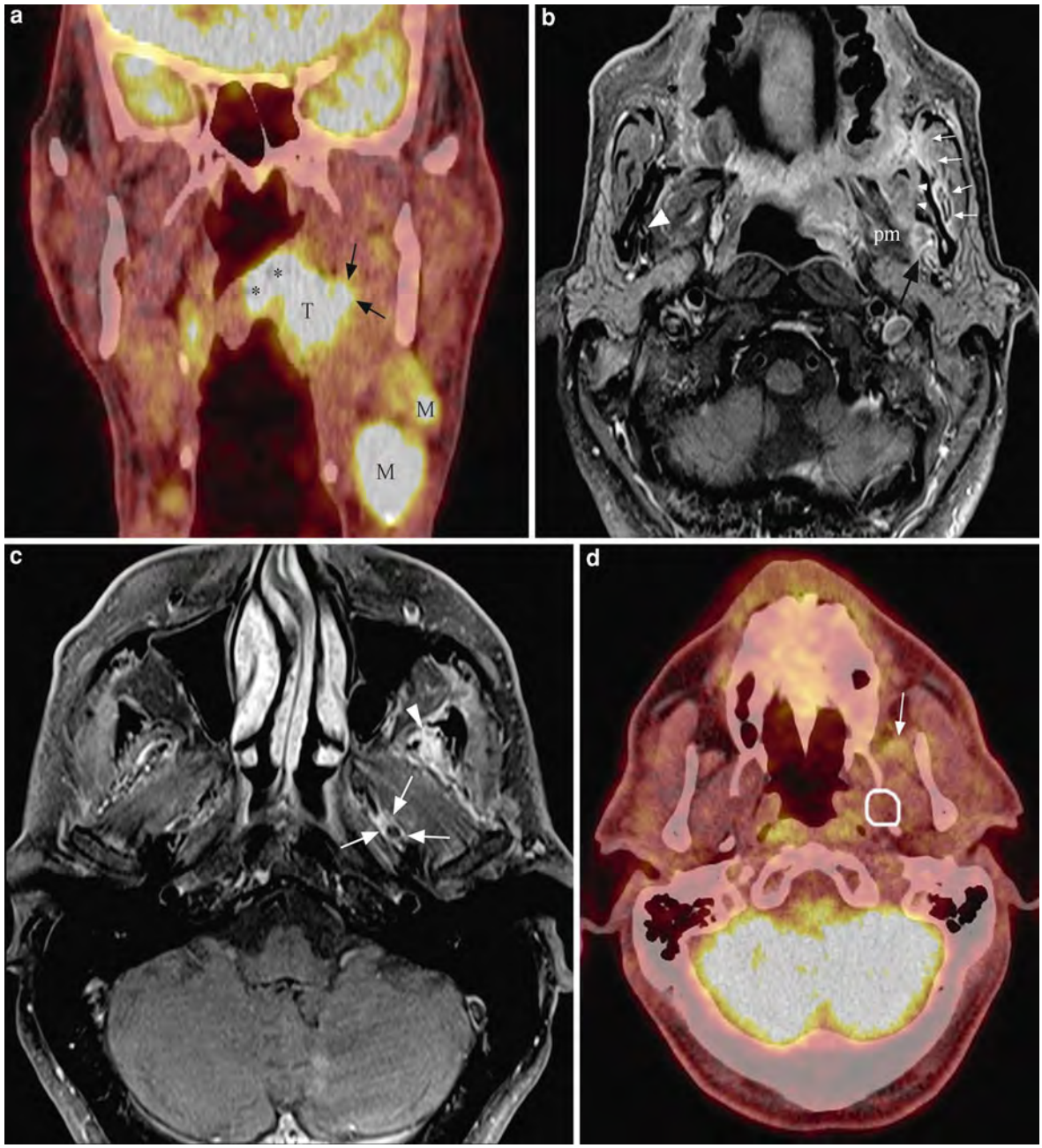

Fig. 4 Fused PET/CT image (**a**) of a patient with known large tonsillar squamous cell carcinoma (*T* in **a**) and trismus reveals gross tumor extension into the soft palate (* in **a**) and more subtle infiltration of the medial pterygoid muscle (*arrows* in **a**) as well as metastatic lymph nodes in group IB (*M* in **a**). The contrast enhanced, fat-suppressed T1 weighted images (**b** and **c**) not only confirm the infiltration of the medial pterygoid muscle (*pm* in **b**) but also show involvement of the left masseter muscle (*white arrows* in **b**) and left mandibular ramus (*small white arrowheads* in **b**). In addition, gross tumor is seen at the mandibular foramen on the left (*black arrow* in **b**) when compared to its normal appearance on the right (*large white arrowhead* in **b**) consistent with perineural tumor spread that extended superiorly to V3 just below the skull base (*arrows* in **c**). Despite the few millimeter thick rind of tumor around V3 no significant FDG uptake (*o* in **d**) was seen on the fused PET/CT image (**d**) at the same level. The false negative results are likely related to the poor spatial resolution of PET when compared to MRI. The subtle FDG uptake (*arrow* in **d**) on MRI markedly enhancing superficial temporalis muscle (*arrowhead* in **c**) is more consistent with denervation rather than tumor infiltration as the size of enhancing abnormality is larger than the resolution limitations of PET

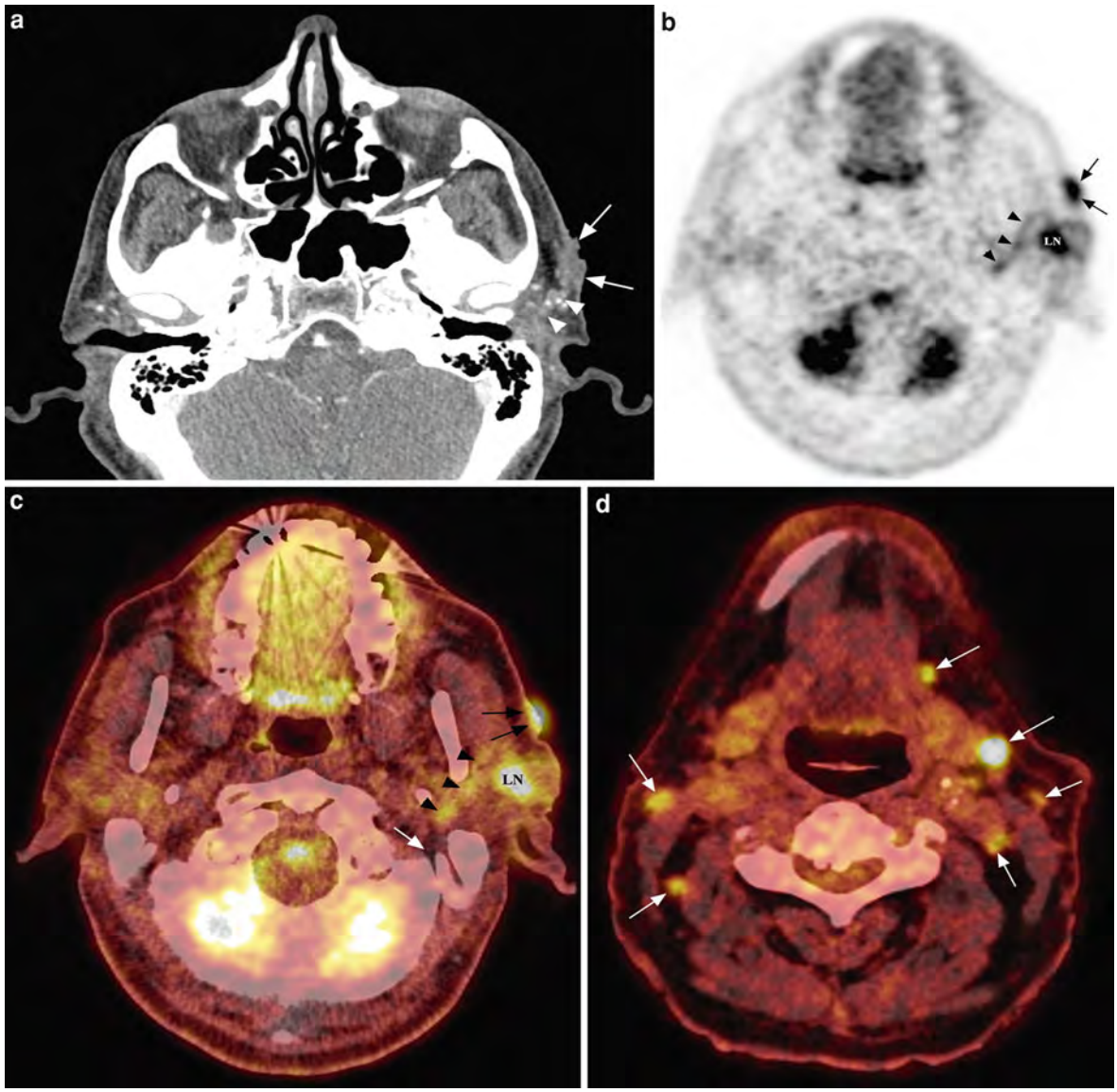

Fig. 5 Axial contrast enhanced CT (**a**) of a 67-year-old male shows a slightly ulcerated skin lesion (*arrows* in **a**) with gross infiltration of the subcutaneous tissues that was biopsy proven to represent squamous cell carcinoma of the skin. Close observation also reveals a linear to partially nodular band extending from the lesion posterior medially (*arrowheads* in **a**) concerning for perineural tumor spread. The PET image (**b**) at a slightly lower level confirms the perineural tumor spread as the linear band of FDG uptake (*arrowheads* in **b** and **c**) follows the course of the facial nerve main trunk towards the stylomastoid foramen (*white arrow* in **c**) as better seen on the fused PET/CT image (**c**). FDG uptake is also noticed within the skin lesion (*black arrows* in **b** and **c**) as well as in a metastatic pretrageal lymph node (*LN* in **b** and **c**) on the *left*. Clinically unexpected additional metastatic disease (*arrows* in **d**) was discovered more inferiorly within the neck bilaterally as seen on the fused PET/CT image (**d**)

an MRI examination (Hanna et al. 2007). So far, CT has been utilized instead. With its reported sensitivity and specificity near 90%, there is potential for improvement when combined with FDG-PET, based on a few published case reports (Bhatnagar et al. 2005; Ngugen and Roarke 2008; Conrad et al. 2004). Nevertheless, the ability to detect perineural tumor spread with FDG-PET/CT is mixed, based on clinical

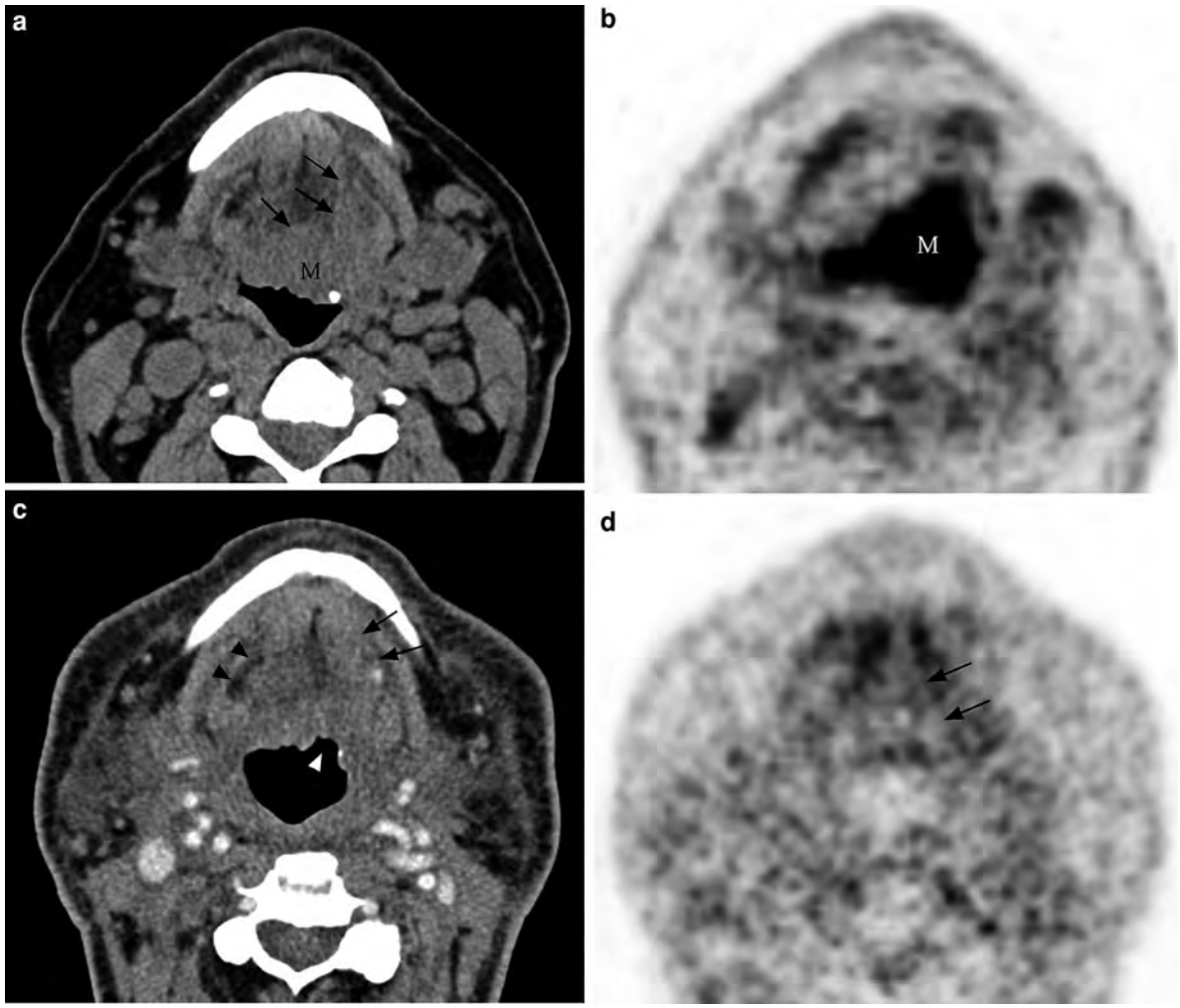

Fig. 6 Non-contrast enhanced CT image (**a**) in a patient with dysphagia shows a large mass involving the tongue base bilaterally (*M* in **a**) with signs of deep infiltration in midline and on the *left side* (*arrows* in **a**) with profound FDG uptake (M in **b**) on the PET image (**b**) that also involves the entire right tongue base. The contrast-enhanced CT image (**c**) performed 3 months after completion of radiation therapy demonstrates a focal ulceration (*white arrowhead* in **c**) on the *left* with associated obscuration of the fat planes medial to the hyoglossus muscle on the *left* (*arrows* in **c**) when compared to their normal appearance on the *right* (*black arrowheads* in **c**) that is concerning for persistent tumor. FDG-PET image (**d**) reveals lack of FDG uptake in the area of concern (*arrows* in **d**) consistent with control at the primary site

experience with no large series of patients published so far (Figs. 4 and 5). In addition, intracranial extension of perineural tumor spread might be missed as it may be indistinguishable from the physiological intense brain uptake, if not specifically searched for.

The variable FDG uptake in muscles, as well as the usual marked uptake in the lymphoid tissues, also hinders the T-staging as the primary tumor may truly infiltrate such tissues or may mimic such involvement by blending of the tumor with the physiological FDG uptake (Fig. 6). In general, asymmetric lymphoid tissue uptake is strongly concerning for tumor involvement, even though asymmetric FDG accumulation might be physiological in nature. When evaluating muscular involvement one should focus more on the FDG uptake distribution within the muscle rather than upon symmetry, with focal FDG uptake being more likely to be caused by tumor involvement than diffuse uptake (Fig. 7). Search for obliteration of intramuscular striations and

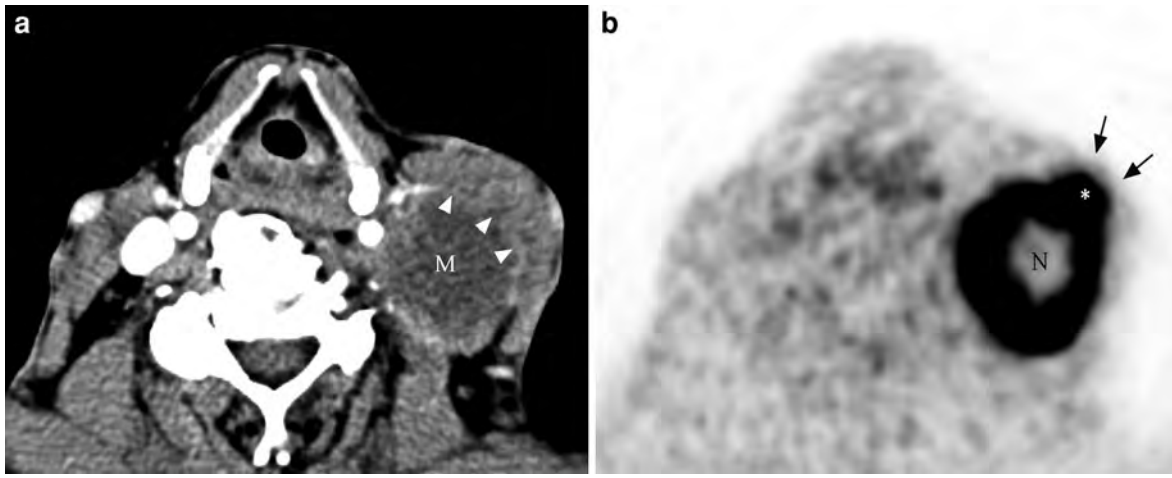

Fig. 7 Contrast enhanced CT (**a**) of a patient with an unknown primary tumor shows a large group III nodal metastasis (*M* in **a**) with lateral displacement of the sternocleidomastoid muscle (*arrowheads* in **a**). The FDG-PET (**b**) at the same level shows lack of FDG uptake (*N* in **b**) in the central, necrotic portion of the lymph node and focal out pouching of the profound, peripheral FDG uptake (* in **b**) with SUV_{max} of 19.6 that extends almost to the skin surface (*arrows* in **b**). Such extensive invasion of the sternocleidomastoid muscle was not suspected on the CT examination

Fig. 8 Coronal fused PET/CT image (**a**) shows intense FDG uptake in the majority of the tongue (*T* in **a**) with extension into the superior alveolar ridge (*arrow* in **a**) on the right. The uptake in the tongue was related to a poorly differentiated squamous cell carcinoma while the FDG uptake within the superior alveolar ridge was caused by marked periodontal disease (*arrow* in **a** and **b**) with adjacent osteitis (*arrowhead* in **b**) as better seen on the coronal CT image displayed in bone window (**b**). The lack of bony invasion significantly alters the treatment plan. The focal FDG uptake along the hard palate (*arrowheads* in **a**) is within minor salivary glands and physiological in nature. As in this patient, it can be very asymmetric in appearance. This patient not only had metastatic disease to group IB lymph nodes (* in **a**) but also multiple hilar (*arrowheads* in **c**) and pulmonary metastases as seen on the coronal FDG-PET image of the chest (**c**). The doughnut-shaped uptake (*arrow* in **c**) corresponds to the expected cardiac uptake

surrounding fat planes on the CT component of the PET/CT study might solidify such a suspicion.

Underlying infectious and inflammatory processes might also compromise the interpretation of the FDG-PET scans. When inflammation is present adjacent to the primary tumor it might mimic more extensive involvement and significantly alter the treatment plan. Most commonly teeth-related infections are observed in the head and neck area. When in close proximity to a primary tumor, e.g. floor of the mouth or hard palate cancer, the tooth-related FDG uptake might be mistaken for tumor involvement and lead to unnecessary

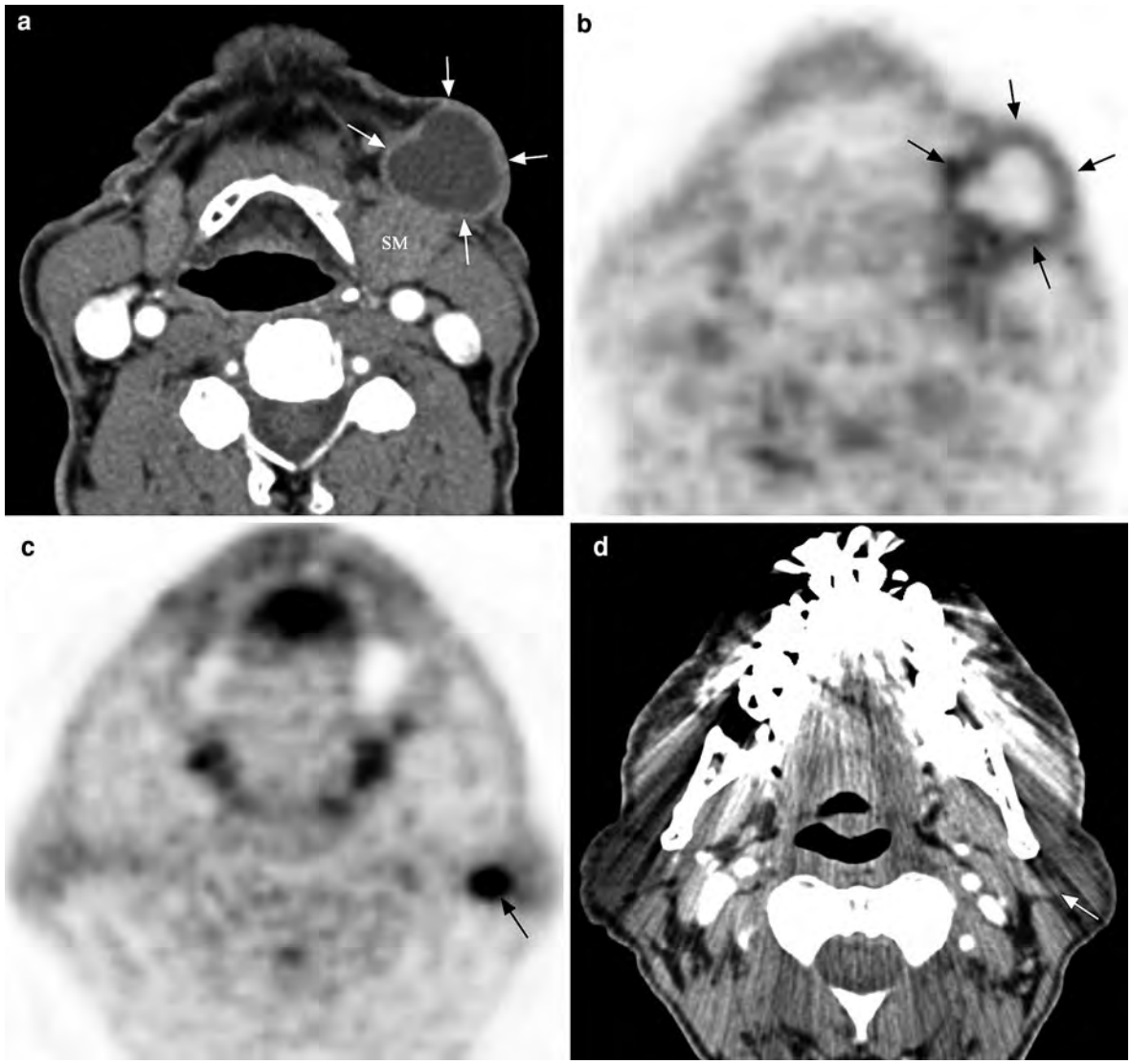

Fig. 9 Axial, contrast enhanced CT (**a**) in a patient presenting with a rapidly growing mass in the left submandibular region shows a large cystic lesion (*arrows* in **a**) anterior to the left submandibular gland (*SM* in **a**) that demonstrates only mild and thin peripheral FDG uptake (*arrows* in **b**) on the PET image (**b**). The FDG uptake is false negative for malignancy due to the very large central necrosis. The clinical examination was otherwise negative while the PET image at a higher level (**c**) reveals an additional, intensely FDG avid lesion (*arrow* in **c** in **d**) within the tail of the left parotid gland that is barely visible on the contrast-enhanced CT image (**d**) because of profound beam hardening artifacts from dental fillings. This is an important finding as it shifts the search for an unknown primary tumor from the visceral compartment to the skin. Since some benign tumors of the parotid gland can show marked FDG uptake a biopsy was performed revealing Warthin's tumor in left parotid gland and squamous cell carcinoma in the left group IB lymph node

removal of the mandible or maxilla (Fig. 8). When located away from the primary tumor, it might be mistaken for a second primary tumor or a metastatic deposit. Careful assessment of other imaging studies, correlation to clinical examination and/or dental films usually solve such a problem.

2.1.2 Nodal Staging

The nodal stage is the most important prognostic factor for survival of patients with head and neck cancer, with reported reduction of long-term survival by 50% with unilateral and 75% with bilateral nodal metastasis (Subramaniam et al. 2010; Chu et al. 2010).

CT and MRI have shown wide range in sensitivity (36–94%) and specificity (50–98%) for detection of nodal metastasis. Only limited number of studies directly compared FDG-PET with conventional imaging, reporting superior performance of FDG-PET with an accuracy of 89% when compared to CT/MRI with 79% (Roh et al. 2007). Even more interesting are the results from a study by Lonneux et al. (2010) that focused upon detailed evaluation of discordant results between CT/MRI and FDG-PET. A discordant TNM stage was found between conventional work-up and whole body FDG-PET in 43% of patients; in 16% of patients the nodal stage was correctly upgraded and in 7% correctly downgraded. In 12% the neck was incorrectly staged by PET-CT. In this study, the change in nodal staging by PET led to an altered treatment planning in 5.2% of patients.

False results with PET are typically attributed to the inability to differentiate reactive from metastatic lymph nodes, decreased FDG uptake in necrotid lymph nodes (Fig. 9a and b), confluence of the primary tumor with the nodal metastatic disease making distinction between the two impossible, and misinterpretation of benign parotid gland tumors such as Warthin's (Fig. 9c and d) or pleomorphic adenomas for metastatic lymph nodes (Subramaniam et al. 2010).

All available imaging modalities struggle with the detection of metastatic foci within subcentimeter lymph nodes leading to modifications of the diagnostic criteria for each imaging modality over time. For FDG-PET imaging, size-based SUV_{max} cut-off values have been shown to be beneficial with lymph nodes considered positive when $SUV_{max} \geq 1.9$ and lymph node <10 mm in diameter, $SUV_{max} \geq 2.5$ and lymph node 10–15 mm in diameter and SUV_{max} of ≥ 3 and lymph node of >15 mm in size (Murakami et al. 2006). Such an approach yielded a sensitivity of 79% and almost perfect specificity of 99% (Fig. 10). However, these criteria are not widely used although they may be of interest in patients with clinically negative necks (Fig. 5d). Currently, mixed results in regard to performance of the FDG-PET in N0 staged patients have been published. Some groups report no benefit while others show a twofold higher detection rate for occult metastasis in patients with oral cavity squamous cell carcinomas (Ng et al. 2006; Brouwer et al. 2004; Krabbe et al. 2008). None of these groups applied the aforementioned modified SUV_{max} criteria.

Extracapsular tumor spread is also an important predictor of patient's prognosis, with reported recurrence rates tenfold higher and 50% reduction of survival when present (Puri et al. 2003). FDG-PET in isolation is unable to directly detect extracapsular tumor spread, however, in combination with CT, in particular with contrast enhanced CT, it may yield the same sensitivity and specificity as CT alone. In addition, a recent study reported significantly higher SUV_{max} of lymph nodes with extracapsular tumor spread (Fig. 7) than without, with mean SUV_{max} of 11.9 and 5, respectively (Kubicek et al. 2010).

2.1.3 Detection of Distant Metastasis and Second Primary Tumors

Presence of distant metastasis alters the treatment strategy from curative to palliative intent in the majority of patients. Distant metastases are associated with markedly reduced survival rates, with an average survival time of about 8 months (Dietl et al. 2007). The incidence at the time of initial diagnosis is low with reported rates of up to 4%, with higher incidence rates (up to 26%) observed within 2 years after completion of initial treatment (Fig. 8c). The majority of metastatic disease occurs to the lung (54–56%) and pleura (40%). Therefore, screening for distant metastasis with chest X-rays or chest-CT has been widely utilized. Other less common sites of involvement include liver (4–7%), skin (6%) and bone (10–12%) which are insufficiently screened with this approach (Dietl et al. 2007; Garavello et al. 2006).

FDG-PET, as a whole body imaging technique, has been shown to have higher detection rates of metastatic deposits with reported rates ranging between 10 and 25% (Subramaniam et al. 2010) at a sensitivity reaching 100%, but lower specificity and accuracy of 80% (Wax et al. 2002). CT alone shows reverse results, with lower sensitivity of 87% but higher specificity and accuracy of 100 and 90%, respectively. Therefore, the combined FDG-PET/CT should be able to yield the most optimal sensitivity, specificity and accuracy and should be considered to be added in the work-up of head and neck cancer patients, in particular when unfavorable risk factors are present. The known unfavorable risk factors for development of distant metastasis range from patient's age over T and/or N stages to tumor site and grade (Garavello et al. 2006) with the highest risk

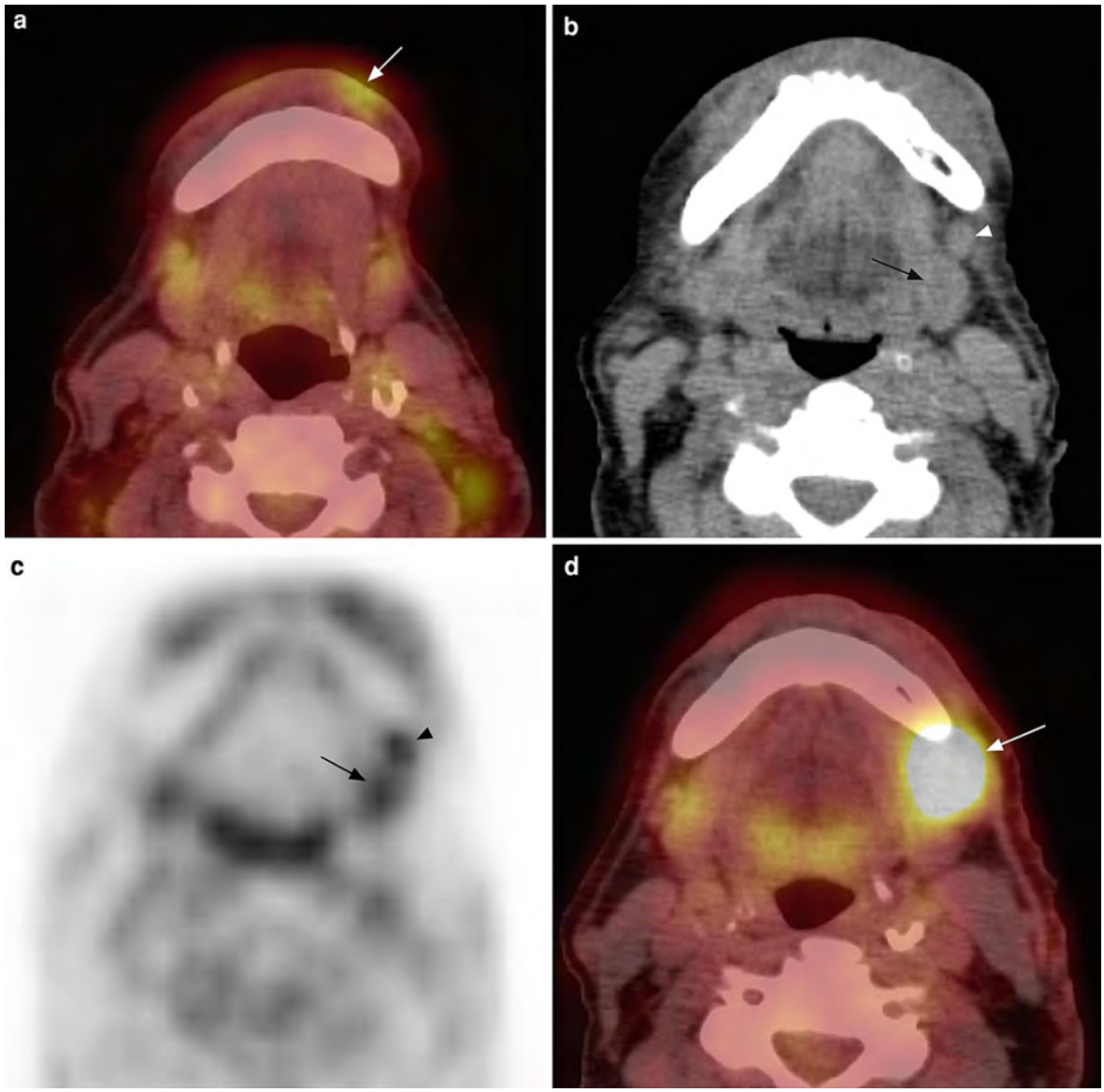

Fig. 10 A 65-year-old patient revealing marked FDG uptake (*white arrow* in **a**) on the fused PET/CT image (**a**) in a left lower lip squamous cell carcinoma. The non-contrast enhanced CT image (**b**) demonstrates a small group IB lymph node on the left (*arrowhead* in **b**) located just anterior to the submandibular gland (*black arrow* in **b**) that shows similar FDG uptake (*arrowhead* in **c**) on the PET image (**c**) as the submandibular gland itself (*black arrow* in **c**) with an SUV_{max} value of 2.0. This lymph node was considered reactive in nature based on the traditional SUV_{max} criteria, however, it should have been interpreted as "strongly suspicious for metastatic disease" based on the modified criteria by Murakami et al. (2006) The metastatic involvement (*arrow* in **d**) of this lymph node demarcated itself on fused PET/CT follow-up image (**d**) and was successfully treated without recurrent disease on follow-up

seen in patients under 45 years of age with high T and N stages presenting with undifferentiated, hypopharyngeal cancer. A recent publication also suggests that SUV_{max} values for nodal metastases over 10 may represent a risk factor for distant metastases but not for local failure (Kubicek et al. 2010).

Patients with head and neck cancer also have increased risk of development of second primary

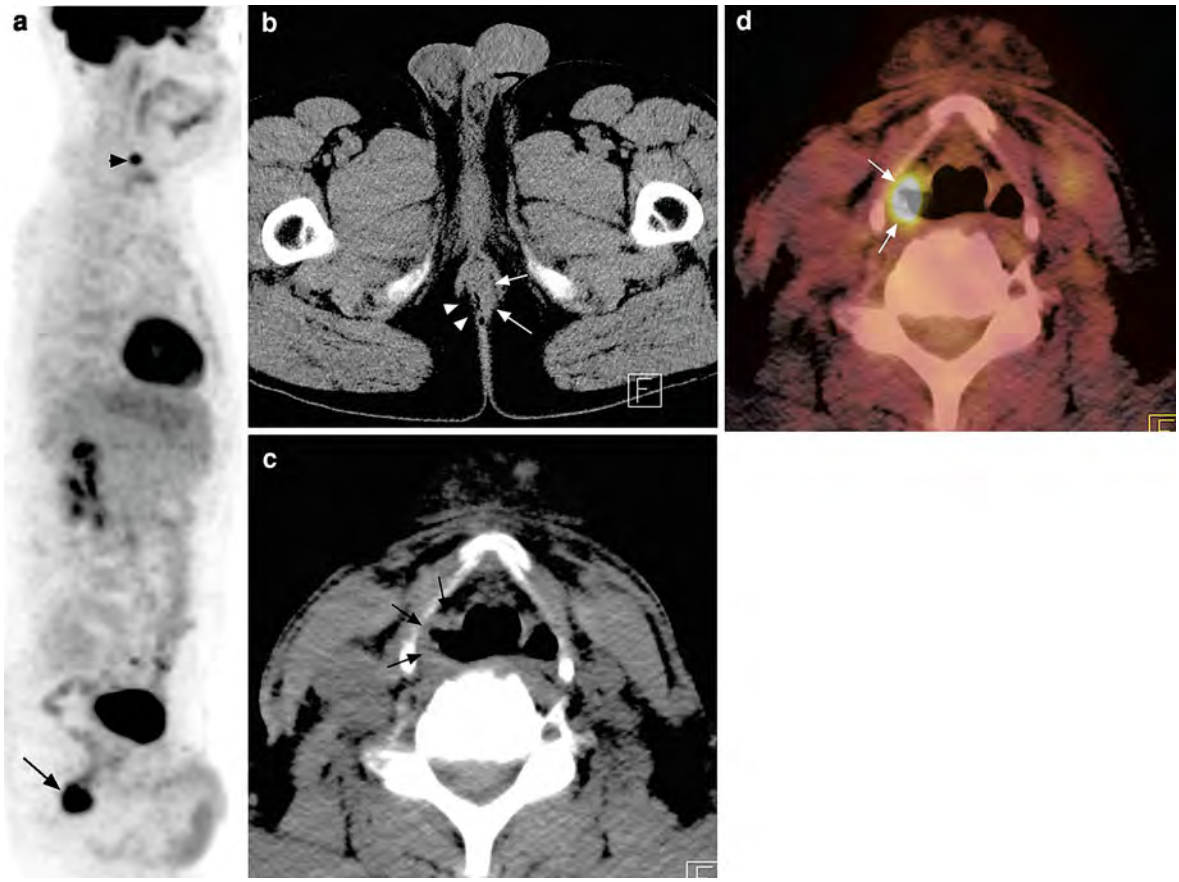

Fig. 11 Whole body PET image displayed in sagittal plane (**a**) shows two areas of marked FDG uptake: very small in the mid neck (*arrowhead* in **a**) and a larger one at the rectoanal junction (*arrow* in **a**). The axial CT image (**b**) through the rectoanal junction confirms an infiltrating lesion on the left (*arrows* in **b**) with marked infiltration of the perianal fat planes when compared to their normal appearance on the right (*arrowheads* in **b**) while the CT image (**c**) through the mid neck reveals subtle thickening of the lateral and anterior piriform sinus walls (*arrows* in **c**). The marked FDG uptake (*arrows* in **d**) on the fused PET/CT image allows a more confident diagnosis of a second primary tumor in the right piriform sinus than the CT alone

tumors with the majority occurring in the lung or upper aerodigestive tract including the head and neck area (Fig. 11). Limited published results show similar superiority of FDG-PET in the detection of second primary tumors as for distant metastases, with reported rates of up to 18% when compared to conventional screening, facilitating more prompt treatment of these tumors (Brouwer et al. 2006; Dietl et al. 2008).

2.1.4 Detection of Unknown Primary Tumors

The reported incidence of unknown primary tumors in the head and neck area with negative clinical examination and CT and/or MRI studies ranges between 3 and 10% (Miller et al. 2008; Subramaniam et al. 2010). Panendoscopy as well as FDG-PET imaging, in particular in combination, have been shown to be valuable tools in the work-up of such patients. The reported detection rate of unknown primary tumors with FDG-PET is about 30% (Miller et al. 2008; Johansen et al. 2008) with a sensitivity, specificity as well as positive and negative predictive values of 64, 94, 90 and 76%, respectively (Miller et al. 2008). Tonsillar fossa, tongue base, hypopharynx, nasopharynx and lungs are the most common sites harboring the primary tumor (Fig. 12). The localization of the unknown primary tumor has been shown to affect the treatment plan in the majority of patients (Fig. 9).

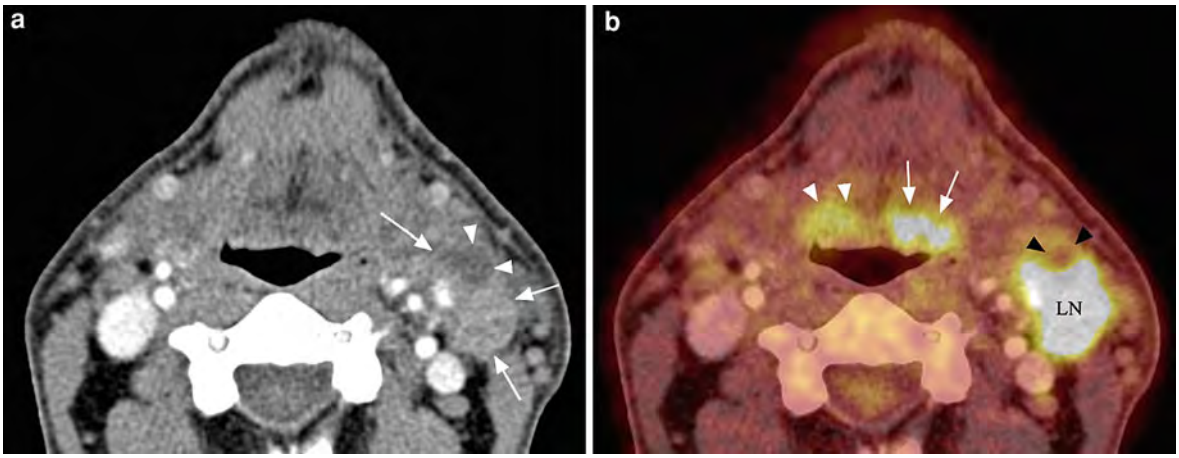

Fig. 12 Contrast enhanced CT (**a**) through the inferior tongue base level shows an ill-defined and heterogeneously enhancing group IIA lymph node (*arrows* in **a**) on the left side. No underlying primary tumor was detectable on clinical examination. The fused PET/CT image (**b**) reveals asymmetric FDG uptake in the lymphoid tissues of the tongue base, left greater (*arrows* in **b**) than right (*white arrowheads* in **b**), guiding the subsequently performed biopsies. Pathological examination confirmed squamous cell carcinoma in the left inferior tongue base with metastatic disease to the left neck. Notice the lack of FDG uptake in the anterior portion (*black arrowheads* in **b**) of the left group IIA lymph node (*LN* in **b**) that corresponded to a focal necrotic area (*arrowheads* in **b**) on the CT image

A false negative rate of FDG-PET of 16% has also been reported which was primarily attributed to the very small size of the primary tumor of 5 mm or less as found on panendoscopy. As mentioned above, such small lesions are unreliably detected with FDG-PET due to its inherent low spatial resolution. Therefore, the work-up of patients with unknown primary tumors should include FDG-PET, followed by panendoscopy (Miller et al. 2008). The reverse order is not recommended as panendoscopy may cause post-procedural inflammation resulting in higher falsely positive FDG-PET rates (Johansen et al. 2008). In addition, FDG-PET might be able to lead the panendoscopist to the concerning sites and so increasing the chance for correct localization of the unknown primary tumor (Fig. 12).

In approximately 70% of patients, neither imaging studies nor panendoscopy with random biopsies were able to identify an underlying primary tumor site. Long-term follow-up of such patients who were primarily treated with lymph node dissection revealed a surprisingly low rate of delayed demarcation of the unknown primary site with reported incidence of 6% (Miller et al. 2008). These study results suggest that in selected patients (N1 disease without extracapsular spread in the neck dissection specimen) with negative FDG-PET and negative panendoscopy with random biopsies a "wait and see approach" with close follow-up might be sufficient instead of the often performed whole neck radiation therapy.

2.2 Treatment Planning

TNM staging is a well-established method for evaluation of head and neck malignancies that is directly linked to certain treatment options. In general, more extensive treatment is done with advanced tumors without distant metastasis while more conservative treatment is preserved for earlier stage tumors.

Stratification of squamous cell tumors into favorable and unfavorable radiation treatment groups based on CT tumor volume has been well established for the different anatomical sites in the past two decades. Early results for FDG-PET imaging suggest that the tumor volume is in general overestimated with all imaging modalities. FDG-PET yielded in average 33% smaller tumor volumes and tended to be closer to the pathological specimen volumes than CT or MRI (De Figueiredo et al. 2009; Daisne et al. 2004). The impact of this observation upon treatment group stratification is so far unknown as the tighter volume might facilitate focused treatment options, such as intensity modulated radiation therapy (IMRT), but

might also provide a smaller "safety" margin between tumor and healthy tissues potentially leading to higher rates of persistent or recurrent tumor. This is even more concerning when considering that the outline of the pathological specimen was not completely encompassed by the outline of any of the imaging modalities examined in a small reported series with the largest non-encompassed area attributed to FDG-PET (Daisne et al. 2004). Therefore, the CT established tumor volumes cannot be directly applied to FDG-PET studies.

A small portion of patients with favorable appearing tumors (e.g. very small tumor volume and stage) on clinical examination and CT/MRI exhibit a very aggressive growth pattern despite appropriate treatment. In contrast to conventional imaging techniques, FDG-PET is able to reveal the biological activity of head and neck cancers and provides an easy to be performed in vivo opportunity to characterize the aggressiveness of individual tumors. Preliminary results indicate that a cut- off value of primary tumor SUV_{max} between seven and eight is able to stratify patients into favorable and unfavorable groups with higher local recurrence rates and shorter survival times observed in patients with SUV_{max} of >8 treated with radiation therapy (Kubicek et al. 2010; Higgins et al. 2011). In addition, "FDG activity maps" of each tumor can be performed offering a magnitude of new radiation therapy modifications such as voxel-intensity-based dose escalation with higher radiation doses prescribed to tumor parts with higher FDG activity (Vanderstraeten et al. 2006). The long-term benefits of such individualized treatment using dose escalation to parts of the tumor based on the FDG-activity intensity-modulated radiation plans are not known yet.

Tumor hypoxia has also been identified as an unfavorable factor in the treatment of head and neck cancers (Gray et al. 1953). Hypoxic tumor cells have been shown to be resistant to chemotherapy and radiation when compared to aerobic tumor cells, leading to higher risk of locoregional failure and decreased overall survival rates (Nordsmark and Overgaard 2004; Nordsmark et al. 2005). Biopsies evaluate only a small portion of the tumor and are prone to sampling errors as the majority of tumors is heterogeneous in nature. In contrast, PET imaging performed with specific tracers such as ^{18}F-labelled Fluoromisonidazole (^{18}F-MISO), allows in vivo mapping of the entire tumor volume for areas of hypoxia. Selective increase of radiation dose to the hypoxic subvolumes by 20% without significant dose escalation to the surrounding normal soft tissues has been reported feasible in a small group of patients with head and neck cancer using IMRT techniques (Lee et al. 2008). Dose escalation by 50% has been shown to be more challenging as larger hypoxic subvolumes make protection of healthy surrounding tissues difficult or impossible. Therefore, radiation sensitizers, vasodilators, hyperbaric oxygen, carbon breathing and/or hypoxic cell cytotoxins have been another focus of recent research projects, for example, promising preliminary results have been reported from the Accelerated Radiotherapy with CarbOgen and Nicotinamide (ARCON) trial (Kaanders et al. 2002).

A more detailed discussion on the use of imaging for radiotherapy planning is found in "Use of Imaging in Radiotherapy for Head and Neck Cancer".

2.3 Treatment Surveillance

Currently, FDG-PET does not play any significant role in evaluation of head and neck cancer patients during chemotherapy and or radiation therapy. A few publications showed promising results for early stratification of responders to non-responders by FDG-PET following two or three cycles of chemotherapy but their impact upon the treatment plan has not been determined yet (Lowe et al. 1997; Dalsaso et al. 2000). Similarly, no significant benefit of FDG-PET during radiation treatment has been shown since the inflammatory changes related to the radiation hamper the interpretation of the FDG-PET images. In addition, adaptation of the prescribed radiation dose to the reduced tumor volume as seen on repeated FDG-PET studies has not shown to significantly reduce the radiation dose to healthy organs at risk within the radiation fields (Geets et al. 2007).

In contrast, FDG-PET is playing an important role in the evaluation of head and neck cancer patients after completion of treatment with recurrence rates of up to 27% reported in patients with clinically and by conventional imaging unsuspected disease (Wong et al. 2002; Salaun et al. 2007). The accuracy of FDG-PET in detection of recurrent or persistent disease is in particular dependent upon the time point of FDG-PET performance in relation to treatment.

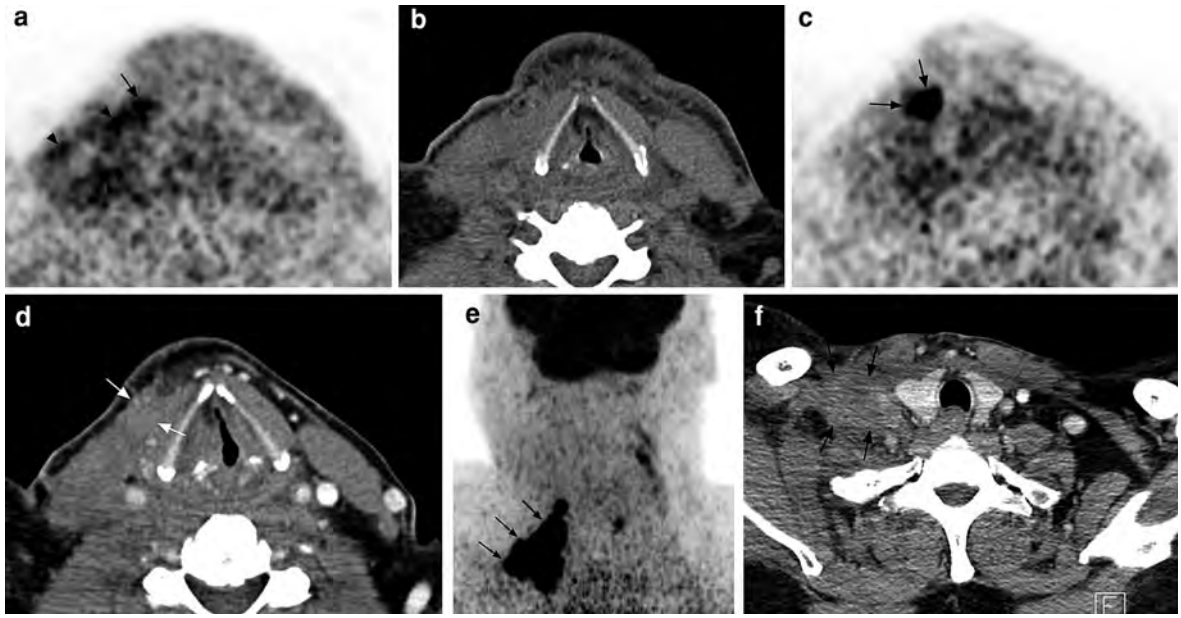

Fig. 13 Axial PET image (**a**) performed 4 weeks after lymph node dissection shows patchy areas of marked FDG uptake (*arrow and arrowheads* in **a**) within the right lateral neck compartment without evidence of focal lesions on the non-enhanced CT image (**b**) at the same level. Such FDG uptake could be related to post-surgical inflammation/granulation tissue or persistent tumor. The PET examination was repeated 3 months later (**c**) revealing a discrete area of intense FDG uptake (*arrows* in **c**) within the region of the more anterior FDG uptake on the prior study (*arrows* in **a**) while the more posterior foci of FDG uptake (*arrowheads* in **a**) resolved. The contrast-enhanced CT image (**d**) performed at the same level shows a subtle lesion (*arrows* in **d**) along the anterior margin of the sternocleidomastoid muscle that could be overlooked without the PET part of the examination. This persistent/recurrent tumor extends into the supraclavicular fossa on the right (*arrows* in **e**) causing complete obliteration of the supraclavicular fat planes (*arrows* in **f**) as seen on the coronal PET image (**e**) and contrast-enhanced CT image at the thoracic inlet level (**f**)

Although early scanning at 4–6 weeks post treatment is clinically preferred, it has shown to have higher false positive and negative results than desired at that time point. The higher false positive results are related to inflammatory changes associated with surgery (Fig. 13) and/or radiation therapy, while the higher false negative results are felt to be related to insufficient time for residual viable cancer cells to grow to a level that can be detected with FDG-PET (Yai et al. 2005; Rogers et al. 2004). Therefore, the current recommendation is to obtain follow-up FDG-PET studies about 12 weeks post completion of treatment. This time point appears to be a well balanced compromise between accuracy of FDG-PET and development of post-treatment fibrosis, while still allowing for salvage treatment if needed.

The utility of follow-up FDG-PET needs to be divided into three aspects: recurrence at the primary site, nodal disease and distant metastases.

2.3.1 Post-treatment Evaluation of the Primary Site

Early detection of persistent or recurrent disease at the primary site is critical as advanced recurrent tumors harbor a significantly poorer prognosis, with reported 2-year survival rates of 70% for early and only 22% for advanced recurrent disease. Clinical examination and conventional imaging are sometimes challenging because of the marked alteration of the soft tissues planes caused by radiation therapy and/or surgery (Figs. 14 and 15). Conventional imaging is in particular reliant upon visibility of fat planes which are often obliterated on post-treatment scans secondary to edema, inflammation and/or scar tissue, making distinction to recurrent or persistent tumor challenging (Fig. 6c and d). The ability of FDG-PET to capture metabolic rates has been shown to be beneficial in earlier detection of recurrent tumor, even in clinically disease-free patients, with reported sensitivities and

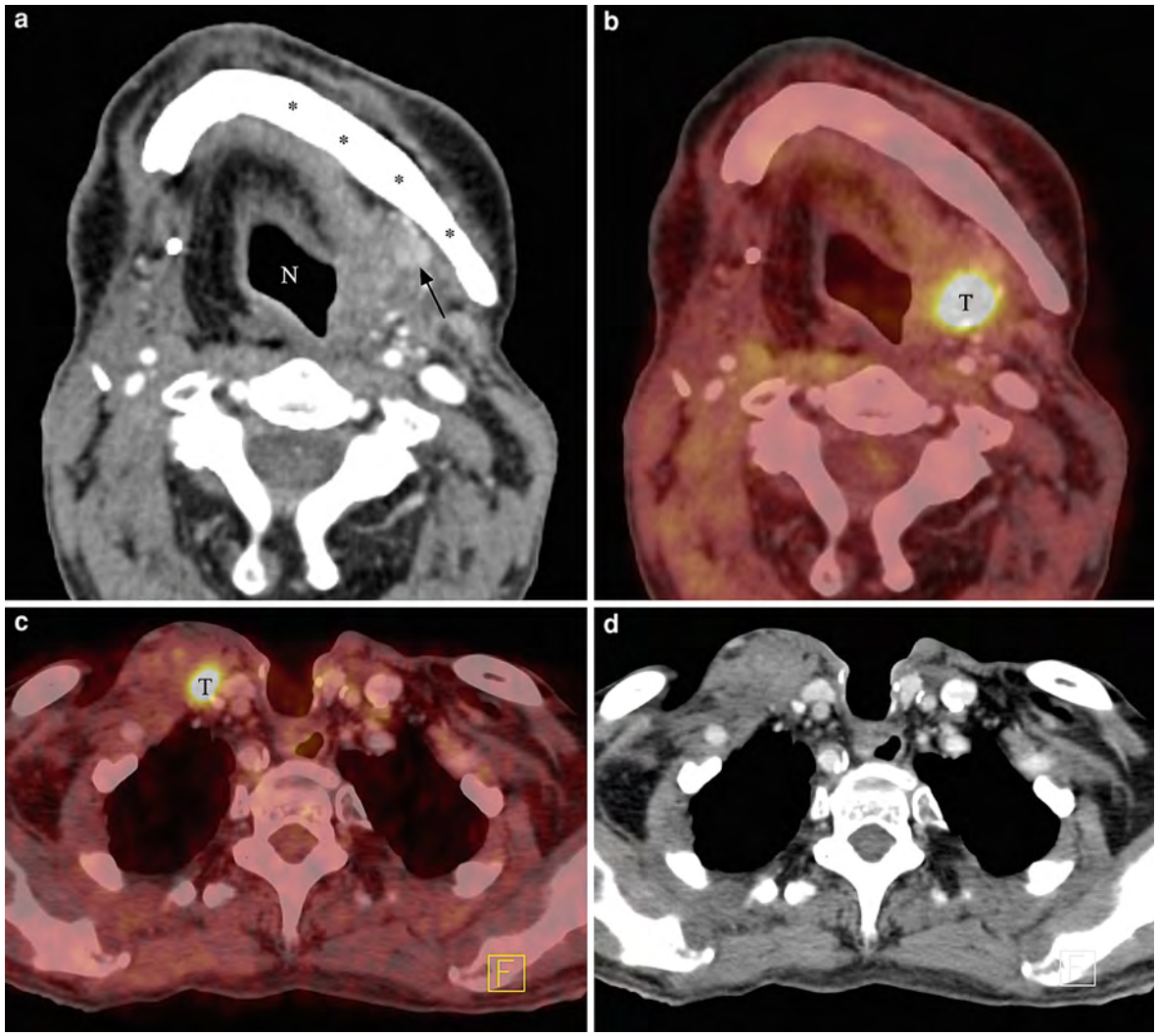

Fig. 14 Fifty-seven-year old patient status post resection of advanced squamous cell carcinoma of the tongue base, pectoralis flap reconstruction and right lymph node dissection presents for follow-up surveillance. The contrast-enhanced CT image at the level of the mandible (**a**) shows asymmetric fat planes lateral to the neopharynx (*N* in **a**) with a small enhancing lesion (*arrow* in **a**) along the residual mandible (* in **a**) on the *left side*. The fused FDG-PET/CT image at the same level (**b**) reveals that the recurrent tumor (*T* in **b**) is actually more medially located than the suspicious area—critical information for the subsequently performed confirmatory CT-guided biopsy. The PET/CT image at the thoracic inlet (**c**) detects another focus of profound uptake (*T* in **c**) along the deep margin of the pedicle of the pectoralis major flap that was unsuspected on the contrast-enhanced CT image at the same level (**d**). This additional information led to significant change in the patient's treatment plan

specificities of FDG-PET of 92–100 and 81–95%, respectively, with a very high negative predictive value of 96% (Wong et al. 2002; Ong et al. 2008). This is markedly higher than reported for clinical examination with 60% sensitivity, 76% specificity and 74% negative predictive value. False positive FDG-PET results have been attributed to inflammation such as related to post radiation mucositis, sialadenitis, healing tissues sites at tracheostomy, voice valve prosthesis, recent biopsy or osteoradionecrosis. Muscular uptake that can be physiological in nature or related to muscle spasm (Fig. 16), denervation or partial muscle resection may also cause false positive findings.

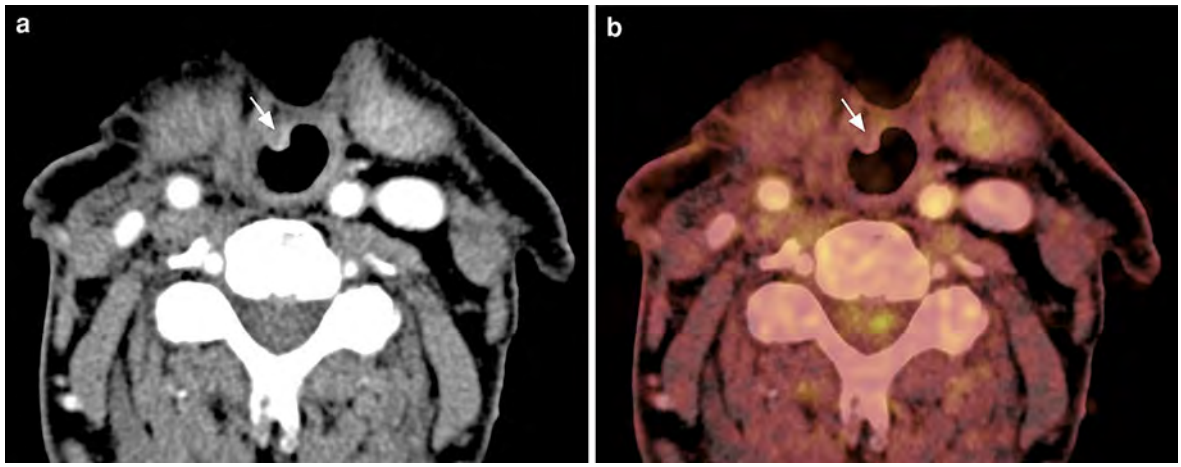

Fig. 15 Axial, contrast-enhanced CT (**a**) in a patient status post total laryngectomy shows a focal polypoid lesion within the neopharynx (*arrow* in **a**) that was concerning for recurrent tumor. This is not confirmed on the fused PET/CT image (**b**) as no FDG uptake is seen within this lesion (*arrow* in **b**)

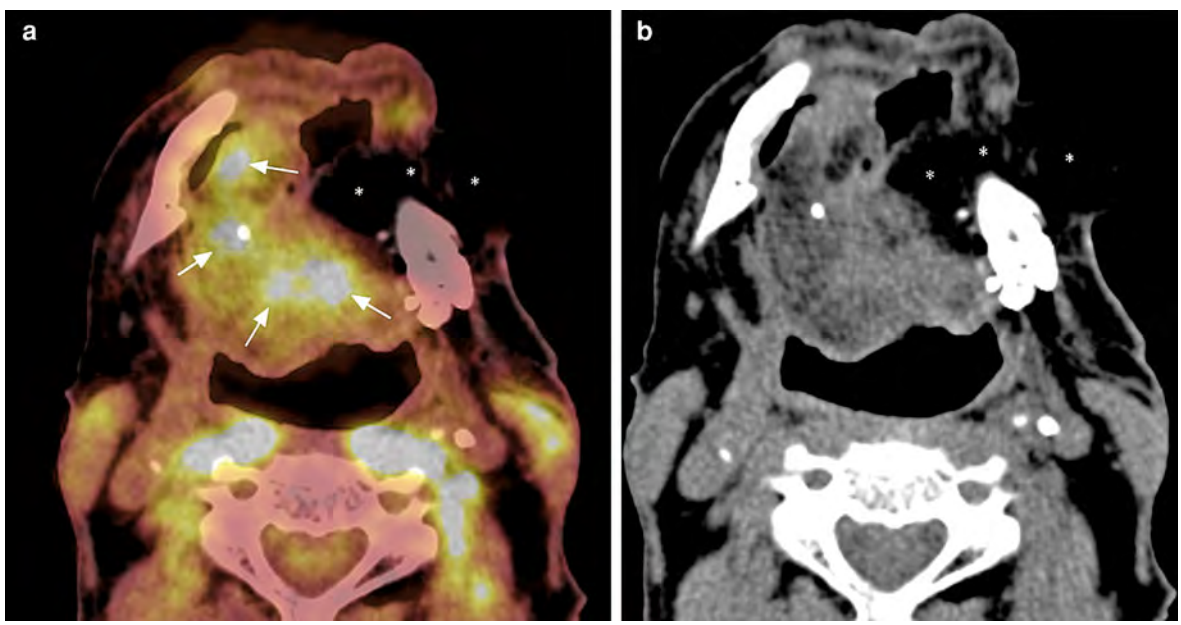

Fig. 16 Fused PET/CT image (**a**) in a patient status post floor of the mouth cancer resection, partial glossectomy and mandibulectomy and myocutaneous flap (* in **a** and **b**) reconstruction shows patchy areas of marked FDG uptake within the residual tongue (*arrows* in **a**) that are concerning for multifocal recurrent tumor. The non-contrast enhanced CT (**b**) at the same level, however, demonstrates preservation of the striation of the intrinsic tongue musculature or focal fat without discrete lesions. Clinical examination revealed rapid fasciculations of the residual tongue. This is a common finding in patient status post extensive oral cavity surgery that can mimic recurrent tumor. In some patients, MRI examination is needed to confirm the physiological nature of the FDG uptake

Significant overlap of SUV_{max} values between benign disease and recurrent tumor occurs. In general, diffusely increased FDG-uptake is typically related to post-treatment inflammatory changes, while localized uptake is more consistent with recurrent or persistent tumor (Fig. 13). A cut-off value for SUV_{max} of 3.2 has been reported to yield the best sensitivity (92%) and specificity (70%) in detection of recurrent tumors

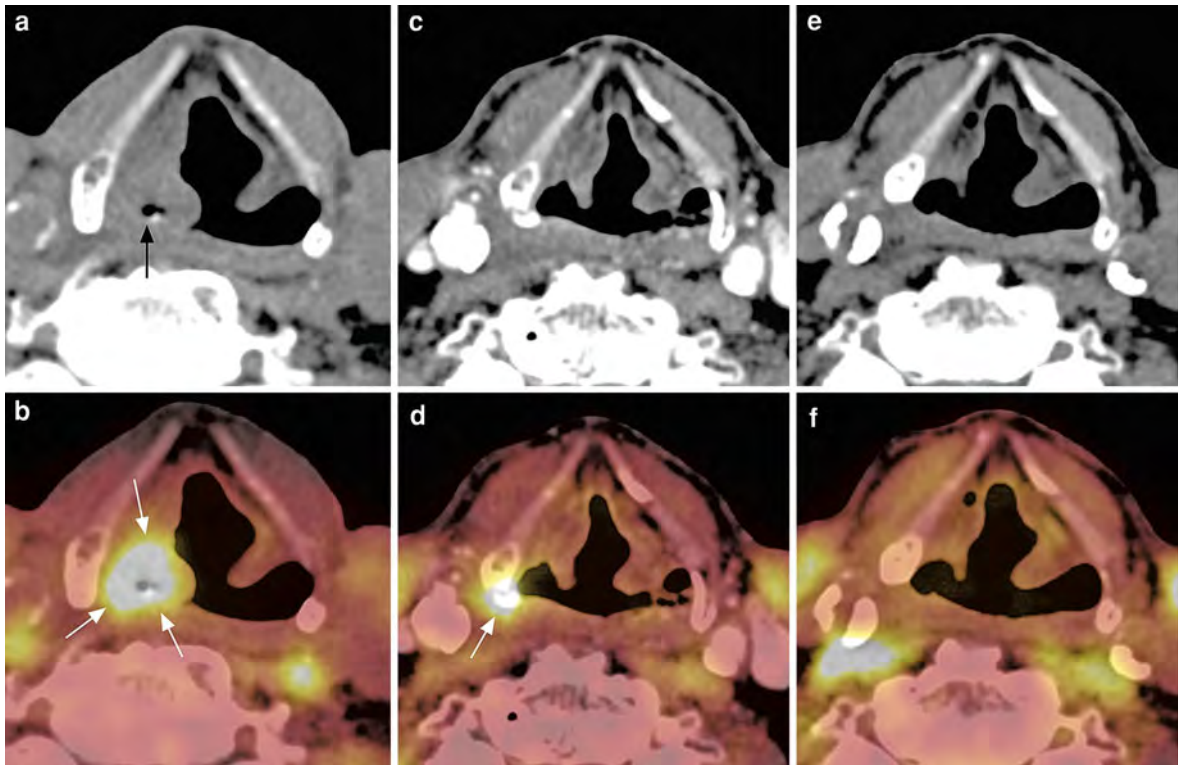

Fig. 17 CT and fused PET/CT images of a patient with piriform sinus cancer show marked obliteration of the right piriform sinus (*arrow* in **a**) with profound, circumferential FDG uptake (*arrows* in **b**) at the initial presentation (**a** and **b**). The follow-up examination (**c** and **d**) performed 3 months following completion of radiation therapy reveals resolution of the mass on the CT portion of the study with persistent small focus of FDG activity (*arrow* in **d**) in the lateral aspect of the piriform sinus raising concerns of persistent tumor. A biopsy was performed without confirmation of residual tumor. The patient was therefore followed with sequential PET/CT studies with decreasing FDG accumulation seen over time. Complete resolution of the FDG activity was achieved on the 18 months follow-up examination (**e** and **f**)

(Wong et al. 2002). Since the specificity is not as optimal as desired, clinical correlation of residual FDG uptake is recommended, with subsequent biopsies depending upon patient risk profile and level of suspicion for recurrent tumor. If a biopsy is not warranted, close clinical and/or imaging follow-up should be done as some patients may demonstrate delay in resolution of FDG activity at the primary tumor site (Fig. 17) while others will show progression and eventual more obvious demarcation of the FDG uptake as recurrent tumor (Fig. 18).

2.3.2 Post-treatment Evaluation of Nodal Disease

The need for lymph node dissection following radiation therapy, without or with additional chemotherapy, is a subject of ongoing debate. Some clinicians are strong proponents of lymph node dissection in patients with initial N2 staging independent of the treatment response, while others support a "wait-and-see" approach in particular in patients with clinically N0 necks post treatment. Several studies have reported a very high negative predictive value of FDG-PET at 3–4 months post-definitive radiation with values ranging between 97 and 100% and this independent of the size of residual nodal mass (Yai et al. 2005; Ong et al. 2008; Nayak et al. 2007). Therefore, the following algorithm has been suggested:

- No response or progression of nodal disease at 4–6 weeks—lymph node dissection is required.
- Nodal response at 4–6 weeks—performance of FDG-PET/CT at 12 weeks post completion of definitive radiation:

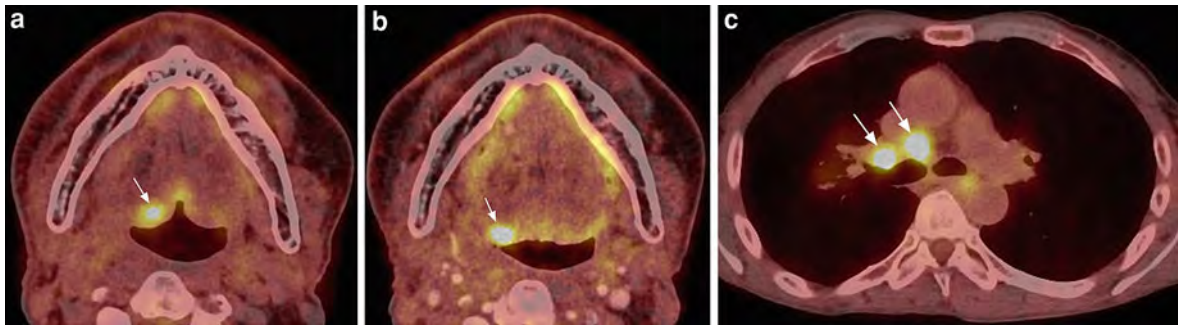

Fig. 18 Fused PET/CT images following radiation therapy of a right tongue base tumor: The study performed 3 months after completion of radiation therapy (**a**) shows a focal area of persistent FDG-uptake (*arrow* in **a**) in the right tongue base that was interpreted as persistent tumor. This was contradicting the clinical examination and the subsequently performed biopsies. Repeated PET CT examination (**b**) was done 3 months later revealing slightly more pronounced FDG uptake (*arrow* in **b**) in the right posterior tongue that was now extending to the tongue surface and was biopsy confirmed to represent persistent tumor. Unfortunately, the patient also developed hilar metastases (*arrows* in **c**) in between these two studies

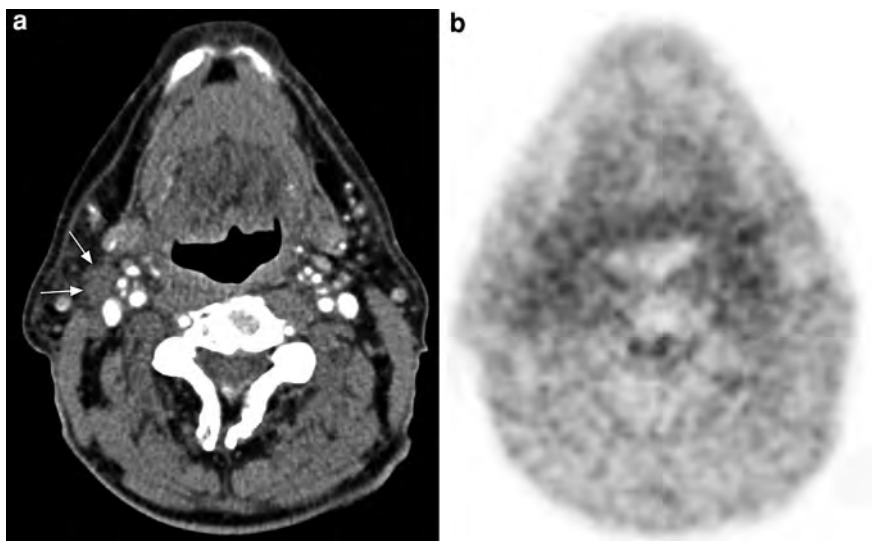

Fig. 19 Axial contrast-enhanced CT (**a**) of a patient 3.5 months after completion of radiation therapy for a tongue base cancer shows a residual, slightly heterogeneously appearing group IIA lymph node (*arrows* in **a**) on the right side measuring 1.4 by 1.1 cm in size. Since the PET image (**b**) shows no FDG activity, a lymph node dissection is not indicated

- negative FDG-PET with residual lymph nodes <2 cm in size—"wait-and-see" approach with close follow-up required (Fig. 19)
- residual lymph nodes larger than 2—lymph node dissection warranted independent of FDG-PET results
- positive FDG-PET—lymph node dissection or at least biopsy is required as the positive predictive values of FDG-PET are less optimal, ranging between 38 and 43%.

Such an algorithm has been shown to result in reduction of planned lymph node dissection by 75–80%, while missing residual neck disease in less than 5% of patients only (Ong et al. 2008; Nayak et al. 2007).

2.3.3 Post-treatment Evaluation of Distant Metastases

The reported incidence of distant metastases detected on post-treatment FDG-PET studies ranges between 20 and 30% with sensitivities and specificities around 93% (Wong et al. 2002; Abgral et al. 2009). Such high incidence rates of metastatic disease are likely related to preferential FDG-PET imaging in patients with more advanced initial disease, or

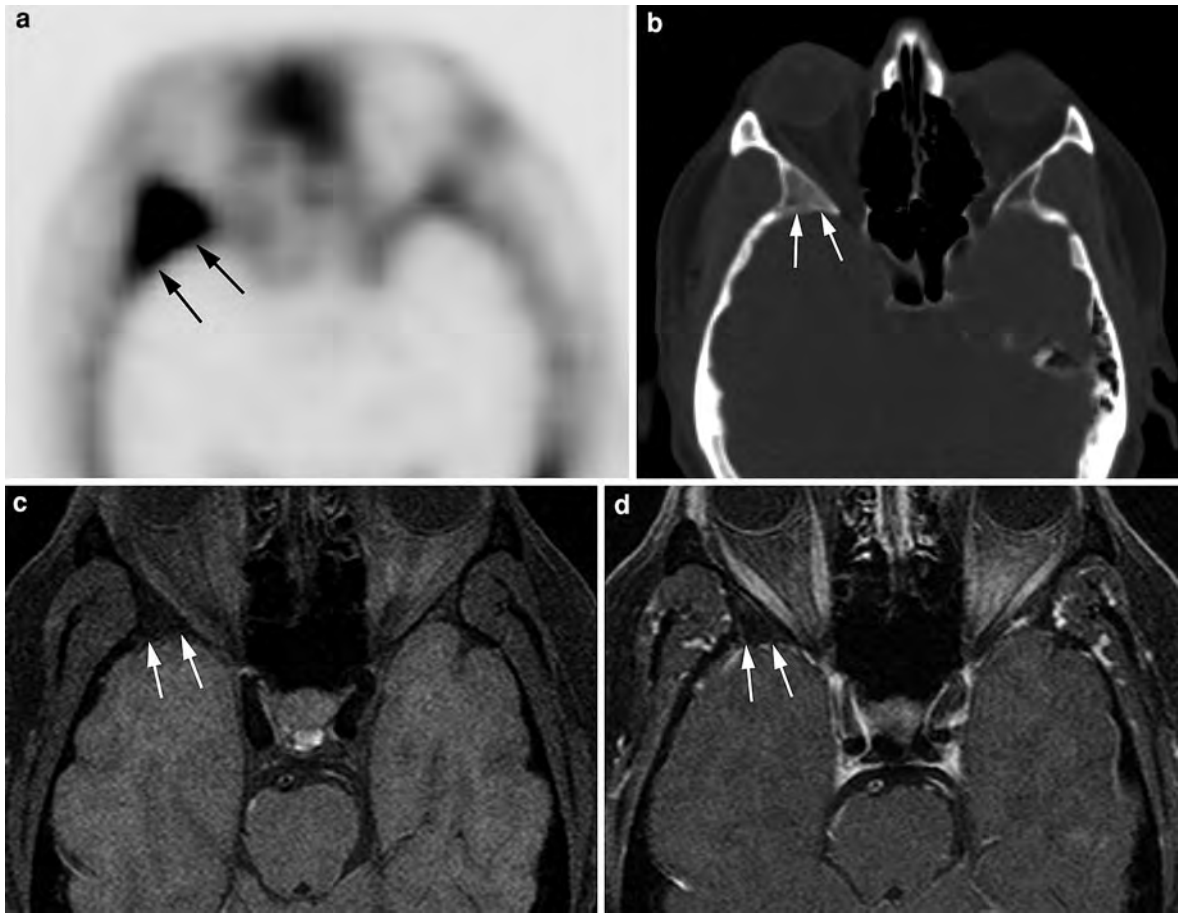

Fig. 20 ^{18}F-NaF PET CT examination (**a**) was performed in a patient with recently diagnosed prostate cancer. The study shows a markedly ^{18}F-NaF avid lesion in the right greater sphenoid wing (*arrows* in **a**) that was initially interpreted as a metastatic lesion. The corresponding CT image (**b**) reveals a markedly expanded greater sphenoid wing on the right when compared to the left with ground glass opacification and preservation of the cortex (*arrows* in **b**). These are characteristic imaging findings of fibrous dysplasia. Confirmation with MRI was obtained demonstrating markedly expanded, low attenuation greater sphenoid wing (*arrow*s in **c**) on the T1 fat suppressed image (**c**) without enhancement (*arrows* in **d**) following Gadolinium administration (**d**)

clinically already suspected disease at the locoregional level. Therefore, it is not surprising that simultaneous recurrence at the primary site has been reported in up to 33% of patients. Distant metastatic disease to the chest was most commonly observed which was clinically silent in up to 50% of patients (Fig. 18).

2.4 Special Considerations for Some Histological Tumor Types

The value of PET imaging for tumor types other than squamous cell carcinoma histological is less well established. Special considerations as delineated below need to be taken into account for some of them.

2.4.1 Salivary Gland Tumors

Differentiation of benign form malignant salivary gland lesions is not reliably possible with FDG-PET, as the majority of Warthin's tumors (Fig. 9) and some pleomorphic adenomas show markedly increased FDG uptake, similar to malignant tumors, leading to a false positive rate of 30–50% (Okamura et al. 1998; Keyes et al. 1994). In addition, a few malignant tumors such as adenoid cystic and mucoepithelial carcinomas have been reported to have lower than for

a malignant tumor expected SUV values. On the other hand, FDG-PET was shown beneficial after the diagnosis of a salivary gland malignancy has been established, leading to a change in treatment plan in up to 35% (Otsuka et al. 2005). The main strength of FDG-PET in such patients was the detection of distant metastatic disease in 25 and 22% of patients during the initial staging and follow up time points, respectively.

2.4.2 Bone Lesions

Bony lesions, in particular of the skull base, pose a challenge for the radiologist as these are often asymptomatic in nature, similar in appearance on conventional imaging and difficult to access by biopsy (see also "Malignant Lesions of the Central and Posterior Skull Base"). Sometimes, bone scans with ^{99m}Tc-MDP are performed to help narrow down the differential diagnostic possibilities. ^{18}Fluoro-Sodium Fluoride (^{18}F-NaF) is a new bone-specific PET agent that results in a high target-to-background ratio. It has been reported to significantly increase the detection rates of metastatic disease when compared with conventional bone imaging and single photon emission tomography (SPECT) (Evan-Spir et al. 2006; Beheshti et al. 2010). However, as ^{99m}Tc-MDP it is not specific for malignant tumors and also taken up by some benign bony lesions (Fig. 20); therefore of limited value in patients with a single bony lesion (Chen et al. 2009).

FDG-PET/CT has been shown to complement the results of bone-specific radiotracer studies. Standard FDG-PET has been reported to be superior to ^{99m}Tc-MDP and ^{18}F-NaF in imaging of plasmocytoma, multiple myeloma and other bone marrow malignancies (Chen et al. 2009). Standard FDG PET has, however, only limited value in distinguishing primary benign and malignant bone lesions, as highest radiotracer uptake values have been reported with histiocytic and giant cell tumors, and similar low values with fibrous dysplasia, osteosarcomas and chondrosarcomas (Aoki et al. 2001). More accurate distinction between benign and malignant bony lesions seems possible with dual-time point FDG PET CT imaging with increased radiotracer uptake in malignant lesions at 2 h when compared to 1 h post FDG injection and stable or decreasing uptake in benign lesions (Tian et al. 2009).

3 Conclusion

In summary, PET represents an important adjunct to conventional imaging in staging and follow-up of patients with head and neck cancers, in particular of squamous cell types. Its ability to capture biological activity and areas of hypoxia within tumors adds other important variables in the stratification of patients into favorable and unfavorable treatments groups and facilitates more individualized treatment planning.

References

Abgral R, Querellou S, Potard G, LeRoux PY, LeDuc-Pennec A, Marianovski R, Pradier O, Bizais Y, Kraeber-Bodéré F (2009) Does 18F-FDG PET/CT improve the detection of posttreatment recurrence of head and neck squamous cell carcinoma in patients negative for disease on clinical follow-up? J Nucl Med 50(1):24–29

Aoki J, Watanabe H, Shinozaki T, Takagishi K, Ishijima H, Oya N, Sato N, Inoue T, Endo K (2001) FDG PET of primary benign and malignant bone tumors: standartized uptake values in 52 lesions. Radiology 219:774–777

Beheshti M, Pirich C, Langsteger W (2010) Convetional Tc-99m-based bone scan versus fluoride positron emission tomography combined with computed tomography in the assessment of bone metastases in prostate cancer patients. Imaging Decis MRI 13:67–129

Bhatnagar AK, Heron DE, Schaitkin B (2005) Perineural invasion of squamous cell carcinoma of the lip with occult involvement of the intra-orbital nerve detected by PET-CT and treated with MRI-based IMRT: a case report. Technol Cancer Res Treat 4(3):251–253

Brouwer J, de Bree R, Comans E, Golding RP, Castelijns JA, Hoekstra OS, Leemans CR (2004) Positron emission tomography using [^{18}F]fluorodeozyglucose (FDG-PET) in the clinically negative neck: is it likely to be superior? Eur Arch Otorhinolaryngol 261:479–483

Brouwer J, Senft A, de Bree R, Comans E, Golding RP, Castelijns JA, Hoekstra OS, Leemans CR (2006) Screening for distant metastases in patients with head and neck cancer: is there a role for ^{18}FDG-PET? Oral Oncol 42:275–280

Chen K, Blebea J, Laredo JD, Chen W, Alavi A, Torigian DA (2009) Evaluation of musculoskeletal disorders with PET. PET/CT, and PET/MR imaging. PET Clin 3:451–465

Chu MM, Kositwattanarerk A, Lee DJ, Makkar JS, Genden EM, Kao J, Packer SH, Som PM, Kostakoglu L (2010) FDG PET with contrast enhanced CT: a critical imaging tool for laryngeal carcinoma. Radiographics 30:1353–1372

Conrad GR, Sinha P, Holzhauer M (2004) Perineural spread of skin carcinoma to the base of the skull: detection with FDG PET and CT fusion. Clin Nucl Med 29:717–719

Daisne JF, Duprez T, Weynand B, Lonneux M, Hamoir M, Reychler H, Grégoire V (2004) Tumor volume in pharyngolaryngeal squamous cell carinoma: comparison at CT,

MR imaging, and FDG PET and validation with surgical specimen. Radiology 233:93–100

Dalsaso TA, Lowe VJ, Dunphy FR, Martin DS, Boyd JH, Stack BC (2000) FDG-PET and CT in evaluation of chemotherapy in advanced head and neck cancer. Clin Positron Imaging 3(1):1–5

De Figueiredo BH, Barret O, Demeaux H, Lagarde P, De-Mones-Del-Pujol E, Kantor G, de Clermont-Gallerande H, Richaud P, Fernandez P (2009) Comparison between CT- and FDG-PET-defined target volumes for radiotherapy planning in head-and-neck cancers. Radiother Oncol 93(3):479–482

Dietl B, Marienhagen J, Schaefer C, Pohl F, Murthum T, Kölbl O (2007) Überleben mit hämatogen metastasierten HNO-Tumoren. HNO 55:785–791

Dietl B, Marienhagen J, Kühnel T, Schreyer A, Kölbl O (2008) The impact of FDG-PET/CT on the management of head and neck tumours: the radiotherapist's perspective. Oral Oncol 44(5):504–508

Evan-Spir E, Metser U, Mishani E, Lievshitz G, Lerman H, Leibovitch I (2006) The detection of bone metastases in patients with high-risk prostate cancer: 99mTc-MDP bone scintigraphy, single- and multi-filed-of-view SPECT, 18F-fluoride PET, and 18F-fluoride PET/CT. J Nucl Med 47(2):287–297

Garavello W, Ciardo A, Spreafico R, Gaini RM (2006) Risk factors for distant metastases in head and neck squamous cell carcinoma. Arch Otolaryngol Head Neck Surg 132:762–766

Geets X, Tomsei M, Lee JA, Duprez T, Coche E, Cosnard G, Lonneux M, Grégoire V (2007) Adaptive biological image-guided IMRT with anatomic and functional imaging in pharyngo-laryngeal tumors: impact on target volume delineation and does distribution using helical tomotherapy. Radiother Oncol 85(1):105–115

Gray LH, Conger AD, Ebert M, Hornsey S, Scott OCA (1953) The concentration of oxygen dissolved in tissues at the time of irradiation as a factor in radiotherapy. Br J Radiol 26:638–648

Ha PK, Hdeib A, Goldenberg D, Jacene H, Patel P, Koch P, Koch W, Califano J, Cummings CW, Flint PW, Tufano RP (2006) The role of positron emission tomography and computed tomography fusion in the management of early-stage and advanced-stage primary head and neck squamous cell carcinoma. Arch Otolaryngol Head Neck Surg 132:12–16

Hanna E, Vural E, Prokopakis E, Carrau R, Snyderman C, Weissman J (2007) The sensitivity and specificity of high-resolution imaging in evaluating perineural spread of adenoid cystic carcinoma to the skull base. Arch Otolaryngol Head Neck Surg 133(6):541–545

Higgins KA, Hoang JK, Roach MC, Chino J, Yoo DS, Turkington TG, Brizel DM (2011) Analysis of pretreatment FDG-PET SUV parameters in head-and-neck cancer: tumor SUV(mean) has superior prognostic value. Int J Radiat Oncol Biol Phys (Epub ahead of print)

Johansen J, Buus S, Loft A, Keiding S, Overgaard M, Hansen HS, Grau C, Bundgaard T, Kirkegaard J, Overgaard J (2008) Prospective study of 18FDG-PET in the detection and management of patients with lymph node metastases to the neck from an unknown primary tumor. Results from the DAHANCA-13 study. Head Neck 30:471–478

Kaanders J, Pop L, Marres H, Bruaset I, Van den Hoogen F, Merkx M, Van der Kogel A (2002) ARCON: experience in 215 patients with advanced head-and-neck cancer. Int J Radiat Oncol Biol Phys 52(3):769–778

Keyes JW, Harkness BA, Greven KM, Williams DW, Watson NE, McGuirt WF (1994) Salivary gland tumors: pretherapy evaluation with PET. Radiology 192:99–102

Krabbe CA, Dijkstra PU, Pruim J, van der Laan B, van der Wal JE, Gravendeel JP, Roodenburg J (2008) FDG PET in oral and oropharyngeal cancer. Value for confirmation of N0 neck and detection of occult metastases. Oral Oncol 44:31–36

Kubicek GJ, Champ C, Fogh S, Wang F, Reddy E, Intenzo C, Dusing RW, Machtay M (2010) FDG-PET staging and importance of lymph node SUV in head and neck cancer. Head Neck Oncol 2:19

Lee NY, Mechalakos JG, Nehmeh S, Lin Z, Squire OD, Cai S, Chan K, Zanzonico PB, Greco C, Ling CC, Humm JL, Schröder H (2008) Fluorine-18-labeled fluoromisonidazole positron emission and computed tomography-guided intensity-modulated radiotherapy for head and neck cancer: a feasibility study. Int J Radiat Oncol Biol Phys 70(1):2–13

Lonneux M, Hamoir M, Reychler H, Maingon P, Calais G, Bridji B, Digue L, Toubeau M, Grégoire V (2010) Positron emission tomography with [18F]fluorodexoyglucose improves staging and patient management in patients with head and neck squamous cell carcinoma: a multicenter prospective study. J Clin Oncol 28(7):1190–1195

Lowe VJ, Dunphy FR, Varvares M, Kim H, Wittry M, Dunphy CH, Dunleavy T, McDonough E, Minster J, Fletcher JW, Boyd JH (1997) Evaluation of chemotherapy response in patients with advanced head and neck cancer using [f-18]fluorodeoxyglucose positron emission tomography. Head Neck 19(8):666–674

Miller FR, Karnad AB, Eng T, Hussey DH, McGuff HS, Otto RA (2008) Management of the unknown primary carcinoma: long-term follow-up on a negative PET scan and negative panendoscopy. Head Neck 30(1):28–34

Murakami R, Uozumi H, Hirai T, Hishimura R, Shiraishi S, Ota K, Murakami D, Tomiguchi S, Oya N, Katsuragawa S, Yamashita Y (2006) Impact of FDG-PET/CT imaging on nodal staging for head-and-neck squamous cell carcinoma. Int J Radiat Oncol Biol Phys 68(2):377–382

Nayak JV, Walvekar RR, Andrade RS, Daamen N, Lai SY, Arigris A, Smith RP, Heron DE, Ferris RL, Johnson JT, Branstetter BF (2007) Deferring planned neck dissection following chemoradiation for stage IV head and neck cancer: the utility of PET-CT. Laryngoscope 117:2129–2134

Ng SH, Yen TC, Chang JTC, Chan SC, Ko SF, Wang HM, Lee LY, Kang CJ, Wong AMC, Liao CT (2006) Prospective study of [^{18}F]fluorodeoxyglucose positron emission tomography and computed tomography and magnetic resonance imaging in oral cavity squamous cell carinoma with palpably negative neck. J Clin Oncol 24:4371–4376

Ngugen BD, Roarke MC (2008) Salivary duct carcinoma with perineural spread to facial canal F-18 FDG PET/CT detection. Clin Nucl Med 33:924–928

Nordsmark M, Overgaard J (2004) Tumor hypoxia is independent of hemoglobin and prognostic for loco-regional tumor control afer primary radiotherapy in advanced head and neck cancer. Acta Oncol 43(4):396–403

Nordsmark M, Bentzen SM, Rudat V, Brizel D, Lartigau E, Stadler P, Becker A, Adam M, Molls M, Dunst J, Terris DJ,

Overgaard J (2005) Prognostic value of tumor oxygenation in 397 head and neck tumors after primary radiation therapy. An international multi-center study. Radiother Oncol 77(1):18–24

Okamura T, Kawabe J, Koyama K, Ochi H, Yamada R, Sakamoto H, Matsuda M, Ohashi Y, Nakai Y (1998) Fluorine-18 fluorodeoxyglucose positron emission tomography imaging of parotid mass lesions. Acta Otolaryngol Suppl 538:209–213

Ong SC, Schröder H, Lee NY, Patel SG, Carlson D, Fury M, Pfister DG, Shah JP, Larson SM, Kraus DH (2008) Clinical utility of 18F-FDG PET/CT in assessing the neck after concurrent chemoradiotherapy for locoregional advanced head and neck cancer. J Nucl Med 49(4):532–540

Otsuka H, Graham MM, Kogame M, Nishitani H (2005) The impact of FDG-Pet in the management of patients with salivary gland malignancy. Ann Nucl Med 19(8):691–694

Puri SK, Fan CY, Hanna J (2003) Significance of extra-capsular lymph node metastases in patients with head and neck squamous cell carcinoma. Current Opin Otolaryngol Head Neck Surg 11(2):119–123

Rogers JW, Greven KM, McGuirt WF, Williams DW, Watson NE, Geisinger K, Cappellari JO (2004) Can post-RT neck dissection be omitted for patients with head-and-neck cancer who have a negative PET scan after definitive radiation therapy? Int J Radiat Oncol Biol Phys 58(3): 694–697

Roh JL, Yeo NK, Kim JS, Lee JH, Cho KJ, Choi SH, Nam SY, Kim SY (2007) Oral Oncol 43:887–893

Salaun PY, Abgral R, Querellou S, Couturier O, Velette G, Bizais Y, Kraeber-Bodéré F (2007) Does 18fluoro-fluoro-deoxyglucose positron emission tomography improve recurrence detection in patients treated for head and neck squamous cell carcinoma with negative clinical follow-up? Head Neck 29(12):1115–1120

Sigg MB, Steinert H, Grätz K, Hugenin P, Stoeckli S, Wyrich GK (2003) Staging of head and nekc tumors: [18F]fluorodeoxyglucose positron emission tomography compared with physical examination and conventional imaging modalities. J Oral Maxillofac Surg 61(9): 1022–1029

Subramaniam RM, Truong M, Peller P, Sakai O, Mercier G (2010) Fluorodeoxyglucose-Positrone-Emission Tomography Imaging of Head and Neck Squamous Cell Cancer. AJNR Am J Neuroradiol 31:598–604

Tian R, Su M, Tian Y, Li F, Li L, Kuang A, Seng J (2009) Dueal-time point PET/CT with F-18 FDG for the differentiation of malignant and benign bone lesions. Skeletal Radiol 38:451–458

Vanderstraeten B, Duthoy W, De Gersem W, De Neve W, Thiersen H (2006) [^{18}F]fluoro-deoxy-glucose positron emission tomography ([^{18}F]FDG-PET) voxel intensity-based intensity-modulated radiation therapy (IMRT) for head and neck cancer. Radiother Oncol 79:249–258

Vierns D, Visser EP, De Geus-Oei LF, Oyen WJG (2010) Methodological considerations in quantification of oncological FDG PET studies. Eur J Nucl Med Mol Imaging 37:1408–1425

Wax MK, Myers LL, Gabalski EC, Husain S, Gona JM, Nabi H (2002) Positron emission tomography in the evaluation of synchronous lung lesions in patients with untreated head and neck cancer. Arch Otolaryngol Head Neck Surg 128: 703–707

Wong RJ, Lin DT, Schröder H, Patel SG, Gonen M, Wolden S, Pfister DG, Shah JP, Larson SM, Kraus DH (2002) Diagnostic and prognostic value of [^{18}F]fluorodeoxyglucose positron emission tomography for recurrent head and neck squamous cell carinoma. J Clin Oncol 20(20):4199–4208

Yai M, Smith RB, Graham MM, Hoffman HT, Tan H, Funk GF, Graham SM, Chang K, Dornfeld KJ, Menda Y, Buatti JM (2005) The role of FDG PET in management of neck metastasis from head-and-neck cancer after definitive radiation treatment. Int J Radiat Oncol Biol Phys 63(4): 991–999

Use of Imaging in Radiotherapy for Head and Neck Cancer

Sandra Nuyts and Alysa Fairchild

Contents

Abstract

Wider availability of and technical improvements in anatomic and biological imaging have facilitated the implementation of high-precision three-dimensional conformal and intensity-modulated radiotherapy (RT) in head and neck cancer. The integration of recent advances in functional and molecular imaging have already improved staging, RT delivery, response prediction, and follow-up. Rational clinical use of all modalities should be encouraged, especially in the setting of imaging-intensive investigational RT protocols such as adaptive therapy. Expanded development of imaging markers which can predict radioresistance or outcome could further customize treatment. Continued successful use of innovative imaging in routine clinical practice will ultimately depend on well-designed clinical studies with adequate follow-up.

1 Introduction

Head and neck cancers (HNC) include malignancies originating in the oropharynx, oral cavity, hypopharynx, and larynx. In the western world, more than 90% of these are squamous cell carcinomas (Hustinx and Lucignani 2010). Nasopharyngeal malignancy is also a subtype of HNC, although with a somewhat different epidemiology and natural history. Most early-stage head and neck tumours can be cured by surgery or radiotherapy (RT), which have similar locoregional control rates. The selection of treatment modality in early disease depends on patient condition and

S. Nuyts (✉)
Department of Radiation Oncology,
University Hospital Gasthuisberg,
Herestraat 49, 3000 Leuven, Belgium
e-mail: Sandra.Nuyts@uz.kuleuven.ac.be

A. Fairchild
Department of Radiation Oncology,
Cross Cancer Institute, 11560 University Avenue,
Edmonton, AB T6G 1Z2, Canada

R. Hermans (ed.), *Head and Neck Cancer Imaging*, Medical Radiology. Diagnostic Imaging,
DOI: 10.1007/174_2011_385, © Springer-Verlag Berlin Heidelberg 2012

preference, organ function, and cosmesis. The majority of patients with HNC, however, have locoregionally advanced disease at diagnosis, and are treated with either curative-intent RT plus or minus chemotherapy, or radical surgery followed by post-operative (chemo)radiotherapy (Hustinx and Lucignani 2010). HNC preferentially spreads to cervical lymph nodes (LN) which, if involved, are an adverse prognostic factor. For patients whose disease is too advanced to be addressed radically, palliative RT may be administered for symptom control. RT is therefore part of the treatment approach in the majority of HNC patients at some point during the course of their disease.

The clinical challenge in radical RT is to attain the highest probability of cure with the least toxicity to surrounding normal structures. It is assumed that improvements in locoregional control can be obtained by increasing the dose of radiation delivered to the gross tumour as well as areas at risk for microscopic involvement. Although radiation damages both normal and neoplastic cells, most normal tissues have a small advantage in their ability to recover from RT injury. In curative treatment, this difference is exploited by using many small dose fractions delivered daily over a period of several weeks to obtain a therapeutic advantage. The total dose that can be delivered is limited by the damage caused to the surrounding normal tissues and consequent risk of complications, which also increases with increased RT dose. Therefore, the more normal tissue that can be spared, the greater potential exists for escalating the tumour dose. Recent advances maximise the ability to accomplish this, including the integration of more powerful computers, hardware developments in delivery machines, and especially advances in imaging.

Wider application of and/or technical improvements in ultrasound (US), computed tomography (CT), magnetic resonance imaging (MRI), and positron emission scanning (PET) have made it possible to design high-precision three-dimensional (3D) conformal and intensity-modulated radiotherapy (IMRT). In HNC for example, the obvious advantage of sparing structures such as the salivary glands from damage has pushed IMRT to the forefront as the new standard of care faster than in other cancer sites. However, success requires exact radiological identification of both the tumour and normal structures. Functional imaging is an area of active investigation and metabolic, physiologic, genotypic, or phenotypic data may contribute to our ability to delivery RT safely and effectively in the near future.

This chapter will focus on recent advances in anatomical and functional imaging as they apply to the field of Radiation Oncology. After a general overview of RT in HNC, the advantages and limitations of various imaging techniques used in RT will be described. This will be followed by a review of the current and potential applications of these technologies in Radiation Oncology, although a comprehensive description of the technical details of these techniques is beyond the scope of this chapter.

2 Radiotherapy for Head and Neck Cancer: General Principles

In the infancy of Radiation Oncology, surface anatomy was used to delineate the site to be treated (Table 1). This necessarily resulted in treatment fields encompassing large amounts of normal tissue, and dose calculation could be performed at only a few selected points. In the 1950s, with the advent of the fluoroscopic simulator, internal bony landmarks were used to guide field determination. Two-dimensional (2D) treatment planning was performed in a single plane with target doses displayed as isodose lines. Typically, patients with HNC planned using this method were treated with two lateral fields encompassing the primary and nodal areas, with a separate low neck field for the supraclavicular fossae (Fig. 1). This field arrangement required the portals to be reduced in size at some point to limit the dose to critical normal structures such as the spinal cord. Further dose was then delivered through smaller ‘boost’ fields to the grossly involved areas.

However, it was extremely difficult with 2D treatment to deliver a tumour ablative dose while limiting damage to an organ at risk (OAR) that may be just a few millimetres away. The toxicity from this type of head and neck RT was therefore among the worst seen in Radiation Oncology. In the 2D field setup, both parotid glands commonly received full dose radiation. The most common acute side effects consisted of mucositis resulting in dysphagia and odynophagia, salivary changes, and dermatitis. Late toxicities, usually permanent, included xerostomia,

Table 1 Progress in radiotherapy planning

Evolution	Target definition based on	Dose calculation
One-dimensional	Surface anatomy landmarks	Few selected points
Two-dimensional	Radiographic anatomy	Planar isodose distribution
Three-dimensional	CT, MRI	Volumetric dose calculation in 3D conformal, intensity-modulated radiotherapy
Functional imaging	PET, functional MRI	Volumetric dose calculation within which selective target dose optimisation e.g. dose-painting
Molecular imaging	Biologic, genotypic, or phenotypic tumour data	Volumetric dose calculation within which selective target dose optimisation e.g. dose painting

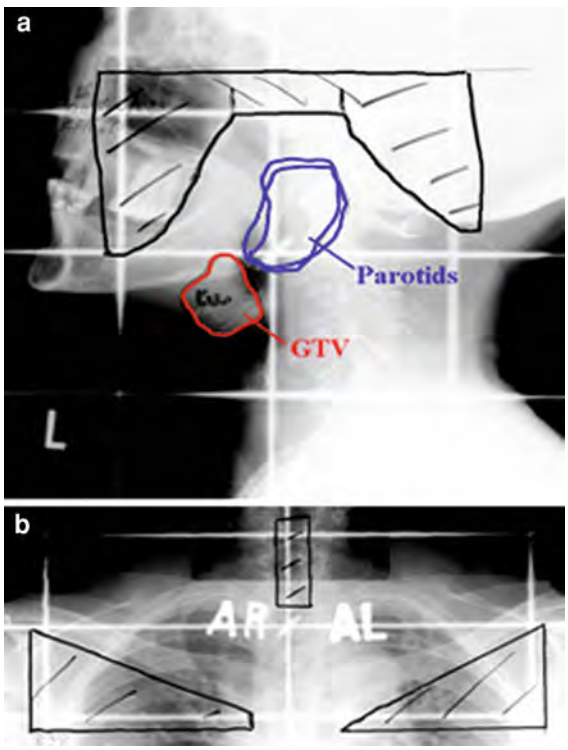

Fig. 1 Standard 2D radiation portals: 2 lateral opposed fields (**a**) and a lower anterior field (**b**). Abbreviation: GTV= gross tumour volume

fibrosis, myelitis, and osteonecrosis. Acute and late toxicity was one of the limitations in the 2D era resulting in an inability to increase the total dose above approximately 74 Gy; others included irradiation of extensive areas of mucosa and the critical issue of matching of sequential fields.

Over the past 20–30 years, these issues led to the development of CT-based RT, during which time CT simulation has become routine. Tumours and OARs are outlined on serial axial CT slices by the radiation oncologist and then reconstructed in three-dimensions. Computer-based treatment planning systems show a 'beam's eye view' projection of the patient's anatomy as seen from the radiation source, demonstrating which structures are present in the beam's path. Based on this geometry, beam and table angles and field sizes can be optimised for each field. Following international guidelines for dose computation, a treatment plan is developed using electron densities and tissue depths from the planning CT. Isodoses are volumetrically overlaid on the CT slice dataset forming a 3D model of the patient (Fig. 2). Dose–volume histograms, graphical representations of the dose delivered to a certain structure by volume, are also displayed. The beams in this 3D conformal radiation therapy (3DCRT) technique are more precisely targeted than in the 2D era, but within each, there is uniform dose intensity.

To improve the therapeutic index further, IMRT was introduced in the 1990s. As its name implies, IMRT allows the modulation of intensity within each radiation beam, so that each may contain one or more areas of high intensity, and other areas of lower intensity. By modulating the intensity within each field as well as the number of fields, radiation dose can be elegantly sculpted around the tumour (Fig. 2). The head and neck is an ideal site for this highly conformal RT due to the complex geometry of this area, the extremely small distances between tumour and critical structures, and the significant impact of radiation-induced toxicity on quality of life (QoL). Advantages of IMRT include: the ability to deliver treatment to an irregularly-shaped or concave volume; administration of different doses to different areas simultaneously [the simultaneous integrated boost

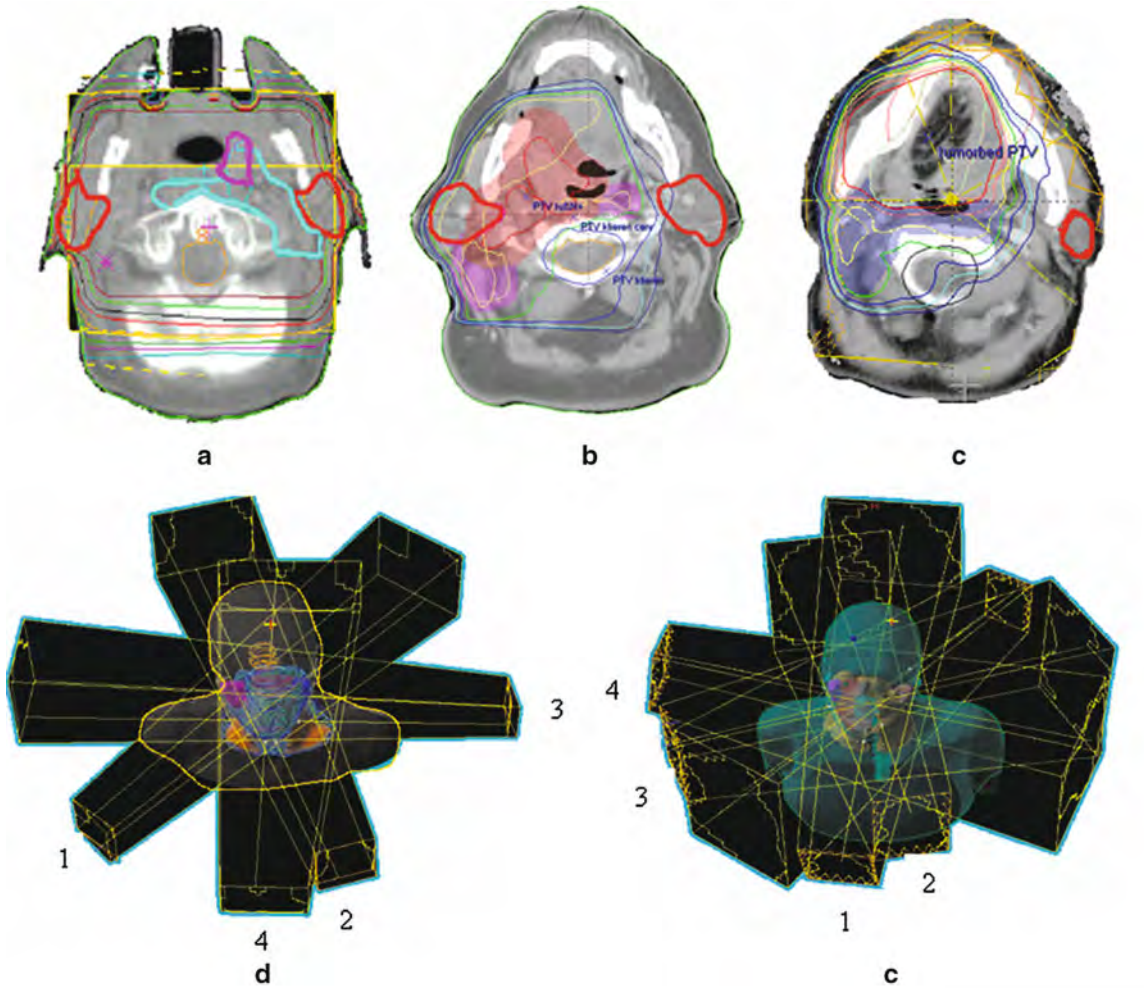

Fig. 2 Comparison between field arrangement and isodoses obtained with 2D, 3D, and IMRT planning showing sparing of contralateral parotid gland from high-dose radiation. **a** 2D plan isodoses, **b** 3D plan isodoses, **c** 5 field IMRT isodoses, **d** 3D-CRT setup with 4 fields, **e** 5 field IMRT field arrangement

(SIB) technique]; eliminating the need for field adjustments and matching; and greater sparing of normal structures such as the spinal cord or salivary glands (Bhide et al. 2010). IMRT and 3DCRT have been prospectively compared in three randomised HNC trials, two of which are published (Kam et al. 2007; Pow et al. 2006). To date, it appears that local control and disease-specific survival are equivalent, with the suggestion of improved salivary function and QoL in the IMRT patients.

Due to the highly conformal nature of the dose distribution and steep dose gradients, accurate localisation of areas to be treated is necessary to avoid geographic miss (Troost et al. 2010a). It is therefore essential that radiation oncologists have an excellent knowledge about the anatomy of the head and neck, as well as the use, advantages and disadvantages, and interpretation of different imaging modalities.

3 Overview of Imaging Used in Radiotherapy

Imaging modalities used commonly in RT delivery can be divided into two main categories: anatomical, which provide structural or morphological information, and functional, which elucidate biological or molecular features. General tumour discrimination

Table 2 Characteristics of imaging modalities used in radiotherapy

Technique	Tumour discrimination	Spatial resolution
Plain radiography	Poor	Poor
CT	Good/average	Excellent
MRI	Excellent	Excellent
PET	Good/average	Average

and spatial resolution are summarised in Table 2, and use, advantages, and limitations from a Radiation Oncology perspective are outlined below. Inter- and intra-observer variation must be taken into account in assessing comparative accuracy, but this may be offset to some degree by using complementary information from multiple imaging modalities.

3.1 CT

3.1.1 Use

CT simulation scans are essential in RT as computer-based treatment planning algorithms require CT electron density data for dose calculation. PET or MRI alone cannot be used but require co-registration or 'fusion' with CT (Dandekar et al. 2010). CT simulation scans are performed with the patient immobilized in the treatment position, on a flat table top to simulate the RT delivery machine (linear accelerator) patient couch. Radio-opaque markers on skin reference marks are used in patient set-up at the time of treatment. CT slices are typically 2–10 mm thick depending on the site to be imaged, and the scanner is ideally networked to treatment planning software to enable direct data transfer.

3.1.2 Advantages

- good contrast between air, fat, and bone
- widespread availability
- relatively inexpensive
- good geometric accuracy
- visualisation of anatomy for comparison with diagnostic imaging
- spiral and multi-slice CT with reduced scanning times
- contrast agents improve tumour discrimination
- provides electron density information for tissue inhomogeneity corrections for accurate dose modelling
- multiplanar reconstruction

3.1.3 Disadvantages

- CT scans represent anatomic information regardless of biological changes making differentiation between malignancy and benign processes that cause morphologic changes difficult (Dandekar et al. 2010)
- differentiation difficulty between tumour edges and adjacent normal soft tissue
- artifacts caused by contrast agents and high-density structures such as tooth fillings can obscure anatomy and pathology in proximity
- high-density structures also hamper the conversion of tissue signal to electron density
- radiation dose

3.2 Magnetic Resonance Imaging

3.2.1 Use

MRI provides multi-planar anatomical information with high-contrast resolution. CT/MRI fusion is standard for HNC RT planning, especially for nasopharyngeal, oral tongue, and paranasal sinus carcinomas (Fig. 3). MRI-visible markers can be used to indicate skin reference marks.

3.2.2 Advantages

- no patient radiation dose
- excellent delineation of soft tissue, intracranial infiltration and perineural spread
- flexibility in imaging sequences and planes allowing optimisation according to tissue of interest
- functional and molecular imaging capabilities such as diffusion-weighted (DW) MRI

3.2.3 Limitations

- does not provide inhomogeneity (electron density) information
- patient positioning may be a problem as scanner aperture is usually small
- long scan times
- geometrical distortion created at the edges of the field must be corrected

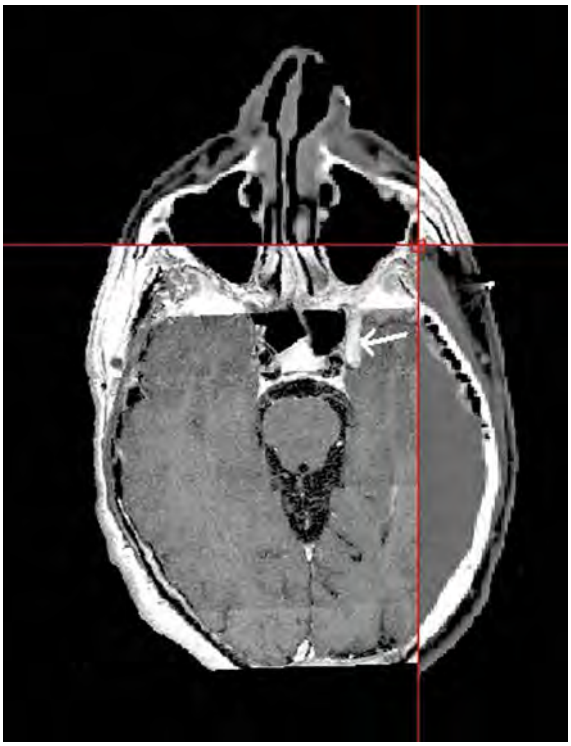

Fig. 3 Example of CT/MRI fusion image. A 48-year-old male presented with recurrence of a squamous cell carcinoma of the facial skin with perineural spread along the infraorbital nerve into the fossa pterygopalatina, and extension to the lateral left cavernous sinus (*arrow*)

- susceptibility artifacts at interfaces between bone and air (Daisne et al. 2003)
- cannot be performed simultaneously with diagnostic CT or CT simulation and fusion can be challenging if slight differences in patient position are present
- use of immobilisation masks (required for RT positioning) during MRI can preclude the use of a dedicated head and neck coil

3.3 PET

3.3.1 Use

Technological advances in PET scanning have increased the use of this modality for RT. The hybrid PET/CT, introduced in 2001, is the technique of choice for imaging HNC for the purposes of treatment planning (Hustinx and Lucignani 2010). As with MRI, PET–CT should be acquired in the treatment position on a flat table top with appropriate RT immobilisation. The presence of RT department staff can help ensure accuracy, consistency, and patient comfort in positioning (Dandekar et al. 2010). Registration of the CT component with the CT simulation scan improves image fusion accuracy (Dandekar et al. 2010).

3.3.2 Advantages

- PET can define a metabolically active biological target volume (BTV) (Dandekar et al. 2010)
- detection of distant metastases or second primary tumours
- hardware fusion of hybrid PET–CT scanners provide better localisation than stand-alone PET scanners (Dandekar et al. 2010)
- new tracers under development
- during follow-up, differentiation of fibrotic scar from residual viable tumour after RT

3.3.3 Limitations

- false positive readings due to physiological tracer uptake in brain, salivary glands, laryngeal muscles, skeletal muscle, heart, and brown fat
- false positives can also be caused by infection, inflammation, or reactive LN
- uptake of ^{18}F-FDG is influenced by tumour blood flow, blood glucose level, glucose consumption, and activity of glucose transporters and hexokinase (Dandekar et al. 2010)
- relatively low specificity
- poor spatial resolution
- radiation dose
- lack of a standardised method of signal segmentation
- does not provide accurate information on external and internal body contours (Daisne et al. 2003)

4 Applications of Imaging Data in Radiation Oncology

Imaging of tumours and surrounding normal tissues is used for several purposes:

a. diagnosis and staging
b. RT planning
c. treatment verification
d. response prediction
e. follow-up

4.1 Diagnosis and Staging

Conventional staging includes clinical examination, US, examination under anaesthesia, endoscopy, CT, and MRI to determine size and location of the primary tumour, extent of LN involvement, and to exclude distant metastases and concurrent second primaries.

4.1.1 Primary Tumour and Cervical Lymph Nodes

US can be used as a diagnostic tool for unexplained neck masses. In 42 patients who ultimately had a confirmed tissue diagnosis of HNC, the sensitivity and specificity of US was 96.8 and 93.3% respectively (Hwang et al. 2009).

^{18}F-FDG PET might be superior to CT or MRI at detecting involved cervical LN (Laudenbacher et al. 1995; Adams et al. 1998). The average sensitivity and specificity of PET is 84 and 96%, respectively, compared to 69 and 68% for CT or MRI. However, other studies have suggested that ^{18}F-FDG PET offers little additional information (Stoeckli et al. 2002; Benchaou et al. 1996). Addition of ^{18}F-FDG PET/CT to CT and MRI did increase the specificity (86 vs. 60%) and sensitivity (89 vs. 62%) for the detection of pathological retropharyngeal LN (Chu 2009). PET is limited in its ability to detect small lesions. Brink et al. (2002) showed a sensitivity of 83% for nodes larger than 1 cm^3, but for smaller LN the sensitivity dropped to 71%.

A recent meta-analysis included 1,236 analysable patients from 32 retrospective and prospective studies investigating ^{18}F-FDG PET scans used for neck staging (Kyzas et al. 2008). The authors excluded from consideration studies with a risk of verification bias, those with planned neck dissection, those without histologic correlation, and those including patients being investigated for recurrence. PET interpretation was both qualitative and quantitative and in only five studies was it performed in a blind fashion. All included studies which used single-modality PET scanners rather than integrated CT/PET. The overall sensitivity and specificity (79 and 86%, respectively) was slightly but not statistically higher than conventional imaging. In patients with clinically negative necks ($N = 311$), sensitivity of PET was 50%, and not statistically better than conventional imaging. The method of PET interpretation did not impact diagnostic accuracy (Kyzas et al. 2008).

For imaging of the primary tumour, as reviewed by Troost et al. (2010a) PET has an overall sensitivity of 93–100%, specificity of 90–100%, and accuracy of 94–98%. For patients with histologically-proven squamous cell carcinoma in a neck LN of unknown origin despite conventional workup, PET can detect the primary in up to 25% of cases (Troost et al. 2010a).

4.1.2 Pathoradiologic Correlation Studies

Eighteen patients with stage II–IVB or recurrent HNC underwent ^{18}F-FDG PET and contrast-enhanced CT followed by surgical resection within 1 month (Burri et al. 2008). PET scans were reviewed in a blinded fashion and no baseline MRIs were performed. Three-dimensional pathologic data were available for 12 tumours. Mean tumour standardised uptake value (SUV) was 14.2 (range 2.6–43.3). PET had a sensitivity of 94% for primary tumours (compared to 82% for CT) but correctly identified five tumours missed by CT. PET sensitivity was 90% for neck disease compared to 67% for CT; specificities were identical at 78%. Although multiple values were investigated, a SUVmax threshold of 40% or greater showed the best compromise between accuracy and risk of underestimating disease extent, and also correlated best with pathologic volumes (Burri et al. 2008).

Three protocols for staging of HNC were compared in 44 patients who underwent surgical resection of the primary and neck dissection within 6 weeks of imaging (Rodrigues et al. 2009). The imaging protocols were contrast-enhanced CT, whole body ^{18}F-FDG PET/CT, and dedicated head and neck high-resolution contrast-enhanced ^{18}F-FDG PET/CT. There was no statistical difference between the two PET protocols, but both were significantly better than CT in evaluation of the primary tumour. The dedicated head and neck PET outperformed whole body PET in detection of cervical LN metastases, particularly those <15 mm (Rodrigues et al. 2009).

In a landmark study, Daisne et al. (2004) compared co-registered CT, MR, and ^{18}F-FDG PET scans in 29 patients with HNC, of whom nine (all T4 larynx) underwent radical surgery. The surgical specimen was

also coregistered with the images in an internally validated technique accurate to within 2.1 mm. Gross tumour volumes (GTVs) were retrospectively delineated on CT and MRI by one investigator and reviewed by another. For PET scans, GTVs were delineated automatically using a signal-to-noise ratio segmentation algorithm. Gross tumour infiltration in the surgical specimen was determined by a pathologist without knowledge of imaging results. The authors found that the average GTV_{PET} was significantly smaller than GTV_{CT} or GTV_{MRI}; however, GTV_{PET} were not totally encompassed by that of the other two modalities. CT and MRI volumes were not significantly different in size, but did not completely overlap. In comparison with the reference surgical specimen, all imaging modalities overestimated actual tumour size with GTV_{PET} closest to reality. CT volumes were up to 107% larger, and PET overestimated by up to 46%. Areas visualised best by CT were the peritumoural soft tissues as well as tumour extension in the region of the pharyngeal wall. MRI best depicted infiltration of muscle, cartilage, extralaryngeal tissues and the parapharyngeal space. All three imaging modalities failed to identify a small fraction of macroscopic tumour, approximately 10%, mainly superficial mucosal or extralaryngeal extension (Daisne et al. 2004).

Alternative PET tracers investigated for HNC staging include 0-2-fluro-(18F)-ethyl-L-tyrosine (FET). In one such study, Balogova et al. prospectively compared the diagnostic performance of ^{18}F-FDG versus ^{18}FET-PET/CT. ^{18}FET-PET had significantly improved specificity (100 vs. 63%) but lower sensitivity (64 vs. 95%). The authors concluded that based on the sensitivity, ^{18}FET was not a suitable tracer for HNC staging (Balogova et al. 2008).

Diffusion-weighted MRI detects differences in tissue microenvironment due to random displacement of water molecules. This movement, occuring between pairs of opposing magnetic field gradients, is detectable as signal loss proportional to the amount of movement and the strength of the gradient. These differences are quantified as apparent diffusion coefficients (ADC) which are inversely correlated with tissue cellularity. From 2004 to 2006, 33 patients scheduled for surgical treatment of biopsy-proven HNC underwent 1.5 T turbo-spin echo (TSE) MRI and DW-MRI the day before surgery (Vandecaveye et al. 2009). DW-MRI images were read a mean of 18 months after surgery in a blinded fashion. The specimen was progressively dissected then matched to the TSE MRI. Nodal stage was determined by consensus between a pathologist, radiologist, and radiation oncologist. Six hundred and fifty LNs were identified in the surgical specimen, 301 identified by DW-MRI and 76 were metastatic. The majority of nodal metastases showed no distinct radiologic morphologic abnormalities. TSE MRI had a sensitivity of 46%, specificity of 96%, and an accuracy of 83% for nodal disease, with DW-MRI sensitivity 84%, specificity 94%, and accuracy 91%. Neither of the MRI protocol could detect LN metastases smaller than 4 mm. The ADC was significantly lower for metastatic than for benign LN likely due to the hypercellularity, cellular polymorphism and increased mitoses of malignancy (Vandecaveye et al. 2009). It must be kept in mind that a false decrease in ADC may be due to nodal reactive changes (germinal centres and fibrotic stroma) acting as microstructural barriers. These changes may be most apparent in small LN close to metastatic ones due to a tumour-induced immunologic response (Vandecaveye et al. 2009). The high negative predictive value of DW-MRI for lymphatic metastatic disease may help decision-making in the setting of planned neck dissection or determination of RT treatment volume.

4.1.3 Distant Metastases and Second Primaries

^{18}F-FDG PET may detect previously unrecognized distant metastases or second primary malignancies (Hustinx and Lucignani 2010). Senft et al. (2008) investigated the added value of ^{18}F-FDG PET in screening HNC patients at high risk for distant metastases (multiple or bilateral LN, low-neck LN, LN $\geq$6 cm, tumour recurrence, or second primary tumours). Of 92 evaluable patients, the mean age was 59 and more than 50% had either oropharynx or oral cavity primaries. All underwent chest CT and PET and the gold standard was clinical status after 12 months' follow-up. Each imaging modality was interpreted without knowledge of the other. Thirty-one percent of patients with a negative CT chest at baseline developed distant metastases or a second primary by 12 months. Fifteen percent of patients with negative screening PET developed distant metastases and 2% a second primary within 12 months. Compared to CT, PET had a higher

sensitivity with a slightly higher negative predictive value and accuracy, while the combination of both had the highest sensitivity (63%). The authors' concluded that screening with both modalities should be performed (Senft et al. 2008).

Haerle et al. (2010) retrospectively reviewed ^{18}F-FDG PET/CT results in 311 patients of mixed HNC subsites undergoing staging panendoscopy between 2002 and 2007. Ninety percent had stages III or IV disease and underwent PET primarily to screen for distant metastases. The gold standard was histologic information (when available) or clinical status after 6 months' follow-up. Panendoscopy detected second primaries in 4.5% compared with 6.1% detected by PET within the coverage area of endoscopy. All lesions detected by endoscopy were also detected by PET, which found five additional malignancies. Sensitivity was 100% for PET/CT versus 74% for panendoscopy; specificity was 96.5 and 99.7%, respectively. The authors felt that PET was not cost-effective in early-stage disease, as panendoscopy was sufficient due to its high accuracy. In patients with advanced HNC, ^{18}F-FDG PET is recommended to routinely exclude distant metastases. But with advanced disease and a negative PET, endoscopy could be restricted to the area of the primary tumour (Haerle et al. 2010).

4.2 Radiotherapy Planning: Anatomic Information

In treatment planning, it is essential to accurately differentiate tumour from normal adjacent tissue. Evidence is growing that complementary morphological information from imaging such as MRI can help decrease variability in tumour delineation.

4.2.1 CT

CT is routinely used for delineation of tumour volumes and is considered to be the gold standard at present. CT-based delineation of metastatic LN is usually less prone to error than that of the primary disease due to differentiation from surrounding fatty tissue (Troost et al. 2010a). However, both inter- and intra-observer variability in volume delineation exists. Hermans et al. investigated this variability in CT studies of 13 laryngeal tumours reviewed by five different observers, each of who repeated the delineation exercise four times. Both inter-, and to a lesser extent, intraobserver variability had a statistically significant effect on resulting volumes. The most experienced participant obtained the most stable mean tumour volume (Hermans et al. 1998). The authors concluded that variability can be reduced by having a single experienced reader to perform all delineations. In practice, however, each physician typically performs the RT planning for their own patients, so several groups have published guidelines to facilitate reproducible delineation of primary tumours and LN regions (Gregoire et al. 2003; Chao et al. 2002; Eisbruch et al. 2002).

4.2.2 MRI

Because of the superior soft-tissue contrast of MRI, it is the preferred imaging modality to demonstrate oral cavity, nasopharyngeal and oropharynx malignancies, for example (Troost et al. 2010a). Rash et al. studied the potential impact of the combined use of CT and MRI on volume delineation in advanced HNC. Four participants outlined the GTV in six patients with cancers involving the base of skull on CT, as well as axial, coronal, and sagittal MRI. GTV_{MRI} were on average 30% smaller, with less interobserver variation than CT-derived GTVs (Rash et al. 1997). Enami et al. examined MRI and CT in eight nasopharyngeal patients. Compared with CT, MRI-based targets were 74% larger and more irregularly shaped. On average, composite CT + MRI GTVs were 10% larger than GTVs drawn from MRI alone. The authors concluded that fusion of MRI and CT images would significantly reduce the possibility of geographic miss in this tumour site (Enami et al. 2003).

4.3 Radiotherapy Planning: Biological Information

4.3.1 ^{18}F-FDG PET

Besides the location, size and extent of the tumour, knowledge about biological features is useful in the management of HNC. Potential roles of ^{18}F-FDG PET include: reduction of inter-observer variability in tumour delineation, reduction of the size of the GTV, identification of tumour extension missed by CT or MRI, decision-making in the case of marginally enlarged LN, the identification of parts of the tumour potentially benefiting from additional radiation dose,

and adaptation of the treatment plan during RT (Troost et al. 2010a). Biological or molecular techniques may allow improved detection of micrometastases either directly, or as a result of better assessment of the characteristics of the primary (Mahfouz et al. 2010).

The definition of "metabolic" or "biological" tumour volume remains a challenging one, however, and there is no consensus regarding the optimal method for segmenting a metabolically active lesion (Hustinx and Lucignani 2010). In order to use ^{18}F-FDG PET to optimally delineate volumes, the way the PET images are interpreted must be known. The best method of PET interpretation for RT applications is unknown at this time and options include:

- visual (qualitative)—generally leads to larger volumes, is operator-dependent, and susceptible to window–level settings
- SUV-based methods—percent maximum peak SUV, fixed arbitrary SUV, threshold SUV, fixed percent SUV relative to the maximum activity in the tumour (usually 40–50%)
- background cutoff (defined with respect to the background FDG signal)—can be automated, and may be affected less by heterogeneity of lesion tracer uptake
- automated or semiautomated methods—provide consistent target delineation with a significant saving in contouring time

The impact of PET imaging on target delineation in RT for HNC has recently been investigated. Syed et al. (2005) examined the impact of ^{18}F-FDG PET/CT in 24 patients and concluded that PET/CT significantly increases interobserver agreement in disease localisation. Scarfone evaluated the influence of ^{18}F-FDG PET on tumour volumes of six patients which were delineated on CT and then modified based on PET data. The resulting GTV_{PET} was larger than the GTV_{CT} by an average of 15%. The final GTV_{PET} LN volume was on average 17% larger (Scarfone et al. 2004). Koshy et al. also used PET in 36 patients with HNC as part of their RT planning. In 14%, PET/CT fusion altered RT volumes, and dose was altered in four patients (Koshy et al. 2005). PET–CT detected 39 positive nodes in contrast to 28 detected by clinical examination, CT, or MRI in a study by Nishioka et al. In four patients, the nodal stage increased, which impacted on target delineation. Parotid-sparing became possible in 71% of patients whose neck was determined to be tumour-free on PET, and, except for one patient, no recurrences were seen 18 months after treatment of the GTV_{PET} (Nishioka et al. 2002).

Schinagl compared co-registered ^{18}F-FDG PET with CT for assessment of LN in 78 patients. Of 108 nodes classified on CT as enlarged (shortest axial diameter of $\geq$10 mm), 75% were also identified as enlarged by PET using visual interpretation, and between 43 and 59% by other PET segmentation methods. Of 100 LN classified as marginally enlarged (7–10 mm), only a minority were visualised by PET. Volume and shape of the resulting GTVs were influenced heavily by the method of segmentation. All automated segmentation methods yielded significantly smaller GTVs than those based on clinical information and CT; visual interpretation yielded volumes closer to that of GTV_{CT}. Depending on the segmentation tool used, more than 20% of the GTV_{PET} was located outside the GTV_{CT}. However without a histologic gold standard, it is possible that PET uptake in this area could be a result of peritumoural inflammation (Schinagl 2009).

Studies addressing integration of PET into IMRT treatment planning, recently reviewed by Troost et al. (2010a), are encouraging, although tend to be retrospective, small and heterogeneous, with short follow-up and historical controls. Paulino et al. compared the GTV identified on CT to that obtained from ^{18}F-FDG PET in 40 patients with HNC treated with IMRT. The GTV_{PET} was smaller, the same size, or larger than the GTV_{CT} in 75, 8, and 18% of cases, respectively. In approximately 25% of patients, tumour would have been underdosed if PET had not been performed. The authors recommended use of both CT and PET in determining the GTV for IMRT in head and neck malignancy (Paulino et al. 2005).

Yu et al. used a co-registered multimodality pattern analysis segmentation system (COMPASS) to automatically delineate radiation targets in HNC using ^{18}F-FDG-PET and CT. This innovative system extracts textural features such as coarseness and contrast from PET and CT voxels, each of which is labelled "normal" or "abnormal". The COMPASS system was applied to the images of ten patients and results compared with those of three PET threshold-based methods (SUV of 2.5, 50% maximal intensity and signal/background ratio). The gold standard was considered to be the manual contouring of three radiation oncologists. The COMPASS tumour

delineations were more similar to those of the physicians than those based on other methods, especially in regions adjacent to tissues with high PET uptake. Validated automated segmentation methods may in future decrease inter-observer variability and uncertainty in target delineation (Yu et al. 2009).

4.3.2 Dose Painting

Most treatment failures occur in the high-dose RT volume, suggesting that the dose delivered is insufficient to ablate malignant cells. Dose escalation to the entire target volume is not possible, however, due to normal tissue toxicity. The term 'dose painting' implies non-uniformity within a target region, to direct dose to subregions of tumour in order to improve local control. IMRT has the ability to deliver non-uniform dose distributions, but the question is, which areas should be targeted? Focusing a high-dose boost to a BTV, the hypermetabolic area on a PET scan could improve response rates (Ling et al. 2000). Likewise, eliminating PET-negative regions from prophylactic radiation volumes could reduce the dose to OARs. Therefore, imaging methods are being developed to provide biological information regarding tumour hypoxia, proliferation, apoptosis, angiogenesis and receptor status, and all aspects of the tumour microenvironment relevant to radiation resistance (Chapman et al. 2003; Bussink et al. 2010).

4.3.3 Hypoxia

Hypoxic cells are 2.5–3 times more resistant to radiation than well-oxygenated cells and hypoxia is therefore a major determinant of tumour response to RT. A variety of methods have been used to measure oxygenation of tumours including needle electrodes (Nordsmark and Overgaard 2004). This technique has several drawbacks including invasiveness, lack of discrimination between necrotic and viable hypoxic tissue, sampling error, and requirement of accessibility. Non-invasive techniques to identify hypoxia have recently sparked interest in terms of suggesting areas which could benefit from dose escalation (Troost et al. 2010a).

Tumour perfusion rate was investigated by Hermans et al. with dynamic CT in 105 patients treated with RT. Intravenous contrast was rapidly injected while dynamic axial data acquisition was performed at the level of the largest tumour dimension. Perfusion rate was calculated using the time–density curve of the tumour and the maximal arterial density. When patients were stratified according to median perfusion value, those with lower perfusion rates had a significantly higher local failure rate (Hermans et al. 2003).

^{62}Cu-diacetylbis-N-4-methyl-thiosemicaarbazone (Cu-ATSM) has been investigated as a PET marker for hypoxia because of its rapid uptake, activity ratio, rapid blood clearance, and washout from normally oxygenated cells. Chao et al. examined the feasibility of dose escalation to areas identified as hypoxic by Cu-ATSM PET in an IMRT planning study. Based on co-registration of Cu-ATSM PET to CT images, 80 Gy total dose in 35 fractions could be safely delivered to the hypoxic target volume, and 70 Gy/35 to the remainder (Chao et al. 2001).

^{18}F fluorinated misonidazole (^{18}FMISO) is reduced and incorporated into cells under hypoxic conditions and has also been investigated as a PET tracer (Koh et al. 1992; Chapman et al. 1983). Jansen explored the microenvironment of neck LN metastases in HNC patients, examining the relationship between tumour perfusion measured by dynamic contrast-enhanced MRI (DCE-MRI) and hypoxia measured by ^{18}FMISO-PET. Matched regions of interest from both modalities were analysed in 13 newly diagnosed patients. The authors found a strong negative correlation between perfusion parameters and ^{18}FMISO SUV, supporting the hypothesis that metastatic neck LN are poorly perfused and therefore likely relatively hypoxic (Jansen et al. 2010).

Eschmann et al. (2005) compared ^{18}FMISO-PET uptake with clinical outcome after treatment. Twenty-six patients with HNC were scanned before RT, and ^{18}FMISO uptake was quantified using SUV and tumour-to-background ratios. Patients with local recurrence could be separated from disease-free patients by the SUV 4 h after injection, at which timepoint all recurrences had SUV >2. All patients with a tumour-to-muscle ratio >1.6 experienced tumour recurrence. The authors also reported temporally inconsistent ^{18}FMISO distribution in that the location of regions which met the criteria for hypoxic changed with time.

The potential of ^{18}F-FDG-PET, ^{18}FMISO-PET, DW-MRI and dynamic contrast-enhanced (DCE)-MRI to provide a potential BTV for dose painting was evaluated by Dirix and colleagues. After intravenous injection of a paramagnetic contrast agent, DCE-MRI

shows tissue signal intensity increase on T1-weighted scans (Dirix et al. 2009). Changes in signal intensity on DCE-MRI are related to tumour permeability, perfusion and interstitial pressures, which may influence treatment response. Fifteen patients with locally advanced HNC participated in a study of sequential CT/PET with ^{18}F-FDG PET, ^{18}FMISO PET and 1.5 T MRI performed before, during, and after radical RT (Dirix et al. 2009). GTVs delineated by the treating radiation oncologist were retrospectively retrieved while the GTV_{PET} was automatically segmented based on source-to-background ratio. The GTV_{MRI} was manually delineated by a radiation oncologist and radiologist in consensus. There was an excellent correlation between CT- and MRI-based volumes, and all volumes showed significant shrinkage over the course of RT, by approximately 50% (Dirix et al. 2009). Both the GTV_{PET} and $GTV_{DW\text{-}MRI}$ were significantly smaller than the GTV_{CT}. Over a median follow-up of 30.7 months, disease recurred in seven patients; all recurrences were located within the area of overlap of the GTV_{CT}, GTV_{MRI}, and GTV_{PET}. There was little residual hypoxia on follow-up ^{18}FMISO PET scan during the fourth week of treatment. DW-MRI showed residual disease in three patients and all developed locoregional recurrence. At 8 weeks after the end of treatment, ^{18}F-FDG PET suggested residual disease in two patients, both of whom ultimately recurred. DFS correlated negatively with baseline maximum tissue-to-blood ^{18}FMISO ratio (T/Bmax), size of the hypoxic volume at baseline, and with T/Bmax on the ^{18}FMISO scan during treatment. Three of the locoregional recurrences were outside the hypoxic volume defined by baseline ^{18}FMISO PET. Compared with lesions that remained controlled, those which recurred had significantly lower ADC on DW-MRI during and after RT, and a significantly higher initial slope on baseline DCE-MRI. The authors caution that interpretation of DW- and DCE-MRI scans in this area is not straightforward, and suggest the use of quantitative or semiquantitative measurements for volume definition assistance (Dirix et al. 2009).

Newer generations of nitroimidazoles have also been studied, including ^{18}F-labelled fluoroerythronitroimidazole (FETNIM), fluoroetanidazole (FETA), and 2-(2-nitro-1[H]-imidazol-1-yl)-N-(2,2,3,3,3-pentafluoropropyl)-acetamide (EF5). FETNIM and FETA are both stable in the context of non-oxygen-dependent metabolism and have higher tumour-to-background contrast secondary to increased hydrophilicity (Lehtio et al. 2001; Rasey et al. 1999; Yang et al. 1995). EF5 has been used for immunohistochemical detection of hypoxia, with a future possibility of correlating this with PET results (Ziemer et al. 2003). FETNIM has been used clinically to determine the oxygenation status of patients undergoing RT.

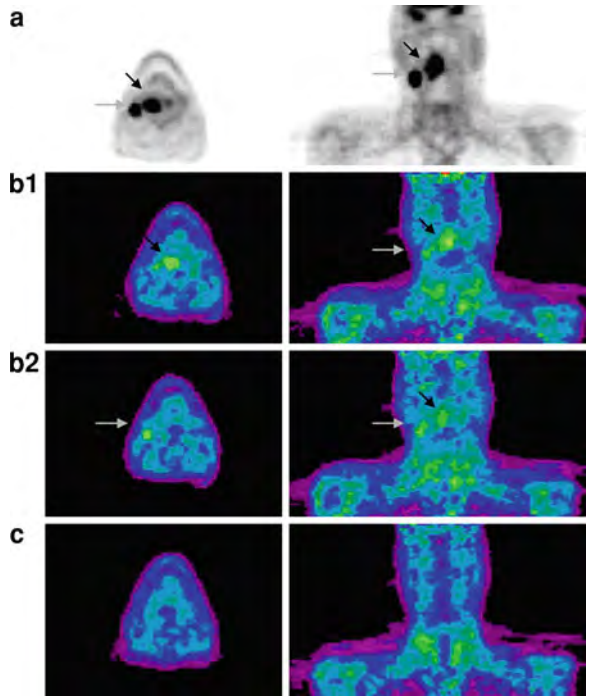

Fig. 4 Temporal change in hypoxia. A 57-year-old patient presented with stage T3N2b squamous cell carcinoma of the oropharynx. Baseline ^{18}F-FDG PET (**a**) shows uptake at the primary tumour (*black arrow*) and regional lymph node (*grey arrow*). ^{18}FMISO PET acquired 1 day later (**b**1–2) indicates hypoxia in both the primary tumour (**b**-1 *black arrow*) and lymph node (**b**-2 *grey arrow*). Repeat ^{18}FMISO PET after 4 weeks of radiotherapy (**c**) shows decreased ^{18}FMISO uptake

Temporal and geographic stability is a significant concern for hypoxia-based dose escalation (Troost et al. 2010b). Acutely this is related to microscopic changes in oxygenation caused by intermittent opening and closing of vessels (Chapman et al. 1983) (Fig. 4). Reoxygenation of regions which are hypoxic at baseline will likely occur over the course of curative-intent RT. Also unknown is what RT dose is required to eliminate hypoxic subpopulations (Troost et al. 2010b). More work is required to elucidate the

evolution in intratumoural hypoxia before single hypoxia-tracer PET images can be used as a basis for dose escalation (Dirix et al. 2009).

4.3.4 Proliferation

Uncontrolled proliferation is one of the hallmarks of malignancy. Tumour subvolumes with evidence of high rates of proliferation may also benefit from dose escalation. The degree of metabolic activity detected by ^{18}F-FDG may be a surrogate for tumour cell density as slowly proliferating tumours generally show less uptake than rapidly proliferating ones. ^{18}F-FDG is prone to false positives, however, for the reasons outlined in Sect. 3. Therefore, more specific tracers have been investigated.

Radiolabelled nucleosides can be used to quantify DNA synthesis and radiolabelled amino acids can be used as markers for protein synthesis. In terms of nucleoside tracers, the most studied is ^{18}F-labelled fluorothymidine (FLT), a pyrimidine analogue (Dandekar et al. 2010). FLT has high-specific activity and good tumour-to-background ratio (Shields et al. 1998). Cobben et al. studied ^{18}FLT PET for visualisation of laryngeal cancer in 21 patients in comparison with ^{18}F-FDG PET. While an equal number of tumours were detected with each modality, higher absolute uptake of ^{18}F-FDG than ^{18}FLT was reported (Cobben et al. 2004). Because less tracer is taken up compared to glucose uptake, sensitivity of FLT imaging may be relatively low (Buck et al. 2003). Troost et al. (2010b) attempted to use ^{18}FLT PET for adaptive RT in oropharyngeal patients, but concluded that PET segmentation methods could not be directly extrapolated to ^{18}FLT as the resulting volumes were unsatisfactory. ^{18}FLT PET may be useful in future to direct RT to primary tumour sites as it is not influenced by peritumoural inflammation. However, it is unlikely that ^{18}FLT neck imaging will be practical as false positives are caused by uptake in germinal centres of metastatic LN.

The most studied amino acid tracers are ^{11}C-methionine (MET) and ^{11}C-tyrosine, which are surrogate markers of high rates of protein metabolism (Dandekar et al. 2010). Amino acid tracers may better discriminate between tumour and inflammation because inflammatory cells have lower protein than glucose metabolism (Kubota et al. 1995). Geets et al. studied the role of MET PET for delineation of tumour volume in pharyngo-laryngeal squamous cell carcinomas. Twenty-three patients were imaged with CT, ^{18}F-FDG PET, and MET PET before treatment (RT or surgery). MET PET volumes did not differ from CT volumes, while the ^{18}F-FDG volumes were significantly smaller. The authors concluded that MET PET does not provide additional value information over CT, probably because of the confounding effect of high-MET uptake by the normal mucosa and salivary glands (Geets et al. 2004).

Another indicator of proliferation is an increased cellular choline level. ^{1}H MR-spectroscopy can be used to estimate choline levels in human tumours. This procedure has successfully localised active disease in other cancer sites but data in HNC have not yet been reported.

4.3.5 Apoptosis

Apoptosis can be an indicator of intrinsic radiosensitivity because it is a major pathway of cell death after ionising irradiation. Annexin V is a protein which binds to membrane-bound phosphatidyl serine and is exposed on the surface of cells undergoing apoptosis. ^{99m}Tc-radiolabeled annexin V is therefore being tested to quantify apoptosis (Green and Steinmetz 2002). Van de Wiele et al. (2003) performed quantitative tumour apoptosis imaging using ^{99m}Tc-radiolabelled annexin V and SPECT in 20 patients planned for surgical resection. Quantitative annexin V tumour uptake values correlated well with the number of apoptotic cells on assays for apoptosis-induced DNA fragmentation, provided samples had minimal necrosis. The authors concluded that this method can be used to monitor treatment response, if treatment does not alter the diffusion-related uptake of peptides. ^{99m}Tc-radiolabelled annexin V scintigraphy has been used to monitor radiation-induced apoptotic cell death in other cancer sites, but has not yet been used in the setting of HNC.

4.3.6 Receptor Status

Proliferation of many tumours is regulated by factors that bind to membrane or intracellular receptors to activate signal transduction pathways. Imaging of receptor status therefore might provide information that can be used to guide treatment and prognosis. For example, epidermal growth factor receptor (EGFR) is a transmembrane glycoprotein involved in activating

several pathways associated with proliferation, migration, stromal invasion, angiogenesis, and resistance to cell death-inducing signals (Dancey 2004). EGFR is overexpressed in 80–100% of HNC (Grandis et al. 1996), and this overexpression is associated with both increased metastatic potential and poor prognosis (Ang et al. 2002). Contrast agents to visualise EGFR are under development, such as radiolabelled cetuximab.

In summary, functional imaging to guide RT planning is promising, but still needs to be validated through clinical studies before it can be incorporated in daily practice. Outcome data on this approach are pending at this time and more work remains before most of the tracers discussed can be used for patient treatment decisions.

4.4 Treatment Verification

Treatment verification refers to the use of imaging to ensure that RT fields are appropriately localised throughout the entire treatment period, taking into consideration factors such as patient immobilisation and positioning. Commonly in head and neck RT, masks or shells are custom-made for the patient's anatomy and are then fixed to the table to prevent movement during treatment (intrafraction) and on a daily basis (interfraction). This ensures the ability to re-establish the patient's position each day, which can be affected by several factors: changes in tumour size and shape; organ movement such as respiration or swallowing; anatomic variation; and patient set-up errors.

Image-guided radiotherapy (IGRT), defined as the use of on-board imaging to improve patient set-up accuracy (Castadot et al. 2010), allows verification of the correct position of the RT field prior to treatment initiation. There are several ways to accomplish this. Traditionally, a 'port film' used the portion of the accelerator beam exiting from the patient to expose commercially available radiographic film. This has less diagnostic quality but it is sufficient for comparison to planning images for gross errors. The next generation is called electronic portal imaging (EPI), which uses fluorescent screens, 2D ion chambers, or matrix flat panel imagers and are again compared with a reference image. These 2D online electronic images have made it possible to correct patient positioning in real time, just before radiation is delivered (Fig. 5).

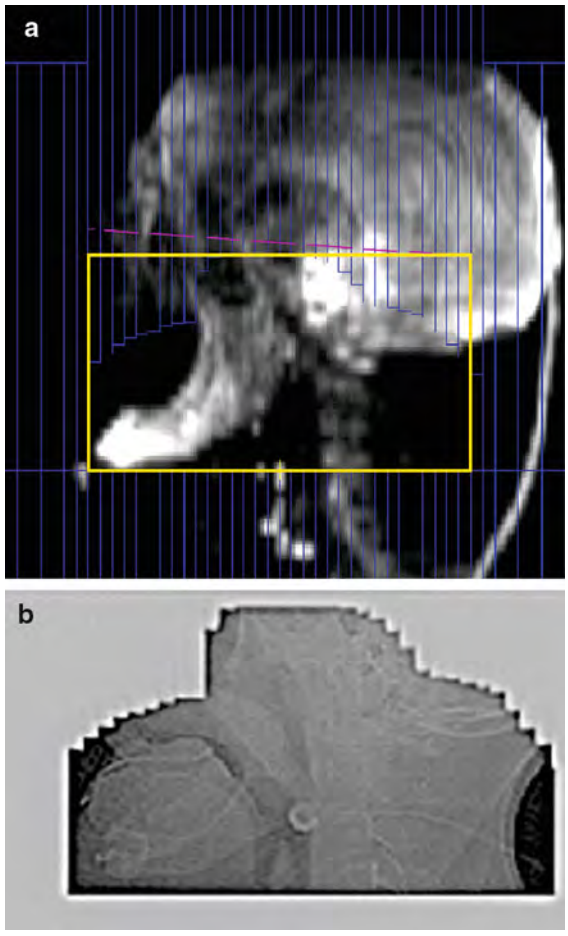

Fig. 5 Comparison between digitally reconstructed radiograph derived from CT simulation images (**a**), and a port film, obtained during irradiation (**b**),which are compared to verify patient positioning and size and shape of the treatment portal

On-board cone beam CT has recently been introduced, which allows 3D verification of fields in relation to other structures, such as OARs. To create these images, an extra tube is mounted on the linear accelerator producing a divergent X-ray beam, which is captured using a portal detector opposed to the CT tube. Both make a 360° rotation around the patient. One study by Han et al. (2008) evaluating the impact of daily helical megavoltage CT-guided set-up correction reported that the median dose to critical normal structures (spinal cord and parotid glands) increased significantly when daily corrections were not applied. Techniques of adaptive RT designed to further customise treatment by minimising both systematic and random positioning errors are well reviewed by Castodot et al. (2010).

4.4.1 Adaptive Radiotherapy: 4D

As alluded to above, it is common for tumours and to some extent OARs to change over the course of curative RT. Tumour and nodal volumes shrink by up to 3% per day, changing size, shape, and position, sometimes asymmetrically. External face and neck contour modifications may be seen as patients lose weight and muscle mass. This further alters the anatomy and geometry of the disease in relation to critical normal structures. Parotid glands not only decrease in volume but also shift medially into the high-dose region with time (Castodot et al. 2010; Barker et al. 2004). Resolving post-operative changes or even disease progression during treatment can also be seen. Spatiotemporal instability of the target and normal structures and/or geometric uncertainty of patient positioning are critical in IMRT because of the sharp dose gradients involved (Castadot et al. 2010). The result of these changes is that location and dose delivered may differ significantly from what was planned.

Four-dimensional (4D) RT is the next generation in conformal treatment, which attempts to account for these changes over time. Latest generation linear accelerators are now equipped to visualise soft-tissue structures with CT while fluoroscopy tracks the breathing cycle in real time. Changes are mapped over the period of RT and treatment volumes are changed accordingly in "adaptive" or response-based therapy. Significant alterations may even involve revising the entire radiation plan (Dandekar et al. 2010).

Megavoltage cone beam CT (MVCT) allows the reconstruction of the actual delivered dose based on a patient's specific anatomy in real time (Pouliot et al. 2003; Ghilezan et al. 2004). Acquiring a low-dose MVCT image on the treatment machine immediately prior to therapy allows online verification of patient position. The same imaging device also records the portal dose during treatment. By converting this portal dose to primary fluence at the plane of the detector and backprojecting through the MVCT model of the patient, the 3D dose delivered at the time of treatment can be obtained (Welsh et al. 2002). This may allow modulation of the next day's RT dose based on the actual dose received to that point, as opposed to delivering the previously planned daily dose (Welsh et al. 2002). Optimisation in this manner could compensate for dosimetric alterations caused by anatomical or positional changes during treatment (Castadot et al. 2010).

Ten patients with stage III/IV pharyngolaryngeal tumours receiving SIB chemoradiotherapy were imaged using contrast-enhanced CT and ^{18}FDG-PET at baseline and then weekly during weeks 2–5 to investigate whether imaging reassessment influenced dose delivery (Geets et al. 2007). Eight patients also underwent MRI. Volumes were manually delineated by one investigator. PET-based volumes were delineated using an in-house validated gradient-based segmentation method. The mean primary tumour GTV significantly decreased over the course of treatment ($P < 0.001$). Functional imaging primary tumour GTVs were always smaller than those based on anatomical imaging. There was no clinically relevant difference between CT- and MRI-based volumes. By completion of 45 Gy, mean primary tumours had decreased by 54–70% compared to baseline, with all imaging modalities suggesting similar rates of reduction. PET-based adaptive IMRT produced significantly tighter dose distributions (i.e. 15–40% reduction of the volume of tissue receiving >60 Gy), but this did not significantly reduce OAR doses. One challenge with use of PET during RT, especially after the fourth week, is that images become more difficult to interpret due to inflammation of the tumour and normal tissue (Geets et al. 2007). While a potential advantage of adaptive RT is the compensation for underdosage of target volumes or overdosage of OARs, because of extra staff workload and cost, the optimal implementation strategy remains to be defined (Castadot et al. 2010).

4.5 Response Prediction Using Biological Imaging

Recognition of nonresponders or early progressors after RT is essential as these patients might benefit from intensified treatment or early surgical salvage (Farrag et al. 2010). The time window for successful salvage surgery is unfortunately limited because operability is determined not only by the likelihood of obtaining oncologic control but also by surgical reconstructive options available (Vandecaveye et al. 2007).

4.5.1 Prediction During Therapy

Farrag et al. investigated whether ^{18}F-FDG PET during treatment can predict outcome for HNC patients treated with radical RT ± chemotherapy. Over three years, 43 consecutive patients were

evaluated by history, examination, lab tests, panendoscopy, CT, and MRI. All patients also underwent PET at baseline and at the end of the fourth week of therapy (approx 47 Gy). Scans were analysed by two physicians with access to complete clinical information. Sixty-three percent of patients had either hypopharynx or oropharynx cancer, 37% received cisplatin-based chemotherapy, and 44% had T3 or T4 disease. RT was given via a SIB technique to a total dose of 66–70.5 Gy to the primary disease and involved LN. Median follow-up was 12.7 months. Two-year overall and disease-free survival was 66 and 52%, respectively. Median SUVmax decreased from baseline to follow-up PET. Both low SUVmax at baseline and on follow-up PET were significantly correlated with overall survival. There was a non-significant trend for patients with a complete metabolic response at follow-up PET to have better outcomes (Farrag et al. 2010).

Baseline and mid-treatment ^{18}FMISO PET/CT scanning has also been prospectively investigated (Lee et al. 2009). Twenty HNC patients, 90% with locally advanced oropharyngeal primaries, underwent concurrent chemotherapy and IMRT. All had pretreatment ^{18}F-FDG and ^{18}FMISO-PET/CT scans, with a mid-treatment ^{18}FMISO PET scan 4 weeks after the start of treatment. However, the authors found that ^{18}FMISO findings on the mid-treatment scan did not correlate with patient outcome (Lee et al. 2009).

Hentschel et al. used ^{18}FDG-PET to adapt RT based on the evolution of tumour metabolic activity. While the median SUVmax decreased, in this study the median sizes of GTV_{PET} and metabolic volumes actually increased during RT, likely as a result of therapy-induced inflammation. The authors concluded that treatment volumes cannot be reduced through PET-based adaptive replanning in this manner, probably due to the use of this particular type of algorithm (Hentschel et al. 2009).

4.5.2 Prediction After Therapy

After completion of RT, ^{18}F-FDG PET may assist in detection of residual viable tumour. This may be particularly useful in patients with persistently enlarged LN, in whom neck dissection may be considered (Hustinx and Lucignani 2010). However, scan interpretation after therapy is difficult because of the altered glucose consumption, necrosis, and infiltration of inflammatory cells within irradiated tissue (Farrag et al. 2010). The appropriate time to image patients post-therapy is not yet clear. Some authors have suggested that an interval of up to 12 weeks may be required before cell debris is sufficiently cleared (Bussink et al. 2010). However imaging done too late may miss the window of opportunity for salvage (Murphy et al. 2010). The reader is referred to "Positron Emission Tomography in Head and Neck Cancer" for more detail.

A retrospective study of DW-MRI in response prediction included 38 patients with pathologically confirmed HNC treated to at least 60 Gy (Hatakenaka et al. 2010). Most received concurrent chemotherapy. Salvage treatment (neck dissection and/or intra-arterial chemotherapy) was ultimately delivered to eight patients. Pretreatment DW-MRI was performed a median of 7 days prior to initial treatment. The primary lesion region of interest was determined by consensus between two radiologists and one radiation technologist without knowledge of locoregional disease status. Tumour volume, T stage, treatment, and ADC correlated significantly with local disease status. ADC had a sensitivity of 77.8%, specificity of 100%, PPV of 100%, and NPV of 80% for the prediction of local failure in stage T3/T4 disease. Low ADC values pretreatment was correlated with high local control. Kim et al. (2009) reported the usefulness of pretreatment ADC for predicting treatment response in 33 cases. They calculated the ADC values of the neck nodes, but not from the primary lesions. Pretreatment ADC value of complete responders was significantly lower than that from partial responders. The authors also performed a repeat MRI after 1 week of RT. The patients with a complete response showed a significantly higher increase in ADC than the partial responders by the first week of chemoradiotherapy. These data suggest that ADC can be used as a marker for prediction and early detection of response to therapy. In general, tumours showing a high ADC increase have a better treatment response than those with little or no ADC increase. The authors speculated that the apoptosis and necrosis of responding tumours present fewer microstructural barriers, thereby increasing ADC.

DW-MRI has also been used prospectively to assess salivary gland function before and at a mean of 9 months after parotid-sparing RT in eight patients (Dirix et al. 2008). RT was delivered to a dose of 60–72 Gy. The mean total dose to the spared parotid

gland was 20 Gy, below the 25 Gy required for functional sparing. There were no dose constraints for the other parotid or either submandibular gland; typically these glands received >40 Gy. Before RT, a biphasic response to stimulation was confirmed in both parotids of all patients, identical to the pattern seen in healthy volunteers (Thoeny et al. 2005). In unspared glands, ADC was significantly higher after RT, possibly due to fibrosis, necrosis, or both. In the spared parotid, ADC value after RT was not significantly different compared to before RT. A comparable response to stimulation as before RT was observed in the spared but not the unspared parotid (Dirix et al. 2008). This suggestion of preserved function in the spared gland was confirmed by low patient-rated xerostomia scores and salivary gland scintigraphy results. The authors hypothesise that based on this data, DW-MRI allows non-invasive assessment of salivary gland functional changes with sufficiently high spatial resolution that it could be used to improve models of dose-response relationships (Dirix et al. 2008).

4.6 Follow-Up

Long-term follow-up after radical RT for HNC aims to evaluate treatment response, manage toxicity, exclude persistent disease, detect locoregional recurrence, and monitor for distant metastases or second primary tumours (Manikantan et al. 2009). Follow-up also provides an opportunity for psychological support, symptom management, and rehabilitation of voice and swallowing. The lack of consensus in the literature on the optimum frequency of follow-up imaging reflects significant variation in clinical practice. Published surveillance protocols often lack a clear evidence base and can be resource-intensive (Manikantan et al. 2009).

Manikantan et al. reviewed the English literature (1980–2009) on follow-up with any imaging modality to compile recommendations for effective surveillance. Publications included chest X-ray, chest CT, ^{18}F-FDG PET, endoscopy, and tumour markers. There are no randomised controlled trials on the subject although expert guidelines have been published by collaborative groups. Manikantan summarised 55 studies, producing a flow chart for suggested timelines of surveillance. The first visit should take place 4–8 weeks after treatment completion and include history and physical exam. Endoscopy is indicated in symptomatic patients, and a new baseline CT or MRI should be obtained 3–6 months after RT. Thyroid function studies should be performed after any RT to the lower neck. PET should only be done if there is a discrepancy between physical findings and other imaging. Untreated clinically negative necks should be followed with examination and US-guided FNA when necessary. Chest CT should be performed in symptomatic patients and those with suspected lung metastases or second primaries. The authors recommend more intense surveillance in the first 3 years and for patients in whom a salvage option is available. There are no data proving greater efficiency for higher cost strategies (Manikantan et al. 2009). A second literature survey on ^{18}FDG PET in HNC indicates that when compared with CT, PET has a higher sensitivity (93 vs. 54%) and specificity (83 vs. 74%) for diagnosing recurrences, and higher sensitivity (84 vs. 60%) and specificity (95 vs. 39%) for monitoring effects of therapy (Gambhir et al. 2001).

However, analysis of follow-up imaging is not always straightforward. Tissue changes after RT may be striking as they evolve over time (Glastonbury et al. 2010). The complexities of image interpretation after RT were pictorially reviewed by Glastonbury et al. Radiation-induced changes may mask or mimic residual disease. Acute RT-related changes include mucositis, interstitial oedema, ischaemia, and inflammation. Late side effects are associated with fibrosis and atrophy and can appear years after treatment. Severe but uncommon late effects include osteoradionecrosis and aerodigestive tract stenosis. Deep ulcers, new enhancing masses, lymphadenopathy, or bone or cartilage destruction must be considered recurrence until proven otherwise (Glastonbury et al. 2010). Dependence on size criteria limits the use of anatomical imaging in the detection of residual subcentimeter nodal disease and in definitive exclusion of tumour in persistently enlarged LN (Vandecaveye et al. 2007).

Emerging reports suggest that DW-MRI may help to distinguish persistent tumour from post-RT changes. RT-associated tissue changes are expected to show lower cellularity (and therefore higher ADC), compared to tumour which is highly cellular (with lower ADC) (Vandecaveye et al. 2007). Twenty-six patients with suspected tumour recurrence after

chemoradiotherapy planned for salvage surgery were prospectively imaged. DW-MRI and TSE sequences were performed the day before surgery in all patients; most also underwent contrast-enhanced CT and some had panendoscopy, biopsy ,and/or ^{18}F-FDG PET. Pathology was considered the gold standard (surgical specimen in 23, biopsy in 3). The ADC was measured in each region with suspected recurrence, in normal-appearing LN and normal-appearing but irradiated head and neck tissue. Fifteen of nineteen suspected lesions were positive for malignancy and all surrounding tissues showed RT-induced tissue changes or necrosis. ADC values were indeed significantly lower for tumour than for tissue with post-RT changes only. When compared with ^{18}F-FDG PET ($N = 17$), DW-MRI correctly excluded tumour in three patients with hypermetabolic areas on PET, and correctly identified subcentimeter contralateral LN metastases without PET uptake in two. DW-MRI identified clinically relevant neck nodal metastases as small as 6 mm. Compared with CT, TSE, MRI and PETand , DW-MRI showed a low false positive rate and correctly charactersed non-tumoural persistent ulcers, persistently enlarged LN and inflammatory lesions. The authors concluded that DW-MRI is optimally interpreted in conjunction with anatomic imaging (Vandecaveye et al. 2007).

5 Conclusions and Future Challenges

No single imaging intervention is perfectly sensitive, specific, inexpensive, safe, and convenient (Manikantan et al. 2009). Anatomic and functional imaging provide complementary information which has already improved staging, RT delivery, response prediction, and follow-up. Knowledge about the capabilities and limitations of all imaging modalities is essential for their rational clinical use, especially in the setting of imaging-intensive investigational RT protocols such as adaptive therapy.

There remain hurdles to be overcome, including optimal timing of mid- and post-treatment imaging for each modality and accounting for spatiotemporal changes in tumour motion and hypoxia. Restrictions on PET use include the preferred method of segmentation and implementation of automated techniques. Many studies published to date have included small numbers of patients with a wide variety of disease sites, stages and treating institutions. This has the potential of confounding results due to differing image acquisition protocols, instrumentation and interpretation methods (Kyzas et al. 2008). Benefits of any imaging modality vary according to the local radiology experience available (Moeller et al. 2010). Interpretation of certain imaging modalities and especially imaging performed after high-dose RT may require special expertise.

Use of emerging technologies may address current challenges. For example, DW-MRI avoids the contrast required by dynamic MRI and CT that may have side effects, cost implications, and cannot be used in renal dysfunction (Hatakenaka et al. 2010). It may also be used as a non-invasive tool to select patients who could potentially benefit from treatment intensification such as dose painting (Dirix et al. 2009). Further development of imaging markers which can predict radioresistance or outcome could assist with prescription of RT based on tumour phenotype or genotype. Successful introduction of functional imaging into routine clinical practice will depend on continued clinical studies with sound methodology and adequate follow-up (Dirix et al. 2009).

References

Adams S, Baum R, Stuckensen T et al (1998) Prospective comparison of ^{18}F-FDG PET with conventional imaging modalities (CT, MRI, US) in lymph node staging of head and neck cancer. Eur J Nucl Med 25:1255–1260

Ang K, Berkey B, Tu X et al (2002) Impact of epidermal growth factor receptor expression on survival and pattern of relapse in patients with advanced head and neck carcinoma. Cancer Res 62:7350–7356

Balogova S, Perie S, Kerrou K, Grahek D, Montravers F, Angelard B et al (2008) Prospective comparison of FDG and FET PET/CT in patients with head and neck squamous cell carcinoma. Mol Imaging Biol 10:364–373

Barker J, Garden A, Ang K et al (2004) Quantification of volumetric and geometric changes occurring during fractionated radiotherapy for head-and-neck cancer using an integrated CT/linear accelerator system. Int J Radiat Oncol Biol Phys 59:960–970

Benchaou M, Lehmann W, Slosman D et al (1996) The role of FDG-PET in the preoperative assessment of N-staging in head and neck cancer. Acta Otolaryngol 116:332–335

Bhide S, Kazi R, Newbold K, Harrington K, Nutting C (2010) The role of intensity-modulated radiotherapy in head and neck cancer. Ind J Cancer 47:267–273

Brink I, Kleznr T, Krause T et al (2002) Lymph node staging in extracranial head and neck cancer with FDG

PET-appropriate uptake period and size-dependence of the results. Nuklearmedizin 41:108–113

Buck A, Halter G, Schirrmeister H et al (2003) Imaging proliferation in lung tumors with PET: ^{18}F-FLT versus ^{18}F-FDG. J Nucl Med 44:1426–1431

Burri R, Rangaswamy B, Kostakoglu L, Hoch B, Genden E, Som P, Kao J (2008) Correlation of positron emission tomography standard uptake value and pathologic specimen size in cancer of the head and neck. Int J Radiat Oncol Biol Phys 71:682–688

Bussink J, van Herpen C, Kaanders J, Oyen W (2010) PET-CT for response assessment and treatment adaptation in head and neck cancer. Lancet Oncol 11:661–669

Castadot P, Lee J, Geets X, Gregoire V (2010) Adaptive radiotherapy of head and neck cancer. Semin Radiat Oncol 20:84–93

Chao C, Bosch W, Mutic S et al (2001) A novel approach to overcome hypoxic tumor resistance: Cu-ATSM-guided intensity-modulated radiation therapy. Int J Radiat Oncol Biol Phys 49:1171–1182

Chao C, Wippold F, Ozyigit G et al (2002) Determination and delineation of nodal target volumes for head-and-neck cancer based on patterns of failure in patients receiving definitive and postoperative IMRT. Int J Radiat Oncol Biol Phys 53:1174–1184

Chapman J, Baer K, Lee J (1983) Characteristics of the metabolism-induced binding of misonidazole to hypoxic mammalian cells. Cancer Res 43:1523–1528

Chapman J, Bradley J, Eary J et al (2003) Molecular (functional) imaging for radiotherapy applications: an RTOG symposium. Int J Radiat Oncol Biol Phys 55:294–301

Chu H, Kim J, Yoon D, Hwang H, Rho Y (2009) Additional diagnostic value of (18)F-FDG PET in detecting retropharyngeal nodal metastases. Otolaryngol Head Neck Surg 141:633–638

Cobben D, van der Laan B, Maas B et al (2004) ^{18}F-FLT PET for visualization of laryngeal cancer: comparison with ^{18}F-FDG PET. J Nucl Med 45:226–231

Daisne J, Sibomana M, Bol A et al (2003) Evaluation of a multimodality image (CT, MRI and PET) coregistration procedure on phantom and head and neck cancer patients: accuracy, reproducibility and consistency. Radiother Oncol 69:237–245

Daisne J, Duprez T, Weynant B et al (2004) Tumor volume in pharyngolaryngeal squamous cell carcinoma: comparison at CT, MR imaging, and FDG PET and validation with surgical specimen. Radiology 233:93–100

Dancey J (2004) Epidermal growth factor receptor inhibitors in clinical development. Int J Radiat Oncol Biol Phys 58:1003–1007

Dandekar P, Partridge M, Kazi R, Nutting C, Harrington K, Newbold K (2010) Challenges in integrating 18FDG PET-CT into radiotherapy planning of head and neck cancer. Ind J Cancer 47:260–266

Dirix P, De Keyzer F, Vandecaveye V, Stroobants S, Hermans R, Nuyts S (2008) Diffusion-weighted magnetic resonance imaging to evaluate major salivary gland function before and after radiotherapy. Int J Radiat Oncol Biol Phys 71:1365–1371

Dirix P, Vandecaveye V, De Keyzer F, Stroobants S, Hermans R, Nuyts S (2009) Dose-painting in radiotherapy for head and neck squamous cell carcinoma: value of repeated functional imaging with (18)F-FDG PET, (18)F-fluoromisonidazole PET, diffusion-weighted MRI and dynamic contrast-enhanced MRI. J Nucl Med 50:1020–1027

Eisbruch A, Foote R, O'Sullivan B et al (2002) Intensity-modulated radiation therapy for head and neck cancer: emphasis on the selection and delineation of the targets. Semin Radiat Oncol 12:238–249

Enami B, Sethi A, Petruzelli GJ (2003) Influence of MRI on target volume delineation and IMRT planning in nasopharyngeal carcinoma. Int J Radiat Oncol Biol Phys 57: 481–488

Eschmann S, Paulsen F, Reimold M et al (2005) Prognostic impact of hypoxia imaging with ^{18}F-misonidazole PET in non small lung cancer and head and neck cancer before radiotherapy. J Nucl Med 46:253–260

Farrag A, Ceulemans G, Voordeckers M, Everaert H, Storme G (2010) Can 18F-FDG-PET response during radiotherapy be used as a predictive factor for the outcome of head and neck cancer patients? Nucl Med Commun 31:495–501

Gambhir SS, Czernin J, Schwimmer J et al (2001) A tabulated summary of the FDG PET literature. J Nucl Med 42(suppl 5):1S–93S

Geets X, Daisne J, Gregoire V et al (2004) Role of 11-C-methionine positron emission tomography for the delineation of the tumor volume in pharyngo-laryngeal squamous cell carcinoma: comparison with FDG-PET and CT. Radiother Oncol 71:267–273

Geets X, Tomsej M, Lee J, Duprez T, Coche E, Cosnard G et al (2007) Adaptive biological image-guided IMRT with anatomic and functional imaging in pharyngo-laryngeal tumours: impact on target volume delineation and dose distribution using helical tomotherapy. Radiother Oncol 85:105–115

Ghilezan M, Yan D, Liang J et al (2004) Online image-guided intensity-modulated radiotherapy for prostate cancer: how much improvement can we expect? A theoretical assessment of clinical benefits and potential dose escalation by improving precision and accuracy of radiation delivery. Int J Radiat Oncol Biol Phys 60:1602–1610

Glastonbury C, Parker E, Hoang J (2010) The postradiation neck: evaluation response to treatment and recognizing complications. Am J Radiol 195:W164–W171

Grandis J, Melhem M, Barnes E et al (1996) Quantitative immunohistochemical analysis of transforming growth factor-alpha and epidermal growth factor receptor in patients with squamous cell carcinoma of the head and neck. Cancer 78:1284–1292

Green A, Steinmetz N (2002) Monitoring apoptosis in real time. Cancer J 8:82–92

Gregoire V, Levendag P, Ang K et al (2003) CT-based delineation of lymph node levels and related CTVs in the node-negative neck: DAHANCA, EORTC, GORTEC, NCIC, RTOG consensus guidelines. Radiother Oncol 69:227–236

Haerle S, Strobel K, Hany T, Sidler D, Stoeckli S (2010) 18F-FDG-PET/CT versus panendoscopy for the detection of synchronous second primary tumours in patients with head and neck squamous cell carcinoma. Head Neck 32:319–325

Han C, Chen Y, Lui A et al (2008) Actual dose variation of parotid glands and spinal cord for nasopharyngeal cancer

patients during radiotherapy. Int J Radiat Oncol Biol Phys 70:1256–1262

Hatakenaka M, Nakamura K, Yabuuchi H, Shioyama Y, Matsuo Y, Ohnishi K et al (2010) Pretreatment apparent diffusion coefficient of the primary lesion correlates with local failure in head and neck cancer treated with chemoradiotherapy or radiotherapy. Int J Radiat Oncol Biol Phys, doi:10.1016/j.ijrobp.2010.05.051 (Epub ahead of print)

Hentschel M, Appold S, Schreiber A, Abramyuk A, Abolmaali N, Kotzerke J et al (2009) Serial FDG-PET on patients with head and neck cancer: implications for radiation therapy. Int J Radiat Biol 85:796–804

Hermans R, Feron M, Bellon E et al (1998) Laryngeal tumor volume measurements determined with CT: a study on intra- and interobserver variability. Int J Radiat Oncol Biol Phys 40:553–557

Hermans R, Meijerink M, Van den Bogaert W et al (2003) Tumor perfusion rate determined noninvasively by dynamic computed tomography predicts outcome in head-and-neck cancer after radiotherapy. Int J Radiat Oncol Biol Phys 57:1351–1356

Hustinx R, Lucignani G (2010) PET/CT in head and neck cancer: an update. Eur J Nucl Med Mol Imaging 37:645–651

Hwang H, Perez D, Orloff L (2009) Comparison of positron emission tomography/computed tomography imaging and ultrasound in staging and surveillance of head and neck and thyroid cancer. Laryngoscope 119:1958–1965

Jansen J, Schoder H, Lee N, Wang Y, Pfister D, Fury M, Stambuk H, Humm J, Koutcher J, Shukla-Dave A (2010) Noninvasive assessment of tumour microenvironment using dynamic contrast-enhanced magnetic resonance imaging and (18)F-fluoro-misonidazole positron emission tomography imaging in neck nodal metastases. Int J Radiat Oncol Biol Phys 77:1403–1410

Kam M, Leung S, Zee B, Chau R, Suen J, Mo F et al (2007) Prospective randomized study of intensity-modulated radiotherapy on salivary gland function in early-stage nasopharyngeal cancer patients. J Clin Oncol 25:4873–4879

Kim S, Loevner L, Quon H et al (2009) Diffusion-weighted magnetic resonance imaging for predicting and detecting of early response to chemoradiation therapy of squamous cell carcinoma of the head and neck. Clin Cancer Res 15: 986–994

Koh W, Rasey J, Evans M et al (1992) Imaging of hypoxia in human tumors with [F-18] fluoromisonidazole. Int J Radiat Oncol Biol Phys 22:199–212

Koshy M, Paulino A, Howell R, Schuster D, Halkar R, Davis L (2005) F-18 FDG PET-CT fusion in radiotherapy treatment planning for head and neck cancer. Head Neck 27:494–502

Kubota R, Kubota K, Yamada S et al (1995) Methionine uptake by tumor tissue: a microautoradiographic comparison with FDG. J Nucl Med 36:484–492

Kyzas P, Evangelou E, Denaxa-Kyza D, Ioannidis J (2008) 18F-Fluorodeoxyglucose positron emission tomography to evaluate cervical node metastases in patients with head and neck squamous cell carcinoma: a meta-analysis. JNCI 100:712–720

Laudenbacher C, Saumweber D, Wagner-Manslau C et al (1995) Comparison of fluorine-18-deoxyglucose PET, MRI and endoscopy for staging head and neck squamous-cell carcinomas. J Nucl Med 36:1747–1757

Lee N, Nehmeh S, Schoder H, Fury M, Chan K, Ling C et al (2009) Prospective trial incorporating pre-/mid-treatment (18F)-misonidazole positron emission tomography for head and neck cancer patients undergoing concurrent chemoradiotherapy. Int J Radiat Oncol Biol Phys 75:101–108

Lehtio K, Oikonen V, Gronroos T et al (2001) Imaging of blood flow and hypoxia in head and neck cancer: initial evaluation with $^{15}OH_2O$ and ^{18}F fluoroerythonitroimidazole PET. J Nucl Med 42:1643–1652

Ling CC, Humn J, Larson S et al (2000) Towards multidimensional radiotherapy (MD-CRT): biological imaging and biological conformality. Int J Radiat Oncol Biol Phys 47:551–560

Mahfouz M, Rodrigo J, Takes R, Elsheikh M, Rinaldo A, Brakenhoff R, Ferlito A (2010) Current potential and limitations of molecular diagnostic methods in head and neck cancer. Eur Arch Otorhin 267:851–860

Manikantan K, Khode S, Dwivedi R, Palav R, Nutting C, Rhys-Evans P, Harrington K, Kazi R (2009) Making sense of post-treatment surveillance in head and neck cancer: when and what of follow-up. Cancer Treat Rev 35:744–753

Moeller B, Rana V, Cannon B, Williams M, Sturgis E, Ginsberg L et al (2010) Prospective imaging assessment of mortality risk after head and neck radiotherapy. Int J Radiat Oncol Biol Phys 78:667–674

Murphy J, La T, Chu K, Quon A, Fischbein N, Maxim P, Graves E, Loo B, Le Q-T (2010) Postradiation metabolic tumour volume predicts outcome in head and neck cancer. Int J Radiat Oncol Biol Phys, doi:10.1016/j.ijrobp.2010.01.057 (Epub ahead of print)

Nishioka T, Shiga T, Shirato H et al (2002) Image fusion between ^{18}FDG-PET and MRI/CT for radiotherapy planning of oropharyngeal and nasopharyngeal carcinomas. Int J Radiat Oncol Biol Phys 53:1051–1057

Nordsmark M, Overgaard J (2004) Tumor hypoxia is independent of hemoglobin and prognostic for loco-regional tumor control after primary radiotherapy in advanced head and neck cancer. Acta Oncol 43:396–403

Paulino A, Koshy M, Howell R et al (2005) Comparison of CT- and FDG-PET-defined gross tumor volume in intensity-modulated radiotherapy for head-and-neck cancer. Int J Radiat Oncol Biol Phys 61:1385–1392

Pouliot J, Xia P, Langen K et al. (2003) Dose-guided radiation therapy using low-dose megavoltage con-beam CT. In: 44th annual AAPM annual meeting, San Diego, Med Phys

Pow E, Kwong D, McMillan A, Wong M, Sham J, Leung L et al (2006) Xerostomia and quality of life after intensity-modulated radiotherapy vs. conventional radiotherapy for early-stage nasopharyngeal carcinoma: initial report on a randomized controlled clinical trial. Int J Radiat Oncol Biol Phys 66:981–991

Rasey J, Hofstrand P, Chin L et al (1999) Characterization of ^{18}F fluoroetanidazole, a new radiopharmaceutical for detecting tumor hypoxia. J Nucl Med 40:1072–1079

Rash C, Keus R, Pameijer F et al (1997) The potential impact of CT-MRI matching on tumor volume delineation in advanced head and neck cancer. Int J Radiat Oncol Biol Phys 39:841–848

Rodrigues R, Bozza F, Christian P, Hoffman J, Butterfield R, Christensen C et al (2009) Comparison of whole-body FDG-PET/CT, dedicated high-resolution head and neck FDG-PET/CT, and contrast-enhanced CT in preoperative staging of clinically M0 squamous cell carcinoma of the head and neck. J Nucl Med 50:1205–1213

Scarfone C, Lavely W, Cmelak A et al (2004) Prospective feasibility trial of radiotherapy target definition for head and neck cancer using 3-dimensional PET and CT imaging. J Nucl Med 45:543–552

Schinagl D, Hoffmann A, Vogel W, van Dalen J, Verstappen S, Oyen W et al (2009) Can FDG-PET assist in radiotherapy target volume definition of metastatic lymph nodes in head and neck cancer? Radiother Oncol 91:95–100

Senft A, de Bree R, Hoekstra O, Kuik D, Golding R, Oyen W et al (2008) Screening for distant metastases in head and neck cancer patients by chest CT or whole body FDG-PET: a prospective multicentre trial. Radiother Oncol 87:221–229

Shields A, Grierson J, Dohmen B et al (1998) Imaging proliferation in vivo with ^{18}F FLT and positron emission tomography. Nat Med 4:1334–1336

Stoeckli S, Steinert H, Pfaltz M et al (2002) Is there a role for positron emission tomography with ^{18}F-fluorodeoxyglucose in the initial staging of nodal negative oral and oropharyngeal squamous cell carcinoma. Head Neck 24:345–349

Syed R, Bomanji J, Nagabhushan N et al (2005) Impact of combined ^{18}F-FDG PET/CT in head and neck tumours. Br J Cancer 92:1046–1050

Thoeny HC, De Keyzer F, Claus FG, Sunaert S, Hermans R (2005) Gustatory stimulation changes the apparent diffusion coefficient of salivary glands: initial experience. Radiology 235:629–634

Troost E, Schinagl D, Bussink J, Oyen W, Kaanders W (2010a) Clinical evidence on PET-CT for radiation therapy planning in head and neck tumours. Radiother Oncol 96:328–334

Troost E, Bussink J, Hoffmann A, Boerman O, Oyen W, Kaanders J (2010b) 18F-FLT PET/CT for early response monitoring and dose escalation in oropharyngeal tumours. J Nucl Med 51:866–874

Van de Wiele C, Lahorte C, Vermeersch H et al (2003) Quantitative tumor apoptosis imaging using Technetium-99m-HYNIC Annexin V single photon emission computed tomography. J Clin Oncol 21:3483–3487

Vandecaveye V, De Keyzer F, Nuyts S et al (2007) Detection of head and neck squamous cell carcinoma with diffusion weighted MRI after (chemo)radiotherapy: correlation between radiologic and histopathologic findings. Int J Radiat Oncol Biol Phys 67:960–971

Vandecaveye V, De Keyzer F, Vander Poorten V et al (2009) Head and neck squamous cell carcinoma: value of diffusion-weighted MR imaging for nodal staging. Radiol 251:134–146

Welsh J, Patel R, Ritter M et al (2002) Helical tomotherapy: an innovative technology and approach to radiation therapy. Technol Cancer Res Treat 1:311–316

Yang D, Wallace S, Cherif A et al (1995) Development of F-18-labeled fluoroerythonitroimidazole as a PET agent for imaging tumor hypoxia. Radiology 194:795–800

Yu H, Caldwell C, Mah K, Poon I, Balogh J, MacKenzie R et al (2009) Automated radiation targeting in head and neck cancer using region-based texture analysis of PET and CT images. Int J Radiat Oncol Biol Phys 75:618–625

Ziemer L, Evans S, Kachur A et al (2003) Noninvasive imaging of tumor hypoxia in rats using 2-nitroimidazole ^{18}F-EF5. Eur J Nucl Med Mol Imaging 30:259–266

Index

R. Hermans (ed.), *Head and Neck Cancer Imaging*, Medical Radiology. Diagnostic Imaging,
DOI: 10.1007/978-3-642-17869-6, © Springer-Verlag Berlin Heidelberg 2012